

DTIC
SELECTE
JUN 1 2 1995
S D
F

11th Annual Review of Progress in

APPLIED COMPUTATIONAL ELECTROMAGNETICS

at the

Naval Postgraduate School

Monterey, CA

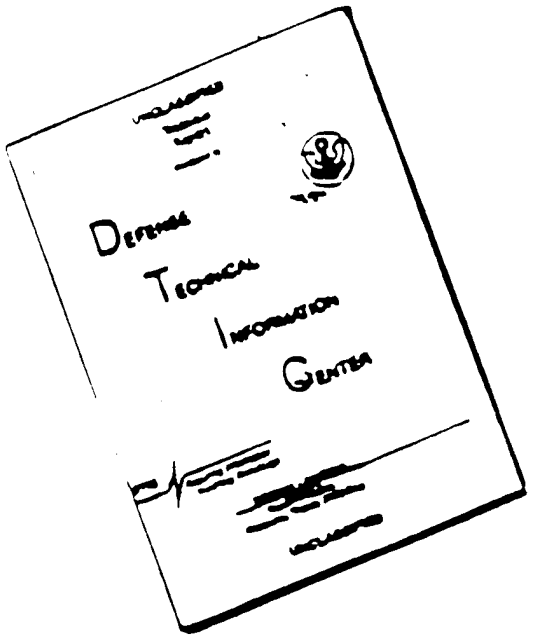
March 20-25, 1995

CONFERENCE PROCEEDINGS

This document has been approved for public release and sale; its distribution is unlimited.

19950608 142

DISCLAIMER NOTICE



THIS DOCUMENT IS BEST QUALITY AVAILABLE. THE COPY FURNISHED TO DTIC CONTAINED A SIGNIFICANT NUMBER OF PAGES WHICH DO NOT REPRODUCE LEGIBLY.

CONFERENCE PROCEEDINGS

VOLUME I

11th Annual Review of Progress in APPLIED COMPUTATIONAL ELECTROMAGNETICS

at the

Naval Postgraduate School

Monterey, CA

March 20-25, 1995

SYMPOSIUM PROGRAM COMMITTEE CHAIRMAN

Raymond Luebbers

Sponsored by

The Applied Computational Electromagnetics Society,

NPS, DOE/LLNL, Penn State University, University of Mississippi,

USAF, DOD AND DOE IN COOPERATION WITH IEEE, URSI, ASEE, SIAM AND AMTA

THE NAVAL POSTGRADUATE SCHOOL

DTIC QUALITY INSPECTED 3

Contents

Table of Contents i

1996 Call for Papers xii

1995 Symposium Program Committee xiii

Conference Chairman's Statement xiv

ACES President's Statement xv

ACES 95 Short Courses xvi

Agenda xvii

VOLUME I

SESSION 1: SCATTERING
Chairs: V. Cable and E. Miller

"A CGFFT Method Applied to the Scattering From Finite Size Microstrip Antenna" by A. McCowen 2

"Analysis of Scattering by Cluster of Nonspherical Particles Based on Complete Mathematic Models" by Y. Eremin, N. Orlov and V. Rozenberg 6

"Analytic Solution for Calculating the Radar Cross-Section and Related Parameters of a Conducting Right Circular Cylinder Surrounded by Multiple Layers of Lossy Dielectrics" by G.W. Jarriel, Jr., M.E. Baginski, and L. Riggs 8

"RCS of High Permittivity Cubes Computed with the TLM Method" by C. Eswarappa and W.J.R. Hoefer 13

"Scattering Analysis of Antenna Installations/Panels on a Curved Surface Using Uniform Field Integration Method" by J.J. Kim and O.B. Kesler 21

"Code Validation of Aircraft Scattering Parameters Using IR Thermograms" by J. Norgard, R. Sega, M. Seifert, T. Blocher, and A. Pesta 29

"A New Method for Solving Scattering Problems with Conducting Media in the Time Domain" by M. Schinke and K. Reiß 37

"Experience and Experiments at Cray Research with JUNCTION-2" by J.A. Crow and Q.M. Sheikh 45

"Quantitative Methods for Measuring and Improving the Performance of Electromagnetic Scattering Codes" by J.P. Meyers, A.J. Terzuoli, Jr., and G.C. Gerace 49

SESSION 2: LOW FREQUENCY
Chairs: K. Kunz and H. Sabbagh

"Numerical Modelling of EMC in Underground Power Cable Systems with the Hybrid FE-BE Method" by J. Shen and A. Kost 58

"New Contribution to the Study of Fault Currents Distribution in the Ground Systems" by H.O. Brodskyn, M.H. Giarolla, J.R. Cardoso, N.M. Abe, and A. Passaro 66

"On the Oscillatory Phenomena of Eddy Currents Along the, $\bar{A}$, V- Ψ Interface" by Z. Cheng, Q. Hu, S. Gao, Z. Liu, M. Wu, and C. Ye 75

"A New MMP-Code for Static Field Computation" by M. Gnos and P. Leuchtmann 81

Dist | A-1

SESSION 2: continued

"Molten Aluminum Flow Induced by High Magnetic Fields" by W.P. Wheless, Jr., and C.S. Wheless 89

"The Electrostatic Characterization of a N-Element Planar Array Using the Singularity Expansion Method" by J.E. Mooney and L. Riggs 98

"A Volume-Integral Code for Electromagnetic Nondestructive Evaluation" by R.K. Murphy, H.A. Sabbagh, J.C. Treece, and L.W. Woo 109

SESSION 3: RESEARCH AND ENGINEERING FRAMEWORK FOR CEM
Organizer: K. Siarkiewicz

"Research and Engineering Framework (REF) for Computational Electromagnetics" (Invited Paper) by B. Hantman, K. Siarkiewicz, J. Labelle, and R. Jackson 118

"Research and Engineering Framework (REF) Data Dictionary Specifications for Computational Electromagnetics" (Invited Paper) by J.A. Evans 126

"DT_NURBS - A Geometry Engine for Integration of MMACE Data" (Invited Paper) by B. Ames and C. Whitcomb 127

"Standardized Grid Generation for the Research and Engineering Framework" (Invited Paper) by L.W. Woo, H.A. Sabbagh, J. LaBelle, and B. Hantman 135

"Visualization and Standards" (Invited Paper) by J.V. Cugini 143

"Visualization Tookkit for Computational Electromagnetics" (Invited Paper) by R.A. Joseph 151

"MMACE - Lessons for the Development of a CEM Computational Environment" (Invited Paper) by R.G. Hicks and K. Siarkiewicz 155

SESSION 4: INTERACTIVE TECHNICAL SESSIONS

SESSION 4A: EM THEORY I

"Pulse Basis Function Implementation of the Radiation Condition Integral Equations" by P.C. Colby 164

"Finite Difference Solutions of Geometrical Optics and Some Related Nonlinear PDEs Approximating High Frequency Helmholtz Equation" by E. Fatemi, B. Engquist, and S. Osher 172

"Conversion of Mechanical Energy to Electromagnetic Energy" by R.M. Bevensee ..... Presentation Only

"Block-Toeplitz-Structure-Based Solution Strategies for CEM Problems" by V.I. Ivakhnenko and E.E. Tyrtyshnikov 181

"The Two-Dimensional Finite Integral Technique Combined with the Measured Equation of Invariance Applied to Transverse Electric Open Region Scattering Problems" by G.K. Gothard and S.M. Rao 189

"Artificial Transparent Boundaries in Computational Quasioptics" by A.V. Popov 195

"A Statistical Electromagnetics (STEM) Research Initiation Report" by W.P. Wheless, Jr., C.B. Wallace, and W.D. Prather 202

SESSION 4A: continued

"Optimization of Aperiodic Conducting Grids" by R.L. Haupt 211

"Accurate MOM Scattering Calculations Using Massively Parallel Computation" by L.D. Vann and J.S. Bagby 216

"A New Angle on a Low Cost Ground Screen for Model Testing in the Undergraduate Antennas Laboratory (Looking at Near Vertical Incidence Skywaves (NVIS) for a Coast Guard Patrol Boat)" by M.E. McKaughan, W.M. Randall and B. Nutter 224

"Efficient Extraction of the Near-Field From CGFFT Methods Applied to Scatterers in the Resonance Region" by A.McCowen 229

SESSION 4B: VISUALIZATION & INTERFACES

"Computer Code for Field Calculation and Visualization in Quasioptics" by Y.V. Kopylov 234

"Dosimetry in a Voxel Model of the Head" by P.J. Dimbylow 240

"A Graphical User Interface for the NEC-BSC" by L.W. Henderson and R.J. Marhefka 245

"MF Communication and Broadcast Prediction System" by M.J. Packer and A.P. Tsitsopoulos 252

"A Finite Difference Time Domain Visualization Tool for Microsoft Windows ™" by A.Z. Elsherbeni, C.D. Taylor, Jr., and C.E. Smith 260

SESSION 4C: VALIDATION

"Transformable Scale Aircraft-Like Model for the Validation of Computational Electromagnetic Models and Algorithms: Initial Configuration and Results" by D.R. Pflug and D.E. Warren 268

"Measurement Study for Validation of Electromagnetics Scattering Codes on a Complex 3D Target" by T.L. Kienberger and D.E. Jurgens 276

"Validation Using a Moment Method Approach with Exact Object Representation" by J.A. Larsson, S. Ljung, and B. Wahlgren 286

"IR Measurements for Validating EM Analysis Tools" by M. Seifert, T. Blocher, and A. Pesta 294

SESSION 4D: EMI/EMC/EMP

"Analysis of Electromagnetic Interference at an Ocean Observation Post" by L. Bai and J.F. Dai 302

"Enforcing Correlation on Statistically Generated EM Cable Drivers" by R. Holland and R. St. John 308

"Analysis of Different Contributions to the Coupling Between Reflector Antennas on a Satellite" by C. Park and P. Ramanujam 321

"Simple Radiation Models in Lieu of EMC Radiated Emissions Testing" by R. Perez 323

SESSION 5: OPTIMIZATION TECHNIQUES IN APPLIED ELECTROMAGNETICS
Organizer: O.A. Mohammed

"An Optimization Approach to Reduce the Discretization Error in Finite Element Explicit Solution Scheme" (Invited Paper) by M. Feliziani, E. Latini, and F. Maradei 334

"Analysis and Design of a Reentrant Resonant Cavity Applicator for Radio Frequency Hyperthermia System" (Invited Paper) by Y. Kanai, T. Tsukamoto, K. Toyama, T. Kashiwa, Y. Saitoh, and M. Miyakawa 342

"Analysis of Loaded Cavities Using the Constitutive Error Approach" (Invited Paper) by R. Albanese, R. Fresa, R. Martone, and G. Rubinacci 350

"The Design of Electromagnetic Devices Using Knowledge Based Systems and Sensitivity Information" (Invited Paper) by D.A. Lowther, D.N. Dyck, and R. Rong 358

"A Computer Program for the Design of Superconducting Accelerator Magnets" (Invited Paper) by S. Russenschuck 366

"Application of Optimization to the Design of Electromechanical Devices" (Invited Paper) by J.K. Sykulski and Y.B. Cheng 378

"Genetic Algorithms for the Optimal Design of Electromagnetic Devices" (Invited Paper) by O.A. Mohammed and G.F. Üler 386

"Linear Constraints - Gradient Technique for the Inverse Problem of Design Optimization" (Invited Paper) by A.A. Arkadan and S. Subramaniam-Sivanesan 394

Session 6: COMPUTATIONAL ELECTROMAGNETICS APPLIED TO SHIP DESIGN
Organizers: J. Newcomb and J. Logan

"The Naval Sea Systems Command Electromagnetic Engineering Program" by D. Cebulski, N. Baron, and J. Eadie" ..... Presentation Only

"EM Engineering System Architecture" by J.A. Winston ..... Presentation Only

"EM Engineering Ray Tracing and Casting Model (RTC) by L. Gray ..... Presentation Only

"Ship Transition-Frequency EM Environment Analysis Requirements" by G.R. Piper ..... Presentation Only

"Finite Volume Time Domain Analysis of Ship Topside EM Environment Features" by W.F. Hall, A.H. Mohammadian, C.M. Rowell, and V. Shankar ..... Presentation Only

"EM Engineering Ship End-to-End Application" by L.R. Carslon, C.F. Juster, and G.R. Allen ..... Presentation Only

"EM Engineering Applied to Patrol Craft (PC-1)" (Invited Paper) by D. Tam, J. McGee, C. Azu, and M. Soyka 403

"Shipboard Antenna Pattern Visualization and Analysis"(Invited Paper) by L. Russell, J. Logan, J. Rockway, and D. Schwartz 410

SESSION 7: FINITE DIFFERENCE TIME DOMAIN
Organizer: J. Beggs

"Computational Analysis of Radiation from an Elliptical Shaped End Radiator" (Invited Paper) by S.A. Blocher, E.A. Baca, and J.H. Beggs 418

"A Time Domain in Harmonic Oscillator Model for an FDTD Treatment of Lossy Dielectrics" (Invited Paper) by K.S. Kunz 425

"FDTD Modeling of Electromagnetic Wave Interactions with Composite Random Sheets" (Invited Paper) by J.G. Maloney and B.L. Shirley 430

SESSION 7: continued

"An Improved Near to Far Field FDTD Algorithm" (Invited Paper) by K.S. Kunz 431

"Unstructured Finite-Volume Modeling in Computational Electromagnetics" (Invited Paper) by D.J. Riley and C.D. Turner 435

"Scattering from Coated Targets Using a Frequency-Dependent, Surface Impedance Boundary Condition in FDTD" by C.W. Penney, R.J. Luebbers, and J.W. Schuster 445

"Hybrid Finite Difference Time Domain and Finite Volume Time Domain in Solving Maxwell's Equations" (Invited Paper) by K.S. Yee and J.S. Chen 453

"Reducing the Number of Time Steps Needed for FDTD Antenna and Microstrip Calculations" (Invited Paper) by RJ. Luebbers and H.S. Langdon 465

"Numerical Simulations of Light Bullets, Using the Full Vector, Time Dependent, Nonlinear Maxwell Equations" by P.M. Goorjian and Y. Silberberg 472

SESSION 8: BERENGER'S BOUNDARY CONDITION
Organizer: J. Fang

"Ultrawideband Termination of Waveguiding and Multilayer Structures for FD-TD Simulations in 2-D and 3-D" (Invited Paper) by C.E. Reuter, R.M. Joseph, E.T. Thiele, D.S. Katz, and A. Taflove 476

"A 3-D Perfectly Matched Medium by Coordinate Stretching and Its Absorption of Static Fields" (Invited Paper) by W.C. Chew, W.H. Weedon, and A. Sezginer 482

"Perfectly Matched Anisotropic Absorbers for Finite Element Applications in Electromagnetics" by D.M. Kingsland, Z.S. Sacks, and J.F. Lee 490

"Modification of Berenger's Perfectly Matched Layer for the Absorption of Electromagnetic Waves in Layered Media" by M. Gribbons, S.K. Lee, and A.C. Cangellaris 498

"Performance of the Perfectly Matched Layer in Modeling Wave Propagation in Microwave and Digital Circuit Interconnects" by Z. Wu and J. Fang 504

SESSION 9: TIME DOMAIN/FDTD
Chairs: L. Long and J. Maloney

"A FVTD Algorithm for Maxwell's Equations on Massively Parallel Machines" by V. Ahuja and L.N. Long 513

"The Piecewise Linear Recursive Convulution Method for Incorporating Dispersive Media into FDTD" by D.F. Kelley and R.J. Luebbers 526

"Combining Different Coordinate Systems in the Time Domain Finite Difference Method" by M. Mrozowski, M. Okoniewski, M.A. Stuchly, and S.S. Stuchly 534

"Time Domain Response of Simulated 2D Composite Scatterers" by A.Z. Elsherbeni and P.M. Goggans 542

"An Object-Oriented Approach to Writing Computational Electromagnetics Codes" by M. Zimmerman and P. Mallasch 551

SESSION 10: "FAST ALGORITHMS FOR COMPUTATIONAL ELECTROMAGNETICS"
Organizers: E. Michelssen and W. Chew

"On the Use of Wavelet-Like Basis Functions in the Finite Element Analysis of Elliptic Problems" (Invited Paper) by R.K. Gordon 559

"Fast Wavelet Algorithm (FWA) for Moment Method Analysis of Electromagnetic Problems" (Invited Paper) by K. Sabetfakhri and L.P.B. Katehi 568

"Fast Far Field Approximation for Calculating the RCS of Large Objects" (Invited Paper) by C.C. Lu and W.C. Chew 576

"The Parameter Estimation Technique (PET): Speeding Up Dense Matrix Methods" (Invited Paper) by Ch. Hafner and J. Fröhlich 584

"A Novel Scheme for Massively Parallel Solution of Maxwell's Equation Using FDTD" (Invited Paper) by M.A. Jensen, Y.Rahmat-Samii, and A. Fijany 592

"Reduction of the Filling Time of Method of Moments Matrices" (Invited Paper) G. Vecchi, P. Pirinoli, L. Matekovits, and M. Orefice 600

"The Fast Multipole Method for Large 2d Scatterers" (Invited Paper) by L.R. Hamilton, J.J. Ottusch, M.A. Stalzer, R.S. Turley, J.L. Visher and S.M Wandzura 606

"A Multilevel Matrix Decomposition Algorithm for Analyzing Scattering From Large Structures" (Invited Paper) by E. Michielssen and M. Boag 614

"A 3D Fast Multipole Method for Electromagnetics with Multiple Levels" (Invited Paper) by B. Dembart and E. Yip 621

"Fast Multipole Method Solution of Combined Field Integral Equation" by J.M. Song and W.C. Chew 629

AUTHOR INDEX 637

VOLUME II

SESSION 11: MICROWAVE AND GUIDED WAVE
Chairs: P. Goggans and A. Terzuoli

"Computer-Simulation of Isotropic, Two-Dimensional Guided-Wave Propagation" by R.A. Speciale 639

"Analysis of Ultra-Short Pulse Propagation on Uniform and Tapered Printed Transmission Lines" by R.O. Veliz and J.R. Souza 648

"Wave-Field Patterns on Electrically Large Networks" by R.A. Speciale 656

"Scattering Characteristics of Dissimilar Waveguide Slot Couplers" by A.K. Singh and S. Christopher 664

"An Alternative Formulation of the Tranverse Resonance Technique" by A.G. Neto, S. Ariguel, H. Aubert, D. Bajon, and H. Baudrand 672

SESSION 12: MOM

Chairs: A. Peterson and R. Ziolkowski

"Moment Method Analysis of Dielectric Covered Radiating Slots Using Alternative Green's Function Approach" by S. Christopher, V.V.S. Prakash, A.K. Singh, and N. Balakrishnan 680

"Computation of E-Field Distribution of Low Gain Antenna on Conducting Body or Revolution" by J. Liu, J. Wang, and Y. Gao 687

"An Implementation of an Exact Scheme for Problem Decomposition Via the Use of Aperture Admittance" by D.L. Wilkes, C.C. Cha, and T. Krauss 695

"Parallelization of the Parametric Patch Moment Method Code" by X. Shen, G.E. Mortensen, C.C. Cha, G. Cheng, and G.C. Fox 702

"A Tool Box for Parallelization of Moments Method Codes" by E. Yip, B. Blakely, L. Johnson, D. Jurgens, and R. Kochhar 710

SESSION 13: RECENT DEVELOPMENTS IN FDTD ANALYSIS

Organizers: M. Piket-May and D. Katz

"Simulation of Microwave Circuits by FDTD Method" (Invited Paper) by C.N. Kuo, B. Houshmand, and T. Itoh 718

"Adaptation of FDTD Techniques to Acoustic Modeling" (Invited Paper) by J.G. Maloney and K.E. Cummings 724

"FDTD Investigation of the Antenna-Tissue Interaction for Cellular and Satellite Systems" (Invited Paper) by Y.Rahmat-Samii and M.A. Jensen 732

"FDTD Modeling of Ground-Penetrating Radar Antennas" by B.J. Zook 740

"FDTD Modeling of Ultrashort Optical Pulse Interactions with Nonresonant and Resonant Materials and Structures" (Invited Paper) by R.W. Ziolkowski 748

"Time Domain Analysis of Electromagnetic Wave Propagation in Nonlinear Dielectric Slab" by G. Miano, C. Serpico, L. Verolino, and F. Villone 753

"An Efficient Sub-gridding Algorithm for FDTD" by D.T. Shimizu, M. Okoniewski, and M.A. Stuchly 762

"Using the Integral Forms of Maxwell's Equations to Modify and Improve the FDTD (2,4) Scheme" by M.F. Hadi and M. Piket-May 767

"From the Berenger PML ABC to Micro-Lasers: Recent Advances in FD-TD Modeling Techniques" (Invited Paper) by A. Taflove 775

SESSION 14: PROPAGATION
Organizer: K. Chamberlin

"Terrain and Refractivity Effects in a Coastal Environment: Results From The VOCAR Experiment" by A. Barrios 784

"Capabilities and Limitations Associated with Using GTD to Model Propagation Path Loss in the Presence of Irregular Terrain" by K. Chamberlin 790

"Comparison of Electromagnetic Wave Propagation Computer Programs" by S.A. Fast and T.H. Koschmieder 798

"A Model for Estimating Electromagnetic Wave Attenuation in a Forest (EWAF) Environment" by C. Welch, C. Lemak, and L. Corrington 801

"Validation of the Radio Physical Optics Propagation Model" by R.A. Paulus 809

"VTRPE: A Variable Terrain Electromagnetic Parabolic Equation Model" by F.J. Ryan 816

"Estimating Tropospheric Refractivity Fields Using a Nonlinear Gauss-Markov Procedure and the PE Model" by D.B. Boyer and F.J. Ryan 824

"Modeling of Radio Wave Ducting Over Regular Boundary" by I.P. Zolotarev 830

SESSION 15: PARALLELIZATION OF EM CODES
Organizers: J. Volakis and A. Chatterjee

"Advances in Time-Domain CEM Using Massively Parallel Architectures" (Invited Paper) by C. Rowell, V. Shankar, W.F. Hall, and A. Mohammadian 839

"Parallel Solutions of Maxwell's Equations on the Meiko CS-2" by N. Madsen, B. Eme, D. Steich and G. Cook 847

"Parallelization of the CARLOS-3D Method of Moments Code" (Invited Paper) by J.M. Putnam, D.D. Car, and J.D. Kotulski 848

"Parallel Computing for Electromagnetism at ONERA" (Invited Paper) by A. de La Bourdonnaye, A. Cosnuau, X. Ferrières, P. Leca, and F.X. Roux 856

"The Performance of the Parallel Solution of the Quasi-Minimal Residual (QMR) Method on 2D Mesh Architectures" (Invited Paper) by L. Hamandi, F. Özgüner and R. Lee 864

"Advanced Parallel Solver Techniques" (Invited Paper) by A.S. King 872

"Parallelized FDTD for Antenna Radiation Pattern Calculations" by Z.M. Liu, A.S. Mohan, T.A. Aubrey, and W.R. Belcher 873

"Calculation of Electromagnetic Fields with the Multiple Multipole Method (MMP Method) on Parallel Computers" by C. Tudziers and H. Singer 881

"Implementation of the Finite-Difference Time-Domain Method on Parallel Computers" by R.S. David and L.T. Wille 889

SESSION 16: EM THEORY II
Chairs: K.Yee and R. Gordon

"FDTD Investigation of the Ability to Increase Electromagnetic Fields Around Head Tumors" by D.B. Dunn, A.J. Terzuoli, Jr., G.C. Gerace and C.M. Rappaport 898

"FDTD and PMM Based Design of a TEM Horn Antenna with Reduced Off-Boresight Fields" by D.J. Wolstenholme, A.J. Terzuoli, Jr., and G.C. Gerace 904

"Determination of the Complex Aperture Distribution of a Planar Spiral Antenna from 3-D Far-Field Radiation Pattern Data" by M. Kluskens, W. Lippincott, and M. Kragalott 910

"Analysis of Micro-Contamination of Silicon Wafers Based on Discrete Sources Method (DSM) by Y.A. Eremin and N.V. Orlov 925

"Analysis of Convergence Properties of Projection Methods for Solving CEM Applications" by V.I. Ivakhnenko, A.V. Kukk, E.E. Tyrtyshnikov, A.Y. Yeremin, and N.L. Zamarashkin 929

SESSION 17: ELECTROMAGNETIC MODELING TECHNIQUES FOR INTEGRATED OPTICS
Organizer: A. Cangellaris

"Analysis and Design of Guided-Wave Optical Devices Using Finite-Difference Time-Domain Method" (Invited Paper) by S.K. Chaudhuri and S.T. Chu 937

"Vectorial Analysis of Optical Waveguides by the Method of Lines" (Invited Paper) by R. Pregla and W.W. Pascher 943

"Vector Finite Element Analysis of Lossless and Lossy Dielectric Waveguides" (Invited Paper) by P. Cheung and A. Gopinath 951

"NL-FDTD Modeling of Linear and Nonlinear Corrugated Waveguiding Systems for Integrated Optics Applications" (Invited Paper) by R.W. Ziolkowski and J.B. Judkins 957

"Analysis of Coupled Nonlinear Optical Waveguides by Matrix Method" by V. Tripathi, A. Weisshaar, and H.S. Chang 962

SESSION 18: TOPICS IN FRACTAL AND WAVELET ELECTRODYNAMICS
Organizers: D.H. Werner and P.L. Werner

"An Overview of Fractal Electrodynamics Research" (Invited Paper) by D.H. Werner 964

"Fractal Arrays and Fractal Radiation Patterns" (Invited Paper) by P.L. Werner, D.H. Werner, and A.J. Ferraro 970

"Wavelet Transforms and Time/Time-scale Analysis" (Invited Paper) by R.K. Young and T.G. Golsberry 979

"Wavelet-based Processing to Efficiently Achieve Broadband Monostatic and/or Passive Cross-sensor Processing" (Invited Paper) by R.K. Young and L.H. Sibul 987

"The Intervallic Wavelets with Applications in the Surface Integral Equations" (Invited Paper) by G.W. Pan and J.Y. Du 993

"Radar Cross Section Data Reduction Using Wavelets" by A.S. Ali, S.E. Duval, and R.L. Haupt 1000

SESSION 19: NEC APPLICATIONS
Organizer: J.K. Breakall

"Computationally Efficient and Accurate Approximations for Impedance Matrix Elements of NEC-Type Method of Moments Formulations" by D.H. Werner, S.E. Metker, and J.A. Huffman 1009

"Development of the Coupled-Resonator Antenna Principle, A Computer Modeling Case History" by G.A. Breed 1017

"Antenna Design and Development Using NEC-WIN" by T.A. Erdley, J.J. Shapiro, J.S. Young, and J.K. Breakall 1025

"The "PAINT" System, A UTD/NEC Hybrid Package for Simulating Antenna Patterns Over 3-Dimensional Irregular Terrain" by J.S. Young and J.K. Breakall 1033

SESSION 20: FEM
Chairs: R. Burkholder and J. Karty

"Numerically Characterizing Electromagnetic Fields Local to the Edge of a Conducting Strip Using a Matched Asymptotic Technique and the Finite Element Method" by A.S. Ali and C.L. Holloway 1040

"An Enhanced "A Posteriori" Remeshing Algorithm for Adaptive Meshing of 2D Finite Element Problems" by P.Girdinio, A. Manella, and G. Molinari 1047

"Finite Element Analysis of Waveguides Using Edge-Based Magnetic Vector Potential and Nodal-Based Electric Scalar Potential" by J.F. Lee, G.Lizalek, and J. Brauer 1054

"A Scattering Analysis of Laser Beam Wave by Groove Pits on Optical Memory Disk by Using FEM with BEM" by Y. Miyazaki and K. Tanaka 1062

"3D Nodal-and Mixed-Based Elements for Unbounded Microwave Problems" by A. Nicolas, L. Nicolas, and J.L. Yao-bi 1070

"A Rationale for the Use of Mixed-Order Basis Functions Within Finite Element Solutions of the Vector Helmholtz Equation" by A.F. Peterson and D.R. Wilton 1077

"Finite Element Waveguide Simulator Techniques" by J.R. Sanford and N.M. Johansson 1085

"A Solution For Open Boundary Electromagnetic Field Problems by Mapped Infinite and Virtual Elements" by L.H.A. de Medeiros and A. Raizer 1094

SESSION 21: EM ANALYSIS TECHNIQUES FOR ELECTRICALLY LARGE CAVITIES
Organizer: D. Pflug

"Application of Modal and Plane Wave Expansions to Modeling Large Jet Engine Cavities" (Invited Paper) by J.L. Karty and J.M. Roedder 1103

"Scattering From Dielectric Loaded Cavities Using Shooting and Bouncing Rays" (Invited Paper) by M.C. Christensen, S.W. Lee, and D.J. Andersh 1111

"XPATCH Simulation of Large Inlet Structures" (Invited Paper) by R. Bhalla and H.Ling 1118

"An Iterative Physical Optics Approach for the EM Analysis of Cavities and Other Multi-Bounce Geometries" (Invited Paper) by R.J. Burkholder 1126

SESSION 21: continued

"Improved Ray Basis in the Hybrid Analysis of EM Scattering by Large Open Cavities" (Invited Paper) by R.J. Burkholder, P.H. Pathak, H.T. Chou, D.J. Andersh,and J. Fath 1134

"Overlapping Modal and Geometric Symmetries for Computing Jet Engine Inlet Scattering" (Invited Paper) by D.C. Ross, J.L. Volakis, H.T. Anastassiu, and D.J. Andersh 1142

SESSION 22: ACCURACY ESTIMATION IN ELECTROMAGNETIC MODELING
Organizer: S.M. Wandzura

"Assessing the Influence of Coefficient Accuracy, Matrix Condition Number, Size and Type, and Computer Precision on Matrix-Solution Accuracy" (Invited Paper) by E.K. Miller 1151

"Numerical Accuracy Issues in Finite Element Frequency Domain Solutions of Radar Scattering Problems" (Invited Paper) by J. D'Angelo 1163

"Accuracy in Computation of Matrix Elements of Singular Kernels" by S.M. Wandzura 1170

"Accuracy Estimation and High Order Methods" by L.R. Hamilton, J.J. Ottusch, M.A. Stalzer, R.S. Turley, J.L. Visher, and S.M. Wandzura 1177

"Accuracy Issues in Time-Domain CEM Using Structured/Unstructured Grid Formulations" (Invited Paper) by V. Shankar, W.F. Hall, and S. Palaniswamy 1185

"An Accuracy Study for the 3D Hybrid Finite Element Method of Moments SWITCH Code" (Invited Paper) by G.E. Antilla and Y.C. Ma 1193

"Modeling Accuracy of Method of Moments" by M.B. Gedera, L.N. Medgyesi-Mitschang, R. Pearlman, J.M. Putnam, D.S. Wang 1194

"Requiring Quantitative Accuracy Statements in EM Data" (Invited Paper) by E.K. Miller 1202

SESSION 23: PDE METHODS IN ELECTROMAGNETICS
Organizers: R. Lee and J.F. Lee

"Optimization Issues in Finite Element Codes for Solving Open Domain 3D Electromagnetic Problems" (Invited Paper) by A. Chatterjee and J.L. Volakis 1212

"A Characteristic-Based 3D Time Domain Maxwell Equation Solver" (Invited Paper) by J.J.S. Shang and K.C. Hill 1220

"Finite Element Solution of Eddy Current Problems in Electromagnetics" (Invited Paper) by O.A. Mohammed and G.F. Üler 1228

"Ten Years of Evolution of the FDTD-Like Conformal Techniques" (Invited Paper) by K.S. Yee 1241

"Whitney Elements Time Domain (WETD) Methods for Solving Three-Dimensional Waveguide Discontinuities" (Invited Paper) by J.F. Lee 1258

"An FDTD/FVTD 2D-Algorithm to Solve Maxwell's Equations" by J.S. Chen, J.V. Prodan, and K.S. Yee 1266

"Spectral Finite Methods for the Simulation of Electromagnetic Interactions with Electrically Long Structures" (Invited Paper) by A.C. Cangellaris and D. Hart 1280

AUTHOR INDEX 1288

THE APPLIED COMPUTATIONAL ELECTROMAGNETICS SOCIETY

1996 CALL FOR PAPERS 1996

The 12th Annual Review of Progress in Applied Computational Electromagnetics

March 18-22, 1996

Naval Postgraduate School, Monterey, CA

Share your knowledge and expertise with your colleagues

The Annual ACES Symposium is an ideal opportunity to participate in a large gathering of EM analysis enthusiasts. The purpose of the Symposium is to bring analysts together to share information and experience about the practical application of EM analysis using computational methods. The Symposium features four areas of interest: technical publication, demonstrations, vendor booths and short courses. All aspects of electromagnetic computational analysis are represented. The Symposium will also include invited speakers and interactive forums. Contact Richard Gordon (601) 232-5388 for details.

1996 ACES Symposium Chairman
Richard Gordon
University of Mississippi
EE Dept. Anderson Hall, Box 41
University, MS 38677
Phone: (601) 232-5388
Fax: (601) 232-7231
Email:eegordon@vm.cc.olemiss.edu

1996 ACES Symposium Administrator
Richard W. Adler
ECE Dept/Code ECAB
Naval Postgraduate School
833 Dyer Road, Room 437
Monterey, CA 93943-5121
Phone: (408) 646-1111
Fax: (408) 649-0300
Email:554-1304@mcimail.com

1996 ACES Symposium Co-Chairman
Jin-Fa Lee
EE Department
Worcester Polytechnic Institute
100 Institute Road
Worcester, MA 01609
Phone: (508) 831-5778
Fax: (508) 831-5491
E-mail: jinlee@ee.wpi.edu

1966 ACES Symposium Co-Chairman
Eric Michielssen
ECE Department
University of Illinois
1406 West Green Street
Urbana, IL 61801-2991
Phone: (217) 333-3803
Fax: (217) 333-8986
E-mail: michiels@decwa.ece.uiuc.edu

1996 ACES Symposium

Sponsored by: ACES, NPS, DOE/LLNL, UNIV OF MISSISSIPPI, USAF, DOD AND DOE IN COOPERATION WITH IEEE, URSI, ASEE, SIAM AND AMTA

THE NAVAL POSTGRADATE SCHOOL

1995 Symposium Program Committee

for the

11th Annual Review of Progress in

APPLIED COMPUTATIONAL ELECTROMAGNETICS

at the
Naval Postgraduate School
Monterey, CA

Symposium Chairman:

Ray Luebbers
Penn State University
320 EE East
University Park, PA 16802
(814) 865-2362/Fax:7065

Co-Chair: Richard K. Gordon
EE Dept. Univ. of Mississippi
Anderson Hall, Box 41
University, MS 38677
(601) 232-5388/Fax:7231

Symposium Adviser:

Dr. Richard W. Adler
ECE Dept. Code ECAB
Naval Postgraduate School
833 Dyer Road, Room 437
Monterey, CA. 93943-5121
(408) 646-1111/Fax: 649-0300

Symposium Short Course Chairman:

Robert Lee
Ohio State Univ. EE Dept.
2015 Neil Ave.
Columbus, OH 43210-1272
(614) 292-1433/Fax: 7596

1996 Symposium Chairman:

Chair: Richard K. Gordon
EE Dept. Univ. of Mississippi
Anderson Hall, Box 41
University, MS 38677
(601) 232-5388/Fax: 7231

Conference Secretary:

Mrs. Pat Adler

Advisory Committee:

Richard W. Adler, Naval Postgraduate School
Pat Foster, Microwave & Antenna System
Richard K. Gordon, Univ of Mississippi
Harold Sabbagh, Sabbagh Assoc., Inc.
Ed Miller, Ohio State University
Robert Bevensee, Consultant
Raymond Luebbers, Penn State University
Andrew Peterson, Georgia Institute of Tech.
Frank Walker, Boeing Defense & Space Group
Perry Wheless Jr., Univ. of Alabama
Duncan Baker, Univ. of Pretoria
James Breakall, Penn State University

A - C - E - S

1995

March 20-24, 1995
Monterey, CA

For more information please contact:

Technical Program Chairman
Raymond Luebbers
Dept. of Electrical Engineering
The Pennsylvania State University
University Park, PA 16802
Phone: (814) 865-2362
FAX: (814) 865-7065
Email: lu4@psuvm.psu.edu

Short Course Chairman
Robert Lee
Dept. of Electrical Engineering
The Ohio State University
Phone: 614-292-1433
FAX: 614-292-7596
Email: lee@ee.eng.ohio-state.edu

Symposium Administrator
Richard W. Adler
ECE Department/Code ECAB
Naval Postgraduate School
833 Dyer Road, Room 437
Monterey, CA 93943-5121
Phone: (408) 646-1111
FAX: (408) 649-0300
Email: 5541304@mcimail.com

Publicity Chairman
Paul M. Goggans
EE Department
University of Mississippi
Anderson Hall, Box 1
University, MS 38677
Phone: (601) 232-5954
FAX: (601) 232-7231
Email: eepmg@cotton.vislab.olemiss.edu

Publication Chairman
Richard K. Gordon
EE Dept., University of Mississippi
Anderson Hall, Box 41
University, MS 38677
Phone: (601) 232-5388
FAX: (601) 232-7231
Email: eegordon@vm.cc.olemiss.edu

APPLIED COMPUTATIONAL ELECTROMAGNETICS SOCIETY

The Eleventh Annual Review of Progress in Applied Computational Electromagnetics

Welcome to the 11th Annual Review of Progress in Applied Computational Electromagnetics.

While this year's conference retains the flavor of past meetings, some changes have been made. In particular, more of the sessions have been organized around a particular theme, with more invited papers than in previous years. The individuals responsible for these sessions are indicated in the agenda as Session Organizers, and their efforts are very much appreciated.

Special recognition should be given to several individuals who contributed significantly to the conference. Paul Goggans provided the advertising for the conference. Rob Lee once again did an excellent job of organizing the Short Courses. Richard Gordon received all the papers and put them together to produce these Proceedings. And of course Richard and Pat Adler must be recognized for arranging for the printing of the Proceedings, for providing access to the NPGS Facilities, and for all their other contributions to the conference.

Please enjoy your time in Monterey as much as possible, whether listening to a paper being presented, catching up on the latest "gossip" in the hallways, or enjoying the sights of Monterey.



Raymond Luebbers
Technical Program Chairman
1995 ACES Conference

ACES PRESIDENT'S STATEMENT

It's nice to be here in California in March, especially since we weren't entirely certain that there was going to be a California in March. This state seems to attract more than its fair share of calamities, ranging from floods, fires, mud slides, and OJ-things.

In any case, we're back at ACES'95, the Eleventh Annual Review of Progress in Applied Computational Electromagnetics, which reverts to the Naval Postgraduate School, our long-time home.

Ray Luebbers and his committee have put together an excellent program, one which embraces 'low frequency' CEM to 'high frequency 'CEM. The subject matter to be discussed ranges from the traditional scattering and radiation problems, so typical of ACES past, to optimization techniques in applied electromagnetics. This area has been of interest to designers of electrical machines, but we see that it is being applied to hyperthermia and superconducting accelerator magnets.

I am pleased to see ACES embrace all aspects of computational electromagnetics, for there is no single 'natural' milieu of CEM for ACES. The problems of CEM are many and varied. If one has an interest in solving Maxwell's equations, he should be at home at any frequency, in any environment.

You will note that Ken Siarkiewicz, a long-time dedicated supporter of ACES, has put together an interesting session entitled 'Research and Engineering Framework for CEM'. Ken then did himself proud by releasing $10,000 of MMACE (millimeter-wave, microwave advanced computational environment) funding so that ACES could properly support this session. This tells me two things: first, that Ken is a pretty good man to have on your side, and second, that ACES is increasingly being viewed as the preeminent vehicle to expose issues in computational electromagnetics.

ACES is reaching this stature because of the dedication of its members especially those who volunteer to do its work. When you publish next, think about the ACES Journal or Newsletter as the publication of choice. When you wish to give your profession extracurricular support, consider working for ACES. A lot of people have, and a lot more will.

Enjoy the Eleventh Annual Review.

Harold A. Sabbagh
Sabbagh Associates, Inc.
4635 Morningside Drive
Bloomington, IN 47408
(812) 339-8273
(812) 339-8292 FAX
email:has@sabbagh.com

ACES 1995 SHORT COURSES

MONDAY MARCH 20 — FULL-DAY COURSE

0830-1630 "Finite Elements for Electromagnetics"
by John Brauer, MacNeal Schwendler Corporation

0830-1630 "GEMACS From A-Z" by Buddy Coffey, Advanced EM.

0830-1630 "Physical Wavelets" by Gerald Kaiser, University of Massachusetts at Lowell.

HALF-DAY COURSE

1300-1630 "The Multiple Multipole Program (MMP): Theory, Practical Use and Latest Features"
by Pascal Leuchtmann, Swiss Federal Instiitute of Technology

1300-1630 "Verification and Validation of Computational Software" by E.K. Miller, Ohio University.

SATURDAY MARCH 25 — FULL-DAY COURSE

0830-1630 "Using Mathematical Software for Computational Electromagnetics"
by Jovan Lebaric, Naval Postgraduate School.

0830-1630 "Wire Antenna Modeling Using NEC" by Dick Adler, Naval Postgraduate School, Jim Breakall, Penn State University, and Gerry Burke, Lawrence Livermore National Lab.

0830-1630 "FDTD, Generalized FDTD and FVTD Techniques in Solving Maxwell's Equations"
by Kane Yee, Lockheed.

FINAL AGENDA

The Eleventh Annual Review of Progress in Applied Computational Electromagnetics

NAVAL POSTGRADUATE SCHOOL
20 - 25 MARCH, 1995

Raymond Luebbers, Technical Program Chairman

Richard Gordon, Proceedings Editor

Robert Lee, Short Course Chairman

Paul Goggans, Publicity Chairman

Richard Adler, Conference Facilitator

MONDAY 20 MARCH

0830-1630	**SHORT COURSE (FULL-DAY)** "Finite Elements for Electromagnetics"	**102 Glasgow** John Brauer, MacNeal-Schwendler Corporation
0830-1630	**SHORT COURSE (FULL-DAY)** "GEMACS from A-Z"	**122 Ingersoll** Buddy Coffey, Advanced EM
0830-1630	**SHORT COURSE (FULL-DAY)** "Physical Wavelets"	**101 A Spanagel** Gerald Kaiser, Univ. of Massachusetts at Lowell
1300-1630	**SHORT COURSE (HALF-DAY)** "The Multiple Multipole Program (MMP): Theory, Practical Use and Latest Features"	**325 Ingersoll** Pascal Leuchtmann, Swiss Federal Institute of Technology
1300-1630	**SHORT COURSE (HALF-DAY)** "Verification and Validation of Computational Software"	**323 Ingersoll** E. K. Miller, Ohio University
0800-2030	**CONFERENCE REGISTRATION**	**103 Glasgow Hall**

TUESDAY 21 MARCH

0700	**CONFERENCE REGISTRATION**	**103 Glasgow Hall**
0700-0800	**CONTINENTAL BREAKFAST**	
0800	**WELCOME** Raymond Luebbers	**102 Glasgow Hall**
SESSION 1: SCATTERING (parallel with Sessions 2 and 3) **CHAIRS: V. CABLE, E. MILLER**		**122 Ingersoll Hall**
0840	"A CGFFT Method Applied to the Scatttering from Finite Size Microstrip Antenna"	A. McCowen
0900	"Analysis of Scattering by Cluster of Nonspherical Particles Based on Complete Mathematic Models"	Y.A. Eremin, N.W. Orlov and V.I. Rozenberg
0920	"Analytic Solution for Calculating the Radar Cross-Section and Related Parameters of a Conducting Right Circular Cylinder Surrounded by Multiple Layers of Lossy Dielectrics"	G.W. Jarriel, Jr., M. E. Baginski, and Lloyd Riggs
0940	"RCS of High Permittivity Cubes Computed with the TLM Method"	C. Eswarappa and W.J.R. Hoefer
1000	**BREAK**	
1020	"Scattering Analysis of Antenna Installations/Panels on a Curved Surface Using Uniform Field Integration Method"	J.J. Kim and O.B. Kesler
1040	"Code Validation of Aircraft Scattering Parameters using IR Thermograms"	J. Norgard, R. Sega, M. Seifert, T. Blocher and A. Pesta

TUESDAY 21 MARCH

SESSION 1: SCATTERING (parallel with Sessions 2 and 3) (CONT) — **122 Ingersoll Hall**

1100	"A New Method for Solving Scattering Problems with Conducting Media in the Time Domain"	M. Schinke and K. Reiß
1120	"Experience and Experiments at Cray Research with JUNCTION-2"	J.A. Crow and Q.M. Sheikh
1140	"Quantitative Methods for Measuring and Improving the Performance of Electromagnetic Scattering Codes"	J.P. Meyers, A. J. Terzuoli, Jr., and G.C. Gerace
	LUNCH	

SESSION 2: LOW FREQUENCY (parallel with Sessions 1 and 3) — **117 Spanagel Hall**
CHAIRS: K. KUNZ, H. SABBAGH

0840	"Numerical Modelling of EMC in Underground Power Cable Systems with the Hybrid FE-BE Method"	J. Shen and A. Kost
0900	"New Contribution to the Study of Fault Currents Distribution in the Ground Systems"	H.O. Brodskyn, M.H. Giarolla, J.R. Cardoso, N.M. Abe and A. Passaro
0920	"On the Oscillatory Phenomena of Eddy Currents Along the $\vec{A}$, $\mathbf{V}$-Ψ Inferface"	Z. Cheng, Q. Hu, S. Gao, Z. Liu, M. Wu and C. Ye
0940	"A New MMP-Code for Static Field Computation"	M. Gnos and P. Leuchtmann
1000	**BREAK**	
1020	"Molten Aluminum Flow Induced by High Magnetic Fields"	W.P. Wheless, Jr. and C.S. Wheless
1040	"The Electrostatic Characterization of a N-Element Planar Array Using the Singularity Expansion Method"	J.E. Mooney and L. Riggs
1100	"A Volume-Integral Code for Electromagnetic Nondestructive Evaluation"	R.K. Murphy, H.A. Sabbagh, J.C. Treece and L. W. Woo
	LUNCH	

SESSION 3: RESEARCH AND ENGINEERING FRAMEWORK FOR CEM (parallel with Sessions 1 and 2) — **102 Glasgow Hall**
ORGANIZER: K. SIARKIEWICZ

0840	"Research and Engineering Framework (REF) for Computational Electromagnetics" (Invited)	B. Hantman, K. Siarkiewicz, J. Labelle and R. Jackson
0900	"Research & Engineering Framework (REF) Data Dictionary Specification for Computational Electromagnetics" (Invited)	J.A. Evans
0920	"DT_NURBS - A Geometry Engine for Integration of the MMACE Data" (Invited)	B. Ames and C. Whitcomb
0940	"Standardized Grid Generation for the Research and Engineering Framework" (Invited)	L.W. Woo, H. A. Sabbagh, J. LaBelle and B. Hantman
1000	**BREAK**	
1020	"Visualization and Standards" (Invited)	J. Cugini
1040	"A Visualization Toolkit for Computational Electromagnetics" (Invited)	B. Joseph
1100	"MMACE - Lessons for the Development of a CEM Computational Environment" (Invited)	R.G. Hicks and K.R. Siarkiewicz
	LUNCH	

1200 **BOARD OF DIRECTORS MEETING** — **Terrace Room, Herrmann Hall**

TUESDAY AFTERNOON 21 MARCH

1330-1730	**VENDOR BOOTHS AND WINE AND CHEESE BUFFET**	**Barbara McNitt Ballroom, Herrmann Hall**
1800	**HAPPY HOUR (NO HOST)**	**Barbara McNitt Ballroom, Herrmann Hall**
1900	**AWARDS BANQUET**	**Barbara McNitt Ballroom, Herrmann Hall**
1330-1530	**SHORT COURSE (PARTIAL DAY, NO FEE)** Bob Bevensee "Time Series Analyses of Equity Stock Prices and a Profitable Investment Strategy"	**102 Glasgow Hall**
1330-1530	**SESSION 4: INTERACTIVE TECHNICAL SESSION**	**Barbara McNitt Ballroom, Herrmann Hall**

SESSION 4A: EM THEORY I — **Barbara McNitt Ballroom, Herrmann Hall**

"Pulse Basis Function Implementation of the Radiation Condition Integral Equations"	P.C. Colby
"Finite Difference Solutions of Geometrical Optics and Some Related Nonlinear PDEs Approximating High Frequency Helmholtz Equation"	E. Fatemi, B. Engquist and S. Osher
"Conversion of Mechanical Energy to Electromagnetic Energy"	R.M. Bevensee
"Block-Toeplitz-Structure-Based Solution Strategies for CEM Problems"	V.I. Ivakhnenko and E.E. Tyrtyshnikov
"The Two-Dimensional Finite Integral Technique Combined with the Measured Equation of Invariance Applied to Transverse Electric Open Region Scattering Problems"	G.K. Gothard and S.M. Rao
"Artificial Transparent Boundaries in Computational Quasioptics"	A.V. Popov
"A Statistical Electromagnetics (STEM) Research Initiation Report"	W.P. Wheless, Jr., C.B. Wallace and W.D. Prather
"Optimization of Aperiodic Conducting Grids"	R.L. Haupt
"Accurate MOM Scattering Calculations Using Massively Parallel Computation"	L.D. Vann and J.S. Bagby
"A New Angle on a Low Cost Ground Screen for Model Testing in the Undergraduate Antennas Laboratory (Looking at Near Vertical Incidence Skywaves (NVIS) for a Coast Guard Patrol Boat)"	M.E. McKaughan, W.M. Randall and B. Nutter
"Efficient Extraction of the Near-Field from CGFFT Methods Applied to Scatterers in the Resonance Region"	A. McCowen

SESSION 4B: VISUALIZATION & INTERFACES — **Barbara McNitt Ballroom, Herrmann Hall**

"Computer Code for Field Calculation and Visualization in Quasioptics"	Y.V. Kopylov
"Dosimetry in a Voxel Model of the Head"	P.J. Dimbylow
"A Graphical User Interface for the NEC-BSC"	L.W. Henderson and R.J. Marhefka
"MF Communication and Broadcast Prediction System"	M.J. Packer and A.P. Tsitsopoulos
"A Finite Difference Time Domain Visualization Tool for Microsoft Windows™"	A. Z. Elsherbeni, C.D. Taylor, Jr. and C. E. Smith

SESSION 4C: VALIDATION — **Barbara McNitt Ballroom, Herrmann Hall**

"Transformable Scale Aircraft-Like Model for the Validation of Computational Electromagnetic Models and Algorithms: Initial Configuration and Results"	D.R. Pflug and D. Warren
"Measurement Study for Validation of Electromagnetic Scattering Codes on a Complex 3D Target"	T. Kienberger and D. Jurgens
"Validation Using a Moment Method Approach with Exact Object Representation"	J.A. Larsson, S. Ljung and B.Wahlgren
"IR Measurements for Validating EM Analysis Tools"	M. Seifert, T. Blocher and A. Pesta

TUESDAY AFTERNOON 21 MARCH

SESSION 4D: EMI/EMC/EMP — **Barbara McNitt Ballroom, Herrmann Hall**

"Analysis of Electromagnetic Interference at an Ocean Observation Post"	L. Bai and J.F. Dai
"Enforcing Correlation on Statistically Generated EM Cable Drivers"	R. Holland and R. St. John
"Analysis of Different Contributions to the Coupling Between Reflector Antennas on a Satellite"	C. Park and P. Ramanujam
"Simple Radiation Models in Lieu of EMC Radiated Emissions Testing"	R. Perez

WEDNESDAY MORNING 22 MARCH

0730 **CONTINENTAL BREAKFAST**

0800 **ACES BUSINESS MEETING** President Hal Sabbagh **102 Glasgow Hall**

SESSION 5: OPTIMIZATION TECHNIQUES IN APPLIED ELECTROMAGNETICS (parallel with Sessions 6 and 7) 361 Ingersoll Hall
ORGANIZER: O.A. MOHAMMED

0840	"An Optimization Approach to Reduce the Discretization Error in Finite Element Explicit Solution Scerne" (Invited)	M. Feliziani, E. Latini, F. Maradei
0900	"Analysis and Design of a Reentrant Resonant Cavity Applicator for Radio Frequency Hyperthermia System" (Invited)	Y. Kanai, T. Tsukamoto, K. Toyama, T. Kashiwa, Y. Saitoh and M. Miyakawa
0920	"Analysis of Loaded Cavities Using the Constitutive Error Approach" (Invited)	R. Albanese, R. Fresa, R. Martone and G. Rubinacci
0940	"The Design of Electromagnetic Devices using Knowledge Based Systems and Sensitivity Information" (Invited)	D.A. Lowther, D. N. Dyck and R. Rong
1000	**BREAK**	
1020	"A Computer Program for the Design of Superconducting Accelerator Magnets" (Invited)	S. Russenschuck
1040	"Application of Optimization to the Design of Electromechanical Devices" (Invited)	J.K. Sykulski and Y.B. Cheng
1100	"Genetic Algorithms for the Optimal Design of Electromagnetic Devices" (Invited)	O.A.Mohammed, G.F. Üler
1140	"Linear Constraints - Gradient Technique for the Inverse Problem of Design Optimization" (Invited)	A.A. Arakadan and S. Subramaniam-Sivanesan
	LUNCH	

SESSION 6: COMPUTATIONAL ELECTROMAGNETICS APPLIED TO SHIP DESIGN (parallel with Sessions 5 and 7) 102 Glasgow Hall
ORGANIZERS: J. NEWCOMB AND J. LOGAN

0840	"The Naval Sea Systems Command Electromagnetic Engineering Program" (Invited)	D. Cebulski, N. Baron and J. Eadie
0900	"EM Engineering System Architecture" (Invited)	J. Winston
0920	"EM Engineering Ray Tracing and Casting Model RTC" (Invited)	L. Gray
0940	"Ship Transition-Frequency EM Environment Analysis Requirements" (Invited)	G. Piper
1000	**BREAK**	
1020	"Finite Volume Time Domain Analysis of Ship Topside EM Environment Features" (Invited)	B. Hall, A. Mohammadian, C. Rowell and V. Shankar
1040	"EM Engineering Ship End-To-End Application" (Invited)	L. R. Carlson, C. F. Juster, G. R. Allen

WEDNESDAY MORNING 22 MARCH

SESSION 6: (CONT) COMPUTATIONAL ELECTROMAGNETICS APPLIED TO SHIP DESIGN (parallel with Sessions 5 and 7) 102 Glasgow

1100	"EM Engineering Applied to Patrol Craft (PC-1)" (Invited)	D. Tam, J. McGee, C. Azu and M. Soyka
1120	"Shipboard Antenna Pattern Visualization and Analysis" (Invited)	L.C. Russell, J.C. Logan, J.W. Rockway and D.F. Schwartz
	LUNCH	

SESSION 7: FINITE DIFFERENCE TIME DOMAIN (parallel with Sessions 5 and 6) 122 Ingersoll Hall
ORGANIZER: J. BEGGS

0840	"Computational Analysis of Radiation from an Elliptical Shaped End Radiator" (Invited)	S. A. Blocher, E. A. Baca and J. H. Beggs
0900	"A Time Domain Harmonic Oscillator Model for an FDTD Treatment of Lossy Dielectrics" (Invited)	K. S. Kunz
0920	"FDTD Modeling of Electromagnetic Wave Interactions with Composite Random Sheets" (Invited)	J.G. Maloney and B.L. Shirley
0940	"An Improved Near to Far Field FDTD Algorithm" (Invited)	K. S. Kunz
1000	**BREAK**	
1020	"Unstructured Finite-Volume Modeling in Computational Electromagnetics" (Invited)	D.J. Riley and C.D. Turner
1040	"Scattering from Coated Targets Using a Frequency-Dependent, Surface Impedance Boundary Condition in FDTD"	C.W. Penney, R.J. Luebbers and J.W. Schuster
1100	"Hybrid Finite Difference Time Domain and Finite Volume Time Domain in Solving Maxwell's Equations" (Invited)	K.S. Yee and J.S. Chen
1120	"Reducing the Number of Time Steps Needed for FDTD Antenna and Microstrip Calculations" (Invited)	R. Luebbers and H.S. Langdon
1140	"Numerical Simulations of Light Bullets, Using the Full Vector, Time Dependent, Nonlinear Maxwell Equations"	P. Goorjian and Y. Silberberg
	LUNCH	

WEDNESDAY AFTERNOON 22 MARCH

SESSION 8: BERENGER'S BOUNDARY CONDITION (parallel with Sessions 10 and 11) 102 Glasgow Hall
ORGANIZER: J. FANG

1320	"Ultrawideband Termination of Waveguilding and Multilayer Structures for FD-TD Simulations in 2-D and 3-D" (Invited)	C.E. Reuter, R.M. Joseph, E.T. Thiele, D.S. Katz and A. Taflove
1340	"A 3-D Perfectly Matched Medium by Coordinate Stretching and Its Absorption of Static Fields" (Invited)	W.C. Chew, W.H. Weedon and A. Sezginer
1400	"Perfectly Matched Anisotropic Absorbers for Finite Element Applications in Electromagnetics"	D.M. Kingsland, Z.S. Sacks and J.F. Lee
1420	"Modification of Berenger's Perfect Matched Layer for the Absorption of Electromagnetic Waves in Layered Media"	M. Gribbons, S.K. Lee and A.C. Cangellaris
1440	"Performance of the Perfectly Matched Layer in Modeling Wave Propagation in Microwave and Digital Circuit Interconnects"	Z. Wu and J. Fang
1500	**BREAK**	

WEDNESDAY AFTERNOON 22 MARCH

SESSION 9: TIME DOMAIN/FDTD (parallel with Sessions10, 11 and 12) **102 Glasgow Hall**
CHAIRS: L. LONG, J. MALONEY

1520	"A FVTD Algorithm for Maxwell's Equations on Massively Parallel Machines"	V. Ahuja and L.N. Long
1540	"The Piecewise Linear Recursive Convolution Method for Incorporating Dispersive Media into FDTD"	D.F. Kelley and R. J. Luebbers
1600	"Combining Different Coordinate Systems in the Time Domain Finite Difference Method"	M. Mrozowski, M. Okoniewski, M.A. Stuchly and S.S. Stuchly
1620	"Time Domain Response of Simulated 2D Composite Scatterers"	A.Z. Elsherbeni and P. Goggans
1640	"An Object-Oriented Approach to Writing Computational Electromagnetics Codes"	M. Zimmerman and P. Mallasch

SESSION 10: FAST ALGORITHMS FOR COMPUTATIONAL ELECTROMAGNETICS (parallel with Sessions 8, 9, 11, and 12)
ORGANIZERS: E. MICHIELSSEN AND W. CHEW **122 Ingersoll Hall**

1320	"On the Use of Wavelet-Like Basis Functions in the Finite Element Analysis of Elliptic Problems" (Invited)	R.K. Gordon
1340	"Fast Wavelet Algorithm (FWA) for Moment Method Analysis of Electromagnetic Problems" (Invited)	K. Sabetfakhri and L.P.B. Katehi
1400	"Fast Far Field Approximation for Calculating the RCS of Large Objects" (Invited)	C.C. Lu and W.C. Chew
1420	"The Parameter Estimation Technique (PET): Speeding Up Dense Matrix Methods" (Invited)	C. Hafner and J. Fröhlich
1440	"A Novel Scheme for Massively Parallel Solution of Maxwell's Equations using FDTD" (Invited)	M.A. Jensen, Y. Rahmat-Samii and A. Fijany
1500	**BREAK**	
1520	"Reduction of the Filling Time of Method of Moments Matrices" (Invited)	G. Vecchi, P. Pirinoli, L. Matekovits and M. Orefice
1540	"The Fast Multipole Method for Large 2d Scatterers" (Invited)	L.R. Hamilton, J.J. Ottusch, M.A. Stalzer, R.S. Turley, J.L. Visher and S.M. Wandzura
1600	"A Multilevel Matrix Decomposition Algorithm for Analyzing Scattering from Large Structures" (Invited)	E. Michielssen and A. Boag
1620	"A 3D Fast Multipole Method for Electromagnetics with Multiple Levels" (Invited)	B. Dembart and E. Yip
1640	"Fast Multipole Method Solution of Combined Field Integral Equaltion"	J.M. Song and W. C. Chew

SESSION 11: MICROWAVE AND GUIDED WAVE (parallel with Sessions 8 and 10) **361 Ingersoll Hall**
CHAIRS: P. GOGGANS, A. TERZUOLI

1320	"Computer-Simulation of Isotropic, Two-Dimensional Guided-Wave Propagation"	R.A. Speciale
1340	"Analysis of Ultra-Short Pulse Propagation on Uniform and Tapered Printed Transmission Lines"	R.A.O. Veliz and J.R. Souza
1400	"Wave-Field Patterns on Electrically Large Networks"	R.A. Speciale
1420	"Scattering Characteristics of Dissimilar Waveguide Slot Couplers"	A. Singh and K.S. Christopher
1440	"An Alternative Formulation of the Tranverse Resonance Technique"	A.G. Neto, S. Ariguel, H. Aubert, D. Bajon and H. Baudrand
1500	**BREAK**	

WEDNESDAY AFTERNOON 22 MARCH

SESSION 12: MOM (parallel with Sessions 9 and 10) **361 Ingersoll Hall**
CHAIRS: A. PETERSON, R. ZIOLKOWSKI

1520	"Moment Method Analysis of Dielectric Covered Radiating Slots Using Alternative Green's Function Approach"	S. Christopher, V.V.S. Prakash, A.K. Singh and N. Balakrishnan
1540	"Computation of E-field Distribution of Low Gain Antenna on Conducting Body of Revolution"	J. Liu, J. Wang and Y. Gao
1600	"An Implementation of an Exact Scheme for Problem Decomposition Via the Use of Aperture Admittance"	D.L. Wilkes, C-C. Cha and T. Krauss
1620	"Parallelization of the Parametric Patch Moment Method Code"	X. Shen, G.E. Mortensen, C.C. Cha, G. Cheng and G. C. Fox
1640	"A Tool Box for Parallelization of Moments Method Codes"	E. Yip, B. Blakely, L. Johnson, D. Jurgens and R. Kochhar

THURSDAY MORNING 23 MARCH

0730	**CONTINENTAL BREAKFAST**	

SESSION 13: RECENT DEVELOPMENTS IN FDTD ANALYSIS (parallel with Sessions 14 and 15) 102 Glasgow Hall
ORGANIZERS: M. PIKET-MAY AND D. KATZ

0840	"Simulation of Microwave Circuits by FDTD Method" (Invited)	C.N. Kuo, B. Houshmand and T. Itoh
0900	"Adaptation of FDTD Techniques to Acoustic Modeling" (Invited)	J.G. Maloney and K.E. Cummings
0920	"FDTD Investigation of the Antenna-Tissue Interaction for Cellular and Satellite Systems" (Invited)	Y. Rahmat-Samii and M.A. Jensen
0940	"FDTD Modeling of Ground-Penetrating Radar Antennas"	B.J. Zook
1000	**BREAK**	
1020	"FDTD Modeling of Ultrashort Optical Pulse Interactions with Nonresonant and Resonant Materials and Structures" (Invited)	R.W. Ziolkowski
1040	"Time Domain Analysis of Electromagnetic Wave Propagation in Nonlinear Dielectric Slab"	G. Miano, C. Serpico, L. Verolino and F. Villone
1100	"An Efficient Sub-gridding Algorithm for FDTD."	D.T. Shimizu, M. Okoniewski and M.M. Stuchly
1120	"Using the Integral Forms of Maxwell's Equations to Modify and Improve the FDTD (2,4) Scheme"	M.F. Hadi and M. Piket-May
1140	"From the Berenger PML ABC to Micro-Lasers: Recent Advances in FD-TD Modeling Techniques" (Invited)	A. Taflove
	LUNCH	

SESSION 14: PROPAGATION (parallel with Sessions 13 and 15) **361 Ingersoll Hall**
ORGANIZER: K. CHAMBERLIN

0840	"Terrain and Refractivity Effects in a Coastal Environment: Results from the VOCAR Experiment"	A. Barrios
0900	"Capabilities and Limitations Associated With Using GTD to Model Propagation Path Loss in the Presence of Irregular Terrain"	K. Chamberlin
0920	"Comparison of Electromagnetic Wave Propagation Computer Programs"	S.A. Fast and T. H. Koschmieder
0940	"A Model for Estimating Electromagnetic Wave Attenuation in a Forest (EWAF) Environment"	C. Welch, C. Lemak, and L. Corrington
1000	**BREAK**	
1020	"Validation of the Radio Physical Optics Propagation Model"	R.A. Paulus

THURSDAY MORNING 23 MARCH

SESSION 14: PROPAGATION (parallel with Sessions 13 and 15) (CONT) — **361 Ingersoll Hall**

1040	"VTRPE: A Variable Terrain Electromagnetic Parabolic Equation Model"	F.J. Ryan
1100	"Estimating Tropospheric Refractivity Fields Using a Nonlinear Gauss-Markov Procedure and the PE Model"	D. Boyer and F.J. Ryan
1120	"Modeling of Radio Wave Ducting Over Regular Boundary"	I.P. Zolotarev
	LUNCH	

SESSION 15: PARALLELIZATION OF EM CODES (parallel with Sessions 13 and 14) — **122 Ingersoll Hall**
ORGANIZERS: J. VOLAKIS AND A. CHATTERJEE

0840	"Advances in Time-Domain CEM Using Massively Parallel Architectures" (Invited)	C. Rowell, V. Shankar, W.F. Hall and A. Mohammadian
0900	"Parallel Solutions of Maxwell's Equations on the Meiko CS-2" (Invited)	N. Madsen, B. Eme, D. Steich and G. Cook
0920	"Parallelization of the CARLOS-3D Method of Moments Code" (Invited)	J.M. Putnam, D.D. Car and J.D Kotulski
0940	"Parallel Computing for Electromagnetism at ONERA" (Invited)	A. de La Bourdonnaye, A. Cosnuau, X. Ferrières, P. Leca and F. X. Roux
1000	**BREAK**	
1020	"The Performance of the Parallel Solution of the Quasi-Minimal Residual (QMR) Method on 2D Mesh Architectures" (Invited)	L. Hamandi, F. Özgüner and R. Lee
1040	"Advanced Parallel Solver Techniques" (Invited)	A.S. King
1100	"Parallelized FDTD for Antenna Radiation Pattern Calculations"	Z.M. Liu, A.S. Mohan, T. Aubrey and W.R. Belcher
1120	"Calculation of Electromagnetic Fields with the Multiple Multipole Method (MMP Method) on Parallel Computers"	C. Tudziers and H. Singer
1140	"Implementation of the Finite-difference Time-Domain Method on Parallel Computers"	R.S. David and L.T. Wille
	LUNCH	

THURSDAY AFTERNOON 23 MARCH

SESSION 16: EM THEORY II (parallel with Sessions 18 and 20) — **361 Ingersoll Hall**
CHAIRS: K. YEE, R. GORDON

1320	"FDTD Investigation of the Ability to Increase Electromagnetic Fields Around Head Tumors"	D.B. Dunn, A.J. Terzuoli, Jr. G.C. Gerace and C.A. Rappaport
1340	"FDTD and PMM Based Design of a TEM Horn Antenna with Reduced Off-Boresight Fields"	D.J. Wolstenholme, A.J. Terzuoli, Jr. and G. C. Gerace
1400	"Determination of the Complex Aperture Distribution of a Planar Spiral Antenna from 3D Far-Field Radiation Pattern Data"	M. Kluskens, W. Lippincott and M. Kragalott
1420	"Analysis of Micro-Contamination of Silicon Wafers Based on Discrete Sources Method (DSM)"	Y.A. Eremin and N.W. Orlov
1440	"Analysis of Convergence Properties of Projection Methods for Solving CEM Applications"	V.I. Ivakhnenko, A.V. Kukk, E.E. Tyrtyshnikov, A.Y. Yeremin and N.L. Zamarashkin

THURSDAY AFTERNOON 23 MARCH

SESSION 17: ELECTROMAGNETIC MODELING TECHNIQUES FOR INTEGRATED OPTICS (parallel with Sessions 18, 19 and 20)
ORGANIZER: A. CANGELLARIS **361 Ingersoll Hall**

1520	"Analysis and Design of Guided-wave Optical Devices Using Finite-Difference Time-Domain Method" (Invited)	S.I. Chaudhuri and S.T. Chu
1540	"Vectorial Analysis of Optical Waveguides by the Method of Lines"(Invited)	R. Pregla and W. Pascher
1600	"Vector Finite Element Analysis of Lossless and Lossy Dielectric Waveguides" (Invited)	P. Cheung and A. Gopinath
1620	"NL-FDTD Modeling of Linear and Nonlinear Corrugated Waveguiding Systems for Integrated Optics Applications" (Invited)	R.W. Ziolkowski and J.B. Judkins
1640	"Analysis of Coupled Nonlinear Optical Waveguides by Matrix Method"	V. Tripathi, A. Weisshaar and H.S. Chang

SESSION 18: TOPICS IN FRACTAL AND WAVELET ELECTRODYNAMICS (parallel with Sessions 16, 17and 20) 102 Glasgow Hall
ORGANIZERS: D.H. WERNER AND P.L. WERNER

1320	"An Overview of Fractal Electrodynamics Research" (Invited)	D.H. Werner
1340	"Fractal Arrays and Fractal Radiation Patterns" (Invited)	P.L. Werner, D.H. Werner and A.J. Ferraro
1400	"Wavelet Transforms and Time/Time-scale Analysis" (Invited)	R.K. Young and T.G. Golsberry
1420	"Wavelet-based Processing to Efficiently Achieve Broadband Monostatic and/or Passive Cross-sensor Processing" (Invited)	R.K. Young and L.H. Sibul
1440	"The Intervallic Wavelets with Application in the Surface Integral Equations" (Invited)	G.W. Pan and J.Y. Du
1500	**BREAK**	
1520	"Radar Cross Section Data Reduction Using Wavelets"	A.S. Ali, S.E. Duval and R.L. Haupt

SESSION 19: NEC APPLICATIONS (parallel with Session 17 and 20) 102 Glasgow Hall
ORGANIZER: J. BREAKALL

1540	"Computationally Efficient and Accurate Approximations for Impedance Matrix Elements of NEC-Type Method of Moments Formulations"	D.H. Werner, S.E. Metker and J.A. Huffman
1600	"Development of the Coupled-Resonator Antenna Principle A Computer Modeling Case History"	G. Breed
1620	"Antenna Design & Development Using NEC-WIN"	T. A. Erdley, J. J. Shapiro, J. S. Young and J.K. Breakall
1640	"The "Paint" System A UTD/NEC Hybrid Package for Simulating Antenna Patterns Over 3-Dimensional Irregular Terrain"	J.S. Young and J.K. Breakall

SESSION 20: FEM (parallel with Sessions 16, 17, 18, and 19) **122 Ingersoll Hall**
CHAIRS: R. BURKHOLDER, J. KARTY

1320	"Numerically Characterizing Electromagnetic Fields Local to the Edge of a Conducting Strip Using a Matched Asymptotic Technique and the Finite Element Method"	A.S. Ali and C. L. Holloway
1340	"An Enhanced "A Posteriori" Remeshing Algorithm for Adaptive Meshing of 2D Finite Element Problems"	P. Girdinio, A. Manella and G. Molinari
1400	"Finite Element Analysis of Waveguides Using Edge-Based Magnetic Vector Potential and Nodal-Based Electric Scalar Potential"	J. -F. Lee, G. Lizalek and J. Brauer
1420	"A Scattering Analysis of Laser Beam Wave by Groove Pits on Optical Memory Disk by Using FEM with BEM"	Y. Miyazaki and K. Tanaka
1440	"3D Nodal- and Mixed-Based Elements for Unbounded Microwave Problems"	A. Nicolas, L. Nicolas and J.L. Yao-bi
1500	**BREAK**	

THURSDAY AFTERNOON 23 MARCH

SESSION 20: FEM (parallel with Sessions 16, 17, 18, and 19) (CONT) — **122 Ingersoll Hall**

1520	"A Rationale for the Use of Mixed-order Basis Functions Within Finite Element Solutions of the Vector Helmholtz Equation"	A.F. Peterson and D.R. Wilton
1540	"Finite Element Waveguide Simulator Techniques"	J.R. Sanford and N.M. Johansson
1600	"A Solution for Open Boundary Electromagnetic Field Problems by Mapped Infinite and Virtual Elements"	L.H.A. de Medeiros and A. Raizer

FRIDAY MORNING, MARCH 24

0730 **CONTINENTAL BREAKFAST**

SESSION 21: EM ANALYSIS TECHNIQUES FOR ELECTRICALLY LARGE CAVITIES (parallel with Sessions 22 and 23)
ORGANIZER: D. PFLUG — **122 Ingersoll Hall**

0840	"Application of Modal and Plane Wave Expansions to Modeling Large Jet Engine Cavities" (Invited)	J. L. Karty and J.M. Roedder
0900	"Scattering from Dielectric Loaded Cavities Using Shooting and Bouncing Rays" (Invited)	M. Christensen, S. W. Lee D.J. Andersh
0920	"Xpatch Simulation of Large Inlet Structures" (Invited)	R. Bhalla and H. Ling
0940	"An Iterative Physical Optics Approach for the Em Analysis of Cavities and Other Multi-Bounce Geometries" (Invited)	R.J. Burkholder
1000	**BREAK**	
1020	"Improved Ray Basis in the Hybrid Analysis of EM Scattering by Large Open Cavities" (Invited)	R.J. Burkholder, P.H. Pathak, H.T. Chou, D. Andersh and J. Fath
1040	"Overlapping Modal and Geometric Symmetries for Computing Jet Engine Engine Inlet Scattering" (Invited)	D.C. Ross, J.L. Volakis, H. T. Anastassiu and D. Andersh
	LUNCH	

SESSION 22: ACCURACY ESTIMATION IN ELECTROMAGNETIC MODELING (parallel with Sessions 21 and 23) 109 Glasgow Hall
ORGANIZER: S.M. WANDZURA

0840	"Assessing the Influence of Coefficient Accuracy, Matrix Condition Number, Size and Type, and Computer Precision on Matrix-Solution Accuracy" (Invited)	E. K. Miller
0900	"Numerical Accuracy Issues in Finite Element Frequency Domain Solutions of Radar Scattering Problems" (Invited)	J. D'Angelo
0920	"Accuracy in Computation of Matrix Elements of Singular Kernels"	S.M. Wandzura
0940	"Accuracy Estimation and High Order Methods"	L.R. Hamilton, J.J. Ottusch, M.A. Stalzer, R.S. Turley, J.L. Visher and S. M. Wandzura
1000	**BREAK**	
1020	"Accuracy Issues in Time-Domain CEM Using Structured/Unstructured Formulations" (Invited)	V. Shankar, W. F. Hall and S. Palaniswamy
1040	"An Accuracy Study for the 3D Hybrid Finite Element Method of Moments SWITCH Code" (Invited)	G.E. Antilla and Y.C. Ma
1100	"Modeling Accuracy of 3D Method of Moments Techniques"	M.B. Gedera, L.N. Medgyesi-Mitschang, R.A. Pearlman, J.M. Putnam, D-S.Y. Wang
1120	"Requiring Quantitative Accuracy Statements in EM Data" (Invited)	E.K. Miller
	LUNCH	

FRIDAY MORNING, MARCH 24

SESSION 23: PDE METHODS IN ELECTROMAGNETICS (parallel with Sessions 21 and 22) 102 Glasgow Hall
ORGANIZERS: R. LEE AND J. -F. LEE

0840	"Optimization Issues in Finite Element Codes for Solving Open Domain 3D Electromagnetic Problems" (Invited)	A. Chatterjee and J.L. Volakis
0900	"A Characteristic-Based 3D Time Domain Maxwell Equation Solver" (Invited)	J.S. Shang and K.C. Hill
0920	"Finite Element Solution of Eddy Current Problems in Electromagnetics" (Invited)	O.A. Mohammed and G. F. Üler
0940	"Ten Years of Evolution of the FDTD-like Conformal Technique" (Invited)	K.S. Yee
1000	**BREAK**	
1020	"Whitney Elements Time Domain (WETD) Methods for Solving Three-Dimensional Waveguide Discontinuities" (Invited)	J. -F. Lee
1040	"An FDTD/FVTD 2D-algorithm to Solve Maxwell's Equations"	J.S. Chen, J.V. Prodan and K.S. Yee
1100	"Spectral Finite Methods for the Simulation of Electromagnetic Interactions with Electrically Long Structures" (Invited)	A.C. Cangellaris and D. Hart
	LUNCH	

SATURDAY, 25 MARCH SHORT COURSES

0830-1630 **SHORT COURSE (FULL-DAY)** — **101A Spanagel Hall**
"Using Mathematical Software for Computational Electromagnetics"
Jovan Lebaric, Naval Postgraduate School

0830-1630 **SHORT COURSE (FULL-DAY)** — **109 Glasgow Hall**
"Wire Antenna Modeling Using NEC"
Dick Adler, Naval Postgraduate School
Jim Breakall, Penn State University
Gerry Burke, Lawrence Livermore National Lab

0830-1630 **SHORT COURSE (FULL-DAY)** — **102 Glasgow Hall**
"FDTD, Generalized FDTD and FVTD Techniques in Solving Maxwell's Equations"
Kane Yee, Lockheed

SESSION 1:

SCATTERING

Chairs: V. Cable, E. Miller

A CGFFT METHOD APPLIED TO THE SCATTERING FROM FINITE SIZE MICROSTRIP ANTENNA

A. McCowen
Department of Electrical and Electronic Engineering
University of Wales, Swansea, UK

Abstract

Conjugate gradient FFT (CGFFT) methods which solve the electric field integral equation (EFIE) have previously been applied to microstrip structures. However, the methods reported assume an infinite planar substrate (or layered substrate) and cannot be applied to finite structures, or structures with recesses or general inhomogeneity in the substrate.

This paper will discuss the CGFFT method which has been used to solve the EFIE for finite structures. Initial results from this technique have shown good agreement with conventional method of moment solutions.for bistatic rcs and induced current distributions.

INTRODUCTION

Conjugate gradient FFT (CGFFT) methods which solve the electric field integral equation (EFIE), have previously been applied to microstrip structures and several authors, eg [1], have demonstrated their efficiency in CPU and memory. However, the methods reported assume an infinite planar substrate (or layered substrate) and ground plane which are modelled by a modified Green's function, and are thus unsuitable for finite structures or structures with recesses and general inhomogeneity in the substrate.

Based on the author's previous works [2, 3], a CGFFT method has been developed to cope with the mixed dielectric/conductor problem associated with microstrip of finite size and having arbitrary planar substrates (presently restricted to isotropic). Similar structures have been modelled in previous works, which includes a recent paper by Sarkar, Rao and Djordjevic [4], but these works have been based on the Method of Moments (MoM) for mixed conductor/dielectric problems which is well-known to be prohibitively expensive in CPU and computer storage for scatterers in the resonance region.

This paper will discuss the CGFFT method which has been used to solve the EFIE for finite size microstrip structures, and show initial results from the scheme. The results of bistatic rcs and current distribution on the scatterers will be given and compared to the results of the method of moments scheme based on the combined field integral equation (CFIE) for mixed dielectric/conductor problems which was developed by Rao, Wilton and Glisson [5] and was also used in [4].

THE CGFFT METHOD

The problem domain comprises 2 subdomains S and V. Firstly S is the set of N two-dimensional pec surfaces stacked parallel to the x-y plane, each separated by Δz and discretised by Δx and Δy in the usual way for CGFFT methods. Secondly the subdomain V is an inhomogeneous dielectric which is uniformily discretised into cells of size $\Delta x \Delta y \Delta z$ which are interleaved between the N pec surfaces of the subdomain S, see Fig. 1. Each cell is assumed to have a constant value of relative permittivity. If J_s and J_v are the current continue distributions on the pec surfaces and the polarization currents respectively then the EFIE takes the form

$$\begin{bmatrix} G_{ss} & G_{sv} \\ G_{vs} & G_{vv} \end{bmatrix} \begin{bmatrix} J_s \\ J_v \end{bmatrix} = \begin{bmatrix} E_s^i \\ E_v^i \end{bmatrix} \tag{1}$$

where E_s^i and E_v^i are the known incident electric fields on S and V respectively. The Green's dyadic terms in the impedance matrix represent the self and mutual coupling between the subdomains. It should be noted that G_{ss} is determined by a straight forward extension of the formulation for resonant pec plates given in [2] in which the null electric boundary condition is applied to S and G_{vv} is as determined in [3] for a 3D inhomogeneous dielectric scatterer. The cross-coupling terms are similar to those in G_{ss} and G_{vv} but are interpolated in the way defined by Shen [5] who applied an FFT-based algorithm to two flat pec plates to form a dihedral reflector. A conjugate gradient FFT based algorithm is then used to drive the left-hand side of (1) to be equal to the known right-hand side.

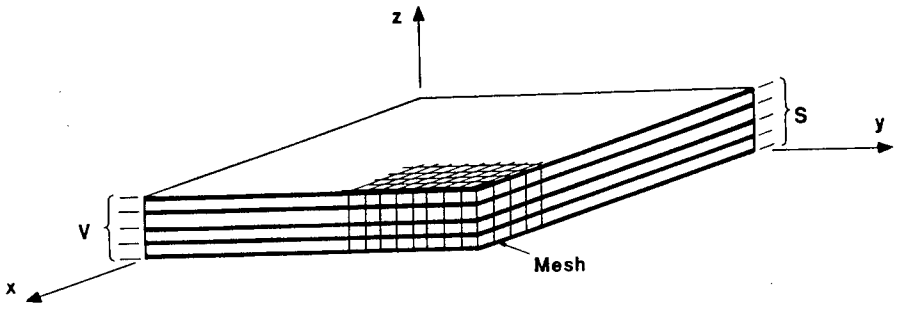


Fig. 1 The domain of the scheme showing the subdomains S, a set of pec plates, and V layers of dielectric.

RESULTS

A typical example of the results to be shown is now given. Fig. 2 shows a rectangular patch antenna of width W and length L with a feed line of width w and length l, over a finite ground plane. For this case the structure comprises the subdomain S which is the set of 2 pec plates, one of which is the ground plane, and the subdomain V, which comprises a single layer of dielectric of thickness h (= Δz). It should be notefd that the scheme is flexible enough to take a similar structure with a thick substrate, ie one in which H - (N-1). Δz).

The far-field in the x-z plane is shown in Fig. 3 for the structure as defined in Table 1 and illuminated by a plane wave at normal incidence and polarised along the x-asis. The results of the present scheme are compared to the results from the method of moments schemes [4] and are shown to be in excellent agreement with $\Delta x = \Delta y = 0.0625\lambda_o$ and $\Delta z = 0.0125\lambda_o$, 1560 unknowns are generated for this case and the storage requirement for the impedance matrix in the spectral domain is 0.7Mbytes. With the initial estimate of the current density taken to be zero the interative scheme took 400 iterations to converge with a relative error tolerance of 0.025. The cpu taken to generate the solution was approximately 2 sec. per iteration on a Dec Alpha 2100. The generation of the impedance matrix is a negligible proportion of the solution time.

Table 1 Data for the structure

Substrate	**Patch and feed**
$\varepsilon_r = 2.56$	
$h = 0.0125\lambda_o$	$L = W = 0.3125\lambda_o$
$L_g = 1.25\lambda_o$	$w = 0.0625\lambda_o$
$W_g = 0.0375\lambda_o$	$l = 0.3125\lambda_o$

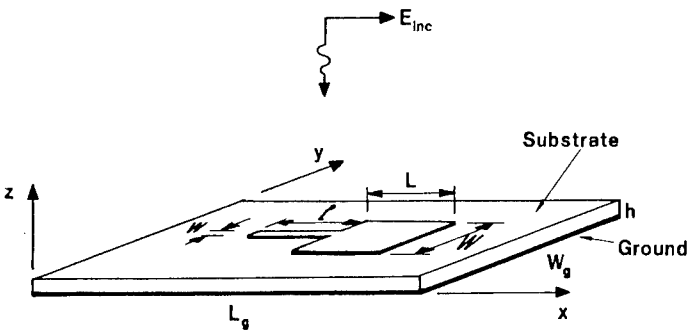


Fig. 2 Geometry of the microstrip structure.

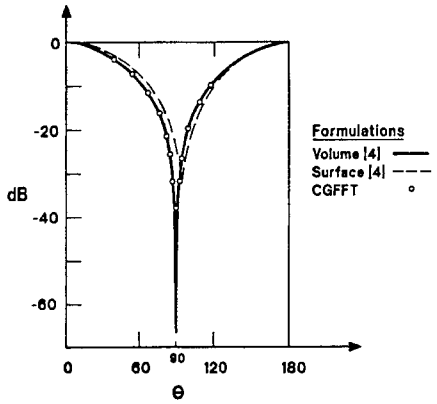


Fig. 3 Far field (20 log|E_q| versus θ in the Z,-x plane for the geometry and data of Fig. 2 and Table 1. Results are compared to those from [4].

REFERENCES

[1] M.F. Catedra and E. Gago, 'Spectral domain analysis of conducting patches of arbitrary geometry in multilayer media using the CGFFT method', IEEE Trans AP-38, pp 1530-36, October 1990

[2] T.V. Tran and A. McCowen, 'An improved pulse-basis CGFFT method for the thin conducting plate problem', IEEE Trans AP-41, pp 185-190, February 1993

[3] T.V. Tran and A. McCowen, 'A unified family of FFT-based method for dielectric scattering problems', J of Electromagnetic Waves and Applic., vd 8, No. 8, pp 973-992, 1994

[4] T.K. Sarkar, S.M. Rao and A.R. Djordjevic, 'Electromagnetic scattering and radiation from finite microstrip structures', IEEE Trans AP-38, pp 1568-75, November 1990

[5] S.M. Rao, D.R. Wilton and A.W. Glisson, 'Electromagnetic scattering by surfaces of arbitrary shape', IEEE Trans. AP-30, pp 409-418, May 1982

[6] C.Y. Shen, 'Application of the Discrete Fourier Transform method of nonorthogonal dihedral reflectors', IEEE Trans. AP-38, pp 1913-19, December 1990

ANALYSIS OF SCATTERING BY CLUSTER OF NONSPHERICAL PARTICLES BASED ON COMPLETE MATHEMATIC MODELS

Yu.Eremin*, N.Orlov*, and V.Rozenberg**

*Faculty of Applied Mathematics & Computer Science,
Moscow State University,
Vorobyov's Hills, 119899 Moscow, Russia
Fax: +7(095)939-2596; Tel: +7(095)939-1776;
E-mail: EREMIN@cs.msu.su

**Faculty of Applied Mathematics, Russian State Pedagogical University,
nab. reki Moiki 48, 191186 Saint-Petersburg, Russia

Problems of EM scattering by atmospheric hydrometeors are very important via plural practical applications. Under tracing atmosphere by whether radars the work wavelength happens to be very sensitive for the presence of atmospheric particles by virtue such effects as attenuation of propagating field, scattering, depolarization effects and so on arise. Discrete Sources Method (DSM) seems to be very appropriate for analysis of such complex scattering problems as multiple scattering by a cluster of strong interacting non-spherical particles [1],[2].

In the frame of DSM the scattered field is represented as a superposition of multipoles' fields. It satisfies to Maxwell' equations and Silver-Muller radiation conditions exactly. Multipoles amplitudes needs to be determined from the boundary condition at the obstacle surface. If the obstacle represents an aggregate of axi-symmetric particles it is found to be possible to examine complete mathematic models on the basis of GMT. To simplify the problem we employ azimuthal Fourier-series expansion both for scattering and exited fields for reduction 3-D space scattering problem to the set of the approximating problems at the surface element of an obstacle.

We use the special construction for EM fields of the multipoles. Multipoles are deposited in the complex plane joining to the axis of symmetry. The harmonics of the multipoles can be represented as a finite linear combination of the elementary functions. Multipole' amplitudes for each harmonic should be determine as a pseudosolution of the overdetermined linear system obtained from the point-

matching approach. It allows to get a minimum of the mean-square norm for the residual of EM fields at the obstacle surface. The efficiency of the DSM code allows to employ any kind of personal computers. One is able to investigate an obstacle having the total meridian length up to 10 exciting wavelengths and to estimate the error of the result obtained.

This technique was applied to the analysis of the scattering of TM/TE plane wave (wavelength was 3.2 cm) by atmospheric hydrometeors. The hydrometeor shape was chosen following to the real hydrometeor forms [3]. Comparison of scattering characteristics for the single particle with results obtained from spherical approximation using for the particle shape was performed. We have established the limits of spherical particles' approximation for atmosphere hydrometeors [4].

The investigation of wave scattering using the dynamic model was performed. It allows to calculate the multiple scattering by the cluster of strong interacting non-spherical particles [5]. The particles differing one from others both by shape and permittivity can be used as elements of the cluster. This model seems to be very useful under investigation of the wave propagation through an active atmosphere "melting layer" in that hydrometeors are in the state of fragmentation and coagulation. Results of complete EM analysis of such systems show the essentially different mechanism of scattering by the cluster of strong interacting particles than by non-interacting ones.

References

[1] Yu. Eremin, N. Orlov, A. Sveshnikov, ***Sov.Phys. Dokl.***, 1992. V.37, No 1, p.31.

[2] Ju. Eremin, N. Orlov, V. Rosenberg, ***Computer Physics Comm.***, 79 (1994), p. 201

[3] C. Cuang, K. Beard., ***J. Atmospheric Sci.***, 1990. No 11, p.1374.

[4] Yu. Eremin, N. Orlov, V. Rosenberg, 'EM Scattering from Single Electrified Raindrops', ***J. Atm. & Terr. Phys.*** (accepted for publication)

[5] Yu. Eremin, N. Orlov, V. Rosenberg, 'Multiple EM Scattering by Linear Array of Electrified Raindrops', ***J. Atm. & Terr. Phys.*** (accepted for publication).

ANALYTIC SOLUTION FOR CALCULATING THE RADAR CROSS-SECTION AND RELATED PARAMETERS OF A CONDUCTING RIGHT CIRCULAR CYLINDER SURROUNDED BY MULTIPLE LAYERS OF LOSSY DIELECTRICS

George W. Jarriel Jr., Michael E. Baginski, Lloyd Riggs
Department of Electrical Engineering
200 Broun Hall • Auburn University, Alabama 36849

January 12, 1995

Abstract

A theoretically exact solution which determines the scattered fields due to TM incidence of an electric plane wave on an infinitely long (no z variation) perfectly electrically conducting cylinder surrounded with variable layers of lossy dielectric materials is presented. This solution is used to calculate the radar cross-section (RCS) of an un-coated cylinder, a cylinder with a lossy dielectric coating where the constitutive parameters are assumed to be invariant with frequency, and cylinders where the constitutive parameters of the lossy coating vary with frequency.

I Introduction

On naval vessels, and other self contained environment, the proximity of RF transmitter/receiver equipment to conduction cables may produce undesirable reflections. Primarily an electromagnetic compatibility (EMC) problem, this investigation presents theoretical data demonstrating the potential for lossy materials, also known as radar absorbant material (RAM), to reduce unwanted reflections as opposed to the difficult task of determining a physical configuration which is designed to minimize these problems. The method chosen for this effort is the exact series solution due to the geometry of the problem as well as the obvious numerical efficiency advantages. The exact series solution require only a fraction of the time for calculation as the MOM or TLM. In addition, unlike the MOM or TLM, the exact series solution is theoretically exact. Only the TM case is presented in this paper, but the techniques presented here can be used to develop the TE scattered field formulation and RCS.

II Analytic Formulation

Shown in Figure 1 is a TM_z electric field incident on an infinitely long (no z-variation) wire with N concentric, dielectric coatings (regions 1 to N) where each region has it's own constitutive parameters (ε_r,μ_r, and k_m). From Harrington [1] we know that the total electric field for the N+1 region (free space) is defined as

$$\mathbf{E}^t_{z,N+1} = \mathbf{E}^i_{z,N+1} + \mathbf{E}^s_{z,N+1} = \mathbf{E}_0 \sum_{n=-\infty}^{+\infty} j^{-n}(J_n(k_{N+1}\rho) + a_n H^{(2)}_n(k_{N+1}\rho))e^{jn\phi} \tag{1}$$

and for regions m≤N, the total electric field is defined as

$$\mathbf{E}^t_{z,m} = \mathbf{E}^i_{z,m} + \mathbf{E}^s_{z,m} = \mathbf{E}_0 \sum_{n=-\infty}^{+\infty} j^{-n}(b_{n,m} J_n(k_m\rho) + c_{n,m} N^{(2)}_n(k_m\rho))e^{jn\phi} \tag{2}$$

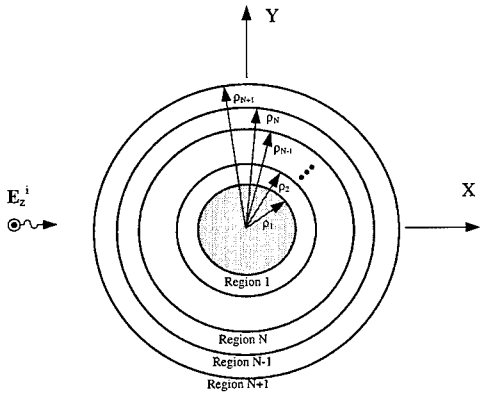


Figure 1: Geometry of Problem. Circular PEC cylinder coated with N layers of dielectric material.

where the subscript m denotes the region, $\mathbf{E}^t_{z,m}$ is the z-component of the total electric field, $\mathbf{E}^i_{z,m}$ and $\mathbf{E}^s_{z,m}$ are the incident and scattered z-directed fields respectively, and E_0 is the magnitude of the incident field. J_n is the Bessel function of the first kind, N_n is the Neumann function, and $H_n^{(2)}$ represents the Hankel function of the second kind. A_n, $b_{n,m}$, and $c_{n,m}$ are all coefficients modifying the Bessel functions. Solving for the coefficients is necessary to determine the scattered field, and thus the RCS. In order to do this, we use the boundary conditions

$$\mathbf{E}^t_{z,Region\ m}(\rho = \rho_1) = 0.0 \tag{3}$$

$$\mathbf{E}^t_{z,Region\ m}(\rho = \rho_{m+1}) = \mathbf{E}^t_{z,Region\ m+1}(\rho = \rho_{m+1}) \text{ for all } \rho_m \ 2{\leq}\text{m}{\leq}\text{N}{+}1 \tag{4}$$

$$\mathbf{H}^t_{\phi,Region\ m}(\rho = \rho_{m+1}) = \mathbf{H}^t_{\phi,Region\ m+1}(\rho = \rho_{m+1}) \text{ for all } \rho_m \ 2{\leq}\text{m}{\leq}\text{N}{+}1 \tag{5}$$

Application of Maxwell's equations and these boundary conditions to 1 and 2 give us the following solution for a_n

$$a_n = -\left(\frac{J_n(k_{N+1}\rho_{N+1}) - J_n'(k_{N+1}\rho_{N+1})D_{n,N+1}}{H_n^{(2)}(k_{N+1}\rho_{N+1}) - H_n'^{(2)}(k_{N+1}\rho_{N+1})D_{n,N+1}}\right) \tag{6}$$

where

$$D_{n,m} = \begin{cases} 0 & \text{if m=1} \\ \frac{\eta_{m-1}}{\eta_m}\frac{J_n(k_{m-1}\rho_m)+F_{n,m-1}N_n(k_{m-1}\rho_m)}{J_n'(k_{m-1}\rho_m)+F_{n,m-1}N_n'(k_{m-1}\rho_m)} & \text{otherwise} \end{cases} \tag{7}$$

and

$$F_{n,m} = -\left(\frac{J_n(k_m\rho_m) - J_n'(k_m\rho_m)D_{n,m}}{N_n(k_m\rho_m) - N_n'(k_m\rho_m)D_{n,m}}\right) \tag{8}$$

In order to determine a_n, $F_{n,1}$ must be solved. This can then be used to solve for $D_{n,2}$ which is used to solve for $F_{n,2}$. This process is repeated until $D_{n,N+1}$ is determined, at which point a_n can be calculated.

Once the coefficient a_n has been determined, the scattered field, $\mathbf{E}_z^s$, is known, and so the RCS can be calculated. The formula for the RCS is defined as

$$\mathbf{RCS} = \lim_{\rho \to \infty} 2\pi\rho \frac{\mid E_z^s \mid^2}{\mid E_z^s \mid^2} \tag{9}$$

$\mathbf{E}_z^i$ is generally give as unity, so using the asymptotic formula of the Hankel function of the second kind reduces the formula to an easily calculable form. The formulas presented here were used to calculate the RCS when the coating is lossless for various cases, and compared against other methods [2]and [3], and shown to be in excellent agreement.

III Numerical Results

In this section analytic data is presented showing the effects of a RAM coating on a right cylinder. The frequency dependence of the relative permittivity and permeability of each material is shown in Figure 2 and the corresponding RCS in Figure 3 (RCS of cylinder without RAM also shown). Several methods for presenting the RCS results were considered and a contrasting of the behavior of each material to an un-coated wire was most appropriate (Figure 3)

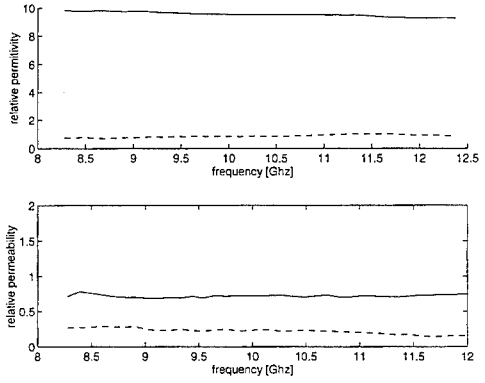


Figure 2: Real(–) and imaginary permittivity and permeability of RAM material over 8 to 12 Ghz range.

The use of frequency independent, but still lossy, RAM (ε and μ frequency independant) was included for the purpose of an additional comparison of the RAM material and is not representitive of any known RAM. However, because the use of a single value for ε and μ for a given RAM commonly occurs for a narrow band analysis of the RCS, both ε and μ were selected accordingly. Mid-band values (freq = 10.28 Ghz) were used as ε and μ for the frequency invariant RAM, and assumed to be constant over the entire X-band. Figure 3 clearly shows that the RCS versus frequency dependance is not strongly effected by the use of the average value of the RAM constituitive parameters. This indicates, at least for the cases considered, that an approximate or average value of certain parameters yield generally acceptable results. Figure 3, considering the permitivity and permeability to be constant over this frequency range gives comparable results to the plot of the RCS when the parameters vary with frequency. Both radar

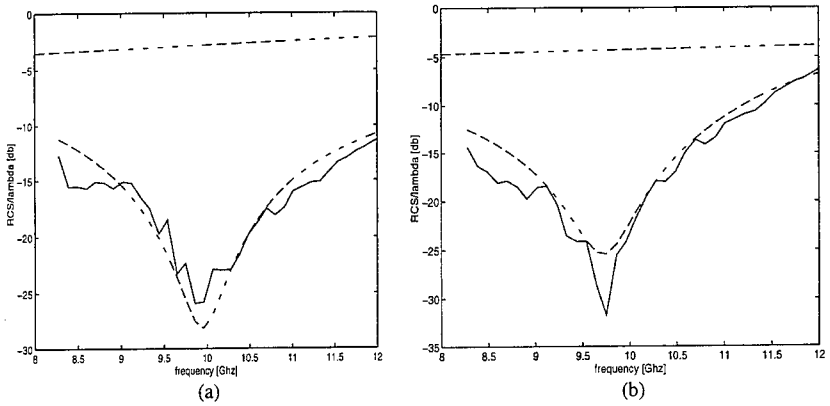


Figure 3: RCS/λ of (a) 5/16 and (b) 3/16 inch diameter wire with no coating (-.), with a 2.543 mm coating where the constitutive parameters are constant ε_r=9.511+i0.8679 μ_r=0.7326-i0.2186 (- -), and with a 2.543 mm thick coating with the frequency dependent parameters shown in Figure 2.

absorbing materials give the maximum attenuation at approximately the same frequency, but for the 5/16 inch wire, the frequency invariant RAM results have a minimum RCS approximately 3 dB lower than the frequency dependent RAM data. Also, for the 8.5 to 9.5 Ghz range, the frequency dependent RAM shows a smaller RCS. For the 3/16 inch wire, the frequency dependant RAM give a smaller RCS ($\approx$7 dB) for the low end of the X-band. This indicates that for a high degree of accuracy, the frequency dependence of the constituitive parameters must be taken into account.

It is also shown in Figure 3 that the frequency dependent RAM gives maximum attenuation at the frequency corresponding to a quarter wavelength in the material for the TM case. Figure 4 shows three RCS curves for varying thicknesses of the frequency independent RAM coating. The peak value of attenuation occurs at frequencies corresponding to a RAM thickness of $\lambda/4$. A comparison of the frequency varying RAM curves is shown in Figure 4.

IV Measurements

The measurements for the experimental data were conducted using a Naval Research Laboratory (NRL) arch arrangement configured with dual-ridged broadBand transmit and recieve horns and a Hewlett Packard 8510 B Network Analyzer with the time domain windowing option. The windowing option was used to isolate the power returns from the bare and RAM coated wires. In all cases the return from the bare and RAM coated wire was significantly higher than any system noise, and therefore a high degree of accuracy can be assumed for the measurements. Samples of the RAM material were analyzed, and the scattering parameters were calculated using the HP analyzer. The constituitive parameters were then extracted from the scattering matrix. Several samples were taken at different locations on each wire as a test for anisotrophies.

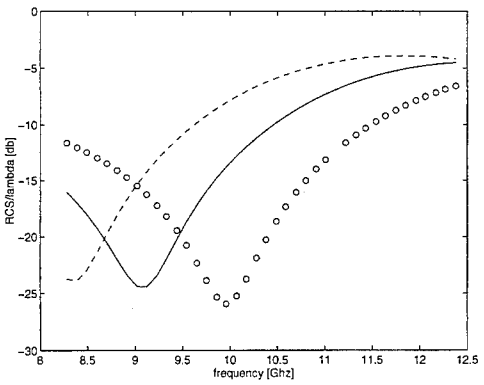


Figure 4: RCS/λ of a 3/16 inch diameter wire with a 2.5 mm RAM coating (oo), 2.75 mm RAM coating (-), and 3.0 mm RAM coating (- -). The constitutive parameters are constant ε_r=9.511+i0.8679 μ_r=0.7326-i0.2186.

V Conclusions

Careful consideration must be taken with the values of the constituitive parameters when modeling radar absorbing materials on conductors at high frequencies. Since variations in these parameters may significantly alter the calculated attenuation due to the concebtric RAM layer, attention must be given to obtain data reflecting the frequency dependence of complex permeability and permitivity if a high degree of accuracy is required. All simulations in the research showed good agreement with the measurements. A peak attenuation of 20-25 decibels was shown in the simulated case. This large value of attenuation was found to occur at frequencies corresponding to a RAM thickness of $\lambda/4$. It was also shown that an average value of ε and μ of the actual RAM (frequency dependent) could be used for approximate RCS values over a narrow frequency range for the TM mode considered.

References

[1] R.F.Harrington, *Time-varying Electromagnetic fields.* McGraw-Hill Inc., 1961.

[2] C. Lin and M. T. Yaqoob, "Electromagnetic scattering from a conducting cylinder covered with a multilayered dielectric," *Journal of Applied Physics*, vol. 72, pp. 788–790, July 1992.

[3] N. Wang, "Electromagnetic scattering from a dielectric coated cylinder," *IEEE Transactions on Antennas and Propagation*, vol. 33, pp. 960–963, Sept. 1985.

RCS OF HIGH PERMITTIVITY CUBES COMPUTED WITH THE TLM METHOD

Channabasappa Eswarappa and Wolfgang J. R. Hoefer

NSERC/MPR Teltech Research Chair in RF Engineering, Department of Electrical and Computer Engineering, University of Victoria, Victoria, B.C., CANADA V8W 3P6

ABSTRACT

In this paper, the three-dimensional time domain Transmission Line Matrix (TLM) method has been applied to compute the RCS of dielectric cubes of relative permittivity 37.84 and 79.46, and comparison has been made with published measurements [1]. Since the high permittivity cubes ring for a very long time, very good quality absorbing boundary conditions having long term stability are required. We have achieved these by modifying Higdon's absorbing boundary conditions. Long term stability has been obtained by using proper discretization of the boundary operators (derivatives), and very low reflections have been obtained by concatenating two first-order boundary operators. We have obtained stability beyond 60,000 time steps by placing the absorbing boundaries just 20 cells away from the cube surfaces (cube size is 15 cells). The RCS data computed with the TLM method agree very well with the measurements published in [1]. The frequency shift between the TLM results and the measurements is negligible, while a considerable frequency shift has been reported between results obtained with FDTD and measurement [1].

1. INTRODUCTION

The Transmission Line Matrix (TLM) method is a numerical technique in which both space and time are discretized [2]. The simulation of propagation of electromagnetic waves is done through scattering of impulses in a 3-D meshed network of transmission lines. This method is suitable for computation of radar cross-section (RCS) of complex bodies. The RCS over a wide frequency bandwidth can be obtained from a single TLM simulation. Earlier studies on computation of RCS using the TLM method have concentrated mainly on perfectly conducting targets [3-6]. This paper studies the scattering properties of high permittivity dielectric cubes. As these cubes ring for a very long time, highly stable absorbing boundary conditions are required for a TLM analysis as compared to the perfectly conducting targets. Eventhough a number of absorbing boundary conditions have been reported in the literature, Higdon's absorbing boundary conditions [7] have been found to perform better than others [8]. The absorption properties in the required frequency range can be optimized by taking advantage of the prior information about the incident angles and by combining several first-order boundary operators [9-10]. Also, the long term stability can be obtained by choosing the proper finite differences for the boundary operators.

We have used the symmetrical condensed node (SCN) TLM [11] (shown in Fig.1) for obtaining the scattered tangential electric and magnetic fields on the fictitious current surfaces. The advantages of this node when compared to the expanded TLM node and Yee's FDTD node are the following: boundary description is easier, and all six field components can be defined at single points in space. It has six branches, each branch consisting of two uncoupled two-wire transmission

lines. The 12 transmission lines linking the Cartesian mesh of nodes together have the characteristic impedance of free space. Each line is associated with two fields. For example, a voltage impulse incident upon the port 3 is associated with the field quantities E_y and H_z.

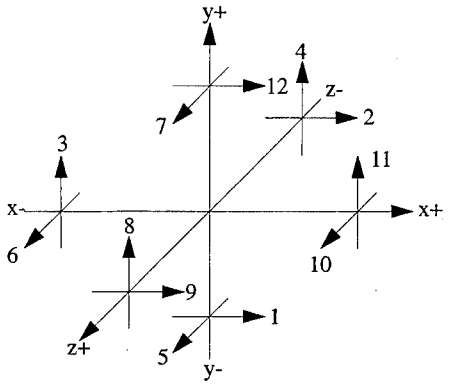


Fig. 1: The Symmetrical Condensed Node

2. ABSORBING BOUNDARY CONDITIONS

To obtain good absorption over a wide range of incident angles, we have concatenated two first-order Higdon's boundary operators to obtain a second-order absorbing boundary condition [9]. A voltage impulse reflected from the absorbing boundary can be computed from the knowledge of impulses in the cells in front of the boundary using the following equation:

$$\begin{aligned} V^n(m,j,k) \;=\; & (\alpha_1+\alpha_2)\,V^{n-1}(m,j,k) - \alpha_1\alpha_2 V^{n-2}(m,j,k) \;+ (\beta_1+\beta_2)\,V^n(m-1,j,k) \\ & + (\gamma_1+\gamma_2-\alpha_1\beta_2-\beta_1\alpha_2)\,V^{n-1}(m-1,j,k) - (\alpha_1\gamma_2+\gamma_1\alpha_2)\,V^{n-2}(m-1,j,k) \\ & -\beta_1\beta_2 V^n(m-2,j,k) - (\beta_1\gamma_2+\gamma_1\beta_2)\,V^{n-1}(m-2,j,k) - \gamma_1\gamma_2 V^{n-2}(m-2,j,k) \end{aligned} \tag{1}$$

The interpolation coefficients are:

$$\alpha_i = \frac{(a-g_i(1-b))}{(a-1-g_i(1-b)-\varepsilon_i\Delta l)},\ \beta_i = \frac{(a-1+g_i b)}{(a-1-g_i(1-b)-\varepsilon_i\Delta l)},\ \gamma_i = \frac{(-a-bg_i)}{(a-1-g_i(1-b)-\varepsilon_i\Delta l)} \tag{2}$$

where coefficients a and b are weighted time and space averages of the space and time differences, respectively. ε_1 and ε_2 are damping factors. The parameter g_i is

$$g_i = \frac{\cos\theta_i}{c}\,\frac{\Delta l}{\Delta t} \tag{3}$$

where Δl and Δt are the space resolution and time step respectively. θ_i are the incidence angles. For the symmetrical condensed node, g_i becomes $g_i = 2\ \cos\theta_i$.

The values of a and b can be chosen to control the stability of the absorbing boundaries. According to Higdon [7], a must be less than or equal to 0.5 (for $a=b$) to get stable absorbing boundary conditions.

3. NEAR-FIELD TO FAR-FIELD TRANSFORMATION

The near-field to far-field transformation technique based on the equivalence principle is well known. According to this principle, the far electromagnetic field components can be computed if the tangential electric and magnetic fields on a closed fictitious surface surrounding the scatterer are known. If the fields outside of the closed surface are E_s and H_s, then the surface electric and magnetic current densities are

$$J_s = \hat{n} \times H_s, \qquad M_s = -\hat{n} \times E_s, \tag{4}$$

where $\hat{n}$ is the local surface unit normal. These current densities can be calculated using the TLM method. These should be calculated at the required number of frequencies and stored for further processing. After the current densities have been computed, the electric and magnetic vector potentials can be calculated from the following equations:

$$A = \frac{\mu e^{-jkr}}{4\pi r} \int_s J_s e^{jk(x_s \sin\theta\cos\phi + y_s \sin\theta\sin\phi + z_s\cos\theta)}\, ds \tag{5}$$

$$F = \frac{\varepsilon e^{-jkr}}{4\pi r} \int_s M_s e^{jk(x_s \sin\theta\cos\phi + y_s \sin\theta\sin\phi + z_s\cos\theta)}\, ds \tag{6}$$

where x_s, y_s, and z_s are the co-ordinates of the source point on the current surface. θ and ϕ are the spherical co-ordinates of the far point. The far-field electric components can be computed from the knowledge of electric and magnetic vector potentials:

$$E_\theta = -j\omega (A_\theta + \eta F_\phi), \quad E_\phi = -j\omega (A_\phi - \eta F_\theta), \tag{7}$$

where η is the free space impedance.

4. NUMERICAL RESULTS

The dielectric cube of size 8.97 mm and permittivity 37.84 was discretized into 15 SCN-TLM cells on each side. The space resolution and time step were 0.598 mm and 0.9966 ps, respectively. A plane wave with a electric field component E_y and magnetic field component H_z was incident on one face of the cube normally (shown in Fig. 2). This was achieved in the symmetrical condensed node by launching the impulses on branch 3. We have used a cosine modulated Gaussian pulse (shown in Fig. 3) as the excitation to make sure that only the frequencies of interest were excited. This also ensured that the D.C. and very low frequencies were not excited, otherwise, the absorbing boundaries could not be placed close to the cube surface. The excitation Gaussian pulse width (corresponding to -34 dB) was 127 Δt. The values of the incidence angles used in the design of the absorbing boundaries were 45^o and 85^o. The absorbing boundaries were placed 20 cells away from the cube surfaces. The time response of the E_y field for two sets of coefficients a

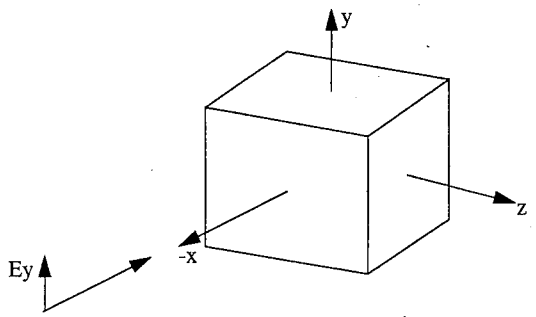


Fig. 2: The high permittivity cube with incident electric field E_y

(weighted time average of the space difference) and *b* (weighted space average of the time difference) are plotted in Figs. 4a and 4b. Note that the oscillations start around 2500 time steps for the case $a=b=0.25$, while there is no stability problem for $a=b=-0.25$. Hence, we have used $a=b=-0.25$ in all our computations. Stability beyond 60,000 time steps has been obtained in both dielectric cubes of permittivity 37.84 and 79.46 with just 20 cells separating the cube edges and the absorbing boundaries, while growing oscillations beyond 32,768 time steps have been reported in the FDTD analysis of the cube of permittivity 79.46 using Mur's absorbing boundaries (in spite of twice the spacing of 40 cells between the cube edges and the absorbing boundaries).

The computed RCS for 15,000 TLM time steps is plotted in Fig. 5. When compared with the measured results (Fig. 6), it can be seen that the convergence is not yet reached. Fig. 6 shows the RCS data computed with 60,000 time steps. They compare well with the measurements.

Next, we have computed the RCS of a cube of size 7.72 mm and $\varepsilon_r=79.46$ [1]. Again, the same TLM discretization as above (i.e., 15 cells along the length of the cube and 20 cells between the cube edge and the absorbing boundaries) was used. The space resolution and time step were 0.5147 mm and 0.8578 ps, respectively. The width of the cosine modulated Gaussian pulse was 148 Δt. Fig. 7 compares the computed RCS (using 60,000 TLM time steps) and measurement. They compare well except for a slight shift in the TLM results towards lower frequencies because of the coarseness error.

5. CONCLUSIONS

The RCS of high permittivity dielectric cubes has been obtained using the TLM method. The results agree very well with the measurements published in [1]. While the frequency shift between the TLM results and the measurements is negligible for $\varepsilon_r=37.84$, it is very small in the case of $\varepsilon_r=79.46$. A much larger shift has been reported in the FDTD analysis.

Our study shows that Higdon's absorbing boundaries have superior absorption and long term stability. Also, they are very efficient since they need to be placed only 20 cells away from the cube surfaces.

The frequency domain near-field to far-field transformation technique requires huge disk space to store the tangential electric and magnetic fields on the fictitious current surfaces (of the order of

100 Mbytes for 100 frequency points). One way of avoiding this is to compute the far-fields directly in the time domain as done in [12]. In that case, Prony's method can be applied to estimate the future time response from a short initial time response, leading to a very fast TLM analysis. Our future work will concentrate on these techniques.

REFERENCES

[1] C.W. Trueman, S.J. Kubina, R.J. Luebbers, S.R. Mishra, and C. Larose, "RCS of High Permittivity Cubes by FDTD and by Measurement", *9th Annual Review of Progress in Applied Computational Electromagnetics* Digest, pp. 2-10, March 22-26, 1993, Monterey, CA.

[2] W. J. R. Hoefer, "The Transmission Line Matrix (TLM) Method", in T. Itoh: *Numerical Techniques for Microwave and Millimeter Wave Passive Structures*, John Wiley & Sons, New York (1989).

[3] F.J. German, G.K. Ghothard, L.S. Riggs, and P.M. Goggan, "The Calculation of Radar Cross-section (RCS) Using the TLM Method", Int. J. Numer. Modelling, vol. 2, no. 4, pp. 267-278, Dec. 1989.

[4] N.R.S. Simons and E. Bridges, "Application of the TLM Method to Two-Dimensional Scattering Problems", Int. J. Numer. Modelling, vol. 5, pp. 93-110, 1992.

[5] M. Khalladi, J.A. Morente, and J.A. Porti, "RCS of Arbitrarily-Shaped Targets with the TLM Method", *IEEE Trans. on Antennas and Propagation*, vol. 42, no. 6, pp.891-893, June 1994.

[6] F.J. German, "General Electromagnetic Scattering Analysis by TLM Method", Electronics Letters, vol. 30, no. 9, pp. 689-690, 28th April 1994.

[7] R. L. Higdon, "Numerical absorbing boundary condition for the wave equation," *Mathematics of Computation*, vol. 49, no. 179, pp. 65-91, July 1987.

[8] D. Steich and R. Luebbers, "Comparison and Generation of Higher Order FDTD Absorbing Boundaries", *10th Annual Review of Progress in Applied Computational Electromagnetics* Digest, pp. 212-233, March 21-26, 1994, Monterey, CA.

[9] C. Eswarappa and W.J.R. Hoefer, "One-Way Equation Absorbing Boundary Conditions for 3-D TLM Analysis of Planar and Quasi-planar Structures", *IEEE Trans. Microwave Theory Techniques*, vol. 42, no. 9, pp. 1669-1677, Sep. 1994.

[10] Z. Chen, M.M. Ney, and W.J.R. Hoefer, "Absorbing and Connecting Boundary Conditions for the TLM Method", *EEE Trans. Microwave Theory Tech.*, vol. MTT-41, no. 11, pp. 2016-2024, 1993.

[11] P. B. Johns, "Symmetrical Condensed Node for the TLM method", *IEEE Trans. Microwave Theory Tech.*, vol. MTT-35, no. 4, pp. 370-377, April 1987.

[12] R.J. Luebbers, K.S. Kunz, M. Schneider and F. Hunsberger, "A Finite-Difference Time-Domain Near Zone to Far Zone Transformation", *IEEE Trans. on Antennas and Propagation*, vol. AP-39, No. 4, pp. 429-433, April 1991.

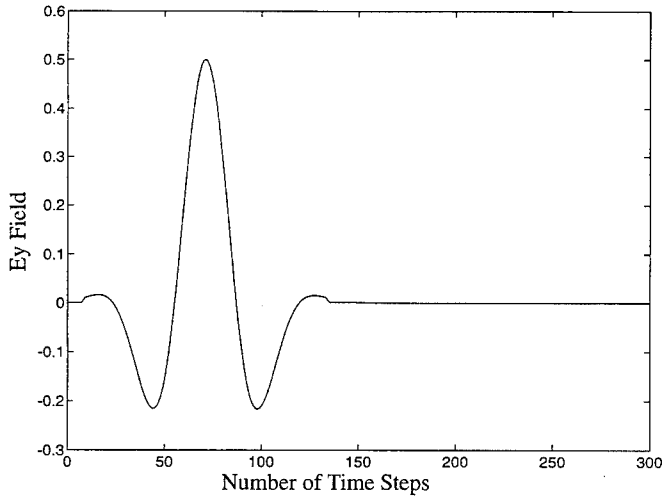


Fig. 3: Cosine modulated Gaussian temporal profile for the plane wave excitation

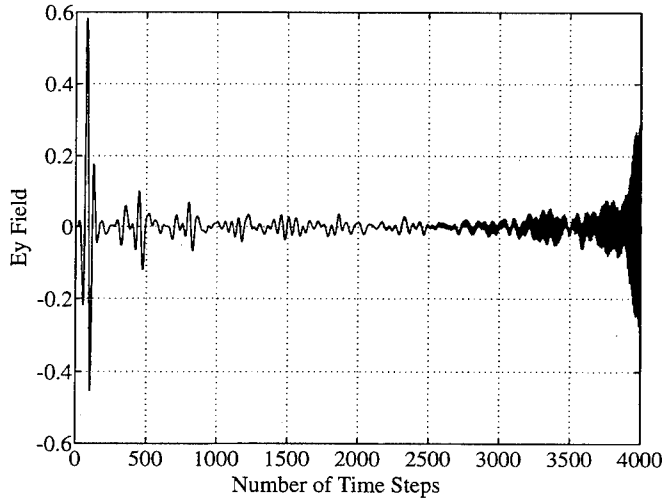


Fig. 4a: Time response of the high permittivity cube for a=b=0.25 (ε_r=37.84, θ_1=45 ^{0}, θ_2=85^0)

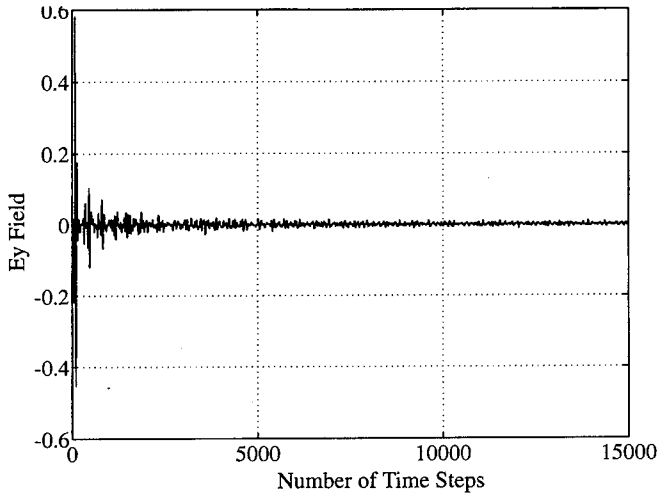


Fig. 4b: Time response of the high permittivity cube for a=b= - 0.25 (ε_r=37.84, θ_1=45 ^{0}, θ_2=85^0)

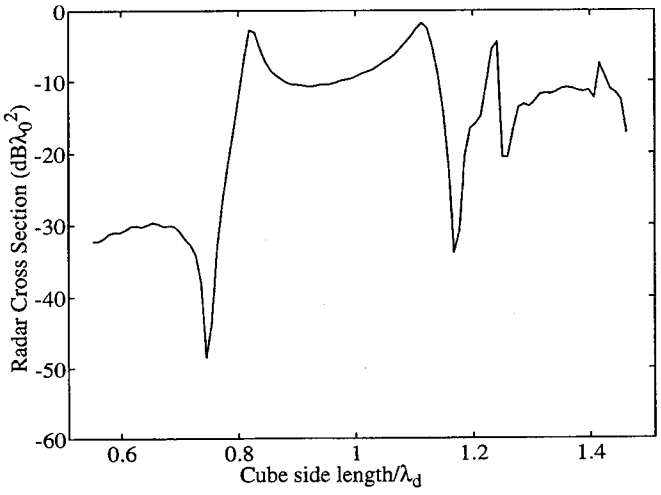


Fig. 5: RCS computed with 15,000 TLM time steps (cube side length = 8.97 mm, ε_r = 37.84, bistatic angle = 8 degrees)

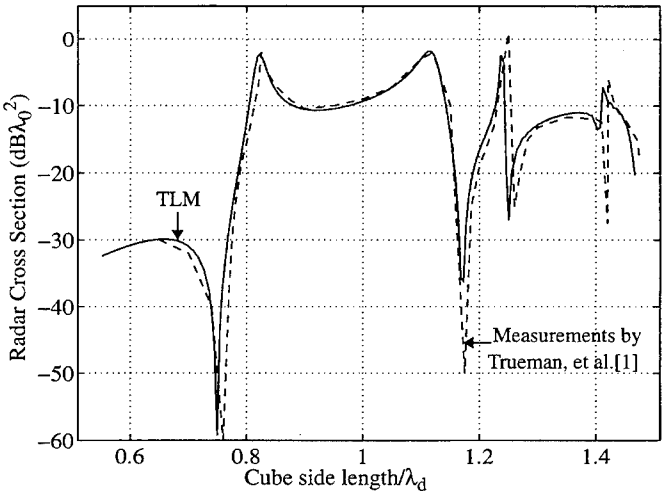


Fig. 6: RCS computed with 60,000 TLM time steps (cube side length = 8.97 mm, $\varepsilon_r = 37.84$, bistatic angle = 8 degrees)

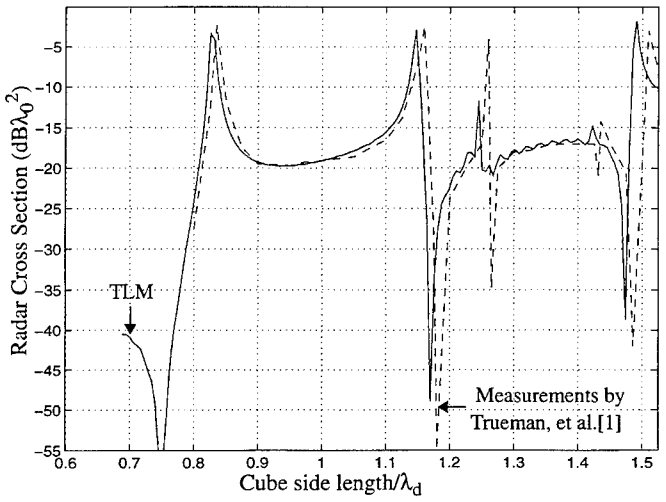


Fig. 7: RCS computed with 60,000 TLM time steps (cube side length = 7.72 mm, $\varepsilon_r = 79.46$, bistatic angle = 8 degrees)

SCATTERING ANALYSIS OF ANTENNA INSTALLATIONS/PANELS ON A CURVED SURFACE USING UNIFORM FIELD INTEGRATION METHOD

Jacob J. Kim and Oren B. Kesler*

Texas Instruments Incorporated
2501 W. University, M/S 8019
McKinney, Texas 75070

ABSTRACT

An efficient computer algorithm has been developed to predict accurate three-dimensional backscattering RCS levels from antenna/array installations or panels/doors on an electrically large curved surface such as aircrafts and missiles. The new algorithm significantly reduces the computation time of a scattering prediction code(UFIM) while maintains the same accuracy of the prediction. This paper describes the new process which was incorporated into the UFIM code and demonstrates its enhanced capability as an efficient design tool for the practical antenna/array installations or panels/doors on a large curved scattering object.

INTRODUCTION

The electromagnetic(EM) contribution from antenna/array installations or panels/doors is a matter of increasing concern in radar scattering, especially for low observable(LO) vehicle design. Accurate RCS prediction of those complex discontinuities on a large scattering object is difficult due to lack of numerically efficient three-dimensional(3-D) analytic solutions or too many unknowns for matrix inversion. Measurement approaches are also limited due to quiet-zone size of indoor RCS measurement ranges and the high cost of the full-scale test model. Last year the Uniform Field Integration Method(UFIM)[1] was introduced as an efficient computational technique to accurately predict 3-D RCS levels from a contour along a piecewise continuous curve on a planar surface. The method utilizes simple two-dimensional(2-D) scattered field formulations. The contour was defined by any localized discontinuities of arbitrary cross section such as small step, slit, groove, dielectric filled gap, bump, impedance discontinuity, and coated or conducting wedges. The UFIM is a hybrid approach, bridging the gap between high frequency techniques for electrically large objects and low frequency techniques for electrically small objects. This paper describes an actual application of the UFIM to practical design problems of antenna/array installations and panels/doors on a large curved scattering object and its significant improvement in computational efficiency.

NEW UFIM PROCESS

A typical UFIM analysis process on a curved surface is shown in Figure 1. The contour on a smooth curved surface can be approximated with a piecewise continuous curve if the size of each piecewise section is very small (e.g., less than 0.1λ). Then the total 3-D RCS levels from the contour can be obtained by summing 3-D scattering contributions from all piecewise sections along the contour. The 3-D scattering contribution from each piecewise section can be obtained by an UFIM process. The UFIM process is very efficient for predicting 3-D RCS levels from any discontinuities on a surface, because only 2-D scattered fields from the discontinuity are required instead of 3-D. It is noted that some assumptions made in the UFIM analysis process are listed in the UFIM Features in Figure 1. The simple 2-D scattered fields may be obtained by full wave computations such as method of moments(MOM), Finite Element Method(FEM), Finite Difference Time Domain(FDTD), or Transmission Line Matrix(TLM), or by simple planar measurements[2]. The UFIM is an efficient 2-D to 3-D conversion process and calculates the 3-D backscattering RCS directly from the 2-D scattered field of the contour. However, in the course of computing the scattering from antenna/array installations on a electrically large curved surface, numerous solutions to the 2-D problem are needed due to many piecewise sections simulating the surface curvature. That results in the major computation time because most 2-D solutions are numerically rigorous but very computationally extensive. Therefore, a new algorithm has been developed and implemented into the UFIM code to reduce the burden of massive 2-D scattered field computation. The reduced computation time is a result of the fact that the cross sectional dimension of a discontinuity is small compared to a wavelength (e.g., typically less than 0.1λ). Figure 2 shows the magnitude and phase plots of the 2-D scattered field from a groove (width = 0.15cm, depth = 0.11cm) computed by SWAG code[3]. The plots show the characteristics of slowly varying magnitude and phase of the 2-D scattered field for the whole elevation angles. Since the 2-D scattered field from an electrically small discontinuity is not sensitive to the elevation angles, one needs to compute a single elevation pattern of 2-D scattered field only once for the whole RCS pattern computation. One may store the 2-D scattering data for discrete elevation angles and retrieve the stored sample data using a simple searching program whenever a 2-D scattered field data is needed. The new process significantly reduces the computation time for discontinuities on a curved surface. A typical 3-D RCS pattern of an antenna installation on a missile body takes only several seconds which previously took an hour or so.

To validate the new UFIM process, a test model with a groove on a curved surface(total length = 95cm, diameter = 8cm) were constructed as shown in Figure 3. The test model consists of an ogive, a cylinder, and an ogive with a groove (width = 0.15cm, depth = 0.11cm) between the front ogive and the cylinder. The results of new UFIM prediction were compared with actual 3-D RCS measurements for both horizontal and vertical polarizations in Figure 3. All comparisons showed very good agreement besides some ripples in the measured data due to the traveling wave contributions. The body scattering from the ogive-cylinder-ogive test model is also computed using Physical Theory of Diffraction(PTD) technique to show the significance of the scattering from the groove even though its cross sectional dimension is less than 0.1λ. A practical antenna installation problem has been analyzed using the new UFIM process. A groove (width = 0.15cm, depth = 0.11cm) along a typical antenna boundary (5cm $\times$ 5cm square patch) is modeled on a cylinder (diameter = 15.25cm). Figure 4 shows a square shaped antenna mounted on a curved surface and its edge is perpendicular to the nose-on direction. Figure 5 shows the same antenna mounted on a

curved surface but its edge is 45° rotated to the nose-on direction. Two 80° conical RCS patterns were calculated for the vertical polarization using the new UFIM process. The comparison of two RCS patterns in Figures 4 and 5 clearly shows the scattering dependency on the antenna edge shape. A few other shapes such as panels and doors on a curved surface were also analyzed using the new process. The efficiency of the UFIM code has been significantly improved by the new process while the new process maintains the same accuracy of the scattering data. Several volumetric RCS patterns were also generated for antenna installations and panels on a curved surface using the new process and took only a few minutes for a typical volumetric pattern. The new UFIM code has demonstrated its full capability as an efficient design tool for the practical antenna/array installations or panels/doors on a large curved scattering object.

CONCLUSIONS

A new computer algorithm has been developed to enhance the capability of the 3-D scattering code(UFIM) for antenna/array installations or panels/doors on an electrically large curved surface. The algorithm significantly reduces the computation time of the UFIM while maintains the same accuracy of the prediction. Several test models were made and the UFIM predictions were compared with 3-D measurements. All test results showed very good agreement. This paper demonstrated its enhanced capability as an efficient design tool for the practical antenna/array installations or panels/doors on a large curved scattering object. Another feature is that one can readily isolate the RCS contribution from electrically small discontinuities on a practical vehicle using the UFIM process. The main advantages of the new process are simplicity, computation efficiency, and its vast application to many complex EM scattering problems which may be occurred in antenna/array installations or panels/doors on a large scattering object.

REFERENCES

[1] Jacob J. Kim and Oren B. Kesler, "Efficient Computational Technique for Backscattering from a Discontinuity along a Piecewise Continuous Curve on a Planar Surface," in Proc. 10th Annual Review of Progress in Applied Computational Electromagnetics, Monterey, CA, pp. 465-472, Mar. 1994.

[2] Jacob J. Kim, Thomas S. Watson, and Oren B. Kesler, "Efficient RCS Measurement Technique of a Complex Discontinuity on a Large Scattering Object," in Proc. Sixteenth Annual Antenna Measurement Techniques Association Symposium, Long Beach, California, pp. 70-75, Oct. 1994.

[3] S.C. Gibson, B.C. Graham-Jones, B.L. Horning, M.M. Jones, O.G. Romero, and C.W. Yang, "Scattering from Generic Surface Discontinuities, Part VI: User Manuals," Northrop Corporation Aircraft Division, December 1989.

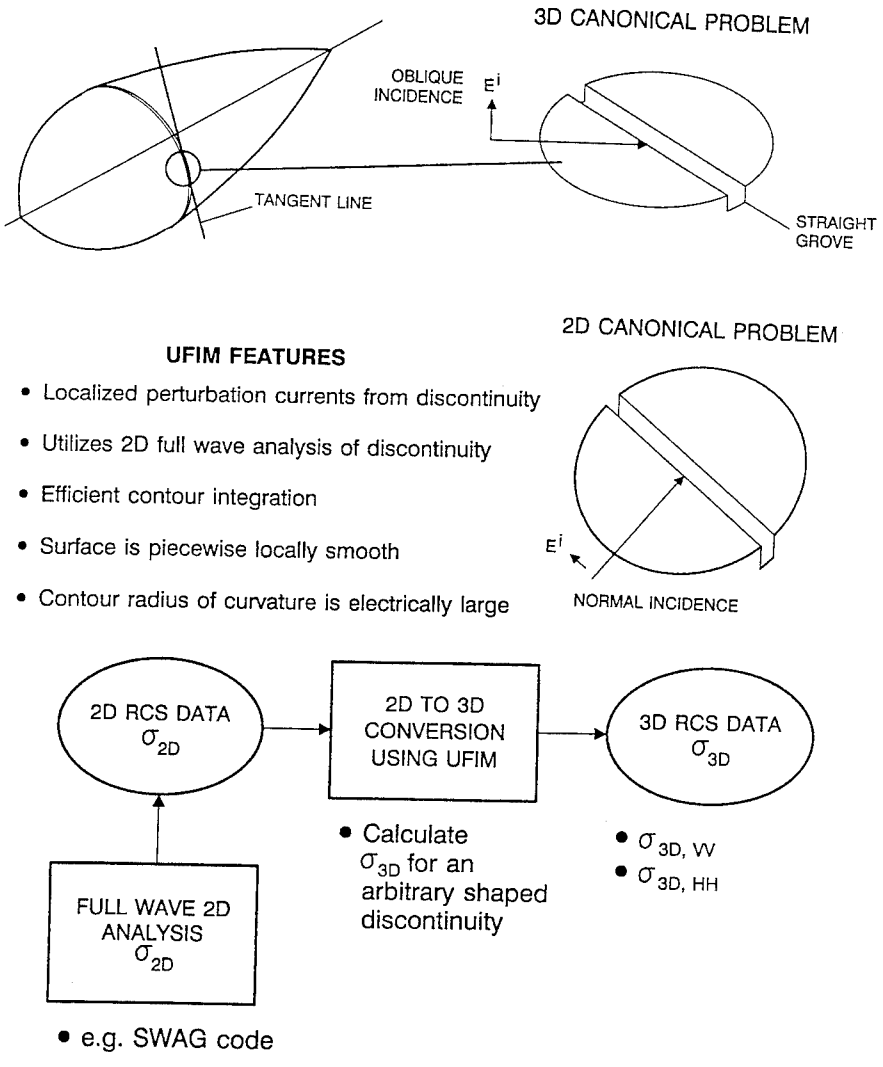


Fig. 1. UFIM analysis process on a curved surface.

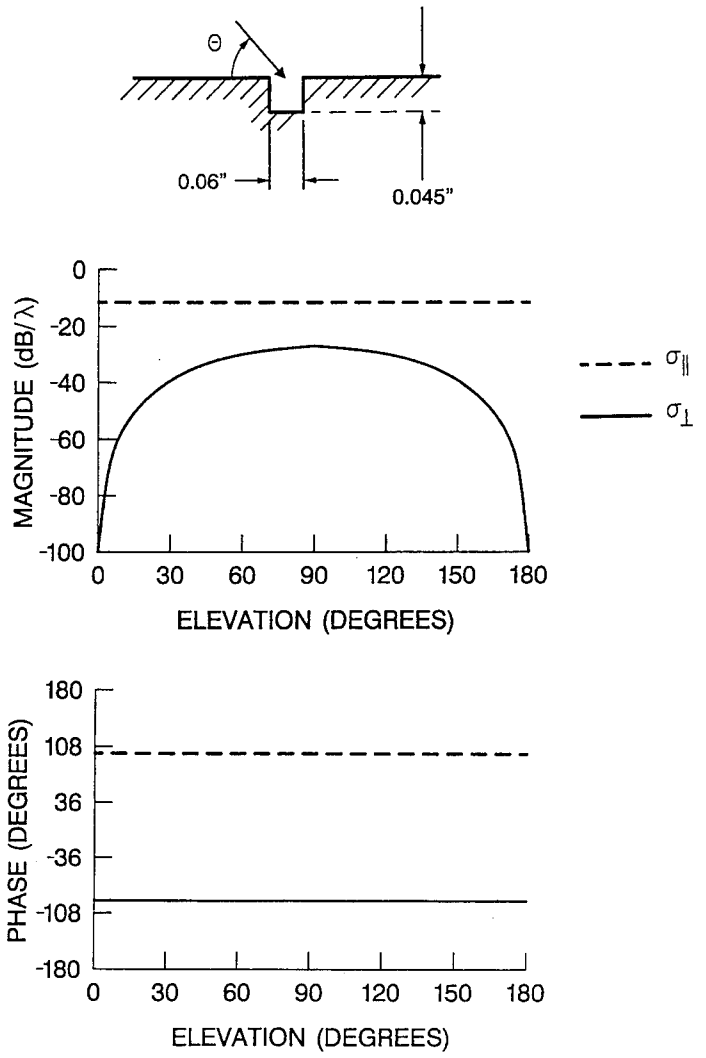


Fig. 2. Two-dimensional RCS data of a groove at 18 GHz.

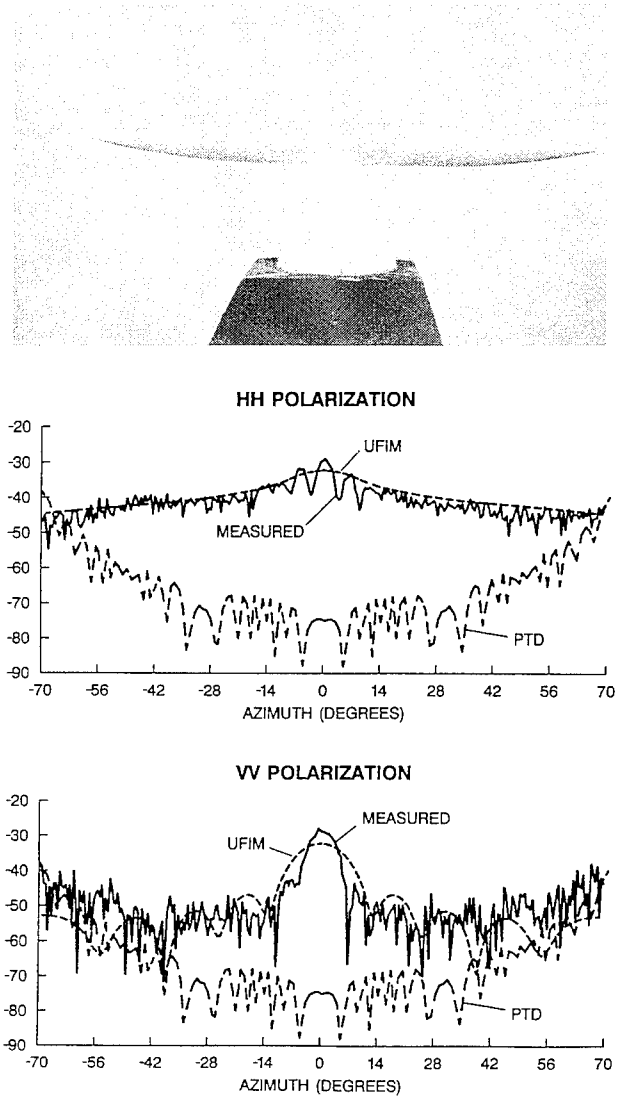


Fig. 3. Azimuth RCS patterns of a groove on a curved surface at 18 GHz.

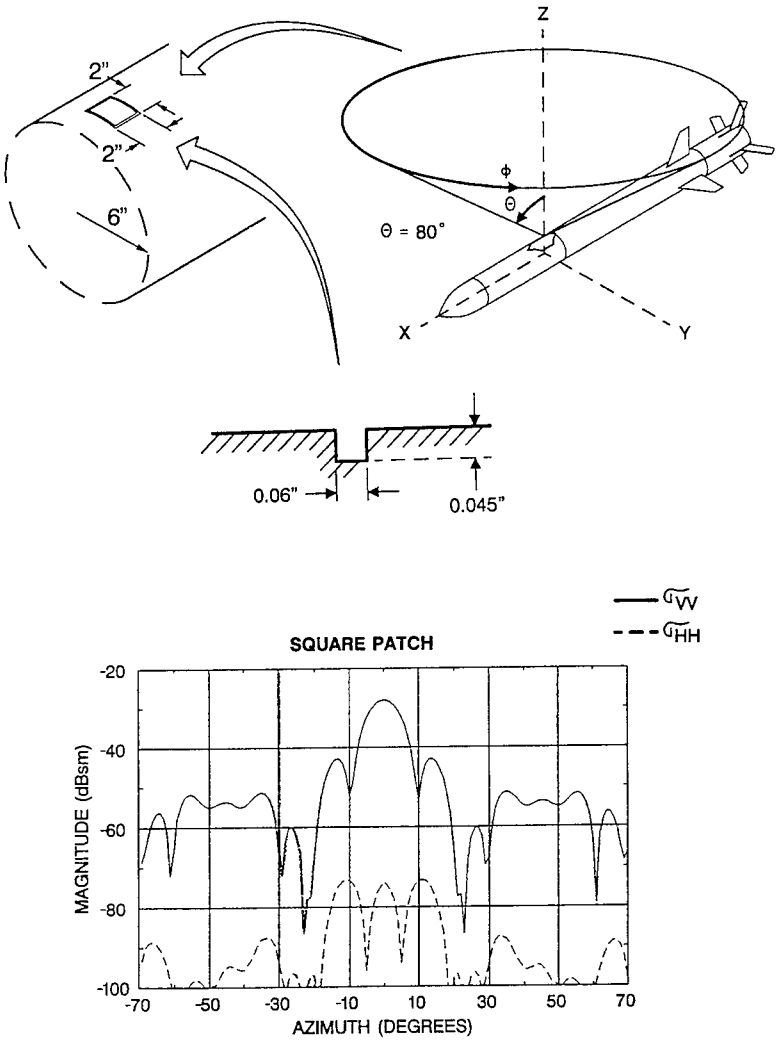
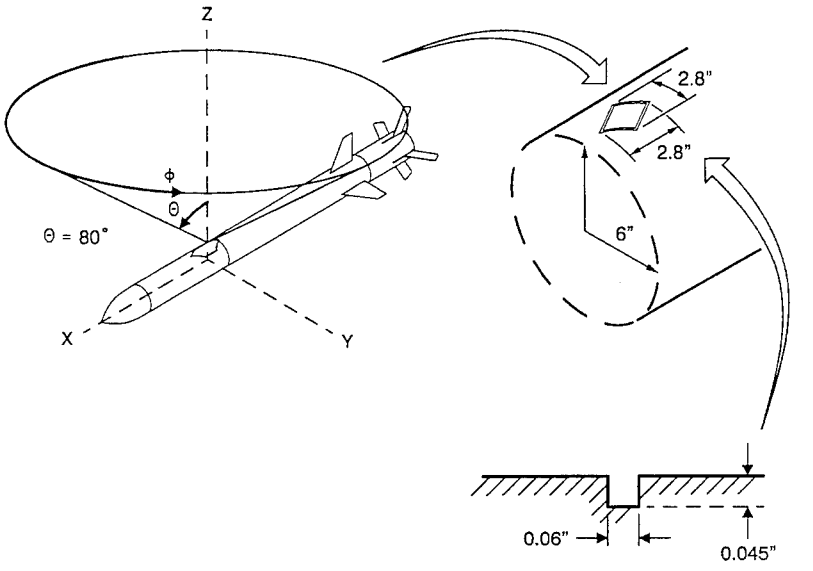


Fig. 4. A 80° conical RCS pattern from antenna installations of a square patch at 18 GHz.



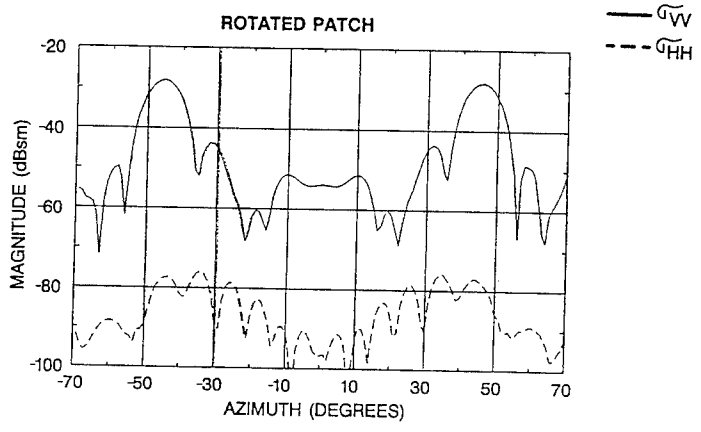


Fig. 5. A 80 ° conical RCS pattern from antenna installations of a 45 ° rotated patch at 18 GHz.

CODE VALIDATION OF AIRCRAFT SCATTERING PARAMETERS USING IR THERMOGRAMS

John Norgard*, Ronald Sega**, **Michael Seifert*****, **Timothy Blocher*****, **Anthony Pesta*****

**US Air Force Academy & University of Colorado*
***NASA Johnson Space Center*
****Rome Laboratory RL/ERST*

Abstract

An infrared (IR) measurement technique is presented which has been developed to measure electromagnetic (EM) fields. This technique uses the thermal absorption properties of a thin, planar, and lossy IR detection screen to map the intensity of the EM energy over any two-dimensional region of interest. This measurement produces a two-dimensional IR thermogram of the electric or magnetic field being measured, i.e. an isothermal contour map of the intensity of the EM field. As an example, IR thermograms are presented for the diffraction pattern of the EM field scattered from an F16 scale model aircraft for various microwave frequencies, angles of incidence, and polarizations of the incident wave and for several different orientations of the aircraft relative to the incoming radiation. The experimentally determined IR thermogram for the scattered electric field for nose-on, horizontally-polarized (plane of the aircraft wings) illumination at 3 GHz is compared to the scattered electric field computed for the same case by the GEMACS numerical electromagnetics code. The agreement between the techniques is discussed and used to validate the results of the code.

1. Introduction

A non-destructive, minimally perturbing infrared (IR) measurement technique has been developed to observe electromagnetic (EM) fields. Metallic surface currents and charges also can be measured with this technique.

This IR measurement technique produces a two-dimensional IR thermogram of the electric or magnetic field being measured, i.e. an isothermal contour map of the intensity of the EM field.

This IR measurement technique recently has been applied to determine microwave induced surface currents[1], radiated fields from antennas and high power microwave (HPM) sources, e.g. near-field intensities and far-field antenna patterns of horns[2-3], diffraction patterns of EM fields scattered from complicated metallic objects[4-7], intensities of EM fields coupled through apertures in shielded enclosures[8-11], and modal distributions of EM fields excited inside cavities[12-15].

Examples of EM energy scattered from an F16 scale model aircraft are presented in this paper. The results are compared to data predicted numerically by the GEMACS numerical electromagnetics code. The advantages and disadvantages of this new IR measurement technique are also discussed.

2. IR Measurement Technique

The IR measurement technique is based on the Joule heating that occurs in a lossy material as an EM wave passes through the material. A thin planar sheet of a lossy carbon loaded material is used to map electric fields; a thin planar sheet of a lossy ferrite loaded material is used to map magnetic fields. The absorbed heat energy is converted into conducted and convected heat energy and into re-radiated EM energy. The radiated EM energy is concentrated in the IR band, and is detected with an IR Scanning Array or an IR Focal Plane Array (FPA) as the energy radiated from a "blackbody".

2.1. IR Experimental Setup

This technique involves placing the lossy IR detection screen in the EM wave in the plane over which the fields are to be measured. The loss mechanisms in the detector material, i.e. the conductivity and the imaginary components of the permittivity and the permeability of the detector material, absorb the incident EM energy as thermal heat energy and cause the temperature of the detector to rise above the ambient temperature of the surrounding environment by an amount that is proportional to the local electric and/or magnetic field intensity (energy) at each point in the screen material. This produces a two-dimensional IR thermogram of the electric and/or magnetic field in the screen material.

2.2. IR Detector Screen

The screen material is tailored to be sensitive to only one component of the field, e.g. by optimizing the values of the electrical conductivity and the imaginary part of the permittivity of the material relative to the imaginary part of the permeability of the material, the detector screen can be made sensitive to only the tangential component of the electric or magnetic field in the plane of the screen. Care is also exercised in the selection of the screen material not to significantly perturb the electric or magnetic field by the presence of the lossy material. The screen is designed to absorb less than 5% of the incident power. The constitutive parameters of the IR detector screen are optimized to produce a large temperature rise in the detector material for a small amount of absorbed energy.

The temperature difference between the screen material and the background is detected, digitized, and stored in the memory of the IR camera on a pixel by pixel basis. The system has 256 by 256 pixels per frame of data. This stored data represents the temperature distribution over the extent of the detector screen and is a map of the intensity of the electric or magnetic field distribution absorbed in the screen. The incident electric or magnetic field can then be determined from a solution of Maxwell's Equations (Fresnel's and Snell's laws) for an EM wave incident on a planar film of lossy material. For small temperature rises, the electric or magnetic field intensity is nearly linearly proportional to the temperature change.

2.3. IR Advantages and Disadvantages

The IR measurement technique provides a quick and accurate method to observe EM fields in a two-dimensional plane. However, only the magnitude of the electric or magnetic field is measured; no phase information is detected. Also, since this technique is based on the thermal mass of a detector material, high energy is required to produce good thermal images of EM fields.

3. Scattering and Diffraction Patterns

As an example of the IR measurement technique, a 1:32 scale model of an F16 aircraft was constructed. A plastic model of an F16 was sprayed with several coats of silver paint to make its surface conductive. The model was irradiated in the far field of a microwave horn antenna, as shown in Figure 1. IR thermograms were made of the diffraction pattern of the EM field scattered from the model.

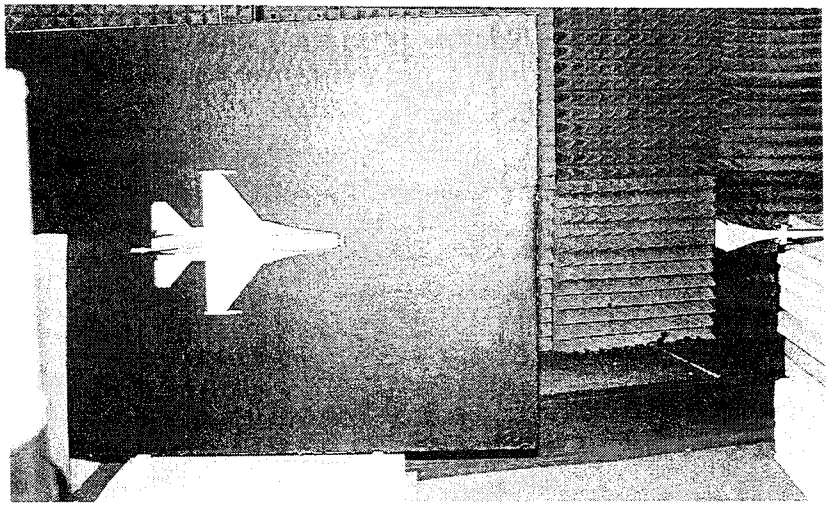


Figure 1. *IR Experimental Setup*

In the experiment, a large IR detector screen of carbon paper was positioned around the aircraft in several different orientations. For one series of IR thermograms, the screen was positioned in the axial plane through the middle of the aircraft. First, the screen was oriented in the plane passing through the wings of the aircraft to map the scattered fields tangent to the plane formed by the wings and the fuselage of the aircraft. Then, the screen was oriented in the plane passing through the tail stabilizer to map the scattered fields tangent to the plane formed by the tail stabilizer and the fuselage of the aircraft. For another series of IR thermograms, the screen was oriented in the transverse plane that intersected the middle of the wings of the aircraft, cf. Figure 1, to map the scattered fields in the cross section of the aircraft.

3.1. IR Measurements

Experimentally obtained IR thermograms of the scattered fields for the case of nose-on illumination are shown in Figure 2. The series of thermograms cover the 2 to 6 GHz range of frequencies. In each IR thermogram, the follow diffraction phenomena are discernable:

i) a standing wave between the source and the nose of the aircraft due to the scattered wave off the front of the aircraft
ii) a surface wave on each side of the aircraft between the nose and the missile rails on the wing tips
iii) a point of diffraction on the aft end of each wing tip
iv) a shadow zone behind the aircraft

Many configurations of the aircraft were tested at various other frequencies, polarizations, and angles of incidence. The IR thermograms shown in Figure 2 are typical of the results.

3.2. GEMACS Predictions

The test case of horizontally-polarized, nose-on illumination in the plane of the wings of the aircraft at 3 GHz was chosen to be modeled by the GEMACS code. The test configuration is shown in Figure 3. The electric field distribution as determined experimentally by the IR imaging technique and as determined numerically by the GEMACS code are both shown in Figure 3. The surface current which created the diffracted fields are also shown in Figure 3. The corresponding IR imaging data for the magnetic field was not determined experimentally.

After examining Figure 3, it can be noted that many features of IR image and the GEMACS data are in agreement, such as the prominent standing wave at the front of the aircraft, the surface waves along both sides of the aircraft, and the diffraction centers behind the wing tips. Overall, the comparison is good.

However, there are some areas of disagreement. The most obvious is the intense zone of scattering behind the aircraft in the GEMACS data, as compared to the shadow zone in the IR image. Some of these differences can be explained based on differences in the IR and

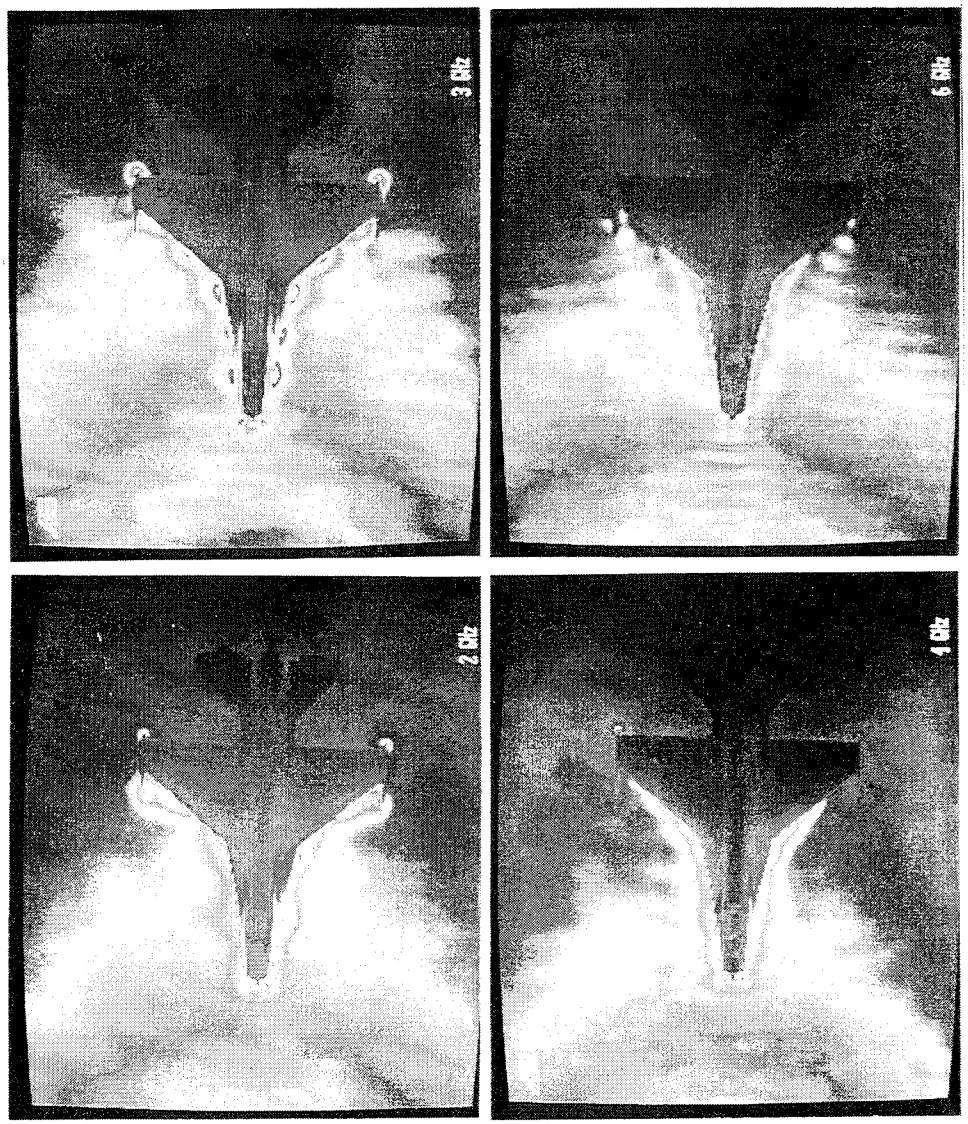


Figure 2. *IR Thermograms* (at 2,3,4 and 6 GHz)
Nose-on Illumination, Horizontal Polarization (plane of the aircraft wings)

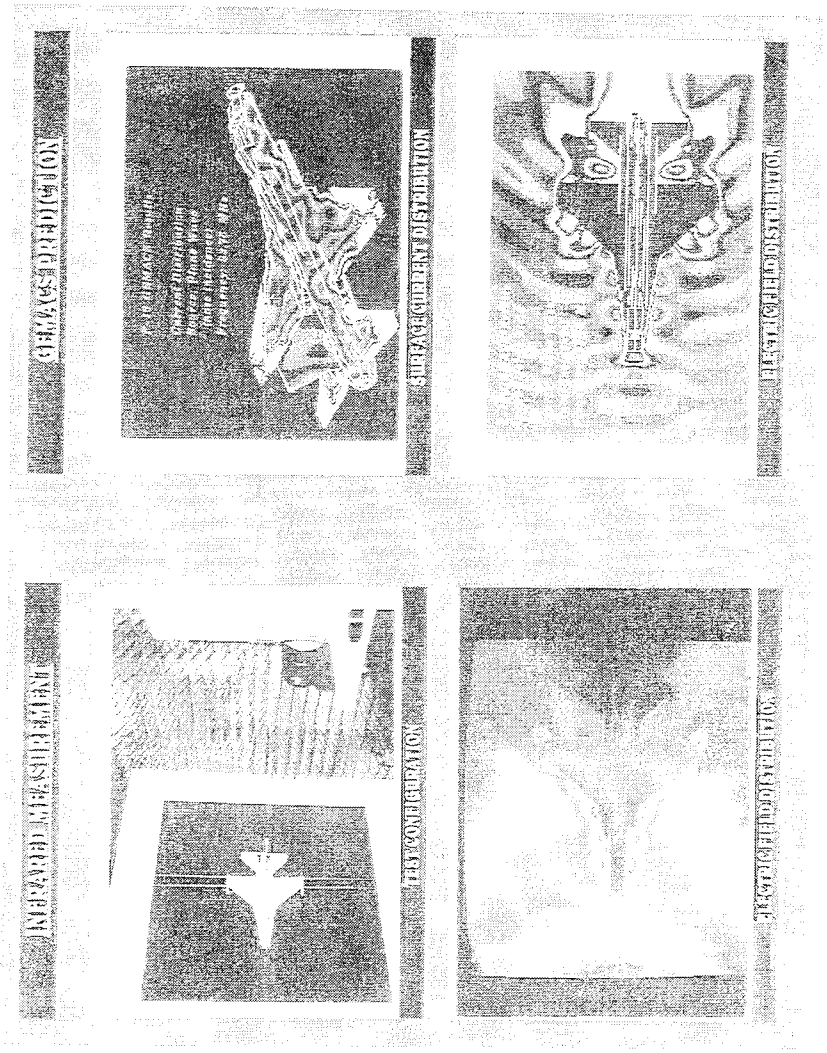


Figure 3. *IR Measurements and GEMACS Predictions* (at 3 GHz)
Nose-on Illumination, Horizontal Polarization (plane of the aircraft wings)

GEMACS models. The IR model of the F16 has missile rails; the GEMACS model does not, due to excessive computational time required to model this detail. Also, in the GEMACS model, the incident wave is truly a plane wave; whereas, in the IR model, the aircraft is being illuminated by a spherical wave.

An updated model of the F16, with missile rails installed and illuminated by a spherical point source, is being prepared for the GEMACS code, since the IR thermograms must be taken in the near field of the source, due to sufficiently high incident energy requirements on the model.

4. Conclusions

The IR measurement technique is a viable method to aid in the determination of EM fields scattered from complex metallic objects such as advanced aircraft models. The IR method allows for rapid observation of EM field activity and interference, resulting in an in-depth understanding of EM scattering phenomena. The technique can be used to verify the accuracy of EM codes by comparing the IR thermograms with the computed results.

Acknowledgements

The authors wish to acknowledge the work of Joseph Sadler at Phillips Laboratory who helped make the F16 scale model aircraft and take the IR thermograms and William Prather at Phillips Laboratory and Buddy Coffey at Advanced EM who ran the GEMACS code.

References

[1] Wetlaufer, G.D., Sega, R.M. and Norgard, J.D. - *Thermographic Detection of Microwave Induced Surface Currents.* Proceedings of the APS/URSI Symposium, May 1985, Vancouver, BC, Canada.

[2] Sega, R.M. and Norgard, J.D. - *Infrared Diagnostic Techniques for High-Power Microwave Measurements.* Proceedings of High Power Microwave Technology Meeting, December 1986, Albuquerque, NM.

[3] Metzger, D.W., Norgard, J.D. and Sega, R.M. - *Numerical Calculation & Experimental Verification of Near Fields from Horns.* IEEE-EMC Transactions, February 1992.

[4] Sega, R.M. and Norgard, J.D. - *Infrared Detection of Microwave Scattering from Cylindrical Structures.* Proceedings of the URSI Winter Meeting, January 1986, Boulder, CO.

[5] Sega, R.M. and Norgard, J.D. - *Infrared Measurement of Scattering and Electromagnetic Penetrations through Apertures.* IEEE-NS Transactions, Vol. NS-33, No.6, December 1986, pp. 1858-1883.

[6] Sega, R.M., Norgard, J.D. and Harrison, M.G. - *Infrared Comparisons of the Electromagnetic Scattering From Conducting and Dielectric Cylinders.* Proceedings of the Nuclear Electromagnetics Symposium, May 1988, San Francisco, CA.

[7] Norgard, J.D., Sega, R.M., Ianacone, K.J., Harrison, M.G., Pesta, A.T. and Seifert, M.A. - *Scattering Effects of Electric and Magnetic Field Probes.* IEEE-NS Transactions, Vol. NS-36, No. 6, December 1989, pp. 2050-2057.
[8] Sega, R.M. and Norgard, J.D. - *An Infrared Measurement Technique for the Assessment of Electromagnetic Coupling.* IEEE-NS Transactions, Vol. 32, No. 6, December 1985, pp. 4330-4332.
[9] Metzger, D.W., Sega, R.M., Norgard, J.D. and Bussey, P.A. - *Experimental and Theoretical Techniques for Determining Coupling Through Apertures in Cylinders.* Proceedings of the Nuclear Electromagnetic Meeting, May 1986, Albuquerque, NM.
[10] Sega, R.M. and Norgard, J.D. - *Expansion of an IR Detection Technique Using Conductive Mesh in Microwave Shielding Applications.* Proceedings of the SPIE Symposium, August, 1987, San Diego, CA.
[11] Smith, M.D., Sega, R.M. and Norgard, J.D. - *Infrared Detection of Electromagnetic Penetration through Narrow Slots in a Planar Conducting Surface.* Proceedings of the URSI National Radio Science Meeting, January 1990, Boulder, CO.
[12] Norgard, J.D. and Sega, R.M. - *Three-Dimensional Determination of Cavity Resonance and Internal Coupling.* Proceedings of the URSI Winter Meeting, January, 1987, Boulder, CO.
[13] Sega, R.M., Norgard, J.D. and Genello, G.J. - *Measured Internal Coupled Electromagnetic Fields Related to Cavity and Aperture Resonance.* IEEE-NS Transactions, Vol. NS-34, No. 6, December 1987, pp. 1502-1507.
[14] Norgard, J.D. and Sega, R.M. - *Measured and Predicted Coupling of Electromagnetic Radiation Into a Cylindrical Cavity Through a Small Aperture.* Proceedings of the 1989 Electromagnetic Compatibility Symposium, March 1989, Zurich, Switzerland.
[15] Norgard, J.D., Fromme, D.C. and Sega, R.M. - *Correlation of Infrared Measurement Results of Coupled Fields in Long Cylinders with a Dual Series Solution.* IEEE-NS Transactions, Vol. NS-37, No. 6, December 1990, pp. 2138-2143.

A NEW METHOD FOR SOLVING SCATTERING PROBLEMS WITH CONDUCTING MEDIA IN THE TIME DOMAIN

Michael Schinke and Karl Reiß

Institut für Theoretische Elektrotechnik und Meßtechnik
Universität Karlsruhe, D-76128 Karlsruhe, Germany
E-mail: schinke@temds2.etec.uni-karlsruhe.de

Abstract The reflection and transmission of nonsinusoidal plane TEM-waves which are perpendicular incident on a planar interface between a perfect dielectric and a lossy semi-infinite medium is analytically investigated in the time domain. In addition the reflected and transmitted waves are calculated for incident impulse waves. Due to the losses, continuous terms evolve. The distribution in reflected and transmitted parts and the propagation of the impulse-shaped parts can easily be described.

1 Introduction

The solution of Maxwell's equations in the time domain especially with the simple and powerful finite difference time domain (FDTD) algorithm [1] is being used very successfully for many years. Nevertheless, the physics of time domain behavior is not understood completely. Perhaps this is due to education methods, which are focussed rather on frequency- than on more complicated time domain methods.

In the present work a new method operating directly in the time domain for solving scattering problems with conducting media is presented. Let us assume the reflection and transmission problem at a planar boundary between a perfect dielectric and a conducting half-space, shown in Fig. 1. The known perpendicular incident uniform plane wave with an arbitrary wave form function $\mathcal{E}_\mathrm{i}(\xi)$ can be expressed in the time domain as

$$\mathbf{E}_\mathrm{i}(z,t) = E_0\,\mathcal{E}_\mathrm{i}\left(t-\frac{z}{v_1}\right)\mathbf{e}_x\,, \qquad \mathbf{H}_\mathrm{i}(z,t) = \frac{1}{Z_1}\,\mathbf{e}_z\times\mathbf{E}_\mathrm{i}(z,t)$$

$$\text{with} \qquad v_1 = 1/\sqrt{\varepsilon_1\mu_1}\,, \qquad Z_1 = \sqrt{\mu_1/\varepsilon_1}\,. \tag{1}$$

If medium 2 would also be lossless ($\sigma_2 = 0$), we could make the time domain ansatz

$$\mathbf{E}_\mathrm{r}(z,t) = r\cdot E_0\,\mathcal{E}_\mathrm{i}\left(t+\frac{z}{v_1}\right)\mathbf{e}_x\,, \qquad \mathbf{H}_\mathrm{r}(z,t) = -\frac{1}{Z_1}\,\mathbf{e}_z\times\mathbf{E}_\mathrm{r}(z,t)\,,$$

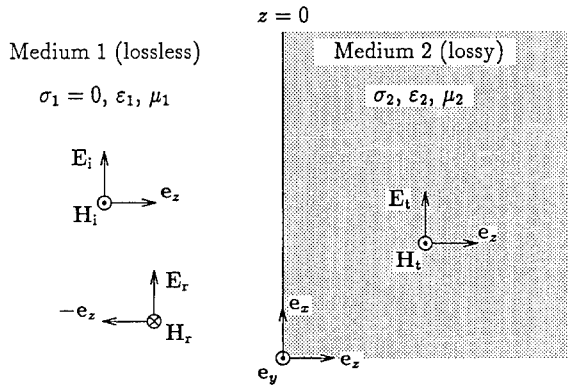


Figure 1: Reflection and transmission problem

$$\mathbf{E}_t(z,t) = d \cdot E_0\, \mathcal{E}_i\left(t - \frac{z}{v_2}\right)\mathbf{e}_x, \qquad \mathbf{H}_t(z,t) = \frac{1}{Z_2}\,\mathbf{e}_z \times \mathbf{E}_t(z,t)$$

$$\text{with} \qquad v_2 = 1/\sqrt{\varepsilon_2\mu_2}, \qquad Z_2 = \sqrt{\mu_2/\varepsilon_2} \tag{2}$$

for the reflected and the transmitted wave with unknown constants r and d, which can be determined by enforcing the boundary conditions at the interface $z = 0$. This leads to the known Fresnel coefficients

$$r = \frac{Z_2 - Z_1}{Z_2 + Z_1}, \qquad d = \frac{2Z_2}{Z_2 + Z_1}. \tag{3}$$

This proceeding is very similar to the frequency domain method for monochromatic waves, where $\mathcal{E}_i(\xi) = \cos(\omega\xi)$ or $\mathcal{E}_i(\xi) = \exp(\mathrm{j}\omega\xi)$.

For $\sigma_2 > 0$ things change dramatically. The main differences between the lossless and the lossy case are, that in the lossy case

- the wave form function (WFF) of the reflected wave is different from the WFF of the incident wave.
- the electric and the magnetic field in the lossy medium cannot be described with a simple WFF and there is *no* connection between the electric and magnetic field like $\mathbf{H}_t(z,t) = \frac{1}{Z_2}\,\mathbf{e}_z \times \mathbf{E}_t(z,t)$ in the lossy medium.
- we have to introduce unknown *functions*, not constant coefficients. The unknown functions will be determined also by the boundary conditions.

Now we try to solve the problem given in Fig. 1 with medium 2 of finite conductivity ($\sigma_2 > 0$).

2 Ansatz functions in lossy media

In the **lossless medium 1** we assume again the incident wave

$$\mathbf{E}_\mathrm{i}(z,t) \;=\; E_0\,\mathcal{E}_\mathrm{i}\left(t-\frac{z}{v_1}\right)\mathbf{e}_x\,, \qquad \mathbf{H}_\mathrm{i}(z,t) \;=\; \frac{1}{Z_1}\,\mathbf{e}_z\times\mathbf{E}_\mathrm{i}(z,t) \tag{4}$$

with $\mathcal{E}_\mathrm{i}(\xi)\equiv 0$ for $\xi<0$. Due to the losses in medium 2, the reflected wave has to be expressed with an unknown WFF $\mathcal{E}_\mathrm{r}(\xi)$:

$$\mathbf{E}_\mathrm{r}(z,t) \;=\; E_0\,\mathcal{E}_\mathrm{r}\left(t+\frac{z}{v_1}\right)\mathbf{e}_x\,, \qquad \mathbf{H}_\mathrm{r}(z,t) \;=\; -\frac{1}{Z_1}\,\mathbf{e}_z\times\mathbf{E}_\mathrm{r}(z,t)\,. \tag{5}$$

As ansatz for the transmitted wave in the **lossy medium 2** we write

$$\mathbf{E}_\mathrm{t}(z,t) \;=\; E_0\,\mathcal{E}_+\left(\frac{z}{v_2\tau},\frac{t}{\tau}\right)\mathbf{e}_x\,, \qquad \mathbf{H}_\mathrm{t}(z,t) \;=\; \frac{E_0}{Z_2}\,\mathcal{H}_+\left(\frac{z}{v_2\tau},\frac{t}{\tau}\right)\mathbf{e}_y \tag{6}$$

with the positive fundamental solutions published by us in [2]:

$$\mathcal{E}_+(z',t') \;=\; \mathrm{e}^{-t'}F_+(t'-z') \;-\frac{1}{2}\,\mathrm{e}^{-t'}\int_{\xi=0}^{t'-z'}\left[\mathrm{I}_0(w_+)-(t'+z')\frac{\mathrm{I}_1(w_+)}{w_+}\right]F_+(\xi)\,\mathrm{d}\xi\,, \tag{7}$$

$$\mathcal{H}_+(z',t') \;=\; \mathrm{e}^{-t'}F_+(t'-z') \;+\frac{1}{2}\,\mathrm{e}^{-t'}\int_{\xi=0}^{t'-z'}\left[\mathrm{I}_0(w_+)+(t'+z')\frac{\mathrm{I}_1(w_+)}{w_+}\right]F_+(\xi)\,\mathrm{d}\xi \tag{8}$$

$$\text{with}\quad w_+ \;=\; \sqrt{(t'+z')(t'-z'-\xi)}$$

and the normalized space and time variables

$$z'=\frac{z}{v_2\tau}\,, \qquad t'=\frac{t}{\tau}$$

with the double relaxation time $\tau=2\varepsilon_2/\sigma_2$ of the lossy medium 2. The real (!) constants $v_{1/2}$ and $Z_{1/2}$ are defined by (1) and (2). In this work we use the convention that *all integrals are zero when the upper limit is less than the lower limit.* This saves us the use of many unit step functions behind the integrals.

These fundamental solutions (7) and (8) for the electric and the magnetic field in a conducting medium are obtained by solving a *characteristic*[1] initial value problem (IVP) with Riemann's method [3] directly in the time domain and can be seen as expansion of d'Alembert's (time domain) solution of the wave equation for conducting media. Both electric and magnetic field depend only on the *characteristic WFF* $F_+(\xi)$.

Many authors before us solved Cauchy IVP's, e. g. [4], [5][2], [11][3], and [12]. For the use as ansatz functions like in the problem shown in Fig. 1 the fundamental time domain solutions are better suited than solutions of Cauchy problems, because at the interface between two media there are no

[1]The initial values are given on the charakteristic directions $t'+z'=0$ and $t'-z'=0$.

[2]very controversially discussed by [6, 7, 8, 9, 10]

[3]only for the electric field strength

impressed field strengths like they are assumed for the solution with Cauchy initial data. The field strengths on both sides of the interface rather adjust themselves due to the boundary conditions at the interface which will be taken into account now. Like in the lossless case, where we have to determine the *constants* r and d, we now look for some expressions for the determination of the unknown characteristic wave form *function* F_+ and the unknown WFF $\mathcal{E}_r$ of the reflected wave.

3 Enforcing boundary conditions

Enforcing continuity on the tangential components of the electric and magnetic fields (4)–(6) across the interface

$$\left[\mathbf{E}_i(z,t)+\mathbf{E}_r(z,t)\right]_{z=0} = \mathbf{E}_t(z,t)\Big|_{z=0}, \qquad \left[\mathbf{H}_i(z,t)+\mathbf{H}_r(z,t)\right]_{z=0} = \mathbf{H}_t(z,t)\Big|_{z=0}$$

and the introduction of $\overline{F}_+(t') = \mathrm{e}^{t'} F_+(t')$ to improve the numerical stability finally yields

$$d\,\mathcal{E}_i(\tau\,t') = \overline{F}_+(t') - \frac{1}{2}\int_{\xi=0}^{t'} \mathrm{e}^{-t'}\left[r\,\mathrm{I}_0(w_b) - t'\,\frac{\mathrm{I}_1(w_b)}{w_b}\right]\mathrm{e}^{\xi}\,\overline{F}_+(\xi)\,\mathrm{d}\xi\,, \tag{9}$$

$$d\,\mathcal{E}_r(\tau\,t') = r\,\overline{F}_+(t') - \frac{1}{2}\int_{\xi=0}^{t'} \mathrm{e}^{-t'}\left[\mathrm{I}_0(w_b) - r\,t'\,\frac{\mathrm{I}_1(w_b)}{w_b}\right]\mathrm{e}^{\xi}\,\overline{F}_+(\xi)\,\mathrm{d}\xi \tag{10}$$

with $w_b = \sqrt{t'(t'-\xi)}$.

Contrary to all expectations the Fresnel coefficients r and d according to (3) for a nonconducting medium 2 can be used to simplify these expressions.

Equation (9) is a Volterra integral equation of the second kind for $\overline{F}_+(\xi)$ which can be solved with little numerical effort. The computation of $\mathcal{E}_t(z',t')$, $\mathcal{H}_t(z',t')$ and $\mathcal{E}_r(\xi)$ follows straightforward.

Without solving these equations we can conclude:

- For $Z_1 \ll Z_2$, i. e. $r = 1$, $d = 2$, follows $\mathcal{E}_r(t) = \mathcal{E}_i(t)$; the reflected wave has the same WFF as the incident wave.
- For $Z_1 \gg Z_2$, i. e. $r = -1$, $d \to 0$, follows $\mathcal{E}_r(t) = -\mathcal{E}_i(t)$; the reflected wave has the same WFF as the incident wave up to the factor -1.
- For $t = 0$ follows at the interface $z = 0$:

  $$\mathbf{E}_r(0,0) = rE_0\,\mathcal{E}_i(0)\,\mathbf{e}_x = r\,\mathbf{E}_i(0,0), \tag{11}$$

  $$\mathbf{E}_t(0,0) = dE_0\,\mathcal{E}_i(0)\,\mathbf{e}_x = d\,\mathbf{E}_i(0,0), \tag{12}$$

  according to (9) for $t' = 0$: $F(0) = d\mathcal{E}_i(0) = d/r\mathcal{E}_r(0)$. From (11) and (12) we now conclude that the distribution of the wave front of the incident wave to the reflected and the transmitted wave front is independent of the losses in medium 2. This will last even for an incident wave with impulse-shaped wave form as it will be shown in the next paragraph.

Note that all these conclusions are independent of the conductivity σ_2.

4 Incident impulse wave

Now we want to investigate an incident wave with Dirac-impulse shaped WFF:

$$\mathcal{E}_i(\tau\, t') = \delta(t')\,.$$

The modified characteristic WFF $\overline{F}$ consists now of two parts — a Dirac impulse and a continuous part. With

$$\overline{F}(t') = d\Big[\delta(t') + \Gamma_0(t')\Big] \tag{13}$$

into (9) we get a new Volterra integral equation of the second kind for the determination of the continuous part Γ_0 of $\overline{F}$:

$$\frac{1}{2}\,\mathrm{e}^{-t'}\big[r\,\mathrm{I}_0(t') - \mathrm{I}_1(t')\big] \;=\; \Gamma_0(t') - \frac{1}{2}\int_{\xi=0}^{t'} \mathrm{e}^{-t'}\left[r\,\mathrm{I}_0(w_\mathrm{b}) - t'\,\frac{\mathrm{I}_1(w_\mathrm{b})}{w_\mathrm{b}}\right]\mathrm{e}^{\xi}\Gamma_0(\xi)\,\mathrm{d}\xi \tag{14}$$

with $\quad w_\mathrm{b} \;=\; \sqrt{t'(t'-\xi)}\,.$

With the solution $\Gamma_0(\xi)$ of (14), the normalized fields in the lossy medium 2 follow from (7) and (8) with (13):

$$\begin{aligned}\mathcal{E}_{t,\delta}(z',t') \;=\; d\Big\{ & e^{-z'}\,\delta(t'-z') + e^{-z'}\,\Gamma_0(t'-z') - \frac{1}{2}\,e^{-t'}\left[\mathrm{I}_0(t') - (t'+z')\frac{\mathrm{I}_1(t')}{t'}\right] \\ & - \frac{1}{2}\int_{\xi=0}^{t'-z'}\left[\mathrm{I}_0(w_+) - (t'+z')\frac{\mathrm{I}_1(w_+)}{w_+}\right] e^{\xi}\,\Gamma_0(\xi)\,\mathrm{d}\xi\Big\}\,,\end{aligned} \tag{15}$$

$$\begin{aligned}\mathcal{H}_{t,\delta}(z',t') \;=\; d\Big\{ & e^{-z'}\,\delta(t'-z') + e^{-z'}\,\Gamma_0(t'-z') + \frac{1}{2}\,e^{-t'}\left[\mathrm{I}_0(t') + (t'+z')\frac{\mathrm{I}_1(t')}{t'}\right] \\ & + \frac{1}{2}\int_{\xi=0}^{t'-z'}\left[\mathrm{I}_0(w_+) + (t'+z')\frac{\mathrm{I}_1(w_+)}{w_+}\right] e^{\xi}\,\Gamma_0(\xi)\,\mathrm{d}\xi\Big\}\end{aligned} \tag{16}$$

with $\quad w_+ \;=\; \sqrt{(t'+z')(t'-z'-\xi)}\,.$

Likewise with the known solution $\Gamma_0(\xi)$ of (14) the WFF of the reflected field with the argument $x = t' + z'$ follows from (10) and (13):

$$\begin{aligned}\mathcal{E}_{r,\delta}(\tau\, x) \;=\; & r\left[\delta(x) + \Gamma_0(x) + \frac{1}{2}\,\mathrm{e}^{-x}\,\mathrm{I}_1(x) + \frac{1}{2}\,x\int_{\xi=0}^{x} e^{-x}\,\frac{\mathrm{I}_1(w_2)}{w_2}\,\mathrm{d}\xi\right] \\ & -\frac{1}{2}\left[e^{-x}\,\mathrm{I}_0(x) + \int_{\xi=0}^{x} e^{-x}\,\mathrm{I}_0(w_2)\,\mathrm{d}\xi\right]\end{aligned} \tag{17}$$

with $\quad w_2 \;=\; \sqrt{x(x-\xi)}\,.$

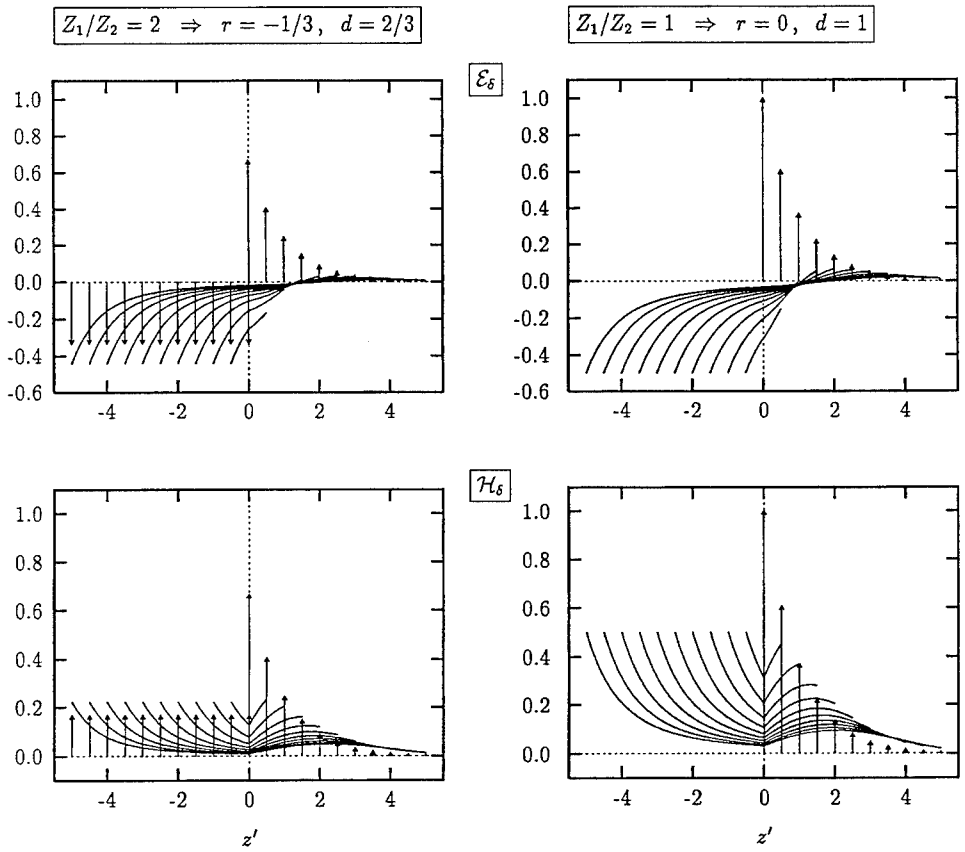


Figure 2: Impulse response of normalized electric (above) and magnetic (below) fields for $t' = 0,\ 0.5,\ 1.0, ...,\ 5.0$ and two different values of Z_1/Z_2

In Fig. 2 and 3 the time evolution of the normalized solutions for an incident Dirac impulse wave and different (always real!) values of Z_1/Z_2 is shown. The incident impulse is omitted in the plots. For $z < 0$ the space variable z' is normalized to $v_1\tau$ and for $z > 0$ to $v_2\tau$. The normalized magnetic field $\mathcal{H}_{r,\delta}$ of the reflected wave is defined by

$$\mathbf{H}_{r,\delta}(z', t') = \frac{E_0}{Z_2}\,\mathcal{H}_{r,\delta}\big[\tau(t' + z')\big] = -\frac{E_0}{Z_1}\,\mathcal{E}_{r,\delta}\big[\tau(t' + z')\big]\,.$$

It is an unexpected result that the Dirac impulses are divided due to the reflection coefficient r and the transmission coefficient d like for the lossless case, which can be seen directly from

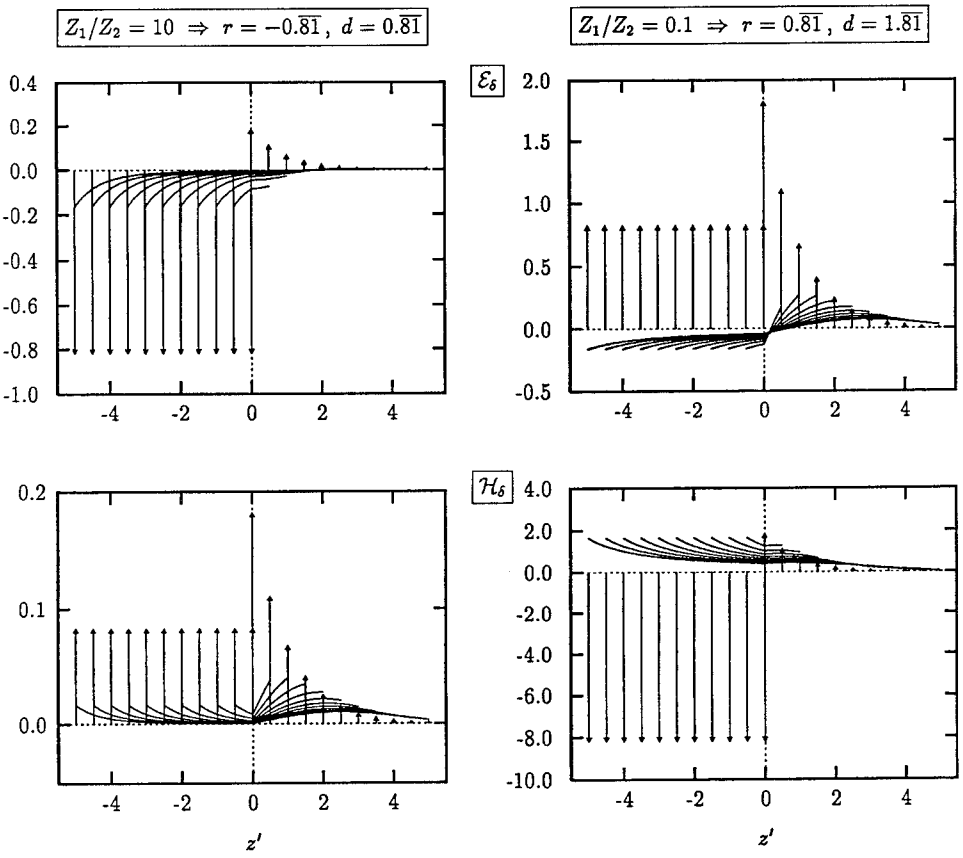


Figure 3: Impulse response of normalized electric (above) and magnetic (below) fields for $t' = 0,\ 0.5,\ 1.0, \ldots,\ 5.0$ and two different values of Z_1/Z_2

(15)–(17). We conclude that the incident impulse does not see the losses in medium 2 when it is reflected for $t' = 0$. After the impulse has passed the interface it is exponentially damped due to the losses and causes *continuous waves*, which are propagating also into the lossless medium 1. This happens also in the case $Z_1 = Z_2$ (Fig. 2 right), which can be concluded from (17). For $r = 0$ the wave front of the only existing continuous part of the normalized reflected wave has always the amplitude 1/2, independent of the conductivity σ, which only has to be greater than zero.

Problems with conducting *layers* can be solved with this method in the same way, when we take into account the "negative" fundamental solution $\mathcal{E}_-$ additional to $\mathcal{E}_+$.

Acknowledgement

This work has been supported by the Deutsche Forschungsgemeinschaft (DFG).

References

[1] K. Yee, "Numerical solution of initial boundary value problems involving maxwell's equations in isotropic media", *IEEE Trans. on Antennas and Propagation*, vol. vol. AP-14, pp. pp.302–307, May 1966.

[2] M. Schinke and K. Reiß, "Fundamental time domain solutions for plane TEM-waves in lossy media", in *1994 Asia-Pacific Microwave Conference Proceedings*, December 6–9, 1994, Tokyo, Japan, vol. I, pp. 277–280.

[3] R. Courant and D. Hilbert, *Methods of Mathematical Physics, volume* II *Partial Differential Equations*, John Wiley & Sons, New York/London, 1962.

[4] H. F. Harmuth, "Correction of Maxwell's equations for signals I", *IEEE Trans. on Electromagnetic Compatibility*, vol. vol. EMC-28, pp. pp.250–258, November 1986.

[5] H. F. Harmuth, "Correction of Maxwell's equations for signals II", *IEEE Trans. on Electromagnetic Compatibility*, vol. vol. EMC-28, pp. pp.259–266, November 1986.

[6] E. F. Kuester, "Comments on "Correction of Maxwell's equations for signals I," "Correction of Maxwell's equations for signals II," and "Propagation velocity of electromagnetic signals"", *IEEE Trans. on Electromagnetic Compatibility*, vol. vol. EMC-29, pp. pp.178–190, May 1987.

[7] J. R. Wait, "Comments on "Correction of Maxwell's equations for signals I and II"", *IEEE Trans. on Electromagnetic Compatibility*, vol. vol. EMC-29, pp. pp.256–257, August 1987.

[8] M. J. Neatrour, "Comments on "Correction of Maxwell's equations for signals I," "Correction of Maxwell's equations for signals II," and "Propagation velocity of electromagnetic signals"", *IEEE Trans. on Electromagnetic Compatibility*, vol. vol. EMC-29, pp. pp.258–259, August 1987.

[9] R. K. Rosich, "Comments on "Correction of Maxwell's equations for signals I and II"", *IEEE Trans. on Electromagnetic Compatibility*, vol. vol. EMC-30, pp. pp.178–179, August 1988.

[10] A. Lakhtakia, "Nonuniqueness of the inverse laplace transform, and the debate on Harmuth's technique", *IEEE Trans. on Electromagnetic Compatibility*, vol. vol. EMC-36, pp. pp.256–258, August 1994.

[11] O. R. Asfar, "Riemann-Green function solution of transient electromagnetic plane waves in lossy media", *IEEE Trans. on Electromagnetic Compatibility*, vol. vol. EMC-32, pp. pp.228–231, August 1990.

[12] J. LoVetri and J. B. Ehrman, "Time-domain electromagnetic plane waves in static and dynamic conducting media: I", *IEEE Trans. on Electromagnetic Compatibility*, vol. vol. EMC-36, pp. pp.221–228, August 1994.

Experience and Experiments at Cray Research with JUNCTION-2 (*Abstract*)

John A. Crow and Qasim M. Sheikh*
Cray Research

January 17, 1995

Abstract

Ongoing work at Cray Research is involved in the evaluation and classification of codes and techniques used in the numerical solution of problems in electromagnetics. Different formulations typically lend themselves to certain types of problems, and a number of codes have sprung up to address the specialities. Part of the evaluation effort involves providing feedback to code developers, whenever possible, on algorithms and coding structures that will allow larger problems to be dealt with effectively and efficiently.

It is the purpose of this note to report on certain experiences at Cray Research with the electromagnetic scattering code, tentatively named *JUNCTION-2*, under development at the University of Houston by D. R. Wilton and his team. The structure of the code, as well as the class of problems it addresses, makes it a good candidate for a new class of iterative linear system solvers. Examples are given for a problem arising in the EMI/EMC analysis of a leaky equipment panel in a shielded room. The results will be presented at the meeting and are not included here.

1 Introduction

Numerical solution techniques for problems in electromagnetics are nearly as diverse as the problems themselves. Problems in antenna design, EMI/EMC, medical imaging, circuit board prototyping, motor design, plasma evolution, etc., all base their formulations on Maxwell's equations. Yet, the success of computer simulation of the fields and processes of interest lies in the ability of the formulation (i) to adapt itself accurately to the geometry, materials, and unknowns of the problem, and (ii) to be amenable to solution by approximate techniques.

For example, thin-wire antenna design problems are well-suited to classical wire-based integral equation moment methods; RCS calculations for conducting bodies are often times naturally handled by patch-based integral equation methods. Thus, these problems have rather

*crow@cray.com, qs@cray.com, Cray Research, Cray Research Park, 655E Lone Oak Drive, Eagan, MN 55121 USA

nice formulations, and further, benefit from the fact that the theory of solution approximation for such problems is rather mature. This combination leads to successful implementations as codes.

The present study arises from ongoing work at Cray Research to evaluate and classify high-quality codes and techniques of interest to engineers and analysts in the electromagnetics community. The goal is to understand better the tools available to such workers, and to provide feedback and assistance on techniques and algorithms when requested. The survey to date has included, in addition to the present code, low-frequency finite element codes used in the design of motors and generators, and the scattering code *CARLOS-3D*. We would like to thank Don Wilton and William Brown of the University of Houston for their assistance in this work.

2 The JUNCTION-2 Code

The code, tentatively referred to as *JUNCTION-2* by D. R. Wilton, is under development at the University of Houston, in conjunction with Lawrence Livermore and Sandia National Laboratories, and the US Navy. It is a method-of-moments code based upon the classical Stratton-Chu integral formulation of scattering problems. As such, it allows the user to formulate problems in terms of electric field, magnetic field, and combined field integral equations. [1]

A rather important aspect of *JUNCTION-2* is its ability to handle structures consisting of both body-type scatterers as well as wire scatterers. Thus scattering from structures and coupling onto wire antennas can be handled reliably. This has application in antenna design and antenna placement problems in which it is important to understand the effects of a conducting environment on antenna performance. Such antennas include long-wire antennas and dipole arrays as found in direction-finding equipment on board naval ships. Also, one can consider coupling to cables and radiation from them.

Element Types Models of the scattering structures are assumed to be made up of flat triangular patches and straight wire elements. The wire elements may be joined to the patches at endpoint-vertex junctions. Impedance loading of the patches is accomodated.

Basis Functions Surface currents are piecewise linear functions, and represented in terms of the Rao-Wilton-Glisson basis functions [2] which guarantee that current flowing into an edge is balanced by the current flowing out of the edge. Possible future work on these basis functions would address the physical field singularity occurring at the edges of nonsmooth patch boundaries. On wire elements, piecewise linear (chapeaux) functions are used.

Excitations Excitation of structures can be in the form of plane waves or voltage sources. However, the modularity of the code is such that is is rather easy to introduce other excitation types. As part of this evaluation, we wrote a general excitation package that was added and used to compute the scattering of a dipole field within a shielded equipment room. [See next section.]

Output The surface current densities computed by code are provided as output. These allow subsequent near- and far-field estimations to take place. In addition, provision is made for far-field patterns to be obtained. In this case, the far-field position of interest is provided by the user in the input deck

3 Examples

A number of test cases were used to evaluate the performance of the code, and were selected in order to represent the computational step in an EMI/EMC analysis and an RCS analysis. Both use the combined-field integral formulation to

avoid problems with internal resonances. Here, we report on the results of the EMI problem.

The EMI/EMC problem models a leaky equipment panel in a shielded room. The room is 13 ft by 6.5 ft, and 8 ft high. Fig. 1 shows a cutaway view of the mesh used for the calculations. Near the right side of the equipment rack is a small, 300 MHz dipole radiator that subsequently produces fields throughout the room. The first step in an EMI/EMC assessment is to determine the ambient fields in the room; once this is done, an estimate of the effect of the field on cabling, circuit boards, etc. is performed. Fig. 2 shows schematically the density of the moment matrix of the CFIE for this example.

To parameterize the problem, the currents induced in the room due to different orientations of the dipole radiator were computed. Specifically, 360 different orientations of the dipole were of interest, and corresponded to 360 excitations of the structure. The orientations were chosen so that the dipole was rotated (parallel to the nearby wall of the equipment rack) through 360 deg in 1 deg steps. Another run was made in which the radiator was translated through the room while its orientation remained fixed. Different levels of mesh refinement were used.

4 Iterative Solvers

There has been a significant amount of attention drawn to iterative solver technology for linear systems of equations. The main attraction of course is that it has been observed in practice that high-quality solution estimates are obtained in a relatively small number of iterations, maybe on the order of ten to fifty, and this makes the solution process $O(N^2)$ in practice. Here, we will discuss some experience with a commercial solver, CDENSE, developed by Elegant Mathematics, Inc.[1] This solver is available for Cray platforms. Contact the vendor for further information.

CDENSE is a robust, fast, iterative linear system solver. Is is applicable to the linear systems with complex, dense coefficient matrices and multiple right-hand sides originating from 3d boundary integral formulated applications such as computational electromagnetics and acoustics.

It uses high-quality, numerically stable, sparse ILU preconditioning strategies for dense coefficient matrices and thus provides an asymptotically $O(n^2)$ iterative solution using preconditioned GMRES-like iterations without restarts. Special optimizing features are available to improve considerably CDENSE's efficiency when solving linear systems having a large number of multiple right-hand sides. Special versions can be configured to handle specific problems.

The key distinguishing characteristics of this solver are its high reliability, its efficiency, and its ability to produce solutions with a user-prescribed accuracy for highly ill-conditioned problems.

A great deal of success has been had with such solvers, and from a practical standpoint to the engineer and analyst, the utility lies in their ability to provide in practice solutions in $O(n^2)$ time.

References

[1] D. S. Jones, *Methods in Electromagnetic Wave Propagation*, vol. 2, Oxford University Press, New York, 1987.

[2] S. M. Rao, D. R. Wilton, and A. W. Glisson, *Electromagnetic scattering by surfaces of arbitrary shape*, IEEE Trans. Antennas Propagation, 30 (1982), pp. 409–418.

[1] rsarbora@sovusa.com, 12142 NE 166th Place, Bothell, WA 98011 USA

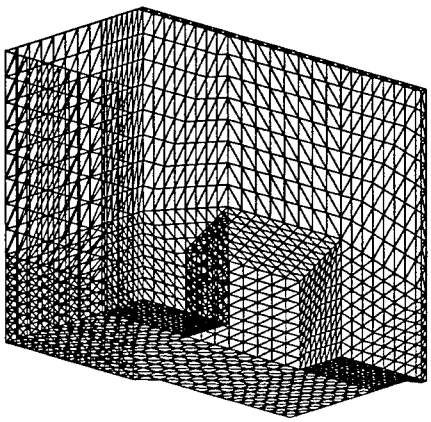


Figure 1: Sample Mesh for EMC/EMI Example

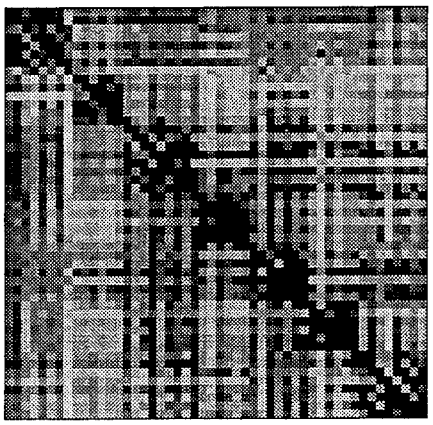


Figure 2: Fill Pattern of Moment Matrix ($N = 6528$)

QUANTITATIVE METHODS FOR MEASURING AND IMPROVING THE PERFORMANCE OF ELECTROMAGNETIC SCATTERING CODES [1]

J. P. Meyers, A. J. Terzuoli, Jr., G. C. Gerace • Air Force Institute of Technology

INTRODUCTION: A set of quantitatively based evaluation methods is presented as an alternative to qualitatively based evaluation methods. These quantitative methods provide a way of making objective evaluations of a code's performance. In addition, these methods can be used to analyze predictions of complicated scattering patterns.

Validating an electromagnetic code involves comparing predicted results with theoretical results for a set of known scattering objects. These comparisons confirm or validate that the code is accurately predicting the electromagnetic field. Although in principle these comparisons sound simple, in reality it is a rather involved problem. Usually, the primary method in use for comparing predicted and theoretical results involves overlaying the plots of the two data sets. This approach allows for a qualitative comparison between the two data sets and clearly identifies gross errors in the predicted results. However, it is not an adequate evaluation procedure for detecting subtle, yet significant differences, nor does it work well when trying to validate the fields from objects with rapidly varying (θ, ϕ) patterns. The evaluation procedures presented use a quantitative approach for making comparisons. The quantitatively based comparisons allow for an unbiased, objective analysis and can be applied to all (θ, ϕ) patterns.

These evaluation procedures should be applicable to a wide range of prediction codes. The procedures focus on the values of the scattered field or the (θ, ϕ) pattern. It is assumed that the scattered field can be obtained from the output of the specific prediction code of interest. Since the procedure does not depend upon specific features of any single prediction code, it is reasonable to assume that they will perform equally well for any prediction code.

SOURCES OF REFERENCE DATA SETS: This section addresses the issue of producing reference data sets with which the predicted results are compared. The limited source of exact analytical solutions is presented followed by a discussion of using measured data. In the section on using measured data, the issue of measurement error is addressed. Solutions for eliminating or accounting for some of the errors are presented.

EXACT ANALYTICAL SOLUTIONS: The evaluation procedures compare predicted results with theoretical data sets. Ideally the comparisons would be made using scattering objects for which an exact analytical solution exists. However, exact analytical solutions are known for few objects. One such object is a perfect electric conducting (PEC) sphere. Other objects for which exact or near exact solutions exist include: flat plates, circular cylinders, and semi-infinite wedges. Definitely absent from the list are objects with many scattering centers [1]. Since so few exact analytic solutions exist, comparisons are usually made with measured scattered field patterns.

MEASURED DATA: All measured data is subject to various measurement errors and system limitations which introduces a level of uncertainty in the evaluation. But if the predictions agree within the measurement error, the code can be considered to produce valid results. Therefore, it is important to either know the error limits of the measured data or be able to estimate it.

Random error (e.g. noise) is not the only source of error that must be addressed during the evaluation procedure. The systematic errors inherent in the measurement process pose a potentially more serious problem. These errors can include, misalignment of the scattering object, calibration errors, and various approximations and assumptions made in the design of the measurement facility. Unfortunately little, if anything, can be done to reduce the effects of calibration error. If significant calibration errors are known to exist in the measured data, the best solution is to repeat the measurements after re-calibrating the measurement system.

[1] This work was supported by the U. S. Air Force Wright Laboratories.

Other common systematic errors are not as critical as calibration errors. It is well known [2, 3, 4, 5] that misalignment by as much as 0.5° in either azimuth or elevation is enough to produce significant but subtle differences especially for objects with many scattering centers. Another common source of systematic errors is the uniform plane wave approximation used by measurement facilities. Ideally, the scattering object should be illuminated with a uniform plane wave (constant amplitude and phase), but this would require an infinite aperture. One method of reducing the error associated with uniform plane wave approximations is to use a compact range. This type of measurement range creates a better uniform plane wave approximation by using a large parabolic reflector to convert the incident spherical wave into a near uniform plane wave over a finite test volume. Uniform plane wave approximation errors tend to create shifts in the overall magnitude of the measured scattered field levels . Therefore, it may be better to compare relative levels instead of absolute levels.

Sometimes systematic errors can be addressed during the comparison process. Scattered field data sets, especially azimuth and elevation sweeps, tend to be characterized by large peaks. For azimuth and elevation sweeps, these peaks can correspond to large specular reflections, which are characteristic of smooth surfaces with large radii of curvature, but can also be created by other phenomena as well. These peaks can be used for alignment purposes in both angular coordinates and field magnitudes. Often approximate calculations can be used to estimate the actual peak value. This value is then used to shift both the measured and predicted values. A short cut that often works equally well, is to shift either one of the two data sets to correspond to the value of the other one. In both cases, the relative changes in field values are compared. This has the added benefit of separating errors in *overall* levels from errors in *relative* changes within the data set.

ERROR METRICS: Once an acceptable reference data set has been obtained, it is necessary to determine exactly how the two data sets will be quantitatively compared. Each data set consists of N *x-y* data points which correspond to the scattered field of the test object as a function of either azimuth, elevation, or frequency. The purpose of the error metric is to accurately describe the overall agreement between the two data sets with as few numbers as possible. Ideally, the level of agreement can be represented with a single numerical value. Several error metrics that measure the level of agreement between two data sets are presented. It is assumed that the two data sets have the same number of data points corresponding to the same values for the independent variable. The metrics proposed are only one set of possible error metrics. Other metrics may exist that work equally well for various circumstances. The best approach for evaluating potential metrics involves observing how they respond to various types of differences between reference and test data. For each of the metrics in this study, the following definition of error is used:

$$e_i = \sigma_{i,reference} - \sigma_{i,predicted} \tag{1}$$

where σ is the echo area (or radar cross section, RCS) measured in either linear area units (m^2) or logarithmic units (dBsm). It is important to note that logarithmic units tend to enhance the effects of nulls whereas linear units tend to suppress nulls. Again, experimentation is the best way to determine which is better for a given set of circumstances.

MEAN SQUARE ERROR (MSE): The mean square error is a simple way of measuring the average error of all data points in a prediction. This measure does not allow positive and negative errors to cancel each other since the error values are squared before summation. This measure is calculated by

$$\text{MSE} = \frac{1}{n}\sum_{i=1}^{n} e_i^2 \tag{2}$$

where the error of the i^{th} data value, e_i, is given by (1). The number of points in each data set is given by n. Small values for MSE indicate good overall agreement between the two data sets. However, a

large MSE does not necessarily mean poor agreement. Since the error values are squared before summation, relatively large error values have more influence on the value of the mean square error.

MEAN ERROR (ME): Like the mean square error, the mean error measures the average error of all data points in a prediction. Unlike the mean square error, the mean error allows positive and negative errors to cancel each other. Due to this cancellation, a relatively poor prediction can result in a low error value. The mean error is calculated as

$$\mathrm{ME} = \frac{1}{n}\sum_{i=1}^{n} e_i \qquad (3)$$

A low value for ME can mean one of two things: good agreement between the two data sets, or large errors were canceled with large or numerous smaller errors of the opposite sign.

STANDARD DEVIATION (STD): The standard deviation measures the degree of variation about the mean. Therefore, it is a good error measure to use when the measured data is relatively constant and the predicted data deviate from that value. An azimuth scan of a sphere or a cylinder is an example where the standard deviation may be a good measure of the error. Since the scattered field of a sphere and cylinder don't change with aspect angle, the scattered field should be constant. However, since many prediction codes use faceted models and the predicted scattered field will vary with aspect angle. The standard deviation is calculated by

$$\mathrm{STD} = \sqrt{\frac{n}{n-1}\left(MSE - ME^2\right)} \qquad (4)$$

PERCENTAGE AGREEMENT (PA): Since most predictions are compared to measured data, it is necessary to account for random measurement error *(noise)* in the measurement system. This percent agreement metric calculates the percentage of the predicted data points which have error values less than the measurement error, or some other acceptable level of error. This error metric is flexible enough to account for measurement errors that vary as a function of the independent variable. In addition, if an acceptable error level has been established, that error level can be used to determine the percentage agreement. Percentage agreement is calculated by

$$\mathrm{PA} = \frac{\#\left(|e_i| < err\right)}{n} \cdot 100 \qquad (5)$$

where *err* is the acceptable error threshold value which can be a constant or a function of the independent variable. The pound sign *(#)* in the numerator is used to indicate the total number of error values which satisfy the expression in parentheses.

NOISE FLOORS: In addition to measurement errors, measured data contains a noise floor which is the level of the background environment which cannot be deleted from measured data. The noise floor depends upon the conditions under which the measurements were made. It varies from one measurement facility to the next and can even depend upon the scattering object being measured. Measured field levels close to the noise floor are indistinguishable from system noise, thus are meaningless. Therefore, each of the error metrics listed can, and generally should, be modified to include only those data values which are significantly above the noise floor.

DATA PROCESSING AND FILTERING: For complicated objects, the back scattered field with respect to azimuth angle tends to have rapid fluctuations separated by only a fraction of a degree, with a dynamic range of *20 to 40 dB* [6]. In addition to these rapid fluctuations, an underlying trend exists based on the geometry and composition of the scattering object. Therefore, filtering of the data such

that the underlying trend becomes apparent is useful. Several methods of *smoothing* scattered field data are traditionally used. In general, they involve a sliding window, in which the center data point is replaced with a value (e.g. mean and median) related to all of the data points in a window of *fixed* but arbitrary width. Since scattered field data is commonly plotted in logarithmic *(dBsm)* or linear *(m^2)* units, the issue arises concerning in which scale the data is best smoothed. However taking the mean of logarithmic data is the same as taking the geometric mean of linear data.

None of the traditional window smoothing methods attempt to take into account the geometry of the scattering object. The spacing of the peaks and nulls in the scattered field data corresponds to how rapidly the relative scattering centers move in and out of phase. For example, in the case of a long narrow object, the peaks and nulls will be spaced more closely when viewed from broadside *(90°)* than when viewed from either end *(0° or 180°)*. The path distances from the transmitter to each end vary more rapidly at broadside than they do at other incident angles, thus creating the higher density of peaks at broadside.

We now present three *filtering* techniques which account for these variations in peak to null separation. All three methods use the sliding window concept, however the width of the window width is *variable* over the entire azimuth of the scattered field data set. Initially, two window widths are calculated, one for the end aspect and the other for the broadside aspect. These two window widths are based on a bounding box which circumscribes the scattering object. In the case of a generic long narrow object, this is a simple rectangular box. The box widths at the two azimuths can be viewed as a rectangular window on the surface currents of the scattering object. In going from the induced currents on the object to the scattered far field, a Fourier Transform may be applied to these windows to get a corresponding *sinc* i.e. *(sin x)/x*. The null-to-null width of the *sinc* main lobe is used as the window width. Since the projection of the scattering object on the transmitter varies as a function of azimuth, the window width should also vary as a function of azimuth. This variation is approximated by a *cosine on a pedestal* given by

$$W(\theta) = W(0°) + W(90°) \cdot \cos(\theta) \tag{6}$$

where W represents the null-to-null width of the *sinc* main lobe. This is also the variable width of the sliding window that is used for filtering. Now that the variable window width has been defined, the next step is to establish the operation that will be applied to the data within the variable window.

POWER SCALE WEIGHT: The first two filtering techniques perform a weighted average of the data points. The weighting will correspond to a $sinc^2$, i.e. $((\sin x)/x)^2$ similar to scattered power raw data which is proportional to the square of the scattered E-field. The first technique averages data in logarithmic units *(dBsm)* while the second technique averages data in linear units *(sm)*. The two filtering techniques are given by

$$\sigma_{1,i} = \frac{1}{2n+1} \sum_{k=i-n}^{i+n} \left\{ \sigma_k \frac{\sin^2(\frac{k}{n}\pi)}{(\frac{k}{n}\pi)^2} \right\} \tag{7}$$

and

$$\sigma_{2,i} = \frac{1}{2n+1} \sum_{k=i-n}^{i+n} \left\{ \left[10^{(\frac{\sigma_k}{10})} \right] \frac{\sin^2(\frac{k}{n}\pi)}{(\frac{k}{n}\pi)^2} \right\} \tag{8}$$

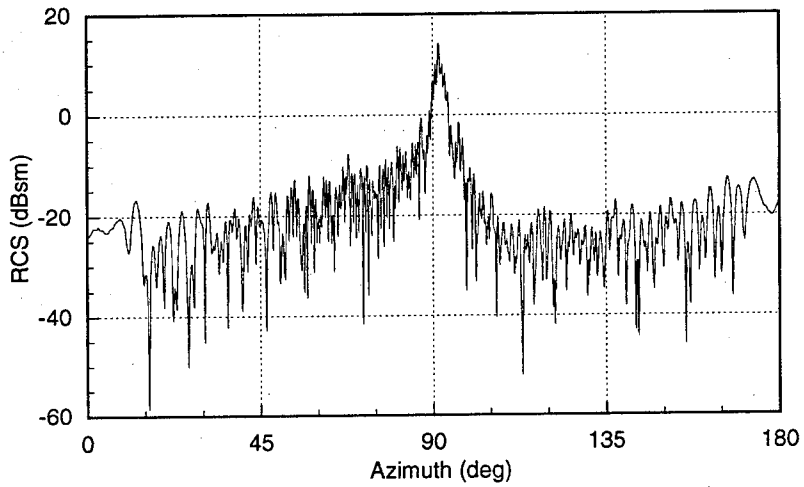


Figure 1. Raw Generic Long Object Scattered Field Data. HH polarization, 18 GHz.

where σ is the magnitude of the echo area in *dBsm* and n is the number of data points in the filtering window centered about the i^{th} data point as given by (6). The numerical subscript on σ indicates the particular filtering technique.

FIELD SCALE WEIGHTS: The third and final technique takes into account that the raw data is actually processed scattered E-filed data. In fact, by using echo area values, the phase information of the scattered E-field is lost. Therefore, the third technique converts the echo area value back into a value proportional to the scattered E-field. As long as the phase of the scattered E-field is recorded along with the magnitude of the echo area, it is possible to recover all of the information obtained during the measurement or prediction process. The echo area (or radar cross section, RCS) σ is defined by

$$\sigma = \lim_{R\to\infty} 4\pi R^2 \left|\frac{\overline{E^s}}{\overline{E^i}}\right|^2 \tag{9}$$

where E^s and E^i are the scattered and incident E-fields respectively.

It is necessary to understand how the scattered field measurements were made in order to be able to extract the desired information about the scattered E-field. Since static scattered field measurements are typically made in the presence of other scatterers, it is necessary to make calibration measurements of a scattering object for which the scattered field is known. Typically, four sets of measurements are made to obtain a single scattered field signature. *First,* the scattering from the support structure for the calibration object is measured. *Second,* the scattering from the calibration object and its support structure is measured. *Third,* if a different support structure is used for the test object, the scattering from it is measured. *Finally,* the scattering from the test object and its support structure are measured. With these four measurements and the known scattered field of the calibration object, it is possible to calculate the echo area of the test object. This calculation is given by

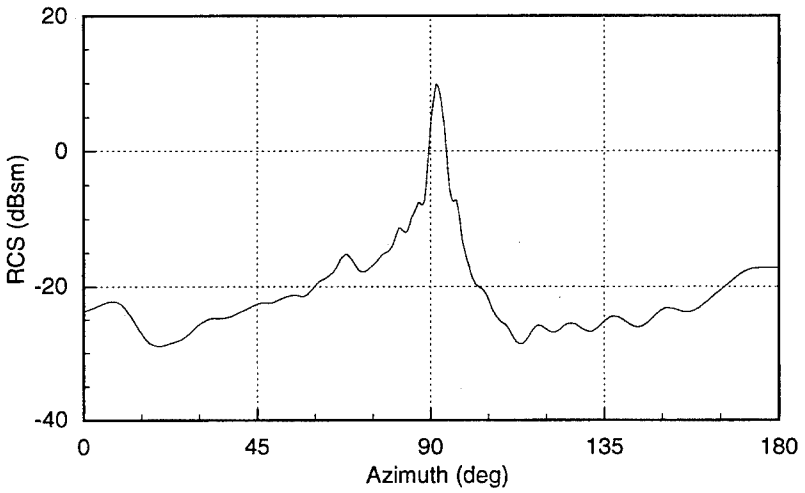


Figure 2. Processed Scattered Field Data by Filtering in Logarithmic Units.

$$\sigma_t = \left| \frac{\overline{E_t^s} - \overline{E_{tb}^s}}{\overline{E_c^s} - \overline{E_{cb}^s}} \right|^2 \sigma_c \tag{10}$$

The subscripts refer to the test *(t)*, test background *(tb)*, calibration *(c)*, and calibration background *(cb)*. Each of the E-fields are complex quantities. The phase recorded with the magnitude of the scattered field is that of the numerator in (10). Therefore, a complex quantity, $\overline{X}$, proportional to the scattered E-field of the test object is given by

$$\left|\overline{X}\right| = \sqrt{10^{\left(\frac{\sigma}{10}\right)}} \tag{11}$$

and

$$\overline{X} = \left|\overline{X}\right|\cos(\phi) + j\left|\overline{X}\right|\sin(\phi) \tag{12}$$

where ϕ is the phase of the scattered E-field which was recorded during the measurement or prediction process.

Instead of processing the magnitude of the scattered field as was done in the first two filtering techniques, the third technique processes the complex quantity $\overline{X}$, which is proportional to the complex scattered E-field. Once again, the sliding window size is given by (6) and a weighted mean is calculated on the data values within each window. Since the complex quantity $\overline{X}$ is proportional to the complex scattered E-field and not the square of the E-field, the weights are given by the *sinc* function instead of a squared $sinc^2$. The third filtering technique is then given by

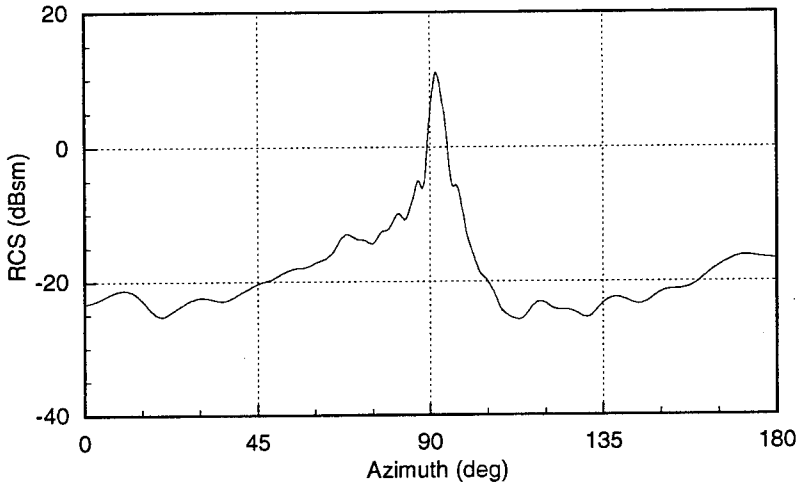


Figure 3. Processed Scattered Field Data by Filtering in Linear Units.

$$\overline{X}_{3,i} = \frac{1}{2n+1}\sum_{k=i-n}^{i+n}\left\{\overline{X}_k \frac{\sin(\frac{k}{n}\pi)}{(\frac{k}{n}\pi)}\right\} \tag{13}$$

Once the complex quantities have been processed, they are converted back into standard echo area values and plotted in units of dBsm. Thus the processed echo area using the third technique is given by

$$\sigma_{3,i} = 10\log_{10}\left(\left|\overline{X}_{3,i}\right|^2\right) \tag{14}$$

COMPARISON OF FILTERING TECHNIQUES: Measured data from a generic long object is used as the sample data set. The measured data was taken at 18 GHz with angular step size of 0.25° using horizontal polarization. Figure 1 is a plot of the raw scattered field data plotted in *dBsm* versus azimuth angle. As indicated earlier, the scattered field varies rapidly over extremely small sweeps in azimuth angle. Figures 2 through 4 correspond to the three filtering techniques. The first two filtering techniques produce fairly similar sets of smoothed data. The peaks and nulls are slightly more pronounced in the first technique which performs the weighted averaging on logarithmic data. An interesting observation is that the main peak at *90°* is almost identical over a span of about *10°* for the first two filtering techniques. As might be expected, the third filtering technique produces a significantly different set of smoothed data. The coherent adding of the complex values is responsible for the increased jaggedness and multiple peaks and nulls at *90°*. Although, not readily evident from the figures, the values resulting from technique #3 are all less than the values resulting from the other two techniques. These lower values are caused by the summation of complex values instead of magnitudes.

It is difficult to make a general choice of processing technique for use in all cases. For the purposes of generic long object data, either one of the techniques that average scattered field values appears to work well. The third technique does not produce smooth results at broadside for this

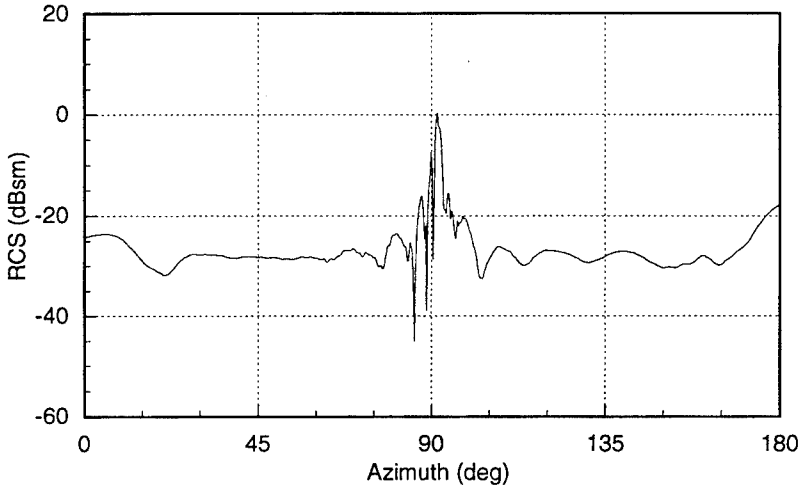


Figure 4. Processed Scattered Field Data by Filtering of complex E-field values in Linear Units.

particular set of data. However, its failure for this data set should not exclude it from considerations for use in other cases.

SUMMARY: Evaluation of an EM scattering prediction code requires several choices and decisions to be made. *First,* a set of test scattering objects must be chosen which will create the various scattering phenomena of interest. *Second,* reference data sets must be obtained for each test object. These reference data sets may come from analytical solutions, measured data, or other prediction codes. If another prediction code is used to create the reference data, it must be generally accepted to produce accurate results, or the evaluation is of little significance. Finally, a method of comparing predicted and reference data must be chosen. It is highly desirable that a quantitative comparison method be chosen to compliment qualitative comparisons. Quantitative comparisons provide unbiased, objective comparisons and accommodate both simple and complicated scattered field patterns. If complicated scattered field patterns are being compared, data processing and filtering may simplify the comparisons.

ACKNOWLEDGMENT: The authors express their gratitude to the following people for their help, assistance, comments, and support: Dennis Andersh, Russ Burleson, Eric Miller, Joe Sacchini, Dave Coulliette, Paul Skinner, Paul Auclair.

REFERENCES

[1] E. F. Knott, et al. *Radar Cross Section.* Artech House, Boston, 1993.

[2] E. M. Miller, D. J. Andersh, A. J. Terzuoli, Jr., "Facetization Level and the Effect on XPATCH Predictions," *Proceedings of the Ninth Annual Review of Progress in Applied Computational Electromagnetics,* Naval Postgraduate School, Monterey, CA, March 22-26, 1993, pp. 610-617.

[3] E. M. Miller, D. J. Andersh, A. J. Terzuoli, Jr., "The Effect of Model Facetization on RCS Predictions," *Digest of the 1993 IEEE/APS International Symposium,* Univ. of Mich.; Ann Arbor, MI, June 28-July 2, 1993, vol. 3, pp. 1404-1407.

[4] R. O. Jernejcic, A. J. Terzuoli, Jr., R. Schindel, "Evaluation of Full Radar Signature Predictions Using XPATCH," *Proceedings of the Tenth Annual Review of Progress in Applied Computational Electromagnetics,,* Monterey, CA, March 21-25, 1994, pp. 343-351.

[5] R. O. Jernejcic, A. J. Terzuoli, Jr., R. F. Schindel., "Electromagnetic Backscatter Predictions Using XPATCH," *Digest of the 1994 IEEE/APS International Symposium, Univ. of Wash.; Seattle, WA,* June 19-24, 1994.

[6] E. F. Knott, et al. *Radar Cross Section Measurements.* Van Nostrand Reinhold, New York, 1993.

SESSION 2:

LOW FREQUENCY

Chairs: K. Kunz, H. Sabbagh

Numerical Modelling of EMC in Underground Power Cable Systems with the Hybrid FE-BE Method[1]

J. Shen and A. Kost
Institut für Elektrische Maschinen, Technische Universität Berlin
Sekr. EM 4, Einsteinufer 10, D-10587 Berlin, Germany

1. Introduction

High voltage transmission lines are the important and necessary components of an electric energy distribution system. The electromagnetic field of the transmission lines may affect human beings and sensitive electronic devices in its neighborhood. The interconnected electromagnetic influences between the active electromagnetic system and its environment which is called Electromagnetic Compatibility (EMC) has become increasingly important recently because of its wide ranging industrial implications. Another name "Electrosmog" for EMC has been introduced to stress the significance of electromagnetic environment pollution [1].

Basically there are two types of high voltage transmission lines. The one is an overhead transmission line and the other an underground cable. The EMC problems in the overhead transmission line power system have been extensively discussed, see e.g. [2]. An obvious negative biological effect of the electromagnetic field caused by the overhead transmission line power system has not been recognized [2, 3].

The influence of the underground power cable systems on the environment is more prominent. This is easy to understand. First, the underground power cable system is generally adopted in the urban district of dense population. Secondly, the distance from the cables to the earth surface is smaller than that in the overhead transmission line power system. Therefore, it is more interesting to investigate the EMC quality of the underground power cable system.

Besides the possible biological effects of the electromagnetic field on human beings, some other medical problems also exist. For example, questions are raised with regard to the behavior of pace-makers under the influence of the electromagnetic field of the underground power cable systems. The new limit value of the magnetic flux density of 30 μT for the normal operation of the pace-makers has been put forward and recognized in Germany. However, in some of the underground power cable systems (400 kV) the magnetic field in the region above the ground may exceed this limited value. Thus, the shielding of the magnetic field produced by such an underground cable system is necessary.

The shielding of the magnetic field has been successfully achieved by using a thin ferromagnetic plate. This is a typical classic open magnetic shielding problem. In order to effectively design the magnetic shielding for the underground cable system, it is essential to compute the magnetic fields of the power cable systems in the existence of the shielding plates or other ferromagnetic materials such as steel girder. For this purpose, a software (HYBEMC 1.0) based on the Hybrid Finite Element (FE) and Boundary Element (BE) method has been developed [4]. In this Hybrid FE-BE solution strategy, the nonlinearity and inhomogeneity of the ferromagnetic materials are treated by the FE method while the infinite exterior space is considered by the BE method. To improve the solution accuracy and the user-pleasantness, an adaptive mesh generation is also implemented.

In this paper, the Hybrid FE-BE method and the features of the developed software are to be reviewed. Then, some application examples will be represented. Consequently, one example of the design of the magnetic shielding system by means of the numerical simulation will be given to show the approach to design the magnetic shielding in the underground power cable systems.

[1] This project was funded by Siemens AG, Germany

2. Hybrid FE-BE Method

In the 2-D electromagnetic field problems in which the exciting current has only one component, say z-component, see Fig. 1, the magnetic vector potential has also one component and automatically satisfies the Coulomb Gauge.

In terms of the magnetic vector potential, the electromagnetic field problems at power frequency can be formulated by:

$$\frac{\partial}{\partial x}\left(\nu\frac{\partial \dot{A}}{\partial x}\right)+\frac{\partial}{\partial y}\left(\nu\frac{\partial \dot{A}}{\partial y}\right)-j\omega\sigma\dot{A}=-\dot{J}_0 \quad (1)$$

$$in\ \Omega_{FE}$$

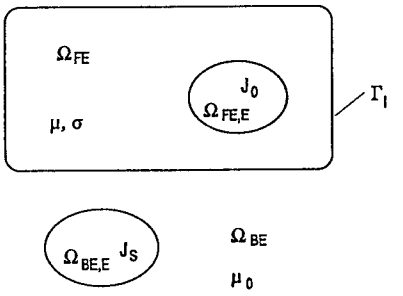


Figure 1 Model configuration of 2-D electromagnetic fields

and

$$\frac{\partial^2 \dot{A}}{\partial x^2}+\frac{\partial^2 \dot{A}}{\partial y^2}=-\mu_0\dot{J}_s \qquad in\ \Omega_{BE} \qquad (2)$$

where $\dot{A}$ is complex phaser of the vector potential, ν reluctivity, μ_0 permeability in vacuum, σ conductivity, ω angular frequency, $\dot{J}_0$ and $\dot{J}_s$ the exciting current sources in Ω_{FE} and Ω_{BE} respectively.

2.1 FEM for the Ω_{FE} region

At first, the weak FEM formulation of eqn. (1) can be written as:

$$\iint_{\Omega_{FE}}\left[\nu\frac{\partial \dot{A}}{\partial x}\frac{\partial W}{\partial x}+\nu\frac{\partial \dot{A}}{\partial y}\frac{\partial W}{\partial y}+j\omega\sigma\dot{A}W\right]dxdy-\oint_{\Gamma_I}W\cdot\nu\frac{\partial \dot{A}}{\partial n}d\Gamma - \iint_{\Omega_{FE}}\dot{J}_0 W dxdy=0 \qquad (3)$$

where W is the weight function and $\vec{n}$ is the outward normal vector at the interface Γ_I. We note here that the contour integral term of eqn. (3) will only be considered when the FE element shares a common boundary with the region Ω_{BE}; otherwise, the contribution of this term is omitted.

2.2 BEM for the Ω_{BE} region

The BE formulation of eqn. (2) can be derived by using the Weighted Residual Method [7]:

$$c_i\dot{A}_i=\int_{\Gamma_I}G^*\frac{\partial \dot{A}}{\partial n}d\Gamma-\int_{\Gamma_I}\frac{\partial G}{\partial n}\dot{A}\,d\Gamma+\int_{\Omega_{BE,E}}G^*\mu_0\dot{J}_s d\Omega \qquad (4)$$

where G^* is the fundamental solution of eqn. (2).

2.3 Coupling the FE and BE equations

At the interface between Ω_{FE} and Ω_{BE}, there exist:

$$\begin{cases} \dot{A}_{BE} = \dot{A}_{FE} \\ \dfrac{1}{\mu_0}\left(\dfrac{\partial \dot{A}}{\partial n}\right)_{BE} = -\dfrac{1}{\mu}\left(\dfrac{\partial \dot{A}}{\partial n}\right)_{FE} \end{cases} \tag{5}$$

By means of eqn. (5), eqn. (3) and eqn. (4) can be coupled into a system of equations, in a matrix form [4]:

$$\boldsymbol{C}\cdot\boldsymbol{X} = \boldsymbol{Y} \tag{6}$$

where $\boldsymbol{X} = \left[(\boldsymbol{A})_{FE} \quad \left(\dfrac{\partial \boldsymbol{A}}{\partial n}\right)_{BE} \right]^T$, $\boldsymbol{Y} = \left[\boldsymbol{F} \quad \boldsymbol{A}_s \right]^T$ and $\boldsymbol{C} = \begin{bmatrix} \boldsymbol{K}' & \dfrac{\mu}{\mu_0}\boldsymbol{T} \\ \Gamma(\boldsymbol{H}) & -\boldsymbol{G} \end{bmatrix}$.

$\boldsymbol{K}'$, $\boldsymbol{T}$ and $\boldsymbol{F}$ are the coefficient matrices of eqn. (3) and $\boldsymbol{H}$, G and A_S the coefficient matrices of eqn. (4). $\Gamma(\boldsymbol{H})$ means that the column of the coefficient matrix $\boldsymbol{H}$ is relocated according to the FE node numbering. In implementation, a mixed element discretization i.e. a linear variation of the vector potential over a FE element and a constant distribution of the normal derivative over a boundary element is used [5,6].

It has to be mentioned that the system matrix $\boldsymbol{C}$ is unsymmetric because of the contribution of the BE equation. This makes the solution of the system equations difficult and partially compensates the advantage of the Hybrid FE-BE method.

3. Features of the Developed Software

3.1 Treatment of nonlinear eddy current problems

For the nonlinear eddy current problems, the physical values are not sinusoidal when the exciting current is yet sinusoidal. In other words, the permeability of the ferromagnetic materials is dependent on not only position but also time. Therefore, the nonlinear eddy currents cannot be represented in terms of the complex phaser with single frequency [7]. However, the real permeability can be replaced by the so-called equivalent permeability when the wave shapes of the physical variables are not interesting. The equivalent permeability is only a function of position. Then, the nonlinear eddy current problems can be still formulated by eqn. (1).

There are two kinds of equivalent permeabilities: RMS model [8,9] and energy model [8]. In this paper, the RMS equivalent permeability is adopted [4].

For the nonlinear problems, the resulting system of equations is the same as eqn. (6) but the system matrix is dependent on the nonlinear reluctivity, i.e.

$$C(\nu)\cdot\boldsymbol{X} = \boldsymbol{Y} \tag{7}$$

To solve this nonlinear equation system, the damped Newton-Raphson method is applied [4]. However, the numerical experiments showed that the convergence of iteration is not ensured in the case of thin ferromagnetic plates. In order to overcome this difficulty, a new method to compute the reluctivity in the iterative process is implemented. In this secant method [10], the new reluctivity in the n.th iteration $\nu^{(n)}$ is derived as the secant $H^{(n)}/B_{new}^{(n)}$, where $B_{new}^{(n)}$ is obtained from the B-H curve

according to the magnetic field strength $H^{(n)} = \nu^{(n-1)} \cdot B^{(n)}$ and $B^{(n)}$ is directly computed from the Hybrid FE-BE method solution. In this way, the iteration convergence can be greatly improved.

3.2 Solution of the system of complex and unsymmetric equation system

As mentioned in section 2.3, the system matrix $\boldsymbol{C}$ is complex and unsymmetric. To solve this kind of equations, various iterative solvers have been numerically investigated. We have tested three iterative solvers: BCG (BiConjugated Gradient method), GMRES (Generalized Minimal Residual method) and CGS (Conjugated Gradient Squared) with several ILU-preconditioners (Incomplete LU decomposition). In the case of the test examples resulted from the Hybrid FE-BE formulation for the EMC problems in the cable systems, the divergence of the solution of the equation systems by using BCG and GMRES has not been recognized. The convergence rate of BCG is faster than that of GMRES [11].

However, the convergence of CGS is not ensured. Whenever convergent, CGS converges more rapidly than BCG and GMRES.

Furthermore, it has been shown that the increase of the fill-in level in the ILU-precondition can raise the convergence rate. For more detailed informations see [11].

3.3 Modelling of the idealized exciting current sources in the FEM

In the EMC problems of the power systems, the electromagnetic field distribution in the area of the exciting current sources is generally not required to be exactly computed. Therefore, the exciting current sources can be simplified into some kinds of ideal current sources, e.g. the ideal line current and the ideal current sheet, in order to reduce the dimension of the solution problem.

However, the surface current density of the idealized exciting current sources is infinite because their cross area is zero. One approach to model the idealized exciting current sources in the FEM is to use the concept of the Dirac Delta function [12]. For example, the ideal line current source can be expressed by:

$$\dot{J}_l = \dot{I}_l \delta_l (P - P_l) \tag{8}$$

where $\dot{I}_l$ is the given ideal line current (Ampere), δ_l the Dirac Delta function and $P_l(x_l, y_l)$ the coordinate of the position of the ideal line current.

The ideal current sheet density can be mathematically represented in terms of the contour integral of the ideal line current source, i.e.:

$$\dot{J}_s(r_{\Gamma_s}) = \int_{\Gamma_s} \dot{J}_s(r_l)\, \delta(r - r_l)\, d\Gamma(r_l) \tag{9}$$

where Γ_s is the contour on which the ideal current sheet source $\dot{J}_s(A/m)$ is distributed.

Numerical examples can be found in [12], which shows the high accuracy of this approach.

3.4 Adaptive mesh generation

The solution accuracy is greatly dependent on the domain discretization. The adaptive mesh generation is such a strategy that the mesh, beginning from any prescribed starting one, is automatically and adaptively refined by means of a Posterior error estimator. The adaptive mesh generator used in this software [13] is based on the error estimator of the Bank & Weiser method [14].

3.5 Calculation of flux density with superconvergence method in post-processing

It has been proven that the global convergence rate of the vector potential is of $O(h^2)$ for the first order triangular elements when h denotes the mesh size. However, the first order derivatives such as flux density show the convergence of O(h) [15]. In the simulation of the EMC problems of the cable systems, the mesh is strongly concentrated near the plate because the variation of the magnetic field in the ferromagnetic plate and its neighborhood is much greater than that in the space above the earth surface, in which the flux density is interested. Thus, the accuracy of the flux density in the space above the earth surface is not sufficient.

In the literature [15], a post processing operator of superconvergence property was proposed. The idea of this post processing operator is to use an analytical solution to calculate the first order derivatives. This analytical solution is the solution of the Laplace equation $\Delta u = 0$ in a small circle surrounding the point at which the flux density is evaluated, together with the boundary condition on the circumference, on which the vector potentials are know from the numerical FEM calculation.

One example is shown in Fig. 2, in which the distribution of the flux density directly evaluated from the Hybrid FE-BE computation is compared with that obtained by using the above post processing operator of superconvergence.

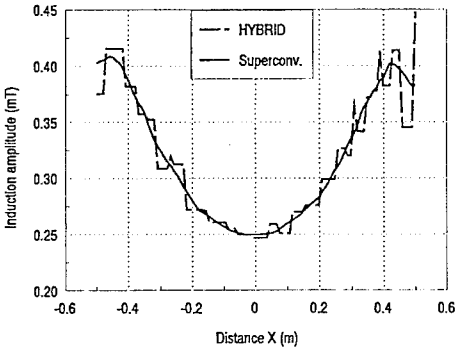


Figure 2 Comparison of the induction amplitude
(Example model: Fig. 3, y = 1 m)

4. Application Examples

4.1 Shielding of a single phase cable system with an iron plate

Fig. 3 shows the equipotential map of an experimental model in which the magnetic field excited by a single phase cable system is screened by a thin iron plate.

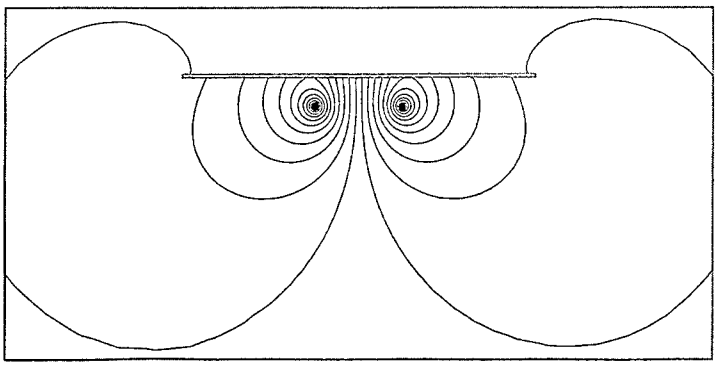


Figure 3 Equipotential map (ωt=0)
Shielding effect of a iron plate on the magnetic field excited by a single phase cable system

4.2 Power cable systems near steel materials

Near the power cable systems there often exist the ferromagnetic materials, for example, the power cables are located on one side of a bridge over a river. As an example, the magnetic field of a three-phase power cable system near a steel girder is shown in Fig. 4.

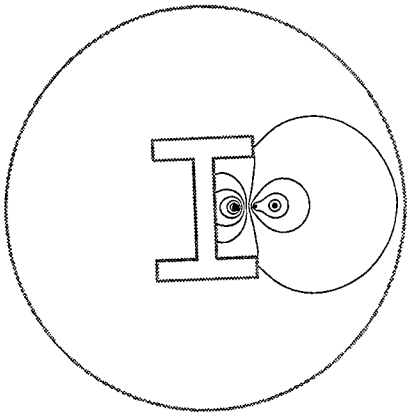


Figure 4 Equipotential map (ωt=0)
A three-phase power cables near a steel girder

4.3 Shielding effect of double iron plates

Two three-phase systems are usually adopted in the underground power cable systems. In these systems the cables are embedded underground e.g. more than 2 m. Thus, a double plates shielding system can be applied to improve the screen effect. One example is shown in Fig. 5, in which both edges of the plates are crooked to reduce the edge effect, i.e. the magnetic field near the top of the plate edge is increased because of the eddy currents.

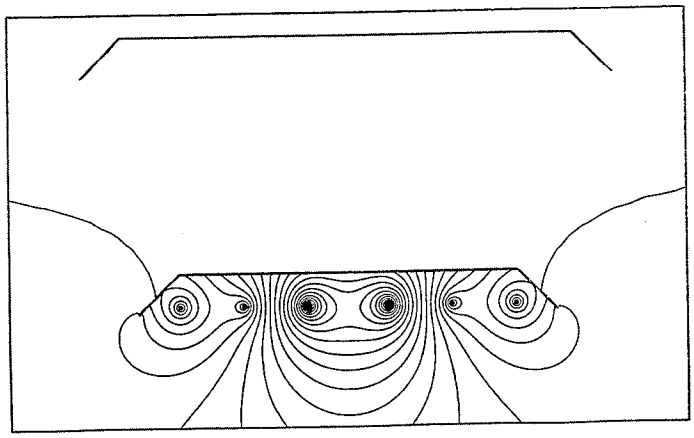


Figure 5 Equipotential map (ωt=0)
Shielding effect of the double iron plates in a two three-phase cable system

5. Design of Shielding Systems by Means of Numerical Simulations

The shielding system can be designed by means of the numerical simulation. For the cable system of a two three-phase cable system, see Fig. 6, the dependency of the maximal values of the screen effect ($SE = 20\log\frac{B_1}{B_2}$ dB, where $\mathbf{B}_1$ and $\mathbf{B}_2$ are the induction amplitude with and without shielding plate respectively), the induction amplitude and the eddy current loss on the distance h is shown in Fig. 7.

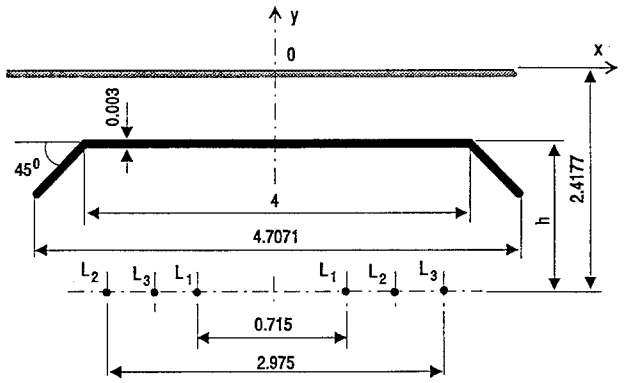


Figure 6 Configuration of the cable system (I = 1602 A, unit: m)

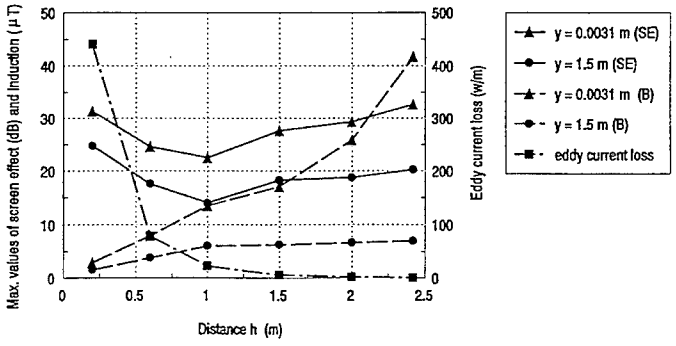


Figure 7 Dependency of screen effect, induction and eddy current loss on distance h (x = -2.5 ··· 2.5)

It can be seen that the maximal induction amplitude at y = 0.0031 m can exceed the limit value of 30 μT when the plate is placed on the ground surface.

As a fact, the screen effect is strongly dependent on the plate width and thickness. The plate thickness should be 3 times the skin depth [4]. Furthermore, it is important to note here that a practical magnetic shielding system is also related with a lot of other factors, e.g. economical and construction consideration.

6. Conclusions

A strategy to analyze and design the shielding systems of the underground power cable systems by using the Hybrid FE-BE method is introduced. Some of the features to treat the nonlinear eddy current problems are reviewed. The examples have shown the effectiveness of the developed method.

7. References

[1] E. David and M. Palic, Elektrosmog-Wirkungen elektromagnetischer Felder auf den Menschen, ETZ, No.3, 1994, 134-139.

[2] R. Belmans and W. Geysen, Environmental implications of high voltage overhead lines, Proc. of the 15.th Congress of World Energy Council, Madrid, Sept. 20-25, 1992, 71-87.

[3] H.-J. Hanbrich, Der Mensch im elektischen und magnetischen Niederfrequenzfeld, ETZ, No.3, 1994, 128-133.

[4] J. Shen and A. Kost, Hybrid FE-BE method for EMC problems in power cable systems, to be presented at COMPUMAG'95, July, 1995.

[5] S. J. Salon and J. M. Schneider, A Hybrid Finite Element-Boundary Integral Formulation of the eddy current problem, IEEE Trans. on Magn., Vol. 18, 1982, 461-466.

[6] T. Onuki, Hybrid Finite Element and Boundary Element method applied to electromagnetic problems, IEEE Trans. on Magn., Vol. 26, 1990, 582-587.

[7] J. Shen, Computation of linear and nonlinear eddy currents with the Boundary Element method, Ph. D. thesis, Berlin, University of Technology, Germany, 1994.

[8] J. D. Lavers, Finite Element solution of nonlinear two dimensional TE-mode eddy current problems, IEEE Trans. on Magn., Vol. 19, 1983, 2201-2203.

[9] Y. D. Terrail, J.-C. Sabonnadiere, P. Masse and J. L. Coulomb, Nonlinear complex Finite Elements analysis of electromagnetic field in steady-state AC devices, IEEE Trans. on Magn., Vol. 20, 1984, 549-552.

[10] O. Biro, K. Preis and K. R. Richter, Various FEM formulations for the calculation of transient 3D eddy currents in nonlinear media, Proc. of CEFC'94, to be published in the May 1995 issue of IEEE Trans. on Magn..

[11] J. Shen, T. Hybler and A. Kost, Comparative study of iterative solvers for the complex and unsymmetric system of equations, to be presented at COMPUMAG'95, July, 1995.

[12] J. Shen and A. Kost, Modelling of the idealized current sources in the FEM, Proc. of CEFC'94, to be published in the May 1995 issue of IEEE Trans. on Magn..

[13] L. Jänicke, Finite Elemente Methode mit adaptiver Netzgenerierung für die Berechnung dreidimensionaler elektromagnetischer Felder, Ph. D. thesis, Berlin University of Technology, Germany, 1994.

[14] R. E. Bank and A. Weiser, Some a Posterior error estimators for elliptic partial differential equations, Mathematics of Computation, Vol. 44, 1985, 283-301.

[15] M. Kasper and J. Franz, Highly accurate computation of field quantities and forces by superconvergence in Finite Elements, Proc. of CEFC'94, to be published in the May 1995 issue of IEEE Trans. on Magn..

NEW CONTRIBUTION TO THE STUDY OF FAULT CURRENTS DISTRIBUTION IN THE GROUND SYSTEMS

Brodskyn, H. O.; Giarolla, M. H.; Cardoso. J. R.; Abe, N. M.; Passaro, A.*

Escola Politécnica da USP
Depto. de Engenharia de Energia e Automação Elétrica
Av. Prof. Luciano Gualberto, Trav. 3, 158
05508-900 - São Paulo - SP

* Instituto de Estudos Avançados - IEAv/CTA

SUMMARY

In previous work [1,2] the author presents a methodology, based on finite elements method (FEM), to calculate the potentials distribution on the grounding area influence. At that time the input to the solver admits as known the split of the system. The aim of this article is to demonstrate the advantages of finite element method (FEM) associated with power systems equations with lumped parameters to intrinsically obtain the distribution of fault current in several offered conductor ways and the potential distribution on the ground, simultaneously. To solve the complex equations system, the methodology adopted was that described by Mesquita [4]. That solution was adopted because of its efficiency and easy to adapt to the FEM software implemented.

1. INTRODUCTION

This work describes a method to calculate the distribution of currents between ground and over head ground wires when a line ground fault occurs in a transmission line as well as the potentials grades that had been developed in the earth.

Most of works had developed techniques that put emphasis on one of two points bellow:

- Calculation of lumped parameters and use traditional network studies, with simplifications mainly on the representation of the ground resistance and their mutual;
- Analyses based on empirical graphics.

This kind of phenomena just on the few last years started to be solved using FEM techniques [1], but even in this case this solution starts from the hypotheses of fault current distribution known.

Our proposal is to mix both FEM techniques on the ground and lumped parameters of the over ground network as well the mutual between line and ground cables in the same solution using a global complex matrix.

The computation in the frequencies domain brings a new contribution to the study.

The application of the Incomplete Cholesky Complex-Bi-Conjugate Gradients method (ICCBCG) was identified as the most appropriated, in the face of encouraging results obtained until the moment, as well as existing symmetry in the resultant matrix.

In the developed methodology, the domain is subdivided in two parts:

1. soil and buried elements;
2. electric network, as show on fig. 1.1.

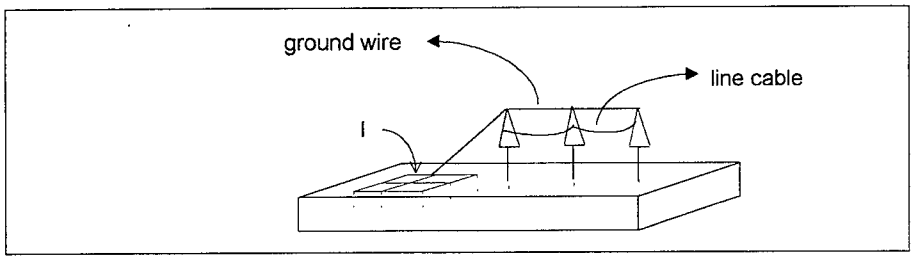


Fig. 1.1 - Schematic Model of the Study Domain

The matrix that simulates the system will be the composition of the global matrix arising from mathematics formulation for the FEM to the ground system, with the insertion of the network lumped parameters, resulting in a system of equation like:

$$Ax = b \qquad \text{(Eq. 1.1)}$$

where A is the complex matrix, resultant of the global matrix composition of the FEM with insertion of lumped parameters of the fault current dispersal system, x is the scalar potential of all domain nodes, and b it is the impress current vector.

The interest to know with better detail the distribution of current in the multiconnected earth system is that of minimize investment on ground grid as well as optimize its design. As by-product, the used methodology allows the study of transference potentials in metallic elements not directly linked up with the electric system, but they are situated in their influence area (problem domain) like: plumbing, metallic structures, armors, with they have contact or they are buried in the soil, in the moment of incident of the line to ground fault.

2. CONSTRUCTION OF THE COMPLEX MATRIX

Following [5] we can simplify the network model, if there are presented just line and over ground wire in a transmission line, to the follow scheme:

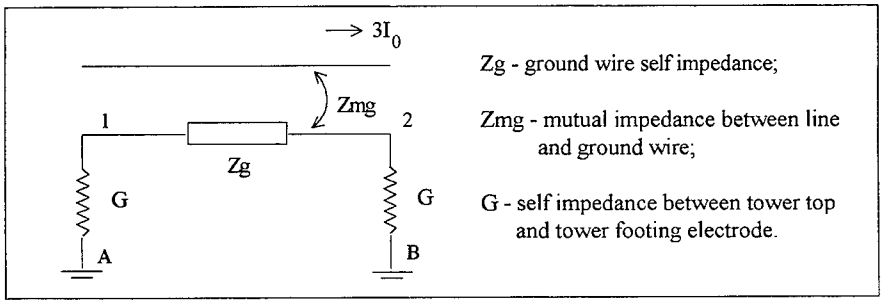


Fig. 2.1 - Impedance model of lumped parameters.

The points A and B are examples of interface between model with lumped parameter and the ground (FEM).

If we change in the over seen model the Zmg impedance by current generator:

$$Ig = \frac{Zmg}{Zg}(3I_0) \qquad \text{(Eq. 2.1)}$$

the interconnection of two substations can be show on fig. 2.2.:

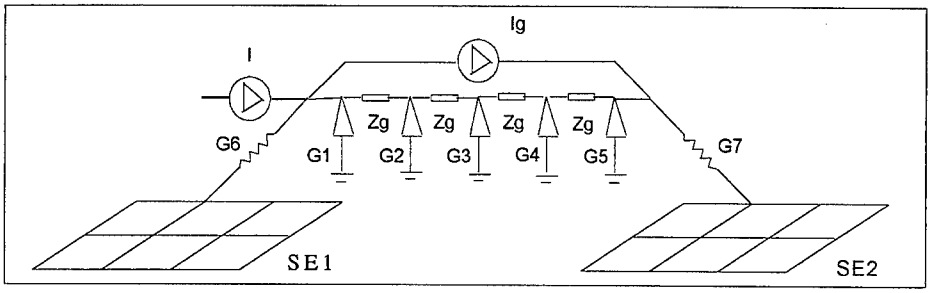
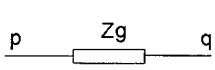
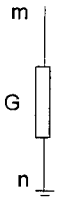


Fig. 2.2 - Interlink of two ground networks of substations.

The construction of the Matrix is done including in the FEM matrix [G] the nodes introduced by the links with the lumped parameters. To do that the impedance of the interconnections between the tower top and the ground electrode, and the self impedance of the over ground wire will be treated as one dimension elements to be include in the main matrix as show bellow:



$$\begin{array}{c} \\ p \\ q \end{array}\begin{array}{c} \begin{array}{cc} p & q \end{array} \\ \begin{bmatrix} 1/Zg & -1/Zg \\ -1/Zg & 1/Zg \end{bmatrix} \end{array}$$



$$\begin{array}{c} \\ m \\ n \end{array}\begin{array}{c} \begin{array}{cc} m & n \end{array} \\ \begin{bmatrix} G & -G \\ -G & G \end{bmatrix} \end{array}$$

Tower interconnections series impedances.

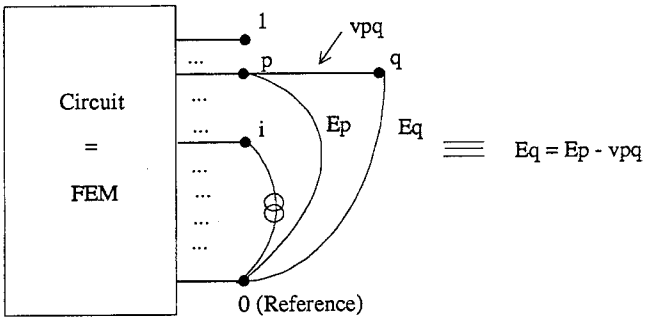
Elements of parallel impedance.

$$\begin{array}{c} \\ n \\ m \\ p \\ q \end{array}\begin{array}{c} \begin{array}{cccc} n & m & p & q \end{array} \\ \begin{bmatrix} +G & -G & & \\ -G & +G & & \\ & & +1/Zg & -1/Zg \\ & & -1/Zg & +1/Zg \end{bmatrix} \end{array}$$

[G] after lumped elements included.

The tower connections with the over ground wires will be considered as resistive so the final matrix will be symmetric with complex elements.

This algorithm is just the inclusion of a element in an already build Y matrix as show bellow [6]:



3. SOLUTION METHODOLOGY

So, to solve the problem defined before, we have the following equation:

$$[G] \cdot [V] = [I] \qquad \text{(Eq.3.1)}$$

where G is symmetric.

To solve this equation it will be used the method of Bi-Complex-Conjugate Gradient[3]. This method, shown on the algorithm III of Jacobs article, is generic and can solve the more simple situations when them arise as the A matrix real, positive defined and symmetric, falling in the CG method. The Bi-Conjugated method explore the minimization of the residue o r, $r_0 = b - Ax_0$, where $\bar{x}$ is the system solution, minimizing the h^2 function, that on the CG method is $r^T A^{-1} r$ and on the Bi-CG real is $x^T (A + A^T) x$, minimizing the calculus effort compared to the form $A^T Ax = A^T b$. In this way the minimum of r will be searched in two orthogonal directions in the space defined in the problem r_i and $\bar{r}_i$.

"Unfortunately on the Bi-CG system is not possible to prove that the residual norm h^2 is strictly decrease at each step of the algorithm for a general complex matrix, as can be proved for CG. In special case of a Hermetian matrix, it is possible to prove the strict monotonicity" [3].

The Complex Bi-Conjugate Gradient Method

$$Ax = b \qquad \text{(Eq. 3.2)}$$

Given: A - a non-singular matrix with complex elements of order n;

b - the vector of right-hand sides of order n;
x_0 - an initial estimate of the solution $\bar{x}$.

The procedure bellow takes into account the Jacobs [3] on the Bi-CG system adopted in the $R^{m.n}$ space:

$$r_0 = b - Ax_0 \quad \text{(Eq. 3.3)}$$
$$\bar{r}_0 = r_0^* \quad \text{(Eq. 3.4)}$$
$$p_0 = r_0 \quad \text{(Eq. 3.5)}$$
$$\bar{p}_0 = \bar{r}_0 \quad \text{(Eq. 3.6)}$$

for i = 0,1,2,...

$$\alpha_i = \frac{(\bar{r}_i, p_i)}{(\bar{p}_i, Ap_i)} \quad \text{(Eq. 3.7)}$$

$$x_{i+1} = x_i + \alpha_i p_i \quad \text{(Eq. 3.8)}$$

$$r_{i+1} = r_i - \alpha_i Ap_i \quad \text{(Eq. 3.9)}$$

$$\bar{r}_{i+1} = \bar{r}_i - \alpha_i^* A^H \bar{p}_i \quad \text{(Eq. 3.10)}$$

$$\beta_i = -\frac{(A^H \bar{p}_i, r_{i+1})}{(\bar{p}_i, Ap_i)} \quad \text{(Eq. 3.11)}$$

$$p_{i+1} = r_{i+1} + \beta_i p_i \quad \text{(Eq. 3.12)}$$

$$\bar{p}_{i+1} = \bar{r}_{i+1} + \beta_i^* \bar{p}_i \quad \text{(Eq. 3.13)}$$

continue until $r_{i+1} = 0$

The bi-orthogonality relationships satisfied by the various vectors are:

$$(\bar{p}_i, Ap_j) = 0 \quad \text{for} \quad i > j \quad \text{(Eq. 3.14)}$$
$$(\bar{r}_i, r_j) = (r_i, \bar{r}_j) = 0 \quad \text{for} \quad i > j \quad \text{(Eq. 3.15)}$$
$$(p_i, A^H \bar{p}_j) = 0 \quad \text{for} \quad i > j \quad \text{(Eq. 3.16)}$$
$$(\bar{r}_i, p_j) = (r_i, \bar{p}_j) = 0 \quad \text{for} \quad i > j \quad \text{(Eq. 3.17)}$$

Notes: * complex conjugate;

^{H} transposed of the vector or matrix of complex conjugate elements.

$$(x, y) = x^H . y \quad \text{(Eq. 3.18)}$$

$$(x, y) = (y, x)^* \quad \text{(Eq. 3.19)}$$

Special Cases:

- If A is Hermetian, that is $A^H = A$, then the complex Bi-CG algorithm becomes the complex form of the basic CG algorithm just as one would expect since Hermetian is the analogue to symmetry. The analogous result as for the basic CG algorithm holds on the strict monotonic of the residual norm per step;
- If the system is real then $\bar{p}_o = p_0$ e $\bar{r}_o = r_0$ and we have the Bi-CG real algorithm;
- If the system is real and the matrix A is positive definite and symmetric we have the CG algorithm.

As described by Mesquita [4] when the matrix A is symmetric and complex, we can use the Incomplete Choleski method before applying the Bi-CCG, making the ICCBCG (Incomplete Complex Bi-Conjugate Gradients) that introduce reductions on the number of iterations to obtain the problem solution.

On the pre-conditioning Incomplete Cholesky method the matrix is:

$$C = T . T^T \quad \text{(Eq. 3.20)}$$

where T is the low triangle of the matrix.

The ICCBCG method:

$$r_0 = b - Ax_0 \quad \text{(Eq. 3.21)}$$

$$\bar{r}_0 = (r_0)^* \quad \text{(Eq. 3.22)}$$

$$CZ_0 = r_0 \quad \text{(Eq. 3.23)}$$

$$p_0 = Z_0 \quad \text{(Eq. 3.24)}$$

$$C^H \bar{Z}_0 = \bar{r}_0 \quad \text{(Eq. 3.25)}$$

$$\bar{p}_o = \bar{z}_0, \quad i = 0 \quad \text{(Eq. 3.26)}$$

$$\alpha_i = \frac{(\bar{r}_i, z_i)}{(\bar{p}_i, Ap_i)} \quad \text{(Eq. 3.27)}$$

$$x_{i+1} = x_i + \alpha_i p_i \quad \text{(Eq. 3.28)}$$

$$r_{i+1} = r_i - \alpha_i A p_i \quad \text{(Eq. 3.29)}$$

$$\bar{r}_{i+1} = \bar{r}_i - (\alpha_i)^* A^H \bar{p}_i \quad \text{(Eq. 3.30)}$$

$$\|r_{i+1}\| < \varepsilon \quad \rightarrow \text{ Stop}$$

$$CZ_{i+1} = r_{i+1} \quad \text{(Eq. 3.31)}$$

$$\beta_i = \frac{(\bar{r}_{i+1}, Z_{i+1})}{(\bar{r}_i, Z_i)} \quad \text{(Eq. 3.32)}$$

$$p_{i+1} = Z_{i+1} + \beta_i \, p_i \qquad \text{(Eq. 3.33)}$$

$$C^H \bar{Z}_{i+1} = r_{i+1} \qquad \text{(Eq. 3.34)}$$

$$\bar{p}_{i+1} = \bar{Z}_{i+1} + (\beta_i)^* \bar{p}_i \qquad \text{(Eq. 3.35)}$$

$$i = i + 1 \qquad \rightarrow \text{ go to Eq. 3.27}$$

4. EXAMPLE AND RESULTS

On the first approach we will utilize the simplified example of figure 4.1.a, with DC current of 1500 A on point 2.

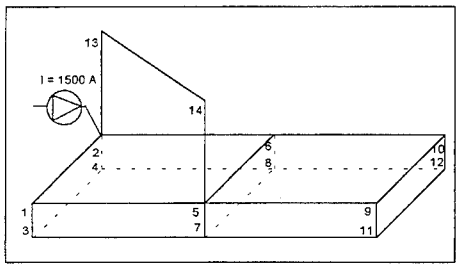


Fig. 4.1.a - Example Scheme

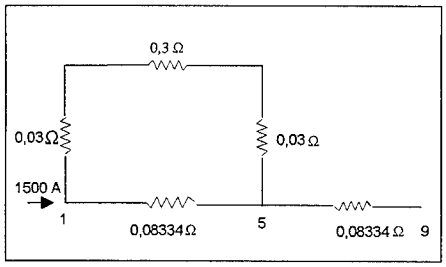


Fig. 4.1.b - Equivalent Model

The solver had considered the elements between the points 2-13, 13-14, e 14-5 as lumped values, and the rest of domain had been simulated with FEM and ICCG (Incomplete Cholesky Conjugate Gradients) solution.

The results are those below:

V_1	= 226.4793 V	V_6	= 124.9714 V	V_{11}	= 0
V_2	= 226.5250 V	V_7	= 124.9691 V	V_{12}	= 0
V_3	= 226.4539 V	V_8	= 124.9757 V	V_{13}	= 218.0702 V
V_4	= 226.4691 V	V_9	= 0	V_{14}	= 133.4464 V
V_5	= 124.9921 V	V_{10}	= 0		

For verification lets take a equivalent system where the FEM domain will be simulated by lumped parameters too.

Considerations:

- Distance between two points: 1m
- Soil Resistivity: $\rho_{solo} = 1/12 \; \Omega.m$
- Resistances: element between points 2-13: 0,03 Ω
  element between points 13-14: 0,3 Ω

element between points 14-5: 0.03 Ω

Then,

$R_{solo} = \rho \frac{l}{s} = 1/12 * 1 = 0{,}08334\ \Omega$

The current is uniformly distributed in the 1-2-3-4 area.

So, we have the solution of the equivalent model of figure 4.1.b :

V_1 = 226.5 V V_5 = 125 V V_9 = 0

To the other result we will use the example of the fig. 4.2:

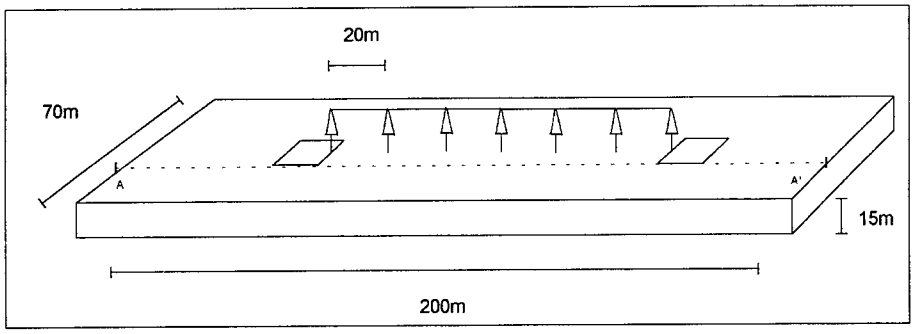


Fig. 4.2 - Example domain

The ground rods of the mesh and of the towers are 6.0 m long, the mesh is buried at 0 m level, and the soil is stratified in three layers following:

0m -3m: 100 Ω.m -3m -9m: 400 Ω.m -9m -15m: 1300 Ω.m

Fig. 4.3, shows the equipotential lines distribution due to a total ground fault (I= 40 A) imposed in the left-side mesh.

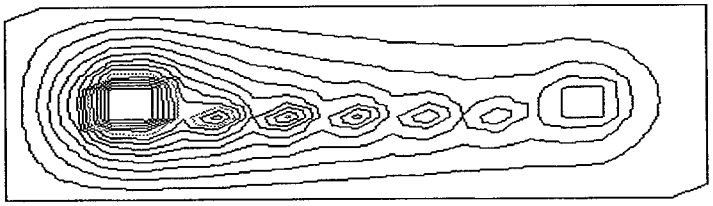


Fig. 4.3 - Equipotential lines

Fig. 4.4.a shows the potential profile in the direction (A-A') as show in fig.4.2, and the fig. 4.4.b shows the potential surface at 0 m level.

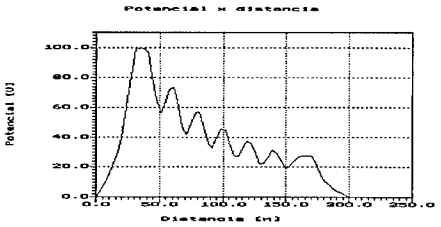


Fig. 4.4.a - Potential profile

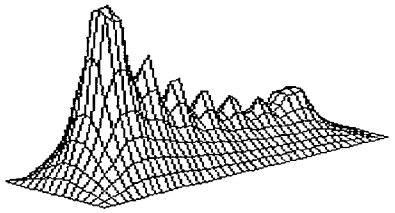


Fig.4.4.b - Potential Surface

5. CONCLUSION

Although we had used just real domain and ICCG solution with no very sofisticated discretization of the soil domain, until now, the results show viability of the solution global matrix with lumped network parameters and FEM matrix, as can be seen in the examples.

ACKNOWLEDGEMENT

PROMON Engenharia that had supported this work..

REFERENCES:

[1] Cardoso, J.R.; GROUND-3D Versão 2.0 - Um software CAD/CAE para análise de sistemas de aterramento em baixa frequência. In: XII SNPTEE - Seminário Nacional de Produção e Transmissão de Energia Elétrica, Recife, Out. 93.

[2] Cardoso, J.R; FEM Modeling of Grounded Systems with Unbounded Approach. In: CONFERENCE ON THE COMPUTATIONAL ON ELETROMAGNETIC FIELDS, 9. Miami, 1993. COMPUMAG: proceedings. Miami,1993.

[3] Jacobs, D.A.H.; Generalization of the Conjugate Gradient Method for solving non -symetric and complex systems of algebraic equations, Central Electricity Generating Board, n. RD/L/N/70/80, 24/03/80.

[4] Mesquita, R.C.;'Cálculo de campos eletromagnéticos tridimensionais utilizando elementos finitos: Magnetostática, Quase-estática e Aquecimento Indutivo.', Tese de Doutorado - Universidade Federal de Santa Catarina, Dez. 90.

[5] Senger, E.C.; Anniochimo, M.W.,'Método numérico para cálculo de distribuição em sistemas de aterramento multiconectado',In: XIV Congresso Ibero Latino Americano de Métodos Computacionais em Engenharia, Dez. 93.

[6] Stagg, G.W.;El-Abiad, A.H.;Computer Methods in Power System Analysis, McGraw-HIII, 1968.

ON THE OSCILLATORY PHENOMENA OF EDDY CURRENTS ALONG THE $\vec{A}$, V-Ψ INTERFACE

Z. Cheng, Q. Hu, S. Gao, Z. Liu, M. Wu, C. Ye
Baoding Transformer Works, Baoding 071056, China

ABSTRACT This paper investigates the oscillatory phenomena of the solution of eddy currents along the interface between the $\vec{A}$, V conductor and the Ψ-current-free region in the $\vec{A}$, V-Ψ approach, and the schemes to remove those strange numerical behaviors have been proposed and carried out .

1. OSCILLATORY PHENOMENA OF $\vec{J}$ IN $\vec{A}$, V-Ψ INTERFACE

The general multi-subregion eddy current problems are often encountered in the design of electromagnetic devices, various advanced analysis facilities have been developed and verified in every aspects. As a way out to cope with the multi-subregion problem involving the multiply connected conductors the combined use of different vector and/or scalar potential sets by no special numerical dealing was investigated[1].

In the combined version the $\vec{T}-\Psi-\Psi$($\vec{T}$: electric vector potential; Ψ: magnetic scalar potential) and the $\vec{A}-V-\vec{A}$ ($\vec{A}$: magnetic vector potential; V: electric scalar potential) as two basic potential sets[5] were alternatively used in the different subregions. It aims to make use of the complementary advantages of every analysis methods to be combined and avoid their shortcomings when used individually, to simplify the numerical implementations, and to reduce the computing cost. Since the numerical solutions of the same field problem by the different analysis tools may not approach to the exact solution in the same trends[6]. It is also expected to improve those numerical solutions of both the eddy current $\vec{J}$ and the magnetic flux densities $\vec{B}$.

However, the oscillatory phenomena of the solution of eddy current $\vec{J}$ have been found along the interface between the conductor described by the $\vec{A}$, V set and current-free region in which Ψ scalar potential was employed only.

We have noticed that O. Biro and A. Kameari have pointed out the oscillatory phenomena of the magnetic flux densities $\vec{B}$ occurred on the interface between $\vec{A}$ and Ψ for magnetostatic case[3, 4], O. Biro has obtained an improved solution of magnetic flux densities by setting up the $\vec{A}-\Psi$ boundary outside $\vec{A}$ -conductor[3].

2. ON THE DUALIZED NUMERICAL TEST

To study the numerical behaviours of the combined potential sets a dualized numerical test has been proposed[2], that is, two simply connected conducting plates of high per-

meability were driven by a time varying and uniform magnetic field, and the $\vec{A}-V$ and the $T-\Psi$ potential sets were adopted in the different plates, respectively, as shown in Fig. 1.

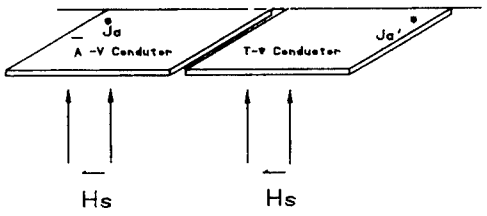
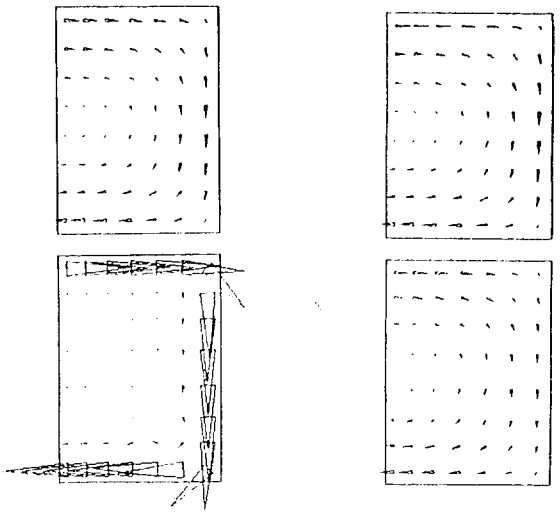


Fig. 1 The dualized test model
Note: Here $\vec{J}a$ and $\vec{J}a'$ are the corresponding positions

Due to the symmetry of the testing conditions described above the distributions of eddy currents induced in the two plates should be the same. However, the numerical test results obtained by the combined code have shown that the distributions of eddy current in the $\vec{A}$, V conductor become strange, especially, along the boundary of the $\vec{A}$, V conductor, as shown in Fig. 2(a).



(a) without penalty-plus factor (Ca=1)

(b) with penalty-plus factor (Ca=33. e3)

Fig. 2 Distributions of eddy currents caused in $\vec{A}$, V and T, Ψ conductors

Notes:

1) Number of brick elem. = 1386
2) Number of unknowns = 3758
3) Number of nodes =1840
4) The upper plate: $\vec{T}, \Psi$ set
   The lower plate: $\vec{A}, V$ set
5) μr : relative permeability of steel plate
   here $\mu r = 500$.
6) PICCG solver used

3. ON THE PENALTY-PLUS FACTOR

In the combined use of the $\vec{A}, V-\vec{A}-\Psi$ and the $\vec{T}, \Psi-\Psi$ presented here the Coulomb gauge was imposed in forms of penalty-function term to the curl-curl equations,

$$\nabla \times \frac{1}{\sigma} \nabla \times \vec{T} - \{\nabla(\frac{1}{\sigma} \nabla \cdot \vec{T})\} + \frac{\partial}{\partial t} \mu \ (\vec{T} - \nabla \Psi) = 0 \tag{1}$$

$$\nabla \times \frac{1}{\mu} \nabla \times \vec{A} - \{\nabla(\frac{Ca}{\mu} \nabla \cdot \vec{A})\} + \sigma \ (\frac{\partial \vec{A}}{\partial t} + \nabla \frac{\partial V}{\partial t}) = 0 \tag{2}$$

Notice that here Ca was introduced into the penalty-function term within {} of (1). we have seen that Ca does enhance the "zero-divergence" condition, therefore it can be referred as a "penalty-plus factor". The distributions of eddy currents can be dramatically improved by tacking a suitable penalty-plus factor, see Fig. 2(b).

What are the reasons to cause the strange numerical behaviours? It is worth to further study. According to the numerical tests done by the authors it can be summarized as follows:

(1) The finite element system of the $\vec{A}, V-\Psi$ is symmetric but non-positive definite and badly ill-conditioned, and the ill-condition of the system will be sharpening when the permeability of the conductor become high;

(2) The "zero-divergence" condition of the Coulomb gauge is poorly realized;

(3) Both the continuity of Bn and Ht (normal component of magnetic flux densities $\vec{B}$ and tangent component of magnetic field intensity H) are weakly satisfied for nodal FEM.

However, it has been shown that both the ill-condition of $\vec{A}-V$ submatrix and the numerical divergence of $\vec{A}$ can be considerably improved. Fig. 3 and table 1 show the variation of the sum total of the non-zero numerical divergence of $\vec{A}$ at the centers of all brick elements with the penalty-plus factor Ca.

Table 1

Ca	$\Sigma \mid \nabla \cdot \vec{A}_{max} \mid$ $*10^{-4}$	$\nabla \cdot \vec{A}_{max}$ $*10^{-5}$
500	2.779	1.488
1000	2.124	1.033
1500	1.736	0.8066
2000	1.473	0.6684
2500	1.281	0.5742
4560	0.8325	0.3716
8630	0.5011	0.2270
12690	0.3742	0.1673
16750	0.3024	0.1338
20820	0.2550	0.1119
24880	0.2208	0.09627
28940	0.1953	0.08456
33000	0.1753	0.07542

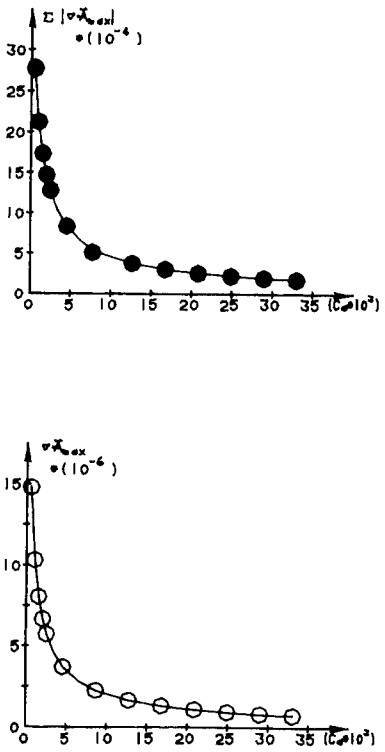


Fig. 3 Variation of div $\vec{A}$ with Ca

Fig. 4 and table 2 show the relation between the penalty-plus factor Ca to be taken and relative permeability μr of $\vec{A}$, V conductor.

Table 2

μr	Ca
1	$0.58*10^3$
25	$3.30*10^3$
50	$5.10*10^3$
100	$8.70*10^3$
200	$15.00*10^3$
300	$21.40*10^3$
400	$27.50*10^3$
500	$33.00*10^3$

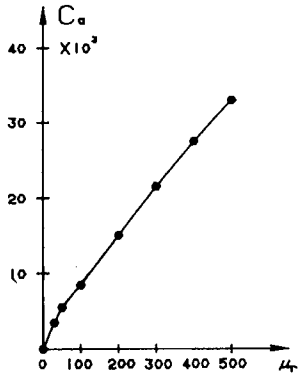


Fig. 4 relation of Ca and μr

The numerical test also showed that the relation between the iteration number of PICCG and the relative permeability of the conductor μr, as shown in Fig. 5.

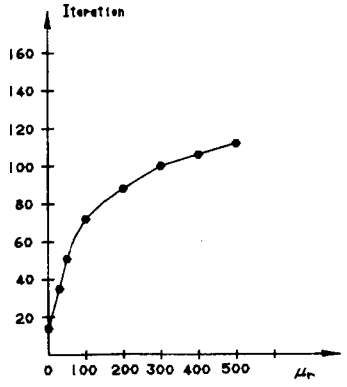


Fig. 5 relation between PICCG and μr

4. CONCLUSIONS

The dualized numerical tests proposed in the paper have been carried out to show the strange phenomena of the solution of eddy currents when run the combined code, and those unexpected numerical phenomena can be removed by taking a proposed penalty-plus factor in Coulomb gauging, and the related performances about the penalty-plus factor Ca have been shown in the paper.

ACKNOWLEDGMENT

This work was supported by The National Natural Science Foundation of China.

REFERENCES

[1] Z. Cheng, S. Gao, C. Ye, J. Wang, P. He, "On the development of the combined eddy current code", Proc. of ACES, 1992, pp. 314-390

[2] Z. Cheng, Q. Hu, S. Gao, Z. Liu, C. Ye, M. Wu, "On the use of combined potential sets to cope with general eddy current problems", paper of the CEM'94, London.

[3] K. Preis, O. Biro, C. Magele, W. Renhart, K. R. Richter, G. Vrisk, "FEM analysis of 3Dmagnetostatic fields",

[4] A. Kameari, " Study on 3-D eddy current analysis using FEM", Proc. of 4th IGTE and European TEAM workshop, 1990, pp. 91-99

[5] O. Biro, K. Preis, "Finite element analysis of 3-D eddy currents", IEEE Trans., Mag-26, 1990, pp. 418-423

[6] T. Nakata, N. Takahashi, K. Fujiwara, Y. Shiraki, "Comparison of different finiteelements for 3-D eddy current analysis", IEEE Trans., Mag-26, pp. 434-437

A New MMP-Code for Static Field Computation

M. Gnos and P. Leuchtmann
Lab. of El.-mag. fields and Microwave Electronics, ETH Zurich
CH-8092 Zurich, Switzerland

Abstract: *A new MMP-code for static field computation based on generalized multipole techniques (GMT) has been implemented. In absence of time variations Maxwell's equations are separated in three formally equal and independent systems of equations referred to as the electrostatic, the magnetostatic and the direct current system. The new program handles all of them.*

Different types of expansion functions are implemented: regular and singular multipole functions for 2D and 3D as well as charge or current distributions on a curved thin wire. In addition to the features of the time harmonic version both scalar and vector potentials are available, as well as zero order pole functions (point charges, inexistant in the time harmonic case due to charge conservation). Complex field components are reduced to real ones and thus simplify the computation.

In electrostatics both the total charge or the potential of electrodes may be either given or computed (by field integration) after having solved the field problem. Additional constraints concerning, e.g., total charge can be applied.

Static solutions may serve as quasistatic expansion functions for low frequency problems and/or for (electrically) small areas.

Examples out of electrostatics (red blood cell detetection using an Ohmmeter), magnetostatics (screening effect of iron rails) and quasistatics (foot point impedance of an antenna) show the wide range of application of the new static MMP-code.

1. Introduction

The MMP-program package [1] is a top level tool for computational electromagnetics in frequency domain for situations smaller than, say five to ten, wave lengths and piecewice homogeneous, linear and isotropic materials. It is possible to calculate quasistatic fields by specifying a very low frequency. However, a few specific and typically static effects — e.g., a net charge on an insulated electrode — are not covered with this approach.

As it is well known, MMP expands the unknown electromagnetic field

$$\begin{pmatrix}\vec{E}\\ \vec{H}\end{pmatrix} = \begin{pmatrix}\vec{E}_0\\ \vec{H}_0\end{pmatrix} + \sum_{k=1}^{N} a_k \begin{pmatrix}\vec{E}_k\\ \vec{H}_k\end{pmatrix} \qquad (1)$$

in a series where each $\begin{pmatrix}\vec{E}_k\\ \vec{H}_k\end{pmatrix}$ is a solution of Maxwell's equations, i.e., the electric field $\vec{E}_k$ and the magnetic field $\vec{H}_k$ are coupled through Maxwell's equations. As a matter of fact this coupling becomes very weak at low frequencies. MMP fulfils this weak coupling analytically but it allows numerical errors for fulfilling the boundary conditions. In almost static cases the rigorous respecting of the very weak $\vec{E} \leftrightarrow \vec{H}$ coupling turns out to be an unnecessary restriction. Using two independent expansions for $\vec{E}$ and $\vec{H}$ respectively gives more freedom to satisfy the boundary conditions. Classic MMP has not only an upper frequency limit but also a lower one. The static MMP program, the subject of this paper,, eliminates the lower frequency limit.

Note that in principal $\vec{E}$ and $\vec{H}$ are still coupled, not field↔field but source↔source (i.e., charge↔current through the charge conservation principle). However, in many practical applications the sources are located on the boundary rather than inside the field domain. The classical MMP approach allows errors on the boundaries but forbids errors in the domain. Concerning $\vec{E} \leftrightarrow \vec{H}$ coupling this is much too restrictive at low frequencies. The (almost) inexistent field↔field coupling in the domain must be dropped.

Moreover, in many practical cases only $\vec{E}$ (or only $\vec{H}$ or the current density $\vec{j}$ respectively) are requested. The remaining fields, though existing, need not to be calculated explicitely. On the other hand, potentials of the fields are often required in statics, in particular when boundary conditions are given in terms of potentials rather than in terms of fields. This leads to a necessary extension of the MMP program. Of course, the purely static procedure allows one only to perform real calculations which are much more efficient than MMP's complex matrix solvers.

2. The Static Theory

In the case of piecewise homogenous, linear and isotropic materials (described by the permittivity ε, the permeability μ and the conductivity σ, the static Maxwell's equations in the field domain are

$$\begin{aligned} \operatorname{rot}\vec{H} = \vec{j}_0, \quad \operatorname{div}\vec{H} = 0, \qquad & \text{(magnetostatics)(2-1)} \\ \operatorname{rot}\vec{E} = \vec{0}, \quad \operatorname{div}\vec{E} = \varrho_0/\varepsilon, \quad & \text{(electrostatics)} \quad (2\text{-}2) \\ \operatorname{rot}\vec{j} = \vec{0}, \quad \operatorname{div}\vec{j} = 0. \qquad & \text{(direct current)} \quad (2\text{-}3) \end{aligned}$$

The only formal difference between the three static domains are the right hand sides in the equations. The homogeneous equations (i.e., if $\vec{j}_0 = \vec{0}$ and $\varrho_0 = 0$) are identical for both $\vec{H}$, $\vec{E}$ and $\vec{j}$. The main task in MMP is finding an expansion for the solution of the *homogeneous* equations. Thus we can treat all static cases (electrostatics, magnetostatics and direct current) in the same way. We write $\vec{F}$ for the field, look for a solution of

$$\operatorname{rot}\vec{F} = \vec{0}, \quad \operatorname{div}\vec{F} = 0 \tag{3}$$

and may state that $\vec{F}$ has both a scalar potential g and a vector potential $\vec{G}$ with[1]

$$\vec{F} = \operatorname{rot}\vec{G}, \quad \vec{F} = -\operatorname{grad} g. \tag{4}$$

Assuming Coulomb gauge ($\operatorname{div}\vec{G} = 0$) for the vector potential all these functions are also solutions of the Laplace equations

$$\Delta\vec{F} = \vec{0}, \quad \Delta\vec{G} = \vec{0}, \quad \Delta g = 0. \tag{5}$$

Thus, a general static MMP expansion $f(\vec{r})$ consists not only of a field but also of the associated potentials:

$$f(\vec{r}) = \begin{cases} \vec{F}(\vec{r}) & \text{vectorial field } (\vec{E}, \vec{H}, \vec{j}\ldots) \\ \vec{G}(\vec{r}) & \text{associated vector potential} \\ g(\vec{r}) & \text{associated scalar potential} \end{cases} \tag{6}$$

and the expansion for a field domain D is

$$f_{\text{tot}} = f_0 + \sum_{k=1}^{N} a_k f_k, \tag{7}$$

where f_0 covers the particular (inhomogeneous) solution[2] while the 'seven dimensional' real spacefunctions f_k satisfy the homogeneous equations (3) to (6). Note that optionally, not all seven components of f are in use for a particular problem. E.g., in magnetostatics the scalar potential is not defined in the presence of currents.

The boundary conditions to be fulfilled on the boundary $\partial\mathrm{D}_{ik}$ between the subdomains D_i and D_k are different in all three static domains. In electrostatics, we have

$$\vec{E}_{i\mathrm{T}} - \vec{E}_{k\mathrm{T}} = \vec{0}, \quad \varepsilon_i E_{i\mathrm{n}} - \varepsilon_k E_{k\mathrm{n}} = \varsigma, \tag{8}$$

where the indices T and n denote the respective components tangential and normal to the boundary and ς is a possible surface charge density.

In magnetostatics, we have

$$\vec{H}_{i\mathrm{T}} - \vec{H}_{k\mathrm{T}} = \vec{0}, \quad \mu_i H_{i\mathrm{n}} - \mu_k H_{k\mathrm{n}} = 0, \tag{9}$$

and in the case of direct current, it is

$$\frac{1}{\sigma_i}\vec{j}_{i\mathrm{T}} - \frac{1}{\sigma_k}\vec{j}_{k\mathrm{T}} = \vec{0}, \quad j_{i\mathrm{n}} - j_{k\mathrm{n}} = 0. \tag{10}$$

All potential components are continuous across a boundary, as long as the same gauge and the same normalization is used on both sides. We simply have

$$\vec{G}_i = \vec{G}_k \quad \text{and} \quad g_i = g_k \tag{11}$$

on the boundary $\partial\mathrm{D}_{ik}$.

3. The MMP Implementation

Similar to the dynamic case, the static MMP approach starts with an expansion (7) in each subdomain D_i and sets up an overdetermined system of equations for the unknowns a_k by introducing the expansion in the respective boundary conditions (8)...(11) being evaluated in the so-called matching points on the boundary. The resulting system of equations is solved in the least squares sense using Givens plane rotations.

3.1 The Static Boundary Conditions

A straightforward least squares technique minimizes the sum of the squares of the errors of each equation. In the computer, this minimization is done with *numbers* rather than with physical quantities. Due to the fact that fields and potentials have different physical units, numerical errors of both quantities may not be compared directly with each other. Further on, considering the normal conditions (8) in the special case of a fictitious boundary, say vacuum at both sides, one finds that the numbers in the right equation in (8) are essentially $\varepsilon_0 \approx 8.854 \cdot 10^{-12}$ times smaller than those in the left equations in (8). This means that the mismatching $\Delta E_{\mathrm{n}} := E_{i\mathrm{n}} - E_{k\mathrm{n}}$ may be ten billion times larger than the *mismatching* of the tangential $\vec{E}$-components, but the least squares routine

[1] The existence of both $\vec{G}$ and g is given in simply connected field domains only.

[2] f_0 need not to have both scalar and vector potential.

still 'sees' a larger error of the tangential components. To avoid such differences, MMP divides the boundary conditions (8)...(11) by appropriate numbers. The user may define two general weighting constants ($K_{s,v}$) for this purpose, one for the scalar potential and one for the vector potential. The actual equations to be fulfilled in a matching point are[3]

$$\begin{aligned}
\lambda_i \vec{F}_i \cdot \vec{u}_1 - \lambda_k \vec{F}_k \cdot \vec{u}_1 &= 0, && (12\text{–}1)\\
\lambda_i \vec{F}_i \cdot \vec{u}_2 - \lambda_k \vec{F}_k \cdot \vec{u}_2 &= 0, && (12\text{–}2)\\
\kappa_i \vec{F}_i \cdot \vec{u}_n - \kappa_k \vec{F}_k \cdot \vec{u}_n &= 0, && (12\text{–}3)\\
K_v \vec{G}_i \cdot \vec{u}_1 - K_v \vec{G}_k \cdot \vec{u}_1 &= 0, && (12\text{–}4)\\
K_v \vec{G}_i \cdot \vec{u}_2 - K_v \vec{G}_k \cdot \vec{u}_2 &= 0, && (12\text{–}5)\\
K_v \vec{G}_i \cdot \vec{u}_n - K_v \vec{G}_k \cdot \vec{u}_n &= 0, && (12\text{–}6)\\
K_s g_i - K_s g_k &= 0. && (12\text{–}7)
\end{aligned}$$

Thereby, $\lambda_{i,k}$ and $\kappa_{i,k}$ are related to the permittivities $\varepsilon_{i,k}$, permeabilities $\mu_{i,k}$ and conductivities $\sigma_{i,k}$, $\vec{u}_1$ and $\vec{u}_2$ are tangential unit vectors and $\vec{u}_n$ is the normal unit vector. The actual values for the constants are:

	el.-stat.	mag.-stat.	current
$\lambda_i =$	1	1	$\sqrt{\frac{\sigma_k}{\sigma_i}}$
$\lambda_k =$	1	1	$\sqrt{\frac{\sigma_i}{\sigma_k}}$
$\kappa_i =$	$\sqrt{\frac{\varepsilon_i}{\varepsilon_k}}$	$\sqrt{\frac{\mu_i}{\mu_k}}$	1
$\kappa_k =$	$\sqrt{\frac{\varepsilon_k}{\varepsilon_i}}$	$\sqrt{\frac{\mu_k}{\mu_i}}$	1

(13)

These values may be overridden by the user in the same way as it may be done in the dynamic MMP program [1,3].

Note that not all boundary conditions need to be used simultaneously. However, MMP's least squares technique makes it reasonable to use all of them in so far as the related quantities occur in the actual problem.

3.2 Available Expansion Functions

As expansion functions, 2D- and 3D-multipoles, 2D- and 3D-regular expansions as well as line charge segments and line current segments are currently implemented. Note that different coordinate origins deliver new functions. MMP uses several origins simultaneously in typical applications. The formulae for the 2D-multipoles of m-th order are (cylindrical coordinates ρ, ϕ and z):

$$\begin{aligned}
F_\rho &= \frac{m}{\rho^{m+1}} \begin{matrix}\cos\\ \sin\end{matrix}(m\phi),\\
F_\phi &= \frac{m}{\rho^{m+1}} \begin{matrix}\sin\\ -\cos\end{matrix}(m\phi),\\
F_z &= 0,\\
G_\rho &= 0,\\
G_\phi &= 0,\\
G_z &= \frac{1}{\rho^m} \begin{matrix}\sin\\ -\cos\end{matrix} m\phi,\\
g &= \frac{1}{\rho^m} \begin{matrix}\cos\\ \sin\end{matrix} m\phi.
\end{aligned} \qquad (14)$$

The corresponding regular expansions are very similar, but with positive powers of ρ. [3]

The formulae for the 3D-multipoles of n-th order and m-th degree are expressed in spherical coordinates r, θ and ϕ:

$$\begin{aligned}
F_r &= \frac{n+1}{r^{n+2}} P_n^m(\cos\theta) \begin{matrix}\cos\\ \sin\end{matrix}(m\phi),\\
F_\theta &= \frac{1}{r^{n+2}} \Big((n+m)\tilde{P}_{n-1}^m(\cos\theta) - \\
&\qquad n\cos\theta \tilde{P}_n^m(\cos\theta) \Big) \begin{matrix}\cos\\ \sin\end{matrix}(m\phi),\\
F_\phi &= \frac{m}{r^{n+2}} \tilde{P}_n^m(\cos\theta) \begin{matrix}\sin\\ -\cos\end{matrix}(m\phi)\\
G_r &= 0,\\
G_\theta &= \frac{-m}{nr^{n+1}} \tilde{P}_n^m(\cos\theta) \begin{matrix}\sin\\ -\cos\end{matrix}(m\phi),\\
G_\phi &= \frac{1}{nr^{n+1}} \Big((n+m)\tilde{P}_{n-1}^m(\cos\theta) - \\
&\qquad n\cos\theta \tilde{P}_n^m(\cos\theta) \Big) \begin{matrix}\cos\\ \sin\end{matrix}(m\phi),\\
g &= \frac{1}{r^{n+1}} P_n^m(\cos\theta) \begin{matrix}\cos\\ \sin\end{matrix}(m\phi)
\end{aligned} \qquad (15)$$

Thereby P_n^m is the associated Legendre polynomial and $\tilde{P}_n^m(\cos\theta) := P_n^m(\cos\theta)/\sin\theta$ is used to avoid numerical instabilities close to the z-axis. Again, the corresponding regular expansions are very similar, but with positive powers of r.

The electric field of a straight homogeneously charged line segment has the following form. The segment lies on the z-axis (between $z = 0$ and $z = l$)

[3] The surface charge density ς is supposed to be zero.

and has the length l.

$$\begin{aligned} F_\rho &= \frac{1}{\rho}\left(\frac{z}{r} - \frac{z-l}{\sqrt{\rho^2+(z-l)^2}}\right), \\ F_\phi &= 0, \\ F_z &= \frac{1}{\sqrt{\rho^2+(z-l)^2}} - \frac{1}{r}, \\ G_\rho &= 0, \\ G_\phi &= \frac{\sqrt{\rho^2+(z-l)^2}}{\rho} - \frac{r}{\rho}, \\ G_z &= 0, \\ g &= \ln\frac{\sqrt{\rho^2+(z-l)^2}-(z-l)}{r-z}. \end{aligned} \tag{16}$$

For simplicity's sake, the cylindrical coordinate $\rho = \sqrt{x^2+y^2}$ and the spherical coordinate $r = \sqrt{x^2+y^2+z^2}$ have been used. Note that $\vec{G}$ is singular on the whole z-axis. This means that the vector potential of this function should not be used if (a part of) the z-axis is in the field domain.

The field of a constant current in the same segment is more sophisticated. The magnetic field $\vec{H}$ and the associated vector potential $\vec{A}$ (with $\mathrm{rot}\,\vec{A} = \mu\vec{H}$) may be formally evaluated using Biot-Savart's integral:

$$\begin{aligned} H_\rho &= 0, \\ H_\phi &= \frac{1}{\rho}\left(\frac{z}{r} - \frac{z-l}{\sqrt{\rho^2+(z-l)^2}}\right), \\ H_z &= 0, \\ A_\rho &= 0, \\ A_\phi &= 0, \\ A_z &= \frac{1}{\mu}\ln\frac{\sqrt{\rho^2+(z-l)^2}-(z-l)}{r-z}. \end{aligned} \tag{17}$$

However, this is a highly *nonphysical field*: The curl equation (3) is not satisfied. Nevertheless we can use it, but only in conjunction with many segments forming a *closed* loop all together. The scalar potential of the field of a single current segment does not exist.

In static MMP long curved lines built up by an arbitrary number of segments may be defined. Thereby, the line specification is the same as that for the curved line multipoles [2,3].

Beside these basic expansion functions, there are the 'connections' — essentially expansion functions built up by a (possibly large) number of other expansion functions. The general procedure for building connections is the same as in time harmonic MMP [1,3].

3.3 Further Features

Most of the special features of the classic (time harmonic) MMP code are also available in the static version. We mention the symmetry feature (up to three symmetry planes may be specified), the constraints (additional equations, often related to line or surface integrals of field quantities) and the integrals (an output feature to obtain integral quantities such as total field energy etc.). A specifically static constraint is the total charge of an electrostatic model: it may be specified by the user.

Both input and output may be performed using the mmptool [4], including all geometric data and the automated choice of the expansion functions (2D- and 3D-multipoles only). However, at present state the mmptool has not been adapted to statics yet. Thus, a few lines of particular static input data must be added to the input file using a text editor.

3.4 Quasistatic Calculations

Static models are theoretical models. No practical application helds the same field unchanged for an infinite amount of time. However, very slowly varying fields show the same spacial dependency as the static field. E.g., we may write

$$\vec{E}_{\mathrm{ex}}(\vec{r},t) \approx \vec{E}_{\mathrm{stat}}(\vec{r})\cdot T(t) \tag{18}$$

where the indices 'ex' and 'stat' stand for exact and static respectively and $T(t)$ is a (slow[4]) time function. Thus, static MMP solutions may be used as special expansion functions in classic (time harmonic) MMP. Let us describe the procedure with an example. Suppose the field in the feeding area of an antenna is calculated by means of static MMP with the results

$$\vec{E}_{\mathrm{stat}}(\vec{r}) = \vec{E}_0(\vec{r}) + \sum_{k=1}^{N_{\mathrm{e}}} \alpha_k \vec{E}_k(\vec{r}), \tag{19-1}$$

$$\vec{H}_{\mathrm{stat}}(\vec{r}) = \vec{H}_0(\vec{r}) + \sum_{k=1}^{N_{\mathrm{m}}} \beta_k \vec{H}_k(\vec{r}) \tag{19-2}$$

with *real* parameters α_k, β_k. These solutions are taken as a connection [1,3] in the expansion of the time harmonic antenna problem, i.e., the time harmonic expansion for the feeding area consists of two members:

$$\begin{pmatrix}\vec{E}_{\mathrm{timhar}}\\ \vec{H}_{\mathrm{timhar}}\end{pmatrix} = a_1\begin{pmatrix}\vec{E}_{\mathrm{stat}}\\ \vec{0}\end{pmatrix} + a_2\begin{pmatrix}\vec{0}\\ \vec{H}_{\mathrm{stat}}\end{pmatrix} \tag{20}$$

where a_1 and a_2 are *complex* unknowns of the full problem and the expansion of the outer area is of

[4] i.e., the field domain is small compared to the minimum wave length related to $T(t)$.

the form (1). Note that the two terms in (20) are not classical MMP expansion functions as those in (1) because they satisfy Maxwell's equations only approximately and only as a pair. Nevertheless a_1 and a_2 are independent and will be determined by matching the feeding area expansion (20) with the outer area expansion of the antenna. NB: The ratio a_1/a_2 is closely related to the foot point impedance of the antenna.

A special version of the MMP code has been worked out to allow (pairs of) static solutions as connections.

4. Examples

We treat three typical examples to illustrate the capabilities of the new static and the quasistatic MMP code. The first example is a direct current problem: The penetration of a red blood cell (RBC) through a hole in a membrane is measured using an ohmmeter. To predict the resistance an accurate calculation of the highly inhomogeneous current density is necessary. The second example treats the magnetostatic problem of cables mounted close to one rail of a railroad. The screening effect of the rail may cause problems when the cable is used for signal transmission to the train. The third example deals with the foot point impedance of an antenna. The feeding area is calculated by quasistatic MMP and then matched with the time harmonic solution.

4.1 Detection of Red Blood Cells

Since the conductivity of red blood cells (RBC) is much lower than that of the fluid around the presence of RBC's may alter the electrical resistance of specific situations. The effect may be used to detect RBC's moving through membrane holes. A simple model with an insulating membrane with a single hole is shown in fig. 1. Between two parallel infinite plates there are an insulating membrane with a single circular hole and an insulating RBC imbedded in a conductive medium. The geometrical shapes of both the (insulating) membrane and the RBC are simplified in order to use the symmetry of revolution. The picture gives a plot of the current density for a particular location of the RBC. The electrical resistance measured between the plates varies strongly when the RBC moves through the hole. Figure 2 shows the relative variation of the resistance when the RBC moves from the top plate downto the bottom plate.

The calculation is split up in two steps: The situation without RBC — yielding a 177 unknowns 'connection'[5] for the second step — and the influence of the RBC. Both memory requirement and cpu times are very moderate for this small problem. Actual values for a generic position (960 matching points model) are 137(+177) unknowns, 28 sec cpu time[6], 0.5 MByte for the data including the matrix and 0.6 MByte for the program. Thereby, the accuracy is $\approx 1\%$ for individual field values.

For computing the resistance $R = U/I$, the total current I is obtained by integrating the current density over the hole area while the voltage U is simply given by the boundary values of the potential.

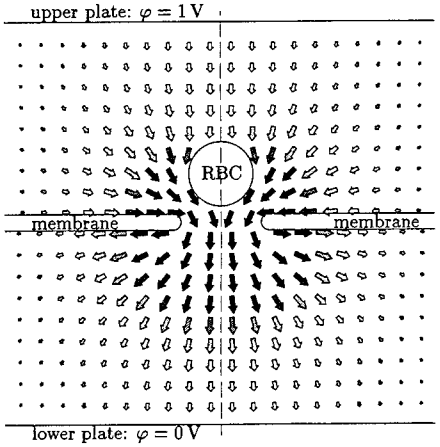


Figure 1: Two infinitely well conducting parallel plates are kept at potentials 0 V and 1 V respectively. Both the membrane and the red blodd cell (RBC) are practically insulating compared to the blood fluid. The shown current density is highly inhomogeneous, particularly when the RBC's position is close to the membrane hole. The dashed vertical line is the axis of rotational symmetry used in this model. Exploiting this symmetry yields a significant reduction of both computation time and storage requirement.

4.2 Magnetostatic Screening of a Rail

For transmitting informations from and to moving trains two wire transmission lines with seperately positioned wires are mounted along the railway line, e.g., one wire very close to one rail and the second wire two meters apart from the rail. The particular shape of the rail and the high relative permittivity ($\mu_r \approx 200$) of the iron deform the magnetic field in the close environment of the wire. Figure 3 shows the strong screening effect with one wire mounted in the groove of the rail.

[5] See end of sect. 3.1

[6] All cpu time values for a Sparc2.

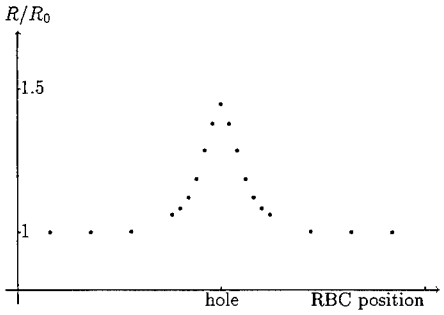


Figure 2: The resistance R — measured between the two plates shown in fig. 1 — depends on the relative position of the RBC. This picture shows the variation of R/R_0 when the RBC is moved along the rotational axis. R_0 is the resistance without any RBC. Note that the maximum value (RBC centered in the hole) may be calculated using an additional reflective symmetry and thus allowing much higher accuracy at the same amount of calculation. The curve is symmetrical with respect to the hole position. Therefore, only one half is calculated.

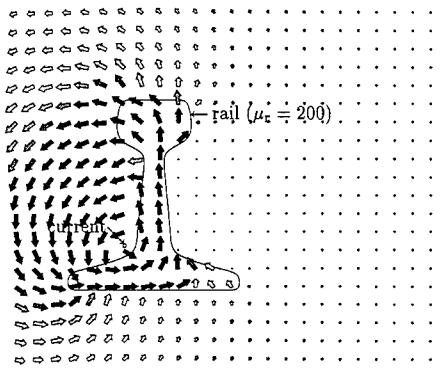


Figure 3: The magnetic field — the picture shows the magnetic induction $\vec{B} = \mu\vec{H}$ — of the current flowing in the wire parallel to a rail is strongly deformed. This is due to the shape of the rail and the high magnetic permeability (μ_r) of the iron. The return path for the current is a few meters apart from the rail. See also fig. 4 for a more general view.

However, as shown in fig. 4, this is only a local effect and must be taken into account when the detector on the train is mounted close to its wheels.

It is important to note that this calculation is purely magnetostatic. This means that no skin effect, eddy current or other dynamic effects are taken into account. Further on, we are discussing a two

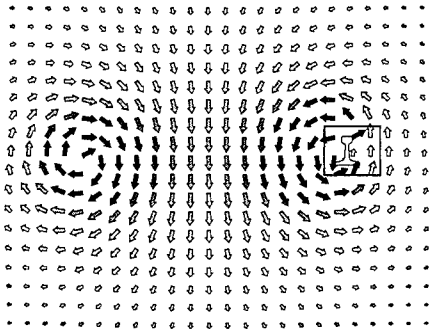


Figure 4: Though the magnetic is deformed in the close neighborhood of the rail (see fig. 3) the effect is small far away from the rail.

dimensional (cylindrical) model here.

The contour of the rail is discretized using 688 matching points and as much as 693 unknowns model the field. This results in 338 sec Sparc2 cpu time for the solution and about 2 MBytes memory requirement for the matrix. The use of so many unknowns for a relatively simple problem yields an almost 'analytical' accuracy: The maximum mismatching is below 0.1%.

4.3 Footpoint Impedance of an Antenna

As already mentioned in section 3.4 appropriate static solutions may also be used to model so-called quasistatic fields. As an example we treat the calculation of the foot point impedance of a $\lambda/2$-monopole antenna mounted on an infinite ground plane. The feeding area is modelled very accurately in order to show the power and the precision of the method.

In a first step the electric field in the feeding area is calculated. Figure 5 shows the situation and the resulting field. A coaxial cable (with a dielectric) feeds the antenna from the bottom, the ground plane has a hole and is connected to the outer conductor of the cable. This calculation step requires 58 unknowns, 120 matching points and about 1 second Sparc2 cpu time. The voltage is given by the potential boundary values.

The second step deals with the magnetic field and requires no unknowns, no matching points and no cpu time. This is due to the fact that the magnetostatic field is just the field of a straight current. The return current which actually flows in the outer conductor of the coaxial cable and — radially — in the ground plane does *not* contribute to the field inside the feeding area and need not to be modelled. Figure 6 shows the result.

The third and last step combines the two static fields and matches them to the dynamic field of the

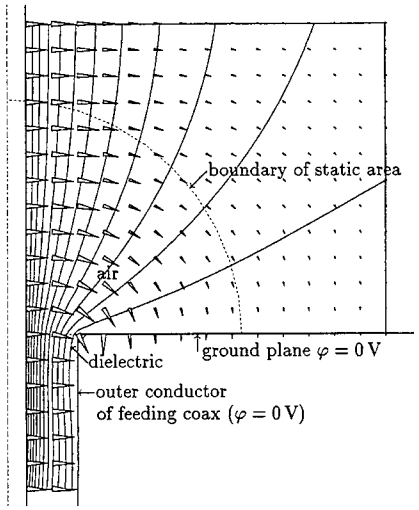


Figure 5: The electric field (triangles) and the associated equipotential lines in the feeding area of an antenna, calculated by means of electrostatics. Only the portion below the dotted arc will be used later. (The outer field will be a true dynamic, i.e., time harmonic field.) Note that even the permittivity of the coaxial feeding cable's dielectric is taken into account. The model has a symmetry of revolution with respect to the dash dotted axis at the left.

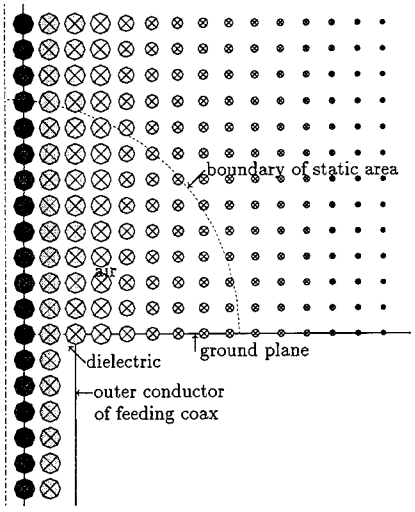


Figure 6: The magnetic field in the feeding area of an antenna is calculated by means of magnetostatics. It is equal to the well known field of a straight current and requires pracitcally no cpu-time. As in fig. 5 only the portion below the dotted arc will be used later.

antenna. Below the bell-shaped boundary shown in figs. 5 and 6, the static fields $\vec{E}_{\text{stat}}$ and $\vec{H}_{\text{stat}}$ each multiplied by separate *complex* constants (a_{E} and a_{H}) are valid while in the outer area a conventional (i.e., time harmonic) MMP expansion is used. Either static fields are matched with the dynamic field on the surface of the bell. The computation leads to certain constants a_{E} and a_{H}. Provided that the static fields are associated with a voltage of 1 V and 1 A respectively, the complex footpoint impedance simply becomes $Z = a_{\text{E}}/a_{\text{H}}$. Figure 7 shows the fitting of the static and the dynamic field and fig. 8 gives the instantaneous values of both the electric field and the Poynting field $\vec{S}$ close to the $\lambda/2$ monopole antenna.

The dynamic problem consists of only 16 unkowns, the current in the antenna modelled with 10 unkowns and a few multipole functions to adapt the solution to the feeding area and the unknown voltage (numerically equal to a_{E}). The current (numerically equal to a_{H}) is set to 1. 148 matching points were used and the cpu worked for 154 seconds.

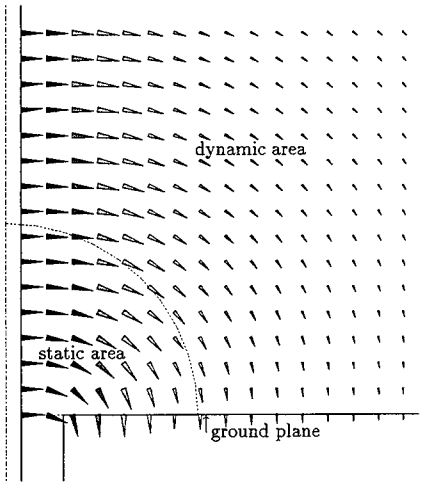


Figure 7: The statically computed electric field in the inner area fits seamlessly to the dynamically computed field in the outer area. The same is true for the magnetic field (not shown in the picture).

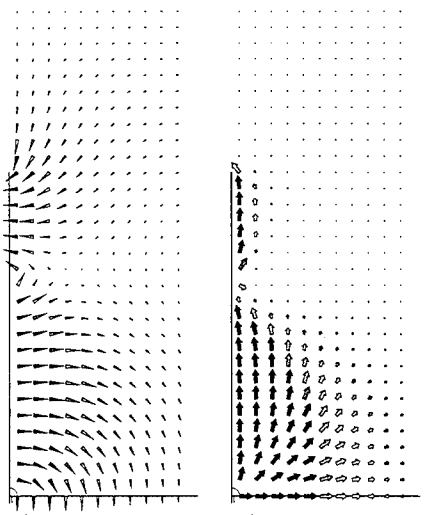


Figure 8: The instantaneous values of both Poynting field (right) and electric field (left) show the dynamic character of the field. Note the small static area indicated at the lower left corner of each picture.

5. Summary

With the new static MMP program both electrostatic, magnetostatic and direct current problems may be solved. Further on, the static solutions may be used as quasistatic expansions in dynamic situations. 2D and 3D multipoles and regular expansion functions as well as finite length line currents and line charges are implemented. Both fields and their scalar and vector potentials may be used. The examples show the high flexibility and the wide range of applications of the new program. A beta-version of the program is available. It is planned to add the static program to the full MMP package.

References

[1] Ch. Hafner and L. Bomholt, The 3D Electrodynamic Wave Simulator (including the 3D-MMP source code), John Wiley & Sons Ltd., 1993.

[2] P. Leuchtmann and M. Gnos, "Curved Line Multipoles for the MMP-Code", in 10-th Annual Review of Progress in Applied Computational Electromagnetics (ACES), Conference Proceedings, (Monterey), Mar. 1994.

[3] P. Leuchtmann, *The Generalized Multipole Technique (GMT) and the Multiple Multipole Program (MMP): Theory and Practical Use in Computational Electromagnetics*, 150 pages, 1995 (a basic introduction, available from the author).

[4] P. Regli, *mmptool*, freeware program, available through ftp anonymous on sirius.ethz.ch (129.132.41.1), directory mmp, ETH Zürich, Nov. 1993.

Molten Aluminum Flow Induced by High Magnetic Fields

W. Perry Wheless, Jr.[†] and C.S. Wheless[‡]
[†]Department of Electrical Engineering [‡]Seebeck Computer Center
University of Alabama, Tuscaloosa, AL 35487

Abstract

Previous work related to the characterization of aluminum reduction pots, in which extremely high currents are used to process bauxite into aluminum, has concentrated on finding the distribution of currents, magnetic fields and forces. With these computed forces and magnetic fields, it becomes possible to model the resultant swirling flow of molten aluminum. The equations that govern the molten metal flow are known as the Navier-Stokes equations. Investigation into a numerical solution of the Navier-Stokes equations, in the context of aluminum reduction pots, is reported here.

1 Introduction

Previous work related to the characterization of aluminum reduction pots, in which extremely high currents are used to process bauxite ore into aluminum, has concentrated on finding the distribution of currents, magnetic fields and forces. With these computed forces and magnetic fields, it becomes possible to describe the swirling flow of molten aluminum in the reduction pots. This is of interest to commercial producers of aluminum because the induced molten metal motion represents a substantial inefficiency, or loss of energy, in the refining process. The equations which govern the motion of the molten metal, and viscous flow in general, are known as the Navier-Stokes equations. This paper reports on an investigation into the numerical solution of the Navier-Stokes equations in the context of aluminum reduction pots.

There are two basic governing equations for incompressible fluid flow, which involve partial derivatives both with respect to time and space variables. These two equations also involve pressure and three forces - magnetic, flow resistance, and acceleration. It is possible to consolidate these into a single equation to be solved [1], but the order of differentiation is increased in the process so that numerical solution instabilities are inherent; also, pressure does not appear explicitly in the final equation, which is apparently linked to convergence problems.

An alternative approach, pursued here, is to solve the governing equations simultaneously, as a system, at a lower level of consolidation. Treating pressure explicitly and writing separate equations for the velocity components, a system of three equations results. A relaxed iterative finite difference solution of the Navier-Stokes

equations has been implemented. A Gauss-Siedel iteration method is utilized for the simultaneous solution of the three equations [2].

Test case results are shown, so that the feasibility of the method is established. The range of validity of this particular numerical solution formulation has not yet been established, and will be a matter for future research through more complex case studies. The influence of system parameter values (and ratios) on convergence are discussed.

2 Governing Equations

The two applicable relations for incompressible fluid flow are

$$\rho\frac{\partial \mathbf{V}}{\partial t} + \nabla P = \mathbf{J} \times \mathbf{B} + \mu\nabla^2\mathbf{V} + \frac{1}{3}\nabla(\nabla \cdot \mathbf{V}) \tag{1}$$

and

$$\frac{\partial P}{\partial t} + \nabla \cdot (\rho\mathbf{V}) = 0. \tag{2}$$

In the above equations, ρ is the specific density of molten aluminum (2.3×10^3 kg/m^3) and μ is the viscosity (1.2×10^{-3} $\frac{kg}{m-\text{sec}}$). The vector quantities are velocity $\mathbf{V}$, current density $\mathbf{J}$, and magnetic flux density $\mathbf{B}$.

As a first order model of the problem of interest, it is assumed that all quantities are invariant with respect to depth, so that work here is in a z = constant plane (taken at z = 0 for convenience). The rectangular geometry of the aluminum reduction pot is shown in Figure 1.

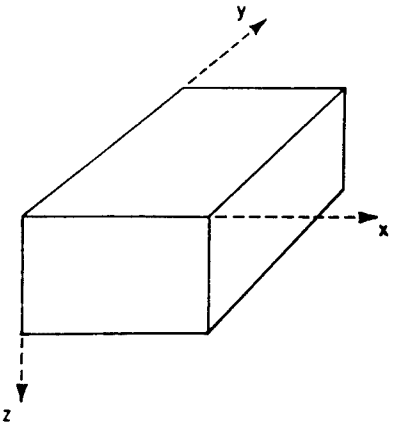


Figure 1. Aluminum reduction pot geometry.

Eqs. 1 and 2 involve pressure P and the forces $\mathbf{F}_m$ (magnetic), $\mathbf{F}_r$ (flow resistance), and $\mathbf{F}_a$ (acceleration). The gravity force, $\mathbf{F}_g$, is absent by virtue of investigating only

horizontal flow. In Eq. 1, the term $\frac{1}{3}\nabla(\nabla \cdot \mathbf{V}) = 0$ and, in Eq. 2, the term $\frac{\partial P}{\partial t} = 0$ for this case.

Dividing Eq. 1 by ρ, noting that $\mathbf{F}_m = \frac{\mathbf{J} \times \mathbf{B}}{\rho}$ (F_{mx} and F_{my} are known from calculation elsewhere), and writing separate equations for the velocity components, one can then write the equations for steady-state incompressible fluid flow as

$$u\frac{\partial u}{\partial x} + v\frac{\partial u}{\partial y} = -\frac{1}{\rho}\frac{\partial P}{\partial x} + F_{mx} + \upsilon\nabla^2 u \tag{3}$$

$$u\frac{\partial v}{\partial x} + v\frac{\partial v}{\partial y} = -\frac{1}{\rho}\frac{\partial P}{\partial x} + F_{my} + \upsilon\nabla^2 v \tag{4}$$

$$\frac{\partial u}{\partial x} + \frac{\partial v}{\partial y} = 0, \tag{5}$$

where $u = V_x, v = V_y$ and the relation $\mu = \rho\upsilon$ has been applied.

Making the assumption of small velocities, which is physically reasonable in this case, the equations to be solved may be somewhat simplified to the useful approximations

$$\upsilon\nabla^2 u \approx \frac{1}{\rho}\frac{\partial P}{\partial x} - F_{mx} \tag{6}$$

$$\upsilon\nabla^2 v \approx \frac{1}{\rho}\frac{\partial P}{\partial y} - F_{my} \tag{7}$$

and

$$\frac{\partial u}{\partial x} + \frac{\partial v}{\partial y} = 0. \tag{8}$$

3 Numerical Method

A Gauss-Siedel iteration method for simultaneous solution of Eqs. 6-8 has been selected. A grid of points is established in the z = constant plane (where the reduction pot spans $0 \leq x \leq \mathbb{L}$ and $0 \leq y \leq \mathbb{D}$) with spacings $\triangle x = \frac{\mathbb{L}}{NX}$ and $\triangle y = \frac{\mathbb{D}}{NY}$, where NX and NY are the number of subdivisions desired in the x and y directions, respectively. Three matrices are utilized, the elements of which are storage locations for the current values of u, v, and (pressure) P corresponding to the individual grid points. Starting with arbitrary initial values, the computation scheme methodically updates the matrix elements in an iterative manner until convergence is achieved or ITMAX (from the program input data) iterations have transpired.

To implement this method on the computer, it is necessary to express all derivatives present in the equations to be programmed by finite-difference operator approximations.

When Eqs. 6 through 8 are programmed using a mixture of forward difference and central-difference operators, the result exhibits very poor convergence behavior. Although convergence to 2% (maximum relative change in any matrix element during an update iteration) has been obtained for two test cases, neither solution was

physically meaningful. That is, convergence to false solutions occurred in both cases. Furthermore, a low $\triangle x$ to $\triangle y$ ratio, on the order of 0.01 or less, has been found empirically to be necessary for convergence to occur at all.

Substantial progress occurs when the problem is re-programmed to incorporate only the central-difference operators

$$\frac{\partial u}{\partial x} = \frac{u_{i+1,,j} - u_{i-1,,j}}{2\triangle x} + \mathcal{O}\left[(\triangle x)^2\right], \tag{9}$$

$$\frac{\partial^2 u}{\partial x^2} = \frac{1}{(\triangle x)^2}\left[u_{i-1,,j} - 2u_{i,,j} + u_{i+1,,j}\right] + \mathcal{O}\left[(\triangle x)^2\right], \tag{10}$$

and

$$\frac{\partial^2 u}{\partial y^2} = \frac{1}{(\triangle y)^2}\left[u_{i,,j-1} - 2u_{i,,j} + u_{i,,j+1}\right] + \mathcal{O}\left[(\triangle y)^2\right]. \tag{11}$$

Lower-case letters u, v, and p, where accompanied by subscripts, indicate elements of the respective matrices U, V, and P. The fact that the error for each of these approximations is on the order of the subject increment ($\triangle x$ or $\triangle y$) squared is emphasized by inclusion of the term $\mathcal{O}\left[(\cdot)^2\right]$ in Eqs. 9 through 11.

The change to exclusive use of central-difference operators makes all error terms in the numerical process the same order of magnitude, and results in a significant performance improvement. Convergence capability improves sharply, $\triangle x$ to $\triangle y$ ratios up to 0.5 become useful, and some physically reasonable solutions may be obtained. We shall return to the matter of final solutions after the numerical form and program are discussed. First, the equations as they are actually programmed are developed below.

Applying $\nabla^2 = \dfrac{\partial^2}{\partial x^2} + \dfrac{\partial^2}{\partial y^2}$ and the relation $\nu = \dfrac{\mu}{\rho}$ to Eq. 6,

$$\frac{\mu}{\rho}\left[\frac{\partial^2 u}{\partial x^2} + \frac{\partial^2 u}{\partial y^2}\right] = \frac{1}{\rho}\frac{\partial P}{\partial x} - F_{mx}. \tag{12}$$

Re-arranging,

$$\frac{1}{\rho}\frac{\partial P}{\partial x} = \frac{\mu}{\rho}\frac{\partial^2 u}{\partial x^2} + \frac{\mu}{\rho}\frac{\partial^2 u}{\partial y^2} + F_{mx}. \tag{13}$$

Multiplying both sides by ρ, one obtains

$$\frac{\partial P}{\partial x} = \mu\frac{\partial^2 u}{\partial x^2} + \mu\frac{\partial^2 u}{\partial y^2} + \rho F_{mx}. \tag{14}$$

If the appropriate finite-difference operator approximations are now used, the equation becomes

$$\frac{P_{i+1,j} - P_{i-1,j}}{2\triangle x} = \mu\frac{u_{i+1,j} - 2u_{i,j} + u_{i-1,j}}{(\triangle x)^2} + \mu\frac{u_{i,j+1} - 2u_{i,j} + u_{i,j-1}}{(\triangle y)^2} + \rho F_{mx}, \tag{15}$$

or, multiplying by $2\triangle x$, we obtain the useful form of

$$P_{i+1,j} - P_{i-1,j} = \frac{2\mu}{\triangle x}(u_{i+1,j} - 2u_{i,j} + u_{i-1,j}) \quad (16)$$
$$+2\mu\frac{\triangle x}{(\triangle y)^2}(u_{i,j+1} - 2u_{i,j} + u_{i,j-1}) + 2\rho\triangle x F_{mx}.$$

It is common practice to add a "relaxation" term as a variable aid to faster convergence. The relaxation term simply contributes a fractional part of the old value into the new value being computed. By re-arranging and adding such a term, the equation for computer implementation is

$$P^*_{i+1,j} = P_{i-1,j} + \frac{2\mu}{\triangle x}(u_{i+1,j} - 2u_{i,j} + u_{i-1,j}) \quad (17)$$
$$+2\mu\frac{\triangle x}{(\triangle y)^2}(u_{i,j+1} - 2u_{i,j} + u_{i,j-1}) + 2\rho\triangle x F_{mx}$$
$$+(1 - R_p)P_{i+1,j}$$

where the asterisk on $P^*_{i+1,j}$ denotes a new element value, replacing the old value $P_{i+1,j}$. Note that the effect of the relaxation term is negated if one inputs "1" as the value of variable R_p. Eq. 17 obviously can be re-arranged to give $P_{i-1,j}$ on the left-hand side, if desired.

Now recall that $\frac{\partial u}{\partial x} + \frac{\partial v}{\partial y} = 0$ from Eq. 8. If the finite-difference operator approximations are directly substituted:

$$\frac{u_{i+1,j} - u_{i-1,j}}{2(\triangle x)} + \frac{v_{i,j+1} - v_{i,j-1}}{2(\triangle y)} = 0 \quad (18)$$

or

$$u_{i+1,j} - u_{i-1,j} + \frac{\triangle x}{\triangle y}(v_{i,j+1} - v_{i,j-1}) = 0 \quad (19)$$

after multiplication by $2(\triangle x)$. The re-arranged form of this equation becomes

$$u_{i-1,j} = u_{i+1,j} + \frac{\triangle x}{\triangle y}(v_{i,j+1} - v_{i,j-1}). \quad (20)$$

Adding a relaxation term and emphasizing the new element value with an asterisk gives

$$u^*_{i-1,j} = u_{i+1,j} + \frac{\triangle x}{\triangle y}(v_{i,j+1} - v_{i,j-1}) + (1 - R_u)u_{i-1,j}. \quad (21)$$

The equation for $u^*_{i+1,j}$ is similar and obvious. Note that each major equation has been assigned its own relaxation term - involving R_u here. As indicated earlier, the effect of this relaxation term can be negated simply by setting the variable R_u equal to 1.0.

Finally, recall from Eq. 7 that $\upsilon\nabla^2 v \approx \frac{1}{\rho}\frac{\partial P}{\partial y} - F_{my}$. Again $\upsilon = \frac{\mu}{\rho}$, and if we substitute for ∇^2 :

$$\frac{\mu}{\rho}\left(\frac{\partial^2 v}{\partial x^2} + \frac{\partial^2 v}{\partial y^2}\right) = \frac{1}{\rho}\frac{\partial P}{\partial y} - F_{my}. \quad (22)$$

Multiplying by $\frac{\rho}{\mu}$,

$$\frac{\partial^2 v}{\partial x^2} + \frac{\partial^2 v}{\partial y^2} = \frac{1}{\mu}\frac{\partial P}{\partial y} - \frac{\rho}{\mu} F_{my}. \tag{23}$$

Application of the finite-difference operator approximations gives

$$\frac{v_{i+1,j} - 2v_{i,j} + v_{i-1,j}}{(\triangle x)^2} + \frac{v_{i,j+1} - 2v(i,j) + v_{i,j-1}}{(\triangle y)^2} = \frac{1}{\mu}\frac{P_{i,j+1} - P_{i,j-1}}{2\triangle y} - \frac{\rho}{\mu} F_{my}. \tag{24}$$

If we multiply through by $(\triangle x)^2(\triangle y)^2$ and re-arrange the equation, the result is:

$$\begin{aligned} v_{i,j}(-2)\left[(\triangle x)^2 + (\triangle y)^2\right] &= -(\triangle y)^2 (v_{i+1,j} + v_{i-1,j}) \\ &\quad -(\triangle x)^2 (v_{i,j+1} + v_{i,j-1}) + \frac{(\triangle x)^2(\triangle y)}{2\mu}(p_{i,j+1} - p_{i,j-1}) \\ &\quad -\frac{\rho}{\mu}(\triangle x)^2(\triangle y)^2 F_{my}. \end{aligned} \tag{25}$$

Finally, dividing by $(-2)\left[(\triangle x)^2 + (\triangle y)^2\right]$ and adding a relaxation term, we obtain the following equation:

$$\begin{aligned} v^*_{i,j} &= \frac{(\triangle y)^2}{2\left[(\triangle x)^2 + (\triangle y)^2\right]}(v_{i+1,j} + v_{i-1,j}) \\ &\quad + \frac{(\triangle x)^2}{2\left[(\triangle x)^2 + (\triangle y)^2\right]}(v_{i,j+1} + v_{i,j-1}) - \frac{(\triangle x)^2(\triangle y)}{4\mu\left[(\triangle x)^2 + (\triangle y)^2\right]}(p_{i,j+1} - p_{i,j-1}) \\ &\quad - \frac{\rho}{2\mu}\frac{(\triangle x)^2(\triangle y)^2}{\left[(\triangle x)^2 + (\triangle y)^2\right]} F_{my}, \end{aligned} \tag{26}$$

which can be implemented as the computer solution of the problem of interest.

4 Test Case

An example has been selected for illustration of the solution of the system of equations 17, 21, and 26. The forcing function of the example problem is depicted in Fig. 2. The function is defined along the mid-line in the x-direction (i.e., at $x = \frac{\mathbb{L}}{2}$). It varies sinusoidally in y as shown, with the periodicity chosen so that one complete cycle exactly spans the $y = 0$ to $y = \mathbb{D}$ range. More grid points were used in the lower plot so that the sinusoidal amplitude variation is more apparent. Convergence in this case was well-behaved, with the solution converging to an EPSMAX of 0.002 in about 55 iterations. The maximum change in any element of all three matrices U, V, and P from one iteration to the next must be less than user-specified EPSMAX for successful convergence to be declared.

The numerical solution results are given graphically in Fig. 3. A finer grid was used in the calculation of Fig. 3b. In both cases, the velocity plots substantially

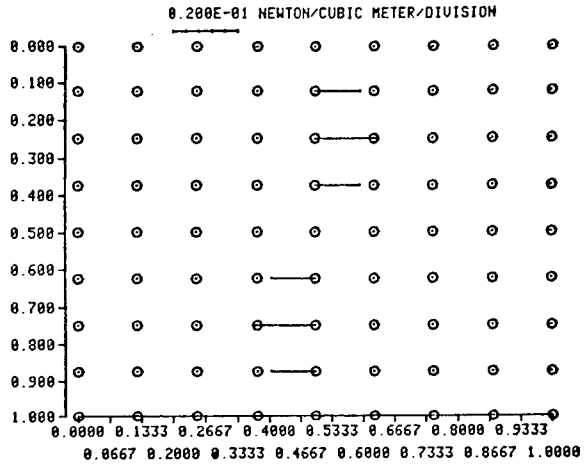


Figure 2a. Coarse grid spacing.

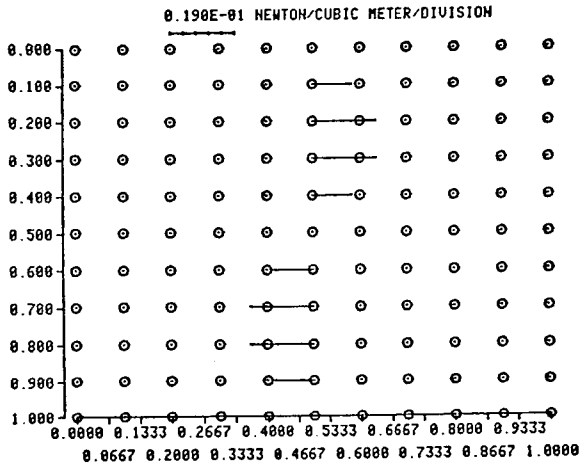


Figure 2b. Fine grid spacing.

Figure 2. Test case forcing function.

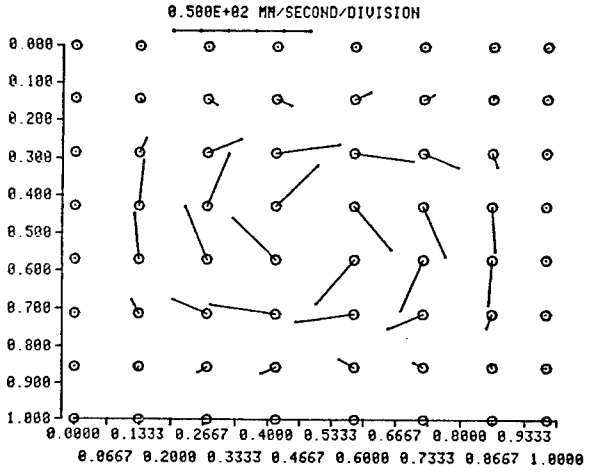


Figure 3a. Coarse grid spacing.

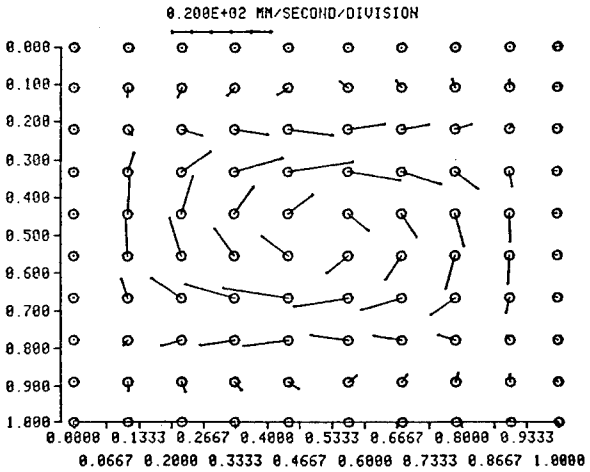


Figure 3b. Fine grid spacing.

Figure 3. Test case solutions.

agree with what one would intuitively expect from the given forcing function. There is a clockwise rotation of the molten metal, with the maximum velocity vector lengths in agreement with the maximum amplitude region of the forcing function. The solution goes to zero along the pot (boundary) walls, as it should.

For this test case, the relaxation factors are chosen to be $R_u = 1.0$ while $R_p = R_v = 1.08$. The convergence rate is somewhat sensitive to the relaxation factors chosen, but the nature of the relaxation is analytically unknown at this time.

5 Conclusions

Numerical solutions to the Navier-Stokes equations, in the context of aluminum reduction pots, have been successfully achieved for rudimentary test cases, as described above. Solutions for other, more complicated, forcing functions are being investigated, but with lesser convergence success. It has been observed that the ratio $\triangle x$ to $\triangle y$ has a strong influence on convergence behavior. Similarly, a fortuitous choice of R_u, R_v, and R_p is essential.

Considerable research and analysis will be required to define the operational limits of this particular numerical formulation. Beyond that, the guidelines for prudent selection of parameters for a given application must be determined. There may be additional aspects for consideration yet to be discovered, artifacts arising from certain classes of complex forcing functions.

Nonetheless, the methodology presented here has demonstrated (through the test case example) a capability heretofore not achieved. There is clearly cause for optimism that the solution method can be extended and successfully generalized from this basis. The progression to more complex cases may have to be in carefully measured steps of increasing difficulty, but the critical matter of feasibility has been substantially resolved by this study to a positive conclusion.

6 Acknowledgments

Discussions and other assistance provided by Dr. Sam S.-Y. Wang toward understanding the nature and scope of the Navier-Stokes equations is gratefully acknowledged. Also, the study by Dr. Mark Tew of an alternative "potential" type formulation provided valuable insight into the problem, which helped motivate the numerical approach described here.

References

[1] C.H. Ma and S. Singh, *private communication.*

[2] B. Carnahan, H.A. Luther, and J.O. Wilkes, *Applied Numerical Methods*, John Wiley & Sons, New York, 1969.

THE ELECTROSTATIC CHARACTERIZATION OF A N-ELEMENT PLANAR ARRAY USING THE SINGULARITY EXPANSION METHOD

Jon E. Mooney and Dr. Lloyd Riggs
Department of Electrical Engineering
200 Broun Hall • Auburn University, Alabama 36849

January 11, 1995

Abstract

In this paper, the Singularity Expansion Method (SEM) is used to describe the electrostatic charge distribution on an array of thin linear antennas placed in a uniform electric field. Using the SEM, the step plane wave induced transient current on the array is expanded in terms of its singularities (poles) in the Laplace transform or complex frequency domain. Transient charge is derived from the induced current expression using the continuity equation. The final value theorem is applied to the transient charge expression to determine the electrostatic charge distribution on the array.

I Introduction

The Singularity Expansion Method allows one to treat a conducting body in a manner similar to that used in classical circuit theory. In circuit theory, the response of a linear circuit excited by an arbitrary waveform may be determined by knowledge of the location of any singularities of the response function as well as the corresponding residues. In a distributed system (e.g., a conducting body), an infinite number of singularities exist and associated with each is a natural modal current and charge distribution. For an arbitrary excitation, one need only determine how much of each natural mode has been excited. This is determined by the coupling coefficient associated with a given natural mode. [1]

The essence of the SEM is its ability to break down the electromagnetic interaction process into meaningful parameters such as poles, modes and coupling coefficients. Definitions for these SEM parameters will be presented employing a method of moments approximation to the continuous operator electric field equation (EFIE) in terms of the current induced on the array. The main intent of this work is to provide a clearer view of the fundamental aspects of electrostatic interaction than is available through conventional analysis methods.

II Theoretical Development

As a starting point, consider the array comprised of perfectly conducting thin cylindrical elements as shown in Figure 1. Impinging on this array is some incident field generated by a distant source. The impinging field induces current and charge on the elements, and these sources in turn radiate a scattered field. Due to the perfectly conducting nature of the elements, the total tangential electric field on the surface of the conductors must be zero; that is, the tangential component of the incident electric field must exactly cancel the tangential component of the scattered electric field. Utilizing standard potential theory [2], the scattered electric field can be expressed in terms of an integro-differential operation on the induced current. This expression and the boundary conditions result in an electric field integral equation (EFIE) in terms of the unknown surface currents on the the elements [3].

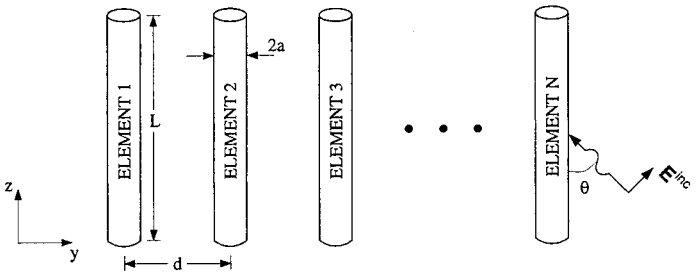


Figure 1: A N-Element Planar Array

An approximate solution to this EFIE can be obtained by employing the method of moments [4]. A pulse expansion of the unknown current, and a pulse testing of the EFIE yields the familiar network matrix equation for the induced current cast explicitly in terms of the complex frequency parameter $s = \Omega + j\omega$,

$$\overline{I}(s) = \mathbf{Z}^{-1}(s)\overline{V}(s) = \mathbf{Y}(s)\overline{V}(s) \tag{1}$$

where

$\mathbf{Z}(s)$ is the system impedance matrix

$\mathbf{Y}(s)$ is the system admittance matrix

$\overline{I}(s)$ is the system current response vector

$\overline{V}(s)$ is the system voltage excitation vector

The inverse of the $\mathbf{Z}(s)$ can be expressed as the ratio of its adjoint to its determinant. Thus, the singularities (poles) of the system are those complex frequencies that force the determinant of $\mathbf{Z}(s)$ to zero. These singularities are termed natural resonance frequencies of the scatterer since they are frequencies for which the body can have a response with no excitation. The poles must lie in the left hand plane to ensure a decaying response. In addition, except for those that lie on the real axis, the poles must occur in conjugate pairs so that a real time response exists. Finally, no poles can lie on the $j\omega$ axis because the body is losing energy through radiation.

Knowing the poles, the system admittance matrix can be expanded in a singularity series, hence the name SEM. Expanding $\mathbf{Y}(s)$, the expression for the induced current becomes

$$\overline{I}(s) = \sum_{\alpha} \frac{\mathbf{R}_\alpha}{s - s_\alpha} \overline{V}(s) + \overline{W}_e(s) \tag{2}$$

where s_α is the αth natural resonance, and $\mathbf{R}_\alpha$ is the residue matrix at the αth resonance. The term $\overline{W}_e(s)$ is a vector whose elements are entire functions, i.e., it has singularities only at infinity [5]. Baum addresses the inclusion of $\overline{W}_e(s)$ in (2) and shows that it is not necessary for the SEM characterization of perfectly conducting cylinders [6].

The residue matrix $\mathbf{R}_\alpha$ at s_α can be evaluated via the Cauchy residue theorem [7], which is

$$\mathbf{R}_\alpha = \frac{1}{2\pi j} \int_{c_\alpha} \mathbf{Y}(s)\, ds \tag{3}$$

where c_α denotes a contour enclosing the pole at $s = s_\alpha$. It can be shown that $\mathbf{R}_\alpha$ is dyadic; that is, its elements can be calculated as the product of elements taken from two column vectors [5]. Furthermore, because the EFIE is used, $\mathbf{R}_\alpha$ is symmetric which means the column vectors are identical. Exploiting the dyadic and symmetric properties, $\mathbf{R}_\alpha$ can written as

$$\mathbf{R}_\alpha = \beta_\alpha \overline{M}_\alpha \overline{M}_\alpha^T \tag{4}$$

where $\overline{M}_\alpha$ is the αth natural modal current distribution and the superscript "T" denotes the matrix transpose operation. The parameter β_α is a complex proportionality constant which is chosen so that the maximum value of $\overline{M}_\alpha$ is real and unity.

Using the factored form of $\mathbf{R}_\alpha$ and dropping the entire function, the expression for the induced currents becomes

$$\overline{I}(s) = \sum_\alpha \frac{\beta_\alpha \overline{M}_\alpha \overline{M}_\alpha^T}{s - s_\alpha} \overline{V}(s) \tag{5}$$

The voltage excitation vector $\overline{V}(s)$ can be written more specifically as

$$\overline{V}(s) = f(s)\overline{\Lambda}(s) \tag{6}$$

where $f(s)$ is the functional form of the system excitation (impulse, step...), and $\overline{\Lambda}(s)$ is the geometry dependent impulsive excitation vector. The elements of $\overline{\Lambda}(s)$ are of the form $b\,exp(-ts)$, where b is proportional to the component of the incident electric field vector along the body. The term $exp(-ts)$ represents a time delay of t seconds. This delay ensures causality in that no point on the body can respond prior to the arrival of the incident wavefront [1].

Using (6) in (7), yields

$$\overline{I}(s) = f(s) \sum_\alpha \frac{\beta_\alpha \overline{M}_\alpha \overline{M}_\alpha^T}{s - s_\alpha} \overline{\Lambda}(s) \tag{7}$$

The SEM parameter known as the coupling coefficient appears in (7), and it is defined as

$$\eta_\alpha(s) = \beta_\alpha \overline{M}_\alpha^T \overline{\Lambda}(s) \tag{8}$$

This parameter, which is dependent on the geometry of the scatterer as well as the polarization and propagation direction of the incident wave, governs how much the αth pole-mode pair couples into the response. Substituting (8) into (7), the current response vector becomes

$$\overline{I}(s) = f(s) \sum_\alpha \eta_\alpha(s) \frac{\overline{M}_\alpha}{s - s_\alpha} \tag{9}$$

To obtain an expression for the charge, the continuity equation is employed:

$$\overline{\rho}(s) = -\frac{1}{s} \nabla \cdot \overline{I}(s) \tag{10}$$

Combining the continuity equation with (9), the expression for the charge becomes

$$\overline{\rho}(s) = -f(s) \sum_\alpha \eta_\alpha(s) \frac{\overline{D}_\alpha}{s - s_\alpha} = f(s)\overline{\Gamma}(s) \tag{11}$$

where $\overline{\Gamma}(s)$ is the "network" impulse charge response and

$$\overline{D}_\alpha = \nabla \cdot \overline{M}_\alpha \tag{12}$$

defines the αth natural charge mode [1]. Through a partial fraction expansion of the $[s(s-s_\alpha)]^{-1}$ term, the expression for the induced charge can be written as

$$\overline{\rho}(s) = -f(s)\left[\sum_\alpha \eta_\alpha(s)\frac{\overline{D}_\alpha}{ss_\alpha} - \sum_\alpha \eta_\alpha(s)\frac{\overline{D}_\alpha}{s_\alpha(s-s_\alpha)}\right] \tag{13}$$

The first term of (13) can be neglected because there is no singularity at $s = 0$ in the complex plane [8].

In order to determine the electrostatic charge distribution, an appropriate excitation function $f(s)$ must be chosen so that the array is immersed in a uniform electric field. Although a variety of waveforms would suffice, a simple step excitation will be used here. Thus, substituting s^{-1} in for $f(s)$ and neglecting the first term, (13) becomes

$$\overline{\rho}(s) = \sum_\alpha \eta_\alpha(s)\frac{\overline{D}_\alpha}{s_\alpha s(s-s_\alpha)} \tag{14}$$

Again expanding the $[s(s-s_\alpha)]^{-1}$ term of (14) in partial fractions yields

$$\overline{\rho}(s) = \sum_\alpha \eta_\alpha(s)\frac{\overline{D}_\alpha}{ss_\alpha^2} - \sum_\alpha \eta_\alpha(s)\frac{\overline{D}_\alpha}{s_\alpha^2(s-s_\alpha)} \tag{15}$$

Applying the final value theorem to obtain the electrostatic charge distribution results in

$$\overline{\rho}(t=\infty) = \sum_\alpha \eta_\alpha(s)\frac{\overline{D}_\alpha}{s_\alpha^2} \tag{16}$$

III Numerical Results

In this section, the electrostatic characterization of two, three, four, and five element arrays will be given. The elements of the planar arrays under consideration have a radius-to-length ratio, a/L, of 0.005, and a separation distance-to-length ratio, d/L of 0.10. The radius a and the separation distance d parameters are illustrated in Figure 1. The electrostatic charge distribution on these arrays using the SEM will be compared to the direct MOM solution for the same obtained from the electrostatic scalar potential equation. In addition to presenting the electrostatic charge distribution, a discussion of some relationships among the the SEM parameters of the N-element arrays will be given.

Before presenting the results for the two, three, four, and five element arrays, it is interesting to give a brief discussion of the SEM parameters associated with a single linear conductor. A SEM characterization of a single linear element reveals that the poles of this object occur in layers roughly parallel to the $j\omega$ axis. The poles in the fundamental layer lie very close to the $j\omega$ axis. Only these poles contribute significantly to the response since their nearness to the jw axis implies a small damping constant. The imaginary parts of the fundamental layer poles, when multiplied by the length of the element L and divided by the speed of light c, occur at approximately $k\pi$, where k denotes an integer. Thus, the first pole of the first layer lies near $\omega L/c = \pi$. Singularities residing in this general vicinity are termed fundamental resonance region poles. Other poles in the layer nearest the imaginary axis are referred to as harmonics of the fundamental and have imaginary parts near 2π, 3π, etc. Another way to view the location of the first layer poles is to note their imaginary parts occur at frequencies where the element length is an integer multiple of a half-wavelength. This relationship is shown as follows

$$\frac{\omega L}{c} = k\pi \;\Rightarrow\; \frac{2\pi L}{\lambda} = k\pi \;\Rightarrow\; L = k\frac{\lambda}{2} \tag{17}$$

where λ is the free space wavelength.

As mentioned previously, associated with each pole is a unique modal current distribution. The modes for poles lying in the first layer have sinusoidal current distributions along the length of each element. The fundamental resonance region pole is observed to have a half-wavelength sinusoidal current distribution as would be expected from (17). Similarly, second harmonic poles have a full wave sinusoidal current distribution. Although (17) may reveal the nature of the distribution for a given harmonic, what is not so obvious is the direction of the current flow on the array associated with a given mode. Examining the location of the poles and the characteristics of their corresponding modal current distributions reveals much about the fundamental electromagnetic interaction process.

Having introduced the SEM parameters for the single element, the pole-mode relationships for the two, three, four, and five element arrays can now be discussed. The SEM factorization of the two element array reveals that two poles reside in the general location of the complex plane where the isolated element has a single pole. Thus, in the fundamental resonance region, the two element array has two poles. Furthermore, two poles exist in each of the higher order harmonic regions as well. Figure 2a illustrates the pole positions for the first five harmonics of the two element array. As one might anticipate, the three element arrays has three poles in the complex plane where the single element has only one. The pole positions for the three element array are shown in Figure 2b. This trend continues as more elements are added to the array such that a N-element array has N poles in the region where the isolated element only has one.

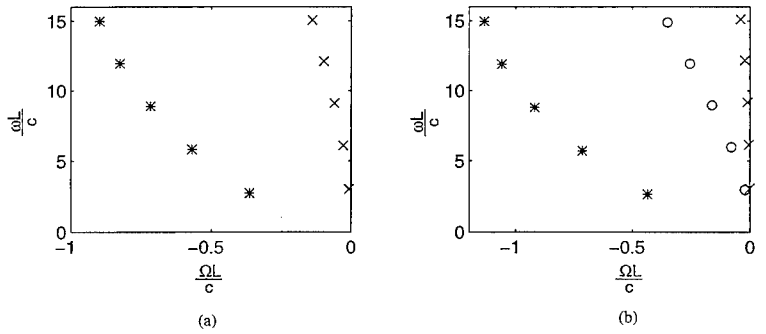


Figure 2: The pole positions for the first five harmonics of the (a) two element array and the (b) three element array.

The addition of a singularity for each element added to the array provides for some interesting pole mode relationships. The two poles for the two element array can be identified as either a radiation pole or a transmission line pole depending on the directions of the modal currents which flow on the elements of the arrays. The radiation pole, designated with the symbol * in Figure 2a, has modal currents that flow in the same direction on both elements. This pole, which is located furthest from the $j\omega$ axis, is low Q (essentially the ratio of stored energy to dissipated energy); therefore, any energy that is coupled into this mode will be rapidly radiated into space. In contrast, the transmission line pole has modal currents that flow in opposite directions. In accordance with Kirchoff's current law, a symmetric two wire array with one ampere flowing on one element must have one ampere flowing in the opposite direction on the other element. The transmission line pole, designated with the symbol X, is located very close to the $j\omega$ axis and, therefore, is high Q (low damping constant). The real part of the modal current distributions

associated with the fundamental radiation and transmission line poles are shown in Figure 3. The imaginary part of the modal current is not shown since it is very small relative to the real part.

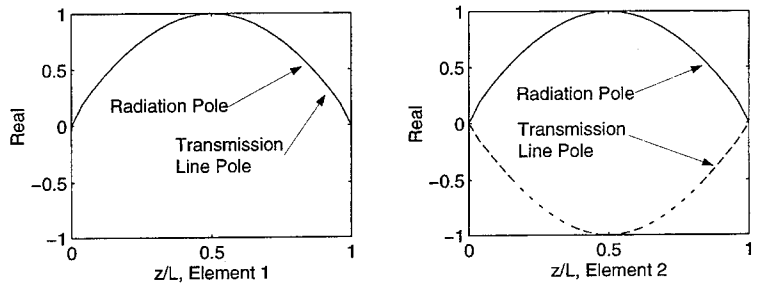


Figure 3: The real modal current distributions for the fundamental radiation and transmission line poles of the two element array.

The three element array, as mentioned previously, has three poles in the area where the isolated element has only one. By inspecting Figure 2b, one can observe the positions of these singularities. The three element array also has a radiation pole and a transmission line pole designated by the symbols $*$ and X, respectively. These poles have the same characteristics of the radiation and transmission line poles of the two element array. Of the pole trio, the radiation pole resides furthest from the $j\omega$ axis and the transmission line pole lies the closest. The radiation pole has modal currents that flow in the same direction on all three elements. Furthermore, it has the highest damping and lowest Q of the three poles. The transmission line pole has modal currents of 0.5 amperes (amplitude) flowing in the same direction on the outer wires and one ampere flowing in the opposite direction on the the center element, which satisfies Kirchoff's current law. Because of its close proximity to the $j\omega$ axis, the transmission line pole has a small damping constant and, therefore, a high Q. The remaining pole is referred to here as the zero-mode pole. As its name suggests, the zero-mode pole has no current on the center element. In Figure 2b, this pole is designated with the symbol O. The real parts of the modal current distributions of the the fundamental radiation, transmission line, and zero-mode poles of the three element array are shown in Figure 4. It should be pointed out here that the poles of the arrays are system poles; that is, a pole does not correspond to any particular element of the array.

The four and five element arrays possess some of the modes of the two and three element arrays as well as having some unique modes of their own. As expected, the four element array has four poles in a given harmonic region which means it has four distinct modal distributions. Two of these poles are the familiar radiation and transmission line poles. These poles have the same characteristic modal current distributions as discussed previously. The radiation pole has modal currents flowing in the same direction on each element, and relative to the positions of the other three poles, it is located furthest from the $j\omega$ axis. An inspection of the modal current distribution for the transmission line pole reveals one ampere flowing in opposing directions on the inner two elements and 0.5 amperes flowing in opposing directions on the outer elements. The other two distinct modal current distributions of the four element array are interesting, but a physical interpretation is not so simple. The current distributions of these modes are oriented such that the net current flowing over all four elements is zero.

As one would expect, the five element array has five distinct modes. Three of these are associated

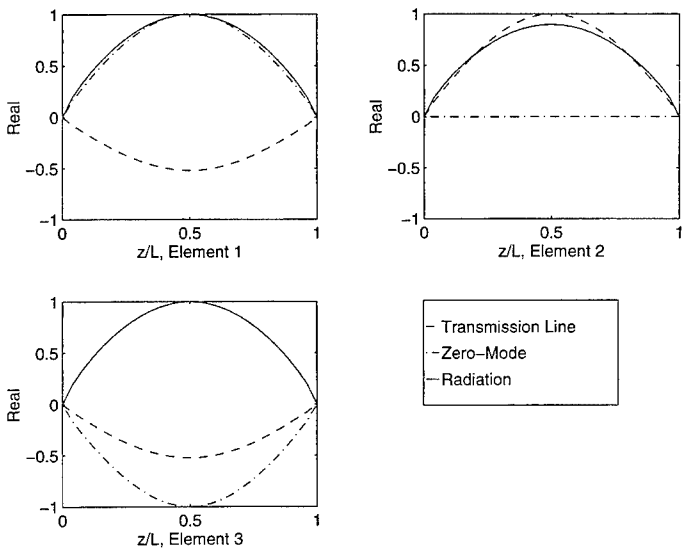


Figure 4: The real modal current distributions for the fundamental radiation, transmission line, and zero-mode poles of the three element array.

with the three element array. Thus, in addition to two more singularities, the five element array has a radiation pole, a transmission line pole, and a zero-mode pole. These three poles have the same characteristic modal distributions described earlier for the three element array. A physical interpretation of the modes of the remaining two singularities is also difficult. One significant feature of these modes is that their distributions, when summed over all five elements, is approximately zero.

As mentioned in the previous section, the coupling coefficient governs how much of each mode couples into the response. The electrostatic coupling coefficient for the two and three element arrays as a function of the angle of incidence θ is shown in Figure 5. The angle of incidence and polarization of the incident electric field is defined in Figure 1. By observing Figures 5a and 5b, one can see that only the odd harmonics of the radiation pole couple significantly into the response. Furthermore, the amount each radiation pole couples into the response decreases with the increase in the order of the harmonic. No mode significantly couples into the response beyond the 7th or 9th harmonic. The strong coupling aspect of the radiation pole is due to the fact that its modal currents flow in the same direction on all the elements. None of the modes of the even harmonics couple into the response because their distributions have an odd symmetry about the center of each element, and the excitation is an even function. Furthermore, except for the radiation pole, the modes of all the other singularities are oriented such that they effectively cancel one another. As an example, observe the modal current distribution associated with the zero-mode pole of the three element array in Figure 4. It is obvious that the currents on the outer elements cancel each other, and the current on the center is already zero. A similar observation can be made about the transmission line mode.

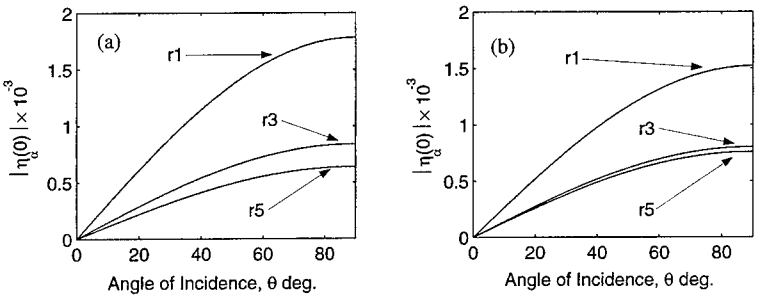


Figure 5: The magnitude of the normalized electrostatic coupling coefficients for the (a) two and (b) three element arrays. The notation r^* represents the harmonic of the radiation pole.

The electrostatic charge distributions for the two, three, four, and five element arrays are shown in Figure 6, 7, 8, and 9, respectively. The electrostatic responses were calculated using a unit step plane wave polarized in the positive z-direction ($\theta = 90°$). Only the fundamental, third, and fifth harmonics were used in computing the responses. The SEM electrostatic responses are compared to the direct MOM solution of the electrostatic scalar potential equation. As one can see, the SEM agrees well with the direct MOM solution in all cases.

IV Conclusions

In this paper, the Singularity Expansion Method was used to determine the electrostatic charge distribution on a N-element planar array. The results obtained using the SEM agreed very well with the more conventional MOM solution of the electrostatic scalar potential equation. In addition to yielding good results, the SEM provided a more meaningful description of the electromagnetic interaction process. This was accomplished by factoring the problem into its SEM parameters: poles, modes, and coupling coefficients.

Through numerical experimentation on planar arrays of two, three, four, and five elements, some interesting relationships among the SEM parameters were observed. Based upon these results, the following conclusions can be made for a N-element (N>2) array:

- A N-element array has N poles in the region where a single element has only one. These poles are system poles and are *not* related to a single element in the array. Associated with each pole is a unique modal distribution.
- Two of the N poles will be a radiation pole and a transmission line pole. Of the N poles, the radiation pole will be located the furthest from the $j\omega$ axis, and the transmission line pole will be closest.
- All odd N-element arrays will have a zero-mode pole.
- A N-element array will have all the modes of the N-2 array plus 2 additional distinct modes.
- The fundamental radiation pole dominates the electrostatic response.

References

[1] L.S.Riggs,T.H.Shumpert,J.M.Lindsey, "Commonalities in the electrostatic characterization of several thin conducting cylinders using the singularity expansion method," *Journal of Electrostatics*, vol. 22, pp. 161–176, 1989.

[2] R.F.Harrington, *Time-Harmonic Electromagnetic Fields.* McGraw-Hill, 1961.

[3] H. Pocklington, *Electrical Oscillations in Wire.* Cambridge Philos. Soc. Proc. London, V.o., 1897.

[4] R.F.Harrington, *Field Computation by Moment Methods.* Macmillan, 1968.

[5] K.R.Umashankar, *The calculation of electromagnetic transient currents on thin perfectly conducting bodies using the singularity expansion method.* PhD thesis, University of Mississippi, 1974.

[6] F.M.Tesche, "On the singularity expansion method as applied to electromagnetic scattering from thin wires," *AFWL Sensor and Simulation Notes*, 1973. Note 177.

[7] L.S.Riggs, *Singularity expansion method (SEM) analysis of thin perfectly conducting cylindrical conductors.* PhD thesis, Auburn University, Auburn University, AL, 1985.

[8] C.E.Baum, "On the singularity expansion method for the solution of electromagnetic interaction problems," *AFWL Interaction Notes*, Dec. 1971. Note 88.

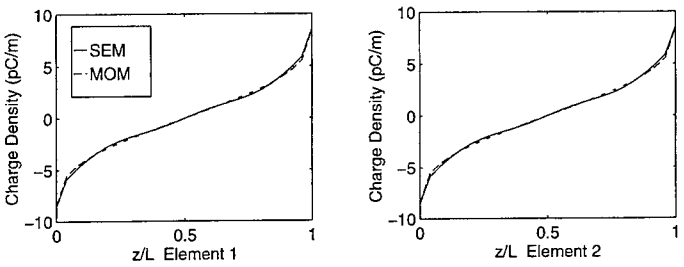


Figure 6: The electrostatic charge distribution for the two element array, $d/L = 0.10$, $a/L = 0.005$. The applied electric field is oriented in the positive z-direction ($\theta = 90$ deg.).

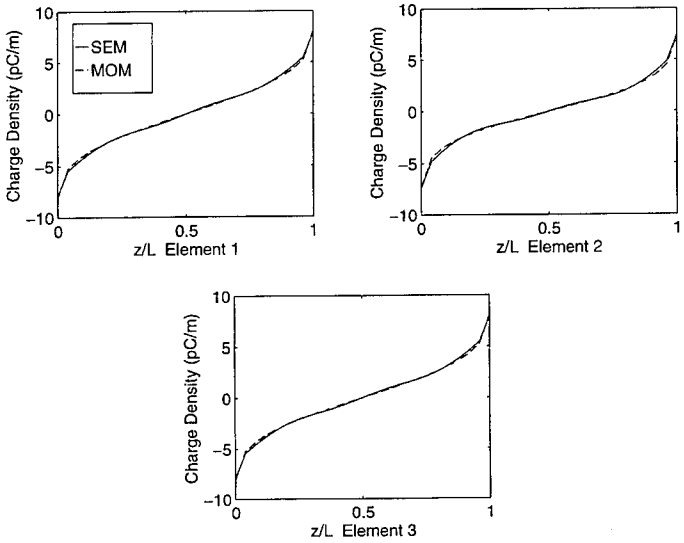


Figure 7: The electrostatic charge distribution for the three element array, $d/L = 0.10$, $a/L = 0.005$. The applied electric field is oriented in the positive z-direction ($\theta = 90$ deg.).

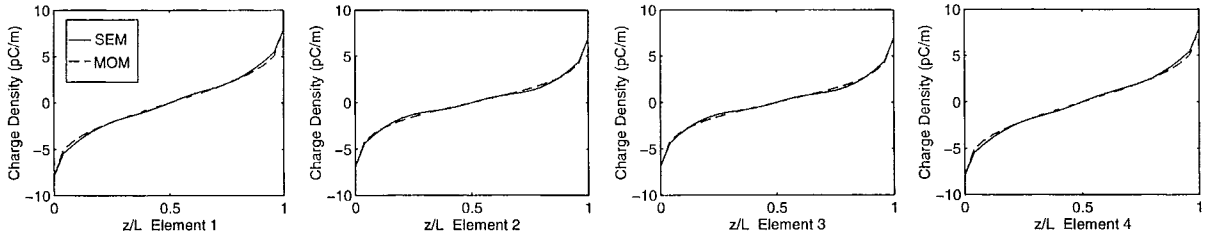


Figure 8: The electrostatic charge distribution for the four element array, d/L=0.10, a/L=0.005. The applied electrostatic field is oriented in the positive z-direction (θ.=90 deg.).

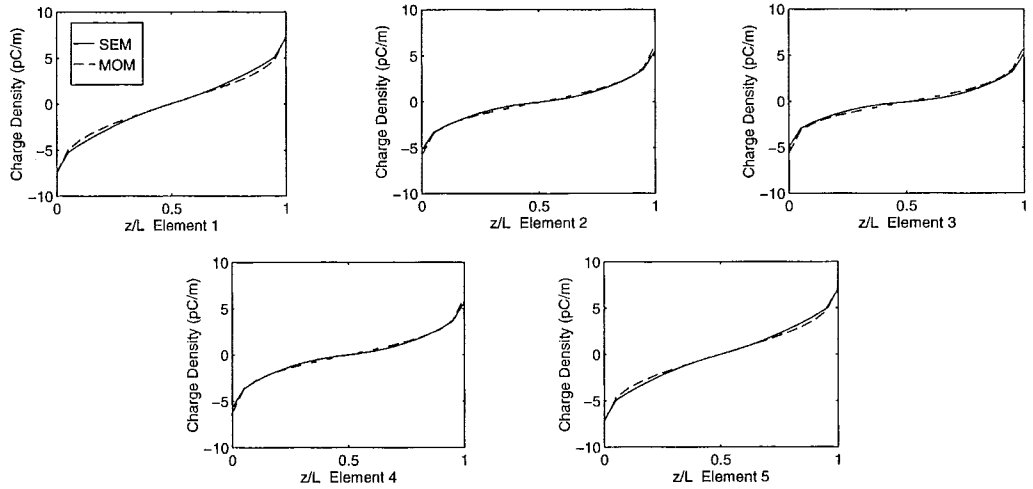


Figure 9: The electrostatic charge distribution for the five element array, d/L=0.10, a/L=0.005. The applied electrostatic field is oriented in the positive z-direction (θ=90 deg.).

A Volume-Integral Code for Electromagnetic Nondestructive Evaluation

R. Kim Murphy, Harold A. Sabbagh, Jeff C. Treece, and Lai Wan Woo

Sabbagh Associates, Inc., 4635 Morningside Drive, Bloomington, IN 47408, USA

Introduction. VIC-3D©[1], a volume-integral code for eddy-current nondestructive evaluation (NDE), solves the problem of computing the interaction between flaws and probe coils (see Figure 1) [2], [3]. The

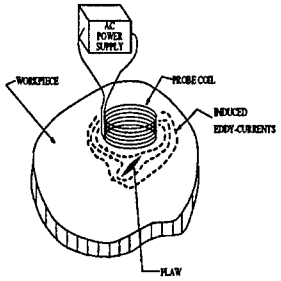


Figure 1: Electromagnetic NDE: showing a probe coil interacting with a flaw.

probes may have either ferrite or air cores [4], [5], and the flaw can exist in either ferromagnetic or non-ferromagnetic plane-parallel, layered workpieces. Because the fields are usually quite small, we can ignore the nonlinear magnetization characteristics of the workpiece, and assign a scalar magnetic permeability to each layer.

Volume-Integral Equations for Ferromagnetic Workpieces. We start with Maxwell's equations

$$\begin{aligned} \nabla \times \mathbf{E} &= -j\omega \mathbf{B} \\ \nabla \times \mathbf{H} &= j\omega \mathbf{D} + \mathbf{J}^{(e)} \, . \end{aligned} \tag{1}$$

Now, $\mathbf{H} = \mathbf{B}/\mu(\mathbf{r}) = \mathbf{B}/\mu_h + \mathbf{B}/\mu(\mathbf{r}) - \mathbf{B}/\mu_h = \mathbf{B}/\mu_h - \mathbf{M}_a$, where μ_h is the host conductivity, and $\mathbf{M}_a$ is the anomalous magnetization vector. Thus, the second of Maxwell's equations may be written

$$\nabla \times \mathbf{B}/\mu_h = j\omega \mathbf{D} + \mathbf{J}^{(e)} + \nabla \times \mathbf{M}_a \, , \tag{2}$$

which makes clear that the Amperian current, $\nabla \times \mathbf{M}_a$, is an equivalent anomalous electric current that arises because of the departures of the magnetic permeability of the workpiece from the host permeability, μ_h. $\mathbf{J}^{(e)}$, on the other hand, is an electric current that includes the anomalous current that arises due to differences in electrical conductivity; $\mathbf{J}^{(e)} = \sigma_h \mathbf{E} + (\sigma(\mathbf{r}) - \sigma_h)\mathbf{E} = \sigma_h \mathbf{E} + \mathbf{J}_a$. Because the host conductivity and permeability are constant within each plane-parallel layer, they can be accounted for by means of Green functions. This leaves us with only the anomalous electric and magnetic sources to be determined.

Even though the Amperian current is electrical (because it appears as a source term in the second Maxwell equation (Ampere's law)), we will refer to it as $\mathbf{J}^{(m)}$, to remind us that it is of magnetic origin, and to distinguish it from $\mathbf{J}^{(e)}$ (which now stands for the anomalous electric current, $\mathbf{J}_a$). The important

point, however, is that because the Amperian current behaves as an electrical current, we need only use electric-electric Green functions in the formulation of the problem.

In establishing the volume-integral equations, we simply make use of the fact that the total electric field and magnetic flux density at a point is the sum of the fields due to the probe coil, which we call the incident fields, and those due to the anomalous currents, $\mathbf{J}^{(e)}$ and $\mathbf{J}^{(m)}$.

Hence, we write

$$\begin{aligned}
\mathbf{E}^{(i)}(\mathbf{r}) &= \frac{\mathbf{J}^{(e)}(\mathbf{r})}{\sigma_a(\mathbf{r})} - \mathbf{E}^{(0)}(\mathbf{r})\left[\mathbf{J}^{(e)}\right] - \mathbf{E}^{(s)}(\mathbf{r})\left[\mathbf{J}^{(e)}\right] - \mathbf{E}^{(0)}(\mathbf{r})\left[\mathbf{J}^{(m)}\right] - \mathbf{E}^{(s)}(\mathbf{r})\left[\mathbf{J}^{(m)}\right] \\
\mathbf{B}^{(i)}(\mathbf{r}) &= \frac{\mu(\mathbf{r})\mu_h}{\mu(\mathbf{r})-\mu_h}\mathbf{M}_a + \frac{1}{j\omega}\nabla\times\mathbf{E}^{(0)}(\mathbf{r})\left[\mathbf{J}^{(e)}\right] + \frac{1}{j\omega}\nabla\times\mathbf{E}^{(s)}(\mathbf{r})\left[\mathbf{J}^{(e)}\right] \\
&\quad + \frac{1}{j\omega}\nabla\times\mathbf{E}^{(0)}(\mathbf{r})\left[\mathbf{J}^{(m)}\right] + \frac{1}{j\omega}\nabla\times\mathbf{E}^{(s)}(\mathbf{r})\left[\mathbf{J}^{(m)}\right] \ . \qquad (3)
\end{aligned}$$

In arriving at the second equation, we have used the fact that $\mathbf{B} = -(1/j\omega)\nabla\times\mathbf{E}$, and $\mathbf{M}_a = ((\mu(\mathbf{r}) - \mu_h)/\mu(\mathbf{r})\mu_h)\mathbf{B}$.

The first part of the first equation in (3) is the electric-electric (ee) interaction, and the second part is the electric-magnetic (em) interaction. The two parts of the second equation are, respectively, the magnetic-electric (me) and the magnetic-magnetic (mm) interactions. We decompose the various interactions into the 'infinite-space' part, designated by the superscript, (0), and the 'layered-space' part, designated by the superscript, (s). This is done for convenience in coding and problem solving.

The electric-electric interaction terms are given by

$$\mathbf{E}^{(0)}(\mathbf{r})[\mathbf{J}^{(e)}] = \int \Phi^{(e)}(\mathbf{r}-\mathbf{r}')\mathbf{J}^{(e)}(\mathbf{r}')d\mathbf{r}' + \frac{1}{k_0^2}\nabla\int\Phi^{(e)}(\mathbf{r}-\mathbf{r}')\nabla'\cdot\mathbf{J}^{(e)}(\mathbf{r}')d\mathbf{r}' \ , \qquad (4)$$

and

$$\begin{aligned}
\mathbf{E}^{(s)}(\mathbf{r})[\mathbf{J}^{(e)}] &= \int d\mathbf{r}' G_{xx}^{(1)(a)}(x-x',y-y',z-z')\mathbf{J}_t^{(e)}(\mathbf{r}') + \mathbf{a}_z\int d\mathbf{r}' G_{xz}^{(a)}(x-x',y-y',z-z')J_z^{(e)}(\mathbf{r}') \\
&+ \int d\mathbf{r}' G_{xx}^{(1)(b)}(x-x',y-y',z+z')\mathbf{J}_t^{(e)}(\mathbf{r}') + \mathbf{a}_z\int d\mathbf{r}' G_{xz}^{(b)}(x-x',y-y',z+z')J_z^{(e)}(\mathbf{r}') \\
&+ \nabla_t\int d\mathbf{r}' G_{xx}^{(2)(a)'}(x-x',y-y',z-z')\nabla_t'\cdot\mathbf{J}_t^{(e)}(\mathbf{r}') \\
&+ \nabla_t\int d\mathbf{r}' G_{xx}^{(2)(b)'}(x-x',y-y',z+z')\nabla_t'\cdot\mathbf{J}_t^{(e)}(\mathbf{r}') \\
&+ \frac{1}{k_0^2}\nabla\int d\mathbf{r}' G_{xz}^{(a)}(x-x',y-y',z-z')\nabla'\cdot\mathbf{J}^{(e)}(\mathbf{r}') \\
&- \frac{1}{k_0^2}\nabla\int d\mathbf{r}' G_{xz}^{(b)}(x-x',y-y',z+z')\nabla'\cdot\mathbf{J}^{(e)}(\mathbf{r}') \ . \qquad (5)
\end{aligned}$$

The electric-magnetic interaction terms are given by substituting $\mathbf{J}^{(m)}$ for $\mathbf{J}^{(e)}$ in (4) and (5); because $\mathbf{J}^{(m)}$ has zero divergence, we have

$$\begin{aligned}
\mathbf{E}^{(0)}(\mathbf{r})[\mathbf{J}^{(m)}] &= \int \Phi^{(e)}(\mathbf{r}-\mathbf{r}')\mathbf{J}^{(m)}(\mathbf{r}')d\mathbf{r}' \\
\mathbf{E}^{(s)}(\mathbf{r})[\mathbf{J}^{(m)}] &= \int d\mathbf{r}' G_{xx}^{(1)(a)}(x-x',y-y',z-z')\mathbf{J}_t^{(m)}(\mathbf{r}')
\end{aligned}$$

$$
\begin{aligned}
&+ \quad \mathbf{a}_z \int d\mathbf{r}' G_{xz}^{(a)}(x-x', y-y', z-z') J_z^{(m)}(\mathbf{r}') \\
&+ \quad \int d\mathbf{r}' G_{xx}^{(1)(b)}(x-x', y-y', z+z') \mathbf{J}_t^{(m)}(\mathbf{r}') \\
&+ \quad \mathbf{a}_z \int d\mathbf{r}' G_{xz}^{(b)}(x-x', y-y', z+z') J_z^{(m)}(\mathbf{r}') \\
&+ \quad \nabla_t \int d\mathbf{r}' G_{xx}^{(2)(a)'}(x-x', y-y', z-z') \nabla_t' \cdot \mathbf{J}_t^{(m)}(\mathbf{r}') \\
&+ \quad \nabla_t \int d\mathbf{r}' G_{xx}^{(2)(b)'}(x-x', y-y', z+z') \nabla_t' \cdot \mathbf{J}_t^{(m)}(\mathbf{r}') \,, \qquad (6)
\end{aligned}
$$

where $\nabla_t = \mathbf{a}_x \frac{\partial}{\partial x} + \mathbf{a}_y \frac{\partial}{\partial y}$; $\nabla_t \cdot \mathbf{J} = \frac{\partial J_x}{\partial x} + \frac{\partial J_y}{\partial y}$; $\mathbf{J}_t = \mathbf{a}_x J_x + \mathbf{a}_y J_y$, and

$$
\begin{aligned}
\Phi^{(e)}(\mathbf{r}-\mathbf{r}') &= -j\omega\mu_0 \frac{e^{-jk_0|\mathbf{r}-\mathbf{r}'|}}{4\pi|\mathbf{r}-\mathbf{r}'|} \\
&= \frac{-j\omega\mu_0}{2\pi} \int_0^\infty \frac{e^{-\lambda_0|z-z'|}}{2\lambda_0} J_0(rl) l dl \,. \qquad (7)
\end{aligned}
$$

In the Bessel transform, $r = [(x-x')^2 + (y-y')^2]^{1/2}$.

The various layered-space Green functions are given by

$$
\begin{aligned}
G_{xx}^{(1)(a)}(x-x', y-y', z-z') &= \frac{-j\omega\mu_0}{2\pi} \int_0^\infty \left[\frac{c(z'-z)}{2\lambda_0} e^{-2\lambda_0 T} G_{1,-1}^{(E)} \right] J_0(rl) l dl \\
G_{xx}^{(1)(b)}(x-x', y-y', z+z') &= \frac{-j\omega\mu_0}{2\pi} \int_0^\infty \left[\frac{e^{\lambda_0(z+z')}}{2\lambda_0} e^{-2\lambda_0 z_0} G_1^{(E)} + \frac{e^{-\lambda_0(z+z')}}{2\lambda_0} e^{2\lambda_0 z_{-1}} G_{-1}^{(E)} \right] J_0(rl) l dl \\
G_{xx}^{(2)(a)'}(x-x', y-y', z-z') &= \frac{-j\omega\mu_0}{2\pi} \int_0^\infty \left[\frac{c(z'-z)}{2\lambda_0} e^{-2\lambda_0 T} \frac{G_{1,-1}^{(E)} - G_{1,-1}^{(M)}}{l^2} \right] J_0(rl) l dl \\
G_{xx}^{(2)(b)'}(x-x', y-y', z+z') &= \frac{-j\omega\mu_0}{2\pi} \int_0^\infty \left[\frac{e^{\lambda_0(z+z')}}{2\lambda_0} e^{-2\lambda_0 z_0} \frac{G_1^{(E)} - G_1^{(M)}}{l^2} \right. \\
&\qquad \left. + \frac{e^{-\lambda_0(z+z')}}{2\lambda_0} e^{2\lambda_0 z_{-1}} \frac{G_{-1}^{(E)} - G_{-1}^{(M)}}{l^2} \right] J_0(rl) l dl \\
G_{xz}^{(a)}(x-x', y-y', z-z') &= \frac{-j\omega\mu_0}{2\pi} \int_0^\infty \left[\frac{c(z'-z)}{2\lambda_0} e^{-2\lambda_0 T} G_{1,-1}^{(M)} \right] J_0(rl) l dl \\
G_{xz}^{(b)}(x-x', y-y', z+z') &= \frac{-j\omega\mu_0}{2\pi} \int_0^\infty \left[-\frac{e^{\lambda_0(z+z')}}{2\lambda_0} e^{-2\lambda_0 z_0} G_1^{(M)} - \frac{e^{-\lambda_0(z+z')}}{2\lambda_0} e^{2\lambda_0 z_{-1}} G_{-1}^{(M)} \right] \\
&\qquad J_0(rl) l dl \,, \qquad (8)
\end{aligned}
$$

where $c(z'-z) = e^{\lambda_0(z'-z)} + e^{-\lambda_0(z'-z)}$, $\lambda_0 = (l^2 - k_0^2)^{1/2}$, and T is the thickness of the 0th layer, which contains the flaw.

Note that the terms with the superscript (a) are convolutional in all three spatial variables, whereas those with (b) are convolutional in $(x-x')$ and $(y-y')$, but are correlational in $(z+z')$, where z is normal

to the layers of the workpiece. This decomposition is of great importance when solving large systems of equations, as we shall see later.

The G's are defined in terms of the TE and TM-mode reflection coefficients:

$$\begin{aligned} G^{(E)}_{1,-1} &= \frac{R^{(E)}_1 R^{(E)}_{-1}}{1 - R^{(E)}_1 R^{(E)}_{-1} e^{-2\lambda_0 T}}, \quad G^{(E)}_1 = \frac{R^{(E)}_1}{1 - R^{(E)}_1 R^{(E)}_{-1} e^{-2\lambda_0 T}}, \quad G^{(E)}_{-1} = \frac{R^{(E)}_{-1}}{1 - R^{(E)}_1 R^{(E)}_{-1} e^{-2\lambda_0 T}} \\ G^{(M)}_{1,-1} &= \frac{R^{(M)}_1 R^{(M)}_{-1}}{1 - R^{(M)}_1 R^{(M)}_{-1} e^{-2\lambda_0 T}}, \quad G^{(M)}_1 = \frac{R^{(M)}_1}{1 - R^{(M)}_1 R^{(M)}_{-1} e^{-2\lambda_0 T}}, \quad G^{(M)}_{-1} = \frac{R^{(M)}_{-1}}{1 - R^{(M)}_1 R^{(M)}_{-1} e^{-2\lambda_0 T}} , \end{aligned} \tag{9}$$

which are, in turn, computed using a recursion relation for stratified media [6].

The magnetic-electric operators are

$$\begin{aligned} \nabla \times \mathbf{E}^{(0)}(\mathbf{r}) \left[\mathbf{J}^{(e)}\right] &= \nabla \times \int \Phi^{(e)}(\mathbf{r} - \mathbf{r}') \mathbf{J}^{(e)}(\mathbf{r}') d\mathbf{r}' \\ \nabla \times \mathbf{E}^{(s)}(\mathbf{r}) \left[\mathbf{J}^{(e)}\right] &= \nabla \times \int d\mathbf{r}' G^{(1)(a)}_{xx}(x - x', y - y', z - z') \mathbf{J}^{(e)}_t(\mathbf{r}') \\ &+ \nabla \times \mathbf{a}_z \int d\mathbf{r}' G^{(a)}_{xz}(x - x', y - y', z - z') J^{(e)}_z(\mathbf{r}') \\ &+ \nabla \times \int d\mathbf{r}' G^{(1)(b)}_{xx}(x - x', y - y', z + z') \mathbf{J}^{(e)}_t(\mathbf{r}') \\ &+ \nabla \times \mathbf{a}_z \int d\mathbf{r}' G^{(b)}_{xz}(x - x', y - y', z + z') J^{(e)}_z(\mathbf{r}') \\ &+ \nabla \times \nabla_t \int d\mathbf{r}' G^{(2)(a)'}_{xx}(x - x', y - y', z - z') \nabla'_t \cdot \mathbf{J}^{(e)}_t(\mathbf{r}') \\ &+ \nabla \times \nabla_t \int d\mathbf{r}' G^{(2)(b)'}_{xx}(x - x', y - y', z + z') \nabla'_t \cdot \mathbf{J}^{(e)}_t(\mathbf{r}') , \end{aligned} \tag{10}$$

with the same expressions holding for $\nabla \times \mathbf{E}^{(0)}(\mathbf{r}) \left[\mathbf{J}^{(m)}\right]$, $\nabla \times \mathbf{E}^{(s)}(\mathbf{r}) \left[\mathbf{J}^{(m)}\right]$.

Discretization via the Method of Moments (Galerkin) Define a regular grid in three-dimensional space, with grid spacing δx, δy, δz. Relative to this grid we define $\pi(x)$ to be the unit pulse

$$\pi(x) = \begin{cases} 1, & \text{if } 0 \le x \le 1 \\ 0, & \text{otherwise,} \end{cases} \tag{11}$$

and $\pi_{m+1}(x)$ to be the mth-order convolution of $\pi(x)$ (we define $\pi_1(x) = \pi(x)$).

Next, expand the current vector as

$$\begin{aligned} J_x(\mathbf{r}) &= \sum_{KLM} J^{(x)}_{KLM} T^{(x)(e)}_{KLM}(\mathbf{r}) \\ J_y(\mathbf{r}) &= \sum_{KLM} J^{(y)}_{KLM} T^{(y)(e)}_{KLM}(\mathbf{r}) \\ J_z(\mathbf{r}) &= \sum_{KLM} J^{(z)}_{KLM} T^{(z)(e)}_{KLM}(\mathbf{r}) ; \end{aligned} \tag{12}$$

the expressions for $T_{klm}^{(q)(e)}$ are:

$$\begin{aligned} T_{klm}^{(x)(e)}(\mathbf{r}) &= \pi_{2k}(x/\delta x)\pi_{1l}(y/\delta y)\pi_{1m}(z/\delta z) \\ T_{klm}^{(y)(e)}(\mathbf{r}) &= \pi_{1k}(x/\delta x)\pi_{2l}(y/\delta y)\pi_{1m}(z/\delta z) \\ T_{klm}^{(z)(e)}(\mathbf{r}) &= \pi_{1k}(x/\delta x)\pi_{1l}(y/\delta y)\pi_{2m}(z/\delta z) \qquad (k,l,m) = (0,0,0),\ldots,(N_x,N_y,N_z)\,, \end{aligned} \tag{13}$$

where $\pi_{1m}(y/\delta y)$ is the mth unit pulse function, and $\pi_{2k}(x/\delta x)$ is the kth tent function, which is the convolution of $\pi_{1k}(x/\delta x)$ with itself.

The $T^{(q)(e)}(\mathbf{r})$ are called facet elements, because the qth element is constant over the qth facet of the klmth cell. They are used to ensure that the divergence of the current density remains bounded. Facet elements have been called 'volumetric rooftop' functions in [7]. Volumetric rooftop functions have also been used in [8] and [9].

Because $\mathbf{J}^{(m)}(\mathbf{r}) = \nabla \times \mathbf{M}_a(\mathbf{r})$, we expand $\mathbf{M}_a(\mathbf{r})$ in edge-elements, which have the required differentiability of the curl operation

$$\begin{aligned} M_x(\mathbf{r}) &= \sum_{KLM} M_{KLM}^{(x)} T_{KLM}^{(x)(m)}(\mathbf{r}) \\ M_y(\mathbf{r}) &= \sum_{KLM} M_{KLM}^{(y)} T_{KLM}^{(y)(m)}(\mathbf{r}) \\ M_z(\mathbf{r}) &= \sum_{KLM} M_{KLM}^{(z)} T_{KLM}^{(z)(m)}(\mathbf{r})\,, \end{aligned} \tag{14}$$

where

$$\begin{aligned} T_{KLM}^{(x)(m)}(\mathbf{r}) &= \pi_{1K}(x)\pi_{2L}(y)\pi_{2M}(z) \\ T_{KLM}^{(y)(m)}(\mathbf{r}) &= \pi_{2K}(x)\pi_{1L}(y)\pi_{2M}(z) \\ T_{KLM}^{(z)(m)}(\mathbf{r}) &= \pi_{2K}(x)\pi_{2L}(y)\pi_{1M}(z)\,. \end{aligned} \tag{15}$$

These functions are called edge-elements because the expansion coefficient, $M_{KLM}^{(x)}$, is the (constant) value of M_x along the x-directed edge, $(y = (L+1)\delta y, z = (M+1)\delta z)$. There are similar interpretations for $M_{KLM}^{(y)}$ and $M_{KLM}^{(z)}$.

The components of the magnetic current vector are given by

$$\begin{aligned} J_x^{(m)} &= \frac{\partial M_z}{\partial y} - \frac{\partial M_y}{\partial z} \\ &= \sum_{KLM} \left[M_{KLM}^{(z)} \pi_{2K}(x)\pi'_{2L}(y)\pi_{1M}(z) - M_{KLM}^{(y)} \pi_{2K}(x)\pi_{1L}(y)\pi'_{2M}(z) \right] \\ J_y^{(m)} &= \frac{\partial M_x}{\partial z} - \frac{\partial M_z}{\partial x} \\ &= \sum_{KLM} \left[M_{KLM}^{(x)} \pi_{1K}(x)\pi_{2L}(y)\pi'_{2M}(z) - M_{KLM}^{(z)} \pi'_{2K}(x)\pi_{2L}(y)\pi_{1M}(z) \right] \\ J_z^{(m)} &= \frac{\partial M_y}{\partial x} - \frac{\partial M_x}{\partial y} \end{aligned}$$

$$= \sum_{KLM} \left[M^{(y)}_{KLM} \pi'_{2K}(x) \pi_{1L}(y) \pi_{2M}(z) - M^{(x)}_{KLM} \pi_{1K}(x) \pi'_{2L}(y) \pi_{2M}(z) \right]$$

$$\nabla_t \cdot \mathbf{J}^{(m)}_t = \frac{\partial^2 M_x}{\partial y \partial z} - \frac{\partial^2 M_y}{\partial x \partial z}$$

$$= \sum_{KLM} \left[M^{(x)}_{KLM} \pi_{1K}(x) \pi'_{2L}(y) \pi'_{2M}(z) - M^{(y)}_{KLM} \pi'_{2K}(x) \pi_{1L}(y) \pi'_{2M}(z) \right] , \qquad (16)$$

where the last term is the transverse divergence of the Amperian current.

Note that we can express $J^{(m)}$ in terms of $J^{(e)}$; i.e., the edge elements and the facet elements are related. This simplifies a number of calculations involving ferromagnetics.

We will discretize (3) by employing Galerkin's method, which uses the same vector functions for expansion and testing. The spatial derivatives that could cause problems will be removed by the testing process. Take moments of each of the first three equations of (3) with the corresponding facet element, and of the second three equations with the corresponding edge element. The result for the electric equation is

$$\begin{bmatrix} \mathbf{E}^{(ix)} \\ \mathbf{E}^{(iy)} \\ \mathbf{E}^{(iz)} \end{bmatrix} = \begin{bmatrix} \mathbf{Q}^{(x)} & \mathbf{0} & \mathbf{0} \\ \mathbf{0} & \mathbf{Q}^{(y)} & \mathbf{0} \\ \mathbf{0} & \mathbf{0} & \mathbf{Q}^{(z)} \end{bmatrix}^{(ee)} \begin{bmatrix} \mathbf{J}^{(x)} \\ \mathbf{J}^{(y)} \\ \mathbf{J}^{(z)} \end{bmatrix}$$

$$+ \begin{bmatrix} \mathbf{G}^{(xx)}_{(0)} & \mathbf{G}^{(xy)}_{(0)} & \mathbf{G}^{(xz)}_{(0)} \\ \mathbf{G}^{(yx)}_{(0)} & \mathbf{G}^{(yy)}_{(0)} & \mathbf{G}^{(yz)}_{(0)} \\ \mathbf{G}^{(zx)}_{(0)} & \mathbf{G}^{(zy)}_{(0)} & \mathbf{G}^{(zz)}_{(0)} \end{bmatrix}^{(ee)} \begin{bmatrix} \mathbf{J}^{(x)} \\ \mathbf{J}^{(y)} \\ \mathbf{J}^{(z)} \end{bmatrix}$$

$$+ \begin{bmatrix} \mathbf{G}^{(xx)}_{(a)} & \mathbf{G}^{(xy)}_{(a)} & \mathbf{G}^{(xz)}_{(a)} \\ \mathbf{G}^{(yx)}_{(a)} & \mathbf{G}^{(yy)}_{(a)} & \mathbf{G}^{(yz)}_{(a)} \\ \mathbf{G}^{(zx)}_{(a)} & \mathbf{G}^{(zy)}_{(a)} & \mathbf{G}^{(zz)}_{(a)} \end{bmatrix}^{(ee)} \begin{bmatrix} \mathbf{J}^{(x)} \\ \mathbf{J}^{(y)} \\ \mathbf{J}^{(z)} \end{bmatrix}$$

$$+ \begin{bmatrix} \mathbf{G}^{(xx)}_{(b)} & \mathbf{G}^{(xy)}_{(b)} & \mathbf{G}^{(xz)}_{(b)} \\ \mathbf{G}^{(yx)}_{(b)} & \mathbf{G}^{(yy)}_{(b)} & \mathbf{G}^{(yz)}_{(b)} \\ \mathbf{G}^{(zx)}_{(b)} & \mathbf{G}^{(zy)}_{(b)} & \mathbf{G}^{(zz)}_{(b)} \end{bmatrix}^{(ee)} \begin{bmatrix} \mathbf{J}^{(x)} \\ \mathbf{J}^{(y)} \\ \mathbf{J}^{(z)} \end{bmatrix}$$

$$+ \begin{bmatrix} \mathbf{G}_{(0)} & \mathbf{G}_{(a)} & \mathbf{G}_{(b)} \end{bmatrix}^{(em)} \begin{bmatrix} \mathbf{M}^{(x)} \\ \mathbf{M}^{(y)} \\ \mathbf{M}^{(z)} \end{bmatrix} , \qquad (17)$$

where the $\mathbf{Q}$'s are tri-diagonal matrices, the $\mathbf{G}_{(0)}$'s the infinite-space matrices, the $\mathbf{G}_{(a)}$'s the convolutional layered-space matrices, and the $\mathbf{G}_{(b)}$'s the correlational layered-space matrices. The infinite-space matrices are convolutional, also. The superscript (ee) denotes electric-electric matrices, and (em) denotes electric-magnetic matrices. The $\mathbf{J}$'s are the unknown electric currents, and the $\mathbf{M}$'s are the unknown magnetic polarization vectors. The last block in (17) is simply a short-hand representation of the three blocks above it, except that it represents electric-magnetic interactions.

The magnetic equation is similar to (17), and is given by

$$\begin{bmatrix} \mathbf{B}^{(ix)} \\ \mathbf{B}^{(iy)} \\ \mathbf{B}^{(iz)} \end{bmatrix} = \begin{bmatrix} \mathbf{Q}^{(x)} & \mathbf{0} & \mathbf{0} \\ \mathbf{0} & \mathbf{Q}^{(y)} & \mathbf{0} \\ \mathbf{0} & \mathbf{0} & \mathbf{Q}^{(z)} \end{bmatrix}^{(mm)} \begin{bmatrix} \mathbf{M}^{(x)} \\ \mathbf{M}^{(y)} \\ \mathbf{M}^{(z)} \end{bmatrix}$$

$$
+ \begin{bmatrix} \mathbf{G}_{(0)}^{(xx)} & \mathbf{G}_{(0)}^{(xy)} & \mathbf{G}_{(0)}^{(xz)} \\ \mathbf{G}_{(0)}^{(yx)} & \mathbf{G}_{(0)}^{(yy)} & \mathbf{G}_{(0)}^{(yz)} \\ \mathbf{G}_{(0)}^{(zx)} & \mathbf{G}_{(0)}^{(zy)} & \mathbf{G}_{(0)}^{(zz)} \end{bmatrix}^{(mm)} \begin{bmatrix} \mathbf{M}^{(x)} \\ \mathbf{M}^{(y)} \\ \mathbf{M}^{(z)} \end{bmatrix}
$$

$$
+ \begin{bmatrix} \mathbf{G}_{(a)}^{(xx)} & \mathbf{G}_{(a)}^{(xy)} & \mathbf{G}_{(a)}^{(xz)} \\ \mathbf{G}_{(a)}^{(yx)} & \mathbf{G}_{(a)}^{(yy)} & \mathbf{G}_{(a)}^{(yz)} \\ \mathbf{G}_{(a)}^{(zx)} & \mathbf{G}_{(a)}^{(zy)} & \mathbf{G}_{(a)}^{(zz)} \end{bmatrix}^{(mm)} \begin{bmatrix} \mathbf{M}^{(x)} \\ \mathbf{M}^{(y)} \\ \mathbf{M}^{(z)} \end{bmatrix}
$$

$$
+ \begin{bmatrix} \mathbf{G}_{(b)}^{(xx)} & \mathbf{G}_{(b)}^{(xy)} & \mathbf{G}_{(b)}^{(xz)} \\ \mathbf{G}_{(b)}^{(yx)} & \mathbf{G}_{(b)}^{(yy)} & \mathbf{G}_{(b)}^{(yz)} \\ \mathbf{G}_{(b)}^{(zx)} & \mathbf{G}_{(b)}^{(zy)} & \mathbf{G}_{(b)}^{(zz)} \end{bmatrix}^{(mm)} \begin{bmatrix} \mathbf{M}^{(x)} \\ \mathbf{M}^{(y)} \\ \mathbf{M}^{(z)} \end{bmatrix}
$$

$$
+ \begin{bmatrix} \mathbf{G}_{(0)} & \mathbf{G}_{(a)} & \mathbf{G}_{(b)} \end{bmatrix}^{(me)} \begin{bmatrix} \mathbf{J}^{(x)} \\ \mathbf{J}^{(y)} \\ \mathbf{J}^{(z)} \end{bmatrix} . \tag{18}
$$

where $\mathbf{B}$ is the incident magnetic flux density due to the coil, the superscript (mm) stands for magnetic-magnetic interactions, and (me) stands for magnetic-electric interactions. The magnetic-magnetic $\mathbf{Q}$ matrices are a little more complicated than the electric-electric ones. The important point is that the electric-magnetic, magnetic-electric, and magnetic-magnetic matrices can be computed from the electric-electric.

We take advantage of the convolutional and correlational structure of the matrices by using conjugate gradients to solve the system of equations. The vector-matrix products are evaluated using three-dimensional FFT's [4].

Impedance of Flaws in Ferromagnetic Bodies. The reaction of field, $\mathbf{E}^{(2)}$, on source, $\mathbf{J}_e^{(1)}$, is

$$
[1,2] = \int \mathbf{J}_e^{(1)} \cdot \mathbf{E}^{(2)} dV . \tag{19}
$$

The source with superscript 1 is the primary source due to the exciting coil, and superscript 2 denotes scattered fields (and their sources) due to the flaw. If I_c is the current in the exciting coil, then the change in impedance due to the flaw, as seen by the coil is

$$
\Delta Z = -\frac{[1,2]}{I_c^2} = -\frac{[2,1]}{I_c^2} , \tag{20}
$$

where we have used the reciprocity theorem. If we normalize the excitation to be $I_c = 1$, then

$$
\begin{aligned}
\Delta Z &= -\int \mathbf{J}_e \cdot \mathbf{E}^{(i)} dV \\
&= -\int (\mathbf{J} + \nabla \times \mathbf{M}) \cdot \mathbf{E}^{(i)} dV \\
&= -\int \mathbf{J} \cdot \mathbf{E}^{(i)} dV - \int \mathbf{M} \cdot \nabla \times \mathbf{E}^{(i)} dV \\
&= -\int \mathbf{J} \cdot \mathbf{E}^{(i)} dV + \int \mathbf{M} \cdot j\omega \mathbf{B}^{(i)} dV ,
\end{aligned} \tag{21}
$$

where we have dropped the superscript 2, and replaced the superscript 1 by (i), to denote incident fields. The transference of the curl operator in going from the second to the third equation is valid for $\mathbf{M}$ with finite support.

Upon substituting the expansions for the electric and magnetic solution vectors, (12) and (14), into (21), we get

$$\Delta Z = -\sum_{KLM} \Big[J^{(x)}_{KLM} E^{(ix)}_{KLM} + J^{(y)}_{KLM} E^{(iy)}_{KLM} + J^{(z)}_{KLM} E^{(iz)}_{KLM} - j\omega \left(M^{(x)}_{KLM} B^{(ix)}_{KLM} + M^{(y)}_{KLM} B^{(iy)}_{KLM} + M^{(z)}_{KLM} B^{(iz)}_{KLM} \right) \Big] \ . \tag{22}$$

This is a sum of dot-products of the electric current and magnetic polarization solution vectors with the incident electric field and magnetic flux-density vectors.

References

[1] VIC-3D: An Eddy-Current NDE Code User's Guide, Sabbagh Associates, Inc., 4635 Morningside Drive, Bloomington, IN 47408, September 1993.

[2] H. A. Sabbagh, L. D. Sabbagh, and J. R. Bowler, "A Volume-Integral Code for Eddy-Current Nondestructive Evaluation," COMPEL, Volume 9 (1990), Supplement A, pp. 67-70.

[3] J. R. Bowler, L. D. Sabbagh, and H. A. Sabbagh, "Eddy-Current Probe Impedance due to a Surface Slot in a Conductor," IEEE Trans. Magnetics, Vol. 26, No. 2, March 1990, pp. 889-892.

[4] J. R. Bowler, L. D. Sabbagh, and H. A. Sabbagh, "A Theoretical and Computational Model of Eddy-Current Probes Incorporating Volume Integral and Conjugate Gradient Methods," IEEE Trans. Magnetics, Vol. 25, No. 3, May 1989, pp. 2650-2664.

[5] H. A. Sabbagh, J. R. Bowler, and L. D. Sabbagh, "A Model of Eddy-Current Probes with Ferrite Cores," Nondestr. Test. Eval., Vol. 5, pp. 67-79.

[6] G. J. Burke, C. G. Dease, E. M. Didwall, R. J. Lytle, "Numerical Modeling of Subsurface Communication," UCID-20439 Rev. 1, Lawrence Livermore National Laboratory, August 1985.

[7] M. F. Catedra, E. Gago, and L. Nuño, "A Numerical Scheme to Obtain the RCS of Three-Dimensional Bodies of Resonant Size Using the Conjugate Gradient Method and the Fast Fourier Transform," IEEE Trans. Antennas and Propagation, Vol. 37, No. 5, May 1989, pp. 528-537.

[8] A. Peter, M. Zwamborn, P. M. van den Berg, J. Mooibroek, and F. T. C. Koenis, "Computation of Three-Dimensional Electromagnetic-Field Distributions in a Human Body Using the Weak Form of the CGFFT Method," Applied Computational Electromagnetics Society Journal, Winter 1992, Vol. 7, No. 2, pp. 26-42.

[9] P. Zwamborn and P. M. van den Berg, "The Three-Dimensional Weak Form of the Conjugate Gradient FFT Method for Solving Scattering Problems," IEEE Trans. Microwave Theory and Techniques, Vol. 40, No. 9, September 1992, pp. 1757-1766.

SESSION 3:

RESEARCH AND ENGINEERING FRAMEWORK FOR CEM

Chair: K. Siarkiewicz

RESEARCH AND ENGINEERING FRAMEWORK (REF) FOR COMPUTATIONAL ELECTROMAGNETICS*

B. Hantman§, K. Siarkiewicz◊, J. Labelle§, R. Jackson‡

Correspondence to:
Barry Hantman
Raytheon Company, Mailstop T3MJ21
Tewksbury, MA 01876
Phone: (508) 858-5778
FAX: (508) 858-5976
Email: hantman@msmg02.msd.ray.com



MMACE / A TRI-SERVICE PROGRAM

ABSTRACT

Scientific and engineering research and design codes are typically FORTRAN-based, having vastly different data structures and I/O, and unique and inconsistent user interfaces resulting in long learning curves and difficulties in usage. This is true of the codes implementing the various computational electromagnetics (CEM) formulations. The result is numerous opportunities for the introduction of human error in the design process because of usage difficulties, the required manual manipulation of data from code to code, the inability to graphically view the geometry and directly access the geometry to build the analysis model, and the inability to ensure that all design codes are working with valid input data. This situation also adversely affects the cost (human and software/hardware) of maintaining and extending design capabilities as the theoretical foundation and design needs advance. The Research and Engineering Framework (REF), developed as part of the Microwave and Millimeter-Wave Advanced Computational Environment (MMACE) program, provides a coherent, heterogeneous design environment which is the first step toward addressing the above problems. Although the REF was initially developed to address the problems of the power tube industry, the underlying framework is open in the sense of accommodating a broad range of scientific and engineering disciplines, including CEM modeling and simulation. The REF focuses on providing enabling technology in several critical areas including: ease of use and consistency; support for a "master" geometry; data sharing; integration of codes at different dimensionalities; heterogeneous networking; numerical grid generation; visual connection of tools and data flows; and configuration management of design data for project teams.

The REF was first released to the US microwave tube industry in January 1994 for evaluation and testing. The lessons learned from development and usage have been used to refine the system and expand on its capabilities. The REF is currently being used in industry, universities, and government laboratories.

This paper provides detail to the concepts outlined in previous ACES symposia [1-2] and other conferences [3]. It contains an overview of the REF architecture, its functionality and its capabilities. Also included is a description of how the REF can be applied to the codes and requirements of the CEM community.

* Work supported by the Office Of Naval Research
§ Permanent Address: Raytheon Co., 50 Apple Hill Dr. T3MJ21, Tewksbury, MA 01876
◊ Permanent Address: Rome Lab./ERST, 525 Brooks Rd. Griffiss AFB, NY 13441-4505
‡ Permanent Address: Naval Research Lab., Code 6840, Washington, DC 20375-5347

BACKGROUND

The MMACE program has been underway for over two years and is now in its second phase. The first phase, which began in 1992, was an investigation phase. Four teams were put in place to study the problems of the Microwave Power Tube industry and develop roadmaps for the implementation of a framework to address those problems. The teams found an existing design environment that: was based largely on in-house developed software; was largely unsupported by commercial vendors; did not take advantage of the latest advances in CAD, visualization, database technology, and networking; was addressing technically difficult problems; contained a collection of tools that were not well integrated with each other; and was crucial to projects deemed important to the US government. While these items were true of the power tube industry, the same can be said of many niche scientific disciplines including CEM. Once the investigation was complete, the four MMACE teams began constructing a prototype system to experiment with some of the proposed solutions. This prototype was released in early 1994 and the system is now in production use.

Phase II of the MMACE program, scheduled to last three years, began in March of 1994. Raytheon Company and Compact Software, along with several subcontractors[1], are under contract to jointly develop the complete framework. However, it became obvious that the problem should be split into two parts. The first part of the problem addresses those areas specific to power tube design. The second part of the problem addresses areas that are common to multiple design disciplines and therefore have far greater applicability. The portion of the system common to multiple disciplines, including CEM, is referred to as REF, the Research and Engineering Framework. Version 1.2 of the REF was shipped in November of 1994 and is now available for both the Hewlett-Packard and Sun platforms. Source code is available for those wishing to port the system to additional platforms.

OVERVIEW

The REF contains programming interfaces, standards, and tools to aid in the integration of codes. In addition, it provides the data management, networking, visualization, and "Master" geometry needed to drive analysis codes. The REF also provides the utilities needed to construct graphical user interfaces including the top level control panel. The REF portion of the system can be compared to a computer operating system: generic, powerful, and providing much functionality but of little interest to the end user who requires software that is written to operate on top of it. Figure 1 shows the structure and major components of the REF.

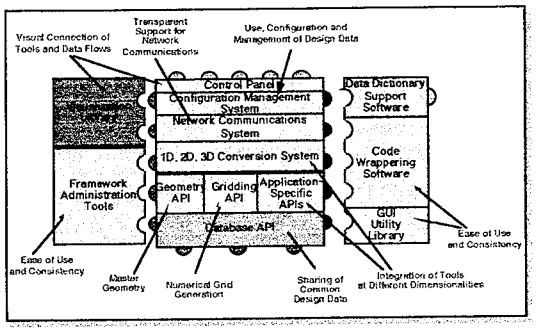


Figure 1 - REF Architecture

---

1 The Compact/Raytheon Team includes Sabbagh Associates, Hughes, Litton, ITT, Teledyne, and Varian as subcontractors.

On top of the REF, one can layer design tools specific to a given design discipline, such as CEM. For the MMACE program, we have tested the REF by integrating a collection of design tools used in the design and analysis of power tubes and the data dictionary describing the data elements needed for that design and analysis. These design and analysis codes can be compared to off the shelf software that can be loaded on a system and accessed by the end users to perform specific functions. However, like off the shelf software, without the underlying operating system (in this case the REF) the software would be useless. Figure 2 shows the REF with discipline specific tools, databases, and data dictionaries connected to provide the user with a complete environment. Although the specific codes that would be integrated for CEM would be different from those that have been integrated to date, the concept is the same.

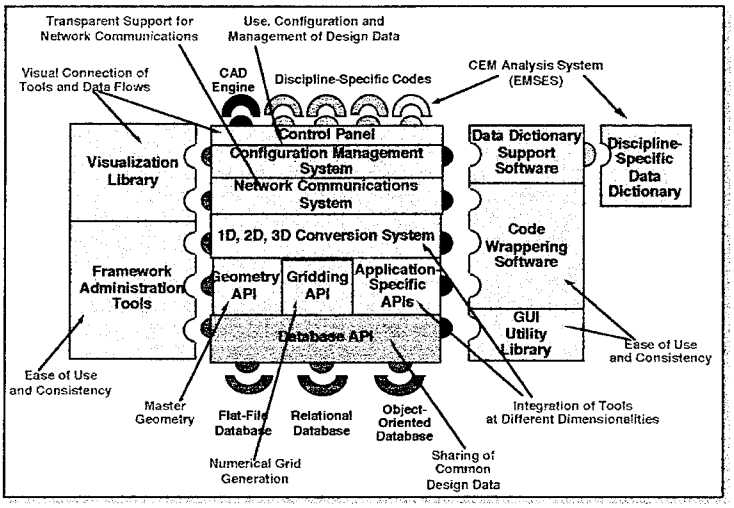


Figure 2 - REF Environment Customized for a Specific Design Discipline

RESEARCH AND ENGINEERING FRAMEWORK (REF) DETAIL

While Phase I of the MMACE program concentrated on developing design requirements and implementation of a prototype framework, Phase II focuses on enhancing, extending, and developing framework technology in eight key areas:

- Ease of use and consistency
- Sharing of common design data
- "Master" geometry driven analysis
- Standard foundation for numerical grid generation
- Integration of tools at different dimensionalities
- Visual connection of tools and data flows
- Use, configuration & management of design data
- Transparent support for network communications & distributed processing

At the same time, the MMACE Team has continued to provide support for standards activities, system validation, tool integration, and system dissemination.

The following is a summary of the REF's features in each of the areas listed . Each of the areas is addressed by a piece of the architecture shown in figures 1 and 2.

Ease of Use and Consistency

During the initial implementation of the REF, a heavy emphasis was placed on making the system usable and extendible by design engineers, not software engineers. This work is currently being enhanced to provide technology in three key areas.

First, code wrappering software and a standard user interface library is being created so that users can easily place existing codes into the framework and provide them with a standardized appearance and behavior.

Second, all documentation is being placed on-line and made accessible over the Internet network. This will ensure that all users, regardless of their location, have the latest and most up-to-date manuals available to them. This will be accomplished by utilizing the NCSA Mosaic software, the software of choice for exploring the Internet.

Third, a standard set of visualization tools is being included with the framework so that code developers need not create their own. The need for proprietary visualization tools will be eliminated and, with their elimination, some of the expense of developing new codes.

Sharing of Common Design Data

A large emphasis has been placed on sharing design data between codes. This concept is currently being extended to allow additional types of data, such as thermomechanical or electromagnetic data, to be shared. This is being accomplished by developing a detailed data model and programmatic data interface. Users are able to extend the data model to access data entities that are not contained in the data model as delivered. A separate data model for CEM is being create at Rome Laboratory.

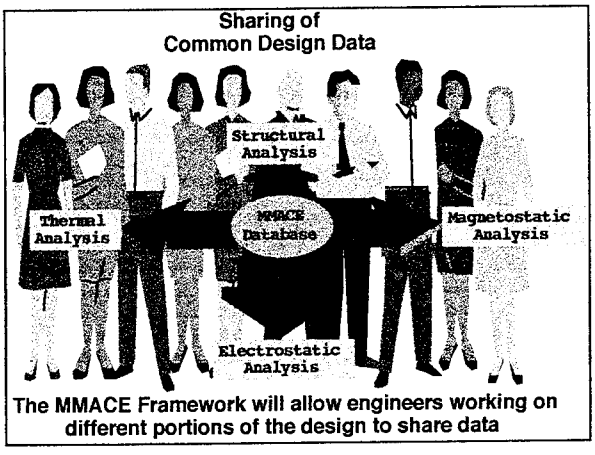


Figure 3 - Sharing of Common Design Data

The REF includes Application Programming Interfaces (APIs) to aid in the development of design and analysis codes. These APIs allow code developers to concentrate on the algorithmic portions of the code and avoid the time consuming data exchange portions of the coding. In addition, these APIs insulate the code developer from changes to the underlying implementation. At present, the REF includes the following APIs to aid data sharing:

- Data API - This programming interface provides direct read and write access to all of the data attributes in the REF database.

- Particle & Field API - This programming interface provides direct read and write access to all of the particle and field data in the REF database. This API can be used for accessing any large matrix of data.

The goal in this area is to promote data reuse while building on existing standards and off-the-shelf commercial products. It is not the REF developer's intent to create a new database product. Rather, the REF will provide the appropriate layers so that users can select the pieces they desire without having to worry about the affect on the analysis codes.

Master Geometry

One of the goals of the REF is to have all codes utilize a single, consistent source to derive a geometry model for analysis. This task would be simplified if a single CAD package were chosen and the framework provided access to that CAD package's database to all codes. However, note that the issue of providing geometry to analysis and simulation codes is far more complex than simply accessing a CAD database. Extensive work would be required, regardless of the CAD package chosen, to enable a heterogeneous mix of codes to share a geometry source.

While many large companies have adopted the single CAD system approach, it has been demonstrated to have several pitfalls:

- The user is tied to a particular CAD package and cannot change without considerable expense.
- Enhancements and bug fixes will be made based on the perceived market for the CAD product. This will usually not help niche scientific areas such as those addressed by the REF.
- Everyone must agree on the CAD package. This is highly unlikely due to different business requirements, cost, corporate standards, etc.

For the REF, the choice of a CAD package is left up to the user. The REF takes the approach of having a buffer around the CAD engine so that the geometry information can be accessed by all codes regardless of the specific CAD package used. To help build this layer, the MMACE Team is using the NASA IGES standard and the DTNURBS library developed by Boeing Computer Services under contract from the Navy's David Taylor Modeling Basin.

An API has been created to access the geometry information regardless of the user's choice of CAD package.

Numerical Grid Generation

A key feature of the REF environment is the support for numerical grid generation. In the current design environment, gridding software is often tied to a particular code and is sometimes embedded within that code. The objective of the MMACE program is to develop standards for the exchange of grid information and, in doing so, allow multiple codes to share grid information. In addition, by creating this standard layer, users will be able to plug-in the latest gridding software as it becomes available. To test this, an existing grid generator will be adapted to use the REF gridding standard. This will then be accessed by both electromagnetic and thermomechanical codes. An example is shown in figure 4.

The REF grid generation requirements for both thermomechanical (TM) and computational electromagnetic (CEM) analysis can be briefly summarized as follows:

- Mixture of line, surface and solid elements - node-based geometric entities in TM, and both node and edge-based in CEM.
- Steep gradient of grid density to accurately model localized phenomena.

- P-type and H-type grid refinements in adaptive gridding
- Specification of boundary codes., loadings, initial conditions and material properties (e.g., density, thermal and electrical conductivities, Young's modulus, Poisson's ratio, permeability, dielectric permitivity, etc.)
- Sliding interfaces and joints in TM, and surfaces of discontinuities in CEM.
- Symmetry (or anti-symmetry) planes
- Computed quantities for post processing - for TM: temperature, displacements, velocities, accelerations, stresses, bending moments, material-dependent variables, etc.; for CEM: electric and magnetic fields, current density, scalar and vector potentials, etc. These may involve complex numbers.
- Rectangular grids used in the finite-difference and volume-integral methods in CEM.

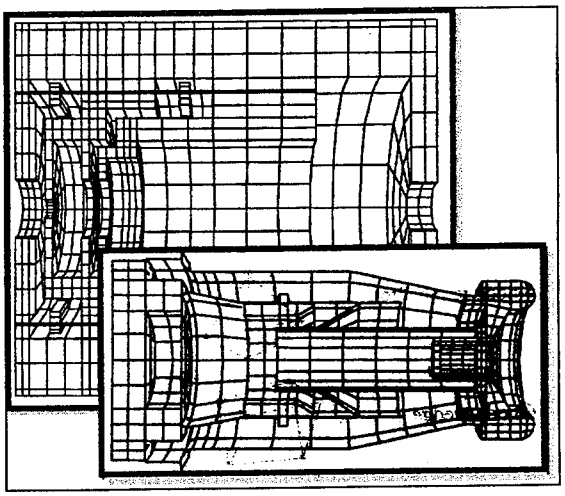


Figure 4 - Gridding

These requirements are being used as input for the design and development of the REF gridding interface.

Integration of Codes at Different Dimensionalities

In the existing MMACE system for power tube design, a link was established between the 1D parametric codes and the 2D geometry driven codes. At present, the link is uni-directional and does not accommodate the users' 3D requirements.

An effort is being made to generalize the existing software to provide a complete integration of codes at different dimensionalities. This is not a trivial problem. For axisymmetric designs, going from 1D information to 2D information or from 2D to 3D is fairly straightforward. However, in the other direction (e.g., going from a 3D database to a 2D database), approximations must be made which may effect the outcome of the analysis. The REF developers are taking a multifaceted approach to connecting codes and data operating at different levels of detail. Basic methodologies and tools are being developed which will interact with the user to select, abstract, and connect/transport parametric and geometric design data to codes at both higher and lower dimensionalities.

Visual Connection of Tools and Data Flows

The REF includes a customizable control panel to allow access to tools and to visually display the design flow. The MMACE Control Panel, shown in Figure 5, is the first thing the user sees when accessing the Framework. While the REF provided the underlying tools for creating the control panel, the specific button layout and dependencies that are shown are specific to power tube design. Obviously, the buttons and layout would be different for CEM. The control panel contains buttons for each of the codes available to the user. These buttons are laid out in the process flow appropriate to a given project. Each design could have a different process. Notice that the arrows indicate the design flow direction as well as whether a particular code is blocked, ready, running, or done. The user simply executes codes by pushing buttons available on the OSF/Motif compliant interface. The control panel has been designed in such a way to make it possible to "plug" in new codes as needed.

CEM design and analysis tools can easily be integrated into the system using the wrappering tools included with the REF.

The control panel also provides access to the data visualization tools and to the version control system. The version control system can be configured to automatically archive key versions of design data at specified points in the design cycle. This allows designers to try several design variants and then easily locate and return to the variant that provided the best results. The underlying REF core manages the versioning of data.

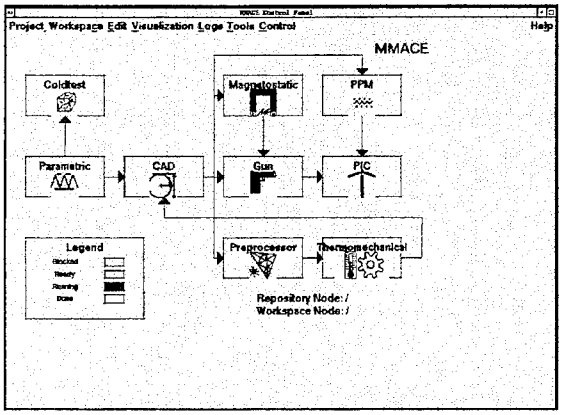


Figure 5 - Control Panel

Configuration and Management of Design Data

Proper management of design data is critical to producing a quality product. Typically, design data has been maintained by the design engineer in hardcopy format. Data is often stored in several filing cabinets and in other places throughout the organization. It is often difficult to find the latest version of the data, especially if people involved in the original design are no longer around.

At present, a configuration and management system is being developed so that the REF can automatically track design data. The system will keep electronic copies of different versions of the data, both for designs under development and for products that have shipped. Users will be able to instantly retrieve data from any version of the product. In addition, by automatically keeping track of the data, users will be able to explore different design variations without having to worry about overwriting information from alternate design options.

Once a design is complete, data for alternate design options can be deleted to conserve space and the final database can be archived in an electronic vault for future reference. Often, this archived version will be used as the starting point for upgrades or even for new designs that are similar to the one archived. An index will make it easy to locate archived designs.

The REF design data management system will be an adjunct to, not a replacement for, more capable and full-featured corporate data management systems. The focus of REF data administration capabilities will be the support of small R&D groups in the configuration and management of their technical data.

Inherent Networking

Users of the REF typically have environments comprised of multiple workstations and mainframe computers. Users want to make use of these resources by performing remote executions of codes and, if supported by the codes themselves, to perform distributed processing. For example, a user in a company's engineering facility might wish to utilize the mainframe resources available at another company facility over a wide area network. The REF includes a complete programmatic subroutine library allowing users to take advantage of the high-performance hardware distributed throughout their company's network. In extreme cases, users could even use this technology to submit large processing jobs to other companies across a wide area network such as the Internet. Long running CEM codes could be set up on a local workstation and executed on a remote, massively parallel processor. Data post-processing could still be accomplished locally. Unfortunately, none of the power tube design and analysis codes that have been integrated into the framework to date are using this networking capability. This is probably due to the fact that the codes integrated to date have been pre-existing codes making incorporation of distributed and/or remote processing difficult. It is expected that this capability will be of greater use for new design and analysis codes currently under development.

SUMMARY

Phase II of the MMACE program will provide a full research and engineering framework for niche technical communities which will approach the functionality, quality, and robustness found in commercial products. The REF core development will focus on some of the problems not addressed adequately by commercial vendors because of the typically small market size of engineering and scientific communities. Specifically, MMACE and its underlying REF core will provide a low-cost environment that is easy to use, has a consistent interface, promotes data sharing, provides a unified source of geometry, supplies standards for numerical grid generation, integrates 1D, 2D, and 3D codes, provides a visual means for the user to view data and data flows, performs configuration management of the design data, and supports the use of heterogeneous networks of computers.

The REF will provide the foundation for design environments that are applicable to a wide variety of technical design disciplines including, power tube design, antenna design, and computational electromagnetics among others. The REF software is distributed at no charge[2] and the developers are eager to work with anyone who desires to make use of the software.

REFERENCES

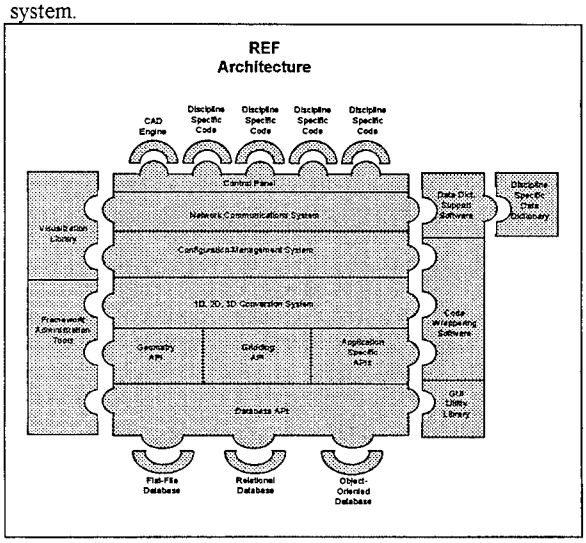
1. Siarkiewicz, K. "The Electromagnetic Modeling and Simulation Environment for Systems (EMSES)." *9th Annual Review of Progress in Applied Computational Electromagnetics Conference Proceedings*, March 1993, pages 114-121.
2. Siarkiewicz, K. "Further Considerations Regarding the Electromagnetic Modeling and Simulation Environment for Systems (EMSES)." *10th Annual Review of Progress in Applied Computational Electromagnetics Conference Proceedings*, Volume II, March 1994, pages 86-93.
3. Hantman, B et. al. "Technical Overview Of The MMACE Phase I Prototype and Phase II Research And Engineering Framework Development." *1994 Microwave Power Tube Conference, May 1994.*

2 Software is available to US defense contractors and universities. Requests for software should be sent to the Naval Research Laboratory.

Research & Engineering Framework (REF) Data Dictionary Specification for Computational Electromagnetics

Mr Jeffrey A. Evans
Decision Science Applications, Inc.

The Research and Engineering Framework (REF) manages data for a variety of design and analysis codes. Each of these different design and analysis codes have their own data requirements (data model) for input and output. The method that the REF uses to handle these different data models is through the use of a data dictionary. REF users will have the ability to switch between data models thereby transforming the generic REF into a discipline-specific design system.



This paper discusses the design and development of a Computational Electromagnetic (CEM) specific data dictionary for REF. Types of data covered by this dictionary include: CEM Analysis Techniques; Geometry Elements; Material Properties; Excitation Information; and Obsevables Information. The CEM data dictionary is being developed as a baseline data dictionary for the wide variety of CEM codes available. A developer need only tie his/her application-specific code into the REF directly or through wrappering to access this data dictionary.

Common areas of CEM, Computation Fluid Dynamics, and Finite Element Analysis for Structural and Thermal investigations were considered to facilitate transfer of information and the future development of discipline-specific REF data dictionaries. These areas are of immediate interest due to their interaction with electromagnetics.

The REF data dictionary and its support software then provide a means for validating application data input and facilitate extending the data model and dictionary to a variety of engineering disciplines.

This work was Sponsored by Rome Laboratory under the Expert Science And Engineering Program (BAA 93-07)

DT_NURBS - A GEOMETRY ENGINE FOR INTEGRATION OF MMACE DATA

Bob Ames
LT Cliff Whitcomb, USN

Naval Surface Warfare Center - Carderock Division
David Taylor Model Basin
Bethesda, Md 20084-5000
ames@oasys.dt.navy.mil
whitcomb@oasys.dt.navy.mil

Abstract

This paper describes the role of the DT_NURBS Spline Geometry Library in the Microwave/Millimeter Advanced Computational Environment (MMACE) system architecture. DT_NURBS provides a common geometry, gridding, and analysis data structure for the MMACE Research and Engineering Framework (REF). The DT_NURBS library also offers the CEM community the means to integrate geometry, gridding, and analysis data into a common product model. This product model allows for multi-discipline integration in a logical and inter-dependent way.

Background

It has become evident over the years that geometry plays a vital role as the common element in the design and analysis of complex systems. In essence, computational geometry is the closest data representation of the actual product of any piece of information. It is not surprising then that when complex systems are designed, the integration of performance data with geometry becomes critical. This is most evident when two dependent disciplines interact with a changing geometry. Consider an example where thermal characteristics effect the geometry which in turn vary electromagnetic performance. Airplane wing design also requires a coupling of aerodynamic load and structural response. Each in turn affects the other and the resultant "in-flight" shape is found through iteration to equilibrium. As efforts at multi-discipline integration increase so will the requirements for a robust and complete common geometry model.

In the early 80's some pioneers in integration schemes and math modeling techniques developed a mathematical characterization called Non-Uniform Rational B-Splines, NURBS. This NURBS math model is very capable of modeling complex geometry structures as well as correctly representing circles, ellipses, etc., which could only be approximated by other splines. This allows for all geometry entities to be based on one math form whether they are lines, arcs, or trimmed contoured surfaces joined to formed a bounded solid. The NURBS math form is also capable of representing other geometry that may have been created from a different math model (i.e. Bezier, uniform non-rational B-splines, Coons patches, CSG primitives like spheres, cones, etc.).

In 1989 a geometry library called DT_NURBS was developed. The objective of the library is to provide a common geometry math model for the integration of geometrically dependent analysis tools with Computer-Aided-Design systems; and to provide tools for unique applications unsupported by commercial programs. In particular, DT_NURBS was developed to provide the tools for integration of computational, physics based codes and other geometrically dependent analysis. These tools include grid and analysis modeling as well a more general CAD related geometry modeling. In addition, DT_NURBS was designed to accommodate more difficult modeling requirements. These include, but are not limited to, designs where geometry, grids, and analysis varying with time, iteration, or configuration. This is accomplished through the use of multi-dimensional NURBS based mathematics.

Implementation

The implementation of DT_NURBS in the engineering world could take almost unlimited form. In general, the objective of DT_NURBS is to provide analysis programs, or their pre- and post-processors, with a library of routines which allow these codes to 1) read CAD generated data; 2) develop, modify, and access grids; and 3) store the resultant geometry, grid, and analysis data in a single topology. A DT_NURBS based application would therefore contain and control all information relating to geometry, grids, and analysis. Since analysis is dependent on grids, and grids on geometry, the coupling of these elements in an object oriented data structure is logical. In some situations, solvers need access to geometry and control of grids. Transient or unsteady analysis of geometry varying with time requires adaptive gridding and multi-discipline coupling in a "hands off" non-interactive framework. The same is true for design optimization.

Figure 1 illustrates this type of configuration where two or more applications directly communicate the same data structure; thereby eliminating the need for data translation, or reformatting. In this configuration, the common geometry used by both codes may have been initially constructed on a CAD system. Once constructed, the geometry is saved in IGES format. This format will contain entities the original developer used in constructing the geometry and its IGES representation of those entities will be set by the CAD vendor. Through an IGES filter program developed by NASA called NIGES, the non-NURBS IGES entities are filtered or translated into Non-Uniform Rational B-Splines, NURBS. No loss of accuracy occurs in this translation because NURBS are a mathematical superset of most CAD entities. Most CAD systems store native data in NURBS format internally as well. Once a NURBS based IGES file is generated the geometry can be read by both applications. Theoretically, DT_NURBS can read an unfiltered IGES file. However, not all entities can be automatically used in calls to DT_NURBS routines. DT_NURBS actually supports an extension of the NASA standard. In the figure it is referred to as DT/NIGES. These DT extensions to the NASA-IGES standard are stored as user defined entities and are ignored by most CAD systems. In this area of the IGES file, DT_NURBS stores geometry, grids, and analysis data in a mapped object topology, called Geometry/Grid/Analysis Objects or GGA. Because IGES is large and not efficient for use as a common flat file format, the DTRC native format will generally be used when sharing data between applications. A DT/NIGES file or standard IGES file can be written at any time for communication with other CAD related applications. The main use of the DT/NIGES file format is for exchange of a single data file where some applications may be 'DT_NURBS aware' while other applications may only be able to use the common geometry stored as standard IGES entities. The association between common geometry (standard IGES) and GGA objects (DT/NIGES) is maintained by being in one IGES file. Future DT_NURBS support for the STEP standard will improve translation of B-rep solids and other product model type data. GGA type data will still require a separate Application Protocol since none of the existing AP's currently support GGA functionality.

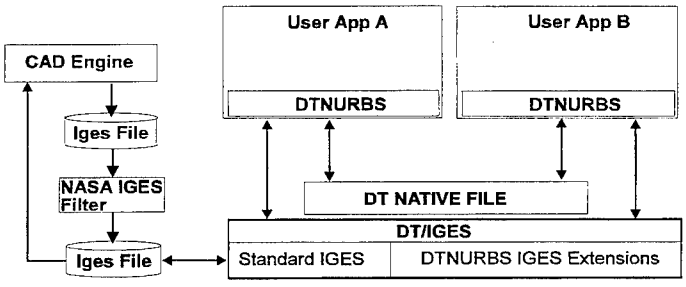


FIGURE 1 - DT_NURBS BASED INTEGRATION

In many situations, however, it may not be prudent to modify analysis codes to accommodate the DT_NURBS data structure and GGA topology. At least not initially. Cost, time, size, maintenance, or other software development issues may preclude the inclusion of DT_NURBS data structures internal to a code. This forces the GGA object topology to reside outside the applications themselves. In these situations DT_NURBS can act as an toolkit or foundation for an Application Program Interface, or API, between applications and the data base (see Figure 2). The best way to visualize

this architecture is to think of DT_NURBS as a toolbox that allows for the construction, evaluation, manipulation, and storage of geometry, grids, and analysis. In this toolbox, DT_NURBS ensures the dependency between geometry, grids, analysis, and attribute data, but requires the maintenance to occur within application wrappers by way of general access API's. It is not the intent to describe completely the different architectures available to DT_NURBS, but rather to illustrate its capabilities in such an environment. The MMACE architecture is very similar to this latter configuration. The MMACE data base description is outlined in more detail in Reference 1.

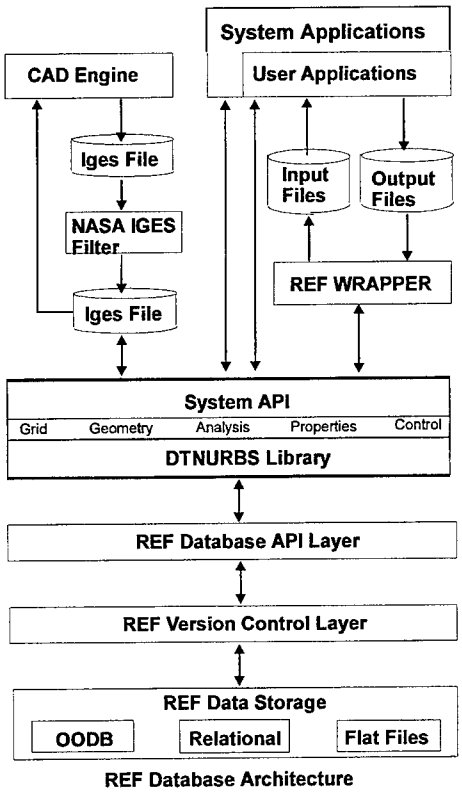


FIGURE 2 - REF DATABASE ARCHITECTURE

The DT_NURBS library provides the MMACE with essential components to the Geometry, Gridding, and Analysis Application Program Interface (API). DT_NURBS provides a suite of subroutines which give the programmer a wide range of capabilities; from simple curve fitting to modeling, manipulating, or evaluating solid objects containing geometry, grid, and analysis data. One unique capability of DT_NURBS is the ability to literally place grid and analysis data inside geometry through the use of GGA objects.

Geometry/Grid/Analysis Objects

DT_NURBS models common geometry, grids, and analysis in an object oriented topology where the dependence between geometry, grids, and analysis solutions are maintained. This architecture is called Geometry/ Grid/ Analysis Objects, or GGA. [Ref. 2]

To understand how GGA objects function it is necessary to outline some of the unique features of DT_NURBS that allow GGA objects to operate as they do. Most DT_NURBS entities have unlimited dimensionality. For example, a point is usually considered to be 3 dimensional, but a vector has variable length. A vector can model all points, but points cannot define all vectors. Using the word 'point' has some meaning beyond the raw data; but in reality it is just a vector of data. We typically associate point with a location in Cartesain space. From a data modeling perspective it is just a vector of length three containing real data. This is the easiest way to think of the differences between DT_NURBS modeling and CAD modeling. DT_NURBS operates on data; some of which happen to be used for the construction of geometry. In CAD systems, all data assumes it is associated with or defining geometry. DT_NURBS would model points as vectors. If the user only wants to store three Cartesian data values that is perfectly acceptable. Should the user decide to store temperature and pressure along with the Cartesian data DT_NURBS will allow it, CAD systems won't. If the user should choose to fit a surface or solid through those vector points DT_NURBS can do that. If the user then chooses to view the model as a 3D image, the three of the five parameters would be chosen. If it happens to be (x,y,z) then only geometry is plotted.

DT_NURBS has the ability to specify the dimensionality of its entities to any dimension. It therefore has the ability to act as a superset of traditional CAD entities. Secondly, spline entities like curves and surfaces have independent parameters that the spline entity is normalized to. For a curve it could be curve length. Traditional spline curve entities have one independent variable, surfaces have two, and solids have three. DT_NURBS has no limit on the number of independent variables for the parameterization of these entities. Consider a traditional surface. Normally it has three dependent variables, namely, (x,y,z). When a surface is constructed it is traditionally parameterized by two independent variables (u,v), see Figure 3.

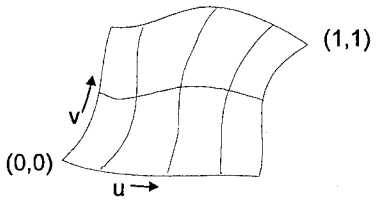


FIGURE 3 - TRADITIONAL SURFACE PARAMETERS

DT_NURBS allows an unlimited number of dimensions for both dependent and independent variables. What this means is the we can add parameters such as iteration, time step, or configuration to the traditional independent parameters used by CAD systems. In this situation, the dependent variables, (x,y,z), can be evaluated given a set of independent variables, or parametric location (u,v,config,time,iter). Written backwards, every point on the geometry is defined by it location along (u,v) at a particular iteration, during a single time step, of one of the design configurations. This is a simple case of variational geometry modeled as a single geometric entity. Consider again the case where geometry is changing with iteration, time, and configuration. Figure 4 depicts a hierarchy of data structure showing iterations per time step and time step simulations per configuration. Perhaps we have an optimization program controlling design configuration. Each design geometry goes through a simulation where it may be changing with time, perhaps because of environmental or operational conditions. Between each time step the geometry iterates to convergence between two analysis applications such as mechanical and thermal.

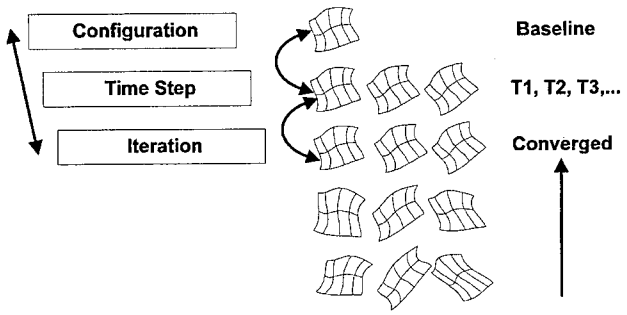


FIGURE 4 - GEOMETRY CHANGING WITH ITERATION, TIME, AND CONFIGURATION

This is just one example of the possible topologies available through DT_NURBS. For example, if we add the parameter (w) we can model a solid changing with these parameters (u,v,w,config,time,iter) as well. The DT_NURBS representation more closely models geometric reality. What is the geometry of a balloon? When its inflated, deflated, deflating, or blowing in the wind? In a CAD system you will get to model only one representation.

GGA objects extend the ability to model variational geometry to include to storage of grid and analysis data along with the geometry. The GGA object is based on an hierarchical object architecture where objects have the same mathematical representation and dimensionality but have dependencies on each other through mappings. Grids are imbedded in surfaces or solids, and analysis is modeled as surface or solid interpolations of solution data stored at grid points. Geometry, grid, and analysis data may change content with time, iteration, or any number of additional parameters without losing their dependence on each other.

Consider the previous example of the geometry varying with iteration, time, and configuration. Suppose now that we attach a grid that is 'stuck' or mapped to this geometry. This grid contains vector nodes that can hold geometric and non-geometric data at each node. The non-geometric data could contain analysis data, property data, or any data that varies over the domain of the geometry. Suppose again that we fit a surface or solid through these vector nodes. This new entity will now interpolate and mathematically define the data over the entire grid domain. Again this analysis entity is 'stuck' or mapped, like the grid, to the parent geometry. As the geometry changes so does the grid and analysis data. For simple grids that contain vector nodes of just parametric geometric data, no additional information is required as the geometry changes; unless of course we choose to change or adapt the grid for each iteration, time step, and configuration. In this scenario, however, we are also storing non-geometric or analysis data at each node. Therefore, the grid will have the same independent dimensionality as the geometry. Its information will change with iteration, time, and configuration. This same analogy holds true for the analysis entity except that as a spline function there are some differences in dimensionality.

Keep in mind that in this example there are only three individual entities in this entire simulation. This allows for coupling of multi-discipline analysis for steady or unsteady analysis. Each multi-discipline application that implements a GGA data structure can define, extract, or interrogate the analytic geometry for solution data derived from another application. This point needs re-emphasizing. A grid point for an application, say finite element analysis, requires a pressure and temperature. By pointing to a parametric location on the parent geometry, (u,v,w,config,time,iter), it can request this information from an analysis entity(s) that contains this information. This other entity is also mapped to the same geometry and shares the same geometry parameterization. When two or more different, but dependent applications are structured this way, communication between them is immediate and automatic. These are fundamental requirements for optimization, design synthesis, and unsteady or transient simulations. Additional benefits of the dependent nature of GGA objects is configuration control. The grid and analysis data is mapped to the parent geometry. There is no question about which geometry the analysis was performed on and what grids were used. Also, a different kind of product model is now available; one that contains solution data, performance information, and property data that varies over the geometry.

An Example Problem

The following problem will illustrate how one discipline, in this case thermal analysis, could go about modeling using GGA objects for use by two other disciplines, mechanical analysis and electromagnetic (EM) analysis. Our problem involves the transient conditions existing within a helix traveling wave tube (TWT) during warm up. A simplified helix TWT, shown in Figure 5, consists of a gun, slow-wave structure (helix), collector, and RF circuit. The gun assembly, consisting of the heater bucket (heater), cathode, focus electrode, anode, and related support structure, is used for our example. As the gun components heat up, the materials expand, causing deformations of the various structures. The gun component geometry must be maintained in a constant relative position during warm up and operation.

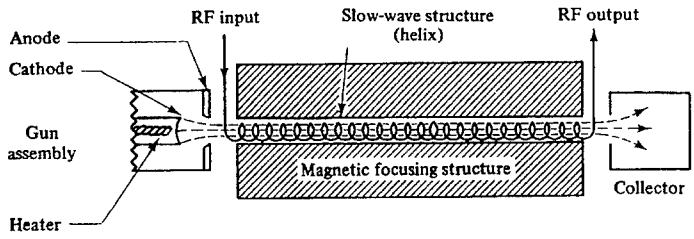


FIGURE 5 - SIMPLIFIED DRAWING OF A HELIX TWT [REF. 3]

The TWT component warm up is a transient event requiring both the thermal analysis code and mechanical analysis code to iterate in an automated fashion at each time step so that component deformations due to thermally induced stresses can be determined. The EM analysis then must compute the resulting electric field for each deformed geometry at each time step. The analysis domain used for this example is shown in Figure 7. A possible GGA object design process implementation is described to show how the data exchange problem between analysis codes is made possible.

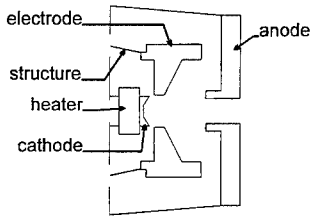


FIGURE 6 - ANALYSIS DOMAIN OF A TWT GUN

To accomplish the TM and EM analyses, we need a method of integrating the gun geometry as a function of time, the grids used in each of the three analyses, and a method of storing the results of the three analyses. Given these, thermal analysts will calculate the temperature distribution within the cathode, focus electrode, anode, heater, and support structure assemblies at each time interval and will store temperature data at every time step. The mechanical analysts will then compute the structural deformations due to the temperature distribution effects on the temperature-dependent mechanical properties of the component materials. The EM analysts, in turn, use the deformed component geometry to model the region bounded by the gun components to update the electric field and the resulting effect on the electron beam. Note that the EM analysts do not directly need any computational results from the TM computations, but only the resulting deformed geometry computed by the mechanical solver.

The data for the modeling requirements can be defined as: (1) a geometry (or geometries); (2) a grid for each of the required analysis, thermal, mechanical, and EM, that is appropriate to each solver being used; and finally, (3) the results of

analysis. In a traditional mode of operation the data is treated separately and it is up to the designer/analyst to manage the interconnections. We want to facilitate management of the disparate data. Specifically, we want the integration to accomplish three things. First, we want all the relevant data to be stored in a compact and efficient form. Second, we want the time dependency integrated seamlessly. This means that, for example, at any point on the gun geometry, and at any time during warm-up, the mechanical solver should be able to easily determine the temperature, density, or any other computed non-geometric or performance variable. Lastly, performance data should be stored locally, associated only with the corresponding component or region, and not stored globally.

It is important to note one of the reasons why traditional approaches to geometry, grids, and analysis fail to provide the seamless integration required. For example, traditional geometry is restricted to planar and space curves described by a single independent parameter, and to surfaces described by two parameters. However, the problems we are discussing require at least three or four independent parameters. Solids require three parameters for geometry and one for time. This means that standard representations such as those provided by IGES or PDES/STEP are not sufficient as a means of storing or sharing this type of data. Next, the data we are attempting to integrate is inherently multi-dimensional as it pertains to dependent variables. Not only do we want to deal with the traditional three coordinates of geometry but we also want to add analysis data such as temperature or potential.

Integration needs a method for treating many independent and many dependent variables as single entities and a method for treating subsets of geometry without having to decompose the overall geometry into pieces. GGA objects can be solid, surface, or curve entities. These entities can be imbedded within one another in a parent/child relationship. The child objects are imbedded and move with the parent entity. For example, the human arm is a solid object containing veins, muscles, bones, and nerves. As the arm moves with time, the shape and orientation of the arm changes, but the body parts within move along with it. In the case of the TWT gun, the parent geometry can be modeled as a solid defining the entire gun domain being analyzed. Within that parent, the child geometries, or components - modeled as either solids, surfaces, curves, and grids - can change position and shape. The geometry decomposition for the TWT gun is shown in Figure 7. The choice of entity type is a function of the topology of the region to be studied. For example, in modeling the arm, a choice of solid bones, tube-surface veins, and curves for nerves might be used. The same analogy is true for the modeling of TWT guns. In this example we might model the parent gun geometry as a solid. The child entities - cathode, anode, heater, and focus electrode - would also be solids. The support structures would be surfaces whose common boundaries with their respective attached components are curves. In addition, each entity, solid, surface, curve, or grid, can include non-geometric data that can vary with that entity. The electrode, heater, cathode, support structures, and anode require TM type data such as temperature, stress, strain, and density. The bounded EM region may include electric field potential or other variables.

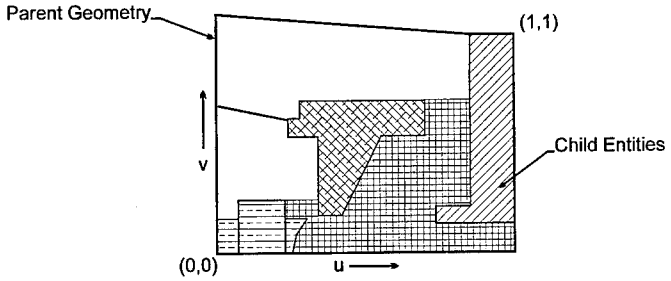


FIGURE 7 - PARENT AND CHILD TOPOLOGY FOR TWT GUN

For the gun, we want to perform three type of analysis. The type of grid used for each analysis is subject to the requirements of each solver. In the thermal analysis case we may choose to use a structured grid and in the mechanical analysis case we may want a unstructured grid. For EM analysis we could use a topological rectangular grid. All different grid types are supported in the GGA architecture. Figure 8 illustrates how different grids are mapped to their respective child components. As evident by the figure, not all components need to be physical geometries. In this figure the bounded

EM region is also defined as a child entity. It shares common boundaries with other child components thus ensuring a robust topology. The common edges, or surfaces, provide the means to transfer or communicate analysis data and also form boundaries for gridding. Additionally, these common boundaries can be used to establish common grid points for both components if this is required.

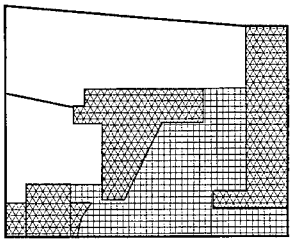


FIGURE 8 - GRIDS AND COMPONENT ENTITIES FOR TWT GUN

The solution to the TWT gun analysis problem then consists of first creating a single geometry of the TWT gun, possibly extracted from a common IGES file of the geometry. Each discipline then creates the grid desired. GGA objects are formed by decomposing the geometry into parent/child entities. The child's entities include geometry and grids. The grids are defined with appropriate vector lengths necessary for the resultant analysis data. The three analysis codes then are executed. The thermal solver performs the temperature solution at the first time step, handing control over to the mechanical solver, which can automatically extracts the temperature values needed to drive deformations from the thermal differences. The deformations to the mechanical grid are used to reshape the component geometry. The EM solver then takes the new deformed geometry as the new starting point and computes the electric field and the resulting electron beam path. These data exchanges and inter-disciplinary iterations continue until the TWT reaches steady state conditions. The path of the electron beam will then be determined for satisfactory positioning throughout the warm up transient. This process allows codes to proceed through the entire simulation without need for intervention. Each analysis still uses the grids necessary to achieve optimum results, and the solution data is now stored with the geometry and grids.

Summary

The use of the GGA objects allows the integration of analysis codes in such a way that the performance data required to be transmitted through grids and geometry can be done without the need to force grid compatability among the codes. The implementation of GGA object based architectures enables multi-disciplinary analysis to be seamlessly and generically performed across any set of computational disciplines. The DT_NURBS library provides the MMACE REF with essential components to the Geometry/Gridding Application Program Interface (API). Similarly, DT_NURBS routine can be embedded in any physics based code such as thermal-mechanical and CEM. This offers a highly coupled relationship between individual codes and MMACE. Optimization techniques are also possible in this environment. Additional benefits of the dependent nature of GGA objects is configuration control, and a product model that contains solution data and other performance information.

References

1 La Belle, Joseph, and Barry Hantman, "Microwave/Millimeter-wave Advanced Computational Environment (MMACE) Database Specification", Raytheon Corporation, 1994.

2 Ames, Robert, David R. Furguson, and Deborah D. Parsons, "Applications of the General Geometry, Grid and Analysis (GGA) Object in DT_NURBS", 1995 (Pending Publication).

3 Liao, Samuel Y., "Microwave Devices and Circuits", Prentice-Hall, New Jersey, 1980.

Standardized Grid Generation for the Research and Engineering Framework

L. W. Woo, H. A. Sabbagh, Sabbagh Associates, Inc., 4635 Morningside Drive, Bloomington, IN 47408, J. LaBelle, and B. Hantman, Raytheon Company, Mailstop T3MJ21, 50 Apple Hill Drive, Tewksbury, MA 01876.

Introduction. In the analysis of microwave devices, the complex geometry inherent to these systems mandates its discretization into smaller, and more tractable pieces. A mesh of grid points (or **nodes**) and the connectivity of these nodes to form **elements** must be generated to describe the geometry. The nodes and elements possess certain attributes: physical and material properties, load, constraints, etc. The attributes may be scalars, vectors, tensors, or fields. In addition, there may be attributes associated with the discretized model, and certain information which controls the analysis. After an analysis is completed, there will be computed quantities associated with the grid points, the elements and the model. Examples of discrete analytical methodologies include finite element, finite difference, boundary and volume elements. Current gridding practice of most analysis codes can be summarised as:

- Gridding algorithms are often embedded into individual codes,
- Grids are tightly coupled to specific codes.

Thus the mesh generated for one code cannot be readily utilized by another code.

The analysis codes thus far integrated into the Research and Engineering Framework (REF) of the Microwave and Millimeter Wave Advanced Computational Environment (MMACE) can be divided into 2 broad categories: thermomechanical (TM) and computational electromagnetic (CEM). The numerical grid and solution data from these codes can be stored in the REF common database, either as a complete archive of the design process, or to facilitate the reuse of the same grid data between different analysis codes. To achieve these goals, we are developing a *top-level* grid Application Programming Interface (API) that will serve as an interface between the analysis tools that are being developed and the REF. The Grid API allows different pre- and post-processors, and analysis codes to be easily integrated or replace existing codes, without affecting other codes in the framework. Grid and solution data can be readily retrieved from or stored in the common database via the API. DT_NURBS[1], a B-spline based geometry library from the David Taylor Model Basin, not only provides a robust and comprehensive set of geometry manipulation functions, but it also affords an excellent method for representing geometry, grid data and associated attributes, and other information required by the various types of analysis codes. This paper provides a brief overview of the requirements of CEM and TM grid and solution data, functionality of the REF Grid API and the use of the DT_NURBS data structure for accessing and manipulating the mesh data.

Grid Generation. Grids can be basically divided into three groups: structured, unstructured, and hybrid.

Structured Grids. We let (x,y,z) and (ξ, η, ζ) denote the co-ordinates in the physical and the computational space respectively; then the grid generation process involves creating a network of lines of constant ξ, η, and ζ such that a one-to-one mapping can be established between physical and computational space. The physical space is mapped into a square or rectangle in two dimensions, and into a cube in three dimensions, as in Figure 1.

Structured grids are primarily divided into two groups, Cartesian and curvilinear grids, which are shown in Figure 2. The domain of Cartesian grids is decomposed by vertical and horizontal lines, and

boundaries are approximated by tracing where the grid lines meet the body. The main drawback of this type of grid is that the application of boundary conditions is difficult. On the other hand, the co-ordinate surfaces of curvilinear grids coincide with all boundaries.

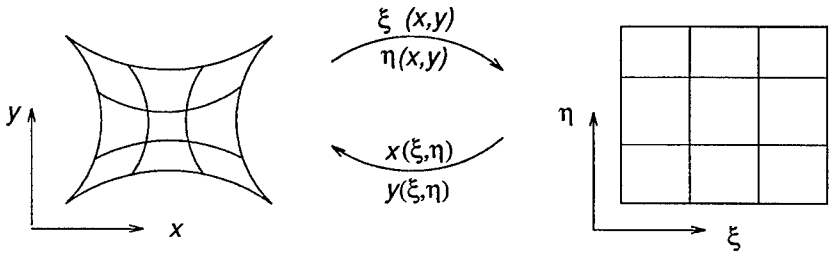


Figure 1: Mapping Computational Space (Left) into Physical Space (Right).

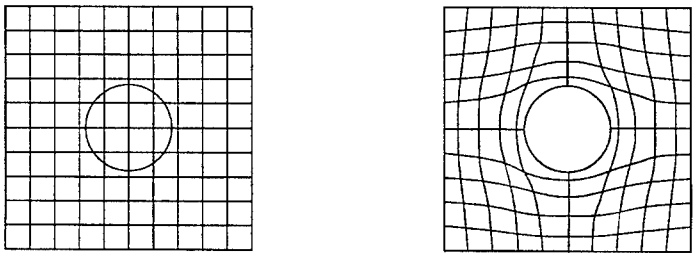


Figure 2: Cartesian (Left) and Curvilinear (Right) Grids.

Structured grid generation methodologies can be grouped into two main categories:

- Direct methods, where algebraic interpolation techniques are utilized - Transfinite interpolation, the most widely used algebraic grid generation method, is based on Langrange and Hermite interpolation. Recently the application of non-uniform rational B-Splines (NURBS) has revolutionized direct methods of generating grids.
- Indirect methods, where a set of partial differential equations are solved to generate the grid - The Poisson equation is solved with different control functions, which controls the grid spacing and smoothness of the grids, to generate the grid.

Unstructured Grids. Unstructured grids are composed of triangular cells in two dimensions and tetrahedral cells in three dimensions, as shown in Figure 3. The grid information is stored in a set of co-ordinates called nodes, and the connectivity, that indicates which nodes are connected to the cell. The advantage of the unstructured grid is that it can be generated around complicated shapes with ease.
Hybrid Grids. Structured and unstructured grids may be combined to form hybrid grids, in which part of the grid is structured and other parts unstructured (Figure 3). Hybrid grids can be generated either by creating structured grids around the body and unstructured grids away from the body, or by creating structured grids around different components and then connecting them by using unstructured grids.

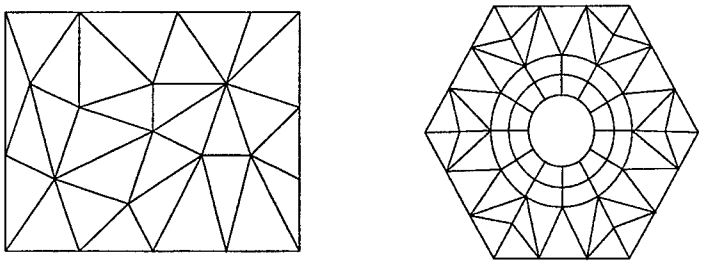


Figure 3: Unstructured (Left) and Hybrid (Right) Grids.

In most practical computations, grid points are clustered near the region where there is a large gradient in the computed variables.

Requirements of CEM Grid and Solution Data. The two dominant themes in CEM are integral equations and differential equations. The method of multigrids is becoming increasingly used in solving the discretized differential equations when the grids are regular, as in the case of the finite difference (FD) method.[2]

The finite-difference time-domain (FDTD) method is often used when solving transient, or broad-band problems, especially those associated with pulse propagation in digital and microwave circuits. The FDTD method typically uses structured grids. However, the use of unstructured grids is gaining popularity with the new generation of FDTD codes.

The finite element method (FEM) [11], [12], although applicable to time-domain problems, seems to find its greatest use in the frequency domain, when dealing with geometries of arbitrary shape, and steady-state calculations at a single frequency. Three-dimensional FEM codes generally use unstructured grids.

Structured and regular grids are much more computationally efficient, since all arrays are directly addressed, and perform more efficiently on vector, as well as RISC, processors. They are limited, however, in the geometries that they can accurately model.

In view of the fact that the method of differential equations is used in the majority of the CEM codes, which includes all the codes thus far integrated into the REF, we will limit our discussions to the FD and FE methods in this section. Furthermore, this allows us to develop a grid API that will be immediately useful to the TM community within MMACE, because all such TM codes are of the FE genre.

In spite of the different numerical algorithms employed by FD and FE solvers, the solvers in both methods operate on similar sets of initial data: a mesh. A mesh consists of geometric data (nodes and elements), material properties, boundary conditions, and all other information required to describe the physics of the problem to be solved. In addition, control information, which may include analysis options, output flags, etc, must be supplied to the analysis code. In some FD codes, the geometry is parametrized as lines, arcs, surfaces, etc, and is read in as part of the input; grid generation is an inherent part of the analysis code. The complexity of the geometry of microwave devices reduces the usefulness of such codes in the REF.

Nodes and Elements. Grid data can be divided into 2 parts: nodes and elements. In FD, the element connectivity is strictly node-based; i.e., each element is completely defined by a list of node numbers. For example, one element in Figure 4 is defined by the set of nodes $\{1, 2, 5, 4, 7, 8, 11, 10\}$, and the second element by $\{2, 3, 6, 5, 8, 9, 12, 11\}$.

In the finite-element analysis of thermomechanical problems, we usually expand the unknown fields

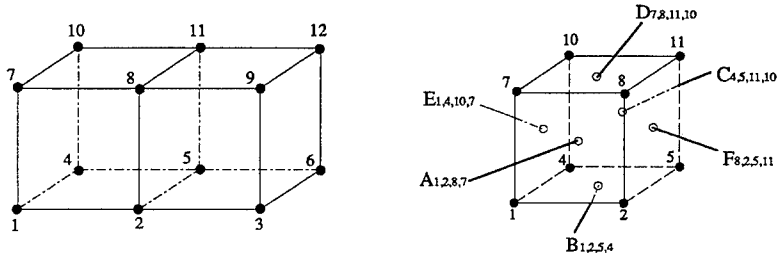


Figure 4: 3D Nodal-Based (Left) and Edge-Based (Right) Elements.

using scalar interpolating basis functions, with the unknown expansion coefficients being three-component vectors; indeed, these expansion coefficients are usually the values of the fields at the nodes of the interpolating functions, which are the nodes of the grid. This is satisfactory if the fields are everywhere continuous, such as the displacement field in a problem of structural analysis, or fluid flow. If, however, there are sliding interfaces involved in the problem, then the Grid API must identify the associated nodes, so that the analysis code can treat them correctly.

In an electromagnetics problem, however, the fields of interest are not everywhere continuous; only the tangential components of the electric field, **E**, and the magnetic field, **H**, are continuous, in the absence of internal singular sources. Hence, the elements of finite-element codes in CEM are not node-based; they are are **edge**-based [2]-[4]. When solving an electromagnetics problem using edge-elements, one uses vector interpolating basis functions (the edge-elements) together with scalar expansion coefficients to define the field. The scalar expansion coefficient is some property of the electromagnetic field, such as the normal component of the current across an edge, that is continuous, and this is the reason such functions are called edge elements. In volume-integral equations, one uses facet elements as the three-dimensional analog of edge elements. Facet elements are vector expansion functions, whose scalar expansion coefficients are the normal component of current through the corresponding face (facet) of an element.

Each edge element is defined by the edges (edges in 2D and facets in 3D), which enclose the area/volume of the element. Thus the first element in Figure 4 is defined by the edge-connectivity, $\{A_{\{1,2,8,7\}}, B_{\{1,2,5,4\}}, C_{\{4,5,11,10\}}, D_{\{7,8,11,10\}}, E_{\{1,4,10,7\}}, F_{\{8,2,5,11\}}\}$, as shown in the figure on the right.

The use of edge-elements, and the associated edge-connectivity description, in the finite-element method in CEM is numerically superior to node-based connectivity, especially in dynamic field problems, for two reasons: (1) when solving for the solenoidal eigenmodes of a waveguide, a node-based finite-element analysis with a penalty method will still give spurious solutions at discrete frequencies; (2) the boundary conditions in node-based FEM are very difficult to enforce. Unless special conditions are carefully specified at every perfect electric and magnetic conductor (PEC and PMC), or impedance boundary, as well as any boundary between two dissimilar media, it is easy to incur errors in the solution. In contrast, boundary conditions are naturally imposed when using edge elements, and little additional effort is needed for their specification.

Material Properties and Boundary Conditions. Material properties can be viewed as scalar attributes of the elements. These attributes are real numbers for time-domain algorithms, including thermomechanical codes, and complex numbers for frequency-domain algorithms. If the constitutive relation associated with the physics of the problem is anisotropic and involves tensor coefficients, the symmetries inherent in the constitutive relation will reduce the number of independent coefficients in the constitutive tensor,

and these coefficients can be derived from a few scalar parameters[1]. Something similar is required when solving electromagnetics problems on conforming grids by means of finite-difference equations, such as the FDTD. In the curvilinear coordinate system that is generated to conform to the scatterer, one computes the contravariant component of the electric field along an 'electric edge' of the cell, and the contravariant component of the magnetic field along a 'magnetic edge' of the dual, or overlapping cell [9]. One needs the covariant components of the electric field along an electric edge, however, in order to calculate the electric circulation that is used in the FDTD algorithm. The transformation from contravariant to covariant components of vectors requires the use of the metric tensor, G, associated with the curvilinear coordinates. Thus, this tensor will have to be stored as input data with the grid. Fortunately, this tensor is symmetric, which means that only six independent components need be stored. Furthermore, one can incorporate permittivity and permeability information into appropriately weighted metric tensors, although basis vectors are needed to reconstruct fields, set up initial conditions, and so forth [10].

When solving eddy-current problems, or coupled thermo-electromagnetic problems, or problems with nonlinear materials, it is necessary to include data that define the conductivity, permeability, and/or permittivity as a function of field strength or temperature.

Volume-integral algorithms in CEM utilize volumetric sources as dependent variables to be determined. Otherwise, when one uses FD or FE techniques in CEM the problems can generally be considered to be completely driven by boundary conditions (BC); problems with volumetric sources are rarely encountered.

Boundary conditions can be associated with the nodes or with the boundary surfaces or edges. For edge elements, the BC only applies to the edges. Vector quantities can be easily represented in their 3-component form: 2 tangential and 1 normal, although only the tangential components of the E and/or H fields have to be specified in edge elements.

Closure. EM analyses cannot be terminated abruptly at the external boundary of the physical domain. It is necessary to approximate the interaction of the system with its environment. However, the closure of a problem cannot be easily treated as a simple nodal or edge-based attribute; its parametrization is highly model-dependent.

There are three commonly used means of closing the analysis domain. The first is to use approximate vector absorbing boundary conditions (ABC) on a sphere [6]. The second approach uses a rigorous boundary integral operator, that is defined over a surface of revolution that contains the problem domain within its interior [7]. The third approach uses a surface, together with its boundary integral operator, that conforms to the surface of the domain of interest [8]. In using this approach, one can take advantage of recent developments in solid geometry that use NURBS (non-unifrom rational B-splines) [5].

Because of the lack of consensus, we are unable to derive a uniform representation of the data structure for closure. As a result, its implementation in the Grid API will be postponed.

Solution Data.

For problems that are solved in the frequency-domain, the E (or H) field solutions will consist of complex vectors. Although the Grid API can be coded to process these data as complex numbers, the imaginary part of the data will be treated as a second (real) vector solution, in order to maintain uniformity between CEM and TM solution data. This allows a tradeoff between transportability and bookkeeping.

Problems that are solved in the time-domain, whether via the finite-element method or the finite-difference time-domain (FDTD) method, will have real vector solutions only, as in TM problems.

Summary. We can briefly summarize the requirements of CEM grid and solution data:

- Nodal definition - node number, (x, y, z) values, attributes

[1] An example is that only two Lamé constants are required to define an isotropic constitutive tensor that has thirty-six coefficients in elasticity theory.

- Element definitions - element number, nodal connectivity, attributes (e.g., material type)
- Edge definitions - edge number, nodal connectivity, attributes
- Boundary conditions
  1. node-based - scalars, vectors
  2. edge-based - scalars, vectors

  The boundary conditions may be temperature- and time-dependent.
- Material definitions - The material properties may be temperature- and frequency-dependent, etc.
- Solution data
  1. node-value - scalars, vector
  2. edge-value - scalars, vectors (real + imaginary parts)
  3. element-value - scalars, vectors (real + imaginary parts)
- Control information - analysis options, solver type, output flag, material definitions, and all other nongeometric information.

Requirements of Thermomechanical Grid and Solution Data. There is only one dominant theme in computational thermomechanics: the finite element method. The development of the Grid API for TM codes is further simplified by the fact that all finite elements are node-based. Furthermore, because one rarely uses frequency-domain methods in thermomechanical models, the solution data will consist of real numbers, only.

In most TM analysis codes, three types of elements are supported: beam (or line), shell (or surface) and solid elements. The beam and shell elements, also known as structural elements, are used in analyses where the aspect ratios between the 3 dimensions are highly skewed. Their use is neccesitated by the fact that, if treated as regular solid elements, these elements will cause the system matrix to be very ill-conditioned, and the computational time is greatly increased. As a result of the very small extent in one (for shells) or two (for beams) of the dimensions, the structural elements possess additional degrees of freedom - twisting and bending - which are not present in solid elements.

The following is a brief summary of the requirements of the TM grid and solution data:

- Nodal definitions - node number, (x, y, z) values, attributes (e.g., nodal constraints, nodal forces, etc),
- Element definitions - element number, nodal connectivity, attributes
- Material definitions - The material properties may be temperature-dependent and anisotropic.
- Boundary conditions
  1. node-based - scalars, vectors
  2. surface-based - scalars, vectors, flux

  The boundary conditions may be temperature- and time-dependent.
- Solution data
  1. nodes - scalars, vector
  2. beam elements - scalars, vectors, tensors
  3. surface elements - scalars, vectors, tensors
  4. solid elements - scalars, vectors, tensors
  5. Computed degrees of freedom associated with the entire model.

- Control information - analysis options, solver type, output flag, material definitions, and all other nongeometric information.

Functionality of the Grid API. The goals of the Grid API are: (1) to allow software developers to develop new, or wrap existing, software to be integrated into the REF; and, equally important, (2) to facilitate the use of the same grid data in multidisciplinary analyses. If the requirements of the CEM and TM grid and solution data are compared strictly in terms of data structure, it becomes clear that there is major overlap between these requirements, in spite of the different physics involved. The fundamental information to be processed are nodal coordinates, element connectivities, and nodal and elemental attributes which may be scalars, vectors, or tensors. It is, therefore, possible to design the Grid API so that, with a few exceptions, most TM and CEM requirements can be met with the same functions.

The data structure implemented in the geometry library, DT_NURBS[1], will be used as the foundation for the storing and retrieving of data performed by the Grid API. Its well-designed, dynamically managed, memory and data structure will accommodate most, if not all, types of data encountered in computational analyses. This includes the storage of grid and solution data as "Grid, Geometry and Analysis" (GGA) entities, and the simple storage of arrays of numbers and characters. The use of DT_NURBS greatly eases the burden of finding a common interface between different data requirements in multidisciplinary analyses. With the use of rational and non-rational B-spline functions, multivariate functions, which can be geometric, solution and field data, can be accurately and efficiently interpolated. In addition, the library provides many sophisticated mathematical tools to manipulate the data. For examples, there are functions to calculate the intersection of surfaces in multi-dimensional space, and functions to extract a constant parameter curve on a surface.

The following is a summary of the basic functionalities provided by the Grid API:

1. The storage and retrieval of Cartesian and curvilinear, structured and unstructured grids, and element connectivity - The coordinate system used in the nodal definition can be either Cartesian, cylindrical or spherical. Hihger order elements, such as those with mid-side nodes, can be processed too.

2. The storage and retrieval of material properties used in the analysis - The material properties can have any number of functional dependencies.

3. The storage and retrieval of the boundary conditions specified in the analysis - This includes pointers to other large array data used as boundary conditions. The large array data may be the temperature distribution calculated by a thermal code which is then used to drive a mechanical analysis in which the stresses due to thermal expansion are computed, or field data.

4. Simple data analysis capabilities - This includes the computation of cell volumes, the normal vector to a surface, the distance of a point from a surface, etc.

5. Simple browsing capabilities through the entire grid data set.

With these high-level, machine-independent functions, grid data can be easily managed in a standardized and highly portable manner by software developers, with the underlying data pipelines and any machine-dependency of the data being the responsibility of the Research and Engineering Framework.

Acknowledgement. We acknowledge private discussions with Profs. Raj Mittra, John Volakis, Ray Luebbers, Alan Taflove, and Steven Gedney, and Drs. Don Pflug and Chris Reuter during the preparation of this report. We are indebted to Prof. Bharat Soni for supplying much of the material on

grid generation. The discussions with the members of the MMACE project have been invaluable in determining the scope and the functionalities of the Grid API.

References

[1] "DT_NURBS Spline Geometry Subprogram Library, Users' Manual," Version 2.2, Prepared by Boeing Computer Services, Ed. United States Navy, Naval Surface Warface Center/Carderock Division, David Taylor Model Basin, Bethesda, MD 20084.

[2] Harold Sabbagh, "Numerical Methods Practices specific to CEM", "CEM Computational Models Including Meshes", "Some Mathematical Methods For Computational Electromagnetics", from the series of 8 notes written for MMACE Phase I, 1992.

[3] A. Bossavit and I. Mayergoyz, "Edge-elements for Scattering Problems," IEEE Trans. Magnetics, Vol. 25, No. 4, July 1989, pp. 2816 – 2821.

[4] Z. J. Cendes, "Vector Finite Elements for Electromagnetic Field Computation," IEEE Trans. Magnetics, Vol. 27, No. 5, September 1991, pp. 3958 – 3966.

[5] L. Valle, F. Rivas, and M. F. Cátedra, "Combining the Moment Method with Geometrical Modelling by NURBS Surfaces and Bézier Patches," IEEE Trans. Antennas and Propagation, Vol. 42, No. 3, March 1994, pp. 373-381.

[6] A. F. Peterson, "Accuracy of 3-D Radiation Boundary conditions for Use with the Vector Helmholtz Equation," IEEE Trans. Antennas and Propagation, Vol. 40, No. 3, March 1992, pp. 351-355.

[7] W. E. Boyse and A. A. Seidl, "A Hybrid Finite Element Method for 3-D Scattering Using Nodal and Edge Elements," IEEE Trans. Antennas and Propagation, Vol. 42, No. 10, October 1994, pp. 1436-1442.

[8] S. Barkeshli, H. A. Sabbagh, D. J. Radecki, and M. Melton, "A Novel Implicit Time-Domain Boundary-Integral/Finite-Element Algorithm for Computing Transient Electromagnetic Field Coupling to a Metallic Enclosure," IEEE Trans. Antennas and Propagation, Vol. 40, No. 10, October 1992, pp. 1155-1164.

[9] K. S. Yee, J. S. Chen, and A. H. Chang, "Conformal Finite-Difference Time-Domain (FDTD) with Overlapping Grids," IEEE Trans. Antennas and Propagation, Vol. 40, No. 9, September 1992, pp. 1068-1075.

[10] J. W. Eastwood, W. Arter, N. J. Brealey, and R. W. Hockney, "Body-Fitted Electromagnetic PIC Software for Use on Parallel Computers," AEA-TPD-260, AEA Technology, Culham Laboratory, Abingdon, Oxfordshire OX14 3DB, UK, December 2, 1994.

[11] M. Calamia, G. Pelosi, and P. Silvester, eds., "Second International Workshop on Finite Element Methods for Electromagnetic Wave Problems," COMPEL, Vol. 13, Supplement A, May 1994.

[12] J. B. Davies and P. P. Silvester, "Finite elements in electromagnetics: A jubilee review," Applied Computational Electromagnetics Society Journal, Vol. 9, No. 2, July 1994, pp. 10-24.

Visualization and Standards

John V. Cugini

Computer Systems Laboratory
National Institute of Standards and Technology
Gaithersburg, MD 20899, USA

ABSTRACT

The basic concepts of scientific visualization are described: visualization itself, associated graphics data, and the application programmer interface (API). The potential role of standards and the extent to which actual standards realize this potential is explored. Although existing standards adequately cover low-level graphics data, there is a need for standardization of higher-level semantically rich data. Standardization of APIs, both officially and de facto, has been an active field, but no clear leader has yet emerged. Visualization tools are explained within this framework.

KEYWORDS: application programmer interface; graphics data; graphics standards; visualization.

1 Introduction

The Microwave/Millimeter Wave Advanced Computational Environment (MMACE) Project must support powerful and intuitive visualization features in order to be successful. Providing these facilities is a real technical challenge because of the wide range of disciplines involved in the design of microwave tubes: manufacturing, thermal analysis, and simulation of electromagnetic phenomena, to cite just a few. Clearly MMACE cannot create a visualization infrastructure from scratch, but must adopt and customize existing visualization standards and conventions. The exercise of applying these conventions to the project also serves to highlight gaps in the visualization standards currently available.

2 Visualization Concepts

Visualization is the generation of a visual representation of some sort of data. *Interactive* visualization includes the ability of the human viewer, in real time, to manipulate the representation

in some way that corresponds to the properties of the data being displayed. The data to be depicted can be generated in many ways, e.g. as the result of:

- an experimental measurement,
- a simulation (or modeling) of some physical phenomenon,
- a mathematical operation,
- the design of an artifact.

Most visualization applications fall into one of two broad categories: realistic or conceptual. In the former, the intent is to represent some physical object as it would actually appear to the human eye. Lighting effects, shading, reflection, shadows, and refraction are all characteristic of realistic rendering. Typical applications are those where the final appearance of the product is of interest, such as automobile body design and architecture.

The purpose of conceptual visualization, on the other hand, is to convey a more abstract understanding. Typical applications might be a blueprint for a mechanical part, or coloring to indicate the value of some variable, such as temperature in a weather map. The objects being represented need not be actually visible, nor indeed real physical objects at all, as would be the case for realistic visualization. Rather, inherently invisible entities such as mathematical functions, isosurfaces, and wind-chill factors can all be mapped into some set of visual shapes and features.

Although the main focus of this paper is on conceptual visualization, the application programmer interface (API) standards discussed herein, such as PHIGS, PEX and OpenGL, also have many features supporting realistic visualization.

Visualization functionality, then, consists of transforming some internal representation of the objects to be visualized into a form directly processible by an external device such as a CRT or plotter. For interactive visualization, external user events, such as mouse clicks, must be interpreted as commands to modify the way in which the object is depicted. This central concept of the "graphics pipeline" is useful to keep in mind in order to understand how the various standards work together to support visualization.

The role of standards is twofold: 1) the definition of intermediate forms of representation — visualization data — within the transformation from internal to visual, and 2) the definition of APIs to allow direct control of the visualization process by platform-independent software.

3 Visualization data

There are a great many graphics data formats, far more than can be discussed here in any detail. For information on formats mentioned below, see recent surveys [KAY92], [MURR94]. Also, see the world-wide web (WWW) reference list, section 7.

Graphics formats can be categorized according to two criteria: representation level and geometric level, as explained below.

Visualization data with a high representation level directly describes the phenomenon of interest in units appropriate to the problem domain; data at a lower representation level corresponds more directly to the appearance of the computer display. The three representation levels we consider are modelling, graphics, and device.

The modelling/graphics distinction indicates whether data is meant to describe real-world entities (properties such as mass, physical size, charge, etc.) or to describe the appearance of graphical entities (dotted line, fonts, etc.) as they are to be displayed. Note that some properties, such as geometry and color, are meaningful in both realms — but in context it should be clear how they are to be interpreted. Of course modelling data is not inherently graphical; our interest here is in data that is susceptible to visualization. Modelling data as such does *not* describe how it is to be displayed e.g. which (graphical) colors to associate with which (real-world) temperatures. Finally, the device level is data which corresponds closely to the primitives of the graphics device; this could be a low-level protocol or even a description of the frame buffer contents, which determines how screen pixels are colored.

Note that visualization almost always involves the implicit or explicit conversion of modelling data to device data, perhaps via the intermediate step of graphics data. Furthermore, after this conversion, the original meaning of the modelling data is usually *not* preserved in the lower level format. E.g. a vector field may become a set of yellow arrows, which in turn become lighted pixels.

The geometric level of data simply indicates whether the basic entities represented have non-trivial spatial extension, such as lines, non-uniform rational B-spline (NURB) surfaces, conic surfaces, etc. (often called vector data) or are merely values at 2D or 3D point locations.

To sum up, with examples:

	vector data	point data
modelling	STEP	HDF
graphics	CGM	GIF
device	PEX	bitblt (bit block transfer)

Figure 1: Examples of Visualization Data Formats

Among the criteria to keep in mind when evaluating which format(s) to use for a given application are:

- functionality (e.g. support for 3D, splines)
- strength of standardization (well-defined, interpretation available, not dependent on single vendor, conformance tests available)

- widespread use and marketplace support
- supporting software tools: cost and power
- storage efficiency
- performance (speed) potential

3.1 Modelling data

Modelling data standards specify the internal representation of a given object or feature in the domain of interest, for instance, how to represent a vector field internally so as to allow calculations on it. There seem to be two broad areas of standardization relevant to MMACE: one for manufacturing and design, exemplified by IGES and STEP, the other for scientific data, exemplified by HDF, CDF, and NetCDF.

In the MMACE program, standardization of modelling data is addressed by the common data dictionary, so that all MMACE applications will use the same format to describe objects of interest. How this common data (geometric or otherwise) interfaces with the available standards is a significant visualization design issue. For instance, if the data dictionary specifies the use of HDF, MMACE would then "inherit" HDF-supporting software, but also be limited to whatever HDF can express. Of course, the choice of modelling data format is a very basic design decision, with implications far beyond visualization support. For instance, the availability of database support for a given format would be a major criterion.

3.2 Graphics data

Vector data (that describing extended spatial objects) provides a somewhat abstract description of the scene to be displayed. It often includes information such as 3D shape and position of points, lines, surfaces, and volumes, intrinsic color of objects, width and style of lines, size and style of markers, position and orientation of virtual camera, lighting effects, etc. Among the formats in common use are CGM and DXF.

Pixel-oriented graphics data, also called bitmap or raster data, often requires a lot of storage; associated compression techniques are therefore important. Generally one cannot easily recover higher-level components from the pixel data alone. Most of these formats are 2D only. Among the more popular are GIF, JPEG, and TIFF.

3.3 Device data

Visualization data at this level is very tightly defined, down to the bit level. It is intended to be interpreted either directly by a graphics device or by a low-level device driver or server. Standardization is especially important here because it allows one vendor's system to generate

graphic data that may be displayed on that of another over a network. The X protocol has been widely adopted by the UNIX workstation world. There are two 3D extensions, PEX and GLX, oriented towards the PHIGS and OpenGL APIs, respectively.

4 Application Programmer Interfaces

Visualization API standards specify the interface between application programs and a supporting graphics library. Typically, they have features to support automatic conversion of data from modelling to screen coordinates, perspective views, transformations, lighting effects, and data visualization. Also, the program should be able to control and interpret input from the user in terms of the model.

Thus, a program written using an API effectively performs the conversion of modelling data to device data, obviating the need to capture the lower level data explicitly. Furthermore, since the program is in control of the whole graphics pipeline at once, it can support richer interactive visualization, since the program "understands" the meaning of the object being displayed, and thus can interpret user input in terms of that object. By contrast, a generic visualizer which accepts graphics data typically cannot do more than perform generic geometric (e.g. rotation) and graphical (e.g. modify color) operations on the displayed object.

We will consider here only 3D graphic APIs which have multi-vendor support. The three major interfaces meeting these criteria are OpenGL [OGL93], PEXlib [PEX92], and PHIGS [PHIGS89]. Again, a detailed comparison is beyond the scope of this paper, but a brief survey of features is presented in the table below. All these APIs are generic graphic libraries; they are not oriented towards any particular domain. If one needed to support a large application, it might well be advisable to build a higher-level utility API on top of one or more of these, first to shield the application programmer from some of the lower-level details of graphics rendering, and second to build in support for the types of objects to be manipulated in the domain of interest.

5 Visualization Tools

Visualization standards support not only the programming of specific applications by the eventual end-user, but also the development of portable general-purpose tools, some of which may be made freely available. Most such tools accept data at the graphics or device level and generate a display as a result. The higher level the data, the higher level operations that may be available. For instance, if the tool starts with 3D graphics data it may well allow the user to rotate selected objects around a specified axis, move them relative to each other, or view them from various perspectives. If the tool accepts only 2D pixel data, such functionality is impractical; the tool is likely to allow only simple operations such as cropping and scaling. At the other extreme, a "domain-savvy" tool would be able to perform operations that were meaningful in the semantic domain of the application. For instance, a tool that visualizes an EM vector field might allow the adjustment of the position and strength of field sources.

	OpenGL	PEXlib	PHIGS
platforms	workstations,PCs	workstations	workstations
level of operations	low	low	medium
flexibility	high	high	medium
performance	high	high	varies
cost	low	free	substantial
standards body	consortium	consortium	ISO committee
GUI support	no	yes	no
graphic input	no	yes	yes
lighting	yes	yes	yes
data visualization	no	yes	yes

Figure 2: Visualization API criteria

The functionality of a tool therefore can be pretty well summarized by asking:

- What level of visualization data does it accept, and which formats in particular?
- What operations does it allow?
- What level of visualization data does it generate, and which formats in particular?
- What environment does it run under?

For instance, xv may be characterized as a tool that accepts graphics-level pixel data (GIF, TIFF, JPEG, etc.), supports operations such as sizing, cropping, and color editing, generates graphics-level pixel data and device level data (i.e. draws picture), and works in the UNIX/X environment.

6 Conclusion

Strong visualization standards can promote the development of portable graphics software tools, and facilitate the exchange of graphics data across different vendors' platforms, and among various applications. In the past standards usually originated either in "official" standards committees, such as those operating under the American National Standards Institute (ANSI) or International Standards Organization (ISO) umbrella, or from a single dominant vendor. It is becoming more common, however, for standards to be promulgated by consortia of vendors and other interested parties, such as the X Consortium and OpenGL Architecture Review Board. The consortium method often allows greater speed and flexibility in the formulation of standards, but it becomes more difficult for the user to decide among competing standards in the same application area.

7 World-wide web (WWW) Reference List

The following Universal Resource Locators (URLs) contain information pertinent to this article.

MMACE project:
http://mmace.nrl.navy.mil:8080/

Computer Graphics and Visualization:
http://www.dataspace.com/WWW/vlib/comp-graphics.html
http://www.khoros.unm.edu/pointers/visualization.html

Scientific data formats:
ftp://rtfm.mit.edu/pub/usenet/news.answers/sci-data-formats or
http://fits.cv.nrao.edu/traffic/scidataformats/faq.html

Graphics data formats:
ftp://ftp.ncsa.uiuc.edu/misc/file.formats/graphics.formats
ftp://zamenhof.cs.rice.edu/pub/graphics.formats
http://gopher.ora.com:70/1/descriptions/soft/gff

X consortium specifications, such as X, PEX, and PEXlib:
http://ftp.x.org

Hierarchical Data Format (HDF):
http://www.ncsa.uiuc.edu/SDG/Software/HDF/HDFIntro.html

NetCDF:
http://www.unidata.ucar.edu/packages/netcdf

PHIGS Validation Tests:
http://speckle.ncsl.nist.gov/~cugini/pvt/hy-top.html

Information on OpenGL:
http://www.sgi.com/tech/openGL/opengl.html

References

[KAY92] *Graphics File Formats*, David Kay and John Levine, Windcrest/McGraw-Hill, 1992.

[MURR94] *Encyclopedia of Graphics File Formats*, James D. Murray and William vanRyper, O'Reilly & Associates, 1994.

[OGL93] *OpenGL Reference Manual*, OpenGL Architecture Review Board, Addison-Wesley, 1993.

[PEX92] *PEXlib Reference Manual*, Steve Talbott, ed., O'Reilly & Associates, 1992.

[PHIGS89] *Computer Graphics — Programmer's Hierarchical Interactive Graphics System (PHIGS) Functional Description, Archive File Format, Clear-Text Encoding of Archive File*, ISO/IEC 9592-1:1989, International Organization for Standardization, 1989.

Visualization Toolkit for Computational Electromagnetics

R. A. Joseph
ARCON Corporation
260 Bear Hill Rd.
Waltham, MA 02154

1. Abstract.

This paper is a brief description of a visualization system under development for use with electromagnetic simulation computer programs[1].

The visualization software is designed to be a generic package capable of operating with several Electromagnetic (EM) codes and various hardware platforms. Geometric models of irradiated and/or radiating objects are obtained using CAD software. These models are translated into data files appropriately formatted as input to the EM code. The output of the EM computation is then processed by the visualization system to display such quantities as surface currents, antenna radiation patterns and EM fields. A platform independent language, OpenGL, is used to visualize intermediate and final results. Execution of the codes is under the control of a graphical user interface.

2. Introduction.

Computer programs for electromagnetic analysis belong to a large class of simulation programs that were developed to model physical systems. These simulation programs provide valuable, often indispensable, assistance to engineers and scientists and are widely accepted and applied in research, development and product design. EM analysis and other physical simulation programs provide an ideal client base for the application of modern graphics and visualization techniques. Because many of these simulation programs were written before graphics workstations and high-speed microprocessors became available, there are many instances in which the formats of the input model data and output information can be substantially modified and improved with visualization software.

GEMACS (General Electromagnetic Model for the Analysis of Complex Systems)[2] is a widely used (distributed to over 50 Government and commercial organizations) modeling code used to analyze the behavior and performance of electromagnetic systems. GEMACS is written in FORTRAN-77 and has the advantage of running on several different platforms, including mainframes, workstations and IBM-PC 486 compatible computers. Although GEMACS modeling capability and the depth and variety of information provided by the electromagnetic analysis are considerable, running the code requires a great deal of work creating a representation of the input geometry in terms of GEMACS primitives. In addition, the run results are usually expressed as tables of numbers which convey far less than a graphical presentation.

We have begun a project to enhance the utility of GEMACS by building on to it an interface which will translate output from any standard CAD program into a suitable format. This interface will also allow the convenient visualization of output from a run of the GEMACS code and will

include a Graphical User Interface allowing the user to issue instructions to the program via a pointing device.

3. Development.

Our development work has been done primarily on a Silicon Graphics Indigo^2 Workstation featuring a MIPS R4400 150MHz processor, 64 MB memory and IRIX Version 5.2.

All of our code is written in ANSI C, with function calls to the X Window system through OSF/Motif. Our graphics programming was done with function calls to OpenGL[3]. OpenGL is a hardware-independent graphics language originally available only on Silicon Graphics Workstations, but now implemented on nearly all workstations, including DEC, HP and Sun. It is supplied with the Silicon Graphics operating system, IRIX version 5.2, or later. It has also been adapted for use in Windows NT for IBM-PC compatibles and will be used in Windows 95 when it becomes available. Programming with OpenGL thus allows us the ability to quickly adapt our program to multiple platforms.

The CAD package used for this project was ACAD75J[4], a CAD package available to members of the Electromagnetic Code Consortium. All that was required of the CAD package was the ability to output geometry information in terms of IGES[5] (Initial Graphics Exchange Specification). Nearly all modern CAD packages are able to do this. Thus, the requirement for the interface is reduced to the ability to translate from IGES graphical entities to GEMACS primitives.

Some of the most important IGES entities used are Non-Uniform Rational B-Spline (NURBS)[6] curves and surfaces. These occur naturally in CAD applications since they allow for the compact encoding of complicated curves and surfaces. Surfaces in GEMACS are not representable by NURBS entities, but rather as combinations of facets.

When we first embarked on this project, we had planned to integrate DT-NURBS[7] into our program to handle NURBS entities. We found, however, that one of the advantages of OpenGL is that it allows the direct interpretation of NURBS curves and surfaces.

In addition, OpenGL can also be used, when operating in feedback mode, to translate NURBS entities into a series of vertices which can then be used to generate the geometry section of a GEMACS command file consisting of plate surface descriptions. Although it is totally transparent to the user, the model image is actually drawn twice. The first time, it appears on the screen. The next time it is drawn, the information that would normally go to the screen is instead sent to an array, which is then written to a temporary file. It is the information in this file that is used to generate the command file for the EM simulation program.

4. Program Function.

Figure 1a shows the program screen after the import of a geometric figure which was created by ACAD75J and stored in the IGES format. The menu bar at the top offers four selections:

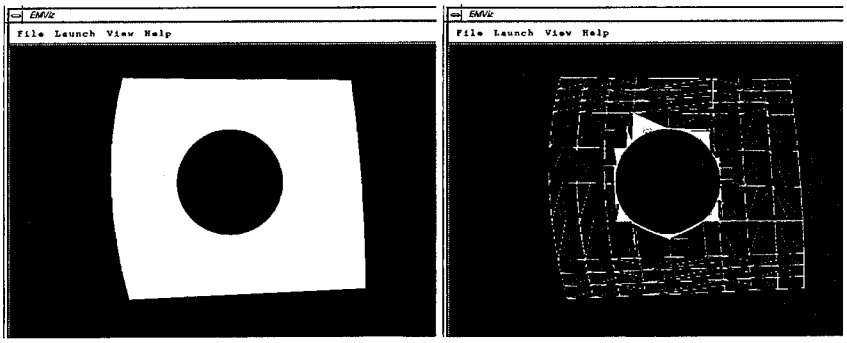
1. File, offers two options:
   a) Open: allows the user the option to import a previously created IGES file.
   b) Quit: to end the program.

2. Launch, offers four options:
   a) ACAD: shells to the CAD program.
   b) Cull: a program which will reduce the number of facets through combination of neighboring facets.
   c) GEMACS: creates a GEMACS command file, and then shells to GEMACS.
   d) MATLAB: strips and reformats the GEMACS output files, then calls Matlab to visualize the results.

3. View, offers two options:
   a) A toggle which will facetize the solid surface, as shown in Figure 1b.
   b) View: offers the user the ability to change viewing angles.

4. Help.

The model shown in Figure 1 was drawn using ACAD specifically for use during the development phases of our project. The figure is a simple two-dimensional surface, but the presence of



(a) (b)

Figure 1. EMViz home window.

the two curved vertical edges causes the CAD program to code the surface as a NURBS surface within the IGES file. One of our primary objectives was to provide a method for the translation of NURBS entities into a format compatible with GEMACS command files.

5. Future Plans.

The program screen shown in Figure 1, EMViz, is a version developed specifically to work with GEMACS. At this stage it is able to translate only a limited number of the 100 different types

of IGES entity types. In addition, the code does not take advantage of all the GEMACS geometry primitives available. In addition to filling in these gaps, we will be extending the User Interface to allow the user to have more control over GEMACS execution.

We also plan to continue the development of our program with the inclusion of other electromagnetic modeling programs such as GRECO[8], and NEC[9], and also other physical modeling situations such as are encountered in mechanical engineering (heat transfer, statics), environmental engineering (fluid flow, particle diffusion), and electronic engineering (charged particle transport) applications, to name a few. We also plan to port our code to all types of workstations, and also to the PC running WindowsNT or Windows 95.

The result of this project will be a product called ArconViz.

6. References.

1. R. A. Joseph and W. F. Bellow, "Visualization for Computational Electrodynamics", Contract No. F30602-94-C-0154 Final Technical Report (to be published).

2. (a)D. L. Kadlec and E. L. Coffey, "General Electromagnetic Model for the Analysis of Complex Systems *(GEMACS)* User Manual (Version 3)", Final Technical Report RADC-TR-83-217, Rome Air Development Center, AFSC, Griffiss AFB, NY, 13441, Sept. 1983. (b) E. L. Coffey, N. W. Coffey, and D. L. Kadlec, "*GEMACS* Source Book", RADC-TR-88-102, Rome Air Development Center, AFSC, Griffiss AFB, NY, 13441, April 1988.

3. J. Neider, T. Davis, and M. Woo, *OpenGL* Programming Guide, Addison-Wesley Publishing Co., Reading, MA, June, 1993.

4. J. P. Abelanet *et al.*, "Advanced Computer Aided Design *(ACAD)* User's Manual, Version 7.2", General Dynamics, Fort Worth Division, 12 May 1990.

5. IGES - Initial Graphics Exchange Specification (Ver. 5.2) ,US PRO/IPO-100, U. S. Product Data Association, Fairfax, VA, January 1993.

6. G. Farin, Curves and Surfaces for Computer Aided Geometric Design, Third Ed., Academic Press, Inc., Boston, MA, 1993.

7. *"DT_NURBS* Spline Geometry Subprogram Library Users Manual", CARDEROCKDIV-92/000, Carderock Division, Naval Surface Warfare Center, Bethesda, Maryland 20084-5000, November 1993.

8. J. M. Rius, M. Ferrando, and L. Jofre, "*GRECO*: Graphical Electromagnetic Computing for RCS Prediction in Real Time", *IEEE Antennas and Propagation Magazine*, Vol. 35, No. 2, April 1993.

9. G. J. Burke and A. J. Poggio, "Numerical Electromagnetics Code *(NEC)* - Method of Moments", Lawrence Livermore Laboratory, Livermore, CA, January, 1981.

MMACE - LESSONS FOR THE DEVELOPMENT OF A CEM COMPUTATIONAL ENVIRONMENT

Ross G. Hicks,
Compact Software,
201 McLean Blvd.,
PATERSON, NJ 07504

and

Ken Siarkiewicz,
Rome Laboratory/ERST,
525 Brooks Road,
GRIFFIS AFB, NY 13441-4505

1.0 Introduction

This paper reviews the development of the MMACE (Microwave and Millimeter-wave Advanced Computational Environment) using the REF (Research Engineering Framework). MMACE is a specific usage of the generic REF framework for the microwave tube industry in which the design environment is being specifically developed in support of power tube design. This paper therefore draws upon experiences gained during the interface of microwave tube design codes with the REF.

Although the examples used in this paper refer to the microwave tube code experience, the discussion will generalize the procedures followed and the lessons learned. It is the intent of this paper to address the scientific code interface process from the point of view of a neophyte who wishes to insert an analysis code into the REF.

Specifically, the following issues will be addressed: (1) the characteristics of codes which are readily inserted into REF, (2) the control panel insertion procedure, (3) the user-interface wrappering procedure for codes, (4) the data connectivity procedure for codes, and (5) the data modeling and data dictionary tasks which ensure re-usability of data within REF. Future directions of REF plug-and-play activities will be discussed and the advantages and disadvantages of these directions will be highlighted.

2.0 MMACE Phase 1 Prototype

During Phase 1 of the MMACE Program, a prototype software environment was produced. During the period of the development of this prototype, the MMACE program concentrated on developing a detailed understanding of the computational requirements for advanced microwave power tube design.

Several of the key concepts which were identified during this 18-month period have been implemented in this prototype design system which includes a subset of existing tube industry design codes. It was a key objective of Phase 1 of the MMACE program that this prototype provide a useful design capability to the tube industry and it was on that basis that the subset of codes was selected. Specifically, the selected subset of codes provides a design capability through to the PIC (particle-in-cell) codes and includes a thermomechanical analysis capability.

The MMACE prototype also focused on providing a first cut at design data management and integration whilst providing a consistent and intuitive interface to the user. A master geometry data model, a first generation of wrapper technology and a control panel (using a design flow paradigm) were also provided. In addition, the prototype was an ideal vehicle to provide the integrators with an opportunity to gain experience with the tube codes, the tube industry itself and the issues particular to the high frequency electromagnetics arena. Further, during the development of the prototype, the difficulty of a variety of implementation issues were evaluated, tested and invaluable lessons learnt for future development. The future development of REF will benefit significantly from the leveraged use of this prototype experience.

3.0 Future REF Development

The REF of the future will be a complete graphically oriented computational environment. It will be a geometry-based, user-oriented, data-driven and team engineering managed environment for high frequency device design. This environment will be an enabling technology for improved manufacturing, particularly with regard to the cost and quality issues so essential to the bottom line of a manufacturing organization.

In order to achieve the above objectives, the following are goals of the REF environment development effort during the MMACE program:

(a) the user will be enabled so that he/she can add/enhance/delete codes in the REF environment;

(b) a comprehensive parametric design data model will be developed complete with a user-extensible data dictionary.

(c) a comprehensive geometry data model to support the use of 2D and 3D tools. The geometry socket approach available in the prototype will continue into the full REF environment and thereby permit the connection of a variety of front-end CAD tools. Selection of the appropriate CAD tools will provide connectivity into the CAD/CAM world;

(d) the complete REF environment will enable the user to move readily up and down the data abstraction pyramid, provide for different views of the same data and provide a consistent set of visualization tools;

(e) a graphical template builder for the wrapper technology rather than the text based builder available in the prototype. The graphical approach will reduce the development and maintenance time for the wrapper technology.

(f) full design data management in order to provide the right data to the right person at the right time. The data management approach will need to capture all data relevant to geometry-based design disciplines including parametric, geometry, array data, grids, test, specifications and materials data.

(g) a user-configurable graphically-driven control panel which through its intuitive look and feel will shorten the user learning curve and reduce errors.

(h) the REF environment will need to provide various facilities including state-of-the-art connectivity and openness as well as data backup and recovery.

By providing such facilities, REF will provide a positive improvement to the design and manufacturing process. The following table captures some of the comparative aspects of a pre-REF and a post-REF scenario.

ITEM	PRE-REF (1993)	POST-REF (1996)
Legacy design data	Disorganized, non-electronic	Organized, accessible, electronic database
Parts re-use	Not common	Enabling, standard parts library complete with test data
Use of new codes	Not easily connectable to existing data, difficult to validate	Straightforward to connect to REF compliant data; readily validate the new code with existing data
Alternative design scenarios	Difficult to add alternative design scenarios	Straightforward to add an alternative design to complement main-stream design
Connection to drafting and machine shop	Not electronic, slow, possibility of error	Electronic, rapid, minimization of errors
Manufacturing	Afterthought to design process	Facilitates concurrent engineering
Design team	Single local location	Distributed computing/ distributed design

Table 1: Pre- and Post-REF Comparison Matrix

4.0 Lessons Learned

4.1 Characteristics of Codes to Facilitate Easy Insertion into REF

It is important to determine what "characteristics" of codes define the relative ease or difficulty of insertion of such codes into the REF framework. Specifically, the term "characteristics" of codes means the syntax and signatures of the data I/O stream and the sequence by which this data is input and output by the code. The paradigm for which REF is geared towards are codes which are batch oriented, i.e. there is very little interactive user input once the code has been given its set of data inputs. These codes then run using this data input and produce the computed data output. Whether the code takes a short or a long time to complete its execution is not relevant; what is relevant is that all data necessary for the code to run through to completion must be present prior to starting the code.

In order for relatively easy insertion of a code to occur, the syntax of the file input and output of the code must be fairly straightforward. Straightforward in this context means that the syntax should not contain significant amounts of branching of syntax, branching in the sense that different sequencing of syntax occurs depending on the value of data in prior lines. Whilst complex branching can be added to REF as REF evolves, there becomes a limit in scope of benefits versus expended effort to incorporate flexibility for extraordinarily complex data syntax.

4.2 REF Control Panel

The control panel is the first and most important interface which a REF user will see (see Figure 1). Consequently, it is important that this screen provide an extremely attractive flexibility. Specifically, the user expects the following functionality:

- The ability to configure the flow of design tools in the sequence that is appropriate for the design that is being contemplated;
- The ability to add and remove design tools as required;
- The ability to invoke core system utilities such as project version control, visualization tools, project load and save commands, etc.;
- The ability to provide help. During the prototype phase of MMACE, it was established that the Mosaic system is the ideal candidate for the provision of help and as such all documentation which is to be used for REF should be configured to run within the MOSAIC system.

In order to connect a new code to the REF control panel, it is important that the following information be available:

- the pathname to the executable of the code;
- the name of the icon which will be used to represent the code on the control panel; and

- the pathname to the templates which are used to wrapper the code to the REF.

REF will provide this capability shortly.

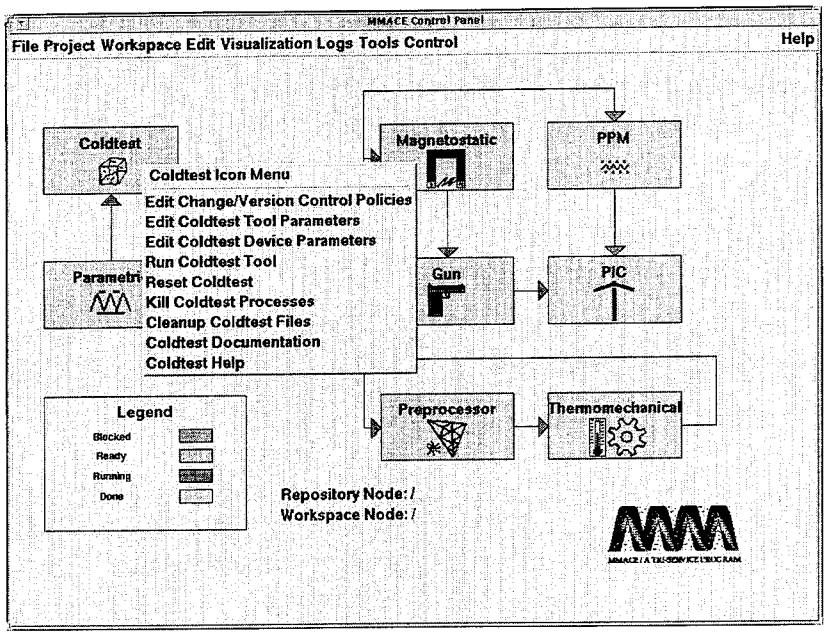


Figure 1: REF Prototype Control Panel

4.3 User Interface Wrappering

The process of user interface wrappering (see Figure 2) is composed of a sequence of steps which provide two separate but related pieces of functionality when wrappering a native code. Firstly, the I/O data needs of the native code need to be connected to the central REF database mechanism. Secondly, the user needs to be able to display the data being input and output for verification and to also provide the user with the opportunity to edit the data, as required.

In order to provide a user-interface to the I/O data entities which are required by the code, the process consists of constructing a template technology in which the user can log an inventory of all of the data entities which need to be viewed or edited. In order to display each of these data entities, the user must provide in the relevant template, the location of the entity in the database, the prompt to be displayed in conjunction with the value of the data entity and any other useful information such as the units in which the data entity will be displayed.

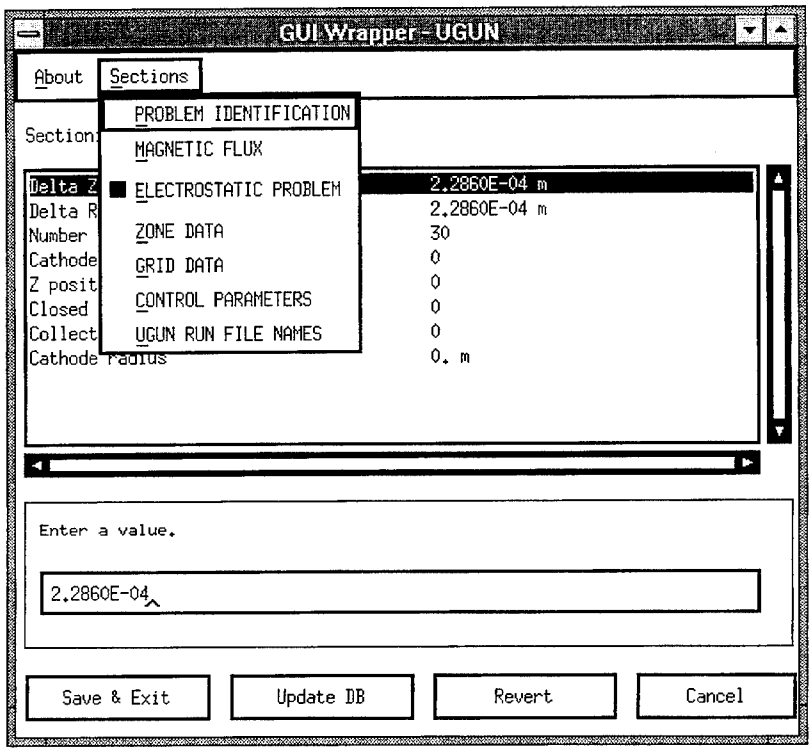


Figure 2: REF Prototype Wrapper Technology

The second piece of the wrapper functionality is to extract the data from the database and provide it in the sequence and syntax of the input file, as required by the native code being wrapped. A similar capability is required for the output from the code. This requires a second piece of technology whose function is to provide for each data item, its location in the REF database and the syntax in which each of the data items should be presented. Clearly, as REF evolves, the allowable syntax will expand to address more types of file syntax. Currently, the following styles of syntax are covered: (1) order-sensitive files, in which there is a strict order in which the data is required in the file and for which there are no significant branches in the order of data; (2) namelist-style files for which order is not important but each data item must be accompanied by a keyword which identifies to the native code the identity of the data item to which the value belongs.

The above discussion has focused on parametric data. REF must also give consideration to geometric data for which several "firmware" implementations have been generated for a variety of tube codes in the REF prototype. "Firmware" is used in the sense that the code can be easily customized by the developers of REF but it is much more difficult for users to make said alterations. It remains one of

the challenges of REF to generate a relatively generic approach to the geometric data connection of native codes via a wrapper to the database. It is expected that no matter what the solution is for this issue that there will be a requirement that users make some minor modifications to their native codes in the area of geometry input.

The current MMACE prototype has focused exclusively on 2D geometry. Clearly, this effort needs to extended to provide a 3D capability. In addition, the future of geometry representations is moving to NURBS and so the REF must have in its plans a means for this transition to be effected. Specifically, during the transition from geometry representation using lines and arcs to that using NURBS, there will be a valid mixture of codes, some of which will require NURBS and some of which will expect lines and arcs. In order to provide a useful framework, it is necessary for REF to deal transparently with the mixture of types of geometry data availability and requirements. This can be most conveniently done by using a bi-directional translator which will be activated when a mismatch between geometry data needs and geometry data availability is detected.

4.4 Data Modeling and Data Dictionary

The data model developed under the MMACE Phase 1 prototype activities was a limited data model which offered the following features. Interwoven in each discussion is the lessons learned and the approach to be pursued for the next generation of REF:

- The ability to separate generic and tool-specific data. By tool-specific data, it is meant data which is needed specifically for that particular tool's usage and has no significance to the actual solution of the generic simulation being performed by the particular tool. This concept will be maintained in future generations of REF.

- Objects of data are recognized by type name. For example, a pole piece in a magnetic analysis solution would be defined in the CAD drawing as having a type of pole_piece and so all magnetic tools would need to identify all such objects with this type. Consequently, in a design where there are multiple pole pieces, all of these would need a unique name but all would be of type pole_piece. This is clearly one of the more inflexible pieces of the current prototype environment. In order for tools to connect to provide simulations, it is necessary for each of them to have an inventory of all of the types of objects which are relevant to their simulation arena. For example, a static magnetic analysis tool will need to know all types of materials which have a permeability issue. This is clearly not in the interests of flexibility. What is more appropriate is that a tiered data model be constructed which provides one view for the user, namely types such as pole_pieces, permanent_magnets, etc. for which a user can tag all of the various objects when drawing the particular design problem to be studied. However, a second and more fundamental view needs to also be generated which contains features such as permeability and permittivity. It is this second view which contains the fundamental physics information that will drive the information which the wrapper for various tools will search for. Therefore, under the revised and more generic REF data modeling approach, tools which perform magnetic analysis will search for all entities whose second view contain magnetic information.

- The object names are used to associate geometric defining lines and arcs with the corresponding parametric information in the database. It is proposed that such a means of connectivity will continue to be used as the REF data modeling continues to evolve.

- Mass quantity information such as the particle and fields information in the database is stored with appropriate headers to define the columns and rows of this high volume information. In moving to the next generation of REF software, the flexibility of this data modeling approach needs to enhanced so as to permit other high volumes of information (such as CEM data) and it be organized in such a manner that a group of visualization tools can be easily targeted to provide a visualization capability for this data.

4.5 Distributed Computing and Distributed Design

In the long term, REF will provide the opportunity for design teams to utilize codes in distant places as well as to enable design teams to work together effectively even when the team members are in widely separated locations. For the distributed computing scenario, the REF environment will provide not only the control information to activate the particular remote codes so desired but to also manage the data flows into and out of the remote codes over the networks. In order to provide for a distributed design environment, a two layered approach will be available. A designer may remotely logon to a REF system and use the X-windows protocols over a high speed line to perform designs on the host REF system. Alternatively, the designer may logon to their own local REF system and "check" data out of the main remote REF data repository, perform the intended design work and then check back the completed design results to the main remote repository.

4.6 Advanced Gridding Technology

REF is enabling in the sense that advanced grid technologies will be available in the environment. An API is being developed such that grids for electromagnetic analysis and thermomechanical analysis can be accomplished. Plug and play gridding tools suitable for various solution tools are also being studied.

5.0 Conclusions

The REF prototype is a platform from which a future advanced design environment can grow and develop. Effective progress for REF in the future requires a strong link with interested parties in order to capture all relevant design issues and to collect suitable feedback so that the REF development can adjust during its evolutionary development period. A users' group has been formed to provide a forum for the discussion and collection of ideas and directions for future generations of REF.

SESSION 4A:

EM THEORY I

Pulse Basis Function Implementation of the Radiation Condition Integral Equations

Paul C. Colby

Lockheed Palo Alto Research Laboratories
colby@chicago.rdd.lmsc.lockheed.com

Abstract

We present a novel Method of Moments (MOM) program for general 3D bodies which is both simple and robust. The algorithm is based on the Radiation Condition Integral Equations (RCIE) which are a weak form of the radiation condition expressed in terms of the fields on the surface of the scatterer. A key element in the development of the RCIE is the separation of the time harmonic Maxwell's equations into two decoupled equations using chiral field combinations. In addition to simplifying the development, this approach yields a particularly stable formulation of the scattering problem. The resulting integral equations are discretized using a very simple pulse basis function which greatly simplifies problems encountered in meshing complex surfaces with overlapping interpolational bases.

1 Introduction

The calculation of scattering from three dimensional targets of general shape is a subtle and complex problem. While many Method of Moments (MOM) algorithms have been developed for 3D scatterers, few are simple to use. One of the principle difficulties faced by the user of a MOM program is the sheer complexity of generating a viable surface mesh. Typically, this surface mesh is composed of surface elements (such as triangles) which are required to share common nodes on common boundaries. In addition one must also provide a list of element interconnections which define the allowed current flow on the surface. Even for very simple geometries, such as a conesphere, the generation of these inputs is a complex problem.

We present a MOM algorithm which removes many of the constraints and difficulties associated with the present surface current modeling schemes. The approach requires only that the target surface be *covered* with elements, rather than requiring a complex (and highly constrained) interlocking mesh of current elements.

In the following section the development of the RCIE is reviewed. To keep the discussion brief, only essential points of the argument will be given. A more complete treatment of the RCIE is to be found in Reference [1]. The geometry model and H-field basis is discussed in Section 3. In Section 4 the example of a conesphere is presented to demonstrate both the stability and the current limitations of the approach.

2 Radiation Condition Integral Equations

We consider the problem of scattering from a body of finite extent. The surface of the scattering body, S_b, is assumed to have a unit normal, $\hat{n}$, directed out of the volume of the body at every point. Generalizations to bodies which have surface singularities (such as edges, corners and cusps) is straightforward provided the surface singularities are sets of measure zero for integration over S_b.

Unlike the Electric (EFIE), Magnetic (MFIE), or the Combined (CFIE) Field Integral Equations, the Radiation Condition Integral Equations do not express boundary conditions on the surface of the scattering body. Rather, the RCIE are the radiation condition in weak form expressed in terms of the total fields on the surface of the scattering body. Since the radiation condition is common to all scattering problems, the RCIE hold for all scattering bodies—independently of any surface boundary conditions. To obtain a system of integral equations which describe a particular scattering problem, the RCIE must be augmented by the boundary conditions on the surface of the scatterer. Incorporating surface boundary conditions is straightforward since the RCIE are expressed in terms of total fields on the surface of the scatterer.

The RCIE have their simplest expression in terms of the chiral field combinations. With an $e^{i\omega t}$ time dependence Maxwell's time harmonic field equations take the form in a vacuum

$$\nabla \times \mathbf{E} = ik\mathbf{H} \tag{1}$$
$$\nabla \times \mathbf{H} = -ik\mathbf{E} \tag{2}$$

where $k = 2\pi/\lambda$ and units have been chosen to make the impedance of free space 1. Chiral field combinations are defined

$$\mathbf{F}^R = \mathbf{H} + i\mathbf{E} \tag{3}$$
$$\mathbf{F}^L = \mathbf{H} - i\mathbf{E} \tag{4}$$

where the R and L superscripts denote *right-handed* and *left-handed* fields, respectively. The origin of the labels "right-handed" and "left-handed" arises from the fact that (4) is zero for fields which are the sum of only right-hand circularly polarized plane waves. In this sense the field (3) may be viewed as the sum of all right-hand polarized plane wave components of the field while (4) is the sum of all left-handed components.

To a large extent expressions involving either right-handed or left-handed fields will be the same up to an occasional sign. To reduce the number of expressions we use the superscript,

α, to denote either an R or an L. In expressions for which the choice of sign depends on handedness, $\pm$ and $\mp$ will be used where the upper sign holds for $\alpha = R$ and the lower sign holds for $\alpha = L$. Using (1) and (2) the chiral fields are seen to obey two decoupled first order differential equations

$$\nabla \times \mathbf{F}^\alpha = \pm k \mathbf{F}^\alpha. \tag{5}$$

The implications of (5) are far reaching and imply that the $\mathbf{F}^R$ and $\mathbf{F}^L$ fields are dynamically independent exterior to the scatterer. Therefore, in the far field the right-handed and left-handed fields obey separate (and independent) radiation conditions.

The chiral fields have a number of interesting properties not shared by the usual E and H-fields. One property of particular importance is that

$$\nabla \cdot (\mathbf{F}_1^\alpha \times \mathbf{F}_2^\alpha) = 0 \tag{6}$$

where $\mathbf{F}_1^\alpha$ and $\mathbf{F}_2^\alpha$ are any two solutions of (5) of the same handedness. From (6) and the divergence theorem it follows that

$$\iint_{\partial V} (\mathbf{F}_1^\alpha \times \mathbf{F}_2^\alpha) \cdot \hat{n}\, dA = \iiint_V \nabla \cdot (\mathbf{F}_1^\alpha \times \mathbf{F}_2^\alpha)\, dV = 0 \tag{7}$$

where the boundary surface of volume, V, is written ∂V.

To apply (7) to scattering problems consider the volume, V, to be all space exterior to the scatterer. Provided V is free of sources, it may be shown that (7) holds with the boundary of V taken as S_b. From (7) one arrives at the following definition for a weak radiation condition; *Let Λ^α be the set of all solutions to (5) on V which obey the radiation condition. A field distribution, $\mathbf{F}$, on S_b satisfies the weak α-handed radiation condition provided*

$$\iint_{S_b} (\mathbf{T}^\alpha \times \mathbf{F}) \cdot \hat{n}\, dA = 0 \tag{8}$$

for all $\mathbf{T}^\alpha \in \Lambda^\alpha$. The fields, Λ^α, are referred to as testing fields and play the role of Green's functions in the development.

The weak radiation conditions (8) is applied to scattering problems by expressing the total chiral fields as a sum of the incident and scattered fields

$$\mathbf{F}^\alpha = \mathbf{F}^\alpha_{Scattered} + \mathbf{F}^\alpha_{Incident}. \tag{9}$$

By definition the scattered fields are members of the sets Λ^α. Integrating both sides of (9) by a general element of Λ^α yields the RCIE

$$\iint_{S_b} (\mathbf{T}^\alpha \times \mathbf{F}^\alpha) \cdot \hat{n}\, dA = \iint_{S_b} (\mathbf{T}^\alpha \times \mathbf{F}^\alpha_{Incident}) \cdot \hat{n}\, dA. \tag{10}$$

Equations (10) are linear integral equations satisfied by the chiral field distributions on the surface of any scatterer. They are incomplete in that the boundary conditions on the surface of the scatterer have not been specified.

To incorporate surface boundary conditions into (10) is straightforward. For perfect conducting bodies the appropriate surface boundary condition is $\mathbf{E}_{\|} = 0$ on S_b. From (3) and (4)

$$\mathbf{F}^R_{\|} = \mathbf{F}^L_{\|} = \mathbf{H}_{\|} \tag{11}$$

at every point on S_b. Substituting $\mathbf{H}_{\|}$ for the total chiral fields in (10) yields the integral equations

$$\iint_{S_b} (\mathbf{T}^R \times \mathbf{H}) \cdot \hat{n}\, dA = \iint_{S_b} (\mathbf{T}^R \times \mathbf{F}^R_{Incident}) \cdot \hat{n}\, dA \tag{12}$$

$$\iint_{S_b} (\mathbf{T}^L \times \mathbf{H}) \cdot \hat{n}\, dA = \iint_{S_b} (\mathbf{T}^L \times \mathbf{F}^L_{Incident}) \cdot \hat{n}\, dA \tag{13}$$

which are solved numerically in the following sections for the tangent H field. It is interesting to note that the only coupling between chiral field components occurs on the surface of the scatterer by virtue of the surface boundary condition (11).

3 Numerical Algorithm

Application of MOM to equations (12) and (13) requires that finite dimensional approximations are made for the surface H-field and the testing fields. Before making these approximations we first consider the geometric model or surface representation problem. Let the surface, S_b, (which is assumed to be closed) be represented by a finite number, N, of parametric patches. A parametric patch is defined as a differentiable vector function, $\mathbf{R}_k(u,v)$, $(k = 1, \cdots, N)$ of two parameters which maps the region, $[0,1] \times [0,1]$, in parameter space onto a region, P_k, of the surface S_b. The N parametric patches are chosen to cover the surface such that every point on S_b is either within a unique patch, P_k, or on the common boundary between patches. Patches, being non-overlapping, permit the surface integrals in (12) and (13) to be written as a sum

$$\iint_{S_b} (\mathbf{T}^\alpha \times \mathbf{H}) \cdot \hat{n}\, dA = \sum_{k=1}^{N} \int_0^1 \int_0^1 (T_{k,u} H_{k,v} - T_{k,v} H_{k,u})\, du\, dv \tag{14}$$

of integrals over each parametric patch. The tangent components of the vector, $\mathbf{H}$, (and similarly $\mathbf{T}$) are given on each patch by the projections

$$H_{k,u}(u,v) = \mathbf{H} \cdot \frac{\partial \mathbf{R}_k}{\partial u} \quad \text{and} \quad H_{k,v}(u,v) = \mathbf{H} \cdot \frac{\partial \mathbf{R}_k}{\partial v}. \tag{15}$$

The pulse basis is defined by approximating the functions (15) as constant over each patch.

The form of the testing fields in (12) and (13) are quite general, however, we will restrict our choices to dipole fields [1] for simplicity. A chiral dipole field is constructed from the

[1] In general all testing fields may be expressed as integrals (sums) of dipole fields. In this sense, dipole fields span the sets, Λ^α, which are linear vector spaces.

vector potential

$$\mathbf{A}_k = \frac{e^{-ik|\mathbf{r}-\mathbf{r}_k|}}{4\pi|\mathbf{r}-\mathbf{r}_k|}\mathbf{p}_k \tag{16}$$

where $\mathbf{p}_k$ is the vector dipole moment and $\mathbf{r}_k$ is the source point location. In general the chiral dipole sources may be chosen anywhere throughout the volume of the scatterer. However, we have found the best performance is attained by choosing the testing field sources on the surface, S_b, such that vector dipole moments are tangent to the surface at the location of the source.

From (15) it is apparent that there are two degrees of freedom per patch. To obtain a square system matrix, i.e. to insure equal numbers of H-field "unknowns" and equations, one must use two chiral dipoles per patch. It is also desirable to treat the right-handed and left-handed equations on an equal footing by selecting one right-handed and one left-handed dipole on each patch. The explicit choices made in this work are

$$\mathbf{r}_k = \mathbf{R}_k(1/2, 1/2) \tag{17}$$

$$\mathbf{p}_k^{\alpha} = \hat{\xi}_k \pm i\hat{\zeta}_k \tag{18}$$

where the unit vector ξ_k is chosen to lie along the u-tangent vector at $\mathbf{r}_k$ and $\zeta_k = \hat{n} \times \xi_k$. With this choice of dipole moments the radiation pattern of the dipoles are rotationally symmetric in the plane tangent to the surface at $\mathbf{r}_k$ with a null along the inward directed normal.

For modeling of general 3D surfaces, bicubic [3] parametric patches are used. Each patch is defined by interpolating 16 surface points, $\mathbf{R}_{i,j}^k$, on the patch using

$$\mathbf{R}_k(u,v) = \sum_{i=0}^{3}\sum_{j=0}^{3} \mathbf{R}_{i,j}^k G_i(u) G_j(v) \tag{19}$$

where the interpolation function, $G_i(u)$, are third order interpolating polynomials. Bicubic parametric patches (19) provide a very robust surface model which is capable of accurately modeling curved as well as flat surfaces. Since no "connection" is required with neighboring patches, the user need only specify the 16 surface points for each patch. The only restrictions on the input data is that the patch normal (defined as the u-tangent vector crossed with the v-tangent tangent) be directed out of the volume of the scatterer and that the patches cover the surface.

The resulting $2N \times 2N$ matrix equation is written in block form as

$$\begin{bmatrix} A_{n,m}^{R,u} & A_{n,m}^{R,v} \\ A_{n,m}^{L,u} & A_{n,m}^{L,v} \end{bmatrix} \begin{bmatrix} h_m^u \\ h_m^v \end{bmatrix} = \begin{bmatrix} \mathbf{p}_n^R \cdot \mathbf{F}_{Incident}^R(\mathbf{r}_n) \\ \mathbf{p}_n^R \cdot \mathbf{F}_{Incident}^L(\mathbf{r}_n) \end{bmatrix} \tag{20}$$

where the coefficients h_m^u and h_m^v are the constants assumed for the functions (15). The right-hand-side vector is obtained by applying the divergence theorem to the right-hand-side of (12) and (13) with the assumption that the incident field is source free throughout the

volume of the scatterer. Matrix elements for which the testing field source is separated by some distance from the H-field patch ($n \neq m$)

$$A^{\alpha,u}_{n,m} = -\int_0^1 du \int_0^1 dv\ T^{\alpha}_{n,v} \tag{21}$$

$$A^{\alpha,v}_{n,m} = \int_0^1 du \int_0^1 dv\ T^{\alpha}_{n,u} \tag{22}$$

are evaluated with guassian quadratures. The "self-terms", for which the dipole sources are on the patch of integration, are evaluated by separating out principle value and pole terms. The pole terms are the familiar $\frac{1}{2}H$ terms from the MFIE and take the form

$$P^{\alpha,k}_{n,m} = \frac{1}{2}\mathbf{p}^{\alpha}_{n} \cdot \mathbf{D}_k \delta_{n,m} \tag{23}$$

where the vectors, $\mathbf{D}_k$, are the dual vectors to the patch tangent vectors at the source point location. The principle value integral is evaluated by first subtracting a potential term of the form, $\nabla\Phi$, where

$$\Phi = -\frac{1}{4\pi k r^2}(1 + ikr - k^2 r^2)e^{-ikr}\mathbf{p} \cdot \hat{\mathbf{r}} \tag{24}$$

from the dipole fields. This reduces the singularity of the integrand from $1/r^3$ to $1/r$. The remaining potential integral has a $1/r^3$ singularity and is reduced to a line integral around the patch boundary. The resulting self-terms are

$$\begin{aligned} A^{\alpha,u}_{n,n} &= P^{\alpha,u}_{n,n} - \int_0^1 du \int_0^1 dv\ \tilde{T}^{\alpha}_{v} \\ &\quad \pm \int_0^1 (\Phi|_{v=0} - \Phi|_{v=1})\, du \end{aligned} \tag{25}$$

$$\begin{aligned} A^{\alpha,v}_{n,n} &= P^{\alpha,v}_{n,n} + \int_0^1 du \int_0^1 dv\ \tilde{T}^{\alpha}_{u} \\ &\quad \pm \int_0^1 (\Phi|_{u=1} - \Phi|_{u=0})\, dv \end{aligned} \tag{26}$$

in which $\tilde{\mathbf{T}}^{\alpha} = \mathbf{T}^{\alpha} \pm \nabla\Phi$. The remaining singularities in $\tilde{T}^{\alpha}$ are illiminated by evaluating the surface integrations in polar coordinates in parameter space. While the choice of parametric patches are bicubic surfaces, the integral forms (25) and (26) are completely general and are valid for patches of general curvature.

4 Numerical Examples

The generation of surface meshes for a conesphere is demonstrated in Figure 1. First, accurate geometric models of the scattering target in terms of bicubic patches were produced. These geometric models are referred to as the coarse meshes since it is often possible to represent curved bodies with relatively few bicubic patches. The top two coarse meshes

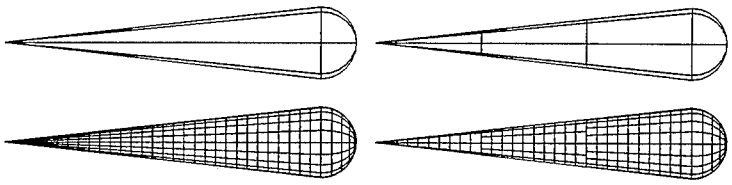


Figure 1: Coarse and fine grain meshes for conesphere

shown in Figure 1 are for a 5 meter long conesphere with a sphere radius of 0.5 meters and are comprised of 12 and 24 patches, respectively. Each bicubic patch is specified by 16 surface points which were obtained using the analytic form of the conesphere[2]. Finer grain meshes were generated using a simple subdivision algorithm as follows. Each coarse mesh patch was evenly divided in parameter space into N_u by N_v subpatches. The number of subdivisions, N_u, was determined by multiplying the desired number of pulses per unit length by the arc length at the value of v for which the width of the patch is a maximum. A similar algorithm is used to determine the number, N_v, of v-subdivisions. Since the RCIE algorithm presented here imposes no constraints on the relative position of element nodes, each coarse patch is subdivided independently of the neighboring coarse patches. This greatly simplifies the subdivision algorithm. The fine grain meshes for a meshing rate of 20 pulses per wavelength at 100 Mhz are shown below the corresponding coarse meshes in Figure 1. Refinement of the two coarse meshes lead to very different meshes. The refinement of the 12 patch mesh resulted in a 630 patches (Mesh 1) while the refinement of the 24 patch mesh yielded a 450 patches (Mesh 2). Mesh 2 had fewer patches than Mesh 1 because larger patches are used at the cone tip. In addition Mesh 1 is a gridded mesh in which neighboring patches share common nodes which is not the case for Mesh 2.

Monostatic cross sections were computed with the refined meshes and compared with a Body of Revolution Program based on the EFIE. The results of these calculations are shown in Figure 2. The system matrix for Mesh 1 was rank 1260 and had an estimated condition number of 200. Mesh 2 resulted in a rank 900 system matrix with and estimated condition number of 243. The maximum difference of 0.3dB between the computeded RCS for Mesh 1 and 2 occurred at a scattering angle of 135 degrees in the theta (horizontal) polarization. This difference is small compared to the 4.2dB difference between the RCIE and EFIE results at 165 degrees. We believe the EFIE results are correct since a convergance study was made and the program used is well validated with range measurements.

Experience with this and other scattering targets indicates that, while the pulse algorithm is quite stable and rapidly convergent for pulse densities below 10 per wavelength, the convergence for densities above 10 per linear wavelength is slow. Our current belief is

[2]For more complex surfaces, bicubic representations may be constructed from IGES data obtained from automated drafting programs.

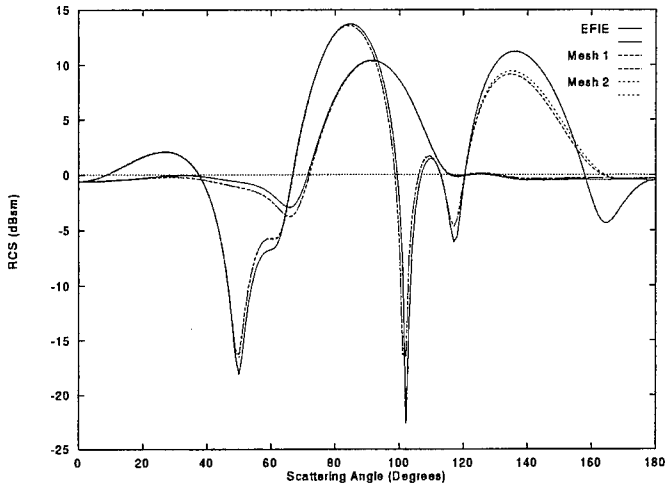


Figure 2: Monostatic RCS of conesphere at 100 Mhz. A scattering angle of 0 degrees corresponds to illumination of the cone tip. The solid curves show the results obtained with an EFIE MOM calculation using a BOR program. The dashed and dotted curves show the RCIE results obtained with Mesh 1 and Mesh 2.

that the poor convergence for high pulse densities is due to the curl free nature of the pulse basis. The pulse H-field bases are not expected to model surface waves effectively since these phenomena involve the normal electric field which is the curl of the tangent H-field.

A natural remedy for the above limitation is to add linearly independent basis elements which have a nonvanishing curl. We are currently pursuing this approach with the hope of improving the convergence rate while not sacrificing the robustness and ease of use of the pulse basis.

References

[1] P. C. Colby, "Application of the Radiation Condition Integral Equations to Electromagnetic Scattering," Submitted for publication in *Trans.* IEEE, AP.

[2] J. A. Stratton, *Electromagnetic Theory*, McGraw–Hill, New York 1941, pp. 32–33

[3] Mickael E. Mortenson, *Geometric Modeling* 1985 John Wiley & Sons, Inc.

Finite Difference Solutions of Geometrical Optics and Some Related Nonlinear PDEs Approximating High Frequency Helmholtz Equation

E. Fatemi, B. Engquist, and S. Osher [1]
University of California, Department of Mathematics, 405 Hilgard Avenue
Los Angeles, CA 90024-1555

1 Introduction

To predict reflection of radar waves from objects and other radar radiation patterns it is necessary to compute high frequency electromagnetic waves in arbitrary domains. Since the wavelength of the electromagnetic waves is in general very small compared to the size of the physical objects of interest, direct finite difference, finite element methods and boundary integral methods for the Maxwell's equations are computationally very expensive and in some situations not practical. Approximate methods have been used extensively for this type of calculations. We have developed finite difference methods for solving the nonlinear partial differential equations that approximate the high frequency solutions of the scalar wave equation, starting from the geometrical optics approximation and then continuing to the classical asymptotic expansion and a new perturbed geometrical optics system. These methods potentially will replace ray tracing methods for high frequency calculations in many cases and are applicable directly for calculation of electromagnetic waves.

The Maxwell's equations for electric and magnetic fields in an isotropic homogeneous material are written as:

$$(\epsilon E)_t = c\nabla\times H - 4\pi J \tag{1}$$

$$(\mu H)_t = \nabla\times E \tag{2}$$

$$\nabla\cdot(\epsilon E) = 4\pi\rho \tag{3}$$

$$\nabla\cdot(\mu H) = 0 \tag{4}$$

where E is the electric field, H is the magnetic field, J is the current, ρ is the charge density, c is the speed of light in the medium; μ and ϵ are respectively electric permittivity and magnetic permeability. The electromagnetic waves are solutions of the following wave equations, derived from Maxwell's equations, for E and H vectors.

$$E_{tt} = \frac{c^2}{\epsilon\mu}\Delta E \tag{5}$$

$$H_{tt} = \frac{c^2}{\epsilon\mu}\Delta H \tag{6}$$

Special time harmonic solutions of Maxwell's equations can be obtained by assuming solutions of the form,

$$E = e(x)e^{i\omega t + i\omega\phi(x)}, \quad H = h(x)e^{i\omega t + i\omega\phi(x)},$$

[1]This research was supported by ONR # N00014-91-J-1034, NSF # DMS 94-04942, and ARPA URI-ONR-N00014-92-J-1890

where ϕ function is the phase of the wave and ω is the frequency of the wave. These solutions locally resemble a high frequency plane wave and arise in important practical applications.

By substituting the above ansatz, one can show that the phase satisfies the eikonal equation [1].

$$(\nabla\phi)^2 = \frac{\epsilon\mu}{c^2(x)} \tag{7}$$

The eikonal equation is a first order nonlinear PDE, a Hamilton-Jacobi type equation. The usual practice has been to solve the eikonal equation by ray tracing methods. Ray tracing in this context is nothing but solving the eikonal equation using the method of characteristics for PDEs. Our approach relies on a direct discretization of the eikonal equation using the recently developed numerical methods for Hamilton-Jacobi equations [4]. From the above ansatz one also derives transport equations for amplitude of the wave. The transport equations are of hyperbolic type and we solve them using high order upwind numerical methods developed for hyperbolic equations.

To develop the methods, here we concentrate on the scalar linear wave equation in two spatial variables, a scalar version of the wave equations for electromagnetic waves. Any method developed for the scalar wave equation is applicable directly for solving the electromagnetic wave equations.

$$u_{tt} = c^2\Delta u = c^2(x,y)(u_{xx} + u_{yy}) \tag{8}$$

x and y are the spatial variables, t is time, u is the amplitude of the wave and $c(x,y)$ is the speed of the wave in the medium. We consider time harmonic solutions of the form

$$u(x,y,t) = e^{i\omega t}v(x,y). \tag{9}$$

Here ω is the frequency of the wave as imposed by the boundary conditions. For time harmonic solutions the wave equation is reduced to the Helmholtz equation.

$$\Delta v + \frac{\omega^2}{c^2}v = \Delta v + k^2n^2(x,y)v = 0 \tag{10}$$

n is the index of refraction and the non-dimensional quantity $k^2 = \frac{\omega^2}{c^2} = \frac{4\pi^2}{\lambda^2}$ represents relative size of the wavelength of the wave with respect to the physical size of the problem. The fundamental difficulty in solving the Helmholtz equation for large values of parameter k is the fact that the necessary mesh size in each coordinate direction is proportional to $\frac{1}{k}$. To resolve each wavelength one approximately needs ten points. For a three dimensional calculation one needs approximately $O((10k)^3)$ number of points to resolve the solution. Values of $k = 1000$ are common for many applications.

Since direct solutions are not practical, approximate methods are of special interest. A qualitatively correct approximation is the geometrical optics approximation, which is correct in the limit of infinite frequency, equivalent to zero wavelength. The geometrical optics could be derived formally by considering a solution of the form

$$u = A(x)e^{ik\phi(x)} \tag{11}$$

for the Helmholtz equation. The amplitude, A, and the phase, ϕ, satisfy

$$\begin{cases} 0 = |\nabla\phi|^2 - n^2 \\ 0 = 2\nabla A\cdot\nabla\phi + A\Delta\phi \end{cases} \tag{12}$$

This approximation is valid for infinite frequency and it does not include all solutions of the Helmholtz equation, notably diffraction phenomena are not represented by the above equations.

A substantial correction to the above approximation could be achieved by expanding solutions of the Helmholtz equation around zero wavelength, in inverse powers of k, in the following form,

$$u(x,y) = e^{ik\phi(x,y)} \sum_{n=0}^{\infty} v_n(x,y)(ik)^{-n}. \tag{13}$$

By substituting the above expansion in the Helmholtz equation and equating the coefficients of different powers of k, partial differential equations for the functions ϕ, v_0, v_1, etc are derived [3].

$$\begin{cases} 0 = |\nabla\phi|^2 - n^2 \\ 0 = 2c^2\nabla\phi\cdot\nabla v_0 + c^2 v_0\Delta\phi \\ 0 = 2c^2\nabla\phi\cdot\nabla v_{n+1} + c^2 v_{n+1}\Delta\phi + c^2\Delta v_n \end{cases} \tag{14}$$

The asymptotic expansion, since it is a correction to the geometrical optics, also fails where geometrical optics fails, notably on shadow lines. The representation (13) requires a unique phase to be defined and it does not allow for crossing rays.

We have investigated a new approximation which we shall name perturbed geometrical optics equations. This system is the geometrical optics equations including the usually omitted terms of order $1/k^2$.

$$\begin{cases} 0 = |\nabla\phi|^2 - n^2 + (1/k^2)(\Delta A/A) \\ 0 = 2\nabla A\cdot\nabla\phi + A\Delta\phi \end{cases} \tag{15}$$

Analytical results suggest that these equations are equivalent to the Helmholtz equation in a compact simply connected domain as long as the amplitude of the solution, $|u|$, is bounded away from zero. Numerical results show that this system has qualitatively correct solutions near shadow lines.

2 Numerical Methods

We use finite difference methods to solve the nonlinear PDEs that we have discussed. We use upwind methods for discretization due to the hyperbolic nature of the equations. To achieve higher order accuracy we use ENO scheme (essentially non-oscillatory) for calculating derivatives. The ENO method is based on an adaptive stencil to calculate the derivative of a function defined on the grid. Use of ENO method allows us to calculate solutions of the eikonal equation with discontinuous first derivatives without smoothing the solution. We use the following notation to denote the discretization. Δx, Δy, and Δt are the mesh sizes. $\phi^n_{i,j}$ is the numerical approximation to the solution of the eikonal equation.

$$\phi^n_{ij} \approx \phi(x_i, y_j, t^n) = \phi(i\Delta x, j\Delta y, n\Delta t) \tag{16}$$

Also we use standard notation for forward, backward, and centered differences.

$$D^+_x\phi_{ij} = \frac{\phi_{i+1,j} - \phi_{i,j}}{\Delta x} \quad D^-_x\phi_{ij} = \frac{\phi_{i,j} - \phi_{i-1,j}}{\Delta x} \quad D^0_x\phi_{ij} = \frac{\phi_{i+1,j} - \phi_{i-1,j}}{2\Delta x} \tag{17}$$

The most important equation of the three approximations that we are considering is the eikonal equation. Our numerical algorithm for the eikonal equation is developed based on the recently devised numerical methods for Hamilton-Jacobi type equations. To solve the eikonal equation we introduce time as an artificial variable.

$$\phi_t = |\nabla\phi|^2 - n^2 = H(\phi_x, \phi_y) \tag{18}$$

The discretization in time is of the forward Euler type.

$$\phi_{i,j}^{n+1} = \phi_{i,j}^{n} + \Delta t \hat{G}(D_x^+ \phi_{i,j}, D_x^- \phi_{i,j}, D_y^+ \phi_{i,j}, D_y^- \phi_{i,j}) \tag{19}$$

The numerical flux, denoted by $\hat{G}$, is calculated based on the exact or an approximate solution of a Riemann problem for the eikonal equation. We use two different numerical fluxes, one is a Lax-Friedrichs type method and the second is a Godunov type. The Lax-Friedrichs flux is defined as

$$\hat{G_{LF}}(u^+, u^-, v^+, v^-) = H((u^+ + u^-)/2, (v^+ + v^-)/2) + \alpha_x(u^+ - u^-) + \alpha_y(v^+ + v^-) \tag{20}$$

Where α_x and α_y are local upper bounds for absolute values of the partial derivatives of the Hamiltonian $H(u, v)$.

$$|\frac{\partial H}{\partial u}| < \alpha_x \quad \text{for} \quad u \in (u^-, u^+) \tag{21}$$

In the second method the flux is defined through a third order ENO interpolation and a Godunov type Riemann solver.

$$\phi_{i,j}^{n+1} = \phi_{i,j}^{n} + \Delta t \hat{G_G}(D_x^{+ENO} \phi_{i,j}, D_x^{-ENO} \phi_{i,j}, D_y^{+ENO} \phi_{i,j}, D_y^{-ENO} \phi_{i,j}) \tag{22}$$

The values of the derivatives, D^{ENO}, are calculated based on third order interpolation with an adaptive stencil [4]. The Godunov flux is defined by

$$\hat{G_G}(u^+, u^-, v^+, v^-) = \text{ext}_{u \in I(u^-, u^+)} \text{ext}_{v \in I(v^-, v^+)} H(u, v) \tag{23}$$

$H(u, v) = c\sqrt{u^2 + v^2}$ and I(a,b)=[min(a,b), max(a,b)] . The function ext is defined by

$$\text{ext}_{u \in I(a,b)} = \max_{u \in I(a,b)} \quad \text{if} \quad a \leq b, \tag{24}$$

$$\text{ext}_{u \in I(a,b)} = \min_{u \in I(a,b)} \quad \text{if} \quad b < a. \tag{25}$$

Note that in general the operations of taking max and min do not commute and the Godunov flux in not always uniquely defined. But for many cases, including our $H(u, v)$, the flux is uniquely defined. Use of a third order ENO interpolation and the exact Riemann solver results in the excellent resolution of the discontinuities in the solution of the phase.

The time dependent transport equations are hyperbolic equations that govern conservation of energy for the wave. For solving the transport equations we use upwind schemes. Higher order ENO methods are easily implemented in our codes. We use centered differences to calculate the velocity vector field, $\nabla\phi$, from the discrete values of ϕ.

$$\nabla\phi_{ij}^{n} = (D_x^0 \phi_{ij}^{n}, D_y^0 \phi_{ij}^{n}) \tag{26}$$

The above values are used for an upwind discretization of the transport equations. For example the term $\phi_x \cdot A_x$ is discretized as $D_x^0 \phi_{ij}^{n} \cdot D_x^u A_{i,j}^{n}$ where

$$D_x^u A_{i,j}^{n} = D_x^{+ENO} A_{i,j}^{n} \quad \text{if} \quad D_x^0 \phi_{i,j}^{n} > 0$$

$$D_x^u A_{i,j}^{n} = D_x^{-ENO} A_{i,j}^{n} \quad \text{if} \quad D_x^0 \phi_{i,j}^{n} < 0 \tag{27}$$

Note that D_x^{+ENO} for a first order stencil is just D_x^+.

We use a time marching scheme to solve the perturbed geometrical optics system. The time marching corresponds to solving the Helmholtz equation as steady state solution of a linear time dependent Schroedinger equation. Here we only consider discretization of the following system for variables(v, ϕ), $A = e^v$. The discretization for variables (A, ϕ) is similar. We discretize the following system.

$$\begin{cases} \phi_\tau = |\nabla\phi|^2 - n^2 - (1/k^2)(\Delta v + |\nabla v|^2) \\ v_\tau = 2\nabla v \cdot \nabla\phi + \Delta\phi \end{cases} \tag{28}$$

Since we are interested only in the steady state case we consider a simple time discretization. The linearized system is of Schroedinger type and a forward Euler time discretization of the system will be unstable. We do a mixed discretization in time of the system. We treat the linear part implicitly and the nonlinear part explicitly. This will enable us to have time steps which are proportional to Δx, since we are treating the nonlinear transport terms explicitly. The numerical scheme for the system is:

$$\begin{cases} \phi_{i,j}^{n+1} + (1/k^2)\Delta t(D_x^+ D_x^- v_{i,j}^{n+1} + D_y^+ D_y^- v_{i,j}^{n+1}) = \\ \phi_{j,j}^n + \Delta t\hat{G}(D_x^+\phi_{i,j}^n, D_x^-\phi_{i,j}^n, D_y^+\phi_{i,j}^n, D_y^-\phi_{i,j}^n) - \Delta t(1/k^2)((D_x^0 v_{i,j}^n)^2 + (D_y^0 v_{i,j}^n)^2) \\ v_{i,j}^{n+1} - \Delta t(D_x^- D_x^+ \phi_{i,j}^{n+1} + D_y^- D_y^+ \phi_{i,j}^{n+1}) = \\ 2\Delta t D_x^v v_{i,j}^n \cdot D_x^0 \phi_{i,j}^n + 2\Delta t D_y^v v_{i,j}^n \cdot D_y^0 \phi_{i,j}^n \end{cases} \tag{29}$$

This discretization is stable for $\Delta t < c\Delta x$ from the explicit discretization of the transport equations. In practice we found out that we could use the above scheme in the range $10 < k \leq \infty$.

3 Numerical Results

We consider reflection of an incident wave off a cylinder with radius one. The source of the wave is at point $(0, 7)$. We use polar coordinates for calculations. The physical problem is posed in the entire R^2 but our computational domain is $[1, 6] \times [-\pi, \pi]$. The solution is assumed to be of the form

$$u = A_1 e^{ik\phi_1} - A_2 e^{ik\phi_2} \tag{30}$$

The geometrical optics equations for the variables A_1, A_2, ϕ_1, and ϕ_2 are solved and then the results are added together to obtain the solution. The two systems are coupled through the boundary conditions at the surface of the cylinder. We specify Dirichlet boundary conditions for phase and amplitude of the incident wave in the region of the domain where it is illuminated by the source. Everywhere else the boundary conditions are based on the local direction of the characteristics. The phase of the reflected wave at the surface of the cylinder is equal to the incident wave and therefore at $r = 1$ we specify the boundary conditions for ϕ_2 and A_2 according to:

$$\phi_2(1, \theta) = \phi_1(1, \theta) \quad A_2(1, \theta) = A_1(1, \theta). \tag{31}$$

The problem is solved numerically in (r, θ) space and the results are interpolated to a Cartesian grid. The equations for variables A_1, A_2, ϕ_1, and ϕ_2 are valid in the limit of infinite k but we have used $k = 3$ to generate figure 1 to compare our solution with an exact solution for $k = 3$. In the next figure we present the exact solution computed from the expansion of the solution in Bessel functions.

The multivalued solutions of the eikonal equation in domains with constant index of refraction outside a convex domain have a simple structure which could be exploited. If one considers a boundary fitted coordinate system where one of the coordinates is radially outward from center of the body and the other two coordinates are local coordinates on the surface of the object, then the incident and reflected solutions of the eikonal equation become unique in this coordinate system. If we consider reflection of a wave from a cylinder we can extend the domain for θ from $(-\pi, \pi)$ to the whole real line. The multivalued solutions in this case are numerated by integers. For computational purposes we have to cut the domain. We show the results of our calculation in the domain $(-2\pi, 2\pi)$ for the phase and log of the amplitude of the reflected wave.

The last computed example corresponds to calculation of the phase and amplitude around a shadow line using the perturbed geometrical optics system. We set up the problem in the domain $[-1,1]\times[-1,1]$. We specify Dirichlet boundary conditions on one side and Sommerfeld radiation boundary conditions on rest of the domain. Let us recall that that the solution u is

$$u = e^{v+ik\phi} \tag{32}$$

For Dirichlet boundary conditions we specify

$$\begin{array}{l} v(-1,y) = 0 \quad \phi(-1,y) = tH(t) \quad \text{if} \quad y > 0 \\ v(-1,y) = -10 \quad \text{if} \quad y < 0 \end{array} \tag{33}$$

For the rest of the boundary we specify $\nabla\phi \cdot \mathbf{n}$ and $\nabla v \cdot \mathbf{n}$. Since the values of $\nabla\phi \cdot \mathbf{n}$ and $\nabla v \cdot \mathbf{n}$ are not known a priori, we extrapolate the values from neighboring points. The obtained amplitude is shown in figure 5. Note that we have used the value $k = 100$ in this calculation and that the amplitude shows the typical oscillatory behavior around the shadow line (compare with [1] p. 434). In the last figure we compute the intensity of the diffracted wave near an straight edge using the Fresnel approximation ([1] p. 434).

4 Acknowledgment

We wish to thank E. Harabetian for many helpful comments and observations about this work.

References

[1] M. Born and E. Wolf, Principles of Optics, Pergamon Press, sixth edition, 1989.

[2] J. B. Keller, A Geometrical Theory of Diffraction, *Calculus of variations and its Applications*, McGraw-Hill, New York, 1958, p. 27.

[3] J. B. Keller, R. Lewis, and B. Seckler, Asymptotic solution of some diffraction problems, *Communications on Pure and Applied Mathematics, IX*, (1965), 207-265.

[4] S. Osher and C-W Shu, High order essentially non-oscillatory schemes for Hamilton-Jacobi equations, *SIAM J. Numer. Analys. XXVIII* (1991), 907-922.

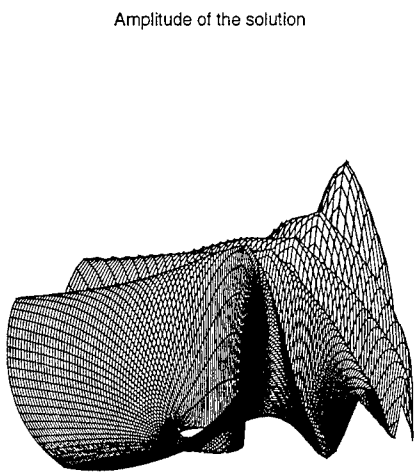


Figure 1: Computed solution outside a cylinder

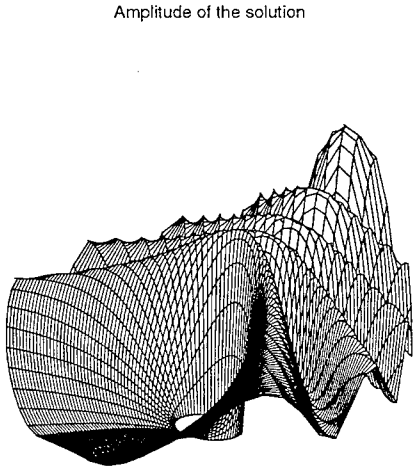


Figure 2: Exact solution outside a cylinder

Phase of the reflected wave

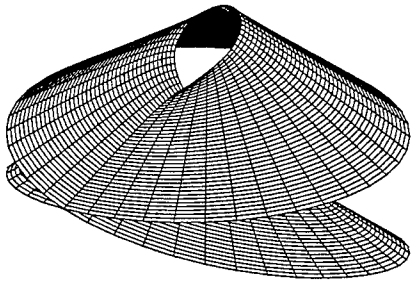


Figure 3: Multivalued phase of the reflected wave outside a cylinder

Amplitude of the reflected wave

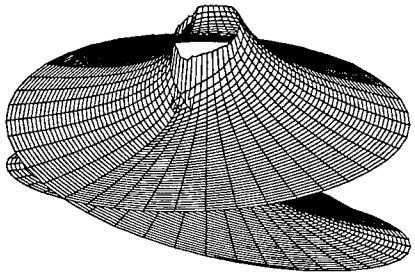


Figure 4: Multivalued amplitude of the reflected wave outside a cylinder

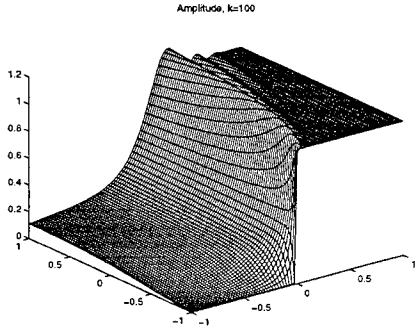


Figure 5: Solution of the perturbed geometrical optics system around a shadow line

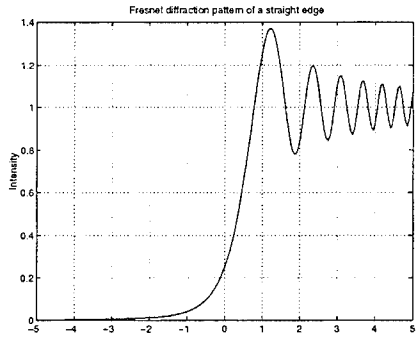


Figure 6: Fresnel diffraction pattern of a straight edge

Block-Toeplitz-Structure-Based Solution Strategies for CEM Problems

Ivakhnenko V. I. and Tyrtyshnikov E. E.

Russian Academy of Sciences and Elegant Mathematics, Inc.(USA)

E-mail: tee@post.inm.ras.ru

Toeplitz matrices and block multilevel Toeplitz matrices frequently arise in many CEM problems (antennas, tomography, geophysical applications, radar cross section computations, and so on). Usually Toeplitz matrices appear when a problem under consideration possesses some symmetries. However, we present the results which clearly show that block Toeplitz matrices can underlie efficient iterative solution methods for problems which possess no evident symmetries.

Consider the diffraction problem of an electromagnetic field on a bounded inhomogeneuos obstacle V with the complex-valued permittivity $\varepsilon(M)$ and the permeability $\mu(M)$, which are assumed to be piecewise continuous functions of $M \in V$. The electromagnetic field should satisfy:

(1) the Maxwell equations at the points where $\varepsilon(M)$ and $\mu(M)$ are continuous

$$\begin{cases} \operatorname{rot} E = i\omega\mu H, \\ \operatorname{rot} H = -i\omega\varepsilon E, \end{cases} \quad M \in V, \quad \begin{cases} \operatorname{rot} E = i\omega\mu_0 H, \\ \operatorname{rot} H = -i\omega\varepsilon_0 E + j_0, \end{cases} \quad M \in R^3/\bar{V};$$

here j_0 is an extraneous current source of the electromagnetic field, ε_0, μ_0 are the permittivity and the permeability of the free space;

(2) the continuity conditions for the tangential components of E and H on the medium boundaries including all discontinuity points of ε and μ;

(3) the radiation conditions at infinity (for the scattered field).

Let E^0, H^0 be the electromagnetic field (induced by j_0) satisfying the Maxwell equations

$$\begin{cases} \operatorname{rot} E^0 = i\omega\mu_0 H^0, \\ \operatorname{rot} H^0 = -i\omega\varepsilon_0 E^0 + j_0, \end{cases} \quad M \in R^3,$$

with no obstacle. Then the scattered fields

$$E^s = E - E^0, \; H^s = H - H^0$$

satisfy the following equations

$$\begin{aligned} &\text{rot } E^s = i\omega\mu_0 H^s + i\omega(\mu - \mu_0)H \equiv i\omega\mu_0 H^s + j^M, \\ &\text{rot } H^s = -i\omega\varepsilon_0 E^s - i\omega(\varepsilon - \varepsilon_0)E \equiv -i\omega\varepsilon_0 E^s - j^E. \end{aligned} \tag{1}$$

Introducing vector potentials

$$A^E(Q) = \int_V G(Q, P) j^E(P) dV_P, \quad A^M(Q) = \int_V G(Q, P) j^M(P) dV_P,$$

where

$$G(Q, P) = e^{\frac{ik_0 R}{4\pi R}}, \quad R = |QP|, \quad k_0 = \omega\sqrt{\varepsilon_0\mu_0},$$

we obtain

$$\begin{aligned} E^s &= -\tfrac{i}{\omega\varepsilon_0}(\text{grad div} + k_0^2) A^E + \text{rot } A^M, \\ H^s &= -\text{rot } A^E - \tfrac{i}{\omega\mu_0}(\text{grad div} + k_0^2) A^M. \end{aligned}$$

Setting

$$\varepsilon_r = \frac{\varepsilon}{\varepsilon_0}, \ \mu_r = \frac{\mu}{\mu_0}, \ w_0 = \sqrt{\frac{\mu_0}{\varepsilon_0}} = 120\pi$$

we arrive at the following integro-differential equations

$$\begin{aligned} E - E^0 &= (\text{grad div} + k_0^2) \int_V G(\varepsilon_r - 1) E dV + ik_0 w_0 \text{rot} \int_V G(\mu_r - 1) H dV, \\ H - H^0 &= -i\tfrac{k_0}{w_0} \text{ rot} \int_V G(\varepsilon_r - 1) E dV + (\text{grad div} + k_0^2) \int_V G(\mu_r - 1) H dV. \end{aligned} \tag{2}$$

Using Mikhlin's formulas for the differentiation of weak singular integrals we obtain

$$\text{grad div} \int_V GF dV = \int_V \text{grad div}(GF) dV - \frac{1}{3} F,$$

$$\text{rot} \int_V GF dV = \int_V [\nabla G, F] dV$$

(the right-hand side integral in the first equation should be understood in the Cauchy principal value sense) and then we rewrite (2) in the form

$$\begin{aligned} &(\tfrac{1}{3}(\varepsilon_r - 1) + 1)E \\ &- \int_V (\text{grad div} + k_0^2) G(\varepsilon_r - 1) E dV - ik_0 w_0 \int_V [\nabla G, (\mu_r - 1) H] dV &= E^0, \\ &(\tfrac{1}{3}(\mu_r - 1) + 1)H \\ &- \int_V (\text{grad div} + k_0^2) G(\mu_r - 1) H dV + i\tfrac{k_0}{w_0} \int_V [\nabla G, (\varepsilon_r - 1) E] dV &= H^0. \end{aligned} \tag{3}$$

The vector fields E and H satisfy the Maxwell equations so long as they solve (3). The scattered fields satisfy the radiation conditions thanks to the properties of the kernel G. It remains only to verify that the tangential components of the fields are continuous at all the medium boundaries. This property can be guaranteed so long as V is a union of a finite number of subdomains and ε_r, μ_r, E, H are continuously differentiable functions in each of them.

A standard approach to solution of (3) requires in general solution of systems of linear algebraic equations with dense coefficient matrices. From the commonly adopted point of view it is hard to believe due to size cosiderations that it is possible to treat the cases of relatively large obstacles using 3D volume integral equations. However, we present an approach that allows one to cover effectively the case of really large obstacles. This approach is based first of all on a change of unknown vector variables in (3) and then on a specific reduction technique producing linear algebraic systems with properly parameterized dense coefficient matrices. In fact the coefficient matrices are embedded into block multilevel Toeplitz matrices. It allows us to make storage requirements to be only linearly dependent on the coefficients matrix size and to reduce dramatically the arithmetic complexity of the coefficient matrix-vector multiplication due to exploitation of the FFT technique (see [1]).

Let us first change the variables:

$$\tilde{E} = (\varepsilon_r - 1)E,\ \tilde{H} = (\mu_r - 1)Hw_0,\ \tilde{H}^0 = -w_0 H^0.$$

Omitting for simplicity the tilde sign we obtain the following integral equations

$$\begin{array}{l} \left(\frac{1}{3} + \frac{1}{\varepsilon_r - 1}\right) E \\ -\int\limits_V (\mathrm{grad}\,\mathrm{div} + k_0^2) GE dV - i \int\limits_V k_0 [\nabla G, H] dV \;=\; E^0, \\ -\left(\frac{1}{3} + \frac{1}{\mu_r - 1}\right) H \\ +\int\limits_V (\mathrm{grad}\,\mathrm{div} + k_0^2) GH dV - i \int\limits_V k_0 [\nabla G, E] dV \;=\; H^0. \end{array} \tag{4}$$

These equations are better to deal with than (3) since they involve integral operators with kernels which do not depend on ε_r and μ_r.

We now embed the region V in a cuboid Π, take up a uniform cubic mesh on Π and approximate V by a union V_h of properly chosen mesh cells. We then apply the Galerkin method with piecewise constant test functions supported on these mesh cells. The Galerkin procedure results in a linear algebraic system

$$Ax = b$$

with a complex symmetric coefficient matrix A. If V is equal to Π we have

$$A = D + T,$$

where D is a diagonal matrix while T is a block three-level Toeplitz matrix. In the general case, when $V \neq \Pi$, $A \in C^{n \times n}$ admits the presentation

$$A = D + P^T T P, \tag{5}$$

where P is a diagonal matrix of order n while T is a block three-level Toeplitz matrix of order $m \geq n$ and P is an $m \times n$ matrix with zeroes everywhere except for a square $n \times n$ permutation submatrix.

Due to presentation (5) A can be multiplied by a vector with only $\mathcal{O}(n \log n)$ arithmetic operations. Such a multiplication procedure is based on the FFT algorithm and on the relation between Toeplitz and circulant matrices. The complexity of conventional iterative algorithms for

solving dense linear algebraic systems depends crucially on the costs of a matrix-vector multiplication procedure. The FFT-based procedure surely provides a very efficient implementation of each iteration step.

We present numerical results for three sample problems with dielectric obstacles. In each case we considered the symmetric with respect to the Z-axis configuration and the incident plane wave comings along the Z-axis.

Problem 1. Consider a penetrable two-layered ball with radii $r_1 = 2$, $r_2 = 4$ and $\varepsilon_r = 8$ for $0 \le r \le r_1$ and $\varepsilon_r = 2$ for $r_1 < r \le r_2$; $k_0 = 0.8$. Figure 1 shows comparison of two graphs of the analytical and the computed components $|E_x|$ of the electric field along the X-axis inside the obstacle.

Problem 2. Consider a penetrable two-layered ball with radii $r_1 = 0.163$, $r_2 = 0.314$ and $\varepsilon_r = 28 + i162$ for $0 \le r \le r_1$ and $\varepsilon_r = 7 + i12$ for $r_1 < r \le r_2$; $k_0 = 1$ (cf. [2]). Figure 2 shows comparison of the computed and the analytical components $|E_x|$ along the X-axis. Figure 3 shows comparison of the computed and the analytical bistatic cross sections σ/λ^2 for the $\Theta - \Theta$ polarization.

Problem 3. Consider a three-layered cube with the edge length $a = 1$ and $k_0 = 1$. The layers have their boundaries orthogonal to the Z-axis. The widths of the layers are equal to 0.25, 0.5 and 0.25 while their relative permittivities are equal to 3, 9, 12, respectively. Figure 4 shows comparison of two diagrams of the bistatic cross sections σ/λ^2 obtained by the suggested numerical procedure proposed using two different mesh sizes ($32 \times 32 \times 32$ and $64 \times 64 \times 64$).

Numerical experiments show that the approach proposed allows one to rather accurately computed the scattered electromagnetic field inside strongly inhomogeneous and rather large objects. They also demonstrate that piecewise constant vector test functions are still functions of very reasonable choice. This conclusion apparently contradicts the conclusion made in [2], where piecewise linear functions were strongly advocated to substitute piecewise constant ones. Another very important implication from the numerical experiments is that the GMRES-based solver requires a rather modest number of iterations to achieve a prescribed accuracy. Hence, the approach proposed permits one to solve very effectively dense linear systems with 1 to 10 millions equations.

Theoretically the above solution strategy can be applied even to the case when the permittivity and the permeability vary within a wide margin. However, in those cases this strategy may require such a fine mesh that we cannot afford. We are interested to present also a generalization of this solution strategy which is free from this drawback. To this end we consider a somewhat limiting case of a perfect conducting metal body covered by a bounded inhomogeneous dielectric layer.

Let V denote the dielectric layer region and let S denote the metal body surface. The scattered fields should satisfy equations (1) but when trying to present the fields using vector potentials we now need to take into account also the fields from the electric current J^E on the metal surface S:

$$E^s = -\frac{i}{\omega\varepsilon_0}(\mathrm{grad\,div} + k_0^2)\int\limits_{V_e} G j^E dV \;-\; \frac{i}{\omega\varepsilon_0}(\mathrm{grad\,div} + k_0^2)\int\limits_{S} G J^E dS + \mathrm{rot}\int\limits_{V_m} G j^M dV,$$

$$H^s = -\mathrm{rot}\int\limits_{V_e} G j^E dV - \mathrm{rot}\int\limits_{S} G J^E dS - \frac{i}{\omega\mu_0}(\mathrm{grad\,div} + k_0^2)\int\limits_{V_m} G j^M dV,$$

where V_e and V_m denote the subregions of V with $\varepsilon \neq \varepsilon_0$ and $\mu \neq \mu_0$, respectively. The perfect conductor condition

$$E_\tau^s + E_\tau^0 = 0$$

results in the following equation on S

$$\frac{i}{\omega\varepsilon_0}(\frac{\partial}{\partial\tau}\mathrm{div} + k_0^2)\int\limits_{V_e} Gj^E dV \;+\; \frac{i}{\omega\varepsilon_0}(\frac{\partial}{\partial\tau}\mathrm{div} + k_0^2)\int\limits_S GJ^E dS + (\tau, \int\limits_{V_m} \mathrm{rot}\,(Gj^M)dV) = E_\tau^0.$$

As previously, having changed the vector variables and keeping the same notation for the new variables we finally obtain the following system of integral equations

$$\begin{aligned}
(\frac{1}{3} + \frac{1}{\varepsilon_\tau - 1})E - \int\limits_{V_e}(\mathrm{grad\,div} + k_0^2)(GE)dV \;&-\; \frac{i}{\omega\varepsilon_0}\int\limits_S(\mathrm{grad\,div} + k_0^2)(GJ^E)dS \\
&-\; i\int\limits_{V_m} k_0[\nabla G, H]dV = E^0, \\
-(\frac{1}{3} + \frac{1}{\mu_\tau - 1})H + \int\limits_{V_m}(\mathrm{grad\,div} + k_0^2)(GH)dV \;&-\; i\int\limits_{V_e} k_0[\nabla G, E]dV \\
&+\; w_0\int\limits_S [\nabla G, J^E]dS = H^0, \\
-\int\limits_{V_e}(\frac{\partial}{\partial\tau}\mathrm{div} + k_0^2)(GE)dV \;&+\; \frac{i}{\omega\varepsilon_0}(\frac{\partial}{\partial\tau}\mathrm{div} + k_0^2)\int\limits_S GJ^E dS \\
&-\; ik_0(\tau, \int\limits_{V_m}[\nabla G, H]dV = E_\tau^0.
\end{aligned}$$

To solve this system we apply the Galerkin method using the same piecewise constant vector test functions to approximate E and H and the Rao-Wilton-Glisson functions to approximate J^E on the metal surface. The coefficient matrix of the resulting algebraic system takes the form

$$A = \begin{bmatrix} V & C \\ C^T & S \end{bmatrix},$$

where V and S correspond to the dielectric–dielectric influence coefficients and the metal–metal ones, respectively, while C accounts for the coupling. To solve the algebraic system we use the GMRES-based solver with a specific preconditioning strategy.

We present sample numerical results demonstrating an agreement of the computed solution with the analytical solution.

Problem 4. Consider a metal ball of radius $r_1 = 0.1$ with a penetrable dielectric spherical layer $r_1 < r \leq r_2$ whith $r_2 = 0.4$ and $\varepsilon_\tau = 4$; $k_0 = 1$. Figure 5 shows comparison of two diagrams of the bistatic cross sections σ/λ^2 obtained using the numerical procedure proposed and the analytical solution.

We observe a rather well agreement between the analytical and the computed solutions. The numerical experiments thus justify the robustness of the approach in the case of highly inhomogeneous objects. In contrast to [2] we see that from the practical point of view it is not at all mandatory to turn to weak formulations and then to refuse from using piecewise constant test functions. Actually being simpler than whatever else functions, the piecewise constant functions prove to be a reliable basis for the Galerkin method applied straighforwardly to "strong" integral formulations.

The proposed approach seems to be especially well suited for the case when the metal body constitutes a relatively small inclusion inside a (possibly rather large) dielectric region. In all cases really large linear algebraic systems with dense coefficient matrices can be solved very effectively by the proposed block-Toeplitz-structure-based solution strategy.

The authors gratefully acknowledge the helpful contribution by A.Kukk in this research and especially his assistance in conducting numerical experiments. Special thanks also goes to A. Yeremin for his help to improve the presentation.

References

[1] E.E. Tyrtyshnikov. Optimal and superoptimal circulant preconditioners. SIAM J. Matrix Anal. Appl., 1992, v.13, no 2, pp.459-473.

[2] Peter Zwamborn, Peter M. van der Berg. Computation of electromagnetic field inside strongly inhomogeneous objects by the weak-conjugate gradient fast-Fourier-transform method. J. Opt. Soc. Am., A, v.11 no 4, 1994, pp.1414-1421.

Figure 1: Problem 1, $|E_x|$

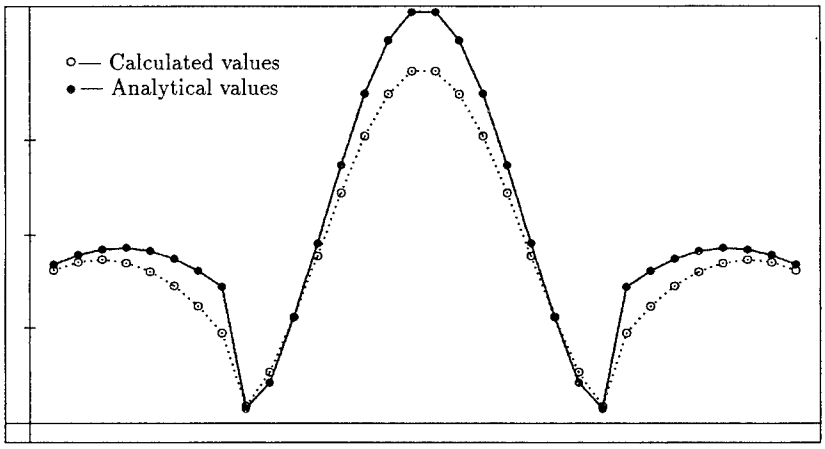


Figure 2: Problem 2, $|E_x|$

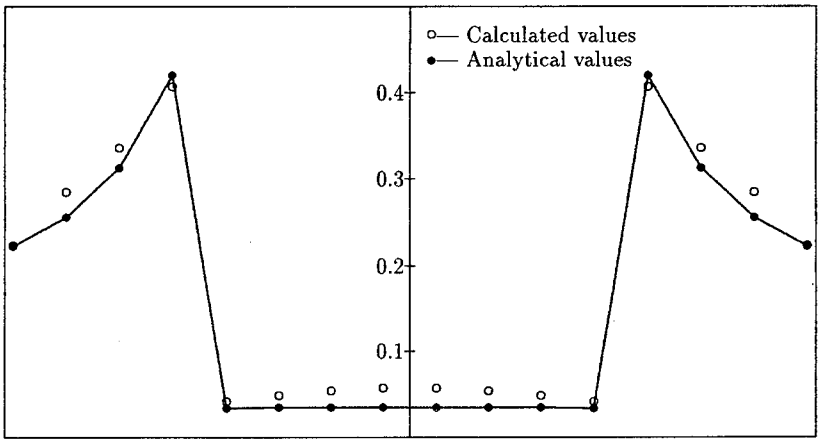


Figure 3: Problem 2, σ/λ^2

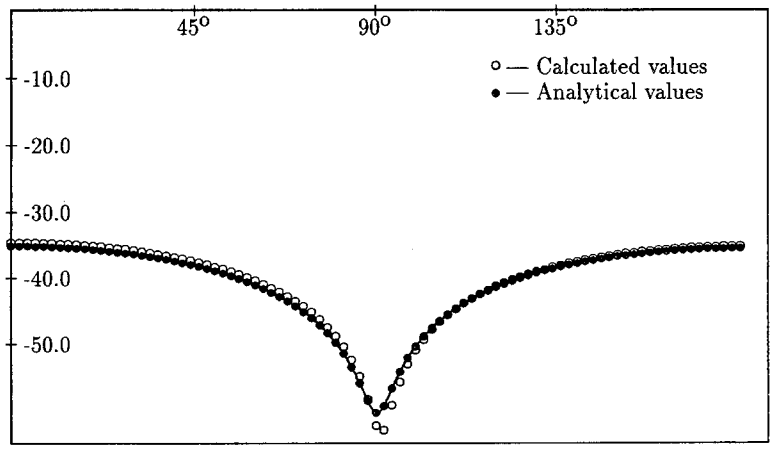


Figure 4: Problem 3, σ/λ^2

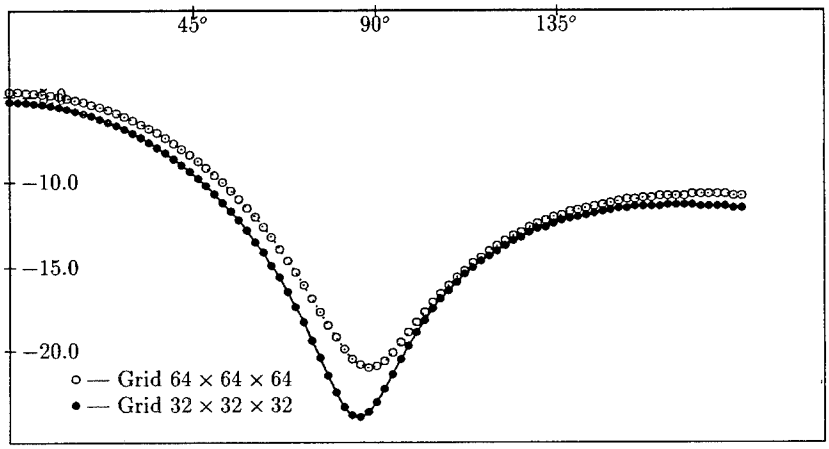
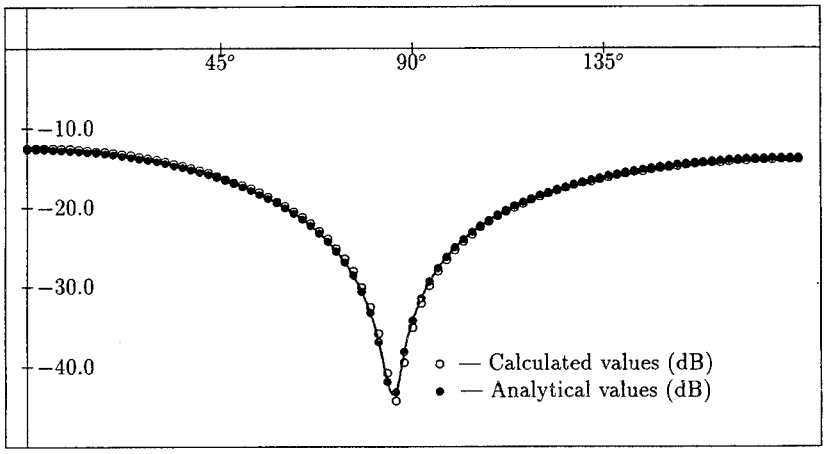


Figure 5: Problem 4, σ/λ^2



THE TWO-DIMENSIONAL FINITE INTEGRAL TECHNIQUE COMBINED WITH THE MEASURED EQUATION OF INVARIANCE APPLIED TO TRANSVERSE ELECTRIC OPEN REGION SCATTERING PROBLEMS

Griffin K. Gothard and Sadasiva M. Rao
Department of Electrical Engineering
200 Broun Hall • Auburn University, Alabama 36849

Abstract

The frequency domain analysis of several open region scattering bodies illuminated by transverse electric (TE) plane waves is accomplished using the two-dimensional finite integral technique (FIT) combined with the measured equation of invariance (MEI). The resulting FIT/MEI solutions are compared with the well known method of moment (MoM) solutions for validation.

I Introduction

The finite integral technique (FIT) uses the integral form of Maxwell's equations applied to a discrete conformal grid. The scattering structure and the surrounding region is subdivided into elements, in this case triangles, and constitutive material parameters are assigned to each triangle thus facilitating the specification of an inhomogeneous body. Then, Maxwell's equations, in the integral form, are applied to each element to generate a sparse matrix. The measured equation of invariance (MEI) is used to truncate the problem space close to the scattering body.

II The Finite Integral Technique

The finite integral technique directly applies the Maxwell's equations in integral form to a discrete grid [1]. The unknown quantities are approximated by explicit basis functions, and therefore the technique is easily derived and implemented. Also, use of the integral form of Maxwell's equation provides a smoothing effect on the problem solution.

Beginning with Maxwell's equations

$$\nabla \times \boldsymbol{H} = -j\omega\epsilon\boldsymbol{E}$$
$$\nabla \times \boldsymbol{E} = j\omega\mu\boldsymbol{H}$$

the two-dimensional integral form (no z variation) may be easily derived, given by

$$\int \boldsymbol{E}_t \cdot d\boldsymbol{l} = -j\omega \int \mu \boldsymbol{H}_z \mathrm{ds}$$
$$\boldsymbol{H}_z^{i+1} - \boldsymbol{H}_z^{i} = j\omega \int \epsilon \boldsymbol{E}_t \cdot \overline{n} d\boldsymbol{l} \qquad (1)$$

where $\boldsymbol{E}_t$ is the transverse electric (TE) field, $\boldsymbol{H}_z$ is the z-directed magnetic field, and $\boldsymbol{H}_z^{i+1}$ and $\boldsymbol{H}_z^{i}$ are the magnetic fields at two adjacent node locations i+1 and i in the mesh, respectively.

Applying the appropriate basis functions and simplifying results in an equation which, if applied to every node in the discrete mesh, generates an edge based sparse finite integral matrix that can then be solved for the unknown quantities [1].

III The Measured equation of invariance

The measured equation of invariance [2,3] technique, applied to the boundary nodes of a discrete grid scheme, enforces the radiation condition for open region scattering problems.

Using the static case as an example, assuming we have an open region perfect electric conductor (PEC) with a charge density q_v on the PEC, we can find the potential $\mathbf{V}(\rho)$ at any point in space using

$$\mathbf{V}(\rho) = \int_c \frac{q_v(\rho') ln|\rho - \rho'|}{2\pi\epsilon_0} dc' \tag{2}$$

where ρ' and ρ represent the position vectors to the source and field points respectively, and q_v is the charge density. Also, at each boundary node, an equation relating the boundary nodes potential with the neighboring nodes potentials can be defined as

$$\sum_{i=1}^{N} \alpha_i V_i = 0 \tag{3}$$

where V_i is the unknown voltage at node i, α_i is an unknown weighting coefficient associated with V_i, and N is the number of potentials considered.

By assuming N-1 orthogonal functions for the purpose of representing q_v in (1), and then solving for the V_i's in (2), a set of N-1 linear equations with N-1 unknown α_i's can be defined at each boundary node. Solving these equations yields a set of weighting coefficients (α_i; i=1, N-1) associated with each boundary node. Using these weighting coefficients in place of the finite difference schemes weighting coefficients, implements the MEI method and enforces the radiation condition. Since N is a finite number (in our case equal to 6), the new finite-difference global matrix is still sparse.

IV Numerical Results

Figure 1 shows the normalized current distribution on the body of a 0.8λ to a side infinite PEC square cylinder illuminated by a normally incident TE plane wave as predicted by the FIT/MEI and MoM. The real and imaginary parts of the current are plotted from the middle of the shadow region to the middle of the illuminated region of the cylinder. The FIT/MEI problem space is truncated 2 layers away from the cylinder and has a total of 336 edges, where 40 are fixed (known) and 296 are the unknowns. The MoM cylinder is subdivided into 40 equal segments. As can be seen in the figure, agreement between the FIT/MEI and MoM predicted currents is good for both the real and imaginary parts.

Figure 2 shows the normalized current distribution on the body of an infinite circular cylinder ($\rho = 0.15\lambda$) illuminated by a TE plane wave as predicted by the FIT/MEI and MoM. The current is plotted from the middle of the shadow region to the middle of the illuminated region of the cylinder. The FIT/MEI problem space is truncated 2 layers away from the cylinder and has a total of 112 edges, where 16 are known and 96 are unknown. The MoM cylinder is subdivided into 16 equal segments. As the figure illustrates, agreement between the FIT/MEI and MoM is good for the imaginary part of the current and fair for the real part.

Figures 3 and 4-5 show the predicted normalized current distributions (electric and magnetic, respectively) on the body of a 0.2λ to a side infinite square dielectric cylinder illuminated by a normally incident TE plane wave as predicted by the FIT/MEI and MoM. For the constitutive material parameters of the cylinder, the permittivity (ϵ_r) is 4.0 and the permeability (μ_r) is 1.0. The currents are plotted from the middle of the shadow region to the middle of illuminated region of the cylinder. The FIT/MEI problem space is truncated 2 layers away from the dielectric cylinder and has a 616 unknowns. The MoM cylinder

has 112 unknowns. In Figure 3, the agreement between the FIT/MEI and MoM predicted electric current distribution is good for both the real and imaginary parts. As Figures 4-5 show, the magnetic current distribution also shows a fair agreement.

V Conclusions

The purpose of this effort was to validate the FIT/MEI method for open region problems illuminated by transverse electric plane waves, and no effort was made to minimize the unknowns for either the FIT/MEI or MOM techniques, nor to maximize agreement between the two methods by increasing the FIT/MEI or MOM unknowns. However, since the FIT/MEI technique generates a sparse matrix, and easily handles inhomogeneous or anisotropic materials and complex geometries, it is ***possible*** that the technique could deal with more complex and electrically larger problems that the MOM. Presently, work is in progress to test this possibility.

References

[1] J. E. Wheeler III, *Formulation and investigation of finite integral techniques for computing electromagnetic fields in the presence of arbitrary inhomogeneous objects*, Ph.D thesis, University of Houston, December 1991.

[2] K. K. Mei, R. Pous, Q. Chen, and Y. W. Liu, "The measured equation of invariance: a new concept in field computation," 1992 IEEE ALS International Symposium, Chicago, USA, pp. 2047-2050.

[3] K. K. Mei, R. Pous, Q. Chen, and Y. W. Liu, "The measured equation of invariance: A new concept in field computation," *IEEE Trans. Antennas Propag.* 42(3), 320-328, 1994.

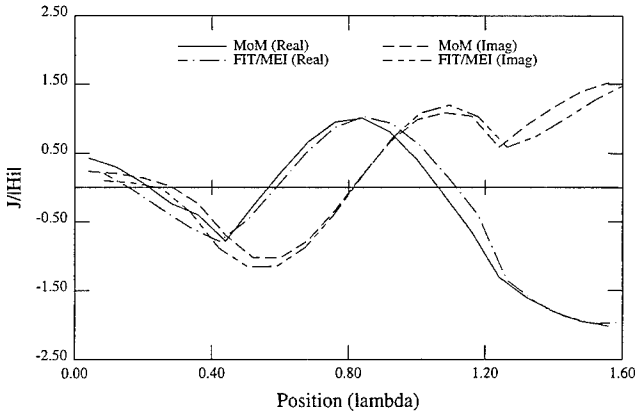


Figure 1: The normalized electric current distribution on the body of a 0.8λ to a side infinite square PEC cylinder illuminated by a normally incident TE plane wave as predicted by the FIT/MEI and MoM. The real and imaginary parts of the current distribution are plotted from the middle of the shadow region to the middle of the illuminated region.

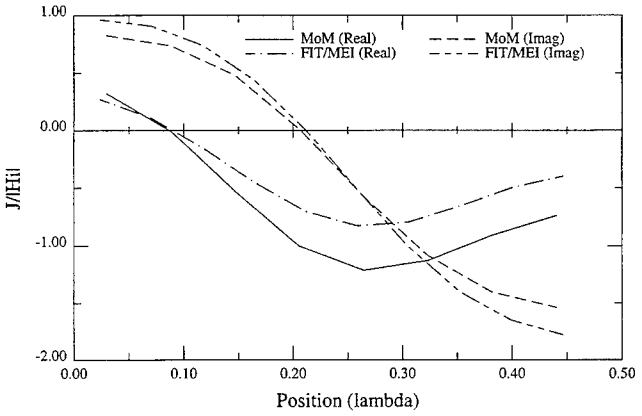


Figure 2: The normalized electric current distribution on the body of a $\rho = 0.15\lambda$ infinite circular PEC cylinder illuminated by an incident TE plane wave as predicted by the FIT/MEI and MoM. The real and imaginary parts of the current distribution are plotted from the middle of the shadow region to the middle of the illuminated region.

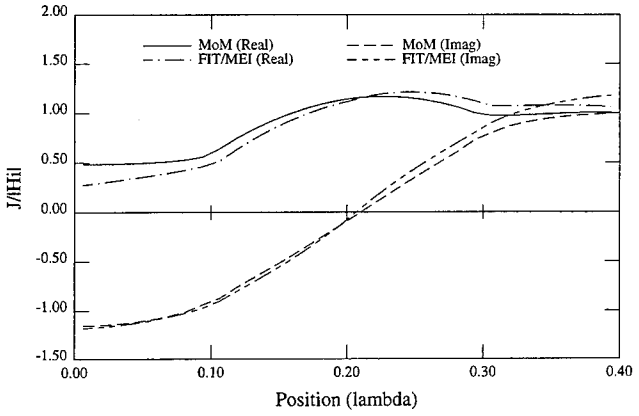


Figure 3: The normalized electric current distribution on the body of a 0.2λ to a side infinite dielectric square cylinder (μ_r=1.0 , ϵ_r=4.0) illuminated by a normally incident TE plane wave as predicted by the FIT/MEI and MoM. The real and imaginary parts of the current are plotted from the middle of the shadow region to the middle of the illuminated region.

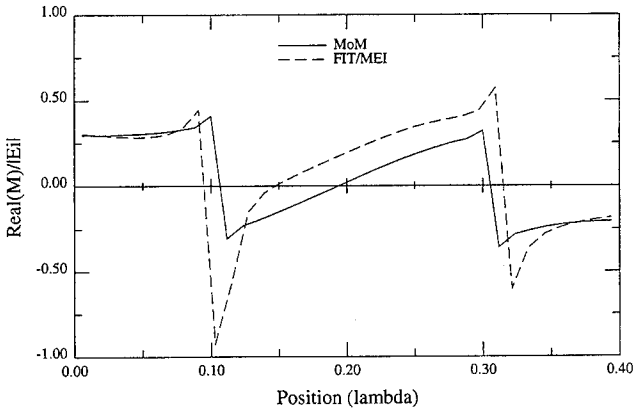


Figure 4: The real part of the normalized magnetic current distribution on the body of a 0.2λ to a side infinite dielectric square cylinder (constitutive parameters μ_r=1.0 , ϵ_r=4.0) illuminated by a normally incident TE plane wave as predicted by the FIT/MEI and MoM. The current is plotted from the middle of the shadow region to the middle of the illuminated region.

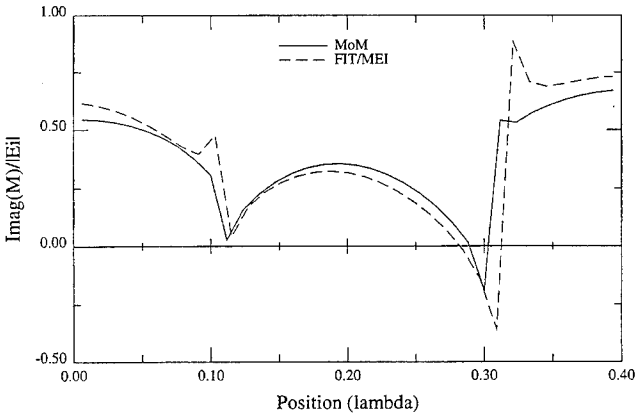


Figure 5: The imaginary part of the normalized magnetic current distribution on the body of a 0.2λ to a side infinite dielectric square cylinder (constitutive parameters μ_r=1.0 , ϵ_r=4.0) illuminated by a normally incident TE plane wave as predicted by the FIT/MEI and MoM. The current is plotted from the middle of the shadow region to the middle of the illuminated region.

ARTIFICIAL TRANSPARENT BOUNDARIES IN COMPUTATIONAL QUASIOPTICS

Alexei V.Popov

Institute of Terrestrial Magnetism, Ionosphere and Radio Wave Propagation
Russian Academy of Science, 142092 Troitsk, Moscow region, Russia

INTRODUCTION

The parabolic wave equation proposed by Leontovich and Fock in the middle forties has many applications to diffraction and wave propagation [1]. It can serve as a powerful computational tool for complicated environments with non-separable variables (radio propagation over a curved terrain, in a nonuniform tropospheric duct etc.). A specific difficulty arises when the wave field is to be found in an infinite domain. In order to handle the problem numerically one has to reduce the region to a finite strip (in two dimensions) or to a cylinder (in $3D$ case) and to transfer the radiation condition posed at infinity onto its border (surface). It is desirable to do that exactly in order to avoid spurious reflections from the artificially introduced boundaries. An exact form of the boundary condition providing full transparency for an arbitrary solution of the parabolic wave equation in two dimensions has been found and tested by Baskakov and Popov [2]. An equivalent formula has been published independently by Marcus [3]. Here, we discuss this result and make necessary generalizations for three-dimensional problems and quasi-stratified environments.

DERIVATION OF TRANSPARENT BOUNDARY CONDITION IN $2D$

The simplest case we consider here is two-dimensional diffraction by a finite dielectric obstacle in the half-space $x > 0$. If the dielectric permittivity $\epsilon(x,z)$ differs not much from unity: $|\epsilon - 1| << 1$, a paraxial wave beam $E = u(x,z)e^{ikx}$ can be described by the parabolic equation

$$2ik\frac{\partial u}{\partial x} + \frac{\partial^2 u}{\partial z^2} + k^2(\epsilon - 1)u = 0 \tag{1}$$

Assuming that variation $\epsilon - 1$ vanishes above the level $z = a$ we can solve Eq.(1) in the quadrant $x > 0$, $z > a$ analytically. So, for a given initial value $u(0,z) = u_0(z)$ and for an arbitrary boundary value $u(x,a)$, the exact solution of Eq.(1) that satisfies the radiation condition can be written in the following form: $u = v + w$ where

$$v(x,z) = e^{-i\pi/4}\sqrt{k/2\pi x}\left[\int_{a-z}^{\infty} u_0(z+t)\exp\left(\frac{ikt^2}{2x}\right)dt - \int_{z-a}^{\infty} u_0(2a-z+t)\exp\left(\frac{ikt^2}{2x}\right)dt\right] \tag{2}$$

and

$$w(x,z) = -\frac{e^{i\pi/4}}{\sqrt{2\pi k}}\frac{\partial}{\partial z}\int_0^x u(\xi,a)\exp\left[ik\frac{(z-a)^2}{2(x-\xi)}\right]\frac{d\xi}{\sqrt{x-\xi}} \tag{3}$$

Now we can calculate the normal derivative $\partial u/\partial z(x,a)$. Differentiating Eqs.(2)-(3) and making

use of Eq.(1) yield the following relation

$$\frac{\partial u}{\partial z}(x,a) = -e^{-i\pi/4}\sqrt{2k/\pi}\,\frac{\partial}{\partial x}\int\limits_0^x u(\xi,a)\,\frac{d\xi}{\sqrt{x-\xi}} + \frac{\partial v}{\partial z}(x,a) \tag{4}$$

It can be considered as a nonlocal generalization of the third-kind boundary condition which enables one to integrate Eq.(1) numerically within the strip $-a < z < a$. A finite-difference approximation of Eq.(4) has been examined by Baskakov and Popov [2]. Numerical tests showed full absorption of arbitrary wave packets encountering the interface $z = a$ from inside of the strip. If the initial function $u_0(z)$ vanishes for $z > a$, the boundary condition (4) takes a homogeneous form

$$\frac{\partial u}{\partial z}(x,a) = -e^{-i\pi/4}\sqrt{2k\frac{\partial}{\partial x}}\,u(x,a) \tag{5}$$

that ensues also from factorization of the differential operator (1):

$$\left(2ik\frac{\partial}{\partial x} + \frac{\partial^2}{\partial z^2}\right)u = \left(\frac{\partial}{\partial z} + e^{-i\pi/4}\sqrt{2k\frac{\partial}{\partial x}}\right)\left(\frac{\partial}{\partial z} - e^{-i\pi/4}\sqrt{2k\frac{\partial}{\partial x}}\right)u \tag{6}$$

THREE-DIMENSIONAL CASE

Consider a $3D$ generalization of the parabolic wave equation

$$2ik\frac{\partial u}{\partial x} + \Delta_\perp u + k^2(\epsilon - 1)u = 0 \tag{7}$$

assuming that variations $\epsilon - 1$ and the initial value $u(0,r,\varphi) = u_0(r,\varphi)$ are localized in a vicinity $r < a$ of the longitudinal axis (a good example is a paraxial wave beam truncated by a finite aperture and propagating through a dielectric quasioptic system). As the parabolic equation (7) can be solved analytically for $r > a$, we are able to transfer the radiation condition from infinity to the cylindrical boundary $r = a$.

Using the Fourier expansion

$$u(x,r,\varphi) = \sum_{m=-\infty}^{\infty} u_m(x,r)e^{im\varphi} \tag{8}$$

and Duhamel principle, one gets an exact expression

$$u(x,r,\varphi) = \frac{1}{2\pi}\,\frac{\partial}{\partial x}\int\limits_0^x\int\limits_0^{2\pi} u(\xi,a,\psi)\,d\xi\,d\psi \sum_{m=-\infty}^{\infty} e^{im(\varphi-\psi)}U_m(x-\xi,r) \tag{9}$$

of the solution $u(x,r,\varphi)$ outside the cylinder $r = a$ in terms of its boundary values $u(x,a,\psi)$. Here,

$$U_m(x,r) = \frac{1}{2\pi i}\int\limits_{c-i\infty}^{c+i\infty} \frac{H_m^{(1)}(r\sqrt{2ikp})}{H_m^{(1)}(a\sqrt{2ikp})}\,e^{px}\,\frac{dp}{p} \tag{10}$$

are partial step functions satisfying the following boundary condition

$$U_m(x,a) = \begin{cases} 1 & for \quad x > 0 \\ 0 & for \quad x < 0 \end{cases} \tag{11}$$

and the radiation condition for $r \to \infty$. Simple calculation yields a perfectly absorbing boundary condition:

$$\frac{\partial u}{\partial r}(x,a,\varphi) = \frac{1}{2\pi}\frac{\partial}{\partial x}\int_0^x\int_0^{2\pi} u(\xi,a,\psi)K(x-\xi,\varphi-\psi)\,d\xi\,d\psi \tag{12}$$

with

$$K(x,\varphi) = \frac{e^{-i\pi/4}}{\pi}\sqrt{\frac{k}{2}}\sum_{m=-\infty}^{\infty} e^{im\varphi}\int_{c-i\infty}^{c+i\infty}\frac{H_m^{(1)\prime}(a\sqrt{2ikp})}{H_m^{(1)}(a\sqrt{2ikp})}\,e^{px}\,\frac{dp}{\sqrt{p}} \tag{13}$$

that enables one to reduce the computation region to the semicylinder $x > 0$, $r < a$.

SHORT-WAVE ASYMPTOTIC

The kernel of the surface integral operator (12) can be simplified in the short-wave limit when the radius of the artificial cylindrical boundary a is large compared with the wavelength $\lambda = 2\pi/k$. Assuming that $ka \gg 1$, replace the Hankel functions in (13) with their Debye asymptotics

$$H_m^{(1)}(t) \sim \sqrt{\frac{2}{\pi m tan\beta}}\;e^{i[m(tan\beta-\beta-\pi/4)]}$$

$$H_m^{(1)\prime}(t) \sim i\sin\beta H_m^{(1)}(t) \tag{14}$$

where $\cos\beta = m/t$. Then the integral can be evaluated analytically:

$$\int_{c-i\infty}^{c+i\infty}\frac{H_m^{(1)\prime}(a\sqrt{2ikp})}{H_m^{(1)}(a\sqrt{2ikp})}\,e^{px}\,\frac{dp}{\sqrt{p}} \sim i\int_{c-i\infty}^{c+i\infty}\sqrt{1-\frac{m^2}{2ikpa^2}}\,e^{px}\,\frac{dp}{\sqrt{p}} =$$

$$= \sqrt{\pi}\int_x^{\infty}\exp\left(-i\frac{m^2}{2ka^2}t\right)\frac{dt}{t^{3/2}} = -\frac{m}{a}\sqrt{\frac{2\pi}{k}}\int_{\frac{m}{a}\sqrt{\frac{x}{2k}}}^{\infty} e^{-i\alpha^2}\,\frac{d\alpha}{\alpha^2} \tag{15}$$

As

$$\int_\tau^\infty e^{-i\alpha^2}\,\frac{d\alpha}{\alpha^2} = \frac{e^{-i\tau^2}}{\tau} - 2i\int_\tau^\infty e^{-i\alpha^2}\,d\alpha \tag{16}$$

the kernel (13) can be expressed in terms of Fresnel integrals:

$$K(x,\varphi) \approx -e^{-i\pi/4}\sqrt{\frac{2k}{\pi x}}\sum_{m=-\infty}^{\infty} e^{im\varphi}\left(e^{-i\tau_m^2} - 2i\tau_m\int_{\tau_m}^{\infty} e^{-i\alpha^2}\,d\alpha\right) \tag{17}$$

where $\tau_m = \frac{m}{a}\sqrt{\frac{x}{2k}}$. This approximation makes the boundary condition (12) ready for an immediate numerical implementation.

TRANSPARENT BOUNDARIES FOR QUASI-STRATIFIED ENVIRONMENTS

A parabolic wave equation for UHF propagation in a tropospheric duct has been introduced by Fock [1]

$$2ik\frac{\partial u}{\partial x} + \frac{\partial^2 u}{\partial z^2} + 2k^2\frac{z}{R^*}[1+g(x,z)]\,u = 0 \tag{18}$$

Here, the height-dependent term z/R^* describes the joint influence of the earth sphericity and barometric refraction (R^* is the equivalent earth's radius), and the correction $g(x,z)$ corresponds to

nonuniform variations of the refraction index localized below some reference height $z = b$ (similar models comprising a horizontally stratified background and localized perturbations are used in ocean acoustics, Tappert [4]). Having in mind numerical integration of Eq.(18), we have derived a boundary condition reducing the problem posed in the half-space $z > 0$ to a strip $0 < z < b$. Omitting details, we just write down the result in dimensionless variables $\xi = (k/2R^{*2})^{1/3}x$, $\zeta = (2k^2/R^*)^{1/3}z$, $\beta = (2k^2/R^*)^{1/3}b$:

$$\frac{\partial u}{\partial \zeta}(\xi,\beta) = \int_0^\xi \frac{\partial u}{\partial \xi}(\xi',\beta)K^+(\xi-\xi')\,d\xi' \tag{19}$$

Here,

$$K^+(\xi) = -\frac{1}{2\pi i}\int_{-\infty-ic}^{\infty-ic} e^{it\xi}\,\frac{w_1'(t-\beta)}{tw_1(t-\beta)}\,dt \tag{20}$$

and $w_1(t)$ is first-kind Airy-Fock function. It is evident that similar transparent boundary conditions can be obtained for other height-dependent backgrounds.

ASYMPTOTIC BEHAVIOR OF BOUNDARY OPERATORS

Our approach to truncation of the computational domain yields a family of special functions being the kernels of integral boundary operators. The simplest $2D$ example (4) shows that the kernel has a weak singularity at the end of the integration path and some non-local "tail". It is interesting to examine the less trivial examples given above from this point of view.

Consider the $3D$ parabolic equation (7). In the most interesting axial symmetric case, the boundary condition (12) takes the form

$$\frac{\partial u}{\partial r}(x,a) = \frac{\partial}{\partial x}\int_0^x u(\xi,a)K_0(x-\xi)\,d\xi \tag{21}$$

with

$$K_0(x) = \frac{e^{-i\pi/4}}{\pi}\sqrt{k/2}\int_{c-i\infty}^{c+i\infty}\frac{H_0^{(1)'}(a\sqrt{2ikp})}{H_0^{(1)}(a\sqrt{2ikp})}\,e^{px}\,\frac{dp}{\sqrt{p}} \tag{22}$$

In can be seen that its asymptotic behavior depends on the magnitude of the Fresnel parameter $q = x/2ka^2$. For $q \ll 1$, substituting the asymptotics $H_0^{(1)}(z) \sim \sqrt{2/\pi z}\,e^{i(z-\pi/4)}$ for the Hankel function, one gets

$$K_0(x) \sim -e^{-i\pi/4}\sqrt{2k/\pi x} \tag{23}$$

We see that the boundary operator (17) has the same singularity as its $2D$ prototype (4) and reduces to the latter for large radii a. The opposite limiting case $x \to \infty$ can be examined by replacing $H_0^{(1)}(z)$ with its approximation $2/\pi \log z$ for small z. It makes possible to evaluate the integral (18) asymptotically:

$$K_0(x) \underset{x\to\infty}{\sim} \int_0^\epsilon e^{-tx}\log\frac{\log(a\sqrt{2kt}) + i3\pi/4}{\log(a\sqrt{2kt}) - i\pi/4}\,dt$$

$$\approx \frac{x}{a}\int_0^\epsilon \frac{e^{-tx}}{\log(a\sqrt{2kt})}\,dt \underset{q\to\infty}{\sim} -\frac{2}{a\log\frac{x}{2ka^2}} \tag{24}$$

This formula shows that in three dimensions the kernel tail descends more slowly than $1/\sqrt{x}$.

A similar analysis for the PWE (18) in a quasi-stratified medium reveals the same type of singularity:

$$K^+(\xi) = -\frac{1}{2\pi i}\int\limits_{-\infty-ic}^{\infty-ic} e^{it\xi}\frac{w_1'(t-\beta)}{tw_1(t-\beta)}\,dt \underset{\xi\to 0}{\approx} \frac{e^{-i\pi/4}}{\sqrt{\pi\xi}} \tag{25}$$

and a "tail", for large ξ,

$$K^+(\xi) = \frac{w_1'(-\beta)}{w_1(-\beta)} - e^{i\beta\xi}\sum_{s=1}^{\infty}\frac{\exp(-t_s\xi e^{-i\pi/6})}{\beta + t_s e^{i\pi/3}} = Const + O(e^{-C\xi}) \tag{26}$$

tending exponentially to a constant limit.

This constant does not give nonlocal contribution to the integral boundary operator, therefore, in this case the transparent boundary has extremely short "memory". It is natural because the rays corresponding to the PWE (18) bend upwards and leave the upper boundary $z = b$ rapidly.

On the contrary, if we write down an analogous boundary condition providing perfect transparency of an arbitrary chosen "bottom" of the nonuniform layer $a < z < b$, we will see that the boundary operator has very long "memory". The corresponding kernel

$$K^-(\xi) = -\frac{1}{2\pi i}\int\limits_{-\infty-ic}^{\infty-ic} e^{it\xi}\frac{v'(t-\alpha)}{tv(t-\alpha)}\,dt \underset{\xi\to 0}{\approx} \frac{e^{-i\pi/4}}{\sqrt{\pi\xi}} \tag{27}$$

by substitution

$$\frac{v'}{v} = \frac{w'_2}{w_2} - \frac{1}{vw_2} \tag{28}$$

$v(t)$ and $w_2(t) = w_1(t) - 2iv(t)$ being Airy-Fock functions, can be reduced to the following form

$$K^-(\xi) = -\frac{w_2'(-\alpha)}{w_2(-\alpha)} + \frac{1}{2\pi i}\int\limits_{-\infty e^{i\pi/3}}^{\infty e^{i\pi/3}}\frac{e^{it\xi}}{tv(t-\alpha)w_2(t-\alpha)}\,dt \tag{29}$$

with $\alpha = (2k^2/R^*)^{1/3}a$. This integral is closely related to the special function investigated by Buldyrev and Lanin [5] in the problem of the whispering gallery wave propagation.

WIDE-ANGLE PARABOLIC EQUATIONS

Like any asymptotic approximation, the parabolic wave equation has its applicability limits. First, it does not hold for the wave packets with wide angular spectrum. Secondly, at great distances, accumulation of phase approximation errors takes place which distorts the calculated field distribution. In order to overcome these limitations, a number of modified equations to replace the original PWE has been put forward. Here, the wide-angle Claerbout approximation [6],

$$2ik\left(1 + \frac{1}{4k^2}\frac{\partial^2}{\partial z^2}\right)\frac{\partial u}{\partial x} + \frac{\partial^2 u}{\partial z^2} = 0 \tag{30}$$

the fourth-order long-range PWE [7]

$$2ik\frac{\partial u}{\partial x} + \left(1 - \frac{1}{4k^2}\frac{\partial^2}{\partial z^2}\right)\frac{\partial^2 u}{\partial z^2} = 0 \tag{31}$$

and the exact correction formula [8]

$$E(x,z) = \frac{x}{\sqrt{\pi i}}\int_0^{\infty} u(\frac{k}{2t}, z)\,\exp\left[i(\frac{k^2}{4t} + x^2 t)\right]\,\frac{dt}{\sqrt{t}} \tag{32}$$

relating the PWE solutions $u(x,z)$ with the rigorous wave field $E(x,z)$ satisfying the one-way Helmholtz equation

$$\frac{\partial u}{\partial x} = i\sqrt{k^2 + \frac{\partial^2}{\partial z^2}}\ u \tag{33}$$

can be mentioned.

All these equations require some boundary conditions eliminating spurious reflections when being solved numerically in a truncated spatial domain. Using the technique describe above, they can be derived in a similar way. As an example, consider the wide-angle PWE (30) in the quadrant $x > 0$, $z > a$. Its general solution satisfying the initial condition $u(0,z) = 0$ and radiation condition by $z \to \infty$ can be expressed in terms of its boundary values $u(x,a)$:

$$u(x,z) = \frac{\partial}{\partial x} \int_0^x U(\xi,a)U(x-\xi,z)\,d\xi \tag{34}$$

where

$$U(x,z) = \frac{1}{2\pi i} \int_{c-i\infty}^{c+i\infty} \exp\left[px + (a-z)\sqrt{\frac{2kp}{i - \frac{p}{2k}}}\right]\ \frac{dp}{p} \tag{35}$$

is the step function - cf. (10) .

Evaluating the normal derivative yields

$$\frac{\partial u}{\partial z}(x,a) = \frac{\partial}{\partial x} \int_0^x u(\xi,a)K(x-\xi)\,d\xi \tag{36}$$

with

$$K(x) = \frac{\partial U}{\partial z}(x,a) = -\frac{1}{2\pi i} \int_{c-i\infty}^{c+i\infty} \sqrt{\frac{2kp}{i - \frac{p}{2k}}}\ e^{px}\,\frac{dp}{p} = \frac{2ik}{\pi} \int_0^1 e^{2ikxs} \frac{ds}{\sqrt{s(1-s)}} = 2ike^{ikx}J_0(kx) \tag{37}$$

Here, $J_0(t)$ is Bessel function. Note that the nonlocal boundary conditions of transparency are constructed in a standard way. What depends on the specific problem is the possibility of reducing the kernel's integral representation to a simple closed-form expression.

APPLICATIONS AND NUMERICAL EXAMPLES

The boundary conditions of transparency described above admit effective numerical implementation in the framework of the finite difference method. They have been used in a number of diffraction and wave propagation problems. Among them are: radio propagation over an irregular terrain or in a tropospheric wave duct, microwave and X-ray quasioptical systems. We demonstrate some examples of field calculation using transparent boundaries to eliminate spurious reflections.

CONCLUSION

The objective of this paper was to find an exact form of boundary conditions providing full absorption of arbitrary paraxial wave packets described by the parabolic equation. It would enable one to reduce rigorously an infinite domain to a strip or cylinder for numerical calculations. We proposed a general approach to this problem and demonstrated some practical examples.

REFERENCES

1. V.A.Fock. Electromagnetic diffraction and propagation problems. *Pergamon Press*, Oxford, 1965.

2. V.A.Baskakov, A.V.Popov. Implementation of transparent boundaries for numerical solution of the Schrödinger equation. *Wave Motion*, 14, No 1, 1991 , pp.123-128.

3. S.W.Marcus. A generalized impedance method for application of the parabolic approximation to underwater acoustics. *J. Acoust. Soc. Am.*, No 1, 1991, pp. 391-398.

4. F.D.Tappert. The parabolic approximation method, in: Lectures Notes in Physics, 70. J.B.Keller, J.S.Papadakis (eds). Wave propagation and underwater acoustics.*Springer*, New York, 1977, pp.224-287.

5. V.M.Babič and V.S.Buldyrev. Short-wavelength diffraction theory (Asymptotic methods). *Springer*, New York, 1991.

6. J.Claerbout, Fundamentals of geophysical data processing with applications to petroleum prospecting, *McGraw - Hill*, New York, 1976).

7. A.V.Popov, S.A.Hoziosky, On a generalized parabolic equation of diffraction theory parabolic equation (in Russian), *J.Comp.Math. and Math. Phys.*, 17, No 2 (1977), pp.527-533.

8. E.A.Polyansky, Method of correction of the parabolic equation solutions in a nonuniform waveguide (in Russian), *Nauka*, Moscow, 1985.

A Statistical Electromagnetics (STEM) Research Initiation Report

W.P. Wheless, Jr.[◇], C.B. Wallace[†], and W.D. Prather[‡]
[◇]University of Alabama, Tuscaloosa, AL
[†]BDM Federal, Inc., Albuquerque, NM
[‡]Phillips Laboratory, Kirtland AFB, NM

1 Statistical Electromagnetics (STEM) Overview

Interest in the statistical properties and treatment of electromagnetic (EM) fields and their interactions has begun to increase in recent years [1]. One cause for this increase is the myriad failures of traditional methods to interpret and make useful predictions from measurement data which, in turn, has created an awareness that new approaches to RF/microwave experiment design are now both appropriate and necessary. The need to better define data requirements and to simultaneously reduce the number of samples/measurements in future experimental programs, strongly driven by economic constraints, gives additional incentive to pursue physics-based statistical modeling techniques for high-precision experimental characterizations.

Another cause for greater interest in STEM is the extremely limited ability, in actual practice, to directly solve Maxwell's equations, subject to given boundary conditions, for problems of practical interest (even of only modest complexity). Recent work has demonstrated the complicated, chaotic nature of the EM response of simple shapes where the boundary conditions render Maxwell's equations non-integrable [2] - [9].

Furthermore, even in a great many cases where deterministic solutions are straightforward, the required computer CPU time to achieve a solution precludes such an approach. For example, consider upset analysis of a circuit comprising 250 gates, so the number of system states is $2^{250} = 1.81 \times 10^{75}$. Simply taking each state as an unknown for numerical solution, at one operation per unknown and with a teraflop computer, the time requirement for one full numerical characterization is 5.7×10^{55} years. Practical overmoded mode-stirred chamber (MSC) analysis and a multitude of other problems dramatically illustrate this same point.

Yet another contributor to interest in STEM is an unsubstantiated, but rather widespread opinion that the fine-grid point calculation of EM fields in space and time may be unnecessary to reach certain final conclusions within some macroscopic 'performance envelope' sense. While such possibilities are now merely conjecture, they do stimulate speculation that future STEM research might address such questions.

One more impetus for STEM is that we must, of necessity, muddle through life making choices and decisions about EM interactions based on incomplete and flawed information. While most of us learn to live comfortably with some level of uncertainty, there is always a common desire to quantify the uncertainty, and to make it precise. It follows from the ability to quantify uncertainty that applied EM practitioners can start to make categorical statements with complete assurance about their level of uncertainty. Thus the preeminent objective in the development of STEM techniques is to be able to extract useful, quantitative conclusions for decision makers and designers from incomplete and imperfect information, either in data or in the specification of a problem environment; this significantly reduces their programmatic risk and enhances confidence in their decisions.

Statistical electromagnetics can be used to resolve problems in many diverse application areas. However, more basic research must be concluded before practical applications will yield to these new techniques. It is anticipated that useful methods for high frequencies can be developed in the reasonably near future, while extensions to lower frequency ranges will require additional time.

So far, most endeavors to describe EM coupling and interactions statistically have relied on collections of measured data, have employed empirical (best-fit) statistics, and/or have relied on expert engineering judgment. The empirical, or curve fitting, approach generally allows significant variation between predictions because one is working with limited, imperfect data sets. Without *a priori* knowledge about the appropriate distribution function(s), the success of empirical data-fitting has been likewise variable. Even the best among these studies are subject to persistent and legitimate questions regarding range of validity. Limited data tends to be concentrated in the vicinity of the mean, so that a good fit may be suggested for several distribution functions. The range of validity can only be extended by taking more measurements, in order to acquire sufficient data distant from the mean. However, the number of measurements required to confidently establish the distribution is usually precluded by time or budget limitations.

Another related and simultaneous objective for STEM is to develop techniques for the meaningful analysis of systems, or classes of problems, which undergo small changes or variations. These problems are distinguished from those of 'fixed' systems, where the principal limitations involve non-integrability coupled with incomplete and inaccurate environment specification, computer speeds and storage capabilities, and measurement noise/errors. In many important practical problems, small system changes or perturbations are observed to produce large variations in observed EM response(s). While these types of problems are highly resistant to treatment by deterministic methods, it is believed that they are amenable to the application of physics-based statistical methods.

Because STEM models are physics-based and begin with a deterministic model, the predictions must not violate known laws of physics and should be verifiable by experiment. Physics-based statistical models can be progressively improved by both improving the underlying physics and substantiating the truth of assumptions; theory, simulation by means of computational electromagnetics (CEM), and experiment are

symbiotic partners in the refinement process.

2 Motivation for STEM Development

Understanding the electromagnetic (EM) response of complex systems is a key risk minimization activity for many programs. Commercial ventures, such as aircraft and automotive manufacturing, face these difficulties as well as DoD, NASA, and other government agencies. Confidence in the ability to explain, and predict, how complicated systems respond to EM radiation facilitates sound program management. Useful conclusions for decision makers, system planners, and design engineers can be extracted by the application of statistical techniques to this important class of applied EM problems.

Statistical methods are justified by two major difficulties. First, the non-integrable nature of many EM response problems renders analytic solutions intractable; the chaotic nature of the resulting eigenfunctions, eigenfrequencies, and EM energy flow (voltages and currents) is best described statistically. Second, statistical techniques are also effectively applicable to system susceptibility analysis when examining the effect of perturbations (topology, measurement location, source parameters, etc.) and incomplete target/source configuration information (which may cause large EM response changes).

The acronym STEM has been coined from STatistical ElectroMagnetics; STEM embraces the study of non-integrability and physics-based statistics as applied to EM response problems. STEM applications include problems associated with large complex system susceptibility, mode-stirred chamber validity and interpretation, development of calibrated measurement techniques, pre-test prediction, far-field EM scattering, target recognition, and problems in other areas of science and engineering such as space science and geophysics.

Some aspects of a research initiation program for the orderly discovery, development, and exploitation of STEM are reported here. Problems areas of immediate interest include EM measurement and testing, fundamental EM interactions and coupling, and programmatic risk reduction.

3 STEM Preliminaries

A comprehensive application of statistics to a given complex EM problem ultimately must include a system model, a statistical model, and the application of probability theory to predict system responses. In the near future, it is expected that exploration and development efforts will emphasize physics-based statistical models, namely, the joint density functions $f(X_1, X_2, \ldots, X_n)$ associated with random variables X_n. The probabilistic modeling process presumes that we can identify distinct variables to be treated statistically, that a valid physics-based model can be constructed, that modeling should be in terms of measurable parameters and, finally, that it should be possible to demonstrate by experiment the conditions for, and ranges of validity for all assumptions.

To the extent possible, a program which develops methodology and results in STEM corresponding to those in statistical mechanics (both classical and quantum) is appealing. While statistical electromagnetics has some obvious differences which must be accommodated (such as spatial correlations, boundary conditions, and 'appropriate' functions), there are also attractive similarities. In principle, it is possible to deterministically arrive at all the details of an electromagnetics problem from solving Maxwell's equations subject to the relevant boundary conditions, clearly analogous to the detailed dynamics encountered in integrable and non-integrable classical and quantum mechanics. Furthermore, profound successes with statistical mechanics inspire the hope that corresponding powerful principles also are valid, in some dual form, for electromagnetics. For example, applied EM practitioners view with great interest (and envy) the statistical mechanics result that the velocity distribution of molecules in a container is Maxwellian, regardless of the container's shape. Of course, we realize this is not true except in the case of blackbody radiation. Most, if not all, practical EM problems involve specular reflections or refractions at boundaries, hence the failure of thermal equilibrium thermodynamics for the useful EM case.

In the case of applied EM, most problems of practical interest have complex geometrical and material environments, with highly intricate boundaries. This non-integrability creates a fundamental inability to completely and deterministically specify eigenfunctions, eigenfrequencies, and the associated EM energy flow. Because statistical modeling has been so effective with related conceptual problems in statistical mechanics, there is reasonable cause for optimism that it can be a valuable tool in applied EM as well.

The developers of statistical mechanics accomplished their feats of mathematical legerdemain principally by exploring the relationships between dynamical invariants of appropriate functions. That is, the final statistical theory was achieved after extensive theoretical work on determination of the properties of distribution functions. A developmental approach for applied EM comprising parallel theoretical, experimental, and numerical/simulation efforts will be necessary to characterize the relationships and behavior of the important corresponding functions of electromagnetic variables.

Different 'appropriate' functions apply to STEM; these functions should represent measurable quantities such as the actions associated with the $\mathbf{E}$ and $\mathbf{H}$ field components, as well as the energy flow (Poynting vector). Also, because the fields at different locations and/or different times are correlated, spatial and temporal correlation functions are of special interest in the EM case. It is appropriate that early work in the discovery phase of STEM should emphasize the development of relationships between these quantities. The motivation for this is the fact that such relationships exist and proved vital for the codification of statistical mechanics as we know it today.

Because eventual statistical model predictions are rigorously required to obey physical laws, any *a priori* distribution functions and their conditions/ranges for validity should be developed from first principles of physics, and based solidly on Maxwell's equations. While there is widespread belief at this time that there are classes of EM problems which share common distributions obtainable from physics-based statistics, that view has not been adequately substantiated by theory, even

though experiments and computer simulations suggest these relationships exist.

4 Frequency Regimes

STEM concepts can be most directly and quickly applied at high frequencies, where wavelengths become small in comparison to component and/or system dimensions. At such relatively high frequencies, the number of modes is large and problems involving cable bundles, multiple EM entry ports, etc., clearly become stochastic in nature as the problem becomes non-integrable.

In contrast, deterministic methods become more powerful at lower frequencies, where few modes exist. Deterministic solutions are directly attainable for integrable shapes at low frequencies, and that this regime generally is viewed as rather simple. Nonintegrable shapes at low frequencies are not as well determined analytically, but numerical methods and/or experimental characterizations are straightforward.

Intermediate frequencies, associated with 'several' modes, are generally intractable. It appears most likely that the successful methods for analysis and prediction in this frequency range will be a hybrid of theory, simulation, and experiments, but it is difficult to foresee the ultimate details of such methods.

As a result, it is now anticipated that STEM developmental projects will first concentrate on the high-frequency regime. Extension of results to progressively lower frequencies, incorporating appropriate modifications to the theory and results, will follow only after the high-frequency results are promulgated and achieve reasonable acceptance among researchers active in the field.

5 First Initiative

The basic thrusts of a current STEM development initiation effort is depicted in Figure 1. The two major short-term goals are (1) to improve the definitions and understanding of basic phenomenology associated with STEM, and (2) to produce a STEM monograph incorporating the principles necessary to tackle advanced applications. The point of view emphasized here is principally that of the EM engineer, tasked with discerning the best applications of STEM to practical circuits and systems.

While a detailed technical review of previous work is beyond the scope of this paper, a few selected references are briefly cited here so that the interested reader can gain a better appreciation for the entries of Figs. 1 and 2. Results from studies and measurement programs at NIST [10] - [13] imply that a wide variety of reverberation chambers, more often called mode-stirred chambers (MSCs), share common EM characteristics to the extent that it is realistic to believe a comprehensive, valid STEM treatment of MSCs can be developed. An early report on statistical distribution of EM field amplitudes in complex cavities was published by JAYCOR [14] in 1988, and a paper based on this report just recently appeared [15]. The JAYCOR report claims, from both best-fit empirical case studies and a theoretical derivation, that the power measured by a unidirectional probe in a 'complex' cavity has a χ^2 distribution

with two degrees of freedom. An overmoded MSC statistical model was reported in 1991 [16] which is useful for some cases. The most ambitious work on statistical behavior of fields in complex cavities published within the applied EM engineering community was just recently completed [17]. A question of the completeness of [17] for cavities with specular walls arises from classical sources such as [18] as well as more modern physics literature which carefully considers the impact of integrability along with boundary conditions (including but not limited to [2] - [9]); this question is now under study.

The "monograph compilation of results" indicated in Figure 1 is expected to encompass and report on theoretical, experimental, and simulation studies. The objective is to achieve cloture on the previous work reported in both the engineering and physics literature, including extensions which clearly become necessary by discovery in the review process. It is now intended that the scope of the first monograph will be restricted to the high-frequency regime; modifications of the theory and techniques to apply at progressively lower frequencies will follow.

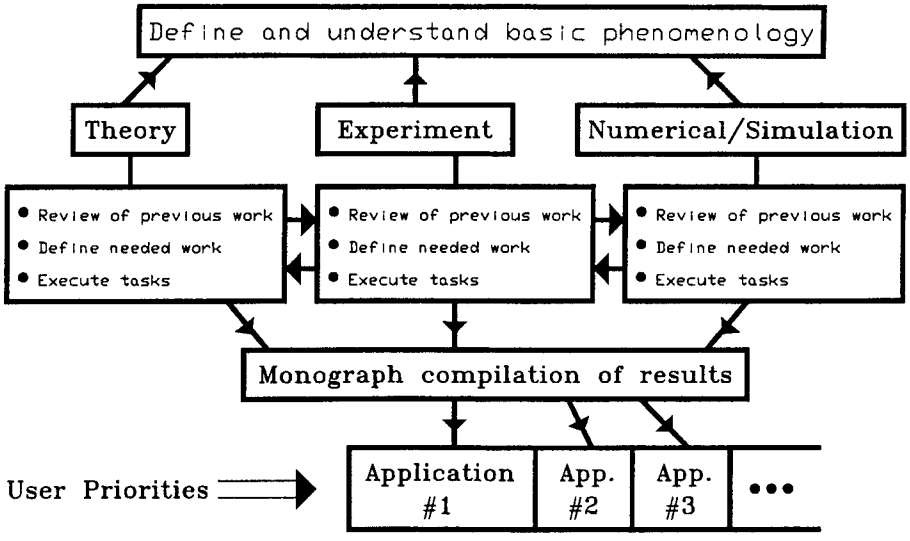


Figure 1. STEM research initiation program plan.

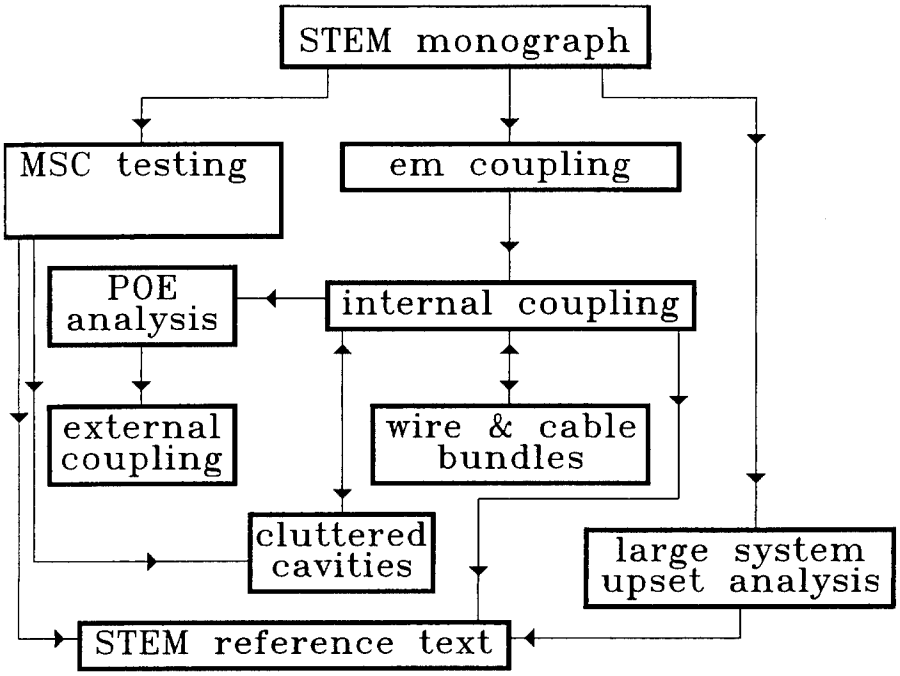


Figure 2. Second-phase subtasks proceeding from STEM monograph.

6 Advanced Applications Research Projects

Various projects to broaden the range of meaningful application of STEM concepts will become possible once a monograph of first principles is available. Figure 2 indicates the three major subdivisions for second-phase applications research as presently envisioned: (1) mode-stirred chamber (MSC) studies, (2) EM coupling problems, and (3) large system upset analysis. Detailed discussion of these areas is precluded by available space here, and would be premature in view of the discoveries which are certain to occur as development of the monograph proceeds. Details regarding advanced projects will be made available as the topic of a future paper, as STEM matures.

7 Acknowledgments

The contributions of Mr. T.H. Lehman and Dr. E.K. Miller to the issues and the research initiation program plan discussed here are gratefully acknowledged.

Support for this work was provided under an I.P.A. agreement between Phillips Laboratory, Kirtland AFB, NM, and The University of Alabama.

References

[1] E.K. Miller, "A rationale for developing and using STEM (STatistical ElectroMagnetics)," presented at EUROEM94 International Symposium on Electromagnetic Environments and Consequences, Bordeaux, France, June 2, 1994.

[2] E.J. Heller and S. Tomsovic, "Postmodern quantum mechanics," *Physics Today*, pp. 38-46, July 1993.

[3] J.L. Vega, T. Uzer, and J. Ford, "Chaotic billiards with neutral boundaries," *Physical Review E*, vol. 48, no. 5, pp. 3414-3420, Nov. 1993.

[4] S. Sridhar and E.J. Heller, "Physical and numerical experiments on the wave mechanics of classically chaotic systems," *Physical Review A*, vol. 46, no. 4, pp. R1728-R1731, 15 Aug. 1992.

[5] S. Sridhar, "Experimental observation of scarred eigenfunctions of chaotic microwave cavities," *Physical Review Letters*, vol. 67, no. 7, pp. 785-788, 12 Aug. 1991.

[6] J. Stein and H.-J. Stöckman, "Experimental determination of billiard wave functions," *Physical Review Letters*, vol. 68, no. 19, pp. 2867-2870, 11 May 1992.

[7] E. Doron, U. Smilansky, and A. Frenkel, "Experimental demonstration of chaotic scattering of microwaves," *Physical Review Letters*, vol. 65, no. 25, pp. 3072-3075, 17 Dec. 1990.

[8] S.W. McDonald and A.N. Kaufman, "Wave chaos in the stadium: Statistical properties of short-wave solutions of the Helmholtz equation," *Physical Review A*, vol. 37, no. 8, pp. 3067-3086, 15 April 1988.

[9] R.J. Riddle, Jr., "Numerical solution of the Helmholtz equation for two-dimensional polygonal regions," *Journal of Computational Physics*, **31**, pp. 42-59, 1979.

[10] B.-H. Liu and D.C. Chang, "Eigenmodes and the composite quality factor of a reverberating chamber," U.S. Department of Commerce / National Bureau of Standards, NBS Technical Note 1066, Aug. 1983.

[11] M.L. Crawford and G.H. Koepke, "Design, evaluation, and use of a reverberation chamber for performing electromagnetic susceptibility/vulnerability measurements," U.S. Department of Commerce / National Bureau of Standards, NBS Tech Note 1092, Apr. 1986.

[12] M.L. Crawford, M.T. Ma, J.M. Ladbury, and B.F. Riddle, "Measurement and evaluation of a TEM/reverberating chamber," U.S. Department of Commerce / National Institute of Standards and Technology, NIST Technical Note 1342, July 1990.

[13] D.I. Wu and D.C. Chang, "The effect of a large rotating scatterer in a rectangular cavity," U.S. Department of Commerce / National Bureau of Standards, NBS Technical Note 1317, Mar. 1988.

[14] R.H. Price, H.T. Davis, R.H. Bonn, E.P. Wenaas, R. Achenbach, V. Gieri, R. Thomas, J. Alcala, J. Hanson, W. Haynes, C. McCrea, C. Montano, R. Peterson, B. Trautlein, and R. Umber, "Determination of the statistical distribution of electromagnetic field amplitudes in complex cavities," JAYCOR, Albuquerque, NM, Report 88JAL129, 1 June 1988.

[15] R.H. Price, H.T. Davis, and E.P. Wenaas, "Determination of the statistical distribution of electromagnetic-field amplitudes in complex cavities," *Physical Review E*, Third Series, vol. 48, no. 6, pp. 4716-4729.

[16] J.G. Kostas and B. Boverie, "Statistical model for a mode-stirred chamber," *IEEE Trans. on Electromagnetic Compatibility*, vol. 33, no. 4, pp. 366-370, Nov. 1991.

[17] T.H. Lehman, "A Statistical Theory of Electromagnetic Fields in Complex Cavities," Phillips Laboratory, Kirtland AFB, NM, Interaction Notes series, Note 494, May 1993.

[18] W.K.H. Panofsky and M. Phillips, *Classical Electricity and Magnetism*, 2nd ed. Reading, MA: Addison-Wesley, 1962, pp. 191-193.

Optimization of Aperiodic Conducting Grids

Randy L. Haupt
HQ USAFA/DFEE
2354 Fairchild Dr, Suite 2F6
USAF Academy, CO 80840-6236
email: haupt@shelter.usafa.af.mil
fax: 719/472-3756
wk: 719/472-3190

Abstract.

This paper presents backscattering patterns from aperiodic grids optimized with genetic algorithms. A method of moments algorithm is used to calculate the induced surface current density on the strips. The optimization procedure is very slow, so several acceleration methods were investigated.

I. Introduction.

Grids are important in the design of reflector antennas and radomes. When uniform grids are very large, they can be accurately represented by infinite periodic grids. Aperiodic grids, small grids or curved grids can't take advantage of the periodicity of the grid to simplify induced current calculations. An aperiodic grid of strips consists of a finite number of infinitely long strips lying in a plane with all the edges parallel to each other. These strips are extremely thin and perfectly conducting, and may have different widths and spacings. By properly choosing the strip widths and spacings, the backscattering patterns from the grid can be modified to achieve a certain sidelobe level or a null in a given direction.

A genetic algorithm is used to optimize the widths and spacings of perfectly conducting strips to obtain the lowest possible relative sidelobe level. Genetic algorithms can optimize a large number of discrete parameters, such as strips in a grating. Other optimization techniques have difficulty dealing with the large number of parameters. Genetic algorithms are ideally suited for parallel computing but are quite slow on serial machines. This paper presents some results of optimizing aperiodic perfectly conducting strips using MATLAB on a Sun Sparc 20 computer and some attempts at accelerating the very slow convergence. Optimized grids have significantly lower sidelobes than uniform grids.

II. Problem Formulation.

Figure 1 shows a model of an aperiodic grid of M perfectly conducting strips lying along the x-axis. The incident plane wave has the electric field parallel to the edges of the strips, and the incident magnetic field is assumed to have a magnitude of one. An integral formulation to find the M current densities is given by

$$e^{jkxcosu} = \frac{k}{4}\sum_{m=1}^{M}\int_{x_m^-}^{x_m^+} J_m(x')\,H_0^{(2)}(k|x-x'|)dx'$$

where

M = number of conducting strips
J_m = surface current density on strip m
$H_0^{(2)}(*)$ = zeroth order Hankel function of the second kind
$k = 2\pi/\lambda$
$u = \cos\phi$
x_m^- and x_m^+ = beginning and ending points of strip m

Expanding the current on strip m into N basis functions and matching the boundary conditions at p = 1,2, ..., P = M x N points transforms the integral equation into

$$e^{jkxcosu} = \sum_{m=1}^{M}\sum_{n=1}^{N}\alpha_{mn}\left[\eta_m J_{mn}(x_p) + \frac{k}{4}\int_{\Delta_p^-}^{\Delta_p^+} J_{mn}(x')\,H_0^{(2)}(k|x-x'|)\,dx'\right]$$

where Δ_p^- and Δ_p^+ are beginning and ending points of pulse p. Once the current density is found, the backscattering is calculated.

A genetic algorithm is used to optimize the width of each strip in the grid and/or the spacings between strips in the grid in order to produce the lowest maximum relative sidelobe level in the backscattering pattern. This algorithm uses ideas from biology to determine the fittest or optimum grid configuration. Details of this algorithm can be found in [1] and [2].

III. Results.

The goal is to optimize a grid of 40 perfectly conducting strips, so that the backscattering pattern has the lowest possible maximum relative sidelobe level. A genetic algorithm performs the optimization using point matching with five collocation points per strip. Strip widths and spacings are limited to increments of 0.03125λ between 0.03125λ and 0.25λ. Five collocation points per strip are used to characterize the current density. The optimization results in a maximum relative sidelobe level of -20.08 dB. Figure 2 shows a diagram of the optimized aperiodic grid. Note that both the strip widths and spacings are nonuniform. Figure 3 shows the resulting backscattering pattern from the grid in Figure 2.

One problem with this optimization procedure is that it takes a considerable amount of time. The impedance matrix has 200x200 elements. Even though genetic algorithms check a very small portion of the solution space, they make a hundred or more function calls every iteration. Every function call requires the decomposition of the matrix and solving for the surface current density and the backscatter for each angle in the far field.

$$\text{flops}_{MOM} = C_H(M\cdot N)^2 + C_{lu}(M\cdot N)^2 + N_A C_{bs}(M\cdot N)^2 + C_{ff}(M\cdot N)^2$$

$$= (C_H + C_{lu}(M\cdot N) + N_A C_{bs} + C_{ff})\cdot (M\cdot N)^2$$

where C_H, C_{lu} , C_{bs}, and C_{ff} are constants representing

C_H = matrix fill-time

C_{lu} = lu decomposition of matrix

C_{bs} = backsubstitution

C_{ff} = far field calculation

If there are 40 strips and 5 collocation points per strip with 200 far field backscattering calculations

$$flops_{MOM} = (C_H + C_{lu}(40 \cdot 5) + 200C_{bs} + c_{ff}) \cdot (40 \cdot 5)^2$$
$$\approx 8 \cdot 10^6 \cdot (C_{lu} + C_{bs})$$

Designing any large grid or trying to design two dimensional grids becomes unreasonable with such large computation times. Consequently, I have tried three other approaches to accelerate the process. First, I tried physical optics, then making the impedance matrix sparse, and finally using fewer collocation points.

Physical optics works well for modeling resistive strips, but doesn't model grids of perfectly conducting strips well [3]. The same optimization was performed with physical optics calculations, then the backscattering pattern was calculated using the MOM. The results were quite poor. Interactions between the strips are too strong to ignore.

Next, I tried working with a sparse impedance matrix. Unfortunately, the coupling between the strips is so strong, that the matrix is very full. Eliminating smaller matrix elements makes the calculations very inaccurate.

Finally, I tried using only one collocation point per strip when calculating the current density. Since the matrix solver takes on the order of $(MN)^3$ operations, the matrix solve time is reduced by 403/2003 = 0.008. This alternative works quite well. Although the backscattering calculations are off by as much as 1 dB, they are accurate enough to give excellent results. Better results could be obtained with an iteration or two of the genetic algorithm calculating the current densities with 5 pulses per strip and using the 1 pulse per strip result as a seed. This acceleration method offers the best tradeoff between accuracy and speed.

IV. Conclusions.

This paper showed how to optimize the backscattering pattern of a grid of perfectly conducting strips by adjusting the widths and spacings of the strips. A 40 element grid was optimized to yield a maximum relative sidelobe level of -20 dB in the backscattering pattern. The genetic algorithm optimization is quite slow on serial machines. In order to accelerate the convergence, the surface current calculations were made using 1 pulse per strip.

References.

[1] J. H. Holland, "Genetic algorithms," Sci. Amer., Jul 1992, pp. 66-72.

[2] D. E. Goldberg, *Genetic Algorithms*. New York: Addison-Wesley, 1989.

[3] R. L. Haupt, "Backscattering from aperiodic resistive grids using physical optics," National Radio Science Meeting, Boulder, CO, Jan 95, p. 292.

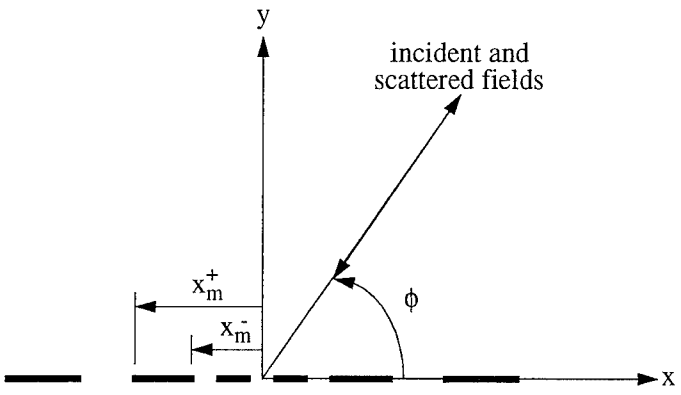


Figure 1. Diagram of an aperiodic grid of perfectly conducting strips.

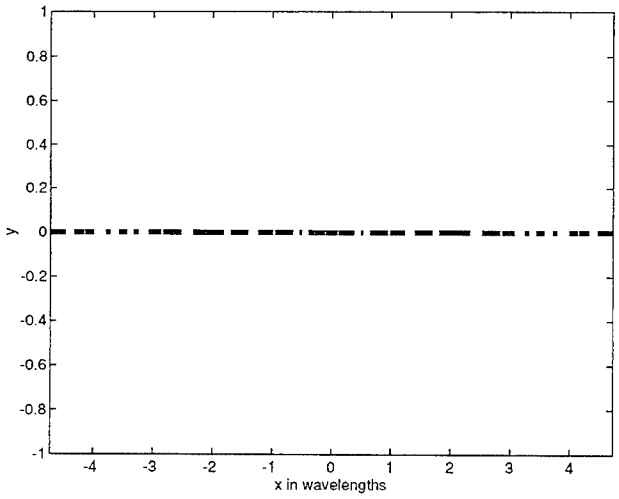


Figure 2. Diagram of optimized perfectly conducting grid.

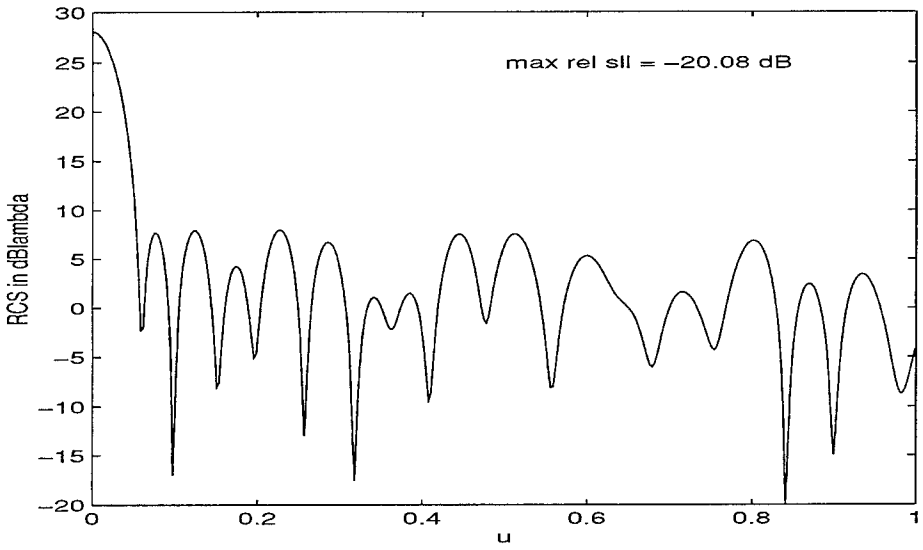


Figure 3. Backscattering pattern from an optimized aperiodic grid of perfectly conducting strips.

ACCURATE MOM SCATTERING CALCULATIONS USING MASSIVELY PARALLEL COMPUTATION

Laura D. Vann and Jonathan S. Bagby
Department of Electrical Engineering
Florida Atlantic University
Boca Raton, Florida 33431
(407)367-3462, FAX (407)367-2336, E-mail bagby@acc.fau.edu

ABSTRACT

Computational accuracy has been widely recognized as a critical issue in applied electromagnetics. At the same time, many applications involve a conflicting design goal of maximum computational efficiency. This paper summarizes a study of applications of massively parallel high performance computing to analysis of electromagnetic scattering from a number of targets. Specifically, this paper focuses on the use of andvanced numerical techniques and massively parallel computing in implementation of the method of moments (MOM) to numerical solution of integral equation electromagnetic scattering formulations. The goal of this effort is to increase numerical accuracy without sacrificing computational efficiency.

The main thrust of the work reported here is to explore several strategies for improving the accuracy of method of moments (MOM) calculations of electromagnetic scattering from metallic, dielectric, and resistive bodies. These strategies, involving more intensive computation than less accurate conventional techniques, are ideally suited for implementation on a massively parallel high-performance computer. The greatly improved capabilities of the computational platform coupled with improved numerical techniques results in greatly enhanced accuracy while maintaining adequate computational efficiency.

The MOM solution technique provides numerical solutions at the cost of requiring manipulation of very large systems of algebraic equations whose coefficients are often given in terms that are computationally expensive. For this reason, this work emphasizes strategies to minimize computation time and storage requirements. Some of these strategies include adaptive partitioning of the scattering body; non-uniform partitioning of the body; and the usage of alternative basis functions, including basis functions incorporating the correct singular behavior near edges. The residual and the singular value decomposition (SVD) are used to diagnose solution convergence and accuracy.

Results to be presented show promise of attaining the goal of simultaneously enhancing accuracy while maintaining acceptable efficiency, especially on massively-parallel platforms. Specific cases to be presented include application of the strategies outlined above to the cases of scattering from 2-dimensional metallic and dielectric scatterers.

1. INTRODUCTION

1.1 Background

Computational accuracy has been widely recognized as a critical issue in applied electromagnetics. At the same time, many applications involve a conflicting design goal of maximum computational efficiency. This paper summarizes a study of new techniques implemented on both scalar and massively

parallel high performance computers to analysis of electromagnetic scattering from a number of targets. The goal of this effort is to use new numerical techniques on scalar and massively parallel computaters to improve computational accuracy without sacrificing computational efficiency.

Integral equation formulations such as the MOM are one of the most widely used analytical approaches in the area of computational electromagnetics, and are the formulations utilized in this work. Some of the reasons for the popularity of integral equation approaches include the following: a) integral equation formulations are typically bounded, unlike their differential counterparts, leading to improved numerical stability; b) such approaches comprise an exact formulation of Maxwell's equations, and approximations are introduce only in the numerical solution of the exact formulation; c) the electromagnetic boundary conditions are incorporated in a natural manner into the formulation; and d) a host of standard, well-understood techniques exist for the numerical solution of integral equations.

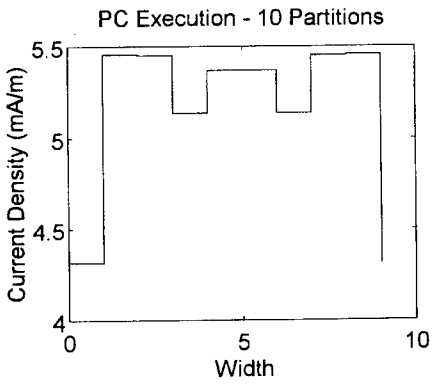
The MOM is noted for its general applicability and accuracy. However, these advantages typically accrue at the cost of requiring manipulation of large systems of algebraic equations whose coefficients are often given in terms that are computationally expensive. For this reason, this work emphasizes strategies to minimize computation time and storage requirements. Some of these strategies include adaptive partitioning of the scattering body; non-uniform partitioning of the body; and the usage of alternative basis functions, including basis functions incorporating the correct singular behavior near edges. The residual and the singular value decomposition (SVD) are used to diagnose solution convergence and accuracy.

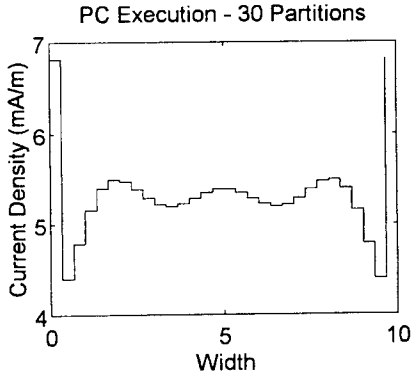
The primary computational platforms used in this study include a Macintosh Quadra (68040 processor), a 486-DX2 PC, a Sun Sparc20, and a massively parallel DECmpp 12000 (MasPar) computer. This SIMD computer, together with five DEC 5000 workstations, has been donated to Florida Atlantic University by Motorola, Incorporated. The data processing unit of the MasPar consists of 4096 processors, each with 64 kB of memory, connected by X-net and a global router. The programming language used is Fortran 90, with C++ available for later applications.

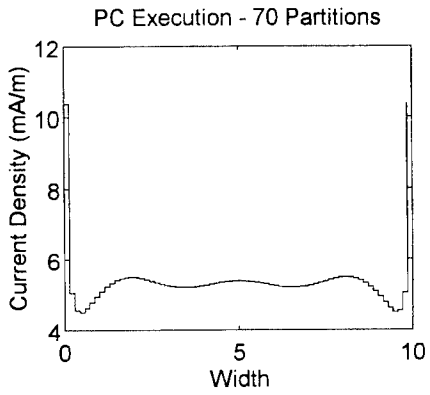
Results to be presented show promise of attaining the goal of simultaneously enhancing accuracy while maintaining acceptable efficiency. Specific cases to be presented include application of the strategies outlined above to the cases of scattering from 2-dimensional metallic and dielectric scatterers.

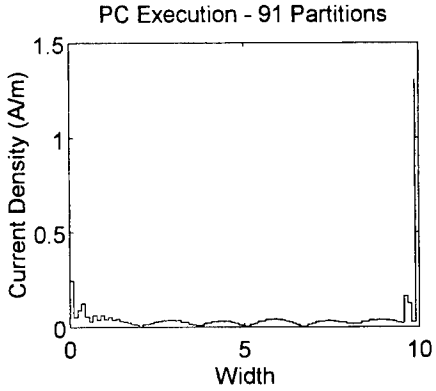
1.2 Typical Results

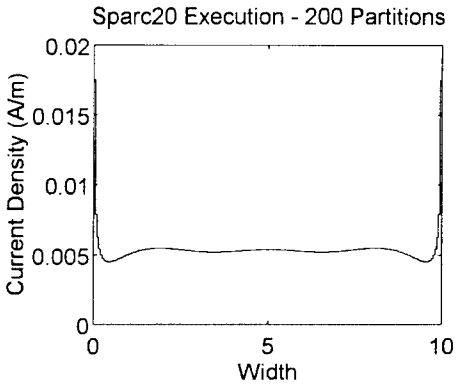
The figures below depict typical results of several computations of the longitudinal current distribution in the TM case on a two-dimensional perfectly-conducting strip.

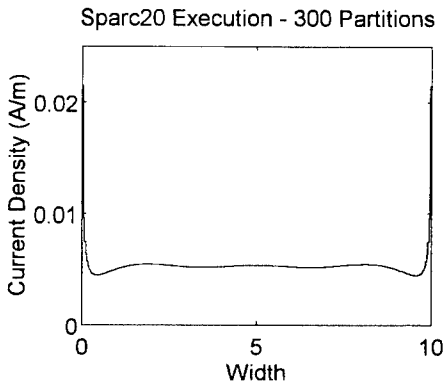


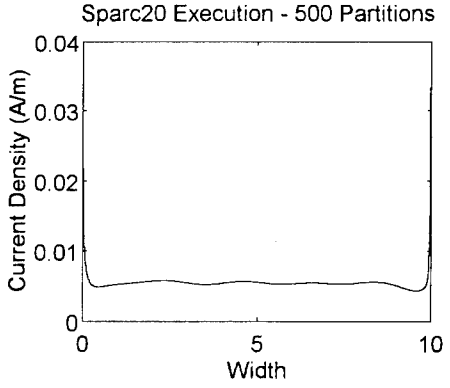



PC Execution - 70 Partitions
Current Density (mA/m)
12
10
8
6
4
0
5
10
Width


PC Execution - 91 Partitions
Current Density (A/m)
1.5
1
0.5
0
0
5
10
Width


Sparc20 Execution - 200 Partitions
Current Density (A/m)
0.02
0.015
0.01
0.005
0
0
5
10
Width


Sparc20 Execution - 300 Partitions
Current Density (A/m)
0.02
0.01
0
0
5
10
Width


Sparc20 Execution - 500 Partitions
Current Density (A/m)
0.04
0.03
0.02
0.01
0
0
5
10
Width


Sparc 20 Execution - 1000 Partitions
Current Density (A/m)
0.06
0.04
0.02
0
0
5
10
Width

The solution technique used is the usual MOM formulation with pulse-function expansion and point matching. The two data sets were obtained from two common computers: a 486-DX2 and a Sun SPARC-20. In each case, the number of partitions of the strip (and hence the number of unknowns in the resultant matrix equation) were gradually increased.

It is obvious that use of too few partitions leads to an unacceptable "stair-step" approximation of the actual continuous current distribution. As the number of partitions is increased the "stair-step" approximation becomes closer to the expected continuous current distribution. The residual R may be used to measure the deviation of the "stair-step" approximation of the current distribution from the actual continuous current distribution. If we denote the exact current distribution on the strip as $J_z(x)$ and denote the MOM approximation to the current distribution on the strip as $\tilde{J}_z(x)$, then the residual is defined as $R = \left\| J_z(x) - \tilde{J}_z(x) \right\|$. It is most usual to use the Euclidian norm, $R = \int \sqrt{J_z^2(x) - \tilde{J}_z^2(x)}\, dx$, in computations.

The residual forms a "figure of merit" which decreases as the MOM approximation to the current distribution increases in accuracy. Note that for partition numbers below a certain limit, the residual decreases as the number of partitions increases. This leads to common conclusion among users of the MOM: a larger number of partitions gives a better result for the unknown.

However, the figures show that this rule of thumb cannot be used indiscriminately. We see that use of too large a number of partitions results in current distributions which are obviously erroneous. A complicating factor is also apparent from the figures: the Sparc20 can handle more partitions than the 486-DX2 before giving spurious results. The qualitative reason for this discrepancy is that the Sparc20 uses a larger binary word-size to represent numbers, and thus the round-off errors causing spurious results for large number of partitions do not become debilitating until a larger number of partitions are used.

The condition number C of the MOM matrix may be used as a figure of merit in determining how nearly singular, and hence how prone to round-off error, the MOM system of equations is. The smaller the condition number of the MOM matrix, the less round-off errors will affect the solution.

There is a well-known numerical routine, called the Singular Value Decomposition (SVD), which may be used to compute the condition number of matrix. We make use of the SVD routine found in LINPAC. The SVD may also be used for many other useful matrix operations. It can be used to invert the linear system, it can be used to solve in cases where the number of equations and unknowns are not equal, and it can be used to give an accurate solution even in cases where the linear system is ill-conditioned (with a condition number which is too large).

Returning to the figures, we see that we have two conflicting sources of numerical error in our solutions: increasing the number of partitions reduces the residual, giving better current distributions, but increasing the number of partitions too far increases the condition number of the linear system, leading to inaccurate solutions due to round-off error.

1.3 Goal of Study

In this study we will use the residual and the condition number in conjunction with the MOM in order to obtain optimally-accurate solutions to electromagnetic scattering problems. Since both the residual and the condition number of a MOM system may be computed automatically, the computer can be programmed to alter the number of partitions used, and can itself decide when the optimal solution is achieved. In addition, the same code can be run on different machines with differing word-sizes, and the optimal solution obtained will be optimal for the particular computer used. For example, on a 486-DX2,

the optimal solution may be obtained for 90 partitions, whereas for a Sparc20 the optimal solution may be obtained for 300 partitions.

The drawback to this automated solution technique is computation time. The SVD routine is an N^4 operation, where N is the number of partitions. Then the solution must be repeated for varying numbers of partitions until an accuracy figure of merit (combining R and C) is minimized. For this reason, this automated solution technique is ideally suited for high-performance computing. Since the bulk of the computation is linear algebra, a massively-parallel SIMD machine, such as the MasPar, is an ideal computational engine.

2. FORMULATION

2.1 Discussion

The mathematical formulation used here is the standard MOM technique adapted to the TM and TE cases of field incidence. In the TM case the incident electric field, and hence the induced currents, are along the axis of the cylindrical body of infinite length. In the TE case the incident field, and hence the induced currents, are transverse to the axis of the cylindrical body of infinite length.

The general integral equation in either case is obtained by equating the total tangential electric field on the conducting body to zero. Denoting the incident electric field as $\vec{E}^i$, the scattered electric field as $\vec{E}^s$, and a unit tangent vector to the conductor as $\hat{t}$, we demand $\hat{t} \cdot \vec{E}^s = -\hat{t} \cdot \vec{E}^i$. In terms of the current $\vec{J}(\vec{\rho})$ on the cylinder, this gives the integral equation

$$\hat{t} \cdot (k^2 + \nabla \nabla \cdot) \int_S G(\vec{\rho}, \vec{\rho}') \vec{J}(\vec{\rho}')\, dS' = -j\omega\varepsilon\, \hat{t} \cdot \vec{E}^i(\vec{\rho}), \quad \vec{\rho} \in S$$

Here $G(\vec{\rho}, \vec{\rho}')$ is the two-dimensional unbounded-space Green's function $G(\vec{\rho}, \vec{\rho}') = \frac{1}{4j} H_0^{(2)}(k|\vec{\rho} - \vec{\rho}'|)$.

This equation will be specialized to the TM and TE cases in numerical implementation. We begin with the TM case.

2.2 TM Case

The above integral equation simplifies for TM incidence to

$$k^2 \int_S G(\vec{\rho}, \vec{\rho}')\, J_z(\vec{\rho}')\, dS' = -j\omega\varepsilon E_z^i(\vec{\rho}), \quad \vec{\rho} \in S$$

We will analyze the simplest case of scattering from a flat, perfectly-conducting strip of width w. Using pulse-function expansion and point-matching results in the linear system $\sum_{j=1}^{N} A_{ij} x_j = b_i, \ i = 1, \cdots, N$. Here the matrix elements and forcing vector are given by

$$A_{ij} = \frac{\omega\mu\Delta}{4} \begin{cases} H_0^{(2)}[k\Delta(i-j)], & i \neq j \\ \left[1 - j\frac{2}{\pi} \log\left(\frac{\gamma k\Delta}{4e}\right)\right], & i = j \end{cases}, \quad b_i = E_z^i\left(k\Delta\left(i + \tfrac{1}{2}\right)\right)$$

This case was implemented on a 486-DX2 and a Sun SPARC-20 with the results shown above.

2.3 TE Case

The above integral equation simplifies for TE incidence to

$$k^2 \int_S G(\vec{\rho}, \vec{\rho}')\, J_t(\vec{\rho}')\, dS' - \frac{\partial}{\partial t} \int_S G(\vec{\rho}, \vec{\rho}')\, \frac{\partial}{\partial t'} J_t(\vec{\rho}')\, dS' = -j\omega\varepsilon E_t^i(\vec{\rho}), \quad \vec{\rho} \in S$$

We will again specialize to the simplest case of TE scattering from a flat, perfectly-conducting strip of width w. Using triangle-function expansion and pulse-function matching results in the linear system $\sum_{j=1}^{N} A_{ij} x_j = b_i, \; i = 1, \cdots, N$. Here the matrix elements and forcing vector are more complicated, and will not be shown.

This case was implemented on a Macintosh Quadra and a Sun Sparc20 with results very similar to those of the TM case.

2.4 Adaptive Uniform Partitions

The figure of merit formed by the residual and the condition number of the linear system may be used to implement an adaptive partitioning scheme. Such a code could find the solution of optimum accuracy on any given machine. The code would begin with a coarse partitioning of the scatterer, such as $N = 15$, and increase the number of partitions by ten in each loop. By monitoring the figure of merit, the number of partitions would keep increasing until the residual grows too large and the condition number of the linear system increases too far.

The adaptive code would increase the number of partitions to approximately 90 on the 486-DX2, to approximately 150 on the Macintosh Quadra, and to over 1000 on the Sparc20.

2.5 Adaptive Non-Uniform Partitions

The condition number of the matrix of the MOM system becomes large when rows of the matrix become nearly equal. This problem occurs in those rows of the MOM matrix which correspond to expansion coefficients which are nearly equal and are far from the edges of the scatterer ($j = 1$ and $j = N$). At such locations the current distribution is slowly varying compared to the current variation near the edges of the structure.

A method of improving the accuracy of the solution while maintaining or reducing the number of partitions exists. This technique is to use larger partition sizes at locations of slowly-varying currents, and smaller partition sizes at locations of rapidly-varying currents (such as edges). We are in the process of implementing this strategy, and numerical results will be available for presentation shortly.

2.6 Singular Edge Basis Functions

Another strategy for improving the accuracy of the solution without increasing the number of

partitions is to use appropriate basis functions near scatterer edges. There are well-known results for the singular behavior of longitudinal currents near edges and angular joints in perfect conductors. The basis functions at these locations may be chosen to incorporate the correct edge singularities in such cases. The fact that the basis function models the actual current better than pulse-functions or triangle-functions should allow for the use of fewer basis functions near these edges, thus improving accuracy while reducing the order of the resultant linear system.

3. IMPLEMENTATION

3.1 Scalar Implementation

The implementation of the adaptive uniform partitioning scheme for the case of TM and TE scattering from a perfectly-conducting strip is complete. Implementation of the technique of non-uniform adaptive partitioning is proceeding, and initial results look promising. Final results will be available shortly.

The formulation involved in utilization of singular edge basis functions is underway. Initial numerical results of this technique should be forthcoming shortly.

3.2 Massively-Parallel Implementation

Initial results for implementation of the adaptive uniform partitioning scheme on the MasPar have been obtained. Porting the scalar code to the MasPar has been greatly facilitated by the extensive linear algebra libraries which exist for the machine (even via the Internet). The most computationally-intensive portion of the code, calculating the Singular Value Decomposition, exists as subroutine ready to use.

To date we have ported our code to the MasPar with only the SVD subroutine executing in Fortran 90. This means that much of the overhead code is executed on the DEC 5000 front-end, and only the most numerically-intensive linear algebra portions (such as SVD) execute on the Data Procession Unit (DPU).

Other portions of the code could benefit from parallel execution, and these segments are currently being re-written for execution on the DPU. Initial results of parallel execution show the expected dramatically-decreased time of execution, but the optimal number of partitions in the MasPar is quite small. Initial results indicate that the optimal number of partitions is on the order of 100, comparable to the results of the 486-DX2. The probable reason for this is that each of the 4096 processors in the DPU are relatively simple, unlike the Alpha processors in the Sparc20.

As the more complex versions of the code are completed for scalar execution, they will be adapted for parallel execution on the MasPar.

4. CONCLUSIONS

4.1 Results to Date

The final results obtained to date indicate that an adaptive uniform partitioning strategy could provide a valuable tool in the accurate MOM analysis of scattering from two-dimensional conducting bodies in a multi-platform environment. The optimal results will be obtained regardless of the machine utilized in the computation.

The adaptive uniform partitioning code has been ported to the MasPar with only the SVD subroutine executing in Fortran 90. Incremental modification of the remainder of the code is underway to reduce the

amount of overhead code that is executed on the DEC 5000 front-end, and total code execution on the (DPU) should be forthcoming shortly..

The non-uniform adaptive partitioning technique is nearly complete for scalar execution. Scalar and parallel results should follow easily. Incorporation of singular edge basis functions is in the formulation stage. Initial results should be available in the near future.

5. ACKNOWLEDGEMENTS

The authors would like to acknowledge the Paging and Telepoint Systems Group of Motorola, Incorporated for their generosity in providing the MasPar and DEC workstations necessary for the massively-parallel portion of this work.

The authors would also like to acknowledge the U. S. Department of Energy for fellowship support provided to L. D. Vann through the Computational Science Graduate Fellowship Program administered by Ames Laboratory.

486DX/2 PC:

PARTITIONS	CONDITION NO.	RESIDUAL
10	2.7513	1.207E-06
30	9.2855	2.4497E-06
70	22.5319	6.0799E-06
90	29.0802	6.9620E-06
91	453.7234	157.0928

SUN Sparc20:

PARTITIONS	CONDITION NO.	RESIDUAL
10	2.7513	1.5926E-06
30	9.2855	5.0160E-06
70	22.5319	1.0479E-06
90	29.0802	7.7640E-06
91	29.4072	1.2630E-05
100	64.9570	1.4202E-05
200	64.9570	1.4202E-05
300	97.5237	2.2250E-05
500	161.931	1.13675
1000	324.253	1.59322

A New Angle on a Low Cost Ground Screen for Model Testing in the Undergraduate Antennas Laboratory (Looking at Near Vertical Incidence Skywaves (NVIS) for a Coast Guard Patrol Boat)

by Professor M. E. McKaughan
LCDR W.M. Randall
United States Coast Guard Academy

and
ENS Brian Nutter
U. S. Coast Guard Cutter Chase

Abstract

For the past five years the U. S. Coast Guard Academy has been conducting research on shipboard antenna patterns using scaled wood models of Coast Guard Cutters painted with a conductive coating. Using a corner of the Antennas Laboratory we set up a anechoic chamber with a horizontal turntable. The results from the models tested have correlated well with the test results from actual cutters and with the Numerical Electromagnetic Code (NEC) approximations.

Last year, as a senior year undergraduate design course project, the Academy was asked to investigate the possibility of using Near Vertical Incidence Skywaves (NVIS) as a method of improving the 110' WPBs (patrol boat) HF communications capabilities. To complete this study, we needed a way to measure the radiation pattern of the antenna/ship/sea surface system. We had previously observed patterns only as a function of equatorial angle, ϕ, with the polar angle, θ, equal to approximately 85 degrees. Other researchers have used an arch system constructed over the ground plane. We attempted to use this technique, but results were unsatisfactory. We came up with a creative way of solving the problem. Instead of moving the illumination antenna over the model, we discovered that we could move the model and ground plane while leaving the illuminating antenna fixed. We constructed a lightweight ground plane that could be mounted vertically. The model was attached to the ground plane, and the entire system was rotated. By changing the aspect of the model on the ground plane through 90°, we were able to collect pattern cuts over the entire hemisphere above the "sea surface".

The results from the testing showed that the rotating ground plane worked and that NVIS showed some promise for the 110' patrol boats. Funding for work on the project was continued. This year, a second student will test alternative NVIS antenna designs, and investigate HF circuit behavior using the "Prophet" propagation prediction software. Finally, we anticipate implementing the most promising antenna design on an actual Coast Guard patrol boat.

It is our hope that the ideas presented here will be of value in the undergraduate Antenna Laboratory to help students better understand the idea of a three-dimensional antenna radiation pattern. We have found the technique helpful in our research and an inexpensive solution to the problem of observing the electromagnetic field over the ground plane.

Background

Our normal method of measuring antenna patterns has been to place the ship model on a copper topped turn table four feet in diameter. This table top rotates through 360°. We illuminate the model and table with a transmitting antenna outside the anechoic corner, and record the magnitude of the signal received on the model antenna. This technique gives us azmuthal information, but no elevation information. Moving the illuminating antenna, while possible presents new problems with in-room reflections since our chamber is only one corner of our Antennas Laboratory room.

To obtain elevation information from our models, one possible approach is to construct an arch over the rotating table top. We could then illuminate the model with an antenna that moved over the arch. This technique is used by the antennas group at the Naval Undersea Warfare Center in New London, CT.

A couple years ago we constructed such an arch to measure elevation information from a simple monopole antenna. After repeated attempts, we concluded that the feed cable for the arch-mounted antenna was contaminating the results, and that this arch method would not work in our simple-minded antenna chamber. To develop a more refined system using an arch arrangement over the ground plane would require the receiver or transmitter to ride on the arch. This sounded expensive and more complex than we were willing to implement.

Azmuthal patterns in the elevation plane

During discussions with the co-authors, our student asked the silly question, "Why not turn the table on edge and rotate the whole thing in the plane that we usually rotate the antennas in the chamber?" We thought about this ridiculous suggestion for a couple minutes, and then we decided that the idea was perhaps not so far out of the plane of possibilities.

Design Considerations

Developing a functioning ground plane required us to consider four major criteria. First, the entire system had to be light enough to be turned by our existing rotating system. This system was capable of turning a weight of less than 25 kg's. Second, we needed a ground plane that would be rigid enough so that it would not flex during rotation. We were able to determine that starting and stopping were the times of largest flex. The third problem area we addressed was how to change the orientation of the model so that we could observe elevation pattern information at different azimuths with respect to the bow of the ship. The final problem to be resolved was how to defy the law of gravity and keep the ship model firmly in contact with the ground plane surface. On the table this had not been a problem because gravity was very cooperative.

Viewed from the completed project side of this effort, many of the aspects of this solution seem obvious. While there is clearly not too much rocket science included in our solution to the problem, I believe that the student was creative in viewing the entire problem from a new angle. A sketch of the final results is presented in Figure 1. While a thousand words have been saved by using this figure, allow me to point out some important details. First, note that while one would first expect that we could have to rotate the model 180° on the ground plane to get an entire set of elevation patterns for the model, after carefully trying a couple orientations, one quickly can see that we only need to move the model through 90° to get complete elevation information. One other consideration which is obvious to us, but not necessarily to the student at first is the requirement that all hardware holding the ship in place should be non-conducting material so as to not interfere with the antenna radiation pattern. Developing a clamping arrangement that would hold the model firmly against the ground plane and made out of wood was rather challenging. Our electronics technician did a wonderful job fabricating the clamps and wooden bolts that are now used.

Advantages of this approach

There are four advantages to this approach based on the anechoic chamber that we have at the Coast Guard Academy. First of all, we were able to use the existing instrumentation that we use for normal equatorial patterns. Second, the solution was inexpensive to implement. Third, we use the same software that we use for azmuthal pattern collection since we are using the same rotation system that we have used previously. Fourth, the entire ground plane and model system attached to a fiberglass pole and can be installed and removed by no more than two people.

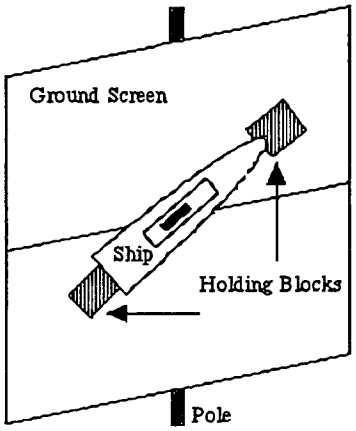


Figure 1. Sketch of vertical ground screen with ship model mounted. This orientation will give a pattern cut over the top of the ship at an azmuthal angle of about 40° off of the starboard bow to 40° off of the port side of the stern.

Disadvantages we have found

One major disadvantage we have found is securely clamping the model to the ground plane. At some aspect angles the model stays in place well, but in other orientations the model wants to jump out of the holding blocks. Our simple solution for this problem is to tie the model in place with a piece of string. A second less significant disadvantage is that the ground plane rotates through 360°. When the ground plane is between the model and the transmitting antenna, the information is meaningless. We choose to ignore this part of the data and present data observed when the antennas on the ship model are "above the horizon."

Experimental Results

Figure 2 presents the results of testing the ship model on the vertical ground screen in our anechoic chamber. Tests were conducted at a scaled frequency of 6.0 MHz and we used four different model orientations of the model. The first pattern (0°) was run with the model oriented so that the pattern cut from from bow to stern over the top of the model. We then did plus and minus 45° and the 90° cut was what we sailor call the athwartship pattern cut. Points that became important, from the student's perspective were the overhead points and points at the horizon. Initially, Mr. Nutter collected the antenna patterns on different days, and did not attempt to normalize anything to what he had observed earlier. When the patterns were superimposed, he concluded that his data was less than perfect because the patterns failed to align at these points. Again, while obvious to us, to the student, this point became a key to understanding of what was really going happening with the patterns. We reran the patterns, paying careful attention to the signal levels and equipment settings, and the results agreed as can be seen in Figure 2.

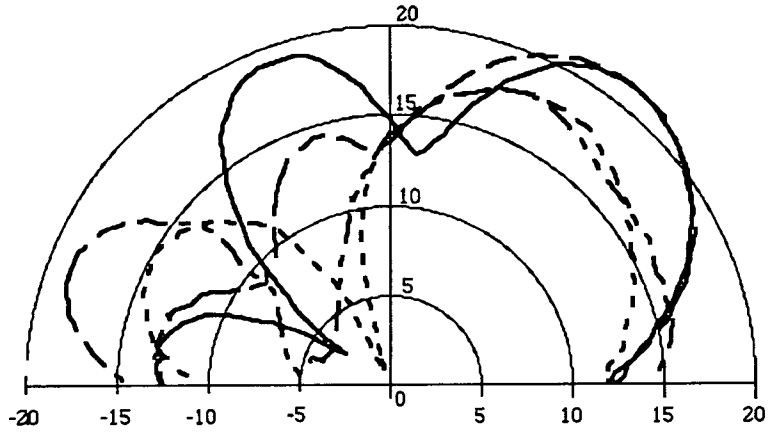


Figure 2. Measured radiation patterns from 110' patrol boat model at scaled frequency of 6.1 MHz. and at angles of -45°, 0°, 45°, and 90° with respect to the ship's bow. Notice agreement at the horizon and directly overhead.

Figure 3 presents the results of one NEC run of our model at a frequency of 6.0 MHz with the pattern cut set for "over the keel" or 0° from stern to bow. Based on general shape of the pattern, we were quite excited about these results. Figure 4 shows a comparison of the data from the anechoic chamber and the NEC generated pattern on the same axis. Obviously, we have some magnitude disparities that must be resolved. One immediate observation that we make is that generally, the shape of the patterns is similar. A second observation is that the NEC pattern is assuming a perfect ground, while our vertical ground screen is not a perfect ground, but appears to be more like we would expect from a sea surface.

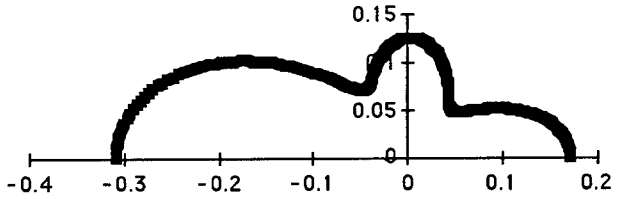


Figure 3. Radiation pattern predicted by NEC at a frequency of 6.0 MHz from bow to stern over the top of the model (0° azmuth).

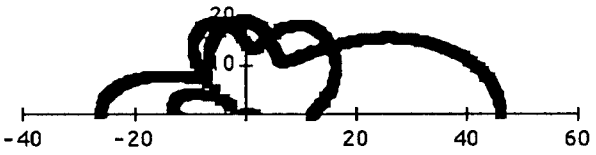


Figure 4. Comparison of the ratiation patterns measured in our anechoic chamber and predicted using NEC code. Note especially the similarity in general shape. The differences in levels at the horizon are still being investigated.

Conclusions

A light weight rotatable ground plane was constructed that would hold a model ship vertically so that elevation antenna patterns could be observed by rotating the ground plane and ship azmuthally. By changing the orientation of the ship model on the ground plane pattern cuts at different angles are recorded. Patterns observed on this ground plane have been compared to numerical results generated by the Numerical Electromagnetic Code. The patterns from both methods agree favorably. This simple technique will be used more as we continue our research into antenna characteristics on Coast Guard Ships. This rotating vertical ground plane is a simple method of observing antenna elevation patterns without resorting to expensive arch systems with the accompanying arch mounted probes.

Acknowledgments

We would like to thank Petty Officer James Lobianco for his initiative and careful craftsmanship in constructing the rotatable ground plane and the ship holding clamps. Without his insight into potential problems, we would probably have destroyed the model by dropping it onto the floor more times that it could tolerate.

EFFICIENT EXTRACTION OF THE NEAR-FIELD FROM CGFFT METHODS APPLIED TO SCATTERERS IN THE RESONANCE REGION

A. McCowen

Department of Electrical and Electronic Engineering

University of Wales, Swansea, UK

Abstract

Conjugate gradient FFT (CGFFT) methods have previously been reported for inhomogeneous dielectric scatterers and planar conductors and both far-fields and current distributions on the scatterer have been included. This paper will explain how the near-fields can be efficiently determined from such methods. A comparison of near-field results will be given with method of moment solutions for mixed dielectric/pec scatterers in the resonance region.

INTRODUCTION

Conjugate gradient FFT (CGFFT) methods have previously been reported to solve the electric field integral equation (EFIE) for scatterers in the resonance region. In common with most method of moment (MoM) schemes CGFFT methods usually solve for the current distribution on the scatterer from which far-fields can be determined with negligibly CPU costs via standard techniques.

The determination of near-fields in a local region to the scatterers is not as straightforward as that for the far-fields. In the MoM schemes the impedance matrix has to be recalculated and this along with further matrix multiplications, can take a significant amount of CPU for a scatterer in the resonance region. This procedure would need to be repeated, possibly many times, to "see" the whole near-field region associated with a scatterer and would rapidly exhaust most computing facilities.

This paper will discuss how near-fields can be efficiently determined via CGFFT methods [1, 2, 3] at a fraction of the computing costs associated with standard MoM schemes. Near-field plots which have been locally validated against a MoM code which solves the combined field integral equation (CFIE) [4], will be given for a range of dielectric and mixed dielectric/pec scatterers in the resonance region.

EVALUATING NEAR-FIELDS

There are basically 3 classes of scatterer to which the CGFFT schemes have been applied, namely inhomogeneous dielectrics [2] resonant pec plates [1] and mixed dielectric/pec scatterers [3]. The computation of the near-fields is similar for each of these schemes and will be discussed for the mixed dielectric/pec scatterer problem. The scheme uses a pulse-basis formulation to solve the EFIE and takes the form

$$\begin{bmatrix} G_{cc} & G_{cd} \\ G_{dc} & G_{dd} \end{bmatrix} \begin{bmatrix} J_c \\ J_d \end{bmatrix} = \begin{bmatrix} E_c^{\,i} \\ E_d^{\,i} \end{bmatrix} \tag{1}$$

where $E_c^{\,i}$ and $E_d^{\,i}$ are the known incident fields on the conductor and dielectric regions respectively, J_c is the unknown induced current on the pec surfaces and J_d the unknown polarization current in the dielectric. The Green's dyadic terms in the impedance matrix represent the self and mutual coupling between the different regions. The significance of the CGFFT scheme is that the FFT of each of the blocks in the impedance matrix requires only a storage of order N, where N is the number of unknowns, whereas the equivalent blocks in the spatial domain of MoM schemes typically require a storage of order N^2 and N can be very large for a resonant structure.

Once a solution to (1) has been computed the matrices G_{cc} etc can be readily expanded to G_{cc}^{exp}, etc with a regular mesh into the whole of the near-field region. The current matrices are also expanded filling in the region outside the scatterer with zeros. Thus whole regions of the scattered near-field E_s, can be computed using expanded versions of either the top or bottom row of (1), eg. using the top row:

$$\begin{bmatrix} G_{cc}^{\,exp} & G_{cd}^{\,exp} \end{bmatrix} \begin{bmatrix} \begin{bmatrix} J_c \\ o \end{bmatrix} \\ \begin{bmatrix} J_d \\ o \end{bmatrix} \end{bmatrix} = \begin{bmatrix} E_s \end{bmatrix} \tag{2}$$

RESULTS

Near-fields will be shown from several mixed dielectric/pec scatterers and these will be compared to the results from the MoM applied to the C.F.I.E. A typical example of the computed near-field is shown for the scatterer given in Fig. 1 which comprises a dielectric cuboid centrally placed in contact with a pec plate in the x-y plane. The scatterer is illuminated along the -z axis with an x-polarised plane wave.

Fig. 2 shows the magnitude of the x-component of a section of the scattered electric field for the case of a $0.2\lambda_o$ dielectric cube of permittivity $\varepsilon_r = 9$ and a square pec plate of side $0.4\lambda_o$. The section is taken perpendicular to the y-axis through the centre of the scatterer. The plot clearly identifies the scattering centres associated with the edges of the pec plate and the faces of the cube. A uniform grid mesh of $0.033\lambda_o$ was used results in a 12 x 12 x 6 solution domain for the CGFFT method. When the solution had been determined the domain was expanded with the same mesh,

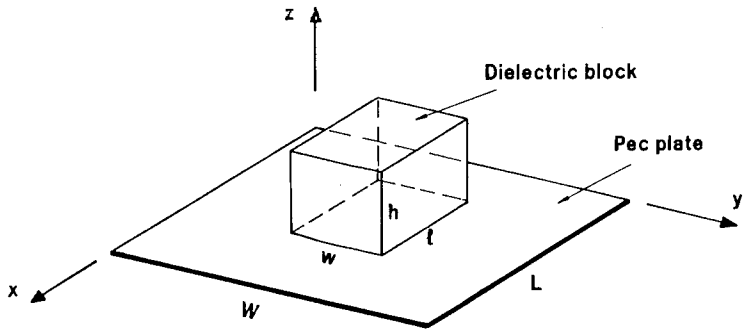


Fig. 1 A mixed dielectric/pec scatterer

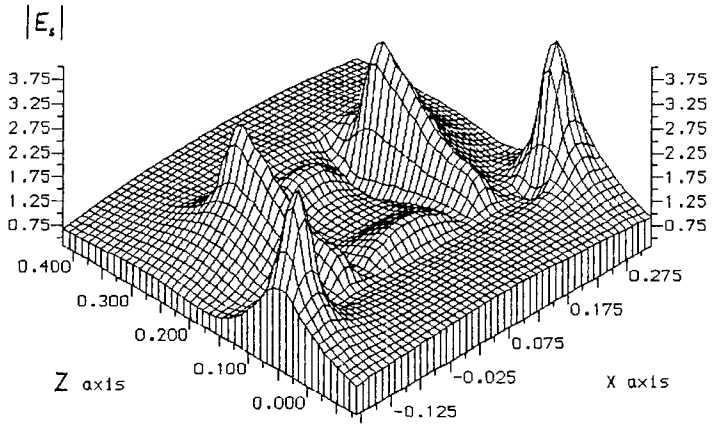


Fig. 2 $|E_x|$ through the centre of the scatterer in Fig. 1 in a plane perpendicular to the y-axis

to 18 x 18 x 12 to compute the near-field surrounding the whole scatterer. Views of the near-field as given in Fig. 2 are then only restricted by the graphics available to the user and further views require no more computations.

REFERENCES

[1] T.V. Tran and A. McCowen, 'An improved pulse-basis CGFFT method for the thin conducting plate problem', IEEE Trans AP-41, pp 185-190, February 1993

[2] T.V. Tran and A. McCowen, 'A unified family of FFT-based methods for dielectric scattering problems', J of Electromagnetic Waves and Applic., vol 8, No. 8, pp 973-992, 1994

[3] A. McCowen, 'A CGFFT method applied to the scattering from finite size microstrip antenna'. see this proceedings.

[4] S.M. Rao, D.R. Wilton and A.W. Glisson, 'Electromagnetic scattering by surfaces of arbitrary shape', IEEE Trans. AP-30, pp 409-418, May 1982

SESSION 4B:

VISUALIZATION & INTERFACES

COMPUTER CODE FOR FIELD CALCULATION AND VISUALIZATION IN QUASIOPTICS

Yuri V.Kopylov

Institute of Terrestrial Magnetism, Ionosphere and Radio Wave Propagation
Russian Academy of Sciences, 142092 Troitsk, Moscow region, Russia

1. Introduction.

For many applications of electromagnetic theory - from radio propagation to X-ray optics, it is extremely useful to have a detailed quantitative and visual representation of the wave field produced by large quasioptic devices being designed and used as antennas, focusing lenses or elements of transmitting lines. An effective tool for interactive computer aided design (CAD) requires selection of a powerful and logically simple computational algorithm and its implementation into a flexible user-friendly computer code. Such program has to permit easy change of the designed system configuration and parameters and immediate display of the effects of each modification.

Quite often, the use of sophisticated analytical methods or time- consuming straightforward numerical algorithms does not allow to reach the desirable effectiveness. A good opportunity to increase the efficiency of field calculations offer the algorithms based on the parabolic equation method. The parabolic equation (PWE) for a slowly varying wave amplitude can be solved numerically much more fast then the exact wave equation. This stimulates an extensive use of the PWE in computer aided design of EM quasioptic systems.

We demonstrate a computer code for IBM-compatible PC's modeling a wide class of quasioptical systems composed from lenses, Fresnel zone plates and similar dielectric elements. Such software can find application in a wide range of EM spectrum including antennas for microwave communication and remote sensing systems, binary optics, X-ray microscopy of biological objects, education and training in optics and diffraction theory, etc.

The mathematical algorithm includes:

- finite-difference approximation of the PWE
- implementation of non-local boundary conditions simulating perfectly transparent boundaries
- a priori applicability criteria of the parabolic equation method
- practical estimates for the finite-difference mesh parameters

The computer code written in C++ programming language provides:

- interactive design and display of the quasioptic system to be simulated
- a restricted library of predefined optical elements
- numerical solution of the PWE
- color graphical display of the calculated field intensity
- interactive calculation regime including breakpoints and field storage.

2. Mathematical Algorithm

We consider diffraction of wave packets with narrow angular spectrum in weak nonuniform media with small permittivity variations $|\varepsilon - 1| \ll 1$. To simplify calculations, we use , instead of the exact wave equation

$$\frac{\partial^2 E}{\partial x^2} + \frac{\partial^2 E}{\partial y^2} + \frac{\partial^2 E}{\partial z^2} + k^2 \varepsilon(x,y,z) = 0 \tag{1}$$

the parabolic wave equation (PWE) [1,2]

$$2ik\frac{\partial u}{\partial z} + \Delta_\perp u + k^2 \left[\varepsilon(x,y,z)E\right] u = 0 \tag{2}$$

for the slowly varying complex amplitude

$$U(x,y,z) = E(x,y,z)e^{-ikz} \tag{3}$$

Being an asymptotic approximation to (1), the PWE (2) describes adequately the main diffraction phenomena ("transversal diffusion" [3]) in the nonuniform dielectric medium as well as the free-space propagation and focusing outside the optical elements. Formally, the applicability conditions of the PWE (2) can be obtained by putting $\varepsilon - 1 = \alpha(x,y,z) = \tilde{\alpha}\left(\frac{x}{a}, \frac{y}{a}, \frac{z}{b}\right)$ where a and b are characteristic scales of transversal and longitudinal nonuniformity of the dielectric permittivity. Estimation of the neglected terms yields:

$$kb \mid \alpha \mid \leq 1, \quad \frac{ka^2}{b} \geq 1 \tag{4}$$

These conditions are usually met for plasma media and X-ray optical elements. In practice, however, the main averaged features of the wave field can be described correctly even under less restrictive assumptions.

If the Fresnel parameter ka^2/b proves to be large, it is possible to omit in (2) the diffusion term Δu which leads to the plane screen approximation

$$u(x,y,b) = u(x,y,0)\exp\left[i\frac{k}{2}\int_0^b \alpha(x,y,z)\,dz\right] \equiv T(x,y)u(x,y,0) \tag{5}$$

for a quasioptical element localized between $z = 0$ and $z = b$.

Outside the optical element, where $\alpha \equiv 0$, the PWE takes the form

$$2ik\frac{\partial u}{\partial z} + \Delta u = 0 \tag{6}$$

and has a general solution

$$u(x,y,z) = \iint_A u(x',y',0)\,G(x-x',y-y',z)\,dx'dy' \tag{7}$$

with

$$G(x-x',y-y',z) = \frac{k}{2\pi iz}\exp\left[ik\frac{(x-x')^2 + (y-y')^2}{2z}\right] \tag{8}$$

Evidently, (7) is nothing but a paraxial approximation of the Kirchhoff integral

$$E(x,y,z) = \frac{k}{2\pi i}\iint\limits_A E(x',y',0)\frac{e^{ikR}}{R}\,dx'dy' \tag{9}$$

However, generally, the complete PWE (2) is to be used to take into account the diffraction processes inside the element body.

Transition from rigorous wave theory to the transversal diffusion approximation leads to the change of kind of the differential equations and to a new formulation of the boundary value problem. In contrast to the elliptic wave equation, the PWE (2) describes the evolution of the wave amplitude in process of almost unidirectional propagation along the optical axis. Physically, it means neglecting the backward reflections from the interfaces and the waves diffracted into large off-axis angles (such approximation is adequate for the variations of the refraction index are supposed to be small).

For the parabolic equation, the Cauchy problem is correct with a given initial distribution $u(x,y,0) = u_0(x,y)$ and with some radiation condition excluding spurious waves coming from infinity. In the process of the numerical solution of the problem demanding truncation of the spatial domain, one has to seek a way of transferring the radiation condition from infinity to a certain finite surface surrounding all the sources and diffractive elements. Since any spurious reflection from this artificial boundary would change the wave field structure, such boundary condition has to provide full transparency for arbitrary radiation from inside.

In a model two-dimensional case, an exact form of the transparency condition

$$\frac{\partial u}{\partial x}(x,\pm A) = \mp e^{-i\pi/4}\sqrt{2k\frac{\partial}{\partial z}}u(x,\pm A)$$

has been found in [4,5].

In three dimensions, we transfer the radiation condition from infinity to an arbitrary cylindric surface $r = A$ surrounding all the dielectric elements using the following generalization of [4,5]:

$$\frac{\partial u}{\partial r}(A,\varphi,z) = \frac{1}{2\pi}\frac{\partial}{\partial z}\int\limits_0^z\int\limits_0^{2\pi} u(A,\psi,\zeta)K(\varphi-\psi,z-\zeta)\,d\zeta d\psi \tag{10}$$

with

$$K(\varphi,z) = e^{-i\pi/4}\frac{\sqrt{k}}{\pi\sqrt{2}}\sum_{m=-\infty}^{\infty} e^{im\varphi}\int\limits_{c-i\infty}^{c+i\infty}\frac{H_m^{(1)\prime}(A\sqrt{2ikp})}{H_m^{(1)}(A\sqrt{2ikp})}e^{pz}\frac{dp}{\sqrt{p}} \tag{11}$$

In the most interesting axial symmetric case, only the term $m = 0$ remains in (11) . Moreover, as usually the integration region is very wide compared with the wavelength ($kA \gg 1$), the Hankel function can be replaced by its far-field asymptotic expression $H_m^{(1)}(t) \sim -\sqrt{2k/\pi t}e^{i(t-\pi/4)}$. Then the zero-order term in (11) can be calculated explicitly:

$$K_0(z) \approx -e^{-i\pi/4}\sqrt{2k/\pi z} \tag{12}$$

which reduces the boundary condition (10) to the form

$$\frac{\partial u}{\partial r}(A,z) = -e^{-i\pi/4}\sqrt{\frac{2k}{\pi}}\frac{\partial}{\partial z}\int\limits_0^z u(A,\zeta)\frac{d\zeta}{\sqrt{z-\zeta}} \tag{13}$$

coinciding the result [4,5].

Confining ourselves to the axial symmetric case, we use the following six-point implicit finite-difference scheme

$$2ik\frac{u_m^{n+1}-u_m^n}{\tau}+\frac{u_{m+1}^{n+1}-2u_m^{n+1}+u_{m-1}^{n+1}+u_{m+1}^n-2u_m^n+u_{m-1}^n}{2h^2}$$

$$+\frac{u_{m+1}^{n+1}-u_{m-1}^{n+1}+u_{m+1}^n-u_{m-1}^n}{4mh^2}+k^2\alpha_m^{n+1/2}\frac{u_m^{n+1}+u_m^n}{2}=0 \tag{14}$$

reducing the PWE (2) to a three-diagonal set of linear algebraic equations. Here, τ and h are the mesh steps in z and r directions, and $u_m^n \approx u(n\tau, mh)$. As the coefficient $\alpha(r,z)=\epsilon-1$ may have discontinuities at the interfaces, a better performance shows the modified scheme where coefficient $\alpha_m^{n+1/2}$ is replaced by its weighted average value

$$\tilde{\alpha}_m^{n+1/2}=\frac{1}{mh^2\tau}\int_{n\tau}^{(n+1)\tau}dz\int_{(m-1/2)h}^{(m+1/2)h}\alpha(r,z)r\,dr \tag{15}$$

given by the integral-interpolation method. The linear equations (14) written for $m=0,1,\ldots,M=A/h$, along with the finite-difference approximation of the transparency condition (13)

$$\frac{u_{M+1}^{n+1}-u_{M-1}^{n+1}}{2h}+2\sqrt{\frac{2k}{i\pi\tau}}\left(u_M^{n+1}-\sum_{s=1}^{n}\gamma_s u_M^{n+1-s}\right)=0 \tag{16}$$

form a complete set of equations which can be solved step by step, from n to $n+1$, by the marching method. The energy balance law

$$\sum_{m=0}^{M} m\mid u_m^n\mid^2 \leq \sum_{m=0}^{M} m\mid u_m^0\mid^2 \tag{17}$$

grants convergence and stability of the scheme (14).

3. Accuracy Estimation

An elementary analysis of accuracy of the PWE approximation can be made, following G.Malyuzhinets, by comparing an exact $2D$ plane wave representation

$$E(z,y)=e^{ik(py+z\sqrt{1-p^2})}, \qquad p=\sin\beta \tag{18}$$

with its "parabolic" analog

$$E^{PWE}(z,y)=e^{ik[py+z(1-p^2/2)]} \tag{19}$$

which satisfies the PWE (6). It is clear that the exponent in (19) corresponds to the first two terms of the Taylor series

$$\sqrt{1-p^2}=1-\frac{p^2}{2}-\frac{p^4}{8}\ldots \tag{20}$$

Demanding the inaccuracy in phase be small compared with π, one gets an applicability criterion of the PWE :

$$p^4 z_{max} \ll 4\lambda \tag{21}$$

It bounds the angle spectrum of the waves accurately described by the parabolic equation at a given distance z_{max}. A more precise approximation of the square root in (4.7) would result in a wide-angle or long-range modification of the PWE.

The same approach can be applied to the error estimation of the finite-difference scheme, used to solve the PWE, on a plane wave functional basis. For the Crank-Nicolson scheme (14) we obtain

$$u_m^n = u(n\tau, mh) = q^n e^{impkh} \tag{22}$$

where

$$q = \frac{1 - i\frac{\tau}{kh^2}\sin^2\frac{pkh}{2}}{1 + i\frac{\tau}{kh^2}\sin^2\frac{pkh}{2}} \tag{23}$$

This solution correctly describes the plane wave (19) in the "parabolic" approximation if the following conditions are met:

$$\frac{pkh}{2} \ll \pi, \qquad \frac{p^2k\tau}{4} \ll 1, \qquad \frac{p^6k^3\tau^2 z_{max}}{96} \ll 1 \tag{24}$$

They allow one to choose the finite-difference grid steps τ and h in order to assure the required accuracy.

The problem encountered in handling practical examples consists in evaluating the spectrum limits of the angles $\beta = sin^{-1}p$ contributing into the wave field in the domain of interest.

For example, the field in the focal region is determined by an integral of the elementary plane waves over the whole aperture of the optical element (lens or zone plate). In this case, the maximum angle of diffraction can be estimated as $\beta_{max} \approx R/f$ where R is the element radius and f is the focal length.

4.Computer Code

The finite-defference algorithm of solving the PWE described above allows for fast calculation of the global wave field distribution even on a personal computer. The diffraction field patterns visualized by means of color graphics contains a large amount of information useful for computer aided design of complex optical systems as well as for education and training in wave theory.

We demonstrate a prototype of the computer code for modeling a wide class of quasioptical systems composed of lenses, Fresnel zone plates, dielectric waveguides, etc.

The main features of this program are:

- interactive design and display of the optical scheme using a built-in library of elements (user has to choose the needed ones and to define only their position and parameters) ;
- a priori accuracy estimations of the PWE and finite-difference scheme realized in the form of warnings and cues ;
- step-by-step numerical solution of the PWE in a truncated domain with transparent boundaries;
- interactive calculation regime with breakpoints, field storage and complex amplitude plotting in desired cross-section ;
- global field visualization using ajustable color intensity palette.

REFERENCES

1. V.A.Fock. Electromagnetic diffraction and propagation problems. *Pergamon Press*, Oxford, 1965.

2. F.D.Tappert. The parabolic approximation method, in: Lectures Notes in Physics, 70. J.B.Keller, J.S.Papadakis (eds). Wave propagation and underwater acoustics.*Springer*, New York, 1977, pp.224-287.

3. G.D.Malyuzhinets, Progress in understanding diffraction phenomena (in Russian), Soviet Physics (Uspekhi), 69, No 2 (1959) pp.312-334.

4. V.A.Baskakov, A.V.Popov. Implementation of transparent boundaries for numerical solution of the Schrödinger equation. *Wave Motion*, 14, No 1, 1991 , pp.123-128.

5. S.W.Marcus. A generalized impedance method for application of the parabolic approximation to underwater acoustics. *J. Acoust. Soc. Am.*, No 1, 1991, pp. 391-398.

Dosimetry in a Voxel Model of the Head

P J Dimbylow

National Radiological Protection Board, Chilton,
Didcot, Oxon OX11 0RQ, Great Britain

1 Introduction

Theoretical dosimetry defines the link between external fields and/or source configurations which can be measured to dose quantities in the body which are difficult to measure. These dose quantities such as the specific energy absorption rate, SAR and current density are related to a possible insult or hazard. The key to future progress in dosimetry is the development of anatomically correct voxel (volume pixel) phantoms from medical imaging data.

This paper presents examples of Finite-Difference Time-Domain (FDTD) calculations of SAR in an anatomically realistic model of the head at frequencies between 900 MHz and 2.45 GHz for a plane wave source and for a monopole representing a generic mobile communications transceiver.

2 Model of the Head

A fine resolution, anatomically detailed model of the head has been constructed directly from a sagittal MRI scan of a single male subject. The MRI data were segmented into 4 million, 1 mm voxels in the shape of cubes. Each cube has a tag which identifies its tissue type. Segmentation which is the identification of the tissue types was performed using the volume rendering code VoxelView (1993) and in particular the merging, arithmetic manipulation and grease pencil features; the latter allows the free-hand insertion and erasure of voxels. The head was split up into convenient segments. Each segment was then divided into high and low greyscale tissues. Each classification was then further differentiated by successive editing and subtraction. Any anomalies were then tidied up with the grease pencil.

The tissues were skin, muscle, bone, brain, cerebrospinal fluid and air (sinuses). The original eye was of poor clarity and so has been replaced by an analytical eye of concentric spheres. The tissues in the eye are the lens, humour and a composite sclera-humour layer. The hypothalamus, pituitary and pineal glands were also edited in by hand, their positions determined from an anatomical atlas of the head. The FDTD calculations were not tractable at 1 mm resolution so the model was rescaled to 2 mm resulting in 490,000 voxels in the head.

Figure 1 shows an annotated axial slice through the eyes of the 2 mm phantom.

3 Numerical Method

The Finite-Difference Time-Domain (FDTD) method has been well documented (see e.g. Taflove and Umashankar, 1990; Kunz and Luebbers, 1993) and only a brief description is given here. The computational domain is divided into a 3D lattice of cells which are assigned individual electrical properties. For a cubic-cell space lattice, the explicit finite-difference procedure, involves positioning the components of the electric field, $\boldsymbol{E}$, on the middle of the edges and the components of the magnetic field, $\boldsymbol{H}$, at the centre of the faces on a unit cell of the lattice. The calculation then leap-frogs, evaluating $\boldsymbol{E}$ and $\boldsymbol{H}$ at alternate half-time steps. Time-stepping proceeds until equilibrium has been reached. A domain enclosing the target and a boundary condition on the surface of the domain must be chosen to absorb the outgoing scattered waves (Mur, 1981). A Faraday's law contour path was used to derive the circumferential $\boldsymbol{H}$ fields immediately adjacent to the wire (Taflove *et al* 1988) in the modelling of the monopole. The monopole was excited by driving a voltage across the one cell gap between the wire antenna and the top surface of the metal box. The conducting metal box was treated by setting the electric fields, tangential to the surfaces, to zero. Further details of the computational method and tissue electrical properties can be found in Dimbylow and Gandhi (1991) and Dimbylow (1993).

4 Results

The specific absorption rate, SAR is defined as

$$SAR = \frac{\sigma |\mathbf{E}|^2}{\rho}$$

where σ is the electrical conductivity, ρ the density and $\mathbf{E}$ is the root-mean square (rms) electric field.

Figure 3 shows a histogram of the SAR across the section through the eyes, depicted in figure 1, for anteroposterior, AP irradiation of the adult at 900 MHz. The front of the head faces the top righthand corner. Energy is preferentially absorbed in the high conductivity tissues such as the eye, brain, muscle and skin. The maximum absorption occurs in the eyes. Bone has a low conductivity resulting in lower power deposition in the skull. The absorption in the brain reveals a complex standing wave pattern. Figure 4 illustrates a surface wave or whispering gallery effect. The head is being irradiated from the side at 2.45 GHz. At this frequency the penetration into the head is small and so the energy absorption should be superficial at the side of the head. However there is significant absorption in the opposite ear from a wave propagating around the surface of the head rather than through the volume of the head.

The interaction between a mobile communication transceiver and the head was modelled using a $\lambda/4$ monopole on a metal box. Three source geometries of the transceiver were considered, viz - vertical alignment in front of the eye denoted AP_v, vertical alignment at the side of the head by the ear denoted LAT_v and horizontal alignment at the side of the head LAT_h (AP is short for antero-posterior and LAT for lateral). The AP_v geometry was chosen to simulate a person talking into the transceiver and more importantly because the feed point of the antenna, near the surface of the eye, will produce the highest local SAR. The LAT geometries represent other typical positions in which the transceiver could be held. Figure 2 shows a volume reconstruction of the 2 mm voxel head and the transceiver for the LAT_v geometry and gives a good impression of the degree of realism that can be achieved by models based on medical imaging data. Also shown is the placement of a simulated hand grasping the lower part of the box.

Figure 5 shows the SAR across the axial slice through the eyes for AP_v irradiation at 900 MHz with the centre of the box 2cm away from the surface of the eye. The energy absorption is far more superficial than in the plane wave case of figure 3 and most of the energy is absorbed in the left eye. Figure 6 shows the SAR distribution for LAT_h irradiation with the antenna 2 cm from the surface of the ear. The energy absorption is principally in the ear with little penetration into the brain and eye.

A complete description of the head-transceiver calculations and a discussion of the implications to safety standards is given in Dimbylow and Mann (1994).

5 Prospectus

A fine-scaled 2 mm resolution voxel model of the human male body is being constructed at NRPB. The raw MRI data were taken from a series of continuous scans of the various parts of the body of a single subject. These blocks of data were then fixed together by rescaling, translocation and rotation. The segmentation of the volume so that each voxel is ambiguously assigned to a tissue type is in progress. The completion of this model will provide a detailed anatomically realistic phantom for comprehensive dosimetry of electromagnetic fields.

References

Dimbylow P J and Gandhi O P, 1991. Finite-difference time-domain calculations of SAR in a realistic heterogeneous model of the head for plane-wave exposure from 600 MHz to 3 GHz. Phys. Med. Biol., 36, 1075-89.

Dimbylow P J, 1993. FDTD calculations of the SAR for a dipole closely coupled to the head at 900 MHz and 1.9 GHz. Phys. Med. Biol., 38, 361-8.

Dimbylow P J and Mann S M, 1994. SAR calculations in an anatomically realistic model of the head for mobile communication transceivers at 900 MHz and 1.8 GHz. Phys. Med. Biol., 39 (10), 1537-1553.

Kunz K S and Luebbers R J, 1993. Finite Difference Time Domain Method for Electromagnetics. CRC Press, Boca Raton.

Mur, G, 1981. Absorbing boundary conditions for the finite-difference approximation of the time-domain electromagnetic field equations. *IEEE Trans. Electromag. Compat.*, **EMC-23**, 377-82.

Taflove, A and Umashankar, K R 1990. The finite-difference time-domain method for numerical modelling of electromagnetic wave interactions with arbitrary structures *Finite Element and Finite Difference Methods in Electromagnetic Scattering*, ed. M A Morgan (New York: Elsevier), pp 287-373.

Taflove, A, Umashankar, K R, Beker, B, Harfoush, F and Yee, F S 1988. Detailed FD-TD analysis of electromagnetic fields penetrating narrow slots and lapped joints in thick conducting screens. *IEEE Trans. Antennas and Propagation.* **AP-36**, 247-57.

Voxel-View/E2.1 (1993). Vital Images Inc., Fairfield, Iowa.

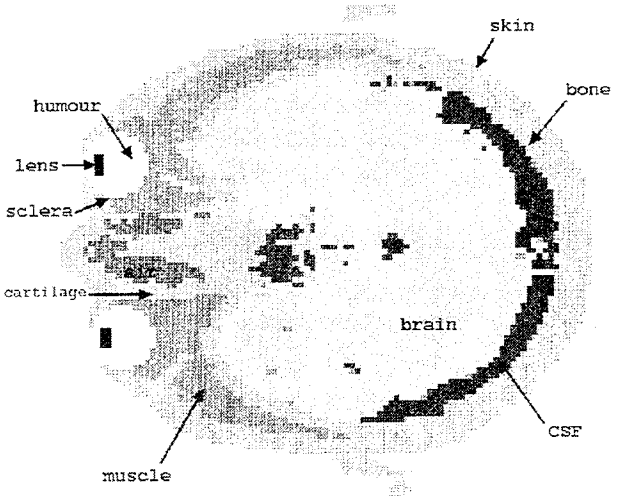


FIGURE 1 Axial slice through the eyes of the 2 mm phantom

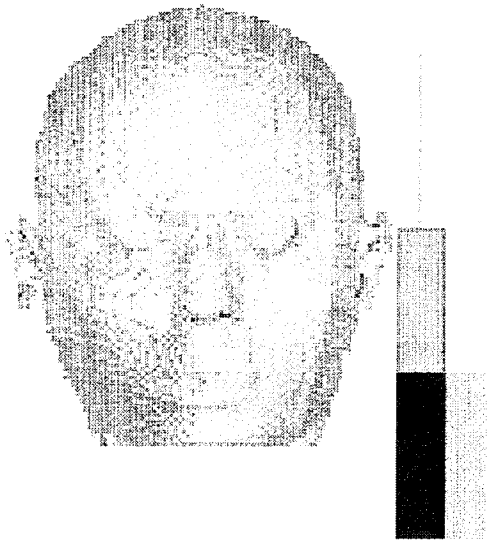


FIGURE 2 Volume reconstruction of the voxel head and the transceiver

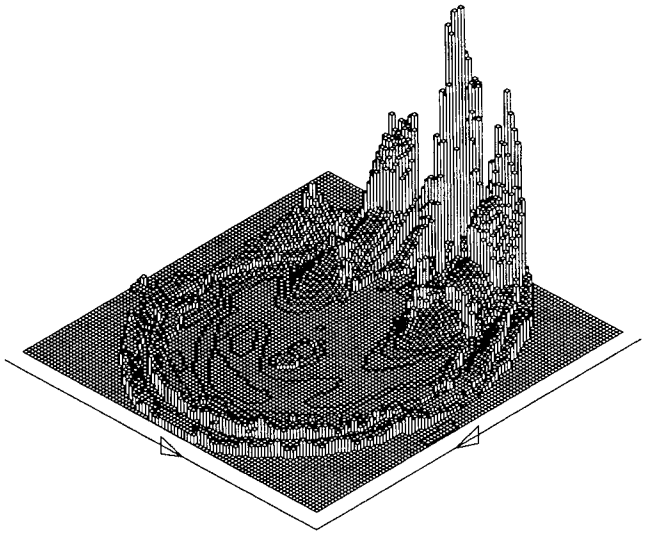


FIGURE 3 A histogram of the SAR through the section at the eyes for AP plane wave irradiation at 900 MHz. The front of the head faces the top right-hand corner

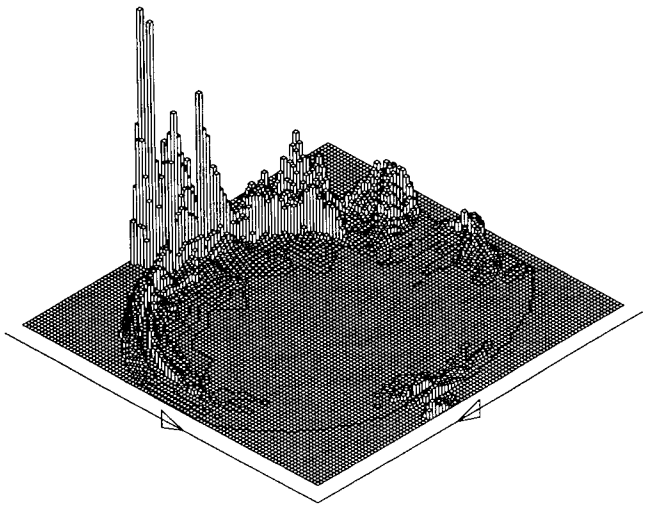


FIGURE 4 SAR at 2.45 GHz for lateral plane wave irradiation

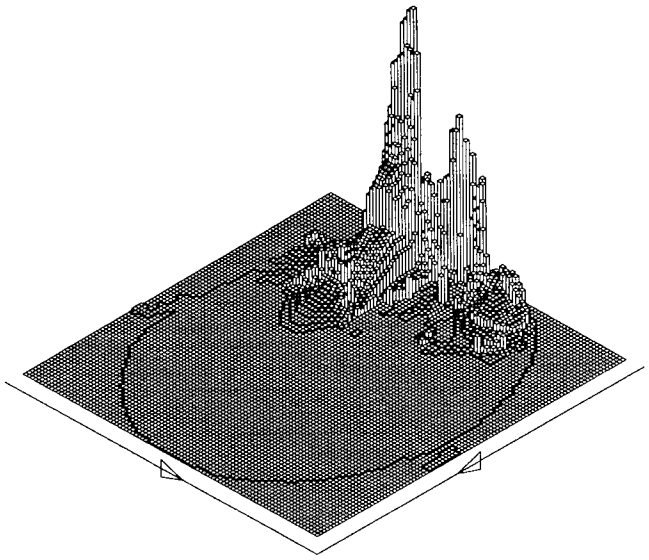


FIGURE 5 SAR at 900 MHz from a generic mobile transceiver in front of the left eye

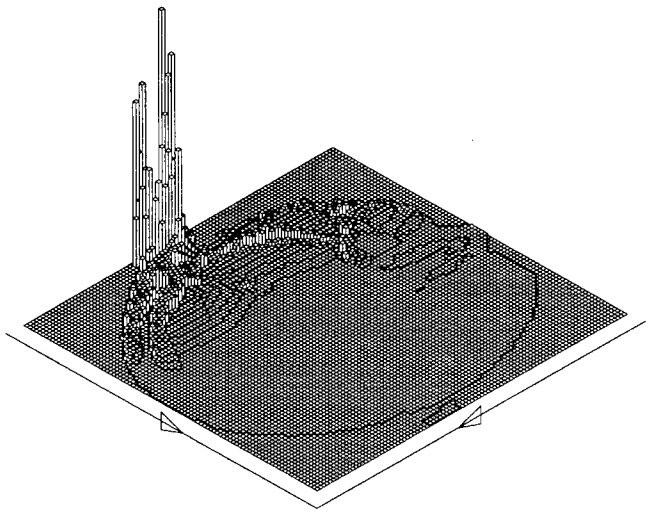


FIGURE 6 SAR at 900 MHz for the transceiver at the side of the head

A Graphical User Interface for the NEC-BSC

L. W. Henderson and R. J. Marhefka
The Ohio State University
ElectroScience Laboratory
1320 Kinnear Road
Columbus, OH 43212-1191
Tel: (614)292-5935
Fax: (614)292-7297
Email: lwh@tiger.eng.ohio-state.edu

I. Introduction

The NEC - Basic Scattering Code (NEC-BSC) [1] has been used for over 20 years for the analysis of high frequency antenna performance on complicated structures such as ships, aircraft, and missiles. The user interface to the program consists of a input file which contains commands and data. This classical mechanism is flexible, transportable and efficient. In contrast, modern graphical user interfaces provide very high levels of user interaction at the expense of transportability. The optimum solution is to retain the classical interface in the NEC-BSC itself, and create a second, companion program which provides a graphical user interface to assist the user in creating the classical input command file. The almost universal acceptance of Microsoft Windows makes it the natural choice for implementing a graphical user interface. This bifurcation of the codes into a graphical user interface code for generating the input file, and an analysis code for generating the numerical results allows the analysis code to remain transportable to any computer that has a FORTRAN compiler. The user can generate the input file on a PC and then run the NEC-BSC on either the PC or a more powerful computer. If the BSC is run on a different computer, then the results can be brought back to the PC for viewing, plotting, etc.

II. Design Philosophy

The NEC-BSC Workbench™ is a windows based environment for creating and manipulating input files for NEC-BSC. The user can open an existing file containing NEC-BSC commands or create new files. The input commands are displayed in a conventional text editing window, and the actual geometry is displayed in separate wireframe views. The design philosophy of the Workbench is based on two fundamental principles. First, the Workbench is intended to be an advanced command text editor with drawing and visualization capabilities where the user can create input files, run NEC-BSC,

and view the results without ever leaving the Workbench. It is not intended to be a CAD program. There are many excellent CAD programs on the market and there is little to be gained by creating another. Rather than spend time and effort creating a new CAD program which merely duplicates the features of existing programs, the Workbench will provide import and export capabilities to existing CAD programs.

The second design principle is a requirement that the Workbench run on a modestly equipped PC. The Workbench does not require massive amounts of memory, special graphics hardware, or the latest 32 bit operating systems. The current version runs well on a 486/33 with Windows 3.1, 4 megabytes of memory, and standard VGA video. In order to accomplish this, it was necessary to use simple wireframe drawing, without hidden lines, rather than more advanced graphics employing hidden lines or solid surface modeling, as shown in Figure 1. The simplicity of the drawing is offset by the speed with which the drawing can be generated. For most geometries, the wireframe drawing can be manipulated in a dynamic, real-time mode. Future versions of the Workbench will provide solid surface model view by using separate, non-dynamic windows. This technique is not new and has been used by CAD programs such as Autocad for many years. In Autocad, the user performs all editing functions using wireframe view without hidden lines, and then generates a solid surface model only when the drawing is complete. Future versions of the Workbench will gain solid surface model capabilities through Open-GL. Open-GL is currently available on Windows NT 3.5 and is expected to be available in an early release of Windows 95. Benchmarks already performed using Open-GL on NT 3.5 are very encouraging. Even without special graphics hardware, the solid model performance is surprisingly good.

III. Geometry Viewing and Editing

Any number of wireframe views can be created, allowing simultaneous viewing of the geometry from several angles as shown in Figure 2. As the user makes changes to the input file, these changes are reflected in the wireframe views. The user can view not only the physical structure, but also sources, receivers, paths of sources and receivers in the near field, and the reference coordinate system. Viewing options include pan, zoom, viewing angle, parallel projections and perspective projections. By selecting a specific command in the input file, the user can load the entire command into a dialog box and thus obtain very high levels of user interaction. The user can also accomplish dialog box editing of commands by picking a geometry item from one of the wireframe views and double clicking on that item. A typical editing dialog and its associated command text is shown in Figure 3.

IV. Ray Viewing and Editing

In a new version of the NEC-BSC, an option to output the ray paths and field information is implemented. The NEC-BSC Workbench can read these files and display the ray paths superimposed on the wireframe views of the geometry. For complicated problems, where the number of rays is large, the Workbench provides various filters for selecting which

rays will be drawn. Rays can be filtered based on the number of interactions or by relative power. The Workbench also supports OLE2 drag and drop for moving rays from one wireframe view to another, and thus allows the user to edit the ray representations in any fashion. The user can obtain information about a particular ray by selecting and double clicking on that ray. Figure 4 shows a typical representation of a corner reflector with a near field source and field point. The different windows show rays that have interacted with the corner reflector from 0 to 3 times.

V. Other Capabilities

Finally, the Workbench allows the user to view and print large output files produced by NEC-BSC. Future versions will include plotting capabilities. At present, the ASCII output files produces by NEC-BSC can be read by most standard spreadsheet type plotting programs. The Workbench was designed to work closely with the NEC-BSC, almost as if it was part of the BSC rather than a separate program. Using a button on the toolbar, the user can launch a special windows version of NEC-BSC. This will cause the current input file to be automatically saved and submitted to the BSC for analysis. Since the BSC runs as a separate program, the user can continue to edit and view other input files while the BSC is executing.

VI. References

[1] R.J. Marhefka and J.W. Silvestro, "Near Zone - Basic Scattering Code User's Manual with Space Station Applications," Technical Report 716199-13, The Ohio State University ElectroScience Laboratory, Department of Electrical Engineering, March 1989.

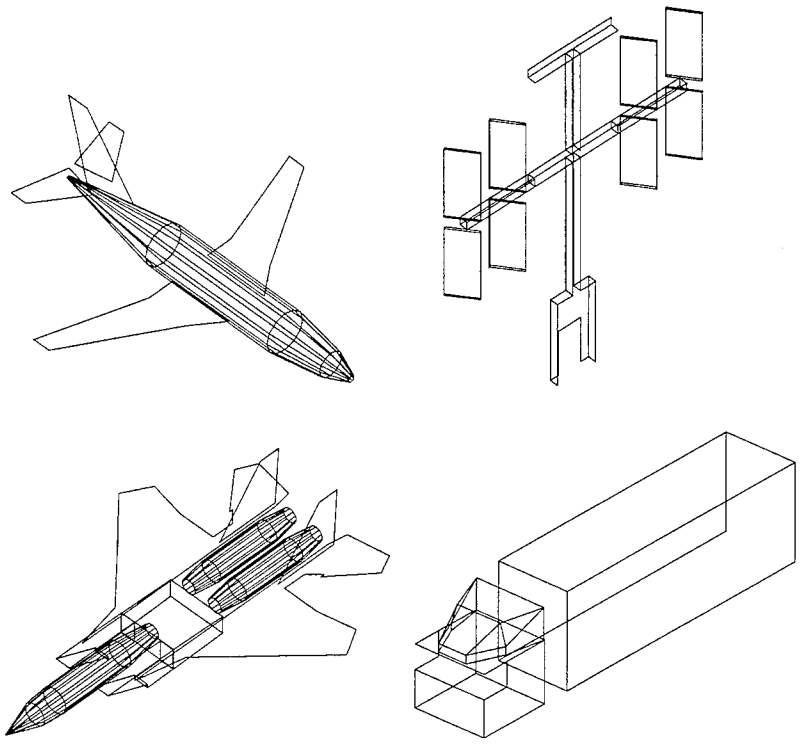


Figure 1. Wireframe drawings produced by the NEC-BSC Workbench.

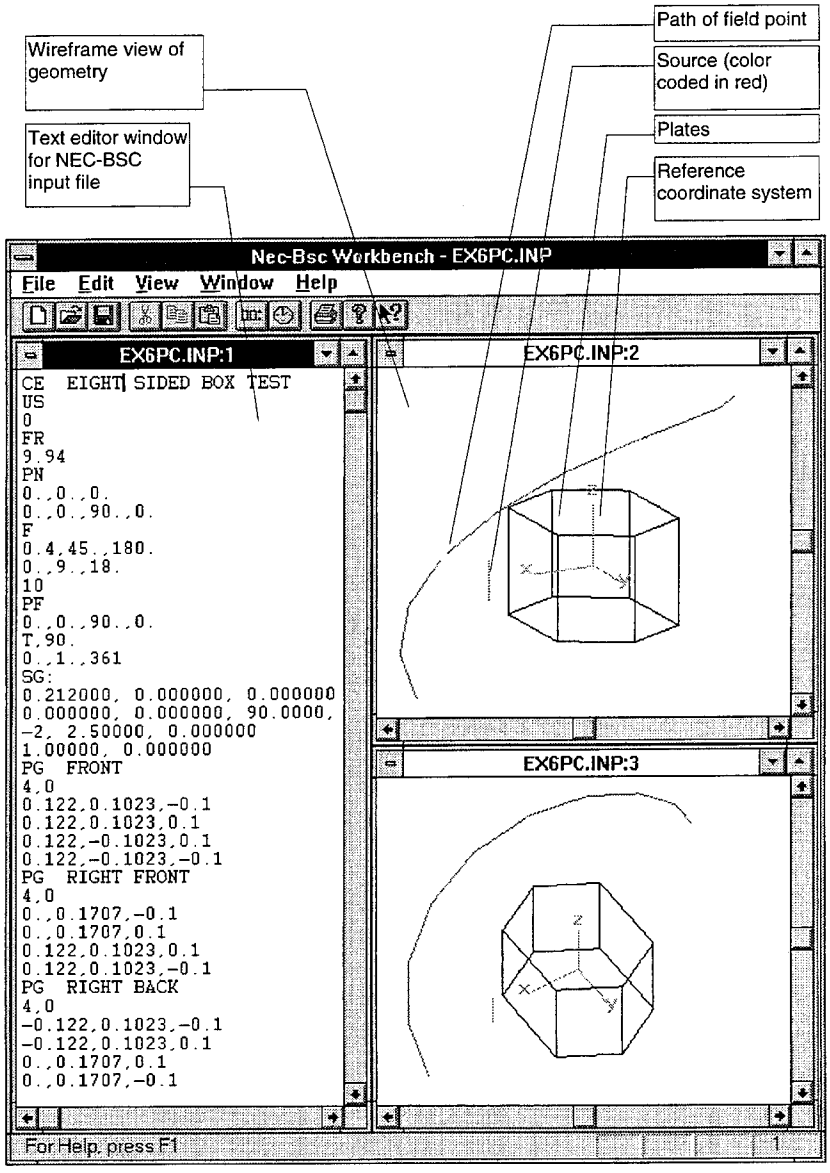


Figure 2. Screen layout and controls

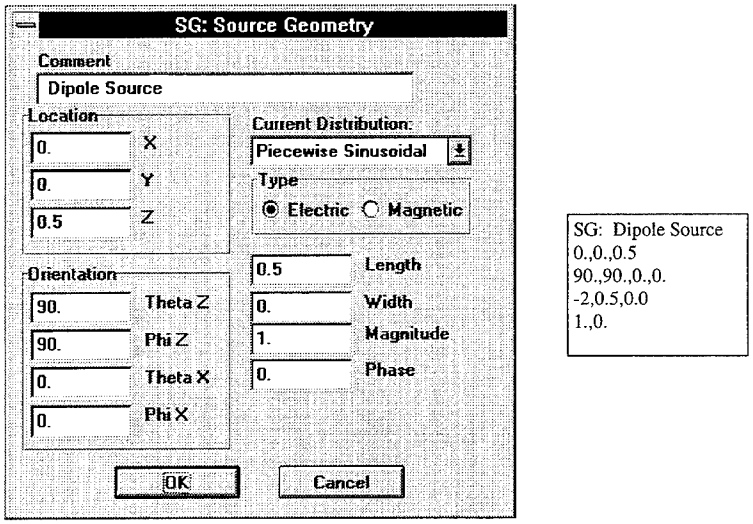


Figure 3. Example of a command dialog. This example shows the dialog box which encapsulates the source command. The actual command file text of the is included for reference. The dialog box can either be invoked by double clicking on the line of text containing the SG: command or by double clicking on the source in a wireframe view.

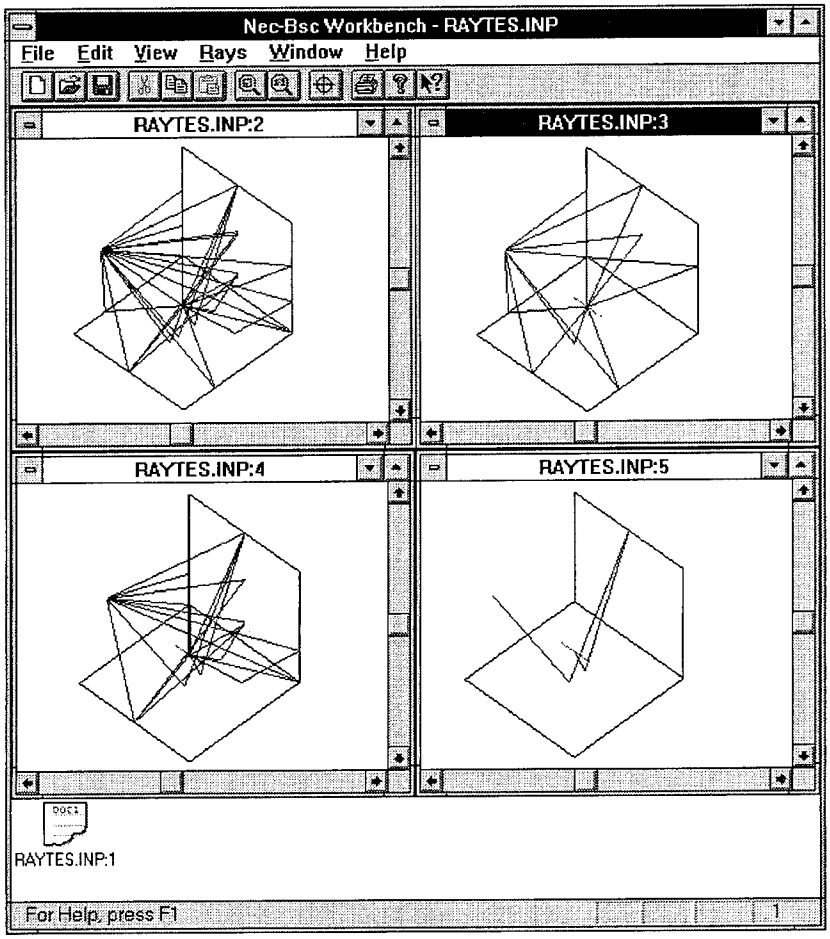


Figure 4. Corner reflector showing rays from source to near field point. Upper left window shows all rays. Other windows show rays that 1, 2, and 3 times respectively.

MF Communication and Broadcast Prediction System

by M.J. Packer and A.P. Tsitsopoulos

Science Applications International Corporation, Communication Engineering Laboratory
261 Cedar Hill Street, Building C, Marlborough, MA 01752
(508) 460-9500

ABSTRACT. A comprehensive antenna and propagation modeling code for the Medium Frequency (MF) band has recently been developed. The code was developed under Windows™ 3.1 on a 80486 PC architecture to provide arrayed antenna analyses, and use the results to perform ground-wave and skywave propagation analyses. A sophisticated user-friendly graphical interface allows quick and easy specification of inputs and displays the results in easy to understand formats. Typical outputs include far field radiation plots and color-coded contour plots that can be easily inserted into documents. Extensive on-line help system and error checking eliminate the most common errors, such as, invalid users input.

INTRODUCTION.

Numerical simulation of wireless communication and broadcast systems is an art, left to engineers and scientists with many years of experience. The Communication Engineering Laboratory (CEL) simplifies user access to this art with modern graphical user-interface (GUI) tools. Three electromagnetic antenna modeling (EAM) codes for quick and intensive antenna analysis were introduced a few years ago. Next, IONWIN, a GUI for IONCAP [1] was developed to simplify the simulation of high frequency skywave propagation. This past year, CEL developed an all inclusive code to simulated MF communication and broadcast predictions called MF Works.

The MF Works code provides a comprehensive system for modeling medium frequency antennas, then uses the results for input to ground-wave propagation analysis. To complete the toolset, skywave analysis was also implemented. This, too, uses the antenna results as an input. Each of these computational modules has a custom designed GUI for input data definition and visualization of the resultant output.

Key features of MF Works are it's map windows. During input definition, the map window assists in specifying the geographical coordinates of the nodes, and during output, contour levels are superimposed on the map. The map window is based on the Defense Mapping Agency's (DMA) high resolution map database and can be used to display any location on the planet. Three different resolutions of the DMA map database are used to decrease disk access time. To simplify operation, the map window contains a Tool Bar, Status Bar, and Scroll Bars. Output data is displayed as colored contours superimposed on maps for the ground-wave and skywave analyses.

THEORETICAL BACKGROUND.

Magnitude and phase of applied current to a directional antenna system controls the directive pattern's lobes and nulls. In the broadcast world, poorly directed lobes or high nulls can cause interference with established service areas of other stations or waste energy over unpopulated areas. Once the energy is radiated from the directional antenna system, the distance it travels while maintaining a useful signal level is very important. Energy is radiated into a space-wave and surface-wave along the earth/air boundary. The space-wave propagates in a spherical wavefront attenuating at $1/r^2$, whereas the surface-wave propagates as a cylindrical wavefront and therefore attenuates at $1/r$. If we just consider wavefront expansion attenuation, then the surface-wave should always outperform the space-wave with terrestrial communication and broadcast. The surface-wave has an additional loss factor caused by currents heating the boundary's media or the ground's constitutive parameters. High conductivity do not impede current flow and allow a surface wave to propagate thousands of kilometers, on the other hand, low conductivity can limit propagation to tens of kilometers.

The standard terms used in communication theory are skywave and ground-wave. Skywave refers to space-waves that are refracted by the Ionospheric and ground-wave is composed of the space- and surface-waves, where the space-wave components include the direct (line-of-sight), ground-reflected, ridge-diffracted, tropospheric-refracted, tropospheric-scattered, and ducted modes, as shown in Figure 1. The surface-wave is composed of propagating electromagnetic waves bound to the earth's surface and refracted in the lower atmosphere. The dominant propagation modes that comprise any ground-wave link are determined by the signal frequency, antenna patterns, and the propagation environment, including terrain and climate. In the MF band, the dominate ground-wave term is the surface-wave bound to the earth/air interface. The propagation environment still determines the distance a radiowave can propagate while remaining above the noise floor.

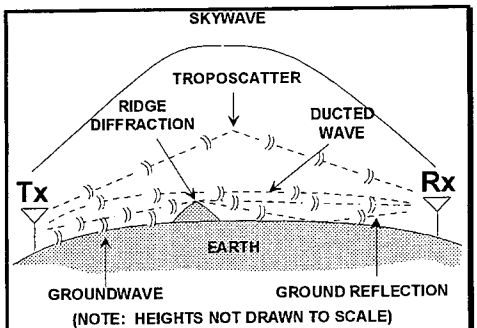


Figure 1. Surface-Wave and Space-Wave Components

Assuming a fixed frequency, then conductivity of the interface along the propagating path is primarily responsible for propagation distance. Conductivity typically varies from 10^{-4} S/m for dry sandy desert, to 5 S/m for salt water. Low conductivity limits the current flow in the ground required by the vertically-polarized electric-field component, the dominant polarization component of surface-wave propagation [2]. In desert climates, these effects are experienced as a significant reduction in effective ground-wave range to just beyond the radio Line-Of-Sight (LOS) [3]. Typically, MF propagation will extend over varying constitutive parameters. Therefore, accurate ground-wave analyses must be capable of analyzing a combined path of multiple constitutive parameters. MF Work's ground-wave analysis performs predictions over both constant homogenous ground and a combined path with up to four ground constitutive parameters changes on each radial path.

ANTENNA ANALYSIS.

Typically, a resonance quarter-wave monopole at one megahertz is 75 meters high with a good ground screen and no loading. Multiple monopoles of this size are commonly arrayed to shape the desired coverage pattern. The MF Works antenna analysis supports arrays of monopole antenna on good ground screens. Array data are specified using a customized input dialog window with all parameters referenced to the first antenna as shown in Figure 2. A minimum of one antenna is required and would result in an omni-azimuthal coverage pattern. A maximum of five antennas can be arrayed to create a complex directional coverage pattern.

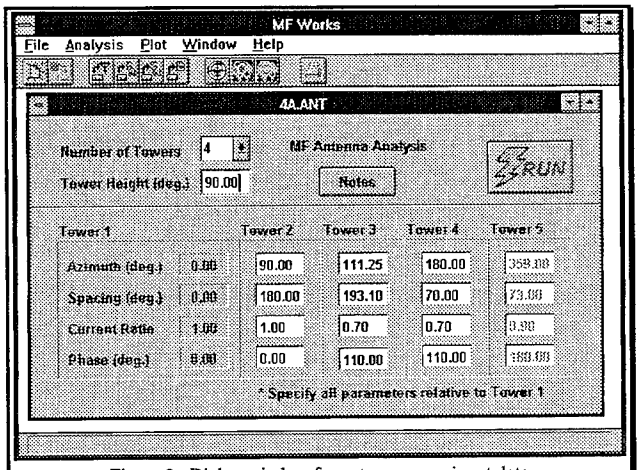


Figure 2. Dialog window for antenna array input data

Once an antenna analysis has been performed, its results are displayed in a polar radiation plot, as shown in Figure 3. The plot displays azimuth cuts of the antenna's three-dimensional power gain pattern using a user-defined elevation angle. The output data are plotted versus compass angles, the top of the plot is North (0°), the right is East (90°), the bottom is South (180°), and the left is West (270°). This is contrary to the customary right hand rule used in antenna theory, but provides a more intuitive visual understanding of the antenna's pattern relative to the maps used in ground-wave and skywave analyses.

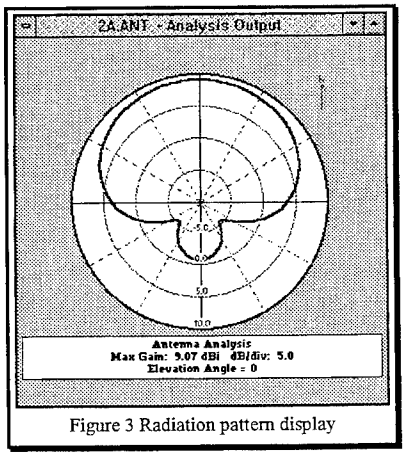


Figure 3 Radiation pattern display

GROUND-WAVE ANALYSIS.

As stated earlier, the ground-wave in the MF band is predominately a surface-wave component bound to the earth/air interface. The following analysis only considers that propagating surface-wave component. Input parameters are easily specified using a customized dialog window as shown in Figure 4.

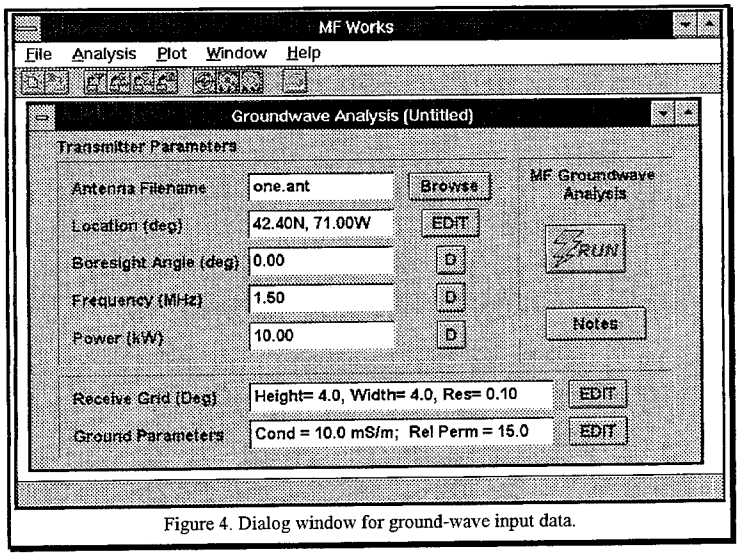


Figure 4. Dialog window for ground-wave input data.

The antenna filename specifies a previously run MF Work's antenna analysis file located at the geographic coordinates entered in the location entry. These geographic coordinates can be entered by typing in the longitude and latitude or by using the map window. The boresight bearing angle, specified in degrees East of North, allows specifying compass direction bearing in which the antenna is pointed. Frequency is entered in units of MHz and must be between 0.3 and 3.0 MHz. Power is entered in units of kilowatts (kW) and must be between 0 and 10,000.

The receive grid dimensions are used to specify a rectangular area of receive locations over which predictions are to be performed. Width, height, and resolution, all in units of geographical degrees are required. MF Works automatically executes ground-wave analyses for each resolution grid point. If the expected ground-wave propagation distance with useable signal power in uncertain then over specify the receiver area and use a course resolution, this will speed up the analysis time. Then, respecify the area of interest and use a finer resolution for smoother output contours.

Ground-wave propagation distances are highly dependent on the ground's constitutive parameters. For homogeneous ground there are two fields to specify: conductivity (mS/m) [σ] and relative permittivity (unitless) [εr]. Conductivity typically varies from 10^{-4} S/m for dry sandy soil to 10^{-2} for average soil to 5 S/m for sea water. Relative permittivity typically varies from 1 for air to 3 for dry sand to 15 for average soil to 81 for sea water [4].

MF Works also performs ground-wave analysis involving varying ground constitutive parameters. The path analysis of successively changing constitutive parameters requires specifying radials paths anchored at the transmitter location. The amount of input data requires specification using an external data file, as shown in Figure 5. Each radial path has a maximum of 4 different constitutive parameters. For example, at a 30° angle, the combined path has two ranges; the first 120 km from the antenna is land and then changes to sea water. At 40°, land extends for 100 km, then changes to salt marsh out to 160 km, then to sea water. The last radial defined is automatically repeated at the same

degree increment to completely define 360 degrees, therefore land exists in all other directions from 80° to 360°, and from 0° to 20°.

Radial Angle (E of N)	Number of Ranges	σ1 (mS/m)	εr1	range 1 (km)	σ2 (mS/m)	εr2	range 2 (km)	σ3 (mS/m)	εr3	range 3 (km)
30	2	10	15	120	5000	80	999			
40	3	10	15	100	111	30	160	5000	80	999
50	3	10	15	80	111	30	140	5000	80	999
60	2	10	15	60	5000	80	999			
70	2	10	15	40	5000	80	999			
80	1	10	15	999						

Figure 5. External text file required for changing constitutive parameters over radial ground paths.

The ground-wave signal strength attenuation is calculated by a series of summation equations as a function of frequency, conductivity, and relative permittivity. As shown in Figures 6a,b,c, this formulation agrees well with FCCGW [5] (Bremmer's extension to Sommerfelds models [6,7]). The only exception is past 200 km over salt water. MF Work's computation seems to be on the conservative side.

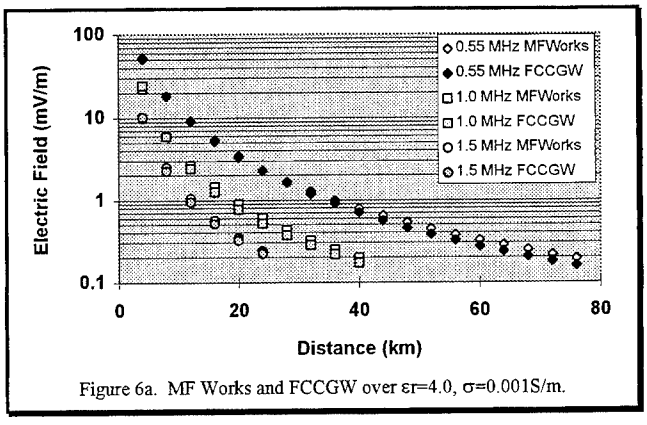


Figure 6a. MF Works and FCCGW over εr=4.0, σ=0.001S/m.

In the past, text-based computer codes only provided the numerical value for attenuation versus distance. The customary initial electric field strength is set to a fixed value at 1 mile. This is electric field delivered from a short lossless vertical radiator (SLVR) radiating energy equally in all directions along the boundary. It was left to the engineer to add or subtract antenna performance after

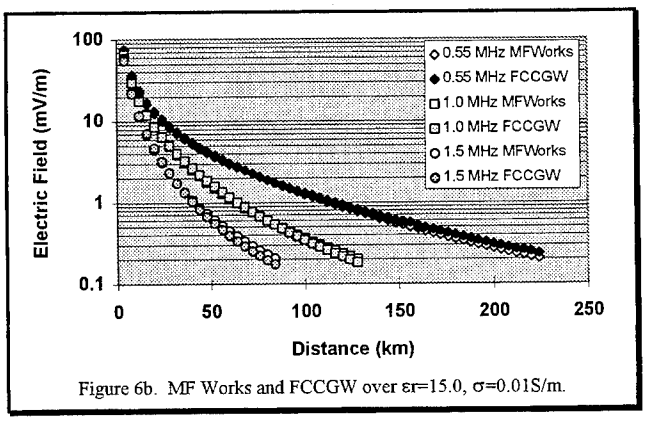


Figure 6b. MF Works and FCCGW over εr=15.0, σ=0.01S/m.

ground-wave computations were completed. In reality, a sophisticated set of antennas are arrayed to provide the ideal coverage pattern which is far from omni-directional. MF Works uses the computed electric field value from the earlier antenna analysis, specified by the antenna filename, to provide the initial electric field values along each radial at 1 mile. Linking antenna analysis results with the ground-wave analysis alleviates a lot of tedious work for the engineer. It also results in an immense amount of output data. This data can be easily viewed as color contours superimposed on to a geographic map, as shown in Figure 7. The map window has several options to better view the results, zoom in and out, add a title, increase or decrease the number of contours, and modify the contour values.

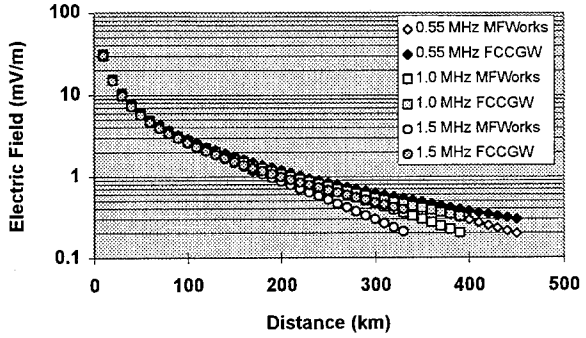


Figure 6c. MF Works and FCCGW over εr=81, σ=4.64 S/m.

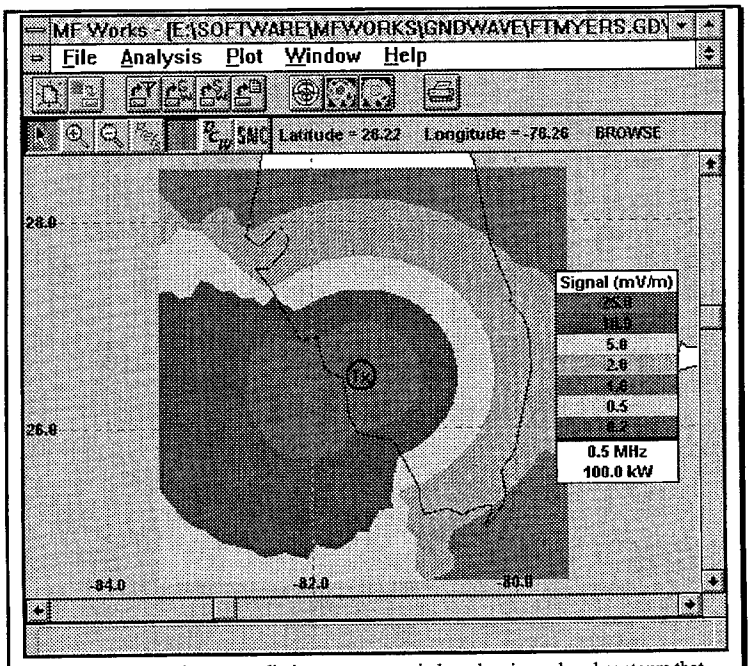


Figure 7. Ground-wave predictions on a map window showing colored contours that represent electric field strength in mV/m with an omni-directional antenna.

SKYWAVE ANALYSIS.

Energy radiated from an antenna launches a ground-wave along the earth/air boundary and also launches a space wave component. Electrons in the ionosphere cause frequency selective bending of electric and magnetic fields as they propagate through different electron densities. The selective bending causes these propagating fields to return to earth at varying distances from the transmitting antenna. The MF Works skywave analysis computes these returned electric field magnitudes versus distance and displays them as colored contours superimposed on a map.

Skywave parameters are specified using a customized dialog window similar to the ground-wave dialog. Outputs are displayed as colored signal level contour maps, as shown in Figure 8.

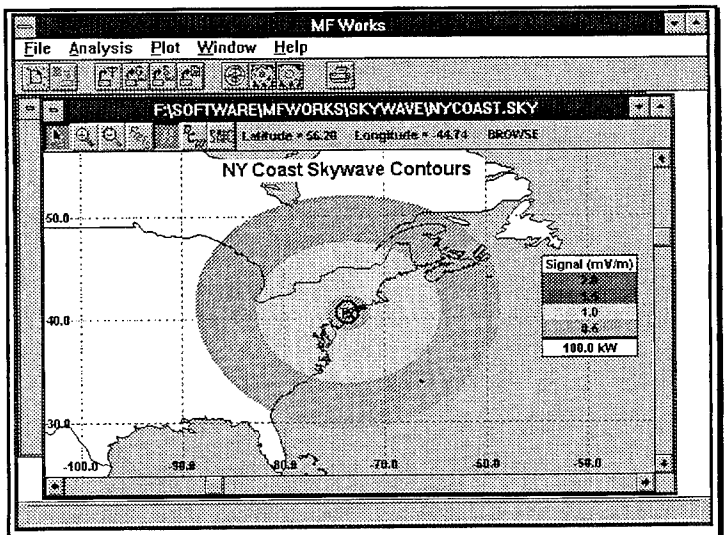


Figure 8. Skywave contour map window displaying electric field magnitude in mV/m.

SUMMARY.

A program now exists to link antenna analysis with ground-wave and skywave analysis from within a sophisticated graphical user-interface. A user with only a basic understanding of PCs and Windows™ will be able to use the GUI to predict the performance of a medium frequency communication or broadcast system. The GUI allows quick and easy specification of inputs and displays the results in easy to understand formats. Outputs includes far field radiation pattern plots and color-coded contour plots that can be easily inserted into documents. Extensive on-line help system and error checking eliminate the most common errors, such as, invalid users input.

CEL continues to develop numerical tools to alleviate the tedious task of linking antenna modeling data with propagation analysis. Several algorithms which modify the Numerical Electromagnetic Code's (NEC) output files to a compatible input format for IONCAP, ICEPAK, and VOACAP have been developed. CEL has developed five other numerical tool's for the analysis of antennas and propagation. An overview of these other tools can be found in reference [8].

All codes were designed for operation on an IBM-compatible personal computer (PC). Minimum system requirements include an 80386-based PC, MS-DOS version 5.0, and Windows™ version 3.1 or later operating in the enhanced mode. The minimum peripheral hardware requirements include a mouse, keyboard, four-Megabytes random access memory, five-Megabytes hard-disk storage capacity, and VGA graphics capability. Optional SAIC-modified DMA map database (geopolitical boundaries only) requires 115 Megabytes of hard-disk storage space. All modules include help systems, error checking, printing, plus all Window's features. MF Works is written in Borland C++ for Windows, version 4.0.

REFERENCES

[1] Teters R.T., Lloyd J.L., Haydon G.W., Lucas D.L., *Ionospheric Communications Analysis and Prediction Program User's Manual*, Institute for Telecommunication Sciences.

[2] K. A. Norton, "The propagation of radio waves over the surface of the earth and in the upper atmosphere, part I", *IRE*, Vol. 24, No. 10, Oct. 1936.

[3] M.J. Packer, R.I Desourdis, Rural And Urban Ground-wave Propagation In A Desert Environment", MILCOM 1993

[4] International Radio Consultative Committee (CCIR), "Electrical Characteristics of the Surface of the Earth", CCIR Rec. 527-1.

[5] R.P Eckert, "Modern Methods for Calculating Ground-Wave Field Strength Over A Smooth Spherical Earth", Federal Communications Commission, February 1986.

[6] H. Bremmer, *Terrestrial Radio Waves, Theory of Propagation*, Elsevier, New York, 1949.

[7] H. Bremmer, "Application of Operational Calculus to Ground-wave Propagation, Particular for Long Waves", IRE A&P, Vol. AP-6, pg. 267-272, July 1958.

[8] M.J. Packer, "Numerical Simulation Of Antennas And Propagation For Wireless Systems", Microwaves and RF, November 1994.

™ Windows is a registered trade-mark of Microsoft Corporation

A Finite Difference Time Domain Visualization Tool for Microsoft Windows™

Atef Z. Elsherbeni, Clayborne D. Taylor, Jr., and Charles E. Smith

Department of Electrical Engineering
The University of Mississippi
University, MS 38677
atef@sphinx.ee.olemiss.edu

Abstract
A user-friendly graphical interface code is developed for the study of electromagnetic interaction with complex geometries using the Finite Difference Time Domain method. This code simplifies the generation of complex scattering geometries through the use of basic shapes such as spheres, cubes, ellipsoids, finite cylinders, and finite strips. The visualization of a source plane wave represented as a Gaussian pulse is also important to determine the valid frequency range. The simulation is visualized through the selection of one of the field components in a plane cut specified by the user.

Introduction
The availability of a more powerful generation of personal computers at low-end workstation prices makes higher level 3D electromagnetic codes possible at lower costs. The study of the interaction of electromagnetic waves with complex scatterers is a difficult task that involves computational methods such as the Finite Difference Time Domain (FDTD) method. Visualization tools previously exclusive to high-end graphics workstations such as the FDTD visualization tool for the SGI [1] can be used on current 486 and Pentium based PC's equipped with high speed graphics cards. However, building up the cells into the FDTD simulation space is a difficult process for practical problems. Therefore, a user-friendly graphical interface is developed and briefly described here for the analysis of an unlimited number of electromagnetic problems through interactive real time visualization of the field components using FDTD. The FDTD code is adapted from Kunz and Luebbers [2]. The source excitation currently supported is a Gaussian pulse plane wave.

Program Startup
Startup of the program shows three windows as shown in Fig. 1. The top window is used to design the geometry and the bottom left window shows a parallel perspective projection of the 3D geometry. The bottom right window is used to show an animated plane cut of one of the six cartesian field components.

Geometry Construction
Before defining the scattering geometry, the user must define the FDTD space that contains the geometry. Selection of the "New" option under the "File" menu will open the space parameters window as shown in Fig. 2.

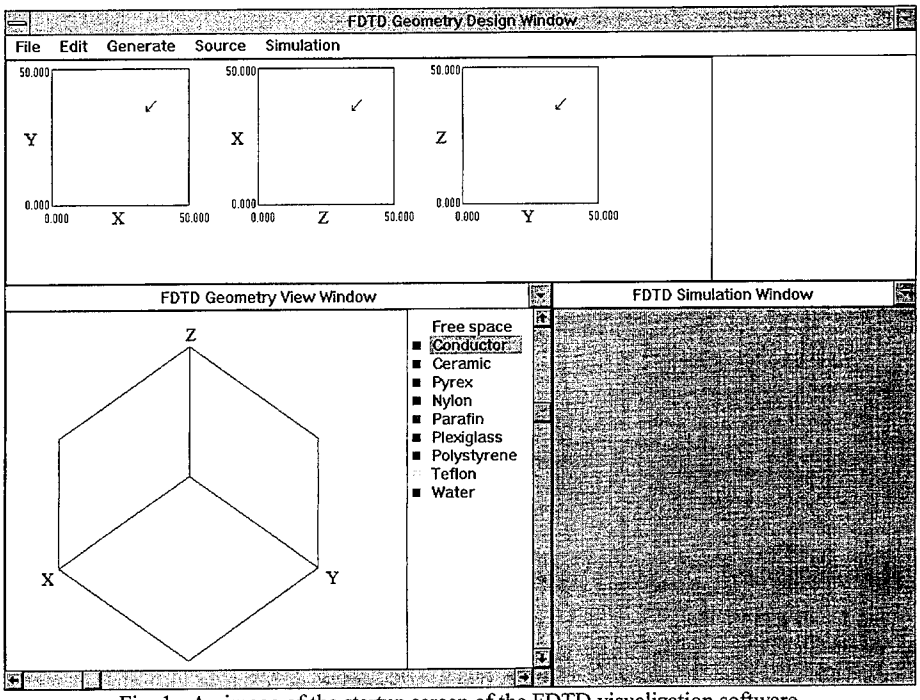


Fig. 1: An image of the startup screen of the FDTD visualization software.

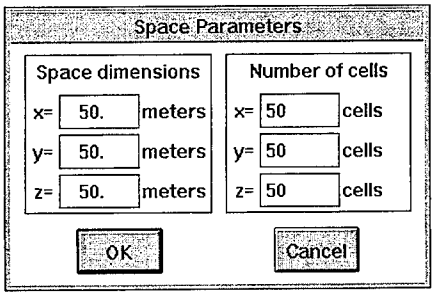


Fig. 2: Space parameters window.

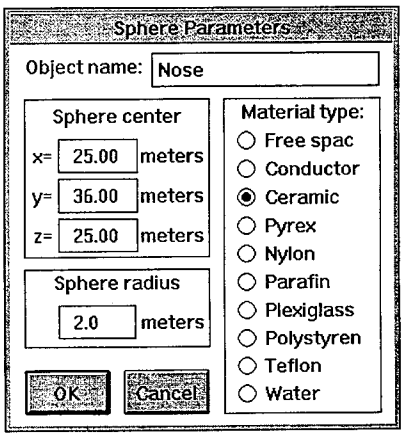


Fig. 3: Sphere placement window.

Once the space is defined, the user may proceed to add objects. The basic shapes available are spheres, cubes, ellipsoids, finite cylinders, or finite strips. These shapes are added by selection of the corresponding name in the 'Generate' menu. A placement window is opened for the selected shape. The object location and dimensions are then defined, along with an optional name for the particular object. As an example, Fig. 3 shows the sphere placement window in which the sphere center location and radius are to be defined.

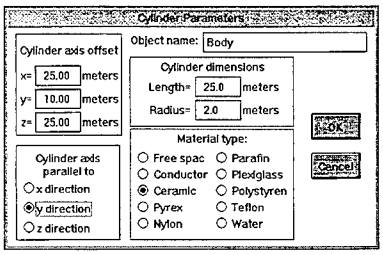


Fig. 4: Cylinder placement window.

The cube placement requires the offset location and x, y, z dimensions while the ellipsoid placement requires the ellipsoid center and major radii parallel to the x, y, and z axes. All offsets must be given from the global origin (0,0,0). The cylinder placement window that is presented in Fig. 4 is more complex. Notice that the cylinder is defined by the length of its axis, the radius of the cylinder, the offset of the starting point of the its axis, and axis orientation. The strip placement window as shown in Fig. 5 may appear quite complex. However, note that the strip should be in one of the xz, yz, or xy planes. Once the plane of the strip is selected, the direction of the length related to the selected plane should be chosen. For example, a strip in the xy plane could have its length in the x or y direction.

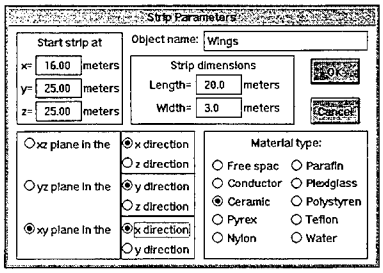


Fig. 5: Strip placement window.

Once the objects are all placed, the parallel perspective view window will show a 3D representation of a constructed model, as demonstrated by the aircraft shown in Fig. 6. The design window will show the 3 views of the space, along with a list of the object names and types, as shown in Fig. 7. This geometry is an adaptation of a generic aircraft similar to that in [3].

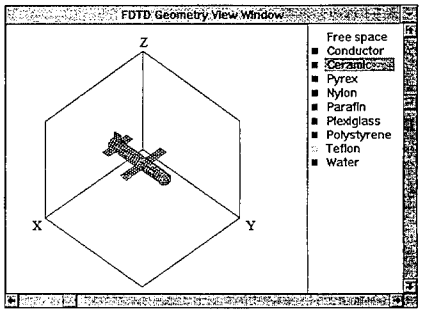


Fig. 6: View of geometry.

Notice that the list of material names with their permittivity and conductivity parameters are obtained

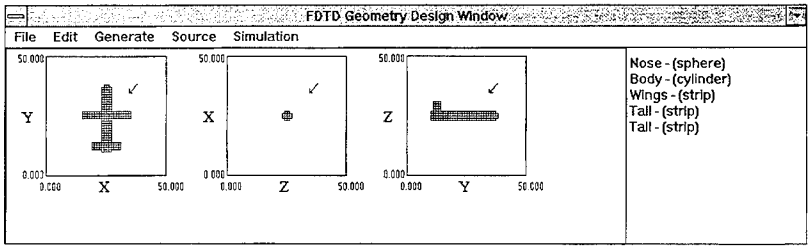


Fig. 7: Edit views and object list of the design window.

from Appendix G in [4]. Items in this list may be changed, except for the conductor and free space. "Double-click" any item and a material type window will appear as shown in Fig. 8.

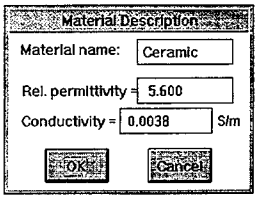


Fig. 8: Material editor.

Source Excitation

Another important part of the FDTD simulation is the parameters of the source excitation. The maximum value of the time step (Δt) and maximum usable frequency are computed from Courant's stability condition.

The user may change the parameters for a Gaussian pulse plane wave by selecting the "Gaussian Pulse" option from the "Source" menu. This calls up the Gaussian parameters window as shown in Fig. 9. The "Inside space" option is for setting a Gaussian pulse type of excitation in a plane or at a point as a source inside of the defined space. The default "Plane Wave" option is currently supported. The definition of the incident angles should be the same as the viewing angles of the parallel perspective view of the 3D geometry. The Gaussian pulse as described by

$$E^i(t) = E_o e^{-\alpha(\tau-\beta\Delta t)^2} \qquad (1)$$

requires input parameters β, Δt, and the time delay τ. The default value for β is given as 64 and Δt is computed by the Courant stability condition

$$\Delta t \le \frac{1}{c\sqrt{\frac{1}{(\Delta x)^2}+\frac{1}{(\Delta y)^2}+\frac{1}{(\Delta z)^2}}} \qquad (2)$$

where c is the speed of light, and Δx, Δy, and Δz are cell dimensions in the x, y, and z directions, respectively. Finally,

$$\alpha = \frac{4}{(\beta\Delta t)^2} \qquad (3)$$

is required to obtain a truncation of the pulse at nearly -140 dB from its maximum amplitude.

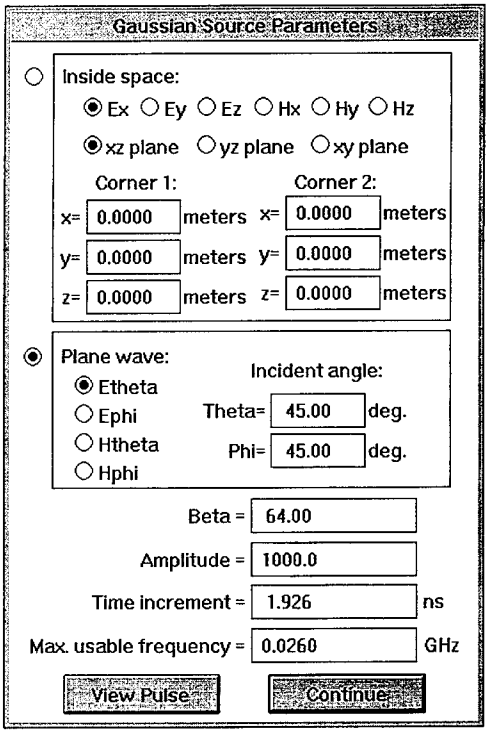


Fig. 9: Gaussian pulse parameters.

Selection of the "View Pulse" button brings up the "Gaussian Pulse" plot window of Fig. 10. From this view, the user can get an idea of the valid frequency range for the simulation. The user may close this window, change the parameters of β and Δt, and then select the "View Pulse" button again to see the effect of the new parameters. The valid frequency range is considered for a pulse with frequencies that correspond to amplitude levels not less than -140dB in the frequency plot. The total time shown as the maximum value of the x axis on the time plot is computed from the total number of time steps given in the simulation parameters window. The amplitude is computed from equation (1) and the frequency response is computed by applying a fast Fourier transform routine [5].

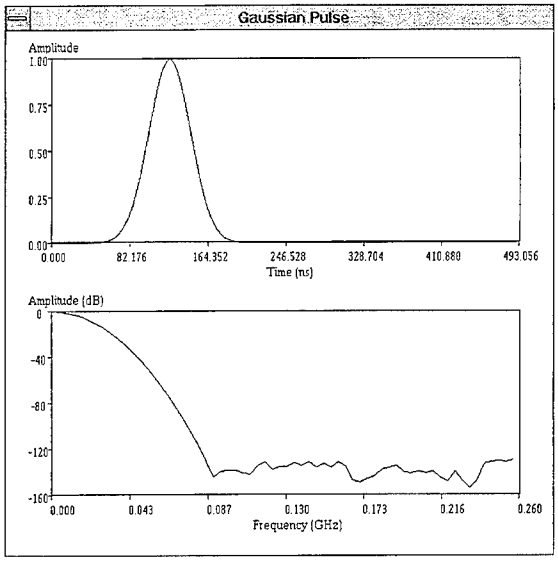


Fig. 10: Gaussian pulse plot window

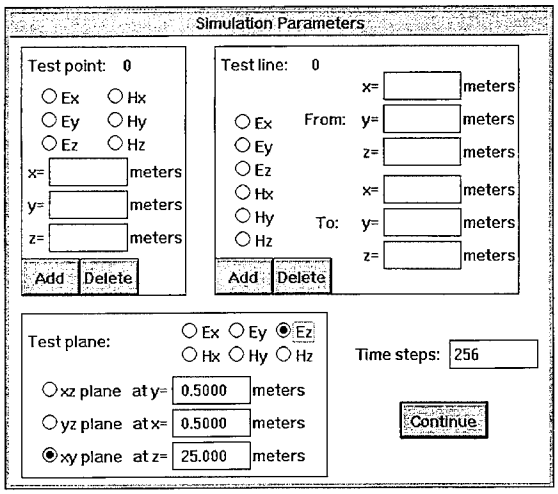


Fig. 11: Simulation parameters window

Simulation

The FDTD computations begin by selection of the "start" option in the "simulation" menu. However, the user may wish to change the default simulation parameters, by selecting the "parameters" option in the "simulation" menu to get the simulation parameters window as shown in Fig. 11. From this window, the user can add sample points and sample lines. The sampled points and lines are recorded in files. The animation window parameters are available in this window. The animation is a color contour-type plot of the selected field components. Selection of the desired field component is done by selecting the appropriate radio button. The selected field component is denoted by a filled circle. When two or more test points or test lines exist, a scroll bar will appear for that group to allow the user to scroll through all of the test points or test line selections. After all the desired simulation parameters are selected, the user may begin the simulation.

After selecting the "start" option, the simulation window will show the selected plane cut, with any geometry cross-section at that plane drawn in white. Other parameters printed in the simulation window are the selected scattered field component, the plane cut with its location, the current time step, and the corresponding simulation time. At the bottom of the simulation is a color scale showing the minimum and maximum amplitudes for the scale. Two examples of the simulation screen are shown in Figs. 12 and 13 where all objects are selected as ceramic. The simulation of a similar aircraft geometry made of perfectly conducting material is shown in Fig. 14.

Conclusion

This FDTD visualization software package is effective in bringing a complex electromagnetics tool to a desktop computer. The computer used was a Gateway 2000 P5-60 with 32 MB RAM. Although the simulation space would be considered small, the animations were smooth and moderately fast. Building the aircraft geometry was completed in a matter of minutes.

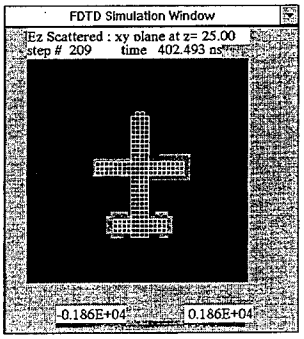


Fig. 12: Animation snapshot

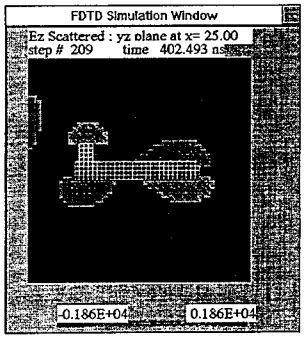


Fig. 13: Another snapshot

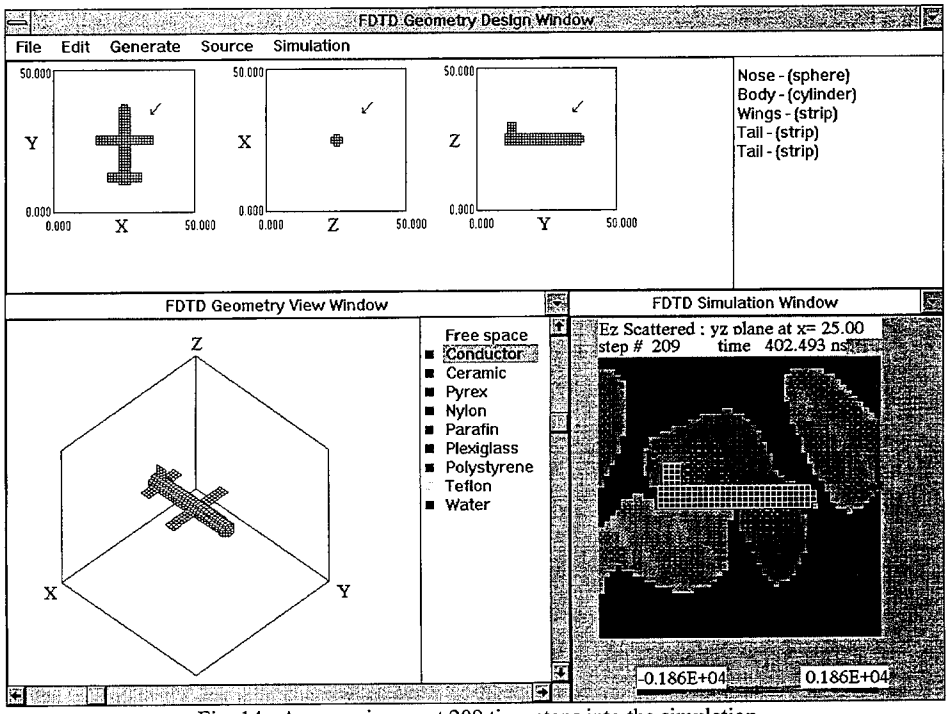


Fig. 14: A screen image at 209 time steps into the simulation

Acknowledgment
This work was supported in part by the U.S. Army Research Office under grant number DAAH04-94-G-0355. The authors would also like to thank Dr. R. J. Luebbers for his constructive comments and for providing the source code of the FDTD method.

References
[1] J.H. Beggs, D.A. Ryan, and R.J. Luebbers, "Visualization of Electromagnetic Fields Using the Finite Difference Time Domain Method," *Applied Computational Electromagnetics (ACES '93)*, pp. 189-194, Monterey, CA, 1993.
[2] K.S. Kunz and R.J. Luebbers, *The Finite Difference Time Domain Method for Electromagnetics*. Boca Raton: CRC Press, 1993.
[3] C.W. Trueman, S.J. Kubina, S.R. Mishra, and C.L. Larose, "RCS of Small Aircraft at HF Frequencies," *Symposium on Antenna Technology and Applied Electromagnetics (ANTEM '94)*, pp. 151-157, Ottawa, Canada, 1994.
[4] D. M. Pozar, *Microwave Engineering*. New York: Addison-Wesley, 1990, p. 715.
[5] D. Kahaner, C. Moler, and S. Nash, *Numerical Methods and Software*. New Jersey: Prentice Hall, 1988.

SESSION 4C:

VALIDATION

Transformable Scale Aircraft-Like Model For the Validation of Computational Electromagnetic Models and Algorithms: Initial Configuration and Results

by

Donald R. Pflug and Daniel E. Warren
Rome Laboratory/ERST
525 Brooks Road
Griffiss AFB, NY 13441-4505

Introduction

A problem common to the development and maintenance of most computational electromagnetics (CEM) codes is validation. This problem becomes particularly acute for large codes involving numerous modules and program paths. The best kind of CEM code validation is good agreement between calculated results and measured data of known accuracy. However, it is usually difficult or impossible to relate differences observed between the CEM code output and measured data to specific limitations within the code quantitatively or even qualitatively. The same problem occurs when comparing calculated results for a standard problem using several CEM codes.

During the past year, Rome Laboratory has constructed a novel test article called the Transformable Scale Aircraft-Like Model (TSAM) that is meant to be used as a CEM code validation tool. Because TSAM is transformable, its configuration can be modified at will allowing measurements to be made on a variety of profiles in contrast to a static test article. Initially, TSAM is designed to accurately mirror the geometry modeling capabilities of a number of CEM codes and, as a result, it holds great promise for allowing algorithm and modeling errors embedded within a CEM code to be estimated qualitatively and even quantitatively using measurements on the TSAM as a guide. Errors then can be adjusted as necessary to achieve a given level of code simulation accuracy. TSAM was designed primarily to study platform effects on the radiation pattern of a co-located antenna (radiation problem) but also can be used to study platform scattering problems if desired.

In this paper, a quick overview of the TSAM concept is presented followed by a description of the TSAM configuration (including the antennas exciting the structure). A representative set of measured antenna patterns and antenna isolation results is given along with an error analysis and accuracy estimates. A description of the Rome Laboratory anechoic chamber measurement facilities also is included.

The TSAM Concept

When the computed results from a CEM code are compared to

measurement, differences are always present. These differences are due to the following factors: 1) limitations within the code on modeling the geometry and physics of the problem (modeling error); 2) limitations in the equations used by the code to describe the electromagnetic phenomena and in their specific implementation (algorithm error); 3) limitations in computational capabilities of the computer platform hosting the code (computation error), and, 4) limitations in measurement accuracy (measurement error). The combination of these errors represents the difference observed between computation and measurements (simulation error). Individual errors usually are not known and may be mutually dependent. If computation error is insignifigent and measurement error is known, simulation error then represents the modeling and algorithm errors.

The novelty of TSAM is making measurements on a scale aircraft-like model that is a duplicate, in both form and substance, of the model in the code. Differences between measured and computed results then is attributable to algorithm error since measured and computed models coincide. These differences now can point to specific causes within the CEM code. TSAM is composed of replaceable components (including antennas) chosen to coincide with the current modeling capabilities of common CEM codes. The goal is for the TSAM components and configuration to evolve and mature over time into a realistic airframe with antennas with detail added incrementally to allow an assessment of the impact of each component to be made.

TSAM Initial Configuration: Structure and Mounted Antennas

The TSAM design described here was chosen to conform roughly to a 1/20 scale model of a wide-bodied aircraft. TSAM is made of aluminum and was fabricated into several canonic shapes to represent wings, fuselage, stabilizers, engine nacelles and pylons. Each canonic shape can be modeled very accurately.

The current TSAM configuration is shown in Figure 1. The fuselage is a hollow elliptical cylinder approximately 93 inches long with diameters 8.5 and 7.5 inches respectively. The cylinder is capped at both ends forming a blunt nose and tapered end. Two thin flat plates serve as wings with rectangular aluminum supporting plates underneath to hold the wings rigid. The wingspread is 76 inches. Three thin plates form the horizonal and vertical stabilizers. Four capped circular cylinder structures represent the engine nacelles and are attached to the wing structures by four thin plates which serve as pylons. All components are hinged and individually removable. Each component geometry can be modeled accurately and the metallic structure is assumed perfectly conducting. The thin plates serving as wings are hinged in order to vary the wing cant. Fuselage rigidity is maintained by an I-beam positioned inside the cylinder.

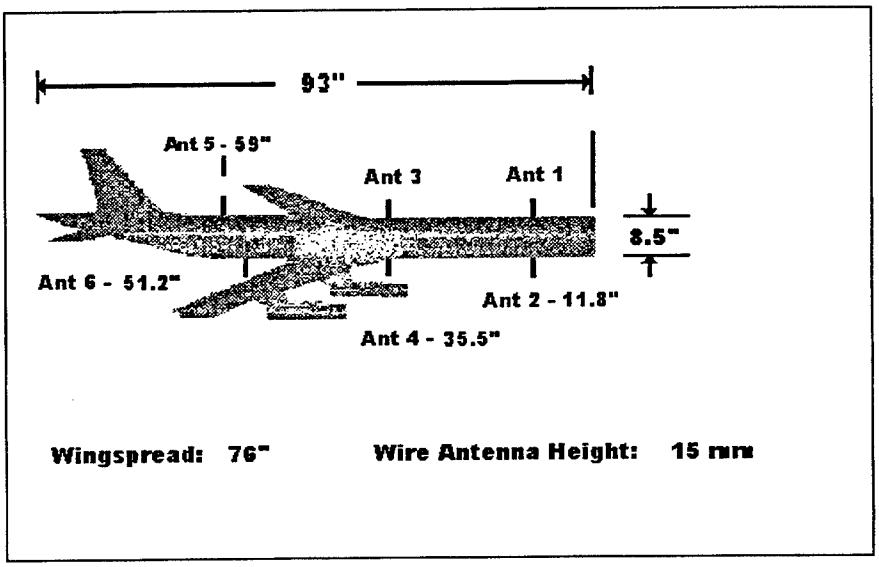


Figure 1. Initial TSAM configuration

Six thin wire monopole antennas, three located directly on top of the cylinder and three on the bottom, are shown schematically in Figure 1. Because each antenna is only 15 mm long they are shown not to scale. Each antenna is labeled numerically and positioned a certain distance away from the blunt nose as shown in Figure 1. The I-beam serves to position and support the mounted antennas and their feed structure.

TSAM Antenna Pattern Measurement Facilities and Procedures:

All antenna radiation pattern measurements were performed in the large anechoic chamber located in the Rome Laboratory Electromagnetic Environmental Effects Research Center. The chamber is designed to provide a 20 cubic foot quiet zone in the center of the chamber. A functional block diagram of the facility set up to determine antenna pattern measurements is shown in Figure 2.

Gain calibrated TSAM antenna radiation pattern data was obtained by rotating the TSAM test article in an incident field radiated from a standard gain horn, at a fixed frequency, while recording the amplitude of power received on each test antenna as a function of

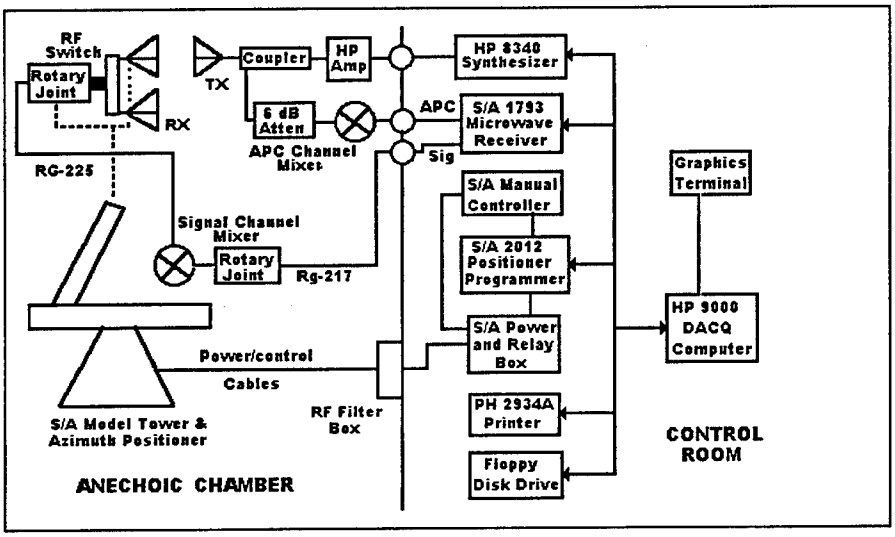


Figure 2. Antenna Pattern Measurement System Functional Diagram

positioner angle. Pattern cuts corresponding to the roll, pitch and yaw (azimuth) principal planes were measured. Gain calibration was obtained through a standard gain antenna substitution method combined with RF cable insertion loss calibration. The S/A 58000 Series model tower with rotary joint provided proper rotation and orientation of TSAM during antenna pattern data collection. A low dielectric constant material was used for the tower and rotating head drive shaft to reduce reflections while the base of the model tower was covered with RF absorber material.

The RF incident field was provided by a synthesized signal source at the frequencies 4.5, 6.0 and 8.0 GHz. This source was connected, as shown in Figure 2, to an American Electronic Laboratory (AEL) H5200 standard gain horn antenna mounted on a telescoping transmit tower near the chamber balcony. The TSAM antennas were connected to the receiver and recording systems, as shown in Figure 2, and the received amplitude signals were recorded as a function of angular position for each frequency.

TSAM Antenna Isolation Measurement Facilities and Procedures:

The same anechoic chamber facility was used to perform the TSAM antenna isolation measurements but with a different test setup as is shown schematically in Figure 3.

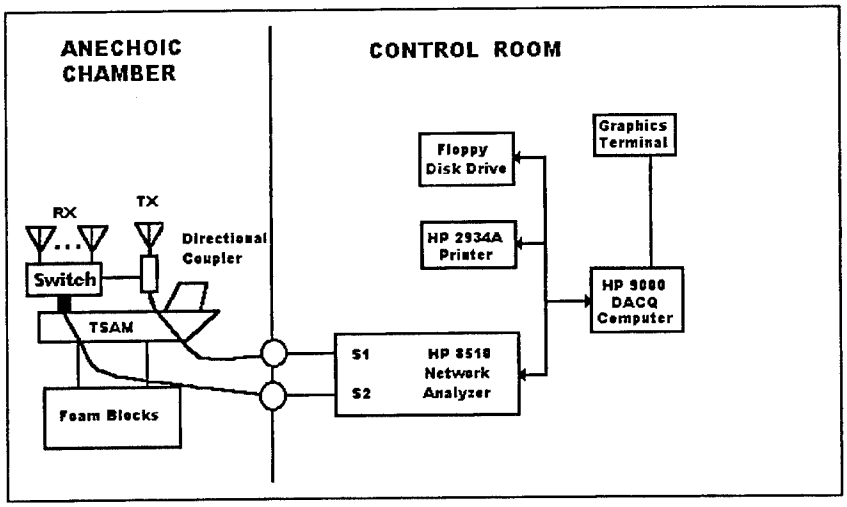


Figure 3. TSAM Antenna Isolation Measurement Block Diagram

TSAM was first positioned on RF transparent foam blocks and set in the chamber. Isolation measurements then were performed between all TSAM antenna pairs. For a given pair, one antenna was chosen to transmit an RF signal and the other one to receive using the RF switch shown in Figure 3. The transmit and receive signals were connected respectively to the S1 and S2 ports of an HP 8510 Network Analyzer and S12 measurements were performed for the transmit antenna and each receive antenna and reference line over the frequency range 4-8 GHz using the RF switch. A different antenna then was chosen for transmit and the process was repeated. The raw antenna isolation data then was calibrated using the reference line data and the results recorded as a function of frequency.

Sources of Error and Measurement Accuracy:

The large anechoic chamber in the Rome Laboratory Electromagnetic Environmental Effects Research Center has been utilized for many years for a variety of antenna measurements and the sources of error and their management are well known. Careful calibration procedures are performed before each set of measurements are recorded and at selected intervals during the measurements. A summary of sources of error, their magnitudes, and an estimated measurement accuracy are given below for both the TSAM antenna pattern measurements and antenna isolation.

Antenna pattern gain measurements are subject to errors in the standard gain antenna radiating source, along the signal propagation

path, in the switching network, the receiver, and the test article positioner. The signal source drifts in both power and frequency. This parameter drift contributes an estimated ±0.3 dB error to the TSAM pattern measurement as well as an additional ±0.2 dB error due to polarization impurity. The signal propagation path is subject to the effects of multipath that exist in the chamber. Chamber reflectivity measurements add an estimated ±0.1 dB error to pattern measurements. The RF switches used for switching between the TSAM antennas and the RF connecting cables will affect signal power levels due to limitations in calibration and temperature drift and insertion loss. Each factor contributes approximately ±0.5 dB to the measurement error. Finally, receiver drift adds about ±0.3 dB to the error. Positioner error is approximately ±0.1° and is not considered a signifigent contributor to antenna gain pattern measurements. The resulting antenna pattern measurement accuracy is estimated to be ±0.8 dB.

Antenna isolation measurements are subject to a similar set of errors. Care was taken to eliminate any systematic errors. The random errors considered in the isolation measurement and their associated estimates of error are: reference line calibration (±0.5 dB VSWR, ±0.7 dB attenuation); losses in the RF switching network and connecting cables (±0.2 dB switch actuation, ±0.5 dB calibration); microwave component temperature drift (±0.3 dB), and receiver drift (±0.1 dB receiver error, ±0.5 dB dynamic settling error). Signal multipath effects were not considered signifigent since the "on TSAM" coupling paths were dominant. The measurement accuracy for antenna isolation measurements was calculated to be ±1.18 dB.

Initial TSAM Pattern and Isolation Measured Results:

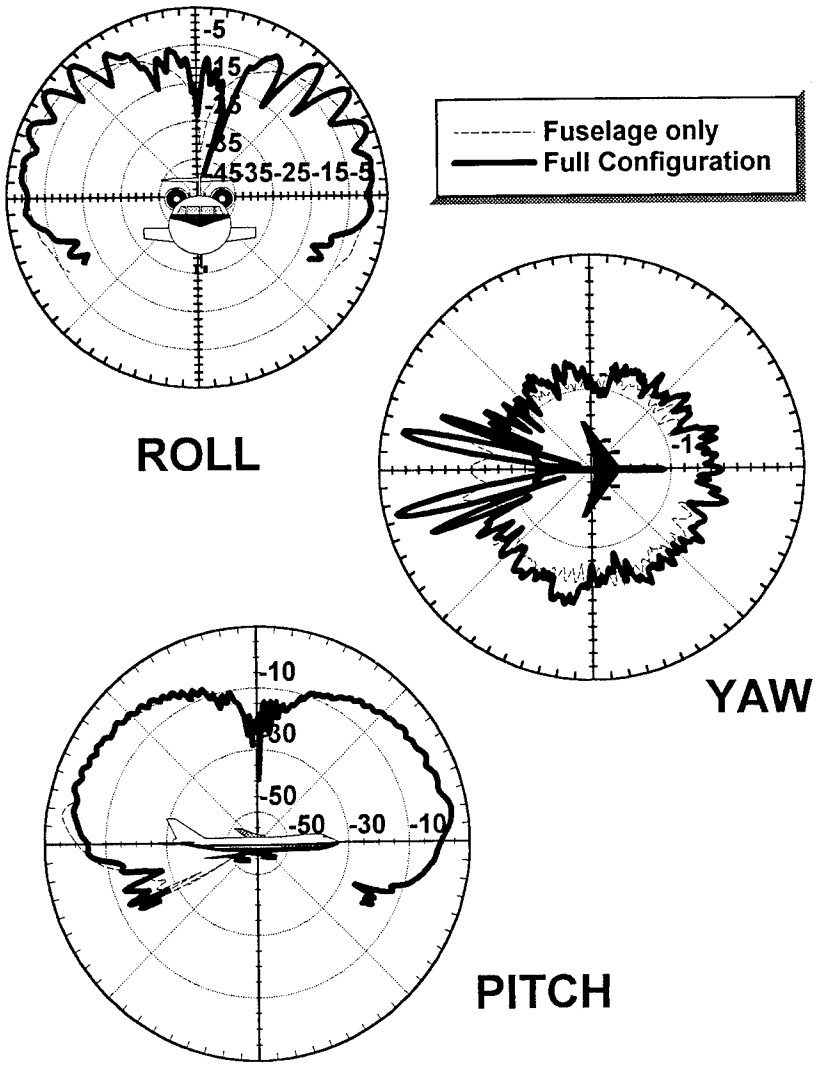
A set of principal plane pattern cuts are shown in Figure 4 at 6 GHz for antenna 3 (see Figure 1) transmitting for the full TSAM configuration and for the cylindrical fuselage only. This choice of measurements illustrates the ease with which large configuration changes can be made. The smooth patterns for the cylinder contrast with the scalloping patterns of the full structure, especially for the roll and yah cuts.

A set of isolation measurements are shown in Figures 5a-c. In each case antenna 2 is the transmitting antenna and the isolation is measured for antennas 1, 3, and 4 over the frequency range 4-8 GHz. for the cases of engines off and on TSAM. Antenna 2 is the bottom front antenna while antennas 1-3 are on top of the cylinder. Even though antennas 1 and 2 are located away from the engines, scattering effects show up as scalloping on the results. The same is true for antennas 3 and 2. Antennas 4 and 2 are located on the bottom of the cylinder and show less isolation.

Acknowledgement:

To Rome Research Corporation, Rome NY, for all TSAM measurements.

Figure 4
TSAM Patterns - Antenna 3 - 6 GHz.



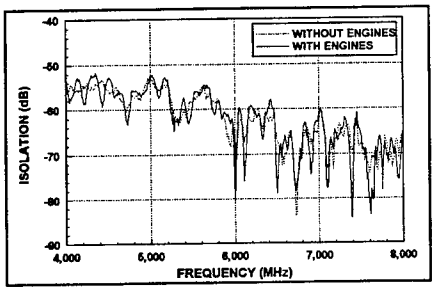


Figure 5a. Antenna 2 - Antenna 1 Isolation

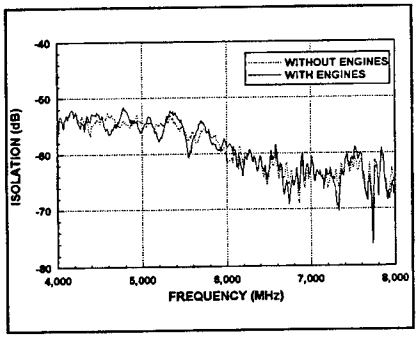


Figure 5b. Antenna 2 - Antenna 3 Isolation

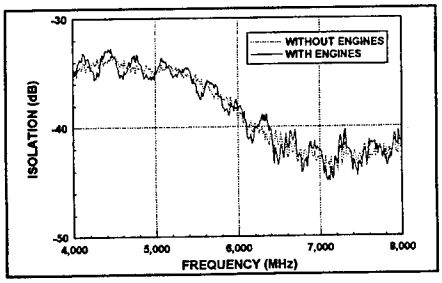


Figure 5c. Antenna 2 - Antenna 4 Isolation

Measurement Study for Validation of Electromagnetics Scattering Codes on a Complex 3D Target

T.L. Kienberger and D.E. Jurgens
Boeing Defense and Space Group

I. INTRODUCTION

Low radar cross section (RCS) targets are becoming prevalent and are presenting several new challenges for electromagnetic scattering codes. The physical target shapes and material characteristics are continually being refined and optimized. Traditionally analysis codes are validated by comparing the predictions to a "trusted" code or against an exact solution. Because RCS levels are decreasing and the complexity of the targets are evolving, the importance of establishing industry standard low-level validation cases with measured data is increasing.

This paper describes one of the methods used by the Boeing Defense and Space Group to validate the accuracy of 3D predictions of low level targets. As previously mentioned, one of the most common ways of validating analytical results is to compare the output to a previously validated code. However, on more complicated targets, when analysis produces varied results it is difficult to know with certainty which of the codes is correct. This study originated from a just such a debate.

A test body was designed with features representative of today's most challenging targets. The target was manufactured and then measured at the Boeing Compact Radar Range. A comprehensive set of angles and frequencies where used to gather data. The primary purpose of this research was to collect data for code validation.

The measured data was compared to predictions from two industry standard method of moments (MoM) codes. The results are presented in Section V along with comments and conclusions.

II. MEASUREMENT PLATFORM

The measurement platform, here after referred to as the target, used for this study was chosen not to demonstrate the capabilities but to explore the limitations of a given code. The target was to have challenging features based on an user's concerns of design problems of interest to Boeing. Thus instead of a series of separate targets to address features such as narrow wedge angles, multiple junctions and material interfaces, one target is desired where these features can be identified but not necessarily isolated from one another. The final consideration in the target design was size. A target and corresponding measured data were desired which would be typical of those run on a massively parallel computer, that is large for a numerical computation. At the same time it was desirable that the physical dimensions allow for ease of handling during data acquisition and that cost of model alterations be minimal. These considerations along with the available measurement facility and its capability resulted in the following model.

The target is an asymmetric triangle in the planform or top view, see figure 1a. The length of the three sides are 176.7, 140.0, and 77.7 inches. It is considered thin in that the volumetric height/depth is

small compared to the length of each planform side, see figure 1b. This model has 1 volumetric edge and two "knife" edges. A knife edge is defined as a contour tapering which approaches a very thin sheet. The volumetric edge has a height of approximately 2 inches. The targets body is coated with a conductive paint, thus it can be modeled as a perfect electrical conductor, or PEC. Further more the target is a closed volume without the addition of any edges. The target is also symmetric in the volumetric direction.

Edges were attached to all 3 sides. The primary reason was to verify multiple surface junction calculations of differing materials. Two of the targets edges, in particular sides B and C as depicted in figure 1, are very thin sheets. The body of the target narrows to knife edges on these sides. The longest side of the target terminates with a wall height. Thus the edge added to this side must have some volumetric thickness

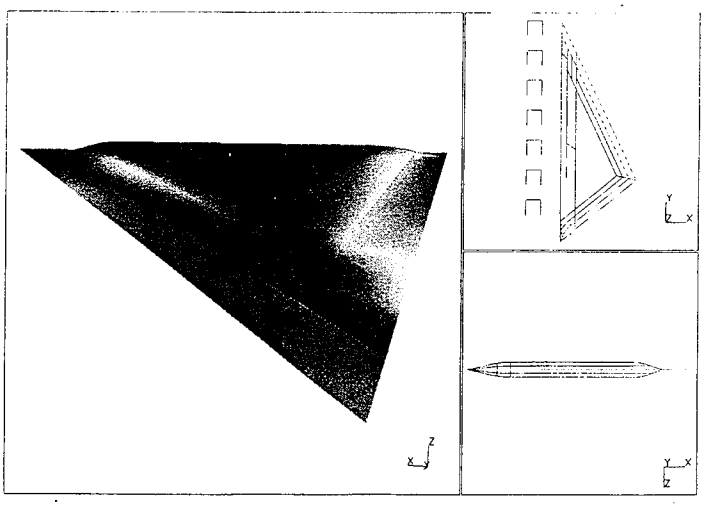


Figure 1, Triangular Measurement Fixture, views produced with IDEAS™

in order to maintain the smooth contour of the target. The edge on this side has the shape of a wedge where the wedge angle is defined such that the shapes contour is continuos to the first order derivative. The edge shape also allows for a bulk material to be placed inside this edge. For this study, however, only tower foam[1] was used for structural support.

This paper presents results from two configurations. They will be referred to as the resistive case (1) and the conducting case (2). The conducting case is simply the same as the resistive case except that aluminum foil was used to cover all edge materials. At the frequencies used in this study the minimal surface irregularities are very small compared to the wavelength. Thereby a PEC for the baseline case in this study is created which effectively simulates a smooth conducting surface. Thus, only the treated case is described in detail here.

[1] Tower foam is similar to ordinary styrofoam. It is lossless which means it does not dissipate radiated energy at any significant level. It can be modeled as a having the properties of free space or, as is customary, it can be completely ignored in the numerical calculation.

The material used for the treated case was very thin sheets of macrofol[2]. Each edge was constructed in the same manner. The knife edges, sides B and C, are the same as the volumetric edge, side A, except collapsed down to two thin sheets adhered together. The edges were constructed in a symmetrical sense thus only one side of any given edge need be described. The edge is approximately 4.5" wide. It is constructed of four strips of macrofol with differing material characteristics. This was done to evaluate the ability to model edge to edge interfaces of differing material properties. Lossless tower foam type material was used for internal support on the volumetric edge and external support on the very thin edges. For target dimensions with the edges installed see figure 2.

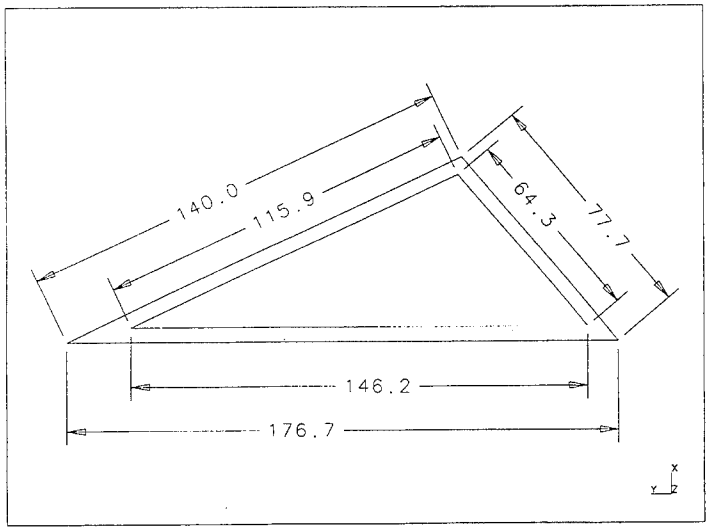


Figure 2, Triangular Measurement Fixture with edges,

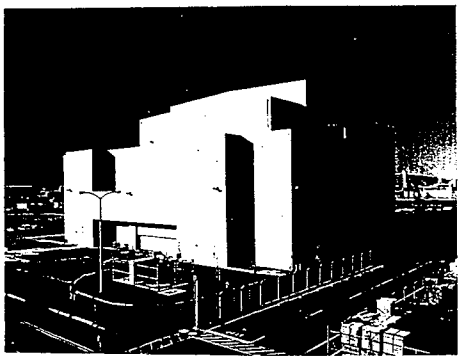
III. TARGET RANGE MEASUREMENT

Range measurements do not produce absolute values, that is exact backscattering levels for a given target. Error mitigation and data processing is usually required even in the best of circumstances. Measurements performed in a controlled environment will produce a good approximation of the backscattering level which is repeatable within a certain tolerance. For this reason the range facility and the data acquisition method deserve some definition.

All range backscattering data presented in this paper was taken at Boeing Defense and Space Group's 9-77 Building Indoor Compact Radar Range[1] over a time period of 4 days. This compact radar range uses 2 reflectors to create a far field condition. That is the wave fronts are propagating nearly parallel after the second reflection. This is easily visualized by comparing to the use of lenses in optics to collimate a light beam. The physical space where models are positioned is referred to as the "quiet zone." This provides a minimum noise area within which a target may be placed, see figure 3.

[2] Macrofol is an impedance sheet material which can be model as having a constant ohms per square value.

The model was hung from four string reels connected to the model at 4 locations. These strings are used to control model yaw and pitch. Unfortunately, the model attachment points were not optimally placed for it's given weight. Thus, as the model was rotated to obtain angular data it flew a slight orbit around the theoretical axis of rotation. The target remained within the quiet zone and thus within the simulated plane wave field at all times, thus only a phase (and not a magnitude) displacement[3] occurs in the data.



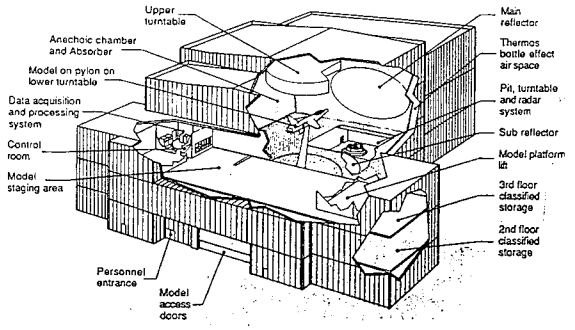


Figure 3, Boeing Defense & Space Group's indoor compact radar range.

The range is characterized by taking various types of data. Some of the more significant are listed here. The range is calibrated using a known target, such as a sphere, positioned in the quiet zone as downrange strobes are collected. A downrange collects scattering data from the full length of the chamber by varying the return signal time at the receive gate. The return of the sphere should occur within the quiet zone at the known level. Adjustments to subsequent radar data are made based on this calibration. Empty chamber data is collected as well. This defines the noise level of the range at any given frequency.

[3] This range facility utilizes a highly precise laser system (POMS [1]) to report exact target position within the global measurement coordinate system. Thus, adjustment for phase displacement in the data can be easily applied

Data was taken in a small/narrow band. Of interest was any set of frequencies with corresponding wavelengths much smaller than the targets overall dimensions. Two transmit-receive horns were used in this band. Presented in this paper are corresponding calculations within the first horn's range. The treated target was near the noise floor at this band, however sufficient data was taken to restore most of the data using standard signal processing methods. For example, the range noise is measured without a target. Then this data is subtracted using the complex field from the data with the target.

The target data was collected for various aspect cuts. The aspect angle is the target's orientation with respect to the incoming field direction or radar look angle. Data for two aspect cuts was collected. First, was a 0° aspect cut. At 0° aspect the target's is horizontal with respect to the look angle. Conversely a 90° aspect cut would position the target normal to the look angle.

The second cut was a 10° great circle. A great circle means a changing aspect angle. That is the target is tilted 10° (aspect 10°) and then rotated without correction to the aspect angle.

Third, a conic of 5° was attempted. A conic maintains the aspect angle of 5° as the target rotates. Unfortunately, due to the target's attachment points this cut could not be accomplished. The length of the strings which hold the target must constantly be adjusted and if the attachment points with respect to the targets weight and center of gravity are not placed optimally it becomes extremely difficult to maintain the constant aspect angle as the target rotates.

For the first two aspect cuts data was collected for both cases, PEC and resistive. Range calibrations taken before and after the above data collection process was within an acceptable tolerance. Thus, all data taken is valid within the same relative error bar.

IV. CALCULATED SCATTERING

Scattering results presented in this paper were calculated with FERM [2], a Method-of-Moments (or MoM) code produced by MIT, and *Carlos*-3D [3], a MoM code produced by McDonnell Douglas. Method-of-Moments is primarily a solution method. Both of these codes use MoM to solve for the scattering from a body in a similar way. The body is discretized using facets, in particular infinitely thin shell triangular facets. One then solves for the currents on these facets induced by an external field. Thus, the number of facets which define the body has an obvious affect on the solution. Also, the induced current is affected by neighboring facets. Therefor, the proximity of surrounding facets must also be considered. In general, the facet definition of a body can have a significant impact on the solution. For this reason the analysis model and the generation there of is described in detail.

The faceted calculation model was generated from a surface representation (IGES 128) of the target. All surfaces on the target were generated from scratch using IDEAS™[4] and TOPGUN [5]. Theses surfaces are only accurate to within +/-0.1 inches, since the target was not originally built with a CAD system. In general, this error would be of concern since, as stated above, the number of facets which define an object affect the solution. However, the number of facets reaches a saturation level which is a frequency dependent. A more exact requirement on the facets is specified by requiring the length of the facet's edges to be defined in terms of the wavelength (λ) at the calculation frequency. Furthermore, resolution beyond a λ per length, e.g. λ /20, will not significantly increase the calculation solution and this quantity could be defined as maximum resolution. Thus the above margin of error in the surface definition is acceptable for calculation frequencies below the maximum resolution quantity.

The facetization of the surfaces, see figure 4, was accomplished using GRIDDER [6] and IDEAS™ [4]. The facet resolution of the target is on the average of λ /10. Figure 5 provides a general gauge for the model resolution. Plotted are the edges sorted by length with various resolution levels depicted. There are other factors involved in creating a faceted model which must also be addressed. These factors are identified in rule-of-thumb meshing criteria which generally produce good results in the calculation. These criteria are termed rule-of-thumb since they are not identified in the user manual provided with the analysis code. These heuristics are a result of trial and error as well as experience with similar numerically complex calculation codes. Two of these factors taken into consideration are 1) the size and spacing of the facets and 2) the distance between facet centers lying in parallel planes.

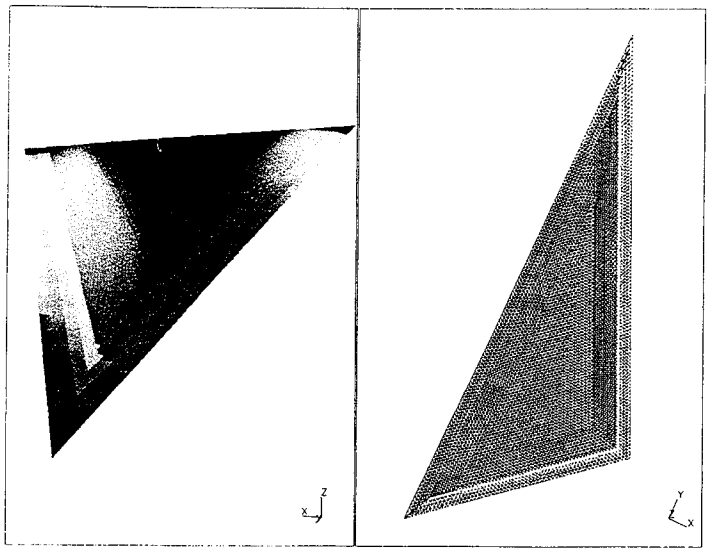


Figure 4, Faceted model, views produced with IDEAS™.

In general, equilateral triangles spaced evenly or spaced such that neighboring facet variation is minimized produces good results in the calculated results. This model maintains a maximum variation of 20% or less. Additionally, the distance between two facets forming a wedge or two facets lying on parallel planes very close together can cause singularity problems in the calculation. This problem was avoided in this model by collapsing facets whose centers were within a 3° wedge angle. Due to the symmetry of the target some of the corner facets of the model were also collapsed.

It is important to accurately define the physical model, or target, however, the accuracy of the calculation model is defined by limiting factors in a numerically complex calculation code. The more significant factors in this study are the per wavelength discretization and singularity criteria which the calculation code can handle. Thus, for the results presented in this study the calculation model is an accurate representation of the physical model.

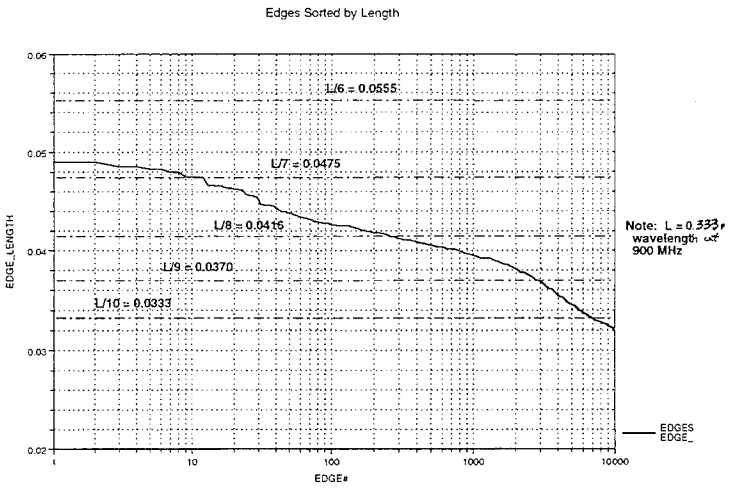


Figure 5, Faceted model edges sorted by length as a resolution gauge.

V. RESULTS/CONCLUSIONS

This study was not conducted to advocate the use of one complex numerical calculation code over the use of another. Several 3D-MoM codes have been created and released within the last few years. This study was initiated to provide a complex platform from which a verification database could be built. At the release of this paper only numerical calculations were accomplished using FERM [2] and *Carlos*-3D [3]. The model contains 25,000 unknowns which even for a MPP is a large problem. Comparisons of the conducting and the treated case are shown only at one frequency.

Comparisons of the conducting case are shown only for FERM and the measured data, see figure 6. The problem of a PEC has been thoroughly studied and it is assumed at a minimum that a 3D-MoM code can accurately calculate scattering for this case. None the less, as a baseline case the conducting model was calculated but this configuration receives a lower priority.

Of greater concern in this study is the treated case. Figure 7 shows a comparison of calculated data from FERM and *Carlos*-3D to the measured data. The data presented here is not shown with error bars. Exact margins of error have not been calculated. The data presented in this study has been processed to provide a clear comparison over several angles. The data is processed by calculating the median for a 5° window around every degree between 0° and 180° at 1° increments. This removes the hashing which is typical in a scattering measurement, see figure 8.

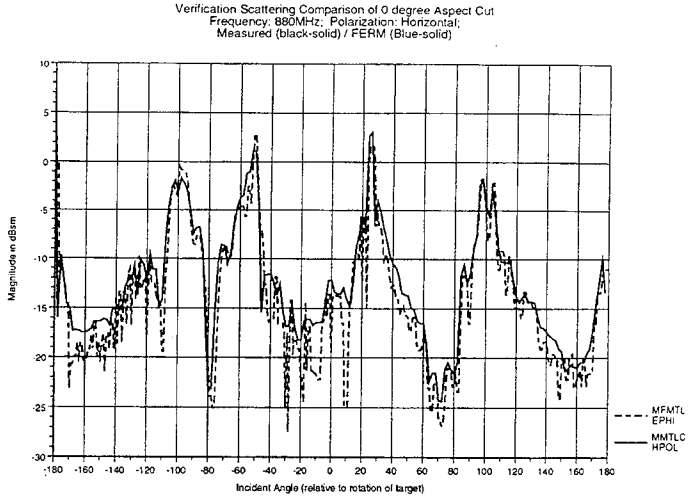


Figure 6, Conducting case results for FERM calculated and measured data.

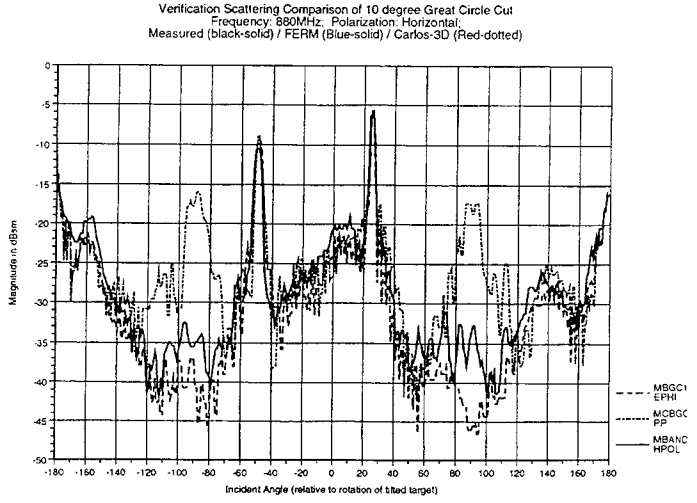


Figure 7, Conducting case results for FERM, and *Carlos*-3D calculated and measured data.

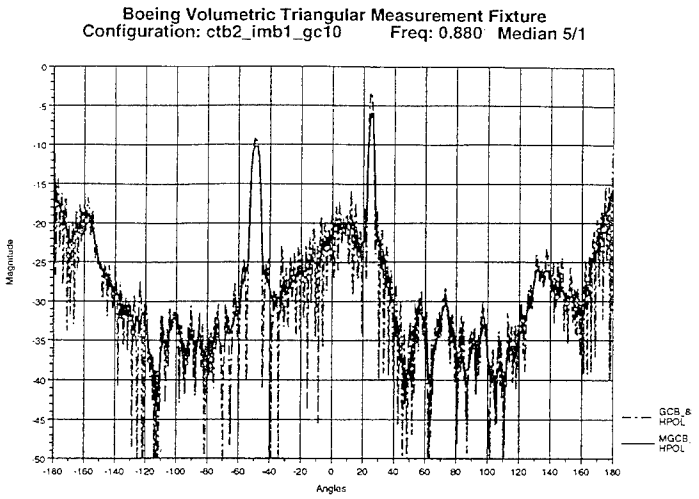


Figure 8, Effect of post processing data.

VI. FURTHER STUDY

As stated above, the primary purpose of this study was to collect data for validation of complex numerical codes. The goal of this study was to create a measurement fixture which could serve to verify several capabilities of a code. This study investigated PEC and infinitely thin sheet impedance surfaces. Two directions of further study have been identified. One evolves changes to the physical model. The other concentrates on refinement of the faceted model and calculations with other complex numerical analysis codes.

Further study needs to collect measurement data from this basic target with each model alteration. Dielectric and magnetic materials should be applied to the model individually and together. Thin materials, which cannot be approximated as infinitely thin sheets, and layered materials need to be addressed as well.

In the other direction, refinement of the faceted model to provide better resolution is planned. Studies on the other polarization, this paper presented on one polarization, and with other 3D-MoM codes, such as PARAMOM [7] will also be addressed.

In closing the authors would like to stress the necessity of a verification platform of this nature. Good measurement data of complex objects is becoming more significant. The ability of numerically complex scattering codes is steadily increasing. Likewise, the availability of MPC (Massively Parallel Computers) and the typical matrix size which can be solved are making jumps in development. A complex verification database should be required as a baseline check to maintain the pace in development of computers, in particular MPCs, and complex numerical codes, specifically electromagnetic scattering codes.

References

1. Boeing Defense & Space Group EM/RF/PHOTONICS System Laboratories, pages 193,194.
2. "FERM, Numerical Modeling of RCS and Antenna Problems," S. Lee, D.A. Shnidman, F.A. Lichauco, Lincoln Laboratories; Massachusetts Institute of Technology (ESD-TR-87-035).
3. "Carlos-3D, Three-Dimensional Method of Moments Code," J.M. Putnam, L.N. Medgyesi-Mitschang, M.B. Gedera; McDonnell Douglas Aerospace East.
4. IDEAS™, Structural Dynamics Research Corporation.
5. TOPGUN, Hyperion Numeric Incorporated.
6. GRIDDER, Boeing Defense & Space Group, Internal Development Program.
7. "Parametric Method of Moments (PARAMOM) RCS Prediction Package," ; Syracuse Research Corporation.

Validation Using a Moment Method Approach with Exact Object Representation

Jan-Åke Larsson, Stefan Ljung and Bo Wahlgren
SAAB SCANIA AB
SAAB Military Aircraft
Linköping, Sweden

1 Introduction

In validating radar cross section or surface current solutions obtained by numerical methods an important issue is to obtain more accurate reference data. As analytical solutions are available only for a limited number of objects, other approaches are needed for more general objects. The approach presented here is also based on numerical calculation, but this method has the advantage of using an exact representation of the object. A drawback of this approach is that only simple geometries can be represented in this way. Nevertheless the method is useful for validating purposes as the object used for validation still can be chosen quite freely.

The validation would be performed as follows: a suitable object, possible to represent as mentioned, is chosen and the scattering problem is solved using both the presented method and the method to be validated. After the two calculations the results are compared, and the accuracy of the method to be validated is estimated. The validated method then can be used to model more complicated objects. Obviously the object selected for validating purposes should be chosen according to the setting in which the validated method will be used.

The presented method solves the Magnetic-Field Integral Equation (MFIE) and the Augmented Magnetic-Field Integral Equation (AMFIE) for the specified geometry. The method consists of five steps:

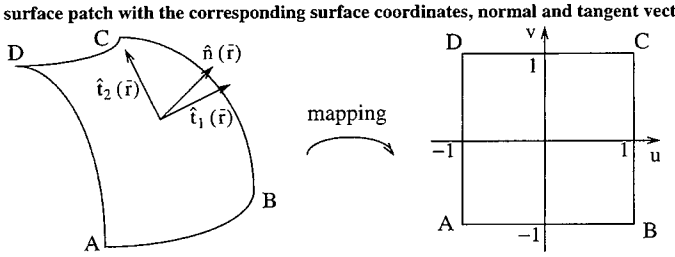
1. Divide the surface into patches.
2. Expand the surface current in appropriate basis functions.
3. Multiply the equation with test functions.
4. Calculate the integrals in question.
5. Solve the system of linear equations that emerges.

The approach has been implemented in MATLAB and FORTRAN. MATLAB is used for user interface, plotting, object generation and so on, while the necessary integrations are carried out by the FORTRAN code. The code is meant to run on a workstation, and not a mainframe, which makes the calculation cheap and simple to perform. The various graphs in this paper have been generated with only workstation hardware. The objects available to the user are such as spheres, cylinders, cones, ogives, boxes, and so on. It is also possible to add new types of objects (and even new patch types). Some results obtained from the code will also be presented, and it will be shown that the accuracy increases significantly by using exact representation of the object.

2 Patch representation and basis functions

The surface must be divided into patches that can be mapped onto some surface where the numerical integration is easy to perform (the patches must of course be numbered, but the patch index is suppressed here for simplicity). One possible and attractive choice is to have patches with four corners, which are easily mapped to a square. This is nice because there are Gaussian 2-dimensional numerical integration (qubature) formulas for a square which are simple but accurate. The patch might look like in figure 1 below.

Figure 1. A surface patch with the corresponding surface coordinates, normal and tangent vectors



The mapping above and the inverse mapping may be represented as

$$\begin{cases} u = u(\bar{r}) \\ v = v(\bar{r}) \end{cases} \quad \text{and} \quad \bar{r} = \bar{r}(u, v) \tag{2-1}$$

The normal and tangent vectors are chosen as

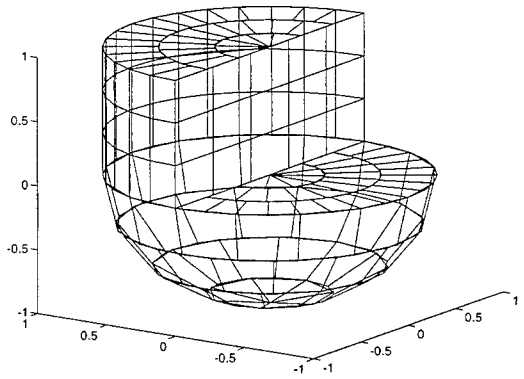
$$\begin{cases} \hat{t}_1 = \dfrac{\partial \bar{r}}{\partial u} \Big/ \left|\dfrac{\partial \bar{r}}{\partial u}\right| \\ \hat{t}_2 = \dfrac{\partial \bar{r}}{\partial v} \Big/ \left|\dfrac{\partial \bar{r}}{\partial v}\right| \\ \hat{n} = \hat{t}_1 \times \hat{t}_2 \end{cases} \tag{2-2}$$

If the mapping used is conformal, the result is that the vectors in (2-2) are orthogonal. This ensures a unique expansion if the needed vector-valued basis functions are based on the vectors $\hat{t}_1$ and $\hat{t}_2$. The basis functions are chosen as follows:

$$\begin{cases} \begin{cases} \bar{I}_1 = \hat{t}_1 \\ \bar{I}_2 = u\hat{t}_1 \\ \bar{I}_3 = v\hat{t}_1 \end{cases}, \begin{cases} \bar{I}_4 = \hat{t}_2 \\ \bar{I}_5 = u\hat{t}_2 \\ \bar{I}_6 = v\hat{t}_2 \end{cases} & \text{on the current patch} \\ \bar{I}_i = \bar{0},\ i = 1 \ldots 6 & \text{elsewhere} \end{cases} \tag{2-3}$$

This choice of basis is made because these basis functions are defined only on one patch, and has no impact on the neighbouring patches. The main benefit is that neighbouring patches need not lie corner-to-corner, which means that if an object with different curvatures on different parts of the surface is to be generated, the different surfaces may be generated separately, and joined without effort (see figure 2 below). Another benefit is that, e g, a spherical surface may be divided into patches which are squares in the θ-φ-plane but all have approximately equal side length in real space. This is important as we want to avoid having many small patches on one part of the surface and some large ones on another part, which would imply wasting computational effort on the small patches while the large ones give rise to a large error.

Figure 2. An object with different curvature on different surfaces. The apparent flatness of the patches arises in the drawing procedure and is not present in the model.



Lastly, the surface element is needed to calculate the integrals in the u-v-plane. Some vector analysis gives

$$ds = \left|\frac{\partial \vec{r}}{\partial u}\right| \left|\frac{\partial \vec{r}}{\partial v}\right| du dv \tag{2-4}$$

The simplest possible patch is the rectangular, flat patch. In this case the mapping becomes quite simple, as the form (i e the curvature) of the patch is not changed from the u-v-plane to real space, just the size, position and attitude. The mapping would look as follows

$$\vec{r}' = \begin{bmatrix} x_1 + (x_2 - x_1)\left(\frac{u+1}{2}\right) \\ y_1 + (y_2 - y_1)\left(\frac{v+1}{2}\right) \\ 0 \end{bmatrix} \tag{2-5}$$

$$\vec{r} = T\vec{r}' + \vec{r}_0$$

where T is a rotational operator and $\vec{r}_0$ is a translation vector. This way of representing the mapping makes it easy to generate a surface in the $\vec{r}'$-space and then rotate and translate it to the desired attitude and position.

A spherical surface has a parameterization which can be divided into patches where $\varphi_1 \le \varphi \le \varphi_2$, and $\theta_1 \le \theta \le \theta_2$ (a square in the θ-φ-plane). The mapping would look like:

$$\begin{bmatrix} \theta \\ \varphi \end{bmatrix} = \begin{bmatrix} \theta_1 + (\theta_2 - \theta_1)\left(\frac{u+1}{2}\right) \\ \varphi_1 + (\varphi_2 - \varphi_1)\left(\frac{v+1}{2}\right) \end{bmatrix} \tag{2-6}$$

$$\vec{r}' = \begin{bmatrix} r\cos\varphi\sin\theta \\ r\sin\varphi\sin\theta \\ r\cos\theta \end{bmatrix}$$

$$\vec{r} = T\vec{r}' + \vec{r}_0$$

An ogival surface has almost the same parameterization as a spherical surface, and therefore almost the same parameterization may be used if $\sin\theta$ is replaced by $(\sin\theta - \sin\theta_0)$.

Circles, cylinders and cones are three types of objects that can be described with the same parameterization:

$$\begin{bmatrix} r \\ \varphi \\ z \end{bmatrix} = \begin{bmatrix} r_1 + (r_2 - r_1)\left(\frac{u+1}{2}\right) \\ \varphi_1 + (\varphi_2 - \varphi_1)\left(\frac{v+1}{2}\right) \\ z_1 + (z_2 - z_1)\left(\frac{u+1}{2}\right) \end{bmatrix} \tag{2-7}$$

$$\bar{r}' = \begin{bmatrix} r\cos\varphi \\ r\sin\varphi \\ z \end{bmatrix}$$

$$\bar{r} = T\bar{r}' + \bar{r}_0$$

The triangular patch is needed for the representation of a pyramid, for instance. Also, if there was a triangulation available on some complex object, it would be nice if the method used here was able to use it.

In the above technique the patches are easy to map conformally from the u-v-plane to the $\bar{r}'$-space. The mapping is sometimes non-conformal at one point of the patch, but this is always at an edge of the patch, so it does not lead to a problem in the above cases. A conformal mapping from a square to a triangle is possible to construct, but it would be rather complicated. It would also imply that the tangent vectors would vary over the surface, as on the curved patches above, which seems a bit inappropriate as the vectors on the surface patch would be easily expressed with two constant orthogonal vectors. A simpler approach would be to copy the expression (2-5), but to contract one side to a point. The result is

$$\bar{r}' = \begin{bmatrix} \left(x_1 + (x_2 - x_1)\left(\frac{u+1}{2}\right)\right) \cdot \left(\frac{1-v}{2}\right) + x_o \cdot \left(\frac{1+v}{2}\right) \\ y_1 + (y_2 - y_1)\left(\frac{v+1}{2}\right) \\ 0 \end{bmatrix} \tag{2-8}$$

$$\bar{r} = T\bar{r}' + \bar{r}_0$$

This mapping is non-conformal on the entire patch. However, this does not impose a problem as the needed normal and tangent vectors may be chosen as

$$\begin{cases} \hat{t}_1 = T\hat{x}' = \dfrac{\partial \bar{r}}{\partial u} \Big/ \left|\dfrac{\partial \bar{r}}{\partial u}\right| \quad (!) \\ \hat{t}_2 = T\hat{y}' \neq \dfrac{\partial \bar{r}}{\partial v} \Big/ \left|\dfrac{\partial \bar{r}}{\partial v}\right| \\ \hat{n} = \hat{t}_1 \times \hat{t}_2 = T\hat{z}' \end{cases} \tag{2-9}$$

Note that the choice of tangent vectors must not necessarily be the one mentioned earlier. We only need orthogonal vectors tangent (and normal) to the patch. The basis functions are obtained from these vectors as usual. As for the surface element, the mapping is non-conformal and (2-4) does not work. We must use the Jacobian instead, and thus the surface element is

$$ds = \left| \begin{bmatrix} \dfrac{\partial x'}{\partial u} & \dfrac{\partial x'}{\partial v} \\ \dfrac{\partial y'}{\partial u} & \dfrac{\partial y'}{\partial v} \end{bmatrix} \right| dudv = \frac{x_2 - x_1}{2} \frac{1-v}{2} \cdot \frac{y_2 - y_1}{2} dudv \tag{2-10}$$

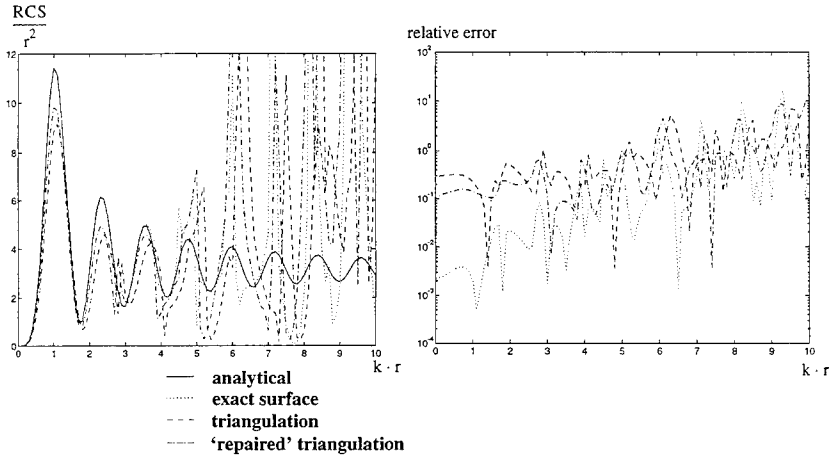
3 Solution of the equations and calculation of RCS

The test functions are chosen to be Dirac's delta functions, and multiplication and integration leads to a system of integral equations which solves the MFIE and AMFIE in certain points at the surface. We thus have a point matching (or collocation) method. The integrals is numerically calculated by FORTRAN subroutines, and finally, the system of equations is solved in MATLAB. Some results calculated with this method is now presented.

First a simple spherical problem is chosen, and since the solution to the problem of a perfectly conducting sphere can be calculated analytically, this solution will be used as reference. In figure 3 the MFIE is used on spheres with 100 patches and different types of surface patches. As can be seen, it is a great benefit to use the exact surface representation. The relative error is reduced with a factor ~30 on the interval (0,3.7). Outside this interval the solutions are not useful, since the relative error increases significantly at higher frequencies.

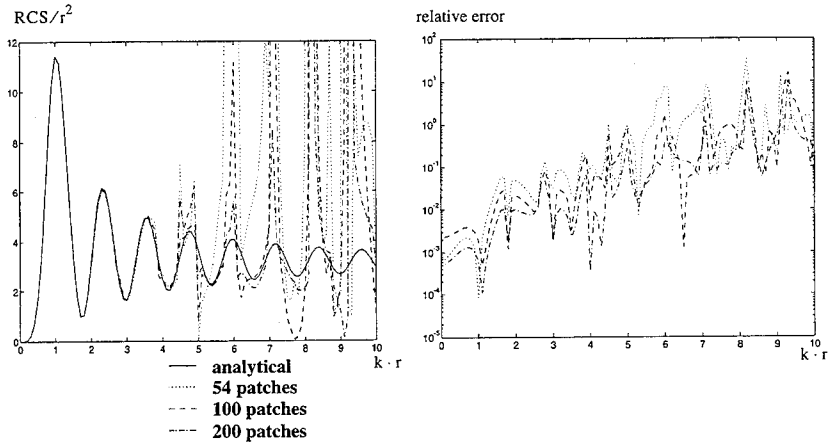
One frequently used way to 'repair' the damage done to an object when triangulating is to increase the size somewhat so that the area of the object is the same in the triangulation as in real space. The effect of such a 'reparation' is also shown in figure 3. The relative error improves with a factor ~1.6 as compared to the ordinary triangulation. One of the improvements of the 'reparation' is rather important, though; the maxima of the RCS appear on the correct frequencies.

Figure 3. Comparison between triangulation and exact surface representation



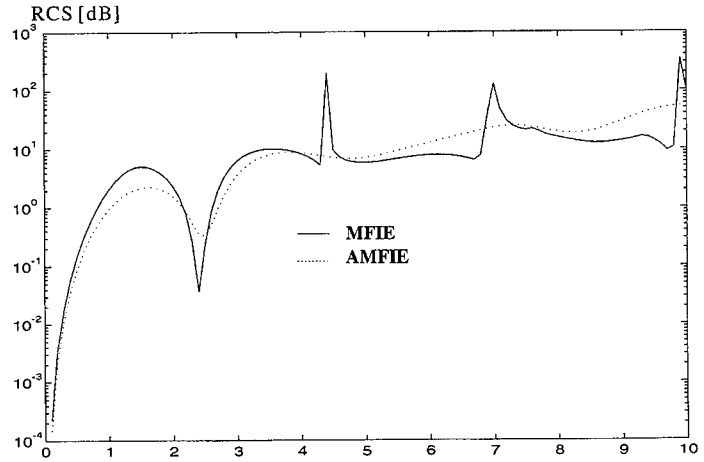
In figure 4 the MFIE is used on the exact surface representation. The number of patches is varied, and it is apparent that doubling the number of patches decreases the relative error by a factor ~2. When using 200 patches, the relative error is less than 1% as high as $k \cdot r \approx 4.5$, except for the resonances (compare with $k \cdot r = 2\pi$, that is equivalent to a wavelength equal to the radius of the sphere). An upper limit to the number of patches is imposed by the available memory, because the method utilizes full matrices. The hardware available for this work set this limit at approximately 200 patches. When exceeding this, a lot of disk swapping starts to take place, which slows down the calculations almost to a dead stop.

Figure 4. Different number of patches



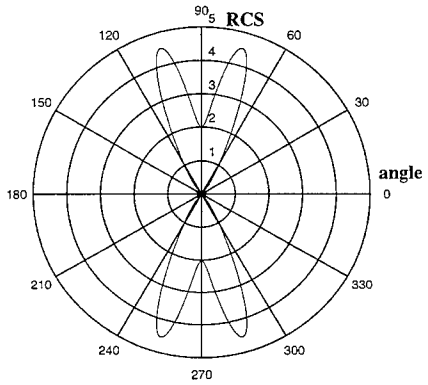
These resonances are now the main problem. A way to remove the spurious solutions is to implement the Augmented MFIE [8]. This is effective if the object in question does not possess any rotational symmetry, and then all the spurious solutions are removed by the AMFIE. Below the result is plotted from usage of MFIE and AMFIE on a cube with 96 patches. Unfortunately, the solutions differ somewhat because the AMFIE is more sensitive to certain errors introduced in the numerical model [1],[8]. Another drawback is that the AMFIE does not remove all the spurious solutions if the object possesses rotational symmetry.

Figure 5. RCS from a cube



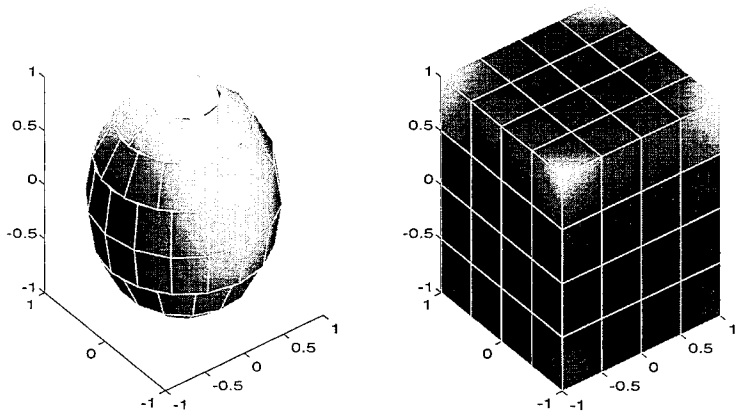
To illustrate another usage of the equation, a calculation has been made on an ogive with 74 patches. Instead of varying the frequency, the incidence angle is varied. The angle is measured from the 'tip' of the ogive. Note the low front and back RCS seen in figure 6.

Figure 6. Calculated RCS for an ogive



One way to visualize the surface currents is to plot the absolute value of the currents on the surface patch. The results of some calculations are shown in figure 7. Darker patches means that less current flow on the patch, but the color scale is only valid in each diagram by itself.

Figure 7. Currents on a sphere and a cube.



4 Conclusions

We have seen that the MFIE and the AMFIE may be solved rather accurately with this approach, especially when compared to an ordinary triangulation (see section 3). The method shows considerable accuracy for k values as high as 4.5, at least for a sphere. A drawback is that the matrices are full, so a full LU- or QR-factorization is needed, which takes a large amount of CPU-time. Also, memory requirements set the upper limit to the number of patches. The calculations are quite possible to perform, though, and the calculations may be done on workstation hardware (which is inexpensive as compared to mainframe CPU-time).

The less accurate AMFIE method may not seem to be useful, but it can still be used in conjunction with the MFIE in a special way. The MFIE is solved, but then the normal component of the magnetic field is checked, and if it is nonzero the AMFIE is solved instead to give a solution where the normal component is zero. This allows for

usage of MFIE at frequencies away from the cavity eigenfrequencies, and so the accuracy of the MFIE is retained, while most of the spurious solutions are eliminated by the AMFIE.

Some closing suggestions for continued work may be in order:

- The Galerkin approach could be utilized in the MFIE and AMFIE equations. This would most probably increase the accuracy, but at the price of increased CPU-time. One great benefit, though, is that this does not demand more memory, and thus it is possible to increase the accuracy somewhat even when the upper limit in memory is reached.
- It has been noted that the MFIE is not well suited to solve thin plate problems [2]. Surfaces inserted in this equation must be closed, but the EFIE can solve problems which contain open surfaces accurately. This means that the implementing the EFIE allows for a larger class of problems to be solved. Some problems in implementing the EFIE in this approach has been noted; e g the collocation method is not possible to use [1].
- Some work could also be done to implement the combined-field or the combined-source equations. The benefit of this would be that *all* the spurious solutions would be eliminated [6],[7]. The same problems as concern the EFIE are present [1].
- Objects generally have sharp corners, and there is reason to suspect that the currents change rapidly there (see for instance figure 7), which may give rise to a large error in the current expansion on patches near the edges. To prevent this, the patches near the corners should be chosen smaller than the other patches. This is currently possible to perform manually, but might be done automatically when setting up a problem.

5 References

[1] J-Å. Larsson, *Calculation of Radar Cross-Section Using the Boundary Element Method and Exact Object Representation*, Final report, LiTH-MAT-Ex-94-06, Department of Mathematics, Linköping University, Sweden, 1994.

[2] C. A. Balanis, *Advanced Engineering Electromagnetics,* Wiley, 1989.

[3] J. J. H. Wang, *Generalized Moment Methods in Electromagnetics,* Wiley, 1991.

[4] A. H. Stroud, D. Secrest, *Gaussian Quadrature Formulas*, Prentice-Hall, 1966.

[5] E. F. Knott, J. F. Shaeffer, and M.T. Tuley, *Radar Cross Section, 2nd ed,* Artech House, 1993.

[6] J. R. Mautz, R. F. Harrington, "H-Field E-Field, and Combined-Field Solutions for Conducting Bodies of Revolution", *Arch. Elektron. Übertraugungstech. (AEÜ)*, Vol 32, No 4, pp.157-164, 1978.

[7] J. R. Mautz, R. F. Harrington, "A Combined-Source Solution for Radiation and Scattering from a Perfectly Conducting Body", *IEEE Trans. Ant. Prop.*, Vol AP-27, pp 445-454, July 1979.

[8] A. D. Yaghjian, "Augmented Electric- and Magnetic-field Integral Equations", *Radio Science*, Vol 16, pp 987-1001, November-December 1981.

[9] L. M. Delves, J. L. Mohamed, *Computational Methods for Integral Equations*, Cambridge University Press, 1985.

[10] I. Gladwell, R. Wait, *A Survey of Numerical Methods for Partial Differential Equations,* Oxford University Press, 1979.

IR MEASUREMENTS FOR VALIDATING EM ANALYSIS TOOLS

Michael Seifert
Timothy Blocher
Anthony Pesta
Rome Laboratory/ERST
525 Brooks Road
Griffiss AFB, NY 13441-4505

Phone: (315) 330-7642
Fax: (315) 330-7083
Email: seifertm@rl.af.mil

Abstract

Infrared (IR) measurement techniques developed to determine electromagnetic (EM) field distributions are used to validate predictions made by Computational Electromagnetic (CEM) simulation tools such as the General Electromagnetic Model for the Analysis of Complex Systems (GEMACS) code. This paper provides comparisons between measured and simulated results from various scattering experiments to demonstrate the feasibility and illustrate the application of the IR measurement technique as validation technique for CEM tools.

A horn antenna was used to generate the fields during the EM scattering experiments. These experiments were performed in the Rome Laboratory anechoic chamber to prevent unintentional EM interference from distorting the measurement results. An IR detector material is placed near the test object to absorb a portion of the EM field. The resulting temperature distribution on the IR detector is measured with an IR measurement system. The temperature distribution is directly related to the intensity of the scattered EM fields.

IR Background

The IR measurement technique is a minimally perturbing measurement technique used to map EM fields and provide a visual two dimensional representation EM field distributions. This technique is based on the thermal heating which occurs when EM energy is absorbed by a lossy dielectric or resistive detector material. The absorbed EM energy is converted into conducted and convected heat energy. The absorbed energy is then re-radiated as EM energy that is concentrated in the IR band. This technique is employed as a diagnostic tool to map the EM fields with and without the presence of measurement probes [1]. A sheet of carbon loaded Kapton with a resistivity of 100 ohms/square is used as the IR detector material. It absorbs a small portion of the EM energy which causes the surface temperature of the detector to rise above the ambient temperature which can be detected by an IR measurement system. The absorbed power in a volume is a function of both the electric and magnetic fields as shown in the following equation:

$$P_{abs} = \int_V (\sigma E^2 + \omega \epsilon'' E^2 + \omega \mu'' H^2) dv \qquad (1)$$

where σ is the conductivity of the detector, ϵ" is the imaginary permittivity of the detector, μ" is the imaginary permeability of the detector and ω is the angular frequency of the incident radiation. A thin lossy detector made of carbon loaded Kapton is placed in the area where the two-dimensional map of the EM field desired. The conductivity and the imaginary components of the permittivity and permeability cause the temperature of the detector to rise above the ambient temperature. The increase in temperature is proportional to the local electric and magnetic field intensity at every location on the detector [2]. Thus, a two-dimensional map of the field intensity is produced. The absolute temperature across the IR detector is recorded, digitized and stored using an Agema Thermovision infrared measurement system. This data can be used to directly obtain the relative field intensity or absolute field intensity through a temperature calibration procedure. This technique has been applied to determine the radiated fields from antennas in both the near and far field, intensity of EM fields coupled through aperture in a shielded enclosure, and modal distributions of EM fields excited inside metal cavities [3]. Another application of the IR measurement technique will be presented in this paper is the validation of CEM analysis tools and models. Minimally perturbing IR measurements will be directly compared to the CEM simulated data, providing insight in the area of model development, model enhancement and simulation techniques.

IR Measurement Procedure

Validation of the CEM predictions were accomplished by performing IR measurements in Rome Laboratory's anechoic chamber. The anechoic chamber is used to minimize unintentional EM fields and EM reflections from distorting the measurement results and to provide a stable temperature environment. The measurement technique involves placing the IR detector (carbon loaded Kapton sheet) in front of the EM radiating source. A 1-2 GHz standard gain horn is used to generate the EM field. The physical dimensions of the horn were measured to allow the horn to be properly modeled for the CEM simulations and to determine how far the IR detector must be placed from the horn in order to be in the far field. The far field condition is determined by using the following equation:

$$\text{Far Field} = 2D^2/\lambda \qquad (2)$$

Where (D) is the largest dimension of the horn antenna (D = .51 meters) and λ is the wavelength of the transmitted frequency, at 1GHz, the calculated far field is 1.7 meters. The IR detector is placed on a styrofoam block to minimize EM reflections and it is positioned directly in front of and at various distances from the face of the horn antenna. A long wave IR scanner has a spectral response of 8-12 microns and can detect temperature changes as small as .08 °C. The scanner is placed on axis with the horn antenna and IR detector as shown in figure 1. The IR scanner samples data at 136 lines per frame and 272 samples per line, the data is digitized and stored. A synthesized sweep generator is used to generate the transmit signal, it is pre-amplified, then amplified by a 200 Watt TWT Amplifier. The output of the TWT is connected to a directional coupler, the output of the coupler is connected to the antenna. The coupler samples the forward and reflected power and is displayed by a power meter, this allows the power transmitted by the antenna to be determined and the power density at the IR detector to be calculated. The IR measurements begin by measuring the background temperature over the IR detector without an EM field applied. The background temperature distribution is stored in memory and is subtracted from the temperature distribution of the EM signal.

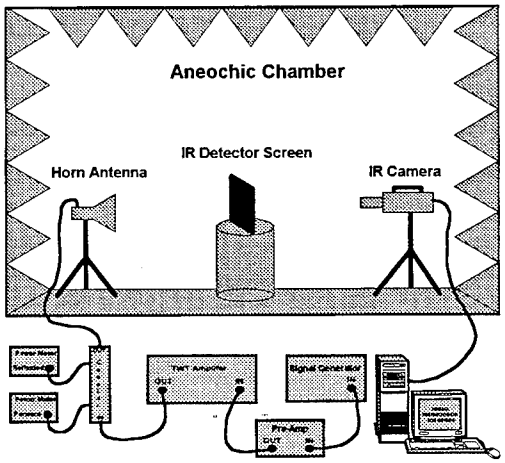


Figure 1.

Computational Electromagnetics (CEM) Tool

The General Electromagnetic Model for the Analysis of Complex System (GEMACS) version 5.3 is used to demonstrate the feasibility of the IR measurement technique in the validation of CEM codes and models. GEMACS is a robust CEM tool that employs multiple solution techniques to determine various electromagnetic observables at high and low frequencies, interior and exterior to scattering objects. These observables include antenna patterns, field distributions, current distributions on structures, and EMI/EMC transfer functions [4].

At Rome Laboratory, GEMACS is primarily used for the "mounted antenna" problem. Antennas tend to perform to specification in "free-space" but can perform poorly when mounted on their host platform. The antenna/system performance can be degraded due to platform scattering or even antenna-to-antenna coupling. In order to accurately characterize the performance of these systems, it is essential for the CEM tool's computations to be valid and also for the antenna and platform models to be constructed very carefully.

Simulations

GEMACS is used to predict the EM field distribution resulting from a horn antenna in free-space and in the presence of a cylindrical scatterer as previously described. GEMACS and the user must, therefore, model the antenna, the cylinder and the EM interactions accurately.

GEMACS has a number of source modeling options that can be categorized as either "stiff" or "soft" [4]. A source having invariant radiating characteristics is called a "stiff" source while the radiating characteristics of a "soft" source are influenced by the presence of other sources and the

host platform. Both types of sources have been applied to the established scenario.

Data Comparison

In the following section the GEMACS simulations results and the IR measurement results are represented as gray scale images, areas of high field levels and high temperatures are white and the lowest field levels and temperatures are black. The first set of simulations involves the use of the GEMACS PSRC command [5]. One feature of the PSRC command analytically represents a far-field horn antenna based upon user supplied geometric and electrical information. This is a "stiff" source which is, therefore, not affected by near field scatterers. The frequency of this horn model is 1 GHz and the field data is computed at 2 meters from the face of the horn. The plane of free-space field data produced by this model is shown in figure 2. The IR measurement of the free-space field distribution is shown in figure 3. The measured and simulation data compare very well, the number of rings is the same as is the relative field intensity. The measured data is somewhat noisy and is not as defined as the simulation data, this is due to the power level available at 2 meters. At a higher power level or closer distance to the source the IR measured data would be more well defined. The cylindrical obstruction, modeled by the Geometric Theory of Diffraction (GTD) capability in GEMACS, was then introduced into the simulation. This cylinder is positioned longitudinally in front of the source centered about the 2 meter distance, this data is shown in figure 4. Note that only half of the measurement plane is simulated to reduce computation time. The correlation between the simulations and the measurements indicate that both the user generated model and the GEMACS computations are valid within the constraints of this particular scenario. The IR measurement of the cylinder positioned longitudinally in front of the source is shown in figure 5. Again the IR measured data compares favorably with the simulation data, the structure is similar with the simulation data being more defined. The hot spot on the side of the cylinder in the simulation data is due to discontinuities at the boundary of the cylinder. The next simulations address the use of "stiff" sources in the presence of near-field scatterers. A 2 GHz PSRC horn source is positioned 0.5 meter from of a GTD cylinder placed sideways. The data is computed from the source to the cylinder as shown in figure 6. The data doesn't compare very well with the IR measurements shown in figure 7. This indicates that the PSRC horn model is not appropriate for use in this situation. Next, a 2 GHz spherical wave [4,6] "stiff" source is applied to the same configuration and the data is shown in figure 8, and compares well with the IR measured results in figure 7. Therefore, the IR measurements helped to identify that the spherical wave source should be used to represent a horn antenna in the presence of a small near-field object. The IR measurement technique has also been used in the validation a Method of Moments (MOM) patch model of a 1 GHz horn antenna. MOM antenna models are "soft" sources which, therefore, accounts for the presence of near field scatterers like those found on aircraft and ships. The results of this simulation are plotted in figure 9 and show a distinct lack of agreement between the simulation and the IR measurements shown in figure 3. This model is therefore not valid, probably due to asymmetry in the patching of the horn model.

Conclusions

IR measurements were used to map the electromagnetic field distributions generated by a standard gain horn and the fields scattered by a metal cylinder for both near and far field conditions. Each measurement scenario was modeled and simulated using the GEMACS code to provide a direct comparison with the measured results. The measured IR data compared favorably to the simulation data, the general shape and relative levels of the radiation patterns are in close agreement. The IR measurement technique

provides a quick and accurate representation of antenna patterns and electromagnetic scattering effects. The IR measurement technique can also be used to identify potential problems in the development of antenna models and simulation techniques. Thus far only simple geometric shaped scatterers have been considered, however as more complex problems are considered the complexity of the simulation problem and the simulation run time will also increases. This paper has demonstrated the feasibility of using IR measurements to validate, enhance and improve the performance of CEM tools.

References

1. Pesta, A.J., and Seifert, M.F. "Infrared Measurements of Electromagnetic Fields", DUAL-USE Technologies and Applications Conference, SUNY Institute of Technology, Marcy, N.Y, May 1993.

2. Norgard, J.D, Metzger, D.W., and Sega, R.M., "Analysis of Probe Measurement Accuracies and Scattering Effects", Technical Report RL-TR-91-252, Rome Laboratory/ERST, Griffiss Air Force Base, NY.

3. Norgard, J.D., Metzger, D.W., and Sega, R.M., Cleary, J, and Seifert, M.F., "Infrared/Microwave Correlation Measurements", Proceedings of the 1991 SPIE Symposium, San Diego, CA, July 1991.

4. Coffey, E.L., Coffey N.W. and Kadlec D.L. 1988. "GEMACS Source Book." Technical Report RADC-TR-88-102. Rome Air Development Center/RBCT, Griffiss Air Force Base, NY.

5. Coffey, E.L., Coffey N.W. and Kadlec D.L. 1994. "General Electromagnetic Model for the Analysis of Complex Systems (GEMACS): Version 5.3 Update Pages" Technical Report RL-TR 90 360. Rome Laboratory/ERST, Griffiss Air Force Base, NY.

6. Coffey, E.L., Coffey N.W. and Kadlec D.L. 1990. "General Electromagnetic Model for the Analysis of Complex Systems (GEMACS) - Version 5, Users Manual" Technical ReportRADC-TR-90-360. Rome Air Development Center/RBCT, Griffiss Air Force Base, NY.

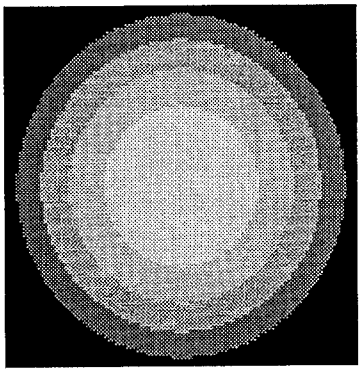


Figure 2: Horn Free Space Simulation Data

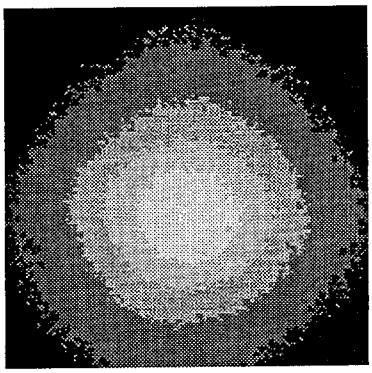


Figure 3: Horn Free Space IR Data

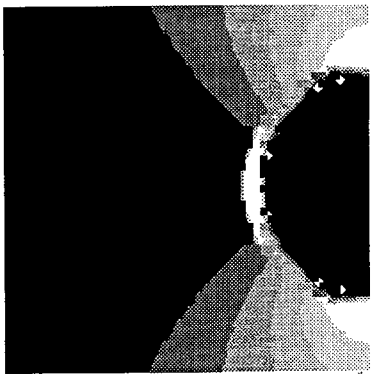


Figure 4: 1/2 Cylinder Simulation Data

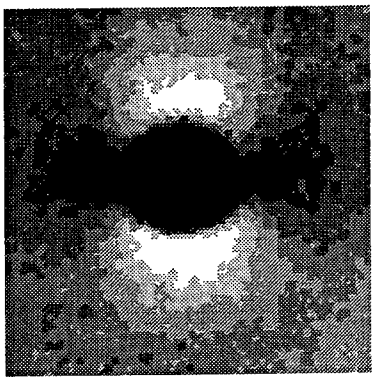


Figure 5: IR Data of Cylinder End View

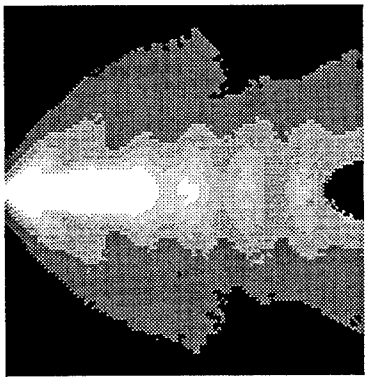


Figure 6: 2 GHz PSRC Horn Source

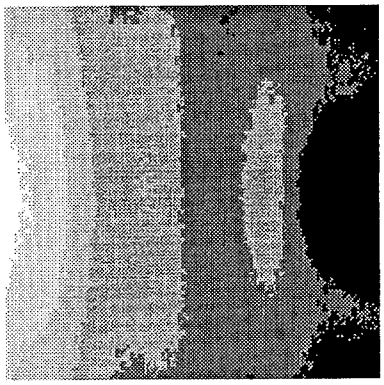


Figure 7: IR Data of Cylinder Side View

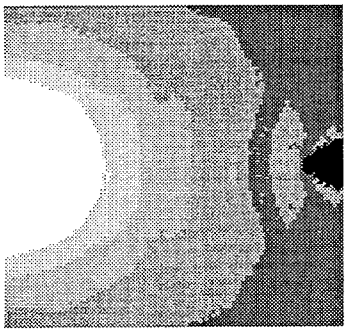


Figure 8: 2 Ghz Spherical Wave Source

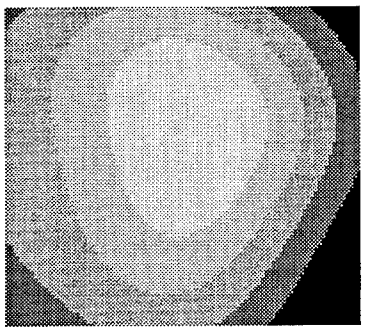


Figure 9: Method of Moments Model

SESSION 4D:

EMI/EMC/EMP

Analysis of Electromagnetic Interference at an Ocean Observation Post

Lizhou Bai, Jin F. Dai
Nanjing Research Institute of Electronic Engineering
P.O.Box 1406--34, Nanjing
China, P.R. (210014)

Abstract

This paper analyses the EMI at an ocean observation post. Detailed calculation in this paper includes five aspects:a) near-field gain of paraboloid antenna, b) gain of communication antenna array,c) coupling prediction between communication antennas of station B and D,d) EMI of communication station B caused by radar station A, and e) EMI of communication station D caused by radar station A.In practice,some arguments we calculated are also measured and given in this paper. We find that the calculated values are very close to the measured. The object of above calculation is to analyse EMI of communication transceiver which would happen caused by radar and to provide the basis for EMC design of the Information Transmitting System.

1.Introduction

It's well known that digital microwave circuits should stay at a distance as far as possible from radar (>10 km). But at the ocean observation post we studied, radar and communication stations are all be located at the same position in order to transfer radar information conveniently.This situation makes it difficult to conduct EMC design of Information Transmitting Systems. There are three aspects of the interference of microwave communication systems caused by radar:a) frequency spectrum of radar signal,b) parasitic oscillation, and c) wide-bands' noise of radar's output signal. Whether it can really cause interference is up to the coupling situation between radar antenna and communication antenna.Of course,there is not only field coupling but also connection of signal lines at the same post,so conduction interference exits too. But this problem can be solved by means of co-site grounding design and necessary wave filtering, thus,conduction interference is not discussed in this paper.

We know that the directional function of radar antenna only gives the far-field EM distribution, but near-field EM distribution also exits because of the short distance between radar and communication station. The arrangement of the observation post we studied is shown as Fig.1.

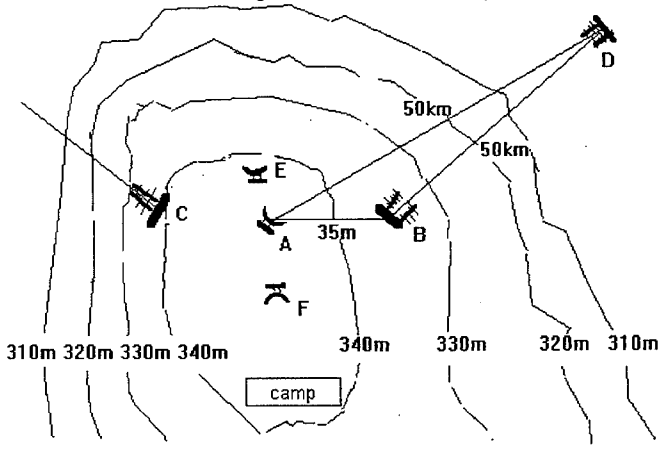


Figure -1. Layout of the observation post we studied

In this small post,there are three radars and two microwave relay stations.Each station is marked with alphabets from A to F, where D is a remote microwave relay station.

Because radar E, and F all work in the SM band, the interference with communication can be ignored when discussing coupling between antennas.

The EMI characteristics of communication station B,C,and D caused by radar A are as follows:

a)Low-frequency partition interference to communication stations, which can be obtained by means of Fourier Analysis.

b)Because the distances,A to B and A to C,are all about 35m,near-field directional function must first be calculated before calculating near-field antenna gain.

c)The distance between radar station A and communication station D is 50km. the angle between two electric axles is 0.5°. It belongs to far-field interference, that is the coupling problem between wave beams, the angle of which is 0.5°.

The procedure of calculating the interference of B and D caused by A is as follows:

a)Calculate the flux of interference power density respectively at B and D produced by radiation field of radar.

b)Calculate the signal power of antenna A at station B and that of antenna B at station A.

c)Compare the intensity of signal and intensity of interference respectively at B and D to obtain the interference of communication B and D caused by radar A .

We know that EMC condition is defined as formula (1):

$P_A = P_t + G_t + G_r - L_i - L_f - L_e$ (1)

P_A: the utilizable power (received through antenna) (dbmw).

P_t: the power of transmitter (peak value of radar power) (dbmw)

G_t: antenna gain of transmitter (db)

G_r: antenna gain of receiver (db)

L_i: wave propagation loss (db)

L_f: transmission loss of feed line from antenna to receiver (db)

L_e: polarization isolation loss of receiver antenna (db)

Formula (2) defines the condition of interference:

$P_A - P_r >= 0$ (2)

P_r: sensitivity of receiver (dbmw)

2. Caculation of Near-field Gain of Paraboloid Antenna

According to the principles of antenna, the field distribution can be seperated into three areas: Rayleigh, Fresnel Approximation, and Frunhofer Approximation, which is shown as Fig.2.

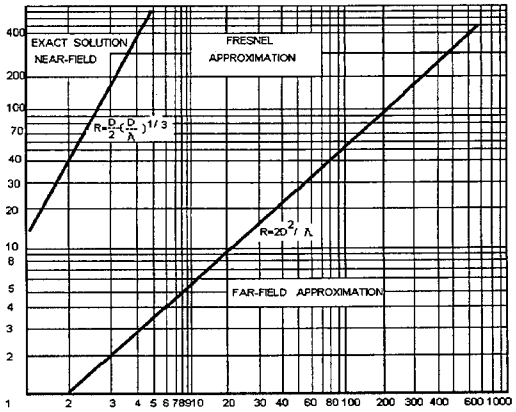


Figure-2. Field integral appoximations for unfocused apertures

Antenna of radar A keeps at a distance of 35m from communication antenna. Together with the technical specification of the antenna of radar A, we get:Reflector calibre D = 15.5 m,Wave band λ = 0.234 m,Distance R =35 m.Thus,R/D = 2.26, D/ λ = 66, therefore, the field we studied falls into Fresnel Approximation. We know that distribution function is:

$$F(\xi,\eta,0)=A(\xi,\eta,0)\exp[-jk\varphi(\xi,\eta,0)] \quad (3)$$

where, A: Amplitude, $k=2\pi/\lambda$, φ: Phase .

At any point P(x,y,z), the field of scalar quantity caused by above distribution function is:

$$\Psi(P)=(1/4\pi)\int_S F(\xi,\eta,0)\{[\exp(-jkr)]/r\}X$$
$$X[(jk+1/r)\cos x + jk\partial\varphi/\partial n -(1/A)\partial A/\partial n]ds \quad (4)$$

In Fresnel Appoximation area, the amplitude factor of integral function in formula (4) can be made the following appoximation: $1/r<<k$, $1/r \cong 1/R$, and $\cos x \cong \cos\theta$. Generally, amplitude $A(\xi,\eta,0)$ is a moderate function of distance, thus, $\partial A/\partial n \cong 0$. So, formula (4) can be made the following approximation:

$$\Psi(P)=j\exp(-jkz)/2\lambda R\int_S F(\xi,\eta,0)\exp\{-jk[(x-\xi)^2/2z - (y-\eta)^2/2z]\}X$$
$$X(\cos\theta+\partial\varphi/\partial n)d\xi\,d\eta \quad (5)$$

To radar A, the antenna of which is paraboloid, we can obtain: $\partial\varphi/\partial n = \partial\varphi/\partial z = 1$, $F(\xi,\eta,0) = F_1(\xi)F_2(\eta)$, we get:

$$\Psi(P)=j(1+\cos\theta)\exp(-jkz)/2\lambda R\int_{sh} F_1(\xi)\exp\{-jk[(x-\xi)^2/2z]\}d\xi\,X$$
$$X\int_{sv} F_2(\eta)\exp\{-jk[(y-\eta)^2/2z]\}d\eta \quad (6)$$

The deduction procedure is omitted here, we obtain:

$$\Psi\Psi^*=(\pi^2/4)\{[\cos(L\pi/2)[C(1/2L^{1/2}-L^{1/2})+C(1/2L^{1/2}+L^{1/2})]$$
$$+\sin(L\pi/2)[S(1/2L^{1/2}-L^{1/2})+S(1/2L^{1/2}+L^{1/2})]^2$$
$$+[\sin(L\pi/2)[C(1/2L^{1/2}-L^{1/2})+C(1/2L^{1/2}+L^{1/2})]$$
$$+\cos(L\pi/2)[S(1/2L^{1/2}-L^{1/2})+S(1/2L^{1/2}+L^{1/2})]^2\} \quad (7)$$

where, $L=R/(2D^2/\lambda)$, C and S are Fresnel integrals, D is the horizontal calibre of antenna, λ is operation wavebandth, R is the distance between antennas. Ψ^* is the conjugate complex of Ψ. The degradation of antenna gain in the near-field yields:$G_d=G_0\Psi\Psi^*$, where G_0 is the antenna gain in far-field. Fig.3 shows the relationship between G_d and L.

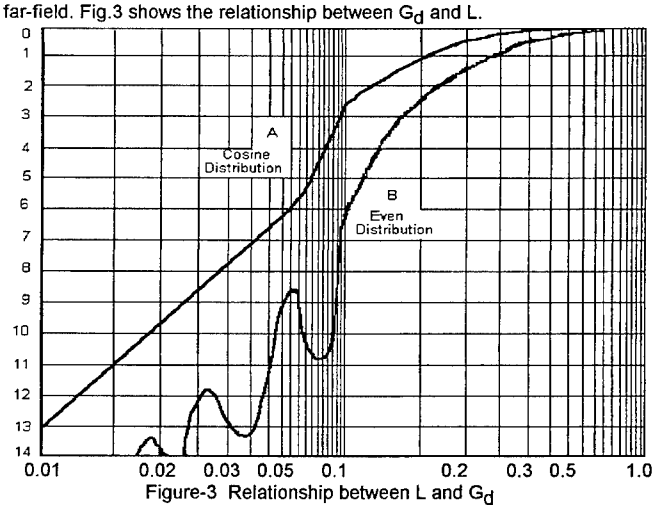
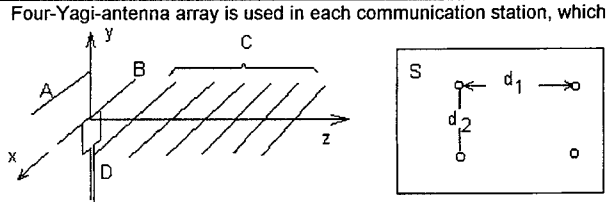


Figure-3 Relationship between L and G_d

To radar A, L = 35m / [2X(15.5m)^2 / 0.234m] = 0.017, thus, G_d = 10.8db according to Fig.3. Therefore the Interference yields: 38db - 10.8db = 27.2db.

3. Calculation of the Gain of Communication Antenna Array

Four-Yagi-antenna array is used in each communication station, which is shown as Figure-4.



(a) (b)

A: Passive reflection oscillator, B: Active emission oscillator
C: Guide oscillator D: Feeding cable S: Reflection net
d_1, d_2: Distance between two neighbour Yagi antennas

Figure--4. (a) Structure of Yagi antenna
(b) Disposition of antenna array

Generally,guide oscillators are apart $\lambda/4$ from each other,the distance between reflection oscillator and active oscillator is also $\lambda/4$.Because the antenna is more than 10m away from ground, effect on radiation caused by ground can be ignored. The directional function is:

$$f(\theta,\varphi)=\{\cos[(\pi/2)\sin\theta\cos\varphi]/\cos\theta\}X$$
$$X\{\sin[(kl/2)(1-\cos\theta\cos\varphi)]/\sin[(kd/2)(1-\cos\theta\cos\varphi)]\}$$
$$X2\cos[(kd_1/2)\cos\theta\sin\varphi]X2\cos[(kd_2\sin\theta\cos\varphi)] \quad (8)$$

where, $d(=\lambda/4)$ is the distance between two guide oscillators, $k=2\pi/\lambda$,l=nd (n is the number of oscillators). The approximate maximum gain of Yagi antenna array is $G_{max}=(MndC)/\lambda$, where M is the number of Yagi antennas, here M=4, C is a factor related to n, here n=6, C=7.8, thus, $G_{max}=[4X6X(\lambda/4)X7.8]/\lambda=46.8$, $10\lg 46.8\cong 17$db. The gain of communication antenna array is:

$$G(\theta,\varphi)=G_{max}[f(\theta,\varphi)/f_{max}(\theta_o,\varphi_o)]^2. \quad (9)$$

The angle between electric axles of radar A and communication antenna D is 0.5^o, according to formula (8), $f_{max}(\theta_o,\varphi_o)=32$, $f(\theta=0.01,\varphi=0.5^o)\cong 32$, thus, the gain of communication antenna array is $G(\theta=0,\varphi=0.5^o)\cong 17$db.

4. EMI Analysis

In this section, we will concretely calculate the EMI of communication station B and D caused by radar station A. We have known the following conditions:

. Location relationship:

A is 35m away from B (distance between antennas) and at the same altitude.
B is 50Km away from D.
A is 50 Km away from D and azimuth $\leqslant 0.5^o$.

. Communication frequency and power:

Frequency ranges from 610~780MHz (up line: B to D), 780~960MHz (down line: D to B), here we use 680MHz (up line) and 780MHz (down line).
Communication power is 5w.

. Radar parameters:

Paraboloid calibre is d(wider side)Xh(narrower side)=15.5mX5.4m,
Maximum gain in the far-field is G_{max}=38db (measured).
Operation frequency is f_o=1280MHz.
Repeat frequency is 1/T = 200Hz,
Pulse width is $\tau=4\ \mu s$.
Peak power is $P^{\wedge}$ = 2X450w = 900w.

4.1 Coupling prediction between communication antennas of station B and D

Here we only analyse the down line communication (D is emitter,B is receiver), we know that:

P_t=10lg5X10^3=36.99dbmw,

G_t=18db (measured),

G_r=18db (measured),

L_f=3db,

L_e=0db,

L_i=20lg(4 π R/ λ)=20lg(4 π Rf/3X10^{-1}) db = 32.44+20lgf(MHz)+20lgR(Km)

= 32.44+20lg780MHz+20lg50Km =124.26 db. Thus:

$P_A = P_t + G_t + G_r - L_i - L_f - L_e$ = - 54.27 dbmw

The sensitivity of receiver P_r=2 μ V, if input resistance is 75 Ω , then, corresponding power can be obtained:

P_{dbmw}=10lg[($10^{-6}V\mu_v$)^2/R]+30db = -120db+20lg$V\mu_v$ - 10lgR+30db = -102.73dbmw,

therefore, P_A-P_r= - 54.27 - (-102.73) = 48.46dbmw.

That's to say the signal power is 48.46dbmw above the sensitivity of receiver.

4.2 EMI of communication station B caused by radar station A

Assume that B is receiver, communication frequency f_1=780MHz(down line).According to the specification of radar A, we get the power of transmitter is:

P_t=P^(2 τ / T)^2[1/ π (f_1-f_o) τ]^2 = 5.836X10^{-5}mw, thus,

$P_{t(dbmw)}$=10lgP_t=10lg5.836X10^{-5}= -42.34dbmw.

Generally, directional function of rectangle paraboloid antenna is D=10.0531(dXh)/ λ^2, we get:

D=10.0531X15.5mX5.4m/(0.234m)^2=15362.43, thus,

D_{db}=10lgD=41.86 db. The efficiency of radar A is ρ =60%, so the gain of radar antenna is G=DX ρ , thus,

G_{db}=41.86db -2.2db=39.66db.

In fact, the measured value of it is 38 db. Degradation of gain (G_d=10.8) in near-field (35m) has been deducted at the end of section 2, thus,

G_t=38 -10.8 =27.2db.

The angle between electric axles of A(radar antenna) and B(communication antenna) is about 135°. We get the values:

$G_r \cong$ -10db,

$L_e \cong$ 0db,

L_f=3db,

R=35m=3.5X10^{-4}Km,

f = 780MHz,

L_i=20lg(4 π R/ λ)=20lg(4 π Rf/3X10^{-1})db=32.44+20lgf(MHz)+20lgR(Km) = 59.82db, thus,

$P_A = P_t + G_t + G_r - L_i - L_f - L_e$ = - 87.96 dbmw

P_A-P_r= - 87.96 - (-102.73) = 14.77dbmw.

That's to say the interference is 14.77dbmw above the sensitivity of receiver.But in section 4.1, we get the signal intensity of B received from D is 48.46dbmw above the sensitivity,so the signal power is 33.69 dbmw above interference power. Although considering the signal degradation (30db), the signal power is 3.69db above interference power. We obtain the result that radar A doesn't interfere with communication B.

4.3 EMI of communication station D caused by radar station A

Assume that D is receiver, communication frequency f_1= 680MHz (up line). According to the specification of radar A, we get the power of transmitter is:

P_t=P^(2 τ / T)^2[1/ π (f_1-f_o) τ]^2 = 4.053X10^{-5}mw, thus,

$P_{t(dbmw)}=10lgP_t=10lg4.053X10^{-5}= -43.92dbmw.$

Because the distance between two stations is 50Km, radar antenna gain in the far-field is G_t=38db (measured). In section 4.2, we have obtained this value which is 39.66 (calculated).

The angle between two electric axles of A and D (antennas) is 0.5^o, thus,

$G_r(\theta=0, \varphi=0.5^o) \cong 17dB$. In fact, the measured value of it is 18db.

$L_e \cong 0db$,

L_f=3db,

R=50Km,

f = 680MHz,

$L_i=20lg(4\pi R/\lambda)=20lg(4\pi Rf/3X10^{-1})db=32.44+20lgf(MHz)+20lgR(Km)=123.07db$,thus,

$P_A = P_t + G_t + G_r - L_i - L_f - L_e = - 113.99$ dbmw

$P_A - P_r = - 113.99 - (-102.73) = -11.26$dbmw.

That's to say the interference is 11.26 dbmw below the sensitivity of receiver. We obtain the result that radar A doesn't interfere with communication D.

5. Conclusion

We mainly analysed the EMI of microwave communication station B (near-field) and station D (far-field) caused by Cm-Band radar (station A) to provide the scientific basis for EMC design of an Information Transmitting System. After calculation, we obtained the result that no EMI will happen in the ocean observation post we studied. This is how things stand.

References

[1] Zhu Xi, Jin F. Dai, *Effect of EMI on the Connectivity of Communication Systems* IEEE 1994 International Symposium on EMC, Chicago, August 1994.

[2] Jin F. Dai, *Analysis of EMC of C^3I Systems* The 6th Academic Conference of Nanjing Research Institute of Electronic Engineering Nanjing, China, November 1993.

[3] W.V.T.Rusch, P.D.Potter, *Analysis of Reflector Antennas* 1970.

[4] T.G.Boone, D.Laack, *Achieving EMI Control In Advanced Highly Integrated Systems* Progress Review of Naval Air Systems Command (NAVAIR) Air Systems Electromagnetic Interference Corrective Action Program (ASEMICAP), Oakridge National Laboratory, Tennessee, May 1989.

ENFORCING CORRELATION ON STATISTICALLY GENERATED EM CABLE DRIVERS

Richard Holland and Richard St. John
Shield Rite, Inc., P. O. Box 8250
Albuquerque, NM 87198
(505) 842-6018

Abstract

This paper deals with probabilistic modeling of the EM response of a complex cavity to HPM penetration. Theoretical studies indicate that the field amplitudes and cable currents squared should have a chi square distribution with two degrees of freedom, but our observations indicate that a log normal fit is empirically better unless the data is first passed through a trend-removing filter. The major innovation reported here is the development of an algorithm which produces cable-drive fields simultaneously having a chi square distribution, and the physically mandated autocorrelation at a point as frequency is swept or at a frequency as the field sensor is moved around to map the cavity response. This algorithm is general enough it can also transform (for instance) a chi square distribution into a normal or log normal distribution.

Statistical Introduction and Empirical Background

It has been established that the power picked up by a dipole antenna in an overmoded cavity obeys a chi square distribution with two degrees of freedom. This statement is true under cw conditions, and applies whether the observations are made at a fixed observation point while frequency is swept or whether the observations are made at a fixed frequency while the antenna is translated or rotated.[1-3] It does, however, depend on the cavity not having a frequency-dependent Q and on all parts of the cavity being equally shielded (i.e., no subenclosures within the enclosure). If these postulates are not obeyed, the antenna power distribution tends to appear log normal instead.[2,3]

In general, for real-world problems, conditions are not ideal, and the dipole antenna response contains a "trend", as well as a rapidly varying response associated purely with the electromagnetic statistics. Then it becomes necessary to filter out this trend if one wishes to see the chi square statistical behavior.[2,3] Price, *et al.*,[1] have produced a lengthy and thorough derivation of the physics and statistics responsible for the chi square attribute of the squared fields (power flux). However, there is a simple approach which relies somewhat on intuition for reaching the same conclusion. Essentially, at any point in the enclosure, the field projected on any dipole consists of two components in phase quadrature, each of which approaches a normal distribution. The power picked up by a dipole antenna is proportional to the summed squares of these quadrature components. (Alternatively, it could be viewed that the power picked up is the summed squaes of the waves going backwards and forwards.) However, this sum is exactly the

This work was supported by the U. S. Air Force Phillips Laboratory under Contract F29601-94-C-0061.

definition of a function which has a chi square distribution with two degrees of freedom.

An empirical result we have observed about data pertaining to the power (current squared) carried by a cable inside an enclosure is that it *also* obeys a chi square distribution with two degrees of freedom after the power is detrended (see Figure 1). (Before detrending, cable powers also tend to appear log normal in distribution.) This result is not predicted or anticipated by the Price work.[1] However, if the power is viewed as the summed squares of two phase quadrature currents, there is no surprise in this observation. (There is an experimentally prompted assumption here that the unsquared phase quadrature current components also have a normal distribution, however.)

In particular, if we have a cable inside an enclosure carrying a sinusoidally varying current with u and v the current phase quadrature components, the cable power will be of the form

$$z = x + y = u^2 + v^2 \tag{1}$$

Moreover, if z has a power density distribution $h(z)$, we can define

$$H(\omega) = \int_{-\infty}^{\infty} h(z) e^{-j\omega z}\, dz \tag{2}$$

It can be shown that the density distribution $h(z)$ is related to the density distributions of x and y, $f(x) = f(y)$ by

$$h(z) = \int_{-\infty}^{\infty} f(x) f(z - x)\, dx \tag{3}$$

so that $f(x)$ is related to $h(z)$ by

$$f(x) = \frac{1}{2\pi} \int_{-\infty}^{\infty} [H(\omega)]^{1/2} e^{j\omega z}\, dz \tag{4}$$

In general, if u and x are related by the transformation function

$$u = g(x) \tag{5}$$

where,

$$g(\ ) = (\ )^{1/2} \tag{6}$$

then the distributions of u and x are related by

$$e(y) = f(g^{-1}(y)) \frac{dg^{-1}(y)}{dy} \tag{7}$$

This relationship is true if the underlying distribution of z is chi square, log normal, or anything else.

In the special case of z having a chi square distribution with two degrees of freedom,

$$\begin{aligned} h(z) &= e^{-z/\mu}/\mu \qquad z>0 \\ &= 0 \qquad\qquad z<0 \end{aligned} \tag{8}$$

and we find that $f(x)$ can be evaluated in closed form,

$$f(x) = \frac{1}{\sqrt{\pi}} \frac{e^{-x/\mu}}{\sqrt{x\mu}} \tag{9}$$

and, thus, $e(u)$ becomes

$$e(u) = \frac{1}{\sqrt{\pi}} \frac{e^{-u^2/\mu}}{\sqrt{\mu}} \cdot 2 \tag{10}$$

where the factor of 2 goes away if we recognize that, unlike z and x, which range form 0 to ∞, u ranges from $-\infty$ to ∞.

We thus see that, if the cable power (current squared) obeys a chi square distribution with two degrees of freedom, the phase quadrature components have a normal distribution with zero mean,

$$e(u) = \frac{1}{\sqrt{2\pi}} \frac{e^{-u^2/(2\sigma^2)}}{\sigma} \tag{11}$$

where the μ and σ are related by

$$\mu = 2\sigma^2 \tag{12}$$

Forcing of Autocorrelation

If a cable is within half a wavelength of a conducting wall, the drive per unit length on the cable is a zero-impedance voltage source of value

$$V = \mu_0 h \frac{dH_{tr}}{dt} \tag{13}$$

where h is the separation between the wall and the cable centerline, and H_{tr} is the component of the surface current on the wall flowing parallel to the cable.

Our first attempt to simulate the chi square power distribution on a cable was performed by partitioning a cable, modeled after one in the EMPTAC facility, into 200 segments and exciting it at 1000 different frequencies. (Test data referenced here was obtained at the Air Force Phillips Laboratory's EM effects EMPTAC [EMP Test AirCraft]
facility. The EMPTAC is essentially a gutted 720 airframe.) The phase quadrature driving fields on each segment were randomly chosen variables from a normal distribution with a mean of 0.00 and a variance of 0.01. In particular, each segment was driven by a field

$$E_I = [A(\omega,n) \cos \omega t + B(\omega,n) \sin \omega t] \tag{14}$$

where $A(\omega,n)$ and $B(\omega,n)$ were obtained from

$$C(\omega,n) = \sigma u(\omega,n) \tag{15}$$

with $\sigma = 0.01$ and $u(\omega,n)$ obtained from

$$R = \frac{1}{\sqrt{2\pi}} \int_{\infty}^{u(\omega,n)} e^{-t^2/2} dt \tag{16}$$

with R a random number uniformly distributed from 0 to 1. In (16), the n is the cable segment index and ω is frequency.

Unlike actual experimental data, this drive did not result in a cable power distribution which was chi square, even after filtering for trend removal. The problem was the $C(\omega,n)$ generated in this manner had no autocorrelation, either between adjacent frequencies or between adjacent cable segments. Thus, the resulting simulated cable powers, unlike the experimentally observed cable powers (see Figure 2), also had no autocorrelation between adjacent frequencies. The first attempt to rectify this problem and to introduce autocorrelation consisted of massaging

the $u(\omega,n)$ given by (16). With R still a random number uniformly distributed between 0 and 1, we associated a u_{lim} with each R through (16).

We then defined a new u through a formula introducing spatial autocorrelation between nearest-neighbor segments

$$u_{space} = \frac{\frac{\lambda}{\Delta l} u_{j-1} + f_{space} u_{\lim}}{\frac{\lambda}{\Delta l} + f_{space}} \tag{17}$$

where u_{j-1} is the u for the previous cable segment, Δl is the cable segment length, and f_{space} is a number around 10. (Making f_{space} zero results in total correlation between adjacent segments; making it >1000 results in no correlation between adjacent segments.) We next defined a second u through a formula to introduce autocorrelation between adjacent frequencies

$$u_{freq} = \frac{\frac{\lambda^2}{L\Delta\lambda} u_{i-1} + f_{freq} u_{space}}{\frac{\lambda^2}{L\Delta\lambda} + f_{freq}} \tag{18}$$

where u_{i-1} is the u for the previous frequency, L is the linear dimension of the cable extent, $\Delta\lambda$ is the change in wavelength between adjacent frequencies, and f_{freq} is another number around 10. (Making f_{freq} zero results in total correlation between adjacent frequencies; making it >1000 results in no correlation between adjacent frequencies.) The actual $u(\omega,n)$ appearing in (15) is u_{freq} of (18).

This procedure succeeds in introducing the desired autocorrelation in cable power over position and frequency (compare Figure 3 with Figure 2). Unfortunately, it also succeeds in distorting the normal distribution that we desire the array of $u(\omega,n)$'s to possess, at least at the tails (see Figure 4). Additionally, the standard deviations σ of the driver ensembles $u(\omega,n)$ and $v(\omega,n)$ are reduced from .01 to about .003.

Restoration of the Normal Distribution

The normal distribution of the $u(\omega,n)$ may be realized along with the desired autocorrelation attribute by the following process: Let us begin by generating the two-dimensional ensemble of numbers along the spatial and frequency axes according to (15)--(18). (Actually, we need two ensembles, one of which will eventually become $A(\omega,n)$ of (14), and the other of which eventually will become $B(\omega,n)$.) Then pick a particular spatial point and examine the one-dimensional array which characterizes the drive versus frequency at this point. To the element of this array having the lowest value, assign the index $i = 1$; to the next, assign $i = 2$; etc.; up to $i = i_{max}$.

In general, the elements of this array (and even the elements of the array of indices i listed versus frequency) will be in a sequence containing autocorrelation information, but the actual values of the elements of this array will have been speciously altered away from a normal distribution in the process of introducing the autocorrelation. We shall now reverse this alteration without destroying the autocorrelation by utilizing the concept that even the array of indices i contains some residual autocorrelation information.

Let us associate a fraction with each point in the one-dimensional array:

$$f_i = i/(i_{max} + \tfrac{1}{2}) \tag{19}$$

If this array actually had a normal distribution with zero mean and σ_g variance, it would be true that, if u_i were the value of element i,

$$\Phi_g(u_i/\sigma_g) = f_i \tag{20}$$

where $\Phi_g(u)$ is the cumulative normal probability distribution function. Since this should be true, we shall force it to be true: Rescale each u_i to obey

$$u_i = \sigma_g \Phi_g^{-1}(f_i) \tag{21}$$

where $\Phi_g^{-1}(f_i)$ is the inverse of the normal cumulative probability distribution function.

Note that this rescaling does not undo the autocorrelation because the i's themselves contain some autocorrelation along the frequency axis. (Very negative numbers tend to be adjacent to other very negative numbers, etc.) It is interesting to point out that this procedure can be used to transform the u_i's into an array with any desired distribution, irrespective of what the underlying initial distribution used to find u_{lim} in (16) was. For instance, if $\Phi_g^{-1}(\,)$ of (21) is the inverse chi square or log normal cumulative distribution function, the u_i's emerging from (21) will become chi square or log normal in distribution.

The following observations now seem in order:

1. This rescaling procedure must, or course, be repeated for the 1D array at each of the spatial drive points.
2. Autocorrelation also existed along the spatial axis before rescaling by virtue of (17) and (18). Since we merely rescale, not resequence, this rescaling will also preserve this autocorrelation along the spatial axis.
3. If we impose a rescaled normal distribution on the u_i's along the frequency axis, and if this rescaled distribution is obtained in the same manner for each spatial point, the distribution of a 1D array of u_j taken in the *other* direction (frequency constant, spatial position variable) will also approach a normal distribution as the number of spatial and frequency observation points both become large.
4. In this entire operation of rescaling the 2D ensemble, there is no reason we cannot reverse the roles of the frequency and the spatial axes across the ensemble.
5. Even in the problem is extended to three spatial (and one frequency) dimensions, rescaling needs only to be done in one direction.

Now let us backup some of these ideas with results. A normal random-distribution generating process set to give 0.00 mean and 0.01 standard deviation was used to initialize all the ensembles which follow. Likewise, f_{space} and f_{freq} were always set to 10, (which gives a fair approximation to the autocorrelation actually observed in the EMPTAC test data we are trying to mimic; see Figures 2 and 3.) Figure 5 illustrates the probability plot for $z = u^2 + v^2$ being chi square in distribution when the u and v ensembles are created with autocorrelation using (16)--(18). On this probability plot, we overlay the result before and after rescaling. It is apparent that the z ensemble based on rescaled u and v is nearly chi square, but the z ensemble based on u and v before rescaling is not. Figure 6 illustrates how far outside the Kolmogorov-Smirnov (K-S) 90% confidence limits for being chi square with $\sigma = .01$ ($\mu = .0002$) the z ensemble is before rescaling, and how close it is after rescaling. (The rescaled ensemble very nearly passes the K-S 90% test.)

The above results give the impression that rescaling pretty well fixes the u and v driver ensembles. Consequently, we next examined the real and imaginary distributions of the phase quadrature components of the simulated EMPTAC cable currents. Figure 7 shows that the cable current quadrature components do not fit a normal probability plot. Figure 8 is a Kolmogorov-Smirnov 90% confidence test of the cable power distribution (after filtering to remove the trend). As anticipated from Figure 7, the cable power distribution does not pass the Kolmogorov-Smirnov test for being chi square, even after being passed through a trend-removing filter. Figure 9 shows, however, that the unfiltered cable power distribution is excellently matched by a log normal probability plot.

At this point, we considered the fact that we had not introduced any mechanism to put the cable current into thermodynamic equilibrium with the electromagnetic environment. To accomplish this, we computed the radiation resistance per unit length of a cable of radius a, with centerline h over a ground plane:

$$R = \mu_o \omega \frac{\left[1 - J_o(2ka)\right]}{2} \approx \frac{\mu_o \omega}{2}(ka)^2 = \mu_o \omega \pi^2 \left(\frac{a}{\lambda}\right)^2 \qquad (22)$$

The EMPTAC tests we are trying to match were performed with frequency swept from 100 MHz to 1 GHz. At 317 MHz, the above formula leads to a radiation resistance of 120 Ω/m. Consequently, this resistance was next inserted in our cable model. (Part of the justification for doing this was the knowledge that an actual cable at some fixed observation point only responds [correlates] to the driving field over a range of a wavelength or two.) Figure 10 shows a considerable improvement results for the cable current quadrature components matching a normal distribution (compare with Figure 7). Also, the cable power distribution with trend removed is now much closer to being chi square (compare Figure 11 with figure 8). The unfiltered cable power distribution does still look much more log normal than chi square, however (see Figure 12).

After all the above procedures had been carried out, a tendency (trend) for the cable drive amplitude, and resulting cable current amplitude to grow with frequency was still present. This trend was eventually traced back to the cable drive-field generating equations (16)--(18). We

observed that if the drive-field advance equations were made over constant frequency increments (Δf, $\lambda^2/(L\Delta\lambda)$ constant), this equation could not contribute to this drive amplitude shifting: Previously, we had always used an exponentially expanding Δf. Making Δf constant implies that the relative proportions of old and new values, i.e., the effective f_{freq}, cannot change during the generation of the drive-field ensembles.

A similar procedure cannot reasonably be applied to the equation which advances the drive-field along the position axis, as keeping ($\lambda/\Delta l$) constant requires using a different cable segmenting scheme (different Δl) at every frequency.

Use of the (17)--(18) scheme where cable drive field is first advanced in the space direction results in the contamination of the subsequent frequency-directed drive advancement as well. Consequently, we reversed the order of the frequency and space cable-drive advancement so the frequency advancement, at least, could be kept pure of changing f_{space}, effects. Also, we changed these equations to make drive-field advancement occur in R space (varying from 0 to 1 in (16)), not u and v space. In other words, (16) is now used to find the u and v ensembles after the R ensembles have been generated. Thus, the equations for creating an R ensemble now become

$$R_{freq} = \frac{\frac{c\Delta f}{L} R_{i-1} + f_{freq} R}{\frac{c\Delta f}{L} + f_{freq}} \tag{23}$$

and

$$R_{space} = \frac{\frac{\lambda}{\Delta l} R_{j-1} + f_{space} R_{freq}}{\frac{\lambda}{\Delta l} + f_{space}} \tag{24}$$

with (16) subsequently applied to R_{space} to find the u and v. (Reversing the order of application of (16) and (17)--(18) should be purely cosmetic, and not change any actual values in the final rescaled drive.) Additionally, we now are very careful to create an entire 2D R_{freq} intermediate arrays, so there can be no possible ambiguity about the definition of the look-back values R_{i-1} and R_{j-1}.

These additional precautions lead to an even more improved (but still not perfect) approach of the u and v ensembles to a normal distribution (compare the probability plots of Figure 13 with those of Figures 7 and 10). Also, the filtered cable power distribution now approaches chi square much more closely (compare Figure 14 with Figures 8 and 11). Also, the unfiltered cable power distribution finally begins to pull away from the ubiquitous log normal form (compare Figure 15 with Figures 9 and 12).

There is still some growth trend remaining on the u and v ensembles as a function of frequency, even after all this correcting. The final tuning of this drive-field generator is now

completed, but resulting cable current quadrature components and powers were not available at the time of this paper deadline.

References

1. Price, R. H., H. T. Davis, and E. P. Wenaas, "Determination of the Statistical Distribution of Electromagnetic-Field Amplitudes in Complex Cavities," *Phys. Rev. E*, Vol. 48, pp. 4716-4729, December 1993.

2. Holland, R. and R. St. John, "Statistical Responses of Enclosed Systems to HPM Environments," *Conference Proceedings*, Vol. 2, pp. 554-568, 10th Annual Review of Progress in Applied Computational Electromagnetics, Monterey, CA, 21-26 March 1994.

3. Holland, R. and R. St. John, "Statistical Response of Enclosed Systems to HPM Environments," PL-TR-94-1006, Air Force Phillips Laboratory, Kirtland Air Force Base, NM, 1994.

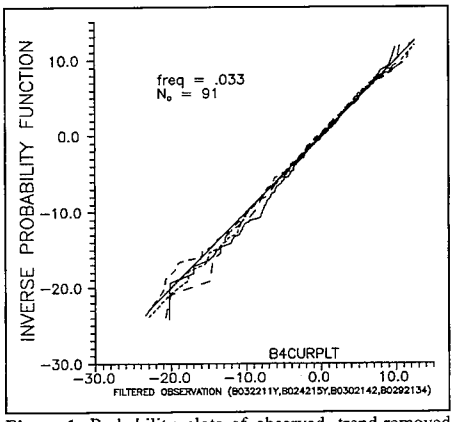


Figure 1. Probability plots of observed, trend-removed EMPTAC cable powers show good fit vs a χ^2 distribution.

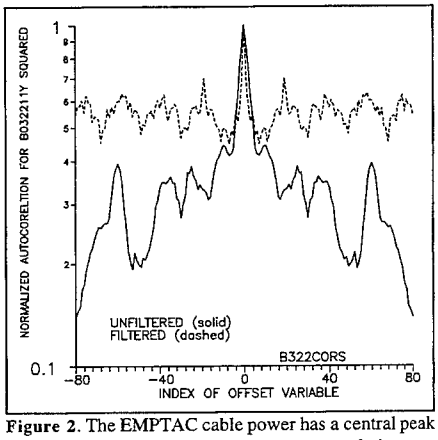


Figure 2. The EMPTAC cable power has a central peak several steps wide in its frequency autocorrelation.

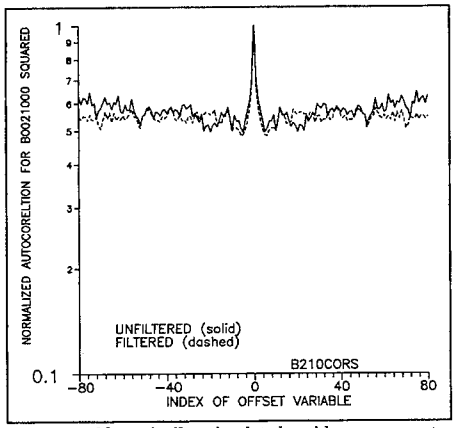


Figure 3. Numerically simulated cable power autocorrelation after forcing autocorrelation onto cable drivers.

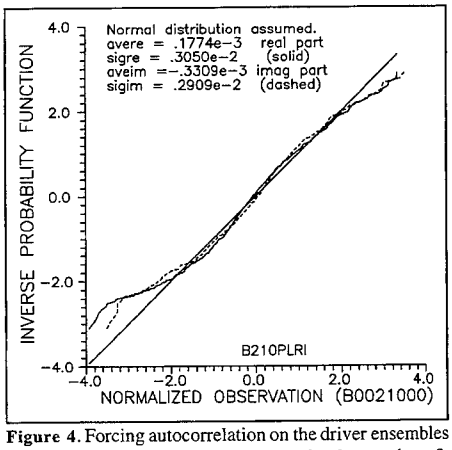


Figure 4. Forcing autocorrelation on the driver ensembles makes distribution tails non-normal and reduces σ by ~.3.

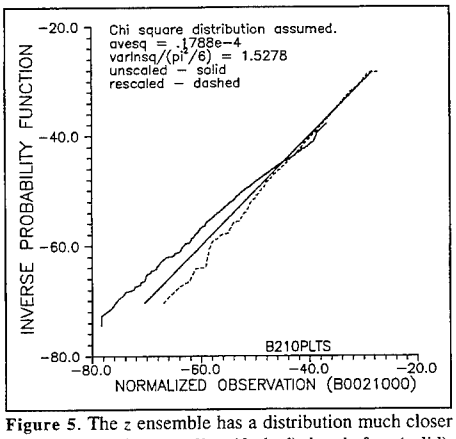


Figure 5. The z ensemble has a distribution much closer to chi square after rescaling (dashed) than before (solid).

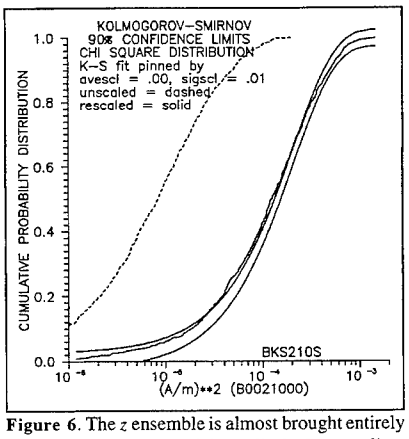


Figure 6. The z ensemble is almost brought entirely inside the K-S 90% confidence limits by rescaling.

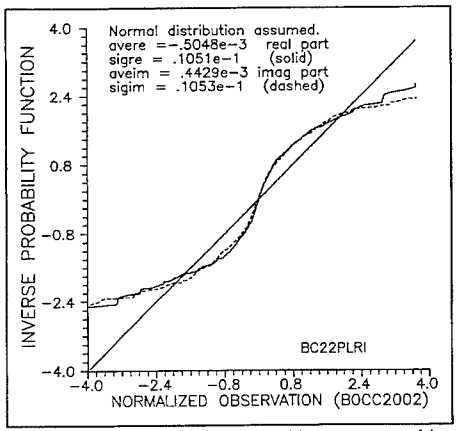


Figure 7. The phase quadrature cable currents resulting from rescaled drive do not fit a normal probability plot.

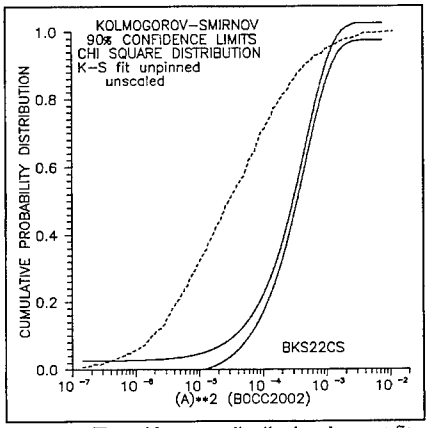


Figure 8. The cable power distribution does not fit a K-S test for being chi square, even after filtering.

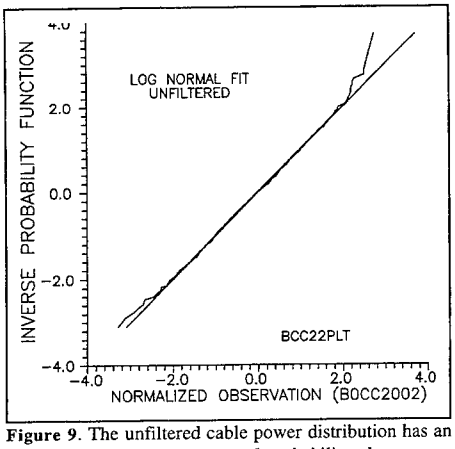


Figure 9. The unfiltered cable power distribution has an excellent match to a log normal probability plot.

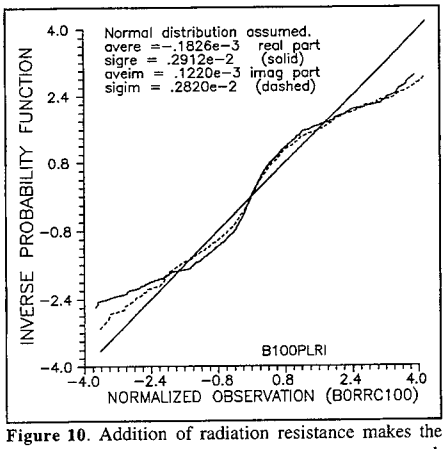


Figure 10. Addition of radiation resistance makes the phase quadrature cable current components more normal.

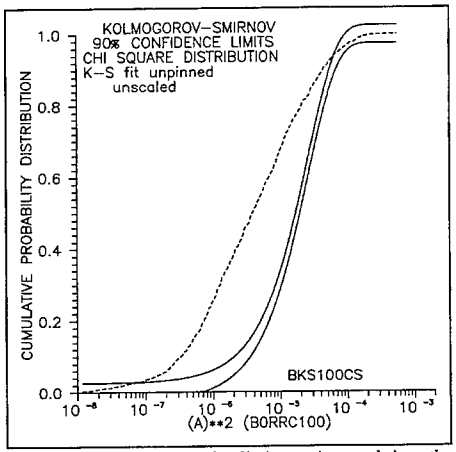


Figure 11. Introduction of radiation resistance brings the filtered cable power distribution closer to being chi square.

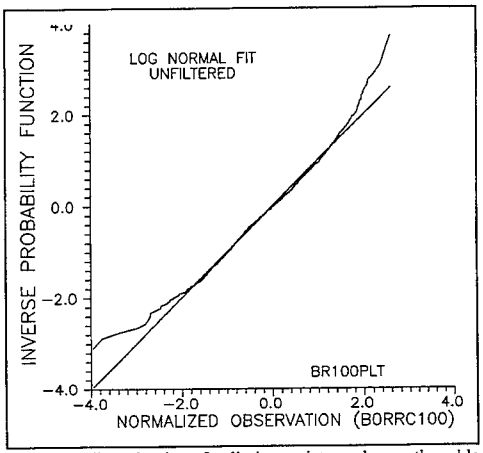


Figure 12. Introduction of radiation resistance leaves the cable power distribution very nearly log normal.

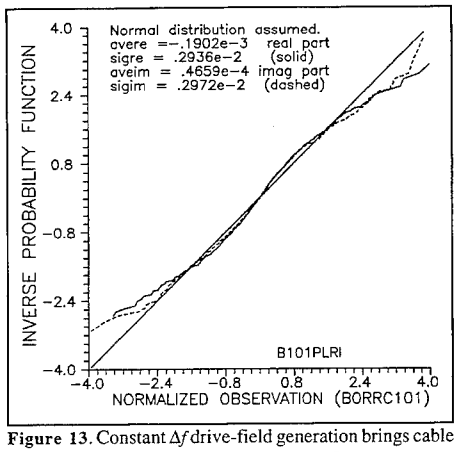


Figure 13. Constant Δf drive-field generation brings cable quadrature currents still more into normal agreement.

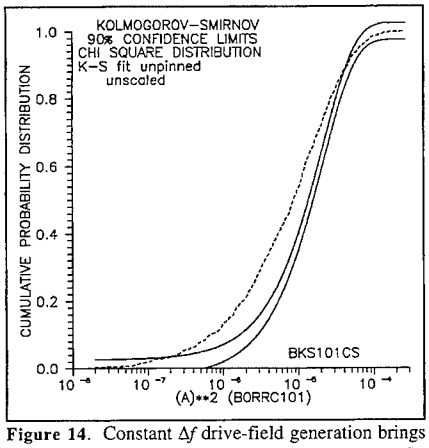


Figure 14. Constant Δf drive-field generation brings cable power distribution still more into a chi square fit.

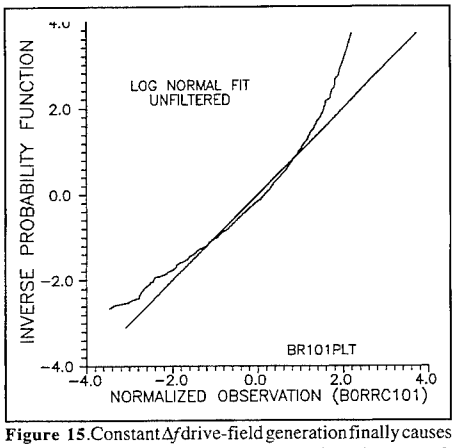


Figure 15. Constant Δf drive-field generation finally causes the cable power distribution to deviate from log normal.

Analysis of different contributions to the coupling between reflector antennas on a satellite

C.Park, P.Ramanujam
Hughes Space and Communications Company,
Los Angeles, CA-90009.

Owing to the complexity in present day satellite requirements it is quite common that many different antennas are mounted on a satellite. The power radiated from some of these can be very high especially for direct broadcast applications. For these applications a separate receive antenna is generally used to increase the isolation between the transmit and receive antennas. Besides, the transmit and receive antennas should be optimally located in order to achieve the maximum advantage with reference to isolation between the two. An accurate analysis of the coupling between the two antennas can aid the antenna designer for optimally locating the different antennas on the spacecraft. This paper discusses the procedure and the techniques used for evaluating an antenna coupling on a typical satellite.

The satellite under consideration has two transmit and one receive antenna. Due to the mechanical considerations, the two transmit antennas were designed to be of dual offset reflector configuration, while the receive was a single offset reflector. The three major components to the coupling are:

(1) Direct transmit horn to receive horn coupling: This corresponds to the coupling between the feed horns illuminating the reflector systems. Since the transmit antenna is a dual reflector and the receive antenna is a single reflector, the two feeds directly face each other although at an angle. Since the horns are sufficiently separated, a simple Friss transmission formula was used to determine this component to the coupling.

(2) Transmit horn-subreflector to receive feed coupling: Due to the smaller size (in wavelengths) and the broad radiation of the subreflector, this contribution was also considered . A simple approach to determining this coupling is to analyze the far-field radiation pattern of the subreflector and to use the Friss transmission formula to obtain the coupling onto the receive feed. A more accurate approach is to analyze the radiation pattern of the subreflector in the near-field using the geometrical theory of diffraction (GTD). Both these approaches were used to determine this component of the coupling.

(3) Transmit horn-subreflector-main reflector to receive feed coupling: This corresponds to the coupling to the receive feed through the aperture fields emanating from the main reflector of the dual reflector. This in turn requires the evaluation of the near-fields over the plane in front of the reflector and containing the receive feed. Near-field Physical optics was utilized to evaluate these nearfields due to the currents on the main reflector, introduced by the feed and subreflector.

Thus the basic techniques used for analyzing the above three components are :

1) Geometrical Optics(GO) - Friis transmission formula
2) Geometrical Optics and Geometrical theory of diffraction(GTD)
3) Near-field Physical Optics (PO)

The numerical results indicating the contributions due to the different components discussed above, obtained using the reflector antenna analysis software GRASP, will be discussed.

SIMPLE RADIATION MODELS IN LIEU OF EMC RADIATED EMISSIONS TESTING

Reinaldo Perez
Jet Propulsion Laboratory
California Institute of Technology
Pasadena, California

Abstract

In mixed analog/digital printed circuit boards the electromagnetic emissions originate mainly from the synchronous (or clocked) circuits present. A good estimate of the radiated emissions from an electronic equipment can often be obtained by analyzing the electromagnetic environment produced by the clocked circuits only. This approach avoids the need for extensive radiated emissions EMC testing over a very large range of frequencies (10 KHz-22 GHz). The method of moments (MOM) is used to calculated the radiated emissions from a clock circuit in a printed circuit board as an example. Simple MOM models can provide good estimates of: a) the frequencies and levels of radiated emissions of most concern, and b) frequency range(s) where accurate emissions measurements needs to be made for compliance with EMC regulatory agencies.

1.0 INTRODUCTION

EMC Testing is required of all electronic assemblies which are capable of editing electromagnetic radiation above certain frequencies (e.g 10KHz for space systems). Commercial (national and international) and military EMC regulatory agencies have established mandatory requirements (or standards) of EMC compliance for all electronic products manufactured for procurement purposes. Radiated Emissions testing is one, of a series of tests, required for EMC compliance. The objective of the test is to assure that the electromagnetic environment emitted by newly designed equipment is not above mandatory radiated emissions limits (in dbμV/m) for a given frequency range. Figure 1, for example, shows the maximum allowed radiated electric fields for aircraft and space systems in the required 10 KHz-20 GHz frequency range at 1.0 meter from the source. When a radiated emission test is performed it is required for measurements to be made over the whole frequency range. This is necessary because test engineers do not know a priori what electromagnetic emissions (frequencies and levels) will be emitted from the designed hardware. It is not uncommon to take measurements over a large frequency range in order to discover that the only emissions present are those within a very limited frequency band.

A considerable amount of effort and time is often spent performing EMC emission tests. EMC testing has implications in the overall cost of hardware design and its time-to-market schedule. It would be of great advantage for test engineers to develop analysis methods that will allow them, not only to identify the emission spectrum of an electronic assembly before testing, but also to calculate, with certain accuracy, the emission levels corresponding to such spectrum. It is possible to justify that if the emission levels calculated are significantly below the allowed emission limits of a given standard, EMC emissions testing could be deemed unnecessary.

2.0 ANALYSIS OF RADIATED EMISSIONS FROM A MIXED ANALOG/DIGITAL PCB

An analysis technique, based on the method of moments (MOM), is discussed to analyze the emissions from mixed an analog/digital Printed Circuit Board (PCB). Mixed analog/digital PCB have become very popular due to the increasing need of many electronic products to process acquired analog data in a digital fashion. Presently, most circuit analysis tools (SPICE-like tools) have incorporated mixed analog/digital simulation in their capabilities to respond to the growing need for such circuits. Furthermore, electronic design automation (EDA) software tools, such as those used in ASIC and MCM design, have also implemented mixed analog/digital analysis algorithms in their software structures.

Analysis of the electromagnetic emissions from mixed analog/digital boards is more simple since the electromagnetic environment generated from such boards is due primarily to the synchronous digital circuits, of which the clocked circuits are the main culprits. Often in mixed analog/digital boards the digital portion occupy less than 50% of the circuitry. The other major source of radiated emissions from digital electronics is that due to common mode currents [1] as manifested in the radiated fields from interface and power cables. Such emissions, which in many cases have the largest magnitude in the radiated spectrum, will not be considered here as will be explained later.

We now consider the electronic assembly described in Figure 2. It shows the Solar Array Deploy Electronics (SADE) which together with the Solar Array Deploy (SAD) mechanism, the Array Control Electronics (ACE), and the Inertial Mechanism Interface Unit (IMIU) constitute the functional hardware for deploying solar arrays in an spacecraft and satellites. The SADE is the assembly of interest in this analysis. A top view (cover removed) and side view (connector inputs) of the SADE is shown in Figure 3. The figure shows the "analog" and "analog/digital" parts of the only PCB in the SADE. Figure 4 shows a partial schematic of the mixed "analog/digital" part of the PCB in the SADE of Figure 3. The schematic shown contains the digital circuits which are part of the SADE board and only a portion of the analog circuits. The digital circuits

involved are an A/D converter and four Flip/Flops as shown in the figure. The SADE PCB is a multilayer board (5 layers). The board contains one power plane, one ground plane and three signal planes. Layer 5 (a signal plane) is where the clock traces of the digital circuits are located. Figure 5 shows the signal and clock traces of the circuits on layer 5. The clock frequency is 3 MHz.

In this analysis the radiated emissions caused by the clock are of greatest importance. Figure 6 shows only the clock traces on layer 5 and it also illustrates some of the aspects in the method of moments modeling.The method of moments code automatically creates an image of the clock trace due to the presence of the ground plane. The clock pulse is of trapezoidal shape (50% duty cycle, only odd harmonics are present) with 5V magnitude and rise time/fall times of 30nS. The spectrum for the first several harmonics is shown in Table 1. The magnitude spectrum of the clock pulse (i.e frequency .vs. voltage level) is calculated as given by equation 1 [2].

$$V(n) = 2*D*V*\left[\frac{Sin\ (n*\pi*D)}{(n*\pi*D)} + \frac{Sin\ (n*\pi*t_r/T)}{(n*\pi*t_r/T)}\right] \qquad (1)$$

where V is the peak amplitude in volts (5V), D is the duty cycle (pulse width/T), t_r is the rise time (seconds), T is the period (units per second), and n is the harmonic number.

The modeled voltage source in Figure 6 is frequency dependent as shown by equation 1. The magnitude voltages are given for each frequency based on the calculated spectrum (all harmonics) of the clock pulse. The clock traces are modeled by equivalent round wires as shown by equation 2 [3].

$$R = 0.335*W*(0.8 + t/W) \qquad (2)$$

for $0.1 \leq t/W \leq 0.8$, where W is the width of the microstrip in meters, t is the thickness of the microstrip in meters and R is the wire radius in meter. The wire diameter is calculated to be 0.82mm diameter. Though not necessary, in the MOM code we assumed perfect conductivity for the microstrip traces in the PCB. Since the fundamental frequency is only 3 MHz, it is assumed that at such low frequencies (including harmonics) the dielectric losses in the PCB are minimum [4], hence, dielectric effects are not included. The total number of segments used in the MOM modeling is 24. Though chip loading could have been included [2] it is neglected in this work for simplicity. To assess the validity of this analytical approach, the fields emitted by the SADE were also measured in an anechoic room.

3.0 MEASURED AND CALCULATED RESULTS

The measured results were obtained as described in Figure 7. In the measurement procedure the top cover of the SADE was removed (see Figure 3) and the motor drive board (see Figure 2) was disabled. Table 2 shows the calculated and measured radiated emissions at 1.0 meter distance (as required per Figure 1) from the source (PCB) for several harmonics of the fundamental clock frequency. The results show that a better accuracy between the calculated and measured data can be obtained at higher harmonics of the fundamental clock frequency.

Finally, we are ready to assess analytically the electromagnetic emissions from the completely assembled SADE (with cover) which is its normal configuration. EMC emissions testing requires the normal configuration. The approximate shielding effectiveness (SE) of the SADE enclosure (thickness of 0.15 inch aluminum with 10 venting round holes, 0.25 inch diameter) is calculated per a procedure described in [5]. The venting holes must be considered in calculating SE since SE depends on the diameter of holes, number of holes and their arrangement. For example, SE decreases as frequency increases and hole diameter increases.

Table 2 also shows the external radiated fields after shielding effectiveness is factored in. The results show that the external emissions are very much well below the limits of Figure 1. For example, at 33 MHz the emissions after SE is -31.2 dBμV/m at 1.0 meter (0.027 μV/m) which is somewhat below the noise floor level of most spectrum analyzer. Though emissions can also come from the cables connected to the SADE (due to the common mode current), flight cables in spacecraft are normally completely shielded (including connectors) and well grounded. Several layers of shields are used on the cables. The emissions from such cables is minimum. Furthermore, though some emissions could have been expected from the motor drive board they are in the low KHz range (< 30KHz for this board) and mostly confined within the SADE enclosure. It can then be concluded from this analysis that there is no need to conduct EMC emission testing for this particular assembly.

In many mixed analog/digital PCB it is often the case than more than one clock frequency is present for different synchronous circuits within the same PCB. Though it could be said simplistically that the above analytical procedure can be repeated for each of the different circuits involved and then superimpose the results, the correct approach is much more complicated. In the near field the coupling of electromagnetic fields to other radiating and non-radiating wire structures (e.g traces, connector pins, chip's connectors) within the PCB must also be considered due to the induced current. Additional work needs to be done in this area.

4.0 CONCLUSION

EMC testing is usually the last "hurdle" for qualification of an electronic product to market. Full scale EMC tests are long and costly. Considerable savings could be achieved if EMC testing could be reduced in scope, only performing the testing that is needed. Computational electromagnetics, and in this particular case the method of moments, can be useful in assessing the need for radiated and conducted emission EMC testing of a prototype assembly.

References

[1] Paul, Clayton and Bush,D.R, "Radiated emissions from common mode currents," IEEE International Symposium on Electromagnetic Compatibility, Atlanta, Georgia, 1987.

[2] Perez, R. "Electromagnetic Compatibility Methods in the Teaching of Electromagnetic Compatibility," ACES Journal, Vol. 8, No. 1, 1993.

[3] Sprinfield, W.K., "Multilayer printed circuitry in computer applications," Fall Meeting of Printed Circuits, Chicago, 1964.

[4] Hoffmann, T.R. Handbook of Microwaves Integrated Circuits, Chapter 3, Artech House, 1987.

[5] Schulz, Richard B. et al. "Shielding Theory and Practice," IEEE Transactions on Electromagnetic Compatibility, Vol. 30, No. 3, August 1988.

Harmonic	Frequency	Harmonic Amplitude in (dB)	Harmonic Amplitude in (volts)
1	3 MHz	-4.038	3.14
2	6 MHz	-151.578	~0.0
3	9 MHz	-14.533	0.938
4	12 MHz	-153.048	~0.0
5	15 MHz	-21.017	0.4447
6	18 MHz	-176.595	~0.0
7	21 MHz	-27.500	0.2108
8	24 MHz	-160.465	~0.0
9	27 MHZ	-36.124	0.078
10	30 KHz	-166.558	~0.0
11	33 MHz	-64.66	0.003

Table 1. Spectrum of the 3 MHz clock in the PCB for several harmonics.

Frequency	E(dBμV/m) Calculated at 1.0 m	E(dBμV/m) Measured at 1.0 m	Δ(dBμV/m)	E(dBμV/m) Calculated after SE
3 MHz	17.4	5.2	12.2	-85.6
9 MHz	22.5	10.8	11.7	-81.2
15 MHz	34.6	23.7	10.9	-74.6
21 MHz	40.15	31.5	8.60	-66.1
27 MHz	49.74	41.9	7.84	-54.8
33 MHz	67.84	60.1	7.74	-31.2

Table 2. Comparison of Calculated and Measured Electric fields for Clock Circuit and the Effect of Shielding Effectiveness (SE).

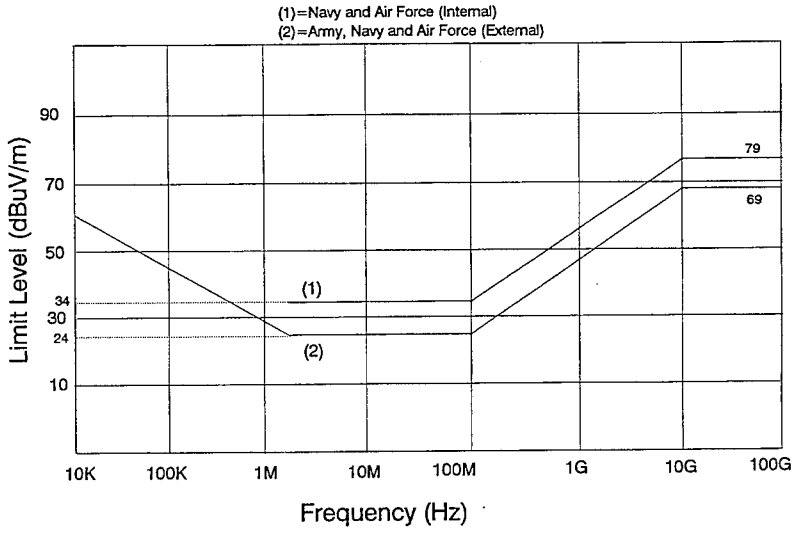


Figure 1. RE102 Limits for Aircraft and Space Systems

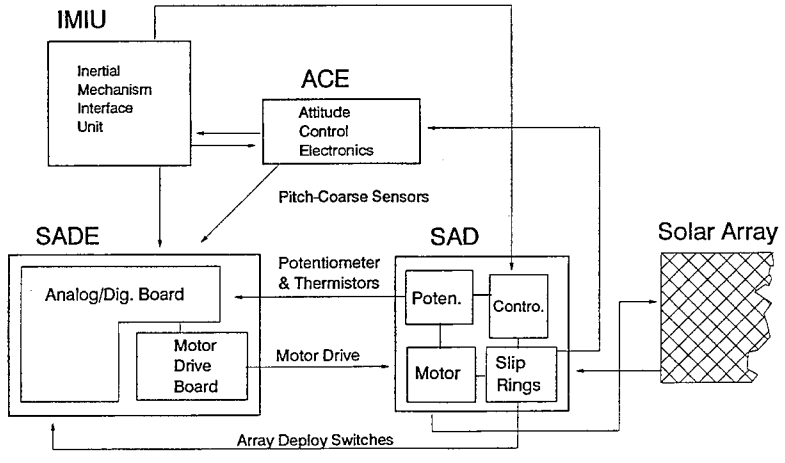


Figure 2. Solar Array Deploy Mechanism.

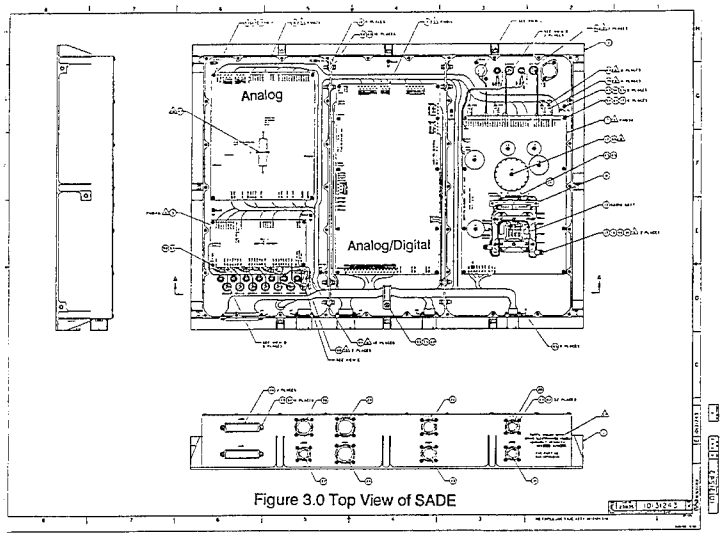


Figure 3.0 Top View of SADE

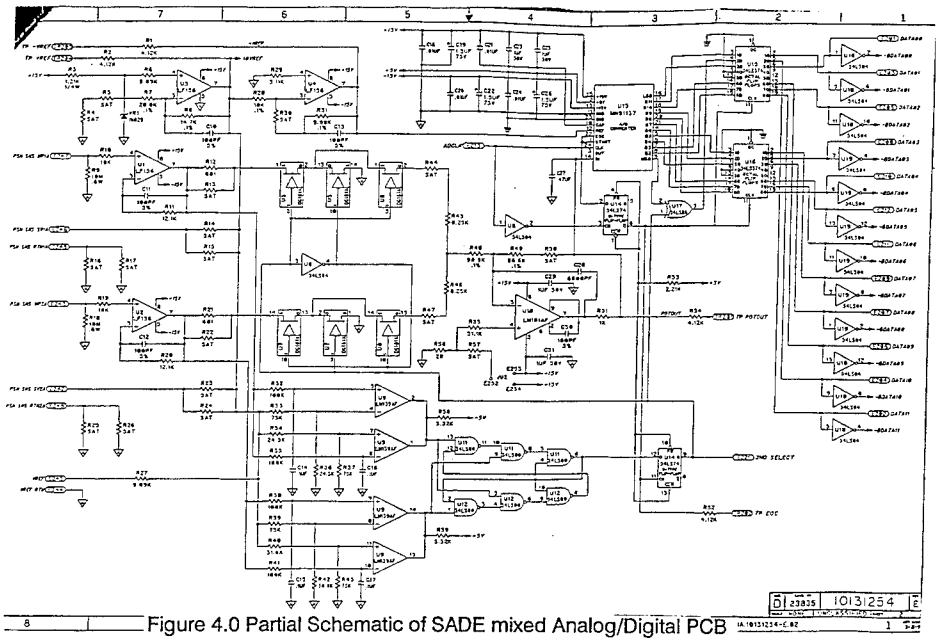


Figure 4.0 Partial Schematic of SADE mixed Analog/Digital PCB

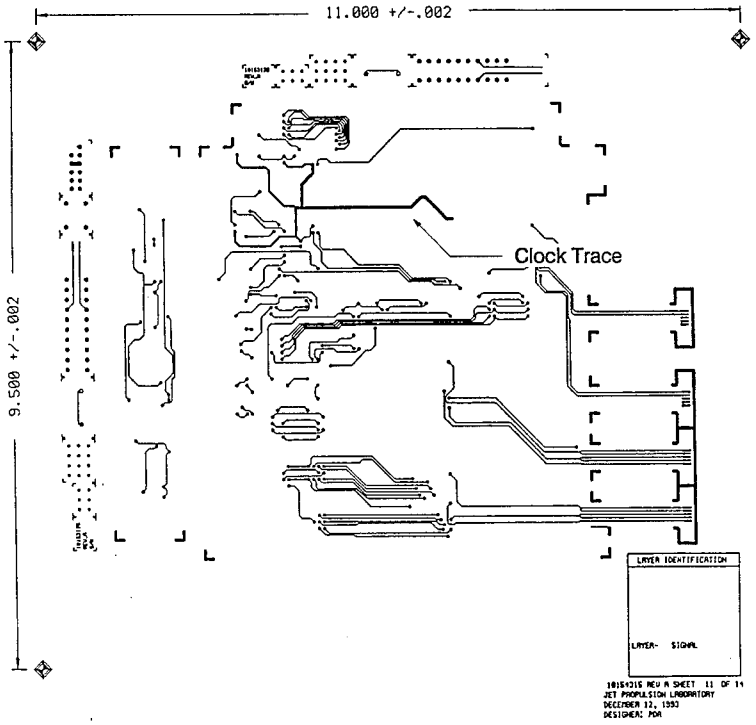


Figure 5.0 Signal and Clock Traces on Layer 5 of PCB

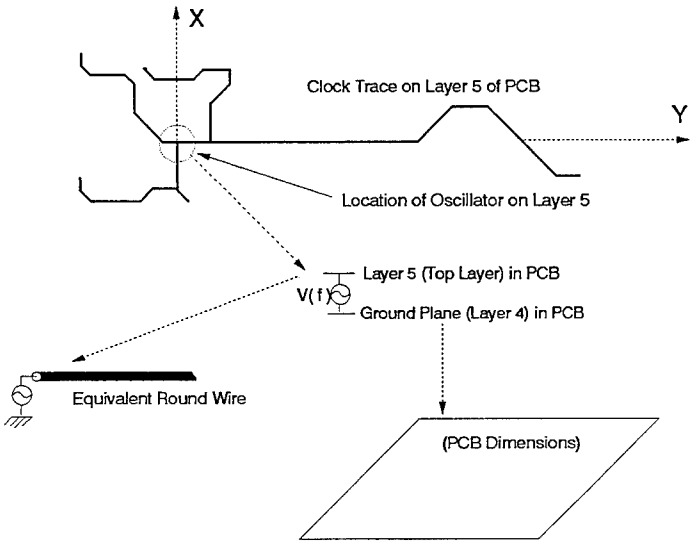


Figure 6. MOM Modeling of Clock Traces in PCB

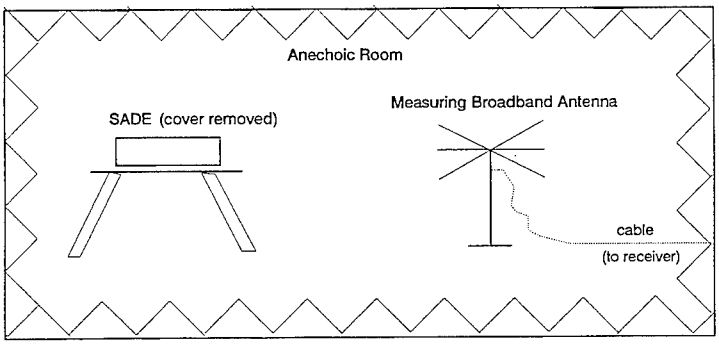


Figure 7. Measuring Radiating Emission from Clock Circuit in the SADE

SESSION 5:

OPTIMIZATION TECHNIQUES IN APPLIED ELECTROMAGNETICS

Chair: O.A. Mohammed

AN OPTIMIZATION APPROACH TO REDUCE THE DISCRETIZATION ERROR IN FINITE ELEMENT EXPLICIT SOLUTION SCHEME

M. Feliziani* E. Latini F. Maradei****

* Dept. of Electrical Engineering - University L'Aquila
Poggio di Roio, 67040 L'Aquila, Italy

** Dept. of Electrical Engineering - University of Rome "La Sapienza"
Via Eudossiana 18, 00184 Rome, Italy

Abstract - Two explicit solution schemes of Maxwell's curl equations based on the *leap-frog* algorithm are presented. The first method is based on a finite element discretization of space and a finite difference integration of time and leads to an explicit solution scheme by applying the *mass lumping* algorithm. The results produced by this method can be inaccurate when nonuniform meshes are adopted since the *mass lumping* algorithm depends strongly on the shape of the elements. The second explicit solution scheme is based on a mixed finite element-finite difference discretization of space and a finite difference integration of time. In order to avoid numerical instabilities and to improve the accuracy, an optimization problem is defined to find a mesh that minimizes the discretization error. In the paper the salient features of a simulated annealing (SA) algorithm are described to generate an optimized two dimensional triangular mesh.

I. INTRODUCTION

New numerical methods based on vector finite elements, edge elements and Whitney elements have been recently developed to solve Maxwell's curl equations in time domain adopting the *leap-frog* scheme [1]-[6]. These methods, named as finite element-time domain (FE-TD) methods, are very powerful since explicit solution algorithms reduce computation time dramatically and finite elements are very convenient to model complex geometrical configurations.

In this paper, a two-dimensional problem is analyzed by two different procedures. In the first method the finite element interpolation is used to solve the fields spatially: the vector magnetic field is approximated by edge elements while the scalar electric field is assumed constant in each element [4]-[5]. The resulting system of equations, obtained by the Galerkin formulation, is nondiagonal. The *mass lumping* algorithm is applied to diagonalize the system and an explicit solution scheme is obtained. The accuracy of the method is strongly dependent on the shape of the triangular elements: the method performs well when grids composed by equilateral triangular elements are used since the dispersion relation is second order accurate [5], but the accuracy decreases for nonregular meshes since right and nonacute triangles lead to zero or negative masses which produce numerical instabilities. In this cases the second method is applied: the diagonalization of the mass matrix is avoided by adopting a mixed finite element-finite difference discretization of space [1]. This approach is less sensitive to the element shape and does not present stability problems.

In practical applications it is not possible to use equilateral triangular meshes to discretize complex configurations. When a nonregular mesh composed by elements of different shape and size is adopted, the main problem of the numerical procedures consists in maintaining good accuracy in the field solution. Therefore global optimization techniques are used in order to find a good discretization of the domain by triangular elements which ensues good numerical accuracy and stability. The optimization strategy consists in minimizing by a simulated annealing (SA) procedure [7]-[8] the error due to the space discretization modifying the position of the mesh nodes and element shapes continuously. An illustrative example is proposed to test the validity of the two different procedures.

II. MATHEMATICAL FORMULATION

Let us consider the following form of Maxwell's curl equation in time domain:

$$\nabla \times \mathbf{H} - \varepsilon \frac{\partial \mathbf{E}}{\partial t} = 0 \tag{1a}$$

$$\nabla \times \mathbf{E} + \mu \frac{\partial \mathbf{H}}{\partial t} = 0 \tag{1b}$$

where **E** and **H** are the electric and magnetic fields, and μ and ε are the permeability and permittivity. In order to simplify the mathematical formulation, the study is limited to a two dimensional problem, i.e. $E_X=E_Y=H_Z=0$.

II.1 Mass Lumping Method

Discretizing the region in triangular elements, the magnetic field in each element is approximated by edge elements as [2]:

$$\mathbf{H}(\mathbf{r},t) \cong \sum_{k=1}^{3} \ell_k^e H_{\tau k}^e(t)\ \mathbf{w}_k(\mathbf{r}) \tag{2}$$

where $\mathbf{r}$ is the position vector, ℓ^e_k the length of the *k-th* edge, $H_{\tau k}$ the magnetic field component along the *k-th* edge, $\mathbf{w}_k$ the Whitney 1-form vector shape function associated to the *k-th* edge [4].

The electric field **E** is assumed to be piecewise constant:

$$\mathbf{E}(\mathbf{r},t) \cong \lambda_c(\mathbf{r}) E_z^e(t)\,\hat{\mathbf{z}} \tag{3}$$

where E_z^e is the constant electric field inside the considered element and λ_c the trial function associated with the node located in the element barycenter satisfying the condition: $\lambda_c(\mathbf{r})=1$ for $\mathbf{r}\in\Omega^e$, $\lambda_c(\mathbf{r})=0$ for $\mathbf{r}\notin\Omega^e$. The adopted field approximations are shown in Fig.1.

Applying Galerkin method to (1) using the field interpolations (2) and (3), the following equations are obtained [4]:

$$\sum_{k=1}^{3} \ell_k^e H_{\tau k}^e \int_{\Omega^e} \lambda_c (\nabla \times \mathbf{w}_k)\cdot\hat{\mathbf{z}}\ d\Omega - \varepsilon^e \frac{dE_z^e}{dt} \int_{\Omega^e} \lambda_c^2\, d\Omega = 0 \tag{4a}$$

$$E_z^e \int_{\Omega^e} \lambda_c (\nabla \times \mathbf{w}_h)\cdot\hat{\mathbf{z}}\, d\Omega + \mu^e \sum_{k=1}^{3} \frac{dH_{\tau k}^e}{dt} \ell_k^e \int_{\Omega^e} \mathbf{w}_k \cdot \mathbf{w}_h\, d\Omega = 0 \tag{4b}$$

where $\mathbf{w}_h$ is the weighting function with h=1,2,3, and μ^e and ε^e are the local permeability and permittivity, respectively.

The systems of equations (4) expressed in matrix form are:

$$[K^e][H_\tau^e] - \frac{dE_z^e}{dt} = 0 \tag{5a}$$

$$[J^e]\,E_z^e+[T^e]\,\frac{d[H_\tau^e]}{dt}=0 \tag{5b}$$

where the coefficients of matrix $[T^e]$ and vectors $[K^e]$, $[J^e]$ are given by:

$$K_k^e=\frac{\ell_k}{A^e\varepsilon^e}\int_{\Omega^e}(\nabla\times\mathbf{w}_k)\cdot\hat{\mathbf{z}}\,d\Omega \tag{6a}$$

$$J_k^e=\int_{\Omega^e}(\nabla\times\mathbf{w}_k)\cdot\hat{\mathbf{z}}\,d\Omega \tag{6b}$$

$$T_{hk}^e=\mu^e\ell_k\int_{\Omega^e}\mathbf{w}_h\cdot\mathbf{w}_k\,d\Omega \tag{6c}$$

where A^e is the element area.

Assembling the local systems (5), the following global systems are obtained:

$$[K]_t[H_\tau]-\frac{d[E_z]}{dt}=0 \tag{7a}$$

$$[J]\,[E_z]+[T]\frac{d[H_\tau]}{dt}=0 \tag{7b}$$

The components of vectors $[E_z]$ and $[H_\tau]$ are equal to the number of elements and edges, respectively.

Time domain is discretized by applying the *leap-frog* technique: the electric field is calculated at the time $t^n=n\Delta t$, while the magnetic field is calculated at $t^{n+1/2}=(n+1/2)\Delta t$, where n is the number of iteration and Δt the time step. Substituting time derivatives in (7) by central finite differences, the following final systems of equations are obtained:

$$\frac{[E_z]^{n+1}-[E_z]^n}{\Delta t}=[K]_t\,[H_\tau]^{n+1/2} \tag{8a}$$

$$\frac{[T]\,[H_\tau]^{n+1/2}-[T]\,[H_\tau]^{n-1/2}}{\Delta t}=-[J]\,[E_z]^n \tag{8b}$$

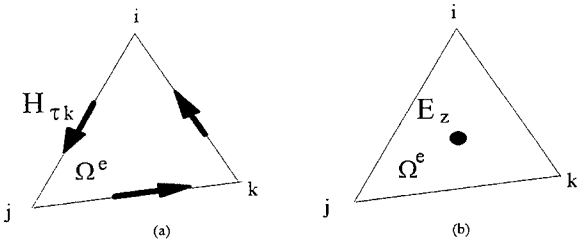


Fig.1. Vector magnetic field (a) and scalar electric field (b) approximations in a triangular finite element.

The electric field vector $[E_z]$ is directly calculated by (8a): at each time step, time derivative of the electric field E_{zp} in the *p-th* element depends on the three components of the magnetic field tangential to the edges of the considered element, as shown in Fig.2a. The calculation of the tangential components of the magnetic field $[H_\tau]$ is performed by (8b): time derivative of the tangential magnetic field component $H_{\tau k}$ depends not only on the electric field in the *p-th* and *q-th* elements which share the *k-th* edge, but also on the time derivative of the magnetic field tangential to the other edges constituting the *p-th* and *q-th* triangles, as shown in Fig.2b. Since the mass matrix [T] is consistent or nondiagonal, the system of equations (8b) must be solved at each time step. In order to obtain an explicit solution scheme, the mass matrix [T] is diagonalized by applying an opportune quadrature scheme, the *mass-lumping* algorithm, to calculate the integral in (6c). Using the tangential components of the magnetic field at mid-points of the edges as quadrature points, the integral in (6c) can be approximated as follows [4]-[5]:

$$\int_{\Omega^e} \mathbf{w}_h \cdot \mathbf{w}_k \, d\Omega = S_i \, \mathbf{w}_h(\mathbf{r}_{j,k}) \cdot \hat{\boldsymbol{\tau}}_{j,k} \; \mathbf{w}_k(\mathbf{r}_{j,k}) \cdot \hat{\boldsymbol{\tau}}_{j,k} +$$

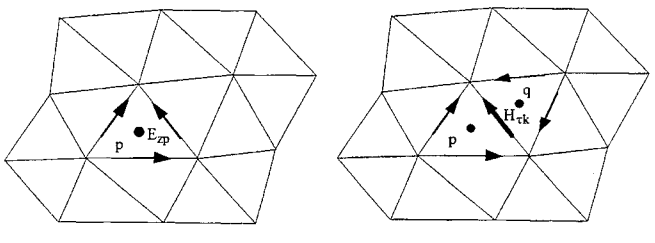
$$S_j \, \mathbf{w}_h(\mathbf{r}_{i,k}) \cdot \hat{\boldsymbol{\tau}}_{i,k} \; \mathbf{w}_k(\mathbf{r}_{i,k}) \cdot \hat{\boldsymbol{\tau}}_{i,k} + S_k \, \mathbf{w}_h(\mathbf{r}_{i,j}) \cdot \hat{\boldsymbol{\tau}}_{i,j} \; \mathbf{w}_k(\mathbf{r}_{i,j}) \cdot \hat{\boldsymbol{\tau}}_{i,j} \qquad (9)$$

where $\hat{\boldsymbol{\tau}}_{i,j}$ is the unit vector tangential to the edge between *i-th* and *j-th* nodes, $\mathbf{r}_{i,j} = (\mathbf{r}_i + \mathbf{r}_j)/2$ is the middle point of the edge between *i-th* and *j-th* nodes, and S_i is the weight given by the following expression:

$$S_i = \frac{\ell_i \, (h_i - d_i)}{2} \qquad (10)$$

where ℓ_i is the length of the *i-th* edge, h_i is the height of the triangle for the *i-th* node and d_i the oriented distance between the ortocenter O of the element and the *i-th* edge according to the notation shown in Fig.3. S_j and S_k are given by expressions analogous to (10).

Using this quadrature scheme the method is efficient when the mesh is composed by acute triangles. When the ortocenter of the element coincides with one vertex of the element (i.e. right triangle) or falls outside the element (i.e. nonacute triangle), the *mass lumping* algorithm leads to zero or negative masses respectively, and the method becomes unstable.



(a) (b)

Fig.2. Explicit calculation of the scalar electric field E_z (a) and implicit calculation of the magnetic field tangential component H_τ (b).

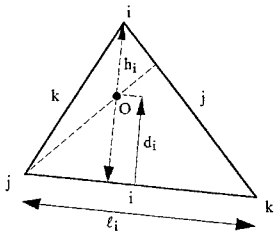


Fig.3. Notation adopted in the calculation of the weight S_i in the *mass lumping* algorithm

II.2 Mixed Finite Element-Finite Difference Method

An explicit solution scheme can be obtained directly by adopting a mixed finite element-finite difference discretization of space [1]. Applying the finite element field approximation (2) and Galerkin method, equation (8a) is still derived. The electric field is assumed to be piecewise constant as in the first method and the tangential component of the magnetic field is obtained by a finite difference approximation. The *k-th* component $H_{\tau k}$ is then given by:

$$\frac{H_{\tau k}^{n+1/2} - H_{\tau k}^{n-1/2}}{\Delta t} = -\frac{2}{\mu_q + \mu_p} \frac{E_{zp}^{n} - E_{zq}^{n}}{d_{qp}} \tag{11}$$

where d_{qp} is the distance calculated normally to the *k-th* edge between the two electric field nodes which share the edge, as shown in Fig.4. In this way the tangential component $H_{\tau k}$ depends only on the electric field in the *p-th* and *q-th* elements.

Assembling (11) the following explicit system is obtained:

$$\frac{[H_\tau]^{n+1/2} - [H_\tau]^{n-1/2}}{\Delta t} = -[M]\,[E_z]^n \tag{12}$$

where [M] is a finite difference matrix with only two nonzero coefficients.

The method based on explicit solution of (8a) and (12) is stable but the accuracy depends clearly on the shape of the elements.

It should be noted that this approach leads to the same solution scheme obtained by using Whitney 1- and Withney 2- forms in a two-dimensional configuration [6].

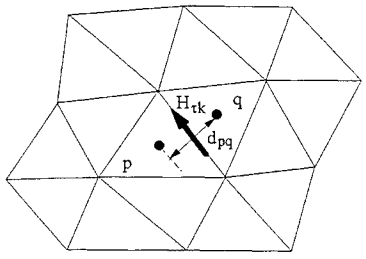


Fig.4. Explicit calculation of the magnetic field tangential component $H_{\tau k}$ in the mixed finite element-finite difference method.

III. MESH OPTIMIZATION BY SIMULATED ANNEALING

When it is not possible to use regular meshes, the discretization error can lead to insufficient accuracy in the field solution. In this case the main problem is to find a mesh that minimizes the discretization error. The problem of finding a good discretization of the domain can be formulated as an optimization problem: for a given configuration the aim of the optimization procedure is to look for the position of the nodes such that the error produced by the discretization is minimum. The element error can be defined as:

$$E^e = 1 - Q^e \tag{13}$$

where Q^e is the quality factor of a triangle given by [10]:

$$Q^e = 8\,(L^e - \ell_i^e)\,(L^e - \ell_j^e)\,(L^e - \ell_k^e) \,/\, (\ell_i^e\,\ell_j^e\,\ell_k^e) \tag{14}$$

where L^e is the triangle semi-perimeter $L^e = (\ell_i^e + \ell_j^e + \ell_k^e)/2$.

The objective function which must be minimized is defined as the sum of the errors associated to each element. A constraint is also imposed to respect the stability condition of the FE-TD methods which states that the time step $\Delta t \leq h_{min}/c$, where h_{min} is the minimum length of the edges and c the propagation velocity.

Let $\mathbf{x}$ be a vector of 2N components, given by the coordinates of the N nodes internal to the domain, and $f(\mathbf{x})$ the function to be minimized, we state the optimization problem as follows:

find the vector $\mathbf{x}$ such that:

$$f(\mathbf{x}) \rightarrow \min$$

with each of the 2N variables ranging in a finite, continuous interval.

Simulated annealing (SA) algorithm in the context of generating a two-dimensional mesh for finite element computation is analyzed. The simulated annealing is a well known powerful global optimization algorithm, used in combinatorial optimizations [7]-[8]. It is based on random moves, and avoids entrapment in local minima by allowing uphill moves, controlled by means of an acceptance criterion. The SA here used is derived from the simulated annealing algorithm for functions of continuous variables proposed in [9].

The algorithm proceeds iteratively: starting from the point $\mathbf{x_0}$ it generates a sequence of points $\mathbf{x_0}$, $\mathbf{x_1}$, .., $\mathbf{x_i}$,.. until it reaches the global minimum of the objective function. At the *m-th* step of the simulated annealing algorithm, a new configuration $\mathbf{x_{m+1}}$ of points is generated by random perturbation of the previous state $\mathbf{x_m}$. The random perturbation is obtained by changing the coordinates of the nodes in turn.

If the value of the function $f(\mathbf{x_{m+1}})$ is less than $f(\mathbf{x_m})$, $\Delta f \leq 0$ and $\mathbf{x_{m+1}}$ is always accepted, however, if $\Delta f > 0$ (uphill moves), $\mathbf{x_{m+1}}$ is accepted with a Boltzmann distribution probability:

$$P(\Delta f) = e^{-\left(\frac{\Delta f}{T}\right)} \tag{15}$$

where T is a control parameter called *temperature*. The method starts with a high value of T and during the minimization process it is gradually lowered in order to focus to the minimum. An established number M_{max} of configurations is generated at each temperature value until the equilibrium is reached. The probability that an uphill move will be accepted diminishes as the

temperature declines until no function cost increasing are accepted anymore.

The algorithm has two termination criteria to decide if the global minimum has been reached. When at the temperature value T_V the M_{max} configurations have been proved, let f_v to be the current value of $f(\mathbf{x_m})$ the search is stopped if:

$$|f_v - f_{v-u}| \leq \beta, \qquad u = 1,.,4$$

and:

$$f_v - f(\mathbf{x_{opt}}) \leq \beta$$

where β is a small quantity which has to be opportunely chosen and $f(\mathbf{x_{opt}})$ is the optimum current value of the objective function.

IV. APPLICATION

The two methods are applied to solve a very simple problem as the plane wave propagation in a homogeneous two-dimensional domain. First, a coarse mesh is generated as shown in Fig.5a. The method based on the *mass-lumping* algorithm is unstable since the mesh presents many nonacute triangles while the mixed finite element-finite difference method is stable but does not produce accurate results.

Second, the proposed SA procedure is applied to build an optimized mesh as shown in Fig.5b. The first method is still unstable while the finite element-finite difference method is stable and the results (non reported in this paper for brevity) are accurate.

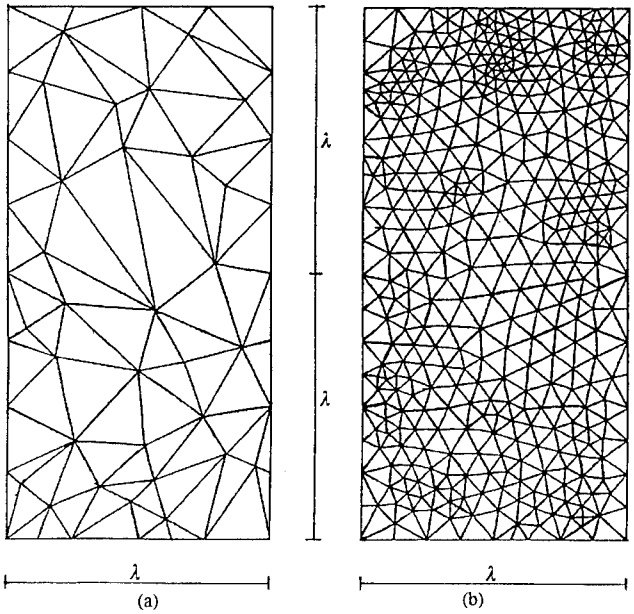


Fig. 5 Nonoptimized mesh (a) and optimized mesh (b).

The method based on the *mass lumping* algorithm produces accurate results only when the mesh is composed by equilateral triangles. In this case the numerical expressions of the two methods coincides. It should be pointed out that the optimized mesh (see Fig.5b) is very similar to a mesh obtained by the application of Voronoi diagrams [11]. This result is relevant because it permits to generate *a priori* mesh based on Voronoi polygons without using any optimization technique. It yields a big reduction of computational cost in the preprocessing and accuracy in the field solution results when the mixed finite elements-finite difference method is utilized. If an automatic mesh generator based on Voronoi polygons is used, care should be taken to respect the stability criterion of the FE-TD methods.

V. CONCLUSIONS

Two explicit methods based on the *leap-frog* scheme have been presented for the solution of Maxwell's curl equations .The first method, based on a finite element discretization of space and a finite difference integration of time, leads to an explicit solution scheme by applying the *mass lumping* algorithm. The accuracy is strongly dependent on the shape of the elements: the mesh must be constituted by nonacute triangles to ensure the stability of the method.

The second method, based on a mixed finite element-finite difference discretization of space and a finite difference integration of time, produces a solution which is less sensitive to the element shape and does not have stability problems.

An optimization problem has been defined to find a FE mesh which produces accurate results avoiding as far as possible nonacute triangles in a two-dimensional mesh and proximating all the triangles to equilateral triangles. This mesh is very similar to a mesh obtained by the use of Voronoi polygons, when the FE-TD stability criterion is respected.

REFERENCES

[1] M. Feliziani, F. Maradei, "Point Matched Finite Element-Time Domain Method Using Vector Elements", *IEEE Trans. Magnetics*, Sep. 1994, vol. MAG-30, no. 5, pp. 3184-3187.

[2] M. Feliziani, F. Maradei, "On the Point-Matched Time Domain Numerical Techniques", *COMPEL*, vol. 13, Supplement A, May 1994, pp. 265-270.

[3] M. Feliziani, F. Maradei, "On the Use of Irregular Grids in the Zeroth-Order Vector Finite Element-Time Domain (VFE-TD) Method", *1994 IEEE AP-S Int. Symp.*, Seattle, WA, June 19-24, 1994, pp.2109-2112.

[4] M.Feliziani, F. Maradei, "Hybrid Finite Element Solution of Time Dependent Maxwell's Curl Equations", *Invited Paper, Sixth Biennial IEEE CEFC'94*, Aix-les-Bains, France, July 5-7, 1994, to appear on *IEEE Trans. Magnetics*, May 1995.

[5] P.B. Monk, A. K. Parrott, "A Dispersion Analysis of Finite Element Methods for Maxwell's Equations", *SIAM J. Sci. Comput.*, vol. 15, no. 4, Jul. 1994, pp. 916-937.

[6] J.F. Lee, "Whitney Element Time Domain (WETD) Method", *Sixth Biennial IEEE CEFC'94*, Aix-les-Bains, France, July 5-7, 1994.

[7] P. J. M. Van Laarhoven, E. H. L. Aarts, "Simulated Annealing: Theory and Applications", D. Reidel, Dordrecht, 1987.

[8] E. H. L. Aarts, J. Korst, "Simulated Annealing and Boltzmann Machines", J. Wiley, New York, 1989.

[9] A. Corana, M. Marchesi, C. Martini, S. Ridella, "Minimizing Multimodal Functions of Continuous Variables with the Simulated Annealing Algorithm", *ACM Trans. Math. Software*, vol. 13, Sep. 1987, pp. 262-280.

[10] D.A. Lindholm, "Automatic Triangular Mesh Generation on Surfaces of Polyhedra", *IEEE Trans. Magnetics*, vol. 19, no. 6, Nov. 1983, pp. 2539-2542.

[11] P.L. George, "Automatic Mesh Generation", J. Wiley, New York, 1991.

ANALYSIS AND DESIGN OF A REENTRANT RESONANT CAVITY APPLICATOR FOR RADIO FREQUENCY HYPERTHERMIA SYSTEM

Y.Kanai, T.Tsukamoto, K.Toyama, T.Kashiwa*, Y.Saitoh and M.Miyakawa
Department of Information Engineering, Niigata Univ., Niigata, 950-21 JAPAN
** Department of Electrical Engineering, Hokkaido Univ., Sapporo, 060 JAPAN*

abstract **-- Analysis and design of a reentrant resonant cavity applicator are investigated. The electricconstants have been measured by the infinitesimal coaxial probe method. Comparisons of calculated and measured temperature distributions for a disk-shaped phantom show that it is necessary to consider the temperature dependences of relative permittivity ε_r and electric conductivity σ of the phantom. By attaching cylindrical conductors to a reentrant resonant cavity applicator, electromagnetic energy is directed toward a specific part of a long phantom and temperature rise in a deep region is achieved.**

I INTRODUCTION

It is important to obtain deep and concentrated heat in a hyperthermia system. For a radio frequency hyperthermia system, the annular phased array [1] or its improved method [2] have been developed. However, it has been pointed out that there are still some difficulties to heat deep-seated cancer tumors selectively [3].

Recently, a reentrant resonant cavity applicator has been utilized [4]. Both calculations [5] and measurements [6] have been carried out, however, only axisymmetrical models have been examined, which is not enough for a practical application. Moreover, it has not been possible to understand the phenomena because the frequency and temperature dependences of the electric and thermal constants for the phantom have been neglected.

In this paper, analysis and design of a reentrant resonant cavity applicator are investigated. In experiments, dielectric phantoms (eg. TX-150) are commonly used, therefore, it is important to measure the frequency and temperature dependences of relative permittivity ε_r, electric conductivity σ, thermal conductivity λ, specific heat capacity c and the volume density of mass ρ. By using the infinitesimal coaxial probe method [7], it is confirmed that ε_r becomes smaller and σ becomes larger as the temperature rises, which means considering the characteristics of ε_r and σ vs. temperature is indispensable. We have also confirmed by calculations that the temperature dependences of λ, c and ρ can be neglected. The frequency dependences (50-100 MHz) of these parameters are found to be not vital for our system.

Next, the calculated and measured temperature distributions of a disk-shaped phantom (240 mm in diameter and 250 mm in thickness) are compared. The 3-D finite difference - time domain method [3] and finite element method are used to obtain electromagnetic field and temperature distributions, respectively, where the iterative calculations are carried out considering the temperature dependences of ε_r and σ. Close agreement between calculated and measured temperature distributions in the phantom show the validity of the calculations.

In order to optimize the cavity structure, the temperature distributions of a long cylindrical phantom (1500 mm in length and 200 mm in diameter) are calculated. Cylindrical conductors are used [8] to direct the electromagnetic energy toward a specific area. Calculated results show that directed heat in a deep region can be obtained, which leads to the possibility of the reentrant cavity applicator with cylindrical conductors being used for a deep-seated cancer tumors.

II REENTRANT RESONANT CAVITY APPLICATOR [4]

Figure 1 shows the schematic structure of the reentrant resonant cavity applicator. In order to direct the electromagnetic energy toward a specific area of the body, this system has been invented. Inside the applicator, there is enough area for one adult. Precise dimensions are shown in section IV. The block diagram of the hyperthermia system is shown in the same figure. First, resonant frequencies of the cavity are measured. When the electromagnetic energy is applied through one-turn coil coupled with the variable capacitor, a resonant state is kept automatically using an impedance controller. In our experiment, the lowest resonant frequency around 50-70 MHz is used. Throughout this paper, the electromagnetic energy of 300 Watts has been applied for 30 minute increments. Next, the phantom is cut and the temperature distribution is measured by the thermogram, however it should be noted that the exact input power is unclear because some energy is consumed by the coil and capacitor. Therefore, we evaluate the temperature rise as arbitrary in our calculations.

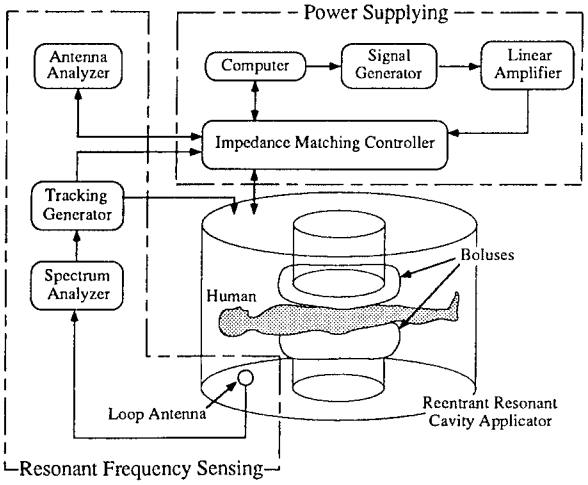


Fig. 1 Schematic structure and block diagram of a reentrant resonant cavity applicator.

III MEASUREMENTS OF ELECTRIC AND THERMAL CONSTANTS

In the experiment, dielectric phantom (eg. TX-150) is commonly used. The dependences of relative permittivity ε_r and electric conductivity σ on temperature and frequency have been pointed out [9], however, in past experiments these dependences have been neglected in both the calculations [5] and the experiments [6]. Therefore, it has not been possible to understand this phenomena.

Here, we have measured the temperature and frequency dependences of ε_r and σ by using the infinitesimal coaxial probe method [7]. Figure 2 shows ε_r and σ vs. temperature at 50 and 100 MHz. As can be seen from the figure, ε_r becomes smaller and σ becomes larger as the temperature rises. These dependences affect the electromagnetic and temperature distributions greatly, which is shown in section IV(c)-(d). From the same figures, frequency dependences of ε_r and σ are found to be small within 50-100 MHz. Because the lowest resonant frequency does not change during the heating

process, it is not necessary to consider frequency dependences of ε_r and σ. Temperature dependences of thermal conductivity λ, specific heat capacity c and the volume density of mass ρ were measured, but we have found by calculations that these dependences can be neglected. Hereafter, only temperature dependences of ε_r and σ are taken into account.

IV VALIDATION OF CALCULATIONS

(a) Calculating methods

We have used the three-dimensional Finite Difference Time Domain (3-D FD-TD) method [3] to solve Maxwell's equations:

$$\nabla \times \boldsymbol{E} = -\mu \frac{\partial \boldsymbol{H}}{\partial t}, \quad \nabla \times \boldsymbol{H} = \sigma \boldsymbol{E} + \varepsilon \frac{\partial \boldsymbol{E}}{\partial t} \tag{1}$$

First, we derive the resonant frequencies of the cavity, the lowest resonant frequency is then applied. After analyzing the electromagnetic field distributions, the electromagnetic energy applied to the phantom is evaluated as

$$\dot{Q} = \frac{1}{2} \sigma \int |\boldsymbol{E}|^2 dt \tag{2}$$

Heat transfer equations

$$\rho c \frac{\partial T}{\partial t} = \lambda \left(\frac{\partial^2 T}{\partial x^2} + \frac{\partial^2 T}{\partial y^2} + \frac{\partial^2 T}{\partial z^2} \right) + \dot{Q} \tag{3}$$

$$q = \alpha_c (T - T_c) \tag{4}$$

are solved by the three-dimensional Finite Element Method (3-D FEM), where ρ, c, λ, q, α_c and T_c are, respectively volume density of mass, specific heat capacity, thermal conductivity, heat flux, heat transfer coefficient and the external temperature.

Note here that the reason we have used FD-TD method to solve Maxwell's equations is the limitation of computer memory at our facility (32 MB RAM).

(b) The model used for calculations and measurements

The dimensions of the cavity used for calculations and measurements are shown in Fig. 3. The diameter and the height of the body are 1900 mm and 1450 mm, respectively. Inside the body there are two reentrants, both of them are 600 mm in diameter and 500 mm in length. The phantom we have used in this section is 240 mm in diameter and 250 mm in thickness. The calculation model is divided into FD cells by using an automatic mesh generator [10]. Variable meshes are used to save computing time and memory while maintaining the accuracy. We have calculated by changing the cell sizes and found that the cell size should be smaller than 5 % of the wave length in the phantom.

(c) Temperature rises for phantoms with different permittivities and conductivities

To understand the differences of electromagnetic and temperature distributions for phantoms with various permittivities and conductivities, both calculations and measurements are carried out and compared. Here, the external temperature was set to 20 °C. Figures 4(a) and (b) show the electromagnetic energy and temperature distributions on the x-y plane, respectively. In these calculations, relative permittivity and conductivity are set to constant ε_r = 80 and σ = 0.50, which correspond to the initial temperature of 10 °C. As can be seen from the figures electromagnetic energy is concentrated and a temperature rise in a deep region is obtained. On the other hand, for the phantom with ε_r = 72 and σ = 0.74 which correspond to the initial temperature of 30 °C, the highest temperature region is found in the periphery as shown in Fig. 5(b). From these results, it is indispensable to consider the nonlinearity

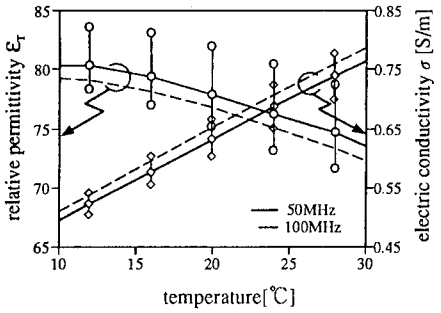


Fig.2 Measured relative permittivity and electric conductivity.

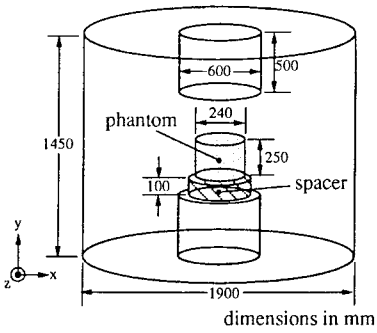
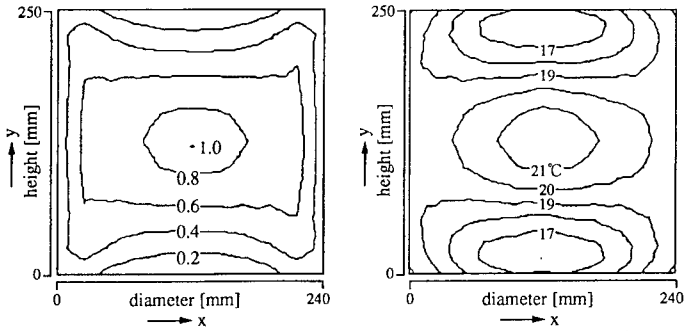


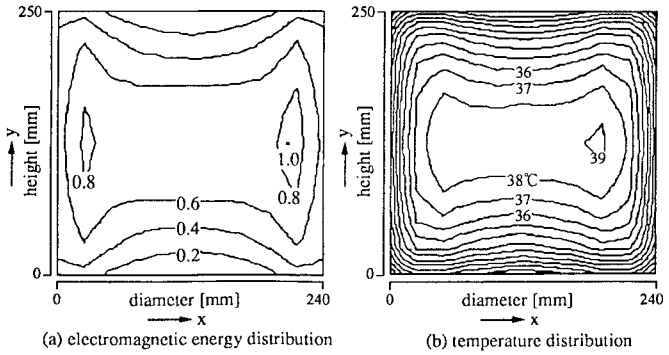
Fig.3 Model used for calculations and mesurements.



(a) electromagnetic energy distribution

(b) temperature distribution

Fig.4 Electromagnetic energy and temperature distributions for ε_r =80 and σ = 0.50, which correspond to the initial temperature of the phantom 10 °C .



(a) electromagnetic energy distribution

(b) temperature distribution

Fig.5 Electromagnetic energy and temperature distributions for ε_r =72 and σ = 0.74, which correspond to the initial temperature of the phantom 30 °C .

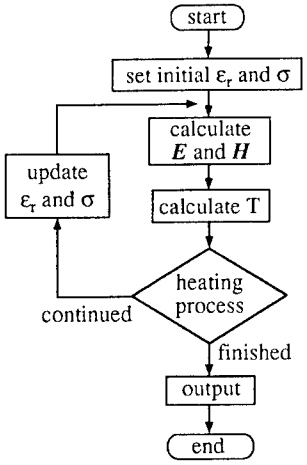


Fig.6 An algorithm to consider the temperature dependences of ε_r and σ.

of ε_r and σ. Therefore, we propose a temperature calculating algorithm considering the temperature dependences of permittivity and conductivity as shown in Fig.6.

(d) Comparisons of calculated and measured results

Figures 7(a) and (b) compare the calculated and measured results on the x-y plane, where the initial temperature of the phantom and the external temperature were 9.2 and 21.7 °C, respectively. In calculating the temperature distributions, the algorithm shown in Fig. 6 is used. By experimenting with an array of different time intervals, it was found that updating the electric constants every five minutes was sufficient for this case. In Figs. 8(a) and (b) the calculated and measured results are compared at the initial temperature of 23.5 °C. The external temperature was 21.0 °C. As can be seen from the figures, close agreements can be found. These show the validity of the proposed algorithm. However, a temperature rise in a deep region is not obtained when the initial temperature was 23.5 °C. In the next section an attempt is made to obtain selective heat in a deep region.

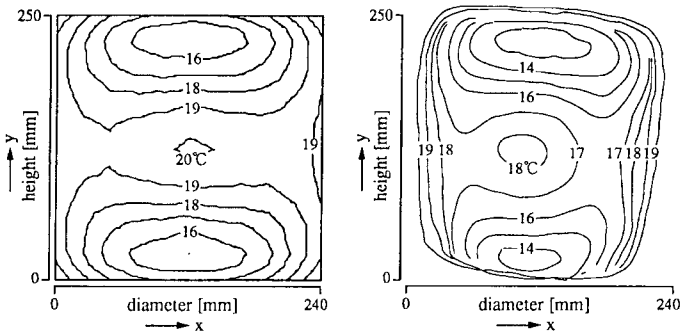
V COMPUTATIONS OF ELECTROMAGNETIC AND TEMPERATURE DISTRIBUTIONS FOR A LONG PHANTOM

In this section, the computations of electromagnetic and temperature distributions for a long phantom are carried out. Considering muscle, relative permittivity and conductivity were set to 75 and 0.75, respectively [11]. The initial temperature of the phantom was set to 20.0 °C. The external temperature was also set to 20.0 °C. Figure 9 shows the model calculated, in this case the phantom is 200 mm in diameter and 1500 mm in length. The conductors were set to direct the electromagnetic energy toward a specific region. To better understand the effect of the conductors [8], calculations were carried out twice, once with and once without the conductors.

Figure 10 shows the electromagnetic energy distribution on the x-y plane without the conductors. The energy is directed toward periphery and we can understand that the directed heat is impossible. The electromagnetic energy distribution on the x-y plane with the conductors are shown in Fig. 11(a). As can be seen from the figure, it is possible to direct the electromagnetic energy toward a deep region. Selective heat in a deep region is found in Fig. 11(b). When comparing Figs. 10 and 11(a), it

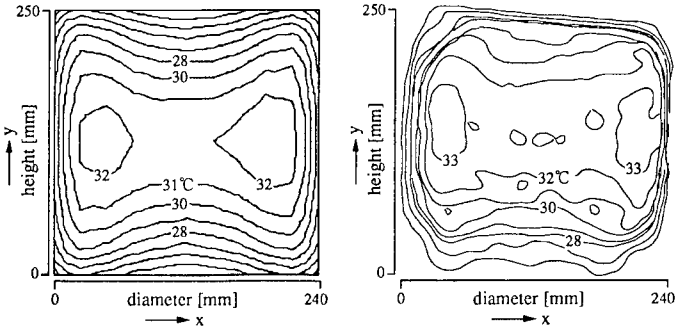
can be seen that when the conductors are utilized an obvious improvement in directed energy toward a specific region is obtained and therefore, the problem noted in section IV(d) may be solved. Note here that the roles of the conductors are 1) shielding the field and 2) directing the field by changing the electromagnetic energy distribution. The energy distribution is found to be critical to the diameters and lengths of the conductors.

This technique using cylindrical conductors can be applied to the phantoms with various shapes and electric constants. This leads to the possibility of the reentrant cavity applicator with cylindrical conductors being used for a deep-seated cancer tumors.



(a) calculated temperature distribution (b) measured temperature distribution

Fig.7 Comparison of calculated and measured temperature distributions, where the initial temperature of the phantom was 9.2 °C.



(a) calculated temperature distribution (b) measured temperature distribution

Fig.8 Comparison of calculated and measured temperature distributions, where the initial temperature of the phantom was 23.5 °C.

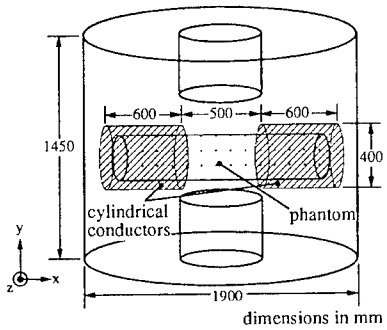


Fig.9 Calculated model for a long phantom.

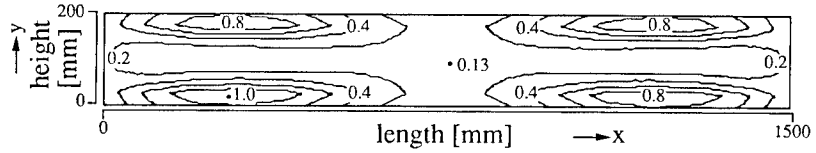
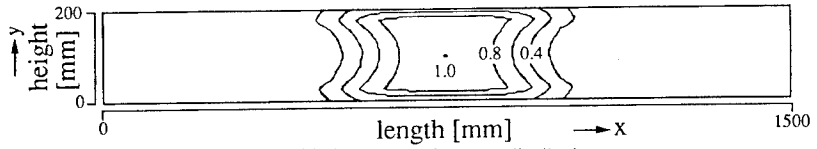
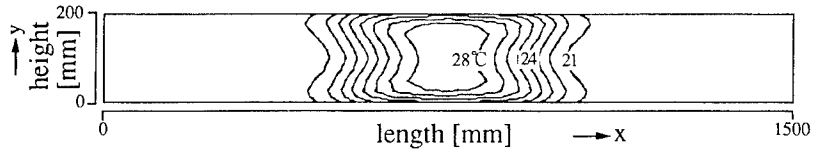


Fig.10 Calculated electromagnetic energy distribution without cylindrical conductors.



(a) electromagnetic energy distribution



(a) temperature distribution

Fig.11 Calculated electromagnetic energy and temperature distributions with cylindrical conductors.

VI CONCLUSION

The electric constants have been measured by using the infinitesimal coaxial probe method. It is confirmed that it is indispensable to consider the temperature dependences of relative permittivity ϵ_r and electric conductivity σ to understand the noted phenomena. We have proposed an algorithm with nonlinearities of electric constants that are taken into account. The calculated and measured results are compared for a disk-shaped phantom and it is found that our algorithm is valid. By using the cylindrical conductors that have been attached to the reentrant resonant cavity applicator, electromagnetic energy is directed toward a specific part of the long phantom and good temperature rise has been obtained. These lead to the possibility of the reentrant cavity applicator with cylindrical conductors being used for a deep-seated cancer tumors.

REFERENCES

[1] P. F. Turner, "Regional hyperthermia with an annular phased array," *IEEE Trans. BME*, Vol. 31, pp.106-114, Jan. 1984.

[2] V. Sathiaseelan, M.F.Iskander, G.C.W.Howard and N.M.Bleehen, " Theoretical analysis and clinical demonstration of the effect of power pattern control using the annular phased-array hyperthermia system," *IEEE Trans. MTT*, Vol.34, pp. 514-519, May 1986.

[3] D. Sullivan, "Three-dimensional computer simulation in deep regional hyperthermia using the finite-difference time-domain method," *IEEE Trans. MTT*, vol.38, pp.204-211, Feb. 1990.

[4] J. Matsuda, K.Kato and Y.Saitoh, "The application of a re-entrant type resonant cavity applicator to deep and concentrated hyperthermia---Computer simulations---," *Jpn. J. Hyperthermic Oncol.*, Vol.4, pp. 111-118, June 1988.

[5] K. Kato, J. Matsuda and Y. Saitoh, "A re-entrant type resonant cavity applicator for deep-seated hyperthermia treatment," *Proc. Annual Int'l Conf. of the IEEE Eng. in Medicine and Biology Society*, Vol. 11, pp.1712-1713, Nov. 1989.

[6] Y.Saitoh, H.Kazuma, M.Miyakawa, J.Matsuda and K.Katoh, " Heating characteristics of phantom with reentrant resonant cavity applicator," *6th Int'l Congress on Hyperthermic Oncology*, vol.1, p.337, Apr. 1992.

[7] M.Miyakawa, "A method of measurement of tissue permittivities by using an infinitesimal coaxial probe," *Trans. of IEICE of Japan*, Vol. J71-D, pp.2450-2456, Nov. 1988.

[8] Y. Saitoh, Y.Kanai, T. Tsukamoto, T.Kashiwa, H.Kazuma and M.Miyakawa, "3-D electromagnetic field analysis of reentrant resonant cavity applicator by FD-TD method," *Jpn. J. Hyperthermic Oncol.*, Vol. 10, p.275, Sep. 1994.

[9] B.J.James and D.M.Sullivan, "Creation of three-dimensional patient models for hyperthermia treatment planning," *IEEE Trans. BME*, Vol.39, pp.238-242, Mar.1992.

[10] M. Miyakawa, "Consideration on the temperature dependency of tissue permittivities in hyperthermia treatment," *Jpn. J. Hyperthermic Oncol.*, Vol. 4, pp.307-315, Sep. 1988.

[11] C.C. Johnson and A.W.Guy, " Nonionizing electromagnetic wave effects in biological materials and systems," *Proc. IEEE*, Vol. 60, pp.692-718, June 1972.

ANALYSIS OF LOADED CAVITIES USING THE CONSTITUTIVE ERROR APPROACH

R.Albanese [1], R. Fresa [2], R. Martone [3], G. Rubinacci [4]

[1] Dip. di Ingegneria Elettronica e Matematica Applicata, Università degli studi di Reggio Calabria, Italy
[2] Dipartimento di Ingegneria dell'Informazione e Ingegneria Elettrica, Università degli studi di Salerno, Italy
[3] Dipartimento di Ingegneria, Seconda Università degli studi di Napoli, Italy
[4] Dipartimento di Ingegneria Industriale, Università degli studi di Cassino, Italy

Abstract *Aim of this paper is to apply an error based finite element formulation to the analysis of the resonant cavities. By suitably choosing two vector potentials for the electric and magnetic fields, the Maxwell equations as well as initial and boundary conditions are automatically satisfied for arbitrary values of these potentials, being the error concentrated in the constitutive equations. The solution is then obtained via minimization of a global error functional related to the constitutive equations. The method provides two complementary solutions and an error estimation that can be effectively used for the refinement of the discretization. The solution is represented by means of edge element based shape functions and the evolution of the system is analysed in the time domain. To calculate the resonant frequencies, the dynamics of suitable field components at proper points of the cavity are Fourier analysed. In addition, by interpreting the solution at time $t=\Delta t$ as the frequency response of the system when forced by a sinusoidal input with $\omega=1/\Delta t$, the eigenfrequencies are located at the peaks of the electromagnetic energy. Since the numerical procedure rigorously satisfies Maxwell equations, the well known problem of the appearance of the spurious modes does not arise. The method is applied to the analysis of inhomogeneously loaded 3D cavities.*

1. Introduction

This paper deals with the analysis of 3D resonant cavities. We apply a numerical formulation for the solution of Maxwell equations which is based on the minimization of the so called constitutive error in the time domain. Usual methods exactly enforce the constitutive relationships and only one of the field equations, satisfying the other one in a weak form. On the other hand, the error-based method makes use of the vector potentials **A** and **F** able to automatically verify both field equations. The numerical solution is then obtained by minimising a functional related to the error on the constitutive relationships and adopting edge element based functions for the vector potentials. This formulation provides two complementary solutions which can be used to obtain an indication of the distribution of the error in the solution domain.

These ideas, originally proposed by Rikabi et al. in [1], have been discussed and applied in the time domain by the authors [2-4] and in frequency domain by Bossavit et al. [5-6].

Some features of the method will be illustrated by determining the resonant frequencies of inhomogeneously loaded 3D cavities. In particular, to calculate the eigenfrequencies, the dynamics of suitable field components at proper points of the cavity are Fourier analysed. In addition, by interpreting the solution at time $t=\Delta t$ as the frequency response of the system when forced by a sinusoidal input with $\omega=1/\Delta t$, the resonant frequencies are located at the peaks of the electromagnetic energy.

2. The error based approach.

A detailed description of the error based approach to the solution of full Maxwell equations is given in [2]. Here, for the sake of simplicity, we will focus our attention to the model of Maxwell equations in non conducting media:

$$\nabla\times\mathbf{E} = -\partial\mathbf{B}/\partial t \qquad (1)$$

$$\nabla\times\mathbf{H} = \partial\mathbf{D}/\partial t \qquad (2)$$

with the proper boundary and initial conditions and the monotonic constitutive properties

$$\mathbf{B} = \mathbf{f}_B(\mathbf{H}) \qquad \mathbf{D} = \mathbf{f}_D(\mathbf{E}) \qquad (3)$$

Introducing the three components vector potentials **A** e **F** as the time integrals of -**E** and **H**, the following fields:

$$\mathbf{E}=-\partial\mathbf{A}/\partial t,\ \mathbf{H}=\partial\mathbf{F}/\partial t,\ \mathbf{B}=\mathbf{B}_o+\nabla\times\mathbf{A},\ \mathbf{D}=\mathbf{D}_o+\nabla\times\mathbf{F} \qquad (4)$$

automatically satisfy Eqs. 1 and 2 and the initial conditions $\mathbf{B}(\mathbf{x},0)=\mathbf{B}_o(\mathbf{x})$ and $\mathbf{D}(\mathbf{x},0)=\mathbf{D}_o(\mathbf{x})$.

From the numerical point of view [2] the vector potentials $\mathbf{A}(\mathbf{x},t)$ and $\mathbf{F}(\mathbf{x},t)$ are approximated in space using edge-element based functions in such a way that the numerical unknowns become the degrees of freedom $\overline{A}(t)$ and $\overline{F}(t)$. A local error functional $\lambda(\mathbf{x},t)\geq 0$, with strict inequality for vector potentials which do not satisfy Eqs 3, is then defined as:

$$\lambda(\mathbf{x},t) = \alpha_H\Big(\int_{H^*}^{H}\mathbf{f}_B(\mathbf{h})\cdot d\mathbf{h} + \int_{B^*}^{B}\mathbf{f}_H(\mathbf{b})\cdot d\mathbf{b} + \mathbf{H}^*\cdot\mathbf{B}^* - \mathbf{H}\cdot\mathbf{B}\Big) + \alpha_E\Big(\int_{D^*}^{D}\mathbf{f}_E(\mathbf{d})\cdot d\mathbf{d} + \int_{E^*}^{E}\mathbf{f}_D(\mathbf{e})\cdot d\mathbf{e} + \mathbf{E}^*\cdot\mathbf{D}^* - \mathbf{E}\cdot\mathbf{D}\Big) \qquad (5)$$

where the local values of the fields are given by Eq. 4; $\mathbf{f}_H$ and $\mathbf{f}_E$ are the inverse mappings of $\mathbf{f}_B$ and $\mathbf{f}_D$; ($\mathbf{H}^*$, $\mathbf{B}^*$) and ($\mathbf{E}^*$, $\mathbf{D}^*$) are two pairs which satisfy Eqs. 3; α_H and α_E are weighting factors. In the linear case ($\mathbf{B}=\mu\mathbf{H}$, $\mathbf{D}=\varepsilon\mathbf{E}$, $\mathbf{H}^*=\mathbf{0}$, $\mathbf{B}^*=\mathbf{0}$, $\mathbf{E}^*=\mathbf{0}$ and $\mathbf{D}^*=\mathbf{0}$) the local error density defined by Eq. 5 becomes

$$\lambda = \alpha_H\{\mu H^2/2 + B^2/2\mu - \mathbf{B}\cdot\mathbf{H}\} + \alpha_E\{\varepsilon E^2/2 + D^2/2\varepsilon - \mathbf{D}\cdot\mathbf{E}\} \qquad (6)$$

Linear approximation is assumed in each of the time steps in which the global interval (0,T) is partitioned. In this way the problem reduces to the solution of a number of subproblems defined in the time steps in which the only unknowns are the vector potentials at final time. Each subproblem can be solved by minimizing a global error functional related to $\lambda(\mathbf{x}, t)$ as:

$$\Lambda = \int_{t_k}^{t_{k+1}}\int_V \lambda(\mathbf{x}, t)\, dv dt \qquad (7)$$

where V is the domain of integration, (t_k, t_{k+1}) is the k-th time step.

With reference for instance to the linear case, the following set of linear algebraic equations is obtained under minimization:

$$\begin{bmatrix} \partial^2\Lambda/\partial\overline{A}_{k+1}\partial\overline{A}_{k+1} & \partial^2\Lambda/\partial\overline{A}_{k+1}\partial\overline{F}_{k+1} \\ \partial^2\Lambda/\partial\overline{F}_{k+1}\partial\overline{A}_{k+1} & \partial^2\Lambda/\partial\overline{F}_{k+1}\partial\overline{F}_{k+1} \end{bmatrix}\begin{bmatrix} \overline{A}_{k+1} \\ \overline{F}_{k+1} \end{bmatrix} = -\begin{bmatrix} \partial\Lambda/\partial\overline{A} \\ \partial\Lambda/\partial\overline{F} \end{bmatrix}_0 \qquad (8)$$

The time integral $\int_{t_k}^{t_{k+1}}\lambda(\mathbf{x},t)dt$ is approximated, according to the θ method, as $\lambda(\mathbf{x}, t_\theta)\Delta t$ with $\Delta t=t_{k+1}-t_k$ and $t_\theta=\theta t_{k+1}+(1-\theta)t_k$. Moreover, the choice $\alpha_H=\alpha_E$ assures the splitting of system (9), i.e. the two unknown potentials $\overline{A}_{k+1}=\overline{A}(t_{k+1})$ and $\overline{F}_{k+1}=\overline{F}(t_{k+1})$ can be obtained as the solution of

two independent systems of equations, since in this case $\left[\partial^2\Lambda/\partial\overline{A}_{k+1}\partial\overline{F}_{k+1}\right]=\left[\partial^2\Lambda/\partial\overline{F}_{k+1}\partial\overline{A}_{k+1}\right]^T=[0]$. This splitting is however different from solving two separate problems for $\overline{A}$ and $\overline{F}$ in (0, T) because in our case each potential at t_{k+1} depends upon both potentials at t_k. We notice that the choice $\theta=0$ leads to a classic explicit scheme which is affected by numerical instabilities. In this case, $\overline{A}$ and $\overline{F}$ are not updated simultaneously, but $\overline{A}_{k+1}$ is conventionally replaced by $\overline{A}_{k+1/2}$ and $\overline{A}_k$ by $\overline{A}_{k-1/2}$. Moreover, since $\overline{A}_{k+1/2}$ and $\overline{F}_{k+1}$ are not explicitly available the dynamic matrix can be diagonalized by using the trapezoidal rule for the numerical evaluation of the relevant space integrals, a treatment similar to the mass lumping [7].

The main difference with the approach of ref. [5] is that the error functional, being expressed in the time domain, is a positive definite quantity, leading to the splitting as a result of a minimization procedure.

3. Numerical Results

The method is applied to the analysis of 3D resonant cavities. The problem has been solved in the time domain starting from the initial conditions $\mathbf{D}(\mathbf{x}, 0)=\mathbf{D}_0(\mathbf{x})=0$ and $\mathbf{B}(\mathbf{x}, 0)=\mathbf{B}_0(\mathbf{x}) = \nabla\times\mathbf{A}_0$ at time t=0. The vector potential $\mathbf{A}_0$ has been selected equal to a linear combination (with random coefficients) of all edge element based shape functions, having excluded those corresponding to edges on the electric walls. The resonant frequencies are then obtained performing a Fourier analysis of the numerical results. This method is particularly useful when dealing with walls of finite conductivity.

On the other hand, in case of a lossless medium, if the potentials **A** and **F** (as well as the fields **E** and **H**) are represented in the frequency domain, one of them will be real and the other one pure imaginary. This allows to obtain a solution of the field problem in the frequency domain using the results of the code running in the time domain. In fact, using an implicit scheme, Maxwell equations at time Δt are approximated as

$$\nabla\times\mathbf{E}(\mathbf{x}, \Delta t) = \hat{\mu}\frac{\mathbf{H}(\mathbf{x}, \Delta t)}{\Delta t} \tag{9}$$

$$\nabla\times\mathbf{H}(\mathbf{x}, \Delta t) = \varepsilon\frac{\mathbf{E}(\mathbf{x}, \Delta t)}{\Delta t} \tag{10}$$

with $\hat{\mu} = -\mu_0$. If we compare these equations with the corresponding ones in the frequency domain

$$\nabla\times\mathbf{E}(\mathbf{x}, \omega)=-j\omega\mu_0\mathbf{H}(\mathbf{x}, \omega) \tag{11}$$

$$\nabla\times\mathbf{H}(\mathbf{x}, \omega)=j\omega\varepsilon\mathbf{E}(\mathbf{x}, \omega) \tag{12}$$

and we pose $\mathbf{H}(\mathbf{x}, \omega)=j\mathbf{h}(\mathbf{x}, \omega)$ and $\mathbf{E}(\mathbf{x}, \omega)=\mathbf{e}(\mathbf{x}, \omega)$, we notice that can be established the following correspondence:

$$\omega=1/\Delta t,\ \hat{\mu} = -\mu_0,\ \mathbf{H}(\mathbf{x}, \Delta t)=\mathbf{h}(\mathbf{x}, \omega),\ \mathbf{E}(\mathbf{x}, \Delta t)=\mathbf{e}(\mathbf{x}, \omega) \tag{13}$$

This means that with these definitions the solution of the system (8) at time $t=\Delta t$ corresponds to the sinusoidal solution in the frequency domain at the angular frequency $\omega=1/\Delta t$. The frequency response can be obtained [8] by forcing the system with a sinusoidal input; the eigenfrequencies correspond to the peaks of the reactive power that, according to Foster's reactance theorem, is an increasing function of the angular frequency.

Notice that the formulation here illustrated is free of spurious modes since Maxwell equations are rigorously satisfied. In particular the fields **D** and **B** are automatically divergence-free. We refer to [5] for a deeper discussion of this point.

Though the proposed method is fully 3D and then applicable to problems of arbitrary geometry, the first example is related to the analysis of the simple cubic resonator as an attempt to validate the proposed procedure and to estimate its accuracy. The 3D resonant frequencies of the cube are given by $f_{lmn} = c\sqrt{l^2 + m^2 + n^2}/2a$, where a is the length of the edge of the cube (a=1 m in our case). The numerical analysis has been performed in the time domain using 8192 time steps of 50 ps, with a Courant number (calculated on the finer mesh) of $Cou = c\frac{\Delta t}{\Delta x}\sqrt{3} = 0.62$. Three meshes (4×4×4, 8×8×8, 12×12×12 equally spaced hexahedral elements) of one eight of the cube have been analysed. With the finer mesh the fundamental mode is discretized with 48 elements per wavelength, while the last depicted mode (l=1, m=5, n=0) has still a sufficient number of elements per wavelength. The modes with same frequency and different shape (the "degenerate modes") have been found by a proper handling of the symmetry conditions on the 3 symmetry planes (which have been considered as either electric or magnetic walls) The results of the Fourier analysis are reported in Table I showing a good agreement with the analytic solution. Notice that there is no evidence of spectrum pollution, i.e. spurious modes do not appear.

Mode	Analytical	Numerical		
	f [MHz]	Coarse mesh f [MHz]	Medium mesh f [MHz]	Fine mesh f [MHz]
110	211.979	215	212	212
111	259.621	263	261	261
012	335.169	351	339	337
112	367.159	381	371	369
220	423.959	446	430	425
221	449.676	471	454	452
130	474.000	532	486	478
113	497.135	551	507	500
222	519.241	546	528	520
203	540.443	598	552	544
132	560.844	618	571	564
223	618.021	676	630	623
401	618.021	774	647	630
330	635.938	718	652	642
114	635.938	784	664	647
331	653.364	734	668	659
420	670.337	878	703	681
421	686.891	910	715	698
332	703.056	925	718	708
224	734.417	>1000	762	745
403	749.460	964	779	762
134	764.302	>1000	793	774
150	764.302	>1000	825	786
333	778.862	878	798	783
423	807.193	>1000	835	818

Table I: Homogeneous cubic resonant cavity. Fourier analysis for three different discretizations. The values refer to E_y or E_z at x=0.375 m, y=0.375 m, z=0.375 m.

The second example refers to a rectangular cavity loaded with a dielectric slab as shown in fig. 1. One eight of the domain has been discretized by imposing $\mathbf{n}\times\mathbf{H}=\mathbf{0}$ at x=a/2 and z=c/2, $\mathbf{n}\times\mathbf{E}=\mathbf{0}$ at y=b/2. Two meshes have been considered: a coarse mesh with 10×4×4 equally spaced hexahedral elements and a fine mesh with 20×8×8 equally spaced hexahedral elements. The analysis has been

carried out again in the time domain (8192 time steps of 50 ps). In fig. 2 the spectra of E_y obtained by a Fourier analysis of the numerical results calculated inside the dielectric at the point P1 (x=0.250 m, y=0.075 m, z=0.100) in case of the coarse mesh and at the point P2 (x=0.050 m, y=0.075 m, z=0.250 m) in case of the fine mesh are shown. The resonance frequencies of the main modes are reported in Table II in comparison with the analytic solutions.

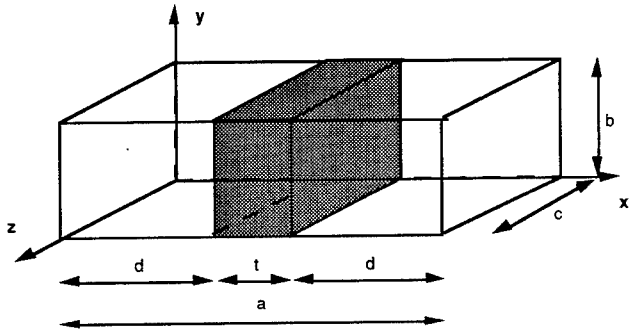


Figure 1: Geometry of the rectangular cavity loaded with a dielectric slab. In the numerical example a=1 m, b=.3m, c =.4m, d=.4m, t=.2m, ε_r =16.

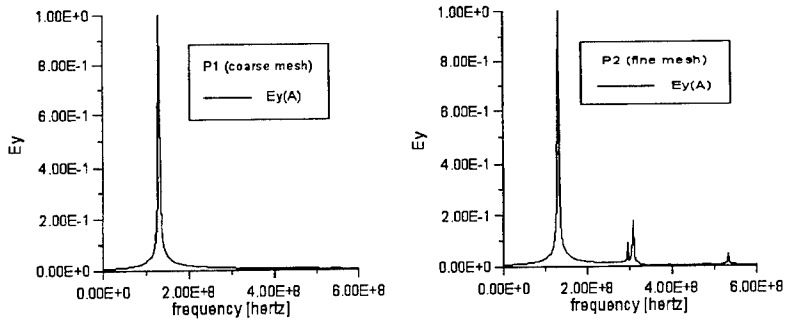


Figure 2: Rectangular cavity loaded with a dielectric slab. Spectra of E_y=-$\partial A_y/\partial t$ at points P1 (coarse mesh) and P2 (fine mesh).

The electromagnetic field distribution for a given mode can also be reconstructed. The eigenfunction of an arbitrary quantity q corresponding to the resonant frequency f_i can be computed by

$$q_i(\mathbf{x}) = A(\mathbf{x}, f_i)\cos\Phi(\mathbf{x}, f_i) \qquad (14)$$

where $A(\mathbf{x}, f)$ and $\Phi(\mathbf{x}, f)$ are amplitude and phase given by the Fourier analysis of $q(\mathbf{x},t)$ at frequency f. For example, fig. 3 shows the E_y distributions in modes TE_{101} and TE_{301} as a function of x for different discretizations, as obtained from the **A** solution ($\mathbf{E}_{(A)}$=$-\partial\mathbf{A}/\partial t$) and from the **F** solution ($\mathbf{E}_{(F)}$=$\nabla\times\mathbf{F}/\varepsilon$). From these results it clearly appears the role of the constitutive error in the estimation of the correctness of the numerical solution.

In fig. 4, the electric field estimates $E_{y(\mathbf{A})}$ and $E_{y(\mathbf{F})}$ are shown as functions of the time at point P2 of the fine mesh inside the dielectric. It can be seen that the constitutive error is much higher than in the mode reconstruction (see fig. 3). The main reason is that the random initial conditions excite the modes whose wavelenght is comparable with the mesh size.

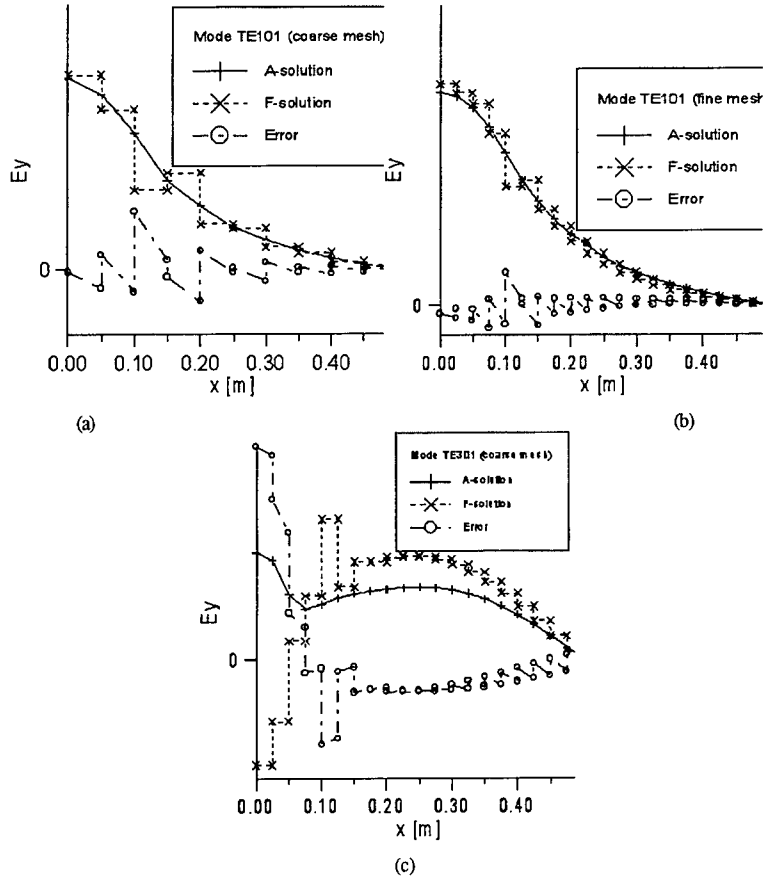


Figure 3: Rectangular cavity loaded with a dielectric slab. Electric field estimates $E_{y(\mathbf{A})}=-\partial A_y/\partial t$ and $E_{y(\mathbf{F})}=(\partial F_x/\partial z-\partial F_z/\partial x)/\varepsilon$ and error field $E_{y(\mathbf{A})}-E_{y(\mathbf{F})}$ as functions of x at y=0.075 m, z=0.100 m: a) TE_{101} eigenfunction (coarse mesh); b) TE_{101} eigenfunction (fine mesh) c) TE_{301} eigenfunction (fine mesh).

Furthermore, we report some results of the analysis based on the correspondence described by Eqs 13. The cavity is excited with an arbitrary sinusoidal input of fixed amplitude.In fig. 5, the reactive power is shown as a function of the frequency of the sinusoidal input. In Table III, the first resonant frequencies for the coarse and the fine mesh, as given by the location of the energy peaks computed using the **A** and **F** variables, respectively. It can be seen that, in this case no upper and

lower bounds are obtained. We notice that our analytical and numerical values of the resonant frequency of the fundamental mode is slightly different from the one reported in [9, 10].

The same analysis has been performed on the inhomogeneously loaded cavity ($0<x<0.200$m, $0<y<0.500$m, $0<z<0.300$m) described and studied f.i. in [5,11,12]. The relative permittivity is $\varepsilon_r=16$ in the dielectric region ($0<x<0.075$m, $0<y<0.125$m, $0<z<0.175$m) and $\varepsilon_r=1$ in the rest of the domain. Magnetic walls are placed at x=0 and y=0 whereas the other walls are perfectly conducting. Some preliminary results obtained in the time domain were already presented in [4]. Here, we present in Table IV the value of the resonant frequency of the fundamental mode as obtained by the first peak of the reactive power computed via Eq. 13 with the fine mesh used in [4].

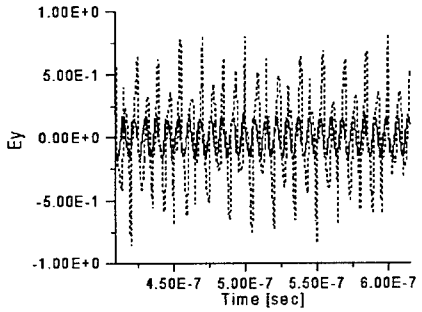


Figure 4: Rectangular cavity loaded with a dielectric slab: $E_{y(A)}$ (solid line) and $E_{y(F)}$ (dashed line) as functions of the time at point P2 of the fine mesh inside the dielectric.

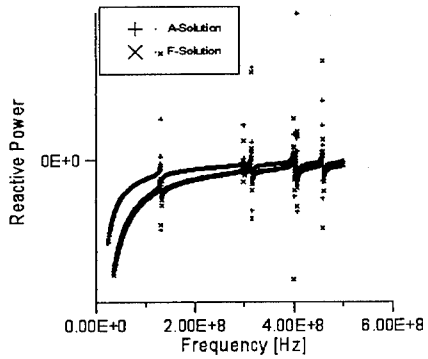


Figure 5: Rectangular cavity loaded with a dielectric slab: reactive power (in arbitrary units) as a function of the frequency of the sinusoidal excitation.

Mode	Analytical	Numerical	
	f [MHz]	Coarse mesh f [MHz]	Fine mesh f [MHz]
101	130.972	132	132
121	297.243	313	300
103	310.873	>450	320
301	392.282	>450	410

Table II: Rectangular cavity loaded with a dielectric slab. Fourier analysis of the estimate of E_y given by the A potential ($E_y=-\partial A_y/\partial t$) at P1 (coarse mesh) and P2 (fine mesh).

Mode	Analytical	Numerical			
	f [MHz]	Coarse mesh: f [MHz]		Fine mesh: f [MHz]	
		A variables	**F** variables	**A** variables	**F** variables
101	130.972	132	131	131	131
121	297.243	305	303	299	299
103	310.873	328	326	315	315
301	392.282	420	418	401	400

Table III: Rectangular cavity loaded with a dielectric slab. The first resonant frequencies for the coarse and the fine mesh, as given by the location of the peaks of the reactive power, computed using the **A** and **F** variables

Formulation	f[MHz]
A-F Time domain	259
A (Reactive power peaks)	256
F (Reactive power peaks)	258
E (Ref. [6])	254.9
H (Ref. [6])	254.5
H (Ref. [9])	267
A-V (Ref. [10])	258
F-ψ (Ref. [10])	259

Table IV: Inhomogeneously loaded 3D cavity. Values of the fundamental resonant frequency given by the Fourier analysis and by the first peak of the reactive power, compared with the results reported in of [6,9,10].

4. Conclusions

In this paper, a numerical formulation of 3D Maxwell equations in the time domain based on the minimization of the constitutive error has been applied to the analysis of resonant cavities. The method present several advantages both in comparison with finite difference schemes on structured meshes, both in comparison with finite element formulations applied to the solution of the vector wave equation on unstructured meshes. In fact, it combines the positive features of the first, in particular the possibility of having stable explicit time domain schemes, with the typical good features of the second with respect to the effective use of unstructured meshes. Moreover, the exact verification of Maxwell equations is guarantied, being the error concentrated in the constitutive equations, henceforth no spurious modes arise; the solution is obtained via minimization of a global error functional and an error estimation is readily available. For the study of 3D resonant cavities the results produced using Foster's reactance theorem are more accurate than those obtained via Fourier analysis.

References

[1] Rikabi, J., Bryant, C.F., Freeman, E.M., An error-based approach to complementary formulations of static field solutions, Int. J. Num. Meth. Eng., Vol.26, 1988.

[2] Albanese, R., Fresa, R., Martone, R., Rubinacci, G., An error based approach to the solution of full Maxwell equations, IEEE Trans. on Mag., Vol.30, No.5,1994

[3] Albanese, R., Fresa, R., Miano, G., Rubinacci, G., Verolino, L., Finite element solution of nonlinear Maxwell equations in the time domain, COMPEL, Vol. 13, Supplement A, 1994, pp. 27-263.

[4] Albanese, R., Fresa, R., Martone, R., Rubinacci, G., On the numerical solution of Maxwell equations in the time domain using edge elements, Proceedings of PIERS'94, Noordwijk, 1994.

[5] Pichon, L., Bossavit, A., A New Variational Formulation Free of Spurious Modes for The Problem of Loaded Cavities, IEEE Trans. on Mag., Vol.29, No.2, 1993.

[6] Golias, N.A., Tsiboukis, T.D., Bossavit, A., Constitutive Inconsistency: Rigorous Solution of Maxwell Equations Based on a Dual Approach, IEEE Trans. on Mag., Vol. 30, No. 5, Sept. 1994, pp. 3586-3589.

[7] Zienkiewicz, O.C., The finite element method, McGraw-Hill Book Company, 1977.

[8] Gomes, J., Ida, N., Calculation of Resonant Frequencies of Aperture Coupled Inhomogeneously Loaded Cylindrical Cavity using Edge Elements (TEAM Workshop Problem No. 19), Proceedings of the International TEAM Workshop, Miami, Nov. 1993.

[9] Akhtarzard S., Johns P.B., Solution of Maxwell Equations in Three Space Dimensions and Time by T.L.M. Method of Numerical Analysis, Proc. IEE, Vol. 122, N.12, 1975.

[10] Sadiku Matthew N.O., Numerical Techniques in Electromagnetics, CRC Press, 1992.

[11] Webb J., Efficient generation of divergence-free fields for the finite element analysis of 3D cavity resonances, IEEE Trans. on Mag., Vol. 24, No. 1, 1988, pp. 162-165.

[12] Bardi I., Biro O., Preis K., Vrisk G., Richter K. R., Nodal and edge element analysis of inhomogeneously loaded 3D cavities, IEEE Trans. on Mag., Vol. 28, 1992, pp.1142-1145.

The Design of Electromagnetic Devices using Knowledge Based Systems and Sensitivity Information

D.A. Lowther, D.N. Dyck and R. Rong

Department of Electrical Engineering
McGill University
3480 University Street
Montreal
Quebec
Canada H3A 2A7

Abstract

This paper describes a system capable of taking an initial set of design specifications and creating and optimizing a complete device. Two basic processes are used coupled with numerically based analysis tools. These processes are those of case based reasoning and sensitivity analysis. The former allows the determination of an initial design choice relatively rapidly while the second provides a basis for the use of first order optimization algorithms. The total system also provides a learning environment in which the system gradually becomes better at designing devices of a particular class.

Introduction

The complete design of an electromagnetic device, as with any other structure, requires an iterative loop of synthesis and analysis. This is often described as a hierarchical process, an iterative process, a waterfall model, or in many other ways; but the essence is that design starts with a requirement for a device to fulfil a purpose subject to a set of constraints and this forms the initial specification. The final device is fully described in terms of a multitude of parameters - often numbering several thousand - and the design 'process' is essentially one of exploring the design space described by these parameters subject to a set of implicit and explicit constraints. In order to make this problem tractable, engineers use a process of information hiding and sub-problem analysis to reduce the dimensionality of the search space such that an exploration of the total design space can be guided in some way. One traditional method for doing this is to examine existing devices, find one that is near to the desired specifications and modify it. The modified device is then tested and remodified. Thus design becomes an evolutionary process. However, building and testing devices is an expensive business and analytical and numerical techniques of ever more increasing complexity provide a method for predicting how the changes might affect the performance without having to build the device. Two- and three-dimensional numerical analysis techniques represent the current state of the art in this area and can almost provide a simulated laboratory for testing designs without actually building them.

Recently, considerable interest has been focussed on optimization processes which automatically modify designs to meet specified performance requirements or goals [1], [2], [3], [4]. These

optimization techniques break into two classes - deterministic methods and stochastic approaches. In the former category are techniques which require knowledge of the derivatives of the cost functions with respect to the design parameters, in the second are approaches such as simulated annealing and genetic algorithms in which the derivatives of the cost functions are determined by exploring the search space by solving sets of examples.

The computer aided analysis tools which currently exist for general purpose two and three dimensional analysis are almost all based on numerical processes and allow the solution of one particular design. Much as in the real laboratory, derivatives of performance variables with respect to the design parameters are not often available and this has led to the recent growth in interest in stochastic systems. However, if sensitivity information can be generated in a form which will allow first order deterministic optimization methods to be applied, it is possible to set up the synthesis, or inverse, problem and to solve it directly [5]. With numerically based systems, this process can be extremely slow, requiring many simulated tests of the device.

An alternate approach is to use existing experience to propose an initial configuration for the device. This allows the final optimization process to concentrate on a small part of the search space with the corresponding gain in speed. Such a combined approach is described below. The knowledge based approach being considered is that of Case Based Reasoning [6] which matches the given specifications onto a database of existing designs. Such an approach provides two pieces of information: the first is a topology for the device which will meet the requirements and the second is an initial set of geometric values providing a starting point for the design search. A new design is then generated based on a combination of the nearest matches found. This device can be modified in shape by using sensitivity information to allow first order optimization processes to be applied.

Identifying an Initial Population of Devices

All electromagnetic devices operate subject to Maxwell's Equations, at least at the macroscopic level, and thus at the highest level they are all similar. In an object oriented sense, a base class of electromagnetic devices can be described which have certain properties, i.e. they are all built out of physical materials, they are all subject to the basic electromagnetic field laws, etc. A hierarchy of classes can now be constructed from this base class, some of these classes involve the coupling of electric and magnetic circuits to transform energy, leading to the classes of transformers and electro-mechanical devices. The latter sub-class includes certain extra topological requirements such that motion can take place. Indeed, this concept of inheritance and derived classes has been implicit in the traditional methods of teaching electromechanical energy conversion.

Any device that is constructed inherits all the properties from all its parent classes (devices) in this class hierarchy. Each physical instantiation of a class can be regarded as a *case* and, in true object oriented fashion, it carries with it all the 'knowledge' of how to function in its environment. Thus a set of switched reluctance motors is made up of several instantiations of a derived class of switched reluctance devices. True to the object oriented paradigm, there is considerable information hiding happening in the final devices - in other words, many of the rules and laws describing the device operation are implicit and can only be determined from a set of tests on the device. In fact, the separation of the rules of the device operation into a single unique set cannot necessarily be done on a single device. Instead, a whole range of devices, i.e. cases, will be needed.

Thus, the knowledge involved in designing a particular kind of device can be described by showing several examples of the device. This is the basis of Case Based Reasoning. The approach

avoids the need to store all the design rules for a device; instead, it uses examples or instantiations as a method of implicitly storing knowledge.

The advantage of this approach is, as with all object oriented systems, a reduction in the dimensionality of the space needed to store the information. The reduction in dimensionality is traded off for storing many examples. Thus, as the number of examples grows, the implicit dimensionality grows in that it should be possible to determine all the parameters and rules governing the device explicitly. However, this would require the choice of exactly the correct set of examples and, since the correct answer is not known, the choice of the correct set is extremely difficult to make. In an industrial environment, the examples are limited to those which have already been produced. An approach of reducing dimensionality in this fashion obviously simplifies the data storage structures but also will lead to storage of redundant information. This latter effect is usually accepted as a reasonable price to pay.

Even with this reduction in dimensionality, the number of parameters to be stored to fully describe a complete device can be extremely high, often running into the thousands. An initial design specification cannot be that detailed - if it was, the design would be complete and there would be no work to do! The problem, then, is still one of accessing the information built into the case database starting with only the initial design specifications. In addition, the initial specifications may consist of any one of many subsets of the total parameter set or may be expressed in terms of combinations of the basic parameters, i.e. higher level functions. For a case based reasoning system to function effectively, it must be able to reason from the specifications provided and choose a set of cases from its database which most closely, in some sense, match the specifications.

These cases, in effect, provide the basis for completing the design - they all contain all the parameters needed to create a final device. The choice of a case immediately provides values for all the unknown parameters, in effect a table lookup system is implemented.

Once an initial population of devices has been found, the next step is to modify these devices to better fit the required specifications. This may be done in several ways, including a genetic or evolutionary approach. However, the method used here tries to avoid such stochastic systems. Rather, an initial structure for the desired device might be obtained by some form of interpolation within the initial population or just the nearest match might be chosen. The next sections describe one approach to finding this initial set.

Feature Extraction

When a device is stored, it exists in a multi-dimensional space but not all these dimensions, or parameters, are useful for retrieving it. In fact, to retrieve it based on a small set of specifications requires that some amount of compaction in the description of the device is necessary. The problem is to match the provided specifications on to the set of stored parameters. This can be achieved in two steps. The first step is that of *feature extraction* - a process routinely used in pattern recognition [7]. A feature is a parameter of a device which best describes the class of the device, i.e. those parameters which most affect the performance of the device. An exhaustive search of all the parameters over a set of devices within a specific class is too expensive so the methods employed are usually based on a heuristic approach.

A major requirement in extracting the key parameters is that they should be linearly independent and orthogonal. This means that one feature at a time can be considered without affecting the others. The question to be answered by any criterion which is established is: 'Which features identify this class

as distinct from any other class?' This leads to the concept of a *separability criterion* which has been more fully described elsewhere [8]. Such a criterion allows a quantitative measure of separability between two classes to be established for each feature of a set of devices and, in turn, provides a method of ranking the importance of each feature within a specific class.

The Algebraic Model

The extraction of important features of a class is not, by itself, sufficient to provide a way of matching specifications onto the database of cases because the choice of the feature set is not unique. However, each choice can be converted into any other choice by suitable transformations. Such transformations can be described by an algebraic model of the device. Many such models have been developed by designers over time and are generally used to determine the implications of certain design choices. A set of algebraic equations basically provides a mechanism for propagating information and deriving (inferring) more information. The equations can be described in terms of a network which provides the mechanism for moving from one parameter set to another. This is the second step in matching stored cases to the provided specifications.

The set of specifications can be used to identify the class of device which is to be used to satisfy the design requirements, the identification of the class activates one particular algebraic model and this allows the parameters in the specifications to be converted into the parameters used to store the current cases. The process for doing this has been implemented as an Algebraic Constraint System [9].

Similarity

At this point in the process, a set of parameters has been generated which can be matched to the stored cases and the final requirement is to determine the 'closeness' or degree of similarity between the required device and the existing designs. This similarity measure is, again, a heuristically based function. The total similarity of the input specification to the retrieved case is measured by the strength of the similarity of each parameter. If there is a direct match between two parameters then the similarity has a value of 1.0. The function used is:

$$\textit{Similarity} = \frac{1}{1+\alpha \times |\log p1 - \log p2|} \qquad (1)$$

where

p1 = stored case parameter value
p2 = input case parameter value
α = *an adjustable constants whose value depends on the application.*

After each parameter is processed the overall similarity value is calculated by the *Nth* root of the individual similarity shown in equation (2).

$$TotalSimilarity = \left(\prod_{1}^{n} S_i \right)^{\frac{1}{n}} \qquad (2)$$

S_i = *the similarity of the ith matched parameter,* n = *the number of matched parameters*

If the total similarity value is below a predetermined threshold the match is abandoned. Those cases with a total similarity value above the threshold will be sorted and retrieved.

At this point, several designs have been retrieved all of which are close to the desired device but none is a perfect match. A final possible device to match the specifications is derived by means of interpolation between the retrieved designs or, more simply, the closest match may be used as a starting point for an optimization process.

Optimizing the Design

While the above process will have generated a possible design, there is no guarantee that it will perform correctly. In fact, if the closest existing design is used it is already known that it is not a perfect match. However, the required design will, in all probability be somewhere close by in the search space. If the design is sufficiently close, the chance of finding a globally optimum solution, rather than a local one will be somewhat increased. To complete the design, it is necessary to investigate the effects of parameter variations on the device performance in somewhat more detail and this work is computationally intensive and thus time consuming. Usually, the variations take the form of shape modifications although material changes might be considered as well.

Two questions to be answered at this point in the design are: 'What is the device which matches the specifications within the required error bounds?' and 'How sensitive is the performance of the device to small variations in shape and/or material properties?' Both these questions can be answered if sensitivity information is available. The first question can be addressed by using the sensitivity information to drive the optimization process in those directions which will be the most profitable and the second question can be answered directly by the various sensitivities at the optimum design.

Such sensitivity information may be derived directly from the underlying field equations and this process is outlined in the following sections.

Design Sensitivity Analysis

This section describes how first order optimization algorithms can be applied to optimizing the device performance using Design Sensitivity Analysis. Sensitivity is the derivative information required by first order optimization methods [10]. The process requires that the design specifications be formulated as a mathematical objective function such that a minimum of the objective function corresponds to a valid design. The objective function will include both the costs associated with the design, such as power dissipation or amount of material, as well as constraints in the design

requirements, for example the required force of an actuator.

Since the objective function encodes the performance of the magnetic device, it will be a function of one or both of the electric and magnetic fields. But what is required is the derivative of the objective function with respect to the design variables. The fields depend implicitly on the design variables through Maxwell's equations. Design Sensitivity Analysis effectively provides the means to compute the derivative of this implicit dependence.

Adjoint System

The sensitivity analysis starts with an adjoint system which has the same material configuration as the original system (system **A**), but the sources (i.e. source current density) of the adjoint system (system **B**) are chosen as follows:

$$\begin{aligned} \hat{J}_{SB} &= \nabla_{\hat{E}_A} F(\hat{E}_A, \hat{H}_A) \\ \hat{L}_{SB} &= -\nabla_{\hat{H}_A} F(\hat{E}_A, \hat{H}_A) \end{aligned} \tag{3}$$

where $\hat{L}_{SB}$ is the magnetic source current density, and the gradients are the partial derivatives of the objective function with respect to the field components at a point (see [11] for details).

Shape Sensitivity

Once the fields for the adjoint system are computed (by solving Maxwell's equations), the sensitivity of the objective function F to variations in shape can be readily computed using the following equation:

$$\begin{aligned} \delta F = \{ & \hat{E}_{Aa} \cdot \hat{E}_{Bb} [(\sigma_a - \sigma_b) + j\omega(\epsilon_a - \epsilon_b)] \\ & - j\omega \hat{H}_{Aa} \cdot \hat{H}_{Bb} (\mu_a - \mu_b) + \hat{E}_{Ba} \cdot (\hat{J}_{SAa} - \hat{J}_{SBb}) \} \delta s \end{aligned} \tag{4}$$

where δF is the perturbation in the objective function due to a displacement δs of the surface in the direction of the surface normal. In this equation, σ_a, ϵ_a and μ_a are the conductivity, permittivity and permeability of the region inside the surface, while the same quantities with a b subscript denote the material properties of the region outside the surface. Also $\hat{J}_{SAa}$ is the source current density in the region inside the surface, and $\hat{J}_{SAb}$ is the source current density outside the surface. Note that continuity requires that the normal component of the source current density must be equal on both sides of the surface. Likewise, since the fields may be discontinuous across the interface, the same subscripts are used to distinguish fields on the inside of the surface (a) from fields on the outside of the surface (b). Thus, for example, $\hat{H}_{Bb}$ is the magnetic field of the adjoint system just outside the surface. The total perturbation in the objective function is found by integrating (4) over the surface of interest. The derivative of the objective function with respect a design parameter which controls the position of the surface is computed using the chain rule after computing the derivative of δs at

every point on the surface.

Design parameters may also control other device properties besides shape, for example material properties and current distributions. The sensitivity to these design variables may also be computed using the fields of the same adjoint system, [11] contains the details for this case.

Interface with Case Based Reasoning

It should be obvious, from the above summary of sensitivity calculations, that setting up the optimization process is not a simple task. Even for relatively basic objective functions, the implementation details of adjoint system sources and surface-parameter relationships can become quite involved, and extensive testing is required to ensure that what is calculated is, in fact, the desired derivative. However, this is where the advantages appear of merging optimization with the case based reasoning system, because the implementation details specific to each device can be worked out before hand and stored with the device in the case based reasoning database. Therefore, the case based reasoning system provides basically everything required for optimization: the parameterized device template, the initial parameter values, the expressions for the adjoint system sources, the partial derivatives of the surface position with respect to the design parameters. The result is that the optimization process becomes entirely automatic.

A Learning System

The sensitivity information and optimization process described above can, in fact, be used in a stand alone mode to create a device directly from the specifications [5]. This is a time consuming process and is likely only to be used when no previous design experience is available. However, once a new device has been designed, either directly from the specifications or by the modification of a previous case(s), it can be added to the case database. This expands the range of experience and knowledge stored in the database and, with time, increases the capability and speed of the system. In effect, the system learns with each new design completed.

Conclusions

This paper has described a complete device synthesis and optimization process which combines the speed of a case based reasoning system to provide good starting point for the optimization process. The combination of case based reasoning with sensitivity analysis provides a mechanism by which designs can be created in the shortest possible time. The system can operate either in a stand alone mode or, more frequently, with a designer to guide the choice of a final design.

Acknowledgments

The authors would like to acknowledge the support of the Natural Science and Engineering Research Council of Canada during this work.

References

[1] S.Russenchuck, "Deterministic Optimization Strategies for the Design of Electromagnetic Devices," *Proceedings of the 6th International IGTE Symposium on Numerical Field Calculation in Electrical Engineering*, September 26-28, Graz, Austria, pp. 233-244.

[2] G.F.Uler, O.A.Mohammed, C.S.Koh, "Design Optimization of Electromagnetic Devices Using Genetic Algorithms," Accepted for publication in *IEEE Transactions on Magnetics*, Vol. 30, November 1994.

[3] J.Simkin, C.W.Trowbridge, "Optimizing Electromagnetic Devices Combining Direct Search Methods with Simulated Annealing," *IEEE Transactions on Magnetics*, Vol. 28, No. 2, 1992, pp. 1545-1548.

[4] A.Gottvald, K.Preis, C.Magele, O.Biro, A.Savini, "Global Optimization Methods for Computational Electromagnetics," *IEEE Transactions on Magnetics*, Vol. 28, No. 2, 1992, pp. 1537-1540.

[5] D.N.Dyck and D.A.Lowther, "The Optimization of Electromagnetic Devices Using Sensitivity Information," *Proceedings of the 6th International IGTE Symposium on Numerical Field Calculation in Electrical Engineering*, September 26-28, Graz, Austria, pp. 251-256.

[6] J.Kolodner, P.Simpson, E.Sycara, "A Process Model of Case-Based Reasoning," *Proceedings of the 9th International Joint Conference on Artificial Intelligence*, Los Angeles, CA, pp. 284-290.

[7] P.A.Devijver, J.Kittler, Pattern Recognition: A Statistical Approach, Prentice-Hall, 1982.

[8] R.Rong and D.A.Lowther, "The Application of Case-Based Reasoning to the Initial Design of Electromagnetic Devices," *Proceedings of the International Symposium on Advanced Computational and Design Techniques in Applied Electromagnetic Systems*, June 22-24, 1994, Seoul, South Korea, to be published in Elsevier Studies in Applies Electromagnetics in Materials.

[9] C.M.Saldanha, "An Algebraic Constraint System for CAD in Magnetics," M.Eng. Thesis, McGill University, 1988.

[10] I.Park, B.T.Lee, S.Y.Hahn, "Sensitivity Analysis based on Analytic Approach for Shape Optimization of Electromagnetic Devices: Interface Problem of Iron and Air," *IEEE Transactions on Magnetics*, Vol. 27, No. 5, 1991.

[11] D.N.Dyck, D.A.Lowther, E.M.Freeman, "A Method of Computing the Sensitivity of Electromagnetic Quantities to Changes in Materials and Sources," *IEEE Transactions on Magnetics*, Vol. 30, No. 5, 1994, pp. 3415-3418.

A COMPUTER PROGRAM FOR THE DESIGN OF SUPERCONDUCTING ACCELERATOR MAGNETS

S. Russenschuck,
CERN, 1211 Geneva 23, Switzerland

CERN is preparing for the construction of the Large Hadron Collider (LHC), to be installed in the existing LEP tunnel. The LHC requires superconducting magnets which are characterized by the dominance of the coil geometry for the field distribution. The program package ROXIE has been developed for the design and optimization of the coil geometries in two and three dimensions. The paper describes the features of the program, the mathematical optimization techniques applied and gives examples of the recent design work carried out.

INTRODUCTION

The Large Hadron Collider (LHC) project is a superconducting accelerator for protons, heavy ions and electron- proton collisions in the multi-TeV energy range to be installed at CERN in the existing LEP tunnel with a circumference of about 27 km. The new facility will mainly consist of a ring of high field superconducting magnets cooled to 1.9 K with superfluid helium [21]. The main dipole magnets will operate at about 8.4 T and the quadrupoles at 220 T/m field gradient. The superconducting magnets are characterized by the dominance of the coil geometry for the field distribution. Therefore, the design computations start by optimizing the coil geometry in two and three dimensions, using analytical integration for computing the magnetic field. Contradictory parameters such as maximum dipole field, minimum content of unwanted multipoles and sufficient safety margin for the conductor must be optimized. The keystoning of the conductors and the grading of the current densities between the two layers complicate the task of finding the best solution. The report describes the ROXIE Fortran program (**R**outine for the **O**ptimization of coil **X**-sections, **I**nverse field computation and coil **E**nd design) which has been developed for the coil optimization and which is available for general use on CERNs Risk6000 workstation cluster PaRC.

It is in the coil end regions of superconducting magnets where most of the quenches occur. Therefore special attention is paid to the design of the coil ends with the objectives of a low peak field and a low integrated multipole content. A 3D option in ROXIE allows the geometric position of the cables and the field in the end region to be calculated with a high accuracy. A further area of application for ROXIE is the need to trace back the origins of measured field imperfections. The mechanical dimensions of the active parts of the coils are impossible to verify under their operational conditions, after their deformation due to manufacture, warm pre-stressing, cool-down and excitation. The inverse problem solving consists of using optimization routines to find distorted coil geometries which produce exactly the multipole content measured. For the solving of the optimization problems and the inverse field calculation a number of mathematical programming techniques have been implemented. They will be described in this paper.

FEATURES OF THE ROXIE PROGRAM

The development of the program was driven by three main objectives: To write an easy-to-use program for the design of superconducting coils considering field quality, quench margin and persistent current multipoles, to include the program into a mathematical optimization environment and to develop an integrated design tool with sophisticated graphic routines, interfaces to CAD systems, numerical field calculation codes and a 5 axis milling machine.

The program includes routines to define geometrically coil cross sections and coil ends of dipoles, quadrupoles, sextupoles, octupoles and decapoles made of Rutherford type superconducting cables. The geometric position of coil block arrangements in the cross section of the magnets is calculated from given input data such as the number of conductors per block, conductor type (to be specified in a separate input file), radius of the winding mandrel and the positioning and inclination angle of the blocks, fig. 1. The

fact that the keystoning of the cables is not sufficient to allow their edges to be positioned on the curvature of a circle, is fully respected. This effect increases with the inclination of the coil blocks versus the radial direction. Rectangular shaped coil blocks are also possible if the cable is not keystoned. Cold conditions can be simulated by means of a contraction coefficient. Furthermore the coil can be subjected to elliptic deformation. The input parameters for the coil end generation are the z position of the first conductor of each coil block, its inclination angle, the straight section and the size of the wedges between the conductors, fig. 5. Four options are available: Coil end design with shims between the turns and conductors placed on the winding mandrel, fig. 5, coil end with grouped conductors aligned at the outer radius of the endspacers, fig. 6, coil end for magnets with rectangular cross sections, fig. 13, and racetrack coil ends. It is assumed that the upper edges of the conductors follow ellipses or circles in the developed sz plane defined by their radial position in the straight subsection and the z position in the yz plane, fig. 7. The curvature of the lower edge of the conductor is then calculated assuming constant perimeter. The geometric positions of bare conductors can be printed in different formats suitable for other numerical field calculation packages such as ANSYS and POISSON. In addition the form of the end spacers is constructed and an option allows to print polylines which give the input to a 5 axis milling machine.

The field calculation part allows the calculation of magnetic field, Lorentz - forces, field quality (multipole content) and quench margin. Each conductor is approximated by line currents carrying the same current located at the strand position inside the conductor. The grading of the current due to keystoning of the cable is therefore considered. By applying Biot-Savart's law for each line current, the field is calculated at a given radius in the aperture and the peak field in the coil itself is evaluated. Thus it is possible to calculate the multipole content and the peak field in the coils with a higher accuracy than with finite-element calculations (this is useful, as the multipoles to be minimized create fields of the order of $10^{-7}T$ at the nominal radius). The influence of the iron yoke can be taken into account by imaging the line currents thus assuming that the yoke iron has an infinite permeability. It is foreseen to apply the volume integral method for the consideration of the iron magnetization. For the peak field calculation the influence of the self field of each strand is neglected. As the critical current density has been measured for a strand without compensation for the self field the correct load line characteristic curves are obtained when the self field is neglected in the calculations. An option allows, however, to take the self field into consideration. The self inductance of the coil is investigated by calculating the vector-potential in the coil and the flux linkage is then evaluated by means of Stokes theorem, neglecting the inner inductance of the strands. From the given self inductance the stored energy is calculated. There is an option for the automatic calculation of the mutual inductances between inner and outer layer blocks in both the upper and lower coil. During ramp of the superconducting LHC magnets from 0.58 to 8.4 T nominal dipole field additional currents (persistent currents) are induced in the filaments. These currents which consist of surface currents and currents in the bulk of the superconductor persist for long periods as they decay only through flux creep. The influence of these currents on the field quality can be evaluated. For the 3D field calculation each conductor is sliced up into "bricks" containing line currents the same way as in the 2 dimensional case. The minimum radius of curvature in the bricks is then approximated by means of central differential quotients. The variation of the field on the position of a line current (roller coaster track) can be plotted versus the number of the brick. In addition the integrated multipole content and the field along a line defined by their 3 start and 3 end coordinates can be calculated and plotted. Another feature is the calculation of the cross talk from one coil end to the other, i.e. the integrated multipole content in the end of aperture 2 is investigated which is excited by the current in aperture 1. For the integrated multipole content the iron yoke can be considered by means of image currents whereas for 3D peak field calculations the influence of the iron yoke has to be neglected as in this case the imaging method gives incorrect results. Asymmetric coil ends can also be evaluated; this is necessary for the connection end of the magnets and for the calculation of effects coming from asymmetric coil block displacements in the ends. A particular effect which can be studied is a different length of the upper and lower pole of the dipole magnets.

From the beginning, the program has been structured to allow the application of mathematical optimization techniques. It has been put into an environment of mathematical optimization, with numerous methods available for decision making, treatment of nonlinear constraints and optimization algorithms. All input data can be addressed as design variables of the optimization problem or as an objective (e.g. when

a certain geometrical dimension has to be minimized). All the evaluated field quantities can be addressed as objectives for the optimization. Decision making methods such as objective weighting, distance function, constraint formulation or the automatic set up of payoff tables are implemented. Nonlinear constraints can be treated either by a feasible domain method, the penalty transformation, the augmented Lagrangian function or the boundary search along active constraints. Optimization algorithms such as EXTREM, Rosenbrock, Levenberg-Marquard, Davidon-Fletcher-Powell and genetic algorithms are implemented. In addition there is a sensitivity analysis with Lagrange multiplier estimation available in order to find the hidden resources of a particular design.

Sophisticated graphic routines have been developed for display of geometry, field, forces etc. both in 2D and 3D. The options for 3D contain hidden surface removal, and depth sort algorithm subroutines. The program uses only a few primitives from the GKS library and can therefore easily be modified for other platforms. ROXIE can plot the geometry of the coil in 2 and 3D, the copper wedges between coil blocks and the end spacers for the coil end region. Displacement vectors for coil positions in the distorted case can be plotted, fig. 4, as well as short circuit currents detected by inverse field calculation from time dependant multipoles. Optional is a heading with comments, time and date. The following field quantities can be displayed in the coil cross section: Magnetic field and Lorentz force components in cartesian or local conductor coordinate systems, Vector potential A, current on strand position, current density in the element, in the superconductor and in the copper, and magnetization vector due to persistent currents. In 3D the graphic routines include: Field along a "roller coaster" track in the conductor, 3D magnetic field in the aperture represented by cones, fig. 11, minimum and maximum local field in the coils, Lorentz forces normal to the cable surfaces, fig. 14, Lorentz forces (cartesian vectors) acting on each cable, and minimum radius of curvature of the conductor.

Fields of application are the calculation and optimization of symmetrical magnet structures with superconducting coils made of Rutherford type conductors, calculation of effects coming from asymmetries (geometric errors in the coils due to manufacturing process) both in 2D and 3D and inverse field problem solving for tracing back these effects from field measurements. Further applications are combined function magnets of various kinds, asymmetries in the ramp and splice region, cross-talk between the apertures in the two-in-one type magnets, design and optimization of the coil end region. The features shall be described in more detail with an example from each of the main fields of application.

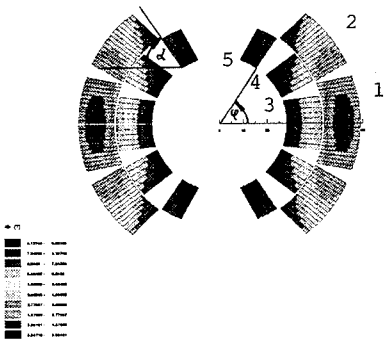


Fig. 1: Optimized dipole coil with 5 block structure (MBPN and MBSMSO models). Display of the magnetic field modulus.

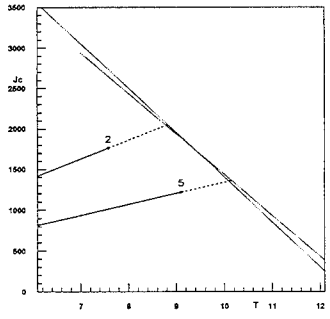


Fig. 2: Load line characteristic curves for the 5 block dipole coil, as displayed in fig.1. Block 2 outer layer, block 5 inner layer.

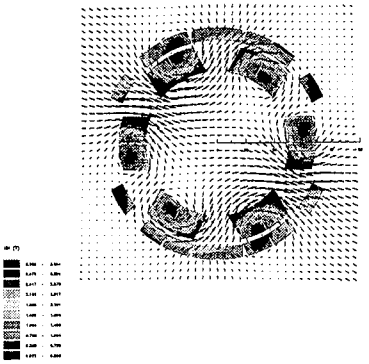


Fig. 3: Cross section of combined dipole-sextupole corrector, with field vector display and $|B|$ in coils

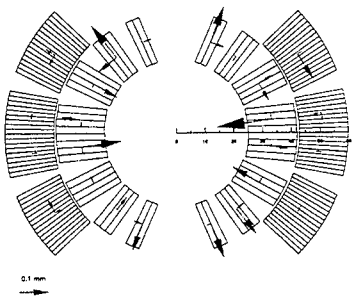


Fig. 4: Displacement vectors for inverse field problem solving for the main dipole model magnet MTA.

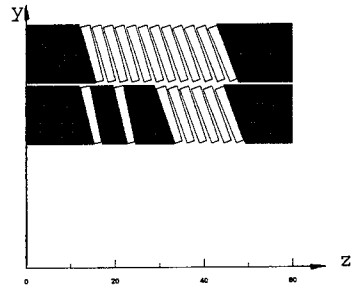


Fig. 5: Cut of main quadrupole end with conductors placed on the winding mandrel.

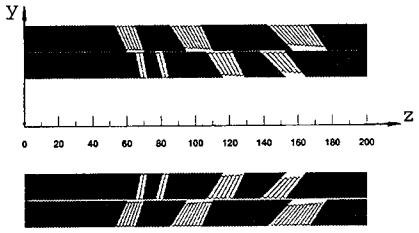


Fig. 6: Cut of model dipole end MBSMSO with grouped conductors aligned on the outer radius.

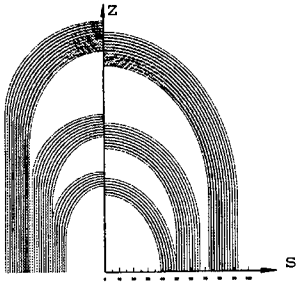


Fig. 7: Developed view on conductors in the dipole end with grouped conductors, outer layer, right: upper edge, left: lower edge.

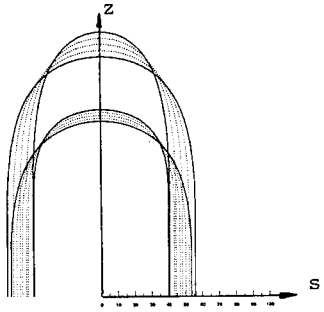


Fig. 8: Polygons for endspacer machining with 5 axis milling machine for dipole model magnet.

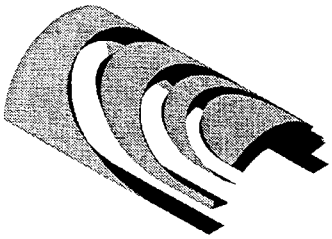


Fig. 9: 3D representation of endspacers for dipole model with grouped conductors (MBSMSO model), outer layer

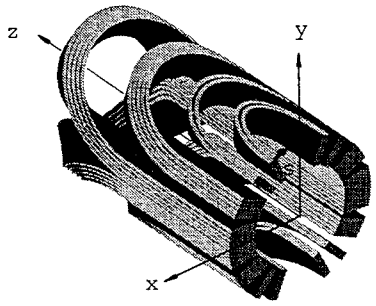


Fig. 10: 3D representation of coil end of the MBFISC dipole model magnet with coordinate system, inner layer only

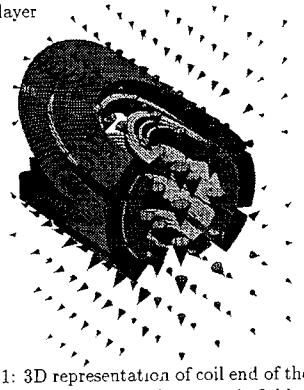


Fig. 11: 3D representation of coil end of the MBTRA dipole model magnet with magnetic field cones.

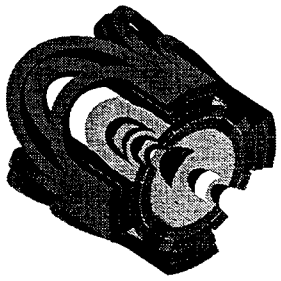


Fig. 12: 3D representation of coil end of the insertion quadrupole

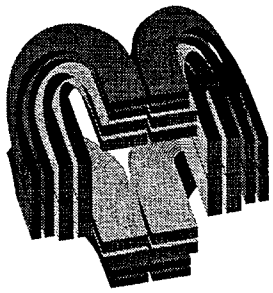


Fig. 13: 3D representation of coil end for a insertion quadrupole design with rectangular coil cross section.

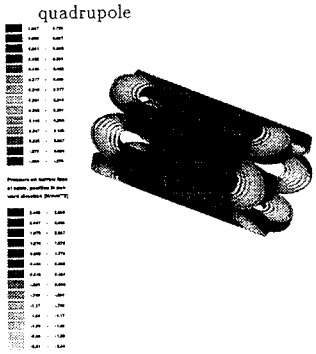


Fig. 14: 3D view of sextupole corrector coil, with pressures due to Lorentz-forces on cables.

MATHEMATICAL OPTIMIZATION TECHNIQUES

Mathematical optimization including numerical techniques such as linear and nonlinear programming, integer programming, network flow theory, and dynamic optimization has its origin in operations research developed in response to military needs of world war II. An optimality criterion for optimization problems with conflicting objectives has been introduced by Pareto in 1896 [20]. The solution process for vector-optimization problems is threefold, based on decision making methods, methods to treat nonlinear constraints and optimization algorithms to minimize the objective function (we shall call this an optimization procedure). Methods for decision making have been introduced and applied on a wide range of problems in economics by e.g. Marglin 1966 [16] and Fandel 1972 [3]. The theory of nonlinear programming with constraints is based on the optimality criterion by Kuhn and Tucker, 1951 [14] which provided the basis for later developments in mathematical programming. Numerous optimization algorithms both using deterministic and stochastic elements have been developed in the sixties. Researchers tend to come back to genetic and evolutionary algorithms recently as they are suited for parallel processing, Fogel 1994 [6], Holland 1992 [10]. While desktop computing power to date is available which was ten years ago only accessible in large computer centers, the combination of mathematical optimization techniques and field calculation has become a modern tool for electrical engineering.

Characteristic for real-world optimization problems are multiple conflicting objectives which should be considered simultaneously Usually the individual solutions for each single objective function differ and a solution that maximizes one objective will not, in general, maximize any of the other objectives. Any improvement of one objective can be achieved only at the expense of another. For the definition of the optimal solution of these so called vector-optimization problems we apply the optimality criterion by Pareto 1896 originally introduced for problems in economics. A **Pareto-optimal** solution (for vector maximum problems also called noninferior solution) is given, if there exists no other solution that will yield an improvement in one objective without degradation in at least one other objective. It is clear that this yields a set of solutions rather than one unique solution. The decision maker (who is not always the design engineer undertaking the optimization) usually picks a solution out of a solution set intuitively. Applying mathematical optimization routines, however, requires a formalized decision making method. Below some methods of decision making are briefly described. It can be proved that they possess a substitute problem to the vector optimization problem with a Pareto-optimal solution (assuming convexity of the objective functions). A comprehensive overview on decision making can be found in Cohon, 1978 [2].

The **objective weighting function** is the sum of the weighted objectives $f_k(\vec{X})$ and results in the minimization problem: $min\{u(\vec{F}(\vec{X})) = \sum_{k=1}^{K} t_k \cdot f_k(\vec{X})\}$ with the weighting factors t_k representing the users preference. The design variables are comprised in the vector $\vec{X}$. The problem is to find the appropriate weighting factors in particular when the objectives have different numerical values and sensitivity. Using objective weighting results therefore in an iterative solution process where a number of optimizations have to be performed with updated weighting factors, a cumbersome process if the decision maker is not the analyst undertaking the calculations. The problem of choosing the weighting factors appropriately also occurs when the **distance function method** is applied. Most common is a least squares objective function. With f_k^* being the requirements for the optimum design, the minimization problem reads: $min \parallel \vec{z}(\vec{X}) \parallel_2^2 = min \sum_{k=1}^{K} t_k (f_k^*(\vec{X}) - f_k(\vec{X}))^2$. The disadvantage of least squares objective functions with the euclidean norm $\| \cdot \|_2$ is the low sensitivity for residuals smaller than one. Therefore sufficiently high weighting factors t_k have to be introduced. If the absolute value norm is applied the disadvantage is the nondifferentiable objective function in the optimum which makes the application of Newton-methods impossible. The problem with the weighting factors can be overcome by defining the problem in the **constraint formulation**. Only one of the objectives is minimized and the others are considered by constraints. The constraints represent the minimum request values specified by the user for the particular objective. The problem is that for badly chosen constraints there exists no feasible solution at all, whereas non active constraints represents a zero weight for the particular objective. However, starting with a design where some engineering expertise was already put into, the analyst should be able to define appropriate constraints. The constraint formulation has the advantage that a **sensitivity analysis** by means of a Lagrange multiplier estimation can be performed using the necessary optimality conditions for constraint optimization problems

introduced by Kuhn and Tucker. The interesting characteristic of the Lagrange multipliers of the corresponding Lagrange function to the constraint problem is that they are a measure of the price which has to be paid when the constraint is decreased. The decision maker can then explore the hidden resources of a design. A tool which provides the decision maker with a lot of information about the hidden resources of a design is the **payoff table**. To create this table K individual constraint optimization problems are solved to find the best solution for each of the K objectives. Best compromise solutions can then be found by minimizing the "distance" from the in general nonfeasible "perfect solution" applying different norms e.g. L_1, L_2 and L_∞ .

Decision making is the most important part and influences the convergence behavior of the whole optimization procedure. For the minimization of constrained and unconstrained objective functions numerous methods have been proposed in the last 30 years. It is most important to find the right minimization method to fit with the method of decision making.

As the design variables of the optimization problem can usually only be varied between upper and lower bounds, a modified objective function is applied $p(\vec{X}) = f(\vec{X})$ if no bound is violated and $p(\vec{X}) = f(\vec{X}^*) + r(\vec{X})$ if a bound is violated. $\vec{X}^* = (x_1, x_2, ..., x_l^*, ...x_n)$ and $r(\vec{X}) = (x_l - x_{lu})^2$ $x_l^* = x_{lu}$ if $x_l > x_{lu}$, $r(\vec{X}) = (x_{ll} - x_l)^2$ $x_l^* = x_{ll}$ if $x_l < x_{ll}$. r_l is a sufficiently high penalty parameter. The advantage of this procedure is that the violation of the bounds are checked before a function evaluation is carried out and that the existing algorithms for unconstrained minimization can be applied without modifications. The objective weighting function as well as the distance function method allows the immediate application of an algorithm for finding the minimum value of an unconstrained objective function as there are no nonlinear constraints to be considered. With the constraint formulation the problem of the treatment of the nonlinear constraints arises. One method is the transformation of the constrained problem into a unconstrained problem by means of a **penalty function** method. The main idea is to add a penalty term to the objective function which depends on the degree to which the constraints are violated and vanishes if the constraints are satisfied. The constraint optimization problem $min\, f(\vec{X})$ subject to equality constraints $h_j(\vec{X}) = 0$ and inequality constraints $g_i(\vec{X}) \leq 0$ transformed into the penalty function to be minimized reads:

$$p(\vec{X}) = f(\vec{X}) + \sum_i p_i \cdot max^2(0., g_i(\vec{X}) - c_i) + \sum_j p_j (h_j(\vec{X}) - d_j)^2 \qquad (1)$$

In order to achieve feasibility of the result the penalty factors p_i, p_j have to be chosen relatively large. Large penalty factors, however, lead to ill-conditioned function topologies, and the optimization algorithms need many function evaluations to find the minimum. It was therefore proposed to solve a sequence of unconstrained minimization problems with increasing penalty factors, **SUMT** or to add the penalty terms to the corresponding Lagrange function, **method of augmented Lagrangian**. Replacing the squares in (1) by the absolute value leads to the **exact penalty transformation** where the penalty factors can be reduced. The problem here is the nondifferentiability of the objective function for active constaints. If the number of design variables does not exceed 5, the method of **boundary search along active constraints** can efficiently be used. The ROXIE user has the choice between the above mentioned methods. It needs some experience to select an efficient procedure consisting of decision making, treatment of nonlinear constraints and a suitable optimization algorithm.

The following optimization algorithms are available: Optimization algorithm **EXTREM by Jacob** [11] which consists of one-dimensional minimizations by means of Powell extrapolations [22] in a main search direction (user supplied) and a orthogonal direction evaluated by Gram-Schmidt orthogonalization. After these one-dimensional searches have been carried out (end of the i-th step) the main search direction is updated by a vector pointing from the initial outline to the minimum of the i-th step. The user has to supply an initial step-size which is taken to $(x_{lu} - x_{ll})/10.$. This user-friendly algorithm is suitable for practically all applications. The **parametric study** evaluates the objective functions for all the combinations of different design variables where for each design variable 10 different values are taken. As the total number of function evaluations is therefore 10^n (for n design variables) the parametric study is only appropriate for up to 3 design variables. The **sensitivity analysis** calculates the sensitivity due to errors in the design variables. A Jacobian Matrix is printed out. It consists therefore of n+1 function evaluations. The **Levenberg-**

Marquard algorithm [13] was originally developed for nonlinear regression problems using least squares objective functions. We can apply it therefore efficiently to the distance function problem. To check the necessary optimality conditions for constraint problems (Kuhn-Tucker equations) a **Lagrange-Multiplier estimation** can be carried out minimizing the corresponding Lagrange- function. The Lagrange function is minimized using the **Davidon-Fletcher-Powell** algorithm where the step-size and direction is given by $\Delta\vec{X} = -H^{-1}\nabla f(\vec{X})$ The Hessian Matrix H does not have to be calculated in each point but is updated iteratively beginning with the unity Matrix I. As the "design variables" are the Langrange - multipliers $\vec{\alpha}, \vec{\beta}$ to be estimated, the derivatives in α_i, β_ican be approximated with a high accuracy. That is the reason for the good convergence behavior of this method when applied to the Lagrange multiplier estimation. It can, however, be applied also to all the other design optimization problems, the convergence behavior is then dependent upon the function topology. In **genetic algorithms**, each trial solution is coded as a vector (chromosome) $\vec{X}$ with elements being described as genes. Holland [10] suggested that the chromosomes are represented by binary strings. It is obvious that this algorithm is specially suited for integer programming. From two sets of chromosomes offspring are produced by use of genetic operators such as crossover and mutation. Crossover means the interchanging of sections of the chromosomes between two parent chromosomes. The position where the chromosomes are split into two sections is chosen randomly. Mutation means that with a certain likelihood single bits in the chromosomes are flipped. As an example, let be the parent chromosomes 000100110|1010111 and 110001010|1100011 , then the offspring is created by crossover (| indicates the crossover point) 000100110|1100011, 110001010|1010111. In order to avoid the dominance of "superindividuals" which leads to an uniform population unable of further evolution, a sufficiently large gene pool has to be chosen from which offspring are created by mating pairs of chromosomes. The likelihood of reproduction for each chromosome is then proportional to the objective function value for the particular design represented by the chromosome. From the offspring the fittest strings are used for the next generation. Only about 60% of the population is used for crossover (crossover probability 0.6). The others simply survive and ensure the genetic diversity of the population. The bit mutation probability is 0.001 which means that only every 1000 th bit is mutated. The problem of genetic algorithms is the dependance of the solution on user supplied and problem dependent input such as crossover probability, size of the gene pool etc. More research has to go into making the algorithm more robust for every day use in optimization of superconducting magnets.

EXAMPLES

Dipole coil optimization (cross section)

Because of the length of the dipole magnets (about 13 m) the design optimization starts with the 2D cross-section of the coils. The design variables for this optimization problem are the positioning angles and the inclination angles of the coil blocks (8 or 10 design variables depending on the number of blocks chosen), c.f. fig. 1.

The field quality of a magnet is usually described by the B_n (called the normal) and the A_n (called the skew components) of the field defined by the expansion of the complex field: $B_y + iB_x = \sum_{n=1}^{\infty}(B_n + iA_n)z^{n-1}$ with $z = x + iy = re^{i\varphi} = r(\cos\varphi + i\sin\varphi)$ and $B_\varphi + iB_r = (B_y + iB_x)e^{i\varphi}$. In ROXIE the r- component of the field is calculated directly by means of the Biot-Savarts law. $B_r(\varphi)$ at a given radius $r = r_0$ is then harmonically analyzed by means of the program TRICOF from the CERN Library which has been set up for double precision for higher accuracy. With A being usually defined as the coefficients of the cos terms and B being the coefficients of the sin terms we get from given equidistant function values in the interval $-\pi \leq \varphi \leq \pi$: $B_r(r_0) = \sum_{n=1}^{\infty}(B_{n(r_0)}\sin n\varphi + A_{n(r_0)}\cos n\varphi) = B_0(r_0)\sum_{n=1}^{\infty}(b_n \sin n\varphi + a_n \cos n\varphi)$. The A and B terms are in agreement with the above definition for the unit radius. The optimization problem possesses a number of different objectives which are partially contradictory:

- A main dipole field of 8.65 T
- A small sextupole field comp. (b_3 = min) and a small decapole field comp. (b_5 = min)
- $b_7 < 0.02 \cdot 10^{-4}$ and $b_9 < 0.005 \cdot 10^{-4}$
- Minimum volume of superconductor
- Maximum margin to quench
- Small multipole content due to persistent currents

By applying the objective weighting function with recursively updated weighting factors and the algorithm EXTREM, a design with only five coil blocks could be found which perfectly meets the requirements concerning field quality as given from beam simulations. All previous design studies considered a six block design. Numerical results are given in Table 2 (MBPN and MBSMSO models), the cross section is displayed in fig. 1. The deterministic optimization procedure converges very well and minimizes the weighting function usually in about 200 function evaluations. However, for each run the number of blocks and the number of conductors per block has to be selected and kept constant. This way, the optimization routine cannot be used to discover a new design principle.

An approach for a "creative" design tool could be the use of genetic algorithms. As they are specially suited for integer programming a optimization problem was set up with predefined conductors (48 in the outer layer, 26 in the inner layer) where by means of genetic algorithms the current was switched on and off, thus resulting in bit strings (genes) of size 74. The size of the gene pool was 65, the crossover probability 0.6 and the bit mutation rate 0.001. As in this case the number of conductors is not fixed, a minimum number of turns was included as an additional objective in the weighting function. Fig. 15 shows some intermediate steps of the minimization after 65, 195 and 4550 function evaluations. The new idea which could be derived is that by piling up some more conductors in the outer layer results in a shielding effect and the pole angle of the inner layer can be increased. A design derived from this idea using the same cable as for the 5 block design (fig. 1) can be seen in fig. 15 on the right. Both designs, although quite different, use the same amount of superconductor, have both the same high field quality and the same margin to quench in the inner layer. Advantageous of the design in fig. 15 is the larger pole angle in the inner layer, which results in easier to wind coil ends. Disadvantages are the higher current density in the cable necessary to produce the same main field (resulting in higher hot spot temperatures at quench) and the reduced margin to quench in the outer layer.

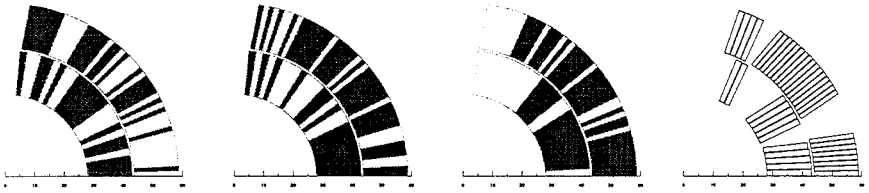


Fig. 15: Intermediate steps of the optimization using genetic algorithms after 65, 195 and solution after 4550 function evaluations (from left to right). A feasible design derived from the solution by means of deterministic methods using the same cable as the 5 block design (fig.1) is displayed on the right.

The main quadrupole as an inverse field problem

With a slightly modified input file ROXIE is able to calculate multipole errors, peak field etc. in asymmetric coil block arrangements. This is the basis of the inverse field calculation option for the tracing back of conductor displacements from given field harmonic measurements. These displacements can well be asymmetric thus requiring individual treatment of each coil block.

The main parameters of the lattice quadrupoles for LHC are a nominal gradient of 252 T/m, a magnetic length of 3.05 m, a nominal current of 15060 A, an inner coil aperture of 50 mm and an operational

temperature of 1.8 K. Before being assembled into their common yoke the two coil-collar assemblies of the second magnet have undergone magnetic measurements at room temperature. Table 1 gives the measured multipole distribution in the straight part of one of these assemblies together with the expected (intrinsic) values.

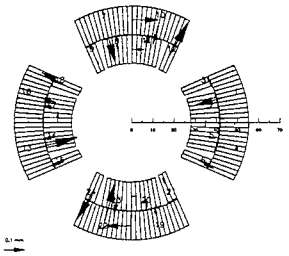


Fig. 16: Displacement vectors for the quadrupole

	Measured		Intrinsic	
n	Normal	Skew	Normal	Skew
1	-	-	-	-
2	-21910.	-	-21910.	-
3	1.972	-5.456	-	-
4	-0.723	-0.920	-	-
5	-0.219	-0.436	-	-
6	-0.066	0.153	-0.79	-
7	-0.004	-0.285	-	-
8	-0.002	0.109	-	-
9	-0.043	-0.022	-	-
10	0.59	-0.044	0.52	-

Table 1: Measured and intrinsic multipole content of the warm quadrupole coils.

The function to be minimized in the inverse field computation problem is a least squares objective function $min\, z(\vec{X}) = min \sum_{i=1}^{10} p_i \cdot ((f_i(\vec{X}))^2 + (g_i(\vec{X}))^2)$ with the residuals $f_i(\vec{X}) = b_i^*(\vec{X}) - b_i$ and $g_i(\vec{X}) = a_i^*(\vec{X}) - a_i$ where $b_i^*(\vec{X}), a_i^*(\vec{X})$ are the calculated and b_i, a_i are the measured multipoles. $\vec{X}$ is the vector of the design variables for the inverse problem. The p_i are weighing factors in order to compensate for the different numerical values of the residuals. The design variables are the possible perturbations of the coil blocks, which determine the content of the multipole components. Because of the non-symmetric nature of the geometrical coil positioning errors a high number of design variables results for the inverse field problem. It had therefore to be assumed that the positioning errors hold for an entire coil block rather than individual conductors. Constraints on the block displacements were introduced: At the poles the collar inserts represent a limitation to any azimuthal motion. The blocks adjacent to the horizontal or vertical planes move together azimuthally; this motion may be different for the two layers. In this way a difference of elastic moduli in the coil layers is accounted for. Each block is allowed to move in the radial direction resulting in a total number of 32 design variables for the inverse field problem. It was solved by means of the Levenberg-Marquard algorithm with about 800 function evaluations. The result is displayed in fig. 16. The displacements show no significant inside movement of inner layer blocks. The adopted collaring procedure, where the coil assembly mandrel is extracted before the final compression of the collars, seems therefore acceptable.

Coil end optimization

The design variables for the optimization are the length of the straight section of each block, the ellipticity of the innermost turn of each block and the inclination angle of each of the blocks in the yz plane, c.f. fig. 6. The positioning angle and inclination angle for defining the cross section (xy plane) (fig. 1) of the magnet was kept constant as found by the 2D cross section optimization. The objectives for the coil end optimization are:

- Minimum integrated multipole content in the coil end
- Low enhancement of the field in the coil
- Minimization of the variation of pressure on the narrow face of the conductor due to Lorentz forces in order to avoid slip between turns
- Maximization of the minimum radius of curvature in each coil block
- Short physical length of the end

A short end length and homogenous Lorentz force distribution in the innermost turn, which can be achieved by placing the inner block of the outer layer closer to the straight section of the magnet, leads to a higher peak field to main field ratio. The problem was solved with objective weighting functions and

successively updated weighting factors and the algorithm EXTREM. Table 2 shows the results of the field calculations for different versions of model dipole magnets. 2D cross section optimizations have been carried out for the models MBFISC, MBTRA and MBPN, but only the MBPN and the MBSMSO coil end (which have the same cross section) has been optimized using the described methods. For the optimization of the integrated multipole content the iron yoke is assumed to end at the onset of the coil end (z=0), in order to reduce the peak field in the coil end region. The peak field is related to the dipole field which would occur for the bare coil.

Design	MTA	MBFISC	MBTRA	MBPN	MBSMSO
Aperture Diameter (mm)	50.	56.	56.	56.	
Cable height, inner layer (mm)	17.	16.7	12.3	15.	
Cable height, outer layer (mm)	17.	16.7	11.7	15.	
Number of turns	74	82	98	82	
Beam distance (mm)	180.	200.	180.	180.	
Yoke radius (mm)	93.	91.5	82.	98	
Length of coil end (mm)	215.	163.	140.	191.	178.
Cable length, Inner layer (mm)	3533	4473	8091	5985.	4591.
Cable length, Outer layer (mm)	10229	11658	12830	12752.	11943.
Nominal current (A)	13987.	12844.	8718.	11614.	
Field at nominal current (T)	9.85	9.46	8.65	8.65	
Quench field (T)	10.37	9.96	9.43	9.65	
Self inductance (mH/m)	6.42	7.82	11.41	7.64	
NI/B	105063.	111352.	98773.	110097.	
$b_3(10^{-4}$ at r=10 mm)	0.690	0.046	0.15	-0.345	
$b_5(10^{-4}$ at r=10 mm)	0.110	0.0015	0.0300	0.0244	
$b_7(10^{-4}$ at r=10 mm)	0.150	-0.0088	0.0173	0.0060	
$b_9/(10^{-4}$ at r=10 mm)	0.020	0.0022	-0.0005	0.0000	
$n_3(10^{-4}$ at r=10 mm)	-4.72	-3.09	-3.62	-3.62	
$n_5(10^{-4}$ at r=10 mm)	0.332	0.111	0.121	0.150	
$n_7(10^{-4}$ at r=10 mm)	-0.019	-0.019	-0.027	-0.027	
$n_9/(10^{-4}$ at r=10 mm)	0.009	0.004	0.005	0.006	
Peak field/main field, inner layer, 2D	1.0235	1.0327	1.057	1.051	
Peak field/main field, outer layer, 2D	0.856	0.908	0.892	0.875	
Peak field/main field, inner layer, 3D	1.0473	1.0668	1.107	1.100	1.18
Peak field/main field, outer layer, 3D	0.921	0.992	0.974	0.923	0.709
$\Delta P\ (N/mm^2)$	15.3	10.6	19.2	18.6	15.9
F_z, inner layer (N)	14460.	10171.	16827.	13279.	13940.
F_z, outer layer (N)	29406.	36897.	25645.	31641.	31419.
Ellipticity ratio, Inner layer	0.998	0.963	0.586	0.864	0.714
Ellipticity ratio, Outer layer	1.027	0.939	0.638	0.636	0.762
Min. radius of curvature, inner layer	4.62	14.36	13.89	6.24	14.32
Min. radius of curvature, outer layer	31.1	15.78	34.54	37.24	30.32
$b_3^{**}(10^{-4}$ at r=10 mm)	52.47	22.55	-33.07	0.000	2.05
$b_5^{**}(10^{-4}$ at r=10 mm)	-0.22	0.189	-1.68	0.000	-0.0065
$b_7^{**}(10^{-4}$ at r=10 mm)	0.135	-0.0036	-0.077	0.0049	-0.0442
$b_9^{**}(10^{-4}$ at r=10 mm)	0.0215	0.0069	-0.0031	0.0048	-0.0071

Table 2: Results for the 2D and 3D coil optimizations. b_n normal relative multipoles (2D), n_n normal relative multipoles due to persistent currents at injection energy. Integration path for relative integrated multipole errors b_n^{**} from z=-100mm to z=250 mm. Iron yoke ends at z=0. Ellipticity ratio given for the upper edge of the innermost turn in each layer, ΔP = Variation of pressure due to Lorentz forces on the narrow face of the innermost conductor of the inner layer. ΔP and F_z are given for a current that would give 8.65 T with a iron yoke of 85 mm.

The multipole content given for the cross section shows that the MBFISC,MBTRA and MBPN dipole models have been already successfully optimized in two dimensions. The MBPN and MBSMSO dipole models show significantly reduced integrated multipole content in the ends. The peak field to main field ratio is difficult to reduce since for the cross section optimization more turns are added in the second block of the outer layer. This is done in order to reduce the b_7 and b_9 components, but considerably increases the

peak field in the coil ends which cannot be compensated with the end design. This effect is particularly pronounced in the MBTRA model which uses the small cable of only about 12 mm height and the 5 block design in the cross section. The reduction of the variation of Lorentz forces acting on the narrow face of the conductor which constitutes a source of slip between the conductors is very difficult. It can be done by shifting the inner block of the outer layer towards the center of the magnet as it is done for the MBFISC and the MBSMSO design. The objective conflicts with the required minimum field enhancement in the ends. Therefore a dipole model will be built with a reinforced mechanical construction, the so called end clamping cage.

ACKNOWLEDGEMENT

I thank T. Tortschanoff and N. Siegel for the discussions and ideas which have been incorporated into the program, which at the current 3.4 version led to more than 14000 lines of computer code. Many thanks to R. Wolf who contributed the subroutines for the calculation of the persistent current effects. I would like to express my gratitude to S. Masso who installed the program on CERN's parallel RISC6000 workstation cluster PaRC, as well as to all colleagues and users of ROXIE who helped me testing the versions or provided me with their designs which I could use as examples.

References

[1] Bertsekas, D.P.: Constrained optimization and Lagrange multiplier methods, Academic Press, 1982
[2] Cohon, J.L.: Multiobjective Programming and Planning, Academic Press, New York, 1978
[3] Fandel, G.: Optimale Entscheidung bei mehrfacher Zielsetzung, Springer, Berlin 1972
[4] Fiacco, A.V., McCormick, G.P.: Sequential unconstrained minimization techniques, Wiley, 1968
[5] Fletcher, R., Powell, M.J.D.: A rapidly convergent descent method for minimization, Computer Journal, Vol. 6, 1963
[6] Fogel D.B.: An Introduction to Simulated Evolutionary Optimization, IEEE-Transactions on Neural Networks, 1994.
[7] Fletcher, R., Reeves, C.M.: Function minimization by conjugate gradients, Computer Journal, Vol. 7, 1964
[8] Gill, P.E., Murray, W., Wright, M.H.: Practical optimization, Academic Press, 1981
[9] Himmelblau, D.M.: Applied nonlinear Programming, McGraw-Hill, 1972
[10] Holland, J.H.: Genetic algorithms, Scientific American, 1992
[11] Jacob, H.G.: Rechnergestützte Optimierung statischer und dynamischer Systeme, Springer, 1982.
[12] Krebs, M.: Vergleich unterschiedlicher Methoden zur Behandlung nichtlinearer Restriktionen in Optimierungsproblemen, Diplomarbeit am Institut fuer Elektrische Energiewandlung, Technische Hochschule Darmstadt, Germany, 1990.
[13] Kuester, J., Mize, J.H.: Optimization techniques with Fortran, Mc Graw-Hill, 1973
[14] Kuhn, H.W., Tucker, A.W.: Nonlinear Programming, Proceedings of the 2nd Berkeley Symposium on Mathematical Statistics and Probability, University of California, Berkeley, 1951
[15] Luenberger, D.G.: Introduction to linear and nonlinear programming, Addison-Wesley, 1973
[16] Marglin, S.A.: Objectives of Water-Resource Development in Maass, A. et al. Design of Water-Resource Systems, Cambridge, 1966
[17] Marquard, D.M.: An algorithm for least squares estimation of nonlinear parameters, Society for Industrial and Applied Mathematics, 1963
[18] Morse P.M., Kimball G.E.: Methods of operations research, Wiley & Sons, New York, 1950.
[19] Nelder, J.A., Mead, R.: A simplex method for function minimization, Computer Journal, Vol. 7, 1964
[20] Pareto, V.: Cours d'Economie Politique, Pouge 1896 or translation by Schwier, A.S.: Manual of Political Economy, The Macmillan Press, 1971
[21] Perin, R.: The Superconducting Magnet System for the LHC, IEEE-Transactions on Magnetics, 1991
[22] Powell, M.J.D.: An efficient method for finding the minimum of a function of several variables without calculating derivatives, Computer Journal, 1964

Application of Optimization to the Design of Electromechanical Devices

Sykulski, J. K.; Cheng, Y. B.
Department of Electrical Engineering
University of Southampton, Southampton SO 5NH, UK

Abstract

The paper presents an automated optimization system which interfaces an external optimizer to a general purpose finite element package. The program, which is easy to use and user friendly with several pull-down menus, searches for constrained shape design variables that fulfil the defined performance criteria. The field analysis forms part of the optimization iterative cycle. The idea of an external optimizer is very attractive as it provides flexibility. The optimization process can be interrupted and restarted easily without loss of accumulated information. The formulation of the Gauss-Newton optimization algorithm with Levenberg-Marquardt modification and its implementation are given in some detail. Two application examples are described. First, a d.c. solenoid actuator with truncated cone pole face is optimized to produce a user specified force-displacement characteristic. Secondly, an actuator solenoid is optimized to produce maximum energy per stroke. The ampere-turn excitation in the coil is governed by the maximum power loss and maximum current density allowable in the coil.

Introduction

The control valve of an electrohydraulic system is operated by a solenoid mounted on the valve block (Fig. 1). The magnetic potential difference produces an attractive force between the pole face and the armature, which moves to close the airgap and minimize its magnetic reluctance. A push pin extending from the centre of the armature acts directly on the spool.

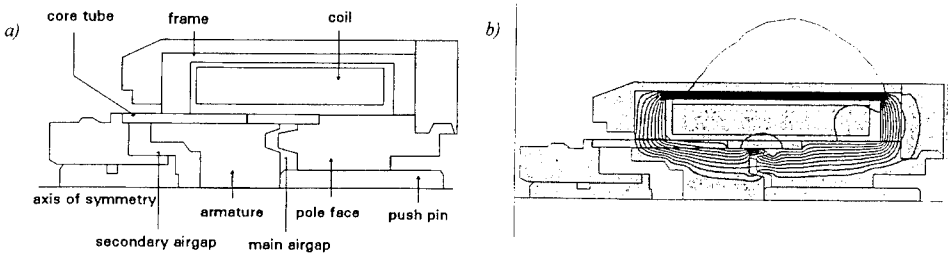


Fig. 1. The electromechanical actuator (*a*) and a typical field plot (*b*)

Accurate field modelling of a d.c. solenoid-operated directional control valve has been conducted using a general purpose finite element package OPERA-2d [27]. Magnetic forces acting on armature at different displacements have been predicted using the Virtual Work Principle and the Maxwell Stress Tensor. Computed characteristics correlate closely with experimental results [3]. The solution is carried out in axis-symmetric mode to reflect the actual symmetry

of the device. The non-linear non-homogeneous equation is solved in terms of magnetic vector potential A

$$\nabla \times \left(\frac{1}{\mu} \nabla \times \boldsymbol{A} \right) = \boldsymbol{J} - \sigma \frac{\partial \boldsymbol{A}}{\partial t} \tag{1}$$

where $\boldsymbol{J}$ is the imposed current density. The total force on armature may be computed from the finite-element solution using the Maxwell Stress Tensor (MST) by performing surface integration in the air surrounding the armature. Because of axial symmetry this reduces to carefully selecting appropriate integration lines in the cross-section of the device. Implementation of the Virtual Work Principle (VWP), on the other hand, requires at least two solutions. The magnetic force along the axial (z) direction is then found from

$$F_z = \frac{\partial W'_m(i,z)}{\partial z} \tag{2}$$

Instead of computing the force from the coenergies at both ends of an incremental displacement, a set of coenergies may be found at several positions along the armature displacement. A least-square polynomial curve is then fitted through these values and more accurate space differentiation is applied to obtain force/displacement characteristic. The coenergy $W'_m(i,z)$ for nonlinear axis-symmetric solutions is given by

$$W'_m = 2\left(\frac{2\pi r}{2} \int_S \boldsymbol{J} \cdot \boldsymbol{A}\, dS \right) - \int_S 2\pi r \left(\int_0^B \boldsymbol{H} \cdot d\boldsymbol{B} \right) dS \tag{3}$$

Automated optimization of solenoid actuators

The nonlinear least-squares problem

Typically m data values (e.g. the desired force in solenoid actuator optimization) $d_1, d_2, \ldots, d_m$ are given, which have been sampled for values $t_1, t_2, \ldots, t_m$ of some independent variable t (e.g. the armature displacement). It is then required to fit a function $\phi(t, x)$ which has n design variables x to be chosen so that the function best fits the data. Therefore, the weighted residuals are given by

$$r_i(\boldsymbol{x}) = w_i[\phi(t_i, \boldsymbol{x}) - d_i], \qquad i = 1,2,\ldots,m \tag{4}$$

with the weighting factors w_i representing the users preference and a least squares solution is sought by minimizing

$$f(\boldsymbol{x}) = \frac{1}{2}\sum_{i=1}^{m} r_i(\boldsymbol{x})^2 = \frac{1}{2}\boldsymbol{R}(\boldsymbol{x})^T\boldsymbol{R}(\boldsymbol{x}) \tag{5}$$

The first-derivative matrix of $\boldsymbol{R}(x)$ is simply the Jacobian matrix $\boldsymbol{J}(x)$ with (i,j)-element $\boldsymbol{J}(x)_{ij} = \partial r_i(x)/\partial x_j$. The gradient of $f(x)$ is

$$\boldsymbol{g}(\boldsymbol{x}) = \nabla f(\boldsymbol{x}) = \sum_{i=1}^{m} r_i(\boldsymbol{x}) \cdot \nabla r_i(\boldsymbol{x}) = \boldsymbol{J}(\boldsymbol{x})^T\boldsymbol{R}(\boldsymbol{x}) \tag{6}$$

Similarly, the Hessian of $f(x)$ is

$$\boldsymbol{G}(\boldsymbol{x}) = \nabla^2 f(\boldsymbol{x}) = \sum_{i=1}^{m} \left[\nabla r_i(\boldsymbol{x}) \cdot \nabla r_i(\boldsymbol{x})^T + r_i(\boldsymbol{x}) \cdot \nabla^2 r_i(\boldsymbol{x}) \right] = \boldsymbol{J}(\boldsymbol{x})^T\boldsymbol{J}(\boldsymbol{x}) + \boldsymbol{S}(\boldsymbol{x}) \tag{7}$$

where

$$\boldsymbol{S}(\boldsymbol{x}) \approx \sum_{i=1}^{m} r_i(\boldsymbol{x}) \cdot \nabla^2 r_i(\boldsymbol{x}) \tag{8}$$

denotes the second-order information in $\nabla^2 f(x)$. Thus, from a truncated Taylor series expansion

$$f(\boldsymbol{x}_k + \boldsymbol{\delta}) \approx q_k(\boldsymbol{\delta}) = f_k + \boldsymbol{\delta}^T\boldsymbol{g}_k + \tfrac{1}{2}\boldsymbol{\delta}^T\boldsymbol{G}_k\boldsymbol{\delta} \tag{9}$$

the quadratic model of $f(x)$ around $\boldsymbol{x}_k$ is given by

$$q_k(\boldsymbol{\delta}) = \frac{1}{2}\boldsymbol{R}(\boldsymbol{x}_k)^T\boldsymbol{R}(\boldsymbol{x}_k) + \boldsymbol{\delta}^T\boldsymbol{J}(\boldsymbol{x}_k)^T\boldsymbol{R}(\boldsymbol{x}_k) + \frac{1}{2}\boldsymbol{\delta}^T\left(\boldsymbol{J}(\boldsymbol{x}_k)^T\boldsymbol{J}(\boldsymbol{x}_k) + \boldsymbol{S}(\boldsymbol{x}_k)\right)\boldsymbol{\delta} \tag{10}$$

for the minimization of objective function of eqn (5). The full Newton step is given by

$$s_k = -G_k^{-1} g_k = -\left[J(x_k)^T J(x_k) + S(x_k)\right]^{-1} J(x_k)^T R(x_k) \tag{11}$$

It is often possible to ignore the second-order term $S(x_k)$ of the Hessian altogether on the grounds that if the nonzero residuals are not of the type that reinforce their nonlinearity [4], then $J(x)^T J(x)$ is a sufficiently good Hessian approximation. In the resulting Gauss-Newton method, the 'Newton step' from x_k is defined by

$$s_k = -\left[J(x_k)^T J(x_k)\right]^{-1} J(x_k)^T R(x_k) \tag{12}$$

Difficulties arise when the Hessian matrix is not positive definite. To solve this problem, an idea of modifying matrices by addition of a multiple of the unit matrix was suggested at an early date by Levenberg [5] and Marquardt [6] and applied to Newton's method by Goldfeld et al [7]. Hence, the step δ_k is determined by solving the system

$$(G_k + \lambda I)\delta_k = -g_k \quad , \qquad \lambda \geq 0 \tag{13}$$

When G_k is close to being positive definite then it may only be necessary to add a small multiple of unit matrix I so as to give a good direction of search. All Levenberg-Marquardt algorithms therefore find a value $\lambda \geq 0$ such that $G_k + \lambda I$ is positive definite and solve eqn (13) to determine δ_k.

Difficulties arise again when the underlying quadratic function $q_k(\delta)$, obtained by truncating the Taylor series for the $f(x_k+\delta)$, does not have a unique minimizer and the method is not defined. Another way of regarding this fact is that the region about x_k in which the Taylor series is adequate does not include a minimizing point of $q_k(\delta)$. A more realistic approach therefore is to assume some neighbourhood Ω_k of x_k is defined in which $q_k(\delta)$ agrees with $f(x_k+\delta)$ in some sense. Then it would be appropriate to choose $x_{k+1}=x_k+\delta_k$, where the correction $\delta(x)$ minimizes $q_k(\delta)$ for all $x_k+\delta$ in Ω_k. Such a method is called a *restricted step method* or sometimes a *trust region method*: the step to a new iterate is obtained by minimizing a local model to the objective function over a restricted ellipsoidal region of validity of the Taylor series centred about the current iterate. The diameter of this region is expanded and contracted in a controlled way based upon how well the local model predicts behaviour of the objective function. It has been shown [8] that this method retain the rapid rate of convergence of Newton's method, but is also generally applicable and globally convergent. Let μ_k be the radius of the neighbourhood. Hence

$$\Omega_k = \{\, x : \| x - x_k \| \leq \mu_k \,\} \tag{14}$$

and seeking the solution δ_k by

$$\underset{\delta}{\textit{minimize}} \quad q_k(\delta) \quad \textit{where} \quad \| \delta \| \leq \mu_k \tag{15}$$

using a double dogleg search technique instead of a line search.

Three optimization algorithms (Gauss-Newton, Levenberg-Marquardt and Trust region methods) have been compared and tested on 18 different functions recommended by More [9] for nonlinear least-square problems. Details of this comparison may be found in a recent conference publication by the authors of this paper [3].

Global optimization with simulated annealing

In recent years a method known as 'Simulated Annealing' has been widely used in combinatorial optimization with classical direct search methods to seek the global minimum of a function $f(x)$. It is essentially an iterative random search procedure with adaptive moves along the coordinate directions. The algorithm permits uphill moves under the control of a probabilistic criterion, thus tending to avoid the first local minima encountered. First, it reaches an area in the function domain where a global minimum should be present, following the gross behaviour irrespectively of small local minima found on the way. It then develops finer details, finding a good, near-optimal local minimum, if not the global minimum itself. This process is based on an analogy from thermodynamics where a system is slowly cooled in order to achieve its lowest energy state. The algorithm was independently introduced by Kirkpatrick et al [10], and Cerny [11]. The name 'simulated annealing' originated from analogy with the physical annealing process of solids. Other names used are Monte Carlo annealing [12], probabilistic hill climbing [13], statistical cooling [14], [15] and stochastic relaxation [16]. An important feature of the simulated annealing algorithm is that it finds high-quality solutions which do not strongly depend on the choice of the initial solution, i.e. the algorithm is effective and robust. However, simulated annealing technique is expensive because many function evaluations are necessary [3].

Concept and main features of the optimization shell

After careful studies of the different optimization algorithms mentioned above, the Levenberg-Marquardt method was chosen and implemented in an improved version of the Electromechanical Actuator Modelling and OptimizatioN (EAMON) shell [2], which also interfaces with the finite element package OPERA-2d. Fig. 2 shows a block diagram of the open architecture system of EAMON. The graphical user interface has been programmed using MATLAB's toolkit. This eliminates the need for long hours of programming in C-language and gives the flexibility to work at a higher, more productive level so that more can be done more quickly and with greater accuracy. For the same reason the optimization routine employing Levenberg-Marquardt algorithm has been written as a MATLAB function in M-file format (i.e. optimizer.m). Any other optimization algorithm which can be written in M-file format can replace the chosen Levenberg-Marquardt algorithm.

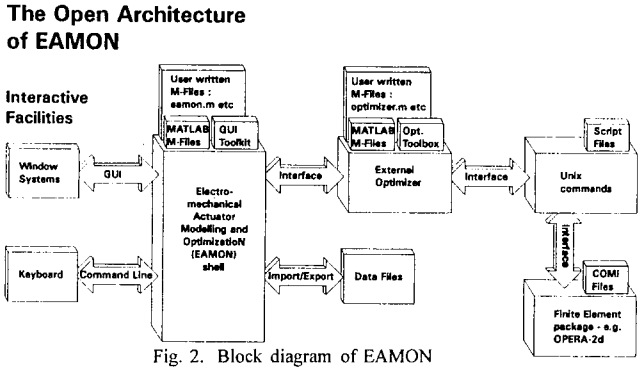


Fig. 2. Block diagram of EAMON

Another important feature of EAMON shell is its capability to interface with a general purpose finite element package, i.e. OPERA-2d, without the need of modifying this commercial software. Script files for various displacements of solenoid armature may be quickly and easily created for any predefined actuator model without any user intervention. Creation of batch files to run finite element analysis is also automated. Finally, the force analysis using Virtual Work Principle is conducted automatically after extensive checks for availability of legitimate finite element solutions and OPERA-2d command files. Any design changes to the actuator model can be made easily and quickly and the whole CAD procedure up to force analysis can be executed in the shortest time possible. The whole CAD operation will be invisible to the user except for a window indicating "Pre-processing", "Running analysis" or "Post-processing" stages of a finite element function call. The computational flowchart illustrating this feature is given in Fig. 3.

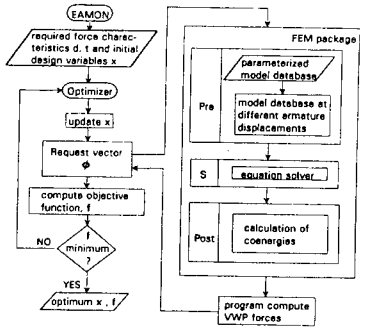


Fig. 3. Computational flowchart

The EAMON shell is easy to use and very user friendly. Pull-down menus appear on the menu bar below the figure title as shown in Fig. 4. Under "Setup" menu, two dialogue boxes can be created. The initial design variables and their bounds can be assigned easily. The desired force characteristic can be specified by assigning forces for the various armature displacements i.e. d_i and t_i in eqn. (4). Up to fifteen displacements can be given, not necessarily in regular intervals. In addition, the weighting factor w_i may also be given. The design variables and force-displacement characteristic will always default to the latest updated values. Under "Options" menu, frequently changed parameters for the optimizer routine can be set; i.e. the maximum number of function evaluations; the termination criteria that is a measure of the worst case precision required of the design variables x; and the termination criteria that is a measure of the precision required of the objective function f at the solution. The optimization does not terminate unless both termination criteria have been met or when the maximum number of function evaluations has been exceeded.

It is useful to have the "Stop" and "Restart" buttons so that the optimization software can be interrupted and restarted easily without loss of accumulated information. Before starting a new iteration, the optimization code checks if the "Stop" button has been clicked to see whether the user wants to interrupt the computation. Users can let an optimization routine run for a small number of iterations, then look at the progress of the calculation in order to decide whether to let it run further. The shell plots force-displacement graphs (required characteristic as x's, initial characteristic in solid line and latest/final characteristic in dotted line) after every iteration and automatically assigns units, title and axis labels so that the user instantly gets the right presentation. A hardcopy can be produced by simply typing "print" in MATLAB command prompt. In addition, optimization results (i.e. number of function calls, number of gradient evaluations, and value of the objective function f at the last evaluated point) will be displayed in the "Comment window".

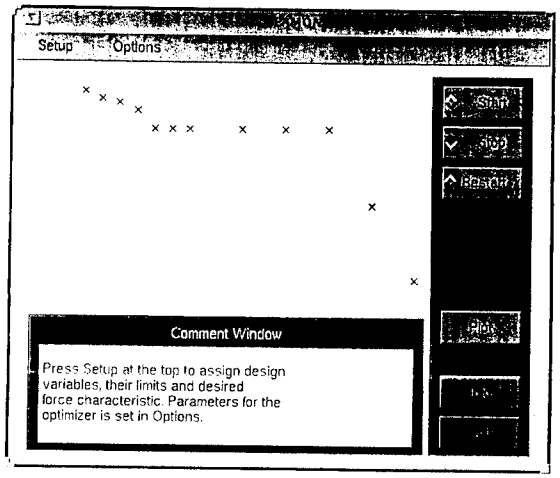


Fig. 4. The EAMON base window

Examples

Example 1 A d.c. solenoid actuator with truncated cone pole face is to be optimized to produce a specified force-displacement characteristic. The five constrained design variables are shown in Fig. 5. Their bounds, initial and optimized values are tabulated below.

design variables	lower bounds	upper bounds	initial values	optimized values
x_1	0	3.1	1.2975	1.2919
x_2	0	45	12.5706	13.9323
x_3	3	8	5.6039	5.5942
x_4	0	10	5.2694	1.6210
x_5	0	3.1	2.9056	2.9256

The optimization terminated successfully after 18 iterations and 108 function evaluations. Fig. 6 shows the required forces, and the initial and final force-displacement characteristics.

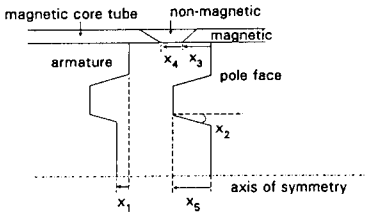


Fig. 5. A section of solenoid actuator with five design variables to be optimized.

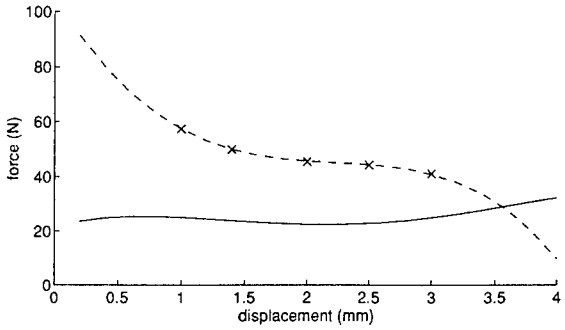


Fig. 6. Required (x's), initial (solid line) and final (dashed line) force-displacement characteristics.

Example 2 The new objective in this example is to maximize the area under the force-displacement curve by varying the radius of the armature (Fig. 7) while maintaining the external diameter of the device constant. The following assumptions are made :

1. the maximum power loss in the coil is 24 watts for a 24 volts d.c. supply;
2. the maximum current density in the copper wire at 100°C temperature rise is assumed 10.67 A/mm^2; and
3. the solenoid coil space factor λ is 0.6353.

The choice of ampere-turns in the coil is limited by assumption (1) or (2) whichever is less. For example, for a design variable x=8mm, the mean radius of coil, r_m = 11.1625 mm, and the cross-section area of coil, A=181 mm^2.

Assuming "single turn" coil, the coil resistance is given by

$$R_t = \frac{\rho_{100} l}{A_c} = \frac{(1.72 \times 1.393 \times 10^{-5}) 2\pi r_m}{A\lambda} = 1.461381 \times 10^{-5}$$

where ρ_{100} is resistivity of copper at 100°C temperature rise, l is the length of the coil turn and A_c cross-section area of copper only. The excitation, assuming a power loss, P=24W, at 24V, is

$$(NI) = \sqrt{\left(\frac{P}{R_t}\right)} = 1281.5\,\text{At}$$

The excitation assuming maximum current density in copper is (NI) = 10.67 × A_c = 1226.94 At. Hence, the solenoid actuator is modelled with 1226.94 At excitation. Consequently,

power loss, $P = (NI)^2 R_t$ = 21.9992 W;
coil current, I = 916.634 mA;
number of turns, N = 1338; and
actual coil resistance, R = 26.1623 Ω.

The design variable (radius) has a lower bound of 6.5 mm, upper bound of 9.5 mm and initial value of 9.2 mm. The initial area under the force-displacement curve is 0.170557 Nm. The optimization terminated successfully after 19 iterations and 36 function evaluations with x = 8.2157 mm, NI = 1168.45 At, P = 21.36 W, and area under the force-displacement curve = 0.191805 Nm. Fig. 8 shows the initial and final force-displacement characteristics.

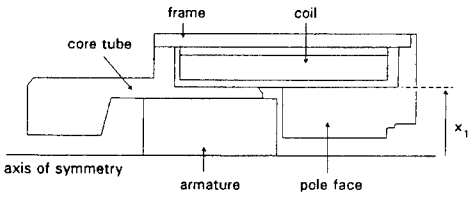


Fig. 7. Solenoid actuator to be optimized.

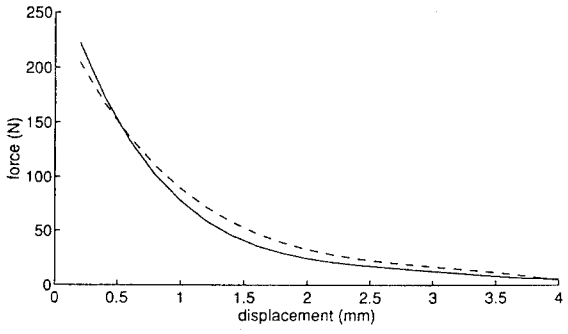


Fig. 8. Initial (solid line) and final (dashed line) force-displacement characteristics.

Acknowledgement

The work has been sponsored by the Vickers Systems Division, TRINOVA Ltd, UK.

References

[1] Y.B. Cheng and J.K. Sykulski: 'A Design Shell for Force Calculations of Solenoid Actuators', *Software Applications in Electrical Engineering*, P.P. Silvester (ed), Computational Mechanics Publications, pp.39-46, 1993

[2] Y.B. Cheng, J.K. Sykulski and R.L. Stoll: 'Force optimization in DC Actuators,' *Compel*, Vol.13 No.1, pp. 163-166, March 1994

[3] Y.B. Cheng and J.K. Sykulski: 'CAD and Optimization of Electromechanical Actuators,' *Proc of ICEM'94*, Vol. 3 pp.187-192, Paris, France, Sept 1994

[4] J.E. Dennis and R.B. Schnabel: *Numerical Methods for Unconstrained Optimization and Nonlinear Equations*, Prentice Hall, 1983

[5] K. Levenberg: 'A Method for the Solution of Certain Nonlinear Problems in Lest Squares', *Quarterly of Applied Mathematics*, Vol. 2, pp. 164-168, 1944

[6] D. W. Marquardt: 'Solution of Nonlinear Chemical Engineering Models', *Chemical Engineering Progress*, Vol. 55, pp. 65-70, 1959

[7] S.M. Goldfeld, R.E. Quandt and H.F. Trotter: 'Maximisation by quadratic hill-climbing', *Econometrica*, Vol. 34, pp. 541-551, 1966

[8] R. Fletcher: *Practical Methods of Optimization*, 2nd edition, Wiley, Ch 5, 1987

[9] J.J. More, B.S. Garbow and K.E. Hillstrom: 'Testing unconstrained optimization software', *ACM Trans. on Math. Software*, Vol. 7, No. 1, pp. 17-41, March 1981

[10] S. Kirkpatrick, C.D. Gelatt Jr., and M.P. Vecchi: 'Optimization by simulated annealing', *Science*, Vol. 220, pp. 671-680, 1983

[11] V. Cerny: 'Thermodynamical approach to the travelling salesman problem: an efficient simulation algorithm', *J. of Optimization Theory and Application*, Vol.45, pp. 41-51, 1985

[12] D.W. Jepsen and C.D. Gelatt Jr: 'Macro placement by Monte Carlo annealing', *Proc. IEEE Int. Conf on Computer Design*, Port Chester, pp. 495-498, 1983

[13] F. Romeo and A.C. Sangiovanni-Vincentelli: 'Probabilistic hill climbing algorithms: properties and applications,' *Proc. Chapel Hill Conf. on VLSI*, Chapel Hell (NC), pp. 393-417, 1985

[14] E. Aarts and P.J.M. van Laarhoven: 'Statistical cooling: a general approach to combinational optimization problems', *Phillips Journal of Research*, Vol.40, pp. 193-226, 1985

[15] J.A. Strorer, J. Becker and A.J. Nical: 'Uniform circuit placement', in P. Bertolazzi and F. Luccio (Eds.): *Proc. Int. Workshop on Parallel Computing and VLSI*, Amalfi, Elsevier Science Publishers, Amsterdam, pp 255-273, 1985

[16] S. Geman and D. Geman: 'Stochastic Relaxation Gibbs Distributions, and Bayesian restoration of images', *IEEE Proc. Pattern Analysis and Machine Intelligence*, Vol. 6, pp. 721-741, 1984

[17] N. Metropolis, A. Rosenbluth, M. Rosenbluth, A. Teller and E. Teller: 'Equation of state calculations by fast computing machines', *Journ. of Chemical Physics*, Vol. 21, pp. 1087-1092, 1953

[18] N.E. Colins, R.W. Eglese, and B.L. Golden: 'Simulated annealing - an annotated bibliography', Cambridge University (preprint), 1987; *Computer* , Vol .21, 1988, and *Communications of the ACM*, Vol. 31, 1988

[19] P.J.M. van Laarhoven and E.H.L. Aarts: *Simulated Annealing: Theory and Applications*, Reidel, Dordrecht, 1987

[20] D. Vanderbilt and S.G. Louie: 'A Monte Carlo Simulated Annealing Approach to Optimization over Continuous Variables', *Journal of Computational Physics*, Vol. 56, pp. 259-271, 1984

[21] A. Corana, M. Marchesi, C. Martini, and S. Ridella: 'Minimizing Multimodal functions of continuous Variables with the 'Simulated Annealing' Algorithm', *ACM Trans. on Mathematical Software*, Vol. 13, No. 3, pp. 262-280, 1987

[22] W.H. Press: *Numerical Recipes in C - The Art of Scientific Computing*, 2nd Edition, Cambridge University Press, p. 450, 1992

[23] W. Spendley, G.R. Hext, and F.R. Himsworth: 'Sequential Applications for Simplex Designs in Optimization and Evaluating Operation', *Technometrics*, Vol. 4, pp. 441-461, 1962

[24] J.A. Nelder and R. Mead: 'A simplex Method for Function Minimization', *Computer Journal*, Vol. 7, pp. 308-313, 1965

[25] F. Freudenstein and B. Roth: 'Numerical solutions of systems of nonlinear equations', *J. ACM.*, Vol. 10, No. 4, pp. 550-556, Oct. 1963

[26] A.R. Colville: 'A comparative study of nonlinear programming codes,' Rep. 320-2949, IBM New York Scientific Center, 1968

[27] 'OPERA-2d - Reference Manual', Vector Fields Ltd, 1993.

Genetic Algorithms for the Optimal Design of Electromagnetic Devices

O. A. Mohammed and G. F. Üler

Department of Electrical and Computer Engineering
Florida International University, Miami, Florida, 33199, USA

Abstract

Genetic Algorithms (GAs) are search methods that mimic some fundamental functions of nature's biological evolution. GAs share natural systems' high level of robustness as result of their being able to adapt to many different environments and to locate the global optimum without being attracted to the local extremes. This study presents an application of GAs to the design optimization of electromagnetic devices. The developed optimization system consists of the search tool and an analysis tool. The finite element method (FEM), serving as the analysis tool is incorporated with the GA. The objective function is formed from the computed field parameters and some penalty terms usually derived from the geometrical constraints. The method is applied to a size optimization problem. The results are highly satisfactory and suggest the inclusion of the GAs in the *search toolbox* of a universal optimization environment.

Introduction

John Holland invented GAs in the early 70s with the goal of creating a computer algorithm that would mimic some functions of natural evolution. If the adaptive and selective mechanism of evolution can be reflected upon an algorithm, this algorithm can then be used to solve complex search problems. The applications that have appeared since the arrival of the technique prove that GAs are powerful in solving complicated problems the way nature does. These applications cover a wide range in the areas of optimization and machine learning problems, including scheduling, pipeline system optimization, image processing and pattern recognition, computer vision, VLSI circuit layout, structural optimization, adaptive filter design, nonlinear equation solving, and neural network design and training [1]. Recently, design optimization of electromagnetic devices has been added to this list by the authors [2].

In nature, evolution works on the chromosomes of individuals in the population, not on the individuals themselves. The information contained in the chromosomes is *decoded* into the individuals in the population. The combinations of genes determine the characteristics of an individual. The rules imposed by the environment govern the survival of the population and, therefore, in which genetic direction it evolves. In a population, the chromosomes that decode into more successful individuals reproduce more often. The less successful ones, and chromosomes representing them, decline in number because they cannot appropriately adapt to the conditions of the environment. Evolution in nature is an ongoing process. It is dynamic because the environment changes continuously. If it is assumed that the rules of the environment do not change for a sufficiently long period, eventually the majority of the members of a population will be well fitted to the environment.

In a GA, three of nature's functions of biological evolution are simulated. These are *reproduction, recombination, and mutation.* In the algorithm, chromosomes are represented by finite length character strings, usually made up of 0s and 1s. Simulated evolution works on a population of strings by means of its operators. The algorithm does not have any information about the problem it is trying to solve. The only information that is provided to it is how the chromosomes are decoded into functional individuals of the population and how successful each individual is in adapting to the environment [1, 3].

Goldberg specifies four main aspects that make the GAs different from other, *more conventional*, search methods:

1. They operate on a population of points in the search space simultaneously, not just on one point.
2. They work with a coded string representing the parameters, not the parameters themselves.
3. They only use the objective function value.
4. Their rules for transition are probabilistic.

Development of a Genetic Algorithm

In the way it mimics the natural selection rule of evolution, the GA offers applicability to any optimization or search problem. Before running the actual program, however, there are four primary steps in preparing to solve a problem using GAs [4]. Prior to solving a problem using GAs, the user must determine the representation scheme, the fitness measure, the stopping rule, and the parameters of GA's operation.

The *representation scheme* is the way the design variables are coded into the finite-length character strings. An alphabet of cardinality K is used. Although some researchers choose to use higher cardinality alphabets, at least in Holland's sense, the alphabet of the representation scheme is binary; $K = 2$, whose elements are '0' and '1.' The coding of the chromosomes is a very important concept directly affecting the performance of the GA. It is user and problem dependent. Binary or Gray coding are possible examples. The representation scheme is responsible for "mapping" every point in the search space onto a unique chromosome [4].

The *fitness measure* is an indication of how successful an individual is. The fitness measure is assigned to the chromosomes. Every chromosome that exists during evolution is evaluated and its fitness measure is calculated. The fitness measure is the only information the GA has relating the population to the environment. In an optimization problem, the environment is the objective function. The objective function value or a function of it can be used. The definition of the fitness measure is also user and problem dependent.

GA's search can continue indefinitely. Even if the population reaches the global optimum, mutations account for a genetically dynamic population. Therefore, a stopping rule is necessary. Some of the popular methods are to fix the number of generations and to use the best individual of all generations as the optimum result; to fix the time elapsed and to select the optimum similarly; to let the entire population converge to an average fitness with some error margin.

The parameters of the GA shape the way the algorithm runs. There are two primary parameters. Population size, μ, is the number of chromosomes in the population; chromosome length, l, specifies the number of characters (genes) used to form one character string. There are two secondary parameters that define the occurrence probabilities of the two of the three main GA operators. Crossover rate, p_c, specifies the occurrence rate of the chromosome. It is measured per chromosome pair; mutation rate, p_m, defines the occurrence rate of a mutation per gene.

The procedure given below is used to obtain the results presented in this paper. There are many variations of implementing a GA. Different versions of algorithms with different performances can be synthesized by manipulating either the algorithm itself or its functions, or both. The algorithm presented here is the *canonical GA* of Holland and De Jong [5, 1].

1. Randomly create an *initial population* of μ chromosomes.
2. Evaluate each chromosome and assign *fitness measures.*
3. If the stopping criterion is satisfied, stop.
4. With the *reproduction* operator, create a new population.
5. Randomly pair the chromosomes to form parents. By means of the *crossover* operator, mate them to form offspring.
6. Apply *mutation* to preserve the genetic diversity.
7. Go to Step 2.

In the above procedure, three fundamental operators of the GAs are introduced; 1) reproduction, 2) crossover and 3) mutation.

Based on the fitness measure of a chromosome and the average fitness of the population, the reproduction operator, also called the selection operator, determines, rather stochastically, the number of copies, if any, that particular chromosome will have in the next generation. There are many ways of designing this operator; however, the underlying idea is to give the chromosomes with higher fitnesses more chance to be represented in the next generation but leave the decision to a random variable. Through reproduction a new generation of the same number of members is generated from the previous population.

Once the reproduction is complete, the chromosomes exchange information through the crossover operator. The crossover operator simulates the recombination process of natural evolution. It mates two parents to create two offspring.

Crossover occurs at a rate determined by p_c, the crossover probability. This GA parameter is defined before running the algorithm. The information exchange between the chromosomes is performed by swapping the bits of two parents' chromosomes. After the individuals of the population are mated, for each pair, all bits from a randomly selected position on the chromosome to the end of the string are swapped. In uniform crossover, there is no positional bias in swapping the bits. This implies that there are crossover methods where the crossover probability of a bit depends on the position of that bit in the chromosome. Another variation is to use multiple point crossover, in which bits positioned between randomly selected sites on the chromosomes are swapped [6]. As an example of the one-point crossover, suppose the coding is binary with an alphabet $A = \{0, 1\}$. Assume that before crossover two strings, $\vec{a}_1$ and $\vec{a}_2$ are mated. Also assume that the crossover site for this pair is 3, as indicated above with the symbol "|". The effect of crossover is shown below.

before crossover	after crossover
$\vec{a}_1 = 110\|010110$	$\vec{a}_1' = 110\|110001$
$\vec{a}_2 = 100\|110001$	$\vec{a}_2' = 100\|010110$

The third fundamental operator of GAs is the mutation operator. Although reproduction and crossover both operate at the chromosome level, mutation operates at the gene level. It occasionally changes the value of a gene acting as a protector against the complete loss of some important genetic information by providing genetic diversity [4]. Mutation is a background operator. Associated with the mutation operator, there is an occurrence probability, p_m, determined along with the other GA parameters. This probability is per gene not per chromosome. The usually high total number of genes in the population combined with the background nature of the mutation operator, p_m, is usually a small number.

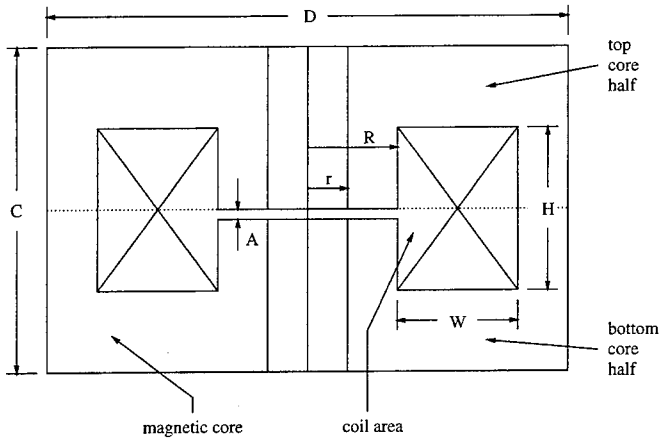


Figure 1: Geometry of the pot core transformer example

Pot core problem

The example used to demonstrate the application of the GAs to the design optimization of electromagnetic devices is a pot core transformer. Mohammed and Jones provided a solution for this problem using a dynamic search method [7]. Here the same geometry is used to provide grounds for comparison of the results. Shown in Figure 1, the design is symmetrical along the vertical line in the middle. Therefore only one half of the problem is modeled and solved. In the original problem, the magnetic material has a nonlinear characteristic. In this application, however, the iron is treated as a linear material and a linear solution is obtained. The permeability used is obtained from the actual $B - H$ curve where the linear region ends as $\mu_r = 1167.14$. Although Mohammed and Jones took them into account, eddy currents are not considered here. Due to these reasons, the comparison of the two methods should not be quantitative.

Design variables

The six design variables indicated on the model in Figure 1 are tabulated in Table 1. The ranges of these variables are based on the two sets of values given by Mohammed and Jones as being starting and end points of the search. Here, lower limits are allowed to be less and upper limits are allowed to be higher than those values. A constraint on the genetic operators are implemented to assure that parameters do not overlap; such as having a coil that is higher than the transformer itself. These ranges are also given in Table 1.

Objective function

The objective of the optimization is to reduce the size of the device while maintaining a certain magnetic flux density. The size of the device is directly dependent on the cross-sectional area modeled. The cross-section can be calculated from the design parameters. A criterion is the magnetic flux density. For each design, the average magnetic flux density in the air gap is

	Design Variables	lower limit (mm)	Upper limit (mm)
D	total width of the transformer (half is modeled)	11.0	15.0
C	height of the transformer	5.0	9.0
H	height of the coil	1.8	3.5
W	width of the coil	3.0	6.5
R	distance of the coil from the center	2.0	3.5
A	width of the air gap	0.007	0.4

Table 1: Design variables of the pot core problem and their ranges

calculated and compared with the value calculated for the smaller device proposed by Mohammed and Jones.

These two comparisons, area and flux density, yield to two fitness parameters which have to be combined to form one fitness value. This is done using

$$\Phi = \Phi_{flux} + \Phi_{area} \tag{1}$$

where

$$\Phi_{flux} = 10 \log \frac{1}{|B_{desired} - B_{calculated}|} \tag{2}$$

$$\Phi_{area} = 1000/Area. \tag{3}$$

The logarithm is used because the reciprocal of the difference in the flux densities may become high. The coefficient should bring the weights of the parameters to the same order.

GA parameters

The GA parameters set used for the pot core optimization problem is given in Table 2. Each of the 30 individuals are made of 48 bits representing 6 design variables with 8 genes each. The representation scheme is Gray coding. A crossover probability of 0.8 is used with uniform crossover. The mutation rate is 0.008. The process is stopped after 100 generations and the best individual is picked as the optimal slotion.

Results of pot core problem

The final values of the 6 design parameters are given in Table 3. In the same table, these values are compared to Mohammed and Jones' results, which utilized dynamic search to reach these values [7]. In Figure 2 the change of the fitness of the best individual is shown. The very high fitness that appears in the first and following three generations is not taken into account as that may be results of a premature convergence phenomenon. As the iterations continue, this unreliable peak disappears. However, one can argue that this particular individual has the best fitness and therefore must be selected as the optimum result. In the results shown here, nevertheless, the best fitness, which appears toward the end of the 100 generations is chosen as the optimum.

In Figure 3 the field solution is shown with isopotential lines. The air region that surronds the transformer is also modeled. For the demonstration purposes, however, these regions are left out of the figures. As one of the objectives is to reduce the size of the device, graphing the best size, the cross-sectional area in this case, against the generations provides valuable insight into how the search proceeds. This is shown in Figure 4 The peak of the first several generations is

GA Parameters	
Number of individuals (μ)	30
Number of chromosome segments	6
Segment length	8
Chromosome length	8
Representation scheme	Gray code
Fitness scaling	linear
Reproduction method	remainder stochastic without replacement
Crossover method	uniform
Crossover probability (p_c)	0.8
Mutation probability (p_m)	0.008
Termination criteria	100 generations

Table 2: GA parameters of the pot core optimization problem

Design variable	Optimized value (mm)	Dynamic search results (mm)
D	11.0471	12.303
C	5.87843	6.655
W	1.96	2.349
H	3.76863	4.724
R	2.95294	2.349
A	0.02087	0.089

Table 3: Final values of the design variables and comparison to the results from the dynamic search method

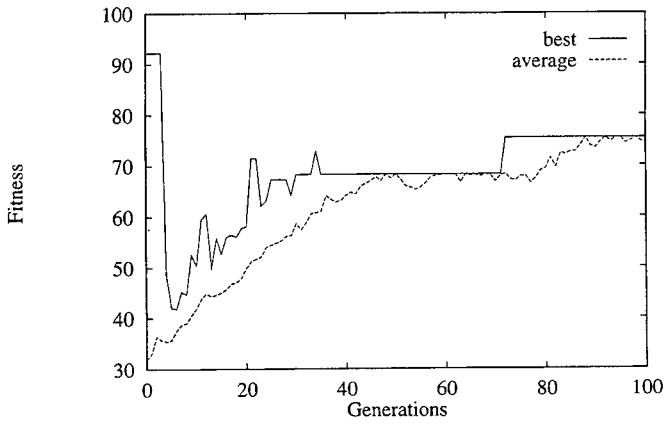


Figure 2: Change of the best and average fitness values over generations

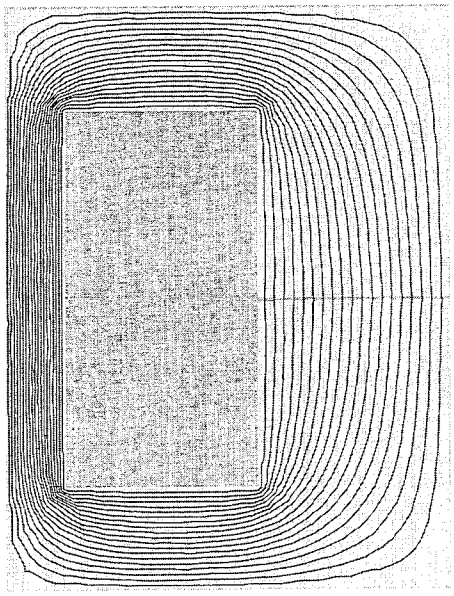


Figure 3: Optimized pot core and the equipotential lines of the corresponding field

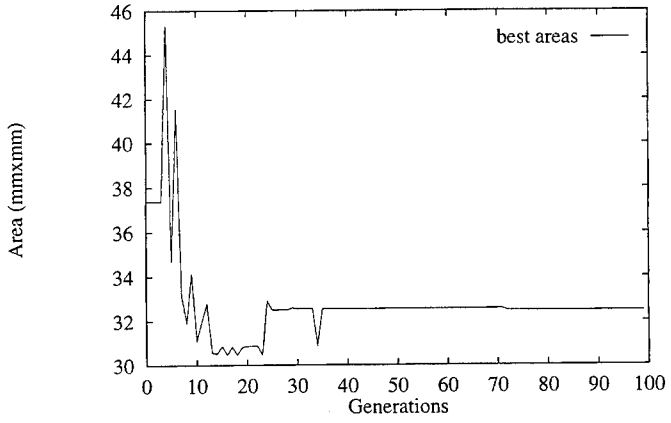


Figure 4: Change of the best areas (smallest size) over generations

observed to represent a bigger size than than that of the selected peak as the optimal solution. This implies that the first peak is a result of a better match in the other criterion, the magnetic field.

It must be noted here that the comparison with the dynamic search method is to establish a performance pattern for GAs with a qualitative insight. The GA solution is linear and does not include eddy currents and losses as the solution by dynamic search did.

Conclusion

Genetic algorithms and the finite element method together are applied to the design optimization of an electromagnetic device.

GAs are search methods that provide a high level of robustness by simulating nature's characteristic of adapting to many different environments. Categorized under stochastic search methods, GAs are distinguished from other random search techniques by their highly structured information exchange schemes. The algorithm explores the search space and exploits the similarities between the traits of the chromosomes to direct the search. GAs perform especially well for multidimensional search problems with nonconvex and nondifferentiable objective functions. They base the search only on the fitness values and do not rely on the derivatives of the objective function or any other auxiliary information. GAs are fully parallelizable.

The performance of GAs is observed to be quite high. For complicated problems, the robust scheme results in comparable speed and guaranteed good solution. Some savings on the CPU time are achieved by keeping the fitness history of the previous generation.

References

[1] D. E. Goldberg, *Genetic Algorithms in Search, Optimization & Machine Learning*, Reading, Massachusetts: Addison-Wesley Publishing Company, Inc., 1989.

[2] G. F. Üler, O. A. Mohammed, and C. S. Koh, "Utilizing genetic algorithms for the optimal design of electromagnetic devices," *IEEE Transactions on Magnetics.*, November 1994 (to be published).

[3] L. Davis, *Handbook of Genetic Algorithms*, New York, New York: Van Nostrand Reinhold, 1991.

[4] J. R. Koza, *Genetic Programming*, Cambridge, Massachusetts: The MIT Press, 1993.

[5] T. Bäck and H. P. Schwefel, "An overview of evalutionary algorithms for parameter optimization," *Evolutionary Computation*, Cambridge, Massachusetts: The Massacusetts Institute of Technology Press, 1993.

[6] L. J. Eshelman, R. A. Caruana, and J. D. Schaffer, "Biases in the crossover landscape," *Proceedings of the Third International Conference on Genetic Algorithms*, San Mateo, California: Morgan Kaufmann Publishers, Inc., pp. 10-19, 1989.

[7] O. A. Mohammed and W. K. Jones, "A dynamic programming - finite element procedure for the desing of nonlinear magnetic devices," *IEEE Transactions on Magnetics*, vol. 26, no. 2, pp. 666-669, March 1990.

Linear Constraints - Gradient Technique for the Inverse Problem of Design Optimization

A. A. Arkadan S. Subramaniam - Sivanesan
Dept. of Electrical and Computer Engineering
Marquette University
Milwaukee, WI. 53233.

ABSTRACT

Classically, the electromagnetic field problem is posed as a direct one in which the device is given and the performance of the device is predicted using numerical analysis techniques. However, in real engineering electromagnetic applications, the problem is posed as an indirect one where the performance is given and the device optimum design parameters are desired. In the design optimization procedure, the indirect problems are also known as inverse problems and are solved by optimizing an object function, which is based on the given performance, with respect to some chosen design parameters. Nowadays deterministic and nondeterministic methods are used for the optimization procedure.

This paper will present an overview of the deterministic gradient based optimization technique. Further difficulties in implementing the technique will be discussed and the results of two case studies employing linear constraints will be presented.

INTRODUCTION

The conventional approach in solving engineering design problems can be classified as direct one. The designer chooses an initial design and modifies the design in such a way to satisfy an expected performance. The modification is based on some heuristic rules and it is a trial and error method [1]. The major drawback of this approach is that the final design hardly satisfies the expected performance. In addition to this, the heuristic rules are based on experience and they are not sufficient enough to achieve an optimum design [2]. Recently, the deterministic and several non-deterministic approaches for design optimization were reported in the literature. Non-deterministic methods do not use the gradients for the optimization. Even though they do not use the computationally expensive gradient, they may also become expensive for a design problem with large number of parameters. However, the application of these non-deterministic methods cannot be avoided for the inverse problems with object functions which have a global minimum and several unrealistic local minima [3, 4]. In this paper the gradient based deterministic approach for the design optimization is discussed.

In the indirect approach the design problem is posed as an inverse one where the aim is to predict the design of a device in such a way to satisfy a given performance as best as possible [1-3, 5-7]. To do so an initial design is chosen and repeatedly modified in a formal manner. Here, at each step, the modification of the device is done based on some analytical methods which have some theoretical background [2]. In the indirect approach the problem is mathematically formulated as an inverse problem and a method based on the sensitivity analysis is applied to optimize the device [1-3, 5-7].

In this work, the indirect design approach for solving the inverse problems is used in the design optimization of electormagnetic devices. To perform the optimization in a formal manner,

(i) the configuration of the device is defined in terms of some chosen design parameters, $\mathbf{p}$, and,
(ii) the performance is expressed as a function, $\mathbf{f(p)}$, in terms of some electromagnetic parameters such as capacitance, inductance, magnitude and/or phase of electromagnetic fields, etc. Then a suitable expression for the desired performance, $\mathbf{f_d(p)}$, is also chosen.
(iii) a suitable optimization procedure is applied to find values of $\mathbf{p}$ in such a way that the corresponding $\mathbf{f(p)}$ is close to $\mathbf{f_d(p)}$ as best as possible.
(iv) a design evaluation criteria, $\mathbf{F(p)}$, which is based on the comparision of $\mathbf{f(p)}$ to $\mathbf{f_d(p)}$ is defined. In practice, the evaluation criteria or object function, $\mathbf{F(p)}$, is chosen in such a way that the optimum design satisfies $\mathbf{F(p)}$ at its extremum point.

The efficient deterministic optimization techniques are based on the computation of the gradient of the function F(**p**) which has to be extremized. In other words, the deterministic methods of the Mathematical Programming requires the gradient of the object function to find the search direction in the optimization. To reduce the cost of the optimization other methods such as Sequential Approximate Optimization (SAO) were used [5].

Sequential Approximate Optimization (SAO)

In the 60's and 70's, the gradient of the object function was computed by perturbing one of the design parameters, **p** at a time [1-3, 5-7]. It is clear that the gradient computation requires the evaluation of F(**p**) hundreads of times and each one needs expensive field computation. Sequential Approximate Optimization (SAO) overcomes this difficulty by analyzing the device for a number of sets of values **p** and predicting the response at some other values of **p** [5, 8, 9]. In SAO, F(**p**) can be approximated either by

(i) fitting a curve with different values of the function, f(**p**) for different sets of **p**, or by

(ii) expressing F(**p**) as a Taylor's series expression of f(**p**) with respect to an initial design with the parameters, $\mathbf{p_0}$ and using the higher order derivatives $f'(\mathbf{p_0})$, $f''(\mathbf{p_0})$,....,$f^{(n)}(\mathbf{p_0})$.

Fast reanalysis techniques, which are among the SAO use the field solution corresponding to **p** to evaluate the field solution corresponding to the parameter values, (**p**+Δ**p**). These techniques are used in static and eigenvalue problems [5]. In this approach, the field corresponding to the set of parameters **p** is evaluated as a solution of the global system, $\mathbf{P}\phi=\mathbf{Q}$. Then the global system corresponding to the parameters, (**p**+Δ**p**) is written in terms of the sensitivities, $\partial\mathbf{P}/\partial\mathbf{p}$ and $\partial\mathbf{Q}/\partial\mathbf{p}$, and the difference vectors $\Delta\phi$ and Δ**p**. The new system has more unknowns than the equations and it can be solved for the $\Delta\phi$ and Δ**p**, if one can obtain some relationships between these unknowns.

SAO give reasonable results for inverse problems having small number of design parameters. But these techniques may become expensive for designs having large number of parameters. In the application of Fast reanalysis techniques one may have to make several assumptions to derive the relationships in between the unknowns. These assumptions may simplify the problem too much and therefore the optimum design may not be practically implemented. To overcome these difficulties the Inverse Problem Methodology (IPM) was introduced [6,7].

Gradient based Inverse Problem Methodology (GIPM)

The Inverse Problem Methodology, the formal method, to solve the inverse problems was evolved in 1989 [6]. In this method, the simple least square based object function, F(**p**) is defined in such a way that the optimum design satisfies F(**p**) at its minimum. In most of the applications, the object function, F(**p**), is differentiable with respect to **p**. The methodology uses this differentiable property of the local matrix equation of the differential [7] or integral methods [10] of the electromagnetic field computation. Eventually the global matrix equation, $\mathbf{P}\phi = \mathbf{Q}$, is differentiated to obtain the derivative of F(**p**). In other words, $\mathbf{P}\phi = \mathbf{Q}$ is analytically differentiated with respect to each of the design parameters. In the direct approach for gradient computation, the differentiated system is solved for the derivative of the field variable with respect to the parameters. Then the gradient of the object function, ∇F(**p**), is computed using these derivatives. Manipulation of the differentiated system results in a matrix equation of the form, $\mathbf{P}(\partial\phi/\partial\mathbf{p}) = \mathbf{R}$. Therefore, solving for the gradient, $(\partial\phi/\partial\mathbf{p})$ is simplified as solving a sytem, $\mathbf{P}(\partial\phi/\partial\mathbf{p}) = \mathbf{R}$ which has the same matrix **P** as that of the original global matrix equation, $\mathbf{P}\phi = \mathbf{Q}$. In otherwords, the same matrix equation is solved several times for different right-hand-side vectors. The IPM reduces the cost of the gradient computation and makes the deterministic methods applicable for the design problems with a large number of parameters. In this section the direct approach for the gradient computation is introuduced; another one known as adjoint approach for the gradient computation will be discussed later.

Method Implementation

As it was mentioned before, the first step of implementing the Gradient based Inverse Problem Methodology (GIPM) for a design optimization problem is choosing **p**, f(**p**) and F(**p**). Then a set of initial values, $\mathbf{p_0}$ are chosen for **p** and then the following procedure is repeated until the optimum design is obtained:

i. Create the mesh for the differential or integral method, form the global matrix equation , $\mathbf{P}\phi = \mathbf{Q}$ and solve for the electromagnetic state variable, ϕ.
ii. Evaluate the object function, $F(\mathbf{p})$, and check whether the design is optimum or not. If the design is an optimum one then stop.
iii. Evaluate the right hand side, $\mathbf{R}$, corresponds to the differentiated system, $\mathbf{P}(\partial\phi/\partial\mathbf{p}) = \mathbf{R}$ and solve for the gradient, $(\partial\phi/\partial\mathbf{p})$. Then compute the gradient, $\nabla F(\mathbf{p})$ using, $(\partial\phi/\partial\mathbf{p})$. A set of new values for the design parameters are given by $\mathbf{p}_{new} = \mathbf{p} - \alpha(\nabla F(\mathbf{p}))'$
iv. Repeat the steps (i). - (iii). until the optimum is reached.

At each iteration of this optimization procedure, the design parameters vary, so a new mesh has to be created for the field computation in step (i). The published literature shows at each step, if the mesh is created independently then the resulting object function may become non smooth with several unrealistic local minima [11, 12]. In [11], the necessity of imposing some regularity constraints implicitly in the mesh by maintaining the mesh topology unchanged throughout the optimization procedure was mentioned. Further, in [12], it was proved that the difficulty of having the local minima can be improved by maintaining the mesh topology.

In some applications, it was observed that the optimum design obtained with the above mentioned regularity constraints may not be smooth enough for practical purposes, even though it satisfies the performance criteria [15, 16]. It was shown that this difficulty is caused by the independent movement of finite element mesh nodes which are having the coordinates as one of the design parameters [15]. Design Element Technique (DET) [15] and Structural Mapping Technique (SMT) [16] are used to overcome this difficulty. SMT has its drawback of using three variables per each node of the finite element mesh. In the DET, a suitable design element is defined by grouping some of the finite elements and the movements of the nodes of the design element are not independent any more. In other words, the movement of the nodes are constrained implicitly. In this paper, it is demonstrated through two example that imposing some linear constraints explicitly on these surfaces in such a way to maintain their smoothness, guarnatees a realistic and practical optimum design.

Sensitivity Derivatives

In the previous sections, the GIPM was introduced as a formal approach to solve inverse problems by choosing some design parameters, $\mathbf{p}$, and defining an object function, $F(\mathbf{p})$, based on the given performance criteria. It is obvious that the electromagnetic fields of a configuration depends on $\mathbf{p}$. The performance, $f(\mathbf{p})$, is expressed in terms of some electromagnetic parameters. Therefore, simply it can be considered as a function of the electromagnetic field, ϕ, and expressed as $f(\phi(\mathbf{p}),\mathbf{p})$. Eventually, the object function, $F(\mathbf{p})$, which is the design evaluation criteria, takes the form,

$$\mathbf{F}(\mathbf{p}) = \mathbf{F}(f(\mathbf{p}),f_d(\mathbf{p}),\mathbf{p}) = \mathbf{F}(f(\phi(\mathbf{p}),\mathbf{p}),f_d(\phi(\mathbf{p}),\mathbf{p}),\mathbf{p}) \equiv \mathbf{F}(\phi(\mathbf{p}),\mathbf{p}) \tag{1}$$

and the most simplest form of $\mathbf{F}$ is a quadratic expression which compares $f(\mathbf{p})$ and $f_d(\mathbf{p})$ in least squares sense.

Even though the computation of the finite-difference approximations of sensitivities are simple and accurate [5], they are computationally expensive. Therefore, the analytical derivatives are frequently used in the GIPM to reduce the cost.

Using the chain rule of differentiation, the derivative of the object function, $d\mathbf{F}(\mathbf{p})/d\mathbf{p}$, is given by

$$\frac{d\mathbf{F}}{d\mathbf{p}} = \frac{\partial\mathbf{F}}{\partial\mathbf{p}} + \frac{\partial\mathbf{F}}{\partial\phi}\frac{\partial\phi}{\partial\mathbf{p}}. \tag{2}$$

The first term of (2) is easy to obtain or in most of the cases zero [5, 7], the computation of the second term is discussed here.

The global matrix equation of the differential or integral method is of the form,

$$\mathbf{P}\phi = \mathbf{Q}. \tag{3}$$

Differentiating (3) with respect to $\mathbf{p}$ results,

$$\mathbf{P}\frac{\partial\phi}{\partial\mathbf{p}} + \frac{\partial\mathbf{P}}{\partial\mathbf{p}}\phi = \frac{\partial\mathbf{Q}}{\partial\mathbf{p}}. \tag{4}$$

Substituting (4) in (2) gives,

$$\frac{d\mathbf{F}}{d\mathbf{p}} = \frac{\partial\mathbf{F}}{\partial\mathbf{p}} + \frac{\partial\mathbf{F}}{\partial\phi}\mathbf{P}^{-1}\left[\frac{\partial\mathbf{Q}}{\partial\mathbf{p}} - \frac{\partial\mathbf{P}}{\partial\mathbf{p}}\phi\right] \tag{5}$$

Eq. (4) can be solved for $(\partial\phi/\partial\mathbf{p})$ since ϕ is already known by solving (3) and the other two sensitivity terms are computable by evaluating the sensitivities of the local matrices element by element. In the direct approach for the gradient computation, $(d\mathbf{F}/d\mathbf{p})$ is evaluated by solving (4) for $(\partial\phi/\partial\mathbf{p})$ and substituting it in

(2). But this approach becomes inefficient in design optimizations with large number of **p** because (4) has to be solved n (= number of parameters) times in each iteration [3].

In the adjoint approach, the following equation is solved for the adjoint vector, λ, corresponding to **F**

$$\mathbf{P}\lambda = \frac{\partial \mathbf{F}}{\partial \phi}, \tag{6}$$

then the gradient is computed by substituting λ for $(\partial \mathbf{F}/\partial\phi)\,\mathbf{P}^{-1}$ in (5):

$$\frac{d\mathbf{F}}{d\mathbf{p}} = \frac{\partial \mathbf{F}}{\partial \mathbf{p}} + \lambda^t\left[\frac{\partial \mathbf{Q}}{\partial \mathbf{p}} - \frac{\partial \mathbf{P}}{\partial \mathbf{p}}\phi\right]. \tag{7}$$

The gradient of a constraint, G can be evaluated in a similar way and it is obvious that the adjoint approach reduces the cost as it requires only one matrix solution.

Case Studies

In this work, design optimization of an electromagnet and a magnetic pole face are considered as examples. In both the cases the objective is to obtain a constant flux density in the air gap. In the first example in addition to this objective minimization of the leakage flux is also considered as a second objective.

Design Optimization of a Magnetic Circuit

The objective is to design a magnetic circuit for a constant flux density of B = 1.0T in the air gap with a minimum leakage inductance. The design parameters chosen for the optimum design are shown in Fig. 1. Four measurement points are chosen along the air gap, (shown by a dashed line in Fig.1) then the values of the computed and desired flux densities are compared in the least squares sense. The leakage inductance is given by [14]

$$L_{leakage} = \frac{N[(A_A - A_B)-(A_C - A_D)]}{I} \tag{8}$$

where

A_A, A_B, A_C and A_D are the MVPs at the points **A**, **B**, **C** and **D** respectively (Fig. 1) and N is the number of turns.

The object function can be simply defined as

$$F = F(B(\mathbf{p}),A(\mathbf{p})) = F_1 + F_2 \tag{9a}$$

where

$$F_1 = \frac{1}{2}\sum_{i=1}^{n}\left(B^{\,i}_{computed} - B^{\,i}_{desired}\right)^2 \quad \text{and} \quad F_2 = \frac{1}{2}\left[\frac{N[(A_A - A_B)-(A_C - A_D)]}{I}\right]^2$$

The derivative is given by

$$\frac{dF}{d\mathbf{p}} = \sum_{i=1}^{n}\left[B^{\,i}_{computed} - B^{\,i}_{desired}\right]\left(\frac{\partial}{\partial \mathbf{p}} B^{\,i}_{computed}\right) + \frac{N}{I}\left[\frac{N[(A_A - A_B)-(A_C - A_D)]}{I}\right]\left[\left(\frac{dA_A}{d\mathbf{P}} - \frac{dA_B}{d\mathbf{P}}\right)\left(\frac{dA_C}{d\mathbf{P}} - \frac{dA_D}{d\mathbf{P}}\right)\right] - \left[\frac{N[(A_A - A_B)-(A_C - A_D)]}{I}\right]\left[\frac{N[(A_A - A_B)-(A_C - A_D)]}{I^2}\right]\frac{dI}{d\mathbf{P}} \tag{9b}$$

MVP is chosen as the state variable for the FEM analysis and at any point in the solution region the flux density, **B** is calculated using the curl equation, $\mathbf{B} = \nabla \times \mathbf{A}$:

$$\frac{\partial \mathbf{B}}{\partial \mathbf{p}} = \frac{1}{B}\left[\left(\frac{\partial A}{\partial y}\right)\frac{\partial}{\partial \mathbf{p}}\left(\frac{\partial A}{\partial y}\right) + \left(-\frac{\partial A}{\partial x}\right)\frac{\partial}{\partial \mathbf{p}}\left(-\frac{\partial A}{\partial x}\right)\right] \tag{10a}$$

Within a first order triangular element, $(\partial A/\partial x)$ is approximated by the equation [14],

$$\frac{\partial A}{\partial x} = [b_1\ b_2\ b_3]\,[A_1\ A_2\ A_3]^t \tag{10b}$$

$$\frac{\partial A}{\partial y} = [c_1\ c_2\ c_3]\,[A_1\ A_2\ A_3]^t \tag{10c}$$

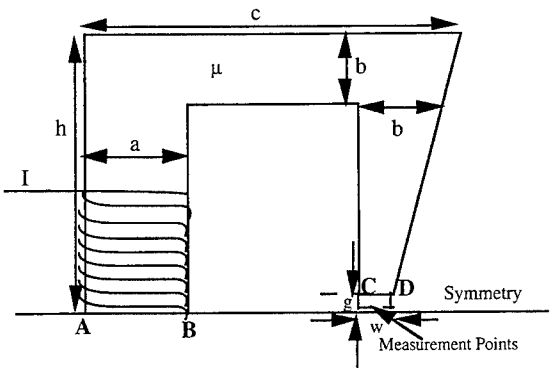


Fig. 1: Parametric description of an Electromagnet

where

$b_i = (y_{i1} - y_{i2})/(2A)$, $c_i = (x_{i2} - x_{i1})/(2A)$ i=1,2,3, i1 = i mod 3 +1, i2 = i1 mod 3 +1,

(x_i,y_i) are the vertices of the triangles

A is the area of the triangle

and A_i is the magnitude of the MVP at the i-th vertex.

Therefore,

$$\frac{\partial}{\partial \mathbf{p}}\left(\frac{\partial A}{\partial x}\right) = \left[\frac{\partial b_1}{\partial \mathbf{p}} \frac{\partial b_2}{\partial \mathbf{p}} \frac{\partial b_3}{\partial \mathbf{p}}\right] [A_1\ A_2\ A_3]^t + [b_1\ b_2\ b_3]\left[\frac{\partial A_1}{\partial \mathbf{p}} \frac{\partial A_2}{\partial \mathbf{p}} \frac{\partial A_3}{\partial \mathbf{p}}\right]^t \quad (10d)$$

$$\frac{\partial}{\partial \mathbf{p}}\left(\frac{\partial A}{\partial y}\right) = \left[\frac{\partial c_1}{\partial \mathbf{p}} \frac{\partial c_2}{\partial \mathbf{p}} \frac{\partial c_3}{\partial \mathbf{p}}\right] [A_1\ A_2\ A_3]^t + [c_1\ c_2\ c_3]\left[\frac{\partial A_1}{\partial \mathbf{p}} \frac{\partial A_2}{\partial \mathbf{p}} \frac{\partial A_3}{\partial \mathbf{p}}\right]^t \quad (10e)$$

Using eqns. (10a - 10e) and (9b), $(\partial \mathbf{B}/\partial \mathbf{p})$ and then $(d\mathbf{F}/d\mathbf{p})$ can be evaluated. Here p has 7 elements with no nonlinear constraints, so application of the adjoint method to calculate the gradient would be more efficient computationally in comparison to the direct method.

Do the parameters have to be constrained? In general, the FEM is applied within a closed boundary. In the GIPM, at each iteration the mesh is changed according to the values of the parameters. The values of some of the parameters take some of the nodes out of the exterior boundary or out of material regions of those particular nodes. To avoid the difficuties in modifying the mesh during the optimization procedure the following linear constraints are imposed on the parameters:

$a \geq 0.0,\ b \geq 0.0,\ c \geq 0.0,\ g \geq 0.0,\ h \geq 0.0,\ I \geq 0.0,\ w \geq 0.0$ (11a)

$b - 3w \geq 0.0$ (11b)

$c - 2a - 2b \geq 0.0$ (11c)

$h - 2b - g \geq 0.0$ (11d)

$h \leq 1.75E\text{-}1$ (11e)

In this case study, a multi-level optimization is implemented. GIPM is initially implemented to the design having initial parameter values (given in the first Row of Table 1). One can see (in Row 2 of Table 1) that the parameter h reached the value 1.749E-1 during that optimization procedure. Even though the active set

Table 1: Optimization Results

a	b	c	g	I	h	w	F1	F2 (L_{link})
5.000E-2	5.000E-2	3.000E-1	2.000E-3	1.0000E1	1.250E-1	1.000E-2	1.036E-1	4.157E-2
5.000E-2	5.000E-2	3.000E-1	2.000E-3	1.0000E1	**1.749E-1**	1.000E-2	8.476E-2	4.088E-2
4.996E-2	4.994E-2	3.000E-1	**2.399E-3**	1.0000E1	1.749E-1	**9.887E-3**	3.186E-3	3.820E-2
4.995E-2	4.992E-2	2.999E-1	**2.394E-3**	1.0000E1	1.749E-1	9.887E-3	3.148E-3	3.820E-2

Row 1: Initial Parametrs and the values of the object functions, F_1 and F_2 (eq. 9a);

Row i: Parametrs and the values of the object functions, F_i and F_2 after level (i-1), i=2,3,4;

(The parameters which have changed more during that level compared to the other ones are high lighted.)

strategy is applied for the optimization with the linear constraints (11a - 11e) the procedure stopped with the parameter values given in Row 2, because the parameter h has the dominant component, (dF/dh), of the derivative, (dF/dp). To continue the optimization procedure further this dominant component having the value of the order, 1E9, has to be discarded, that is , the component is set to zero. In other words, at the second level, the optimization procedure is proceeded further with 6 parameters. At the second level of the optimization procedure, changes were observed in the values of the parameters, g and w (Row 3 of Table 1). It also observed that the component, (dF/dw), has a higher value compared to the other components. So at the third level, both of the dominant components, (dF/dw) and (dF/dh) were discarded by setting to zero and the optimization was continued with 5 parameters and the optimized values are listed in Row 4.

Columns 7 and 8 shows that the object functions, F_1 and F_2, (eq. 9a) which correspond to both the objectives decrease during the optimization. At the third level it was observed that the object function, F_2, has a tendency to increase. Therefore, the optimum design obtained during the third level was considered as the final one and the authors stopped at the third level. One who concerns more on the objective corresponding to the object function, F_1 , can give more weights to F_1 and proceed further for a more accurate optimum design.

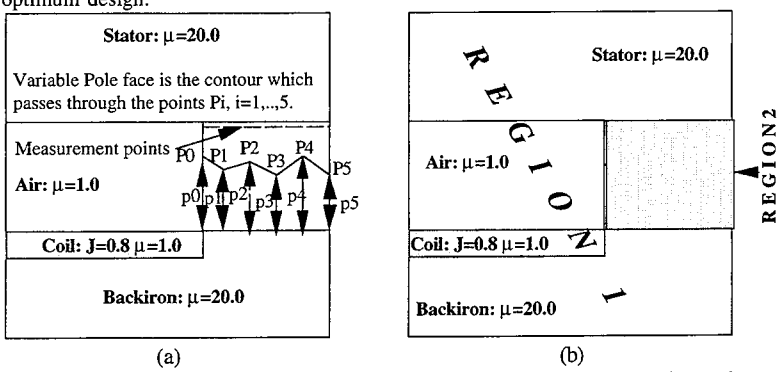


Fig. 2: a. Parametric description of a Pole Face **b.** Subregions of the solution region

Design Optimization of a Magnetic Pole Face

The objective is to design a magnetic pole face with a constant flux density of $B_y = 1.0T$, in the air gap. The design parameters chosen for the optimum design are shown in Fig. 2a. Here the width of the air gap is wider than the length, so n measurement points are chosen along the air gap, (shown by a dashed line in Fig.2a) then the values of the computed and desired flux densities are compared in the least squares sense. The object function is defined as [17, 18],

$$F = F(B_y(\mathbf{p})) = \frac{1}{2}\sum_{i=1}^{n}(B_{y_{computed}}^{i} - B_{y_{desired}}^{i})^2 \qquad (12a)$$

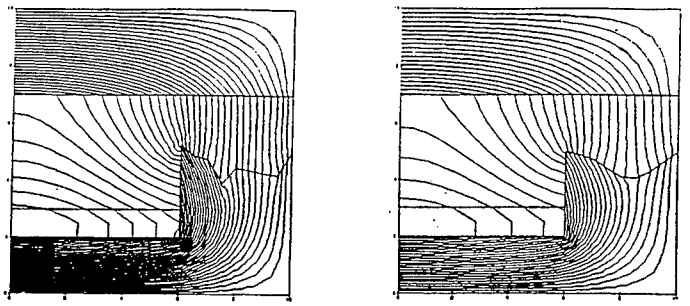
where n is the number of measurement points and ($B_{y_{computed}}^{i}$ and $B_{y_{desired}}^{i}$) are the y-component of the computed flux density and the desired flux density at the i-th measurement point.

The derivative is given by

$$\frac{dF}{d\mathbf{p}} = \sum_{i=1}^{n}(B_{y_{computed}}^{i} - B_{y_{desired}}^{i})\left(\frac{\partial}{\partial \mathbf{p}} B_{y_{computed}}^{i}\right) \qquad (12b)$$

Here also the MVP is chosen as the state variable for the FEM analysis and an approach similar to that of the first case study is applied to compute the derivative of the object function. In this case study, to avoid the difficuties in modifying the mesh during the optimization procedure the following linear constraints are imposed on the parameters:

$$p_0 = 5.0 \qquad (13a)$$



(a) (b)

Fig. 3: Optimum Designs **a.** with out linear constraints **b.** with the linear constraints

$$p_i \geq 0.01,\ i = 1,...,5 \qquad (13b)$$

The solution region is divided into two regions (Fig. 2b), Region 1 does not change during the optimization procedure and can be considered as fixed. The nodes of Region 2 are allowed to move homothetically along the y-direction [15]. This approach is considered here to maintain the mesh topology and to apply the subdomain technique [18] for the solution of the algebraic system.

The optimum design (shown in Fig. 3a) obtained with the maintenance of the mesh topology and the linear constraints, (13a) and (13b), seems to be not smooth enough and cannot be implemented [16-18]. But it was shown that the imposing the following quadratic constraints along the pole face smoothen the surface [17]:

$$\left[\frac{p_0 - p_i}{x_{pi} - x_{p0}} - \frac{p_i - p_{i+1}}{h_{i+1}}\right]^2 < \varepsilon, \qquad i=1 \qquad (14a)$$

and

$$\left[\frac{p_{i-1} - p_i}{h_i} - \frac{p_i - p_{i+1}}{h_{i+1}}\right]^2 < \varepsilon, \qquad i > 1 \qquad (14b)$$

where ε is a very small positive value, x_{pi} is the x-coordinate of the selected node P_i and h_i is the distance between the x-coordinates corresponding to the selected nodes P_{i-1} and P_i.

These quadratic constraints are equivalent to the linear constraints:

$$-\varepsilon < \left[\frac{p_0 - p_i}{x_{pi} - x_{p0}} - \frac{p_i - p_{i+1}}{h_{i+1}}\right] < \varepsilon, \qquad i=1 \qquad (15a)$$

and

$$-\varepsilon < \left[\frac{p_{i-1} - p_i}{h_i} - \frac{p_i - p_{i+1}}{h_{i+1}}\right] < \varepsilon, \qquad i > 1 \qquad (15b)$$

The active set strategy is applied to implement these linear constraints in the optimization procedure. The optimum design (shown in Fig. 3b) obtained with these linear constraints is smooth enough and the implementation of the linear constraints is very simple in comparison to the above mentioned structural mapping and design element techniques.

Conclusion

An overview of the deterministic gradient based optimization was given. Further difficulties in implementing the technique were discussed and the results of two case studies employing linear constraints

were presented. In the first case study, GIPM is successfully applied at multi-levels to optimize a magnetic circuit to obtain a constant flux density in a air gap with a low leakage inductance. It was shown that some design optimizations require multi-level optimizations to reach an optimum design, when some of the components of the derivative, (**dF**/d**p**), of the object function are dominant. In the second case study, some linear constraints are efficiently implemented to avoid the unrealistic optimum designs of the shape optimization of a magnetic pole face.

References

[1]. Eschenauer, H. A., "Structural Optimization - a Need in Design Progress?," in Eschenauer, H. A., Mattheck, C. and Olhoff, N., (eds.), *Engineering Optimization in Design Process, Proceedings of the International Conference Karlsruhe Nuclear Research Center, Germany, Sept. 3-4, 1990*, Lecture Notes in Engineering, Vol. 63, Springer-Verlag, New York, pp. 1-13.

[2]. Hernandez, S., "From CAD to CHAOSD: Structural design and optimization techniques," in Hernandez, S., ed., *Advanced Techniques in the Optimum Design of Structures*, Computational Mechanics Publications, Southampton, 1993, pp. 1-25.

[3]. Arkadan, A., Sareen, T. and Subramaniam, S., "Genetic Algorithms for Nondestructive Testing in Crack Identification," Accepted for publication in IEEE Trans. on Magn, Nov. 1994.

[4]. Arkadan, A., Chen, Y., Subramaniam, S. and Hoole, S. R. H., "NDT Identification of a Crack using ANNs with Stochastic Gradient Descient, " Accepted for publication in IEEE Trans. on Magn, May 1995.

[5]. Haftka, R. T., Gurdal, Z. and Kamat, M. P., *Elements of Structural Optimization*, Kluwer Acadamic Publishers, Doerdrecht, The Netherlands, 1990.

[6]. Gitosusastro, S., Coulomb, J. L. and Sabonnadiere, J. C., "Performance derivative calculations and optimization process," IEEE Trans. on Magn., Vol. 25, No. 4, July 1989, pp. 2834-2839.

[7]. Hoole, S. Ratnajeevan H., Subramaniam, Srisivane, Saldanha, Rodney, Coulomb and Sabonnadiere, "Inverse Problem Methodology and Finite Elements in the Identification of Cracks, Sources, Materials, and their Geometry in Inaccessible Locations," IEEE Trans. on Magn., Vol. 27, No. 3, May 1991, pp. 3433-3443.

[8]. Mlejnek, H. P., Jehle, U. and Schirrmacher, R., "Some Approaches for Shape Finding in Optimal Structural Design," in Eschenauer, H. A., Mattheck, C. and Olhoff, N., (eds.), *Engineering Optimization in Design Process, Proceedings of the International Conference Karlsruhe Nuclear Research Center, Germany, Sept. 3-4, 1990*, Lecture Notes in Engineering, Vol. 63, Springer-Verlag, New York, pp. 35-50.

[9]. Papalambros, Panos Y. and Wilde, Douglass, J., *Principles of Optimal Design : Modeling and Computation*, Cambridge University Press : New York, 1988.

[10]. Hoole, S. Ratnajeevan H., Subramaniam, S., "Inverse Problems with Boundary Elements: Synthesizing a Capacitor," IEEE Trans. on Magn., Vol. 28, No. 2, Mar. 1992, pp. 1529-1532.

[11]. Morrocco, A. and Pironneau, O., "Optimum Design with Lagrangian Finite Elements: Design of an Electromagnet," Comput. Meth. Appl. Mech. Eng., Vol. 53, 1985, pp. 119-148.

[12]. Hoole, S. Ratnajeevan, H., Weeber, Konrad and Subramaniam, S., "Fictitious Minima of Object Functions, Finite Element Meshes, and Edge Elements in Electromagnetic Device Synthesis," IEEE Trans. on Magn., Vol. 27, No. 6, 1991, pp. 5214-5216.

[13]. Salon, S. J. and Istfan, B., "Inverse nonlinear finite element problems," IEEE Trans. on Magn., Vol. 22, No. 5, Sept. 1986, pp. 817-818.

[14]. Hoole, S. Ratnajeevan, H., *Computer Aided Design of Electromagnetic Devices*, Elsevier Press: New York, 1989.

[15]. Haftka, R. T. and Grandhi, R. V., "Structural Shape Optimization - A Survey," Comput. Meth. Appl. Mech. Eng., Vol. 57, 1986, pp. 91-106.

[16]. Weeber, K. and Hoole, S. R. H., "A Structural Mapping Technique for Geometric Parametrization in the Synthesis of Magnetic Devices," Int. J. Num. Meth. Eng., Vol. 33, 1992, pp. 2145-2179.

[17]. Subramaniam, S., Arkadan, A. A. and Hoole, S. Ratnajeevan, H., "Optimization of a Magnetic Pole Face using Linear Constraints to avoid Jagged Contours," IEEE Trans. on Magn., Vol. 30, No. 5, Sept. 1994, pp. 3455-3458.

[18]. Weeber, K. and Hoole, S. Ratnajeevan H., "The Subregion Method in Magnetic Field Analysis and Design Optimization," IEEE Trans. on Magn., Vol. 28, No. 2, Mar. 1992, pp. 1561-1564.

SESSION 6:

COMPUTATIONAL ELECTROMAGNETICS APPLIED TO SHIP DESIGN

Chairs: J. Newcomb, J. Logan

EM Engineering Applied to Patrol Craft (PC-1)

Daniel Tam, Jodi McGee, Charles Azu
Naval Command, Control and Ocean Surveillance Center
Research, Development, Testing, and Evaluation Division (NRaD Code 822)
San Diego, CA

Mick Soyka
Naval Sea Systems Command
Arlington, VA

Abstract

This paper presents the electromagnetic engineering analysis of an HF communication antenna system on the PC-1 Coastal Patrol Class ship using NAVSEA Electromagnetic Engineering (EMENG) computer tools. Shipboard antenna system modeling techniques are addressed. The geometry of the ship is represented by a NEC-MoM wire grid model extracted from a 3-D solid drawing. Geometry and segmentation processing checks of the wire grid model are made simple using the Numerical Electromagnetic Engineering Design System (NEEDS), which color codes the model for visual analysis. Antenna performances are predicted by the Numerical Electromagnetic Code (NEC4), and the results are post-processed by NEEDS, which provides three-dimensional plots for visualization. Electromagnetic Compatibility (EMC) analysis of the co-located HF communications systems is then performed by the Communications Engineering Design System (COEDS) running the Cosite Analysis Model (COSAM 3.0).

Introduction

Much of the communications equipment onboard U.S. Navy ships operates at HF frequencies, where wavelengths range from 10 m (at 30 MHz) to 150 m (at 2 MHz). Because ships and objects typically found onboard are often of dimensions comparable to these wavelengths, the characteristics of the shipboard HF antennas are altered by their physical surroundings. In order to accurately predict antenna performance, the effects of the entire ship must be taken into account. This goal may be achieved through measurements performed on brass scale models of the ships and their antennas, which has been done for many years at NRaD. Alternatively, the ship may be modeled numerically by a wire grid, and calculations substituted for measurements of antenna parameters. This discussion steps through the process of creating a wire grid model of the PC-1 coastal patrol class ship, calculating antenna parameters, postprocessing and visualization of the results, and the use of these results to perform shipboard EMC analysis.

I. The Wire Grid Model

For the PC-1 project, the NEC-MoM wire grid model was extracted from a CAD-II 3-dimensional solid drawing. The shipyard-provided solid drawing is given in Figure 1 below. Using the Intergraph

Engineering Modeling System (EMS) 2.2 on the CAD-II workstation, the command "Extract Part of Curve" creates a line element from a portion of an existing curve. This is the first project to successfully utilize this technique, which resulted in the most accurate wire grid model developed for a ship in numerical modeling history. The PC-1 NEC-MoM numerical wire grid model consists of 1820 elements, as shown in Figure 2.

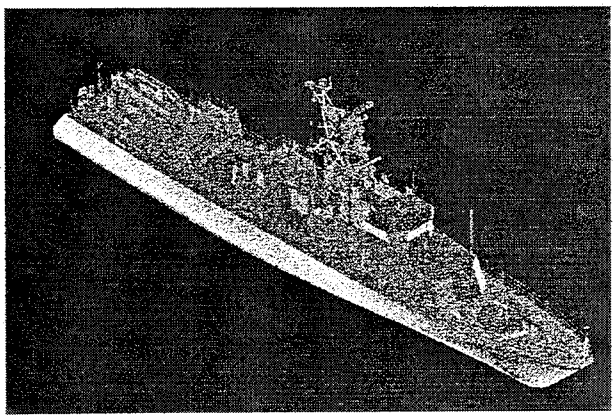


Figure 1. PC-1 Solid Drawing

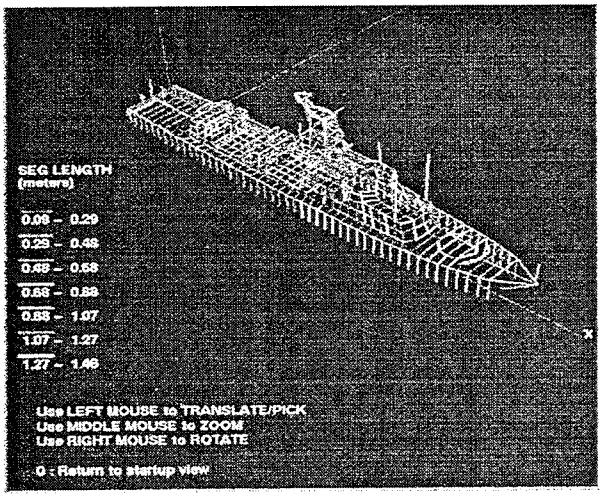


Figure 2. PC-1 NEC-MOM Wire Grid Model

II. Model Validation

The newly extracted wire grid model must be validated before it can be used to analyze the on-board antennas. The necessary checks are performed on NRaD's NEEDS (Numerical Electromagnetic Engineering Design System) workstation, which was developed under NAVSEA's EM Engineering program to assist in making the NEC-MoM process less tedious and more error-free. The geometry checks include verification of wire segmentation, radius, and connections. These are visual checks which involve color-coding the individual segments of the wire grid model. The topside engineer may thus tell by a glance where problems occur within the model.

In the segmentation check, each wire segment is color coded by length. For HF analysis, segment lengths of about one meter are desired (0.1 to 0.007λ for HF). Color coding allows for a quick check that most of the wires are one meter long and that none are outside the allowable range. For the wire radius check, almost all of the wires forming the ship's surface will show a radius of 0.16 meter (0.016 to 0.001λ), which has been chosen to produce the equivalent surface area for a one-meter wire spacing. The only wires which should be colored differently are the antennas and any other non-surface wires, for which the actual radii are entered. Finally, for the connections check the wire segments are color-coded to indicate: (a) both ends are connected, (b) one end is connected, or (c) the wire is completely unconnected to anything else. This check enables stray wires to be picked up as well as verification that the nodes of the wire grid mesh are properly joined. The color coding for connection of a single end indicates antennas, flagpoles, guns, and other non-surface objects which are only connected to other conductive structures on one end.

If problems are found in the wire grid model, the wires are simply modified using AutoCAD and then run through this process again, until no further errors occur.

III. NEC Calculations

Once an error-free wire grid model has been created, NEC4 is used to calculate HF antenna performances. For the PC-1 project, the two forward 23' HF whip antennas are designated P1 and S1 for port and starboard. The NEC-generated results include coupling between these antennas (see Figure 3). Additionally, the impedance of each antenna is calculated as a function of frequency by exciting the antenna under study and solving for the current distribution. Figure 4 shows the impedance of antenna P1, which is almost identical to the impedance calculated for S1, since the ship is symmetrical along its lengthwise axis. Antenna mismatch loss is calculated using the NEC impedance information. The mismatch loss and coupling data will be used later as part of the EMC analysis. Among the most interesting results provided by NEC calculations are the radiation patterns, which can be used as part of the communications system performance evaluation and link studies.

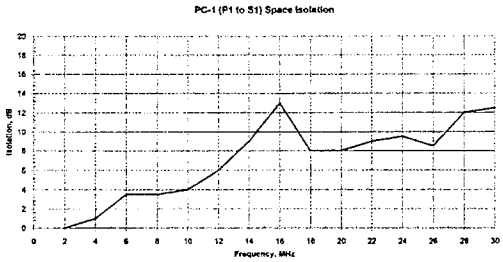


Figure 3. Antenna Coupling

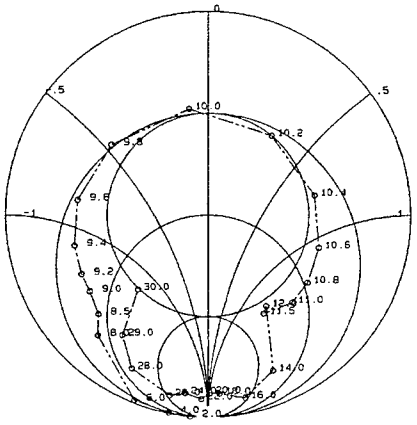


Figure 4. P1 Antenna Impedance

IV. Postprocessing and Visualization

Postprocessing of the NEC calculations is performed using the NEEDS workstation once more. This system has the capability of providing two- and three-dimensional plots of the ship along with the NEC-calculated results. This display is an important part of being able to interpret the large amount of data generated by a NEC run. For example, the near field generated by an onboard transmitter may be represented by color-coded dots of increasing size and intensity as a function of field strength, allowing for a visual interpretation of where the strongest fields occur. NEEDS allows the user to step through the frequency band, keeping the ship stationary and changing only the intensity and patterns of the near

field. Additionally, the display can be set to show only the fields above a certain threshold value, such as the level defined for Hazardous Electromagnetic Radiation for Personnel (HERP) or for Ordinance (HERO). A NEEDS-generated display of the near field due to the P1 antenna radiating at 400 watts and 14 MHz is shown in Figure 5.

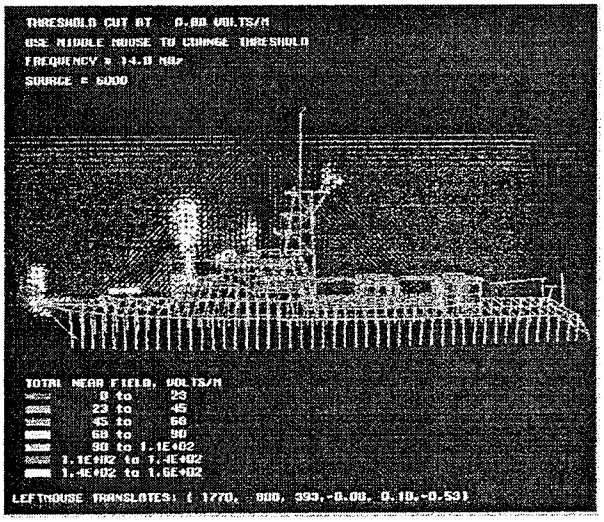


Figure 5. Near field due to P1 radiating at 400 W, 14 MHz

Among the other possibilities for 3-D, color-coded visualization using the NEEDS workstation are the current distributions, charges, near electric field, near magnetic field, and radiation patterns. A NEEDS visualization of the radiation pattern appears in Figure 6. For this plot, the relative magnitude of the field is represented by distance from the origin, and color-coding indicates the E-field phase.

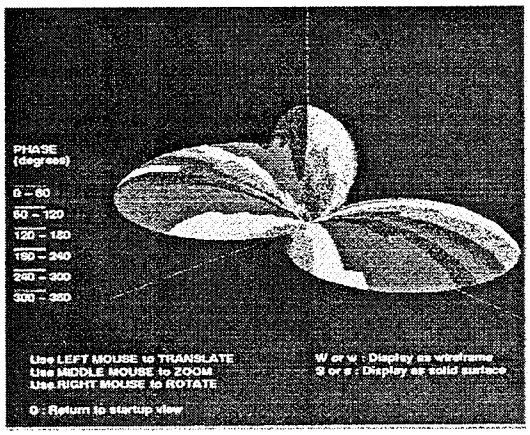


Figure 6. Radiation pattern due to P1 radiating at 400 W, 10 MHz

V. EMC Analysis Using COEDS

The Communications Engineering Design System (COEDS) workstation is another part of the NAVSEA EM engineering (EMENG) program. Electromagnetic Compatibility (EMC) analysis is performed to determine the effects of transmitters on co-located receive systems. In COEDS, a database is created from measurement or from specifications data for each piece of equipment in the communications subsystems. Mathematical models are built to describe the operation of receivers, transmitters, couplers, and antennas. Then the elements of different shipboard transmitting and receiving subsystems may be configured by selecting them from the database and connecting them in the form of a block diagram. The isolation between transmit and receive antennas calculated earlier using NEC may be input into the system, as well as antenna mismatch losses calculated from the NEC impedance data. Thus COEDS takes into account the effects of the shipboard environment on antenna behavior (through the incorporation of NEC data) as well as the behavior of the communications equipment.

COEDS may be used to compute the excess interference levels due to the following interference types: (1) receiver adjacent signal, (2) broadband transmitter noise, (3) spurious emissions, (4) spurious response, (5) receiver intermodulation, and (6) transmitter intermodulation. The goal of communications system design is that receiver performance be noise limited, i.e., that the interference due to on-board transmitters should be less than the maximum of receiver noise and ambient noise. In the design stage, the two major EMC interference interaction parameters which have a great impact are receiver adjacent signal and transmitter broadband noise.

If the COEDS results show that interference levels exceed the noise levels, several mitigation techniques are available. These include the following:

1. Equipment changes
2. Addition of filtering on the receive side
3. Addition of filtering on the transmit side
4. Change of antenna location to increase space isolation

5. Frequency management (increase of frequency separation between transmitter and receiver)
6. Reduction of transmitter power
7. Time management of equipment use
8. Compromise of design goals

Option 4 can be simulated using the NEC-MoM wire grid model, while the effects of options 1-3 and 5-6 can be computed with COEDS. In a single COEDS run, several of these options may be combined at once. In the case of the PC-1 EMC analysis, the interactions between the following transmit and receive configurations were calculated using COEDS:

Transmitters
1. Transmitting at 400 W
2. Transmitting at 200 W
3. Transmitting at 100 W
4. Transmitting at 50 W
5. Postselector filter added, 400 W
6. Postselector filter added, 200 W
7. Postselector filter added, 100 W
8. Postselector filter added, 50 W

Receivers
1. Baseline receiver
2. One preselector filter added
3. Two preselector filters added

COEDS calculates the interference interactions for every combination of these subsystems at a variety of user-chosen receiver-tuned frequencies and transmitter offsets. An interaction matrix for every combination of these transmit and receive systems is then formed, indicating the predicted interference levels in each case. From these results, an accurate assessment of shipboard electromagnetic compatibility is accomplished.

References

Li, S. T., J. C. Logan, and J. W. Rockway. "Automated Procedure for Shipboard Exterior Communication RF System Design", IEEE Transactions on Electromagnetic Compatibility, Vol. EMC-22, No. 4. November 1980.

Li, S. T., J. C. Logan, and J. W. Rockway. "Ship EM Design Technology", Naval Engineers Journal, May 1988.

Rockway, J. W. and D. W. DuBrul. "Performance Prediction Analysis For Shipboard Antenna Systems", Naval Engineers Journal, October 1977.

Tam, D. and C. Azu. "HF Analysis of the PC-1 Coastal Patrol-Class Ship Using the Numerical Electromagnetic Design System (NEEDS) and the Communication Engineering Design System (COEDS)", NRaD Technical Note 1748, September 1994.

Shipboard Antenna Pattern Visualization and Analysis

L. Russell, J. Logan, J. Rockway, D. Schwartz
Naval Command Control and Ocean Surveillance Center
RDT&E Division
San Diego, Ca 92152-5000

ABSTRACT

New visualization tools are being developed to aid in interpreting the output from computational codes and measurements used in the design and analysis of the electromagnetic topsides of Navy ships. One of the principal outputs of interest is the radiation pattern of shipboard antennas systems (e.g., communication, electronic warfare, surveillance, ...). A large quantity of data can be generated by both computational electromagnetic codes and measurement. This paper demonstrates the support that advanced visualization provides to the analysis of shipboard antenna patterns.

1.0 INTRODUCTION

The objective of a ship topside antenna study is to determine an antenna's impedance, near fields, radiation pattern, and coupling to other antenna elements. These technical parameters are necessary to determine the performance of the total shipboard antenna system. Impedance can be related to component compatibility. Near fields are used to evaluate radiation hazards to personnel, fuel and ordnance. Coupling between antennas is necessary for the evaluation of the effect of electromagnetic interference. The radiation patterns are used as part of an evaluation of the link performance of the individual antenna system.

Both computational electromagnetic codes and measurement can generate a large quantity of pattern data. Fast and efficient analysis of this large amount of data requires sophisticated visualization techniques. A user friendly interface improves utilization of the entire visualization capability. Initial visualization programs were written using the Silicon Graphics (SGI) proprietary IRIS GL (Graphics Library). The SGI IRIS Inventor, OSF Motif and MATLAB are now being used to provide user friendly scene interaction for a suite of electromagnetic visualization programs. Inventor is a C++-callable library of functions which allows simplified development of GL-based scene building and scene interaction. MATLAB is a computation environment for numeric computation, data analysis, and visualization. Commensurate with the increasing capability in visualization tools is the need for an easily accessible user interface.

2.0 THREE DIMENSIONAL SURFACE

Two types of three dimensional surfaces can be used for displaying three dimensional pattern data. The radiation pattern is complex (i.e., magnitude and phase) data which is a function of theta and phi. The theta angle is defined from the z-axis toward the x-y plane. The phi is defined from the x-axis in the x-y plane. The radiation pattern also has two components in the theta and phi directions, respectively. For a given component the pattern can be displayed as a colorful three dimensional polar surface. The distance from a point on the surface to the origin is proportional to the log of the magnitude of the data at that point. The color is coded to the phase of the data. This creates a very interesting display as shown in figure 1. This display can be rendered as a solid or as a wire grid. It can be rotated to allow it to be viewed from any direction. Depending on the user's preference, there are several variations on this display. The color can be coded to magnitude to emphasize magnitude. Another display emphasizes the elevation angle by coding the color to elevation angle. A second type of three dimensional display plots the magnitude as a surface on a rectangular grid of theta and phi values. As displayed in figure 2, this type of three dimensional plot helps to visualize the sidelobe and backlobe structure of directional antennas. The principal sidelobes and backlobes can be emphasized by applying a threshold to this type of plot and only displaying magnitudes above the threshold.

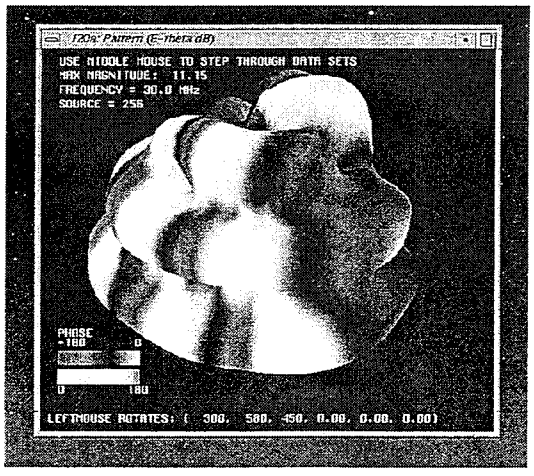


Figure 1. Three dimensional polar radiation pattern.

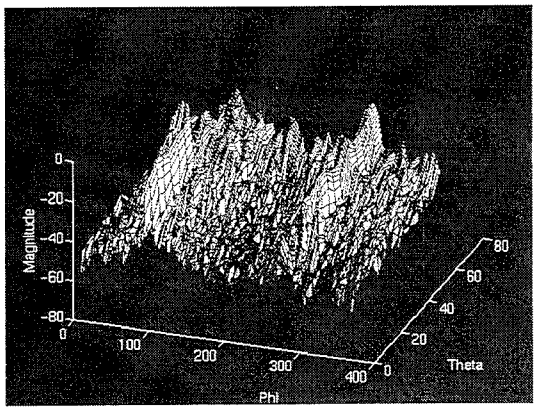


Figure 2. Three dimensional surface radiation pattern.

3.0 TWO DIMENSIONAL SURFACE

Several two dimensional displays for visualization radar cross section (RCS) have been suggested [1]. As a variation of these suggested RCS displays, the radiation pattern could also be displayed as a two dimensional polar surface. The distance from the center is the theta angle and the distance around a circle at a given distance from the center is the phi angle. The color is coded to the magnitude of the radiation pattern. This again creates an interesting display. The two dimensional polar display for figure 1 is given in figure 3.

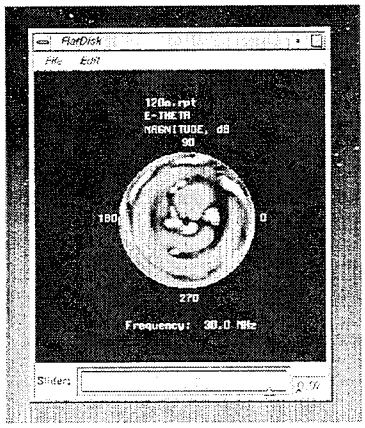


Figure 3. Polar display of radiation pattern.

4.0 THRESHOLDING

The three dimensional radiation pattern display provides wonderful qualitative information regarding the performance of an antenna system, but often what is needed is quantitative information. As a result a three dimensional thresholding technique has been developed using a semitransparent thresholding grid. This allows a reference antenna such as a quarter wave monopole to be overlaid with the original display. The reference antenna provides a threshold for the pattern. The reference can be stepped in 1 decibel step sizes. This allows a quick interpretation of the antenna performance for a given pattern at a particular theta and phi value. An example of this display is shown in figure 4. The portion of the radiation pattern above the threshold is quite apparent.

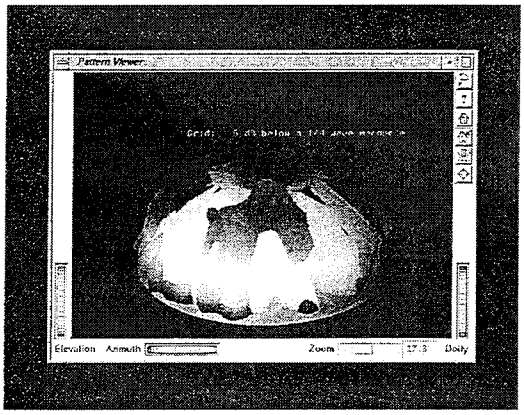


Figure 4. Radiation pattern with thresholding grid.

5.0 SLICING

In this section two methods are described for presenting a "slice" of the three dimensional data to better visualize aspects of the radiation pattern. A visualization capability was developed for interactive slicing of the radiation pattern on planes with arbitrary orientation. This would allow the user to quickly analyze the directional performance of an antenna system. This capability would also facilitate inclusion of radiation pattern data in reports and presentations. Using IRIS Inventor on the Silicon Graphics workstation, a program was developed to provide interactive slicing through three dimensional radiation pattern data. The name of this program is PatternCut. Data is displayed on a polar plot. A slider bar is provided to allow the user to interactively slice through the data. A version of the program exists which displays the data on a linear graph. This version is named LinCut. Examples of the displays

generated by PatternCut and LinCut are shown in figures 5 and 6, respectively.

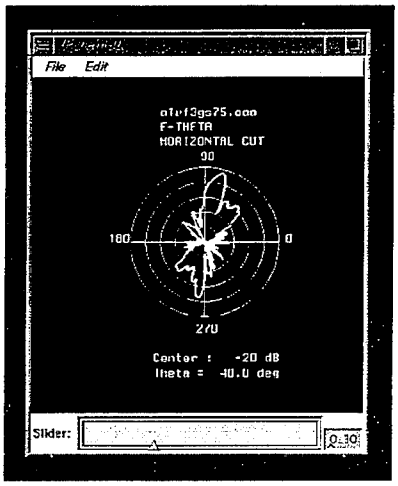


Figure 5. Example display generated by PatternCut.

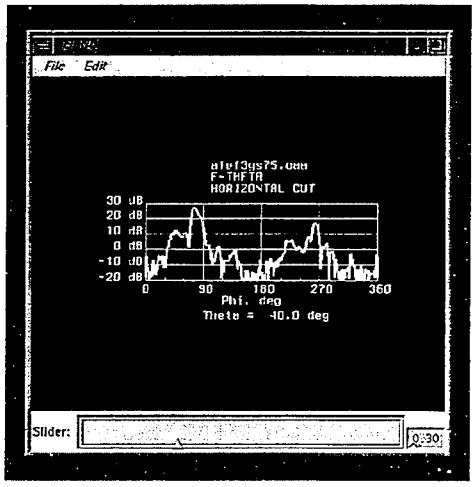


Figure 6. Example display generated by LinCut.

The radiation pattern which is displayed is read from a user-specified file. At this time the program is designed to accept the format for the file created by the Numerical Electromagnetic Code - Basic Scattering Code (NEC-BSC) [2]. The output pattern files

created by NEC-BSC have the extension .oaa. The first line of each file is a text header line. After that each row of the file contains data for a particular theta and phi location. Each output file contains six columns of data. These six columns are for: theta, phi, E-theta (magnitude in dB), E-theta (phase in degrees), E-phi (magnitude in dB), E-phi (phase in degrees).

The user may provide the name of the file containing the pattern data on the command line when first starting the program or a Motif File Selection Dialog Box will appear. When the program is initiated, a window opens. This window has a pull-down menu bar at the top. Below the menu bar is a graphics display area and below this display area is a slider widget.

The menu bar has two items: File and Edit. The sub-menu under File consists of Open and Quit. The hot key for Open is 'Alt + o'. The hot key for Quit is 'Alt + q'. Selecting Open causes a Motif File Selection Dialog Box to appear. Selecting Quit closes the program. The submenu under Edit consists of three sets of radio button menus. The first set lets the user choose between displaying the E-Theta or E-Phi component of the data. E-Theta is the vertical component of the data; E-Phi is the horizontal component of the data. The second set of radio buttons allows the choice of a Horizontal Cut or a Vertical Cut. The final set of radio buttons allows the user to select between Change Cut or Animate.

If Horizontal Cut is selected, the radiation pattern is displayed on a conical cut. The slider bar is used to select the theta value. All data at that given theta value is displayed. In the display window the angle around the outside of the polar plot is phi. The polar plot displays the data in decibels (dB) and has a 50 dB dynamic range. If Vertical Cut is selected, the data is displayed on a vertical cut. The slider bar is used to select the phi level. All data at that given phi value is displayed. In this case the angle around the outside of the polar plot is theta.

If more than one file has been selected (such as by repeated use of the File/Open menu choice), then the Animate option allows the user to slide through the radiation pattern in the several files. In this case the slider bar is used to select the file. This is of use in cases where a sequential series of output files has been created. An example of this occurs when a radar system is sweeping through a range of angles and an analysis has been run at incremental scan steps. Animating the data in this fashion allows for analysis of time dependent effects.

Selecting the radio button Change Cut returns to the case where the slider bar changes either theta or phi (depending on whether Horizontal Cut or Vertical Cut is selected).

A vertical slice as a range-height radar surface is presented in figure 7 [3]. This plot emphasizes the significance of the beam pattern in the low elevation angles and was formed using MATLAB.

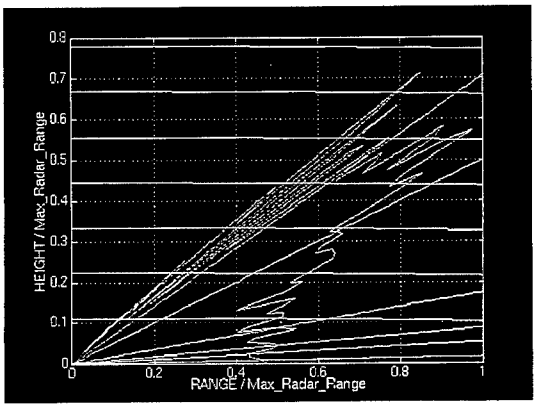


Figure 7. Radar range-height plot.

7.0 SUMMARY

Although much of the presented visualization products were developed on a Silicon Graphics workstation, this software is currently being converted to a format usable on many UNIX workstations. This will be accomplished by converting from SGI's proprietary IRIS GL and Inventor to the multiplatform versions OpenGl and Open Inventory. MATLAB is already available on a variety of platforms. As a future objective, the radiation pattern visualization options will be consolidated into a single program with a graphical user interface.

The radiation pattern is one of several measures of antenna performance that an engineer uses to evaluate a given antenna design. Several different forms of radiation pattern visualization have been presented. A measure of performance of a given visualization of a radiation pattern is its value in guiding an engineer to an optimal design. High performance visualization enhances an engineer's appreciation for some of the design criteria utilized in antenna design.

8.0 REFERENCES

1. C. L. Larose, S. R. Mishra, and C. W. Trueman, "Graphics for Visualization RCS as a Function of Frequency and Angle," IEEE Antennas and Propagation Magazine, Vol. 36. No. 3, June 1994.

2. R. J. Marhefka, "Numerical Electromagnetic Code - Basic Scattering Code User's Manual", Ohio State University Electroscience Laboratory.

3. M. Skolnik, "Radar Handbook", McGraw-Hill Publishing Company, New York, 2nd Edition, 1990.

SESSION 7:

FINITE DIFFERENCE TIME DOMAIN

Chair: J. Beggs

Computational Analysis of Radiation from an Elliptical Shaped End Radiator

S.A. Blocher, E.A. Baca, J.H. Beggs[1]
Phillips Laboratory Electromagnetic Sources Division
Kirtland AFB, NM 87117-5776

Abstract

The Finite Difference Time Domain (FDTD) method has been extensively used to study radiation from a variety of radiating structures, including various shaped end radiators (SER)[1]. In this paper we discuss the application of FDTD to a novel high gain SER, which efficiently radiates the TM_{01} mode. This structure is a transition from a circular to elliptical waveguide which feeds an empirically shaped radiating surface. Included will be descriptions of the geometry, techniques for generating the computational domain, and direct comparisons between FDTD calculated results, on an orthogonal Yee grid, and the experimentally measured directivity of this radiator. Additionally, comments will be made regarding the application of such a radiator as well as the usefulness of FDTD for analyzing such antennas.

1 Introduction

As needs in the RF propagation community continue to grow, so will the requirement for compact efficient non fundamental mode radiating antennas. Many RF power sources produce energy in the circularly symmetric TM_{01} mode within a cylindrical waveguide. The standard approach to radiation involves mode conversion to the fundamental TE_{11} mode and radiation from a conical horn. Alternatively, one may efficiently radiate the TM_{01} mode directly into a high gain, high quality beam from an SER. As with any antenna design process, numerical simulations can provide important information regarding performance characteristics. Due to the ever increasing cost of experimental investigations, well planed and executed computational analysis tend to guide the antenna designer in their efforts. With this in mind, we have

[1]With the Department of Electrical and Computer Engineering, Mississippi State University, Mississippi State, MS 39762.

been utilizing the FDTD method to study the radiation characteristics from an in-house developed novel radiating device. In this paper we will show how FDTD is suited for investigations of this sort and provide some preliminary results of the simulations compared with experiment. Additionally we will include discussions of how the numerical simulations are augmented through the use of symbolic mathematical packages such as Mathematica©to both develop the computational grid as well as analyize the data.

2 Shaped End Radiator

The SER features an elliptical waveguide transition from some input eccentricity to a final output eccentricity. The eccentricity is given by

$$e = \frac{\sqrt{a^2 - b^2}}{a} \tag{1}$$

where a is the minor axis radius and b is the major axis radius. The output transition then feeds an approximately shaped radiating surface. This particular SER, as shown in Figure 1, has a zero input eccentricity (cylindrical waveguide) and smoothly transitions over approximately three guide wavelengths to $e = 0.9$ before scattering onto a radiating surface that is approximately an offset rotated parabolic ellipsoid. The resulting geometry then only be adequately described as a spoon shaped-end radiator (SSER).

The input SER waveguide is fed with a TM_{01} cylindrical waveguide mode. For each TM_{mn} mode of a cylindrical waveguide, there exists a corresponding even and odd mode (TM^e_{mn} and TM^o_{mn} respectively) of an elliptical waveguide except for the TE_{01} and TM_{01} modes for which there is only a corresponding even mode. Since a cylindrical waveguide is an elliptical waveguide of zero eccentricity, the input TM_{01} mode can be viewed as a TM^e_{01} elliptical waveguide mode. The SER functions by maintaining the input TM^e_{01} elliptical through the transition until it is scattered onto a radiating surface inducing a current distribution that leads to a highly directive, high quality beam. to help maintain the TM^e_{01} mode, the present SSER is designed so as to hold a constant mode impedance of 296 Ω through the transition. The remainder of the SSER is then empirically shaped. The actual SSER input waveguide diameter is 1.44λ and the output aperture is approximately 4.75λ by 4.00λ

at the 18 GHz test frequency. Using the largest aperture dimension and the standard criterion for the near to far field boundary ($r \geq 2D^2/\lambda$), we see that the far field is any distance greater than 32λ. Since the wavelength is 0.01667 meters, the far field for this device is any distance greater that 0.5333 meters.

The SSER was tested in a 10' by 10' by 8' anechoic chamber fully lined with 12 " pyramidal absorber utilizing an automated spherical mapping data acquisition system. The anechoic absorber had a rated return loss for normal incident energy of 50 dB from 10 to 30 GHz. The antenna's input was generated by an HP 8673 synthesized signal generator, amplified by an HP 8349A power amplifier. Just prior to the SSER input, the signal was sensed by an HP 8484A power sensor for analysis of the incident waveform. The antenna's radiated pattern was received by another HP 8484A sensor attached to the input of a Ku band pyramidal horn antenna positioned one meter from the radiator. The sensed powers were then measured by an HP 438A dual channel power meter. The TM_{01}^c mode was launched at the input of the SER by a half guide wavelength antenna located on axis at the terminated beginning of the mode launcher. The TM_{01}^c mode was then verified by the far field pattern measurement of a flat circular cut cylindrical waveguide attached to the launching section. Measurement data for the SSER was taken over the azimuthal angle $0 \leq \phi \leq 180$ in five degree increments and over the polar angle $0 \leq \theta \leq 120$ in two degree increments.

For generating the computational domain, the radiator is positioned along the z axis and is approximately described in rectangular coordinates by

$$\frac{x^2}{a^2(z)} + \frac{(y - f(z))^2}{b^2(z)} = 1 \tag{2}$$

where the major and minor axes of the waveguide are polynomial functions of the distance along the z axis given by

$$a(z) = a_0 + a_1 z + a_2 z^2 + a_3 z^3 + a_4 z^4 \tag{3}$$

$$b(z) = b_0 + b_1 z + b_2 z^2 + b_3 z^3 + b_4 z^4. \tag{4}$$

Some sections of the waveguide and the radiating surface involve an offset function given by $f(z)$ in Equation (2). In the waveguide, towards the radiating surface feed, the offset maintains a flat waveguide bottom as indicated

in Figure 2 while the offset in the radiator is approximately an offset rotated parabola.

A simple cubic cell mesh generator was written using the above equations as the cell boundary. The routine was written in Mathematica© because of the ease of programming and debugging within its interpretive environment. Its graphic visualization capabilities also proved very valuable for validating the accuracy of the final generated mesh. As shown in Figure 3, the mesh generator did indeed produce a clean computational domain for FDTD simulation.

3 FDTD Analysis

The computational domain described in the previous section was used in all FDTD simulations. The antenna was excited by a half guide wavelength monopole radiator positioned one cell from the closed end cap in the model [2]. The gap was then excited by a $\hat{z}$ electric field component with a ramped sinusoid function of the form

$$E_z(t) = r(t)\sin(\omega_0 t) \tag{5}$$

where $r(t)$ is the ramping function. As with the experimental investigation, the operating frequency was chosen to be 18 GHz. To allow adequate transients in the guide, the simulation was run for 2048 timesteps with each timestep being 0.863 picoseconds. In the FDTD code, Liao boundary conditions enclosed the computational domain with a spacing of five white space cells from the mesh. When developing the mesh, the spatial discretization was 37 cells per free space wavelength (or 46 cells per guide wavelength). This fine cell size ($\delta = 0.448$ mm) allowed the curvature of the object to be resolved, especially in the curved radiating surface of the antenna. In the code we were utilizing, the fields are saved on an integration surface after the driving function reaches steady state. The data was then post processed to calculate the far zone radiated fields. We sampled data for $-90 \leq \theta \leq 90$ in two degree increments and $0 \leq \phi \leq 180$ in five degree increments. This produced a complete field map over the entire upper half plane.

The computed field data were post processed into contour field plots through the use of the software package Mathematica©. We utilized an in-house developed program to produce such contour maps. This allowed

us to quickly compare the computed results with those obtained from the experimental portion of the study.

4 Results

Initial results indicate reasonably good agreement with the experimental data for this antenna. The FDTD computed results show slight flutter in the far zone contour plots. This discrepancy can be attributed to a number of possible problems with the simulations and are currently being investigated. Possible sources of this error include scattering from cubical discretization used to model the antenna, especially in the spoon shaped radiating surface, grid dispersion, and improper launching of the initial fields at the antenna's feed. This error can be reduced by creating a finer mesh at the cost of significantly increased burdens on computer resources as well as careful consideration of the feeding of the antenna. Work on this problem is continuing.

5 Conclusions

Preliminary data from the antenna indicates that two important factors must be considered when using FDTD for a geometry of this sort. First, a well constructed computational domain must be used in all simulations. This can potentially reduce sources of error in the simulations such as specular reflections ad grid dispersion. Secondly, careful attention must be paid to the launching the initial mode distribution inside the waveguide. If the initial feed is placed incorrectly in the model, an asymmetric field distribution will be generated which will significantly effect the far-zone radiated fields. Work with this radiator and the application of the FDTD method is on going in an effort to reduce the previously described effects. Due to time constraints with the publication deadlines, full corrected simulations have yet to be compleated. At presentation, corrected data for the antenna will be shown with discussion of the errors and their remedies.

References

[1] J. H. Beggs, R. J. Leubbers and B. G. Ruth, "Analysis of Electromag-

netic Radiation from Shaped-End Radiators Using the Finite Difference Time Domain Method," *IEEE Trans. Antennas Propagat.*, vol. 41, pp. 1324-1327, Sept. 1993.

[2] K. S. Kunz, R. J. Luebbers, *The Finite Difference Time Domain Method for Electromagnetics*, CRC Press, Boca Raton, 1993.

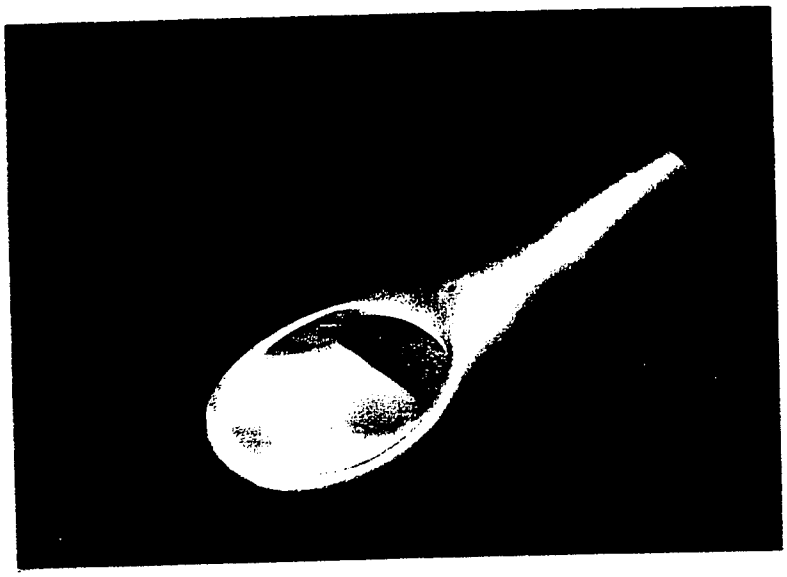


Figure 1: Photograph of SSER.

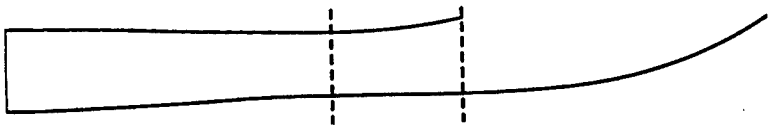


Figure 2: Minor axis plane cross section.

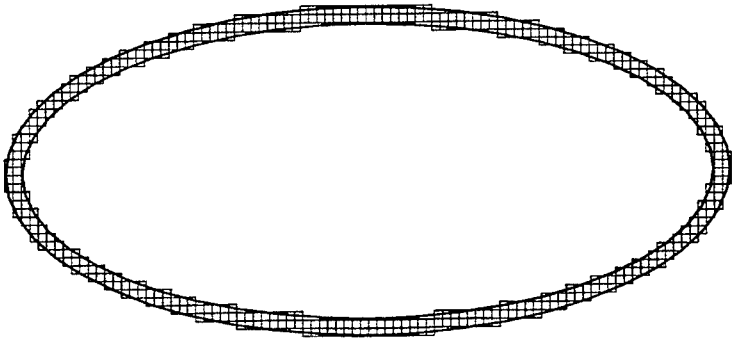


Figure 3: Cross section of elliptic waveguide showing computational domain.

A Time Domain Harmonic Oscillator Model for an FDTD Treatment of Lossy Dielectrics

K.S. Kunz

Department of Electrical Engineering
Penn State University

Introduction

An harmonic oscillator model of polarization in a lossy dielectric material provides a useful alternative to the usual FDTD treatment of lossy dielectrics best characterized by (1) where

$$\nabla xH(t) = \epsilon_\infty \epsilon_0 \frac{\partial E(t)}{\partial t} + \epsilon_0 \frac{\partial \chi_e(t)}{\partial t} * E(t) + \sigma E(t) \quad \nabla xE(t) = -\frac{\partial B(t)}{\partial t} \qquad (1),\ (2)$$

In this alternative formulation the first curl equation is replaced by

$$\nabla xH(t) = \epsilon_0 \frac{\partial E(t)}{\partial t} + \frac{\partial P(t)}{\partial t} + \sigma E(t) \quad , \quad P(t) \equiv N q_0 x(t) \quad (3),\ (4)$$

The displacement x(t) is found in the time domain from the harmonic oscillator equation

$$m\ddot{x} + d\dot{x} + kx = f(t) = q_0 E(t) \qquad (5)$$

The formulation then is entirely in the time domain and permits modeling nonlinearities through the extension of $kx+k_2x^2+k_3x^3+\cdots$ and can include breakdown effects as well as material modulation effects.

Derivation of Harmonic Oscillator Constants

Two widely occurring cases will be treated. They are Debeye and Lorentz materials. Debeye materials such as water are characterized by molecules with permanent dipole moments that are randomly oriented until acted on by an external electric field. Under the influence of this external field they align to produce a net polarization. Lorentz materials have no permanent dipole moment. The positive and negative charges contained within them separate under the influence of an external electric field and thereby produces a polarization field.

Debeye Materials

The harmonic equation used to describe a Debeye material incorporates only damping with a zero spring constant (k=0). The governing differential equation is then

$$m\ddot{x} + d\dot{x} = f(t) = q_0 E(t) \qquad (6)$$

For impulsive excitation

$$f(t) = q_0 E(t) = \delta(t) \tag{7}$$

and the corresponding impulsive polarization is

$$P_\delta(t) = N q_0 \, x_\delta(t) \tag{8}$$

so that

$$x_\delta(t) = P_\delta(t)/N q_0 \tag{9}$$

The impulsive polarization in the frequency domain is defined in terms of the susceptibility $\chi(\omega)$ as

$$P_\delta(\omega) \equiv \epsilon_0 \chi(\omega) E(\omega) = \epsilon_0 \chi(\omega)/q_0 \tag{10}$$

where

$$E(t) = \delta(t)/q_0 \tag{11}$$

has been used to find

$$E(\omega) = 1/q_0 \tag{12}$$

For Debeye materials $\chi(\omega)$ is given by

$$\chi(\omega) = \left(\frac{\epsilon_s - \epsilon_\infty}{t_0}\right) \frac{1}{(1 + j\omega t_0)} \tag{13}$$

Substituting this expression into (10) and inverse transforming yields the corresponding time domain expression for the impulsive polarization

$$P_\delta(t) = \epsilon_0 \chi(t)/q_0 \tag{14}$$

where

$$\chi(t) = \left(\frac{\epsilon_s - \epsilon_\infty}{t_0}\right) e^{-t/t_0} \, u(t) \tag{15}$$

Substituting this expression for $P_\delta(t)$ into the equation for $x_\delta(t)$ in terms of $P_\delta(t)$ yields

$$x_\delta(t) = \epsilon_0 \chi(t)/N q_0^2 = \frac{\epsilon_0}{N q_0^2}\left(\frac{\epsilon_s - \epsilon_\infty}{t_0}\right) e^{-t/t_0} \, u(t) \tag{16}$$

For the harmonic oscillator equation to return this selection for impulsive excitation the constants m and d must be suitably adjusted. Substituting $x_\delta(t)$ into

$$m\ddot{x} + d\dot{x} = 0 \tag{17}$$

yields

$$A_0\left[m\frac{e^{-t/t_0}}{t_0^2} - d\frac{e^{-t/t_0}}{t_0}\right] = 0 \;, \; A_0 = \frac{\epsilon_0}{N q_0}\left(\frac{\epsilon_s - \epsilon_\infty}{t_0}\right) \tag{18}$$

so that

$$m = d t_0 \tag{19}$$

At t = 0

$$dx(t=o) = 1 \tag{20}$$

so that

$$d = 1/A_0 \tag{21}$$

The constant m and d are now determined and $m\ddot{x} + d\dot{x} = q_0E(t)$ becomes

$$\frac{Nq_0^2}{\epsilon_0}\left(\frac{t_0}{\epsilon_s - \epsilon_\infty}\right)(t_0\ddot{x} - \dot{x}) = qE(t) \tag{22}$$

or

$$\frac{Nq_0}{\epsilon_0}\left(\frac{t_0}{\epsilon_s - \epsilon_\infty}\right)(t_0\ddot{x} - \dot{x}) = E(t) \tag{23}$$

Lorentz Materials

The same derivation holds for $x_\delta(t)$, namely that it is given by

$$x_\delta(t) = \epsilon_0\chi(t)/Nq_0^2 \tag{24}$$

The susceptibility of a Lorentz material in the frequency domain is

$$\chi(\omega) = (\epsilon_s - \epsilon_\infty)/(\omega_0^2 + 2j\omega x - \omega^2) \tag{25}$$

with the corresponding time domain expression

$$\chi(t) = \left\{\left[(\epsilon_s-\epsilon_\infty)\,\omega_0^2/(\omega_0^2-\alpha^2)^{1/2}\right]e^{-\alpha t}\sin(\omega_0^2-\alpha^2)^{1/2}t\right\}u(t) \tag{26}$$

Thus

$$x_\delta(t) = \frac{\epsilon_0}{Nq_0}\left\{\left[(\epsilon_s-\epsilon_\infty)\,\omega_0^2/(\omega_0^2-\alpha^2)^{1/2}\right]e^{-\alpha t}\sin(\omega_0^2-\alpha^2)^{1/2}t\right\}u(t) \tag{27}$$

For the harmonic oscillator equation to return this solution for impulsive excitation the constants m, d and k must be suitably adjusted. Following the same lines as for the Debeye material the constants m, d and k are determined to be

$$m = \frac{Nq_0^2}{(\epsilon_s-\epsilon_\infty)\,\omega_0^2}\ ,\ d = 2m\alpha\ ,\ k = m\omega_0^2 \tag{28}$$

The harmonic oscillator equation $m\ddot{x} + d\dot{x} + kx = q_0E(t)$ becomes

$$Nq_0^2\ \frac{1}{(\epsilon_s-\epsilon_\infty)\,\omega_0^2}\left[\ddot{x} + 2\alpha\dot{x} + \omega_0^2x\right] = q_0E(t) \tag{29}$$

Scattered Field Implementation

A scattered field implementation is readily effected by differencing the curl equations as in equation (2) except that for the curl of H total equation (3) is employed so that

$$\nabla xH^{t,n+\frac{1}{2}} = \epsilon_0\frac{(E^{t,n+1}-E^{t,n})}{\Delta t} + Nq_0\frac{(x^{n+1}-x^n)}{\Delta t} + \sigma E^{t,n+1} \tag{30}$$

$$-\left[\nabla xH^{t,n+1} = \epsilon_0\ \frac{(E^{i,n+1} - E^{i,n})}{\Delta t}\right] \tag{31}$$

$$\nabla xH^{s,n+1} = \epsilon_0\frac{(E^{s,n+1}-E^{s,n})}{\Delta t} + Nq_0\frac{(x^{n+1}-x^n)}{\Delta t} + \sigma\,(E^{s,n+1}+E^{i,n+1}) \tag{32}$$

This resulting curl of H scattered equation must be further expanded. In particular the harmonic oscillator equation can be solved for x^{n+1} so that

$$x^{n+1}=\left[\frac{m}{(\Delta t)^2}(2x^n-x^{n-1})+\frac{d}{\Delta t}x^n+q_0(E^{s,n+1}+E^{i,n+1})\right]/\left[\frac{m}{(\Delta t)^2}+\frac{d}{\Delta t}+k\right] \quad (33)$$

For notational compactness define

$$\gamma=\left[\frac{m}{(\Delta t)^2}+\frac{d}{\Delta t}+k\right] \quad (34)$$

Substituting the expression for x^{n+1} into the curl of H scattered equation yields

$$\frac{\Delta t}{\epsilon_0}(\nabla x H^{s,n+\frac{1}{2}})=E^{s,n+1}-E^{s,n}+\frac{Nq_0}{\epsilon_0}\left[\frac{m}{\gamma(\Delta t)^2}(2x^n-x^{n+1})+\frac{d}{\gamma\Delta t}x^n+\frac{q_0}{\gamma}(E^{s,n+1}+E^{i,n+1})\right]+\sigma\frac{\Delta t}{\epsilon_0}(E^{s,n+1}+E^{i,n+1}) \quad (35)$$

This can be solved for $E^{s,n+1}$ to complete the algorithm with

$$E^{s,n+1}=\{\epsilon_0 E^{s,n}+\Delta t(\nabla x H^{s,n+1/2})-((Nq_0/\gamma)+\sigma\Delta t)E^{i,n+1}$$
$$(Nq_0/\gamma)\left[\left(\frac{2m}{(\Delta t)^2}+\frac{d}{\Delta t}-\gamma\right)x^n-\frac{m}{(\Delta t)^2}x^{n-1}\right]\}/(\epsilon_0+Nq_0^2/\gamma+\sigma\Delta t) \quad (36)$$

Results

The completed harmonic oscillator model of lossy dielectrics is not unlike the frequency independent implementation and only requires one additional add and multiply. It therefore runs in a nearly comparable time. Memory requirements are increased by as much as a factor of two by the need for storing the one and two time step prior displacements in the x,y and z directions for the three E field components of each cell.

Figure 1 is a one dimensional calculation of scattering from a half space of water, a Debeye material, that replicates the frequency dependent lossy dielectric model behavior of (2) in figure 8.5 demonstrating the harmonic oscillator model's capability to replicate the frequency dependent lossy dielectric model's prediction. The water air interface is at the 500th cell and the gaussian probe has already encountered the interface and been mostly reflected. The calculation was made with a three dimensional algorithm modified for one dimensional geometries.

(1) R. Luebbers, D. Steich and K. Kunz, "FDTD Calculation of Scattering from Frequency-Dependent Materials," IEEE Transactions on Ant. and Prop., Sept. 1993.

(2) The Finite Difference Time Domain Method for Electromagnetics, K.S. Kunz and R.J. Luebbers, CRC Press 1993.

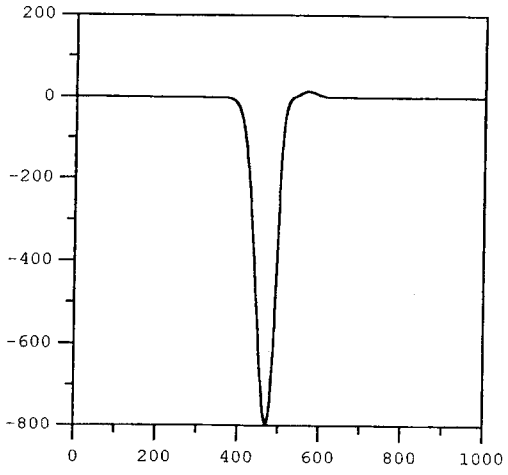


Figure 1

FDTD Modeling of Electromagnetic Wave Interactions with Composite Random Sheets

James G. Maloney and **Brian. L. Shirley**

Signature Technology Lab, Georgia Tech Research Institute
Georgia Institute of Technology
Atlanta, Georgia 30332

We will present a new approach to computing the interaction of electromagnetic plane waves with composite sheets (conductor/dielectric mixtures). The approach is based on using the finite-difference time-domain (FDTD) method to solve Maxwell's equations subject to the relevant boundary conditions imposed by the composite sheets. Specifically, the cases considered were thin sheets (thickness < wavelength) composed of a random distribution of: parallel bars (1D randomness), patches (2D randomness), and small cubes (3D randomness). The constituents (bars, patches, cubes) were either dielectric or conductor (both finite and infinite conductivity were considered). The relative fraction of constituents was varied from below, to near, to above the percolation threshold. The quantity of interest for this research was the frequency dependence of the transmission and reflection coefficients as a function of fill fraction and degree of randomness. During the presentation, visualizations (movies) of the electromagnetic waves interacting with composite sheets will be shown to illustrate the different mechanisms involved for the different degrees of randomness. Comparison of numerical predictions with experimental measurements for the high conductivity cases will also be presented.

An Improved Near to Far Field FDTD Algorithm

K.S. Kunz

Penn State University
Department of Electrical Engineering

Introduction

A commonly employed near to far field algorithm (1) can be derived from the expression (eq. 4.22, Stratton (2))

$$E(x',y',z') = -\frac{1}{4}\pi\int_s (i\omega\mu(n \times H)\phi + (n \times E) \times \nabla\phi + (n \cdot E)\nabla\phi)\, da \quad (1)$$

where $\phi = e^{ikr}/r$, by replacing $i\omega$ by $\partial/\partial t$ and ik by $\partial/\partial r$. The result is

$$E_\theta = -\eta W_\theta - U_\phi \text{ and } E_\phi = -\eta W_\phi + U_\theta$$

where

$$W(t) = \frac{1}{4\pi RC}\frac{\partial}{\partial t}\left\{\int_{s'} J_s(t+(\vec{r}'\cdot\hat{r})/c - R/c)\, ds'\right\}, \quad J_s = \hat{n} \times H(t)$$

$$U(t) = \frac{1}{4\pi RC}\frac{\partial}{\partial t}\left\{\int_{s'} M_s(t+(\vec{r}'\cdot\hat{r})/c - R/c)\, ds'\right\}, \quad M_s(t) = -\hat{n} \times E(t)$$

A worthwhile improvement to this approach is to turn to equation 4.26 of Stratton

$$\nabla' \times E(x',y',z') = \frac{i\omega\mu}{4\pi}\int (n \times H(x,y,z)) \times \nabla\phi\, da$$

This is derived from (1) straightforwardly by noting the ∇' x is in the primed coordinates. Now

$$\nabla' \times E(x',y',z') = i\omega\mu H'(x',y',z') \quad (2)$$

thus

$$H(x',y',z') = -\frac{1}{4\pi}\int_s (n \times H(x,y,z)) \times \nabla\phi\, da \quad (3)$$

Equation (3) can now be employed to formulate a near to far algorithm, instead of (1). The advantage is treating only one field quantity, a gain in simplicity and computational cost.

Time Domain Evaluation of the Far Field Expression

Starting with (3) where

$$\nabla\phi = \left(\frac{1}{r} - ik\right) \frac{e^{ikr}}{r} \hat{f}_0 \qquad (4)$$

and in the limit $r \to \infty$ so only the -ik term survives, the expression for H(x', y', z') becomes the far field expression

$$H(x',y',z') = \frac{ik}{4\pi} \int_s [(nxH(x,y,z)) x\hat{f}_0] \frac{e^{ikr}}{r} da \qquad (5)$$

Now setting $k=\omega/c$

$$H(x',y',z') = \frac{i\omega/c}{4\pi} \int_s [(nxH(x,y,z) x\hat{f}_0] e^{i\omega\left(\frac{r}{c}\right)} da \qquad (6)$$

Fourier transforming this expression to the time domain, noting that $i\omega$ becomes $\partial/\partial t$ and $e^{i\omega t_{ret}}$ is a time retardation which can be ignored, yields the time domain expression for the far field response

$$H(x',y',z',t) = \frac{1}{4\pi cr} \frac{\partial}{\partial t} \int_s [nxH(x,y,z,t) x\hat{f}_0] \, da \qquad (7)$$

In evaluating this expression r is normalized to unity and $\hat{f}_0$ is the unit vector pointing from anywhere on the surface to the observation point.

Far Field Implementation

A rectangular problem space is assumed with a "white space" four cells wide or more. This allows an interior surface to be defined that is one and a half cells in from the faces of the problem space and free of the scatterer. This inner boundary surface cuts through two H field components that are tangential to the inner boundary. The surface integral equation, equation (7), can be evaluated using these components at a selected number of observation points, each defined by observation angles $\phi_{obs}(n)$ and $\theta_{obs}(n)$. A relative delay time is associated with the contributions from each field component. It is derived from the offset of the field point compared to the problem space center along the direction of observation. The contribution of each field point is weighted by the area of a cell face centered about the component. One exception is the components along the edges of the inner boundary. They are weighted by a half cell face area.

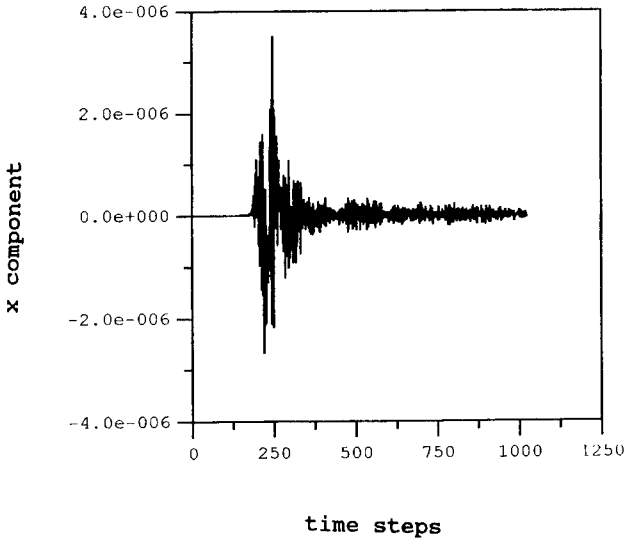
The relative delay is in general not an integral multiple of the time step Δt. Therefore the delayed contribution is divided into two contributions to the two closest time intervals given by integral multiple of Δt using a simple linear interpolation scheme. Each H field component on a face can contribute to two field components at the observation location. At each time step the contribution of a single component on the inner boundary to a single component at the observation location can occur at two

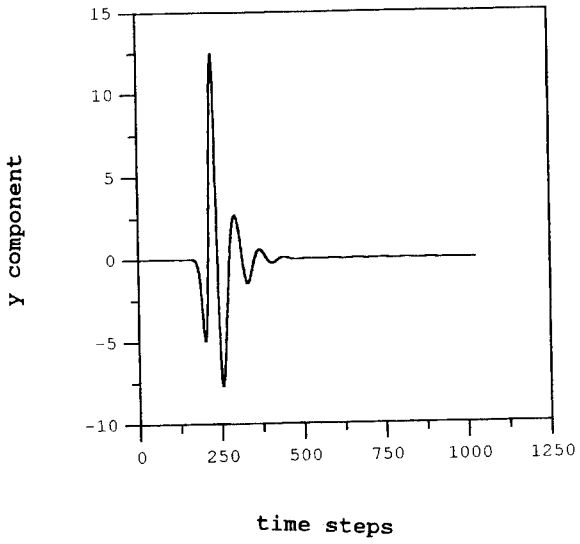
adjoining time intervals. A running accumulation in time of these contributions from all inner boundary components yields an accurate time history of the total scattered response at the observation point.

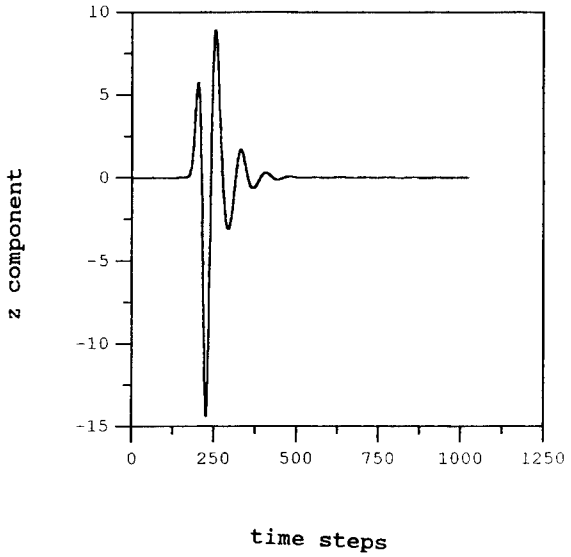
Results

Figures 1-3 are the three far field H field components (x,y,z respectively) for a square metal plate 17 x 17 cells in size illuminated by a 256 time step wide Gaussian pulse. The response is essentially the same as that seen in reference 1 figure 7.2 for a similar geometry and angle of incidence (θ = 45°, ϕ = 30°) for the backscattered radiation.

1) K.S. Kunz and R.J. Luebbers, The Finite Difference Time Domain Method for Electromagnetics, CRC Press, 1993.
2) J.A. Stratton, Electromagnetic Theory, McGraw Hill, 1941.




y component
15
10
5
0
-5
-10
0
250
500
750
1000
1250
time steps


z component
10
5
0
-5
-10
-15
0
250
500
750
1000
1250
time steps

Unstructured Finite-Volume Modeling in Computational Electromagnetics

Douglas J. Riley and C. David Turner
Radiation and Electromagnetic Analysis Department
Sandia National Laboratories
Albuquerque, New Mexico 87185-1166
e-mail: djriley@sandia.gov

Abstract

The finite-volume hybrid-grid (FVHG) algorithm combines unstructured finite-volume grids with traditional finite-difference time-domain (FDTD). The grids are completely coupled without the need for spatial interpolation. The finite-volume grid is defined to terminate on a rectangular surface that may be located very close to the geometry under study, which minimizes overhead. Absorbing boundary conditions with >40 dB attenuation are easily applied in the bounding FDTD grid. In this paper, the FVHG algorithm is extended to free-meshed, tetrahedral-element unstructured grids. This provides finite-element-like modeling flexibility with explicit time differencing. Multi-material regions can be solved. The FVHG algorithm is efficient and accurate, even with complex free meshes generated by advanced solid-modeling software. Long-term stabilization, material averaging, and complications with tetrahedral grids are discussed.

1.0 Introduction

Traditional finite-difference time-domain (FDTD) codes have been used extensively over the past ten to twenty years for the electromagnetic (EM) analysis of geometries with low to moderate complexity. These codes are based on structured cubical-hexahedral cells that model geometries with a staircase approximation. The advancement technique uses the Yee algorithm that can be written in terms of simple contour integrations [1]. Much research has been invested in the development of grid truncation techniques [2,3], near-to-far-field transformations [4], and sub-grid algorithms [5,6]. For geometries that conform to a rectangular grid, FDTD is efficient and accurate using 10-20 cells per wavelength. For arbitrary geometries, traditional FDTD can become impractical because hundreds of cells per wavelength may be required to adequately approximate curvature, with the required resolution being dependent on incident angle and polarization [7,8].

Although FDTD will remain popular for many years, there is considerable interest in the development of accurate and efficient body-conforming volumetric algorithms. Transient solvers based on computational fluid dynamics (CFD) techniques [9], finite-volumes [10,11,12], local contour modifications [13], and overlapping non-rectangular and rectangular grids [14] are under development. Finite-element approaches, although primarily used in the frequency domain, are receiving attention in the time domain [15]. The accuracy and efficiency associated with various non-orthogonal cell shapes is of considerable importance with all methods, and late-time stability becomes an additional concern with transient approaches. Some algorithms, such as the CFD-based approaches, advance both the electric and magnetic fields on a single grid, whereas the approaches described in [10-14] use two offset grids. The latter techniques reduce identically to the FDTD Yee algorithm when the grid is rectangular and can be referred to as generalized-Yee algorithms.

Much of the previous work on transient non-orthogonal algorithms is based on grids generated by mapped-meshing techniques. Such grids are generally composed of hexahedral- and/or wedge-shaped cells and are block-structured, although the grids can be referenced using unstructured techniques. Mapped-meshing usually requires partitioning the geometry to construct the mesh and is therefore not as flexible as free-meshing algorithms. Free meshing generally gives rise to fully unstructured tetrahedron grids, although free-meshing hexahedral algorithms are presently being developed with the CUBIT project at Sandia National Laboratories [16]. Mapped-mesh grids provide a more visually satisfying mesh than grids obtained from free-meshing, but the overall quality of the grid with regard to cell stretch and distortion is often superior with tetrahedral elements.

The present paper emphasizes free-meshing with linear tetrahedrons when used in conjunction with the finite-volume hybrid-grid (FVHG) technique [12]. For open-region problems, the FVHG algorithm embeds the unstructured grid in a traditional FDTD code. Either an analytic or a Berenger-type absorbing boundary condition

is easily applied in the structured grid without incurring considerable overhead. The unstructured region is designed to terminate so that a direct connection to the structured grid occurs without grid interpolation. The overlapping grid algorithm [14] requires spatial interpolation between grids. Many complications have been experienced with free-meshed tetrahedrons that did not occur with mapped meshes, and these will be discussed throughout the paper. The notation in this paper differs somewhat from that used in [12] to simplify the generalization presented here.

Unstructured finite-volume algorithms demand considerably more computer resources than FDTD. Thus, the ideal finite-volume code provides complete solid-modeling flexibility while minimizing overhead. Indeed, one of the most powerful aspects of volumetric solvers lies in their ability to accommodate the inhomogeneous materials that can be easily generated using advanced solid-modeling programs. Key to the FVHG algorithm is a transition to the structured, external FDTD grid as quickly as possible. As described below, this transition has been accomplished within a minimum of 1-2 FDTD spatial steps from solid models generated using commercial products. This distance is remarkably close to the solid model and has lead to highly resolved grids without an excessive number of non-orthogonal cells. For example, the NASA 9.936-inch almond was modeled to 3.5 GHz at 13 "cells" per wavelength using 65 thousand tetrahedral elements, of which 15 thousand elements filled the almond's interior. This particular grid could accommodate different materials within the almond.

Of course, an alternative approach is not to transition to a structured grid at all and instead terminate the grid using simple impedance-matched absorbing layers [17,18] filled with unstructured, non-orthogonal cells. Although satisfactory damping of the transient response can be obtained and parallelization of the field advancement occurs, many (> 10) layers are often required. Because the number of non-orthogonal cells required to fill these layers can become extremely large the hybrid-grid approach has been found to be preferable, at least when using free-meshed tetrahedral elements in the non-orthogonal region. An area of future research that may show promise is the extension of a Berenger-type perfectly matched layer to non-orthogonal cells, but only if it can be applied such that it is nearly adjacent to the solid model and provides >40 dB damping with only a few layers of limited thickness.

The scope of the paper is as follows. In Section 2, grid-generation programs applicable to the FVHG algorithm are discussed. In Section 3, a technique to interface free-meshed unstructured grids to the structured FDTD mesh is presented. In Section 4, the mathematical foundation of the FVHG algorithm is developed and results are presented. Conclusions are given in Section 5.

2.0 Grid Generation

Many commercial and non-commercial programs exist to generate either mapped or free meshes. The FVHG algorithm requires that the non-orthogonal region terminates on a rectangular parallelepiped such that structured, cubical hexahedrons can be directly interfaced. Mapped-mesh programs are well suited to this form of termination. INGRID [19], CUBIT [16], and I-DEAS [20] are three examples that have been used successfully. A fourth example that shows promise for large-scale mapped-mesh grid generation is based on the parallel mesh project at Lawrence Livermore National Laboratory. PMESH [21] possesses an ACIS solid-modeling kernel and is capable of generating tens of millions of cells.

Programs that are capable of generating free tetrahedral elements that terminate with the required properties for use with the FVHG algorithm are much more difficult to obtain. Two commercial products have been evaluated: (1) PRO/Engineer [22], and (2) I-DEAS [20]. PRO/Engineer permits the user to terminate the grid on a parallelepiped with specified fixed-node locations. It does not, however, generally adhere to specified maximum and minimum edge lengths on the terminating surface. As a consequence, additional nodes may be placed on the parallelepiped and/or the tetrahedral-element bases may not possess a required isosceles form. Either of these situations fail to establish the interface of the surrounding structured grid.

I-DEAS permits the surface bounding the unstructured grid to be partitioned into subsurfaces, which obviates the meshing problems experienced with PRO/Engineer. In addition, the meshing module of I-DEAS has been found to be much more flexible, particularly with regard to using symmetry and reflecting elements. I-DEAS was used for all free-meshed FVHG results in this paper. Because the FDTD structured grid can be interfaced extremely close to the free-meshed grid, I-DEAS shows promise for the transient FVHG analysis of complex problems ranging from circuit boards to biomedical applications. However, I-DEAS currently does not provide a parallel-processing capability, and thus grids are limited to a practical number of 1-2 million cells. It is noted that CUBIT's 3D plastering algorithm for the generation of free-meshed *hexahedral* elements may be of future interest when the algorithm matures to accommodate complex geometries.

An I-DEAS tetrahedron grid of a sphere embedded in a closely spaced cubical box with the proper termination characteristics is shown in Fig. 2.1.

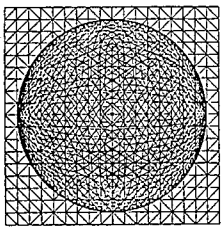


Fig. 2.1

3.0 Unstructured/Structured Mesh Interface

A hexahedral element interfaced to the bases of two tetrahedral cells is shown in Fig. 3.1. For use with the FVHG algorithm, one face of this hexahedron is split into two isosceles triangles; this element is treated as a seven-faced element. A layer of these special hexahedral elements is wrapped completely around the unstructured grid. This layer is referred to as the *interface region.* The tetrahedron grid terminates on the *inner boundary* of this region while the FDTD grid connects to the *outer boundary.* Standard cubical FDTD cells interface directly to the special hexahedral elements without spatial interpolation.

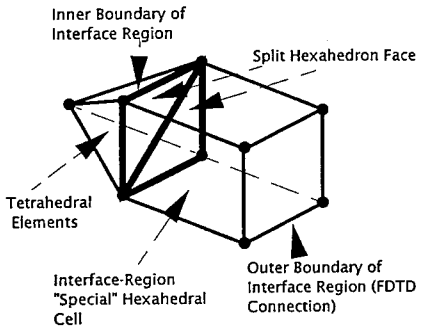


Fig. 3.1 Interface region

The field advancement scheme is as follows. The electric (**E**) fields in the structured grid are initially advanced. The FDTD **E**-fields on the outer boundary of the interface region are second-order time interpolated and mapped into the unstructured-grid registers. The unstructured region is advanced (possibly) several sub-time steps as dictated by the Courant condition in this region. The unstructured **E**-fields are subsequently mapped into the FDTD registers on the inner boundary of the interface region. Advancing the FDTD magnetic (**H**) fields in the structured grid completes the overall time step.

The scheme provides a seamless spatial connection between the unstructured and structured regions. The time-interpolation could be eliminated by using the same Δt for both grids; however, the interpolation can reduce the overall execution time without introducing lower-order error.

4.0 FVHG Algorithm

The non-orthogonal region is defined in terms of a primary grid and a dual (or derived) grid. The basic structure of the primary grid is generated from the solid-modeling/grid-generation program; a preprocessor forms the dual grid along with all necessary cell information for both grids. The centroids of the primary-grid cells correspond to the vertices of the dual-grid cells. Vector **H**-fields are defined at primary-cell centroids, whereas vector **E**-fields are defined at primary-cell vertices. The vertices of the primary cells are contained within the dual cells, but they do not, in general, fall precisely at the location of the dual-cell centroid. Because the vector **H**-fields are advanced using primary cells, the primary grid is equivalently labeled an **H**-grid. Similarly, the dual grid is equivalently labeled an **E**-grid because vector **E**-fields are advanced using the dual cells. The algorithm accommodates primary cells that are arbitrary convex polyhedrons.

For mapped-mesh grids composed mainly of hexahedral elements, the number of cells on the primary and dual grids is roughly equal. For free-meshed tetrahedron grids, the number of dual cells has been found to be roughly one-fourth to one-sixth the number of primary cells, with each cell containing many nodes, faces, and edges, but this can vary considerably depending on the form of the primary grid. The distribution of dual cells is output from the preprocessor.

A typical **H**-grid tetrahedral element, referenced as $\mathbf{H}_i$, is shown in Fig. 4.1. Dual cells (not shown) surround the four vertices; these are referred to as $\mathbf{E}_j$, j = 1-4. The dual edge, s_l^e, connects the centroids of primary-cell i with a neighboring cell, referenced as primary-cell k. The primary edge, s_p^h, connects $\mathbf{E}_1$ and $\mathbf{E}_2$. The volume of primary-cell, i, is denoted V_i^h, while the volume of dual-cell, j, is denoted V_j^e. The area of face, l, on primary-cell, i, is denoted by $A_{i,l}^h$, while the (average) area of face, p, on dual-cell, j, is denoted $A_{j,p}^e$. $\mathbf{n}_{i,l}^h$ and $\mathbf{n}_{j,p}^e$ denote average outward normals for each face of the primary and

dual cells, respectively. (Average face areas and normals are used because the (dual-cell) faces may be non-planar.)

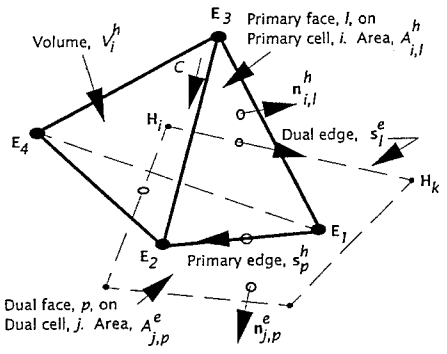


Fig. 4.1. Cell definitions.

In total and scattered forms, Maxwell's equations are:

Total:

$$\mu\frac{\partial}{\partial t}\mathbf{H}^{\mathbf{t}} + \sigma_m \mathbf{H}^{\mathbf{t}} = -\nabla\times\mathbf{E}^{\mathbf{t}} \tag{4.1a}$$

$$\varepsilon\frac{\partial}{\partial t}\mathbf{E}^{\mathbf{t}} + \sigma_e \mathbf{E}^{\mathbf{t}} = \nabla\times\mathbf{H}^{\mathbf{t}} \tag{4.1b}$$

Scattered:

$$\mu\frac{\partial}{\partial t}\mathbf{H}^{\mathbf{s}} + \sigma_m \mathbf{H}^{\mathbf{s}} = -\nabla\times\mathbf{E}^{\mathbf{s}} - (\mu-\mu_o)\frac{\partial}{\partial t}\mathbf{H}^{\mathbf{i}} - \sigma_m \mathbf{H}^{\mathbf{i}} \tag{4.2a}$$

$$\varepsilon\frac{\partial}{\partial t}\mathbf{E}^{\mathbf{s}} + \sigma_e \mathbf{E}^{\mathbf{s}} = \nabla\times\mathbf{H}^{\mathbf{s}} - (\varepsilon-\varepsilon_o)\frac{\partial}{\partial t}\mathbf{E}^{\mathbf{i}} - \sigma_e \mathbf{E}^{\mathbf{i}} \tag{4.2b}$$

Here, ε, σ_e, μ, σ_m, denote permittivity, electric conductivity, magnetic permeability, and magnetic conductivity, respectively. Total fields have a superscript **t**, while scattered and incident fields have superscripts **s** and **i**, respectively. The scattered field equations (4.2a, 4.2b) require linearity. Although either formulation can be used, the scattered-field equations have been found to provide increased accuracy and dynamic range with open-region problems by eliminating grid reflection of the incident field at the interface between unstructured tetrahedrons and the structured FDTD grid. In the following, only the scattered-field form of the equations will be presented, with the total-field results being similar.

By integrating over each cell on the primary and dual grids, the finite-volume time-domain (FVTD) form of the scattered-field equations is

$$\mu_i\frac{\partial}{\partial t}\iiint_{V_i^h}\mathbf{H}_i^{\mathbf{s}}\,dV_i^h + \sigma_{mi}\iiint_{V_i^h}\mathbf{H}_i^{\mathbf{s}}\,dV_i^h = -\sum_l \iint_{A_{i,l}^h}\mathbf{n}_{i,l}^h\times\tilde{\mathbf{E}}^{\mathbf{s}}\,dA_l -$$

$$(\mu_i-\mu_o)\frac{\partial}{\partial t}\iiint_{V_i^h}\mathbf{H}_i^{\mathbf{i}}\,dV_i^h - \sigma_{mi}\iiint_{V_i^h}\mathbf{H}_i^{\mathbf{i}}\,dV_i^h \tag{4.3a}$$

$$\tilde{\varepsilon}_j\frac{\partial}{\partial t}\iiint_{V_j^e}\mathbf{E}_j^{\mathbf{s}}\,dV_j^e + \tilde{\sigma}_{ej}\iiint_{V_j^e}\mathbf{E}_j^{\mathbf{s}}\,dV_j^e = \sum_p \iint_{A_{j,p}^e}\mathbf{n}_{j,p}^e\times\tilde{\mathbf{H}}^{\mathbf{s}}\,dA_p -$$

$$(\tilde{\varepsilon}_j-\varepsilon_o)\frac{\partial}{\partial t}\iiint_{V_j^e}\mathbf{E}_j^{\mathbf{i}}\,dV_j^e - \tilde{\sigma}_{ej}\iiint_{V_j^e}\mathbf{E}_j^{\mathbf{i}}\,dV_j^e \tag{4.3b}$$

Because the basic structure of the primary grid is output from the solid-modeling program, all materials are defined relative to primary cells. For magnetic materials, this is the natural definition. However, electric materials are associated with the spatially staggered dual cells and therefore the permittivity and electric conductivity require averaging. The average values are denoted by $\tilde{\varepsilon}_j$ and $\tilde{\sigma}_{ej}$, respectively (more will said about material averaging techniques in Sections 4.5, 4.6).

4.1 Area-Integral Approximation

There are at least two possibilities for the evaluation of the area integrals in Eqs. 4.3, which is why the symbol, ~, was used over the area-integral vector fields: (1) For each face, the vector fields at all of the vertices are first (linear or volumetric) averaged and then vectorially crossed with the average face normal. This result is finally multiplied by the average face area to complete the calculation for that face (note that edge fields are not required). (2) The vector fields at two vertices are initially used to construct an approximation for the field along the connecting edge. The cross product is then expanded as a vector triple product at each vertex, and finally an average value for the area integral is constructed by summing over all vertices of the face. Although the evaluation described by the first scheme is simpler to implement, it has been found to lead to degraded accuracy and increased late-time instability for all but the simplest of cell shapes (it is recommended only for mapped-mesh grids with limited cell distortion). The second scheme has been found to be generally more accurate and robust, but it also has been found to suffer similar difficulties for complex cell shapes.

4.2 Volume-Integral Approximation

The volume integrals in Eqs. (4.3) are easily evaluated by assuming the vector field remains constant throughout the cell volume. This is the approach used throughout the paper and leads to the following equations:

$$\mu_i \frac{\partial}{\partial t}\mathbf{H}_i^{\mathrm{s}} + \sigma_{m_i}\mathbf{H}_i^{\mathrm{s}} =$$

$$-\frac{1}{V_i^h}\sum_l \iint_{A_{i,l}^h} \mathbf{n}_{i,l}^h \times \tilde{\mathbf{E}}^{\mathrm{s}}\, dA_l - (\mu_i - \mu_o)\frac{\partial}{\partial t}\mathbf{H}_i^{\mathrm{i}} - \sigma_{m_i}\mathbf{H}_i^{\mathrm{i}} \quad (4.4a)$$

$$\tilde{\varepsilon}_j \frac{\partial}{\partial t}\mathbf{E}_j^{\mathrm{s}} + \tilde{\sigma}_{e_j}\mathbf{E}_j^{\mathrm{s}} =$$

$$\frac{1}{V_j^e}\sum_p \iint_{A_{j,p}^e} \mathbf{n}_{j,p}^e \times \tilde{\mathbf{H}}^{\mathrm{s}}\, dA_p - (\tilde{\varepsilon}_j - \varepsilon_o)\frac{\partial}{\partial t}\mathbf{E}_j^{\mathrm{i}} - \tilde{\sigma}_{e_j}\mathbf{E}_j^{\mathrm{i}} \quad (4.4b)$$

A first-order approximation to the vector fields within cells can be constructed by expanding the fields in a first-order Taylor series and applying the relationship $\iiint \nabla\psi\, dV = \iint \psi\, \mathbf{n}\, dA$, where ψ denotes a scalar field and $\mathbf{n}$ denotes an outward normal. This relationship enables the field derivatives to be easily evaluated. The expansion has been implemented on a variety of cell types and has been found to have a minor effect on the accuracy of the geometries examined. The improvement has not been found to outweigh the added implementation complexity, but an exhaustive study has not been done. It is noted that the expansion may be useful on the dual grid when the dual-cell centroid is far removed from the corresponding primary-cell vertex.

4.3 Contour-Integral Correction

A further improvement, and natural extension, to an edge-projection scheme is made by correcting the normal component of the average field along an edge by using contour integration around the face pierced by this edge. *Note that this correction will ensure that the integral of the field divergence over each independent cell is constant in time and that the FVTD algorithm will reduce identically to the traditional FDTD form when the face-normal is parallel to the edge piercing the face.* Specifically, for primary-face (i, l) pierced by dual-edge $\mathbf{s}_l^e$, and dual-face (j, p) pierced by primary-edge $\mathbf{s}_p^h$ (cf. Fig. 4.1):

$$\tilde{\mu}_l^f \frac{\partial}{\partial t}\iint_{A_{i,l}^h} H_l^{\mathrm{s}}\, dA_{i,l}^h + \tilde{\sigma}_{m_l}^f \iint_{A_{i,l}^h} H_l^{\mathrm{s}}\, dA_{i,l}^h = -\oint_C \tilde{\mathbf{E}}^{\mathrm{s}} \cdot d\mathbf{l} -$$

$$(\tilde{\mu}_l^f - \mu_o)\frac{\partial}{\partial t}\iint_{A_{i,l}^h} \mathbf{H}^{\mathrm{i}} \cdot \mathbf{n}_l^h\, dA_{i,l}^h - \tilde{\sigma}_{m_l}^f \iint_{A_{i,l}^h} \mathbf{H}^{\mathrm{i}} \cdot \mathbf{n}_l^h\, dA_{i,l}^h \quad (4.5a)$$

$$\tilde{\varepsilon}_p^f \frac{\partial}{\partial t}\iint_{A_{j,p}^e} E_p^{\mathrm{s}}\, dA_{j,p}^e + \tilde{\sigma}_{e_p}^f \iint_{A_{j,p}^e} E_p^{\mathrm{s}}\, dA_{j,p}^e = \oint_C \tilde{\mathbf{H}}^{\mathrm{s}} \cdot d\mathbf{l} -$$

$$(\tilde{\varepsilon}_p^f - \varepsilon_o)\frac{\partial}{\partial t}\iint_{A_{j,p}^e} \mathbf{E}^{\mathrm{i}} \cdot \mathbf{n}_p^e\, dA_{j,p}^e - \tilde{\sigma}_{e_p}^f \iint_{A_{j,p}^e} \mathbf{E}^{\mathrm{i}} \cdot \mathbf{n}_p^e\, dA_{j,p}^e \quad (4.5b)$$

Here, $H_l^{\mathrm{s}}, E_p^{\mathrm{s}}$ denote the (face) normal component of the scattered magnetic and electric fields as obtained from contour integration (similar to traditional FDTD). The fields are assumed to remain constant over the area integrals. Because the evaluation faces are located at the interface between two cells, both electric and magnetic materials are volumetric averaged (denoted by the symbol, ~, over all materials and a superscript, f, to distinguish "face average" (cf. Sections 4.5, 4.6)).

The (scattered) magnetic field projected along dual-edge $\mathbf{s}_l^e$ is finally constructed by forming

$$\mathbf{H}_i^{\mathrm{s}} \cdot \mathbf{s}_l^e \approx \frac{V_i^h \mathbf{H}_i^{\mathrm{s}} + V_k^h \mathbf{H}_k^{\mathrm{s}}}{V_i^h + V_k^h} \cdot \mathbf{s}_l^e +$$

$$\left[H_l^{\mathrm{s}} - \left(\frac{V_i^h \mathbf{H}_i^{\mathrm{s}} + V_k^h \mathbf{H}_k^{\mathrm{s}}}{V_i^h + V_k^h} \right) \cdot \mathbf{n}_{i,l}^h \right] \left(\mathbf{n}_{i,l}^h \cdot \mathbf{s}_l^e \right) \quad (4.6)$$

The (scattered) electric field projected on primary-edge $\mathbf{s}_p^h$ is similar, as are the projected fields based on the total-field formulation. Linear, instead of volumetric, averaging of the vector fields has also been used successfully, and has been found to provide improved accuracy and stability on the dual grid when adjoining cells differ considerably in their volumes. The use of the contour correction has been found to be most significant when cells possess non-planar faces, which typically occurs on the dual grid. Although formulated and implemented differently here, Eq. (4.6) leads to a scheme that is identical to the modified finite-volume algorithm [10] (which may not be obvious). Note that the FVTD algorithm of Yee [14] incorporates a relation similar to Eq. (4.6) only on the primary-grid edges that connect to a conducting surface.

It is noted that for highly distorted meshes, primary edge, s_p^h, or dual edge, s_l^e, may not pierce the common face shared by two adjoining cells and can lead to computational errors. These "edge/face misses" can be minimized by ensuring that the primary cells are reasonably well shaped, which can be accomplished with free-meshed tetrahedral algorithms by placing controls on the cell aspect ratio, stretch and/or distortion.

4.4 Time Integration

The finite-volume method can develop a late-time weak instability that may manifest itself after several thousand, or perhaps only several hundred, time steps depending on grid complexity. As previously noted, the rate of late-time growth is affected by the manner in which the spatial aspects of the algorithm are implemented. The discrete surface integration (DSI) method [11] represents another spatial variation that improves, but may not eliminate, non-physical growth on complex grids.

Late-time growth can often be completely controlled by using dissipative time integration (it is noted that dissipative time integration is used to stabilize the upwind schemes used in CFD-based formulations). A desirable dissipative scheme behaves as an ideal low-pass filter that only attenuates frequencies above the resolution of the grid; however, such a filter is not practical to implement. An approximation to the ideal filter is described below.

A simple time-averaging technique similar to that used to improve the stability of the transient electric-field integral equation [23] has been found to considerably improve the late-time stability of the finite-volume method on complex grids. The DSI technique will also benefit from the following scheme, but generally later in time.

The traditional second-order centered time difference (applied to the scattered magnetic field) is written as

$$\left.\frac{\partial}{\partial t}\mathbf{H}_i^s\right|_{t=(n+1)\Delta t} \rightarrow \frac{\left(\mathbf{H}_i^s\right)^{n+3/2}-\left(\mathbf{H}_i^s\right)^{n+1/2}}{\Delta t} \qquad (4.7)$$

A time average for $\left(\mathbf{H}_i^s\right)^{n+1/2}$ is the following

$$\left(\mathbf{H}_i^s\right)^{n+1/2} = \frac{1}{\alpha+2}\left(\left(\mathbf{H}_i^s\right)^{n+3/2}+\alpha\left(\mathbf{H}_i^s\right)^{n+1/2}+\left(\mathbf{H}_i^s\right)^{n-1/2}\right) \qquad (4.8)$$

where $\alpha \geq 2$. Time discretization of (4.4a) with (4.7) and (4.8) leads to the advancement form

$$\left(\mathbf{H}_i^s\right)^{n+3/2}\left[A-\frac{B}{\alpha+2}\right]=$$

$$\frac{B}{\alpha+2}\left[\alpha\left(\mathbf{H}_i^s\right)^{n+1/2}+\left(\mathbf{H}_i^s\right)^{n-1/2}\right]-\frac{1}{V_i^h}\sum_l \iint_{A_{i,l}^h}\mathbf{n}_{i,l}^h\times\tilde{\mathbf{E}}^s\,dA_l$$

$$-(\mu_i-\mu_o)\left.\frac{\partial}{\partial t}\mathbf{H}_i^i\right|_{t=(n+1)\Delta t} - \sigma_{m_i}\left.\mathbf{H}_i^i\right|_{t=(n+1)\Delta t} \qquad (4.9)$$

where $A=\left(\frac{\mu_i}{\Delta t}+\frac{\sigma_{m_i}}{2}\right), B=\left(\frac{\mu_i}{\Delta t}-\frac{\sigma_{m_i}}{2}\right)$. The vector electric field is similar, as are the advancement equations for a total-field formulation and also Eqs. (4.5). For the case $\alpha = 2$, the time average provides a cosine frequency profile. For values greater than 2 the profile increasingly flattens, such that as $\alpha \rightarrow \infty$ Eq. (4.9) returns to the usual centered time-difference form and offers no dissipation.

The grid complexity and the level of cell distortion generally dictate how small α must be chosen to obtain long-term (tens-of-thousands of time steps) stability. Grids that require values in the range of 2-3 generally possess very poorly shaped cells and/or a very wide range between the maximum and minimum edge lengths (> 40 to 1). It may not be possible to long-term stabilize these grids and re-generation of the grid is often required. Mapped-mesh grids have been found to require smaller values of α than grids generated using free-meshed tetrahedrons. This is consistent with the previous comments that mapped meshes often possess greater cell stretch and distortion. Stabilization values in the range of 4-6 are typical for mapped meshes. Tetrahedral primary meshes are generally long-term stable using the FVHG default value of 10 (an exception is when there are wide variations in the maximum-to-minimum edge lengths, which is presently under investigation).

Figure 4.2 shows results for back scattering from a finite cylinder with flat end caps. The grid was generated using mapped-mesh techniques and the primary grid contained a highly distorted collection of wedges and hexahedrons. Curve 1 is the FVHG result using $\alpha \rightarrow \infty$ in the unstructured grid (unstable at 0.6 μs), curve 2 is based on the non-dissipative DSI algorithm (unstable at 2 μs), while curve 3 uses FVHG with $\alpha = 4$. Curve 3 represents 21,000 time steps in the unstructured mesh. Up to the DSI instability, curves 2 and 3 are indistinguishable.

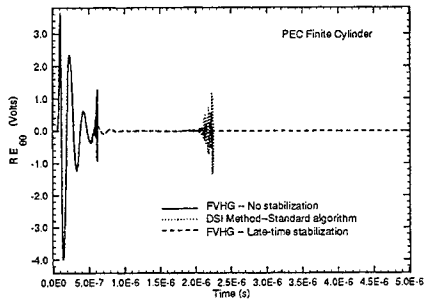


Fig. 4.2. Far back scattered field from a PEC cylinder. Axial polarization.

4.5 Electric Materials

The average permittivity on dual face, p, is defined by

$$\tilde{\varepsilon}_p^f = \frac{\sum_i \varepsilon_i V_i^h}{\sum_i V_i^h} \tag{4.10}$$

where the sums are taken over the primary cells associated with the dual face. The average permittivity for dual cell, j, is then constructed by forming

$$\tilde{\varepsilon}_j = \frac{\sum_p^{N_j^f} \tilde{\varepsilon}_p^f}{N_j^f} \tag{4.11}$$

where N_j^f denotes the number of dual faces associated with dual cell, j. The average electric conductivities, $\tilde{\sigma}_{e\,j}$ and $\tilde{\sigma}_{e\,p}^f$, are similarly defined. Fig. 4.3 shows the FVHG bistatic radar cross section (RCS) for a sphere of radius, a, with $\varepsilon = 4\ \varepsilon_o$. The primary grid contained 144,000 free-meshed tetrahedrons, and the dual grid contained 26,000 cells. The combined number of edges (degrees of freedom) on both grids was approximately 500,000. The incident field was φ polarized and $\sigma_{\varphi\varphi}$ is shown.

4.6 Magnetic Materials

To obtain the vector magnetic field at the primary-cell centroids (cf. Eqs. 4.3a, 4.4a) no material averaging is required. For Eq. 4.5a, primary face, l, is assumed to fall between primary cells, i and k. The average permeability, $\tilde{\mu}_l^f$, at this face is defined by

$$\tilde{\mu}_l^f = (V_i^h \mu_i + V_k^h \mu_k)/(V_i^h + V_k^h) \tag{4.12}$$

$\tilde{\sigma}_{m\,l}^f$ is defined similarly. Fig. 4.4 shows the FVHG bistatic RCS for a sphere of radius, a, with $\mu = 4\ \mu_o$. The grid was the same as that used in Section 4.5.

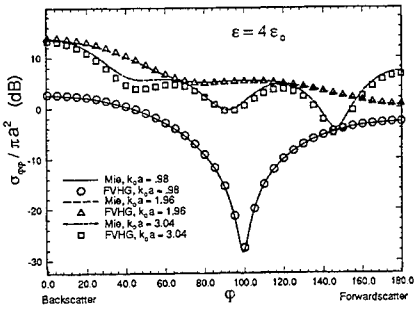


Fig. 4.3. Bistatic RCS for a dielectric sphere. k_o denotes free-space wavenumber.

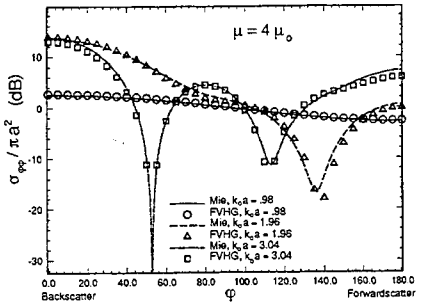


Fig. 4.4. Bistatic RCS for a magnetic sphere.

4.7 Surface Impedance Boundary Condition

To reduce total cell count when thin-material coatings are present, surface-impedance boundary conditions are required. A leading-order impedance boundary condition (IBC) using a simple 3x3 matrix inversion for surface

cells was introduced in [12] based on a total-field formulation (which is easily extended to the scattered-field form). The approximation simply replaced $-\mathbf{n}\times\mathbf{E}^{\mathbf{t}}$ in the area integrals for the cell faces on the object's surface by $Z_s\,\mathbf{n}\times\mathbf{n}\times\mathbf{H}_i^{\mathbf{t}}$, where Z_s denotes the local impedance and $\mathbf{n}$ denotes an outward local surface normal. The approximation was developed for mapped-mesh hexahedral cells that form a regular, "stacked", cell pattern to the surface of the scatterer. Representative results for a resistive sphere (with $Z = Z_s/377$) are shown in Fig. 4.5; the grid was generating using mapped-meshing techniques.

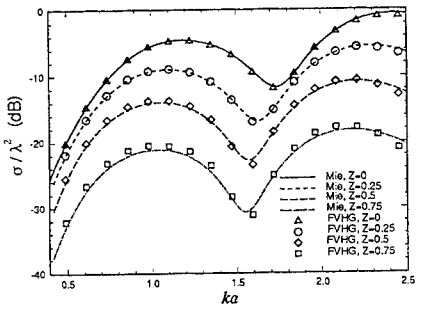


Fig. 4.5. Monostatic RCS for an impedance sphere.

Although the technique works extremely well for such mapped-meshes, it has subsequently been found to greatly underestimate the effect of the coating when using free-meshed tetrahedral grids. A possible explanation is that the formulation modifies the surface integral over the tangential surface face without explicitly modifying the edges bounding this face. Tetrahedral grids lack the ordered cell pattern of mapped-meshes, and elements may possess surface-tangential edges without possessing a tangential surface face. Thus, an edge-based generalization appears to be necessary and is presently under investigation. The alternative finite-volume IBC formulations described in [24] are similarly not expected to be directly applicable to free-meshed tetrahedral grids.

4.8 Miscellaneous Results

Geometry, measurements, and method-of-moment (MoM) calculations for the monostatic RCS of the 9.936-inch NASA almond were presented in [25]. The FVHG analysis of this object is presented here. Dimensions, orientation, and illumination are identical to those described in [25]; the reader is referred to this reference for details. The upper half of the almond embedded in a rectangular box is shown in Figs. 4.6a,b. Note the closeness of the box to the almond's surface. A tetrahedral grid of the isolated almond is shown in Fig. 4.7. The total tetrahedral grid included approximately 65,000 elements, of which 15,000 filled the almond's interior. Based on a maximum (over both grids) average edge length, the grid provides 13 "cells" per wavelength at 3.5 GHz. The monostatic RCS at 1.19 GHz for the vertical/vertical (VV) and horizontal/horizontal (HH) cases [25] are shown in Fig. 4.8. Measured data are only provided at 5-degree intervals. Although the HH FVHG results differ from the measurements by 2-4 dBSM (dB square meters) for certain angles, the results are globally very close to the published MoM calculations for this geometry (included in Fig. 4.8).

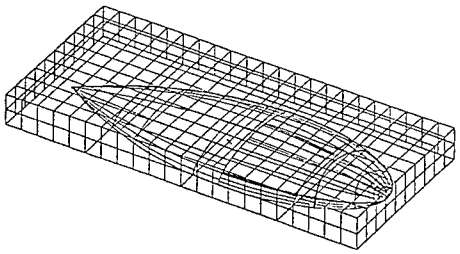


Fig. 4.6a. NASA almond in box (top half).

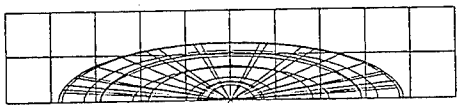


Fig. 4.6b. Top half of embedded almond (end view).

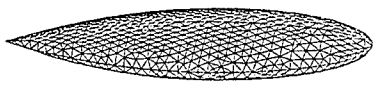


Fig. 4.7. Tetrahedron grid of isolated almond.

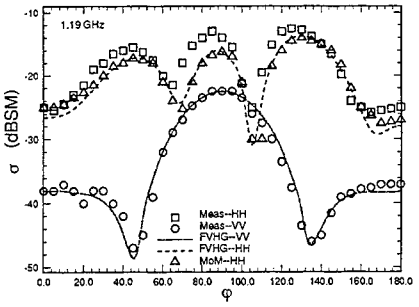


Fig. 4.8. Monostatic RCS for 9.936-inch NASA metallic almond.

5.0 Conclusions

The FVHG algorithm provides a seamless connection between unstructured and structured grids that is free from spatial interpolation across grid boundaries. By treating a non-orthogonal region as a local problem within a structured computational volume, computer resources are greatly reduced while adding considerable modeling flexibility. Multi-material regions are easily accommodated within the unstructured grid. The FVHG algorithm was designed as a general-purpose solver and is presently being used for applications ranging from microelectronics to radar cross section.

The FVHG technique accommodates cells of arbitrary shape. Indeed, although the primary grid may contain only tetrahedral and/or hexahedral elements, the dual grid may have elements with forty or more faces, each with numerous edges. The FVTD algorithm used with FVHG incorporates an FDTD correction along with late-time-stabilizing time integration; this approach has been found to be accurate and generally stable even for very complex grids. Simpler FVTD algorithms can be implemented, but their accuracy and late-time stability have been found to suffer when the grid becomes increasingly complex. Formulations that succeed with one cell type applied to certain geometries may experience difficulties with other cell types and/or other geometries. The authors know of no FVTD algorithm that is *guaranteed* to provide long-term stability for arbitrary grids.

The free-meshing, tetrahedral-element application of the FVHG algorithm presented here provides a powerful transient analysis tool. Although the unstructured region requires considerably more computer resources than the FDTD grid, the rapid transition from the unstructured mesh to structured FDTD permits efficient use of computer resources. The transition can be accomplished within only 1-2 FDTD cells from the modeled geometry. This rapid transition has been realized with the solid-modeling/finite-element software, I-DEAS. However, to permit the efficient generation of very large grids (>1-2 million cells), parallelization of the grid-generation algorithms will be necessary.

The present implementation of the FVHG algorithm encloses the entire modeled geometry in a single rectangular box. To further increase efficiency, various sized, interconnected rectangular boxes may be desirable. These are easily included at the solid-modeling/primary-grid-generation level. The only added complexity is identification of the location where the unstructured/structured interfaces exist. This straightforward extension is presently under investigation.

Acknowledgment

The authors thank Structural Dynamics Research Corporation (SDRC) for their assistance in adapting the I-DEAS finite-element software to the mesh-termination requirements of the FVHG algorithm.

References

[1] A. Taflove, K.R. Umashankar, B. Becker, F. Harfoush, K.S. Yee, "Detailed FD-TD analysis of electromagnetic fields penetrating narrow slots and lapped joints in thick conducting screens," *IEEE Trans. Ant. Prop.*, vol-36, 2, pp. 247-257, Feb. 1988.

[2] D. Steich, R. Luebbers, K. Kunz, "Absorbing boundary condition convergence comparison," *IEEE Ant. Prop. Symp. Digest*, pp. 6-9, Ann Arbor, MI, June 28-July 2, 1993.

[3] Berenger, J.-P., "A perfectly matched layer for the absorption of electromagnetic waves," *J. Comp. Physics*, vol. 114, pp. 185-200, 1994.

[4] R. Luebbers, K. Kunz, M Schneider, F. Hunsberger, "A finite-difference time-domain near zone to far zone transformation," *IEEE Trans. Ant. Prop.*, vol-39, 4, pp. 429-433, April 1991.

[5] R. Holland and L. Simpson, "Finite difference analysis of EMP coupling to thin struts and wires," *IEEE Trans. EMC*, vol. 23, pp. 88-97, May 1981.

[6] D.J. Riley and C.D. Turner, "Hybrid thin-slot algorithm for the analysis of narrow apertures in finite-difference time-domain calculations," *IEEE Trans. Ant. Prop.*, vol. 38, 12, pp. 1943-1950, Dec. 1990.

[7] R. Holland, "Pitfalls of staircase meshing," *IEEE Trans. EMC*, vol. 35, 4, pp. 434-439, Nov. 1993.

[8] R. Holland, V.P. Cable, and L.C. Wilson, "Finite-volume time-domain (FVTD) techniques for EM scattering," IEEE Trans. EMC, vol. 33, pp. 281-294, Nov. 1991.

[9] V. Shankar, A.H. Mohammadian and W.F. Hall, "A time-domain, finite-volume treatment for the Maxwell equations," *Electromagnetics*, vol. 10, 1-2, pp. 127-145, 1990.

[10] N.K. Madsen and R.W. Ziolkowski, "A three-dimensional modified finite volume technique for Maxwell's equations," *Electromagnetics*, vol. 10, 1-2, pp. 147-161, 1990.

[11] N.K. Madsen, "Divergence preserving discrete surface integral methods for Maxwell's curl equation using non-orthogonal unstructured grids," RIACS Tech. Report 92.04, NASA Ames Research Center, CA, Feb. 1992.

[12] D.J. Riley and C.D. Turner, "Finite-volume hybrid-grid (FVHG) technique for the solution of the transient Maxwell's equations," *Applied Computational Electromagnetic Society (ACES) Newsletter*, pp. 25-32, July 1994.

[13] T.G. Jurgens and A. Taflove, "Three-dimensional contour FDTD modeling from single and multiple bodies," *IEEE Trans. Ant. Prop.*, vol. 41, 12, pp. 1703-1708, Dec. 1993.

[14] K.S. Yee and J.S. Chen, "Conformal hybrid finite-difference time-domain (FDTD) with finite-volume time domain," *IEEE Trans. Ant. Prop.*, vol. 42, 10, pp. 1450-1455, Oct. 1994.

[15] G. Mur, "The finite-element modeling of three-dimensional time-domain electromagnetic fields in strongly inhomogeneous media," *IEEE Trans. Magnetics*, vol-28, 2, pp. 1130-1133, March 1992.

[16] Sandia National Laboratories, Albuquerque, NM, Dept. 1425, personal communication, March, 1994.

[17] R. Holland and J.W. Williams, "Total-field versus scattered-field finite-difference codes: a comparative assessment," *IEEE Trans. Nuc. Sci.*, vol. 30, 6, pp. 4583-4588, Dec. 1983.

[18] J.S. Chen and K.S. Yee, "Artificial tapered damping near the outer computational boundary in FDTD," personal communication, June 1994.

[19] M.A. Christan and D. Dovey, "INGRID, A 3-D mesh generator for modeling nonlinear systems, user manual," LLNL Tech. Report UCRL-MA-109790, Livermore, CA, Sept. 1992.

[20] I-DEAS, Structural Dynamics Research Corporation, 2000 Eastman Drive, Milford, OH 45150-2789..

[21] D.D. Hardin, "PMESH: A parallel mesh generator," Nuclear Explosives Code Developers' Conf., Las Vegas, NV, Oct. 1994.

[22] PRO/Engineer, Parametric Technology Corporation, 128 Technology Dr., Waltham, MA 02154.

[23] A. Sadigh and E. Arvas, "Treating the instabilities in marching-on-in-time method from a different perspective," *IEEE Trans. Ant. Prop.*, vol. 41, 12, pp. 1695-1702, Dec. 1993.

[24] K.S Yee and J.S. Chen, "IBC simulation in the FDTD/FVTD hybrid," Personal communication, June, 1994.

[25] A.C. Woo, H.T.G. Wang, M.J. Schuh, M.L. Sanders, "Benchmark radar targets for the validation of computational electromagnetics programs," *IEEE Ant. Propag. Mag.*, vol. 35, 1, pp. 84-89, Feb. 1993.

Scattering from Coated Targets Using a Frequency-Dependent, Surface Impedance Boundary Condition in FDTD

C. W. Penney, R. J. Luebbers, and J. W. Schuster
Department of Electrical Engineering
The Pennsylvania State University
University Park, PA 16802

Abstract

One method for reducing the radar-cross section of objects such as aircraft and missiles is the application of a lossy coating. Computing scattering from targets coated with dielectric/magnetic materials is challenging for many computational methods due to the reduced wavelengths of an incident field inside the coating. These smaller wavelengths require increased sampling of the fields and thus more memory and computation time. A technique for implementing this calculation without greatly increased memory requirements or computation times has recently been developed using a finite-difference, time-domain (FDTD) code and tested in one-, two- and three-dimensions. The method requires knowledge of the frequency behavior of the complex permittivity and permeability and the thickness of the dielectric coating. The surface impedance at the surface of the coating is computed based on the given information and then approximated using a summation of causal functions. The approximated impedance is Z-Transformed and added to the FDTD code in special update equations for the fields at the surface of the coating. No computations are required inside the coatings, so the FDTD grid can be sized based on the free space wavelength. The result obtained is valid over the entire frequency range of interest assuming that the approximated surface impedance is a good match over the entire range. Comparisons with analytical solutions in one-dimension and measurements in three-dimensions show very good agreement.

Introduction

The idea of using a surface impedance which describes the interaction of the tangential fields on the surface of an object as a replacement for computing the actual fields inside an object was first presented by Leontovich[1] in 1948. The advantage of such a method is that when materials with high values of permittivity, permeability, and/or conductivity are encountered, the fields inside the material need not be calculated. If the calculations within the lossy dielectric/magnetic material are replaced by a relationship at the surface of the material, a great savings in computer memory and computation time can be obtained. Leontovich's idea was not greatly pursued (with the exception of a paper by Senior[2] in 1960) until computer methods became more common in the early 1990's. Several relevant papers have since been published by Tesche[3], Riley and Turner [4], Maloney and Smith[5] and Beggs et al.[6]. The work by Maloney and Smith [5] and Beggs et al [6] are most related to the current topic of scattering from coated targets.

Previous authors ([5], [6]) have proposed methods of applying the surface impedance concept to FDTD. The difference between the work of these authors and this paper is that they made the assumption that any fields transmitted into the dielectric would be dissipated within the

material and no energy would be reflected at the terminating surface. This assumption limits the application of their approaches, but it also allows the surface impedance to be described in a relatively simple expression. In the case of a thin coating over conductor, their assumption of no reflection from the terminating surface can not be applied because the layer is typically thin enough for significant energy to reach the conducting surface and be reflected. Indeed, thin coatings that are designed to absorb most of the incident energy include the effects of multiple reflections from the conductor surface.

Implementation

The surface impedance vs. frequency for a thin lossy layer over a perfect conductor is relatively complicated and therefore it is very difficult to use the methods suggested by [5] and [6]. As an alternative to these methods, a new approach was used in which the impedance expression is replaced by an approximation. The approximation is made using a least-squares curve fitting algorithm. Basis functions are given with variable parameters, and these parameters are adjusted for the least amount of difference between the actual data (the impedance) and the approximation. The basis functions chosen must be causal since these functions will be transformed from the frequency domain into the time domain and non-causal functions could cause the FDTD code to become unstable.

The material parameters for a commercially available radar absorbing material (RAM) are shown in Figure 1. This is GDS material available from Emerson and Cuming. The relative permittivity over the frequency range of interest (1 to 18 GHz) varies from 17 to 12 while the relative permeability is as high as 4.5 at some frequencies. Both the permittivity and the permeability have loss terms (imaginary parts) associated with them. The surface impedance of this material is computed assuming that the coating is applied to an infinite conducting sheet, so transmission line methods are used. The surface impedances and the resulting approximations obtained for a 0.09" layer of this material is shown in Figure 2. Getting a nearly exact fit between the actual impedance and the approximation is difficult and may require a large number of basis functions in the curve fit. This results in added complexity and the possibility that the calculations will go unstable. It was found that a reasonably close fit, as shown in Figure 2, provided stability and very good agreement using only two basis functions.

To implement the curve-fit approximation of the surface impedance into the FDTD algorithm requires the application of a transformation since the impedance expression is in the frequency domain and the calculations must be done in the time domain. Since the FDTD code is very similar to a digital system due to the discrete sampling times at which the fields are calculated, it was decided that the Z-Transform would be used. Previous work by Sullivan [8] has shown that the Z-Transform is viable alternative to the Fourier transform for FDTD applications.

Once the approximated impedance has been transformed, it must be added to the FDTD field update equations. The electric field tangential to the surface of the scatterer is defined by the expression [3]

$$\hat{n} \times \overline{E}^{tot} = \hat{n} \times (Z_s \overline{J}_s) \tag{1}$$

$$\overline{J}_s = \hat{n} \times \overline{H}_s \tag{2}$$

where $\overline{E}^{tot}$ = the surface total electric field, $\overline{J}_s$ = the surface current, $\overline{H}_s$ = the surface magnetic field, and Z_s = the surface impedance. From this relationship, an expression for the tangential

electric field just inside the surface of the coating can be found and substituted into the one-dimensional FDTD magnetic field update equation

$$\frac{E_x^n(k+1) - E_x^n(k)}{\Delta z} = -\mu_0 \frac{H_y^{n+\frac{1}{2}}(k+\frac{1}{2}) - H_y^{n-\frac{1}{2}}(k+\frac{1}{2})}{\Delta t} \tag{3}$$

as a replacement for the $E_x^n(k+1)$ term. Here Δz is the spatial increment and Δt is the time step size. In two and three dimensions, a similar substitution would be required for all the electric fields tangential to the surface with special attention paid to the vector nature of Equation 1 to obtain the proper sign. Fields on the surface of the scatterer will use this special equation while all exterior fields will use the usual FDTD equations. Any fields interior to the surface do not affect the calculation results are updated as if they were perfect conductor.

Results

An FDTD code, modified as described above, was written for one, two, and three dimensional problems. The one dimensional code was tested against analytically computed reflection coefficients with excellent results. Analytical solutions in two dimensions are difficult to compute, so the surface impedance code was validated against an unmodified FDTD code which used very small cells and was re-run for every frequency. Finally, the three dimensional results were compared to measurements of 8 inch square conducting plates and a generic model missile (Figure 6). The measurements of both targets were performed a several incidence angles with the most interest being in the RCS of the missile at angles near the nose.

The missile (Figure 3) was constructed from a sealed copper tube and coated with a 0.025" layer of GDS RAM with material parameters shown in Figure 1. The ends of the cylinder are not coated. It has fins made from a high permittivity (relative = 10.4) dielectric that are attached to the copper cylinder through slits cut into the RAM coating. There is also a dielectric (relative permittivity = 2.3) nose cone attached directly to the end of the copper cylinder. An identical missile model but without the GDS RAM coating was also constructed and measured to gauge the effect of adding the coating.

The FDTD approximation of the missile of Figure 3 used cubical FDTD cells 2 mm on a side. The dimensions of the FDTD problem space were 84 x 84 x 347 cells. Due to the thinness of the fins, the permittivity was reduced using a sheet impedance approximation. This resulted in a relative permittivity of 4.5 instead of 10.4. A minimum border of 20 cells surrounded the missile on all side which terminated in a second order stabilized Liao boundary condition [9],[10]. A modulated Gaussian pulse plane wave which had frequency content over the range of 1 to 14 GHz was used as the excitation. Plane wave incident angles from 0 to 90 degrees measured from the nose, with the missile cylinder rotated horizontally, were computed using 2000 time steps. The time step size was 3.85 ps.

As was mentioned previously, FDTD calculations of an uncoated missile were performed and measurements were made so that the effects of the RAM coating could be seen. Figure 4 shows a comparison of the measurements and FDTD calculations in a plot of the RCS of the uncoated missile at 4 degrees off the nose (Vertical Polarization). The coated missile has a very different response, especially at the higher frequencies, as can be seen in Figure 5. The frequency dependent surface impedance FDTD code (FDTDRAMSI) gives good results for the coated missile over the entire range. Additional comparisons at 12.6 degrees shown in Figures 6-7 show the significant

effects of the coating, and the accuracy of the FDTDRAMSI code in predicting these effects. The FDTDRAMSI results for other angles and horizontal polarization are of similar quality.

Conclusion

An FDTD surface impedance approximation can be applied to scattering from conducting targets coated with a thin lossy dielectric/magnetic layer. The formulation described in this paper gives broad frequency band results in a single FDTD calculation with only a minor increase in memory and execution time over usual FDTD. In comparison to normal FDTD calculations for coated targets, the savings in memory and execution time are very significant. This is in large part due to the ability to size the grid based on the free space wavelength instead of the dielectric/magnetic material wavelength since no computations actually take place inside the coating. Three dimensional results for a complex, realistic target have been shown with good agreement to measurements.

References

1 M. A. Leontovich, "On the approximate boundary conditions for electromagnetic fields on the surface of well conducting bodies", in *Investigations of Propagation of Radio Waves*, B. A. Vvedensky, Ed. Academy of Sciences USSR, Moscow, pp. 5-20, 1948.

2 T. B. A. Senior, "Impedance boundary conditions for imperfectly conducting surfaces", *Appl. Sci. Res. B*, vol. 8, pp. 418-436, 1960.

3 F. M. Tesche, "On the inclusion of loss in time-domain solutions of electromagnetic interaction problems", *IEEE Trans. Electromagn. Compat.*, vol. 32, pp. 1-4, Feb. 1990.

4 D. J. Riley and C. D. Turner, "The inclusion of wall loss in Finite- Difference Time-Domain thin-slot algorithms", *IEEE Trans. Electromagn. Compat.*, vol. 33, pp. 304-311, Nov. 1991.

5 J. G. Maloney and G. S. Smith, "The use of surface impedance concepts in the Finite-Difference Time-Domain Method", *IEEE Trans. Antennas Propagat.*, vol. 40, pp. 38-48, Jan. 1992.

6 J. H. Beggs, R. J. Luebbers, K. S. Yee, and K. S. Kunz, "Finite-Difference Time-Domain implementation of surface impedance boundary conditions", *IEEE Trans. Antennas Propagat.*, vol. 40, pp. 49-56, Jan. 1992.

7 D. M. Sullivan, "A frequency-dependent FDTD method using Z-Transforms", *IEEE Trans. on Antennas Propagat.*, vol. 40, pp. 1223-1230, Oct. 1992.

8 Z. P. Liao, H. L. Wong, G. P. Yang, and Y. F. Yuan, "A transmitting boundary condition for transient wave analysis", *Scientia Sinica, Series A*, vol. 27, no. 10, pp. 1063, Oct. 1984.

9 M. Moghaddam and W. C. Chew, "Stabilizing Liao's absorbing boundary condition using single precision arithmetic", *Proc. of the IEEE AP-S Int. Symp.*, London, Ontario, pp. 430, 1991.

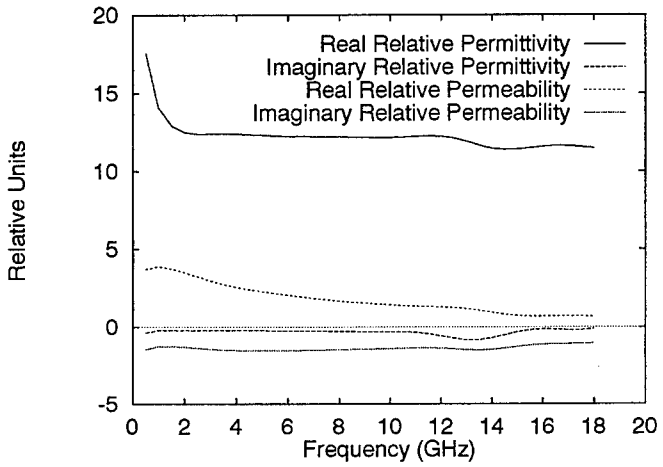


Figure 1: Complex permittivity and permeability of the GDS RAM material over the frequency range of interest.

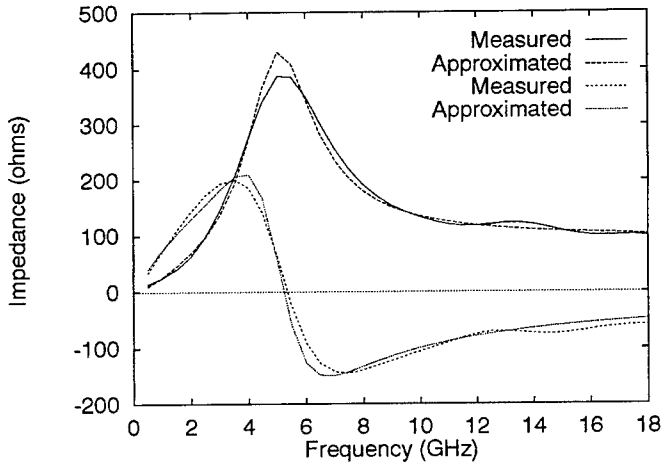


Figure 2: The computed and approximated surface impedances of a 0.09" layer of GDS RAM material on an infinite PEC plane.

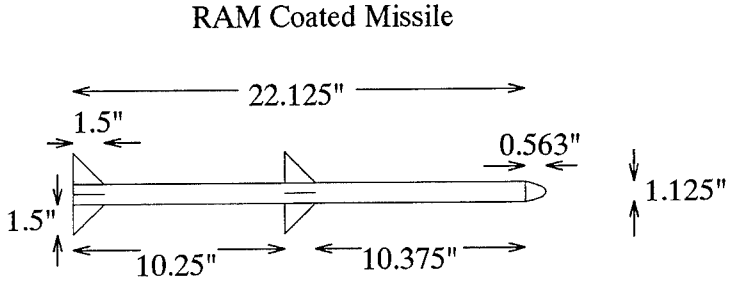


Figure 3: Diagram of the generic missile used. The coated version has a 0.025" layer of GDS RAM material on the tube.

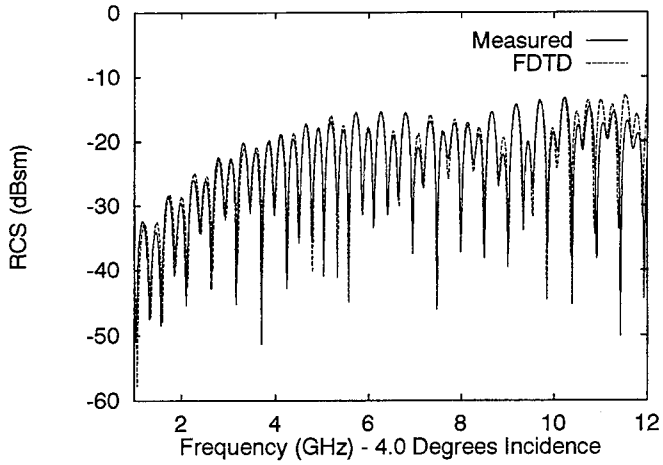


Figure 4: RCS of the uncoated missile of Figure 3 at an incident angle 4 degrees off the nose. The plot is for a vertically polarized incident plane wave and shows the comparison of the measurements and a regular FDTD code.

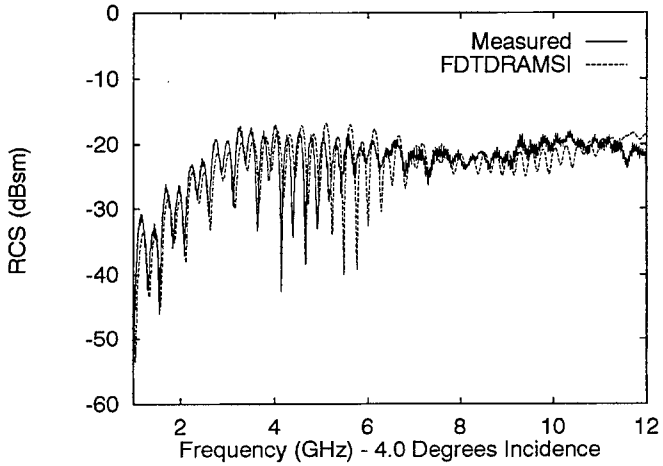


Figure 5: RCS of the coated missile of Figure 3 at an incident angle 4 degrees off the nose. The plot is for a vertically polarized incident plane wave and shows the comparison of the measurements and modified FDTDRAMSI code which uses the approximated input impedance to give broad band results.

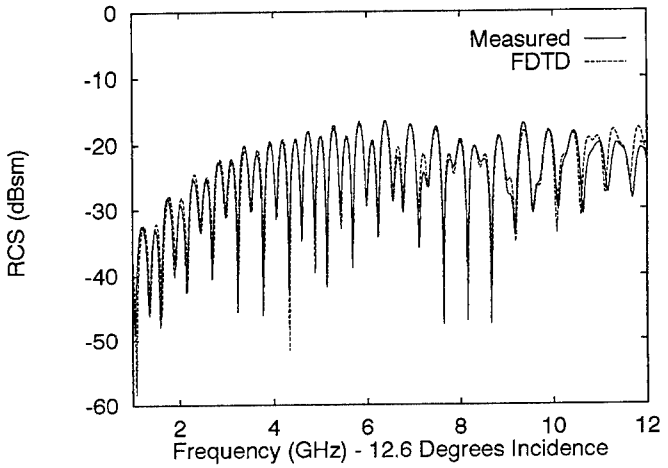


Figure 6: RCS of the uncoated missile of Figure 3 at an incident angle 12.6 degrees off the nose. The plot is for a vertically polarized incident plane wave and shows the comparison of the measurements and a regular FDTD code.

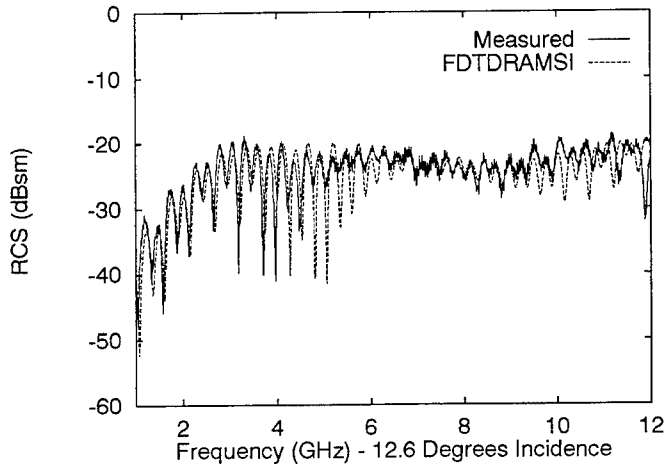


Figure 7: RCS of the coated missile of Figure 3 at an incident angle 12.6 degrees off the nose. The plot is for a vertically polarized incident plane wave and shows the comparison of the measurements and modified FDTDRAMSI code which uses the approximated input impedance to give broad band results.

Hybrid Finite Difference Time Domain and Finite Volume Time Domain in Solving Maxwell's Equations

Kane S. Yee and Jei S. Chen
Lockheed Palo Alto Research Laboratory

Abstract

A hybrid method which combines the FDTD and the FVTD methods is presented. The FVTD based on a unstructured/structured and conformal grid is used in the near vicinity of the surface of a scatterer and the FDTD is used to model the fields in the surrounding area. The two are coupled together through interpolation. The vertex based FVTD allows for more convenient and accurate interpolations than a conformal FDTD method. The hybrid method is validated through two examples -- the RCS of a PEC sphere and the RCS of an ellipsoid of revolution -- by comparison with the exact Mie series solution and with a MOM code calculation.

1. Introduction

This paper will gives details on our work in the conformal time domain technique during the past several years. It is a re-written version of a number of papers we have submitted to the IEEE Transaction on Antennas and Propagations [1-6]. Therefore we shall not give a historical account of the method nor shall we discuss the relation of our work with other published work in conformal FDTD-like time domain methods [7-20]. Such accounts have been given in the quoted papers. Interested readers are urged to consult the references in [1-6].

2. The FDTD and the FVTD

There are two integral forms of Maxwell's equations that are useful in time domain numerical solutions of electromagnetic problems:

$$-\int_A \dot{\vec{B}} \bullet d\vec{a} = \int_{\partial A} \vec{E} \bullet d\vec{l} \qquad \text{(1a)}$$

$$\int_A \dot{\vec{D}} \bullet d\vec{a} = \int_{\partial A} \vec{H} \bullet d\vec{l} \qquad \text{(1b)}$$

$$-\int_V \dot{\vec{B}}\, dv = \int_{\partial V} \hat{n} \times \vec{E}\, da \qquad \text{(2a)}$$

$$\int_V \dot{\vec{D}}\, dv = \int_{\partial V} \hat{n} \times \vec{H}\, da \qquad \text{(2b)}$$

The discretizations based on equations (1a) and (1b) have been commonly known and will be referred to as Finite Difference Time Domain (FDTD, generalized), and the discretizations based on equations (2a) and (2b) have been known and will be referred to as Finite Volume Time Domain (FVTD). The equations (1a) and (1b) are the mathematical description of the Faraday's law and Ampere's law, whereas the equations (2a) and (2b) can be obtained through integrating Maxwell's partial differential equations over a volume. Under smoothness assumptions they are equivalent. Our new proposed conformal method will be a combination of FDTD and FVTD.

3. The Leapfrog FDTD and FVTD

The numerical approach we shall present is very simple. It involves no more than accurate evaluation of line integrals, surface integrals, and volume integrals. We shall use time leapfrog in updating the electric field and the magnetic field. In order to be not too wordy in our discussions, we use the FDTD notations and it is advantageous to introduce the following terminology:

The line integral on the right hand side of (1a) is the **electric circulation** around the curve ∂A; and the curve ∂A **is an electric contour.**

The line integral on the right hand side of (1b) is the **magnetic circulation** around the curve ∂A; and the curve ∂A **is a magnetic contour.**

The surface integral on the right hand side of (2a) is the **electric vorticity** over the surface ∂V.

The surface integral on the right hand side of (2b) is the **magnetic vorticity** over the surface ∂V.

The leapfrog time discretized equations corresponding to (1a)-(2b) are:

$$\frac{1}{\Delta t}\int_A \left(\vec{B}^{n+1/2}-\vec{B}^{n-1/2}\right)\bullet \hat{n}ds=-\int_{\partial A}\vec{E}^{n}\bullet d\vec{l}$$

(3a);

$$\frac{1}{\Delta t}\int_A \left(\vec{D}^{n+1}-\vec{D}^{n}\right)\bullet \hat{n}dS=\int_{\partial A}\vec{H}^{n+1/2}\bullet d\vec{l}$$

(3b);

$$\frac{1}{\Delta t}\int_V \left(\vec{B}^{n+1/2}-\vec{B}^{n-1/2}\right)dv=-\int_{\partial V}\hat{n}\times\vec{E}^{n}\,da$$

(4a);

$$\frac{1}{\Delta t}\int_V \left(\vec{D}^{n+1}-\vec{D}^{n}\right)dv=\int_{\partial V}\hat{n}\times\vec{H}^{n+1/2}\,da$$

(4b).

The above identities are subject to the right-handed orientation of vector analysis. Many time domain algorithms can be obtained by judicious choices of the curves and surfaces. In fact our updating schemes are almost self evident from equations (1a)-(2b). In equations (1a)-(1b) we notice that $\mathbf{A}=\int \mathbf{n}\,da$ is the vector area enclosed by the curve ∂A. From vector analysis it is known that this vector area is independent of the area A. It is specified uniquely by the curve ∂A. It is called the area vector A enclosed by ∂A. Therefore another convenient approximation of (3a)-(3b) is:

$$\frac{1}{\Delta t}(\vec{B}^{n+1/2}-\vec{B}^{n-1/2})\bullet\vec{A}=-\int_{\partial A}\vec{E}^{n}\bullet d\vec{l}$$

(5a)

$$\frac{1}{\Delta t}(\vec{D}^{n+1}-\vec{D}^{n})\bullet\vec{A}=\int_{\partial A}\vec{H}^{n+1/2}\bullet d\vec{l}$$

(5b)

Now the FDTD and FVTD algorithm can be loosely stated:

For FDTD

Use the electric circulation around a curve to update the component of the magnetic field along the area vector of the surface enclosed by the curve.

Use the magnetic circulation around a curve to update the component of the electric field along the area vector of the surface enclosed by the curve.

For FVTD

Use the electric vorticity over a surface to update the magnetic vector in the center of the volume enclosed by the surface.

Use the magnetic vorticity over a surface to update the electric vector in the center of the volume enclosed by the surface.

The accuracy of the algorithm depends on how carefully we choose the curves enclosing the surface and the surfaces enclosing the volume. For example the electric or magnetiic field variables in (4a)-(4b) should be evaluated as close to the centroid of the area as possible. To be explicit let us consider the curve (Figure 1) ∂A = (i,j,k) —>(i+1,j,k) —>(i+1,j+1,k) —>(i,j+1,k) —>(i,j,k). The area vector enclosed by the curved is: $\vec{A}=\hat{z}\Delta x\Delta y$.

The centroid of the area is (i+1/2, j+1/2, k) and the electric circulation is approximately:

$$\int_{\partial A}\vec{E}^{n}\bullet d\vec{l}=Ex^{n}(i+1/2,j,k)\Delta x+Ey^{n}(i+1,j+1/2,k)\Delta y-Ex^{n}(i+1/2,j+1,k)\Delta x-Ey^{n}(i,j+1/2,k)\Delta y\,.$$

Substituting these approximations in (4a) one obtains the following equation:

$$B_z^{n+1/2} = B_z^{n-1/2} - \frac{\Delta t}{\Delta x \Delta y}\{Ex^n(i+1/2,j,k)\Delta x + Ey^n(i+1,j+1/2,k)\Delta y$$
$$- Ex^n(i+1/2,j+1,k)\Delta x - Ey^n(i,j+1/2,k)\Delta y\} \quad (6)$$

Equation (6) is one of the FDTD equations to update the component of the magnetic field. But the equations (3a)-(3b) can be applied to arbitrary curve even when the curve is not planar! This is the power of the area-curve integral form of the Maxwell's equations. If we include sources on the right hand side of (1a)-(1b), the integral form can be used to model circuit elements as well. To facilitate the discussion of the FVTD algorithm we use the rectangular grid topology. We define $(i, j, k) = (x_i, y_j, z_k)$. The grid points need not be equally spaced. This grid will be called an **electric grid** (see Figures 2 and 3 for electric elements). These vertices are the **electric vertices.** Located at the electric vertices is the electric vector **E** (we store the three rectangular components of the electric field there). A computational element is a distorted cube, called an **electric cube** or **an electric element.** The faces of an electric element are the **electric faces.** In rectangular grid an electric cube is an FDTD cube. The "center" of an electric cube is denoted by (i+1/2, j+1/2, k+1/2). This will be called a **magnetic vertex.** Two magnetic vertices are connected if the two corresponding electric elements share a common face. We thus generate a collection of magnetic elements; and the collection constitutes the **magnetic grid.** Located at the magnetic vertices are the magnetic vector **B** (or **H**). The updating of **E** and **H** (we assume that $\mathbf{B}=\mu\mathbf{H}$ and $\vec{D}=\varepsilon\vec{E}$ for simplicity) are carried out with the help of equations (4a) and (4b). The volume in equation (4a) is an electric element and the volume in equation (4b) is a magnetic element. If the faces of an electric element are not coplanar, the volume of the electric element is not defined. So far in our discussion an electric face has four vertices which may not be coplanar. We make the electric face definite by adding the **barycenter** of the four vertices. The rectangular coordinates of the barycenter is the average of the rectangular coordinates of the four vertices. Now the specific electric face we use is the collection of triangles, each of which is formed with two vertices and the barycenter (Figure 4). With the electric faces made definite we have now a definite volume for the electric element. In the evaluation for the electric vorticity we have to make sure that the unit surface normal is pointing away from the volume. Therefore the collection of oriented triangles (use the right hand rule: as the fingers curl along the perimeter of a triangle, the normal of the triangle is in the direction of the thumb) must be such that the area vector points away from the volume. Thus if (i+1/2, j+1/2, k+1/2) denotes the "center" of an electric element, the electric face consisting of the vertices (i, j, k), (i+1, j, k), (i+1, j+1, k) and (i, j+1, k) will have the following four oriented triangles:
{(i+1, j, k), (i, j, k), **b**}, {(i+1, j+1, k), (i+1, j, k), **b**},
{(i, j+1, k), (i+1, j+1, k), **b**}, and {(i, j, k), (i, j+1, k), **b**}
where **b** is the barycenter which can be denoted by (i+1/2, j+1/2, k).
To evaluate the partial contribution to the electric vorticity from this face, we first define the value of the electric vector at the barycenter to be the average of its values at the four vertices. The surface integral over the face is now the sum of the integral over the triangles. Over each triangle we approximate the integral by taking the cross product of the approximate value of the electric field at the centroid of the triangle and the area vector of the triangle.

4. The Overlapping-Grid FDTD / FVTD hybrid

Our FDTD/FVTD hybrid uses a composite grid consisting of a rectangular grid intersecting a body conformal grid. The conformal grid consist of an electric grid and a magnetic grid. The electric grid is a few layer of prisms erected along the normal of the scattering surface. Our main goal is to make use of the triangular surface grid usually generated for the MOM frequency domain integral equation methods. Therefore our conformal electric grid will consist of layers of triangular prisms (Figure 3). No more than five layers are needed. The conformal electric grid intersects an outer rectangular grid in which the FDTD algorithm is used. Constructed from the conformal electric grid is the magnetic grid. The height of the prisms is approximately the same as Δx, the spatial length of the FDTD grid. The lengths of the sides of the surface triangles are comparable to Δx. In the interior electric vertices or the magnetic vertices (points which are neither grid boundary points nor physical boundary points) the FVTD algorithm is used for updating. The interior boundary of our rectangular grid is $0.5\Delta x$ (0.5 zone) to Δx (1 zone) away from the scatterer (Figure 5). The outer boundary electric field on the FVTD primary grid is obtained through interpolation of the calculated rectangular FDTD electric field; the rectangular FDTD electric field at the inner boundary of the rectangular is obtained through interpolating the calculated FVTD field (Figures 6a,b). For the electric vertices at the boundary, we make use of the physical boundary condition and interpolation. This procedure will be explained more fully in the section on boundary conditions.

5 The Double Interpolation

At each time step we carry out a double interpolation for the data from one grid to another grid.

The interpolation from the rectangular FDTD to obtain the electric vector at the outer boundary of the conformal body grid is discussed first. From the rectangular coordinate of an outer boundary point we can find out to which FDTD cube it belongs and where in this FDTD cube it is located. The electric vector at the vertices of this FDTD cube is obtained first through interpolation from the FDTD edge components. The values of the electric vector at the vertices of the electric cube is now used to interpolate the electric vector at the outer boundary vertex through bilinear interpolation.

To interpolate for the rectangular component of the electric field at the midpoint of an edge in the interior boundary of the rectangular grid, we find out which triangular prism this midpoint belongs to and where in this prism this point is located. It is a little tricky for this process. We therefore explain in a little more detail. Let **a** be a point where a rectangular component of the electric field is to be interpolated. We first enumerate those electric vertices which is closest to the point **a**. We then enumerate the triangular prisms sharing the point **a**. One of these prisms will contain the point **a**. The boundary of the prisms are faceted (the upper and lower faces are triangles, and each of the lateral faces is the union of four triangles each of which has the barycenter as a vertex). Each of these prisms has a definite volume. For each of the triangles from the collection of triangles forming the boundary of one of these prisms, construct a pyramid with the addition of point **a**. The sum of the volumes of these pyramids will be larger than the volume of the prism unless the point **a** is in the closure of this prism. In that case the sum of the volumes of the pyramids equals the volume of the prism. The point **a** may lie at the boundary of more than one prisms but we need only to find one such prism. Having found one prism the point **a** belongs to, we subdivide the "vertical" edges of the prism into a large number of points with equal but small distance between two consecutive points (Figure 7). We thus establish equal discrete "vertical" coordinates along the vertical edges. The three points on the three vertical edges with the same vertical coordinate forms a triangle (Figure 7). We form a pyramid with each triangle and the point **a**. We compute the volume of each of these pyramids and find one with the minimum volume! Call the base triangle a minimum triangle. The "vertical" coordinate of the point **a** is approximately the "vertical" coordinate of the minimum triangle. In other words, the point **a** is approximately contained in this minimum triangle. Now we can find the area coordinates of the point **a** in this minimum triangle. The value of the electric vector at the vertices of the minimum triangle is obtained through linear interpolation from the values at the vertices of the prism. Making use of the area coordinates of **a** we can now use linear interpolation to get an approximate value for the electric vector **E** at **a**. Finally the rectangular component of the electric field at the point **a** is obtained.

6. Locally-Distorted-Grid FVTD and FDTD

The FVTD algorithm, when applied to a primary grid consisting of cubes, is almost identical to the rectangular FDTD. If the outer boundary vertices of the FVTD are the same as the inner vertices of the FDTD, it is quite simple to interpolate the FVTD field from the FDTD field and vice versa on the interface between these two algorithms. Thus when a locally distorted electric grid is available, one could use the FVTD on the distorted part of the grid and the FDTD on the undistorted part of the grid. One can also use FVTD throughout. The only reason one uses FDTD at all in this case is because of the bookkeeping simplicity of FDTD.

7. Boundary Condition Simulations in the FDTD/FVTD Hybrid

The discretized equations for FDTD listed in section 3 can only be used for "interior" field points where the electric or magnetic circulations can be obtained from the variables in the computational volume. Also the discretized equations for FVTD listed in the previous section can only be used for "interior" field points where the electric or magnetic vorticities can be obtained from the variables in the computational volume. Near the boundary the algorithms have to be modified. Whatever modification used is governed by trying to make maximum use of the information given by the physical boundary conditions. As a habit of computation we always put the electric nodes on the physical boundary and the magnetic nodes half a zone away from the boundary.

In the following we present two approximate boundary condition simulations for a PEC boundary condition. These are listed as **PEC 0** and **PEC 1** respectively. Undoubtedly there exist many more approximate boundary condition simulations. They are all very similar. **PEC 0** was introduced in our previous work [2]; it works well for smooth surfaces. **PEC 1,** on the other hand, is more general and is more convenient to implement. It has also been generalized for surfaces with edges and conical tips. More discussion on boundary condition simulations are included in our work [3,4].

PEC Boundary Condition Simulation 0 (PEC 0)

Shown in Fig. 8a is a triangular prism representing an electric element. This prism has a triangular base 1-4-8 at the surface of the scatterer. In the updating of the magnetic field at the centroid of this element we need the calculations of the electric vorticity (the surface integrals $\int_{\partial e} \hat{n} \times \vec{E}\, da$) over the boundary of the element. We

show how to approximate the electric vector at the center (point **d**) of the lateral surface 1-4-3-2. Point **a** is the midpoint of the edge 1-2 and point **b** is the midpoint of the edge 3-4. We denote the unit normal to the triangle 1-4-8 by $\hat{n}$. Surrounding the point **a** is a collection of magnetic vertices half a zone from the scatterer. In these vertices the magnetic vectors are located. The procedures to approximate the boundary condition are:

1. Make use of the magnetic vector in this collection and FDTD (this collection forms a dual face) to obtain the component $\hat{A} \bullet \vec{E}(a)$; where $\hat{A}$ is the unit vector of the vector area of the dual surface surrounding the edge 1-2.

2. Since $\vec{E}(1)-\hat{n}(\hat{n}\bullet\vec{E}(1))$ is known from the boundary condition and $\vec{E}(2)$ is calculated, we have the approximation

$$\vec{E}(a)=\hat{n}(\hat{n}\bullet\vec{E}(a))+\frac{1}{2}\left\{\left(\vec{E}(2)-\hat{n}(\hat{n}\bullet\vec{E}(2))\right)+\left(\vec{E}(1)-\hat{n}(\hat{n}\bullet\vec{E}(1))\right)\right\}.$$

3. Solve for

$$\hat{n}\bullet\vec{E}(a)=\frac{\hat{A}\bullet\vec{E}(a)}{\hat{A}\bullet\hat{n}}-\frac{1}{2\hat{A}\bullet\hat{n}}\hat{A}\bullet\left\{\left(\vec{E}(2)-\hat{n}(\hat{n}\bullet\vec{E}(2))\right)+\left(\vec{E}(1)-\hat{n}(\hat{n}\bullet\vec{E}(1))\right)\right\}.$$

4. Similarly, solve for $\hat{n}\bullet\vec{E}(b)$.

5. Approximate $\hat{n}\bullet\vec{E}(d)=\frac{1}{2}\{\hat{n}\bullet\vec{E}(a)+\hat{n}\bullet\vec{E}(b)\}$; this is the component of the electric field at the point **d** normal to the boundary triangle.

6. Also approximate $\vec{E}(d)-\hat{n}(\hat{n}\bullet\vec{E}(d)=\frac{1}{2}\{(\vec{E}(7)-\hat{n}(\hat{n}\bullet\vec{E}(7))+(\vec{E}(6)-\hat{n}(\hat{n}\bullet\vec{E}(6))\}$; this is the projection of the electric field at the point **d** in the plane of the triangle.

7. Approximate $\vec{E}(d)=\hat{n}(\hat{n}\bullet\vec{E}(d))+(\vec{E}(d)-\hat{n}(\hat{n}\bullet\vec{E}(d))\}$, making use of the approximation in step 5 and step 6.

8. The electric vorticity from the lateral face 1234 for this triangular prism is approximated by $\vec{E}(d)\times\vec{A}$; where $\vec{A}$ is the vector area of the lateral surface 1432.

PEC Boundary Condition Simulation 1 (PEC1)

Shown in Fig. 8b is an edge of a triangular prism representing an electric element. Point **a** is the midpoint of the edge 1-2. This prism has a triangular base at the surface of the scatterer. In the updating of the magnetic field at the centroid of this element we need the calculations of the electric vorticity (the surface integrals $\int_{\partial e}\hat{n}\times\vec{E}\,da$) over the boundary of the element. We denote the unit surface normal at the point 1 by $\hat{n}$. Surrounding the edge 1-2 is a collection of magnetic vertices half a zone from the scatterer. In these vertices the magnetic vector are located. The updating of the magnetic vector at the centroid of the prism requires the electric vorticity over its boundary faces. In this approximate simulation the electric vorticity over the upper and lower triangular faces is calculated the same way as in **PEC 0**. We deviate from **PEC 0** in the calculation of the electric vorticity over the lateral faces. Instead we approximate the electric vector at the point 1. We follow:

1. Make use of the magnetic vector in surrounding the edge 1-2 and FDTD (this collection forms a magnetic face) to obtain the component $\hat{A} \bullet \vec{E}(a)$; where $\hat{A}$ is the unit vector of the vector area of the magnetic surface surrounding the edge 1-2.

2. Since $\vec{E}(1)-\hat{n}(\hat{n}\bullet\vec{E}(1))$ is known from the boundary condition and $\vec{E}(2)$ is calculated; we have the approximation

$$\vec{E}(a)=\hat{n}(\hat{n}\bullet\vec{E}(a))+\frac{1}{2}\left\{\left(\vec{E}(2)-\hat{n}(\hat{n}\bullet\vec{E}(2))\right)+\left(\vec{E}(1)-\hat{n}(\hat{n}\bullet\vec{E}(1))\right)\right\}.$$

3. Solve for

$$\hat{n}\bullet\vec{E}(a)=\frac{\hat{A}\bullet\vec{E}(a)}{\hat{A}\bullet\hat{n}}-\frac{1}{2\hat{A}\bullet\hat{n}}\hat{A}\bullet\left\{\left(\vec{E}(2)-\hat{n}(\hat{n}\bullet\vec{E}(2))\right)+\left(\vec{E}(1)-\hat{n}(\hat{n}\bullet\vec{E}(1))\right)\right\}.$$

4. Extrapolate to get $\hat{n}\bullet\vec{E}(1)$

$$\hat{n}\bullet\vec{E}(1)=2\hat{n}\bullet\vec{E}(a)-\hat{n}\bullet\vec{E}(2).$$

5. Approximate $\vec{E}(1)=\hat{n}(\hat{n}\bullet\vec{E}(1))+\left[\vec{E}(1)-\hat{n}(\hat{n}\bullet\vec{E}(1))\right]$.

With the electric vector given at the vertices, the calculation of the electric vorticity over the lateral faces follows the same procedures as that in the FVTD algorithm.

8. A Stabilizing Technique

There have been reports of late time growth in the FDTD-like codes [15-18]. We also experienced such late time growth sometimes in our FDTD/FVTD hybrid. This can be a serious defect. It has prevented meaningful calculations for a long period of time. In [1,4] a time averaging for the magnetic vector is used to stabilize the calculation. We discovered that a a spatial averaging of the magnetic field works well in our FDTD/FVTD hybrid. From the way our rectangular grid overlaps the bodily conformal grid, it can be seen that calculations can be carried out if at each time step we pass the boundary electric field data from one grid to the other. Thus at each time step the electric vector at the outer boundary of the curvilinear grid must be supplied through interpolation from the electric field calculated in the rectangular grid by the FDTD algorithm; and the FDTD rectangular field component at the inner rectangular grid boundary must be obtained through interpolation of the electric vector calculated by the FVTD algorithm. The magnetic field in each grid can be obtained through the regular algorithm. We discovered that the procedures discussed above produce computation with a late time growth! The growth is not a strong instability and it always happened (for the small objects we tried) after the dominant return has passed. We heuristically explain the instability in the following:

The curvilinear grid with the inner boundary being the scattering object and the outer boundary being the curvilinear outer boundary form a "numerical resonator" very much like a physical resonator consisting of the PEC boundary. From theory we know that there exist resonant modes that satisfy the PEC condition. The excitation of these resonant modes is the truncation error of the double interpolation. The rectangular FDTD field is a radiating field. The resonant field gets artificially radiated through the interpolation. We therefore thought of a scheme to "disrupt" the numerical resonant modes. We noticed that in the overlapping region there will be curvilinear magnetic field locations where the magnetic vector, in addition to being updated by the curvilinear FVTD algorithm, can be approximated through interpolation of the calculated rectangular components. **We take an average of the calculated (by FVTD) value and the interpolated (data from FDTD) value.** For our unstructured curvilinear grid, it is more convenient to "mix" the magnetic field than to "mix" the electric field. This late growth phenomenon also occurs in our FDTD/FDTD hybrid algorithm [1]. In our numerical simulation for a finite circular cylinder we tried several types of "mixing" and found that averaging the calculated and interpolated magnetic field works quite satisfactorily. When we observed the late time growth in our FDTD/FVTD we employed the same "mixing" as in the FDTD/FDTD. And it works! Undoubtedly there are other legitimate approaches one might try. In our FDTD/FDTD hybrid [1] we carried out other types of mixings.

9 Sample Calculations

We have performed two sample calculations with our algorithms. Example 1 is a PEC sphere and example 2 is a PEC ellipsoid of revolution. The outer boundary of the rectangular FDTD grid is about one wavelength from the smallest box containing the scatterer. In the outer boundary of the rectangular FDTD grid we use our tapered damping [5] for the sphere calculations and for the ellipsoid of revolution we used the Mur absorbing boundary approximation. The incident wave is a linearly polarized plane Gaussian pulse. The far field scattered time signal is Fourier transformed to yield the frequency response. The radius of the sphere is 1 meter. We present two sets of calculations based on the number of surface triangles used. Our bodily conformal grid consists of four layers of triangular prisms. This body grid intersects an outer rectangular grid. The Δx of the rectangular grid depends on the number of surface triangles used; and the height of the triangular prisms, Δr, is comparable to Δx. For a surface grid of about 1200 triangles with the lengths of the triangles varying from .08 meters to .15 meters, we chose Δx=0.10 meter. and Δr = 0.1meter The FDTD inner boundary is in the neighborhood of $0.5\Delta x$ to $1.0\Delta x$ from the sphere. When the number of triangles is 4800 (four times that with 1200 triangles) we used Δx= .05m

and Δr=.05m. The boundary condition simulation is **PEC 1.** In Figures 9a, and 9b we show the RCS calculations (for two different numbers of surface triangles) and compared them to the Mie series calculation. Also included in Figure 9a is the staircase calculations. In Figure 10 we show the RCS calculation at 150 MHz of the PEC ellipsoid of revolution. The boundary condition simulation is **PEC 0.** This calculations are compared with that of a MOM BOR code. It should be pointed out that the size of the rectangular cell should be comparable to the size of the surface triangles. Therefore, as the number of surface triangles increases, the number of rectangular cells will also increase. For the same Δx the computation time for the FDTD/FVTD hybrid is roughly four times that required for the staircase FDTD; and the memory requirement can easily exceed two times that for the FDTD as one has to store the interpolation coefficients. On the other hand, the FDTD/FVTD hybrid is much more accurate than the staircase FDTD as illustrated in Figure 9a.

10. Conclusion

We have presented in this paper a time-domain hybrid FDTD/FVTD scheme. For smooth scatterers the conformal volume grid can be generated with a surface grid for which a number of commercial grid generators are available. Because the conformal grid is only a few layers of prisms, it is rather simple to generate compared to a full-fledged three dimensional grid that existing generalized FDTD scheme would required. We believe that we have introduced a new technique which may be applicable to a larger number of boundary-value problems in the time domain numerical electromagnetics.

Acknowledgement

Dr. Gordon Strate's assistance in editing the paper is greatly appreciated.

References

1. Kane S. Yee, J. S. Chen, and A. H. Chang, "Conformal Finite Difference Time Domain (FDTD) with Overlapping Grids", *IEEE Trans on Ant. and Propagation*, vol. 40, No. 9, pp.1068-1075, Sept., 1992.

2. Kane S. Yee and J. S. Chen, "Conformal Hybrid Finite Difference Time Domain and Finite Volume Time Domain ", *IEEE. Trans. Antennas Propag.* vol. 42. No. 10, Oct. 1994.

3 K. Yee and J. Chen, " IBC Simulation in the FDTD/FVTD Hybrid," Submitted to IEEE Trans. Antennas and Propag.

4. J. Chen and K. Yee, "Numerical Experiments on Late Time Growth Involving the FDTD/FVTD HYbrid Code," to be submitted to *IEEE Trans. on Antennas and Propagation.*

5. J. Chen and K. Yee, "Artificial Tapered Damping near the Outer Computational Boundary in FDTD," submitted to *IEEE Trans. on Antennas and Propagation*

6. J. Chen, J. Prodan and K. Yee, " An FDTD/FVTD 2D-algorithm to Solve Maxwell's Equations," *1995 ACES conference proceeding.*

7. R. Holland, "Finite-difference solutions of Maxwell's equations in generalized non orthogonal coordinates", *IEEE Trans. Nuc. Sci.*, vol. NS-30, pp.4589-4591, 1983.

8. Kane S. Yee, "Numerical Solution to Maxwell's Equations with Non-orthogonal Grids", *Proc. of 1st Review of Numerical Electromagnetic Codes*, March 19-21,1985. Also Lawrence Livermore Technical Report UCRL-93268, April 1987.

9. Weiland, T, "On the numerical solution of Maxwell's equations and applications in the field of accelerator physics. *Particle Accelerators*, 15; pp.245-292, 1984

10. Fusco, M. A."FDTD Algorithm in Curvilinear Coordinates," *IEEE Trans. Antennas and Propagation*, vol.-38 pp. 76-89, Jan. 1991

11. Fusco, M. A., M. V. Smith, and L. W. Gordon, "A three-Dimensional FDTD Algorithm in Curvilinear Coordinates," *IEEE Trans. Antennas and Propagation*, vol-39 pp. 1463-1472, Oct.1991

12. Taflove, A. K.Umashankar, B. Beker, F. Harfoush, and K. S. Yee, "Detailed FD-TD Analysis of Electromagnetic Field Penetrating Narrow Slots and Lapped Joints in Thick Conducting Screens", *IEEE Trans. Ant. and Propagation*, Feb. 1988.

13. Jurgen, T. G., A. Taflove, and K. R. Umashankar, and T. G. Moore, " Finite difference time domain modeling of curved surfaces," *IEEE Trans. AntennasPropagation*, vol. 40, April 1992.

14. Jurgen, T. G., and A. Taflove, " Three-Dimensional Contour FDTD Modeling of Scattering from Single and Multiple Bodies," *IEEE Tran. AntennasPropag.* vol. 41, No. 12, pp.1703-1708.

15. Madsen, N. K. and R. W. Ziolkowski, " Numerical solution of Maxwell's equations using irregular nonorthogonal grid," *Wave Motion*, vol.10, pp. 583-596, March 1988.

16. N. K. Madsen and R. W. Ziolkowski, " A Three-dimensional Modified Finite Volume Technique for Maxwell's Equations," *Electromagnetics*, vol. 10, nos.1-2,pp.147-161, Jan. 1990.

17. K. N. Madsen, "Divergence Preserving Discrete Surface Integral Methods for Maxwell's Curl Equations Using Non-Orthogonal Unstructured Grids", Lawrence Livermore National Laboratory UCRL JC-109787, Feb. 1992.

18. Riley, D. and C. D. Turner, "Finite-Volume Hybrid-Grid (FVHG) Techique for the Solution of the Transint Maxwell's Equations," *ACES Newsletter*, July 1994.

19. Fang, Jiayuan and Jishi Ren, "A Locally Conformal Finite-Difference Time-Domain Algorithm of Modeling Arbitrary Shape Planar Metal Strips," *IEEE Transactions on Microwave Theory and Techniques*, Vol. 41, No. 5, May 1993.

20. Chan, C. H., H. Sangani, K. S. Yee, and J. T. Elson, "A Finite-Difference Time-Domain Method Using Whitney Elements, " *Microwave and Optical Technology Letters*, Vol. 7, No. 14, Oct. 1994 pp. 673-676.

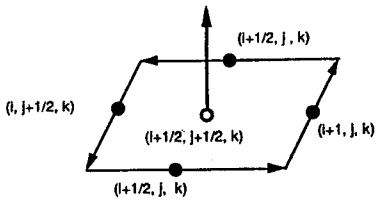


Fig. 1. An Electric Contour and Its Enclosed Area Vector.

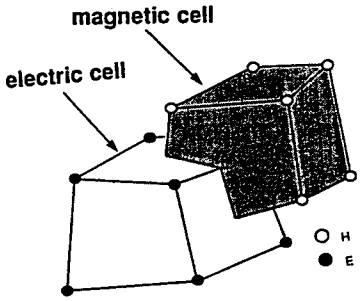


Fig. 2 An Electric Element and a Magnetic Element When They Are Hexahedral.

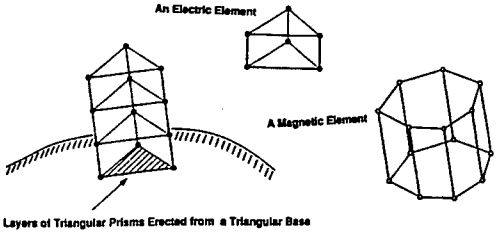


Fig. 3 The Trangular Prismatic Conformal Body Grid.

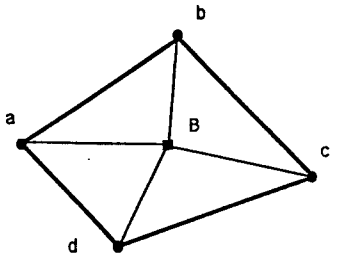


Fig. 4 The Four Vertices of a Face and Its Barycenter B.

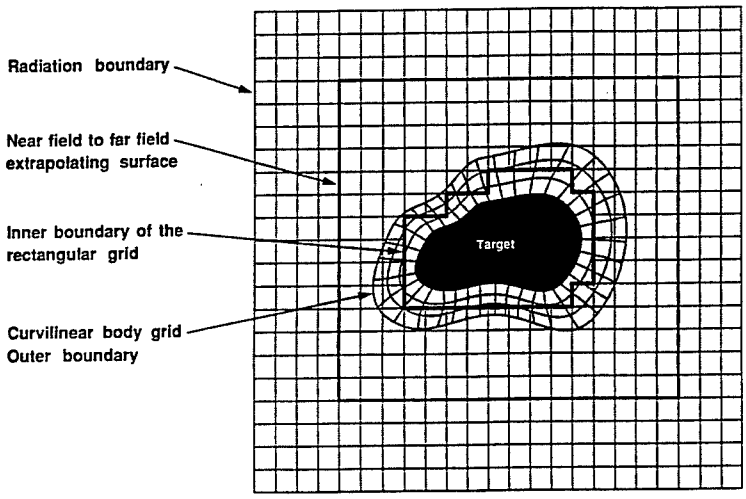


Fig. 5 The Overlapping Conformal FDTD/FVTD Grid

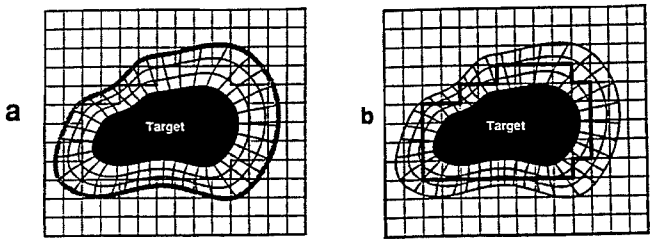


Fig. 6 The Outer Boundary of the Conformal Grid (a) and the Inner Boundary of the Rectangular Grid (b).

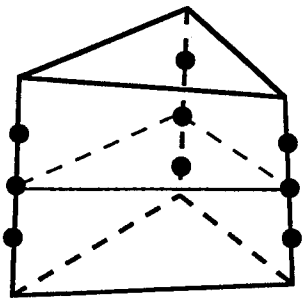


Fig. 7 Triangles of a Prism.

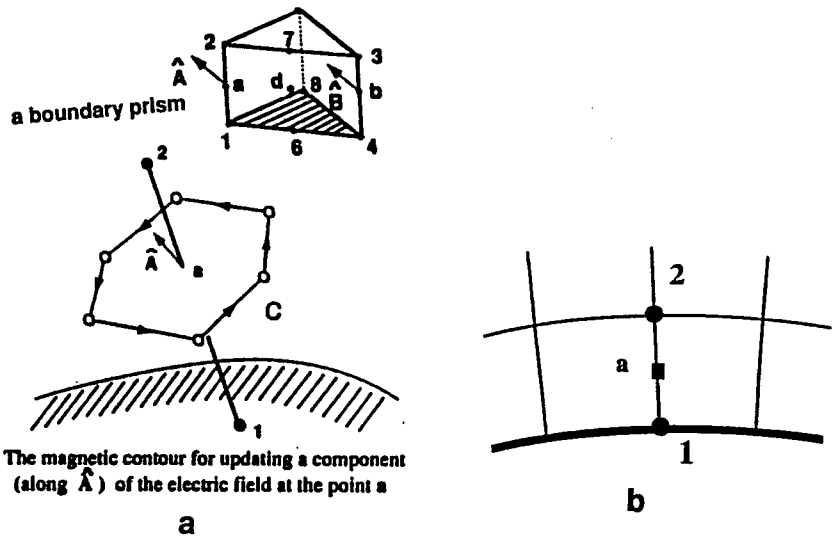


Fig. 8 PEC Boundary Condition Simulation -- a. for PEC 0 and b. for PEC 1

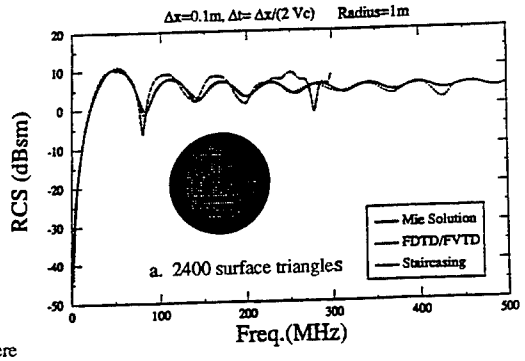
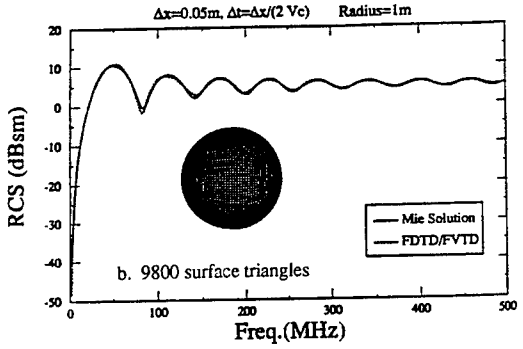


Figure 9 RCS for a PEC Sphere
a. 2400 surface triangle; b. 9800 surface triangles



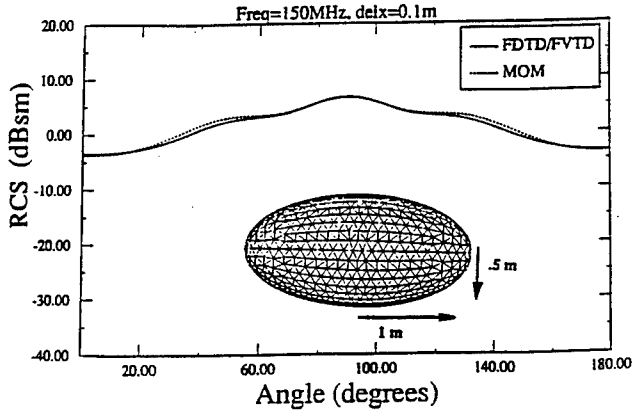


Fig 10 RCS for an Ellipsoid of Revolution
Major axis = 2m; Minor axis = 1m

Reducing the Number of Time Steps Needed for FDTD Antenna and Microstrip Calculations

R. J. Luebbers and H. S. Langdon
Electrical Engineering Department
The Pennsylvania State University
University Park, PA 16802

INTRODUCTION

The finite difference time domain (FDTD) method [1,2] has become an increasingly popular approach for analyzing the electromagnetic performance of antennas and microstrip devices. With transient excitation it provides impedance and scattering parameters over a wide frequency band with one calculation and application of the fast Fourier transformation (FFT). One difficulty with FDTD is that tens or even hundreds of thousands of time steps may be required for the transient fields to decay.

Previous authors have used different approaches to try to reduce the number of required time steps. In [3] for example, the transient excitation source for a microstrip line is located near the FDTD outer boundary. After the transient source amplitude has fallen to zero, the source is removed and replaced with the FDTD absorbing boundary. While this approach reduced the number of time steps needed, it is cumbersome to apply for general geometries. It also requires that the feed location be far enough from any geometry features so that no reflections return to the feed location before the source is removed and the outer absorbing boundary switched on. For these reasons, this approach does not appear to be applied very often in the literature.

A more common approach is to apply signal processing methods to predict the voltages and currents at later times from the results computed for early times. Instead of making FDTD calculations for the full 30,000 time steps required for transients to dissipate, one might make actual FDTD calculations for 8,000 time steps and use these results to predict those for the later times. A number of papers advocating variations of this approach have appeared. Two recent ones are [4,5], and there are a number of earlier attempts cited in these.

Applying the various prediction methods adds additional complexity to the FDTD calculation process. The prediction methods are complicated, and may require care and skill by the user to obtain accurate results. Most of the methods described require the user to determine the order of the prediction process, related to the number of terms of whatever expansion function is used to approximate the FDTD time signal. A poor choice for the order of the prediction model can result in large prediction errors.

In this paper we present an extremely simple approach for reducing the number of FDTD time steps needed for many resonant antenna and microstrip calculations. The approach is based on using a source with an internal resistance to excite the problem. An internal source resistance was used in [6] for excitation of

microstrip patch antennas. However, no illustration of the advantages of using and internal source resistance for reducing FDTD calculation time was presented.

In the following sections of this paper the approach will be presented, and an example calculation for a microstrip antenna will be used to illustrate the advantages.

RESISTIVE SOURCE FDTD EXCITATION

FDTD antenna or microstrip transient calculations are typically excited by a "hard" voltage source. That is, the internal source resistance is zero ohms. These source are very easy to implement in an FDTD code. The electric field at the mesh edge where the source is located is determined by some function of time rather than by the FDTD update equations. A common choice is a Gaussian pulse, but other functions may be used. The Gaussian pulse is significantly greater than zero amplitude for only a very short fraction of the total computation time, especially for resonant geometries such as many antennas and microstrip circuits. Once the pulse amplitude drops the source voltage becomes essentially zero, the source effectively becoming a short circuit. Thus any reflections from the antenna or microstrip circuit which return to the source are totally reflected. The only way the energy introduced into the calculation space can be dissipated is through radiation, or by absorption by lossy media or lumped loads. For resonant structures there are frequencies for which this radiation or absorption process requires a relatively long time in order to dissipate the excitation energy. Using a source with an internal resistance to excite the FDTD calculation provides an additional loss mechanism for the calculations.

Consider that it is desired to excite an FDTD calculation with a voltage source that corresponds to an electric field E in the z direction at a certain mesh location. The corresponding equivalent circuit for a voltage source which includes an internal source resistance Rs is illustrated in Figure 1. If the source resistance Rs is set to 0, then the usual FDTD electric field at the source location is simply given by E=Vs/Δz. Vs is any function of time, often a Gaussian pulse.

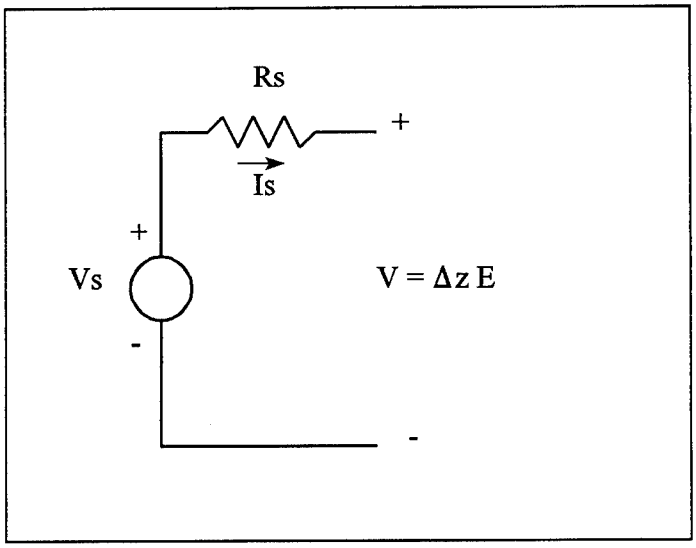


Figure 1 FDTD source with source resistance Rs.

But with the source resistance included, the calculation of the source field E at each time step is complicated slightly. In order to determine the terminal voltage V and thus the FDTD electric source field E, the current through the source must be determined. This can be done by taking the line integral of magnetic field. Example Fortran code for performing the required calculation for a Gaussian pulse is:

```
IF (T.LE.PRIOD) THEN
 EZS(22,15,4)=VS/DELZ*
$ EXP(-ALPH*((T-BETADT)**2))+
$ ((HX(22,14,4)-HX(22,15,4))*DELX+
$ (HY(22,15,4)-HY(21,15,4))*DELY)*
$ RS/DELZ
 ELSE
 EZS(22,15,4)=
$ ((HX(22,14,4)-HX(22,15,4))*DELX+
$ (HY(22,15,4)-HY(21,15,4))*DELY)*
$ RS/DELZ
 ENDIF
```

For this example RS is the source resistance Rs, EZS is the Source Electric Field in the z direction, in this case at mesh location (22,15,4). T is time, and PRIOD is the time duration of the Gaussian pulse, outside of which it is approximated as zero amplitude. VS is the Vs internal source voltage, DELZ is the z dimension mesh size, ALPH and BETADT control the Gaussian pulse width, and HX and HY are the magnetic fields surrounding the electric field source location. If the constant RS is set to 0 in the example Fortran, corresponding to Rs=0, then the usual hard voltage source results. Clearly it is quite simple to implement a voltage source with internal resistance.

EXAMPLE RESULTS

To illustrate the advantage of using a source with an internal resistance, S_{11} vs frequency for a rectangular microstrip antenna over a dielectric

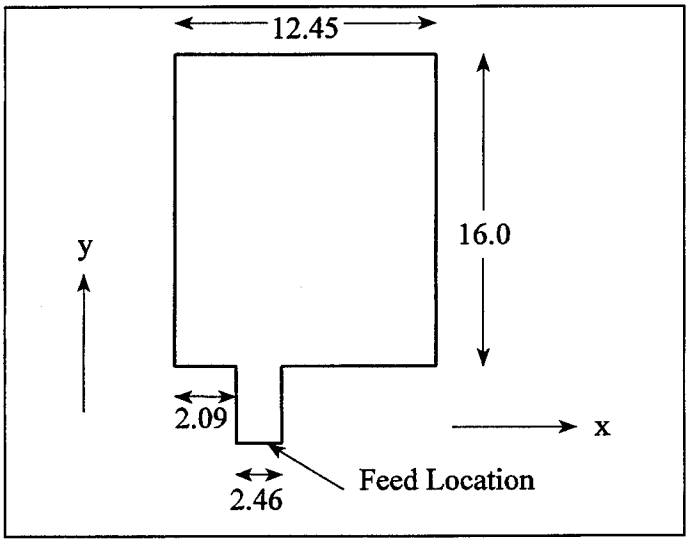


Figure 2 Geometry of microstrip patch antenna from [3]. All dimensions in mm.

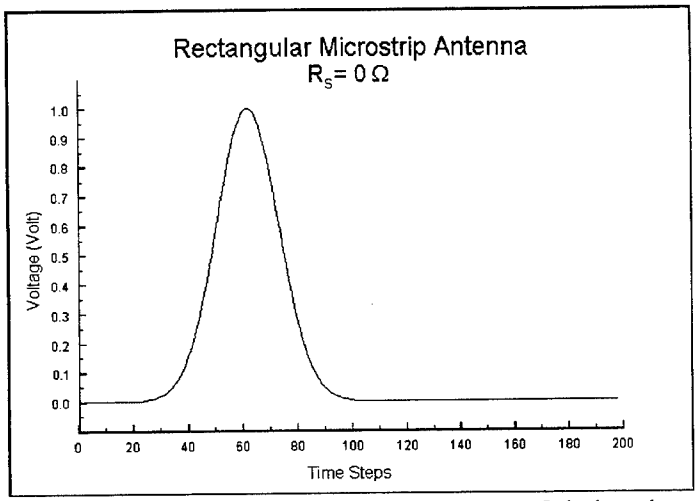


Figure 3 Source voltage V with source resistance Rs=0. Only the early time steps are shown.

substrate will be calculated. The geometry is similar to that shown in Fig. 3 of [3]. The only difference is that the 50Δy long feed line (2.46 mm wide in Figure 2) is reduced to 10Δy in the example calculation done here. Thus the feed location now coincides with the reference plane for phase in [3]. This allows the FDTD space to be smaller, reducing calculation time and memory requirements. The microstrip antenna is located on a 0.794 mm thick dielectric substrate of relative permittivity 2.2 over a ground plane. The cell sizes used are Δx=0.389mm, Δy=0.40mm, and Δz=0.265mm, the same as in [3]. However the time step used is 6.407×10^{-13} seconds, larger than used in [3]. The problem space size is 69x80x18 cells. The antenna is fed using a z-directed electric field just above the ground plane and directly below the end of the stripline as marked in Figure 2. This electric field feed mesh location is then connected to the end of the feed line by additional z-directed mesh edges of perfect conductor. The outer boundary is second order stabilized Liao [7 ,8] except for the x=0 surface which is the perfectly conducting substrate. All calculations were made with the XFDTD software package [9].

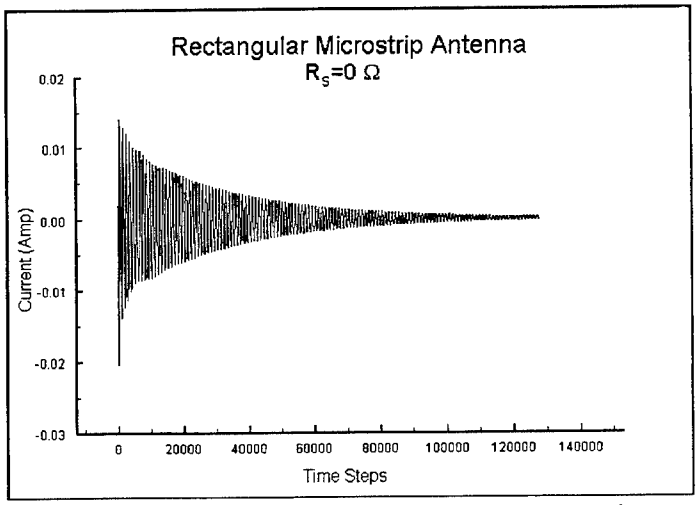


Figure 4 Source current Is with source resistance Rs=0, 128,000 time steps.

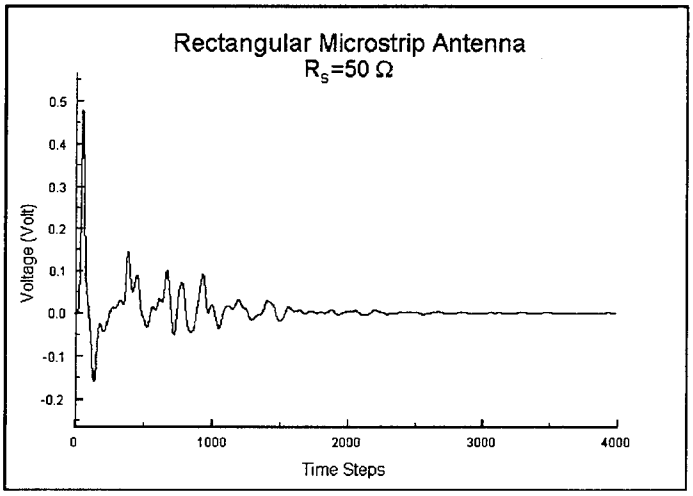


Figure 5 Source voltage V with source resistance Rs=50 Ohms. All 4,000 time steps are shown.

For the first set of calculations the source resistance Rs was set to 0 Ohms, which corresponds to the typical FDTD hard source. The source voltage V which determines the FDTD source electric field vs time is shown in Figure 3. For the hard source with no internal resistance, this is of course just the Gaussian pulse. The corresponding source current Is calculated by FDTD is shown in Figure 4. This calculation was made for 128,000 time steps, and still the current has not completely dissipated.

The corresponding calculations with a source resistance Rs=50 Ohms are shown in Figures 5 and 6. The same Gaussian pulse Vs was used for both calculations. The source voltage V shown in Figure 5, determined by saving the source electric field vs time, is no longer just the Gaussian pulse since the voltage across the source resistance Rs is also included. The source current Is converges much faster to zero amplitude, reducing the FDTD calculation time by

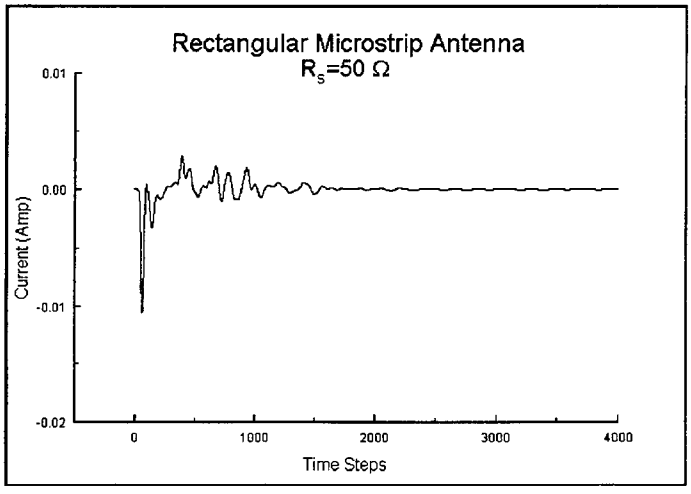


Figure 6 Source current Is with source resistance Rs=50 Ohms. All 4,000 time steps are shown.

a factor of 32. Indeed, it appears from Figure 6 that fewer than 4,000 time steps would be sufficient.

What about accuracy? Using the results from both FDTD calculations shown above, the source voltages and currents are Fourier transformed using an FFT with the same number of terms. The result V and IS results for 4,000 time steps were padded with zeroes to fill the FFT. Then the resulting complex voltages and currents were divided at each frequency to determine the input impedance Z_{in} at the feed location. The stripline characteristic impedance Z_0, as in [3], was taken to be 50 Ohms. Then $S_{11} = (Z_{in} - Z_0)/(Z_{in} + Z_0)$.

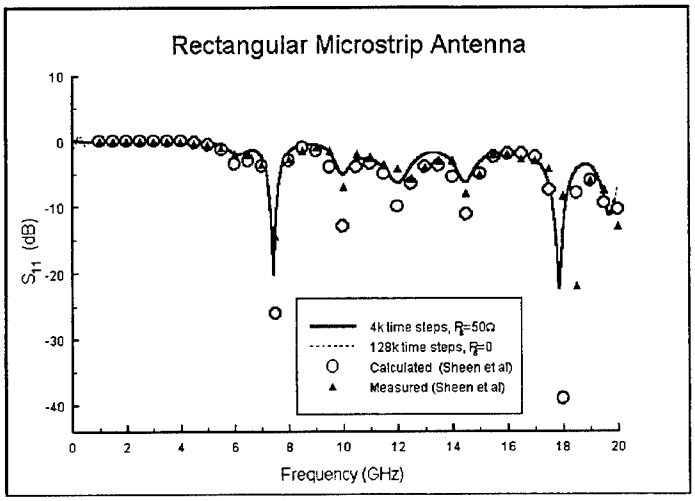


Figure 7 Return loss parameter S_{11} for both FDTD calculations of this paper, compared with calculations and measurements from [3].

The results obtained for both calculations are shown in Figure 7. The agreement between the two calculations is excellent, with the 4,000 and 128,000 time step curves being indistinguishable for most of the plot. The result obtained with Rs=50 is actually more accurate at the lower frequencies. The result with Rs=0 still has not quite converged after 128,000 time steps, and this causes the ripple in the corresponding low frequency S_{11} results. More importantly, the result with the 50 Ohm source resistance required 1/32 of the computation time of the calculation made with the hard source with Rs=0. Both results agree well with the measured and calculated results of Sheen et al [3], which are also shown Figure 7. Even with the longer stripline feed and removal of the source, the FDTD calculations of [3] required 8,000 time steps.

CONCLUSIONS

A simple approach for reducing the number of time steps required for FDTD calculations for resonant antennas and microstrip has been presented. It requires no additional memory, and can be implemented with a few lines of computer code. No time-varying calculation parameters or complicated post-processing is required. For the example shown, accurate results were obtained with 1/32 of the calculation time compared with the typical FDTD calculation.

REFERENCES

1. K. S. Yee, "Numerical solution of initial boundary value problems involving Maxwell's equations in isotropic media," IEEE Trans. Antennas and Propagat., vol. AP-14, pp 302-307, May 1966.

2. K. Kunz, R. Luebbers, The Finite Difference Time Domain Method for Electromagnetics, CRC Press, 496 pp, 1993.

3. D. M. Sheen et al, "Application of the Three-Dimensional Finite-Difference Time-Domain Method to the Analysis of Planar Microstrip Circuits," IEEE Trans. Microwave Theory and Techniques, vol. MTT-38, pp 849-857, July 1990.

4. V. Jandhyala et al, "FDTD Signal Extrapolation Using the Forward-Backward Autoregressive (AR) Model," IEEE Microwave and Guided Wave Letters, vol. 4, pp 163-165, June 1994.

5. J. Chen et al, "Using Linear and Nonlinear Predictors to Improve the Computational Efficiency of the FD-TD Algorithm," IEEE Trans. Microwave Theory and Techniques, vol. MTT-42, pp 1992-1997, October 1994.

6. A. Reineix and B. Jecko, "Analysis of Microstrip Patch Antennas Using Finite Difference Time Domain Method," IEEE Trans. Microwave Theory and Techniques, vol. MTT-37, pp 1361-1969, November 1989.

7. Z. P. Liao, H. L. Wong, G. P. Yang, and Y. F. Yuan, "A transmitting boundary for transient wave analysis," Scientia Sinica, vol. 28, no. 10, pp 1063-1076, Oct. 1984.

8. M. Moghaddam and W. C. Chew, "Stabilizing Liao's Absorbing Boundary Conditions using Single Precision Arithmetic," Proceedings of the IEEE AP-S International Symposium (London, Ontario), pp 430-433, 1991.

9. Available from REMCOM, Inc., Calder Square, PO Box 10023, State College, PA, 16805.

NUMERICAL SIMULATIONS OF LIGHT BULLETS, USING THE FULL VECTOR, TIME DEPENDENT, NONLINEAR MAXWELL EQUATIONS

Peter M. Goorjian
Mail Stop T27B-1
NASA Ames Research Center
Moffett Field, CA 94035-1000
(415) 604-5547
FAX (415) 604-1095

Yaron Silberberg
Dept. of Physics of Complex Systems
The Weizmann Institute of Science
76100 Rehovot, Israel
972-8-342034
FAX 972-8-344109

I. Introduction

From the exact Maxwell's equations, solutions have been obtained that are similar to light bullets [1], i.e. optical pulses that are self-supporting under the effects of diffraction, anomalous dispersion and nonlinear refraction. These pulses propagate stably, without any essential changes in shape or spectral content. For comparison, standard theory, which uses the nonlinear Schrodinger equation (NLSE), (an approximation to Maxwell's equations), predicts [1] that under the effects of nonlinear refraction, self-focusing will lead to the collapse of optical pulses. Also, additional calculations show that when two of these pulses are counter-propagating, upon interacting, they change each others' trajectories. These pulses are extremely small, approximately 25 fs in duration and contain about 5 wavelengths.

The solutions are computed by solving the time dependent, vector, nonlinear Maxwell's equations in two space dimensions [2-5]. The linear dispersion is modeled by a Lorentzian model with a single resonance and the nonlinear refraction is modeled by a Kerr-like instantaneous nonlinearity. The optical carrier is retained in the calculations so that each wavelength in the pulse is resolved. Also, since the Maxwell's equations are solved exactly, all higher order effects, such as higher order dispersion, are automatically accounted for in these simulations.

For comparison, standard methods of analysis and numerical simulation use the NLSE. That approach solves only for the envelope of the pulse. It assumes that the envelope is slowly-varying and that it contains one hundred to one thousand wavelengths [6]. Also, additional terms must be added to the NLSE to account for higher order effects [7]. Hence the NLSE cannot be used for the simulation of the small pulses in this study. Its approximations may account for its inability to predict stable light bullets.

The numerical algorithm employed in this paper is described in Refs. 2-5. It was used for calculations of propagating and interacting temporal [2-3,5] and spatial [4,5] solitons. In those simulations, the nonlinear effects included Kerr-like instantaneous as well as Raman dispersive nonlinearities. Convolution integrals described the linear and nonlinear dispersive effects. Their evolution was determined by a coupled system of nonlinear, ordinary differential equations. These equations were nonlinearly coupled to Maxwell's equations through the electromagnetic field. This entire system of equations was solved by a finite-difference algorithm, as described in Ref. 3. With that development, it became possible, for the first time, to solve the nonlinear, vector Maxwell's equations exactly, without having to go use approximations such as the NLSE. In this paper, that algorithm is used under the simplification that the nonlinearity is entirely instantaneous.

In order to isolate each material effect on the optical wave, the sequence of calculations were done methodically. In the first calculation, only dispersion acted on a pulsed plane wave. Next diffractive effects on a beam were calculated. These two effects were then allowed to act together on a pulse. Next nonlinear refraction was introduced as the third effect, with the result that a stable self-supporting pulse was created. Finally, two of these pulses interacted, while counter-propagating, and they deflected each other.

II. Results

The results are shown by displaying the variation of the electric field in the computational domain. The computational domain is 62 μm along the direction of propagation and 21 μm in the transverse direction.

Figure 1 shows the results of dispersion on a pulsed plane wave at four instants of time in its propagation. The source is turned on at the left side of the domain. The results are shown in a window in the computational domain that is centered in the transverse direction and that is 13 μm wide. The dispersion

in the material is characterized by a single Lorentzian resonance and is described by the following first order susceptibility function: $\chi^{(1)}(\omega) = (\omega_r^2(\epsilon_s - \epsilon_\infty))/(\omega_r^2 - \omega^2)$. Here $\epsilon_\infty = 9, \epsilon_s = 21$ and $\omega_r = 6.0 \times 10^{14}$ rad/sec. The wave length of the plane wave is $\lambda = 1.55\mu$m (in vacuum), with $\nu = 1.94 \times 10^{14}$ Hz or $\omega = 1.22 \times 10^{15}$ rad/sec, which is in the anomalous dispersion range. The electric field strength is 2.9×10^{10} Volts/m. The pulse has a hyperbolic secant envelope with a characteristic decay time constant of 10.3 fs. Notice that as the wave propagates, the pulse lengthens due to dispersion. Each band represents one wavelength.

Figure 2 shows the results of diffraction of a beam. Again the source is turned on at the left side and the four plots show the progression of the beam, including the beam's front edge. The cross sectional profile of the beam source is a hyperbolic secant envelope with a characteristic length of 0.517 μm, which is one wavelength of the optical carrier in a dielectric with an index of refraction equal to three. As the beam propagates, it widens due to diffraction.

Figure 3 shows the effects of both dispersion and diffraction acting on a pulse. The parameters of dispersion and diffraction are those from the previous two calculations. The plot at each time step is scaled by the maximum and minimum values of the electric field at that instant, rather than using global values, which would wash out the pulse's appearance at the later times due to its diminishing amplitude. Notice that the spreading rates of the pulse due to dispersion and diffraction are approximately equal. Also the individual wavelengths are clearly discernible and there are additional wave patterns in the pulse.

Figure 4 shows the pulse propagating under the combined effects of anomalous dispersion, diffraction and nonlinear refraction. The strength of the nonlinearity is given by the nonlinear index coefficient $n_2^I = 3.2 \times 10^{-20}$ m^2/W, (characteristic of silica at $\lambda = 1.55$ μm). Here the length of the computational domain has been reduced to 47 μm from 62 μm, since the longer length is no longer needed. Notice that the pulse is now self-supporting, without any essential changes in size or shape. The wavelengths are distinguishable and there are about five wavelengths in the pulse. Around the core of the pulse, which supports itself, is a surrounding low level outer coat, which disperses and diffracts away from the core.

Figure 5 shows a plot of the electric field values along the centerline of the computational domain at the four times shown in the previous figure. Again this figure shows that the essential shape of the pulse is maintained. Figure 6 shows the temporal power spectrum of the pulse at four locations along the centerline. Here the peak of the spectrum remains essentially unchanged. Hence, the results in Figs. 4-6 show that the pulse is essentially self-supporting and stable, viz. similar to a light bullet. Also, calculations were performed in which the pulse traveled twice the distance shown in Fig. 4 and the pulse maintained its support.

Figure 7 shows that when two of these pulses are counter-propagating, upon interacting, they change each others' trajectories. Initially, the right pulse is slightly upward in comparison to the left pulse. At the third instant plotted, the pulses have just passed each other and the initially higher pulse is still slightly higher. By the four instant, the plot shows that the two pulses have become aligned vertically. Although the effect is small, it shows that one of these light bullet like pulses can alter the path of another through an interaction.

The calculations were performed on a Cray C-90 computer and took 180 seconds per case, relatively minor calculations. The first author thanks Allen Taflove of Northwestern University for many helpful discussions.

III. References

1. Y. Silberberg, *Opt. Lett.* , **15**, No. 22, 1282-1284 (1990).
2. P. M. Goorjian and A. Taflove, *Opt. Lett.* , **17**, No. 3, 180-183 (1992).
3. P. M. Goorjian, A. Taflove, R. M. Joseph and S. C. Hagness, *IEEE J. Quantum Electronics* , **28**, 2416-2422 (1992).
4. P. M. Goorjian, A. Taflove and R. M. Joseph, *OSA Proceedings* , **17**, Short Wavelength V: Physics with Intense Laser Pulses, 66-69, (March 1993).
5. P. M. Goorjian, A. Taflove and R. M. Joseph, Nonlinear Guided-Wave Phenomena, OSA and IEEE/LEOS, Cambridge, England, Sept. 19-22, 1993.
6. G. G. Luther, A. C. Newell and J. V. Moloney, to appear in *Physica D* (1994).
7. G. P. Agrawal and C. Headley, *Phys. Rev. A*, **46**, No. 3, 1573-1577 (1992).

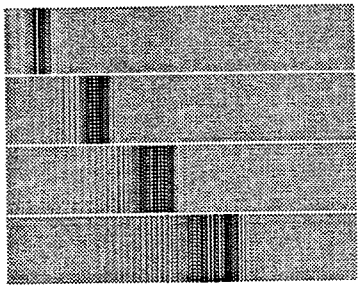


Fig. 1. The electric field of a plane wave in a dispersive medium after 155 fs, 310 fs, 465 fs and 620 fs of propagation.

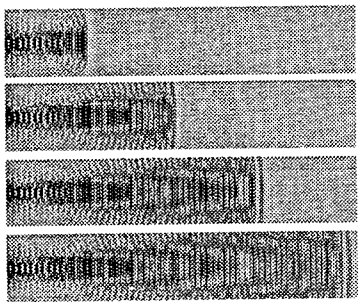


Fig. 2. The electric field of a beam undergoing diffraction after 155 fs, 310 fs, 465 fs and 620 fs of propagation.

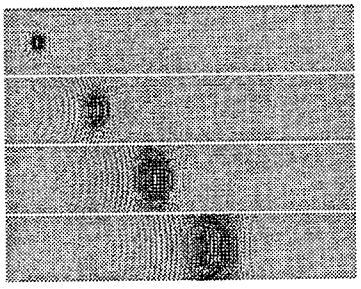


Fig. 3. The electric field of a pulse undergoing dispersive and diffraction after 155 fs, 310 fs, 465 fs and 620 fs of propagation.

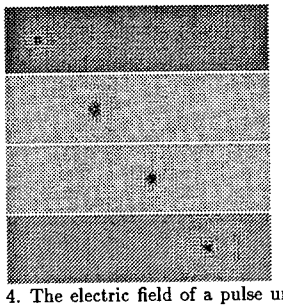


Fig. 4. The electric field of a pulse undergoing dispersive, diffraction and nonlinear refraction after 155 fs, 310 fs, 465 fs and 620 fs of propagation.

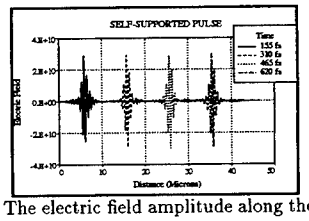


Fig. 5. The electric field amplitude along the centerline of the computational domain after 155 fs, 310 fs, 465 fs and 620 fs of propagation.

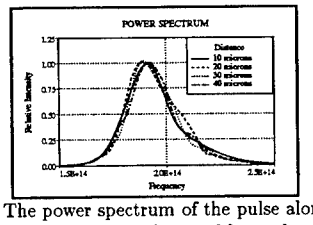


Fig. 6. The power spectrum of the pulse along the domain centerline and located at 10 μm, 20 μ, 30 μ and 40 μ.

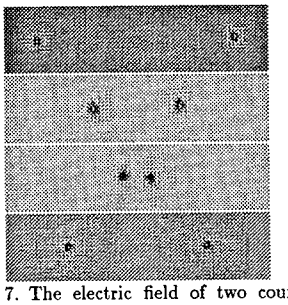


Fig. 7. The electric field of two counter-propagating light bullet-like pulses after 155 fs, 310 fs, 465 fs and 620 fs of propagation.

SESSION 8:

BERENGER'S BOUNDARY CONDITION

Chair: J. Fang

Ultrawideband Termination of Waveguiding and Multilayer Structures for FD-TD Simulations in 2-D and 3-D

Christopher E. Reuter*[1], Rose M. Joseph[2], Eric T. Thiele[4], Daniel S. Katz[3], Allen Taflove[2]

[1]Rome Laboratory/ERST, 525 Brooks Road, Griffiss AFB, NY 13441-4505
[2]Northwestern University, EECS Department, Evanston, IL 60208
[3]Cray Research, Inc., 222 N. Sepulveda Blvd, Ste. 1406, El Segundo, CA 90245
[4]University of Colorado, ECE Department, Boulder, CO 80309

Abstract

We describe a new termination for FD-TD models of metallic and dielectric guided-wave structures and multilayer structures employing the perfectly matched layer (PML) absorbing boundary condition (ABC) introduced by Berenger. The technique is accurate over a wide range of group velocities and requires no a priori knowledge of the propagating modes or dispersive properties of the structure.

Introduction

Both metallic (perfect electrically conducting, PEC) and dielectric waveguiding structures are now commonly modeled using the finite-difference time-domain (FD-TD) method. A problem has existed in the termination of the FD-TD grid for the case where the structure of interest extends beyond the bounds of the model. Since the propagating energy can be multimodal and dispersive, the termination must absorb energy with both a varying group velocity and varying transverse distribution. Previous approaches to this boundary condition problem have included one way wave equations [1], error-cancelling super-absorbers [2], outgoing wave annihilators [3], and the Liao theory [4]. These techniques are limited to a narrow spectrum (allowing the assumption of constant group velocity) or to a discrete number of known spectral components or modes such that each component could be accounted for individually, thus requiring a priori knowledge of the group velocity and modal distribution. More recently, Moglie, et. al [5] derived an analytical waveguide termination by Laplace transformation of the exact expression for the group velocity within the waveguide. This, however, is computationally burdensome requiring the evaluation of a convolution integral for each mode within the guide.

In this paper we describe a termination for FD-TD simulation of guided wave structures employing the perfectly matched layer (PML) absorbing boundary condition (ABC) introduced by Berenger[6]. Using PML absorbing material as a waveguide termination does not require the propagating field energy to be characterized in advance. No a priori knowledge of the propagating modes or dispersive properties of the waveguiding structure is required. Furthermore, the approach is local in time and space, general, and extremely accurate over a wide range of group velocities.

PML Waveguide Termination

The Berenger PML ABC is a new approach to terminate FD-TD grids using a numerical analog of a nonphysical material impedance matched to the standard FD-TD grid which it surrounds. Impedance matching between the FD-TD grid and the PML is attained by splitting certain field components into two subcomponents. Using two split subcomponents to represent one regular FD-TD field component gives an additional degree of freedom for specification of material parameters. Thus it is possible to specify a material in which waves of arbitrary frequency and angle of propagation are caused to decay rapidly while maintaining the velocity and impedance of the numerical media from which they originated. Complete details of the PML technique are reported [6, 7]. Application of the PML to 2-D metallic and dielectric waveguiding structures is reported in [8]. It is a straightforward extension of this work to apply the PML to 3-D metallic and dielectric waveguides.

It is to desirable obtain the minimum possible reflection from the PML. Three parameters control the magnitude of the numerical reflections at grid-PML interfaces; 1) the PML thickness, 2) the theoretical reflection at normal incidence, R(0), as defined by Berenger, and 3) the spatial profile of the conductivity within the PML. Berenger reported limited results for conductivity profiles having constant, linear, and parabolic distributions [6]. Furthermore, since computer resources are limited, the above three parameters must be optimized to meet the required model fidelity and to enable solution of the problem within limits of the available computer system. A thicker PML generally reduces reflections but requires larger memory and longer CPU run time. Modification of the remaining two parameters has insignificant effect on the required memory and run time. However, the relationship between these two parameters and the magnitude of the reflection is not obvious and warrants investigation. We have performed numerical experiments to determine the optimal values for these parameters while limiting computational requirements. The results reported for 2-D and 3-D waveguides in this paper were obtained using the optimized parameters.

Results

The first case reported is that of an an air-filled PEC parallel-plate waveguide having a plate separation of 40 mm (f_{cutoff} = 3.75 GHz). Excitation consists of an 83.3-ps Gaussian pulse

(FWHM) modulating a 7.5 GHz carrier that launches a TM_1 mode towards the PML termination. The spectrum of the excitation and the normalized group velocity for the TM_1 mode are shown in Fig. 1. Note that the input pulse has significant energy in the region of high dispersion on the group velocity curve. The reflection coefficient versus frequency is obtained by dividing the reflected spectrum by the incident spectrum as observed at the air-PML interface. We report the reflection coefficient of the PML termination for two sets of PML parameters. For the first set we used an 8 cell thick PML having a quadratic conductivity profile and an $R(0) = 10^{-6}$. These are typical PML parameters that would be used in a situation where memory is limited. The second type of PML tested has a cubic conductivity profile, an $R(0) = 10^{-7}$, and is 32 cells thick. These parameters would be used in simulations where it is required to obtain the absolute lowest possible reflection from the PML.

Fig. 2 graphs the reflection coefficient versus frequency for these two sets of PML parameters. Reflections better than -60 dB are obtained throughout the entire propagation regime for the first set of PML parameters. If less reflection is required, the 32 cell PML could be implemented yielding a reflection coefficient of better than -100 dB for the majority of the propagation regime.

The next case reported is a three-dimensional, 20 x 40 mm PEC waveguide with $f_{cutoff} = 3.75$ GHz. A pulse with spectral content similar to that of the 2-D case above was used to excite a TE_{10} mode in the waveguide. Again we report two PML terminations having different properties. The first PML is 8 cells thick, has a fourth order conductivity profile, and an $R(0) = 10^{-6}$. The second PML is 24 cells thick, has a fourth order conductivity profile, and $R(0) = 10^{-9}$. Fig. 3 graphs the resulting reflection coefficients versus frequency for both PML terminations. The reflection coefficient is better than -60 dB for the 8 cell PML and better than -80 dB for the 24 cell PML throughout most of the propagation regime. Thus, the PML can be tuned to obtain less reflection.

Reference [8] gave results for PML termination of a 2-D dielectric optical slab waveguide. In the oral presentation we will provide additional results for such structures with optimized PML parameters and also extend the work to 3-D modeling of strip-lines. We will also present results for using PML to improve FD-TD modeling of multi-layer structures, particularly the earth-air interface.

Conclusion

We have demonstrated the Berenger PML to be a wideband termination for FD-TD simulations of dielectric and PEC waveguides in both 2-D and 3-D. It has advantages over previously reported tecnniques including; 1) it is local in time and space, 2) it appears to be effective for dispersive, multimodal, and evanescent energy, and 3) it is easily implemented and computationally efficient.

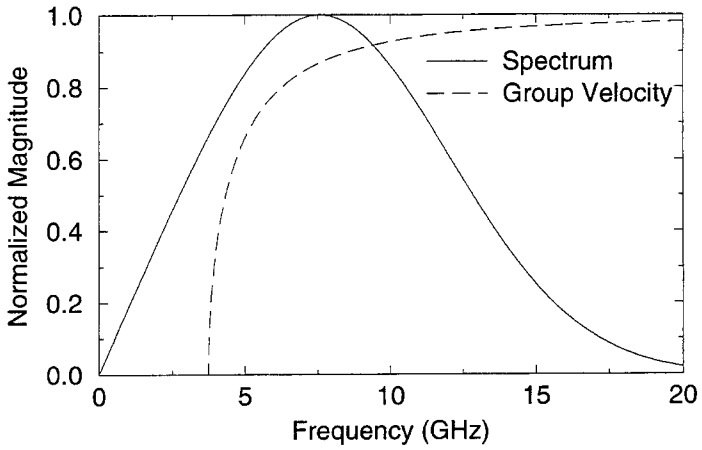


Figure 1. Normalized excitation spectrum and group velocity versus frequency for the TM_1 mode in the 2-D PEC parallel plane waveguide ($f_{cutoff} = 3.75$ GHz).

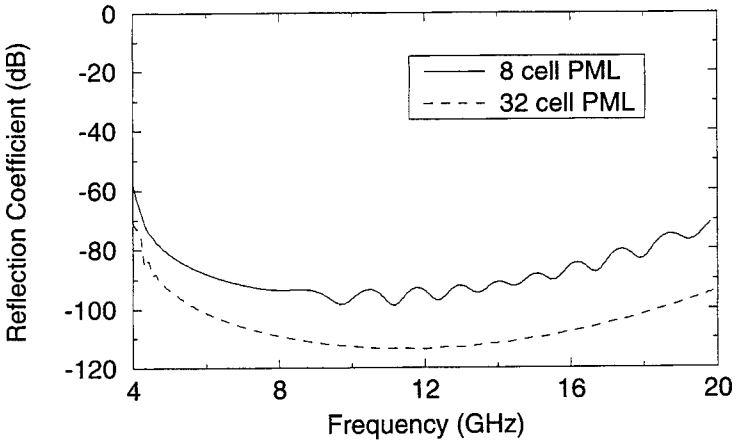


Figure 2. PML reflection coefficient versus frequency observed just outside the PML layer for two PML terminations having different properties: 2-D PEC waveguide test case.

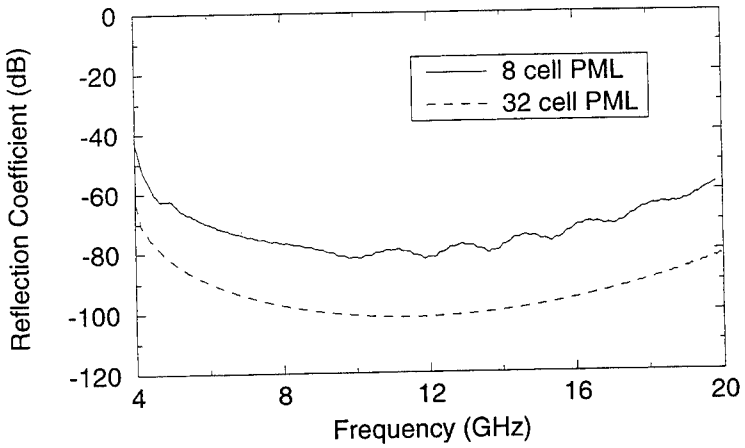


Figure 3. PML reflection coefficient versus frequency observed just outside the PML layer two PML terminations having different properties: 3-D PEC waveguide propagating a pulsed TE_{10} mode with $f_{cutoff} = 3.75$ GHz.

References

[1] G. Mur, "Absorbing boundary conditions for the finite-difference approximation of time-domain electromagnetic field equations," IEEE Trans. Electromagn. Compat., vol. EMC-23, pp. 377-382, Nov. 1981.

[2] K. K. Mei and J. Fang, "Superabsorption-a method to improve absorbing boundary conditions," IEEE Transactions on Antennas and Propagation, vol. AP-40, pp. 1001-1010, Sept. 1992.

[3] A. Bayliss and E. Turkel, "Radiation boundary conditions for wave-like equations," Commun. Pure Appl. Math., vol. 33, pp. 707-725, 1980.

[4] Z. P. Liao, H. L. Wong, B. P. Yang, and Y. F. Yuan, "A transmitting boundary for transient wave analysis," Scientia Sinica (series A), pp. 1063-1076, Oct. 1984.

[5] F. Moglie, T. Rozzi, P. Marcozzi, and A. Schiavoni, "A new termination condition for the application of fdtd techniques to discontinuity problems in close homogeneous waveguide," IEEE Microwave and Guided Wave Letters, vol. 2, pp. 475-477, Dec. 1992.

[6] J. Berenger, "A perfectly matched layer for the absorption of electromagnetic waves," Journal of Computational Physics, 114, pp. 185-200, 1994.

[7] D. S. Katz, E. T. Thiele, and A. Taflove, " Validation and extension to three dimensions of the berenger pml absorbing boundary condition for fd-td meshes," IEEE Microwave and Guided Wave Letters, vol. 4, pp. 268-270, 1994.

[8] C. E. Reuter, R. M. Joseph, E. T. Thiele, D. S. Katz, and A. Taflove, "Ultrawideband absorbing boundary condition for termination of waveguiding structures in fd-td simulations," IEEE Microwave and Guided Wave Letters, vol. 4, pp. 344-346, 1994.

A 3-D Perfectly Matched Medium by Coordinate Stretching and Its Absorption of Static Fields †

WENG CHO CHEW AND WILLIAM H. WEEDON
ELECTROMAGNETICS LABORATORY
DEPARTMENT OF ELECTRICAL AND COMPUTER ENGINEERING
UNIVERSITY OF ILLINOIS, URBANA, IL 61801

APO SEZGINER
SCHLUMBERGER-DOLL RESEARCH
OLD QUARRY ROAD
RIDGEFIELD, CT 06877

Key Terms: Maxwell's equations, coordinate stretching, perfectly matched layer, finite difference time domain, massively parallel computer, static field absorbing boundary condition.

ABSTRACT—A modified set of Maxwell's equations is presented that includes complex coordinate stretching along the three Cartesian coordinates. The added degrees of freedom in the modified Maxwell's equations allow the specification of absorbing boundaries with zero reflection at all angles of incidence and all frequencies. The modified equations are also related to the perfectly matched layer that was presented recently for 2-D wave propagation. We have demonstrated that absorbing material boundary conditions are of particular interest for finite difference time domain (FDTD) computations on a single-instruction multiple-data (SIMD) massively parallel supercomputer.

In addition, we will show that PML will absorb static field and can be used to truncate a finite-difference mesh for electrostatic and magnetostatic simulations.

1. Introduction

The finite difference time domain method [1, 2] is widely regarded as one of the most popular computational electromagnetics algorithms. Although FDTD is conceptually very simple and relatively easy to program, the method is actually quite efficient since it involves $O(N^{1.5})$ computational complexity in 2-D and $O(N^{1.33})$ computational complexity in 3-D [3]. In fact, FDTD can be considered an optimal algorithm since $O(N^{\alpha})$ numbers are produced in $O(N^{\alpha})$ operations.

FDTD is also ideally suited for implementation on a single-instruction multiple-data (SIMD) massively parallel computer. The reason is that the stencil operations that must be computed at each node of the space grid involve only nearest-neighbor interactions and may be implemented at a minimum communication cost [4]. A major challenge, however, is in implementing absorbing boundary conditions (ABCs) at the edges of the FDTD grid. On scalar and vector computers, these boundary conditions are typically computed using methods such as the Engquist-Majda [5], Mur [6], Liao [7] or Higdon [8] ABC. However, these methods are not ideal for parallel supercomputers since they all involve communication with many elements normal to the grid boundary, which can easily surpass the time spent computing core FDTD operations in the grid interior. Also, they do not allow for SIMD operation on a parallel machine without the use of masking.

An alternate method of implementing an ABC is to use a conventional absorbing material boundary [4, 9–14] . For SIMD parallel computation, these methods have the advantage that the ABC may be implemented with the same FDTD stencil operation as the interior nodes by modifying the conductivity material parameter at the edge of the FDTD grid. The disadvantage is that the reflection coefficient at the absorbing border is zero only at normal incidence and is both angle and frequency dependent. Consequently,

† This work is supported by the Office of Naval Research under grant N000-14-89-J1286, the Army Research Office under contract DAAL03-91-G-0339, the National Science Foundation under grant NSF-ECS-92-24466, and NASA under grant NASA-NAG-2-871. Computer time is provided by the National Center for Supercomputer Applications at the University of Illinois, Urbana-Champaign.

the absorbing material border region must be made quite large—typically 20–100 grid points along each edge in order to minimize reflections.

Recently, Berenger [15] suggested a more general method of implementing an absorbing material boundary condition. Berenger proposed a procedure for 2-D wave propagation whereby Maxwell's equations are generalized and added degrees of freedom are introduced. The added degrees of freedom allow the specification of absorbing borders with zero reflection coefficient at all angles of incidence and all frequencies. Moreover, the generalized Maxwell's equations reduce to the familiar Maxwell's equations as a special case and hence the same generalized equations can be used to propagate fields in both the interior region and absorbing region. Although the interface between the interior region and the absorbing boundary is reflectionless, there is still a reflection from the edge of the grid. The advantage of using Berenger's procedure is that much larger conductivity values may be specified in the absorbing region, leading to a drastic reduction in the number of grid points required for the absorbing boundary.

A formulation similar to the Berenger idea has been derived for 3-D wave propagation from first principles using a coordinate stretching approach [16]. The advantage of the new method is for SIMD parallel computation. The method is validated with 3-D FDTD numerical computations on a Thinking Machines Corporation Connection Machine CM-5.

2. Modified Maxwell's Equations

For a general medium, we define the modified Maxwell's equations in the frequency domain, assuming $e^{-i\omega t}$ time dependence, as

$$\nabla_e \times \boldsymbol{E} = i\omega\mu\boldsymbol{H} \tag{1}$$

$$\nabla_h \times \boldsymbol{H} = -i\omega\epsilon\boldsymbol{E} \tag{2}$$

$$\nabla_h \cdot \epsilon\boldsymbol{E} = \rho \tag{3}$$

$$\nabla_e \cdot \mu\boldsymbol{H} = 0 \tag{4}$$

where

$$\nabla_e = \hat{x}\frac{1}{e_x}\frac{\partial}{\partial x} + \hat{y}\frac{1}{e_y}\frac{\partial}{\partial y} + \hat{z}\frac{1}{e_z}\frac{\partial}{\partial z} \tag{5}$$

$$\nabla_h = \hat{x}\frac{1}{h_x}\frac{\partial}{\partial x} + \hat{y}\frac{1}{h_y}\frac{\partial}{\partial y} + \hat{z}\frac{1}{h_z}\frac{\partial}{\partial z}. \tag{6}$$

In the above, e_i, h_i, $i = x, y, z$ are coordinate-stretching variables that stretch the x, y, z coordinates for ∇_e and ∇_h. For a plane wave, we can show that for a homogeneous medium, this gives the dispersion relation

$$\omega^2\mu\epsilon = \boldsymbol{k}_e \cdot \boldsymbol{k}_h \tag{7}$$

where $\boldsymbol{k}_e = \hat{x}\frac{k_x}{e_x} + \hat{y}\frac{k_y}{e_y} + \hat{z}\frac{k_z}{e_z}$ and $\boldsymbol{k}_h = \hat{x}\frac{k_x}{h_x} + \hat{y}\frac{k_y}{h_y} + \hat{z}\frac{k_z}{h_z}$, or

$$\kappa^2 = \frac{1}{e_x h_x}k_x^2 + \frac{1}{e_y h_y}k_y^2 + \frac{1}{e_z h_z}k_z^2 \tag{8}$$

where $\kappa^2 = \omega^2\mu\epsilon$. Equation (8) is the equation of an ellipsoid in 3-D and is satisfied by [16]

$$k_x = \kappa\sqrt{e_x h_x}\sin\theta\cos\phi, \tag{9}$$

$$k_y = \kappa\sqrt{e_y h_y}\sin\theta\sin\phi, \tag{10}$$

and

$$k_z = \kappa\sqrt{e_z h_z}\cos\theta. \tag{11}$$

Note that when e_i, h_i, $i = x, y, z$ are complex, the wave in the x, y, and z directions are attenuative and can be independently controlled. Under the matching condition, $e_x = h_x$, $e_y = h_y$, and $e_z = h_z$, we have $|\boldsymbol{k}_e|^2 = |\boldsymbol{k}_h|^2 = \kappa^2$. The wave impedance is then given by

$$\eta = \frac{|\boldsymbol{E}|}{|\boldsymbol{H}|} = \frac{|\boldsymbol{k}_h|}{\omega\epsilon} = \sqrt{\frac{\mu}{\epsilon}}, \tag{12}$$

irrespective of the values for $e_i, i = x, y, z$ and the direction of propagation.

3. Single Interface Problem

Assume that a plane wave is obliquely incident on the interface $z = 0$. Furthermore, we may assume that the plane wave is of arbitrary polarization. The incident field may be decomposed into a sum of two components, one with electric field transverse to z (TE^z) and the other with magnetic field transverse to z (TM^z).

We can derive their reflection and transmission coefficients as [16]

$$R^{\mathrm{TE}} = \frac{k_{1z}e_{2z}\mu_2 - k_{2z}e_{1z}\mu_1}{k_{1z}e_{2z}\mu_2 + k_{2z}e_{1z}\mu_1} \tag{13}$$

and

$$T^{\mathrm{TE}} = \frac{2k_{1z}e_{2z}\mu_2}{k_{1z}e_{2z}\mu_2 + k_{2z}e_{1z}\mu_1}. \tag{14}$$

Similarly, we have

$$R^{\mathrm{TM}} = \frac{k_{1z}h_{2z}\epsilon_2 - k_{2z}h_{1z}\epsilon_1}{k_{1z}h_{2z}\epsilon_2 + k_{2z}h_{1z}\epsilon_1} \tag{15}$$

and

$$T^{\mathrm{TM}} = \frac{2k_{1z}h_{2z}\epsilon_2}{k_{1z}h_{2z}\epsilon_2 + k_{2z}h_{1z}\epsilon_1}. \tag{16}$$

4. A Perfectly Matched Interface

The phase matching condition requires that $k_{1x} = k_{2x}$ and $k_{1y} = k_{2y}$, or

$$\kappa_1\sqrt{e_{1x}h_{1x}}\sin\theta_1\cos\phi_1 = \kappa_2\sqrt{e_{2x}h_{2x}}\sin\theta_2\cos\phi_2 \tag{17}$$

and

$$\kappa_1\sqrt{e_{1y}h_{1y}}\sin\theta_1\sin\phi_1 = \kappa_2\sqrt{e_{2y}h_{2y}}\sin\theta_2\sin\phi_2 \tag{18}$$

where $\kappa_1 = \omega\sqrt{\mu_1\epsilon_1}$ and $\kappa_2 = \omega\sqrt{\mu_2\epsilon_2}$. For a perfectly matched medium, we choose $\epsilon_1 = \epsilon_2$, $\mu_1 = \mu_2$, $e_x = h_x$ and $e_y = h_y$. Equations (17) and (18) become

$$e_{1x}\sin\theta_1\cos\phi_1 = e_{2x}\sin\theta_2\cos\phi_2 \tag{19}$$

and

$$e_{1y}\sin\theta_1\sin\phi_1 = e_{2y}\sin\theta_2\sin\phi_2. \tag{20}$$

If we now choose $e_{1x} = e_{2x}$ and $e_{1y} = e_{2y}$, then $\theta_1 = \theta_2$, $\phi_1 = \phi_2$ and we can show that both $R^{\mathrm{TE}} = 0$ and $R^{\mathrm{TM}} = 0$ for all angles of incidence and all frequencies.

If region 1 is a vacuum, then $\mu = \mu_0$, $\epsilon = \epsilon_0$, and

$$(e_{1x}, e_{1y}, e_{1z}, h_{1x}, h_{1y}, h_{1z}) = (1, 1, 1, 1, 1, 1). \tag{21}$$

In order to have a lossy region 2 with no reflections at the region 1/region 2 interface, we choose

$$(e_{2x}, e_{2y}, e_{2z}, h_{2x}, h_{2y}, h_{2z}) = (1, 1, s_2, 1, 1, s_2) \tag{22}$$

where s_2 is a complex number. In this case,

$$k_{1x} = k_{2x} = \kappa_0 \sin\theta \cos\phi \tag{23}$$

$$k_{1y} = k_{2y} = \kappa_0 \sin\theta \sin\phi \tag{24}$$

$$k_{1z} = \kappa_0 \cos\theta \tag{25}$$

$$k_{2z} = \kappa_0 s_2 \cos\theta \tag{26}$$

where $\kappa_0 = \omega\sqrt{\mu_0\epsilon_0}$. If $s_2 = s_2' + is_2''$, the wave will attenuate in the z direction. This kind of interface is useful for building material ABCs in a FDTD simulation.

In realistic simulation, we will have to choose $s_2'' \sim \frac{1}{\omega}$. Hence, when the frequency goes to zero, k_{2z} above becomes a purely imaginary number. Therefore, it attenuates static fields as well.

5. Modified Equations in the Time Domain

For the general case of a matched medium, we let $e_x = h_x = s_x$, $e_y = h_y = s_y$ and $e_z = h_z = s_z$. Next, we let $s_x = 1 + i\sigma_x/\omega\epsilon$, $s_y = 1 + i\sigma_y/\omega\epsilon$ and $s_z = 1 + i\sigma_z/\omega\epsilon$. Writing the equations in the time domain [16], we have

$$\mu\frac{\partial \boldsymbol{H}_{s_x}}{\partial t} + \frac{\sigma_x\mu}{\epsilon}\boldsymbol{H}_{s_x} = -\frac{\partial}{\partial x}\hat{x} \times \boldsymbol{E} \tag{27}$$

$$\mu\frac{\partial \boldsymbol{H}_{s_y}}{\partial t} + \frac{\sigma_y\mu}{\epsilon}\boldsymbol{H}_{s_y} = -\frac{\partial}{\partial y}\hat{y} \times \boldsymbol{E} \tag{28}$$

$$\mu\frac{\partial \boldsymbol{H}_{s_z}}{\partial t} + \frac{\sigma_z\mu}{\epsilon}\boldsymbol{H}_{s_z} = -\frac{\partial}{\partial z}\hat{z} \times \boldsymbol{E} \tag{29}$$

and

$$\epsilon\frac{\partial \boldsymbol{E}_{s_x}}{\partial t} + \sigma_x\boldsymbol{E}_{s_x} = \frac{\partial}{\partial x}\hat{x} \times \boldsymbol{H} \tag{30}$$

$$\epsilon\frac{\partial \boldsymbol{E}_{s_y}}{\partial t} + \sigma_y\boldsymbol{E}_{s_y} = \frac{\partial}{\partial y}\hat{y} \times \boldsymbol{H} \tag{31}$$

$$\epsilon\frac{\partial \boldsymbol{E}_{s_z}}{\partial t} + \sigma_z\boldsymbol{E}_{s_z} = \frac{\partial}{\partial z}\hat{z} \times \boldsymbol{H}. \tag{32}$$

Equations (27) – (32) described 3-D wave propagation in a perfectly matched medium. The wave propagation phenomenon described by these equations is very similar to that described by Maxwell's equations with the exception that attenuation may be controlled through the σ_x, σ_y and σ_z variables. The FDTD implementation of these equations on a Yee FDTD grid is straightforward. Absorbing boundaries at the edges of the simulation region may be created by choosing appropriate values of σ_x, σ_y and σ_z. Equations (27) – (32) may be seen to include Berenger's equations [15] as a subset for the 2-D TE or TM case.

6. Computer Simulation Results

To study the PML, we calculate the reflection coefficient for a plane wave incident with different values of k_x. The reflection coefficient is calculated for a step conductivity (σ_z) profile of 7 layers (with a metal backing) shown in Figure 1a. Figure 1b shows the reflection coefficient magnitude as a function of k_x/k_0 where $k_x = k_0$ corresponds to grazing incidence. Notice that the reflection coefficient magnitude is always 1 at grazing incidence. σ_{max} is the maximum value of σ_z for the step profile which increases in conductivity toward the metal backing. The overall reflection amplitude is smaller for increasing σ_{max}. Notice that the evanescent wave ($k_x > k_0$) are well absorbed.

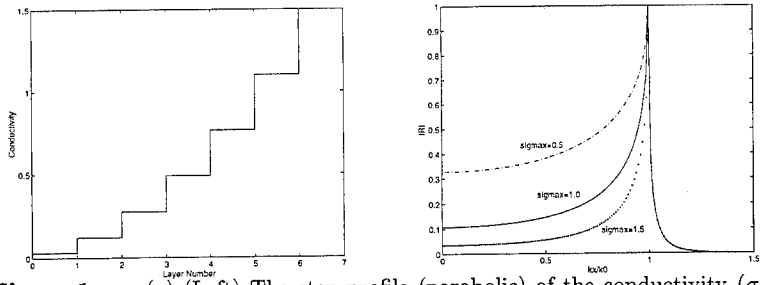


Figure 1: (a) (Left) The step profile (parabolic) of the conductivity (σ_z) used in the PML absorbing boundary. (b) (Right) The reflection coefficient magnitude as a function of a plane wave incident with different k_x's (x being the direction parallel to the interface) and different σ_{max}.

In Figure 2, we solve the Sommerfeld problem of a line source over a PML medium backed by a ground plane. The line source is located at the origin, with the first interface of the medium at a distance h_t below the line source. The observation point is located at (x, z). The amplitude of the field is plotted as a function of x for a fixed z. Notice that as σ_{max} increases, the result agrees with the ideal exact result, which is the case in the absence of the ground-plane-backed PML. Also, for large x, the discrepancy cannot be remedied by choices of σ_{max}. This is because the observer at larger x receives most of the reflected field through grazing reflection, where the PML medium does not absorb well.

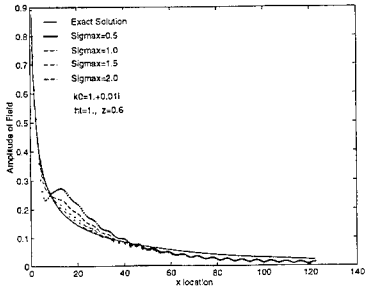


Figure 2: The field magnitude as a function of x for an electric line source over a PML medium backed by a ground plane for different σ_{max} in a seven layer parabolic profile. The thickness of each PML is 0.6.

In order to demonstrate the new method, a 3-D orthogonal grid FDTD algorithm was developed based on Equations (27) – (32). The FDTD algorithm was implemented as a SIMD code on the Thinking Machines Corporation Connection Machine CM-5. The algorithm operates very efficiently on the CM-5 because the FDTD stencil operations that need to be computed at each node involve only nearest-neighbor interactions. The communication operations resulting from the nearest-neighbor interactions are at a minimum cost.

The FDTD solution was solved in a cubic region of dimension $(N_x, N_y, N_z) = (128, 128, 32)$ grid points. The grid parameters chosen were $\Delta x = \Delta y = \Delta z = 2.5$ mm, $\Delta t = 4.5$ ps and $N_t = 512$ time steps were computed.

The infinitesimal electric dipole was simulated by exciting the E_y field in a single grid cell with the source pulse

$$J_y(t) = \frac{1}{\Delta x \Delta y \Delta z} \left[4(t/\tau)^3 - (t/\tau)^4\right] e^{-t/\tau} \tag{33}$$

where $\tau = 1/4\pi f_0$ and a value of $f_0 = 1.0$ GHz was chosen. The dipole source was located at grid location $(n_x, n_y, n_z) = (91, 64, 16)$. The E_x and E_y fields were obtained by sampling the fields at grid location $(n_x, n_y, n_z) = (37, 91, 16)$.

The absorbing boundaries used for the FDTD simulation consisted of planar layers of thickness 8 grid points on all surfaces. Along the borders parallel to x axis, the value of σ_x was specified, while σ_y and σ_z were specified on the borders parallel to the y and z axis, respectively. The conductivity values were chosen with a parabolic taper.

The E_x field computed using both the analytic formulation and the FDTD algorithm are overlaid in Figure 3. The curves due to the analytic and numerical solutions are barely distinguishable, indicating excellent agreement.

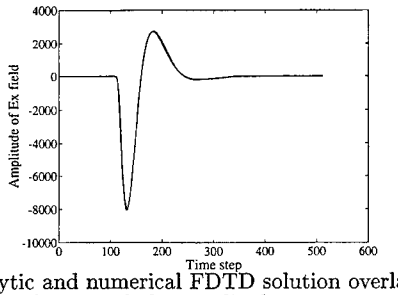


Figure 3: Analytic and numerical FDTD solution overlaid for the E_x field resulting from an infinitesimal electric dipole.

The CM-5 machine used to solve the FDTD problem is located at the National Center for Supercomputing Applications (NCSA) at the University of Illinois. The program was written in CM Fortran and compiled using CMF version 2.1. The CM-5 at the NCSA has 512 nodes with vector units. CPU times were determined by running the problem on 32, 64, 128 and 256 node partitions. For this problem, a total of 1.5 million unknown field quantities per time step

($128 \times 128 \times 32$ grid) were determined for 512 time steps. The CPU times are shown in Table 1.

In Figure 4, we show the absorption of electrostatic field by a PML medium. The plots are for the x-components of the electric field as a function of x due to a line of electric

Table 1: CPU times for FDTD Problem on CM-5

Nodes	CPU sec (Run 1, Run 2, Run 3, Avg.)
32	50.5, 50.2, 50.6; 50.4
64	29.9, 30.0, 30.0; 30.0
128	17.9, 18.4, 18.4; 18.2
256	12.4, 13.2, 12.7; 12.8

dipole pointing in the x-direction. The dotted line is the closed-form solution. The dotted-dashed line is the simulation with PML absorbing boundary condition. The solid line is the result from simulation using a modified impedance boundary condition. It is seen that the static field diminishes exponentially fast near the edge of the simulation region. In the simulation region of interest, the PML result agrees much better than the impedance boundary condition simulation when compared to the closed form solution.

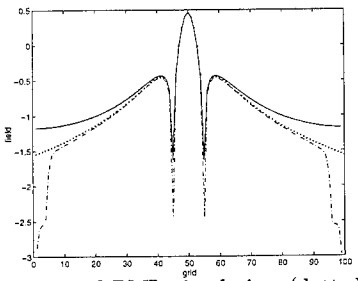


Figure 4: Comparison of PML simulation (dotted-dashed), impedance boundary condition simulation (solid) and closed form (dotted) for the x component of the electric field due to a line source of static electric dipole.

7. Conclusions

A modified set of Maxwell's equations have been introduced using complex coordinate stretching factors along the three Cartesian coordinate axis. This modification introduces additional degrees of freedom in Maxwell's equations such that absorbing boundaries may be specified with zero reflection coefficient at all frequencies and all angles of incidence. The formulation was shown to be related to the perfectly matched layer that was recently derived by Berenger for 2-D wave propagation. A 3-D FDTD algorithm was developed from the modified Maxwell's equations that uses the reflectionless absorbing interface property to implement radiation boundary conditions at the edges of the FDTD grid, and was implemented on the Connection Machine CM-5 and timing results were presented. This breakthrough in absorbing material boundary conditions allows EM scattering to be computed very efficiently on SIMD parallel computers. In addition, we show that PML does not absorb for waves at grazing incidence, but it could absorb static electromagnetic field.

References

[1] K. S. Yee, "Numerical solution of initial boundary value problems involving Maxwell's equations in isotropic media," *IEEE Trans. Antennas Propagat.*, vol. AP-14, pp. 302–307, 1966.

[2] A. Taflove, "Review of the formulation and applications of the finite-difference time-domain method for numerical modeling of electromagnetic wave interactions with arbitrary structures," *Wave Motion*, vol. 10, pp. 547–582, 1988.

[3] W. C. Chew, *Waves and Fields in Inhomogeneous Media.* New York: Van Nostrand, 1990.

[4] W. H. Weedon, W. C. Chew, and C. M. Rappaport, "Computationally efficient FDTD simulation of open-region scattering problems on the connection machine CM-5," in *IEEE Antennas and Propagation Society International Symposium Digest,* (Seattle, WA), June 19–24, 1994.

[5] B. Engquist and A. Majda, "Absorbing boundary conditions for the numerical simulation of waves," *Math. Computation,* vol. 31, pp. 629–651, 1977.

[6] G. Mur, "Absorbing boundary conditions for the finite-difference approximation of the time-domain electromagnetic field equations," *IEEE Trans. Electromag. Compat.,* vol. EMC-23, pp. 377–382, 1981.

[7] Z. P. Liao, H. L. Wong, B. P. Yang, and Y. F. Yuan, "A transmitting boundary for transient wave analysis," *Scientia Sinica. (Series A),* vol. 27, no. 10, pp. 1063–1076, 1984.

[8] R. L. Higdon, "Numerical absorbing boundary conditions for the wave equation," *Math. Comput.,* vol. 49, pp. 65–90, 1987.

[9] I. Katz, D. Parks, A. Wilson, M. Rotenberg, and J. Harren, "Non-reflective free space boundary conditions for SGEMP codes," *Systems, Science and Software,* vol. SSS-R-76-2934, 1976.

[10] R. Holland and J. W. Williams, "Total-field versus scattered-field finite-difference codes: A comparative assessment," *IEEE Trans. Nuclear Sci.,* vol. NS-30, pp. 4583–4588, 1983.

[11] J.-P. Berenger in *Actes du Colloque CEM,* (Tregastel, France), 1983.

[12] C. Cerjan, D. Kosloff, R. Kosloff, and M. Reshef, "A nonreflecting boundary condition for discrete acoustic and elastic wave equations," *Geophysics,* vol. 50, pp. 705–708, 1985.

[13] R. Kosloff and D. Kosloff, "Absorbing boundaries for wave propagation problems," *J. Computational Physics,* vol. 63, pp. 363–376, 1986.

[14] C. M. Rappaport and L. Bahrmasel, "An absorbing boundary condition based on anechoic absorber for EM scattering computation," *J. Electromag. Waves Appl.,* vol. 6, no. 12, pp. 1621–1634, 1992.

[15] J.-P. Berenger, "A perfectly matched layer for the absorption of electromagnetic waves," *J. Computational Physics,* vol. 114, pp. 185–200, 1994.

[16] W. C. Chew and W. H. Weedon, "A 3d perfectly matched medium from modified maxwell's equations with stretched coordites," *Micro. Opt. Tech. Lett.,* vol. 7, pp. 599–604, 1994.

Perfectly Matched Anisotropic Absorbers for Finite Element Applications in Electromagnetics[1]

David M. Kingsland, Zachary S. Sacks, and Jin-Fa Lee
Department of Electrical and Computer Engineering
Worcester Polytechnic Institute
100 Institute Road
Worcester, MA 01609

Abstract

A new type of "Perfectly Matched Layer" (PML) is developed for mesh truncation in frequency domain finite element applications. The concept is based on using diagonally anisotropic media in an artificial absorber. The interface between the absorber and the computation domain can be made reflectionless for any angle of incidence and polarization, leading to a mesh truncation scheme with much less reflection than other local absorbing boundary conditions. The scheme was implemented in a 3-D tetrahedral finite element code and applied to solving a TEM waveguide problem and a sphere scattering problem.

1 Introduction

Traditionally, the truncation of finite element solution domains has been accomplished through the application of local or global boundary operators to the outer surface of the finite element mesh. There is a tradeoff involved between the accuracy of global operators (boundary integral solutions) and the efficiency of local operators (ABC's). Alternative methods of truncation based on placing a layer of absorbing material at the outer boundary of the solution domain have been widely investigated in the past. These absorbers posses the same desirable property as local boundary operators: they preserve the sparse structure of the system matrix generated by the finite element method. Unfortunately, their accuracy is also similar to that of local boundary operators.

Recently, J.P. Berenger [1] introduced a high performance absorbing layer for 2-D FDTD simulations by splitting the H_z field component into two subcomponents ($H_z = H_{zx} + H_{zy}$). This "Perfectly Matched Layer" (PML) approach yields a reflectionless interface between free space and the artificial absorber. Chew and Weedon [2] described an alternative method of deriving a perfectly matched layer based on complex coordinate stretching along the cartesian axes. Both methods involve generalizations of Maxwell's equations which introduce added degrees of freedom. However, neither of these approaches is well suited for finite element implementations of a perfectly matched layer.

Fortunately, a reflectionless interface between free space and a lossy material absorber can also be achieved when the bulk properties of the material are anisotropic. Specifically, if ϵ and μ are appropriately chosen complex diagonal tensors, the impedance of the medium will be independent of the frequency, polarization, and incident angle of the wave at the interface. A perfectly matched layer of this anisotropic material can be used for truncation of finite element solution domains.

In this work, an anisotropic absorber is presented and implemented to truncate FEM solution domains in 3-D. The accuracy of the anisotropic layer is examined by solving a guided TEM wave propagation problem and computing

[1]This work supported by a grant from Motorola, Inc.

the electromagnetic scattering from a plane wave incident on a conducting sphere.

2 Anisotropic Absorbers

The development of a perfectly matched absorber using anisotropic material properties is briefly described in this section. A more detailed derivation can be found in [?]. The material properties of the absorbing medium are assumed to be complex diagonal tensors: $\bar{\epsilon}$, $\bar{\mu}$. To match the wave impedance of the absorber to that of free space, the following condition is required:

$$\frac{\bar{\mu}}{\bar{\epsilon}} = \frac{\mu_0}{\epsilon_0} \tag{1}$$

Thus, $\bar{\mu} = \mu_0\bar{\gamma}$ and $\bar{\epsilon} = \epsilon_0\bar{\gamma}$ where

$$\bar{\gamma} = \begin{bmatrix} a & 0 & 0 \\ 0 & b & 0 \\ 0 & 0 & c \end{bmatrix} \tag{2}$$

a, b, and c are complex numbers. When $a = b = c = 1$, the medium reduces to free space. It can be shown that plane waves are eigensolutions of Maxwell's equations in the diagonally anisotropic media and the plane wave propagation vector $\vec{k}$ is governed by the following dispersion relation:

$$\frac{k_x^2}{bc} + \frac{k_y^2}{ac} + \frac{k_z^2}{ab} = k_0^2 \tag{3}$$

The solution of (3) is an ellipsoid:

$$\begin{aligned} k_x &= k_0\sqrt{bc}\sin\theta\cos\phi \\ k_y &= k_0\sqrt{ac}\sin\theta\sin\phi \\ k_z &= k_0\sqrt{ab}\cos\theta \end{aligned} \tag{4}$$

Next, the reflectivity of a planar interface between two diagonally anisotropic media is examined. In order to determine the reflection and transmission characteristics of the interface, consider the problem of a plane wave produced by a source at $z = -\infty$ in region 1 incident upon the interface at $z = 0$. The geometry of the problem is shown in Figure 1.

The propagation vector $\vec{k}$ is confined to the xz plane, so the general solution to the dispersion relation (3) is:

$$\begin{aligned} k_x &= k_0\sqrt{bc}\sin\theta \\ k_y &= 0 \\ k_z &= k_0\sqrt{ab}\cos\theta \end{aligned} \tag{5}$$

In each region, any arbitrary plane wave whose direction is given by (5) can be decomposed into a linear combination of TE and TM polarizations. The $\vec{E}$ and $\vec{H}$ fields for the case of TE polarization are:

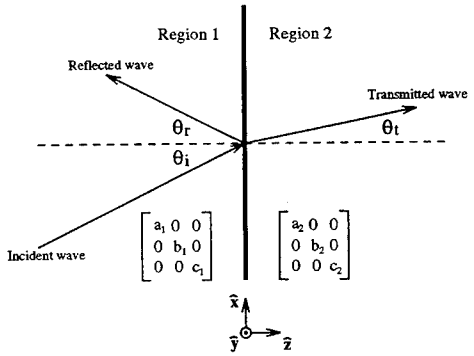


Figure 1: Plane wave incidence on an interface between two diagonally anisotropic half-spaces.

$$
\begin{aligned}
\vec{E}_i(x,z) &= E_0\hat{y}e^{-jk_0(\sqrt{b_1c_1}\sin\theta_i x+\sqrt{a_1b_1}\cos\theta_i z)} \\
\vec{E}_r(x,z) &= R^{TE}E_0\hat{y}e^{-jk_0(\sqrt{b_1c_1}\sin\theta_r x+\sqrt{a_1b_1}\cos\theta_r z)} \\
\vec{E}_t(x,z) &= T^{TE}E_0\hat{y}e^{-jk_0(\sqrt{b_2c_2}\sin\theta_t x+\sqrt{a_2b_2}\cos\theta_t z)} \\
\vec{H}_i(x,z) &= \left(-\sqrt{\frac{b_1}{a_1}}\cos\theta_i\hat{x}+\sqrt{\frac{b_1}{c_1}}\sin\theta_i\hat{z}\right)\frac{E_0}{\eta_0}e^{-jk_0(\sqrt{b_1c_1}\sin\theta_i x+\sqrt{a_1b_1}\cos\theta_i z)} \\
\vec{H}_r(x,z) &= R^{TE}\left(\sqrt{\frac{b_1}{a_1}}\cos\theta_r\hat{x}+\sqrt{\frac{b_1}{c_1}}\sin\theta_r\hat{z}\right)\frac{E_0}{\eta_0}e^{-jk_0(\sqrt{b_1c_1}\sin\theta_r x+\sqrt{a_1b_1}\cos\theta_r z)} \\
\vec{H}_t(x,z) &= T^{TE}\left(-\sqrt{\frac{b_2}{a_2}}\cos\theta_t\hat{x}+\sqrt{\frac{b_2}{c_2}}\sin\theta_t\hat{z}\right)\frac{E_0}{\eta_0}e^{-jk_0(\sqrt{b_2c_2}\sin\theta_t x+\sqrt{a_2b_2}\cos\theta_t z)}
\end{aligned}
\tag{6}
$$

Similarly, the $\vec{E}$ and $\vec{H}$ fields for the case of TM polarization are:

$$
\begin{aligned}
\vec{E}_i(x,z) &= \left(+\sqrt{\frac{b_1}{a_1}}\cos\theta_i\hat{x}-\sqrt{\frac{b_1}{c_1}}\sin\theta_i\hat{z}\right)E_0e^{-jk_0(\sqrt{b_1c_1}\sin\theta_i x+\sqrt{a_1b_1}\cos\theta_i z)} \\
\vec{E}_r(x,z) &= R^{TM}\left(-\sqrt{\frac{b_1}{a_1}}\cos\theta_r\hat{x}-\sqrt{\frac{b_1}{c_1}}\sin\theta_r\hat{z}\right)E_0e^{-jk_0(\sqrt{b_1c_1}\sin\theta_r x+\sqrt{a_1b_1}\cos\theta_r z)} \\
\vec{E}_t(x,z) &= T^{TM}\left(+\sqrt{\frac{b_2}{a_2}}\cos\theta_t\hat{x}-\sqrt{\frac{b_2}{c_2}}\sin\theta_t\hat{z}\right)E_0e^{-jk_0(\sqrt{b_2c_2}\sin\theta_t x+\sqrt{a_2b_2}\cos\theta_t z)} \\
\vec{H}_i(x,z) &= \frac{E_0}{\eta_0}\hat{y}e^{-jk_0(\sqrt{b_1c_1}\sin\theta_i x+\sqrt{a_1b_1}\cos\theta_i z)} \\
\vec{H}_r(x,z) &= R^{TM}\frac{E_0}{\eta_0}\hat{y}e^{-jk_0(\sqrt{b_1c_1}\sin\theta_r x+\sqrt{a_1b_1}\cos\theta_r z)} \\
\vec{H}_t(x,z) &= T^{TM}\frac{E_0}{\eta_0}\hat{y}e^{-jk_0(\sqrt{b_2c_2}\sin\theta_t x+\sqrt{a_2b_2}\cos\theta_t z)}
\end{aligned}
\tag{7}
$$

Now, the reflection coefficient for TE and TM polarizations can be determined by enforcing boundary conditions at the interface. In the TE case, enforcing tangential continuity of $\vec{E}$ and $\vec{H}$ at the interface requires matching the magnitude and phase of the E_y and H_x components of the fields in both regions at $z = 0$. Matching the E_x and H_y components is required in the TM case. Magnitude matching in both TE and TM cases results in the following relations:

$$\begin{aligned} 1 + R^{TE} &= T^{TE} \\ 1 + R^{TM} &= T^{TM} \\ \sqrt{\frac{b_1}{a_1}}\cos\theta_i - R^{TE}\sqrt{\frac{b_1}{a_1}}\cos\theta_r &= T^{TE}\sqrt{\frac{b_2}{a_2}}\cos\theta_t \\ \sqrt{\frac{b_1}{a_1}}\cos\theta_i - R^{TM}\sqrt{\frac{b_1}{a_1}}\cos\theta_r &= T^{TM}\sqrt{\frac{b_2}{a_2}}\cos\theta_t \end{aligned} \tag{8}$$

Phase matching results in:

$$\begin{aligned} \theta_i &= \theta_r \\ \sqrt{b_1 c_1}\sin\theta_i &= \sqrt{b_2 c_2}\sin\theta_t \end{aligned} \tag{9}$$

(8) and (9) can be used to solve for the reflection coefficient, resulting in:

$$R^{TE} = R^{TM} = \frac{\sqrt{\frac{b_1}{a_1}}\cos\theta_i - \sqrt{\frac{b_2}{a_2}}\cos\theta_t}{\sqrt{\frac{b_1}{a_1}}\cos\theta_i + \sqrt{\frac{b_2}{a_2}}\cos\theta_t} \tag{10}$$

If $b_1 c_1 = b_2 c_2$, it follows that $\theta_i = \theta_t$ and the reflection coefficient is not a function of the angle of incidence. For a perfectly reflectionless interface ($R = 0$ for any polarization and angle of incidence), the following conditions must hold:

$$\frac{a_2}{a_1} = \frac{b_2}{b_1} = \frac{c_1}{c_2} \tag{11}$$

If the interface is in the yz plane (x = const.) instead of the xy plane (z = const.), the conditions for no reflection become:

$$\frac{a_1}{a_2} = \frac{b_2}{b_1} = \frac{c_2}{c_1} \tag{12}$$

Similarly, for an interface in the xz plane:

$$\frac{a_2}{a_1} = \frac{b_1}{b_2} = \frac{c_2}{c_1} \tag{13}$$

It is important to consider the special case where region 1 in Figure 1 above is free space. In this case, (11) reduces to:

$$a_2 = b_2 = \frac{1}{c_2} \tag{14}$$

Equations (12) and (13) reduce to similar forms. These result can be used to create a perfectly matched absorbing medium which will damp any incident wave radiating from the adjacent free space region without reflecting radiation back from the interface. Equation (14) indicates that only one complex number is needed to characterize the absorbing region. For example, the diagonal tensor $\bar{\bar{\gamma}}$ required in the absorbing region associated with an interface in the xy plane is:

$$\bar{\bar{\gamma}} = \begin{bmatrix} a & 0 & 0 \\ 0 & a & 0 \\ 0 & 0 & \frac{1}{a} \end{bmatrix} \tag{15}$$

If a is a complex number of the form $a = \alpha - j\beta$, where α and β are positive real numbers, the transmitted wave will be damped:

$$\vec{E}_t(x,z;t) = \vec{E}_t 0 e^{-k_0\beta\cos\theta z} e^{-jk_0(\sin\theta x + \alpha\cos\theta z)} e^{j\omega t} \tag{16}$$

The parameter α determines the wavelength of the transmitted wave in the absorbing region and the parameter β determines the rate of attenuation in the absorbing region. It should be noted that an absorber of this form is not a passive medium since the z component of electric and magnetic conductivity tensors is negative.

For practical purposes, the absorbing region must have a finite thickness. Therefore, the termination of the absorbing region results in reflection of energy back into the free space region. The overall reflection coefficient $R(\theta)$ of a finite thickness absorber with termination is given by:

$$|R(\theta)| = |R_T(\theta)| e^{-2\beta k_0 \cos\theta d} \tag{17}$$

where $R_T(\theta)$ is the reflection coefficient of the termination. If the absorber is terminated by a perfect electric conductor, $|R_T(\theta)| = 1$.

3 Finite Element Implementation

Finite element implementation of the anisotropic absorber in the frequency domain is straightforward. In this work, a tetrahedral vector finite element code was modified to accommodate the diagonal tensor material properties required for implementation of the absorber. The method is based on an $\vec{E}$ field formulation using Whitney 1-Forms (edge elements) as a basis for the test and trial functions ($\vec{E}$ and $\vec{W}$). It is convenient to terminate the absorbing regions with a metal backing, since the surface integral term in the weak form of the wave equation vanishes. The functional (weak form) becomes:

$$\mathcal{F}(\vec{W},\vec{E}) = \int_\Omega \left[(\nabla\times\vec{W})\cdot([\mu_r]^{-1}\nabla\times\vec{E}) - k_0^2\vec{W}\cdot[\epsilon_r]\vec{E} \right] dV \tag{18}$$

The Galerkin testing procedure results in a complex, symmetric linear system:

$$(\mathbf{S} - k_0^2\mathbf{T})\,\mathrm{e} = \mathrm{f} \tag{19}$$

$$\begin{aligned} \mathrm{S}_{ij} &= \int_\Omega (\nabla\times\vec{w}_i)\cdot(\bar{\bar{\mu_r}}^{-1}\nabla\times\vec{w}_j)dV \\ \mathrm{T}_{ij} &= \int_\Omega \vec{w}_i\cdot\bar{\bar{\epsilon_r}}\vec{w}_j dV \end{aligned} \tag{20}$$

$\vec{w}_i$, $\vec{w}_j$ are edge element basis functions. The most efficient solver for (19) appears to be the Bi-Conjugate Gradient method with diagonal scaling.

4 Numerical Results

Numerical studies were conducted using two example problems. TEM wave propagation in a simple parallel plate waveguide was considered as well as the electromagnetic scattering from a conducting sphere. The geometry of the example problems is shown in Figure 2 below.

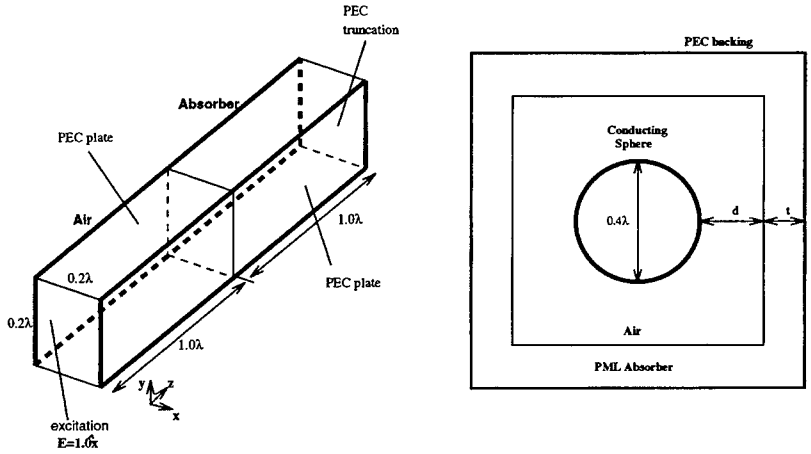


Figure 2: Geometry of TEM and sphere scattering examples

4.1 TEM waveguide

The side walls of the structure are perfectly conducting. The structure is terminated by a metal backed absorbing layer. A TEM wave is excited at the opposite end. Two example results for this problem are shown in the next figure and compared to the exact solutions.

The TEM waveguide problem revealed a drawback of using the anisotropic absorber for mesh truncation. Specifically, the matrix condition number grew as the parameter β was increased. This led to unacceptable rates of convergence in the iterative matrix solver. Further investigation revealed that the condition number is sensitive to the value of α as well as β. Based on a convergence study using the TEM waveguide problem, a near optimal choice of α appears to be $\alpha = \beta$.

4.2 Scattering by a conducting sphere

Scattering from a perfectly conducting sphere of radius 0.4λ was used to characterize the performance of the absorber. The total electric field present in the problem domain is the sum of incident and scattered field components: $\vec{E}^t = \vec{E}^i + \vec{E}^s$. The incident field is a plane wave traveling in the $+z$ direction, polarized in the x direction. The scattered electric field $\vec{E}^s$ is used as the unknown quantity in the FEM field computation instead of the total

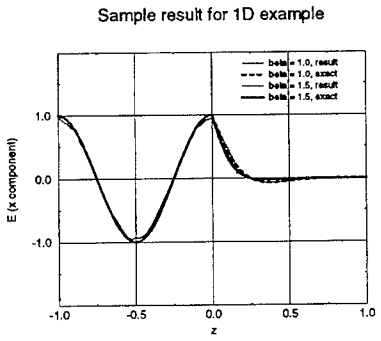


Figure 3: Result and exact solutions for $\beta = 1.0$ and $\beta = 1.5$

electric field. The excitation due to the incident plane wave is incorporated via the boundary condition on the surface of the sphere, where $\vec{E}_t^s = -\vec{E}_t^i$.

For this problem, the J_θ component of the surface current on the sphere was compared to the exact series solution. The results were obtained using meshes with a density of approximately 6- elements / wavelength. The performance of the absorber was characterized by studying the effect of several parameters on the accuracy of the surface current calculation.

First the effect of the parameter β on the solution accuracy was studied. For this comparison, the thickness of the absorber was 0.3λ and the absorber was placed 0.3λ away from the surface of the sphere. β was varied between 0.5 and 3.0. There was no additional accuracy to be gained by using a value of β greater than 3.0 since the rate of damping was limited by the coarse mesh in the absorbing region. In this range for β, the reflection coefficient for normal incidence varies from 0.15 to 1.2×10^{-5}. The surface current distribution for varying values of β is shown in Figure 4.

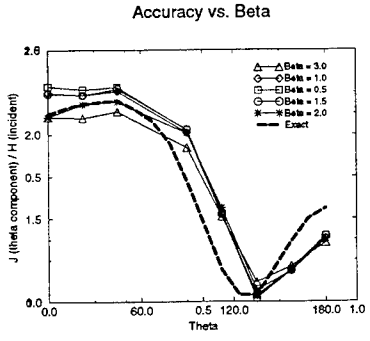


Figure 4: J_θ component of the surface current

Next, the solution accuracy was examined as the absorber thickness was varied. In this study, a β value of 1.5 was used and the absorber was again placed 0.3λ away from the sphere. The thickness of the absorber was varied

from 0.1λ to 0.5λ, resulting in reflection coefficients in the range from 0.15 to 8.1×10^{-5} for normal incidence. The resulting current distributions are plotted in Figure 5.

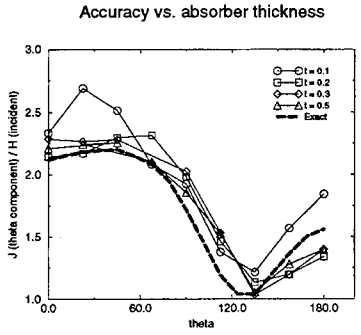


Figure 5: Sphere scattering solution for varying absorber width

5 Conclusions

A new method of mesh truncation for frequency domain finite element analysis was developed. The method is based on using an artificial anisotropic absorber whose material properties are complex diagonal tensors. If the tensors are chosen appropriately, the interface between the computational domain and the absorber will be reflectionless for all angles of incidence. This approach offers the potential for much lower reflection coefficients than other local absorbing boundary conditions.

The new method of mesh truncation was implemented and verified using two example problems. The preliminary results appear promising. Reasonable performance can be achieved with relatively thin absorbing layers (as little as two elements thick). Also, because there is no surface integral term in the metal backed implementation, the method is easy to implement and is well suited for parallel computations. The drawback of this method is that the resulting linear systems are ill-conditioned, which sometimes causes convergence problems with iterative solvers.

References

[1] Berenger, J.P. "A Perfectly Matched Layer for the Absorption of Electromagnetic Waves," *J. Comp. Physics*, 114 : 185-200, 1994.

[2] Chew, W.C. and Weedon, W.H. "A 3-D Perfectly Matched Medium from Modified Maxwell's Equations with Stretched Coordinates," *Microwave and Optical Technology Letters*, September, 1994, p.599-604.

[3] Wangsness, Roald K. *Electromagnetic Fields.* New York: John Wiley & Sons, 1986.

MODIFICATION OF BERENGER'S PERFECTLY MATCHED LAYER FOR THE ABSORPTION OF ELECTROMAGNETIC WAVES IN LAYERED MEDIA

Michael Gribbons, Seung-Kim Lee and Andreas C. Cangellaris
Electromagnetics Laboratory
and the Center for Electronic Packaging Research
Department of Electrical and Computer Engineering
University of Arizona
Tucson, AZ 85721
Phone: (602)621-4521, FAX: (602)621-2999
e-mail: cangellaris@ece.arizona.edu

Abstract

A modification is proposed to Berenger's perfectly matched layer (PML) numerical grid truncation method to provide for efficient absorption of surface waves in the direction transverse to the interface that supports them. Analytic results from wave propagation in dielectric slab waveguides and numerical results from the dispersion analysis of a microstrip line using the finite-difference time-domain method are used to show that, unless this modification is effected, the PML layer cannot be brought arbitrarily close to the interface that supports the surface wave without affecting the propagation characteristics of the wave.

1. Introduction

Berenger's perfectly matched layer (PML) approach to the truncation of FDTD grids has been used successfully in conjunction with electromagnetic radiation and scattering problems in two and three dimensions [1-3]. An alternative approach to the construction of the PMLs, directly from Maxwell's equations using streched coordinates, was presented also in [4]. However, up to this point there has been no detail investigation of the performance of PMLs with regards to absorption of surface waves of the type encountered in layered media and waves with evanescent behavior transverse to their direction of propagation tytpically encountered in practice in conjunction with various types of planar waveguiding structures. Except from a brief discussion in [3], there has been no careful investigation of the effect that a PML layer, positioned parallel to the media interface that supports a surface wave, might have on the propagation characteristics of the wave, especially when the layer is brought close to the interface.

Results in the literature from FDTD simulations of radiation and scattering problems indicate that the PMLs can be brought very close (as close as 2 FDTD cells) to the radiator/scatterer. Such a capability is highly desirable for the FDTD analysis of integrated microwave, millimeter wave and optical circuits, in order to keep computer memory requirements at a minimum without sacrificing the numerical accuracy of the simulations. Such circuits include a variety of resonant structures, the electromagnetic behavior of which is dependent on the dispersive propagation characteristics of the waves supported by the waveguiding sections that comprise them. Cosequently, it is important to investigate and comprehend the impact of PMLs on the dispersive characteristics of planar waveguiding structures before any circuit-level FDTD simulations using PMLs can be performed with confidence.

A first attempt to this investigation is presented in this paper. Through an analytic study of the eigenvalue problem of wave propagation in a dielectric slab waveguide with PMLs present on either side of the slab, we demonstrate that Berenger's PML disturbs the efective index of the propagating wave. Furthermore, we introduce a modification to the original PML that is shown to alleviate this difficulty. The numerical implementation of the modified PML is presented also.

2. Theory

Using the stretched coordinate approach proposed in [4], Maxwell's curl equations are written as

$$\frac{\partial}{\partial t}\epsilon\vec{E} = \nabla_s \times \vec{H} \tag{1}$$

$$-\frac{\partial}{\partial t}\mu\vec{H} = \nabla_s \times \vec{E} \tag{2}$$

where

$$\nabla_s = \hat{x}\frac{1}{s_x}\frac{\partial}{\partial x} + \hat{y}\frac{1}{s_y}\frac{\partial}{\partial y} + \hat{z}\frac{1}{s_z}\frac{\partial}{\partial z} \tag{3}$$

We restrict our attention to the two-dimensional case with $\partial/\partial y = 0$. As it is well known, Maxwell's equations decouple into two independent sets, one involving the field components H_y, E_x, and E_z (TM polarization), and one involving the field components E_y, H_x, H_z (TE polarization). The pertinent equations for the TM polarization are

$$\begin{aligned} j\omega\epsilon E_{z_x} &= \frac{1}{s_x}\frac{\partial}{\partial x}(H_{y_x} + H_{y_z}) \\ &= \frac{1}{s_x}\frac{\partial}{\partial x}H_y \end{aligned} \tag{4}$$

$$\begin{aligned} j\omega\epsilon E_{x_z} &= -\frac{1}{s_z}\frac{\partial}{\partial z}(H_{y_x} + H_{y_z}) \\ &= -\frac{1}{s_z}\frac{\partial}{\partial z}H_y \end{aligned} \tag{5}$$

$$j\omega\mu H_{y_x} = \frac{1}{s_x}\frac{\partial}{\partial x}E_{z_x} \tag{6}$$

$$j\omega\mu H_{y_z} = -\frac{1}{s_z}\frac{\partial}{\partial z}E_{x_z} \tag{7}$$

where the split-component formalism used with Berenger's PML condition, H_{y_x}, H_{y_z}, E_{x_z} and E_{z_x}, has been used. In order to derive the wave equation for the TM polarization, we substitute Eq. (4) in Eq. (6) and Eq. (5) in Eq. (7), giving

$$-\omega^2\mu\epsilon H_{y_x} = \frac{1}{s_x}\frac{\partial}{\partial x}\frac{1}{s_x}\frac{\partial}{\partial x}H_y \tag{8}$$

$$-\omega^2\mu\epsilon H_{y_z} = \frac{1}{s_z}\frac{\partial}{\partial z}\frac{1}{s_z}\frac{\partial}{\partial z}H_y \tag{9}$$

Since $(H_{y_x} + H_{y_z}) = H_y$ we obtain

$$-\omega^2\mu\epsilon H_y = \frac{1}{s_x}\frac{\partial}{\partial x}\frac{1}{s_x}\frac{\partial}{\partial x}H_y + \frac{1}{s_z}\frac{\partial}{\partial z}\frac{1}{s_z}\frac{\partial}{\partial z}H_y \tag{10}$$

Next, we consider the eigenvalue problem associated with the TM-modes of the slab dielectric waveguide shown in Figure 1. Nonmagnetic materials are assumed. The waveguide has thickness $2w$, constant permittivity ϵ_1, and its axis coincide with the z axis. Due to the symmetry of the structure, only the top half is shown. A slab of thickness l and permittivity $\epsilon_2 < \epsilon_1$ represents the medium outside the guide. Notice that $s_x = s_z = s = 1$ for both the guide and the adjacent slab. Beyond the ϵ_2 slab we introduced an M-layer structure terminated by a perfectly conducting plane. All layers in the structure have the same permittivity, ϵ_2; however, their thicknesses, d_m, and the values of s_x, s_{x_i}, are allowed to vary, while $s_{z_i} = 1$. Let β be the unknown propagation constant for even TM-mode propagation in z. A straightforward analysis of the eigenvalue problem results in the following eigenvalue equation

$$\tan(k_{x_1} w) = \frac{k_{x_2}\epsilon_1}{k_{x_1}\epsilon_2}\left[\frac{1+\exp(-2k_{x_2}l)exp(-2k_{x_2}\sum_{i=1}^{M} s_{x_i}d_i)}{1-\exp(-2k_{x_2}l)\exp(-2k_{x_2}\sum_{i=1}^{M} s_{x_i}d_i)}\right] \tag{11}$$

where $k_{x_1}^2 = \omega^2\mu_0\epsilon_1 - \beta^2$ and $k_{x_2}^2 = \beta^2 - \omega^2\mu_0\epsilon_2$. For propagating modes, k_{x_2} is real and positive. At this point, it is appropriate to recall that the eigenvalue equation for the even TM modes for the case of the standard slab waveguide of thickness $2w$ and ϵ_1 embedded in a homogeneous medium ϵ_2 is given by $\tan(k_1 w) = (k_2\epsilon_1)/(k_1\epsilon_2)$. Thus the term in brackets in Eq. (11) may be thought of as the "error" term caused by the truncated domain and the presence of the layered structure. It can be seen that as $l \to \infty$ in Eq. (11), the eigenvalue equation for the standard slab waveguide is recovered. This equation also suggests that instead of having $l \to \infty$ the eigenvalue equation for the standard waveguide can be reclaimed by letting s_{x_i} assume large values. How large these values have to be is dependent on the problem. Further, we notice that s_{x_i} needs to be positive to cause the error terms to become negligible compared to 1. At this point, it is appropriate to recall that for Berenger's PML s_{x_i} is of the form $s_{x_i} = 1 - j(\sigma_i/\omega\epsilon_i)$ and, as such, it does not cause any additional attenuation (since k_{x_2} is real) to help reduce the error term in Eq. (11).

As an example, consider a guide with a core of $2w = 1.0$ cm and index of refraction of $n_1 = 1.3$, surrounded by air. Fig. 2 shows the results of Eq. (11) for the efective index of refraction, $n_{eff} = \beta/(\omega\sqrt{\mu_0\epsilon_0})$, for free-space wavelength of 3.0 cm, $l = 0.5$ cm, and a 10 cell layer with each layer being 1.0 mm thick and having a real value of s_x given by the equation $s_{x_i} = s_{avg}(i/10)^2 + 1$, $i = 1, 2, \ldots, 10$. The dotted line denotes the value of n_{eff} for the case of the standard problem where the syrrounding medium is homogeneous and infinite in extent. This value is $n_{eff} = 1.07941$. This plot suggests that, by a proper choice of s_{avg}, it is possible to recover a solution corresponding to the open computational domain and recover a solution corresponding to the open domain problem, using a small computational domain. More specifically, Figure 2 suggests that a value of $s_{avg} = 10$ should give good agreement with the analytical solution of the infinite domain problem. Notice that the computational domain in the x direction would then be 20 cells in extent (5 in the guide, 5 in the air medium, and 10 in the modified PML medium).

For the sake of comparison, Fig. 3 shows the results of Eq. (11) when each $s_{x_i} = 1.0$. As mentioned earlier, the presence of an imaginary part in s_{x_i} of the form $\sigma_i/\omega\epsilon_i$, would have no impact in reducing the error term in Eq. (11). The independent variable is the number of cells in addition to the 5 cells used to model the air medium around the guide. We see that in order to get an accurate solution approximately 40 extra cells are needed. This means the the computational domain in the x-direction would have to be 50 cells. This represents over a doubling of the domain in the x-direction.

3. Nunerical Implementation

The aforementioned analysis suggests the use of s values in the streched-coordinate formulation of the PML with $Re\{s\} > 1$ in order to facilitate rapid absorption of evanescent waves without affecting their propagation characteristics. Therefore, in order to encompass the general case of planar structures that have both radiating and waveguiding properties, we allow s to assume complex values with real part greater than 1. More specifically, s_i takes the form

$$\begin{aligned} s_i &= s_i' - j s_i'' \\ &= s_i' \left(1 - j \frac{s_i''}{s_i'}\right) \\ &= s_i' \left(1 - j \frac{\sigma_i}{\omega \epsilon}\right) \end{aligned} \tag{12}$$

where $i = x, y, z$. Notice that in addition to the real part of s_i, s_i', being greater than 1, the ratio $\sigma_i/epsilon$ is scaled by s_i' also. With this notation for s_i, the modified Maxwell's system for the TM case takes the form

$$\left(\epsilon \frac{\partial}{\partial t} + \sigma_x\right) E_z = \frac{1}{s_x'} \frac{\partial}{\partial x} (H_{y_x} + H_{y_z}) \tag{13}$$

$$\left(\epsilon \frac{\partial}{\partial t} + \sigma_z\right) E_x = -\frac{1}{s_z'} \frac{\partial}{\partial z} (H_{y_x} + H_{y_z}) \tag{14}$$

$$\left(\mu \frac{\partial}{\partial t} + \frac{\sigma_x \mu}{\epsilon}\right) H_{y_x} = \frac{1}{s_x'} \frac{\partial}{\partial x} E_z \tag{15}$$

$$\left(\mu \frac{\partial}{\partial t} + \frac{\sigma_z \mu}{\epsilon}\right) H_{y_z} = -\frac{1}{s_z'} \frac{\partial}{\partial z} E_x \tag{16}$$

For a numerical application of the aforementioned modified system, we consider the FDTD simulation of wave propagation in our model slab waveguide. From Fig. 2 we see that using a value of $s_x' = 10$ should give good agreement with the analytical solution. We excited the structure with the first even TM mode and used the FDTD generated time histories to calculate numerically the effective index for the mode. The grid size was 1.0 mm, and the modified PML was placed 5 cells away from the core. The calculated numerical value for n_{eff} was 1.07875 which, compared to the analytic value of $n_{eff} = 1.07941$, exhibits only 0.06% difference. Furthermore, the mode profile obtained from the FDTD simulation is almost indistinguishable from the analytic one outside the PML region. We note that the magnitude of the normalized field at the PML interface is around 0.46, showing that it is not necessary to let the field decay significantly before introducing the modified PML.

4. Conclusions

In conclusion, we have shown that the originally proposed PML does not facilitate absorption of surface waves in the direction transverse to their direction of propagation. More importantly, it can alter their propagation characteristics if brought close to the material interface that supports the waves. To provide for evanescent wave absorption, we proposed a modified version of the original PML medium. The modification was effected using the streched-coordinate formalism of the PML. FDTD simulations of wave propagation in dielectric slab waveguides were used to verify numerically the proposed modification.

On-going work examines the application of the proposed modified PML to the FDTD modeling of microwave integrated circuits involving various types of planar waveguides, delay lines, filters, and radiating elements.

Acknowledgements

This work was supported in part by the Advanced Technology Program of the U.S. Department of Commerce through a grant to the National Storage Industry Consortium. The authors would like to thank William Pinello for helpful discussions.

References

[1] J.P. Berenger, "A perfectly matched layer for the absorption of electromagnetic waves," *J. Computational Physics*, in press.

[2] J.P. Berenger, "A perfectly matched layer for free-space simulation in finite-difference computer codes," submitted to *Annales des Télécommunications*, preprint 1994.

[3] C. E. Reuter, R. M. Joseph, E. T. Thiele, D. S. Katz and A. Taflove, "Ultrawideband absorbing boundary condition for termination of waveguiding structures in FD-TD simulations," *IEEE Microwave and Guided Wave Lett.*, vol. 4, pp. 344-346, Oct. 1994.

[4] W. C. Chew and W. H. Weedon, "A 3D perfectly matched medium from modified Maxwell's equations with stretched coordinates," *Microwave and Optical Tech. Lett.*, vol. 7, pp. 599-604, Sept. 1994.

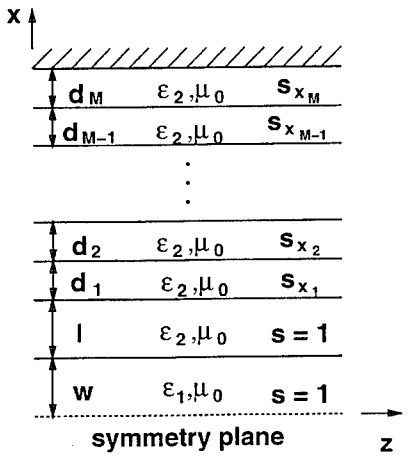


Figure 1: Slab waveguide geometry for analytically soluble problem.

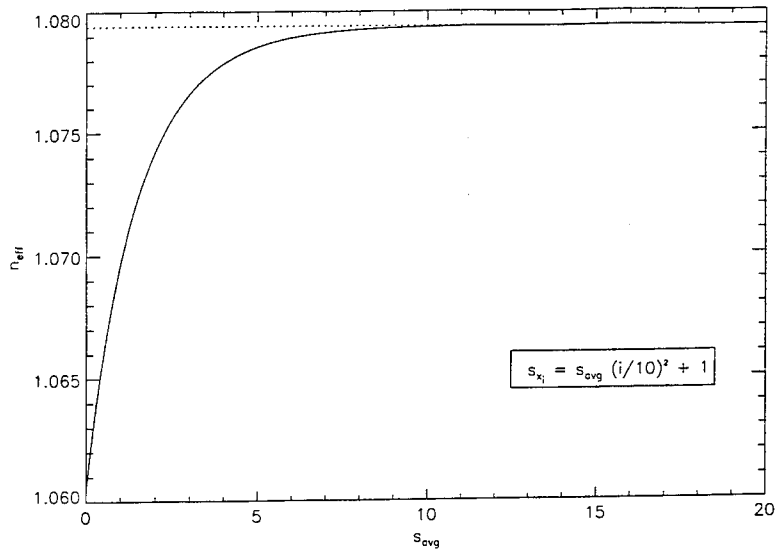


Figure 2: Analytical results of Eq. (11) for example problem.

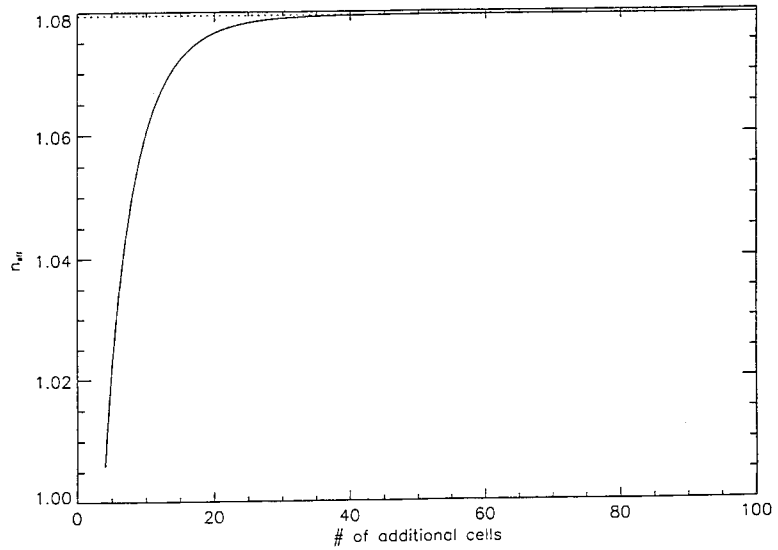


Figure 3: n_{eff} as a function of distance of the perfectly conducting plane from the dielectric slab.

Performance of the Perfectly Matched Layer in Modeling Wave Propagation in Microwave and Digital Circuit Interconnects

Zhonghua Wu and Jiayuan Fang
Department of Electrical Engineering
State University of New York at Binghamton, Binghamton, NY 13902

Abstract

This paper reports the evaluation of the Perfectly Matched Layer (PML) as the numerical absorbing boundary in modeling wave propagation in microwave passive components and digital circuit interconnects. Some computational issues on the finite-difference implementation of PML are discussed. Theoretical analysis and numerical tests show that the PML is very effective for absorbing TEM and quasi-TEM waves, as well as non-TEM waves somewhat above cutoff frequencies, but ineffective for absorbing evanescent waves and non-TEM waves near cutoff frequencies.

I. Introduction

The Perfectly Matched Layer, recently proposed by Berenger, is an artificial absorber for the truncation of numerical computation domains [1-2]. The unique feature of PML, compared to other previously proposed lossy absorbers, is that PML matches interior media for outgoing waves of any incident angles and frequencies. The Perfectly Matched Layer absorbing boundary condition, once it was proposed, immediately drew large attention and enthusiasm in the computational electromagnetic community. Several papers have appeared, shortly after Berenger's invention, that verified and extended the method of PML and applied it to various disciplines, such as wave propagation, scattering and waveguide structures [3-4].

We tested the performance of the PML absorbing boundary condition for both scattering problems and wave propagation in microwave and digital circuit transmission components. It is found that PML exhibits excellent performance for typical scattering problems. For modeling of wave propagation along waveguide components, PML works well in some circumstances, but it can be totally ineffective in other circumstances, mainly in absorbing waves near cutoff frequencies and evanescent waves. This paper discusses the mechanism of the performance of PML for propagating and evanescent waves, and presents the test results of using PML in modeling wave propagation in metal waveguide and microstrip line structures.

II. Electromagnetic Waves in Perfectly Matched Layers

Consider the media shown in Figure 1, where the free-space is in the region $x<0$ and the PML is in $x>0$. According to Berenger's papers [1-2], parameters of the PML should be chosen as

$$\sigma_y = \sigma_y^* = 0$$
$$\sigma_x/\varepsilon_0 = \sigma_x^*/\mu_0 \qquad (1)$$

where σ_x and σ_y are electric conductivities, σ_x^* and σ_y^* are magnetic conductivities. Suppose a plane wave propagating in the direction which has an angle φ with the x axis. As long as the condition in (1) is satisfied, the Perfectly Matched Layer would not cause reflection to the incident wave from the free-space for any incident angle φ and frequencies. Let ψ be any component of the fields in the PML, then ψ can be expressed as [1]:

$$\psi = \psi_0 \, e^{j\omega\left(t - \frac{x\cos\varphi + y\sin\varphi}{c}\right)} \, e^{-\frac{\sigma_x \cos\varphi}{\varepsilon_0 c} x} \qquad (2)$$

If there is no PML, the term $e^{-\frac{\sigma_x\cos\varphi}{\varepsilon_0 c}x}$ will not be there in (2).

For propagating waves in the x direction, $\cos\varphi$ is a real number, and the term $e^{-\frac{\sigma_x\cos\varphi}{\varepsilon_0 c}x}$ in (2) contributes to the attenuation of the fields. As this attenuated wave reaches the end boundary in the x direction (typically a perfect electric wall), it is reflected and further attenuated as it propagates back towards the free-space region. For cases where $\cos\varphi$ is not close to zero, with a proper selection of σ's and a sufficient width of the PML, waves in PML can be attenuated to a sufficiently small value.

On the other hand, if the variation of the fields in the x direction is of evanescent nature, $\cos\varphi$ will be an imaginary number, and the term $e^{-\frac{\sigma_x\cos\varphi}{\varepsilon_0 c}x}$ no longer decays in the x direction. In this case, the presence of the PML does not add any additional attenuation of the wave beyond the original attenuation of the evanescent wave itself.

From the nature of the PML discussed above, one can predict that, for the modeling of wave propagation in waveguide components, PML can be effective for waves somewhat above the cutoff frequencies, but ineffective for waves near cutoff frequencies (when $\cos\varphi$ is close to zero) and evanescent waves (when $\cos\varphi$ is an imaginary number). Numerical tests presented in later sections of this paper confirm this prediction.

III. Time-Marching Schemes in Perfectly Matched Layers

The exponential time marching scheme was used in the papers of Berenger's [1-2], and was also used and advocated by some other investigators [3-4]. Our comparisons made from numerical tests show no noticeable differences between the exponential time-marching scheme and the standard Yee's scheme. The reason for this can be explained as follows. Inside PML, fields do decay rapidly in space, but not in time. Therefore, it is not essential to use the exponential time-marching scheme to achieve the high absorbing property in applying PML.

Figure 2 shows the numerical reflection coefficients, with normal incident angle, of a 8-cell PML implemented with the exponential time-marching scheme and the standard Yee's scheme. The numerical reflection coefficient is obtained by the ratio of the Fourier transformed reflected field and the incident field. In this test, the analytic reflection coefficient of the PML are chosen as 10^{-3} and 10^{-6} respectively, and the variation of the conductivity with space is parabolic. As can be seen from Figure 2, there is virtually no difference on the absorbing property of PML between the exponential

time-marching scheme and the standard Yee's scheme. Same observation is obtained when the incident wave is not of normal incidence angle.

IV. PML Applied to Waveguide Components

First consider a parallel-plate waveguide shown in Figure 3. The separation between the two metal plates is $a = 40$ mm. The lowest order mode of this structure is the TM_0 mode which is actually a TEM mode with a cutoff frequency at dc. The propagation of the TM_0 mode fields along the parallel-plate waveguide is essentially a one-dimensional wave propagation problem. The PML boundary condition can absorb outgoing waves very well in an ultra-wide frequency spectrum, as reported in [4].

The lowest order non-TEM mode in the waveguide shown in Figure 3 is the TM_1 or TE_1 mode which has a cutoff frequency of 3.75 GHz. First let us examine how the TM_1 mode wave is attenuated in the PML. Choose the conductivity σ_x of the PML to be constant with space. From (1), it can be easily found that the attenuation constant of the TM_1 mode in the waveguide is:

$$\alpha = \begin{cases} \sqrt{(\frac{\pi}{a})^2 - k^2} & (f < f_c) \\ \frac{\sigma_x}{\varepsilon_0 c k} \sqrt{k^2 - (\frac{\pi}{a})^2} & (f > f_c) \end{cases} \qquad (3)$$

When $f < f_c$, the attenuation in PML is the same as that in air-filled waveguide. When $f > f_c$, the attenuation is due to the contribution of PML. Expression (3) can be numerically verified by launching a TM_1 mode in the waveguide filled with PML medium, and extracting the attenuation constant of the wave propagating along the waveguide. Let us choose the constant conductivity of the PML to be $\sigma_x = 0.1$ S/m. Figure 4 shows that the attenuation constant expressed in (3) agrees very well with that extracted from numerical solutions of the wave in the waveguide filled with PML.

Figure 5 displays the numerical reflection coefficient of the PML versus frequency for an incident wave of TM_1 mode. The conductivity profiles in PML are all chosen to be parabolic. It can be seen from Figure 5 that, unlike the case for the TM_0 mode, PML performs well only when the frequency is somewhat above the cutoff frequency. The total reflection is reached near the cutoff frequency. When the frequency is less than the cutoff frequency, the attenuation of the wave in PML makes the reflection coefficient less than 1. Notice that the PML does not contribute additional attenuation to the evanescent waves.

Next let's consider a regular rectangular waveguide. The width of the longer side of the rectangular waveguide is chosen as 40 mm. The numerical reflection coefficients for TE_{10}, TE_{20} and TE_{30} modes are shown in Figure 6. Similar conclusions can be drawn from results of Figure 6 as those from Figure 5. In order to achieve low reflection in the spectrum below cutoff frequencies, PML needs to be placed sufficiently away from sources or discontinuities to let evanescent waves fully die out.

V. PML Applied to Microstrip Lines

To simulate a wave propagation along a microstrip line, PML is placed near the outer computation domain as shown in Figure 7. At the end surfaces perpendicular to the metal strip, where outgoing waves incident upon outer boundaries in near normal incident angles, PML is found to be very effective. On the top and the side surfaces of the computation domain, where fields are mostly evanescent in the direction normal to outer surfaces, PML is found to be less effective.

Figure 8 shows the percentage errors in the computed voltage of the microstrip line for different widths of the PML placed at different distances away from the center of the microstrip. The reference data for the voltage is obtained with a very large computation domain. Figure 9 is the corresponding computed effective dielectric constant ϵ_{reff} of the microstrip line. As can be seen from Figure 9, PML needs to be placed at certain distance away from the metal strip and of enough thickness to ensure the reliability of the computed electrical properties of the microstrip line.

VI. Conclusion

This paper presents the performance of PML for modeling wave propagations in waveguides and microstrip lines. It is demonstrated through theoretical analysis and numerical tests that PML is very effective for absorbing outgoing propagating waves somewhat above cutoff frequencies, but ineffective in regions near and below cutoff frequencies. To terminate computation boundaries where evanescent waves are significant, PML needs to be placed sufficiently away from modeled objects to let evanescent waves die out.

Acknowledgement

This work is supported in part by the National Science Foundation under contract MIP-9357561, and the Integrated Electronics Engineering Research Center (IEEC) at the State University of New York at Binghamton.

References

[1] J. P. Berenger, "A Perfectly Matched Layer for the Absorption of Electromagnetic Waves," J. *Comput. Physics*, 114, Oct. 1994, pp. 185-200.

[2] J. P. Berenger, "A Perfectly Matched Layer for Free-space Simulation in Finite-Difference Computer Codes," Euro Electromagnetics 94, Bordeaux, France, May 30 - June 4, 1994.

[3] D. S. Katz, E. T. Thiele, and A. Taflove, "Validation and Extension to Three Dimensional of the Berenger PML Absorbing Boundary Condition for FD-TD Meshes," *IEEE Microwave and Guided Wave Letters*, Vol. 4, No. 8, Aug. 1994, pp. 268-270.

[4] C. E. Reuter, R. M. Joseph, E. T. Thiele, D. S. Katz, and A. Taflove, "Ultrawideband Absorbing Boundary Condition for Termination of Waveguiding Structures in FD-TD Simulations," *IEEE Microwave and Guided Wave Letters*, Vol. 4, No. 10, Oct. 1994, pp. 344-346.

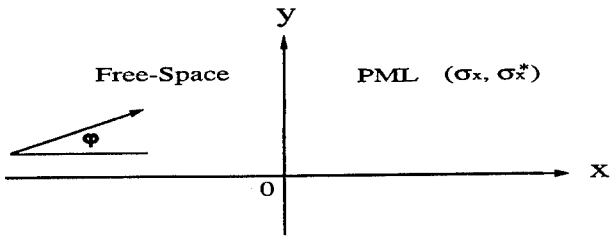


Figure 1. The region of free-space on the left and the PML on the right. The incident wave propagates in the direction which has an angle φ with the x axis.

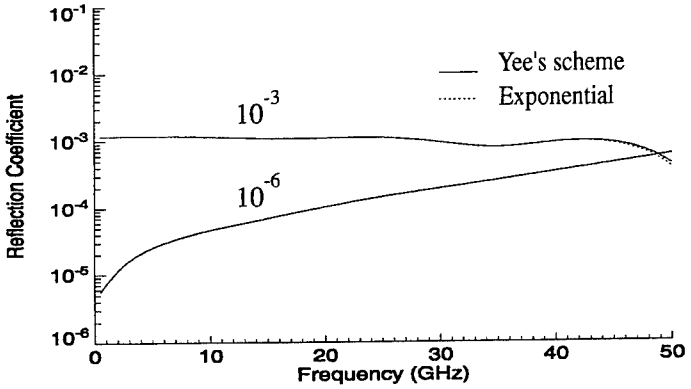


Figure 2. Comparison of reflection coefficients of 8-cell PML implemented with the exponential time-marching scheme and Yee's scheme. The analytic reflection coefficients of PML are chosen as 10^{-3} and 10^{-6}.

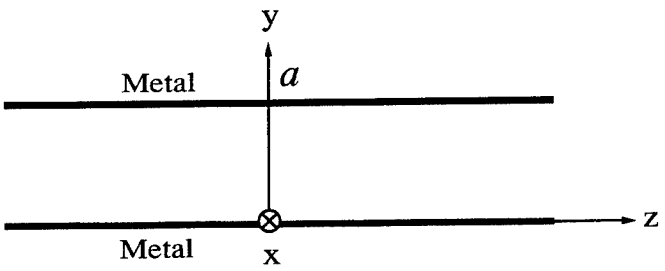


Figure 3. Configuration of a parallel-plate waveguide.

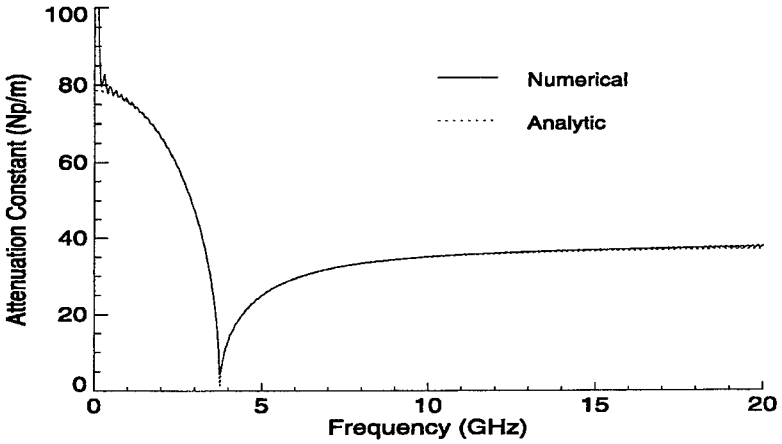


Figure 4. Attenuation constant in PML. The dash line is the analytic solution expressed in eqn (3). The solid line is obtained from the numerical solution of a wave propagating in PML.

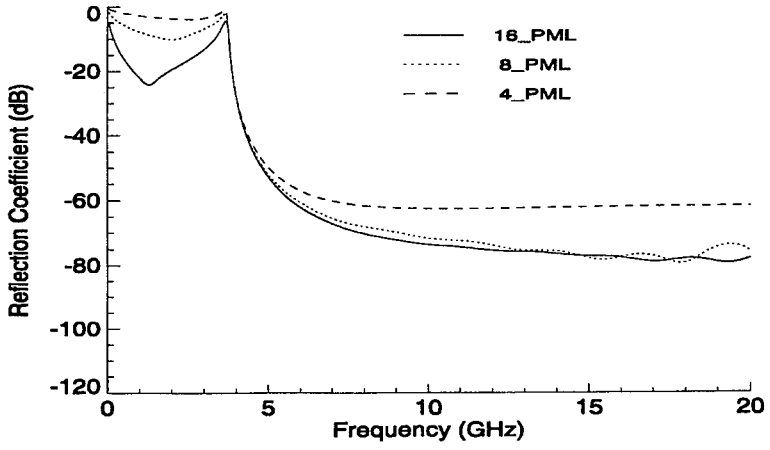


Figure 5. Reflection coefficients of TM1 mode. The width of the PML is 16, 8 and 4 cells respectively. The analytic reflection coefficients of the PML are all chosen as 10^{-4}.

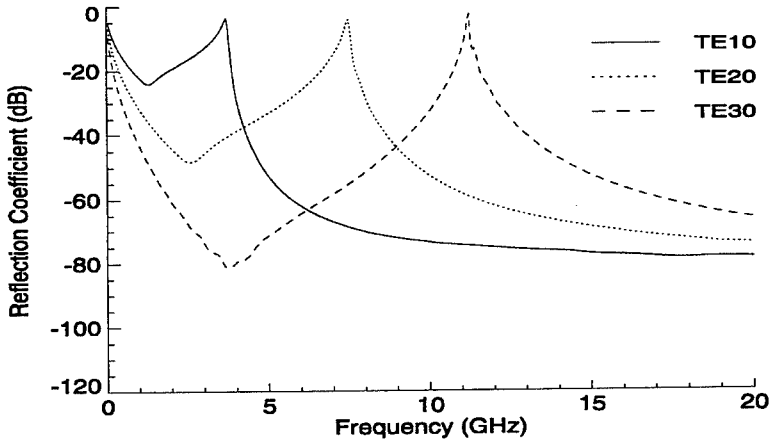


Figure 6. Reflection coefficients of TE10, TE20 and TE30 modes. The width of the PML is of 16 cells, and the analytic reflection coefficients of the PML are all chosen as 10^{-4}.

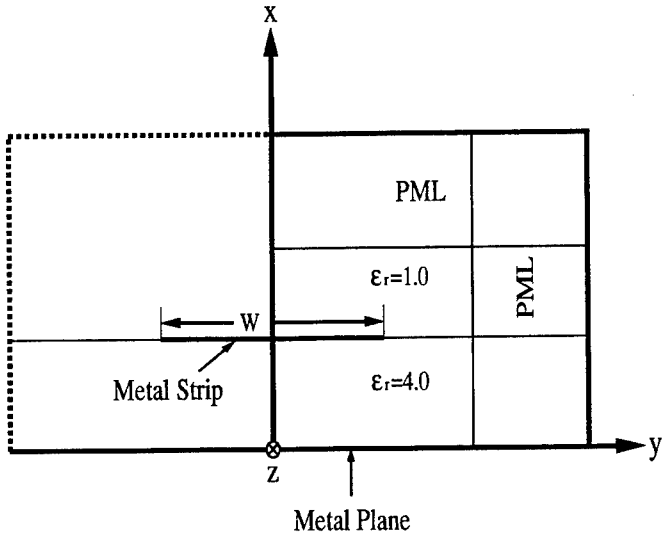


Figure 7. Cross section of the computation domain for a microstrip line. Due to the symmetry of the structure, wave propagation in half of the physical structure is simulated.

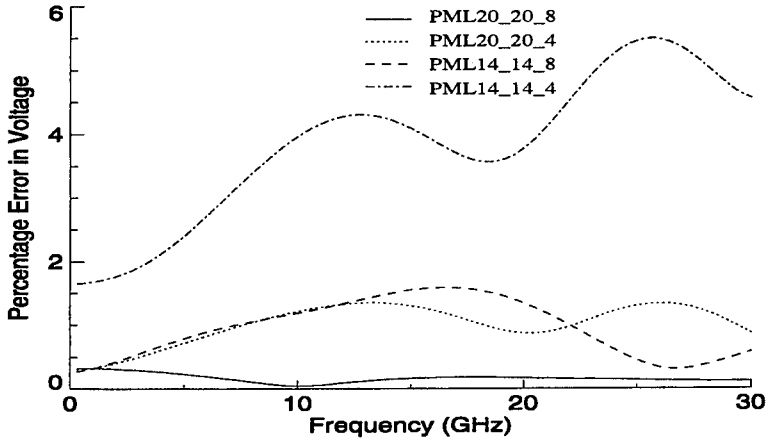


Figure 8. Percentage errors in the computed voltage of the microstrip line. The computation domain of the cross section is of 20 by 20 or 14 by 14 cells. The width of the PML is 8 or 4 cells.

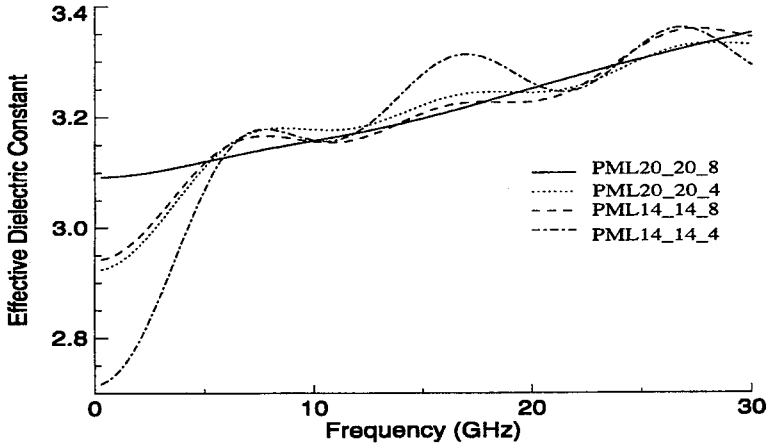


Figure 9. Numerically computed effective dielectric constants of the microstrip line. The computation domain of the cross section is of 20 by 20 or 14 by 14 cells. The width of the PML is 8 or 4 cells.

SESSION 9:

TIME DOMAIN/FDTD

Chairs: L. Long, J. Maloney

A FVTD Algorithm for Maxwell's Equations on Massively Parallel Machines

Vineet Ahuja and Lyle N Long

Dept of Aerospace Engineering
The Pennsylvania State University
University Park, PA

1 Abstract

A 3-D finite volume algorithm for the Maxwell's equations has been developed on generalized body conformal curvilinear grids. The algorithm is explicit in nature and is especially suited to a massively parallel environment. It utilizes the four stage Runge-Kutta time integration method. Integration of the Maxwell's equations is carried out on a dual grid wherein the electric and magnetic field quantities are evaluated on different grids. The algorithm has been successfully tested on the CM-200/CM-5 in solving scattering problems of electromagnetic waves from various targets. Results are presented for the problem of scattering from a perfectly conducting sphere and a perfectly conducting ogive. These results are in extremely good agreement with the exact solution and with results obtained with a standard finite difference time domain code. The formulation used in this case is for the scattered field and the Liao boundary condition is used at the outer non-reflecting boundary. The far zone transformation has also been implemented efficiently in a parallel manner to evaluate the far zone scattering results.

2 Introduction

The Finite Difference Time Domain (FD-TD) effort in computational electromagnetics has been primarily geared towards efficient development of the Yee algorithm [1] on a staggered uniform grid. Although this algorithm is robust, efficient and lacks the propagation of spurious waves due to non-uniform grid size, it is prone to staircasing errors. In order to eliminate these staircasing errors a host of finite difference and finite volume algorithms [2]-[6] have been developed for body-conformal orthogonal grids. However, most of these algorithms are limited by low CFL numbers or cannot be exploited in a data parallel manner. In the present paper we make use of the finite volume approach with the Runge-Kutta time integration method that has been successfully used in aerodynamic [7] and aero-acoustic type problems [8]-[9]. The Finite Volume Time Domain (FV-TD) algorithm is based on the four-stage Runge-Kutta explicit time stepping method on a dual grid. All three electric field components are computed at the same grid points and three magnetic field components are solved for on the same dual grid points. The reason for adopting a dual grid based approach is to avoid adding artificial dissipation explicitly (typical of central differencing

schemes) or make the code dependent on algorithmic dissipation (upwind/characteristic schemes). Explicitly adding artificial dissipation requires tuning certain parameters to prevent odd-even decoupling or killing the unwanted high frequency waves. Algorithmic dissipative schemes, more often than not tend to be too dissipative, thereby requiring a very high resolution for the waves to appear as low frequency waves to the grid.

3 Numerical Model

Maxwell's equations can be written in the conservative vector form as

$$\frac{\partial \mathbf{B}}{\partial t} = -\nabla \times \mathbf{E} \tag{1}$$

$$\frac{\partial \mathbf{D}}{\partial t} = \nabla \times \mathbf{H} - \mathbf{j} \tag{2}$$

Assuming the scatterer to be a perfect conductor and rewriting the equations in their integral form for free space we have

$$\frac{\partial}{\partial t} \int \int_V \int \mathbf{H} dV = -\frac{1}{\mu} \int \int_S \mathbf{n} \times \mathbf{E} dS \tag{3}$$

$$\frac{\partial}{\partial t} \int \int_V \int \mathbf{E} dV = \frac{1}{\epsilon} \int \int_S \mathbf{n} \times \mathbf{H} dS \tag{4}$$

Since the system of Maxwell's equations are linear, the equations are solved only for the scattered fields since the analytical solution for the incident field is known. Henceforth the fields written without any superscripts will be understood to be the scattered fields ($E \equiv E^{scatt} and\ H \equiv H^{scatt}$). If the total or incident fields have to be alluded to they will be explicitly denoted by their respective superscripts.

A finite volume formulation is used to solve the above system of equations. A dual grid is used in this formulation. Each E-field point is located at the centroid of the cube whose corners are H-field points and similarly each H-field point is located at the centroid of an E-field cube. Figure 1 depicts the combination of a E-field cell and an H-field cell that form the dual grid. This formulation differs from the Yee cell formulation in that although the E-field points and the H-field points are not collocated all the E-field components are solved at the same point and all the H-field components are solved at the same dual grid point. The dual grid is generated by first using a standard grid generator to generate the grid for the E-field points for a scatterer that is a perfect conductor (and this grid would correspond to a H-field grid if the scatterer was composed of a magnetic material). The H-field grid is then generated from the E-field grid by taking the average of the coordinates of the corners of each E-field cell.

The system is solved using a four-stage Runge-Kutta time integration method given by

$$\mathbf{Q}_i^m = \mathbf{Q}_i^n - \gamma_m \Delta t \mathbf{R}_i^{m-1} \qquad m = 1, 2, 3, 4$$

$$\mathbf{Q}_i^{n+1} = \mathbf{Q}_i^n + \mathbf{Q}_i^{m=4}$$

The time step is denoted by n and each stage of the Runge-Kutta method by m, where the coefficients are $\gamma_m = \frac{1}{4}, \frac{1}{3}, \frac{1}{2}, 1$ respectively.

$$\mathbf{Q_1} = \begin{bmatrix} H_x \\ H_y \\ H_z \end{bmatrix} \qquad \mathbf{Q_2} = \begin{bmatrix} E_x \\ E_y \\ E_z \end{bmatrix} \tag{5}$$

The residuals $\mathbf{R_i}$ are defined as

$$\mathbf{R_1} = \frac{1}{\Delta V}(\Delta \mathbf{F} + \Delta \mathbf{G} + \Delta \mathbf{K}) \tag{6}$$

$$\mathbf{R_2} = \frac{1}{\Delta V_d}(\Delta \mathbf{L} + \Delta \mathbf{M} + \Delta \mathbf{N}) \tag{7}$$

where

$$\Delta \mathbf{F} = \frac{1}{\mu}\left(\mathbf{S}^{\xi}_{i+1,j+1/2,k+1/2} \times \mathbf{E}^{\xi}_{i+1,j+1/2,k+1/2} - \mathbf{S}^{\xi}_{i,j+1/2,k+1/2} \times \mathbf{E}^{\xi}_{i,j+1/2,k+1/2}\right)$$

$$\Delta \mathbf{G} = \frac{1}{\mu}\left(\mathbf{S}^{\eta}_{i+1/2,j+1,k+1/2} \times \mathbf{E}^{\eta}_{i+1/2,j+1,k+1/2} - \mathbf{S}^{\eta}_{i+1/2,j,k+1/2} \times \mathbf{E}^{\eta}_{i+1/2,j,k+1/2}\right)$$

$$\Delta \mathbf{K} = \frac{1}{\mu}\left(\mathbf{S}^{\zeta}_{i+1/2,j+1/2,k+1} \times \mathbf{E}^{\zeta}_{i+1/2,j+1/2,k+1} - \mathbf{S}^{\zeta}_{i+1/2,j+1/2,k} \times \mathbf{E}^{\zeta}_{i+1/2,j+1/2,k}\right)$$

In the above expressions $\mathbf{S}^{\xi}, \mathbf{S}^{\eta}, \mathbf{S}^{\zeta}$ represent the projected surface areas of constant ξ, η, ζ faces respectively. They are calculated by taking half the vector cross product of the two diagonal vectors that join the four vertices of a cell face. For example the area of the surface abcd as seen in Figure 2 is calculated as

$$\mathbf{S}^{\xi} = \frac{1}{2}\begin{bmatrix} (y_c - y_a)(z_d - z_b) - (z_c - z_a)(y_d - y_b) \\ (z_c - z_a)(x_d - x_b) - (x_c - x_a)(z_d - z_b) \\ (x_c - x_a)(y_d - y_b) - (y_c - y_a)(x_d - x_b) \end{bmatrix}$$

It should be noted that the electric field points used in the evaluation of the above fluxes lie in the center of the cell faces and are not computed directly from the integration process. Instead they are extrapolated from the electric field points that make up the corners of the cell faces. For example from Figure 3

$$\mathbf{E}^{\xi}_{i,j+1/2,k+1/2} = 0.25 \times (\mathbf{E}_{i,j,k} + \mathbf{E}_{i,j+1,k} + \mathbf{E}_{i,j,k+1} + \mathbf{E}_{i,j+1,k+1})$$

Kordulla and Vinokur [10] have proposed an efficient method of calculating cell volumes for three-dimensional flow predictions. The volume ΔV is calculated by partitioning the hexahedron cell into five tetrahedra and computing the volume of each tetrahedron separately. This decomposition helps avoid gaps and overlaps in computing cell volumes and is computationally very efficient.

The residual $\mathbf{R_2}$ used to evaluate the E-field components can be computed in a similar manner:

$$\Delta \mathbf{L} = -\frac{1}{\epsilon}\left(\mathbf{Sd}^{\xi}_{i+1,j+1/2,k+1/2} \times \mathbf{H}^{\xi}_{i+1,j+1/2,k+1/2} - \mathbf{Sd}^{\xi}_{i,j+1/2,k+1/2} \times \mathbf{H}^{\xi}_{i,j+1/2,k+1/2}\right)$$

$$\Delta \mathbf{M} = -\frac{1}{\epsilon}\left(\mathbf{Sd}^{\eta}_{i+1/2,j+1,k+1/2} \times \mathbf{H}^{\eta}_{i+1/2,j+1,k+1/2} - \mathbf{Sd}^{\eta}_{i+1/2,j,k+1/2} \times \mathbf{H}^{\eta}_{i+1/2,j,k+1/2}\right)$$

$$\Delta \mathbf{N} = -\frac{1}{\epsilon}\left(\mathbf{Sd}^{\zeta}_{i+1/2,j+1/2,k+1} \times \mathbf{H}^{\zeta}_{i+1/2,j+1/2,k+1} - \mathbf{Sd}^{\zeta}_{i+1/2,j+1/2,k} \times \mathbf{H}^{\zeta}_{i+1/2,j+1/2,k}\right)$$

The expressions $\mathbf{Sd}^{\xi}, \mathbf{Sd}^{\eta}, \mathbf{Sd}^{\zeta}$ represent the projected surface areas of constant ξ, η, ζ faces of the dual grid respectively. It must be pointed out the subscripts i,j,k used in the calculation of the above fluxes are subscripts on the dual grid.

4 Boundary Conditions

We have to consider the boundary conditions at the surface of the scatterer and the radiation condition at the outer boundary. In both cases we have only the E-field points located at the boundaries. The H-field points lie half a cell away from the boundaries and are considered as interior points. Hence, we have to determine the boundary conditions for only the E-field components.

4.1 Surface Boundary Condition

At the surface of a perfectly conducting scatterer we know that the tangential components of the total electric field is equal to zero.

$$\mathbf{n}_{\eta} \times \mathbf{E}^{total} = 0$$

where $\mathbf{n}_{\eta}$ is the unit normal to the surface of the conductor.

This condition can be approximated as

$$S^{\eta}_{y} E^{total}_{z} - S^{\eta}_{z} E^{total}_{y} = 0 \qquad S^{\eta}_{z} E^{total}_{x} - S^{\eta}_{x} E^{total}_{z} = 0 \qquad S^{\eta}_{x} E^{total}_{y} - S^{\eta}_{y} E^{total}_{x} = 0$$

It can be easily seen that the above three equations are not enough to compute the three components of the electric field at the surface of the scatterer. We need an additional condition in order to make the system determinate. In this case we take into consideration Gauss's electric law which can be written in the integral form as

$$\int\int\int_{V} (\nabla \cdot \mathbf{D})\, dV = 0 \tag{8}$$

or

$$\int\int_{S} (\mathbf{n} \cdot \mathbf{D})\, dS = 0 \tag{9}$$

We need to apply Gauss's electric law to each cell that lies on the boundary. Assuming that the sides perpendicular to the conducting surface have zero flux through them (Figure 4) we obtain

$$\mathbf{S}^{\eta} \cdot \mathbf{E}^{total}_{\eta=1} = \mathbf{S}^{\eta} \cdot \mathbf{E}^{total}_{\eta=2}$$

Combining this condition with the fact that the tangential components of the total fields are equal to zero we can write explicit expressions for the scattered field components of the electric fields at the boundaries.

$$E_x^{scatt}{}_{\eta=1} = \frac{\left(\left[S_x E_x^{total}\right]_{\eta=2} + \left[S_y E_y^{total}\right]_{\eta=2} + \left[S_z E_z^{total}\right]_{\eta=2}\right)\left[S_x^{\eta=1}\right]}{\left(\left[S_x^{\eta=2}\right]^2 + \left[S_y^{\eta=2}\right]^2 + \left[S_z^{\eta=2}\right]^2\right)} - E_x^{inc}{}_{\eta=1} \tag{10}$$

$$E_y^{scatt}{}_{\eta=1} = \frac{\left(\left[S_x E_x^{total}\right]_{\eta=2} + \left[S_y E_y^{total}\right]_{\eta=2} + \left[S_z E_z^{total}\right]_{\eta=2}\right)\left[S_y^{\eta=1}\right]}{\left(\left[S_x^{\eta=2}\right]^2 + \left[S_y^{\eta=2}\right]^2 + \left[S_z^{\eta=2}\right]^2\right)} - E_y^{inc}{}_{\eta=1} \tag{11}$$

$$E_z^{scatt}{}_{\eta=1} = \frac{\left(\left[S_x E_x^{total}\right]_{\eta=2} + \left[S_y E_y^{total}\right]_{\eta=2} + \left[S_z E_z^{total}\right]_{\eta=2}\right)\left[S_z^{\eta=1}\right]}{\left(\left[S_x^{\eta=2}\right]^2 + \left[S_y^{\eta=2}\right]^2 + \left[S_z^{\eta=2}\right]^2\right)} - E_z^{inc}{}_{\eta=1} \tag{12}$$

In the above expressions the quantities $[S_x^\eta], [S_y^\eta], [S_z^\eta]$ are the average of the respective surface areas of the four cells surrounding the E-field point on the boundary.

4.2 Far Field Boundary Condition

Most body conformal grid algorithms in electromagnetics [4]-[6] use a simple outer boundary condition that either solves the one-dimensional wave equation directly or is based on the one-dimensional method of characteristics in cartesian coordinates. These boundary conditions are analogous to the Mur-type boundary condition that is frequently used in computational electromagnetics. They generally work well when the outgoing wave is a plane wave travelling perpendicular to the boundary.

In order to improve the outer boundary condition the Liao [14] form of the non-reflecting boundary condition has been implemented. This can be written in its discrete form as

$$E_{\eta=jmax}^{n+1} = T_{11} E_{\eta=jmax}^{n} + T_{12} E_{\eta=jmax-1}^{n} + T_{13} E_{\eta=jmax-2}^{n} \tag{13}$$

where

$$T_{11} = \frac{(2-s)(1-s)}{2} \qquad T_{12} = s(2-s) \qquad T_{13} = \frac{s(s-1)}{2}$$

and

$$s = \alpha \frac{c\triangle t}{\triangle n} \qquad where \qquad 0 \leq \alpha \leq 2$$

5 Far Zone Transform

One of the most important applications of solving the Maxwell's equations in the time domain is the analysis of the scattered fields from radar targets. For this purpose, it is important to compute the far zone scattered fields. In this section we have used the method developed in [13] and modified it for the FV-TD algorithm. It should be mentioned that although the method developed in [13] is quite generic, the discussion of its application was limited to the Yee algorithm.

In [13] the authors show that the retarded potentials **w** and **u** can be computed from the scattered surface currents using the following formulas:

$$\mathbf{w}\left[t-\left(\vec{r}\cdot\hat{r}\right)/c\right]=\left(\frac{1}{4\pi c}\right)\frac{\partial}{\partial t}\left\{\int_s \mathbf{j}_s(t)\,ds\right\} \tag{14}$$

$$\mathbf{u}\left[t-\left(\vec{r}\cdot\hat{r}\right)/c\right]=\left(\frac{1}{4\pi c}\right)\frac{\partial}{\partial t}\left\{\int_s \mathbf{m}_s(t)\,ds\right\} \tag{15}$$

Assuming that the surface $\eta = constant$ denotes the integration surface for the far zone transform the equations can be recast in discretized form as follows:

$$\mathbf{u}\left[t-\left(\vec{r}\cdot\hat{r}\right)/c\right]=\left(\mathbf{E}\times\mathbf{S}^{\eta}\right)^{n+1}-\left(\mathbf{E}\times\mathbf{S}^{\eta}\right)^{n} \tag{16}$$

At each time step the contribution of each cell surface that makes up the integration surface $\eta = constant$ is calculated and placed in its corresponding **w** bin whose index is computed by subtracting the time delay factor from the elapsed time and dividing the result by the time step Δt.

The retarded potential **w** has to be computed in a slightly different manner since the magnetic field points do not lie on the surface $\eta = constant$. Instead, there exists a magnetic field point half a cell above and half a cell below the surface. Therefore we can take the average of the time derivatives of the cell above and below and compute the retarded potential **w**.

$$\mathbf{w}\left[t-\left(\vec{r}\cdot\hat{r}\right)/c\right]=\mathbf{S}^{\eta}\times\frac{\left(\mathbf{H}^{n+1}-\mathbf{H}^{n}\right)_{\eta+\frac{1}{2}}+\left(\mathbf{H}^{n+1}-\mathbf{H}^{n}\right)_{\eta-\frac{1}{2}}}{2} \tag{17}$$

The far zone scattered fields can be computed from the above potentials as

$$E_\theta=-Zw_\theta-u_\phi \qquad E_\phi=-Zw_\phi+u_\theta$$

6 Parallelization Issues and CM Performance

A CM-Fortran (essentially High Performance Fortran) version of the FV-TD code has been developed. Some of the issues that came up during the development process are discussed:

Since High Performance Fortran supports array based data structures most of the "Do Loop" processes in the Fortran 77 version of the FV-TD code were transformed into simple array operations.

Extensive use is made of the CMF LAYOUT command. This command instructs the compiler as to how the arrays should be laid out in the computers memory. For example the compiler directive

$$CMF\$\ LAYOUT\ A(:news,:news,:news)$$

would force A to be spread across all the parallel processors. All the electromagnetic variables are assigned to parallel arrays using the :news directive. In other words, all the six components of the electric and magnetic fields are stored as parallel variables spread across all the processors.

The more difficult parts of code conversion lie in the implementation of the outer radiation boundary condition. The Liao boundary conditions use 3-dimensional arrays but one of the dimensions is less than the other two. Additional arrays are defined that store the electromagnetic variables at previous time steps and a masking function is used to perform the boundary condition operations only at the boundaries. This method is not very efficient since most of the processors are sitting idle while the boundary operations are being performed.

However, the most significant issue was that of the implementation of the far zone transformation. The far zone transformation is essentially a serial process since the time delay factor dictates the index of the potential arrays where the contribution of the surface arrays have to be accounted for. This is being achieved by a process called *send with add* and the use of indirect array referencing, where the time delays of different points on the far zone surface are stored in an array that acts like a set of pointers for the potential arrays. Since the electric and magnetic currents on the far zone transformation surface are cross products of surface areas and the time derivatives of the electromagnetic field components they are computed as two-dimensional quantities.

Once the components of the magnetic and electric field currents are computed, their contribution is added to the potential arrays which are essentially one-dimensional quantities. Hence the current arrays are converted to one-dimensional quantities using the RESHAPE function. For example :

$$dcrntmx = reshape\,(mold = [imax1 * kmax1]\,, source = curntmx)$$

Issuing the above command converts the two-dimensional array CURNTMX into a one-dimensional array DCURNTMX with a length of imax1 x kmax1.

For the currents corresponding to each grid point on the far zone transformation surface there is a time delay factor that is computed that determines the appropriate potential array into which the contribution of the current is added to. In other words the time delay factor array acts as a pointer array to the currents array.

$$FORALL\,(I = 1 : N) \quad WPOT\,(I) = WPOT\,(I) + SUM\,(DCURNTX\,(1 : lfzc)\,, MASK = MM3\,(1 : lfzc)\,.eq.I)$$

Here WPOT is a potential array, and MM3 is a pointer array. The contribution of dcurntx is added to the appropriate potential array block by the masking condition provided by the pointer array MM3. This, essentially is the logic behind the SEND-WITH-ADD process.

A run on the 32 node $CM-5$ took 19.92 micro-sec/grid point/time-step. This time included the overhead of reading/writing files. With the far zone process excluded, an equivalent run on the 32 node $CM-5$ takes 17.38 micro-sec/grid point/time-step.

7 Results

The first test case considered here is that of scattering of a wideband pulse from a perfectly conducting sphere. The grid used for this case was an O-O type grid and consisted of 37x46x73 grid points. The sphere is of radius 0.1 meters. The incident pulse is represented by the derivative of the Gaussian and can be explicitly written as

$$f\,(t) = -2\alpha\,(\tau - \beta\Delta t)\,e^{-\alpha(\tau-\beta\Delta t)^2} \tag{18}$$

where τ is the time delay parameter

$$\tau = t - (\vec{r} \cdot \hat{r})/c$$

$$\alpha = \left(\frac{4}{\beta \Delta t}\right)^2$$

and β is a user defined parameter that dictates the width of the pulse. The value of β used for the FVTD run in this case was 756. It should be mentioned at this point that the FVTD results are being compared to the results obtained with the PSU-FDTD code that employs the Yee algorithm. An equivalent β of 64 was used in the FDTD run. (The FDTD run was made with a cell size of 0.01m or ten cells per radii) The difference in the β value can be attributed to the difference in the time step, because the value of $\beta \Delta t$ has to be the same for both codes. Since the value of β defines the spectral band width it has to be chosen judiciously so as not to create any unnecessary noise. Figure 5 is a comparison of the backscatter cross-section against frequency of the FVTD and FDTD algorithms and the exact solution. The comparison between the exact solution and the FVTD solution is exceptionally good especially at low frequencies and is seen to be an improvement over the FDTD solution. Figure 6 is a comparison of far zone backscatter E_θ component between the serial version of the FVTD algorithm and a parallel implementation on the CM-5. The parallel far zone implementation seems to match the serial algorithm exactly.

The second test case investigated was that of the metallic ogive. The ogive has a half angle of 22.62 degrees and an aspect ratio of 5:1. The length of the ogive is 10 inches. An O-H type grid was used in this case (Figure 7). The grid consisted of 200 x 31 x 32 cells and was clustered near the leading and trailing edges and close to the surface of the scatterer. A wideband Gaussian pulse is incident normal to the leading edge. The direction of propagation of the incident pulse is parallel to the major axis of the ogive. In Figure 8 the co-polarized RCS is plotted versus frequency for the FVTD and FDTD algorithms. The FDTD results were obtained in this case with 4 million grid points.

A third test case was run with a metallic ellipsoid of the same aspect ratio as the ogive. This case is important because the ellipsoid is representative of the fuselage of an airplane. An O-O type grid was used with 50 x 31 x 72 grid cells. An ultra-wideband Gaussian pulse is incident normal to the leading edge. Figure 9 depicts the evolution of the scattering process.

8 Conclusions and Future Work

A finite volume code has been developed based on a dual grid approach for the CM-200/CM-5 machines. Processes like the far zone, that are inherently serial in nature, have been efficiently parallelized. The algorithm and the code can be used to solve scattering problems for bodies of arbitrary shapes. The results obtained are in good agreement with the exact solution and conventional FD-TD methods. In some cases, like the metallic ogive reasonable results were obtained with 20 times less grid points.

Further testing of the algorithm and the computer code is underway for various other EMCC (Electromagnetic Code Consortium) benchmark configurations like the NASA almond. The code is also being tested for the RCS (Radar Cross Section) of the GE C1A engine inlet.

9 Acknowledgements

The work done here was supported by NASA under grant NAG2-867. The authors would also like to thank NAS (National Aerodynamic Simulation) and the Center for Academic Computing at Penn State for the computing facilities made available.

References

[1] Yee, K.S., "Numerical Solution of Initial Boundary Value Problems Involving Maxwell's Equations in Isotropic Media", *IEEE Transactions on Antennas and Propagation* Vol. AP-14, No. 3, May 1966.

[2] Goorjian, P.M., "Algorithm Development for Maxwell's Equations for Computational Electromagnetism", AIAA Paper 90-0251, Reno, Nevada, Jan 1990.

[3] Madsen, N.K., and Ziolkowski, R.W., "A Three-Dimensional Modified Finite Volume Technique for Maxwell's Equations", *Electromagnetics* Vol 10, pp 147-161, 1990.

[4] Shankar, V., "A Gigaflop Performance Algorithm for Solving Maxwell's Equations of Electromagnetics", AIAA Paper 91-1578, Honolulu, June 1991.

[5] Noack, R.W. and Anderson, D.A., "Time Domain Solutions of Maxwell's Equations Using a Finite Volume Formulation", AIAA Paper 92-0451, Reno, Nevada, Jan 1992.

[6] Shang, J.S. and Gaitonde D., "Scattered Electromagnetic Field of a Reentry Vehicle", AIAA Paper 94-0231, Reno, Nevada, Jan 1994.

[7] Weinberg, Z. and Long L.N., "A Massively Parallel Solution of the Three Dimensional Navier-Stokes Equations on Unstructured Adaptive Grids", AIAA Paper 94-0760, Reno, Nevada, Jan 1994.

[8] Ozyoruk, Y., and Long L.N. "A Navier-Stokes/Kirchhoff Method For Noise Radiation From Ducted Fans", AIAA Paper 94-0462, Reno, Nevada, Jan 1994.

[9] Chyczewski, T.S., and Long, L.N., "A Higher Order Accurate Parallel Algorithm for Aeroacoustic Applications", AIAA Paper 94-2265, Colorado Springs, Colorado, June 1994.

[10] Kordulla, W., and Vinokur, M., "Efficient Computation of Volume in Flow Predictions", *AIAA Journal*, Vol. 21, No. 6, pp 917-918, June 1983.

[11] Agarwal, R.K., and Deese, J.E., "Transonic Wing-Body Calculations Using Euler Equations", AIAA Paper 83-0501, Reno, Nevada, Jan 1983.

[12] Jameson, A., Schmidt, W., and Turkel, E., "Numerical Solutions of the Euler Equations by Finite Volume Methods Using Runge-Kutta Time-Stepping Schemes", AIAA Paper 81-1259, Palo Alto, California, June 1981.

[13] Luebbers, R.J., Kunz, K.S., Schneider, M. and Hunsberger, F., "A Finite-Difference Time-Domain Near Zone to Far Zone Transformation", *IEEE Transactions on Antennas and Propagation*, Vol 39, No. 4, April 1991.

[14] Liao, Z.P., Wong, H.L., Yang, G.P., and Yuan Y.F. "A Transmitting boundary for Transient Wave Analysis", *Scietia Sinica*, Vol. 28, No. 10, pp 1063-1076, Oct 1984.

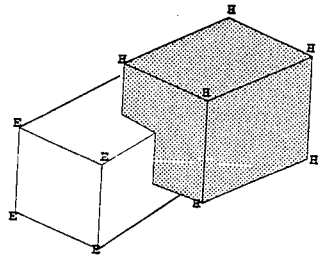


Figure 1 Combined E-field and H-field cells

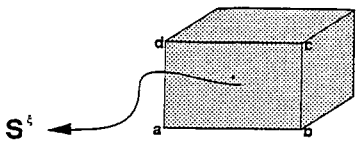


Figure 2 Surface area calculation

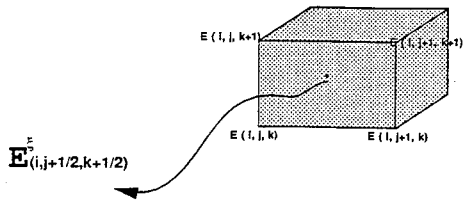


Figure 3 Points contributing to calculation of flux

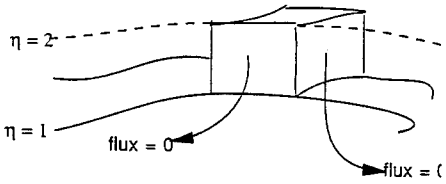


Figure 4 A typical boundary cell with zero flux

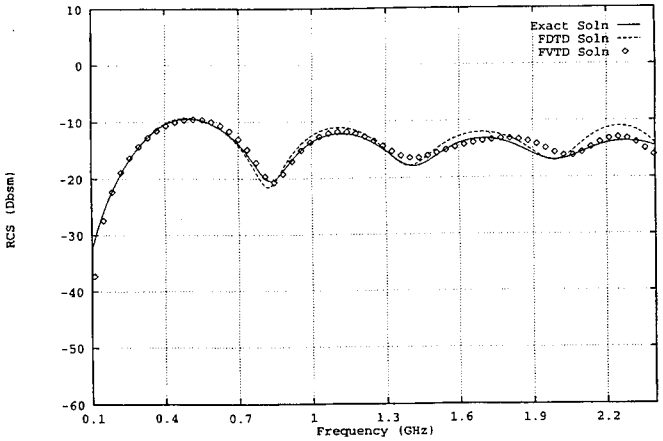


Figure 5 Backscatter RCS vs Frequency for PEC Sphere

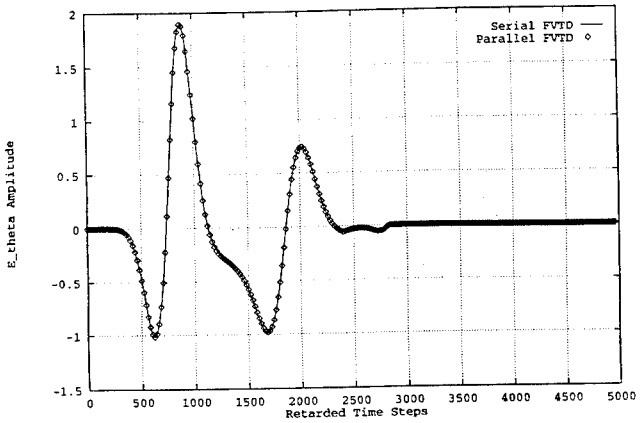


Figure 6 Farzone Backscatter Parallel/Serial Comparison

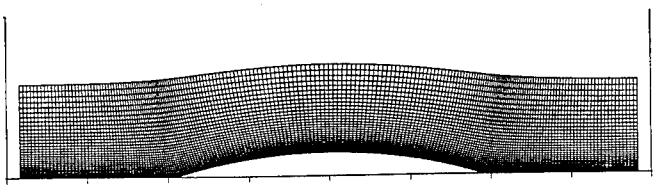


Figure 7 Plane Slice of grid used for Ogive

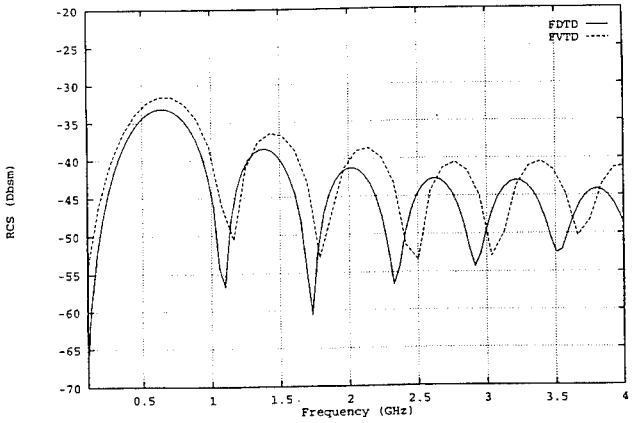


Figure 8 Backscatter RCS vs Frequency for PEC Ogive

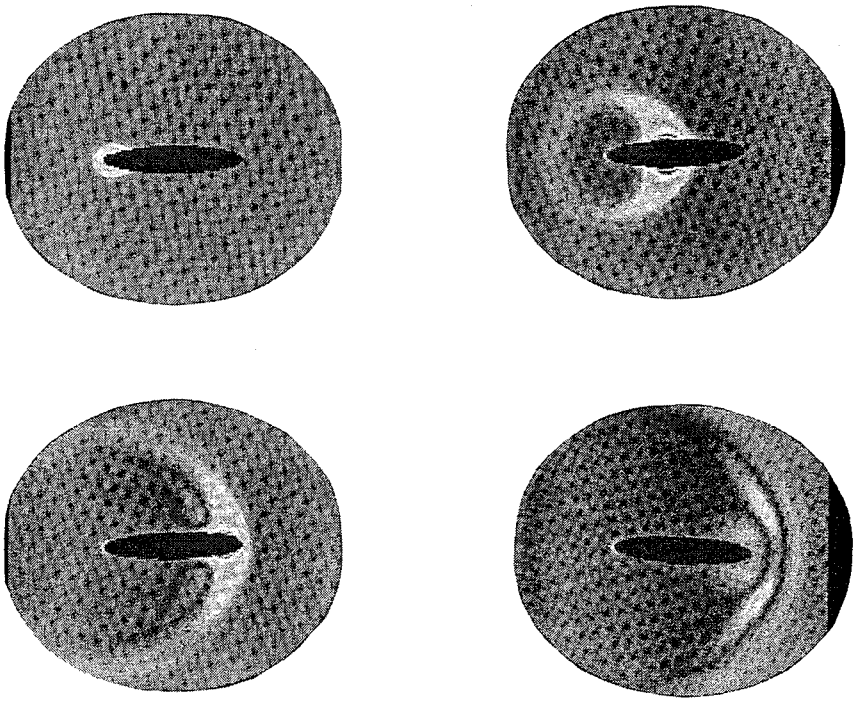


Figure 9 Scattering Process for an Ellipsoid

THE PIECEWISE LINEAR RECURSIVE CONVOLUTION METHOD FOR INCORPORATING DISPERSIVE MEDIA INTO FDTD

David F. Kelley* and Raymond J. Luebbers
Department of Electrical Engineering
The Pennsylvania State University
University Park, Pennsylvania 16802

Abstract - The recursive convolution (RC) method, developed by Luebbers, *et al.*[1], [2], provides a fast and efficient procedure for treating dispersive media in the finite-difference time-domain (FDTD) method. However, the method is somewhat less accurate than other formulations. A new *piecewise linear recursive convolution* (PLRC) method is described here that has greatly improved accuracy over the original RC approach but that retains the speed and efficiency advantages of the original method. Example calculations are presented to demonstrate the improvement in accuracy achieved by the PLRC method.

I. INTRODUCTION

Several approaches have emerged to incorporate the treatment of linear dispersive, or frequency-dependent, media into the standard FDTD algorithm of Yee [3]. In the approach taken by Luebbers, *et al.* [1], [2], the convolution of the susceptibility function and the electric field in the time domain is expressed in discrete time form. Because of the exponential nature of the susceptibility function for most materials of interest, the convolution can be performed efficiently using recursion, and the method is therefore known as the *recursive convolution* (RC) approach. In the convolution integral, the electric field is assumed to be piecewise constant over each time step. In effect, the electric field is approximated as a staircase function in time, resulting in a method that, though accurate enough for most practical cases, nevertheless exhibits less accuracy than other existing approaches. A new method is presented here, however, that approximates the electric field within the convolution integral using a piecewise linear function. The resulting *piecewise linear recursive convolution* (PLRC) method achieves accuracy that rivals or exceeds that of other methods but retains most of the speed and efficiency of the original RC method.

Because of space limitations, this paper describes the PLRC method for a linear dispersive medium characterized by a single Lorentz complex conjugate pole pair only. The formulations for Debye media and multiple poles follow similar procedures. Also, though the discussion is couched in terms of one-dimensional problems, the extension to multiple dimensions is straightforward. The new method is compared to the original Lorentz RC method of Luebbers, *et al.* [2].

II. GENERAL FORMULATION OF THE METHOD

In a dispersive medium, the time domain electric flux density $D(t)$ is related to the electric field $E(t)$ by the convolution

$$D(t) = \epsilon_o \epsilon_\infty E(t) + \epsilon_o \int_0^t E(t-\tau)\,\chi(\tau)\,d\tau \tag{1}$$

where ϵ_o is the permittivity of free space, ϵ_∞ is the dielectric constant of the medium at infinite frequency, and $\chi(t)$ is the susceptibility function of the medium. Using the notation $D^n = D(n\Delta t)$ and $E^n = E(n\Delta t)$, the convolution can be written in discrete time form as

$$D^n = \epsilon_o \epsilon_\infty E^n + \epsilon_o \int_0^{n\Delta t} E(n\Delta t - \tau)\,\chi(\tau)\,d\tau \tag{2}$$

In the RC formulations presented in [1] and [2], the electric field is assumed to be constant over each time interval Δt as shown in Fig. 1. Greater accuracy can be achieved, however, if the electric field is assumed to vary in a piecewise linear manner. Referring to Fig. 1, a piecewise linear approximation to the electric field $E(t)$ over a given interval $[i\Delta t, (i+1)\Delta t]$ can be expressed in terms of the discrete time values E^i and E^{i+1} as

$$E(t) = E^i + \frac{(E^{i+1} - E^i)}{\Delta t}(t - i\Delta t) \tag{3}$$

The form of the time-reversed and offset electric field as used in (2) is given by

$$E(n\Delta t - \tau) = E^{n-m} + \frac{(E^{n-m-1} - E^{n-m})}{\Delta t}(\tau - m\Delta t) \tag{4}$$

Substitution of (4) into (2) gives, after some manipulation,

$$D^n = \epsilon_o \epsilon_\infty E^n + \epsilon_o \sum_{m=0}^{n-1} \left\{ E^{n-m} \chi^m + (E^{n-m-1} - E^{n-m})\,\xi^m \right\} \tag{5}$$

where

$$\chi^m = \int_{m\Delta t}^{(m+1)\Delta t} \chi(\tau)\,d\tau \tag{6}$$

and

$$\xi^m = \frac{1}{\Delta t} \int_{m\Delta t}^{(m+1)\Delta t} (\tau - m\Delta t)\,\chi(\tau)\,d\tau \tag{7}$$

Substituting the expression for D^n evaluated at times $t = n\Delta t$ and $t = (n+1)\Delta t$ into the discrete time form of Ampere's Law,

$$\nabla \times H^{n+1/2} = \frac{D^{n+1} - D^n}{\Delta t} + \sigma E^{n+1} \tag{8}$$

yields

$$\begin{aligned} \Delta t \nabla \times H^{n+1/2} = {} & \epsilon_o \epsilon_\infty \left(E^{n+1} - E^n\right) + \sigma \Delta t E^{n+1} + \epsilon_o \sum_{m=0}^{n} \left\{ E^{n-m+1} \chi^m + \left(E^{n-m} - E^{n-m+1}\right) \xi^m \right\} \\ & - \epsilon_o \sum_{m=0}^{n-1} \left\{ E^{n-m} \chi^m + \left(E^{n-m-1} - E^{n-m}\right) \xi^m \right\} \end{aligned} \tag{9}$$

After much algebraic manipulation, the general form of the FDTD update equation for the electric field becomes

$$\begin{aligned} E^{n-1} = {} & \frac{\epsilon_\infty - \xi^0}{\epsilon_\infty + \frac{\sigma \Delta t}{\epsilon_o} + \chi^0 - \xi^0} E^n + \frac{\Delta t}{\epsilon_o \left(\epsilon_\infty + \frac{\sigma \Delta t}{\epsilon_o} + \chi^0 - \xi^0 \right)} \nabla \times H^{n+1/2} \\ & - \frac{1}{\epsilon_\infty + \frac{\sigma \Delta t}{\epsilon_o} + \chi^0 - \xi^0} \sum_{m=0}^{n-1} \left\{ E^{n-m} \Delta \chi^m + \left(E^{n-m-1} - E^{n-m}\right) \Delta \xi^m \right\} \end{aligned} \tag{10}$$

where

$$\Delta \chi^m = \chi^{m+1} - \chi^m \qquad \text{and} \qquad \Delta \xi^m = \xi^{m+1} - \xi^m \tag{11}$$

From this point on, the derivation depends on whether the dispersive medium under consideration is of Debye or Lorentz type. Though only the derivation for a Lorentz medium is shown here, the derivation for a Debye medium follows a similar procedure.

III. FORMULATION FOR LORENTZ MEDIA

The frequency domain susceptibility function of a Lorentz medium is characterized by one or more pairs of complex conjugate poles. For a medium characterized by a single pole pair, the susceptibility function can be written as

$$\chi(\omega) = \frac{\left(\epsilon_s - \epsilon_\infty\right) \omega_o^2}{\omega_o^2 + j 2 \omega \delta - \omega^2} \tag{12}$$

where ϵ_s is the static, or zero-frequency, dielectric constant, ϵ_∞ is the infinite-frequency dielectric

constant, ω_o is the resonant frequency of the medium, δ is the damping coefficient, and $j = \sqrt{-1}$. The $\exp(j\omega t)$ time convention is assumed. It is convenient to rewrite (12) in the form

$$\chi(\omega) = \frac{\gamma\beta}{(\alpha^2 + \beta^2) + j2\omega\alpha - \omega^2} \tag{13}$$

where

$$\alpha = \delta\,, \qquad \beta = \sqrt{\omega_o^2 - \delta^2}\,, \qquad \text{and} \qquad \gamma = \frac{(\epsilon_s - \epsilon_\infty)\,\omega_o^2}{\beta} \tag{14}$$

The Fourier transform of (13) gives the time-domain susceptibility function

$$\chi(t) = \gamma\, e^{-\alpha t} \sin(\beta t)\, u(t) \tag{15}$$

The susceptibility function in the form of (15) does not allow the development of a simple recursive convolution algorithm. This problem was solved in [2] by introducing the quantity

$$\hat{\chi}(t) = -j\,\gamma\, e^{(-\alpha + j\beta)t}\, u(t) \tag{16}$$

where the carat "^" indicates a complex-valued quantity. The quantity $\hat{\chi}(t)$ has the property

$$\chi(t) = \mathrm{Re}\{\hat{\chi}(t)\} \tag{17}$$

Substitution of $\hat{\chi}(t)$ for $\chi(t)$ into (6) and (7) yields the complex quantities

$$\hat{\chi}^m = \frac{-j\,\gamma}{\alpha - j\beta}\left[1 - e^{(-\alpha + j\beta)\Delta t}\right] e^{(-\alpha + j\beta)m\Delta t} \tag{18}$$

and

$$\hat{\xi}^m = \frac{-j\,\gamma}{(\alpha - j\beta)^2}\left\{e^{(-\alpha + j\beta)\Delta t}\left[-\frac{1}{\Delta t} - \alpha + j\beta\right] + \frac{1}{\Delta t}\right\} e^{(-\alpha + j\beta)m\Delta t} \tag{19}$$

The quantities in (18) and (19) have the properties

$$\hat{\chi}^{m+1} = e^{(-\alpha + j\beta)\Delta t}\,\hat{\chi}^m \qquad \text{and} \qquad \hat{\xi}^{m+1} = e^{(-\alpha + j\beta)\Delta t}\,\hat{\xi}^m \tag{20}$$

and it is easy to show that they are related to the real quantities χ^m and ξ^m by

$$\chi^m = \mathrm{Re}\{\hat{\chi}^m\} \qquad \text{and} \qquad \xi^m = \mathrm{Re}\{\hat{\xi}^m\} \tag{21}$$

Likewise, it is easy to show that the quantities

$$\Delta\hat{\chi}^m = \hat{\chi}^{m-1} - \hat{\chi}^m \qquad \text{and} \qquad \Delta\hat{\xi}^m = \hat{\xi}^{m-1} - \hat{\xi}^m \tag{22}$$

have the properties

$$\Delta\hat{\chi}^{m+1} = e^{(-\alpha+j\beta)\Delta t}\,\hat{\chi}^m \qquad \text{and} \qquad \Delta\hat{\xi}^{m+1} = e^{(-\alpha+j\beta)\Delta t}\,\hat{\xi}^m \tag{23}$$

and are related to the real-valued quantities $\Delta\chi^m$ and $\Delta\xi^m$ by

$$\Delta\chi^m = \mathrm{Re}\{\Delta\hat{\chi}^m\} \qquad \text{and} \qquad \Delta\xi^m = \mathrm{Re}\{\Delta\hat{\xi}^m\} \tag{24}$$

IV. THE RECURSIVE ACCUMULATOR

The recursive convolution algorithm calculates the summation in (10) at each time step in a computationally efficient manner. In order to derive the algorithm, let

$$\psi^n = \sum_{m=0}^{n-1} \left\{ E^{n-m}\Delta\chi^m + \left(E^{n-m-1} - E^{n-m}\right)\Delta\xi^m \right\} \tag{25}$$

The quantity ψ^n is called the *recursive accumulator*. With the introduction of ψ^n, the electric field update equation in (10) becomes

$$E^{n+1} = \frac{\epsilon_\infty - \xi^0}{\epsilon_\infty + \dfrac{\sigma\Delta t}{\epsilon_o} + \chi^0 - \xi^0} E^n + \frac{\Delta t}{\epsilon_o\left(\epsilon_\infty + \dfrac{\sigma\Delta t}{\epsilon_o} + \chi^0 - \xi^0\right)} \nabla\times H^{n+1/2} - \frac{1}{\epsilon_\infty + \dfrac{\sigma\Delta t}{\epsilon_o} + \chi^0 - \xi^0}\,\psi^n \tag{26}$$

A complex recursive accumulator $\hat{\psi}^n$ can be defined for Lorentz media as

$$\hat{\psi}^n = \sum_{m=0}^{n-1} \left\{ E^{n-m}\Delta\hat{\chi}^m + \left(E^{n-m-1} - E^{n-m}\right)\Delta\hat{\xi}^m \right\} \tag{27}$$

Note that, using (24),

$$\psi^n = \mathrm{Re}\{\hat{\psi}^n\} \tag{28}$$

Equation (27) can be rewritten as

$$\hat{\psi}^n = E^n \Delta\hat{\chi}^0 + (E^{n-1} - E^n)\Delta\hat{\xi}^0 + \sum_{m=0}^{n-2} \left\{ E^{n-m-1}\Delta\hat{\chi}^{m+1} + (E^{n-m-2} - E^{n-m-1})\Delta\hat{\xi}^{m+1} \right\} \tag{29}$$

The summation in (29) is equivalent to $\hat{\psi}^{n-1}$ with the terms $\Delta\hat{\chi}^m$ and $\Delta\hat{\xi}^m$ replaced by $\Delta\hat{\chi}^{m+1}$ and $\Delta\hat{\xi}^m+1$, respectively. Substituting (23) into (29) leads to the recursion relation

$$\hat{\psi}^n = (\Delta\hat{\chi}^0 - \Delta\hat{\xi}^0)E^n + \Delta\hat{\xi}^0 E^{n-1} + e^{(-\alpha+j\beta)\Delta t}\,\hat{\psi}^{n-1} \tag{30}$$

At each time step during the execution of the PLRC algorithm for Lorentz dispersive media, the complex recursive accumulator is updated using (30). The electric field is then updated using (26), incorporating the new recursive accumulator value found via (28). The values of χ^0 and ξ^0 that are required in the electric field update equation (26) are found by setting $m = 0$ in (18), (19) and (21).

The recursive accumulator update equation (30) is very similar to equation (20) in [2]. The PLRC method for Lorentz media requires only one additional real backstore variable (the electric field value at time $(n\text{-}1)\Delta t$) over those required for the original RC method, regardless of the number of poles. However, the PLRC method achieves much greater accuracy than the original method with only a minor sacrifice in program speed and memory requirements.

V. NUMERICAL RESULTS

To demonstrate the improvement in accuracy achieved by the PLRC method over the original RC method, both methods were applied to the problem of finding the reflection coefficient as a function of frequency at the interface between free space and a dispersive half-space for normal incidence. The dispersive half space used in the example is a Lorentz medium characterized by a single pair of complex conjugate poles with parameters $\epsilon_s = 3.0$, $\epsilon_\infty = 1.8$, $\omega_o = 2\pi \times 20$ GHz and $\delta = 0.1\omega_o$. The conductivity σ is zero. The incident pulse used in the FDTD solution is Gaussian with a width of 33 cells at the 0.001-amplitude points and contains significant energy at frequencies up to approximately 100 GHz. Since this is a 1-D problem, simple first order Mur absorbing boundary conditions [4] were used at the edges of the computation space.

The FDTD solution used a cell size of 250 μm and a time step size of 0.125 ps (the Courant limit). The FDTD space was 450 cells wide, and the interface was located 45 cells from the "incident" edge. A total field FDTD formulation was used. The reflection coefficient was calculated by taking the FFT of the reflected pulse on the "air" side of the interface and the FFT of the incident pulse at the same location. Dividing each frequency component of the FFT of the reflected pulse by the corresponding component of the FFT of the incident pulse gives the reflection coefficient as a function of frequency. The FDTD algorithm was allowed to run for 825 time steps to ensure that all transients dissipated before the FFTs were performed.

The reflection coefficient magnitudes at the interface computed using the PLRC method and the original RC method are compared to the analytical solution in Fig. 2. The RC solution strays significantly from the analytical solution near the resonance peak and around 40 GHz. The PLRC solution, however, follows the analytical curve closely at all frequencies. The error of the computed reflection coefficient for the PLRC and RC methods is compared in Fig. 3. In the resonance region, the error obtained using the PLRC method is an order of magnitude less than that obtained using the RC method. Both error curves diverge from zero at the higher frequencies where the spatial sampling begins to become inadequate.

VI. CONCLUSIONS

The PLRC approach described here for analyzing propagation through linear dispersive media achieves greatly improved accuracy over that of the original RC method of Luebbers, *et al.*, yet retains excellent speed and computational efficiency. The number of real storage variables required beyond the standard (non-dispersive) FDTD algorithm to implement the PLRC method is only $2P+1$ for Lorentz media, where P is the number of complex pole pairs in the susceptibility function, compared to the $2P$ real variables required by the original method. The PLRC approach also requires only one extra complex multiplication and one extra complex addition per pole per cell per dimension beyond that required for the original RC method.

REFERENCES

[1] R. J. Luebbers, F. P. Hunsberger, K. S. Kunz, R. B. Standler and M. Schneider, "A frequency-dependent finite-difference time-domain formulation for dispersive materials," *IEEE Trans. Electromagn. Compat.*, vol. EMC-32, pp. 222-227, August 1990.

[2] R. J. Luebbers and F. Hunsberger, "FDTD for *N*th-Order Dispersive Media," *IEEE Trans. Antennas Propagat.*, AP-40, pp. 1297-1301, November 1992.

[3] K. S. Yee, "Numerical solution of initial boundary value problems involving Maxwell's equations in isotropic media," *IEEE Trans. Antennas Propagat.*, AP-14, pp. 302-307, May 1966.

[4] G. Mur, "Absorbing boundary conditions for finite-difference approximation of the time-domain electromagnetic-field equations," *IEEE Trans. Electromagn. Compat.*, vol. EMC-23, pp. 1073-1077, Nov. 1981.

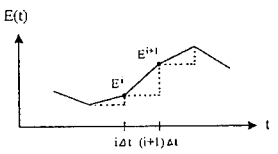


Fig. 1. Piecewise linear (solid) and staircase (dotted) approximations to electric field.

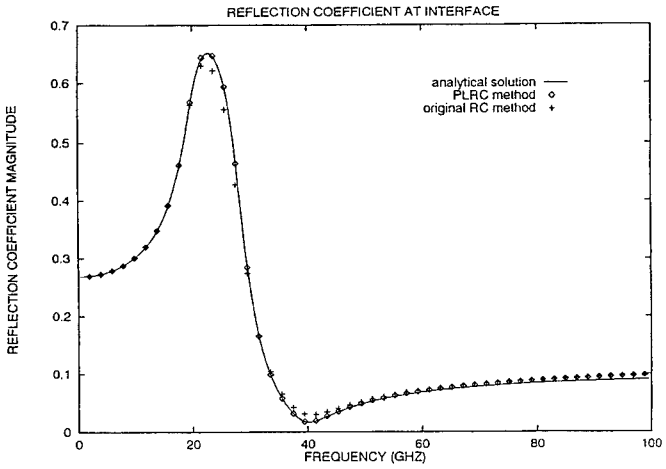


Fig. 5. Reflection coefficient magnitude at interface computed using the PLRC method and the RC method compared to the analytical solution. The FDTD cell size is 250 μm.

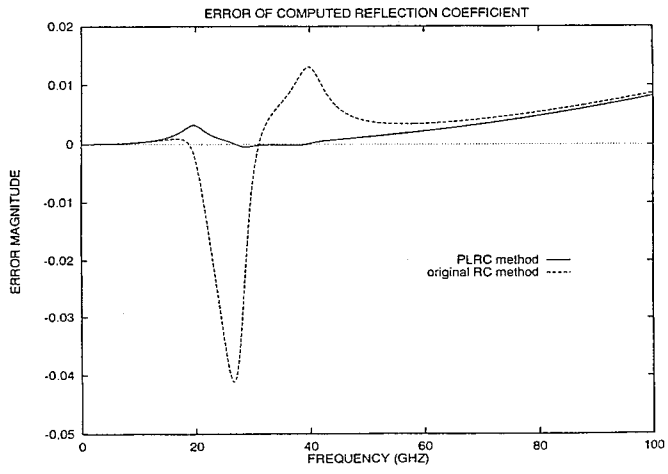


Fig. 6. Error of computed reflection coefficient magnitude obtained using the PLRC method compared to that obtained using the RC method. The cell size is 250 μm.

Combining Different Coordinate Systems in the Time Domain Finite Difference Method

M.Mrozowski[†], M.Okoniewski[‡], M.A.Stuchly[‡], S.S.Stuchly[‡]

[†]Department of Electronics
Technical University of Gdansk,
Gdansk, Poland

[‡] Department of Electrical and Computer Engineering
University of Victoria,
Victoria, B.C., Canada

1 Introduction

Typically, in explicit time domain electromagnetic simulators, the problem space is discretized in a selected orthogonal coordinate system, usually a rectangular one. Since there are apparent limitations of such meshes, other solutions have been previously developed, e.g. unstructured meshes[1] and numerically generated orthogonal, conformal meshes[2]. While very elegant and allowing for a coarser discretization, these solutions are not easy to implement, require extensive data preprocessing and introduce significant computational overhead associated with the complicated nature of the mesh.

In various electromagnetic problems, for instance those involving antennas or waveguide discontinuities, the geometry of the elements(substructures) is simple and can be readily described in one of the common orthogonal coordinate systems. More efficient mesh schemes can be accomplished in such cases. For example, in [6] a technique was described and applied to solve Maxwell equations using a classical FDTD scheme, where local simple meshes (cylindrical, spherical or rectangular) conforming to the structure boundaries were introduced and interfaces were created to "stitch" them with the global mesh of the problem. A similar approach was described in [4] for solving Maxwell equations using Lax–Wendorff explicit scheme.

The interfacing of different grids involves a few numerical problems. In order to transfer the data from one grid to another it is necessary to interpolate the fields obtained in one coordinate system to the points located at mesh nodes in the second grid. Yee *at al.* [6] used linear interpolation for both electric and magnetic fields. They observed that when interfacing rectangular grid with a curvilinear one, instabilities occur if the grids are too loosely coupled. As a remedy to this problem some overlapping of two grids was recommended for the magnetic field in the curvilinear grid, using an average of values obtained through interpolation from rectangular grid and the curvilinear FDTD algorithm. This approach implies that in fact the simulation is done twice within the overlap zone. Additionally, since the structure investigated in [6] was open, it was imposible to infer if any late time instabilities, sometimes occuring in finite difference scheme, actually occured when two grids were used.

Since in theory it suffices to pass only the boundary values from one grid to the other we decided to investigate whether a stable and accurate interfacing can be done with minimal overlap, ie. with an overlap zone only one mesh layer deep. The minimal overlap is important, especially for modern latest multi processor workstations in which the computations for two grids can be carried out in parallel by different CPUs. An increase of the overlap between grids increases the amount of information exchanged between the processors which in turn degrades the overall performance of parallelized computations.

2 Formulation

In brief the procedure of interfacing of two grids is as follows:

- A global grid is selected.
- an auxiliary grid(s) is(are) selected which conforms to the selected element(s) of the structure. The boundary between the grids is determined.
- within each grid the nodes are either:
  - internal — if all its neighbors are also internal
  - boundary — if at least one of its neighbors lies in the complementary mesh.
- if the element is internal, a standard leap-frog algorithm is used to advance time.
- if the element is the boundary one, an interpolation is used to compute the field quantity from the surrounding four nodes of the complementary mesh (Fig.1). This interpolation scheme creates a link between the two meshes.

It is assumed that the boundary is situated in a homogeneous region of the structure, ensuring proper differential properties of the fields and thus the accuracy of the interpolation.

To implement this procedure, it suffices to overlap the two grids by one mesh layer. In order verify if this minimal overlap works in practice, we have examined a canonical 2D problem of

TM field propagation in a cylindrical waveguide with perfectly conducting walls and normalized radius $R = 1$. This choice of the model problem has two important advantages. First, the analytical solution is known, and second, since a shielded problem is considered, no energy is radiated (dissipated) from the structure allowing for the occurence of late time instabilities to be easily detected and studied.

The rectangular grid is selected in the center of guide, while the cylindrical one, conforming to the shape of boundary, is employed outside the central region. The interface between grids is implemented for $r = r_{\text{int}} < 1$.

The wave propagation inside the guide can be expressed by the following initial value problem

$$c^2 \nabla_t^2 \phi(r,\varphi,t) - \frac{\partial^2}{\partial t^2}\phi(r,\varphi,t) = 0 \quad (1)$$

$$\phi(1,\varphi,t) = 0 \quad (2)$$

$$\phi(r,\varphi,0) = \phi_0(r,\varphi) \quad (3)$$

where ϕ is the scalar potential for TM modes and c is the velocity of light.

The above equations involve only one scalar potential instead of usual 5 field components required for classical FDTD formulation using Yee's mesh for TM modes. The formulation based on a scalar wave equation is particularly advantageous for interfacing grids.

To ensure a smooth transition, grids should be *seamed* in a homogeneous region of the structure. It was shown, however [5], that in homogeneous regions it is possible to replace the usual vector formulation of the FDTD scheme with an equivalent version based on two scalar wave equations for TE and TM modes. Thus an algorithm based on two scalars can be devised rather than on 6 field quantities leading to a simplified and hopefully more efficient process of interfacing of meshes.

3 Interpolation methods

There are a few algorithms which can be used for interpolating scalar potential from one grid to another. The simplest one is the bilinear interpolation. This algorithm requires only knowledge of the potential values at four inner nodes surrounding the boundary node. But the bilinear interpolation does not guarantee the continuity of the derivatives. By using more than four inner nodes it is possible to use higher order interpolation schemes. Since the interface is at $r = r_{\text{int}}$ it is easier to implement the higher order schemes when passing from cylindrical grid to rectangular one. For numerical tests we implemented the following algorithms.

For the interpolation from rectangular grid to cylindrical one:

1. bilinear (BL)
2. bicubic (BC)

For the interpolation from cylindrical grid to rectangular one:

1. bilinear (BL)
2. bicubic (BC)
3. bicubic splines (BCS)
4. splines under tension (SUT)

The bicubic interpolation involves only the information on the potential and its derivatives at four nearest neighbors. For calculating splines we used potential values calculated at all points located in the ring containing the boundary points of the rectangular grid. For the bicubic interpolation and bicubic splines we used the procedures from [7], while for the splines under tension we applied the subroutines from the FITPACK library [8].

4 Numerical results

For the time domain solution of equation (1) the leapfrog explicit scheme was used. The numerical simulations were carried out for the interface between grids located at $r = r_{\text{int}} = 0.4$ and $r = r_{\text{int}} = 0.6$ In both cases the cylindrical grid was assumed to have 30 by 62 points in the radial and angular direction, respectively. The rectangular grid was assumed to be based on square cells but the discretization step was different for $r = 0.4$ and $r = 0.6$. It was selected to match the size of a rectangular cell with the cylindrical one at the interface.

The errors relative to analytical results are shown for different interpolation schemes in Tables 1 and 2. In all cases 8000 iteration steps were performed.

Table 1: The errors relative to analytical results and CPU time for different interpolation schemes and interface between grids at $r_{\text{int}} = 0.4$

Interpolation scheme	Relative error				Normalized CPU
From rect-from cyl	TM_{01}	TM_{11}	TM_{21}	TM_{02}	
BC-BC	-0.014	-0.0027	-0.012	-0.0009	1
BL-BCS	-0.012	-0.0024	-0.012	-0.0009	0.52
BL-SUT	-0.012	-0.002	-0.012	-0.0009	0.53
BL-BL	-0.011	-0.001	-0.013	-0.0023	0.43

In the Tables, the codes the first column describe the scheme used for interpolation from the rectangular to cylindrical grid and vice versa. The codes are explained in the preceding section. The last column in Table 1 shows the total CPU time normalized to the CPU time required by BC-BC interpolation i.e. bicubic interpolation. It can be seen that low order bilinear interpolation scheme is much faster than the higher order bicubic interpolation. Since BL-BL may be expected to be the least accurate, a good compromise between speed and interpolation accuracy may be

Table 2: The errors relative to analytical results for different interpolation schemes and interface between grids at $r_{\text{int}} = 0.6$

Interpolation scheme	Relative error			
From rect-from cyl	TM_{01}	TM_{11}	TM_{21}	TM_{02}
BL-BCS	-0.0082	0.0035	-0.0038	0.001
BL-SUT	-0.009	0.0027	-0.004	0.001
BL-BL	-0.0086	0.0048	-0.0035	0.002

achieved by combining the bilinear interpolation for passing from rectangular to cylindrical grid with splines for interpolating in the other direction.

To investigate the difference between the interpolation schemes we have plotted in Fig.2 the local relative difference between time samples obtained from BL-BL and BC-BC scheme. It can be seen that the local difference at some instances is quite significant and generally increases as the simulation progresses. This local error does not, however, influence the results of the spectral analysis.

5 Early and late time instabilities

In the preceding section we showed that accurate results can be obtained with minimal mesh overlap for realistic simulation times (8000 samples). In order to evaluate instabilities, we investigated the case when there is a mismatch between mesh cells. This situation takes place for instance when $r_{\text{int}} = 0.2$ and the grid step in the angular direction is increase two times in the cylindrical grid. Fig.3 shows the the time record of the samples taken every 100th iteration. It can be noted, that instabilities develop after 2000th iteration. The instability occurs for all interpolation schemes which we tested. It was interesting to observe that improving the approximation order does not postpone the moment the instability starts to develop. This may indicate that the reason for the instabilities may be not the approximation error, but different numerical dispersion properties of the grids that become apparent when cells do not match.

Having discovered the early time instability and their immunity to the interpolation scheme we decided to look back at the examples discussed in the previous section but run this time the simulation much longer. Fig.4 shows the results for 24000 samples and $r_{\text{int}} = 0.6$ using BL-BL interpolation. It is seen that no signs of instabilities occur for the first 20000 time steps but after that instability develop slowly. At this time we are not certain if this late time instability can be attributed to the accumulation of approximation errors or different dispersion properties. We expect to address this problem in the future research.

6 Conclusions

We have demonstrated that interfacing of the grids of different type is possible even with minimal overlap provided the mesh cell sizes are matched at the interface. Although the interface works well for realistic simulation times, very late time instabilities may develop in extremely long simulations.

7 Acknowledgment

This work has been performed during one of the authors (MM) visit at the University of Victoria. Grants from the Natural Sciences and Engineering Research Council of Canada, B.C.Hydro, TransAlta Util., and TR Labs are greatfully acknowledged.

References

[1] N.K. Madsen, R.W.Ziolkowski, "Numerical solution of Maxwell's equations in time domain using irregular non-orthogonal grids," Wave Motion, vol.10, ..583-596, Dec. 1988

[2] M.Fusco, "FDTD Algorithm in Curvlinear Coordinates", *IEEE Trans. Antennas Propag.*, vol AP-38, No.1, pp76-89, Jan 1990.

[3] K.S. Kunz, R.J. Luebbers, *"Finite Difference Time Domain Method for Electromagnetics"*, CRC Press Inc., 1993.

[4] M.D.White J.J.Chattot, "Investigation of the Use of Chimera for Solving Maxwell's Equations for Electromagnetic Propagation in the Time Domain", Proc. 9th Annual Rev. Applied Computational Electromagnetics, pp352-359, Monterey, March 22-26, 1993.

[5] P.Aoyagi, J.F.Lee and R.Mittra, "A hybrid Yee algorithm/scalar-wave equation approach, " *IEEE Trans. Microwave Theory Tech.*, vol MTT-41, pp.1593–1600, Sept. 1993.

[6] K.S.Yee., J.S.Chen, A.H.Chang, "Conformal Finite Difference Time Domain (FDTD) with Overlapping Grids," *IEEE Trans. Antennas Propag.*, vol AP-40, No.9, pp1068-1075, Sept. 1992.

[7] W.H. Press, B.P. Flannery, S.A. Teukolsky and W.T. Vetterling, *Numerical recipes: The art of scientific computing*, Cambridge University Press, Cambridge, 1986.

[8] Netlib software library avaliable via e-mail (netlib@ornl.gov)

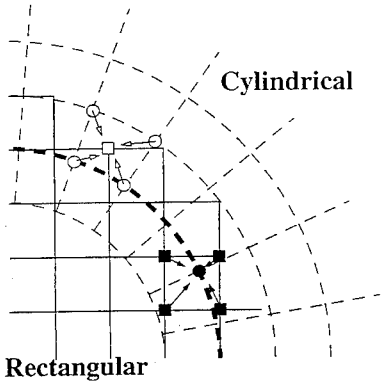


Figure 1: An interface between a rectangular and cylindrical meshes. Rectangles represent nodes of rectangular mesh, circles of cylindrical one. Filled symbols depicts the interpolation of cylindrical nodes, while open symbols explain the interpolation of nodes of the rectangular mesh.

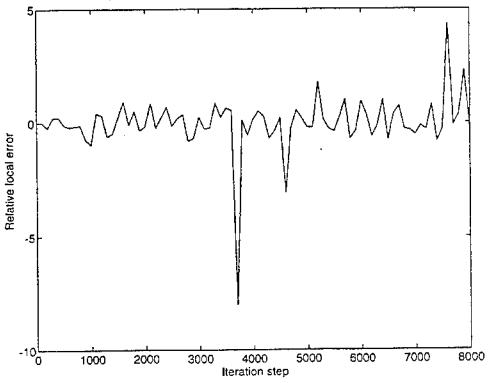


Figure 2: The time record of a local error between BL-BL and BC-BC interpolation (interface at $r_{\text{int}} = 0.4$). Only every 100th sample is shown

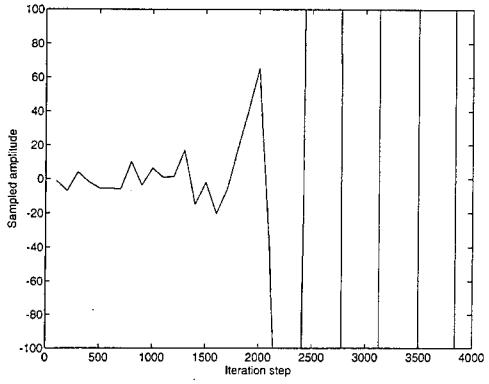


Figure 3: The time record for interface at $r_{\text{int}} = 0.2$ and unmatched cells in both grids. Only every 100th sample is shown

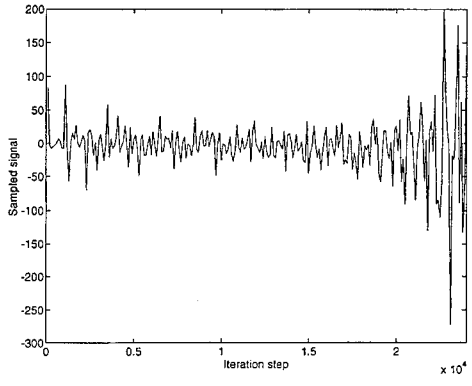


Figure 4: The time record for interface at $r_{\text{int}} = 0.4$ and BL-BL interpolation between grids with matched cell size in both grids. Only every 100th sample is shown

Time Domain Response of Simulated 2D Composite Scatterers

Atef Z. Elsherbeni and Paul M. Goggans
Department of Electrical Engineering
The University of Mississippi
University, MS 38677

Abstract

Two-dimensional composite objects can be simulated by dividing the object into small cells and then replacing each cell with a homogeneous circular cylinder. This paper investigates the ability of the simulation technique to calculate the time domain response of composite scatterers. In this work, the transient plane-wave incident on the scatterer has a center frequency and is band-limited. The time domain scattering data is generated using an appropriate inverse fast Fourier transform of the time-harmonic far-field scattering data determined at discrete frequencies. Results of the simulation method are compared with moment method results.

Introduction

Calculating the field scattered from two-dimensional composite objects is a difficult problem if the inhomogeneity does not follow any particular spatial pattern. However, if the scattering object is discretized into small cells and if each cell is simulated by a homogeneous circular cylinder, efficient solutions are available to predict the scattering width of the composite structure [1]. The validity of the simulation of two dimensional composite scatterers by small circular cylinders has been proved through the years for a TM polarized wave [2, 3]. In recent publications [4, 5], a successful simulation for TE polarized waves is presented. The main advantage of using circular cylinders for simulation is that the cylinders are canonical objects and an exact series solution for each type of cylinder is easily obtainable. The scattering from the composite scatterer, however, incorporates the exact solution of each cylinder and the infinite multiple interaction between them. The solution is theoretically exact and the only approximation involved for obtaining numerical data is due to the truncation of the interaction matrix. This type of approximation is similar to those used in many other numerical techniques.

Although the simulation technique works very well for calculating time-harmonic far and near fields, we are not aware of any attempt to use the simulation of composite scatterers with cylinders for time domain analysis. The objective of this paper is to investigate the validity of the simulation technique for calculating the time domain response of composite scatterers. In this work, the transient plane-wave incident on the scatterer has a center frequency and is band-limited. The time domain scattering data is generated using an appropriate inverse fast Fourier transform of the time-harmonic far-field scattering data determined at discrete frequencies [6].

Here we investigate the ability of the simulation technique to predict the transient electromagnetic wave returned from structures with local as well as non-local and resonant scattering behavior. For this study, two-dimensional (2D) conducting bodies in the upper resonance region were chosen because they are the simplest targets that demonstrate all of the desired scattering behavior. Scattering bodies considered here are a flat plate and a rectangular cavity. Numerical comparison between the data from the simulation technique and the moment method (MM) is presented. Using this comparison, we show the advantages and disadvantages of the simulation technique for predicting the time domain response of these two scatterers. Note that the results presented here are for perfect electric conductor (PEC) scatterers only. This is because of the large execution time required for obtaining reference

results for composite scatterers using the MM. However, we believe that the real advantage of the simulation method is its ability to calculate the transient scattering from inhomogeneous bodies rapidly when compared to other methods [1].

Technical Discussion

A detailed description of the MM solution for the time-harmonic electric field in the far field of a 2D scatterer is given in [7]. A similar description for the simulation method is given in [1, 4].

Because we assume that the reader is in general familiar with these numerical techniques, we have chosen to devote this section to describing the calculation of the scatterers' transient response from the calculated time-harmonic electric field. The definitions and descriptions in this section are presented for the general three dimensional case. Definitions are then specialized to the 2D case only if they are different from the general expressions.

The Target Signature

For a particular scatterer, the received radar signal is here referred to as the target signature. The target signature, g(t), represents some field, voltage, or current quantity in the radar receiver. If the scatterer is stationary and has no moving parts, the target signature is described by the following equation in which convolution is denoted by an asterisk (*):

$$g(t) = a_R(t) * a_P(t) * h(t) * a_P(t) * a_T(t) * f(t) \tag{1}$$

In the expression above, h(t) is the target impulse response function, $a_T(t)$ is the impulse response of the transmitter and transmit antenna, $a_R(t)$ is the impulse response of the receiver and receive antenna, and f(t) is the transmitted signal. The signal f(t) represents some field, voltage, or current quantity in the radar transmitter. In (1), $a_P(t)$ accounts for propagation of the signal between the radar and the target and is taken to be

$$a_p(t) = \frac{\delta(t - R/c)}{\sqrt{4\pi}\,R} \tag{2}$$

where R is the range from the radar to the target, c is the speed of light and δ is the Dirac delta function.

The target impulse response, the impulse response of the transmitter, and the impulse response of the receiver are easiest to define in terms of their Fourier transforms, H(f), $A_t(f)$, and $A_r(f)$. Here the standard engineering definition of the Fourier transform is used so that the target transfer function is related to the target impulse response by the following equation:

$$H(f) = \int_{-\infty}^{\infty} h(t) e^{-j2\pi ft} dt \tag{3}$$

The value of H(f) at a particular frequency f can be determined by considering a time-harmonic plane-wave incident on the target and traveling in the direction of the unit vector $\hat{\mathbf{k}}$. The incident electric and magnetic fields written in phasor form (with $e^{j2\pi ft}$ time variation assumed and suppressed) are

$$\mathbf{E}_i(\mathbf{r}) = E_o \hat{\mathbf{p}} e^{-j2\pi f \mathbf{r}\cdot\hat{\mathbf{k}}/c} \tag{4}$$

and

$$\mathbf{H}_i(\mathbf{r}) = (E_o/\eta_o)\left(\hat{\mathbf{k}} \times \hat{\mathbf{p}}\right) e^{-j2\pi f \mathbf{r}\cdot\hat{\mathbf{k}}/c} \tag{5}$$

where E_o is the constant amplitude of the incident electric field, $\hat{\mathbf{p}}$ is the unit polarization vector (here linear polarization is assumed for simplicity), and η_o is the characteristic impedance of free space. Quantities in boldface type are vectors. The origin of the coordinate system used to define $\mathbf{r}$ is picked at a convenient point close to, inside, or on the scatterer. The origin is denoted with the symbol $\mathcal{O}$. For a monostatic radar system, the Fourier transform of the target impulse response is given by the expression

$$H(f) = \frac{\mathbf{E}_s(-R\hat{\mathbf{k}})\cdot\hat{\mathbf{p}}}{\mathbf{E}_i(\mathcal{O})\cdot\hat{\mathbf{p}}}\left[\sqrt{4\pi}\, R\, e^{(j2\pi fR/c)}\right]. \tag{6}$$

In the expression above it is assumed that the polarization of the receive antenna is matched to the polarization of the transmit antenna. For a radar, the distance R from the origin to the antennas is assumed to be electrically large so that the scattered electric field due to the target, $\mathbf{E}_s$, in (6) can be calculated using the standard far-field approximations. The incident electric field at the origin in (6) can be approximated as a plane wave as expressed in (4) because the variation of the incident field with R is unimportant in this equation (identical variation with R occurs in $\mathbf{E}_s$ and hence cancels the variation in the incident field) and because the spherical wave fronts are approximately planar at the target in the far-field of the transmit antenna. For a 2D scatterer, a slightly different definition of H(f) is used. For the 2D case

$$H(f) = \frac{\mathbf{E}_s(-\rho\hat{\mathbf{k}})\cdot\hat{\mathbf{p}}}{\mathbf{E}_i(\mathcal{O})\cdot\hat{\mathbf{p}}}\left[\sqrt{2\pi\rho}\; e^{(j2\pi fR/c)}\right] \tag{7}$$

where ρ is the distance from the z-axis in the cylindrical coordinate system.

The Equivalent Transmitted Signal

To obtain a more convenient form for analysis, equation (1) can be rewritten using the commutative property of convolution to obtain the following:

$$g(t) = \left\{\frac{a_T(t) * a_R(t) * f(t - 2R/c)}{4\pi R^2}\right\} * h(t). \tag{8}$$

In the expression above, the total time delay is accounted for in f(t). The quantities in the curly brackets in (8) are assumed known and so it is convenient to combine them and define them as a single quantity. This quantity is here referred to as the equivalent transmitted signal, $f^e(t)$.

$$f^e(t) = \frac{a_T(t) * a_R(t) * f(t - 2R/c)}{4\pi R^2}. \tag{9}$$

Using the equivalent transmitted signal the target signature can be expressed as

$$g(t) = f^e(t) * h(t). \tag{10}$$

The form of (10) is useful because $f^e(t)$ includes the effect of the receive antenna and receiver, the transmit antenna and transmitter, and the range to the target; while the target impulse response h(t) isolates the scattering characteristics of the target (note however that h(t) is also a function of the transmit and receive polarization).

Because the Fourier transform of the equivalent transmitted signal is band-limited, it is only necessary to determine H(f) for frequencies in the pass band of $F^e(f)$ in order to calculate g(t). To investigate the target signature any suitable band-limited function can be chosen for the equivalent transmitted signal. To aid in the interpretation of the time-domain results, a standard window function is

used for $F^e(f)$. The window function is normalized so that the peak value of $f^e(t)$ is unity. Here a Blackman window is used. This is expressed in the following form:

$$2\Delta f\, F^e(f) = \text{rect}\left[(f-f_o)/\Delta f\right]\left\{\begin{array}{l}1+\dfrac{a_1}{a_0}\cos\left[2\pi(f-f_o)/\Delta f\right]\\ +\dfrac{a_2}{a_0}\cos\left[4\pi(f-f_o)/\Delta f\right]\end{array}\right\} + \text{rect}\left[(f+f_o)/\Delta f\right]\left\{\begin{array}{l}1+\dfrac{a_1}{a_0}\cos\left[2\pi(f+f_o)/\Delta f\right]\\ +\dfrac{a_2}{a_0}\cos\left[4\pi(f+f_o)/\Delta f\right]\end{array}\right\} \tag{11}$$

where

$$\text{rect}(x) = \begin{cases}1 \text{ for } |x| \le \frac{1}{2}\\ 0 \text{ otherwise}\end{cases}. \tag{12}$$

In (11), f_o is the center frequency and Δf is the bandwidth. The coefficients a_0, a_1, and a_2 are as follows: $a_0 = 0.42$, $a_1 = 0.50$, and $a_2 = 0.08$.

The Radar Profile

Because it is a band-limited function the target signature, g(t), can be expressed in the form

$$g(t) = g_i(t)\cos(2\pi f_o t) + g_q(t)\sin(2\pi f_o t) \tag{13}$$

where $g_i(t)$ and $g_q(t)$ are the in-phase and quadrature portions of g(t). Equation (13) can also be written in envelope and phase form.

$$g(t) = p(t)\cos\left\{2\pi f_o t + \tan^{-1}\left[g_q(t)/g_i(t)\right]\right\} \tag{14}$$

where

$$p(t) = \sqrt{g_i^2(t) + g_q^2(t)}\,. \tag{15}$$

Because it is a low-pass limited function, the envelope of g(t) is used to illustrate the scatterers transient response rather than g(t) itself. The envelope of the target signature is here referred to as the radar profile and is denoted p(t).

Haykin introduces the complex envelope notation to make band-pass limited signal and system problem isomorphic to the base-band signal and system problem [8]. Using the complex envelope notation the radar profile can be determined in a straight-forward manner from $F^e(f)$ and H(f). The complex envelope of g(t) is denoted as $\tilde{g}(t)$ and is defined as

$$\tilde{g}(t) = g_i(t) + jg_q(t)\,. \tag{16}$$

The function g(t) can be recovered from $\tilde{g}(t)$ using the following expression:

$$g(t) = \text{Re}\left\{\tilde{g}(t)\exp(j2\pi f_o t)\right\}. \tag{17}$$

The Fourier transform of the complex envelope can be determined from the Fourier transform of g(t) using the equation

$$\tilde{G}(f) = G(f+f_o) + \text{sgn}(f+f_0)\,G(f+f_o) \tag{18}$$

where

$$\mathrm{sgn}(f)=\begin{cases}1 & \text{for } f>0\\ 0 & \text{for } f=0\\ -1 & \text{for } f<0\end{cases}. \tag{19}$$

In an identical manner the complex envelope of the equivalent transmitted signal can be defined so that

$$\tilde{f}^{e}(t)=f_i^{e}(t)+jf_q^{e}(t) \tag{20}$$

$$f^{e}(t)=\mathrm{Re}\left\{\tilde{f}^{e}(t)\exp(j2\pi f_o t)\right\} \tag{21}$$

and

$$\tilde{F}^{e}(f)=F^{e}(f+f_o)+\mathrm{sgn}(f+f_0)F^{e}(f+f_o) \tag{22}$$

where $f_i^{e}(t)$ and $f_q^{e}(t)$ are the in-phase and quadrature portions off $f^{e}(t)$.The complex envelope of the target impulse response is defined slightly different manner so that

$$\tilde{h}(t)=h_i(t)+jh_q(t) \tag{23}$$

$$h(t)=\mathrm{Re}\left\{2\tilde{h}(t)\exp(j2\pi f_o t)\right\}=2h_i(t)\cos(2\pi f_o t)-j2h_q(t)\sin(2\pi f_o t) \tag{24}$$

and

$$\tilde{H}(f)=\left[H(f+f_o)+\mathrm{sgn}(f+f_0)H(f+f_o)\right]/2 \tag{25}$$

where $h_i(t)$ and $h_q(t)$ are the in-phase and quadrature portions of h(t). The complex envelopes are defined so that

$$\tilde{g}(t)=\tilde{h}(t)*\tilde{f}^{e}(t). \tag{26}$$

According to (26), the complex envelope of g(t) can be expressed in terms of $\tilde{F}^{e}(f)$ and $\tilde{H}(f)$ so that

$$\tilde{g}(t)=\int_{-\Delta f/2}^{\Delta f/2}\tilde{F}^{e}(f)\tilde{H}(f)\exp(j2\pi ft)\,df. \tag{27}$$

The radar profile p(t) is the magnitude squared of (27). For the Blackman window

$$\tilde{F}^{e}(f)=\frac{\mathrm{rect}(f/\Delta f)}{\Delta f}\left\{1+\frac{a_1}{a_0}\cos\left[2\pi f/\Delta f\right]+\frac{a_2}{a_0}\cos\left[4\pi f/\Delta f\right]\right\}. \tag{28}$$

The quantity $\tilde{H}(f)$ in (27) is determined from the positive frequency portion of H(f) as illustrated in (25) so that

$$\tilde{H}(f)=H(f+f_o). \tag{29}$$

Here the radar profile is calculated from H(f) using (27), (28), and (29). The Fourier transform in (27) is calculated from the values of $\tilde{H}(f)$ (determined at discrete values of f from the time-harmonic electromagnetic calculations) using the complex fast Fourier transform (FFT).

Results and Conclusions

This section presents the radar profile of a number of 2D targets. The idea of a reference plane is useful in interpreting the radar profiles given here. The reference plane passes through the origin of the scatterer and is orthogonal to the unit normal pointing in the direction of the incident wave, $\hat{\mathbf{k}}$. A local scatterer on the target will result in a peak in the radar profile at a time corresponding to twice the distance from the reference plane to the scatterer along a $\hat{\mathbf{k}}$ directed path.

Figure 1 illustrates the envelope of the equivalent transmitted signal, $\tilde{f}(t)$, used here. For this illustration and the calculations in this section the center frequency, f_o, is 10 GHz and the bandwidth, Δf, is 4 GHz. The center frequency was chosen arbitrarily; however, the bandwidth was chosen so that a time resolution of approximately 0.5 ns is achieved. The Blackman window has a first time-domain side-lobe which is -58 dB below the peak and a side-lobe fall-off rate of -18 dB/octave.

Figure 2 illustrates a 1 m wide PEC strip with a TE polarized incident plane wave. The strip is at a 45 degree angle to the direction of the incident plane wave and the origin is 1 m from the center of the strip. Figure 3 illustrates the radar profile of the PEC strip. The first two return pulses in Figure 3 are due to edge diffraction from the lower and upper edges of the strip. The latter pulses are due to waves traveling up and down the strip that are then diffracted at the upper or lower edge. Figure 3 demonstrates that the simulation technique does an excellent job of positioning in time the return from edges and traveling waves. The amplitudes of the returns, however, differ in some cases from the MM results. We believe that these differences are due to the finite thickness of the strip in the simulation technique. In the simulation technique, the 1 m strip is modeled using 100 circular cylinders each of radius 5 mm.

Figure 4 illustrates a 45 cm by 10 cm rectangular cavity with a plane wave incident upon the open end of the cavity. The center of the open face of the cavity is 1 m from the origin. The cavity is simulated by 102 cylinders each of radius 5 mm. Figure 5 illustrates the radar profile of the rectangular cavity for a TM polarized plane wave. The first return pulse in Figure 5 is due to edge diffraction from the front edge of the cavity. The second return pulse is due to the wave which travels down the parallel-plate waveguide in the lowest order TM mode and is reflected from the back inside face of the cavity. The third return pulse appears to be due to a wave which travels down the waveguide in a fifth order mode and is reflected from the back face of the cavity. The return after the third pulse cannot be classified as separate return pulses. This portion of the radar profile is the resonant response of the cavity.

Acknowledgment

This work was supported in part by the MICOM Research, Development, and Engineering Center (Dr. C. Ray Smith) under the auspices of the U.S. Army Research Office Scientific Services Program administered by Battelle (Delivery Order 0182, Contract No. DAAL03-91-C-0034).

References

[1] A. Z. Elsherbeni, "A comparative study of two-dimensional multiple scattering techniques," *Radio Science*, Vol. 29, pp.1023-1033, August-July 1994.

[2] A. C. Ludwig, "Wire grid modeling of surfaces," *IEEE Trans. Antennas Propagat.*, AP-35, p. 1045, 1987.

[3] H. A Ragheb and M. Hamid, "Scattering by N parallel conducting circular cylinders," *Int. J. of Electronics*, vol. 59, p. 407, 1985.

[4] A. Z. Elsherbeni and A. Kishk, "Modeling of cylindrical objects by circular dielectric or conducting cylinders," *IEEE Trans. Antennas Propagat.*, AP-40, pp. 96-99, 1992.

[5] A. Z. Elsherbeni and A. Kishk, "Author's reply to comments on "Modeling of cylindrical objects by circular dielectric or conducting cylinders"," *IEEE Trans. Antennas Propagat.*, AP-41, pp. 1343-1344, 1993.

[6] P. M. Goggans, "Calculation of transient scattering from two-dimensional objects using a frequency domain method of moments approach," *Proceedings of the 9th Annual Review of Progress in Applied Computational Electromagnetics (ACES)*, pp.72-80, 1993.

[7] P. M. Goggans and T. H. Shumpert, "CFIE MOM Solution for TE and TM incidence on a 2-D conduction body with a dielectric filled cavity," *IEEE Trans. Antennas Propagat.*, AP-38, October 1990.

[8] S. S. Haykin, *Communication Systems.* second edition, John Wiley & Sons, 1983.

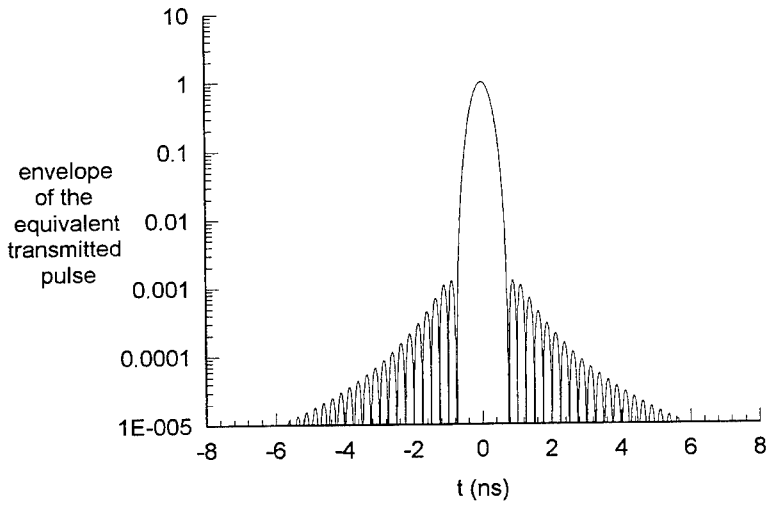


Figure 1. Envelope of the equivalent transmitted pulse.

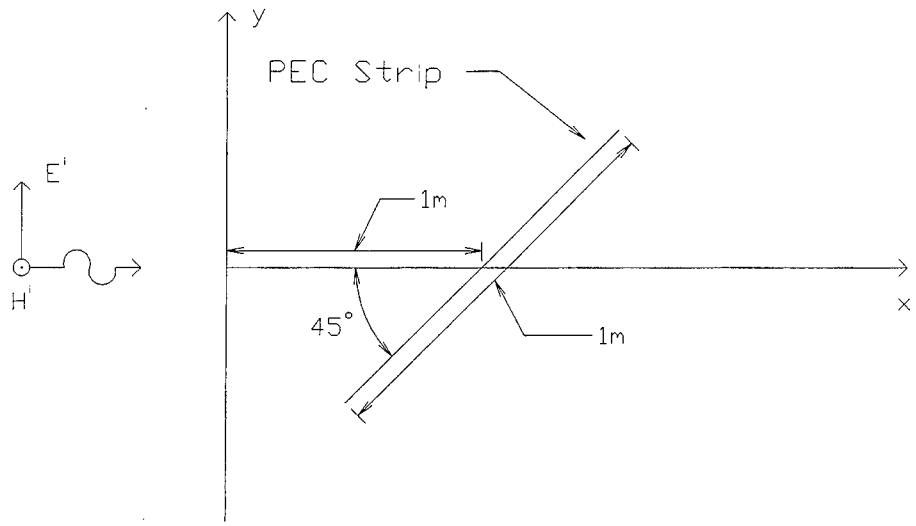


Figure 2. Illustration of a PEC strip with a TE polarized incident wave.

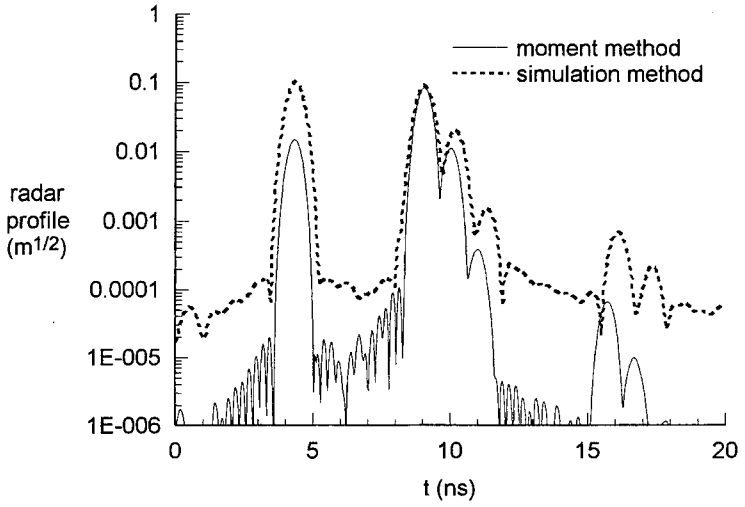


Figure 3. Radar profile of a PEC strip with a TE polarized incident wave.

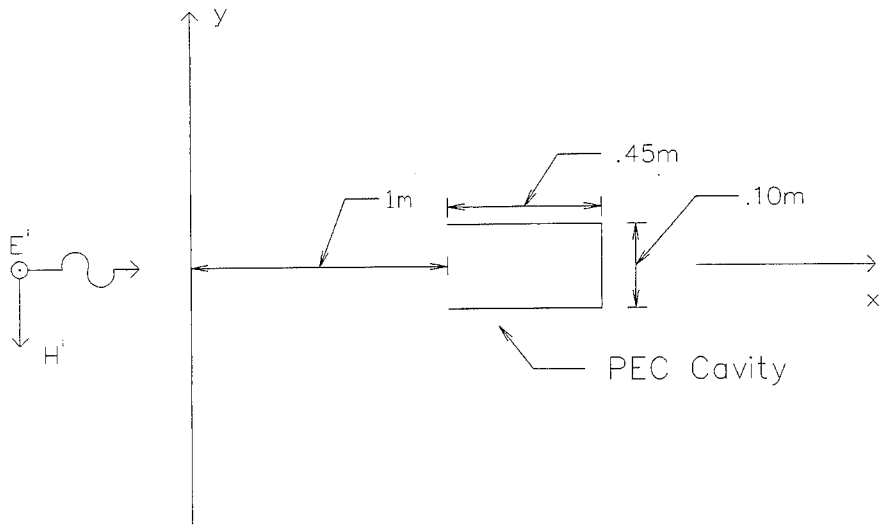


Figure 4. Illustration of a PEC rectangular cavity with a TM polarized incident wave.

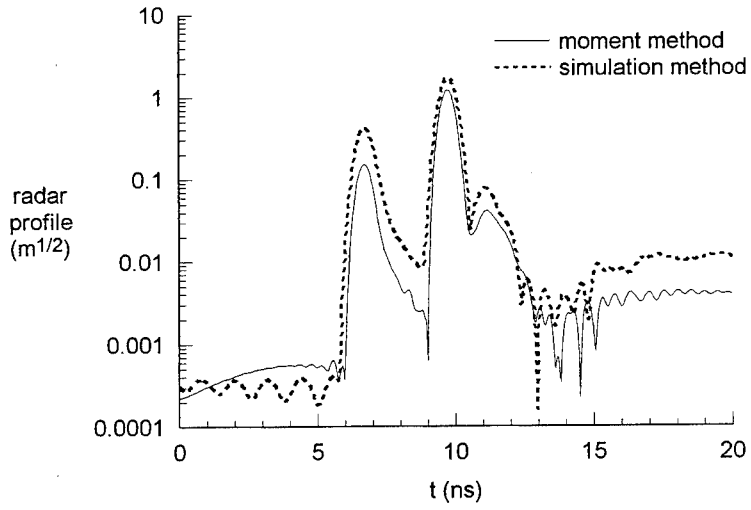


Figure 5. Radar profile of a rectangular cavity for a TM polarized incident wave.

An Object-Oriented Approach to Writing Computational Electromagnetics Codes*

by
Martin Zimmerman and Paul Mallasch
Analex Corporation
Cleveland, Ohio

Abstract

Presently, most computer code development in the Computational Electromagnetics (CEM) community is done in the structured programming paradigm, particularly with the FORTRAN language. Other segments of the programming community have switched to the Object Oriented Programming (OOP) paradigm in recent years in order to ease the development of highly complex codes. This paper examines how OOP is being used in the design of a time-domain numerical analysis CEM code. Comparisons will be made between the OOP code and a structured programming paradigm code in terms of code maintenance, portability, flexibility, and speed.

Introduction

There has been a great deal of work done in the Electromagnetics community in recent years involving the development of numerical algorithms that will solve EM problems quickly and accurately. The vast majority of these codes have been written in a "conventional" manner, using the FORTRAN language and the structured programming paradigm. There are a number of aspects of CEM that make the task of writing numerical analysis quite challenging. These include:

- Parallelism
- Efficient memory usage
- Boundary conditions
- Multiple coordinate systems
- Hybrid methods using more than one numeric algorithm
- Handling rectangular structured, conformal structured, and unstructured grids

Object Oriented Programming (OOP) is a paradigm that has been used to replace structured programming for the production of very large, complex computer programs. Object-oriented languages such as C++ have rapidly gained acceptance in many programming communities. In some areas of numerical analysis, such as Computational Fluid Dynamics, object-oriented codes have made an appearance [1].

How do we define efficiency?

A goal of every programmer is efficient code. In the traditional programming paradigm, efficiency meant speed of execution. A better metric might be the life-cycle costs of the code. In addition to execution time, life-cycle costs include the time to develop the application code, time spent maintaining it, and time spent building the input file. Money also must be factored in; the developer must know whether the end user is willing to pay for additional speed or a "friendlier" interface. There are numerous examples of situations where a user may take days (or longer) to build a model that can be solved in hours on a modern supercomputer. Using the old metric, spending 2 man-months modifying a code so that it would run 50% faster made sense. Under the life-cycle costs metric this might not be cost effective. In addition, the life-cycle costs metric implies that a slower-executing code that is easier to maintain may be more efficient than a faster code that is difficult to maintain. This metric caused the

*This work was carried out at the NASA Lewis Research Center under NASA contract NAS3-25776.

move away from assembly languages towards high-level languages for application programs. In recent years, this same metric caused many software engineers to move from the structured programming paradigm to the OOP paradigm.

What is OOP?

OOP is a programming paradigm; a conceptual model of how a computer program should look. The structured programming paradigm is modeled after the microprocessor. A series of "machines" called procedures or subroutines execute operations on data. In structured programming, data and functions are separate entities. Data are always passive (operated upon) and functions are active.

In the real world the separation between data and functions is not so clear. An engineer, for example, is a person with a name, address, etc. An engineer also has skills which can be applied to problems. An engineer is really a "thing" with both attributes (data) and methods (functions). In the OOP paradigm, "things" are called objects. Each object has attributes and methods that allow it to accurately represent a specific concept. In OOP, data takes the active role because it knows what to do through its methods [2]. The OOP paradigm can be used to some extent in any language, even FORTRAN [3]. However, hybrid OOP languages such as C++ and pure OOP languages such as Smalltalk contain language constructs that allow the attributes and methods of objects to be bound together.

Encapsulation

There are three main concepts in OOP - encapsulation, inheritance, and polymorphism. Encapsulation involves the the way attributes and methods of an object are packaged together. With full encapsulation the attributes of an object are accessible only to other objects of the same type. An object type (in C++ the word "class" is used) defines specific attributes and methods that an object possesses.When encapsulation is enforced, the outside world must access the values of an object's attributes through its methods. Pure OOP languages require full encapsulation while hybrid OOP languages let the programmer decide the level of encapsulation. Encapsulation allows implementation details of the high-level concept the object represents to be hidden from the outside world. The object becomes a "black box", limiting the possibility for error by overwriting memory or applying functions incorrectly. An end result is more readable and portable application code.

Object methods may be divided into several types. First, there are constructors and destructors. A constructor is used to create an object, similar to declaring a variable. Memory required for an object is allocated as the object is created, which can be at any point in the code. The destructor deletes the object, freeing up memory allocated to the object. Normally destructors are called automatically when objects go out of scope. For example, an object created in a loop goes out of scope at the exit from the loop and at this time the destructor is called. This dynamic memory allocation/deallocation makes memory management much easier in C+ than it would be in FORTRAN. Another method is the accessor, which is used by foreign objects to access values of data inside an object. Accessors allow the object creator to give specific read/write access to each object attribute. Many objects contain a print method. Instead of writing an external function that outputs an object's attributes, the object's print method is invoked, causing the object to print itself.

Inheritance

OOP languages allow creation of objects that are "children" of another object. In C++, the terms "base class" and "subclass" are used. Inheritance is the ability of a subclass to inherit all of its parent's attributes and methods. Usually the subclass represents a specialization of the base class. The definition of the subclass only needs to include those methods and attributes that are not part of the general base class. In addition, methods that are different in the subclass than in the base class may be redefined. Anything that doesn't change need not be included in the subclass definition.

Inheritance is a powerful property in terms of code reuse. Objects can be used over and over in new applications, either as is, or as base class objects for some new specialized object. Inheritance also allows the complexity of a concept to be spread across a number of classes. A good example in the present code is the Feed Class, which represents the forcing function applied to the EM time-domain

boundary-value problem. The base Feed Class contains all the information that is common to all forcing functions.The primary method or service is the application of a time-dependent source term to the EM fields in a problem space. The nature of the time-dependent source term (e.g. pulse or sinusoid) is an attribute as is the feed region definition (the region that the forcing function is applied over). There are a number of specializations of the base Feed Class. For example, the weighting across the feed region is different for a coax feed than for a rectangular waveguide. A plane-wave forcing function (used in a scattered field formulation) has a very different implementation from a fixed region feed used in a total field formulation. These differences are contained in the subclass definitions.

Polymorphism

The third and possibly most important concept in the OOP paradigm is polymorphism, representing an abstract concept in different ways. The application programmer works at a high-level, using object methods to accomplish tasks without worrying about the implementation details of the methods. If different forms of a single method are used to accomplish the same task, then polymorphic functionality is present. The key to polymorphism is allowing run-time binding. Objects can invoke methods of other objects without knowing the type (or class) of the other object. In C++ this is done with the virtual function. While C++ is strongly typed, a base class pointer may be used to point to a sub-class object. When a virtual function is invoked through a base class pointer, the base object method is not called. Instead, the object method of the object the pointer points to is called. Polymorphism builds upon the previous two concepts. Encapsulation ensures that the outside world works with an object method rather than working directly upon the object's attributes. Inheritance provides for subclasses that contain the same methods with different implementations.

An example of polymorphism used in this computer code is the Parallel Class. The Parallel Class handles the work of spawning child processes, deciding which processes are neighbors, deciding the domain decomposition, and handling interprocess communication. The implementation is a function of the message passing library used (e.g. PVM, APPL). So a base Parallel Class can have several sub-classes, each of which corresponds to a different message passing library that uses library specific commands. A default Parallel Class whose methods do nothing would be used on a serial machine.

Algorithmic polymorphism

Hybrid method computer codes are by definition polymorphic. Each implementation is capable of reaching the same result (accurate computation of EM fields) using different algorithms. For the present work, the hybrid method utilizes Finite Difference Time Domain (FDTD) and Finite Volume Time Domain (FVTD). Both methods use fields discretized over cell grids. Both methods (in at least some formulations) use similar processes (i.e. update E fields, step in time, update H fields, step in time, apply boundary conditions, save output, repeat). FDTD is much more memory efficient since it is not necessary to describe each cell individually. FVTD has the advantage of being applicable to unstructured grids as well as structured grids. Each algorithm can be represented by a subclass of the same base class that would contain the common methods (e.g. update E fields, etc.). An application of a hybrid FDTD/FVTD method is a complex conformal object surrounded by a regular grid that contains the outer boundary radiating condition [4,5]. This hybrid method also could be used to solve a problem entirely with FDTD or FVTD. By standardizing the interface between regions where different algorithms are used, it is possible to have communication between these regions.

One implementation method would divide the problem space into subspaces. Each subspace uses either FDTD or FVTD and is represented by the appropriate subclass object. The subspaces are collected into an array or list that contains base class pointers to the subspace objects. The application code then traverses the list, invoking the methods for each subspace object in turn without knowing how the object will accomplish its task.

Data Parallelism

Both FDTD and FVTD lend themselves to data parallelism implemented as domain decomposition. From the viewpoint of the application programmer, the mechanics of the domain decomposition should be hidden. Just as each process working on a subset of the problem space acts as

if it is working on the entire problem, the application programmer and user need to work on the entire problem as if it is not broken up. In the present case two class hierarchies, the Field Class and the Focus Class, work together. The Field Class contains the discrete EM field data for the problem space. The data set is amorphous, neither structured nor unstructured. The Focus Class provides the framework for describing how the Field Class data should be ordered. An analogy is that the Field Class is tent fabric and the Focus Class is the set of tent poles defining the shape of the tent. The Focus Object knows what subset of a Field Object to iterate over and how to iterate over that subset. This subset is also a function of the data decomposition among processes. The Focus Object takes position information listed in a global sense and converts it to process local information that is used to control iterations over the Field Classes (Fig. 1). Since this algorithm is implemented in different ways for structured and unstructured grids, different sub-classes of the Focus Class will be needed for these grids.

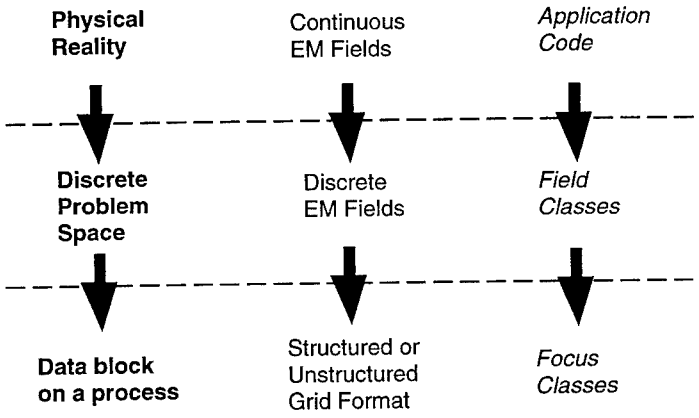


Figure 1. Relationship between levels of abstraction and the OOP classes.

Both FDTD and FVTD use nearest neighbor information and therefore require message passing of EM field information between processes. The Focus Class works in conjunction with the Parallel Class for this task with the Focus Object containing a Parallel Object as an attribute. The Parallel Object determines whether data must be passed. If so, the Focus Object loads a message with the appropriate data and sends it using member functions (methods) of its Parallel Object.

The dynamic memory allocation ability of C++ is very useful for data parallelism. Arrays can be dimensioned to the correct size as a function of the number of processes used. The code uses the minimum amount of memory without recompilation every time the number of processors is adjusted. This is particularly important for people using clusters of workstations that have load distributions that vary from day to day.

Boundary Conditions

Boundary conditions often represent one of the most difficult aspects of numerical analysis programming. Boundary conditions often use a small fraction of the code's execution time while comprising a large number of lines of actual source code. The boundary condition is a concept that can be represented by a class hierarchy. All boundary conditions provide the same service; modification of fields in a subset of the problem space. In addition, all boundary conditions use data, mostly multiplicative constants required by the boundary condition. The actual data needed and the implementation used vary from boundary condition to boundary condition. Differences in

implementation can be handled by creating different sub-classes to represent the different boundary conditions, such as 1st order Mur or 2nd order Liao.

One challenge of applying boundary conditions is that an operation is applied only to a portion of the EM fields in the problem space. Since the Focus Object handles iteration for the data set in the Field Object, the Focus Object must also keep track of what portion of the data set is to be iterated over (the active region). This service also is needed for applying forcing functions and applying material attributes (Fig. 2). The boundary condition may contain smaller Field Objects that cover only the boundary region. The Focus Object must ensure that a mathematical operation on two Field Objects only occurs if the objects have the same size active region.

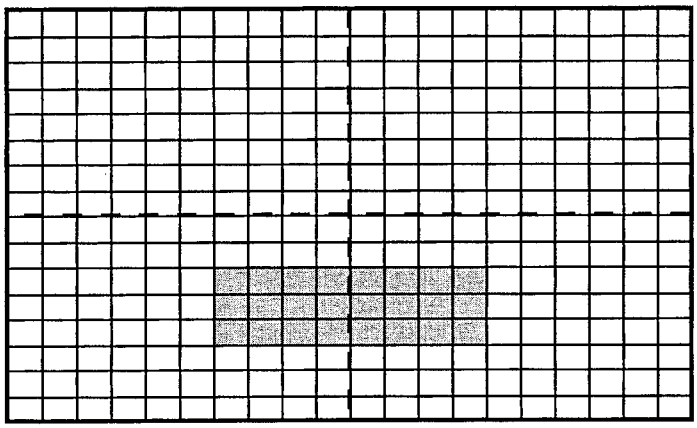


Figure 2. There are various subsets of the entire grid that must be operated on during the course of the numerical analysis.

Comparisons with a structured programming code

The present C++ code is compared to FDTD_ANT, a non-conformal structured-grid FDTD program that is based upon the Luebbers and Kunz FDTDA code [6]. Both codes use the same FDTD formulation and may be used with either scattered field or total field formulation. These codes are compared for code development, code maintenance, flexibility, portability, memory efficiency, and speed efficiency. A version of the FDTD_ANT code is parallelized for domain decomposition along any one of the three Cartesian axes. The C++ code may be domain decomposed along any combination of the three axes (including all three at once).

Code Development

Writing an OOP code often involves more design overhead than writing a similar code in the structured programming paradigm. In Object Oriented Design (OOD) the overall scenario must be divided into individual concepts which are modeled by objects. The designer then decides whether the concept is better represented by one object or a hierarchy of objects. In some cases, classes may already exist that have some of the necessary capabilities. Using existing classes as a foundation for new classes is a hallmark of code reuse. Note that the term code reuse refers to using already created and tested

classes in different applications. Code reuse is different from code copying, which is taking portions of code from one file and copying them into another file. With code reuse less total code is created and there are fewer opportunities for typographical errors than with code copying.

Code maintenance

Code maintenance is a key issue in life-cycle costs since most CEM codes are undergoing almost constant modification. The OOP paradigm specifically addresses code maintenance in several ways. Encapsulation makes the code more modular, which prevents new code from affecting unrelated existing code. In addition, much less global data (including common blocks) exists, making it less likely that memory will be overwritten. The additional code is usually simpler to write. For example, the iterator indices of the Field Object are all encapsulated within the Focus Object that is itself encapsulated within the Field Object. Application code using Field Objects contain no indices or "do-loops". Use of "index-free" notation at the application code level makes the code easier to read and avoids the potential for typographical errors that often accompany nested "do-loops".

Flexibility

The OOP code is far more flexible due to polymorphism. By using class hierarchies that contain virtual functions and functors (functions that are really objects and can be treated like data) it is much easier to write hybrid method codes. In particular, it is possible to write hybrid method codes that don't appear to use multiple methods or algorithms. The versatility of code can be increased by adding new subclasses which need only define the methods whose implementation has changed.

Portability

One clear portability advantage that emerged involved parallelization. The FORTRAN code has two versions, a serial version and a parallel version. To execute the parallel version on a serial machine it would be necessary to remove all the message passing library calls since that library would not be installed on a serial machine. In the OOP paradigm, each type of computer would have a library containing the Parallel subclass relevant to the computer's configuration. A serial machine would have a "stub" subclass that would do nothing. The application code which only deals with the base Parallel Class becomes completely portable. This portability could just as easily be applied to other classes, with highly-optimized algorithm kernels being stored in Class libraries that vary from machine to machine. Application codes would invoke the methods in these libraries without having to know the implementiation details.

Memory efficiency

FORTRAN tends to be very memory inefficient due to the lack of dynamic memory allocation. This is a problem for parallel codes where the data set size is a function of the number of processes running. The C language has dynamic memory allocation through the malloc command, but an additional command must be used in C to deallocate memory. The C++ language goes a step further with automatically called destructors that take care of memory deallocation.

Speed efficiency

While the project has not concentrated on speed of execution, it is certainly an important issue. At the present time the OOP code runs significantly slower than the structured FORTRAN code, by a factor of 8.5. In reference 7, the authors compared versions of a Computational Fluid Dynamics (CFD) code written in FORTRAN, C, and C++ (the first two codes used structured programming and the C++ code used OOP). On a variety of machines the C code was faster than the C++ code by a factor of roughly 2 (the FORTRAN code was roughly equivalent to the C code in speed). For many numerical applications this would be an acceptable loss in execution efficiency. The work in [7] suggests that many things could be done to make the present OOP code faster.

Results

To date, an OOP code has been written in C++. This code is fully parallelized (3-dimensional

domain decomposition) using the PVM message passing library. It uses the FDTD algorithm on a structured grid with either PML or 1st order Mur boundary conditions. Agreement with the FDTD_ANT code is good for a sample problem (agreement is not exact since the codes use different boundary conditions). At present the unstructured grid classes and FVTD solver are being added to the code and will be further reported on during the presentation.

References

[1] I. G. Angus and W. T. Thompkins, "Data storage, concurrency and portability: an object oriented approach to fluid mechanics", The Fourth Conference on Hypercubes, Concurrent Computers, and Applications, 1989.

[2] J. Dutemann, "Our object all sublime," *PC Techniques*, pp. 14-22, April/May 1990.

[3] K. D. Wampler, "The object-oriented programming paradigm (OOPP) and FORTRAN programs," *Computers in Physics*, pp. 385-394, July/August 1990.

[4] K. S. Yee, J. S. Chen, and A. H. Chang, "Conformal finite difference time domain (FDTD) with overlapping grids," *IEEE Trans. Antennas Propagat.*, vol. 40, no. 9, pp. 1068-1075, Sept. 1992.

[5] K. S. Yee and J. S. Chen,"Conformal hybrid finite difference time domain and finite volume time domain," *IEEE Trans. Antennas Propagat.*, vol. 42, no. 10, pp. 1450-1455, Oct. 1994.

[6] J. H. Beggs, R. J. Luebbers, K. S. Kunz, and H. S. Langdon, "User's Manual for three dimensional FDTD version A code for scattering from frequency-independent dielectric materials," short course at the 8th Annual Review of Progress in Applied Computational Electromagnetics, March 1992.

[7] I. G. Angus and J. L. Stolzy, "Experiences in converting an application from Fortran to C++: Beyond *f2c*," *Proceedings of the C++ at Work Conference,* Nov. 1991.

SESSION 10:

FAST ALGORITHMS FOR COMPUTATIONAL ELECTROMAGNETICS

Chairs: E. Michielssen, W. Chew

On the Use of Wavelet-Like Basis Functions in the Finite Element Analysis of Elliptic Problems

Richard K. Gordon
Department of Electrical Engineering
University of Mississippi
University, MS 38677

Introduction

It has been recently shown that the use of wavelet-like basis functions in the finite element solution of elliptic problems yields a global matrix that, after simple diagonal preconditioning, has a condition number that is bounded by a constant as the number of points of discretization is increased [1]. This contrasts sharply with the situation that arises when the traditional finite element or finite difference method is used; in either of these cases the usual preconditioning methods make the condition number $O\left(\frac{1}{h}\right)$; and if simple diagonal preconditioning is used, the condition number will go to infinity as, at best, $\frac{C}{h|h\log h|}$ as the number of points of discretization is increased, i.e., as h goes to zero. This is important because when iterative algorithms are employed, ill conditioning can lead to numerical instabilities, slow convergence, or even lack of convergence. Thus, the use of wavelet-like basis functions appears to have significant potential as an efficient method for solving elliptic problems over large and highly heterogeneous problem domains.

A wavelet is a function that is localized in both the spatial and frequency domains and is such that any L^2 function can be expressed in terms of translations and dilations (or compressions) of the wavelet. This is a relatively new area of research in computational electromagnetics. Steinberg and Leviatan discuss the use of wavelet expansions in an integral equation technique in [2]. In [1] and [3], Jaffard and Laurencot present wavelet methods for elliptic problems. In the 1994 IEEE AP-S Symposium and URSI Meeting, there were several presentations related to wavelets, including [4]-[7].

Construction of the Basis of Wavelet-like Functions

The technique that is employed in this paper is explained in detail in [1]; its application in this paper can be summarized as follows. An initial, coarse discretization of the problem domain is chosen. The traditional finite element basis functions associated with the nodes in this initial discretization are orthonormalized with respect to each other using the procedure described in [1]. The resulting, orthonormalized functions are the first functions in the basis of wavelet-like functions. If finer discretization is desired, new nodes are introduced at the midpoints of the intervals between the existing nodes. The traditional finite element basis functions associated with these new nodes are then orthogonalized against the functions in the basis. Then, the resulting functions are orthonormalized with respect to each other. The functions that result from this are then added to the basis. This procedure is repeated, with more nodes being introduced into the mesh and new functions being added to the basis at each step, until the discretization is as fine as desired. Then, the standard finite element method is employed using the wavelet-like functions constructed in this procedure.

As an illustration of these ideas, consider the finite element solution of the problem:

$$-\nabla\cdot(a\nabla u)+bu=g \text{ on } \Omega$$
$$u=h \text{ on } \partial\Omega$$
$$a(\vec{x})\geq C>0$$
$$b(\vec{x})\geq 0$$

For the sake of simplicity, consider a one dimensional problem in which Ω is the line segment from $x=0$ to $x=3$ and:

$$a(x)=1.1+\sin(25x)$$
$$b(x)=1.0$$
$$g(x)=10.0x$$
$$u(0)=2.0$$
$$u(3)=4.0$$

When the technique described in [2] is used to solve this problem, the first few wavelet-like basis functions are as shown in figures 1-5. (Figure 5 is presented simply to provide an uncluttered view of one of the wavelet-like basis functions shown in figure 4.) Figure 1 shows the first function added to the basis; the initial, coarse discretization used in this case contains only one interior node which is located at the midpoint of the interval. In the next step, one node is placed at the midpoint of each of the two sub-intervals of the initial discretization. The traditional finite element basis function associated with each of these nodes is then

orthogonalized against the function shown in Figure 1. Then, the orthonormalization procedure is applied to the two resulting functions to yield the final wavelet-like functions shown in Figure 2. These functions are orthogonal to each other and to the function shown in Figure 1 as well. At this point there are three interior nodes in the discretization and three wavelet-like functions in the basis. At the next step, nodes are placed at the midpoints of each of the current four sub-intervals. The above procedure is repeated to yield the four wavelet-like functions shown in Figure 3. The next stage in the procedure yields the eight functions presented in Figure 4. It should be noted that the fifteen wavelet-like basis functions shown in Figures 1-4 span the same space as do the fifteen traditional finite element basis functions described by:

$$g_i(x) = \left\{ \begin{array}{ll} 0 & \text{for } x < (i-1)\Delta \\ \dfrac{x-(i-1)\Delta}{\Delta} & \text{for } (i-1)\Delta \le x \le i\Delta \\ \dfrac{(i+1)\Delta - x}{\Delta} & \text{for } i\Delta \le x \le (i+1)\Delta \\ 0 & \text{for } x > (i+1)\Delta \end{array} \right\} \text{for } i = 1,\ 2,\ \cdots,\ 15$$

where $\Delta = \frac{3}{16}$. This procedure is continued until the discretization is as fine as desired.

Numerical Results

The advantage of using the wavelet-like basis functions rather than the traditional finite element basis functions is demonstrated in figures 6-9. The problem above was solved using 3, 7, 15, 31, 63, 127, 255, 511, 1023, and 2047 wavelet-like basis functions and 3, 7, 15, 31, 63, 127, 255, 511, 1023, and 2047 traditional basis functions. In figure 6, the condition number of the preconditioned global matrix is shown for these various numbers of basis functions for both wavelet-like and traditional finite element basis functions. (When wavelet-like basis functions were employed, simple diagonal preconditioning was used; when the traditional finite element basis functions were employed, incomplete Cholesky preconditioning was used.) As can be seen in this figure, the effect on the condition number of using wavelet-like rather than the traditional basis functions is dramatic; while the condition number climbs to more than 2.5 million when the traditional basis functions are used, it reaches a peak value of 65.48 and then actually declines as the number of basis functions increases, when the wavelet-like basis functions are used. In fact, the condition number for the wavelet cases is so much smaller than that for the traditional basis functions that the details of the behavior cannot be seen in figure 6; thus figure 7 is presented to provide a more detailed picture of the behavior of the condition number when the wavelet-like

functions are used. Clearly, even though a much simpler preconditioning is being used in the wavelet than in the traditional cases, the global matrix arising from the use of wavelet-like functions is much better conditioned than that arising from the use of the traditional basis functions. The importance of this is demonstrated in figures 8 and 9. In these figures we see plots of the number of steps required for the convergence of the conjugate gradient algorithm for each of the cases presented in figures 6 and 7. (The conjugate gradient algorithm was applied using the preconditioned global matrix for which the condition number is plotted in figures 6 and 7.) In figure 6 it is seen that when the traditional basis functions are used, the number of steps required for convergence increases without bound as the number of basis functions is increased; but when the wavelet-like basis functions are employed, the number of steps remains quite low. In fact, as was the case in figure 6, the performance obtained using the wavelet-like basis functions is so much better than that obtained using the traditional basis functions that it is impossible to depict both in detail on the same scale; so, figure 9 is presented to provide a more detailed picture of the variation of the number of steps required when the wavelet-like functions are used. From this picture we can see that the number of steps required for a matrix of order 2,047 is the same as that required by a matrix of order 511 and is only 11.4% greater than the number of steps required for a matrix of order 127.

Conclusions

In this paper, the use of wavelet-like basis functions in the solution of elliptic problems over one-dimensional domains is discussed. In this case, the use of such basis functions yields matrices that, with simple diagonal preconditioning, are much better conditioned than are those resulting from the use of traditional finite element basis functions and more sophisticated preconditioning schemes. This leads to much more rapid convergence of the conjugate gradient algorithm when these wavelet-like basis functions are employed.

REFERENCES

[1] Stephane Jaffard, "Wavelet methods for fast resolution of elliptic problems," *SIAM Journal on Numerical Analysis*, vol. 29, num. 4, pp. 965-986, August 1992.

[2] Ben Zion Steinberg and Yehuda Leviatan, "On the use of wavelet expansions in the method of moments," *IEEE Transactions on Antennas and Propagation*, vol. 41, num. 5, pp. 610-619, May 1993.

[3] S. Jaffard and Ph. Laurencot, "Orthonormal wavelets, analysis of operators, and applications to numerical analysis," Wavelets: A Tutorial in Theory and

Applications, Ed. C. K. Chui, Academic Press, Inc., San Diego, CA, pp. 543-601, 1992.

[4] J. C. Goswami, A. K. Chan, and C. K. Chui, "An analysis of two-dimensional scattering by metallic cylinders using wavelets on a bounded interval," *1994 Digest of the IEEE Antennas and Propagation Society International Symposium*, vol. 1, p. 2, June 1994.

[5] O. P. Franza, R. L. Wagner, and W. C. Chew, "Wavelet-Like basis functions for solving scattering integral equations," *1994 Digest of the IEEE Antennas and Propagation Society International Symposium*, vol. 1, pp. 3-6, June 1994.

[6] T. K. Sarkar, L. E. Garcia-Castillo, and M. S. Salazar-Palma, "Utilization of wavelet concepts in finite elements for efficient solution of Maxwell's equation," *1994 Digest of the IEEE Antennas and Propagation Society International Symposium*, vol. 1, p. 7, June 1994.

[7] R. K. Gordon and J. Brown, "Iterative analysis on a parallel computer of the global matrices arising in wavelet and finite element methods," *1994 Abstracts & Program URSI Radio Science Meeting*, p. 296, June 1994.

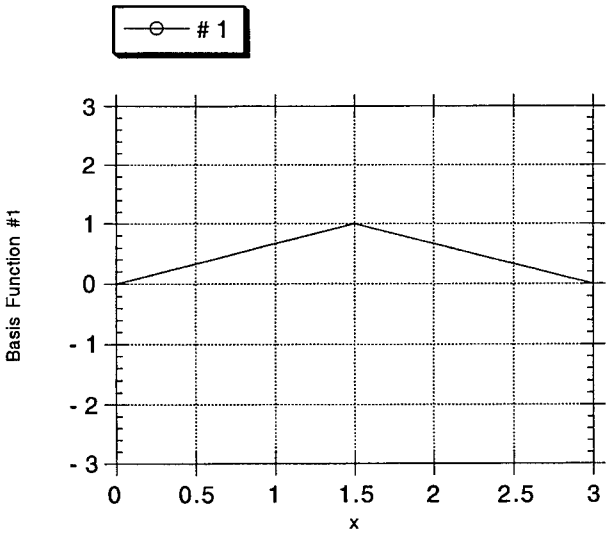


Figure 1. Wavelet-like basis function #1

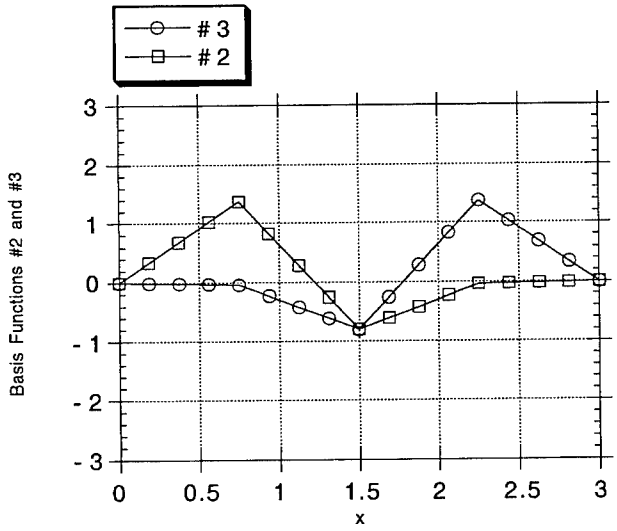


Figure 2. Wavelet-like basis functions #2 and #3

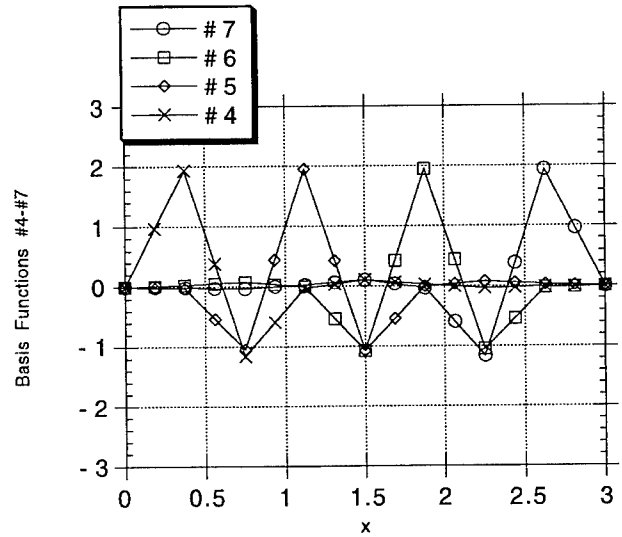


Figure 3. Wavelet-like basis functions #4-#7

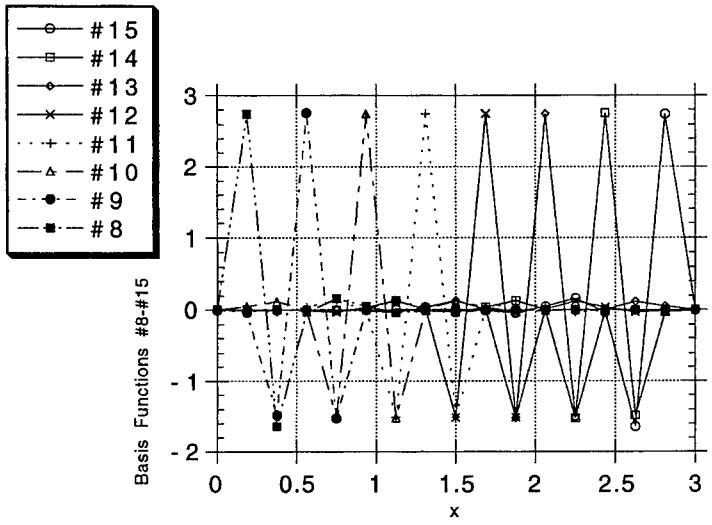


Figure 4. Wavelet-like basis functions #8-#15

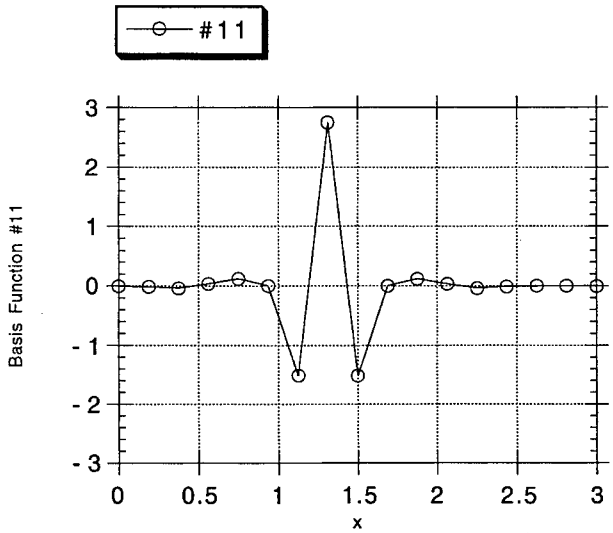


Figure 5. Wavelet-like basis function #11

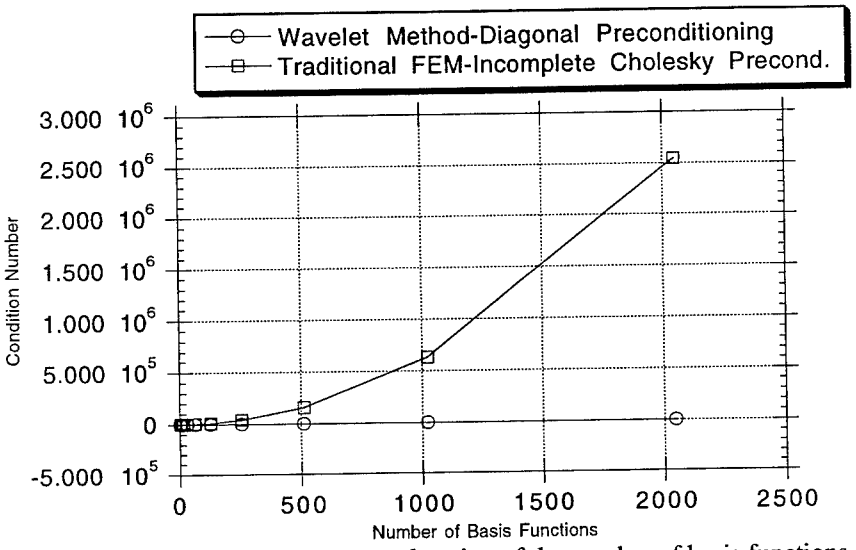


Figure 6. Condition number as a function of the number of basis functions

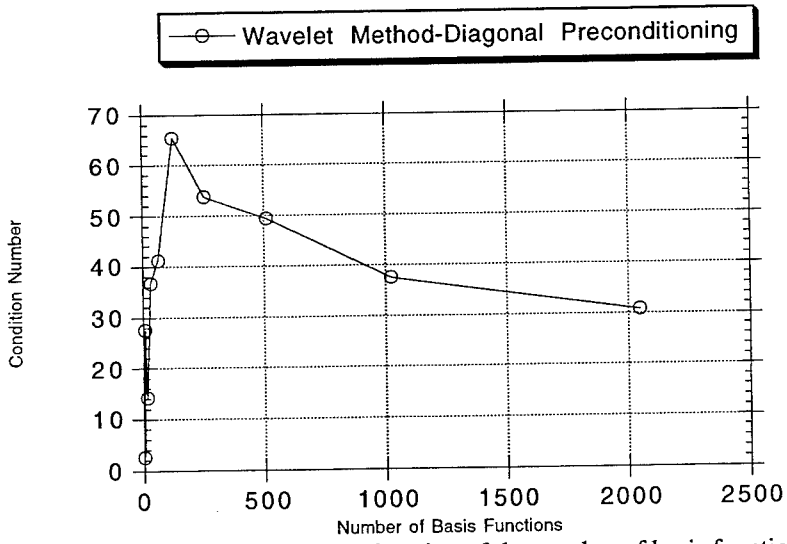


Figure 7. Condition number as a function of the number of basis functions

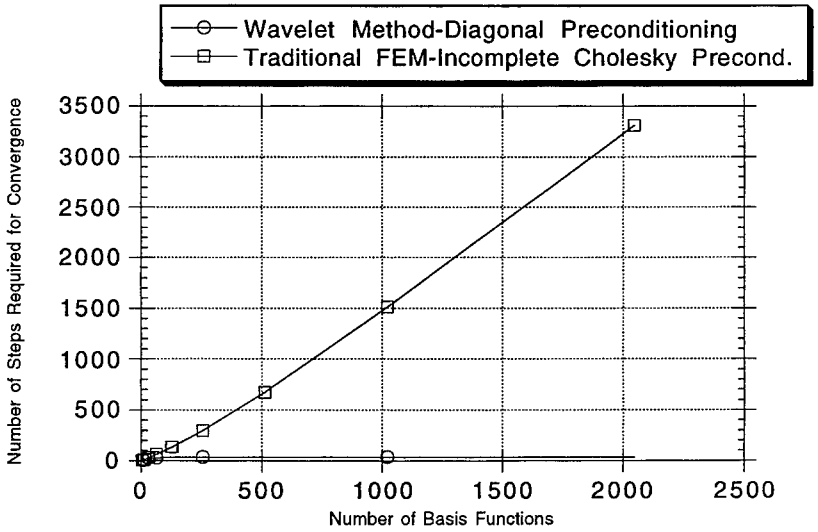


Figure 8. Number of steps required for convergence as a function of the number of basis functions

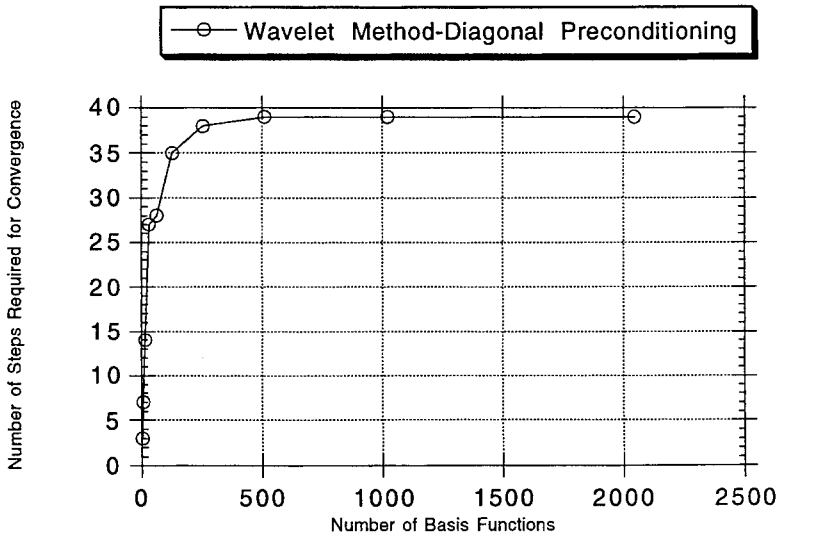


Figure 9. Number of steps required for convergence as a function of the number of basis functions

FAST WAVELET ALGORITHM (FWA) FOR MOMENT METHOD ANALYSIS OF ELECTROMAGNETIC PROBLEMS

Kazem Sabetfakhri* and Linda P.B. Katehi

Radiation Laboratory
Department of Electrical Engineering and Computer Science
The University of Michigan
Ann Arbor, MI 48109-2122

1. Introduction

In the study of complex, large-scale electromagnetic problems, two factors are of key importance: (1) a powerful computer with sufficient speed and memory space, and (2) a rigorous numerical technique characterized by a high degree of accuracy and efficiency. With the rapid advances in the high speed computer technology, the numerical analysts are being provided with ever-increasing computing power. In the meanwhile, the numerical techniques for electromagnetics have reached such a level of maturity that the full-wave analysis of many complex structures is no longer an unrealistic computational goal. As the complexity of the geometries under study increase, the speed factor becomes more prominent due to the enormous volume of the computational load. It is essential to complement the speed of the computing machinery by an increase in the efficiency of the numerical codes. This prompts an urgent need for the development of fast algorithms for the numerical solution of electromagnetic problems.

The Method of Moments (MoM) has long been used as one of the primary tools for the rigorous study of electromagnetic problems [1]. This method in conjunction with the integral equation technique provides the most accurate and in many cases an exact formulation of the related the boundary value problem. In spite of all its advantages over the other numerically intensive techniques, the major challenge in the method of moments is the choice of appropriate basis functions that would provide the required accuracy and computational efficiency. An impeding characteristic of this approach is that the resulting matrices are full and have very poor condition numbers. This challenge becomes even bigger as the geometry under study becomes non-canonical and complex, involving larger numbers of unknowns.

The past two years have witnessed the successful application of the newly developed theory of orthonormal wavelets to various electromagnetic problems [2]-[4]. It has been established that the use of wavelet expansions in conjunction with the method of moments leads to highly sparse moment matrices. This property is based on the fact that the condition number of the resulting matrices is so good that performing a thresholding procedure by discarding a large number of the matrix entries which fall below a certain threshold level does not degrade the accuracy of results. Such a sparsity makes it possible to employ a wide range of numerical methods especially developed for the fast and efficient storage and inversion of this type of matrices.

The orthonormal wavelets have some other interesting properties which can be properly exploited to speed up the moment method computations significantly. One such feature is the Fast Wavelet Algorithm (FWA) which has been used extensively in signal processing applications [5]. In brief, this property enables one to compute the wavelet expansion coefficients at a certain resolution from those of the next higher resolution. Thus, in a moment method solution, it is possible to construct a recursive algorithm to compute all the moment matrix elements in consecutive resolution levels from those of the highest resolution. In the following, first we present a short account of the

theory of one-dimensional multiresolution analysis (MRA) to set up the definitions and conventions. Then, the fast wavelet algorithm (FWA) is described in its one-dimensional version. This is followed by the construction of two-dimensional multiresolution analysis and the associated FWA algorithm. Finally, the implementation of these algorithms for MoM speed-up are discussed and some numerical results are presented.

2. One-Dimensional Multiresolution Analysis

A multiresolution analysis (MRA) of $L^2(R)$ is a sequence of nested approximation subspaces of $L^2(R)$, denoted by $\{V_m\}_{m\in Z}$, such that all subspaces are scaled versions of a central space V_0 obtained through dilation by integral powers of 2 [6]. Each subspace V_m, which is said to have a resolution of 2^{-m}, possesses details twice as fine as those of its predecessor, V_{m-1}, on this approximation ladder. Each subspace V_m by definition has an orthonormal basis, denoted by $\{\phi_{m,n}\}_{n\in Z}$, which consists of properly scaled and shifted versions of a function $\phi(x)$, called the scaling function, such that $\phi_{m,n}(x) = 2^{m/2}\phi(2^m x - n)$. Given an arbitrary square-integrable function $f(x)$, one can then express its approximation at a resolution of 2^{-m} by defining a projection operator $P_m(f)$ onto the subspace V_m in the following form:

$$P_m(f) = \sum_{n\in Z} < f, \phi_{m,n} > \phi_{m,n}(x) \tag{1}$$

where $< f, g >$ denotes the inner product of the two functions $f(x)$ and $g(x)$. We denote the orthogonal complement of V_m in V_{m+1} by W_m and write $V_m \oplus W_m = V_{m+1}$. It can be shown that for each complement subspace W_m, there exists an orthonormal basis, denoted by $\{\psi_{m,n}\}_{n\in Z}$, which consists of scaled and shifted versions of another function $\psi(x)$, called the mother wavelet, such that $\psi_{m,n}(x) = 2^{m/2}\psi(2^m x - n)$. Then, one can write:

$$P_{m+1}(f) = P_m(f) + \sum_{n\in Z} < f, \psi_{m,n} > \psi_{m,n}(x) \tag{2}$$

It can be shown that the entire set $\{\psi_{m,n}\}_{m,n\in Z}$ constitutes a complete orthonormal basis for $L^2(R)$. Now, having a crude approximation of the function $f(x)$ at a coarse resolution level, say m_1, one can improve it to a finer resolution level, say m_2, by exploiting the wavelets of the intermediate levels in the following manner:

$$P_{m_2}(f) = P_{m_1}(f) + \sum_{m=m_1}^{m_2-1} \sum_{n\in Z} < f, \psi_{m,n} > \psi_{m,n}(x), \quad m_2 > m_1 \tag{3}$$

The definition of a multiresolution analysis requires that $\int_{-\infty}^{\infty} \psi(x)dx = 0$, implying that a wavelet is a bandpass function with no dc component. The scaling function, by contrast, is a lowpass function with $\int_{-\infty}^{\infty} \phi(x)dx = 1$. Hence, a multiresolution expansion of a square-integrable function $f(x)$ with an arbitrary spectral content can be expressed in the following form:

$$f(x) = \sum_{k\in Z} c_{m_0,k}\phi_{m_0,k}(x) + \sum_{m=m_0}^{\infty} \sum_{n\in Z} d_{m,n}\psi_{m,n}(x) \tag{4}$$

where m_0 is an initial resolution level, and $c_{m,n}$ and $d_{m,n}$ are the respective expansion coefficients given by

$$c_{m,n} = < f, \phi_{m,n} >$$
$$d_{m,n} = < f, \psi_{m,n} > \quad (5)$$

Various multiresolution analyses with different mathematical properties have been introduced in recent years. The Battle-Lemarie MRA, which is constructed based on polynomial spline functions, has been efficiently used for the MoM analysis of electromagnetic problems [2]-[4]. Fig.1 shows the plots of the cubic spline Battle-Lemarie scaling function and mother wavelet.

3. The Fast Wavelet Algorithm

The foundation of the fast wavelet algorithm is based on the following two-scale property of the multiresolution analysis:

$$\phi(x) = \sqrt{2} \sum_{n \in Z} h_n \, \phi(2x - n)$$
$$\psi(x) = \sqrt{2} \sum_{n \in Z} g_n \, \phi(2x - n) \quad (6)$$

where $\{h_n\}_{n \in Z}$ is a zero-centered symmetric discrete sequence with fast decay, and

$$g_n = (-1)^{n-1} h_{1-n}. \quad (7)$$

Table 1 provides the values of the first few positive h_n coefficients for a cubic spline Battle-Lemarie multiresolution analysis.

Table II
h_n Coefficients for the Cubic Spline Battle-Lemarie MRA

n	h_n
0	0.76613005
1	0.43392265
2	-0.05020169
3	-0.11003702
4	0.03208086
5	0.04206833
6	-0.01717627
7	-0.01798229
8	0.00868520

In view of properties (6), it is not difficult to derive the two following relations:

$$< f, \phi_{m,n} > = \sum_{k \in Z} h^*_{k-2n} < f, \phi_{m+1,k} >$$
$$< f, \psi_{m,n} > = \sum_{k \in Z} g^*_{k-2n} < f, \phi_{m+1,k} > \quad (8)$$

where $*$ denotes the complex conjugate. Using definitions (5), the above relations can be written in the following manner:

$$\begin{aligned} c_{m,n} &= \sum_{k\in Z} h^*_{k-2n}\, c_{m+1,k} \\ d_{m,n} &= \sum_{k\in Z} g^*_{k-2n}\, c_{m+1,k} \end{aligned} \tag{9}$$

Equations (9) are the mathematical statement of the fast wavelet algorithm. Note that according to these equations, the scaling and wavelet coefficients at each resolution can be computed by a discrete convolution from a knowledge of only scaling coefficients at the next higher resolution. Fig.3 shows the signal flow diagram for the fast wavelet algorithm, where the filters H and G involve a discrete convolution plus a decimation by 2. When several resolution levels are required, it is therefore sufficient to compute the scaling coefficients only at the resolution level immediately following the highest resolution involved. All the expansion coefficients at the lower resolution levels can be evaluated recursively using equations (9).

4. Two-Dimensional Multiresolution Analysis

A two-dimensional multiresolution analysis is a ladder of successive nested approximation subspaces $\boldsymbol{V}_m$ of $L^2(\boldsymbol{R}^2)$. Each subspace $\boldsymbol{V}_m$ at a resolution of 2^{-m} is constructed from the Cartesian product of two one-dimensional MRAs at the same resolution, i.e., $\boldsymbol{V}_m = V_m \otimes V_m$ [6]. An orthonormal basis for $\boldsymbol{V}_m$ would consist of the functions $\Phi_{m,n_x,n_y}(x,y) = \phi_{m,n_x}(x)\phi_{m,n_y}(y), n_x, n_y \in Z$, where the one-dimensional functions in x and y are properly dilated and shifted versions of the scaling functions $\phi(x)$ or $\phi(y)$, respectively, as described in section 2. The orthogonal complement of $\boldsymbol{V}_m$ in $\boldsymbol{V}_{m+1}$ is denoted by $\boldsymbol{W}_m$, and it can be shown that

$$\boldsymbol{W}_m = (W_m \otimes V_m) \;\oplus\; (V_m \otimes W_m) \;\oplus\; (W_m \otimes W_m) \tag{10}$$

where W_m is the one-dimensional complement space of V_m. Hence, the orthonormal basis for $\boldsymbol{W}_m$ consists of three sets of wavelets: $\Psi^v_{m,n_x,n_y}(x,y) = \psi_{m,n_x}(x)\phi_{m,n_y}(y)$, $\Psi^h_{m,n_x,n_y}(x,y) = \phi_{m,n_x}(x)\psi_{m,n_y}(y)$, and $\Psi^d_{m,n_x,n_y}(x,y) = \psi_{m,n_x}(x)\psi_{m,n_y}(y)$, with $\psi(x)$ and $\psi(y)$ being the mother wavelet. These wavelets are called vertical, horizontal and diagonal, respectively, in that they sample variations of the expanded function primarily along the corresponding directions.

Now, one can approximate a doubly square-integrable function $f(x,y)$ at a resolution of 2^{-m} by defining the following projection operator onto the subspace $\boldsymbol{V}_m$:

$$P_m(f) = \sum_{n_x\in Z}\sum_{n_y\in Z} < f, \Phi_{m,n_x,n_y} > \Phi_{m,n_x,n_y}(x,y), \tag{11}$$

with the improved approximation at the next finer resolution, 2^{-m-1}, given by

$$P_{m+1}(f) = P_m(f) + \sum_{i=v,h,d}\sum_{n_x\in Z}\sum_{n_y\in Z} < f, \Psi^i_{m,n_x,n_y} > \Psi^i_{m,n_x,n_y}(x,y). \tag{12}$$

The improvement can be continued to any arbitrary resolution by including the intermediate 2-D wavelets.

The two-dimensional counterpart of equation (4) for the multiresolution expansion of a doubly square-integrable function $f(x,y)$ is expressed in the following way:

$$f(x,y) = \sum_{k_x \in Z} \sum_{k_y \in Z} C_{m_0,k_x,k_y} \Phi_{m_0,k_x,k_y}(x,y) + \sum_{m=m_0}^{\infty} \sum_{i=v,h,d} \sum_{n_x \in Z} \sum_{n_y \in Z} D^i_{m,n_x,n_y} \Psi^i_{m,n_x,n_y}(x,y) \quad (13)$$

where m_0 is again the initial resolution level, and C_{m,n_x,n_y} and D^i_{m,n_x,n_y} are the respective expansion coefficients given by

$$\begin{aligned} C_{m,n_x,n_y} &= < f, \Phi_{m,n_x,n_y} > \\ D^i_{m,n_x,n_y} &= < f, \Psi^i_{m,n_x,n_y} >, \quad , i = v,h,d \end{aligned} \quad (14)$$

Then, the two-dimensional fast wavelet algorithm takes the following form:

$$\begin{aligned} C_{m,n_x,n_y} &= \sum_{k_x \in Z} \sum_{k_y \in Z} h^*_{k_x-2n_x} h^*_{k_y-2n_y} C_{m+1,k_x,k_y} \\ D^v_{m,n_x,n_y} &= \sum_{k_x \in Z} \sum_{k_y \in Z} g^*_{k_x-2n_x} h^*_{k_y-2n_y} C_{m+1,k_x,k_y} \\ D^h_{m,n_x,n_y} &= \sum_{k_x \in Z} \sum_{k_y \in Z} h^*_{k_x-2n_x} g^*_{k_y-2n_y} C_{m+1,k_x,k_y} \\ D^d_{m,n_x,n_y} &= \sum_{k_x \in Z} \sum_{k_y \in Z} g^*_{k_x-2n_x} g^*_{k_y-2n_y} C_{m+1,k_x,k_y} \end{aligned} \quad (15)$$

Fig.4 shows the signal flow diagram for the two-dimensional fast wavelet algorithm. Here again, when different resolution levels are required, we only need to compute the scaling coefficients at the resolution level immediately following the highest resolution involved. All the expansion coefficients at the lower resolution levels can be evaluated recursively using equations (15).

5. Numerical Results and Conclusion

In the implementation of the fast wavelet algorithm in the method of moments, it is important to note that the moment integrals involve twice as many variables as the dimension of the integral equation, counting for the source and observation variables. In other words, for a one-dimensional boundary value problem, the integration is performed with respect to two variables x and x'. Similarly, in a two-dimensional problem, the moment integrals involve four variables x, y, x' and y'. For instance, a typical two-dimensional moment integral has the following form:

$$\bar{\bar{K}}_{ij} = \int \int_S \int \int_S F_i(x,y) \bar{\bar{G}}(x,y \mid x',y') F_j(x',y') dx dy dx' dy' \quad (16)$$

where $\bar{\bar{G}}(x,y \mid x',y')$ is the dyadic Green's function of the problem, and $F_i(x,y)$ and $F_j(x',y')$ are the test and expansion functions, respectively. Equation (16) in fact involves a shorthand notation where the pair of indices (i,j) have been used to replace a complex combination of dilation and

shift indices, which would otherwise have been written in the following manner:

$$\bar{\bar{K}}_{ij} = \bar{\bar{K}}^{f_{xi},f_{yi}|f_{xj},f_{yj}}_{m_i,n_{xi},n_{yi}|m_j,n_{xj},n_{yj}} \tag{17}$$

Here, the superscripts $f_{xi}, f_{yi}, f_{xj}, f_{yj}$, denote the generating functions for the respective variables and are either ϕ (scaling function) or ψ (wavelet). The fast wavelet algorithm for this problem can now be written in the following way:

$$\bar{\bar{K}}_{ij} = \sum_{k_{xi}\in Z}\sum_{k_{yi}\in Z}\sum_{k_{xj}\in Z}\sum_{k_{yj}\in Z} \gamma^{xi*}_{k_{xi}-2n_{xi}}\gamma^{yi*}_{k_{yi}-2n_{yi}}\gamma^{xj*}_{k_{xj}-2n_{xj}}\gamma^{yj*}_{k_{yj}-2n_{yj}}\bar{\bar{K}}^{\phi,\phi|\phi,\phi}_{m_i+1,k_{xi},k_{yi}|m_j+1,k_{xj},k_{yj}} \tag{18}$$

where $\gamma^{xi}_k, \gamma^{yi}_k, \gamma^{xj}_k, \gamma^{yj}_k$, are either h_k or g_k depending on the type of the respective generating functions. Equation (18) implies that once we have the interactions between all the 2-D scaling functions at the resolution level immediately following the highest resolution involved, then all the moment integrals at different resolution levels including inter-level interactions can easily be computed by simple discrete convolutions. Note that the quadruple sum in this equation involves the product of four h_n or g_n coefficients, which becomes extremely small for the majority of index combinations. Moreover, the shift indices usually vary over a finite range because the electromagnetic quantities like fields and current are defined over finite regions.

The fast wavelet algorithm has been applied to a variety of 2-D and 3-D electromagnetic problems. In this paper, we consider the full-wave analysis of dielectric structures. A rectangular dielectric slab waveguide of dimensions $a \times b$ and a rectangular dielectric resonator of dimensions $a \times b \times h$, both embedded in free space, have been studied. In the slab case, the 2-D volume polarization current is expanded in a 2-D basis consisting of a 1-D multiresolution expansion in the transverse direction and a sub-domain pulse expansion along the normal direction. In the resonator case, the 3-D volume polarization current is expanded in a 3-D basis consisting of a 2-D multiresolution expansion in the transverse plane and a sub-domain pulse expansion along the normal direction. It has already been demonstrated that in both cases, the resulting moment matrices are highly sparse, and using iterative techniques such as the bi-conjugate gradient method can improve the computation speed drastically.

In the present study, we have implemented the fast wavelet algorithm for the slab and resonator problems. Fig.4 shows the variation of the normalized propagation constant of the dominant mode of a rectangular dielectric slab with $a = 2b$, and $\epsilon_r = 2.25$ versus a normalized frequency defined as $V = (2b/\lambda_0)(\epsilon_r - 1)^{1/2}$. The results have been compared to those of a conventional moment method with a 2-D pulse basis [7]. In this case, each application of FWA algorithm plus the Bi-CG method for the solution of the resulting sparse system takes a fraction of a second on a SUNSPARK 20 workstation. The results for rectangular dielectric resonators have been presented in [4], where a comparison with other approximate methods have been made. For example, for a dielectric resonator of dimensions $a = 10mm$, $b = 8mm$, $h = 5mm$, and $\epsilon_r = 20$, the technique described in this paper using the FWA yields a resonant frequency of $5.532GHz$ for the resonator dominant mode. The computed resonant frequency based on the effective dielectric constant (EDC) method is $5.651GHz$ [8]. In this 3-D volume integral equation problem, each application of FWA algorithm plus the Bi-CG method takes typically four to six minutes on a SUNSPARK 20 workstation, depending on the number of the sub-domain pulses involved.

Finally, it is important to note that the nature of the fast wavelet algorithm, in its 4-D or higher-dimensional versions for the computation of intra-level and inter-level MoM integrals, easily

renders itself to a code parallelization. Although this process has not yet been carried out by the present authors, some preliminary code optimizations indicate a promising improvement in the efficiency and speed especially for three-dimensional electromagnetic problems.

Acknowledgment. This work has been supported by the US Army Research Office.

References

[1] R.F. Harrington, *Field Computation by Moment Methods.* New York: Macmillan, 1968.
[2] B.Z. Steinberg and Y. Leviatan,"On the use of wavelet expansions in the method of moments," *IEEE Trans. Antennas Propagat.*, vol. 41, pp. 610-619, May 1993.
[3] K. Sabetfakhri and P.B. Katehi,"Analysis of integrated millimeter-wave and submillimeter-wave waveguides using orthonormal wavelet expansions," *IEEE Trans. Microwave Theory Tech.*, vol. MTT-42, pp. 2412-2422, Dec. 1994.
[4] K. Sabetfakhri and P.B. Katehi,"Fast wavelet analysis of 3-D dielectric structures using sparse matrix techniques," to appear in *1995 IEEE MTT-S Int. Microwave Symp. Digest.*
[5] S.G. Mallat,"A theory for multiresolution signal decomposition: The wavelet representation," *IEEE Trans. Pattern Anal. Machine Intell.*, vol. PAMI-7, pp. 674-693, July 1989.
[6] I. Daubechies, *Ten Lectures on Wavelets*, Philadelphia, PA: Society for Industrial and Applied Mathematics, 1992.
[7] J.S. Bagby, D.P. Nyquist and B.C. Drachman, "Integral formulation for analysis of integrated dielectric waveguides," *IEEE Trans. Microwave Theory Tech.*, vol. MTT-33, pp. 906-915, Oct. 1985.
[8] R.K. Mongia, "Theoretical and experimental resonant frequencies of rectangular dielectric resonators," *IEE Proc.-H*, Vol.139, pp. 98-104, Feb. 1992.

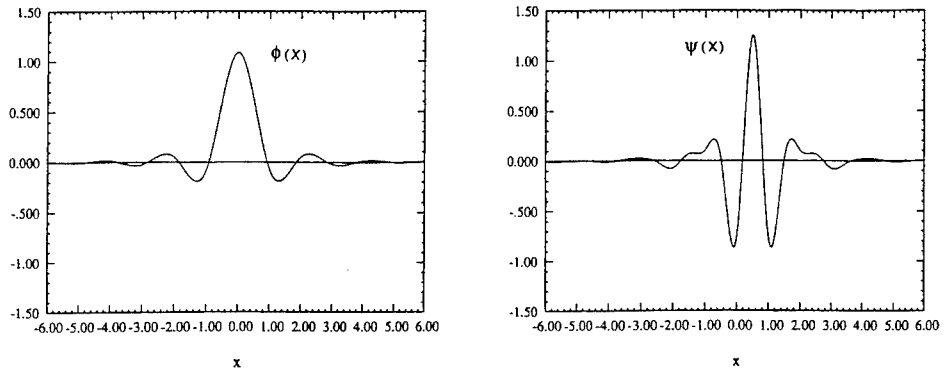


Fig.1. Cubic spline Battle-Lemarie scaling function and mother wavelet.

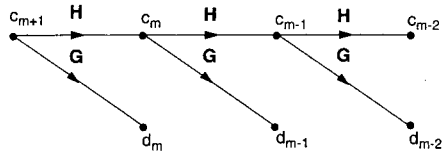


Fig.2. Signal flow graph for 1-D FWA.

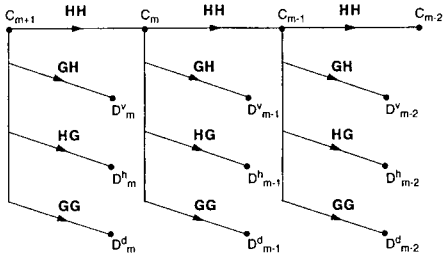


Fig.3. Signal flow graph for 2-D FWA.

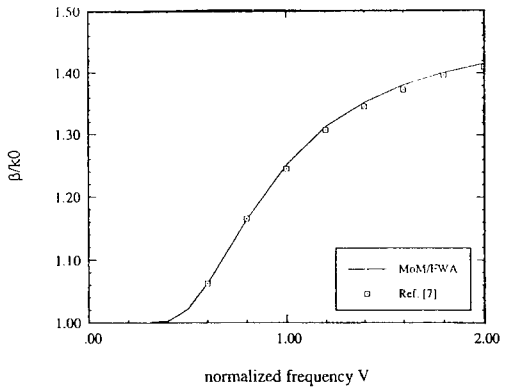


Fig.4. Variation of the normalized propagation constant of the dominant mode of a dielectric slab vs. normalized frequency V.

FAST FAR FIELD APPROXIMATION FOR CALCULATING THE RCS OF LARGE OBJECTS †

CAI-CHENG LU AND WENG CHO CHEW
DEPARTMENT OF ELECTRICAL AND COMPUTER ENGINEERING
UNIVERSITY OF ILLINOIS
URBANA, IL 61801

1. Introduction

In many practical high frequency scattering problems, the scatterers are very large compared to wavelength. When high frequency RCS is required, exact solution is impossible with current computer resources. In this case, approximate methods are very helpful. Typical approximate techniques are geometric optics (GO), physical optics (PO), geometric theory of diffraction (GTD), and physical theory of diffraction (PTD). These approximations have been incorporated into the shooting and bouncing ray (SBR) method [1].

In this paper, we develop another RCS estimation technique called the fast far field approximation (FAFFA). The idea of this method is to compute the interactions between elements using different methods depending on the electrical distance between the elements. When the distance is small, exact interaction is calculated; when the distance is large, a far field approximation is used. The field interactions are calculated iteratively using conjugate gradient (CG) method. The iteration process is equivalent to taking into account the higher order terms in GO, PO or PTD approximations. After several iterations, we find the results to be greatly improved over that of a simple PO or GO. On the other hand, this method can deal with small scale target geometry variations since it computes the near field interaction exactly hence it is more flexible to be applied to arbitrary complex targets. This algorithm has a computational complexity of $O(N^{1.33})$ and memory requirement of $O(N)$ for N unknown problems.

In the following, we first discuss the algorithm mathematically, and then give numerical results to validate the algorithm and show its applications to large size objects. The formulation is presented for electric field integral equation (EFIE) for TM polarization. The numerical simulation contains both 2D and 3D results. In this paper, the time factor of $e^{-i\omega t}$ is assumed and suppressed.

† This work was supported by the Office of Naval Research under grant N00014-89-J1286, the National Science Foundation under grant NSF ECS 92-24466, the Army Research Office under contract DAAL03-91-G-0339 and NASA under contract NAG 2-871. The computer time was provided by the National Center for Supercomputing Applications (NCSA) at the University of Illinois, Urbana-Champaign.

2. Formulation

Consider a TM (to z) plane wave incident on a two dimensional conducting cylinder in free space. The integral equation satisfied by the induced current J can be written as,

$$\frac{\omega\mu_0}{4}\int_S d\mathbf{r}' J(\mathbf{r}')H_0^{(1)}(k|\mathbf{r}-\mathbf{r}'|) = E^{inc}(\mathbf{r}), \tag{1}$$

where $H_0^{(1)}(x)$ is a 0-th order Hankel function of first kind. The integration is over the contour of the cylinder. $E^{inc}(\mathbf{r}) = E_0\exp(-i\mathbf{k}^i\cdot\mathbf{r})$. The subscript z for J and E^{inc} is implied here. Moreover, $\mathbf{r} = \hat{x}x + \hat{y}y$ is a 2D vector, $\mathbf{k}^i = k(\hat{x}\cos\theta^i + \hat{y}\sin\theta^i)$, where θ^i is the incident angle, and $k = 2\pi/\lambda$ is the free space wave number.

To discretize Equation (1), we first divide the surface into strips, and assume that the induced current on each strip is a constant J_j. Thus the discretized form of Equation (1), according to the method of moments, is [2],

$$\sum_{j=1}^{N} g_{ij}J_j = E_i/(30\pi k), \qquad i = 1,2,\cdots,N, \tag{2}$$

where,

$$g_{ij} = \begin{cases} \Delta_j H_0^{(1)}(kr_{ji}) & i \neq j, \\ \Delta_j\left[1 + i\frac{2}{\pi}\ln(0.163805k\Delta_i)\right], & i = j, \end{cases}$$

Δ_j is the strip width, $E_i = E^{inc}(\mathbf{r}_i)$ and $r_{ji} = |\mathbf{r}_i - \mathbf{r}_j|$.

Equation (2) can be solved using the conjugate gradient (CG) method [3]. The most costly part of a CG iteration is the performance of the matrix-vector multiply, i.e., to compute the summation on the left hand side of Equation (2) for $i = 1,2,\cdots,N$. Hence, the operation count of a matrix-vector multiplication is of $O(N^2)$.

Various methods have been explored to accelerate the matrix-vector multiply [4–10]. In this paper, we describe an algorithm which approximately performs the matrix-vector multiply of Equation (2) with $O(N^{1.33})$ operations. The method makes use of the two-level algorithm as proposed in the original fast multiple method [4,7,8], but we arrive at a two level algorithm with lesser complexity compared to the original two-level fast multiple method.

In the first step, we divide the N unknowns into groups as shown in Figure 1. The rules for the division are that: (1) each group should have roughly the same number of unknowns, and (2) the members of each group are as close to each other as possible. Assuming that each group has M unknowns, the number of groups will be N/M. In the following, we use index i and j to number unknowns, and use G_l and $G_{l'}$ to denote groups l and l', respectively.

With this notation, Equation (2) can be rewritten as,

$$\sum_{l'=1}^{N/M}\sum_{j\in G_{l'}} g_{ij}J_j = E_i, \qquad i \in G_l, l = 1,2,\cdots,\frac{N}{M}. \tag{3}$$

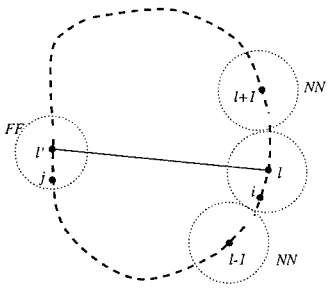


Figure 1 The discredited scatterer is divided into groups. The interaction between groups with large distance is calculated using far field approximation; the near field groups' interaction is calculated exactly. For group l, groups $l-1$, l, and $l+1$ are considered as near field groups (NN); For group l', it is considered as far field group (FF).

Depending on the distance $r_{l'l}$, we define two neighboring regions for each group G_l. One is the near field (NN) region, the other is the far field (FF) region. A group $G_{l'}$ is said to be in the far field region of group G_l if the distance between the two groups is larger than a certain quantity. Otherwise, $G_{l'}$ is in the near field region of G_l. Consequently, the summation in Equation (3) can be split into two parts: one corresponding to the near field (NN) contribution, while the other corresponding to the far field (FF) contribution, namely,

$$\sum_{l'\in NN}\sum_{j\in G_{l'}} J_j H_0^{(1)}(kr_{ji})\Delta_j + \sum_{l'\in FF}\sum_{j\in G_{l'}} g_{ij}J_j = E_i/(30\pi k), \qquad i =\in G_l, l = 1,2,\cdots,\frac{N}{M}. \tag{4}$$

The far field contribution, which is proportional to,

$$I_{li} = \sum_{l'\in FF}\sum_{j\in G_{l'}} J_j H_0^{(1)}(kr_{ji}), \tag{5}$$

can be calculated approximately by first applying the large argument approximation to $H_0^{(1)}(kr_{ji})$:

$$H_0^{(1)}(kr_{ji}) \sim \sqrt{\frac{2}{\pi i}}\frac{e^{ikr_{ji}}}{\sqrt{kr_{ji}}}, \qquad kr_{ji} \gg 1. \tag{6}$$

Next, we write

$$\mathbf{r}_{ji} = \mathbf{r}_{jl'} + \mathbf{r}_{l'l} + \mathbf{r}_{li}.$$

Thus, if $r_{l'l} \gg r_{jl'}$ and $r_{l'l} \gg r_{li}$, then,

$$r_{ji} \sim r_{l'l} + \hat{r}_{l'l} \cdot \mathbf{r}_{li} + \hat{r}_{l'l} \cdot \mathbf{r}_{jl'}. \tag{7}$$

Substituting Equations (6) and (7) into Equation (5), we have

$$I_{li} = \sum_{l' \in FF} \sqrt{\frac{2}{\pi i}} \frac{e^{ikr_{l'l}}}{\sqrt{kr_{l'l}}} e^{ik\hat{r}_{l'l} \cdot \mathbf{r}_{li}} \sum_{j \in G_{l'}} J_j e^{ik\hat{r}_{l'l} \cdot \mathbf{r}_{jl'}} = \sum_{l' \in FF} e^{ik\hat{r}_{l'l} \cdot \mathbf{r}_{li}} \sqrt{\frac{2}{\pi i}} \frac{e^{ikr_{l'l}}}{\sqrt{kr_{l'l}}} b_{l'l}, \tag{8}$$

where,

$$b_{l'l} = \sum_{j \in G_{l'}} J_j e^{ik\hat{r}_{l'l} \cdot \mathbf{r}_{jl'}}. \tag{9}$$

Calculation of Equation (8) for all pairs of (l, i) requires $NM + N^2/M$ operations. The near field operation count is proportional to NM, and the total CPU is

$$CPU \sim C_1 NM + C_2 M \left(\frac{N}{M}\right)^2. \tag{10}$$

where, C_1 and C_2 are constants. Optimization yields $M = \sqrt{N}$ and $CPU \sim N^{1.5}$.

Equation (8) consists of three steps. The first step is called aggregation. It is represented by the summation in Equation (9). The second step is translation, corresponding to,

$$b'_{l'l} = \sqrt{\frac{2}{\pi i}} \frac{e^{ikr_{l'l}}}{\sqrt{kr_{l'l}}} b_{l'l} \tag{11}$$

Finally, the third step is disaggregation, corresponding to,

$$I_{li} = \sum_{l' \in FF} b'_{l'l} e^{ik\hat{r}_{l'l} \cdot \mathbf{r}_{li}}. \tag{12}$$

The reduction in operation from N^2 to $N^{1.5}$ is attributed to replacing the translation matrix by a scalar number.

To further reduce the operation count, we consider the aggregation step more carefully. Computation of Equation (9) for all l, l' requires N^2/M operations. However, we know that $b_{l'l}$ depends only on $\hat{r}_{l'l}$ which is a function of an angle $\alpha \in (-\pi, \pi)$. The oscillation of $b_{l'l}$ with respect to α will depend on $\max(kr_{jl'})$ which is the electrical size of a group. Hence, it motivated us to compute the summation in Equation (8) in two steps. The first step is to compute it on equal samples of α over $[-\pi, \pi]$, and then to compute $b_{l'l}$ by interpolating with the known values on the samples. The number of α samples can be chosen to be proportional to the number of unknowns in the group. The interpolation process is shown in Figure 2. Figure 2a shows the original operation which is the direct aggregation. Figure 2b shows the

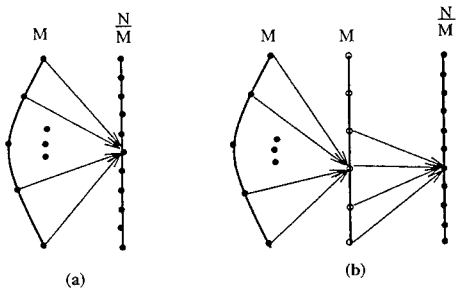


Figure 2 (a). Direct aggregation. (b). Aggregation using interpolation.

aggregation using interpolation. It is clear that if N/M is larger than M, than interpolation procedure is more efficient.

In order to reduce the total computational cost, the cost for the disaggregation stage (Equation (9)) should also be reduced. This can be achieved by smoothing [11], which is just the converse of interpolation. In this manner, the operation count or the $CPU \sim N^{4/3}$.

The above method can easily be extended to the TE polarization, and also to the combined field integral equation.

3. Numerical simulations

In this Section, we give numerical examples to compare the calculated RCS using fast far field approximation (FAFFA) with the result by CG using exact moment matrix. In all the examples, combined field integral equation (CFIE) is used. The numerical results include both TM and TE cases.

Our first example is a 2D open ended cavity. The cavity is of length length, width and thickness 10m, 5m and 1m, respectively. The E_z polarized plane wave is incident at $\theta^i = 30^0$, as shown in Figure 3. The result from fast far field approximation agrees well with the exact solution.

The second example, shown in Figure 4, is the RCS of a 3D 90° dihedral which consists of two flat plate of same size (1m $\times$ 20m, 20m side as the common edge). Vertical polarized plane wave is incident from the direction of $(\theta^i, \phi^i) = (45°, 270°)$ with a frequency 300 MHz.

The above two figures show that FAFFA takes into account of multiple reflections such as in corner reflector and in cavity like targets. Our next example show that FAFFA will also takes into account the small scale target geometry variations. Figure 5 plots the RCS of a two dimensional cylinder whose cross section is also shown in the figure. The geometry variation is in less than a wavelength scale.

From Figures 3 to 5, one can see that the RCS predicted by FAFFA are very close to the exact solution. The advantage of FAFFA is that it has lower computational complexity ($O(N^{4/3})$) and small memory requirement ($O(N)$).

Hence it can be applied to predict RCS for targets with very large electrical size. Figures 6 and 7 are two examples.

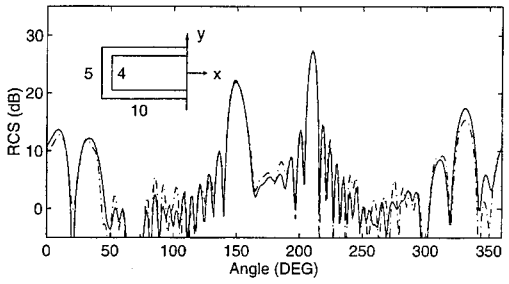


Figure 3 RCS of a 2D open ended cavity.

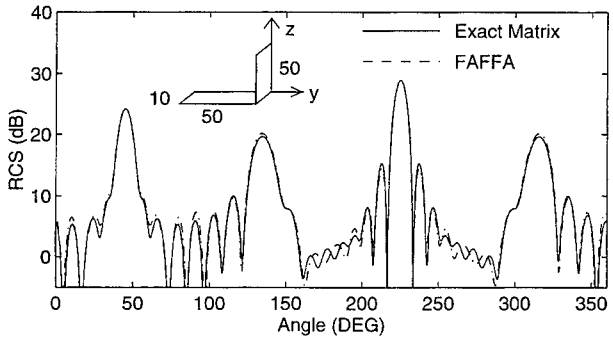


Figure 4 The RCS of a 3D dihedral corner reflector.

4. Conclusions

A fast far field approximation (FAFFA) for RCS calculation of larger size targets is developed. This method considers near field and far field interactions differently so that the complexity for performing a matrix-vector multiplication is reduced from $O(N^2)$ to $O(N^{1.33})$ and the memory requirement is of $O(N)$ for N unknown problems. The method differs from exact method since far field approximation is used. It also differs from pure PO since the solution is calculated iteratively so that the higher order scattering field, such as edge diffraction, surface wave and multiple-reflection, are automatically taken into account. Numerical simulations show that this method predicts RCS which are very close to the exact solution, and is greatly improved over

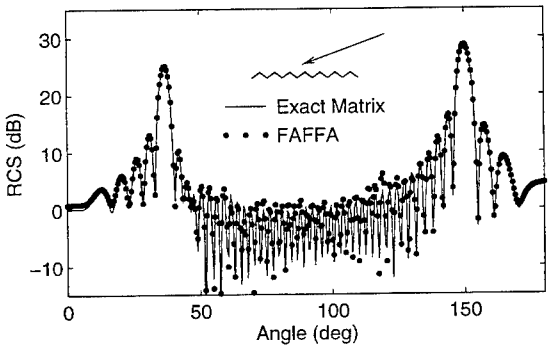


Figure 5 The RCS of a 2D cylinder with zigzag contour of cross section.

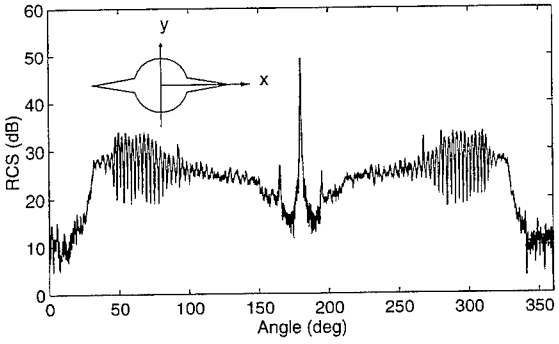


Figure 6 The RCS of a 2D complex target. Plane wave of frequency 300 MHz is incident from $\theta^i = 0^o$ and is polarized in z direction. $N = 52,788$.

that from applying pure PO. Also, due to the reduced computational complexity and memory requirement, the method can be applied to calculate RCS for targets with very large electrical size. Our ongoing work is to apply this method to three dimensional scatterers, which will be reported.

References

[1] Ling, H., R. C. Chou and S. W. Lee, "Shooting and bouncing rays: calculating the RCS of an arbitrary shaped conductor," *IEEE Trans. Antennas and Propgat.,* Vol. 37, pp. 194-205, 1989.

[2] Harrington, R. F., Field computation by moment method, Krieger, Mar-

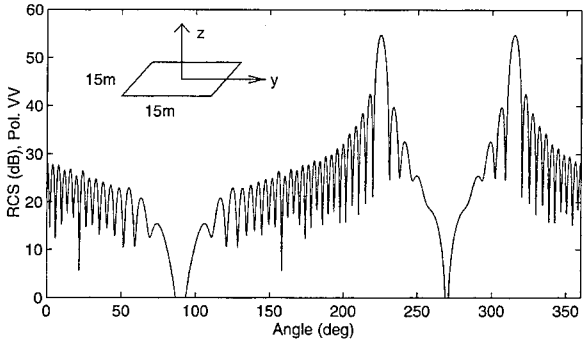


Figure 7 The RCS of a 3D square plate of size $15m \times 15m$. Plane wave incident at $\theta^i = 45^o$, $\phi^i = 0^o$ and is of frequency 300 MHz. $N = 44,700$.

labar, Florida, 1982.

[3] Press, W. H., S. A. Teukolsky, W. T. Vetterling and B. P. Flannery, Numerical Recipes, Cambridge University Press, 1992.

[4] Rokhlin, V., "Rapid solution of integral equations of scattering theory in two dimensions," *J. Comput. Phys.*, 86, (2), pp. 414-439, 1990.

[5] Canning, F. X., "Transformations that produce a sparse moment method matrix," *J. Electromagnetic Waves and Applications,* vol. 4, pp. 903-913, 1990.

[6] Anderson, C. R., " An implementation of the fast multiple method without multipoles," *SIAM J. Sci. Stat. Comput.,* Vol. 13, no. 4, pp. 923-947, 1992.

[7] Coifman, R., V. Rokhlin, and S. Wandzura, "The fast multiple method for the wave equation: a pedestrian prescription," *IEEE Antennas Propagat. Mag.,* Vol. 35, no. 3, pp.7-12, June 1993.

[8] Lu, C. C. and W. C. Chew, "Fast algorithm for solving hybrid integral equations," *IEEE Proc., Part-H,* Vol. 140, No. 6, pp. 455-460, Dec. 1993.

[9] Wagner, R. L. and W. C. Chew, "A ray propagation fast multipole algorithm," *J. Micro. Opt. Tech. Lett.,* Vol. 7, No. 10, pp. 435-438, July 1994.

[10] Lu, C. C. and W. C. Chew, "A multilevel algorithm for solving a boundary integral equations of wave scattering," *J. Micro. Opt. Tech. Lett.,* Vol. 7, No. 10, pp. 466-470, July 1994.

[11] Brandt, A., "Multilevel computations of integral transforms and partical interactions with oscillatory kernal," *Comput. Phys. Commun.,* Vol. 65, pp. 24-38, 1991.

THE PARAMETER ESTIMATION TECHNIQUE (PET): SPEEDING UP DENSE MATRIX METHODS

Ch. Hafner, J. Fröhlich
IFH, ETH-Zentrum, CH-8092 Zurich, Switzerland
E-mail hafner@ifh.ee.ethz.ch, fax ++411 632 1198, phone ++411 632 5135

Abstract

The Parameter Estimation Technique (PET) is a new technique that can be applied to numerical codes based on dense matrices as a power booster for the computation of the response of the physical system at different frequencies, etc. It is applied to the Multiple Multipole Program (MMP) in conjunction with the method of Conjugate Gradients (CG) for iteratively and efficiently solving the rectangular MMP matrix. The PET takes advantage of the a priori knowledge obtained from previous computations and allows to a dramatic reduction of the computation time in various situations. The computation time considerably depends on the PET basis functions. Although useful results had already been obtained with simple power functions, it is shown that the PET can be drastically improved when a more general basis is optimized by a Genetic Algorithm.

1. Introduction

One of the most important benefits of time domain methods such as the Finite Difference Time Domain (FDTD) technique [1] comes from the fact that the information on the EM field of the previous time steps can be used as a starting value for the computation of the actual EM field. This rigid use of the a priori knowledge [2,3] allows the iterative computation of the EM field in each time step with typically one iteration only - provided that the time step is sufficiently small. As a consequence, the method is efficient and fast.

Today, iterative matrix solvers such as the method of Conjugate Gradients (CG) are most frequently applied to large sparse matrices although the CG algorithm was originally designed for small, dense matrices [4]. Variants of the CG have also been applied to the Method of Moments (MoM) and other integral methods [5]. Although CG is very helpful in many situations, it has important drawbacks: Its convergence depends to a great extent on the choice of the preconditioner and of the starting values. Moreover, CG is often either robust or efficient rather than robust and efficient as desired.

The MMP codes [6-8] are based on an overdetermined system of equations characterized by a dense, rectangular matrix. The condition number of the MMP matrix is often very high. Therefore, many of the simple matrix solvers cannot successfully be applied - except for almost trivial problems [9]. This is the most important reason why the CG matrix solver in the 2D MMP code [10] was rarely used in the past. It is important to note that the bad condition of the matrix does not cause inaccurate results. In contrary, it has been shown [2,3] that the accuracy of the results can often be increased by increasing the condition number of the matrix. Moreover, ill-conditioned matrices simplify the modelling and are important for the user-friendliness of the code.

For the reasons outlined above, iterative MMP matrix solvers were discarded [10] and Block-Iterative Techniques (BIT) [8,11] were preferred for computing large MMP models. MMP-BIT is a sophisticated technique that can be applied by MMP wizards only. It

is helpful for solving large problems, but it usually does not allow to considerably reduce the computation time. In inverse scattering and other optimization problems where a large number of slightly varying MMP models must be computed, one is interested in a robust and simple method that allows to keep the computation time as small as desired and MMP-BIT is not well suited for this purpose.

It is very important to recognize that CG and other iterative matrix solvers can handle ill-conditioned matrices. The main problem for the efficient use of such techniques is a sufficiently accurate estimation of the initial values. The key to finding good starting values is governed by some a priori knowledge [2,3] obtained from previous computations. As soon as the EM field has been computed for a specific model, one possesses some a priori knowledge for the computation of slightly modified models. This knowledge should be recycled rather than wasted. The main idea of the Parameter Estimation Technique (PET) is the recycling of knowledge. This technique is explained in the following sections.

The second problem for iterative techniques is the stopping criterion. Unfortunately, the convergence of the CG algorithm applied to overdetermined systems of equations shows a staircase behaviour and the maximum number of iterations required for a given accuracy is not known in advance. It has been shown in [12] that the PET provides both an appropriate estimation of the starting values and an appropriate stopping criterion. In the following, we will outline the PET and emphasize a further improvement of this technique obtained by an optimization of the PET basis using a Genetic Algorithm [13]. Before we start with the description of the PET, we have to resume some MMP features that are relevant for the PET.

2. Some important MMP features

In MMP and other matrix methods, the EM field is defined by a series expansion of the form

$$Field = \sum_{k=1}^{K} A_k Basis_k + Error \qquad (1)$$

Since MMP is based on a boundary method, the basis functions are analytic solutions of Maxwell's equations inside the domain where they are applied to approximate the EM field. Multipole expansions are most frequently used due to their local behaviour and efficient recursive computation [6-8].
The parameters A_k of the MMP expansion (1) are determined by the Generalized Point Matching (GPM) technique [8]. This technique is relatively simple. It leads to an overdetermined system of equations that is solved in the least squares sense. Since the different equations are weighted, this method is also called the method of weighted residuals. The GPM implicitly minimizes an error function defined along the boundaries of all domains and has interesting advantages when the condition number of the matrix is large.

The MMP codes offer several direct and iterative methods for solving the matrix equations. Although the Singular Value Decomposition (SVD) is optimal for ill-conditioned matrices, this technique is rarely applied because it is very time- and memory consuming. In the following, SVD has only been used for computing the condition numbers. Householder transformations and Cholesky factorization are faster than the Givens updating procedure, but these methods are rarely used because they fail when the condition number is large. Therefore, Givens updating is the most frequently used direct matrix solver in MMP. Among the iterative matrix solvers, CG seems to be most appropriate. This is the first choice in conjunction with the PET.

It should be pointed out that the often ill-conditioned, rectangular MMP matrices cause special problems that are not encountered in other matrix methods. Therefore, it is assumed that the application of the PET to the MMP code is more demanding than the application of the PET to other codes.

3. The Test Examples

In [10] the EM scattering of a plane wave at a cylindrical, perfectly conducting plate with the cross section shown in Figure 1 has been considered for testing the performance of the CG algorithm in the 2D MMP code. Although this example is very simple, it shows all the main effects. Therefore, it is well suited as a test case for the MMP-CG-PET implementation.

It is well known that the number and location of the multipoles used for simulating the scattered EM field is critical for the accuracy. Simple rules for setting the multipoles and automatic pole setting procedures are

described in [8,15]. Here, it seems to be reasonable to set all multipoles on the y axis as shown in Figure 1. Both the accuracy and the condition number of the MMP matrix considerably depend on the number of multipoles. A detailed study of this dependence has been presented in [12]. It has been shown that the most accurate results are obtained when the number of multipoles is relatively high, i.e., when the condition number is relatively large.

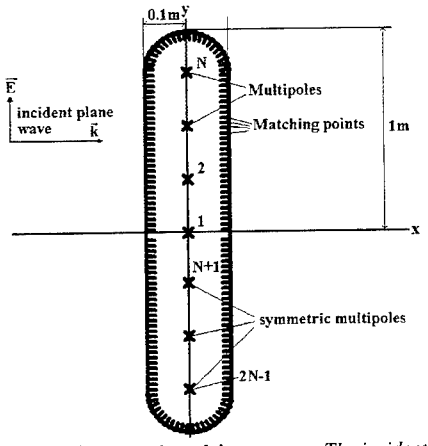


Figure 1: Cross section of the test case. The incident EM field is a plane wave with wave vector in the x direction and either the electric field or the magnetic field in the y direction.

According to [14], the critical points of a such model are at the connections of straight lines and circles. Thus, the efficiency and accuracy can considerably be increased when off-axis multipoles are located near the critical points. In the following, we will use two different MMP models, one with equally spaced multipoles on the axis and another one with a higher number of off-axis multipoles.

For testing the generality of the PET, we will consider a dielectric cylinder of the same shape as in Figure 1 with the relative permittivity equal to four. For this model, two sets of multipoles are used, one with multipoles on the y axis for modelling the scattered field and one with off-axis multipoles outside the cylinder for modelling the field inside the dielectric.

3. Parameter Estimation Technique (PET)

The Parameter Estimation Technique (PET) is based on the concept of recycling the information obtained from previous computations of a similar problem. When equation (1) holds, this information is stored in the parameters A_k, in the basis functions $Basis_k$, and in derived quantities. When the basis functions are kept unchanged during several computations, the parameters A_k (and all derived quantities) are functions of the variables of the computations. These functions are known in all the points where they were computed in previous runs. This allows to apply any extrapolation or interpolation technique for estimating the parameters to be computed in the current run. If the estimation is sufficiently accurate, one has excellent starting values for iterative techniques.

Although the PET can be applied to any variable, we consider the frequency as a single variable for reasons of simplicity, i.e., we consider the functions $A_k(f)$. At low frequencies, these functions are very simple and smooth. Therefore, it is easy to obtain an accurate estimation of the parameters $A_k(f)$ when one already has computed $A_k(f_i)$ for at least one frequency f_i that is not too far away from f. At the beginning of the computation of the frequency dependence, one usually has no knowledge on the size of the parameters for the first frequency f_1. Therefore, one has no good starting value for the CG computations of the parameters $A_k(f_1)$. Although one can start CG iterations with an arbitrary set of parameters, the CG computation of the first parameter set turns out to be much more time consuming than the Givens solution. Therefore, it is reasonable to compute the parameter set for the first frequency with the Givens updating procedure. For all other frequencies one can assume that the parameter set of the previous frequency is a good estimate for the parameter set of the actual frequency.

If we consider the frequency dependence of the parameters in an interesting area where one observes resonances of the structure, we observe a very strong variation of all the parameters which makes the parameter estimation more complicated. Nonetheless, we can assume that the parameter set of a given frequency provides a useful starting value for the iterative computation of the parameter set for a slightly higher or lower frequency.

The parameter estimation $A_k(f)=A_k(f_i)+Error$ is simple and crude. It corresponds to a zero order extrapolation. Of course, one can expect more accurate parameter

estimations from extrapolations with higher order power series approximations of the functions $A_k(f)$. For an n-th order extrapolation one has

$$A_k(f) = \sum_{j=0}^{n} a_{kj} f^j + Error, \qquad (2)$$

with $n+1$ basis functions f^j. For computing the unknowns a_{kj}, at least $I=n+1$ values $A_k(f_i)$ must be stored $(i=1...I)$. With $I=n+1$ one obtains the following I equations for the $n+1$ unknowns:

$$\sum_{j=0}^{n} a_{kj} (f_i)^j = A_k(f_i). \qquad (3)$$

Note that one has to solve a system of I equations for each of the K parameters A_k. Since the same basis functions $(f_i)^j$ are used for the estimation of all parameters, the matrices of all these systems of equations are identical and can be solved simultaneously. Thus, the computation time for the parameter estimation is negligible - except for very high orders n.

At the beginning of the computation of the frequency dependence with n-th order PET, one uses a Givens solution. Since the parameter sets of $n+1$ frequencies are required, one could compute the first $n+1$ frequencies with the direct Givens matrix solver. According to our experience, already a zero order PET allows to save computation time with an iterative CG matrix solver. Therefore, one only computes the first frequency with Givens and all other frequencies with CG based on a k-th order PET, where k is either equal to n or equal to the frequency step number minus one.

It has been shown in [12] that the first order PET allows to considerably reduce the number of CG iterations, but the second order PET is already much worse. This disappointing result can be removed by more sophisticated extrapolation techniques as discussed in [2,3]. First, one can use $I>n+1$ equations for an n-th order PET. This requires the introduction of appropriate weights w_i and leads to the following overdetermined systems of equations that are similar to the matrix equations of the MMP codes:

$$\sum_{j=0}^{n} w_i a_{kj} (f_i)^j = w_i A_k(f_i) + \varepsilon_i \qquad (4)$$

Since the solution of an overdetermined system of equations depends very much on the choice of the weights, one has to find appropriate weights first. This is a demanding task, because we would like to use the same weights for computing all parameters simultaneously and because the frequency dependence of the different parameters in an MMP expansion may be very complicated. Nonetheless, one can apply a genetic algorithm for finding appropriate weights. Although we observed some improvement of higher order PET with appropriate weights, we do not describe this technique in detail because the technique described below is much more successful.

4. Optimized PET

The main problem of the higher order PET is caused by the fact that higher order power series are not useful for the extrapolation of functions. Therefore, we have to replace the basis functions f^j in (2) by more appropriate and more general basis functions:

$$A_k(f) = \sum_{j=0}^{n} a_{kj} basis_j(f) + Error \qquad (5)$$

The search of appropriate basis functions $basis_j(f)$ is an even much more demanding task than the search of appropriate weights mentioned in the previous section. First of all, it is important that these basis functions should be appropriate for simultaneously estimating all the parameters of any MMP expansion for any MMP model.

Since the frequency can vary in a wide range, it is reasonable to replace f in (5) by another variable x that is restricted to the interval 0...1. This should be done in such a way that all frequencies f_i used in the PET are transformed to points x_i in the interval 0...1. If one traces the frequencies starting at the lowest frequency of the frequency range, the actual frequency f is the highest frequency when the PET is performed. Therefore, one maps the lowest frequency f_1 of the PET on $x_1=0$ and the actual frequency f on $x=1$. The basis functions $basis(x)$ need to be known in the points $x_1, x_2, ...x_I$ and $x=1$ rather than in the entire interval 0...1. Therefore, one could replace these functions by simple sets of $I+1$ values $b_i=basis(x_i)$, where $i=1,2,...I+1$. On one hand, this would simplify the search of an appropriate basis, on the other hand, this could cause problems when different spacing of the points x in the interval 0...1 are applied. Since one often prefers logarithmic frequency scales instead of linear ones, we preferred to search continuous basis functions rather than sets of discrete values.

The selection of an appropriate set of basis functions is a typical task for Genetic Algorithms (GAs) [13]. GAs are based on concepts of natural evolution, i.e., mutation, crossover, and selection. GAs optimize bitstrings in

such a way that their fitness is increased. In our case, the bitstrings contain sets of PET basis functions. The coding of the bitstrings is the most crucial part of the GA user. First of all, each of the admitted PET basis functions can be characterized by several parameters. Each of these parameters is characterized by several bits. If one wants to admit a large variety of functions with many parameters or if many bits are used for each parameter, the bitstrings become very long and the performance of the GA becomes slow. For example, when we would like to optimize the five basis functions of a fourth order PET and if we would admit five real and two integer parameters with 32bit per parameter, the length of our bitstring would exceed 1000. In this case, the GA would have to select the fittest of more than 1E300 possible bitstrings. If the computation of the fitness of one individual takes about one second, the GA can check about 3E7 bitstrings within one year, which is a very small fraction of 1E300. It is important to note, that we do not need to know the fittest among the possible bitstrings. The GA must not test all of them for finding a sufficiently fit bitstring. Nonetheless, we should support the GA by making the bitstrings as short as possible. This requires some knowledge and experience of the GA user. First, we characterized our basis functions with a 3 bit integer and two 10 bit real numbers, i.e., 23 bits per basis function. In addition, our bitstring contained eight weights characterized by 10 bit real numbers. Later we removed the weights and used only 2 bits for the integer and 9 bits for the real numbers. We tested several types of common functions (sin, cos, exp, log, etc.) and combinations of such functions, e.g., a*sin(b+x*x), a*exp(-x*x/b), where a,b are real parameters. Finally, we used only the following functions with 0.1<a<10.0 and 0<n<22:

1/(1+a*x)^n,
(1-x/a)^n,
2-1/(1+a*x)^n,
2-(1-x/a)^n.

For running a GA, we must give a precise definition of the fitness. Each bitstring of the GA is decoded and gives us a set of PET basis functions. To test, whether this set is useful for our MMP-CG-PET code, we must run several test examples and we must compute the frequency dependence of these examples. The total number of CG iterations required is a measure of the fitness. The most simple definition of the fitness is

fitness=1/total number of CG iterations.

This definition is not unique, but it seems that it plays a minor role for the GA performance.

First of all, we must specify the frequency range and the MMP models of our test cases. Like in the selection of our set of allowed PET basis functions, we first tried several combinations of frequency ranges and MMP models. If many different MMP models are involved in the definition of the fitness, the computation of the fitness becomes very time consuming. Since a GA typically requires the computation of the fitness of hundreds of individuals, i.e., bitstrings, we are forced to use only a few, simple MMP models.

We first started with only two excitations of one MMP model: the TE and the TM excitation of the cylinder shown in Figure 1 with 9 multipoles on the axis. The frequency range was chosen from 30 MHz up to 300 Mhz. We first used a linear frequency scale and 100 frequency steps. This allowed us to find many PET basis functions causing an average of almost 1 CG iteration per frequency. Since at least one CG iteration is performed anyway, we decided to use a logarithmic frequency scale and only 9 frequency steps. Such a rough discretization of the frequency range causes a very bad performance of the PET based on power series. We expected that a genetically optimized basis for the PET allows to reduce the total number of iterations considerably, maybe by a speedup factor of 10. This factor is related to the first order unoptimized (linear) PET because this is the best PET that had been found in [12]. But we found that even larger factors can be obtained. Since a further reduction of the number of frequency steps makes not much sense (at least 6 frequencies are required for performing a fourth order PET), we replaced our MMP model by one with more unknowns and with a total number of 20 off-axis multipoles. At the same time we increased the desired accuracy in the stopping criterion of the CG algorithm. This test case caused a total number of 575 CG iterations when a first order (linear) PET was applied. Since the minimum number of CG iterations would be 9 for 9 frequency steps, this allows to obtain a speedup factor of about 60.

We used a GA for finding several sets of basis functions for optimized n-th order PET with n= 0,1,2...4. The results were both surprising and encouraging. The speedup was so drastic that we feared that the optimized PET basis functions are adapted to our test case only, and that a much worse speedup could be observed when either the frequency range or the MMP model would be changed. Therefore, we applied the optimized PET to

three different MMP models (two with ideally conducting cylinders and one with a dielectric cylinder) with TE and TM excitation and we used linear frequency scaling in addition to the logarithmic scaling. Moreover, we traced the frequency backwards, i.e., starting with the highest frequency.

Some of the PET basis functions that had been optimized with the GA, required much more CG iterations (especially when the frequency was traced backwards), but many of them turned out to be very robust. The speedup for the more complicated MMP model (dielectric cylinder) was even considerably higher than for the model that had been used in the GA optimization procedure. Therefore, we are confident that these optimized basis functions will be useful for any MMP model.

It should be pointed out that we found our robust optimized PET bases with an evolutionary procedure on three levels: On the first level, we provided a set of basis functions that seemed to be reasonable to us. This was a selection based on our 'a priori' knowledge and on our experience. On the second level, the GA selected the most appropriate basis functions for a given test case; i.e., the GA optimized the parameters characterizing the basis functions provided on the first level. On the third level, we applied the best basis functions found on the second level, to a larger number of test cases and we selected the most robust sets of basis functions.

The best set that has been found up to now is much better than we had ever hoped, but it is certainly not optimal. Therefore, the time-consuming search for better solutions goes on and the MMP users can take advantage of a code with an excellent performance that is further improved when a better PET basis is found by our PET-optimizer running in the background.

5. Results

For optimizing the PET basis functions, we used three different MMP models of the "2D ACES cylinder" (see Figure 1 and Table 1). All models were excited with a TE and a TM plane wave travelling in x direction.

The frequency range from 30MHz-300MHz was scanned with very rough steps. Only 10 values were computed for the entire decade. Four different frequency models were considered: 1) logarithmic upward, 2) logarithmic downward, 3) linear upward, 4) linear downward. These rough frequency models cause a huge number of CG iterations when the simple linear PET is applied. When one runs downward, one starts in an area close to a resonance of the structure where the parameters of the MMP expansion vary rapidly. In this case, the CG convergence is so slow that considerably more iterations than unknowns are required. More than 10'000 CG iterations were required for computing a single frequency of the third MMP model. Since the direct Givens solution is more efficient than the CG solution when more than about 50 CG iterations are required for this model, it seems to be hopeless to find PET basis functions that allow such a drastic reduction of the CG iterations. As one can see from Table 2, we found even zero order PET solutions with an average of less than 7 CG iterations per frequency.

Material	Expansion	Matrix
ideal conductor	9 multipoles on y-axis	164*75
ideal conductor	20 off-axis multipoles	164*49
dielectric, ε_r=4	5 multipoles on y-axis +8 off-axis multipoles	144*95

Table 1: Expansion and matrix size of the three MMP models of the "2D ACES cylinder" used for the PET optimization.

Especially the CG computation of the second frequency of a frequency plot gives rise to a problem. Here, one has only one set of parameters that is known from the initial Givens solution of the first frequency. Therefore, one can only use a zero order PET with a single basis function. Since one does not know whether the parameter to be estimate is increasing or decreasing, it seems to be reasonable to use a constant as the first PET basis function. It may be surprising, that the first basis function in Table 1 is much better than that. When the third MMP model is computed with this PET basis function instead of a constant one, only a few CG iterations are required instead of thousands. In the interval x=0...1, the first PET function decays very rapidly from one to zero. It is important to note that the first basis functions for all optimized higher order PET are similar. The optimized zero order PET estimates the MMP parameters of a frequency by a multiplication of the MMP parameters of the previous frequency with a very small factor of about 10E-11. It seems that it is good to start the CG with such an estimate of the MMP parameters. This is surprising, because setting all MMP parameters equal to zero is not a good starting point for

the CG algorithm in the MMP code. Maybe, the strange optimized zero order PET basis functions can be explained by the bad condition of the MMP matrices.

Order	PET basis functions	Iterations
0	1/(1+2.6185897*x)**20	6.72
1	1/(1+7.9270093*x)**12 2-1/(1+8.8181974*x)**8	6.13
2	1/(1+9.7093954*x)**13 2-1/(1+3.2772961*x)**3 (1-x/3.1223116)**3	5.806
3	1/(1+8.9344432*x)**18 2-1/(1+8.9344432*x)**18 2-(1-x/5.9121316)**2 2-(1-x/5.5246555)**19	5.815
4	1/(1+4.0909969*x)**18 2-1/(1+3.4710391*x)** 6 (1-x/6.0283774)**17 1/(1+3.8197666*x)**20 2-1/(1+8.5469671*x)**12	5.889

Table 2: some of the preliminary 'optimal' PET basis functions for the 2D MMP found before January 6, 1995. The iterations indicated are the average of CG iterations required for one frequency step of our test cases with the rough frequency steps. The corresponding number of CG iterations with a linear (first order) PET was not explicitly computed because more than 10000 iterations were required for a single frequency step of some test cases. The basis functions for the PET orders 0...3 are plotted in Figure 2.

It is important to recognize that the optimized second order PET is better than the optimized first and zero order PET, whereas the unoptimized first order PET was better than any unoptimized higher order PET (based on power series). However, the optimized third order PET is slightly slower than the optimized second order PET. It seems that this is caused by the fact that the corresponding GA search is slower, i.e., the higher order PET that have been found up to now are further away from the optimum. Although it is very likely that we will find more efficient higher order PET basis functions, we cannot expect these solutions to be much more efficient than lower order PET, when we continue with large frequency steps for the following reason. For a fourth order PET we need five previous frequencies for estimating the MMP parameters, i.e., the first frequency used in the PET is about half a decade away from the actual frequency. In our third MMP model we have more than one resonance within half a decade. Therefore, we do not assume that the information in the first frequency allows to considerably improve the estimate of the parameters.

6. Conclusions

The optimized PET presented in this paper is a very powerful and promising new technique that can be applied as a power booster to many numerical codes. It takes advantage of the knowledge obtained from previous computations and allows to replace direct matrix solvers by efficient iterative matrix solvers even when the condition of the matrix is so bad that the iterative matrix solvers would fail without the PET.

The optimization of the appropriate basis functions for the PET is extremely time consuming and difficult. With the help of a genetic algorithm we were able to find promising basis functions for the PET that allowed to drastically reduce the number of CG iterations for all of our test cases. Since we found these basis functions within a few days (during our Christmas holidays) on a DEC Alpha PC, we are confident to find even better basis functions in the near future, i.e., we consider the results presented in this paper to be intermediate.

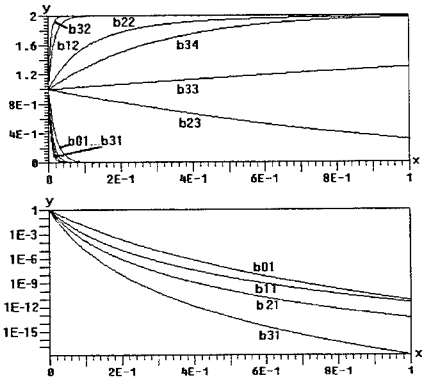


Figure 2: Some of the optimized PET basis functions bnm, where n indicates the PET order and m indicates the number of the basis function. Note that one has n+1 basis functions for an n-th order PET, i.e., m=1...n+1.

The PET optimization is an almost endless job that can be performed very well in the background - with a low priority. The intermediate results of the PET optimization reduce the computation time of MMP computations. Therefore, our MMP code with the PET optimization in the background behaves like a code that is continuously learning to faster compute MMP models.

It is important to note that both the PET itself and the PET optimization can be applied not only to MMP but also to any code based on a matrix method with a sufficiently dense matrix. Since the application of CG matrix solvers to 2D MMP (with its ill-conditioned, rectangular matrices) is relatively hard and requires a well optimized PET, we expect that this technique can easily be adapted to other codes. It should also be pointed out that the PET is neither restricted to the computation of frequency dependeces nor to computational electromagnetics. We assume that it will be one of the most important instruments for a successful and efficient MMP solution of inverse scattering and similar tasks.

REFERENCES

[1] K.S. Yee, "Numerical Solution of initial boundary value problems involving Maxwell's equations", *IEEE Transactions on AP*, Vol.14, 1966.

[2] Ch. Hafner, "'A Priori' Knowledge, Non-Orthogonal Basis Functions, and Ill-Conditioned Matrices in Numerical Methods", *ACES Journal* Vol.8, No.2, 1993.

[3] Ch. Hafner, "On the Design of Numerical Methods", *IEEE AP Magazine*, Vol.35, No.4, 1993.

[4] M.R. Hestenes and E.Stiefel, "Methods of Conjugate Gradients for Solving Linear Systems", *Journal of Research of the National Bureau of Standards*, Vol.49, No.6, 1952.

[5] A.P.M. Zwamborn, *Scattering by Objects with Electric Contrast*, Delft University Press, 1991.

[6] Ch. Hafner, *2D MMP: Two-Dimensional Multiple Multipole Software and User's Manual*, Artech House Books, Boston, 1990.

[7] Ch. Hafner and L. Bomholt, *The 3D Electrodynamic Wave Simulator*, John Wiley & Sons, 1993.

[8] Ch. Hafner, *The Generalized Multipole Technique for Computational Electromagnetics*, Artech House Books, Boston, 1990.

[9] A.C. Ludwig, N. Kuster, A. Glisson, and A. Thal, "5:1 dipole benchmark case", *The ACES Collection of Canonical Problems, Set* 1, 1990.

[10] Ch. Hafner and N. Kuster, "Iterative and block iterative solutions of overdetermined systems of equations in the MMP code", *ACES Conference Proceedings*, Vol. 8, 1992.

[11] N. Kuster and L.H. Bomholt, "A block iterative technique to expand MMP's applicability to EM problems of higher complexity", *IEEE Transactions on MTT*, Vol 42, May 1994.

[12] Ch. Hafner, "MMP-CG-PET: The Parameter Estimation Technique Applied to the MMP Code with the Method of Conjugate Gradients", *ACES Journal*, Vol. 9, No. 3, pp. 28-38, 1994.

[13] S. R. Mangano, *EOS The Evolutionary Object System*, Man Machine Interfaces Inc., New York, 1993.

[14] Ch. Hafner, "MMP Computation of Periodic Structures", *will be published in the Journal of the Optical Society of America.*

[15] P. Regli, *Automatische Wahl der sphaerischen Entwicklungsfunktionen fuer die 3D-MMP Methode*, Diss. ETH No. 9946, Zurich, 1992.

A Novel Scheme for Massively Parallel Solution of Maxwell's Equations using FDTD

Michael A. Jensen†, Yahya Rahmat-Samii‡, and Amir Fijany††

†Department of Electrical Engineering
Brigham Young University
Provo, UT 84602
Tel. (801) 378-5736
Fax. (801) 378-6586

‡Department of Electrical Engineering
University of California, Los Angeles
Los Angeles, CA 90024-1594
Tel. (310) 206-3847
Fax. (310) 206-8495

††Jet Propulsion Laboratory
California Institute of Technology
Pasadena, CA 91109
Tel. (818) 354-9552

I. Introduction

A major emphasis within the computational electromagnetics (CEM) community concerns the solution of Maxwell's differential equations using finite-difference time-domain (FDTD) techniques. These algorithms generally require considerable computational time and storage resources, and as a result their application to very large problems has been somewhat limited. New efforts to alleviate these computational obstacles have focussed on the use of parallelism in the FDTD solutions. Traditionally, these algorithms use spatial domain decomposition or "space-parallelism" in which each processor performs the differencing in a given spatial region at each time step. For many of these schemes, however, communication and synchronization requirements tend to limit the computational speed-up enabled.

This limited potential for enhanced computational efficiency implies that if full exploitation of the capabilities of emerging multiple instruction multiple data (MIMD) architectures is to be realized, approaches must be developed which represent a drastic departure from traditional FDTD techniques. The aim of this paper is to present such a computational strategy. Unlike traditional approaches which rely solely on space-parallel solutions, this methodology exploits parallelism in the temporal dimension as well [1]. This "time-parallelism" is achieved by using the decoupling mechanism of an eigenvalue-eigenvector (EE) decomposition of the FDTD matrix to diagonalize the time-stepping matrix equation. Parallelism can then be used to efficiently solve the resulting diagonal linear recurrence. The algorithm is highly coarse grain and has minimum communication and synchronization requirements, and is therefore suitable for implementation on emerging MIMD machines. Preliminary practical implementation of the algorithm show that large computational speed-up for a given size problem can be achieved.

This paper provides the theoretical and computational bases for the time-parallel solution approach through its application to the Crank-Nicolson (CN) solution of the time-domain scalar wave equation. The algorithm realm of applicability is discussed, and the classes of problems for which the technique provides results superior to those of other techniques are highlighted. The incorporation of absorbing boundary conditions into the algorithm is also demonstrated. The results of practical implementations of the algorithm on the Intel Touchstone Delta supercomputer are provided for several representative configurations.

II. Theoretical Formulation

A. CN Discretization of the Wave Equation

An understanding of the use of time-parallelism in finite-difference solutions of partial differential equations (PDEs) is perhaps best gained by applying the algorithm to a familiar problem. To this end, consider a general form of the scalar wave equation in a homogeneous medium. This PDE can be written as

$$\frac{\partial^2\psi(\vec{r},t)}{\partial t^2} = c^2\nabla^2\psi(\vec{r},t) - \sigma c\eta\frac{\partial\psi}{\partial t} \qquad \vec{r}\in\Omega,\ 0<t<T \tag{1}$$

where Ω is a bounded domain with boundary Ω' and the initial and boundary conditions are specified. The constants c, σ, and η represent the speed of light, medium conductivity, and material intrinsic impedance respectively. Let the vector $\psi^{(m)}$ represent a spatial ordering of the discretized field ψ, where the superscript denotes the time index ($t = m\Delta t$). With this notation, the CN discretization of Eq. (1) can be written as a matrix equation which assumes the form

$$[(1+\gamma)\mathbf{I} - \alpha\mathbf{A}]\,\psi^{(m+1)} = 2\psi^{(m)} - [(1+\gamma)\mathbf{I} - \alpha\mathbf{A}]\,\psi^{(m-1)} + 2\gamma\psi^{(m-1)} + f^{(m+1)} \tag{2}$$

for $1 \le m \le M-1$ where

$\mathbf{I}$ is the unit matrix
$\mathbf{A}$ is the matrix arising from the discretization of the Laplace operator
$\psi^{(m)}$ is the spatially-ordered solution vector at the mth time step
$f^{(m+1)}$ is a source vector
$\alpha = c^2\Delta t^2/2$ and $\gamma = \sigma c\eta\Delta t/2$ are constants
$M = T/\Delta t$, where Δt is the time step size
$\psi^{(0)}$ and $\psi^{(1)}$ are the given initial conditions
N represents the spatial grid size.

The linear matrix recurrence given in Eq. (2) provides a basis for discussing the mathematical implications of space- and time-parallelism. With reference to Eq. (2), space-parallelism generally refers to performing the matrix operations in a parallel fashion at *each time step*. In contrast, time-parallelism refers to a parallel solution of the linear recurrence such that part or all of the time steps are simultaneously computed. The goal of this work is to allow a combination of the two types of parallelism in order to obtain a coarse-grain algorithm which is suitable for emerging MIMD architectures.

It is noteworthy that the CN discretization is an implicit method which offers unconditional stability and therefore reduces the number of time steps required to complete a given computation. However, this savings comes at the cost of a linear system solution at each time step, which can be very expensive in comparison to the solution of an explicit time-stepping procedure.

B. Time-Parallelism

To motivate the idea of time-parallelism, notice that Eq. (2) simply represents a Second-Order Inhomogeneous Linear Recurrence (SOILR) which can be cast into a first-order form. This recurrence solution can be fully parallelized and computed in $O(\log_2 M)$ by using the Recursive Doubling Algorithm (RDA) [2] or Cyclic Reduction Algorithm (CRA) [3]. Unfortunately, such an approach is not *computationally practical* since both RDA and CRA compute powers of the matrices in Eq. (2), resulting in increasingly dense and ultimately full matrices. Nevertheless, this observation indicates that, insofar as the data dependency in the computation is concerned, the time-stepping procedures can be fully parallelized in time.

The goal of the time-parallel algorithm is therefore to manipulate Eq. (2) to allow *efficient* parallelization of the linear recurrence solution. To see this, consider the Eigenvalue/Eigenvector (EE) decomposition of the nonsingular matrix $\mathbf{A}$ given by

$$\mathbf{A} = \Theta \mathbf{\Lambda} \Theta^{-1} \tag{3}$$

where Θ is the set of eigenvectors and $\mathbf{\Lambda}$ is a diagonal matrix representing the set of eigenvalues of $\mathbf{A}$. Substituting Eq. (3) into Eq. (2) and taking Θ and Θ^{-1} outside the parentheses gives the expression

$$\begin{aligned} \Theta\left[(1+\gamma)\mathbf{I} - \alpha\mathbf{\Lambda}\right]\Theta^{-1}\psi^{(m+1)} &= 2\psi^{(m)} - \Theta\left[(1+\gamma)\mathbf{I} - \alpha\mathbf{\Lambda}\right]\Theta^{-1}\psi^{(m-1)} \\ &\quad + 2\gamma\psi^{(m-1)} + f^{(m+1)}. \end{aligned} \tag{4}$$

Defining the diagonal matrix $\mathbf{S} = [(1+\gamma)\mathbf{I} - \alpha\mathbf{\Lambda}]^{-1}$ and multiplying both sides of Eq. (4) by the nonsingular matrix Θ^{-1} gives

$$\mathbf{S}^{-1}\Theta^{-1}\psi^{(m+1)} = 2\Theta^{-1}\psi^{(m)} - \mathbf{S}^{-1}\Theta^{-1}\psi^{(m-1)} + 2\gamma\Theta^{-1}\psi^{(m-1)} + \Theta^{-1}f^{(m+1)}. \tag{5}$$

Defining the vectors $\tilde{\psi}^{(m)} = \Theta^{-1}\psi^{(m)}$ and $\tilde{f}^{(m)} = \mathbf{S}\Theta^{-1}f^{(m)}$ allows us to write Eq. (5) as

$$\tilde{\psi}^{(m+1)} = 2\mathbf{S}\tilde{\psi}^{(m)} - (\mathbf{I} - 2\gamma\mathbf{S})\tilde{\psi}^{(m-1)} + \tilde{f}^{(m+1)}. \tag{6}$$

In contrast to Eq. (2), Eq. (6) is diagonalized and can be efficiently solved in parallel using RDA or CRA. For two and three dimensional problems, Eq. (6) can be computed in $O(N^2 \log_2 M)$ and $O(N^3 \log_2 M)$ respectively by using $O(M)$ processors.

C. Algorithm Structure

To facilitate the discussion of the time-parallel algorithm, we subdivide it into four steps as illustrated in Figure 1. Step 1 involves determining the EE decomposition of the matrix $\mathbf{A}$ and forming the matrix $\mathbf{S}$. In general, since a standard EE decomposition routine returns only Θ and $\mathbf{\Lambda}$, it is necessary to explicitly compute Θ^{-1} by computing the EE decomposition of $\mathbf{A}^T = (\Theta^{-1})^T\mathbf{\Lambda}\Theta^T$. Note that this can be performed in parallel with the EE decomposition of $\mathbf{A}$. The source vectors $f^{(m)}$ are computed and multiplied by $\mathbf{S}\Theta^{-1}$ in Step 2 to obtain the vectors $\tilde{f}^{(m)}$. The parallel solution of the SOILR in Eq. (6) is accomplished in Step 3. Finally, the solution vectors $\psi^{(m)}$ are obtained in Step 4 by performing the matrix-vector multiplication $\Theta\tilde{\psi}^{(m)}$.

It is noteworthy that the computations in Steps 2 and 4 are completely decoupled and can be performed in parallel with no inter-processor communication. Step 3 does involve communication, but this data transfer has a rather simple structure and can be efficiently implemented on MIMD parallel architectures since it involves the exchange of large vectors.

From a standpoint of *computational complexity*, it can be shown that the matrix-vector multiplications of Steps 2 and 4 and the EE decompositions in Step 1 have the potential to dominate the overall algorithmic computational cost. In light of this, two key requirements for the efficient application of the algorithm are

1. an efficient scheme for determining the eigenpairs of $\mathbf{A}$, and
2. an efficient scheme for the matrix-vector multiplications in Steps 2 and 4.

The second issue is particularly important since multiplication of a dense matrix by a vector leads to a computational cost of $O(N^4)$ and $O(N^6)$ for two and three dimensional problems respectively. This fact, coupled with the first issue, motivates the exploitation of the sparse structure of $\mathbf{A}$ and the use of factored forms of Θ and Θ^{-1} to increase the efficiency of these steps.

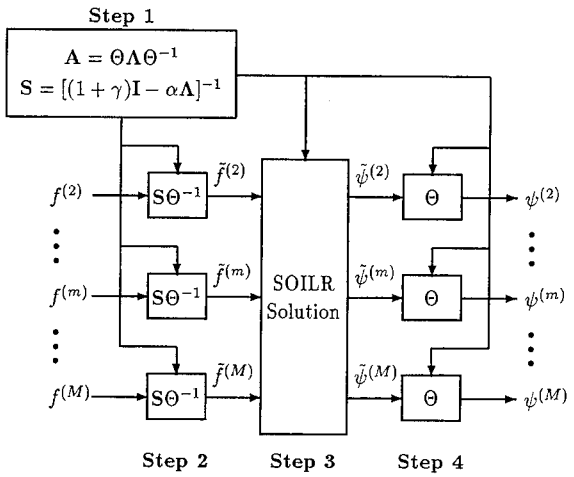


Figure 1: Flow diagram illustrating the computational structure of the time-parallel algorithm.

D. Parallel Recurrence Solution

As mentioned, the parallel solution of Eq. (6) can be accomplished using a conventional method such as RDA or CRA. However, because of the decoupled nature of this equation, it is also possible to exploit both time- and space-parallelism to perform the solution using a pipelining scheme. Preliminary numerical implementations performed by the authors have shown that such a scheme can be more efficient than the RDA for implementations where the number of time steps M is significantly larger than the number of available processors (J). This pipelining scheme is depicted in Figure 2. In this algorithm, processor $\#P$ initially computes the M/J source vectors $f^{(k)}$ for $(P-1)M/J+1 \leq k \leq PM/J$. The matrix recurrence is then divided into J blocks each containing L/J equations, where L is the total number of equations in the system. Processor #1 computes the recurrence for the first block for the first M/J time steps and passes the result to processor #2 before working on the second block. Processor #2 then receives that data, performs the next M/J steps in the recurrence for that block while processor #1 is computing the recurrence for the second block, and passes the result to processor #3. This process is repeated until the recurrence is complete.

E. Absorbing Boundary Conditions

For many problems, particularly enclosed problems involving resonant cavities or wave-guiding structures, the time-parallel algorithm may be readily applied since typically either a Dirichlet or Neumann condition is enforced on the outer spatial domain boundary. However for open problems encountered in radiation and scattering, the issue of incorporating an absorbing boundary condition (ABC) [4] at the outer domain boundary must be addressed. Without proper termination of the grid, outgoing waves in the domain will be artificially reflected by the grid truncation. For the time-parallel scheme, proper choice of an ABC is of critical importance. This arises because the algorithm derivation depends upon the fundamental assumption that all matrices in Eq. (2) are simultaneously diagonalizable. While this assumption holds for conventional boundary conditions (i.e. Dirichlet, Neumann, Mixed, and Periodic), it is not necessarily

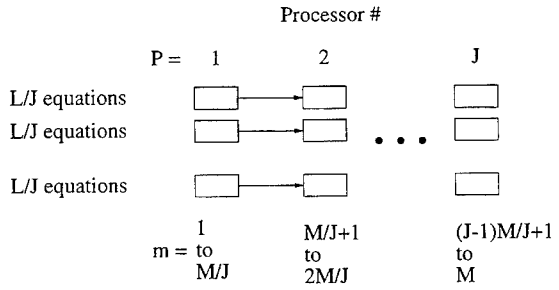


Figure 2: Pictorial description of the pipelined time- and space-parallel SOILR solution.

valid for all existing forms of ABCs.

The method for incorporating ABC's into the algorithm depends somewhat upon the geometry under investigation. However, in general, the goal is to simultaneously *reduce* the matrix equation to a form amenable for parallel computation. For the case of circularly cylindrical structures examined below, it is found that the CN matrix equation can be reduced to a block-diagonal matrix where the blocks are tridiagonal. Such a system can be efficiently solved using the pipelining SOILR solution discussed above.

III. Application to Circular Cylindrical Geometries

The geometry to which the time-parallel algorithm will be applied is the circular cylindrical geometry depicted in Figure 3. In this figure, the inner cylinder boundary at ρ_o is considered a perfect electric conductor while the outer cylinder boundary will be either a conductor or an ABC. These two geometries will be used to compute the fields inside a coaxial cavity as well as the plane-wave scattering from a cylindrical structure. It will be assumed that in all computations the fields are TM^z.

Application of the time-parallel algorithm requires first a knowledge of the EE decomposition for the matrix $\mathbf{A}$. Because this derivation is somewhat involved, only the final results will be presented here. Those interested in specific details should consult Reference [5].

A. Conducting Outer Surface

When a conductor is placed at the outer domain contour, the boundary condition on the z-polarized electric field will be of the homogeneous Dirichlet type. For this configuration, with N azimuthal and K radial discretization points in the spatial grid, the EE decomposition of the matrix $\mathbf{A}$ can be shown to yield

$$\Theta = \mathcal{F}\mathcal{P}\mathcal{Q} \tag{7}$$

where

$\mathcal{Q} = \text{Diag}\{\mathbf{Q}_j\} \in \mathcal{R}^{NK\times NK}$, $1 \le j \le N$

$\mathcal{P} \in \mathcal{R}^{NK\times NK}$ is a permutation matrix

$\mathcal{F} = \text{Diag}\{\mathbf{F}\} \in \mathcal{R}^{NK\times NK}$, where $\mathbf{F}$ is a $N \times N$ one-dimensional discrete Fourier transform (DFT).

Therefore, multiplying a vector $\psi^{(m)}$ by the matrix Θ is tantamount to multiplying $\psi^{(m)}$ by a block diagonal matrix with $K \times K$ blocks, performing a permutation, and performing K DFT's of length N. It should also be mentioned that computing the matrix Θ amounts to finding the N matrices $\mathbf{Q}_j$ by computing the EE decomposition of N $K \times K$ sign-symmetric matrices. This operation can be performed in parallel.

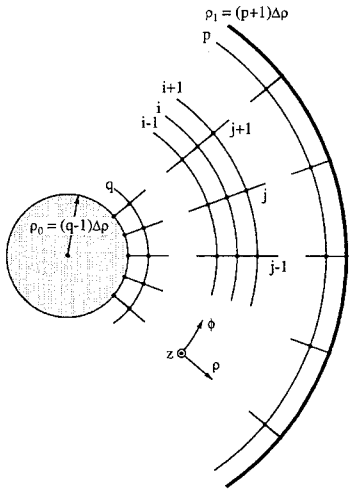


Figure 3: Geometry and gridding for the CN solution of Maxwell's equations near a perfectly conducting circular cylinder.

B. ABC at Outer Surface

When the outer domain boundary is an ABC, the resulting CN matrix equation assumes the general form

$$(\mathbf{I} - \underline{\mathbf{A}})\psi^{(m+1)} = 2\psi^{(m)} - (\mathbf{I} - \underline{\mathbf{A}})\psi^{(m-1)} + 2\underline{\mathbf{V}}\psi^{(m-1)} + f^{(m+1)} \tag{8}$$

where $\underline{\mathbf{V}}$ is a diagonal matrix. It can be shown that the matrix $\underline{\mathbf{A}}$ is reducible to a convenient form using the decomposition $\underline{\mathbf{A}} = \Theta_o \overline{\mathbf{L}} \Theta_o^{-1}$ where $\Theta_o = \mathcal{FP}$ and $\overline{\mathbf{L}}$ is block diagonal, $\overline{\mathbf{L}} = \text{Diag}\{\overline{\mathbf{L}}_j\}$, $1 \le j \le N$, where $\overline{\mathbf{L}}_j \in \mathcal{R}^{K \times K}$ is tridiagonal. Using this decomposition in Eq. (8) results in the equation

$$(\mathbf{I} - \overline{\mathbf{L}})\hat{\psi}^{(m+1)} = 2\hat{\psi}^{(m)} - (\mathbf{I} - \overline{\mathbf{L}})\hat{\psi}^{(m-1)} + 2\overline{\mathbf{V}}\hat{\psi}^{(m-1)} + \hat{f}^{(m+1)} \tag{9}$$

where $\hat{\psi}^{(m)} = \Theta_o^{-1}\psi^{(m)}$, $\hat{f}^{(m)} = \Theta_o^{-1}\psi^{(m)}$, and $\overline{\mathbf{V}}$ remains diagonal but has been transformed by a permutation. Defining $\underline{\psi}^{(m+1)} = \hat{\psi}^{(m+1)} + \hat{\psi}^{(m-1)}$ and $\mathbf{b}^{(m)} = 2\hat{\psi}^{(m)} + 2\overline{\mathbf{V}}\hat{\psi}^{(m-1)} + \hat{f}^{(m+1)}$ allows expression of Eq. (9) as

$$(\mathbf{I} - \overline{\mathbf{L}})\underline{\psi}^{(m+1)} = \mathbf{b}^{(m)}. \tag{10}$$

Because of the block diagonal structure of $\overline{\mathbf{L}}$, the linear system solution in Eq. (10) is equivalent to N *decoupled* tridiagonal system solutions. This decoupled form allows the recurrence solution to be performed using the pipelining method.

IV. Results of Algorithm Implementation

In this section, the results of applying the algorithm to the circular cylindrical geometry on the Touchstone Delta supercomputer will be presented. In all of the computations, the parameters are $M = 512 = \#$ time steps, $K = 32 = \#$ of radial grid points, and $\Delta\rho = 0.1\lambda =$ radial discretization size, and $\rho_1 - \rho_0 = 3\lambda$.

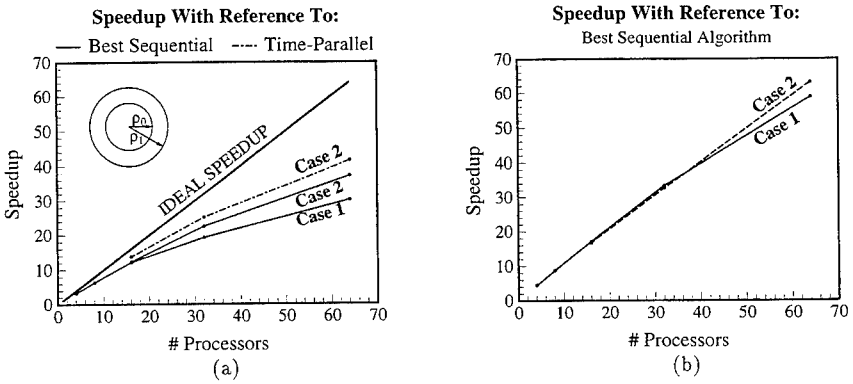


Figure 4: Computational speedup versus the number of processors used to solve for the fields in the coaxial cylinder using the time-parallel approach with pipelining in the SOILR: (a) single computation; (b) 64 computations with different source configurations for the same geometry. Case 1: $\rho_0 = 1.6\lambda$; Case 2: $\rho_0 = 16\lambda$.

A. Closed Coaxial Cavity

As a first example, let us consider the closed coaxial cavity configuration such that a Dirichlet boundary condition is used on the outer computational domain boundary. The inset of Figure 4 illustrates the geometry for the problem and lists the dimensions for the two cylinders under investigation. The excitation is uniform about the interior cavity perimeter. The azimuthal discretization uses $N = 128$ and $N = 1024$ for Cases 1 and 2 respectively.

Figure 4(a) illustrates the speedup achieved as the number of processors assigned to the problem increases. The "IDEAL SPEEDUP" curve suggests that in the absence of communication and synchronization costs, the speedup equals the number of processors used. In reality, however, the achieved speedup is less than ideal, as expected. The speedup is measured with reference to two different sequential computation times. The "Best Sequential" time T_s^{BS} for solution of this problem corresponds to using the Fast Poisson Solver [6] for the linear system solution. The "Time-Parallel" time T_s^{TP} represents the time required to perform the algorithm introduced here on a *single* processor. In all cases, a very good speedup is achieved using the time-parallel approach. It is noteworthy that the computational speedup improves as the problem size increases due to a corresponding increase in the computational grain size.

Close investigation of the relative times required to complete each of the steps in Figure 1 reveals that Steps 1 and 3 represent a significant portion of the algorithm computational time. This occurs because of the communication overhead associated with these steps. It is noteworthy that if the methodology is applied to problems for which the EE decomposition is known explicitly, then the time devoted to Step 1 is reduced to an almost negligible level. For the problem at hand, it becomes evident that the time-parallel algorithm will perform particularly well for problems in which the same geometry is simulated for many different source configurations. In such a situation, the EE decomposition needs to be computed only once for *all* of the CN solutions. As an example, consider that the source in the cavity is non-zero only over a specified azimuthal region, and it is desired to determine the region size for which optimal coupling into the cavity occurs. The speedup of the algorithm assuming that 64 different source region sizes are used is provided in Figure 4(b). These results show significantly improved algorithmic speedup, as expected. This demonstrates the importance of minimizing the relative computation time of the EE decomposition in order to obtain an algorithm with high speedup for a fixed problem size.

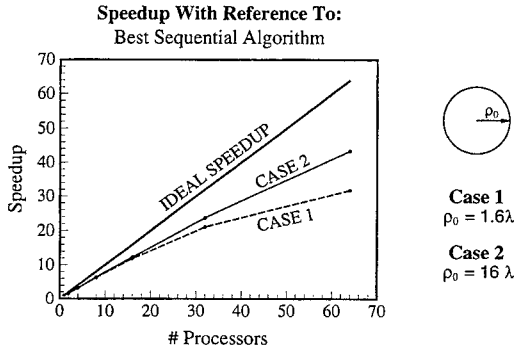


Figure 5: Computational speedup versus the number of processors used to solve for the fields scattered by a cylinder using the time-parallel approach with pipelining in the SOILR.

B. Scattering from a Circular Cylinder

As a second example, consider the computation of scattering from a circular cylinder where an ABC must be placed at the outer domain boundary. Figure 5 illustrates the geometry and computational speedup achieved in this investigation. The azimuthal grid sizes used are identical to those used for the computation in Figure 4. Here again, the speedup results show that the computational grain size is larger for the larger problem, resulting in an improved speedup result. It is also interesting that the speedup performance is very similar to that seen in Figure 4(a) where a purely diagonal system was obtained. It would appear from this simple study therefore that for this configuration, the use of the block diagonal form does not severely degrade the achievable computational speedup.

V. Conclusions

In this paper, a novel approach for the time- and space-parallel solution of FDTD algorithms has been presented. The theoretical and computational bases of the scheme have been detailed, and its practical application on a MIMD architecture has been demonstrated.

References

[1] M. A. Jensen, A. Fijany, and Y. Rahmat-Samii, In *1994 IEEE AP-S Intl. Symposium Digest*, vol. 1, pp. 380–383, Seattle, WA., June 19-24 1994.

[2] P. M. Kogge and H. S. Stone, *IEEE Trans. on Computers*, C-22(8):786–793, 1973.

[3] R. Hockney and C. Jesshope, *Parallel Computers*. Adam Hilger Ltd., 1981.

[4] G. Mur, *IEEE Trans. Electromagnetic Compat.*, EMC-23:377–382, Nov. 1981.

[5] Michael A. Jensen, PhD thesis, University of California, Los Angeles, 1994.

[6] P. N. Swarztrauber and R. A. Sweet, *SIAM J. Numer. Anal.*, 10(5):900–907, Oct. 1973.

Reduction of the Filling Time of Method of Moments Matrices

G.Vecchi, P.Pirinoli, L.Matekovits and M.Orefice
Dipartimento di Elettronica, Politecnico, I-10129 Torino, Italy

Abstract — A technique is presented to reduce the computation time for the evaluation of the impedance matrix for Method of Moments (MoM) discretization of the integral equation formulation of antenna and scattering problems. This technique, called "matrix synthesis", requires that only a fraction of the matrix entries be computed exactly, while the rest is derived through an approximation scheme. Here it is described for printed structures on plane-stratified media, and applications to microstrip structures are presented.

Introduction

We consider here the full-wave, standard integral-equation formulation for antenna or scattering problems, discretized according to the Method of Moments (MoM), so that N unknowns are obtained. The computation time T_c is the sum of the time T_f necessary to fill in the matrix (filling time), and the time T_s required for the factorization (or inversion) of the linear system. Although typical estimates yield $T_s \propto N^3$, and $T_f \sim \frac{1}{2} t_{int} N^2$, where t_{int} is the time required for the evaluation of a typical reaction integral, because of the complexitiy of the integrals, T_f is always important, and often dominant. Here we present a scheme that allows a reduction of the filling time T_f.

In the technique, briefly called *Matrix Synthesis* hereafter, only a selected fraction of the total number of required matrix entries is computed, the rest being obtained through an approximation scheme. The scheme is based on the consideration that the quantity of information required for the representation of a field (degrees of freedom, [1]) is usually less that the number ($\sim N^2/2$) of independent matrix entries. This scheme has the same objectives as those reported in [2]; however, although it achieves a lower efficiency, it has the advantages of a greater simplicity, and of being directly applicable to any existing code (e.g. NEC).

Here we will assume sub-domain basis functions (e.g. rooftops, linear functions on triangular domains, etc.) such as those used for describing general structures, so that the entire set of functions can be divided in classes of spatially translated/rotated equal basis functions (e.g. triangles of the same size). We further assume a Galerkin testing scheme.

Matrix Synthesis

In the global system ("impedance") matrix, we consider here any of the submatrices related to any of the subsets in which the sub-domain basis functions can be divided. This (sub)matrix $\mathsf{Z} = [Z_{mn}]$ is a mapping between the set of integer pairs $\{(m,n), m,n = 1:N\}$ and the complex plane Z. First, the mapping between the indices (m,n) and the matrix entry $Z_{mn} = Z(m,n)$ is regarded as a collection of samples of the mapping between a *continuous* set (x,y) and Z; that is, the discrete variables (m,n) are replaced by the continuous ones (x,y).

The function $Z(x,y)$ can then be *approximated* by fitting a suitable set of functions $\{f_\alpha(x,y), \alpha = 1:M\}$ (e.g. polynomials) to a small number N_s of samples of the function $Z(x,y)$, each sample being a reaction integral. The matrix Z is then obtained by evaluating the approximated function $Z(x,y)$ at discrete points of the (x,y) plane. The number of required points and their location clearly depends on the properties of the kernel of the reaction integrals: in particular, the approximation works well only when the dependence of Z on (x,y) (that is, on (m,n)) is smooth enough. The reaction integral between two current distributions $\underline{J}_m$ and $\underline{J}_n$ has the form $Z_{mn} = \langle \underline{J}_m, \underline{\underline{G}} * \underline{J}_n \rangle$ where $\underline{\underline{G}}$ is the appropriate dyadic Green's function and '$*$' stands for the convolution integral. This integral depends on the centers $\underline{r}_m$ and $\underline{r}_n$ of the sub-domains, on the relative orientation of the sub-domains and of the currents. Therefore, the global matrix Z has to be partitioned into blocks that represent interactions between current components that vary smoothly (or do not vary at all) from one node to another (e.g. azimuthal or radial current component on a disk, the two orthogonal current components on a rectangular plate, etc.). Clearly, matrix elements representing interactions from sub-domains at, or close to, an abrupt discontinuity (e.g. a right-angle bend in a microstrip) are excluded from this considerations.

Printed Structures

As an application of this technique, we consider here a plane, or plane-stratified structure, with sub-domain basis functions. Further, we consider the reaction $Z_{mn} = Z_{mn}^{(12)}$ between the basis functions $\underline{J}_m(\underline{r}) = \hat{u}_1 J_0(\underline{r} - \underline{r}_m)$ and $\underline{J}_n(\underline{r}) = \hat{u}_2 J_0(\underline{r} - \underline{r}_n)$ with $\hat{u}_{1,2}$ being two unit vectors that do not depend on the locations $\underline{r}_{m,n}$, and J_0 is the chosen "elemental" basis function (e.g. a rooftop). With these assumptions, the entries Z_{mn} of the considered sub-matrix are a function of the distance $\underline{q}_{mn}$ between these two points only, $Z_{mn} = Z(\underline{q}_{mn})$, $\underline{q}_{mn} = (\underline{r}_m - \underline{r}_n)$ and by direct replacement of $\underline{q}_{mn}$ by a continuous (vector) variable $\underline{q} \to (x,y)$ one proceeds then to the approximation of the function $Z(x,y)$. Although other forms of fitting could be used, here we will consider Least-Squares (LSQ) fitting of suitable functions $f_\alpha(x,y)$ to the N_s samples $\{Z_i = Z(\underline{q}_i), i = 1:N_s\}$.

Both in free-space and in a layered medium, one can extract from the Green's function $\underline{\underline{G}}$ a strongly singular term $\underline{\underline{G}}_s$, that behaves like $1/q^3$ for $x \to 0$, and a "regular" (integrable) term $\underline{\underline{G}}_r$ that is bounded by $1/q$. The singular term can be rendered independent of frequency, is purely real or imaginary, and represents the static part. Therefore, it is convenient (in general) to separate Z in two terms according to the above: these will have a rather different dependence on the separation distance q.

The term $Z_s(\underline{q})$, due to the static, singular part of $\underline{\underline{G}}$, will be sharply peaked about $q = 0$ and decay abruptly for growing separations q, with a variation at most equal to $1/q^3$. Note that this part is frequency-independent.

Conversely, the term $Z_r(\underline{q})$ due to the "regular" part of $\underline{\underline{G}}$ is smoother for $x = 0$, and dominated by the oscillating behaviour of Green's function; in fact, for small enough sub-domains $Z(\underline{q})$ is approximated by the Green's function itself. The spatial frequency of the oscillations can be readily obtained by inspection of the appropriate Green's function, and this will set the spatial sampling rate and the number of samples per wavelength. On the basis of the spectral representation theory and contour deformation, (e.g. [3]) one can ascertain that away from $q = 0$ the dominant contribution will have a spatial period not smaller than the shortest wavelength in

the layered medium.

Applications and validation

This matrix synthesis technique has been applied, for the sake of validation, to the following different configurations: a microstrip line, an L-shaped patch, subdivided in rectangular subdomains, and a narrow rectangular patch with a general mesh (triangular based).

1. On a microstrip line, only the longitudinal current component is considered, so that the matrix elements Z_{mn} depend only on the longitudinal distance between centers. The line has a length $L = 4.27\lambda_d$ (λ_d is the wavelength in the medium, $\epsilon_r = 2.33$), and the current on it is expanded in terms of 105 rooftop basis functions: the relevant Z-matrix is a Toeplitz, symmetrical matrix and it is only necessary to evaluate and approximate one row. Following the scheme described above, the "singular" and the "regular" part of the matrix are approximated separately. For the singular part $Z_s(q)$, whose variation is expected to be between $1/q^3$ and $1/q$, with a wide dynamics, two possible types of approximation have been compared, both obtained by fitting N_s equispaced samples: a) a direct approximation of $Z_s(q)$ by means of a rational function, and b) a polynomial approximation of $\log Z_s(q)$.

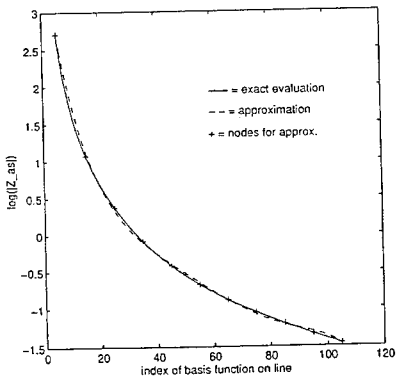


Figure 1. Singular part of $Z^{(II)}$: polynomial approximation of $\log Z_s$

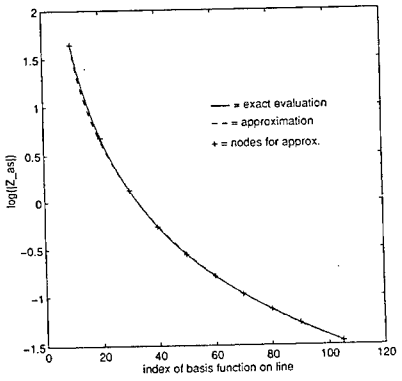


Figure 2. Singular part of $Z^{(II)}$: log of rational approximation of Z_s

Figs. 1 and 2 show that both approximations work well; however, the "logarithmic+polynomial" is easier and preferable, because the fitting of $\log Z_s(q)$ corresponds to a linear LSQ fit while the rational fit relies on a non-linear optimization. Moreover, the rational fit is less efficient in covering the small separation range. In both cases, the number of samples could be further on reduced, by using a non-uniform spacing sampling.

The real and immaginary part of the regular matrix Z_r are approximated separately, polynomially. The results, not reported here, show that $N_s = 18$ samples are sufficient to correctly reproduce all the matrix entries within a 1% error bound.

2. The L-shaped patch can be seen as a pair of ortogonal, partly overlapping microstrips; on each arm the current can be considered only longitudinal ($\hat{x}$ or $\hat{y}$ directed), so that in the non-overlapping zones only one current component is present, while where the two strip are superimposed both current components are present. Each arm has a length $L = 0.28\lambda_d$ and is divided in $N = 25$ rooftop basis functions. The resulting Z-matrix can be partitioned in four submatrices: $\mathsf{Z}^{(xx)}$, $\mathsf{Z}^{(yy)}$ that express the interaction between current elements with the same direction and $\mathsf{Z}^{(xy)}$, $\mathsf{Z}^{(yx)}$, that are the coupling matrices between ortogonal current elements.

The entries of the first two matrices depend only on the longitudinal distance between the basis functions, so that the approximation can be carried out in the same way described above for the microstrip line. In the case of the coupling submatrices, the distance between two subdomains depends either on the longitudinal or on the transverse coordinate; so the elements Z_{mn} are samples of a function of both x and y coordinates, that is suitably approximated via a two-dimensional fitting. The approximation has been applied separately to the singular and to the regular part of $Z^{(xy)}$, $Z^{(yx)}$: the results reported in Tab. 1 show a substantial reduction of the number of reaction integral evalution, with an error between the exact and the synthetized matrix less than 1%; it must be observed that, while for the regular part the whole matrix has been approximated, in the case of the singular part the approximation concerns only the smoother section of the matrix, i.e. the one not involving overlapping subdomains, that is the only portion of the matrix in which the approximation is meaningful: aside from their abrupt variation, the elements in the overlapping zone are very few.

	N_f	N
sing. part $\mathsf{Z}^{(xy)}$ (only a section)	7×7 (49)	18×18 (324)
reg. part $\mathsf{Z}^{(xy)}$ (whole matrix)	8×8 (64)	25×25 (625)

Table 1: Comparison between the number of reaction integrals evalution without (N) and with (N_f) approximation

3. The matrix synthesis technique is applied to a triangular mesh on which linear functions are defined and then suitably grouped to obtain pyramidal basis fuction. Such a mesh has the advantage of being suitable for any patch shape, but it has the drawback that the elements of the associated Z-matrix are significantly more time-expensive: it is therefore particularly important to reduce the number of entries to be evaluated.

Here the case of a dipole, where the current is only longitudinally directed, is considered: the triangular subdomains are grouped in one row of $n_H = 20$ hexagonal sub-domains plus two

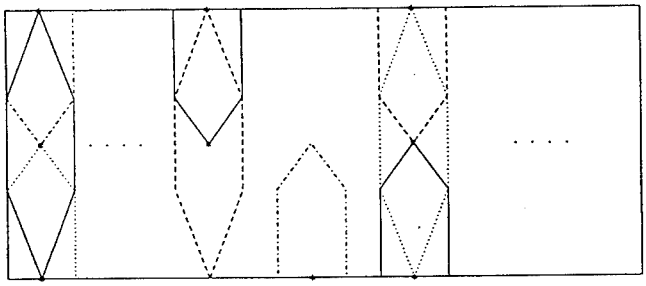


Figure 3: Example of grouping of the trangular sub-domains on a rectangular geometry

outer rows of n_H pentagonal sub-domains (see Fig. 3); this means that the corresponding matrix can be partitioned in different submatrices, expressing the interaction between two hexagonal pyramids ($\mathsf{Z}^{(hh)}$), two pentagonal pyramids ($\mathsf{Z}^{(p_ip_j)}$) or a pentagonal and a hexagonal pyramidal basis function ($\mathsf{Z}^{(hp_i)}$, $\mathsf{Z}^{(p_ih)}$). The interaction between sub-domains on the i-th and j-th row depends only on longitudinal distance between centers and the matrix elements can be seen again as samples of a one-variable function.

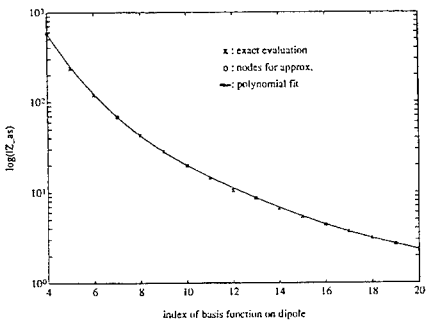


Figure 4. Singular part of $Z^{(hh)}$

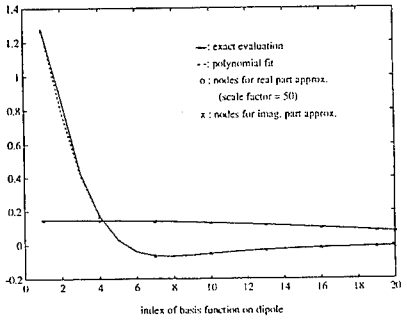


Figure 5. Real and imaginary part of regular term of $Z^{(hh)}$

The results of the approximation for the elements $Z_n = Z_{|i-j|}$ of the self-impedance matrix $\mathsf{Z}^{(hh)}$ are shown in Figs. 4 and 5 for the singular and regular parts, respectively; the solid line shows the exact values of Z_n, the dotted line represents the polynomial approximation obtained by fitting the $N_s = 8$ samples, equispaced except in the final portion of the curves, as emerges from the plots.

Figs. 6 and 7 show the results relative to the approximation of the $\mathsf{Z}^{(hp_i)}$ sub-matrix: also in this case 8 samples are sufficient for correctly synthetize the entire row, and consequently the

whole matrix.

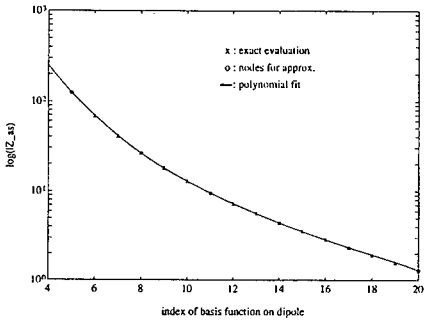


Figure 6. Singular part of $Z^{(hp_i)}$

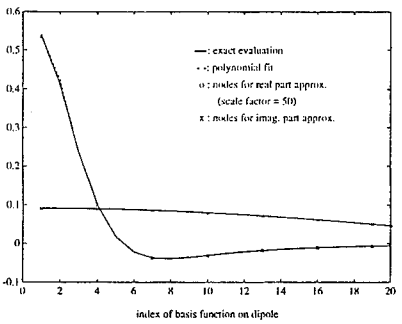


Figure 7. Real and imaginary part of the regular part of $Z^{(hp_i)}$

The results concerning the other submatrices are similar, and for this reason are not reported here: in fact those shown in Figs. 4 to 7 are sufficient to conclude that also in this case the approximation is good: the differences between the exact and approximated values are negligible, and a reduction of a factor of 2-3 of the matrix entry evaluation time is achieved.

Concluding, we can say that this technique leads to a drastical reduction of the filling time, which becomes $T_f \propto \frac{1}{2}(rN^2)t_{int}$ where the reduction factor r is typically in the range $1/2 \div 1/9$.

References

[1] O.M.Bucci, G.Franceschetti, *IEEE Trans. Antennas Propagat.*, vol. AP-37, pp. 918-926, 1989.

[2] E.Michielssen, A.Boag, *IEEE Antennas and Propagat. Symp. Digest*, Seattle, USA, June 1994, pp. 420-423.

[3] L.B.Felsen and N.Marcuvitz, *Radiation and Scattering of Waves*, Secs.5.2, 5.3; Engelwodd Cliffs (NJ): Prentice-Hall, 1973.

The Fast Multipole Method for Large 2d Scatterers[†]

L.R. Hamilton J.J. Ottusch M.A. Stalzer
R.S. Turley* J.L. Visher S.M. Wandzura

Hughes Research Laboratories, Malibu, CA 90265

Abstract

The Fast Multipole Method(FMM) is a technique for computing scattering and radiation from large objects using less memory and CPU time required by dense techniques. When combined with high-order discretizations of the surface currents, the FMM can be used to solve problems on workstations that require supercomputers using dense techniques. We will present the results of cross section calculations for bodies whose cross sections have a large dynamic range. When using low-order basis functions, the FMM requires less memory and cpu time than dense techniques for objects above a certain size. When high-order basis functions are used, the crossover point occurs for larger objects. However, for bodies larger than this threshold, the FMM and high-order discretizations combine to permit solutions with lower memory and cpu requirements than either enhancement used alone.

1 Introduction

The Fast Multiple Method(FMM)[1] can reduce the asymptotic complexity of iterative scattering cross section computations by a factor of $\mathcal{O}(N/\log(N))$ compared to that required by dense matrix techniques. When used with a Galerkin discretization of the scattering integral equations, it depends on the basis functions being localized on the wavelength scale. Use of high-order basis functions with relatively broad support permits more efficient and accurate cross section calculation than using low-order basis functions[2].

When both of these techniques are used together, the optimal basis function order and support size for dense techniques is not the optimal one for the FMM. For relatively small problems, it is more efficient to use dense techniques than the FMM. Even when the FMM is more efficient than dense techniques that use pulse or rooftop basis functions, it is sometimes better to use dense techniques with high-order basis functions having broad support than to use the FMM with basis functions which are more localized.

We will illustrate the interplay of the FMM and high-order basis functions in optimizations of computations for boomerang- and bat-shaped objects of various sizes. When the size of these objects increases beyond one hundred wavelengths, the cross section has a large dynamic range (more than one million to one for a boomerang with 600λ long arms, for instance). Accurate computation of the cross section requires careful numerical integrations and high-order discretizations.

We solved these scattering problems by discretizing the 2d electric field integral equation using the Galerkin technique. Our basis functions consist of localized polynomials in the parametric surface coordinate. We used the single stage FMM with a theoretical asymptotic complexity of $\mathcal{O}(N^{3/2})$, where N is the number of unknowns in the problem. The data for memory usage and CPU time per iteration follow this theoretical prediction remarkably well.

We will present our technique for reliably determining the accuracy for our solutions to these problems. Given this accuracy measure, we will show how CPU time and memory for a given accuracy can be optimized as a function of quadrature order, basis function order, FMM group diameter, and patch size.

[†]This research was supported in part by the Advanced Research Projects Agency of the Department of Defense and was monitored by the Air Force Office of Scientific Research under Contract Number F49620-91-C-0064. The United States Government is authorized to reproduce and distribute reprints for governmental purposes notwithstanding any copyright notation hereron.

2 Background

In this section, I will provide a brief summary of the FMM and the high-order techniques employed in these computations.

2.1 General Background

We are interested in solving the scalar Helmholtz equation

$$(\nabla^2 + k^2)\,\psi = 0 \tag{1}$$

subject to the Dirichlet boundary condition $\psi = 0$ on the scatterer surface S and the radiation condition at ∞.

Let the field ψ consist of an incident plane wave $\phi(\mathbf{x})$ and a scattered wave φ having the asymptotic form

$$\varphi = f(\theta)\frac{e^{ikr}}{\sqrt{r}} \quad ; \quad r \to \infty\,. \tag{2}$$

The differential cross section is given by

$$\frac{d\sigma}{d\theta} = |f(\theta)|^2\,. \tag{3}$$

Eq. (1) can be transformed into the integral equation

$$\phi(\mathbf{x}) = -\int_S d\mathbf{x}'\,G(\mathbf{x},\mathbf{x}')\sigma(\mathbf{x}') \quad ; \quad \mathbf{x}\,\text{on}\,S\,, \tag{4}$$

where

$$\sigma(\mathbf{x}') = -\lim_{\mathbf{x}\to\mathbf{x}'}\hat{n}\cdot\nabla\psi(\mathbf{x})\,, \tag{5}$$

$\hat{n}$ being the unit normal pointing outward from S.

Eq. (4) was discretized for numerical solution by the Galerkin technique. One expands σ in terms of a set of basis functions $\{b_i\}$

$$\sigma(\mathbf{x}) = \sum_i I_i b_i(\mathbf{x})\,, \tag{6}$$

obtaining the matrix equation

$$V = ZI \tag{7}$$

where

$$V_j = i\int_S d\mathbf{x}'\,b_j(\mathbf{x})\phi(\mathbf{x}) \tag{8}$$

$$Z_{ij} = -i\int_S d\mathbf{x}\,b_j(\mathbf{x})\int_S d\mathbf{x}'\,G(\mathbf{x},\mathbf{x}')b_i(\mathbf{x})\,. \tag{9}$$

Efficient numerical solutions of Eq. (4) depend on the appropriate choice of basis functions. We have found that orthogonal polynomials in a parametric surface coordinate provide a choice that is efficient to compute and provides rapid solution convergence[2]. For maximum efficiency, one must use accurate representations of the scattering surface[3]. The basis functions are defined to be non-zero only on localized regions of the surface, we call "patches".

2.2 Fast Multipole Method

The FMM is a sparse factorization of the impedance matrix Z defined in Eq. (9). In its simplest form, the matrix Z can be expressed to arbitrary precision as a combination of three sparse operators: a "near" interaction term Z', a far field transformation V and a translation operator T,

$$Z \approx Z' + V^{\dagger}TV\,. \tag{10}$$

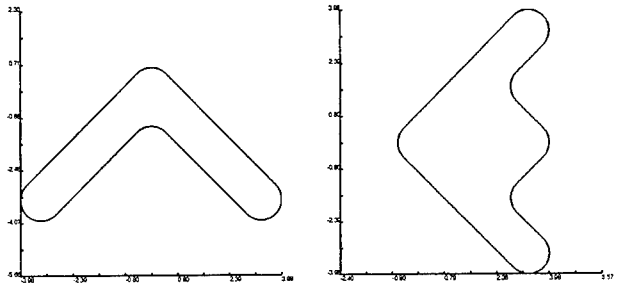


Figure 1: Geometry of 6λ boomerang and 6λ bat

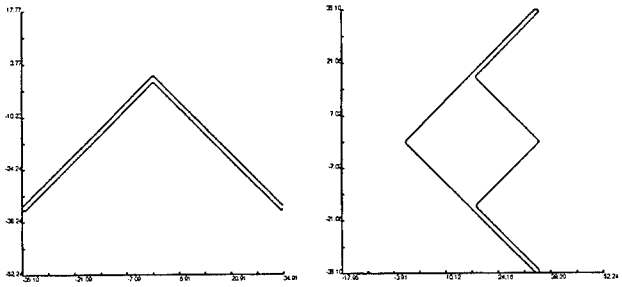


Figure 2: Geometry of 50λ boomerang

The FMM operator is constructed by arranging the basis functions into groups where the basis functions in each group have supports that are near each other. The diameter of a group D is the diameter of the smallest circle enclosing the supports of all basis functions in the group. The optimal group size occurs when the number of groups is approximately equal to the square root of the number of unknowns.

Clearly, the group diameter D can be no smaller than the largest support of the basis functions in the group. Sometimes one must trade-off the optimum group size for the most efficient FMM factorization against the patch size that takes best advantage of high order basis functions.

3 Geometries

We used two geometries for this study, the boomerang and bat shown in Figure 1. oriented so that 0° is nose-on. We will characterize the size of each object by the distance L from the nose to the tip of the leading edge. The variously sized objects are obtained by increasing the length L and keeping the radius of curvature of the corners constant. For example, larger geometries are shown in Figure ??.

These geometries were chosen to be geometrically simple, but challenge the numerical capabilities of our computer program because of their large dynamic range of cross sections. Nose on, the cross section of both objects is approximately that of a circle with the same radius as the radius of curvature of the nose ($r = 0.625\lambda$, $d\sigma/d\theta = 0.3217\lambda$). On the other hand, the tails look like one or two corner reflectors. The cross sections for waves incident on the tail is approximately equal to the square of the span of the objects. For an object with a length of 1500λ the ratio of monostatic cross sections from the tail and nose of the objects is 1.4×10^7.

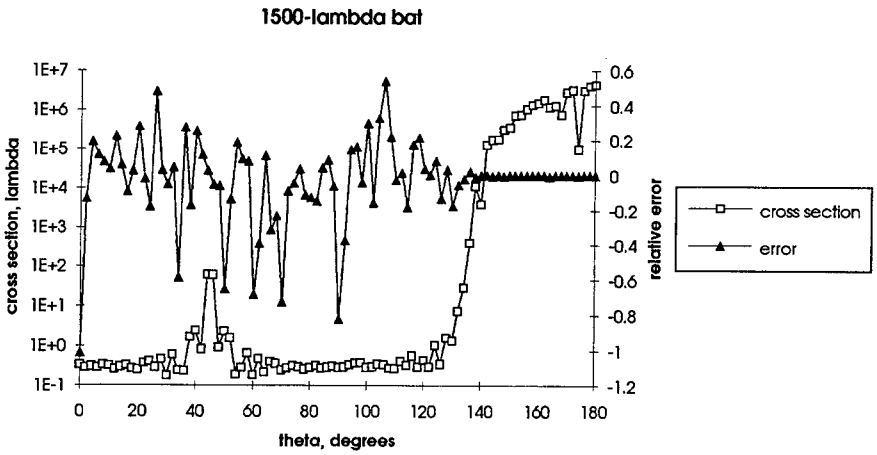


Figure 3: Cross section and relative error as a function of angle for a 1500λ bat.

4 Error Analysis

Meaningful comparisons of various techniques for computing cross sections require accurate error estimates. Our use of high-order methods makes reliable estimates fairly inexpensive to compute. Given a solution with a particular estimated accuracy, we can compute another solution with an order of magnitude smaller error with a modest increase in computation time and memory. We estimate the error in the second solution to be the difference between the two solutions.

We have verified the postulated high-order solution convergence by following the above procedure with scattering from circles, where an independent series solution is available. We have also found that the solutions with increasing order converge rapidly to the assumed exact solutions for the problems reported here.

As mentioned in the introduction, these targets were chosen to have a large dynamic range in their cross sections. For the largest target, a 1500λ bat, there is a dramatic difference between the relative errors in regions of low and high cross sections as shown in Figure 3. Because of this, denser discretizations and more accurate quadratures were required for the larger scatterers than for the smaller ones.

5 Results

In order to illustrate the separate and combined effects of the FMM and high-order techniques, we will compare CPU and memory requirements for four situations:

- low-order dense solutions,
- high-order dense solutions,
- low-order FMM solutions, and
- high-order FMM solutions.

The CPU time reported is the total time to solve the problem. In the dense case (using a direct sovler), it is the sum of the time to fill the impedance matrix, the time to do an LU decomposition of the matrix, and the time to solve Eq. (7) for multiple right-hand sides. Let N be the number of unknowns in the problem. The fill time is

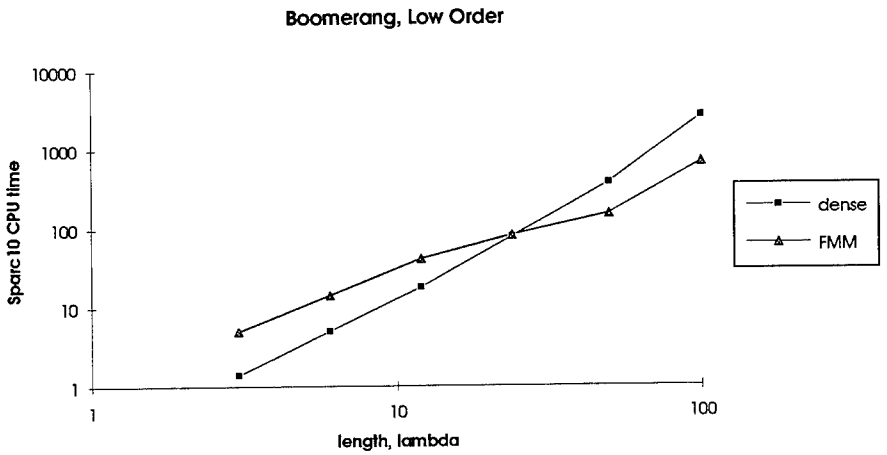


Figure 4: CPU time required for dense and FMM computation of the cross section of a boomerang. Low-order basis functions were used in both cases.

proportional to N^2 and dominates for small problems. For a given N it is usually faster to compute the matrix elements using high-order basis functions than low-order ones. The LU decomposition time is proportional to N^3 and dominates for large problems. The solution time of Eq. (7) is proportional to N^2, but has a smaller coefficient than the fill time (unless the far field is grossly oversampled).

In the case of the FMM, there are two significant components of the CPU time: the computation of the FMM operator, and the iterative solution of the matrix equation at each angle. The FMM setup time has an asymptotic complexity of $\mathcal{O}\left(N^{3/2}\right)$. In small to medium problems where a limited number of scattering angles are computed, this time dominates. For a given N and FMM group diameter D, it is usually faster to compute the FMM operator using high-order basis functions than low-order ones. For the largest problems, the CPU time is dominated by the FMM solution time. Each iteration in the FMM solution has an asymptotic complexity of $\mathcal{O}\left(N^{3/2}\right)$. The complexity of the iterative solver we used is an open question. We use a simple block-diagonal preconditioner, the biconjugate gradient iterative solver, and intelligent starting guesses for the surface currents. This combination appears to have a complexity no higher than $\mathcal{O}\left(N^{1/2}\right)$.

When the desired accuracy could be achieved in single precision, the impedance matrix and FMM operator were stored that way. This was possible on all but the largest problems. In addition, the matrices Z and Z' use packed symmetric storage reducing the required memory by a factor of 2. Although similar packed storage of the T component of the FMM operator is possible, it has not been implemented.

In the following subsections all times are CPU seconds on a Sun Sparc10. Memory is measured in kilobytes.

5.1 Boomerang

Figure 4 shows a comparison of the CPU time required for low-order basis functions and a dense direct solver to the time required using the same basis functions with the FMM. The computations were done with an rms relative error of 0.1. Using these low-order basis functions, the FMM provides a savings in CPU time for boomerangs longer than 25λ. Figure 5 is a similar comparison of the memory required in these two cases. The memory required in the dense case is proportional to the length to the power 2.2. It increases a little faster than the square of the length because of the need to use a finer discretization as the length increases in order to keep the error constant. The FMM memory is proportional to the length to the power 1.6.

Figure 6 is a comparison of the CPU time required for low-order basis functions and high-order basis functions,

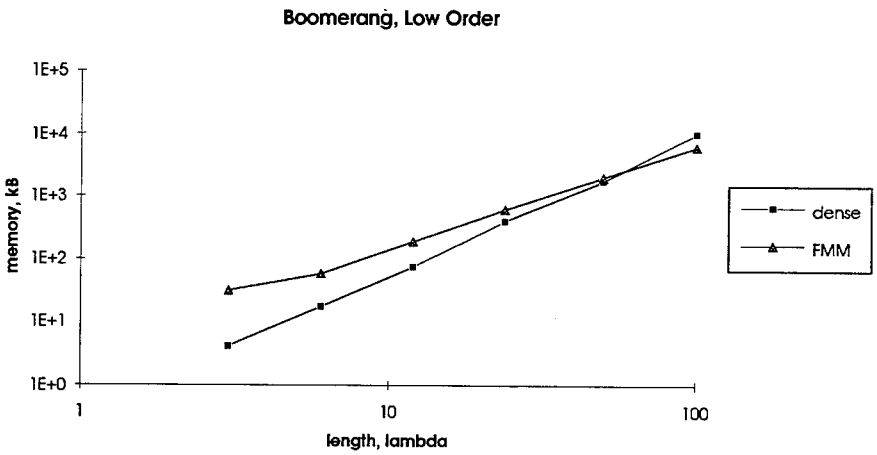


Figure 5: Memory required for dense and FMM computation of the cross section of a boomerang. Lower order basis functions were used in both cases.

using the dense direct solver in both cases. The computations were done with an rms relative error of 0.01. Use of high-order basis functions dramatically reduces the CPU time required, but does not change the asymptotic complexity of the solution.

Figure 7 shows the combined effect of using high-order basis functions and the FMM, comparing the CPU time required for low-order basis functions with a dense matrix and high-order basis functions with the FMM. The computations were done with two significant digits of accuracy. The crossover from where the FMM is faster than a low-order dense solver occurs at a shorter length of 10λ than when the FMM is used alone.

5.2 Bat

Scattering from the bat produces results that are very similar to the ones shown in the previous section. As an illustration, Figure 8 compares the memory required to compute scattering from a bat using a dense matrix and using the FMM. High-order basis functions are used in both cases. Note that the crossover occurs for a longer length of 64λ than in Figure 5 where low-order basis functions are used. The most efficient discretization of the smaller bats uses patches that are so large, they force the FMM group diameters to be larger than is necessary (and optimal) in the low-order case. The slope of the two curves are 2.0 and 1.5 as expected.

6 Conclusion

Use of the FMM in conjunction with high-order discretizations dramatically increases the maximum size of problems which can practically be solved on a given computer to a given accuracy. The use of high-order methods and the FMM becomes especially important for problems with a large dynamic range of cross sections such as the bat and boomerang examples used here. In these problems, denser discretizations are required than in problems with smaller dynamic ranges. Use of high-order methods decreases the number of unknowns required to obtain sufficient accuracy. Use of the FMM reduces the time and memory required to solve the resulting large systems of linear equations. Using both techniques provides more improvement than is possible using either technique separately.

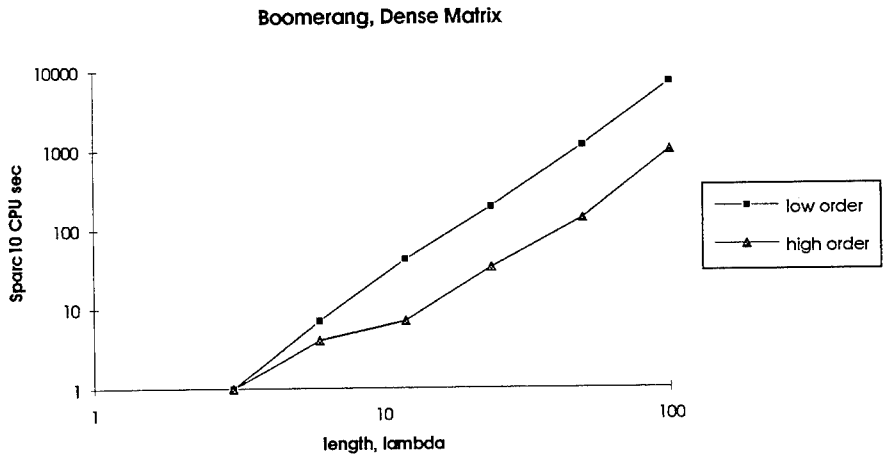


Figure 6: CPU time required for computing the cross section of a boomerang with low-order and high-order basis functions

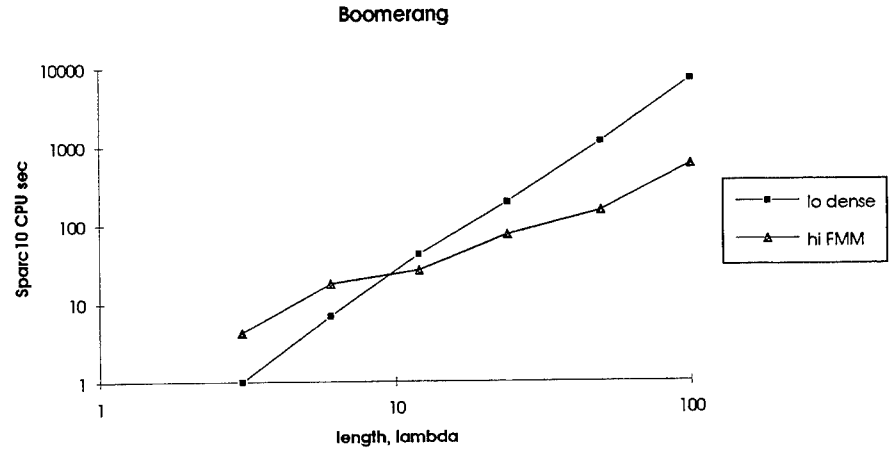


Figure 7: CPU time required for computing the cross section of a boomerang with low-order basis functions and a dense matrix with the time required using high-order basis functions and the FMM

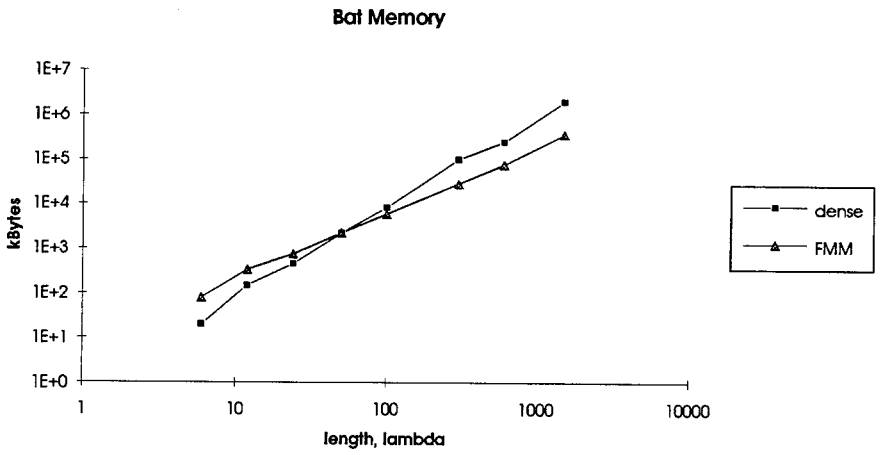


Figure 8: CPU time required to compute the cross section of a bat using high-order basis functions.

References

[1] Ronald Coifman, Vladimir Rokhlin, and Stephen Wandzura. The fast multipole method: A pedestrian prescription. *IEEE Antennas and Propagation Society Magazine*, 35(3):7–12, June 1993.

[2] Lisa Hamilton, Mark Stalzer, R. Steven Turley, John Visher, and Stephen Wandzura. Method of moments scattering computations using high-order basis functions. In *IEEE Antennas and Propagation Society Symposium Digest*, volume 3, pages 1132–1135, Ann Arbor, MI, June 1993. IEEE.

[3] Lisa Hamilton, Vladimir Rokhlin, Mark Stalzer, R. Steven Turley, John Visher, and Stephen Wandzura. The importance of accurate surface models in RCS computations. In *IEEE Antennas and Propagation Society Symposium Digest*, volume 3, pages 1136–1139, Ann Arbor, MI, June 1993. IEEE.

A Multilevel Matrix Decomposition Algorithm For Analyzing Scattering From Large Structures

Eric Michielssen and Amir Boag
Electromagnetic Communication Laboratory
University of Illinois at Urbana-Champaign
Urbana, IL 61801
Tel : (217) - 333 3803 Fax : (217) - 333 8986
e-mail: michiels@decwa.ece.uiuc.edu

Abstract

A multilevel algorithm is presented for analyzing scattering from electrically large conducting and/or penetrable objects. The algorithm accelerates the iterative solution of integral equations that arise in computational electromagnetics. The algorithm permits a fast matrix-vector multiply by decomposing the traditional Method of Moment matrix into a large number of blocks, each describing the interaction between distant scatterers. The multiplication of each block with a trial solution vector is executed using a multilevel scheme that resembles an FFT and that only relies on well-known algebraic techniques. The computational complexity and the memory requirements of the proposed algorithm are $O(N \log^2 N)$. The algorithm is applicable to the analysis of scattering from two- and three-dimensional structures. To date, the algorithm has been successfully applied to the analysis of scattering from large, two-dimensional, perfectly conducting and dielectric scatterers.

1. Introduction.

Recently, the electromagnetics community has shown a renewed interest in iterative solvers as a means for solving very large scattering problems. A number of techniques has been proposed that permit a fast evaluation of a matrix-vector multiplication for matrices that arise in the Method of Moments (MoM) based solution of such problems. Therefore, these techniques may drastically reduce the computational cost associated with the iterative solution of large scattering problems. Examples include, but are not limited to, the Impedance Matrix Localization (IML) technique [1], the Complex Multipole Beam approach (CMBA) [2], the Fast Multipole Method (FMM) [3], and the Adaptive Integral Method (AIM) [4]. Both the IML and the CMBA rely on forming directive radiation beams by using special basis and testing functions and are limited in scope to scattering by sufficiently smooth bodies. The FMM and AIM rely on a multilevel geometrical partitioning of the scatterer and an expansion of the fields in terms of spherical harmonics, and are applicable to arbitrarily shaped scatterers.

It is well-known that a conventional MoM matrix contains all the information needed to solve a scattering problem. This served as our motivation for seeking methods that: (i) are applicable to arbitrary scatterers, (ii) rival the FMM and the AIM in efficiency, and (iii) make direct use of the MoM matrix elements in conjunction with commonly available algebraic techniques. Based upon these requirements we developed a Multilevel Matrix Decomposition Algorithm (MLMDA) [5, 6], that exploits the limited number of Degrees of Freedom (DoF) that characterize a field observed over a domain that is 'well-separated' from a source domain. In the MLMDA, a matrix-vector multiplication is performed by (i) subdividing the overall MoM matrix into a large number of submatrices, (ii) performing the required multiplication on each of these submatrices separately, and (iii) assembling the resulting sub-vectors into the sought after vector. Both the memory requirements and the computational complexity of the algorithm are $O(N \log^2 N)$, where N is the number of unknowns describing the current on the scatterer. The MLMDA evaluates the multiplication of the above mentioned submatrices with a trial solution vector

using an algorithm that resembles an FFT. The MLMDA can easily be incorporated into existing Method of Moment (MoM) programs.

This paper is organized as follows. Section 2 briefly outlines the proposed multilevel scheme. Sections 3 discusses the computational complexity of the proposed algorithm and compares it to other fast algorithms, notably the FMM and the AIM. Sections 4 and 5 describe numerical results and outline conclusions and suggestions for future work, respectively.

2. Formulation of the Multilevel Scheme.

This section outlines the proposed multilevel solver for a two-dimensional TM_z scattering problem. The algorithm can be generalized to solve two-dimensional TE_z and three-dimensional scattering problems with minor effort. The proposed multilevel algorithm relies on a multilevel geometrical decomposition of the scatterer and the corresponding MoM matrix and a multilevel multiplication algorithm for accelerating the matrix-vector product of the decomposed MoM matrix with a trial solution vector.

The multilevel decomposition of the scatterer is performed by enclosing the scatterer in a large (typically square) box and by recursively subdividing this box into smaller boxes. Starting from the coarsest box-discretization, all pairs of non-empty boxes that are geometrically non-adjacent to one another and whose parent boxes are touching one another, are identified at every level (Fig. 1). Each identified pair of boxes corresponds to a submatrix of the global MoM matrix (Fig. 2), and the multiplication of each of these submatrices with a trial solution vector is performed using a multilevel scheme outlined below. The multiplication of those portions of the MoM matrix that are not embedded in any of the identified submatrices, with a trial solution vector, is performed using direct multiplication.

Upon decomposing the MoM matrix into submatrices, the multiplication of a given submatrix with a trial solution vector is performed independently from that of all other submatrices using the three-stage algorithm outlined below and illustrated in Fig. 3.

During the first stage of the multiplication algorithm, each source in the source block is identified and replaced by equivalent sources that reside on the surface of the finest level box that encloses the source. These equivalent sources do not regenerate the fields radiated by the original sources everywhere in space. Rather, the excitation coefficients of these equivalent sources are chosen such that the field radiated by the equivalent sources equals that radiated by the original sources over the observation block. The number of equivalent sources is equal to the number of DoF, N_{dof}, that characterize the field in the observation block due to the actual sources that reside in each of the finest level blocks contained in the source block. It can be shown that [7, 8]:

$$N_{dof} \propto \frac{a_{source} a_{observation}}{r} + \ln\left(\frac{1}{\varepsilon}\right) \tag{1}$$

where a_{source} and $a_{observation}$ are the radii of the circles circumscribing the finest level source blocks and the observation block, r is the distance between the blocks, and ε the tolerated error in the field that is regenerated by the equivalent sources over the observation region. Upon estimating N_{dof}, equivalent sources, N_{dof} in number, are placed on the surface of each finest level non-empty box contained in the source box, and their excitation coefficients, I_{eq}, are computed from those of the original sources, I_{so}, using:

$$I_{eq} = (Z_1)^{\dagger} Z_2 I_{so} \tag{2}$$

where Z_1 is the MoM matrix describing the field due to the equivalent sources at a similarly selected set of N_{dof} observation points on the observation box, Z_2 is the MoM matrix describing the field due to the actual sources at these same N_{dof} observation points, and $\dagger$ denotes a Moore-Penrose pseudo inverse. At the end of the first stage, all sources in the source box corresponding to the submatrix have been replaced by equivalent sources residing on the surface of the finest level box that contains the source.

During the second stage of the execution of the multiplication algorithm, the finest level source blocks are recursively combined, while the observation block is recursively subdivided, until the original source block has been recovered and the finest level observation blocks contained in the observation block are reached. In doing so, the product of the number of non-empty source and observation regions considered at each level remains approximately constant. For each pair of non-empty source and observation regions considered at each level, a set of N_{dof} coefficients is computed which, when associated with the N_{dof} sources on the surface of the source box being considered, regenerate the field over the observation box being considered. The number of DoF of the fields considered at each level remains constant: as the size of the source region increases, the size of the observation regions being considered shrinks, and, by virtue of equation (1), N_{dof} remains constant. The excitation coefficients for each pair of source and observation regions at a given level are computed using equation (2), where the role of the actual sources is replaced by that of the equivalent sources considered at the previous level. At the end of the second stage, a large number of N_{dof} equivalent source excitation coefficients has been computed, each of which, when associated with the N_{dof} excitation coefficients on the source box, regenerates the original field in a different finest level observation box.

During the third stage of the multiplication algorithm, each of these sets of excitation coefficients is used to regenerate the fields due to all original sources contained in the source box at the observation points in the corresponding non-empty finest level box in the observation block.

The execution of the above three stages results in the butterfly-like submatrix-vector multiplication scheme that exhibits a resemblance to the well-known FFT algorithm.

3. Computational Complexity and Comparison to Other Techniques.

The computational complexity of the MLMDA is $O(N\log^2 N)$. Let C_1 denote the cost of multiplying the submatrices describing coarsest level interactions. It is easily verified that $C_1 \propto N\log N$. The cost C_2 of multiplying those blocks describing interactions at the next to coarsest level is proportional to C_1: although the cost of multiplying a single submatrix with a trial solution vector is only halve of that at the coarsest level, there are twice as many non-empty blocks at the next to coarsest level, and, hence, $C_2 \propto C_1$. A similar reasoning holds true for all subsequent levels, and since there are $\log N$ levels the overall cost of the algorithm becomes $O(N\log^2 N)$. It is easily verified that the memory requirements of the algorithm are also $O(N\log^2 N)$. The computational cost associated with the evaluation of fields due to near neighbors, and the storage requirements associated with this operation, are both $O(N)$ and hence subdominant to computational and storage costs associated with the evaluation of the field due to distant sources.

The MLMDA exhibits similarities with the FMM, especially with the ray-propagation version (RPFMA) developed by Wagner and Chew [9]. When compared to the FMM and RPFMA, the MLMDA augments a traditional MoM code solely by well-known algebraic techniques. Hence, the MLMDA is straightforward to implement and the differences between two- and three-dimensional implementations of the MLMDA are minimal. The computational complexity of the multilevel FMM (MLFMM) is $O(N\log^2 N)$ but can decrease to $O(N\log N)$ for very large scatterers [10]. In contrast, the computational complexity of the MLMDA cannot decrease below $O(N\log^2 N)$. This is a direct consequence of the non-recyclable nature of the MLMDA when compared to MLFMM. The MLMDA also exhibits similarities with the AIM [4]. Like the AIM, the MLMDA represents distant fields due to sources residing on the scatterer in terms of those due to sources residing on a regular grid. However,

in contrast to the AIM, which exhibits a computational complexity of $O(N^{1.5}\log N)$ for two-dimensional surface scatterers, the MLMDA does not perform an FFT on the entire grid, which results in a more favorable computational complexity for the MLMDA.

4. Numerical Results.

This section summarizes sample results obtained using an implementation of the above described algorithm for the analysis of TM_z scattering from perfectly conducting and coated strip-like structures. Numerical results obtained using the MLMDA for the TE_z polarization will be described in an forthcoming paper.

Consider the conducting L-shaped profile and its coated version shown in Figures 4a and 4b. Each side of the profile measures $l\,\lambda_o$, the total length of the profile therefore is $2\,l\,\lambda_o$. The coating consists of a perfect dielectric of permittivity ε_r=4 and thickness t=0.05 λ_o. The pec strip was modeled using 10 unknowns per wavelength, and the polarization current in the coating was modeled using a single layer of volumetric cells. The structure is illuminated by a TM_z plane wave as shown in Fig. 4. The CPU-time requirements for solving this scattering problem using the MLMDA are shown in Figure 5 as a function of N. The maximum number of unknowns used to solve this scattering problem was N=16,384, however, we have analyzed structures with up to 50,000 unknowns using the MLMDA. The graph also indicate the number of levels used in the analysis, the maximum being 10. All analysis were performed on a SUN SPARC 10 Workstation. The conduction and polarization currents (not shown) are in perfect agreement with those obtained using a standard MoM program up to N=4192, beyond this point the direct solver becomes impractical on the workstation. Analysis of the data reveals that the memory requirements and the CPU-time closely tracks the theoretical $O(N\log^2 N)$ trend. Although no formal analysis of error propagation of the algorithm has been developed, the algorithm has proven to be stable for all investigated cases.

5. Conclusions.

A multilevel matrix decomposition algorithm was presented for analyzing scattering from electrically large, conducting and/or penetrable, objects. The algorithm permits a fast matrix-vector multiply by decomposing the traditional MoM matrix into a large number of blocks, each of which describes the interaction between distant scatterers. The multiplication of each block with a trial solution vector is executed using a multilevel scheme that resembles an FFT and that only relies on well-known algebraic techniques. Fields due to nearby sources are evaluated directly. The computational complexity and the memory requirements of the proposed algorithm are $O(N\log^2 N)$. The algorithm is applicable to the scattering analysis of both two- and three-dimensional structures. Numerical results obtained for two-dimensional scatterers have demonstrated the usefulness of the proposed approach. A three-dimensional version of the algorithm is currently being implemented and applied to the analysis of scattering from large free-standing structures and structures embedded in a multilayered medium.

References.

[1] F. X. Canning, "A new combined field integral equation for impedance matrix localization (IML)," in *IEEE-AP/S International Symposium*, 1993, Ann Arbor.

[2] A. Boag and R. Mittra, "Complex multipole beam approach to electromagnetic scattering problems," *IEEE Trans. Antennas Propagat.*, vol. 42, 1994.

[3] R. Coifman, V. Rohklin, and S. Wandzura, "The fast multipole method for the wave equation: a pedestrian prescription," *IEEE Atn. Propag. Mag.*, vol. 35, pp. 7-12, 1993.

[4] E. Bleszynski, M. Bleszynski, and T. Jaroszewicz, "A fast integral-equation solver for electromagnetic scattering problems," in *IEEE Int. Conf. AP-S*, pp. 416-419, 1994, Seattle, WA.

[5] E. Michielssen and A. Boag, "Multilevel evaluation of scattered fields," *Micr. and Opt. Tech. Lett.*, to appear, 1994.

[6] E. Michielssen and A. Boag, "Reduced representations of matrices generated by the method of moments," in *IEEE Int. Conf. AP-S*, pp. 420-423, 1994, Seattle, WA.

[7] G. T. D. Francia, "Degrees of Freedom of an Image," *J. Opt. Soc. Am.*, vol. 59, pp. 779-804, 1969.

[8] O. M. Bucci and G. Franceschetti, "On the degrees of freedom of scattered fields," *IEEE Trans. Antennas Propagat.*, vol. 37, pp. 918-926, 1989.

[9] R. L. Wagner and W. C. Chew, "A ray-propagation fast multipole algorithm," *Micr. Opt. Tech. Lett*, Vol. 7, No. 10, pp. 435-438, 1994.

[10] C. C. Lu and W. C Chew, "A multilevel algorithm for solving boundary integral equation of wave scattering," *Micr. and Opt. Tech. Lett.*, Vol. 7, No. 10, pp. 466-470, 1994

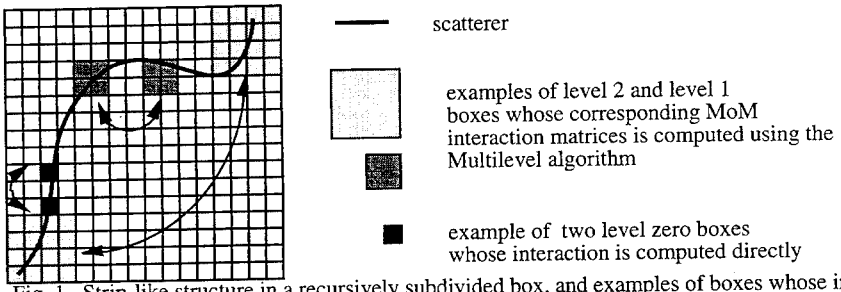


Fig. 1. Strip-like structure in a recursively subdivided box, and examples of boxes whose interactions are computed using the multilevel algorithm.

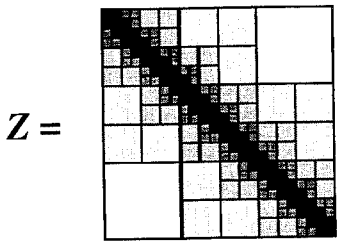


Fig. 2. Example of a decomposed matrix for a flat strip structure.

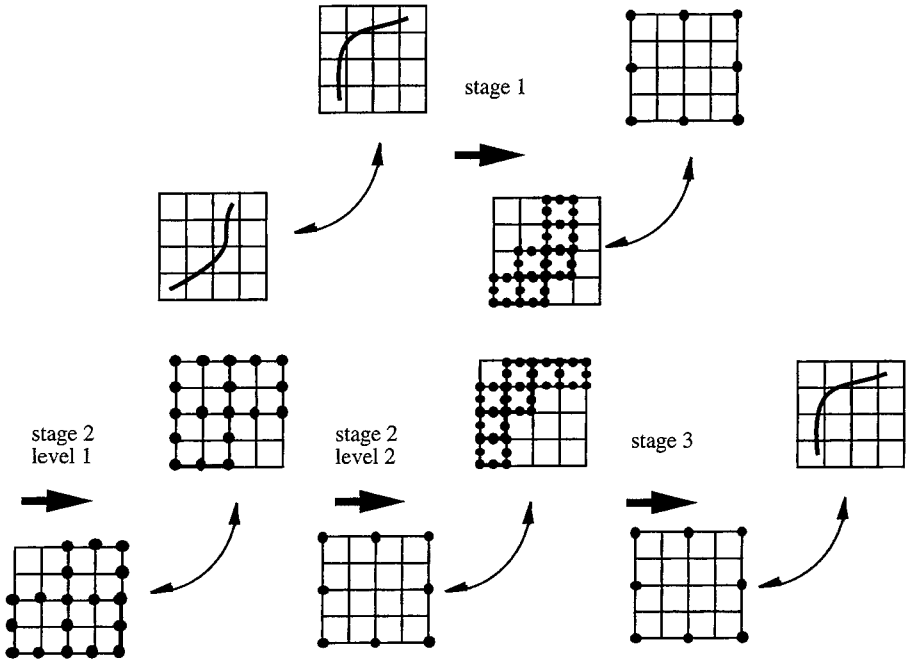


Fig. 3. Multiplication of a submatrix describing the interaction between two distant subsections of the scatterer using MLMDA. During stage 1, the actual sources are replaced by equivalent sources on a regular grid, during stage 2, a multilevel scheme replaces these sources by equivalent sources on a coarser grid while shrinking the corresponding observation domain, and during stage 3 the fields due to each set of equivalent sources is computed at the respective observers.

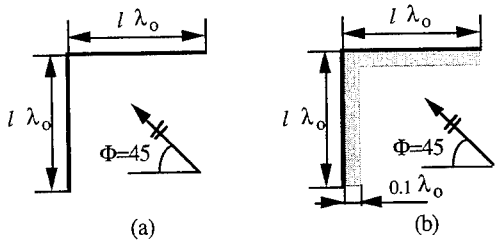


Fig. 4. Uncoted and coated L-shaped profiles.

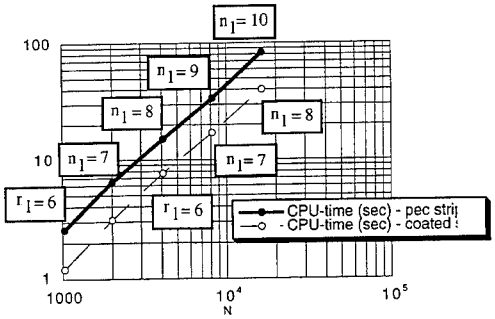


Fig. 5. CPU-time per iteration for MLMDA for the pec strip and coated strip shown in Figs 4a and 4b, respectively.

A 3D Fast Multipole Method for Electromagnetics with Multiple Levels

Ben Dembart and Elizabeth Yip
P.O. Box 3999 Mail Stop 7L-21
The Boeing Company
Seattle, WA 98124

1 Introduction

The fast multipole method is no longer new, and several implementations have been discussed in the literature for accelerating method of moments calculations. See for example [1], [2], and [3] for 2–D implementations, and [4], and [5] for 3–D implementations. In [3] a 2–D multilevel implementation is discussed, the other articles discuss one level implementations.

The general principals are now quite well understood. The addition theorem for spherical Bessel functions provides a mechanism for translating the origin of multipole expansions. Translation allows us to take several multipole expansions and translate them to a common reference frame and then to aggregate them into a single expansion. It is the aggregation of expansions that ultimately provides the speedup.

The objective of this paper is to address the difficulties that arise when a multilevel implementation is attempted.

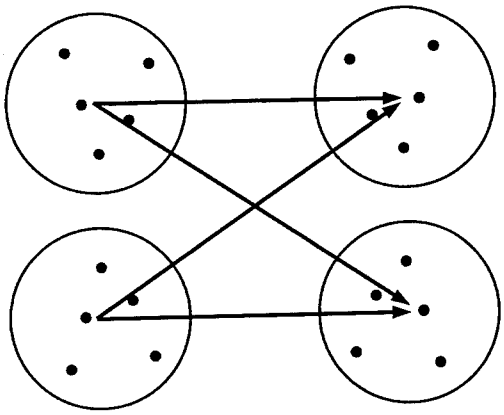
2 One Level FMM

When FMM is implemented with one level the N unknown sources are divided into approximately $N^{1/2}$ clusters with approximately $N^{1/2}$ sources in each cluster. The outer multipole expansion for each cluster will have $O\left(N^{1/2}\right)$ coefficients. The complexity of computing an outer multipole expansion for each source centered at its cluster center is $O\left(N^{1/2}\right)$ making the complexity of computing all outer expansions $O\left(N^{3/2}\right)$.

After the outer expansions have been computed for each cluster, inner expansions are computed as shown in figure 1. The complexity of computing an inner expansion centered at a remote cluster, when both outer expansion and inner expansion have $O\left(N^{1/2}\right)$ coefficients is $O(N)$. Since $O(N)$ of these translations are required this results in a complexity of $O\left(N^2\right)$ for the translation process. This is too high for a fast method.

The solution to this problem was provided by Rokhlin in [6]. Rokhlin showed that one could use the radiation function instead of the multipole expansion, and that this reduced the complexity of the translation to $O\left(N^{1/2}\right)$, making the complexity of the entire translation process $O\left(N^{3/2}\right)$.

Figure 1 One Level FMM



3 The Radiation Function

The concept of the radiation function is not new. It is well known that the radiation function of a scattered field uniquely defines the field [7], but the use of the radiation function to accelerate calculations is novel.

If the scattered field is defined by an outer multipole expansion

$$O(r,\theta,\phi) = \sum_{n=0}^{P} \sum_{m=-n}^{n} O_n^m h_n(kr) Y_n^m(\theta,\phi)$$

then the outer radiation function is given by

$$\widehat{O}(\theta,\phi) = \sum_{n=0}^{P} \sum_{m=-n}^{n} (-i)^{n+1} O_n^m Y_n^m(\theta,\phi) = \lim_{r\to\infty} r \cdot e^{-ikr} \cdot O(r,\theta,\phi)$$

The radiation function is a function defined on the unit sphere, and it is convenient to use the notation $O(\hat{s})$ where $\hat{s}$ is any unit vector (i.e. $\hat{s}$ lies on the unit sphere). For the purpose computation, a finite array of points, $\hat{s}_1, \ldots, \hat{s}_k$ are selected and the array of values $O(\hat{s}_1), \ldots, O(\hat{s}_k)$ is the radiation function. The number and location of the points in the array must be selected so that it is possible to reconstruct the multipole coefficients O_n^m from the radiation function. In particular this means that the number of multipole coefficients must not exceed the number of points in the radiation function.

$$k \geq (P+1)^2$$

If the field inside a region is given by the inner multipole expansion

$$I(r,\theta,\phi) = \sum_{n=0}^{P} \sum_{m=-n}^{n} I_n^m j_n(kr) Y_n^m(\theta,\phi)$$

then the inner radiation function is given by

$$\widehat{I}(\theta,\phi) = \sum_{n=0}^{P} \sum_{m=-n}^{n} (-i)^{n+1} I_n^m Y_n^m(\theta,\phi)$$

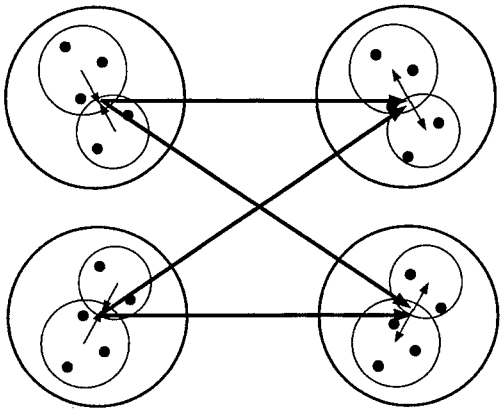
To the best of our knowledge the inner radiation function was invented by Rokhlin [6] and has no obvious physical interpretation.

The advantage provided by using the radiation function instead of the multipole expansion is that computing the inner radiation function from an outer radiation function is quite simple, and has a computational complexity of $\mathbf{O(k)}$.

4 Two Level FMM

When FMM is implemented with two levels the N unknown sources are divided into approximately $\mathbf{N^{2/3}}$ clusters with approximately $\mathbf{N^{1/3}}$ sources in each cluster. Then the clusters are grouped with about $\mathbf{N^{1/3}}$ clusters in each group. The outer radiation function for each cluster will have $\mathbf{O\left(N^{1/3}\right)}$ array values, and the complexity of computing the radiation function is $\mathbf{O\left(N^{1/3}\right)}$ for each source point, or $\mathbf{O\left(N^{2/3}\right)}$ for each cluster, or $\mathbf{O\left(N^{4/3}\right)}$ for the entire problem.

Figure 2 Two Level FMM



The next step is to translate the radiation function for each cluster to the center of its parent group (see figure 2). The outer radiation function for each group will require $\mathbf{O\left(N^{2/3}\right)}$ array values. Thus the radiation functions will have to be interpolated to a denser grid before they can be translated and aggregated. This interpolation process maps an array of length $\mathbf{O\left(N^{1/3}\right)}$ into an array of length $\mathbf{O\left(N^{2/3}\right)}$ and requires $\mathbf{O(N)}$ operations unless a fast algorithm can be found. Since $\mathbf{O\left(N^{2/3}\right)}$ of these interpolations are required an $\mathbf{O(N)}$ interpolation algorithm would result in an $\mathbf{O\left(N^{5/3}\right)}$

complexity for this stage of FMM, making it more complex than the one level algorithm. Clearly if an overall complexity of $\mathbf{O}\left(\mathbf{N^{4/3}}\right)$ is to be achieved, an $\mathbf{O}\left(\mathbf{N^{2/3}}\right)$ interpolation algorithm is required. No such algorithm has been published to out knowledge, and we will not be presenting one here. However, we will present an interpolation algorithm for interpolating from an array of length k to an array of length $\bar{k}$ with complexity $\mathbf{O}\left(\bar{k}\right)\log\left(\bar{k}\right)$.

Once the outer radiation functions have been computed for each group they are used to compute inner radiation functions for each remote group. The complexity is $\mathbf{O}\left(\mathbf{N^{2/3}}\right)$ per translation with $\mathbf{O}\left(\mathbf{N^{2/3}}\right)$ translations required giving an overall complexity of $\mathbf{O}\left(\mathbf{N^{4/3}}\right)$ for this step.

The next step is to take the inner radiation function for each group and to translate it to the center of each cluster the group contains (see figure 2). The group inner radiation functions contain $\mathbf{O}\left(\mathbf{N^{2/3}}\right)$ array values, the cluster inner radiation functions require only $\mathbf{O}\left(\mathbf{N^{1/3}}\right)$ array values. After the radiation functions have been translated it is necessary to reduce the grid density from $\mathbf{O}\left(\mathbf{N^{2/3}}\right)$ back to $\mathbf{O}\left(\mathbf{N^{1/3}}\right)$. If this is not done the next step will have a complexity that exceeds $\mathbf{O}\left(\mathbf{N^{4/3}}\right)$. Reducing the grid density requires removing the high harmonics from the radiation function and then regriding on a courser grid. Removing the high harmonics is necessary before regriding to avoid aliasing. This process of removing the high harmonics and regriding is called filtering. The filtering process is a mapping from an array of $\mathbf{O}\left(\mathbf{N^{2/3}}\right)$ points to an array of $\mathbf{O}\left(\mathbf{N^{1/3}}\right)$ points and must be accomplished with complexity $\mathbf{O}\left(\mathbf{N^{2/3}}\right)$ to achieve an overall complexity of $\mathbf{O}\left(\mathbf{N^{4/3}}\right)$. No filtering algorithm has been published to out knowledge either. We will present an algorithm for filtering an array of length $\bar{k}$ to an array of length k with complexity $\mathbf{O}\left(\bar{k}\log\left(\bar{k}\right)\right)$.

The final step is, for each source point, to translate the inner radiation function of its cluster to it's location, and then to integrate. There are $\mathbf{N}$ source points, and if the inner radiation functions contain $\mathbf{O}\left(\mathbf{N^{1/3}}\right)$ array values then the complexity of this step is $\mathbf{O}\left(\mathbf{N^{4/3}}\right)$.

Thus in order to achieve an $\mathbf{O}\left(\mathbf{N^{4/3}}\right)$ algorithm it is necessary to be able to interpolate from an $\mathbf{O}\left(\mathbf{N^{1/3}}\right)$ array to an $\mathbf{O}\left(\mathbf{N^{2/3}}\right)$ array in $\mathbf{O}\left(\mathbf{N^{2/3}}\right)$ operations, and to filter an $\mathbf{O}\left(\mathbf{N^{2/3}}\right)$ array in $\mathbf{O}\left(\mathbf{N^{2/3}}\right)$ operations.

5 Interpolation and Filtering

Interpolation can be defined as follows. Given a radiation function of degree P on a grid $\hat{r}_1,\ldots,\hat{r}_k$ with $k \geq (P+1)^2$, evaluate the radiation function on a new grid $\hat{\bar{s}}_1,\ldots,\hat{\bar{s}}_{\bar{k}}$ with $\bar{k} \geq k$.

Filtering can be defined as follows. Given a radiation function of degree P on a grid $\hat{r}_1,\ldots,\hat{r}_k$ with $k \geq (P+1)^2$, remove all harmonics $n > \bar{P}$ and then evaluate the radiation function on a new grid $\hat{\bar{s}}_1,\ldots,\hat{\bar{s}}_{\bar{k}}$ with $k \geq \bar{k} \geq \left(\bar{P}+1\right)^2$. Either operation can be accomplished by first computing the required multipole expansion coefficients, and then evaluating the radiation function on the new grid.

Given a radiation function F, its multipole coefficients can be computed by

$$F_n^m = \frac{2n+1}{4\pi} \int_{\mathbf{S}} Y_n^{-m}(\hat{r}) F(\hat{r}) da$$

where $\mathbf{S}$ is the unit sphere [8](2.16). Then if we let $\Omega = P$ for interpolation or $\Omega = \bar{P}$ for filtering we get

$$\bar{F}(\hat{s}) = \sum_{n=0}^{\Omega} \sum_{m=-n}^{n} F_n^m Y_n^m(\hat{s}) = \frac{1}{4\pi} \int_{\mathbf{S}} F(\hat{r}) \sum_{n=0}^{\Omega} (2n+1) \sum_{m=-n}^{n} Y_n^{-m}(\hat{r}) Y_n^m(\hat{s}) da_{\hat{r}}$$

$$= \frac{1}{4\pi} \int_{\mathbf{S}} F(\hat{r}) \sum_{n=0}^{\Omega} P_n(\hat{r} \cdot \hat{s}) da_{\hat{r}} \tag{1}$$

$$= \frac{1}{4\pi} \int_{\mathbf{S}} F(\hat{r}) \delta_{\Omega}(\hat{r} \cdot \hat{s}) da_{\hat{r}}$$

where

$$\delta_{\Omega}(x) = \frac{P_{\Omega+1}(x) - P_{\Omega}(x)}{x-1}$$

These equalities follow from the addition theorem for spherical harmonics and the Christoffel-Darboux formula for Legendre polynomials.

Thus both interpolation and filtering are simple integral transforms, and we seek yet another fast integral transform.

6 Fast Interpolation and Filtering

Fast algorithms can be developed for interpolation and filtering by exploiting the symmetry of the integral transform (1). The kernel of the transform is $\delta_{\Omega}(\hat{r} \cdot \hat{s})$. If U is any real unitary transformation in 3 dimensions (i.e. a rotation and/or refection) then $(U\hat{r}) \cdot (U\hat{s}) = \hat{r} \cdot \hat{s}$. Thus the symmetry of rotation and reflection can be exploited to accelerate interpolation and filtering.

The first step is to select a finite symmetry group G which is a subgroup of $O(3)$. G is a group of 3x3 real orthogonal matrices. The next step is to replace (1) with a quadrature rule that is symmetric with respect to G. If the order of the group G is $\mathbf{Q}$, such a rule has the form

$$\int_{S} F(\hat{r}) da_{\hat{r}} = \sum_{j=1}^{k} w_j \sum_{U \in G} F(U' \hat{r}_j)$$

The $k \cdot \mathbf{Q}$ quadrature points are given by $U'\hat{r}_j$ where $1 \leq j \leq k$ and $U \in G$. The weights are w_j.

The rule must be of sufficiently high order to give exact results. Since in (1) F has order $\mathbf{P}$ and δ_{Ω} has order Ω the rule must have order $\mathbf{P} + \Omega \leq 2\mathbf{P}$. In [9] McLaren shows how to develop efficient quadrature rules that are consistent with symmetry groups of rotations and reflections in three dimensions.

When symmetry is being exploited it is efficient to represent radiation functions as rectangular arrays of values with $\mathbf{Q}$ columns and k rows.

$$F_{jU} = F\left(U'\widehat{\tau}\right)$$

If we wish to interpolate or filter to a new grid defined by $\widehat{\bar{s}}_1, \ldots, \widehat{\bar{s}}_{\bar{k}}$ and G then (1) reduces to (see [10])

$$\begin{aligned} \bar{F} &= \frac{1}{4\pi}\left[\sum_{U\in G} \boldsymbol{\Delta}^U \otimes R_U\right][W \otimes I]F \\ &= \frac{1}{4\pi}[I \otimes T]\left[\sum_{U\in G} \boldsymbol{\Delta}^U \otimes T^{-1}R_U T\right]\left[W \otimes T^{-1}\right]F \end{aligned} \tag{2}$$

where

$$\boldsymbol{\Delta}^U_{ij} = \delta_\Omega\left(\widehat{\bar{s}}_i \cdot U'\widehat{\tau}_j\right)$$

The similarity transformation $T^{-1}R_U T$ transforms each of the regular representations R_U to block diagonal form, significantly reducing the complexity.

This approach can be applied to the groups of rotations and reflection associated with the regular polyhedra, or to the groups of rotations about the polar axis $\mathbf{C_Q}$ or $\mathbf{C_{Qh}}$ (without or with reflection about the equator).

7 Symmetry Groups of the Regular Polyhedra

The groups in this category are the tetrahedral group $\mathbf{T}$ with order 12, $\mathbf{T_d}$ with order 24, the octahedral group $\mathbf{O}$ with order 24, $\mathbf{O_d}$ with order 48, the icosahedral group $\mathbf{I}$ with order 60, and $\mathbf{I_d}$ with order 120 (see [10]).

When equation (2) is implemented using one of these groups the computational complexity is $O\left(k^2\mathbf{Q}\right) = O\left((k\mathbf{Q})^2\right)/\mathbf{Q}$. Note that $k\mathbf{Q}$ is the number of values in the radiation function, and the group order $\mathbf{Q}$ is a constant. Thus there is no theoretical reduction in the computational complexity of $O\left((\#values)^2\right)$, but there is a significant reduction in the constant (by a factor of 120 for $\mathbf{I_d}$).

In spite of the high theoretical complexity, the practical advantage of a very low constant probably makes this the method of choice for interpolating and filtering radiation functions with degree less than 40. This implies scatters with diameters around 6 wave lengths.

We have not yet implemented this approach.

8 The Groups $\mathbf{C_Q}$ and $\mathbf{C_{Qh}}$

These groups have three advantages over the groups in the previous section. First, groups of arbitrarily high order can be achieved by selecting $\mathbf{Q}$ to be large. Quadrature rules of sufficiently high order can be found with $\mathbf{Q} \approx k$, so the computational complexity for filtering and interpolation becomes $\mathbf{O}\left(k^2\mathbf{Q}\right) = \mathbf{O}\left((k\mathbf{Q})^{3/2}\right) = \mathbf{O}\left((\#values)^{3/2}\right)$. Second, the transformation T in equation (2) reduces to the discrete Fourier transform for $\mathbf{C_Q}$ and $\mathbf{C_{Qh}}$, and thus operations involving T or T^{-1} can be performed in $\mathbf{O}(\mathbf{Q}\log(\mathbf{Q}))$ operations, and furthermore $T^{-1}R_U T$ is diagonal. Third, because $\mathbf{C_Q}$ is

a subgroup of $\mathbf{C_{2Q}}$ it is easy to change groups as the FMM calculation proceeds from level to level, making this approach well suited for multilevel FMM.

Interpolation and filtering based on the groups $\mathbf{C_Q}$ or $\mathbf{C_{Qh}}$ provide a theoretical improvement in the computational complexity of FMM. Using this algorithm two level FMM has a complexity of $\mathbf{O}\left(\mathbf{N^{5/3}}\right)$, and multilevel FMM has a complexity of $\mathbf{O}\left(\mathbf{N^{3/2}}\right)$. Thus multilevel FMM and one level FMM have the same order of complexity. However, the constant is significantly lower for multilevel FMM.

This approach to filtering and interpolation has been implemented and proven to work.

9 Faster than Fast

When using the group $\mathbf{C_Q}$ or $\mathbf{C_{Qh}}$ the term in equation (2)

$$\sum_{U\in G} \mathbf{\Delta}^U \otimes T^{-1} R_U T$$

can be shown [11] to take the form

$$\sum_{U\in G} \mathbf{\Delta}^U \otimes T^{-1} R_U T = \begin{bmatrix} \widetilde{\mathbf{\Delta}}^{(0)} & & & \\ & \widetilde{\mathbf{\Delta}}^{(1)} & & \\ & & \ddots & \\ & & & \widetilde{\mathbf{\Delta}}^{(\mathbf{Q}-1)} \end{bmatrix} \tag{3}$$

where

$$\widetilde{\mathbf{\Delta}}^{(q)}_{ij} = 4\pi \mathbf{Q} \frac{P^q_\Omega(\bar{z}_i) P^q_{\Omega-1}(z_j) - P^q_{\Omega-1}(\bar{z}_i) P^q_\Omega(z_j)}{\bar{z}_i - z_j} \tag{4}$$

where $\bar{z}_i$ and z_j are the z-axis components of $\widehat{\bar{s}}_i$ and $\widehat{r}_j$ respectively.

The matrix $\widetilde{\mathbf{\Delta}}^{(q)}$ is k by k, but its action can be computed in $\mathbf{O}(k)$ operations by expanding

$$\frac{1}{\bar{z}_i - z_j} = \frac{1}{(\bar{z}_i - z_0) - (z_j - z_0)} = \frac{1}{\bar{z}_i - z_0} \cdot \frac{1}{1 - \frac{z_j - z_0}{\bar{z}_i - z_0}}$$
$$= \frac{1}{\bar{z}_i - z_0} \cdot \sum_l \left(\frac{z_j - z_0}{\bar{z}_i - z_0} \right)^l$$

This is just a multipole expansion in one dimension and converges rapidly if $\frac{z_j - z_0}{\bar{z}_i - z_0} << 1$. Using this approach multiplication by $\widetilde{\mathbf{\Delta}}^{(q)}$ is reduced to $\mathbf{O}(k)$ and the complexity of the entire interpolation or filtering process is $k\mathbf{Q}\log(\mathbf{Q}) + \mathbf{O}(k\mathbf{Q})$.

Although this algorithm has a superior complexity, the constant associated with the $\mathbf{O}(k\mathbf{Q})$ term is sufficiently high that it will not be effective until the degree of the radiation functions exceeds 200, or the scatter is larger than 30 wavelengths.

This approach reduces the computational complexity of two level FMM to $\mathbf{O}\left(\mathbf{N^{4/3}}\log(\mathbf{N})\right)$ and multilevel FMM to $\mathbf{O}\left(\mathbf{N}\log(\mathbf{N})^2\right)$

This algorithm is currently being implemented.

10 Conclusions

In order to have a fast multilevel implementation of the fast multipole method one needs to use radiation functions of different orders at the different levels. This requires an interpolation operation to increase order going from small source clusters to large clusters. A filtering operation is also required going from large clusters of field points to small clusters. These two operations are very similar and they can be performed with a common algorithm. If a quadrature rule with a sufficiently high order is used equation (2) is an exact representation of that algorithm.

Equation (2) exhibits symmetry and that symmetry can be exploited to accelerate the algorithm. Equations (3) and (4) show how the symmetry group C_Q or C_{Qh} can be used to reduce the complexity of multilevel FMM to $O\left(N \log (N)^2\right)$. These algorithms are exact in that they give the same results as would be achieved by using truncated multipole expansions instead of radiation functions.

Ultimately we expect that approximate algorithms will emerge that are faster than the exact algorithms discussed in this paper. When those approximate algorithms are proposed it will be necessary to have exact algorithms such as those presented here so that the "degree of approximation" of the algorithm can be assessed.

Bibliography

[1] V. Rokhlin. Rapid solution of integral equations of scattering theory in two dimensions. *J. Comp. Phys., Vol. 86, No. 2*, Feb. 1990.

[2] N. Engheta, W. D. Murphy, V. Rokhlin, and M. S. Vassiliou. The fast multipole method (fmm) for electromagnetic scattering problems. *IEEE Trans. Antennas Propagat.,Vol. AP-40, No. 6*, June 1992.

[3] C-C. Lu and W. C. Chew. A multilevel algorithm for solving a boundary integral equation of wave scattering. *Microwave Opt. Technol. Lett., Vol. 7 No. 10*, July 1994.

[4] R. Coifman, V. Rokhlin, and S. Wandzura. The fast multipole method for the wave equation: A pedestrian prescription. *IEEE Antennas Propagat. Mag., Vol 35, No. 3*, June 1993.

[5] J. M. Song and W. C. Chew. Fast multipole method solution using parametric geometry. *Microwave Opt. Technol. Lett., Vol. 7, No. 16*, Nov. 1994.

[6] V. Rokhlin. Diagonal form of translation operators for the helmholtz equation in three dimensions. Technical report, YALEU/DCS/RR-894, March 1992.

[7] C. Muller. *Foundations of the Mathematical Theory of Electromagnetic Waves*. Springer-Verlag, 1969.

[8] M. Epton and B. Dembart. Multipole translation theory for the 3-d lapalce and helmholtz equations. *SIAM J Appl. Math., Vol. 16, No. 4*, (to appear) July 1995.

[9] A. D. McLaren. Optimal numerical integration on a sphere. *Math. Comp. Vol. 17*, 1963.

[10]Michael Tinkham. *Group Theory and Quantum Mechanics*. McGraw-Hill, 1964.

[11]M. Epton. Private communication. .

FAST MULTIPOLE METHOD SOLUTION OF COMBINED FIELD INTEGRAL EQUATION †

J. M. Song and W. C. Chew
Electromagnetics Laboratory
Department of Electrical and Computer Engineering
University of Illinois
Urbana, IL 61801

ABSTRACT— The electromagnetic (EM) scattering from three-dimensional (3D) conducting bodies has been studied. The electric field integral equation (EFIE), magnetic field integral equation (MFIE), and combined field integral equation (CFIE) are approximated by matrix equations using the method of moments (MOM). The fast multipole method (FMM) has been implemented to speed up the matrix-vector multiply in the CG method when it is used to solve EFIE, MFIE, and CFIE. FMM reduces the complexity of a matrix-vector multiply from $O(N^2)$ to $O(N^{1.5})$. With a multilevel fast multipole algorithm (MLFMA), the complexity is further reduced to $O(N\log N)$.

1. Introduction

The EM field scattering by arbitrarily shaped conductor can be obtained by finding the solution of an integral equation where the unknown function is the induced current distribution. The integral equation is discretized into a matrix equation by the method of moments (MOM). The resultant matrix equation is then solved by Gaussian elimination, which requires $O(N^3)$ floating-point operations if Gaussian elimination is used to solve N linear equations, or $O(N^2)$ operations per iteration if the conjugate gradient (CG) method is used.

The fast multipole method (FMM) [1-6] speeds up the matrix-vector multiply in the conjugate gradient (CG) method when it is used to solve the matrix equation iteratively. In this paper, FMM is applied to solve the electromagnetic scattering from three dimensional arbitrary shape conducting bodies. The electric field integral equation (EFIE), magnetic field integral equation (MFIE), and combined field integral equation (CFIE) are considered. FMM formula for CFIE has been derived, which reduces the complexity of a matrix-vector multiply from $O(N^2)$ to $O(N^{1.5})$, where N is the number of unknowns. With a nonnested method, using the ray-propagation fast multipole algorithm (RPFMA) [5,6], the cost of a FMM matrix-vector multiply is reduced to $O(N^{4/3})$. We have implemented a multilevel fast multipole algorithm (MLFMA), whose complexity is further reduced to $O(N\log N)$. The FMM also requires less memory, and hence, can solve a larger problem on a small computer.

2. The Combined Field Integral Equation (CFIE)

Practical electromagnetic problems are often three-dimensional and involve arbitrary geometry. The arbitrary surface is described by dividing it into a number of connected patches which are mathematically described as parametric quadratic surfaces [6,7]. For conducting objects, the electric field integral equation (EFIE) is given by

† This work was supported by NASA under grant NASA NAG 2-871, Office of Naval Research under grant N00014-89-J1286, the Army Research Office under contract DAAL03-91-G-0339, and the National Science Foundation under grant NSF ECS 92-24466.

$$\hat{t} \cdot \int_S \overline{\mathbf{G}}(\mathbf{r}, \mathbf{r}') \cdot \mathbf{J}(\mathbf{r}') dS' = \frac{4\pi i}{k\eta} \hat{t} \cdot \mathbf{E}^i(\mathbf{r}), \tag{1}$$

for $\mathbf{r}$ on surface S, where $\hat{t}$ is any unit tangent vector on S, and

$$\overline{\mathbf{G}}(\mathbf{r}, \mathbf{r}') = (\overline{\mathbf{I}} - \frac{1}{k^2} \nabla\nabla') g(\mathbf{r}, \mathbf{r}'), \tag{2}$$

$$g(\mathbf{r}, \mathbf{r}') = \frac{e^{ikR}}{R}, \quad R = |\mathbf{r} - \mathbf{r}'|. \tag{3}$$

For closed conducting objects, the magnetic field integral equation (MFIE) is given by

$$2\pi \mathbf{J}(\mathbf{r}) - \hat{n} \times \nabla \times \int_S dS' g(\mathbf{r}, \mathbf{r}') \mathbf{J}(\mathbf{r}') = 4\pi \hat{n} \times \mathbf{H}^i(\mathbf{r}) \tag{4}$$

for $\mathbf{r}$ approaches to S from outside, where $\hat{n}$ is an outwardly directed normal. MFIE (4) can be written as

$$2\pi \hat{t} \cdot \mathbf{J}(\mathbf{r}) - \hat{t} \cdot \hat{n} \times \nabla \times \int_s dS' g(\mathbf{r}, \mathbf{r}') \mathbf{J}(\mathbf{r}') = 4\pi \hat{t} \cdot \hat{n} \times \mathbf{H}^i(\mathbf{r}). \tag{5}$$

Then combined field integral equation (CFIE) for closed conducting objects is simply a linear combination of EFIE (1) and MFIE (5) and is of the form:

$$\alpha \text{EFIE} + (1 - \alpha) \frac{i}{k} \text{MFIE}. \tag{6}$$

The combination parameter α ranges from 0 to 1 and can be chosen to be any value within this range. It is found $\alpha = 0.2$ to be an overall good choice.

Let us apply the method of moments (MOM) to the CFIE. The unknown current $\mathbf{J}(\mathbf{r})$ is first expanded in an appropriately chosen set of basis functions $\{\mathbf{j}_i\}$. The CFIE for $\mathbf{J}(\mathbf{r})$ is discretized by substituting the expansion in terms of unknowns a_n. Then, rather than forcing the CFIE to be satisfied for $\mathbf{r}$ approaching S from the outside, it is multiplied by a set of N testing functions $\{\mathbf{t}_j\}$ and the inner products are taken:

$$\sum_{i=1}^{N} A_{ji} a_i = F_j, \qquad j = 1, 2, \cdots, N, \tag{7}$$

where

$$\begin{aligned} A_{ji} = {} & \alpha \int_S dS \mathbf{t}_j(\mathbf{r}) \cdot \int_S dS' \overline{\mathbf{G}}(\mathbf{r}, \mathbf{r}') \cdot \mathbf{j}_i(\mathbf{r}') \\ & + (1 - \alpha) \left[\frac{2\pi i}{k} \int_S dS \mathbf{t}_j(\mathbf{r}) \cdot \mathbf{j}_i(\mathbf{r}) - \frac{i}{k} \int_S dS \mathbf{t}_j(\mathbf{r}) \cdot \hat{n} \times \nabla \times \int_S dS' g(\mathbf{r}, \mathbf{r}') \mathbf{j}_i(\mathbf{r}') \right]. \end{aligned} \tag{8}$$

Finally, the integral equations are approximated by matrix equations (7) using the method of moments (MOM). The specially designed basis functions for subdomains which contain surface curvature are the generalized "rooftop" basis functions with a constant charge density and without line charge accumulation on the surfaces [7].

3. The Fast Multipole Method (FMM)

Letting $\mathbf{r}_j$ and $\mathbf{r}_i$ be the field point and source point, respectively, we have

$$\mathbf{r}_{ji} = \mathbf{r}_j - \mathbf{r}_i = \mathbf{r}_j - \mathbf{r}_m + \mathbf{r}_m - \mathbf{r}_{m'} + \mathbf{r}_{m'} - \mathbf{r}_i = \mathbf{r}_{jm} + \mathbf{r}_{mm'} - \mathbf{r}_{im'}. \tag{9}$$

Thus, using the addition theorem [2,8] the scalar Green's function can be rewritten as

$$\frac{e^{ikr_{ji}}}{r_{ji}} = \frac{ik}{4\pi} \int d^2\hat{k} e^{i\mathbf{k}\cdot(\mathbf{r}_{jm}-\mathbf{r}_{im'})} \alpha_{mm'}(\hat{r}_{mm'} \cdot \hat{k}), \tag{10}$$

where

$$\alpha_{mm'}(\hat{r}_{mm'} \cdot \hat{k}) = \sum_{l=0}^{L} i^l (2l+1) h_l^{(1)}(kr_{mm'}) P_l(\hat{r}_{mm'} \cdot \hat{k}). \tag{11}$$

We have truncated the infinite summation in (11). The integration $\int d^2\hat{k}$ in (10) represents the integrals over the unit sphere, and will be evaluated by Gaussian quadratures with $K = 2L^2$ points. Substituting the scalar Green's function (10) into the dyadic function (2) leads to

$$\overline{\mathbf{G}}(\mathbf{r}_j, \mathbf{r}_i) = \frac{ik}{4\pi} \int d^2\hat{k} (\overline{\mathbf{I}} - \hat{k}\hat{k}) e^{i\mathbf{k}\cdot(\mathbf{r}_{jm}-\mathbf{r}_{im'})} \alpha_{mm'}(\hat{r}_{mm'} \cdot \hat{k}). \tag{12}$$

Substituting Equations (10) and (12) into (8), we get a formula to calculate the matrix elements in non-nearby group pairs,

$$A_{ji} = \frac{ik}{4\pi} \int d^2\hat{k} \mathbf{V}_{fmj}(\hat{k}) \cdot \alpha_{mm'}(\hat{k} \cdot \hat{r}_{mm'}) \mathbf{V}^*_{sm'i}(\hat{k}), \tag{13}$$

where

$$\mathbf{V}_{fmj}(\hat{k}) = \alpha \int_S dS e^{i\mathbf{k}\cdot\mathbf{r}_{jm}} (\overline{\mathbf{I}} - \hat{k}\hat{k}) \cdot \mathbf{t}_j(\mathbf{r}_{jm}) - (1-\alpha)\hat{k} \times \int_S dS e^{i\mathbf{k}\cdot\mathbf{r}_{jm}} \mathbf{t}_j(\mathbf{r}_{jm}) \times \hat{n}, \tag{14}$$

$$\mathbf{V}_{sm'i}(\hat{k}) = \int_S dS e^{i\mathbf{k}\cdot\mathbf{r}_{im'}} (\overline{\mathbf{I}} - \hat{k}\hat{k}) \cdot \mathbf{j}_i(\mathbf{r}_{im'}). \tag{15}$$

When we use CG method to solve the matrix equations (7), matrix-vector multiply is needed to be computed in each iteration. Then, we can write the matrix-vector multiplication as

$$\sum_{i=1}^{N} A_{ji} a_i = \sum_{m' \in B_m} \sum_{i \in G_{m'}} A_{ji} a_i + \frac{ik}{4\pi} \int d^2\hat{k} \mathbf{V}_{fmj}(\hat{k}) \cdot \sum_{m' \notin B_m} \alpha_{mm'}(\hat{k} \cdot \hat{r}_{mm}) \sum_{i \in G_{m'}} \mathbf{V}^*_{sm'i}(\hat{k}) a_i. \tag{16}$$

The first term in (16) is the contribution from nearby groups (including the self-group), and the second term is the far interaction calculated by FMM. The FMM idea is first to divide the subscatterers into groups. Then, addition theorem is used to translate the scattered field of different scattering centers within a group into a single center. Hence, the number of scattering centers is reduced. Similarly, for each group, the field scattered by all the other group centers can be first "received" by the group center, and then "redistributed" to the subscatterers belonging to the group. It is proven that the computation cost using (16) with 2-level FMM is in order $O(N^{1.5})$ [6].

To implement a multilevel fast multipole algorithm (MLFMA), the entire object is first enclosed into a large cube, which is partitioned into eight smaller cubes. Each subcube is then recursively subdivided into smaller cubes until the edge length of the finest cube is about half of a wavelength. Cubes at all levels are indexed. At the finest level, we find which cube each basis function reside in by comparing the coordinates of the center of the basis function with the center of cube . We further find nonempty cubes by sorting. Only nonempty cubes are recorded using tree-structured data at all levels [9]. Thus, the computational cost depends on only the nonempty cubes, not all cubes.

The basic algorithm for matrix-vector multiply is broken down into two sweeps [10]: the first sweep consists of constructing outer multipole expansions for each nonempty cube at all levels. The second consists of constructing local multipole expansions contributed from the well-separated cubes at all levels. When the cube becomes larger from the finest level to the coarsest level, the numbers of multipole expansions should increase. In the first sweep, the outer multipole expansions are computed at the finest level, then the expansions for larger cube are obtained using shifting and interpolation. Let $\mathbf{r}_{m_l'}$ and $\mathbf{r}_{m_{l-1}'}$ be the cube centers at level l and $l-1$, respectively, then the outer multipole expansions for coarser level should be

$$\mathbf{V}_{sm_{l-1}'i}(\hat{k}) = e^{i\mathbf{k}\cdot\mathbf{r}_{m_l'm_{l-1}'}}\mathbf{V}_{sm_l'i}(\hat{k}). \tag{17}$$

But $\mathbf{V}_{sm_l'i}(\hat{k})$ has only K_l values, we need K_{l-1} values of $\mathbf{V}_{sm_{l-1}'i}(\hat{k})$. Then we will interpolate $\mathbf{V}_{sm_{l-1}'i}(\hat{k})$ to K_{l-1} values first, then

$$\mathbf{V}_{sm_{l-1}'i}(\hat{k}_{(l-1)n'}) = e^{i\mathbf{k}_{(l-1)n'}\cdot\mathbf{r}_{m_l'm_{l-1}'}}\sum_{n=1}^{K_l} W_{n'n}\mathbf{V}_{sm_l'i}(\hat{k}_{ln}), \tag{18}$$

where interpolation matrix W is a sparse matrix.

At the coarsest level, the local multipole expansions contributed from well-separated cubes are calculated using the second part of (16). At the second sweep, the local expansions for smaller cubes include the contributions from parent cube using shifting and anterpolation [11], and from the well-separated cube at this level but not well-separated at the parent level. If the local multipole expansions received by the cube center al level $l-1$ is $\mathbf{B}(\hat{k})$, then the contribution from all well-separated cubes can be written as

$$I = \int d^2\hat{k}\mathbf{V}_{fm_{l-1}j}(\hat{k})\cdot\mathbf{B}(\hat{k}) = \sum_{n'=1}^{K_{l-1}} w_{n'}\mathbf{V}_{fm_{l-1}j}(\hat{k}_{(l-1)n'})\cdot\mathbf{B}(\hat{k}_{(l-1)n'}), \tag{19}$$

where $w_{n'}$ is the weighting function. Substituting the interpolation expression for $\mathbf{V}_{fm_{l-1}j}(\hat{k}_{(l-1)n'})$ into (19), and changing the order of two summations lead to

$$I = \sum_{n=1}^{K_l} w_n\mathbf{V}_{fm_lj}(\hat{k}_{ln})\cdot\sum_{n'=1}^{K_{l-1}} W_{n'n}\mathbf{B}(\hat{k}_{(l-1)n'})e^{i\mathbf{k}_{(l-1)n'}\cdot\mathbf{r}_{m_l'm_{l-1}'}}w_{n'}/w_n. \tag{20}$$

The above operation is called anterpolation [11]. At the finest level, the contributions from non-well-separated cube are calculated directly. Since only nonempty cubes are considered, the complexity for MLFMA is further reduced to $O(N\log N)$.

4. Results and Conclusions

In Figure 1, we plot the normalized residual norm in CG method as functions of the number of iterations for EFIE, MFIE, and CFIE. It is found that CFIE converges much faster than EFIE and MFIE. EFIE and MFIE may not converge or converge too slowly at specific frequencies corresponding to the eigenvalues of the interior resonator problem, and give a wrong solution. This phenomenon is called the internal resonance corruption, because the tangential components of a single incident field (either the electric or magnetic field) at the scatterer surface lack sufficient information to uniquely determine the desired surface currents at a resonance frequency. It has been proven that the CFIE eliminates the effect of these resonances. At all frequencies, CFIE has an unique solution, and converges faster than EFIE and MFIE if the matrices are solved by an iteration method since the matrix for CFIE has smaller condition number than those for EFIE and MFIE.

Figure 2 shows the comparison of the CPU time versus the number of unknowns for the solution of CFIE with the FMM, standard CG, and LU decomposition for calculating the bistatic RCS of a conducting sphere. It is seen that the FMM outperforms the standard CG in terms of matrix filling and matrix solving. The FMM also requires less memory, and hence, can solve a larger problem on a small computer. The simulation is performed on a SUN-SPARC-2 with 64 MB of RAM. The final residual norm in CG method is less than 10^{-4}.

Figure 3 shows the validation of the numerical result from combined field integral equation (CFIE) with FMM against the Mie series solution of the bistatic RCS of a metallic sphere of radius 1m at frequency of 0.72GHz for the parallel polarization. 9,408 unknowns with 2-level FMM are used. The solutions of CFIE with FMM agree with Mie series very well.

Figure 4 shows the RCS of a one-meter long NASA almond at 2.5 GHz in the xy plane with $\theta = 90°$. Five unknowns are used per wavelength. The calculation is done by using CFIE with LU decomposition on a SUN-SPARC-10 with 128 MB RAM, and it consumes about 24 hr of CPU time. Some points computed using CFIE with 2-level FMM are shown. These points took 0.5 hr/point to compute, and much less than 3 hr/point to compute with EFIE using FMM. The numerical results are compared with experimental measurement from Ohio State University [12]. There is a good agreement between our results and the measurement.

Figure 5 shows the bistatic RCS of a one-meter long metallic square plate at 4.5GHz in the xy plane with incident angle $\theta = 45°$. 32,512 unknowns with 6-level FMM are used. It is done by solving EFIE on a SUN-SPARC-2 with 64MB RAM. The agreement between our results and the approximation by physical optics is good when the RCS is bigger than 0 dB.

In conclusion, the fast multipole method (FMM) has been implemented to speed up the matrix-vector multiply when CG method is used to solve EFIE, MFIE, and CFIE. At all frequencies, CFIE has an unique solution, and converges faster than EFIE and MFIE. FMM approach reduces the complexity of a matrix-vector multiply from $O(N^2)$ to $O(N^{1.5})$. With a multilevel fast multipole algorithm (MLFMA), the complexity is reduced to $O(N\log N)$. The FMM also requires less memory, and hence, can solve a larger problem on a small computer.

REFERENCES

[1] V. Rokhlin, "Rapid Solution of Integral Equations of Scattering Theory in Two Dimensions," *J. Comput. Phys*, vol. 86, no. 2, pp. 414-439, February 1990.

[2] R. Coifman, V. Rokhlin, and S. Wandzura, "The fast Multipole Method for the Wave Equation: A Pedestrian Prescription," *IEEE Antennas Propagat. Mag.*, vol. 35, no. 3, pp. 7-12, June 1993.

[3] C.C. Lu and W.C. Chew, "A Fast Algorithm for Solving Hybrid Integral Equation," *IEE Proceedings-H*, vol.140, no.6, pp.455-460, December 1993.
[4] B. Dembart and E. Yip, "A 3D Moment Method Code Based on Fast Multipole," *Digest of the 1994 URSI Radio Science Meeting*, p. 23, Seattle, Washington, June 1994.
[5] R.L. Wagner and W.C. Chew, "A Ray-Propagation Fast Multipole Algorithm," *Micro. Opt. Tech. Lett.*, vol.7, no.10, pp.435-438, July 1994.
[6] J.M. Song and W.C. Chew, "Fast Multipole Method Solution Using Parametric Geometry," *Micro. Opt. Tech. Lett.*, vol.7, no. 16, pp.760-765, November 1994.
[7] J.M. Song and W.C. Chew, "Moment Method Solution Using Parametric Geometry," *J. of Electromagnetic Waves and Appl.*, to be published.
[8] M. Abromowitz and I.A. Stegun, *Handbook of Mathematical Functions*, Dover Publication, New York, 1972.
[9] J. Barnes and P. Hut, "A Hierarchical $O(NlogN)$ Force-calculated Algorithm," *Nature*, Vol. 324, pp. 446-449, December 4, 1986.
[10] C. R. Anderson, "An Implementation of the Fast Multipole Method without Multipole," *SIAM J. Sci. Stat. Comput.*, Vol. 13, No. 4, pp. 923-947, July 1992.
[11] A. Brandt, "Multilevel Computations of Integral Transforms and Particle Interactions with Oscillatory Kernels," *Comput. Phys. Commun.*, Vol. 65, pp. 24-38, 1991.
[12] M.I. Sancer, R.L. McClary, and K.J. Glover, "Electromagnetic Computation Using Parametric Geometry," *Electromagnetics*, vol. 10, no. 1-2, pp. 85-103, 1990.

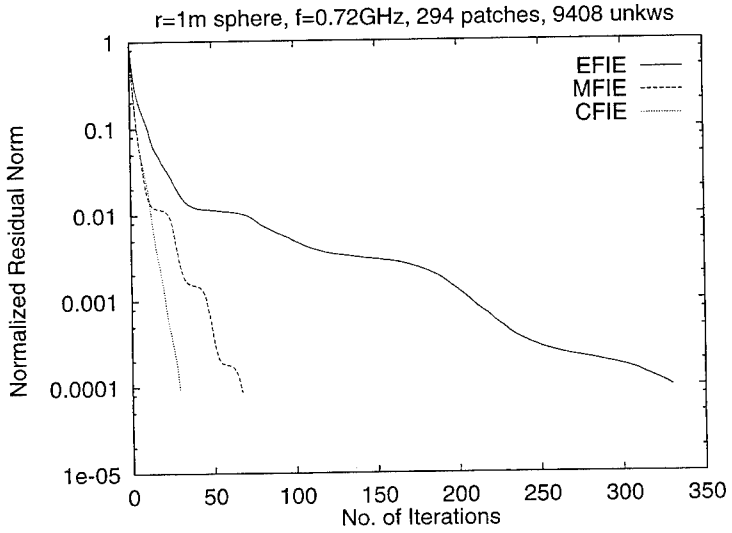


Figure 1. Comparison of the convergence of solutions of EFIE, MFIE, and CFIE for a conducting sphere of radius 1 m at 0.72 GHz for parallel polarization (9,048 unknowns, 7.2 unknowns per wavelength).

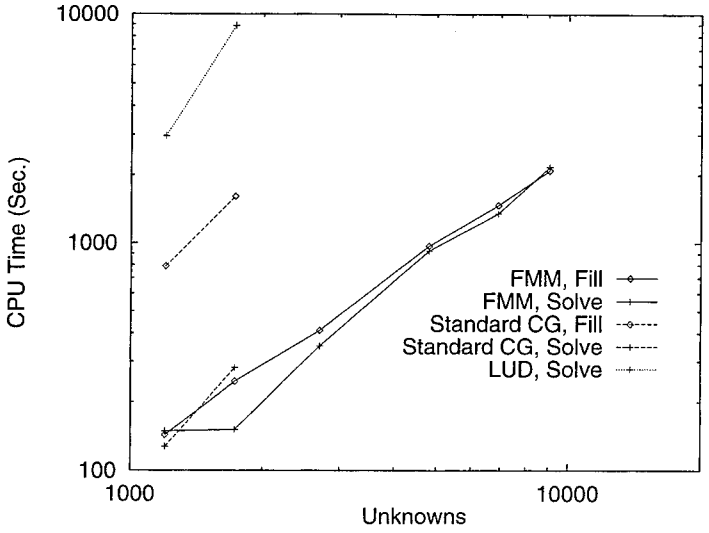


Figure 2. Comparison of the CPU time versus the number of unknowns for FMM, standard CG and LU decomposition for a metallic sphere.

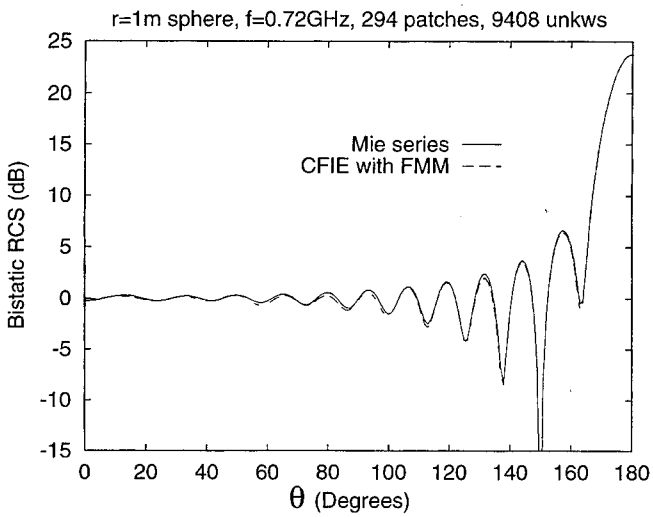


Figure 3. Validations of CFIE with FMM against the Mie series of the bistatic RCS of a metallic sphere of radius 1m at 0.72GHz for VV polarization. The RCS is normalized by πa^2.

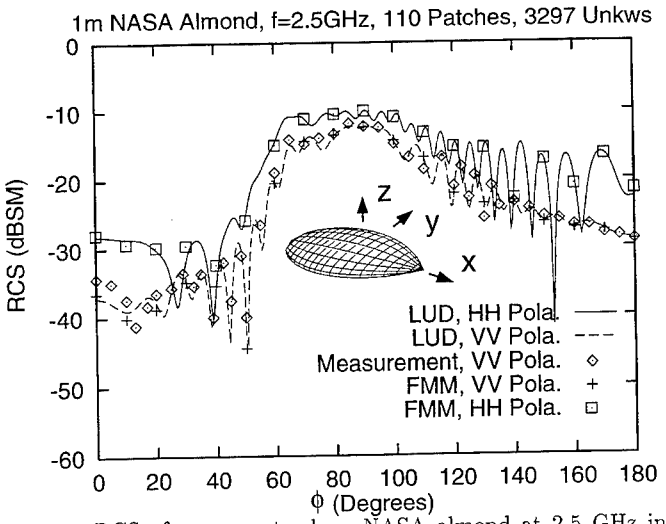


Figure 4. RCS of a one-meter long NASA almond at 2.5 GHz in the xy plane with $\theta = 90°$. Five unknowns are used per wavelength. The results are computed with LU decomposition, and partially with FMM. The experimental measurement by Ohio State University [12] is also given for comparison.

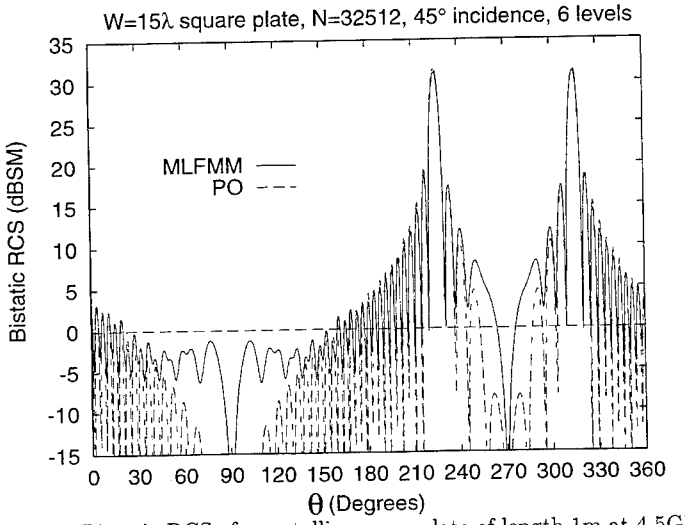


Figure 5. Bistatic RCS of a metallic square plate of length 1m at 4.5GHz for VV polarization with 45° incident angle.

AUTHOR INDEX

VI = Volume I
VII = Volume II

Abe, N.M. VI-66
Ahuja, V. VI-513
Albanese, R. VI-350
Ali, A.S. VII-1000, 1040
Ames, B. VI-127
Anastassiu, H.T. VII-1142
Andersh, D.J. VII-1111, 1134, 1142
Antilla, G.E. VII-1193
Ariguel, S. VII-672
Arkadan, A.A. VI-394
Aubert, H. VII-672
Aubrey, T.A. VII-873
Azu, C. VI-403
Baca, E.A. VI-418
Bagby, J.S. VI-216
Baginski, M.E. VI-8
Bai, L. VI-302
Bajon, D. VII-672
Balakrishnan, N. VII-680
Barrios, A. VII-784
Baudrand, H. VII-672
Beggs, J.H. VI-418
Belcher, W.R. VII-873
Bhalla, R. VII-1118
Blakely, B. VII-710
Blocher, T. VI-29, 294, 418
Boag, M. VI-614
Boyer, D.B. VII-824
Brauer, J. VII-1054
Breakall, J.K. VII-1025, 1033
Breed, G.A. VII-1017
Brodskyn, H.O. VI-66
Burkholder, R.J. VII-1126, 1134
Cangellaris, A.C. VI-498, VII-1280
Car, D.D. VII-848
Cardoso, J.R. VI-66
Cha, C.C. VII-695, 702
Chang, H.S. VII-962
Chaudhuri, S.K. VII-937
Chamberlin, K. VII-790
Chatterjee, A. VII-1212
Chen, J.S. VI 453, VII-1266
Cheng, G. VII-702
Cheng, Y.B. VI-378
Cheng, Z. VI-75
Cheung, P. VII-951
Chew, W.C. VI-482, 576, 629
Chou, H.T. VII-1134
Christensen, M.C. VII-1111
Christopher, S. VII-664, 680
Chu, S.T. VII-937
Colby, P.C. VI-164
Cook, G. VII-847
Corrington, L. VII-801
Cosnuau, A. VII-856
Crow, J.A. VI-45
Cugini, J.V. VI-143
Cummings, K.E. VII-724
Dai, J.F. VI-302
D'Angelo, J. VII-1163
David, R.S. VII-889
De La Bourdonnaye, A. VII-856
De Medeiros, L.H.A. VII-1094
Dembert, B. VI-621
Dimbylow, P.J. VI-240
Du, J.Y. VII-993
Dunn, D.B. VII-898
Duval, S.E. VII-1000
Dyck, D.N. VI-358
Elsherbeni, A.Z. VI-260, 542
Eme, B. VII-847
Engquist, B. VI-172
Erdley, T.A. VII-1025
Eremin, Y. V. VI-6, VII-925
Eswarappa, C. VI-13
Evans, J.A. VI-126
Fang, J. VI-504
Fast, S.A. VII-798
Fatemi, E. VI-172
Fath, J. VII-1134
Feliziani, M. VI-334
Ferraro, A.J. VII-970
Ferrières, X. VII-856
Fijany, A. VI-592
Fox, G.C. VII-702
Fresa, R. VI-350
Fröhlich, J. VI-584
Gao, S. VI-75
Gao, Y. VII-687
Gedera, M.B. VII-1194
Gerace, G.C. VI-49, VII-898, 904
Giarolla, M.H. VI-66
Girdinio, P. VII-1047
Gnos, M. VI-81
Goggans, P.M. VI-542
Golsberry, T.G. VII-979
Goorjian, P.M. VI-472
Gopinath, A. VII-951
Gordon, R.K. VI-559
Gothard, G.K. VI-189
Gribbons, M. VI-498
Hadi, M.F. VII-767
Hafner, Ch. VI-584
Hall, W.F. VII-839, 1185
Hamandi, L. VII-864
Hamilton, L.R. VI-606, VII-1177
Hantman, B. VI-118, 135
Hart, D. VII-1280
Haupt, R.L. VI-211, VII-1000
Henderson, L.W. VI-245
Hicks, R.G. VI-155
Hill, K.C. VII-1220
Hoefer, W.J.R. VI-13
Holland, R. VI-308
Holloway, C.L. VII-1040
Houshmand, B. VII-718
Hu, Q VI-75
Huffman, J.A. VII-1009
Ivakhnenko, V.I. VI-181, VII-929
Itoh, T. VII-718
Jackson, R. VI-118
Jarriel, Jr. G.W. VI-8
Jensen, M.A. VI-592, VII-732
Johansson, N.M. VII-1085
Johnson, L. VII-710
Joseph, R.A. VI-151
Joseph, R.M. VI-476
Judkins, J.B. VII-957
Jurgens, D.E. VI-276, VII-710
Kanai, Y. VI-342
Karty, J.L. VII-1103
Kashiwa, T. VI-342
Katehi, L.P.B. VI-568
Katz, D.S. VI-476
Kelley, D.F. VI-526
Kesler, O.B. VI-21
Kienberger, T.L. VI-276
Kim, J.J. VI-21
King, A.S. VII-872
Kingsland, D.M. VI-490
Kluskens, M. VII-910
Kochlar, R. VII-710
Kopylov, Y.V. VI-234
Koschmieder, T.H. VII-798
Kost, A. VI-58
Kotulski, J.D. VII-848
Kragalott, M. VII-910
Krauss, T. VII-695
Kukk, A.V. VII-929
Kunz, K.S. VI-425, 431
Kuo, C.N. VII-718
Labelle, J. VI-118, 135
Langdon, H.S. VI-465
Larsson, J.A. VI-286
Latini, E. VI-334
Leca, P. VII-856
Lee, J.F. VI-490, VII-1054, 1258
Lee, R. VII-864
Lee, S.K. VI-498
Lee, S.W. VII-1111
Lemak, C. VII-801
Leuchtmann, P. VI-81
Ling, H. VII-1118
Lippincott, W. VII-910
Liu, J. VII-687
Liu, Z. VI-75
Liu, Z.M. VII-873
Lizalek, G. VII-1054
Ljung, S. VI-286
Logan, J. VI-410
Long, L.N. VI-513
Lowther, D.A. VI-358

Lu, C.C. VI-576
Luebbers, R.J. VI-445, 465, 526
Ma, Y.C. VII-1193
Madsen, N. VII-847
Mallasch, P. VI-551
Maloney, J.G. VI-430, VII-724
Manella, A. VII-1047
Maradei, F. VI-334
Marhefka, R.J. VI-245
Marlone, R. VI-350
Matekovits, L VI-600
McCowen, A. VI-2, 229
McGee, J. VI-403
McKaughan, M.E. VI-224
Medgyesi-Mitschang, L.N. VII-1194
Metker, S.E. VII-1009
Meyers, J.P. VI-49
Miano, G. VII-753
Michielssen, E. VI-614
Miller, E.K. VII-1151, 1202
Miyakawa, M. VI-342
Miyazaki, Y. VII-1062
Mohammadian, A. VII-839
Mohammed, O.A. VI-386, VII-1228
Mohan, A.S. VII-873
Molinari, G. VII-1047
Mooney, J.E. VI-98
Mortensen, G.E. VII-702
Mrozowski, M. VI-534
Murphy, R.K. VI-109
Neto, A.G. VII-672
Nicolas, A. VII-1070
Nicolas, L. VII-1070
Norgard, J. VI-29
Nutter, B. VI-224
Okoniewski, M. VI-534, VII-762
Orefice, M. VI-600
Orlov, N. V. VI-6, VII-925
Osher, S. VI-172
Ottusch, J.J. VI-606, VII-1177
Özgüner, F. VII-864
Packer, M.J. VI-252
Palaniswamy, S. VII-1185
Pan, G.W. VII-993
Park, C. VI-321
Pascher, W.W. VII-943
Passaro, A. VI-66
Pathak, P.H. VII-1134
Paulus, R.A. VII-809
Pearlman, R. VII-1194
Penney, C.W. VI-445
Perez, R. VI-323
Pesta, A. VI-29, 294
Peterson, A.F. VII-1077
Pflug, D.R. VI-268
Piket-May, M. VII-767
Pirinoli, P. VI-600
Popov, A.V. VI-195
Prakash, V.V.S. VII-680
Prather, W.D. VI-202
Pregla, R. VII-943
Prodan, J.V. VII-1266
Putnam, J.M. VII-848, 1194
Rahmat-Samii, Y. VI-592, VII-732
Raizer, A. VII-1094
Ramanujam, P. VI-321
Randall, W.M. VI-224
Rappaport, C.M. VII-898
Rao, S.M. VI-189
Reiß, K. VI 29, 37
Reuter, C.E. VI-476
Riggs, L. VI-8, 98
Riley, D.J. VI-435
Rockway, J. VI-410
Roedder, J.M. VII-1103
Rong, R. VI-358
Ross, D.C. VII-1142
Roux, F.X. VII-856
Rowell, C. VII-839
Rozenberg, V. VI-6
Rubinacci, G. VI-350
Russell, L. VI-410
Russenschuck, S. VI-366
Ryan, F.J. VII-816, 824
Sabbagh, H.A. VI-109, 135
Sabetfakhri, K. VI-568
Sacks, Z.S. VI-490
Saitoh, Y. VI-342
Sanford, J.R. VII-1085
Schinke, M. VI-29, 37
Schuster, J.W. VI-445
Schwartz, D. VI-410
Sega, R. VI-29
Seifert, M. VI-29, 294
Serpico, C. VII-753
Sezginer, A. VI-482
Shang, J.J.S. VII-1220
Shankar, V. VII-839, 1185
Shapiro, J.J. VII-1025
Sheikh, Q.M. VI-45
Shen, J. VI-58
Shen, X. VII-702
Shimizu, D.T. VII-762
Shirley, B.L. VI-430
Siarkiewicz, K. VI-118, 155
Sibul, L.H. VII-987
Silberberg, Y. VI-472
Singer, H. VII-881
Singh, A.K. VII-664, 680
Smith, C.E. VI-260
Song, J.M. VI-629
Souza, J.R. VII-648
Soyka, M. VI-403
Speciale, R.A. VII-639, 656
Stalzer, M.A. VI-606, VII-1177
Steich, D. VII-847
St. John, R. VI-308
Stuchly, M.A. VI-534, VII-762
Stuchly, S.S. VI-534
Subramaniam-Sivanesan, S. VI-394
Sykulski, J.K. VI-378
Taflove, A. VI-476, VII-775
Tam, D. VI-403
Tanaka, K. VII-1062
Taylor, Jr., C.D. VI-260
Terzuoli, Jr., A.J. VI-49, VII-898, 904
Thiele, E.T. VI-476
Toyama, K. VI-342
Treece, J.C. VI-109
Tripathi, V. VII-962
Tsitsopoulos, A.P. VI-252
Tsukamoto, T. VI-342
Tudziers, C. VII-881
Turley, R.S. VI-606, VII-1177
Turner, C.D. VI-435
Tyrtyshnikov, E.E. VI-181, VII-929
Üler, G.F. VI-386, VII-1228
Vann, L.D. VI-216
Vecchi, G. VI-600
Veliz, R.O. VII-648
Verolino, L. VII-753
Villone, F. VII-753
Visher, J.L. VI-606, VII-1177
Volakis, J.L. VII-1142, 1212
Wahlgren, B. VI-286
Wallace, C.B. VI-202
Wandzura, S.M. VI-606, VII-1170, VII-1177
Warren, D.E. VI-268
Wang, D.S. VII-1194
Wang, J. VII-687
Weedon, W.H. VI-482
Weisshaar, A. VII-962
Welch, C. VII-801
Werner, D.H. VII-964, 970, 1009
Werner, P.L. VII-970
Wheless, C.S. VI-89
Wheless, Jr., W.P. VI-89, 202
Whitcomb, C. VI-127
Wilkes, D.L. VII-695
Wille, L.T. VII-889
Wilton, D.R. VII-1077
Wolstenholme, D.J. VII-904
Woo, L.W. VI-109, 135
Wu, M. VI-75
Wu, Z. VI-504
Yao-bi, J.L. VII-1070
Ye, C. VI-75
Yee, K.S. VI-453, VII-1241, 1266
Yeremin, A.Y. VII-929
Yip, E. VI-621, 710
Young, J.S. VII-1025, 1033
Young, R.K. VII-979, 987
Zamarashkin, N.L. VII-926
Zolotarev, I.P. VII-830
Zimmerman, M. VI-551
Zielkowski, R.W. VII-748, 957
Zook, B.J. VII-740